

Journal of

Geophysics

Zeitschrift für

Geophysik

Volume 44 1977/1978

Managing Editors: W. Dieminger, J. Untiedt

Editorial Board

Professor K.M. Creer, University of Edinburgh, Department of Geophysics,
James Clerk Maxwell Building, King's Buildings, Mayfield Road, Edinburgh EH9 3JZ, Scotland

Professor W. Dieminger, Max-Planck-Institut für Aeronomie,
D-3411 Lindau ü. Northem/Hann., Federal Republic of Germany

Professor K. Fuchs, Geophysikalisches Institut der TU,
Hertzstraße 10, Bau 42, D-7500 Karlsruhe, Federal Republic of Germany

Professor C. Kisslinger, Director, Cooperative Institute for Research in Environmental Sciences,
University of Colorado, Boulder, CO 80302, USA

Professor Th. Krey, Prakla-Seismos GmbH,
Postfach 47 67, D-3000 Hannover 1, Federal Republic of Germany

Dr. G.C. Reid, Deputy Director, Aeronomy Laboratory, National Oceanographic and Atmospheric Administration,
Boulder, CO 80302, USA

Professor J. Untiedt, Institut für Geophysik der Westfälischen Wilhelms-Universität,
Gievenbecker Weg 61, D-4400 Münster/Westf., Federal Republic of Germany

Professor S. Uyeda, Earthquake Research Institute, University of Tokyo,
Tokyo 113, Japan

Advisory Board

G. Angenheister, München A.A. Ashour, Cairo W.I. Axford, Lindau/Harz J. Behrens, Berlin
H. Berckhemer, Frankfurt a.M. V. Bucha, Praha J. Cain, Greenbelt, MD N. Fukushima, Tokyo
B. Haurwitz, Fort Collins, CO I.P. Kosminskaja, Moskwa W. Krauss, Kiel St. Müller, Zürich
A. Roche, Strasbourg O. Rosenbach, Clausthal-Zellerfeld S. Saxov, Aarhus U. Schmucker, Göttingen
H. Soffel, München L. Stegena, Budapest H. Stiller, Potsdam



Springer International

With the acceptance of the manuscript for publication the exclusive copyright for all languages and countries, including the right for photomechanical and any other reproduction, also in microform, is transferred to the Deutsche Geophysikalische Gesellschaft, Hamburg.

The use of registered names, trademarks, etc. in this publication does not imply, even in the absence of a specific statement, that such names are exempt from the relevant protective laws and regulations and therefore free for general use.

Printed in Germany by Univ.-Druckerei H. Stürtz AG, Würzburg

© by the Deutsche Geophysikalische Gesellschaft, Hamburg, 1977/1978



Author Index

- Ahorner, L. 481
Amann, V. 165
Arnold, F. 125
- Bäte, J. 147
Bamford, D. 219
Bangert, W. 165
Baumjohann, W. 373
Becker, M. 147
Beran, D. 155
Berg, A.P., van den 499
Bhimasankaram, V.L.S. 353
Boldt, B. 557
Boldyrev, S.A. 283
Bonjer, K.-P. 203
Borchers, R. 179
Bourmin, V.Yu. 283
Bradenstein, H.J. 81
- Channell, J.E.T. 613
Cloetingh, S.A.P.L. 499
- Doornbos, D.J. 499
Drescher, A. 173
Dürschner, H. 281
- Elling, W. 27
Enescu, D. 203
Eshghi, I. 663
- Franke, A. 639
Friedrich, M. 91
Friedrich, V.H. 139
Frisch, W. 623
Fuchs, K. 567
- Gidskehaug, A. 317
Grandal, B. 99
Greenwald, R.A. 373
Gutdeutsch, R. 639
- Hagen, O. 99
Hahn, A. 189
Hanuš, V. 473
Harjes, H.-P. 511
Heller, F. 341, 525
Henriksen, K. 401
- Holback, B. 401
Hussain, A.G. 333
- Jacobs, J.A. 675
Jeremic, M.L. 651
Joos, W. 125
- Kent, D.V. 297
Killeen, T.L. 47
Kind, R. 603
Kingsley, S.P. 39
Kohnen, H. 545
Krankowsky, D. 125
Küppers, F. 373
- Langlie, Aa. 317
Lauche, H. 35
Leppin, M. 557
Leydecker, G. 277
Loidl, A. 107, 117
Lowrie, W. 297
- Marien, K.H. 125
Maurer, H. 415
Mauritsch, H.J. 623
McKenzie, D. 441
Meyer, J. 427
Mironova, V.I. 283
Mooney, W.D. 573
Mostaanpour, M.M. 663
Müller, G. 203
Muller, H.G. 39
Murthy, I.V.R. 257
Murty, B.V.S. 353
Musmann, G. 357
- Nergård, A. 317
Niederlöhner, U. 147
- Offermann, D. 1, 139
Ott, W. 81
- Papanikas, D.G. 147
Prodehl, C. 573
- Rao, B.S.R. 257
Rao, D.B. 257
- Rao, S.M.V. 353
Rees, D. 47, 57
Richter, F. 441
Rietsch, E. 273
Röttger, J. 393
Rose, G. 15, 65, 179
Rosenhauer, W. 481
Rounce, P. 47
- Sarma, S.B.S.S. 385
Schmedes, E. 277
Schult, A. 333
Schwentek, H. 27, 107, 117
Scriba, H. 341
Sebulke, J. 245
Seiberl, W. 639
Seidl, D. 511
Seiler, E. 357
Sharma, M.C. 385
Sobouti, M. 663
Soffel, H.C. 333
Spenner, K. 81
Steinhauser, P. 395, 639
Stöckl, H. 203
Storetvedt, K.M. 317
Suckfüll, E. 155
Svalestad, S. 317
- Theile, B. 415
Thomassen, K. 317
Thrane, E.V. 99
Torge, W. 679
Torkar, K. 91
Trinks, H. 139
- Ugletveit, F. 99
Ulrich, S. 91
- Vaněk, J. 473
Vetter, U.R. 231
- Westkämper, H. 545
Widdel, H.U. 15, 65, 179
Wilhelm, H. 435
Witt, G. 401
- Zahn, U., von 139
Zverev, S.M. 283

Subject Index

Airglow

- Observations of the Oxygen Green Line Airglow During the Winter Anomaly Campaign 1975/76 (Lauche, H.) 35
- Measurement of the $O_2(^1\Delta_g)$ Height Profile During a Winter Anomaly Event (Bangert, W., Amann, V.) 165
- A Two Channel Rocket Photometer for 5577Å OI Nightglow Measurements (Drescher, A.) 173

Asthenosphere

- Stress and Viscosity in the Asthenosphere (Vetter, U.R.) 231

Aurora

- Variations in the Auroral Spectrum at the Latitude of the Polar Cleft (Henriksen, K., et al.) 401

Auroral Electrojets

- Joint Magnetometer Array and Radar Backscatter Observations of Auroral Currents in Northern Scandinavia (Baumjohann, W., et al.) 373
- Parameters of the Auroral Electrojet From Magnetic Variations Along a Meridian (Maurer, H., Theile, B.) 415

Crustal Structure

- Crustal Structure of the Rhenish Massif and Adjacent Areas; a Reinterpretation of Existing Seismic-Refraction Data (Mooney, W.D., Prodehl, C.) 573

Earthquake Risk

- Seismic Risk Evaluation for the Upper Rhine Graben and Its Vicinity (Ahorner, L., Rosenhauer, W.) 481

Earthquakes

- The Romanian Earthquake of March 4, 1977. I. Rupture Process Inferred From Fault-Plane Solution and Multiple-Event Analysis (Müller, G., et al.) 203
- Macroseismic Intensity Map of the Federal Republic of Germany for the Friuli Earthquake of May 6, 1976 (Schmedes, E., Leydecker, G.) 277
- Shamil-Siahou Earthquake "North-East of Bandar-Abbas" of 21st March, 1977 (Sobouti, M., et al.) 663

Earth's Core

- Anomalous P-Velocities in the Earth's Outer Core (Jacobs, J.A.) 675

Earth Tides

- Upper Mantle Structure and Global Earth Tides (Wilhelm, H.) 435

Electromagnetic Induction

- Modellversuche zur elektromagnetischen Induktion in langgestreckten Strukturen. Analogue Model Experiments for Electromagnetic Induction in Elongated Structures (Leppin, M., Boldt, B.) 557

Equatorial Electrojet

- Detection of Meridional Currents in the Equatorial Ionosphere (Musmann, G., Seiler, E.) 357

Explosion Seismology

- Interpretation of Wide-Angle Reflection Travel Times in Realistic Crust-Mantle Structures (Bamford, D.) 219
- Crustal Structure of the Rhenish Massif and Adjacent Areas; a Reinterpretation of Existing Seismic-Refraction Data (Mooney, W.D., Prodehl, C.) 573

Extreme Models

- Extreme Models From the Maximum Entropy Formulation of Inverse Problems (Rietsch, E.) 273

Geoelectrical Prospecting

- The Theoretical Investigation of Resistivity Methods for Geoelectrical Prospecting in Marine Areas (Sebulke, J.) 245

Geomagnetic Activity

- The Recurrence Tendency of Geomagnetic Activity During Solar Cycle 20 (Meyer, J.) 427

Gravimeters

- Scale Factor Determinations of a LaCoste and Romberg Gravimeter Model D (Steinhauser, P.) 395

Gravity Anomalies

- Zur Korrelation zwischen der Vertikalintensität des erdmagnetischen Feldes und dem Schwerefeld im ostalpinen Raum. Correlation Between Magnetic and Gravimetric Data in the East Alpine Area (Seiberl, W., et al.) 639

Iceland

- Weak Earthquakes in the Northern Part of the Rift Zone of Iceland (Zverev, S.M., et al.) 283

In Memoriam

- In Memoriam Ulrich Fleischer (Dürschner, H.) 281
 In Memoriam Alfred Schleusener (Torge, W.) 679

Ionosphere

- A Study of the D-Region Winter Anomaly in Western Europe, 1975/76 (Offermann, D.) 1
 D-Region Radio Wave Propagation Experiments, Their Significance and Results During the Western European Winter Anomaly Campaign 1975/76 (Rose, G., Widdel, H.U.) 15
 Behaviour of Ionospheric Absorption in Winter 1975/76 at about 52° N, 9° E (Schwentek, H., Elling, W.) 27
 Co-Ordinated Meteor Wind Observations From Sheffield During the January 1976 Winter Anomaly (Muller, H.G., Kingsley, S.P.) 39
 Plasma Measurements During the Western European Winter Anomaly Campaign (Spenner, K., et al.) 81
 A Rocket Borne Experiment to Measure Plasma Densities in the D-Region (Friedrich, M., et al.) 91
 Intensity of Solar X-rays in the E Region Measured by Proportional Counters Carried on Rockets (Loidl, A., Schwentek, H.) 117
 A Mass Spectrometer Probe for Composition and Structure Analysis of the Middle Atmosphere Plasma and Neutral Gas (Arnold, F., et al.) 125
 Payload B III—an Instrument Package for the Measurement of Conductivity, Concentration and Mobility of Positive and Negative Ions in the Mesosphere (Widdel, H.U., et al.) 179
 New Methods of Separating F Region Absorption From the Cosmic Radio Noise Absorption (Sarma, S.B.S.S., Sharma, M.C.) 385

Lower Mantle

- A Comparison of PKP Precursor Data From Several Seismic Arrays (Berg, A.P., van den, et al.) 499

Magnetic Anomalies

- Zur Korrelation zwischen der Vertikalintensität des erdmagnetischen Feldes und dem Schwerefeld im ostalpinen Raum. Correlation Between Magnetic and Gravimetric Data in the East Alpine Area (Seiberl, W., et al.) 639

Magnetic Interpretation

- Interpretation of Magnetic Anomalies With Fourier Transforms, Employing End Corrections (Rao, B.S.R., et al.) 257

Mesosphere

- Winter Anomaly – Trace Constituents Sounding Rocket Campaign (Daytime Neutral Wind Measurements in the Mesosphere and Lower Thermosphere (Rees, D., et al.) 47
 Payload BI: A Compact and Economic D-Region Experiment Package for Use on Small Sounding Rockets (Rose, G., Widdel, H.U.) 65
 Measurements of Lyman- α Extinction and Energetic Charged Particle Precipitation During the European Winter Anomaly Campaign 1975–76 (Thrane, E.V., et al.) 99
 Mesospheric Molecular Oxygen Density, Pressure and Temperature Profiles Obtained From Measurements of Solar H Lyman- α Radiation (Loidl, A., Schwentek, H.) 107
 A Mass Spectrometer Probe for Composition and Structure Analysis of the Middle Atmosphere Plasma and Neutral Gas (Arnold, F., et al.) 125
 Pitot Pressure Measurements for Atmospheric Density Determination Between 50 and 120 km (Western Europe Winter Anomaly Campaign, January 1976) (Bäte, J., et al.) 147
 Intensity Measurement of the (1,0) γ -Band of NO at 2150 Å With a Polarizing Nitric Oxide Photometer (Beran, D., Suckfüll, E.) 155

Microearthquakes

- Weak Earthquakes in the Northern Part of the Rift Zone of Iceland (Zverev, S.M., et al.) 283

Palaeomagnetism

- Magnetic Discordance in Gran Canaria/ Tenerife and Its Possible Relevance to the Formation of the NW. African Continental Margin (Storetvedt, K.M., et al.) 317
- Palaeomagnetism of Cretaceous Nubian Sandstone, Egypt (Schult, A., et al.) 333
- Palaeosecular Variation Studies of the Brunhes Epoch in the Volcanic Province of the East-Eifel, Germany (Kohnen, H., Westkämper, H.) 545
- Dual Magnetic Polarity Measured in a Single Bed of Cretaceous Pelagic Limestone From Sicily (Channell, J.E.T.) 613
- Palaeomagnetic Data From the Central Part of the Northern Calcareous Alps, Austria (Mauritsch, H.J., Frisch, W.) 623

Petrophysics

- Petro-Physical Properties (Density and Magnetic-Susceptibility) and Lithologic Composition of Some Dolerite Dykes of Andhra Pradesh, India (Rao, S.M.V., et al.) 353
- Some Aspects of Athabasca Oil Sand Behavior, Alberta, Canada (Jeremic, M.L.) 651

Plate Dynamics

- Simple Plate Models of Mantle Convection (Richter, F., McKenzie, D.) 441

Rock Magnetism

- Characteristics of VRM in Oceanic Basalts (Lowrie, W., Kent, D.V.) 297
- Measurements of Anisotropy of Magnetic Susceptibility Using Inductive Magnetometers (Scriba, H., Heller, F.) 341
- Rockmagnetic Studies of Upper Jurassic Limestones From Southern Germany (Heller, F.) 525

Seismic Arrays

- A Comparison of PKP Precursor Data From Several Seismic Arrays (Berg, A.P., van den, et al.) 499
- Digital Recording and Analysis of Broad-Band Seismic Data at the Graefenberg (GRF)-Array (Harjes, H.-P., Seidl, D.) 511

Subduction Zones

- Tonga-Lau System: Deep Collision of Subducted Lithospheric Plates (Hanuš, V., Vaněk, J.) 473

Theoretical Seismograms

- The Reflectivity Method for a Buried Source (Kind, R.) 603

Thermosphere

- Winter Anomaly – Trace Constituents Sounding Rocket Campaign (Daytime Neutral Wind Measurements in the Mesosphere and Lower Thermosphere (Rees, D., et al.) 47
- Winter Anomaly – Trace Constituents Sounding Rocket Campaign (A High Resolution Photometer for Observing Daytime Lithium Releases (Rees, D.) 57
- Payload BI: A Compact and Economic D-Region Experiment Package for Use on Small Sounding Rockets (Rose, G., Widdel, H.U.) 65
- The Cryo Mass Spectrometer in the Winter Anomaly Campaign (Friedrich, V.H., et al.) 139
- Pitot Pressure Measurements for Atmospheric Density Determination Between 50 and 120 km (Western Europe Winter Anomaly Campaign, January 1976) (Bäte, J., et al.) 147

Troposphere

- Evidence for Partial Reflection of VHF Radar Signals From the Troposphere (Röttger, J.) 393

Units

- Die Einheiten des internationalen Systems in der Geomagnetik. SI Units in the Field of Geomagnetism (Hahn, A.) 189

Upper Mantle

- Upper Mantle Structure and Global Earth Tides (Wilhelm, H.) 435
- Simple Plate Models of Mantle Convection (Richter, F., McKenzie, D.) 441

Book Reviews 397, 569*Presentation* 567

Copyright

It is a fundamental condition that submitted manuscripts have not been published and will not be simultaneously submitted or published elsewhere. By submitting a manuscript, the authors agree that the copyright for their article is transferred to the publisher if and when the article is accepted for publication. The copyright covers the exclusive rights to reproduce and distribute the article, including reprints, photographic reproductions, microform or any other reproductions of similar nature, and translations.

Photographic reproduction, microform, or any other reproduction of text, figures, or tables from this journal is prohibited without permission obtained from the publisher.

Special Regulations for the USA

The Article Fee Code on the first page of an article in this journal indicates the copyright owner's consent that in the USA copies may

be made for personal or internal use, provided the stated fee for copying beyond that permitted by Section 107 or 108 of the United States Copyright Law is paid through the Copyright Clearance Center, Inc.

If a code does not appear copies of the article may be made without charge, provided permission is obtained from the publisher.

The copyright owner's consent does not extend to copying for general distribution, for promotion, for creating new works, or for resale. Specific written permission must be obtained from the publisher for such copying.

The use of general descriptive names, trade names, trade marks, etc., in this publication, even if the former are not specifically identified, is not to be taken as a sign that such names are exempt from the relevant protective laws and regulations and may accordingly be used freely by anyone.

R.D. BALLARD, J.G. MOORE

Atlas of the Mid-Atlantic Ridge Rift Valley

With a preface by J.R. Heirtzler

196 figures. Approx. 130 pages. 1977

Cloth DM 43,30; US \$ 19.90

ISBN 3-540-90347-3

Prices are subject to change without notice

This atlas presents a unique view of the ocean floor at a diverging plate boundary. About 180 photographs are collected of fresh sea floor volcanic terrain in the rift valley of the Mid-Atlantic Ridge near 37 north latitude. They were selected from more than 15,000 taken mostly from the submersible ALVIN at depths of about 2,600 meters during the French-American Mid-Ocean Undersea Study (Project FAMOUS). A morphologic classification of volcanic features including types of pillow faults and fissures is developed and illustrated with sketches and diagrams in

addition to the underwater photos. This book provides a basis for the interpretation of ocean floor photographs of comparable areas.

Contents:

Preface.—Introduction.—Geological Setting.—Photographic Techniques.—Submarine Volcanic Products: Volcanic Vents, Major Flow Units, Individual Flow Units, Features of Pillow Crust.—Faults and Related Tectonic Features: Tension Fissures, Fault Scarps of Inner Floor, Patterns of Faulting, Faulted Sedimentary Rock, Rift Valley Walls.—Acknowledgements. References Cited. Figure Captions.



Springer-Verlag
Berlin Heidelberg New York

Physics and Chemistry in Space

Editors:

J.G. Roederer, J.T. Wasson

Volume 1

J.A. JACOBS

Geomagnetic Micropulsations

81 figures. VIII, 179 pages. 1970

Cloth DM 52,-; US \$ 22.90

ISBN 3-540-04986-X

Contents: The Earth's Magnetic Field. The Morphology of Geomagnetic Micropulsations. Magneto-Hydrodynamic Waves. Theories of the Origin of Pc 1 Pulsations. Theories of Pc 2-5 and Pi Oscillations. Micropulsations and the Diagnostics of the Magnetosphere. Subject Index.

Volume 2

J.G. ROEDERER

Dynamics of Geomagnetically Trapped Radiation

94 figures. XIV, 166 pages. 1970

Cloth DM 43,-; US \$ 19.00

ISBN 3-540-04987-8

Contents: Particle Drifts and the First Adiabatic Invariant. Bounce Motion, the Second Adiabatic Invariant and Drift Shells. Periodic Drift Motion and Conservation of the Third Adiabatic Invariant. Trapped Particle Distributions and Flux Mapping. Violation of the Adiabatic Invariants and Trapped Particle Diffusion. Appendices. References. Subject Index.

Volume 3

I. ADLER, J.I. TROMBKA

Geochemical Exploration of the Moon and Planets

129 figures. X, 243 pages. 1970

Cloth DM 69,-; US \$ 30.40

ISBN 3-540-05228-3

Contents: Introduction. Instruments Used for Compositional Exploration. Instruments and Techniques Under Development. Apollo Surface Missions and the Lunar Receiving Laboratory Program. Data Processing and Analysis. Orbital and Surface Exploration Systems After Early Apollo. Subject Index.

Volume 4

A. OMHOLT

The Optical Aurora

54 figures. XIII, 198 pages. 1971

Cloth DM 69,-; US \$ 30.40

ISBN 3-540-05486-3

Contents: The Occurrence and Cause of Auroras: a Short Introduction. The Electron Aurora: Main Characteristics and Luminosity. The Proton Aurora. The Optical Spectrum of Aurora. Physics of the Optical Emissions. Temperature Determinations from Auroral Emissions. Pulsing Aurora. Optical Aurora and Radio Observations. Auroral X-Rays. Subject Index.

Volume 5

A.J. HUNDHAUSEN

Coronal Expansion and Solar Wind

101 figures. XII, 238 pages. 1972

Cloth DM 68,-; US \$ 30.00

ISBN 3-540-05875-3

Contents: History and Background. The Identification and Classification of Some Important Solar Wind Phenomena. The Dynamics of a Structureless Coronal Expansion. Chemical Composition of the Expanding Coronal and Interplanetary Plasma. High-Speed Plasma Streams and Magnetic Sectors. Flare-Produced Interplanetary Shock Waves. Concluding Remarks. References. Subject Index.

Volume 6

S.J. BAUER

Physics of Planetary Ionospheres

89 figures. VIII, 230 pages. 1973

Cloth DM 85,-; US \$ 37.40

ISBN 3-540-06173-8

Contents: Introduction. Neutral Atmospheres. Sources of Ionization. Thermal Structure of Planetary Ionospheres. Chemical Processes. Plasma Transport Processes. Models of Planetary Ionospheres. The Ionosphere as a Plasma. Experimental Techniques. Observed Properties of Planetary Ionospheres. Appendix: Physical Data for the Planets and their Atmospheres. References. List of Symbols. Subject Index.

Volume 7

M. SCHULZ, L.J. LANZEROTTI

Particle Diffusion in the Radiation Belts

83 figures. IX, 215 pages. 1974

Cloth DM 85,-; US \$ 37.40

ISBN 3-540-06398-6

Contents: Introduction. Adiabatic Invariants and Magnetospheric Models. Pitch-Angle Diffusion. Radial Diffusion. Prototype Observations. Methods of Empirical Analysis. Summary. References. Frequently used Symbols. Subject Index.

Volume 8

A. HASEGAWA

Plasma Instabilities and Nonlinear Effects

48 figures. XI, 217 pages. 1975

Cloth DM 82,-; US \$ 36.10

ISBN 3-540-06947-X

Contents: Introduction to Plasma Instabilities. Microinstabilities – Instabilities Due to Velocity Space Nonequilibrium. Macroinstabilities – Instabilities Due to Coordinate Space Nonequilibrium. Nonlinear Effects Associated with Plasma Instabilities. Appendix. General References. List of Symbols. Subject Index.

Volume 9

A. NISHIDA

Geomagnetic Diagnosis of the Magnetosphere

167 figures. Approx. 250 pages. 1977

Cloth approx. DM 70,-;

approx. US \$ 30.80

ISBN 3-540-08297-2

Contents: Geomagnetic Field under the Solar Wind. Power Supply through the Interplanetary Field Effect. Implosion in the Magnetotail. Dynamical Structure of the Inner Magnetosphere. Magnetosphere as a Resonator. Subject Index.

Prices are subject to change without notice



Springer-Verlag
Berlin
Heidelberg
New York

5310/5/1

Instructions to Authors

General

Papers should preferably be written in *English*. Editorial scrutiny can proceed more quickly if manuscripts are submitted *in duplicate* (illustration copy should comprise original drawings etc. plus one copy).

The text should be as *clear and concise* as possible. Submitted papers should be no longer than 20 *printed pages* (30 pages of typescript) including figures. If a paper exceeds 20 printed pages in length page charges of DM 100.— will be levied. Invited papers can be up to 30 printed pages in length. To allow faster publication, the text is made up into pages before the proofs are sent out. Therefore the author should mark in the manuscript where figures and tables may be inserted, and both *form and*

content of the paper should be *carefully checked* to exclude the need for corrections in proof. A charge will be made for changes introduced after the manuscript has been set in type. New results may be given at the end of the paper in a "Note added in proof". Short reports of new results of special interest can be published out of turn as *Short Communications*. They should not be longer than 3 printed pages, including any tables. The Editors reserve the right to decide what constitutes a Short Communication. When setting out his manuscript the author should consult a copy of the journal and conform with its normal practice. *Manuscripts* should be typed on one side of the paper only in double-line spacing with wide margins.

Arrangement of the Manuscript

The *title page* should comprise: title of paper, first name(s) and surname(s) of author(s), laboratory or institution, any footnotes to the title (indicated by asterisks), short version of the title for page heading (not more than 72 typewriter strokes, including spaces), and the address to which proofs are to be sent.

Each paper — except Letters and Short Communications — should be preceded by a brief *abstract* in English stating the methods used and the experimental results, which should be presented in such a way that it is possible for the reader to assess their significance. The abstract should be as short as possible and should not exceed 200 words. Papers not in English should have in addition an English translation of the title of the paper.

Immediately following the abstract up to ten *key words* indicating the scope of the paper should be supplied.

Footnotes which do not refer to the heading of the article should be numbered consecutively and typed on a separate sheet.

References to the literature in the text should be by author and year; where there are two authors both should be named but with three or more only the first author's name plus "*et al.*" need be given. The list at the end of the paper should include only papers mentioned in the text and should be arranged alphabetically by first author's name. References should be cited as follows; *journal papers* — names and initials of all authors, full title, journal as abbreviated in Chemical Abstracts, volume number, first and last page numbers, year; *books* — names

and initials of all authors, full title, edition, place of publication, publisher and year. The author is responsible for the accuracy and completeness of all references. He is urged therefore to make a full record of the necessary bibliographic data at the time he examines the literature. When information is missing, the manuscript will be returned to the author for completion.

Citation of "unpublished results" or papers "in preparation" will not be accepted.

Example of a journal paper citation:

Macdonald, K. C., Luyendyk, B. P., Von Herzen, R. P.: Heat flow and plate boundaries in Melanesia. *J. Geophys. Res.* **78**, 2537–2546, 1973

Example of a book citation:

Jeffreys, H.: The earth, its origin, history, and constitution, 5th ed. London: Cambridge University Press 1970

Example for an article quoted from a book:

Ginzburg, V. L., Ruhadze, A. A.: Waves and resonances in magnetoactive plasma. In: Encyclopedia of physics, Vol. XLIX/4, K. Rawer, ed.: pp. 395–560. Berlin-Heidelberg-New York: Springer 1972

Figures are costly and should be used with discretion. An illustration is only justified if it clarifies or replaces text. Information given in captions should not be repeated in the text. Colored or previously published illustrations are not usually accepted. Figures and graphs should always be mentioned in the text and should be numbered with arabic numerals. A brief descriptive legend should be provided for

each figure; legends are part of the text and should be appended to it. Original drawings and photographs in a form suitable for reproduction should be submitted separately from the text. Use a soft pencil to indicate the top and to note the author's name and the number of the figure on the back of each.

Illustration copy should comprise:

Original line drawings: clean lines of uniform thickness in Indian ink, the whole about twice the size of the final block. Inscriptions should allow for reduction (e.g. for the figure 1 to be about 2 mm high in the final version it must be 4 mm high for reduction $\times 1/2$).

Tables in the form of *computer printouts* will be accepted, provided that they are black enough and fit into the print area after photographic reduction to a letter height of 1.2 mm.

Photographs: sharp, well-contrasted glossy prints trimmed at right angles; areas that are not essential should be cut off. Authors should label photographs with Letraset (Instant Lettering). Photos should be of a size permit reproduction without (or with only slight) reduction within the print area of 122×194 mm. Where possible, figures *should be grouped* so as to utilize the full print area; in general it should be assumed that the same scale of reduction will apply to all figures in the same paper.

Equations should be typewritten whenever possible, showing special typefaces (alphabets) by underlining in color. Special attention should be given to the placing of subscripts and superscripts so that they

are recognizable as such. Formulae should preferably be written in the "linear" form. Equations should be numbered sequentially with arabic numerals in parentheses on the right hand side of the page. In the text they are cited, e.g. Eq. (7), Eqs. (7) and (8).

Marking: Letters in formulae are normally printed in italics, numbers, trigonometric, logarithmic and analytic symbols upright.

The following symbols are frequently confused:

$\cup, \cup, U; \circ, o, O, 0; \times, x, X, \kappa; \vee, v, \nu;$
 $\theta, \Theta, \phi, \varphi, \Phi, \varnothing, \emptyset; \psi, \Psi; \varepsilon, \epsilon;$

a', a^1 ; the symbol a and the indefinite article a ;
also the handwritten Roman letters:

$c, C; I, J; k, K; e, l; o, O; p, P; s, S; u, U; v, V;$
 $w, W; x, X; z, Z.$

Please take care to distinguish them in some way. Underlining to denote special types should be done in accordance with the following code:

single underlining = small letter

double underlining = capital letter

yellow = upright: abbreviations as, e.g., \AA , Re, Im,
grad, div, lim, exp, sin, cos, tan, ctan,
all elements and units.

brown = boldface

violet = the numeral 1 and zero to distinguish them
from the small letter l and the small/capital
letter o, O .

Words or sentences to be set in italics should be marked by single underlining.

**Journal of
Geophysics
Zeitschrift für
Geophysik**

2 1549.4137

44
1977/78

Volume 44 · Number 1/2 · 1977 Last issue of this volume

207 ol.

1-675

82 West 2148

**A Study of the
D-Region Winter Anomaly
in Western Europe, 1975/76**

X, 501



Springer International

Niedersächsische Staats- u.
Universitätsbibliothek
Göttingen

Jh. Geophys. — ISSN 0340-062X — ZEGEA7 44(1/2) 1—188 (1977) — 12. XII. 1977

4. Jan. 1978

Journal of Geophysics – Zeitschrift für Geophysik

Edited for the
Deutsche Geophysikalische Gesellschaft
by

W. Dieminger and J. Untiedt

Letters to the Editors
Book Reviews

The Journal accepts
Review Articles (invited by the Editors)
Original Papers
Short Communications

**in the field of Geophysics and
Space Physics.**

Manuscripts may be addressed to any of the Editors. For addresses see last cover page. Manuscripts should conform with the journal's accepted practice as described in the Instructions to Authors.

Members of the Deutsche Geophysikalische Gesellschaft are entitled to purchase the Journal for their own use at a privilege price of DM 76.— payable with the Membership dues. Orders should be sent to the Society's office at the following address: Binderstr. 22, D-2000 Hamburg 13.

Subscription Information

Volume 43 (6 issues each totalling about 656 pages) will appear in 1977. Information about obtaining back volumes and microform editions available upon request.

North America. Subscription rate: \$85.10, including postage and handling. Subscriptions are entered with prepayment only. Orders should be addressed to: Springer-Verlag New York Inc., Service Center Secaucus, 44 Hartz Way, Secaucus, N.J. 07094, USA. Tel. (201) 348-4033, Telex 0023-125994.

All Other Countries. Subscription rate: DM 210.—, plus postage and handling. Orders can either be placed with your book-dealer or sent directly to: Springer-Verlag, Heidelberger Platz 3, D-1000 Berlin 33, Tel. (030) 822001, Telex 01-83319.

Fifty offprints of each paper are provided free of charge. Additional copies may be ordered at cost price.

It is a fundamental condition that submitted manuscripts have not been and will not be, simultaneously submitted elsewhere.

With the acceptance of a manuscript for publication the publisher acquires the sole copyright for all languages and countries.

The use of general descriptive names, trade names, trade marks, etc., in this publication, even if the former are not specifically identified, is not to be taken as a sign that such names are exempt from the relevant protective laws and regulations and may accordingly be used freely by anyone.

Photographic reproduction, microform, or any other reproduction of text, figures, or tables from this journal is prohibited without permission obtained from the publisher.

Offices

Springer-Verlag, Heidelberger Platz 3, D-1000 Berlin 33, Tel. (030) 822001, Telex 01-83319

Springer-Verlag, Journal Production Department II
Postfach 105280, D-6900 Heidelberg 1, Tel. (06221) 487-1, Telex 04-61690

Springer-Verlag New York Inc., 175 Fifth Avenue, New York, N.Y. 10010, USA.
Tel. (212) 477-8200, Telex 0023-23223

Responsible for Advertisements:

G. Sternberg, Kurfürstendamm 237, D-1000 Berlin 15, Tel. (030) 8821031, Telex 01-85411

Printed in Germany by Univ.-Druckerei H. Stürtz AG, Würzburg

© by the Deutsche Geophysikalische Gesellschaft, Hamburg, 1977

A Study of the D-Region Winter Anomaly in Western Europe, 1975/76

D. Offermann*

University of Bonn, Phys. Dept., Federal Republic of Germany

Abstract. A campaign of integrated groundbased, balloon- and rocketborne experiments for the study of the D-region winter anomaly was performed in winter 1975/76 in Western Europe. Twenty-three balloons and 47 rockets were successfully launched from the range El Arenosillo in southern Spain. Coordinated ground observations took place in Spain, France, Great Britain, Italy, Austria, and Germany. The scientific objectives of the campaign, its structure, performance and geophysical background are described in the present introductory paper. Individual experiments are described in the subsequent papers.

Key words: Winter anomaly – D-region – Mesosphere – Lower thermosphere – GBR campaign.

The dynamical, photochemical and energetic behaviour of the mesosphere and lower thermosphere is still a largely unknown domain. This is on the one hand due to the complexity of processes controlling the atmosphere and ionosphere in this altitude regime (50–140 km). On the other hand this region is not readily accessible to remote measurements, either ground based or satellite borne, and therefore our knowledge is mostly based on a rather limited number of rocket experiments. To improve this situation it is not sufficient to launch a few more rockets. The above mentioned complexity makes it mandatory to concentrate a large number of rockets in one campaign and thus measure as many atmospheric parameters as possible at a time (or at nearly the same time). Complementary and coordinated ground based and satellite measurements are of course very important. Balloon borne experiments in the stratosphere help to define the conditions at the lower boundary of the altitude regime considered.

To understand a complex system like the atmosphere, it is sometimes very helpful to study it under disturbed conditions rather than in the normal state. A suitable disturbance in the altitude region of interest is the winter-anomaly

* Now at: University of Wuppertal, D-5600 Wuppertal, Federal Republic of Germany

of the electron density in the ionospheric D-region. This anomaly is believed to reflect—at least under certain conditions—a profound disturbance not only in the ionosphere but also in the neutral atmosphere.

Enhanced electron densities in the D-region may be caused by- or associated with the following events:

Solar flares (see for instance Mitra, 1975; Beynon and Williams, 1976).

Magnetic storms and storm after effects (for a collection of references see Denny and Bowhill, 1973; Sechrist, 1975; Paulikas, 1975. Recent measurements are reported for instance by Wratt, 1976).

Meteorological events (This was first suggested by Dieminger, 1952. For detailed references of more recent work see Denny and Bowhill, 1973; Sechrist, 1975).

The “meteorological” type of electron enhancement is considered to be the most promising one for a study of atmospheric behaviour. It is therefore mandatory for such study to select events of this type and to exclude the other disturbances as far as possible.

Several different explanations for this winter anomaly have been suggested:

Vertical and/or horizontal transport of atmospheric constituents with low ionization potential as NO (Gregory, 1965; Geisler and Dickinson, 1968; Christie, 1970; Manson, 1971; Geller et al., 1976).

Changes in the ion chemistry (water cluster ion chemistry) as caused by transport of trace constituents like O and H₂O (Newell et al., 1966; Newell, 1968; Sechrist, 1970; Geller and Sechrist, 1971; Sechrist, 1972).

Changes in the neutral and ion chemistry by temperature variations (Sechrist, 1967; this paper was discussed by Geisler and Dickinson, 1968; Reid, 1970).

To take these possibilities into account, it is not sufficient to measure electron and ion densities and composition only (to define the status of the ionosphere), but also the relevant neutral atmosphere parameters have to be determined. This pertains especially to the neutral gas density and composition with emphasis on specific minor constituents as O, NO etc., the temperature profile, and transport processes as winds and turbulence. Obviously the study of the D-region winter anomaly requires a set of atmospheric and ionospheric measurements as complete as possible with respect to structure, dynamics, and chemistry of the atmosphere.

A number of respective groundbased, balloon and rocket borne experiments was therefore integrated in one GBR campaign, which was performed in Western Europe from December 1975 to February 1976. Table 1 shows a list of the participating scientific groups (in an alphabetic order of the respective institutions) and of the experiments performed by them. A total of 22 experimenters groups took part in the campaign and performed 38 different types of measurements. Some of the experiments were duplicate and thus allow for a check on the reliability of the instruments. Also were a number of atmospheric parameters determined by two or more different techniques. This applies especially to the winds, the neutral composition, density and temperature, and the electron density. Thus a valuable intercomparison is possible. The rockets and balloons

Table 1

Institution	Experiment	Atmospheric parameter
<i>Rocket and balloon experiments</i>		
1. DFVLR, Köln (Becker, Papanikas)	Pitot tube, ion gauge	Neutral gas density, temperature
2. DFVLR, Oberpfaffenhofen (Beran)	NO photometer	NO
3. DFVLR, Oberpfaffenhofen (Drescher)	5577 Å photometer	Atomic oxygen
4. INTA, Madrid (Satrústegui, Cisneros)	Walmet sonde Radiosonde balloon wind Balloon ozone sonde	Wind, temperature temperature, pressure, ozone
5. IPW, Freiburg (Spenner)	Retarding potential analyzer	Electron density, temperature
6. IPW, Freiburg (Unger)	Radio propagation	Electron density
7. MPAE, Lindau (Widdel, Rose, Borchers)	Chaff Guard ring sonde Gerdien condenser Thermotron	Wind, density Electron density Ion mobility, conductivity Density
8. MPAE, Lindau (Loidl, Schwentek)	Ly- α photometers X-ray spectrometer	O ₂ , neutral gas density, pressure, temperature Solar emission
9. MPK, Heidelberg (Arnold, Krankowsky)	Cryo pumped mass spectrometer	Ion and neutral gas density and composition
10. NDRE, Kjeller (Thrane)	Ly- α photometer Particle detectors	O ₂ , neutral gas density, pressure and temperature Energetic electrons
11. TU Graz, (M. Friedrich, Riedler)	Faraday rotation Gerdien condenser Balloon	Electron density Ion density Wind, pressure, temperature
12. Universität Bonn (V. Friedrich, Offermann)	Cryo mass spectrometer	Neutral gas composition
13. Universität München (Bangert, Bolle)	Infrared radiometer	O ₂ (¹ Δ)
14. University College, London (Rees)	Lithium vapour trail, ground photometers at Mazagon (near the rocket range) and San Fernando (near Cadiz)	Winds, turbulence
<i>Ground based experiments</i>		
15. CNET, Issy les Moulineaux (Testud, Bernard)	Incoherent Scatter Radar (St. Santin, Nançay, Mende, St. Cassien)	E-region wind and temperature
16. CNET, Issy les Moulineaux (Glass, Fellous)	Meteor wind radars (Garchy, Montpazier)	D-region winds
17. CNR, Bologna (Verniani, Formigini)	Meteor wind radar (Bologna)	D-region winds

Table 1 (continued)

Institution	Experiment	Atmospheric parameter
18. INTA, Madrid (Satrustegui, Cisneros)	Ozone sonde (El Arenosillo)	Total ozone
19. MPAE, Lindau (Rose, Widdel, Lauche, Lange-Hesse)	Ionosonde (El Arenosillo)	Electron density
	Magnetometers (El Arenosillo)	Magnetic activity
	Airglow photometer (El Arenosillo)	Atomic oxygen
	A3 absorption (El Arenosillo, Balerna, Tortosa, transmitter at Aranjuez)	Electron density
20. MPAE, Lindau (Schwentek)	A1 and A3 absorption (Lindau, transmitter for A3 at Norddeich)	Electron density
21. Ulster College, Jordanstown (Smith)	5577 Å Doppler width (Jordanstown)	Temperature (90–100 km)
22. TU Graz (M. Friedrich, Riedler)	A3 absorption (Graz, transmitter near Coburg)	Electron density
23. Universität Bonn (Volland)	VLf propagation (Stockert)	
24. University of Sheffield (Muller)	Meteor wind radar (Sheffield)	D-region winds

were launched from the Spanish rocket range El Arenosillo (37°6' N; 6°44' W). Groundbased stations were operated in Spain, France, Italy, Great Britain, Austria and Germany. Their geographical distribution is shown in Figure 1.

A number of experiments listed in Table 1 was used to forecast launch opportunities, to define the launch criteria, or to verify that these criteria had been fulfilled. The A3 absorption measurement on the range was used for launch decisions. A noon absorption larger than 50 dB (measured between 11.20 UT and 12.20 UT) was assumed to indicate an anomalous winter day. This corresponds roughly to >47 dB in the afternoon (14.00 UT–15.00 UT). A noon absorption smaller than 25 dB was taken to define a low absorption day. These measurements were supplemented by the data obtained at Balerna. The A3 absorption was monitored continuously. Therefore also the development in time of the absorption was used for launch decisions. Further information was contributed by the ionosonde on the range. A second important launch criterion was defined by the ground photometers for tracking the day light lithium vapour trails: Very clear sky was needed around the range for the optical site at Mazagon (37°8' N; 6°49' W), a second optical site at San Fernando (36°28' N; 6°44' W) near Cadiz, and in the direction of the rocket trajectory. Happily this condition was fulfilled during most part of January, 1976.

As mentioned above the major experiments should not be launched during solar flares, magnetic storms, or storm after activity. To achieve this Ursigrams and magnetic forecasts were obtained on a daily basis from the Observatoire de Paris at Meudon. These data were supplemented by magnetometers on the



Fig. 1. Geographical distribution of ground based stations

range. Solar x-ray data from the SMS satellite and flare forecasts were obtained every day from the Space Environment Center, NOAA Boulder, USA.

As there is a correlation between winter anomaly events and stratospheric warmings (for a review see Bowhill, 1969; Patel and Kotadia, 1972), stratospheric weather was monitored during the campaign. Daily STRATALERT messages of the WMO and respective forecasts were received from the Institut für Meteorologie, Freie Universität, Berlin. During high activity phases of the campaign, there were – in addition to the daily routine messages – person to person contacts with the three stations at Meudon, Boulder, and Berlin for detailed discussion of the geophysical situation. Finally, a number of rocket experiments (x-ray-spectrometers, particle detectors) were used to verify that the launch criteria concerning flares and magnetic disturbances had been fulfilled.

The rocket and balloon experiments listed in Table 1 were allocated to 7 different types of rocket payloads and 2 types of balloon payloads. Table 2 shows this allocation together with the number of successful rocket or balloon flights. (Only experiments which had at least one successful flight, are contained in Table 2.) As is seen from this table, there was a large number of launches of the small payloads BI and BVII, and only 2–3 launches of the medium or heavily equipped payloads BII, BIII, BIV, and BV. Also only three vapour trails were available. Therefore the rockets were divided into three groups:

Table 2. Payload allocation of experiments

Payload designation	Vehicle	Number of Typical successful apogee launches	Atmospheric parameter	Technique	Experimenter
B I	Skua 2, 3	15	Wind, density Electron density	Chaff Guardring sonde	Widdel, Rose, MPAE, Lindau Widdel, Rose, MPAE, Lindau
B II	Skyllark 3	2	Neutral gas density, temperature Neutral composition NO O ₂ (Δ) Ly- α X-rays Electron density, temperature	pitot tube, ion gauge Mass spectrometer with shock-freezing cryo ion source Filter photometer Infrared filter photometer Ionization chambers 0, 1-60 Å spectrometer Retarding potential analyzer	Becker, Papanikas, DFVLR, Köln V. Friedrich, Offermann, Univ. Bonn Beran, DFVLR, Oberpfaffenhofen Bolte, Bangert, Univ. München Loidl, Schwentek, MPAE, Lindau Loidl, Schwentek, MPAE, Lindau Spenner, IPW, Freiburg
B III	Petrel	3	Ion mobility-conductivity, gas density	Gerdien-Condenser Thermotron	Widdel, Rose, Borchers, MPAE, Lindau
B IV	Nike-Apache	2	Ion composition and density (positive and negative), neutral gas composition and density Electron density Electron density Ion density Ly- α Energetic electrons	Cryopumped mass spectrometer Radio propagation Faraday rotation Gerdien condenser Ionization chambers Solid state detector	Krankowsky, Arnold, MPK, Heidelberg Unger, IPW, Freiburg M. Friedrich, Riedler, TU Graz M. Friedrich, Riedler, TU Graz Thrane, NDRE, Kjeller Thrane, NDRE, Kjeller
B V	Skua 4	3	Wind, neutral gas density atomic oxygen	chaff 5577 Å filter photometer	Widdel, Rose, MPAE, Lindau Drescher, DFVLR, Oberpfaffenhofen
B VI	Petrel	3	Wind, turbulence	Li-trail	Rees, Univ. College London
B VII	Super-loki	19	Wind, temperature	walmet sonde	Satrustegui, Cisneros, INTA, Madrid
A II	Balloon	4	Wind, pressure, temperature		M. Friedrich, Riedler, TU Graz
R	Radio-Balloon	19(+1)	Wind, temperature, pressure, ozone		Satrustegui, Cisneros, INTA, Madrid

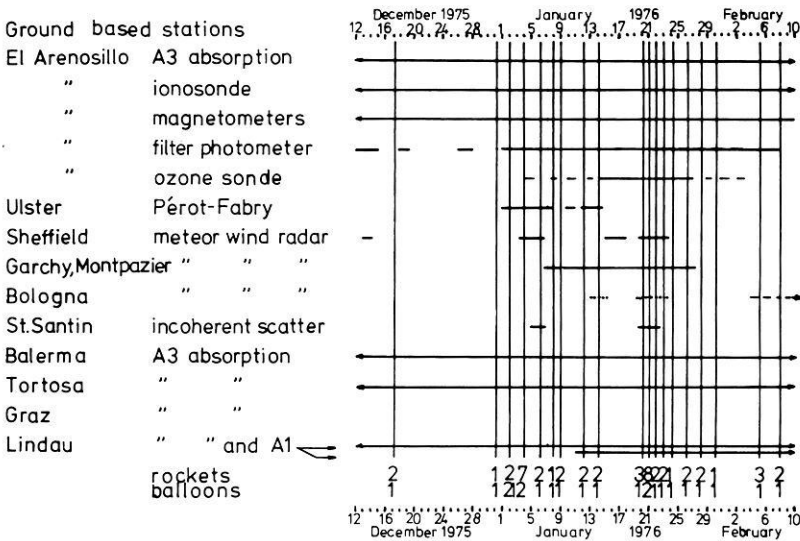


Fig. 2. Periods and dates of ground based, balloon and rocket measurements. Numbers of launches per day are given in the bottom

groups 1 and 2 were called “salvoes” because their rockets were launched on two days with strong winter anomaly within a timespan as short as possible. The first salvo contained one round of each type of rocket and balloon payloads, amounting to 7 rocket and 2 balloon launches. The second salvo also contained one round of each payload. In addition it contained the spare vapour trail and a second AII balloon payload. (This payload AII and a radio balloon payload R were flown on the same balloon). The remaining third group of rockets mainly consisted of the small payloads BI and BVII. Most of them were launched in pairs BI–BVII because this yielded a nearly continuous wind profile from 20 km–95 km. These pairs were normally accompanied by a radio balloon (payload R) which extended the wind and temperature profile down to the ground. The launches of these pairs plus balloon were about evenly distributed over the month of January and begin of February, 1976. They sensed days of high as well as of low winter anomaly activity, thus providing a data background for the two salvoes (see Fig. 2). Table 3 shows the launch times and dates of all successful rocket and balloon flights together with the apogee or maximum flight altitude, and the nominal azimuth of launcher setting. The A3 absorption (noon values) of the respective days are also given. It is seen from this table that a total of 47 rockets and 23 balloons were successfully launched during this campaign.

Table 3 shows that the rockets of the two salvoes (Jan. 4 and Jan. 21, 1976) were launched in a specific sequence (BIII, IV, II, I, VI, VII, V). This sequence and the time intervals between the respective launches resulted from a number of scientific and operational requirements:

1. The central part of the salvo should be launched in the early afternoon.
2. The rockets should follow one another as quickly as possible.

Table 3. Successful rocket and balloon flights

Date	Time	Payload/vehicle	Apogee (approx)	Nominal Azimuth	A3-Absorption (noon)
17. 12. 1975	11:04:00 GMT	B I/Skua 3	93 km	206°	25 dB
	12:00:00 GMT	B VII/Super-Loki	69 km	210°	
	13:35:00 GMT	R /Radio-Balloon	110 km		
31. 12. 1975	10:46:00 GMT	B VII/Super-Loki	66 km	200°	45 dB
	12:39:00 GMT	R /Radio-Balloon	33 km		
2. 1. 1976	11:14:00 GMT	A II/Balloon	15 km		51 dB
	14:59:00 GMT	B I/Skua 3	95 km	200°	
	15:59:00 GMT	B VII/Super-Loki	62 km	200°	
	17:42:00 GMT	R /Radio-Balloon	17 km		
3. 1. 1976	13:49:00 GMT	R /Radio-Balloon	12 km		46 dB
4. 1. 1976	13:40:00 GMT	B III/Petrel	86 km	195°	56 dB
	14:30:00 GMT	B IV/Nike-Apache	131 km	200°	
	15:30:03 GMT	B II/Skylark 3	117 km	200°	
	15:47:00 GMT	B I/Skua 3	103 km	197°	
	16:00:00 GMT	B VI/Petrel	132 km	202°	
	16:52:00 GMT	B VII/Super-Loki	57 km	197°	
	17:06:00 GMT	A II/Balloon	35 km		
	19:35:00 GMT	R /Radio-Balloon	33 km		
	22:58:00 GMT	B V/Skua 4	96 km	200°	
6. 1. 1976	15:46:00 GMT	B I/Skua 2	97 km	200°	50 dB
	16:40:00 GMT	B VII/Super-Loki	70 km	200°	
	18:42:00 GMT	R /Radio-Balloon	32 km		
8. 1. 1976	12:00:00 GMT	B VII/Super-Loki	70 km	200°	60 dB
	13:13:00 GMT	R /Radio-Balloon	31 km		
9. 1. 1976	15:53:00 GMT	B VII/Super-Loki	70 km	200°	25 dB
	16:11:00 GMT	B I/Skua 2	99 km	220°	
	18:47:00 GMT	R /Radio-Balloon	31 km		
12. 1. 1976	15:50:00 GMT	B VII/Super-Loki	56 km	200°	30 dB
	16:20:00 GMT	B I/Skua 3	92 km	220°	
	17:47:00 GMT	R /Radio-Balloon	31 km		
14. 1. 1976	15:50:00 GMT	B VII/Super-Loki	70 km	200°	61 dB
	16:10:00 GMT	B I/Skua 3	91 km	230°	
	17:53:00 GMT	R /Radio-Balloon	24 km		
20. 1. 1976	13:40:00 GMT	B III/Petrel	59 km	195°	35 dB
	15:50:00 GMT	B VII/Super-Loki	63 km	190°	
	16:10:00 GMT	B I/Skua 3	93 km	225°	
	17:38:00 GMT	R /Radio-Balloon	32 km		
21. 1. 1976	11:48:30 GMT	A II/Balloon	4 km		67 dB
	13:40:00 GMT	B III/Petrel	82 km	195°	
	14:32:09 GMT	B IV/Nike-Apache	129 km	200°	
	15:31:00 GMT	B II/Skylark 3	117 km	200°	
	15:40:00 GMT	B I/Skua 2	98 km	197°	
	15:55:00 GMT	B VI/Petrel	134 km	202°	
	16:40:00 GMT	B VII/Super-Loki	70 km	197°	
	18:17:00 GMT	B VI/Petrel	125 km	202°	
	18:57:00 GMT	A II/R/Balloon	29 km		
	22:30:00 GMT	B V/Skua 4	109 km	235°	

Table 3 (continued)

Date	Time	Payload/vehicle	Apogee (approx)	Nominal azimuth	A3-Absorption (noon)
22. 1. 1976	15:56:00 GMT	B VII/Super-Loki	70 km	200°	44 dB
	16:16:00 GMT	B I/Skua 2	93 km	221°	
	17:54:00 GMT	R /Radio-Balloon	33 km		
23. 1. 1976	15:50:00 GMT	B VII/Super-Loki	70 km	195°	51 dB
	16:10:00 GMT	B I/Skua 2	104 km	230°	
	18:05:00 GMT	R /Radio-Balloon	33 km		
24. 1. 1976	13:09:00 GMT	R /Radio-Balloon	33 km		53 dB
	16:41:00 GMT	B VII/Super-Loki	70 km		
26. 1. 1976	12:28:00 GMT	R /Radio-Balloon	31 km		44 dB
	15:59:00 GMT	B VII/Super-Loki	70 km	180°	
	16:19:00 GMT	B I/Skua 3	100 km	200°	
28. 1. 1976	12:58:00 GMT	R /Radio-Balloon	31 km		64 dB
	15:50:00 GMT	B VII/Super-Loki	63 km	220°	
	16:10:00 GMT	B I/Skua 3	94 km	190°	
30. 1. 1976	12:29:00 GMT	R /Radio Balloon	28 km		30 dB
	15:58:00 GMT	B VII/Super-Loki	70 km	220°	
5. 2. 1976	11:39:00 GMT	R /Radio Balloon	28 km		18 dB
	15:51:00 GMT	B I/Skua 2	104 km	205°	
	16:27:00 GMT	B VII/Super-Loki	70 km	205°	
	22:30:00 GMT	B V/Skua 4	103 km	190°	
8. 2. 1976	11:05:00 GMT	R /Radio Balloon	32 km		31 dB
	15:34:00 GMT	B I/Skua 2	100 km	193°	
	16:20:00 GMT	B VII/Super-Loki	70 km	195°	

3. The Li vapour trail must not disturb other measurements.

4. Spare rockets (in case of a misfire) were available only for the smaller payloads.

5. The number of launchers, telemetry and radar stations was limited. One launcher had to be reloaded during the sequence.

As is seen from the table it was managed to launch the first 6 rockets of a salvo within about 3 h. This is certainly sufficient for the study of medium and large scale atmospheric variations as tidal and planetary waves. It could, however, be marginal for short period disturbances as gravity waves. The BV payloads were intended to search for night effects possibly connected with a winter anomaly event. Two of them were therefore launched in the nights after the 2 salvoes. The third Li vapour trail (spare of payload BVI) was launched after the second salvo at twilight conditions in 100 km altitude. The balloons had low priorities on the salvo days and were launched at times when they did not disturb the rocket flights.

The ground based measurements which were coordinated with the balloon and rocket flights are listed in Table 1. Not all of these stations were able to operate continuously. Therefore their activities were concentrated on certain time periods, which were especially centered around the two salvoes. For this

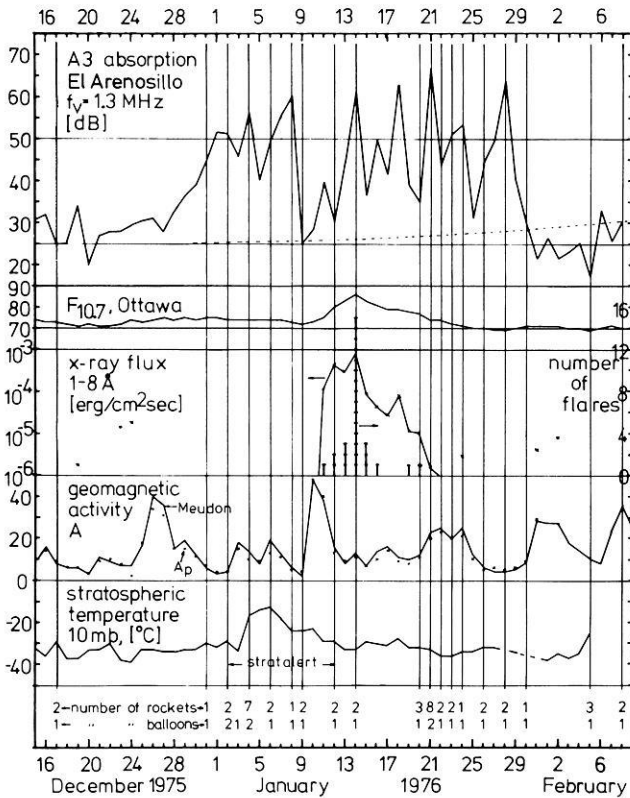


Fig. 3. Geophysical data. Dates of balloon and rocket flights are indicated as vertical lines. Numbers of flights per day are given in the bottom

purpose the ground stations were in permanent twx contact with the rocket range. Figure 2 shows the activity periods of the groundbased stations together with the number and dates of balloon and rocket launches. It is seen from this picture that the period documented best is that from January 20–January 24, 1976. This includes the second salvo on January 21, 1976, which was launched on the day with the strongest winter anomaly event (67 dB) of that winter.

Figures 3 and 4 show a number of geophysical parameters for the duration of the campaign. The data are shown as they were available on the range. The A3 absorption values given in Figure 3 show an unexpectedly strong winter anomaly activity during all of the month of January, 1976. It is interesting to note that the time span between every two strong absorption events (> 50 dB) is in nearly all cases 3–4 days. The rocket and balloon launches are indicated by vertical lines in Figure 3. The number of launches is given in the bottom of the picture. It is seen that the two salvos on January 4 and January 21, 1976 met strong winter anomaly events. The solar activity is shown in Figure 3 in terms of the 10.7 cm radio flux F numbers (Ottawa), by the 1–8 Å x-ray flux, and by the number of flares per day (SMS satellite data, Boulder).

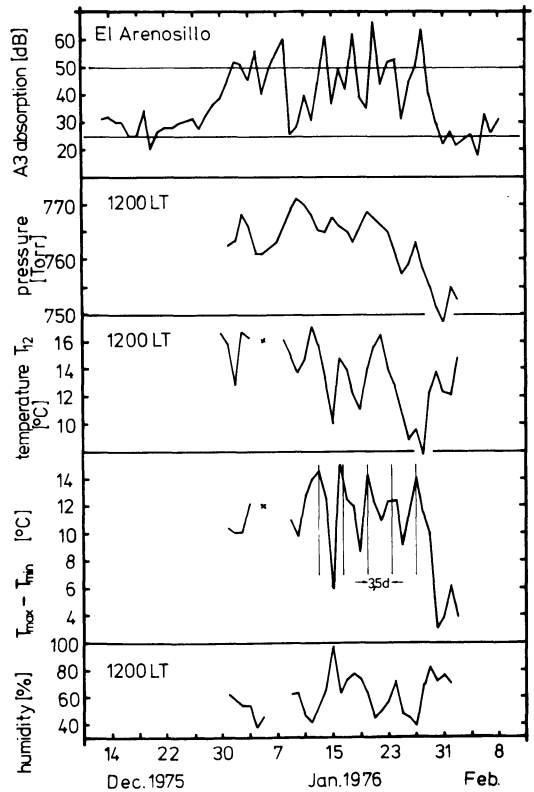


Fig. 4. Meteorological data from ground based measurements on the range. A3 absorption is given for comparison

The first salvo (January 4, 1976) was launched under very quiet solar conditions. By mid of January, however, a sun spot appeared which strongly expresses in all solar data shown in Figure 3. The second salvo (January 21, 1976) therefore was not launched until this activity decayed and had nearly disappeared (note the logarithmic scale of the x-ray flux in Fig. 3). The geomagnetic field was characterized by moderate recurrent disturbances. The planetary Ap index as well as the local Meudon index are given in Figure 3. It is seen that the first salvo was launched under quiet conditions whereas the second salvo went into the beginning of a small recurrent disturbance. The local magnetometers on the range showed, however, that this disturbance had not fully developed by the time when the salvo was finished.

Figure 3 also shows the 10 mb stratospheric temperatures as supplied by the Berlin Stratalerts. Maximum temperatures which occurred in the northern hemisphere are given to characterize the overall situation. A minor stratospheric warming occurred in the beginning of January 1976 (including a stratalert). Most of it, however, did not take place over Western Europe but over Siberia.

Figure 4 shows some meteorological data as they were measured on the range. For comparison the A3 data of El Arenosillo are also given. As mentioned above the weather was unexpectedly good during most part of January, 1976.

Figure 4 shows that this was due to a pronounced high pressure period. It is tempting to look for a link between this high ground pressure and the winter anomaly, because the periods of generally high A3 absorption and high pressure coincide. Superimposed on the mean ground pressure there is a wavelike structure which appears to be present in a similar but time shifted form in the noon temperatures T_{12} (see Fig. 4). Again superimposed on this wave structure there is a diurnal and semidiurnal variation of the ground pressure (not shown in Fig. 4). It reaches peak to peak values up to 4 Torr! The maximum daily temperature variation $T_{\max} - T_{\min}$ is also given in Figure 4. It exhibits a wavelike structure with a period of about 3.5 days. Longer periods may have been eliminated by the method of taking differences of temperature values so close together in time. Periods similar to this and longer ones were found in various balloon and rocket data at higher altitudes during the campaign. Generally speaking it appears that the geophysical situation by the time of the campaign was characterized by pronounced wavelike structures in the atmosphere.

Acknowledgement. The winter anomaly campaign was conceived by U. von Zahn, Bonn. It was supported by various institutions, especially by the Bundesministerium für Forschung und Technologie, Bonn, through DFVLR/BPT, Köln, and by the Instituto Nacional de Tecnica Aeroespacial (INTA), Madrid. Rockets and balloons were launched in cooperation of INTA and Mobile Raketenbasis (MORABA) and GSOC of DFVLR, Oberpfaffenhofen.

At any time when they were needed, geophysical alert and forecast data were supplied by K. Labitzke, Freie Universität Berlin; P. Simon, Observatoire de Paris, Meudon; and H. Heckman and H. Sargent, Space Environment Center, NOAA, Boulder. The campaign success was very much dependent on these data, and they are gratefully acknowledged. Other geophysical and meteorological data presented in this paper were kindly supplied by G. Rose, Max-Planck-Institut, Lindau, and by J. Satrustegui and J.M. Cisneros, INTA, Madrid.

References

- Beynon, W.J.G., Williams, E.R.: The long term variation in the ionospheric winter absorption anomaly. *J. Atmospheric Terrest. Phys.* **38**, 423–429, 1976
- Bowhill, S.A.: Interactions between the stratosphere and ionosphere. In: *Annals of the IQSY*, Vol. 5, pp. 83–95. Cambridge: MIT Press 1969
- Christie, A.D.: D-region winter anomaly and transport near the mesopause. *J. Atmospheric Terrest. Phys.* **32**, 35–56, 1970
- Denny, B.W., Bowhill, S.A.: Partial reflection studies of D-region winter variability, Aeronomy Report No. 56, University of Illinois, Urbana, USA, 1973
- Dieminger, W.: On the causes of excessive absorption in the ionosphere on winter days. *J. Atmospheric Terrest. Phys.* **2**, 340, 1952
- Geisler, J.E., Dickinson, R.E.: Vertical motions and nitric oxide in the upper mesosphere, *J. Atmospheric Terrest. Phys.* **30**, 1501–1521, 1968
- Geller, M.A., Hess, G.C., Wratt, D.: Simultaneous partial reflection and meteor radar wind observations at Urbana, Illinois, during the winter of 1974–1975. *J. Atmospheric Terrest. Phys.* **38**, 287–290, 1976
- Geller, M.A., Sechrist, Jr., C.F.: Coordinated rocket measurements on the D-region winter anomaly-II. Some implications. *J. Atmospheric Terrest. Phys.* **33**, 1027–1040, 1971
- Gregory, J.B.: The influence of atmospheric circulation on mesospheric electron densities in winter. *J. Atmospheric Sci.* **22**, 18–23, 1965
- Manson, A.H.: The concentration and transport of minor constituents in the mesosphere and lower thermosphere (70–110 km) during periods of anomalous absorption. *J. Atmospheric Terrest. Phys.* **33**, 715–721, 1971

- Mitra, A.P.: D-region in disturbed conditions including flares and energetic particles. *J. Atmospheric Terrest. Phys.* **37**, 895–913, 1975
- Newell, R.E.: The general circulation of the atmosphere above 60 km, *Meteorological Monographs*, 9 (31), pp. 98–113. American Meteorological Society 1968
- Newell, R.E., Wallace, J.M., Mahoney, J.R.: The general circulation of the atmosphere and its effect on the movement of trace substances. *Tellus* **18**, 363–380, 1966
- Patel, J.C., Kotadia, K.M.: Relationship between stratospheric warming and ionospheric absorption. *Ann. Geophys.* **28**, 803–807, 1972
- Paulikas, G.A.: Precipitation of particles at low and middle latitudes. *Rev. Geophys. Space Phys.* **13**, 709–734, 1975
- Reid, G.C.: Production and loss of electrons in the quiet day time D region of the ionosphere. *J. Geophys. Res.* **75**, 2551–2562, 1970
- Sechrist, Jr. C.F.: A theory of the winter absorption anomaly at middle latitudes. *J. Atmospheric Terrest. Phys.* **29**, 113–136, 1967
- Sechrist, Jr. C.F.: Interpretation of D-region electron densities. *Radio Sci.* **5**, 663–671, 1970
- Sechrist, Jr. C.F.: Theoretical models of the D-region. *J. Atmospheric Terrest. Phys.* **34**, 1565–1589, 1972
- Sechrist, Jr. C.F.: Ionospheric D and E regions. *Rev. Geophys. Space Phys.* **13**, 894–900, 1975
- Wratt, D.S.: Ionization enhancement in the middle latitude D-region due to precipitating high energy electrons. *J. Atmospheric Terrest. Phys.* **38**, 511–516, 1976

Received May 2, 1977

***D*-Region Radio Wave Propagation Experiments, Their Significance and Results during the Western European Winter Anomaly Campaign 1975/76**

G. Rose and H. U. Widdel

Max-Planck-Institut für Aeronomie, D-3411 Katlenburg-Lindau 3, Federal Republic of Germany

Abstract. During the Western European Winter Anomaly Campaign 1975/76 at ‘El Arenosillo’ (Huelva/Spain) *D*-layer radio wave absorption was measured ‘on line’ in Spain, Germany and Austria using the continuous wave propagation (A_3) method.

The task of the receiving station at the launching site was to announce absorption events of the winter anomalous type. Further, the results of both its absorption and ionosonde measurements were integrated into a number of ground based and rocket measurements in order to calibrate in situ electron density profiles.

Common quasi-periodic oscillations of *D*-layer absorption at the widely separated stations became evident together with the drifts of the associated spatial patterns from the analysis of the records. Comparisons of the daily absorption with *D*-region winds between about 80 and 100 km measured simultaneously by rocket experiments from the same site show correlations between winter anomaly and transport processes at *D*-layer heights.

Key words: Aeronomy – Ionospheric absorption – Winteranomaly.

1. Method of Measurement and the Average Daily Variation of *D*-Layer Absorption during a Year in Southern Europe

During the Western European Winter Anomaly Campaign of 1975/76 at ‘El Arenosillo’ (Huelva/Spain) *D*-layer radio wave absorption was continuously measured in Spain, Germany and Austria. The geographical locations and the distribution of the stations are shown in the preceding paper (Offermann). The transmissions paths in Spain were continuously operated for several years. In each year of observation (1967/68, 1970/71, 1971/72, 1972/73, 1973/74, 1974/75) winter-anomalous conditions were found to be present, January being the month in which the probability of its occurrence was highest and to meet both, high winter-anomalous absorption and conditions of very low absorption. This result

of a rather long period of monitoring which was supplemented by observations of winter-anomalous conditions over Sardinia on an earlier occasion (1964/65) were one of the reasons for planning the campaign and for *D*-layer in situ experiments performed over Arenosillo during the past years (Rose et al., 1972a, 1972b; Rose and Widdel, 1972, 1973). There was no sound reason or support for the belief that winter-anomalous conditions should not be present over a sufficiently long time during December 1975 and January 1976.

The so-called A_3 method was used (Schwentek, 1958; Dieminger et al., 1966; Rose, 1967; Rose et al., 1971, 1974; Friedrich et al., 1976). The amplitudes of the sky waves of continuously transmitting short radio wave transmitters were recorded at receiving stations which were located at distances up to about 500 km. (The transmission was interrupted every five minutes for one minute to discriminate the noise and interference level.) Antennas, distances and transmitting frequencies were well selected according to the local ionospheric propagation conditions in order to be able to determine *D*-layer absorption quasi 'on line' all over the year between about sunrise and sunset.

The absorption measurement is obtained by the transmission of a wave frequency that is reflected at *E*-layer heights ($h' \approx 100 \dots 125$ km) during daytime. In this case the absorption-free reference value which is necessary to determine absorption does not depend too much on the height of reflection if the antennas are designed to favour $1 \times E$ hop propagation. This mode is advantageous because the signal observed from different *E*-layer heights during the day can then be related to one constant (mean) reference value (instead of using a strongly height-dependent one for which the height has to be determined independently in each case) without introducing a significant error.

A proof of this is given in Figure 1 which shows the change of apparent absorption on the Aranjuez-Arenosillo transmission path when the height of reflection

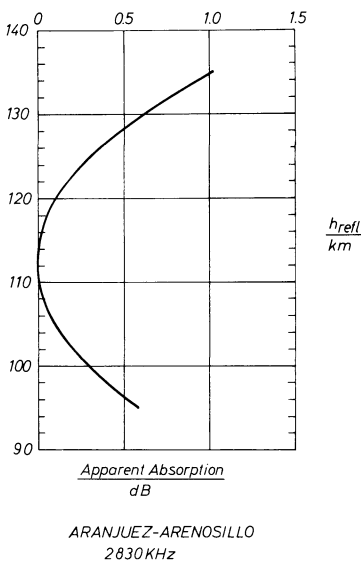


Fig. 1. Change of (virtual) absorption as a mere function of reflection height at vanishing *D*-layer absorption calculated for the technical equipment of the Aranjuez-Arenosillo path

changes (at vanishing D -layer absorption). The error introduced by using a mean constant instead of a height dependent reference value is only of the order of half a dB and can therefore be neglected for most of the day. For this reason the absorption L can readily be determined 'on line' by using the simple formula:

$$L(t) \text{ (dB)} = E_0 \text{ (dB)} - E(t) \text{ (dB)} \quad (1)$$

E_0 is the mean reference receiver input voltage (e.g. in dB over 1 μV) without absorption. It is determined and controlled in principle by averaging a great number of night-time values obtained during blanketing sporadic E -layer propagation conditions. $E(t)$ is the relevant (mean) input voltage centered around the time t of observation. For the different A_3 paths only ordinary mode propagation is of importance. This is because of the orientations of the propagation paths relative to the geomagnetic field and because of the antenna geometries.

The length of the transmission path Aranjuez-Arenosillo is 424 km and the transmission frequency is 2830 kHz. Ground wave propagation is therefore practically non existent. As was proved by simultaneous ionosonde observations, E -layer propagation occurs during the day on this path all over the year for solar zenith distances $\chi < 80^\circ$. At the same time, absorption can be as high as about 60 dB relative to the corresponding absorption-free nighttime value when strong winter anomalous conditions are present. These are values which can still be handled by the receiving equipment without significant loss of accuracy.

In order to investigate what would happen to different E -layer propagated wave frequencies along this transmission path during average winter anomalous conditions, relative differential absorption profiles $(1/L_{\text{tot}}) \cdot (dL/dh) \cdot (\cos\varphi)^{-1} \varphi$ for the more strongly absorbed downcoming wave were calculated and plotted for 2.0, 2.5 and 3.0 MHz in Figure 2. (The measured profile for 2.83 MHz is not included in this figure.)

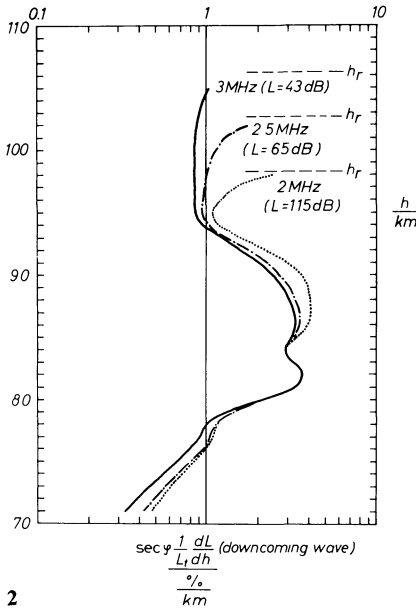
Some consequences are evident from Figure 2: A 2 MHz wave is absorbed so strongly during anomalous conditions that it cannot be measured over that distance. At the same time it is clear, that waves which penetrate increasingly into the E -layer with increasing wave frequency undergo an increasing amount of (unwanted) deviative E -layer loss (Bibl and Rawer, 1951; Rose, 1967). As another example of the response of the transmission path Aranjuez-Arenosillo to low and winter anomalous high absorption conditions, 3 relative differential absorption profiles $(1/L_{\text{tot}}) \cdot (dL/dh) \cdot (\cos\varphi)^{-1} \varphi$ one of them belonging to low absorption conditions, are displayed in Figure 3.

The propagation paths in Spain and Germany have been operated very close to optimum experimental conditions, whereas the path from Meeder (Coburg/Germany) to Graz (Austria) might have been somewhat shorter, but this was impossible because of technical difficulties.

As is well known, the daily variation of absorption can be approximated by a $\cos^n \chi$ law according to (Best and Ratcliffe, 1938):

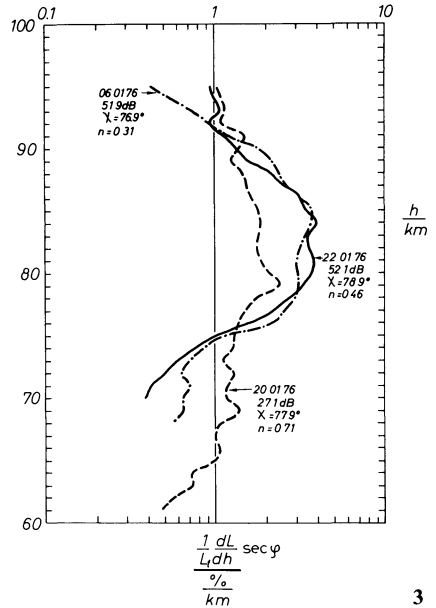
$$L(t) \text{ (dB)} = L_0 \text{ (dB)} \cdot \cos^n \chi(t) \quad (2)$$

where $L(t)$ is the absorption relative to the absorption-free reference value and χ is the solar zenith angle at the time of observation. The exponent " n " may vary



2

Fig. 2. Relative differential absorption $(1/L_{t01}) \cdot (dL/dh) \cdot (\cos \phi)^{-1} \phi$ for the parameters of the Aranjuez-Arenosillo path and different wave frequencies during winter anomalous conditions. The stronger absorbed down-coming wave is presented



3

Fig. 3. Relative differential absorption for 2830 kHz during winter anomalous ($L=52.1$ dB and $L=51.9$ dB) and during normal conditions ($L=27.1$ dB) in winter. Propagation path: Aranjuez-Arenosillo. (Stronger absorbed down-coming wave)

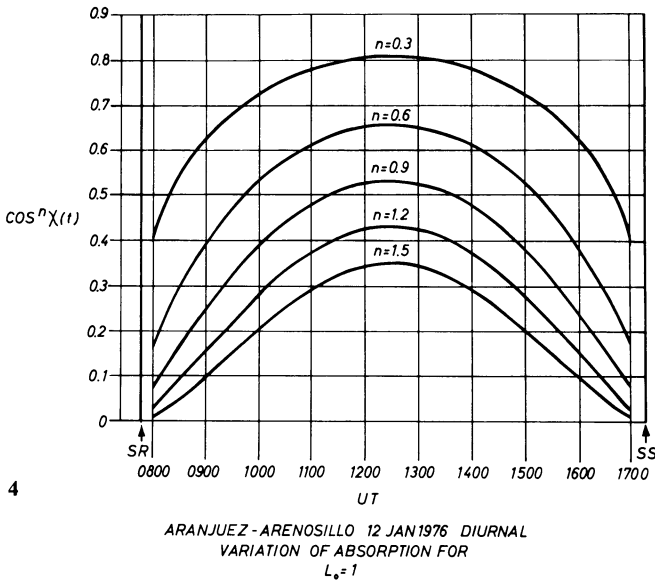
between about 0.5 and 1.5 and determines the shape of the daily curves of absorption; L_0 is the subsolar absorption.

In Figure 4 some $\cos^n \chi$ curves with different exponents are plotted, which were calculated as examples for the midpoint of the Aranjuez-Arenosillo path for 12 January 1976. As is seen from (2) and Figure 4 absorption increases with decreasing “ n ” and increasing L_0 . This property of the daily variation of absorption must be considered if a suitable parameter, characterizing the absorption of a whole day, has to be defined. If in (2), $\cos \chi$ is chosen as the independent variable and the expression is integrated from $\cos \chi=0$ to $\cos \chi=1$, one obtains:

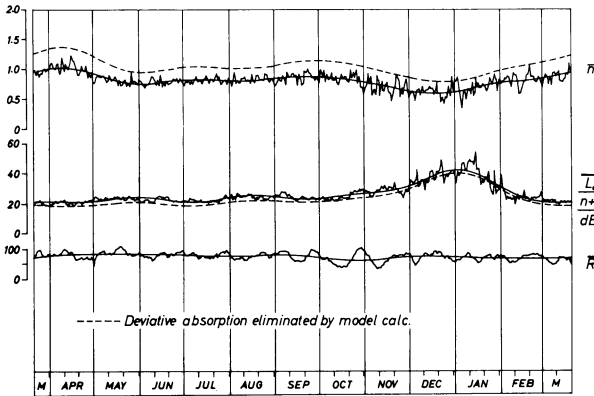
$$L_0/(n+1) = \int_0^1 L(\cos \chi) \cdot d(\cos \chi) \tag{3}$$

with $L_0/(n+1)$ being the parameter with the desired features (Rose, 1967).

The actual process by which $L_0/(n+1)$ is determined is quite different from a real integration: One determines the best fit straight line through all the points $\log L(t)$, $\log \cos \chi(t)$ belonging to E -layer propagation of the relevant day (e.g. $\chi < 80^\circ$ for the Spanish transmission paths). The slope of this line equals “ n ” and



4



5 ARANJUEZ-BALERMA, MEANS: 1967/68, 70/71, 71/72, 72/73 AND 73/74

Fig. 4. Dependence of the diurnal variation of absorption on the exponent “n” in Equation (2), calculated for January 12, 1976. Propagation path: Aranjuez-Arenosillo

Fig. 5. Average variation of the absorption parameters “ \bar{n} ” and “ $\overline{L_0/(n+1)}$ ” (and of the sunspot numbers \bar{R}) during a year. Average from five years of observation

the intersection of the line with the ordinate at $\log \cos \chi = 0$ equals $\log L_0$. The “integrated absorption parameter” $L_D = L_0/(n+1)$ has the advantage that it merges L_0 and “n” in one meaningful parameter. This turns out to be very useful for comparison purposes.

The average daily variations of \bar{n} , $\overline{L_0/(n+1)}$ and of the Zürich sunspot numbers \bar{R} which were obtained from five years of observations (1967/68, 1970/71, 1971/72,

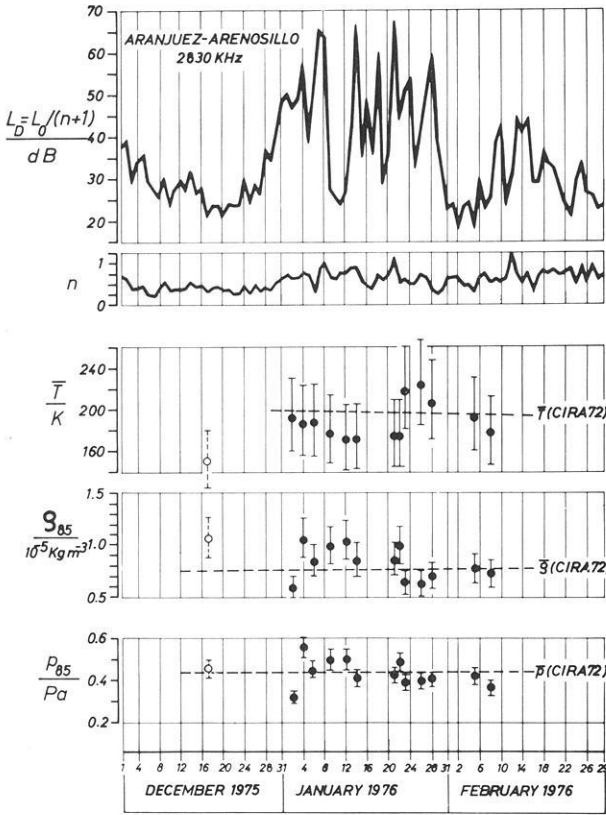


Fig. 6. Variation of the daily absorption parameters “ L_D ” and “ n ” (upper half) and of the rocket temperature data \bar{T} (83–95 km), density at 85 km ρ_{85} , and pressure at 85 km p_{85} observed during the Winter Anomaly Campaign

1972/73 and 1973/74) are plotted in Figure 5. The solid lines are Fourier synthesized by using the coefficients up to the fifth order. Winter-anomalous high absorption is generally evident between November and February as seen from the high $L_0/(n+1)$ values and the relatively large variations of absorption from day to day during the winter season, which do not average out even if five years of observations are superimposed. At the same time the exponent “ n ” is on the average significantly lower during winter too.

The dashed lines in Figure 5 were obtained from model calculations which were performed to estimate the influence of deviate absorption (mainly occurring close to the level of reflection in the E -region) on the measurements (Rose, 1967). As far as $L_0/(n+1)$ is concerned deviate absorption is of the order of 10% and is therefore of no significant importance for the conditions found on our transmission path in Spain. The same is true for the absorption $L(t)$ as long as it is not observed during those periods in the early morning or late afternoon, when the waves are deeply penetrating into the E -layer.

2. The Forecast Capabilities of Ground Based D-Layer Measurements at the Launching Site and Their Integration into Rocket Borne Experiments

The special task of the A_3 receiving station at the El Arenosillo launching site was to announce anomalously high or subnormally low absorption events as early as possible in order to allow sufficient time for the extensive payload and launching preparations. Together with the ionosonde and chaff cloud measurements (Rose et al., 1972a; Rose and Widdel, 1972, 1973) performed at the range, the A_3 measurements were also used to calibrate the rocket borne guarding probes in terms of electron densities versus height.

Our ability to forecast winter anomalous high or low absorption events are based on statistical considerations because no other reliable methods for forecasts exist. In this respect the experience which was gained from the A_3 measurements in Spain during the different previous winters before the campaign (Rose, 1976) was of great value. These data were used for model forecasts and reliability evaluations.

From this experience we decided to define a day of high absorption as a day for which the average absorption \bar{L} between 11.30 and 12.30 UT was higher than 50 dB for the Aranjuez-Arenosillo transmission path. A day of low absorption was one in which \bar{L} was smaller than 25 dB during that time interval. These two characteristic values corresponded on a statistical basis to 47 dB and 23 dB as far as the interval from 14.00 to 15.00 UT was concerned. This time interval was centered around the different launching times of the rockets.

From inspection of the individual daily variations of absorption during the different winters before the campaign it was clear, that winter anomalous conditions or normal conditions continued in nearly all cases over the whole day but changed from one day to the other (if at all). Because of this behaviour no useful forecasts were possible from one day to the other.

A first indication of the conditions to be expected for a given day could be anticipated in the morning at about 09.00 UT, however, with low reliability. If, moreover, the average values for the interval between 09.30 and 10.00 UT were larger than 40 dB or smaller than 20 dB, the probability that the desired conditions would be present during the launch period was between 65 and 70%. If the absorption of the days were larger than 50 dB or smaller than 25 dB around noon, the desired conditions were present in more than about 80% of the launching hours. This outlined procedure worked sufficiently well during the campaign. Only low absorption conditions did not appear as often as expected from the observations of the previous winters.

In the upper part of Figure 6 the variation of the daily absorption $L_D = L_0/(n+1)$ between December and February 1975/76 is shown for the transmission path Aranjuez-Arenosillo together with the daily variation of the exponent "n". Air temperatures, densities and pressures measured by the rocket borne chaff cloud experiment (Rose and Widdel, 1972, 1973) are displayed in the lower part of Figure 6 in comparison with the average CIRA 72 values.

From the air pressure values electron collision frequencies were estimated for D-region heights (Phelps and Pack, 1959) and were used together with the simultaneously measured (integrated) absorption and the virtual height of wave

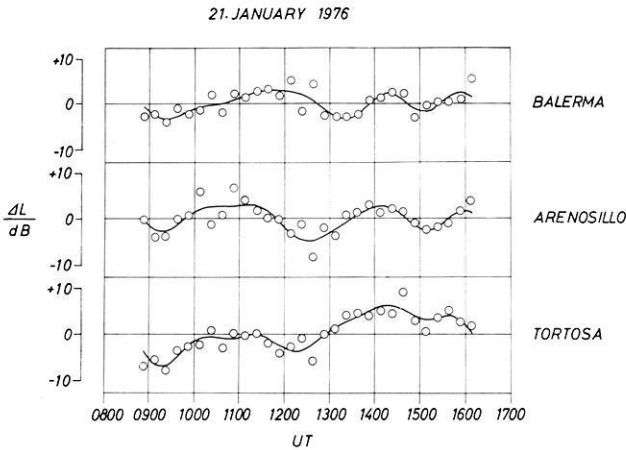


Fig. 7. Wave-like fluctuations of absorption around their associated $\cos^n \chi$ curves of best fit at the three Spanish stations observed on January 21, 1976

reflection to calibrate the relative electron density profiles as obtained from the rocket borne guarding probes. The virtual reflection height was determined by using the transmission curve technique applied to the Arenosillo ionograms with regard to the Aranjuez-Arenosillo transmission path. A more detailed description of this method will be given elsewhere.

3. On the Existence of Common Quasi-Periodic Oscillations of Different Scales at the Separated A_3 Stations

From the results collected with the different A_3 paths in Spain (from Aranjuez to Arenosillo—midpoint: 38.58° N, 5.21° W, $D=424$ km; to Balerma (Almeria)—midpoint: 38.38° N, 3.23° W, $D=374$ km; and to Tortosa—midpoint 40.45° N, 1.57° W, $D=360$ km) it became clear that the days of winter anomalous low or high absorption generally appeared simultaneously all over Spain (the correlation coefficient was $r=0.97$).

Small deviations of absorption from the best fit smoothed $\cos^n \chi$ curves were observed at the different Spanish stations. Suitably filtered, they could be traced in some cases to irregularities moving at speeds of several tens to up to about 100 m/s. An example for this type of moving wave-like structure is shown in Figure 7. In this figure the above mentioned deviations (“fadings”) of absorption around the relevant $\cos^n \chi$ curves for the three Spanish stations observed during 21 January 1976 are displayed. The points are average values for each quarter/h. The curves are Fourier-synthesized. Coefficients up to the fifth order for the displayed time interval were used. The average drift velocity of the associated pattern during that day (calculated by cross correlation) was about 30 m/s. The direction of the movement was from the north-east to the south-west. The drift direction can also be estimated by comparing the temporal locations of the valleys

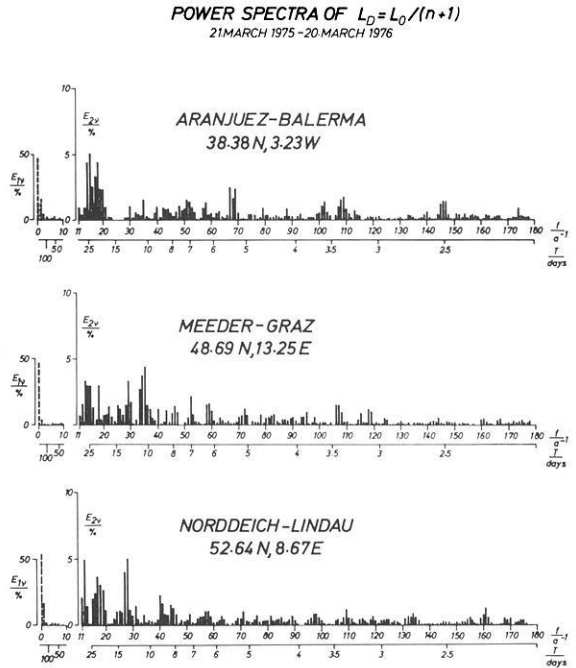


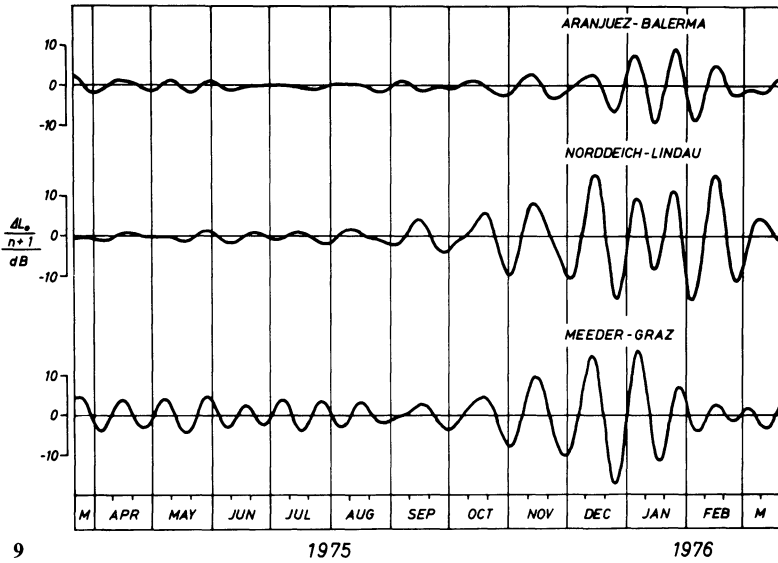
Fig. 8. Relative power spectra of the daily variations of absorption for one year of measurements in Spain, Austria and Germany. The first ten power lines at the left are drawn relative to the relevant total annual energies, the rest in each diagrams is related to the remaining energies

between about 12.30 and 13.30 UT of Figure 7 with the geographic locations of the midpoints of the different Spanish paths.

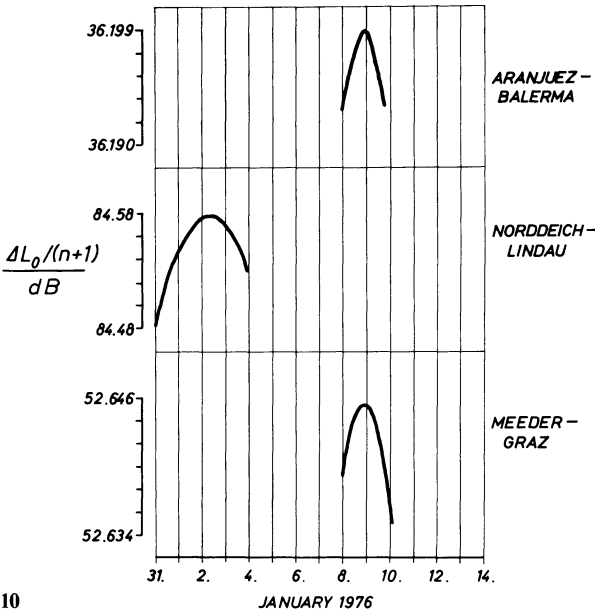
Common quasi periodic oscillations of absorption of the order of 3 weeks became evident from the spectral analysis of the daily variations of absorption L_D observed during one year of measurements in Spain, Germany and Austria. The power spectra of the absorption parameters L_D of the mentioned widely separated stations are shown in a (double) normalized form in Figure 8. If the filtered partial waves, significantly present at all the 3 stations at the same time, are synthesized (e.g. $11 a^{-1} \leq f \leq 20 a^{-1}$), maximum and rather similar amplitude variations for all the three stations were only present during the winter months starting at about November 1975 and lasting to about the beginning of March 1976 (see Fig. 9). Cross correlation calculations including the 100 days from 1 December–9 March revealed a drift of the associated spatial pattern from the west-north-west to the east-south-east at an average speed of about 3 m/s. This value corresponds roughly to an average wave-length of 5000 km.

Other quasi-periodic oscillations of absorption common to all 3 stations contained spectral components with periods around 7 and about 3.5 days (e.g. $40 a^{-1} \leq f \leq 59 a^{-1}$ and $95 a^{-1} \leq f \leq 115 a^{-1}$). These components exhibited the same trend as above: namely large amplitudes are present only during the winter months.

The trends of winter anomaly as observed during the year 1975/76 at the widely separated stations in Germany, Austria and Spain were compared with each other in different ways: The sums of the annual, half-annual and 1/3-annual



9



10

Fig. 9. Fourier-synthesized waves including $11 a^{-1} \leq f \leq 20 a^{-1}$ for the widely separated stations

Fig. 10. Trends of winter anomaly (sums of the annual, half-annual and 1/3-annual waves) for the widely separated stations at expanded scales

waves of the daily absorption resulted in single winter maxima of these synthesized trend curves which occurred simultaneously on the Spanish (Aranjuez-Balerna) and the German-Austrian (Meeder/Coburg-Graz) transmission paths, whereas the maximum was reached one week earlier in Germany on the Norddeich-Lindau path. This is evident from Figure 10 where these maxima are displayed

for clarity at a rather expanded scale. If one confines the calculations to the simple sinoidal trends of the 180 days from 24 September, 1975–21 March, 1976 only for these 3 stations, one arrives at exactly the same result as mentioned above. This corresponds to an average virtual drift of the whole “absorption front” in Central Europe during that winter from the north-east to the south west at a speed of roughly 80 km/day e.g. 1 m/s.

4. Winds at D-Region Heights and A_3 Absorption

Comparisons of the daily absorption with the D-region winds which were measured simultaneously during the last winters by in-situ rocket experiments between about 80 km and 100 km show a correlation between winter anomaly and transport processes at D-region heights. These comparisons were performed by a special correlation-finding procedure (Rose et al., 1972b) which resulted in beam diagrams which indicate the directions in the different heights from which, on the average, increasing winds were accompanied by increasing A_3 absorption.

This procedure was accomplished with all afternoon measurements performed during the Winter Anomaly Campaign and with all other winter observations which were gathered during daytime since 1972/73. The oval beam diagrams obtained for the different heights are shown in Figure 11. They are positioned like maps with the north at top and the directions from which winds were accompanied by the most significant increase of A_3 absorption on the average are indicated by arrows. The circular arcs in the figures represent the 95% or, if in the case when two are drawn, the 95% and 99% significance levels. The numbers of the measurements available for the different heights are given in brackets below the indicated height of each individual diagram of Figure 11.

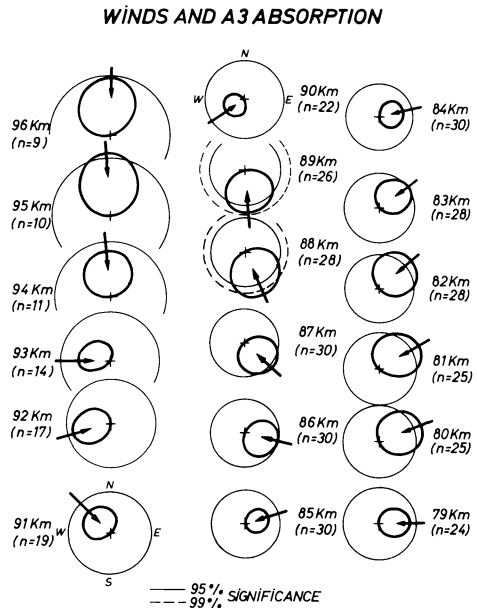


Fig. 11. Beam diagrams which indicate the directions from which increasing winds in the different heights were accompanied most significantly by increasing (integrated) absorption

There appear to be at least three levels of significance, each separated by about a scale height. It was further found by comparisons that the directions of maximum correlations at the different heights were not necessarily the same as the prevailing wind directions observed in these heights.

Acknowledgements. We are gratefully indebted to the Technische Hochschule Graz; this institution took care of the measurements of our Meeder to Graz transmission path, and to Dr. M. Friedrich for the data exchange. Our sincere thanks go also to our colleague Dr. H. Schwentek who kindly made available to us his A_3 absorption measurements collected on the Norddeich-Lindau path.

The work was sponsored by the Bundesminister für Wissenschaft und Technologie.

References

- Best, J. E., Ratcliffe, J. A.: The diurnal variation of the ionospheric absorption of wireless waves. *Proc. Phys. Soc.* **50**, 233, 1938
- Bibl, K., Rawer, K.: Les contributions des régions *D* et *E* dans les mesures de l'absorption ionosphérique. *J. Atmospheric Terrest. Phys.* **2**, 51, 1951
- Dieminger, W., Rose, G., Widdel, H. U.: On the existence of anomalous radio wave absorption during winter in 40° northern latitude. *J. Atmospheric Terr. Phys.* **28**, 317–318, 1966
- Friedrich, M., Riedler, W., Torkar, K., Ulrich, S., Urban, A., Wallner, W.: Ionospheric parameters measured during the winter anomaly campaign 1975/76. INW 7607, 1976. Report of Inst. f. Nachrichtentechn. u. Wellenausbreitung, T. U. Graz, A-8010 Graz, Austria
- Phelps, A. V., Pack, J. L.: Electron collision frequencies in nitrogen and in the lower ionosphere. *Phys. Rev. Letters* **3**, 340, 1959
- Rose, G.: Determination of *D*-layer absorption along a 2000 km path including the end points. Authorized Stanford Res. Inst. translation, pp. 1–105. Stanford Res. Inst. Menlo Park, California USA, 1967
- Rose, G.: A survey of experimental *D*-region data 1967–1975. MPAE-W-46-76-07, pp. 1–67. Report of M.P.I. f. Aeronomie, D-3411 Katlenburg-Lindau 3, FRG, 1976
- Rose, G., Schubart, W., Weber, J., Widdel, H. U.: Ergebnisse von Bodenmessungen der Kurzwellenabsorption in Spanien. *Kleinheubacher Berichte* **14**, 239–246, 1971
- Rose, G., Weber, J., Widdel, H. U., Galdon, P.: Experimental results of radio wave absorption measurements in Southwest Europe. In: *Methods of measurements and results of lower ionospheric structure*, K. Rawer, ed., pp. 331–339. Berlin: Akademie-Verlag 1974
- Rose, G., Widdel, H. U.: On the possibility of a simultaneous measurement of wind speed, wind direction, air density and air temperatures at heights which correspond to the upper *D*-region (max. 95 km) with chaff cloud sensors. *Planetary Space Sci.* **20**, 877–889, 1972
- Rose, G., Widdel, H. U.: Results of air temperature, density and pressure measurements obtained with the aid of foil cloud sensors in the height region between 80 and 95 km. *Planetary Space Sci.* **21**, 1131–1140, 1973
- Rose, G., Widdel, H. U., Azcárraga, A., Sanchez, L.: A payload for small sounding rockets for wind finding and density measurements in the height region between 95 and 75 km. *Phil. Trans. Roy. Soc. London Ser. A* **271**, 509–528, 1972a
- Rose, G., Widdel, H. U., Azcárraga, A., Sanchez, L.: Results of an experimental investigation of correlations between *D*-region neutral gas winds, density changes and short wave absorption. *Radio Sci.* **7**, Nr. 1, 181–191, 1972b
- Schwentek, H.: Bestimmung eines Kennwertes für die Absorption der Ionosphäre aus einer automatisch-statistischen Analyse von Feldstärkeregistrierungen. *AEÜ* **12**, 301–308, 1958

Received May 2, 1977

Behaviour of Ionospheric Absorption in Winter 1975/76 at about 52° N, 9° E

H. Schwentek and W. Elling

Max-Planck-Institut für Aeronomie, D-3411 Katlenburg-Lindau 3, Federal Republic of Germany

Abstract. In winter 1975/76, the diurnal variation of ionospheric absorption was measured daily at 1.73 MHz and 2.28 MHz by the pulse-reflection method, and at 2.61 MHz by field-strength recording of the transmitter DAN of Norddeich Radio. These measurements were made as a contribution to an Aeronomy Programme carried out mainly at El Arenosillo (Spain) in January 1976. The behaviour of characteristic absorption data in the period March 1975 to September 1976 is presented and discussed. It is stressed that the term “winter anomaly” can be applied to the variation of many parameters of the middle atmosphere, ionospheric absorption being only one of these.

Key words: Aeronomy – Ionospheric absorption – Winter anomaly.

Introduction

As a contribution to an Aeronomy Programme carried out in January 1976 at El Arenosillo, Spain, at Lindau, continuous measurements of ionospheric absorption were made. This work was mainly done from a synoptic point of view, using the behaviour of absorption as a diagnostic tool, in order to check to which extent the behaviour of absorption at El Arenosillo would be similar to that at Lindau, particularly, as far as excessive absorption, pointing to winter-anomaly conditions (Schwentek, 1976) is concerned. What could be expected? From synoptic studies it was clear that El Arenosillo, situated at 38°N, is near the southern border of the winter-anomaly zone (Elling et al., 1974; Schwentek, 1976). Moreover, the aeronomy programme had to be carried out near sunspot minimum, when the amount of winter-anomalous absorption is lowest (Röttger and Schwentek, 1974). Thus, the probability to meet winter-anomaly conditions was low. But monitoring absorption at Spain, conditions of winter-anomaly could be and were detected there (Rose and Widdel, 1977).

Concerning a correlation between the behaviour of absorption at Lindau (52.6°N) and El Arenosillo (38°N), it was shown earlier (Schwentek, 1974), that at the distance of 2000 km between Lindau and El Arenosillo, in general, the threshold of significance for a correlation is reached, but that just for these two stations still a significant correlation could be expected.

In this paper, the data obtained at Lindau are only discussed with respect to the behaviour of absorption at Lindau. But the data were made available to some other participants in the campaign mainly for correlation analysis.

A Remark Concerning the Term “Winter Anomaly”

Since the aeronomy programme carried out at El Arenosillo/Spain was mainly aimed at the study of the “winter anomaly”, it seems to be reasonable to recall shortly the anomalous phenomena occurring in winter at middle latitudes. Originally, the term winter anomaly pointed to the fact that the seasonal variation of absorption of radio waves in the ionosphere does not depend merely on solar zenith angle χ . Whereas absorption is constant for constant χ at low latitudes, at middle latitudes it shows a considerable enhancement in winter, and very often superimposed excessive values. Moreover, during days of excessive absorption, the reflection heights are found to be relatively low, about 80 km, as was pointed out already by Dieminger (1952).

Considering other parameters of the middle atmosphere than absorption which are available as time series, as, for instance, the maximum electron density of the E layer, a very similar behaviour was found as for absorption; the same is true for stratospheric temperature (stratospheric warmings) Schwentek (1968). In other words, at temperate latitudes, the entire middle atmosphere, shows a more or less anomalous behaviour in winter. An effect should be found also on other parameters as atmospheric temperature, pressure, composition, wind systems etc. Since the variation depends on time as well as on space a region should be considered with a diameter of at least 2000 km, or even the entire Northern and Southern Hemisphere. As a matter of fact the events of excessive absorption appear as weather-like phenomena of regional extent distributed in patches over the entire middle latitude band of a hemisphere (Schwentek, 1974). – Finally, even if the particular electron-density profiles appearing during winteranomalous days may be attributed to corresponding height profiles of NO, as is suggested, it remains still unclear, how these particular NO profiles were produced, and how they are geographically distributed. This point is made in order to encourage a synoptic study of the NO distribution.

Methods of Measurement and Data Reduction

At Lindau, measurements were continued at 2.61 MHz, at oblique incidence of the waves, by recording the signal strength of the transmitter DAN of Norddeich Radio. By means of a statistical counter, frequency distributions of signal strength were produced for every half an hour (Schwentek, 1966). Simultaneously, measurements were made at 1.73 and 2.28 MHz, at vertical incidence, applying the pulse-reflection method; the equipment used was the same as earlier on board a ship (Barke et al., 1974). Details concerning the methods can

Table 1. Number of days and percentage of ranges in the correlation coefficients calculated from daily regression lines $\log L$ vs. $-\log \cos \chi$

A: 2.61 MHz; summer: 21 June–22 September 1975 plus 22 March–22 June 1976. B: 2.61 MHz; winter: 23. September 1975–21 March 1976. C: 1.73 MHz; winter 11 November 1975–21 March 1976. D: 2.23 MHz; winter: 11 November 1975–21 March 1976. C and D: corrected for τ

Correlation coefficient	1.0–0.951	0.95–0.901	0.90–0.851	0.85–0.801	0.80–0.751	0.75–0.701	0.70–0.651	0.65–0.601	< 0.60
A (days)	37	69	31	30	5	3	2	0	2
%	20.7	38.5	17.3	16.7	2.8	1.7	1.1	0	1.1
B (days)	31	50	21	20	18	8	6	6	20
%	17.2	27.8	11.7	11.1	10.0	4.4	3.3	3.3	11.1
C (days)	41	43	20	14	4	4	2	2	3
%	30.8	32.3	15.0	10.5	3.0	3.0	1.5	1.5	2.2
D (days)	40	32	24	12	12	2	1	3	4
%	30.8	24.6	18.5	9.2	9.2	1.5	0.8	2.3	3.1

be found in the Manual of Ionospheric Absorption Measurements edited by Rawer (1976).

The photographic recording of the reflected pulses used gives not only absorption data, but also accurate heights of pulse-reflection. The shapes of the reflected pulses give hints on irregularities in the layers, and on dynamic processes.

Data reduction was carried out by electronic desk calculators. The diurnal variation of absorption $L(t)$ was approximated by the equation

$$L(f; t) = L_0 \cos^n \chi(t - \tau), \quad (1)$$

with f operational frequency, t time, χ solar zenith angle, τ a delay time, L_0 subsolar absorption.

Characteristic values of the diurnal variation are subsolar absorption L_0 , exponent n , and absorption at $\cos \chi = 0.2$; these data were obtained from plots of $\log L$ vs. $-\log \cos \chi$. Consecutive median values of five half (or quarter) hours were used to determine automatically the regression line. Experience showed that this special procedure gives the most reliable data for characterizing the average behaviour of absorption for each day and that short deviations in absorption due to local or solar effects are eliminated. Calculated distributions of correlation coefficients are given in Table 1. They show a rather regular behaviour in the diurnal variation of absorption in summer, and a larger scatter during winter, thus pointing to particular, disturbed conditions in the lower ionosphere. That is, the correlation coefficient may be considered to be a measure of the regularity or irregularity, respectively, of the diurnal variation of absorption.

The daily average of τ , which was applied to the data obtained by vertical-incidence pulse-amplitude measurements, was determined as follows.

At first, consecutive median values of absorption, L , were calculated for sets of every 5 consecutive absorption values floating over the entire diurnal variation. From such values, a series of regression lines $\log L(t) = \log L_0 + n \log \cos \chi(t - \tau)$ was determined, varying τ until the standard deviation of the data pairs

$\log L$ vs $-\log \cos \chi$ reached a minimum. Then, the corresponding value of τ is the wanted delay time. A comparison of the data in Table I shows that the procedure of taking into account τ leads to better correlation coefficients (C, C); such a computation, however, is time consuming.

Results of Measurements

A survey on the behaviour of absorption at constant zenith angle $\chi=78.5^\circ$, $L(\cos \chi=0.2)$, in winter 1975/76, is given in Figure 1. Values $L(\cos \chi=0.2)$ may be considered as a characteristic parameter of the day. Since the period March 1975–September 1976 is near sunspot minimum, in summer (21 March–21 September) $L(\cos \chi=0.2)$ is nearly constant showing a pronounced minimum in April (see also Schwentek, 1971b). A weak period should be noted; it is not yet quite clear whether it is significant or not. In winter 1975/76, again the well known two types of absorption were found: the regular increase of absorption until the winter solstice, then the decrease until the end of March, and, superimposed on this regular trend, days of excessive absorption (Schwentek, 1971a).

Concerning the correlation of these data with those obtained at El Arenosillo see the analysis made by Rose and Widdel (1977).

In Figure 2 the variation in winter of reflection height h' (upper part), and absorption at $\cos \chi=0.2$ (lower part) is shown for the frequency 1.73 MHz. It shows that, in general, periods of days, or single days, of excessive absorption correlate with the occurrence of low reflection heights. This indicates that during extreme winter-anomalous conditions increased electron densities at lower heights have to be expected. This correlation can be understood by considering electron-density profiles obtained from rocket-measurements in summer, and in winter, showing in winter a marked enhancement of electron concentration between 78 and 88 km (Dickinson et al., 1976). Correspondingly, during conditions of excessive winter-anomalous absorption, at 1.73 MHz, and partly also at 2.28 MHz, stable reflections from heights between 70 and 85 km have been observed, the amplitudes of echoes simultaneously reflected from heights above 85 km being very weak because of strong deviative absorption; that is, the associated profiles are thought to have ledges in the 70–85 km height range causing strong partial reflections.

The electron-density profiles presented by Dickinson et al. (1976) show also that the height gradients of electron density dN/dh , considered at 1.73 and 2.28 MHz, (electron densities 3.7×10^4 and 6.5×10^4 el/cm³, respectively) are greater in summer than in winter. Because the deviative absorption is inversely proportional to dN/dh , the deviative absorption near the point of reflections is greater in winter than in summer. That is, in winter, in the morning and afternoon, the used operational frequencies are often rather near to E-layer critical frequency.—It was thought and discussed to check at El Arenosillo during the winter anomaly campaign the relation mentioned above between absorption, heights of reflection, and electron-density profile in detail by combining a multifrequency absorption measurement and a partial reflection measurement. But these experiments could not be carried out.

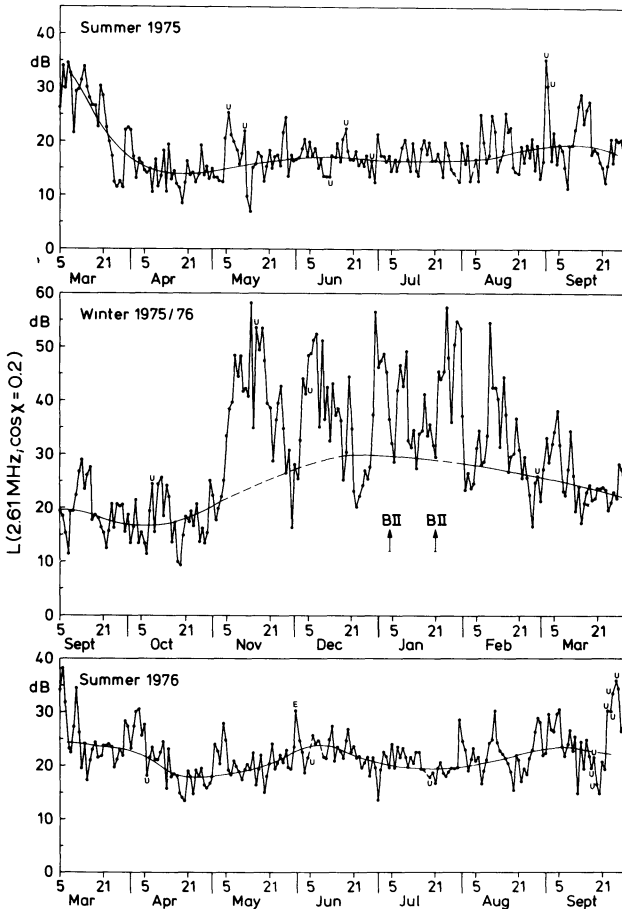


Fig. 1. Absorption in the ionosphere at a constant zenith angle $\chi = 78.45^\circ$, $L(\cos \chi = 0.2)$, derived from the diurnal variation of each day in the period March 1975–September 1976. Method A3 (field-strength recording), frequency $f = 2.614$ MHz, distance transmitter–receiver $d = 296$ km; equivalent frequency 1.5 ± 0.25 MHz corresponding to virtual heights of reflection of 105 ± 25 km. The point of reflection is at 52.6°N , 8.7°E . In summer, the included curve was drawn according to overlapping median values taken for 15 days periods; in winter, however, the regular seasonal variation is tentatively shown; on this the excessive, winter-anomalous absorption is considered to be superimposed. –BII, day on which the payload BII was launched at El Arenosillo/Spain. *U* uncertain value. *E* extraordinary diurnal variation

In winter the average height of reflection at noon is 103 km at 1.73 MHz, and 124 km at 2.28 MHz.

In Figure 3 the seasonal variation of an average of exponent n is presented. This exponent may be considered as the basic parameter for describing the diurnal variation of absorption. It depends not only on season, but also on geographic latitude, operational frequency, and angle of incidence of the radio wave. Two features should be noted in Figure 3, a wave-like variation, and a winter-anomalous enhancement with a maximum around 15 January. It should

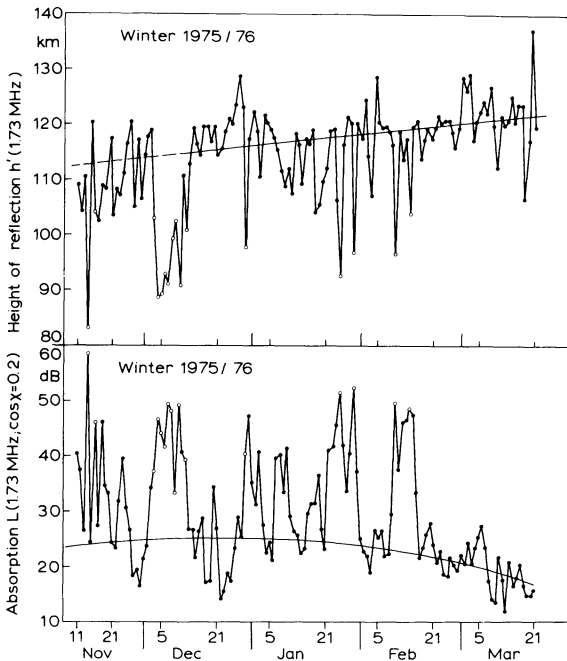


Fig. 2. Upper part: Daily mean values of apparent height of reflection h' taken from the time spans ± 18 min around the time of $\cos \chi = 0.2$ in the morning and in the afternoon; method A1 (vertical incidence), f : 1.73 MHz. Lindau: $51^{\circ}39'N$; $10^{\circ}7.5'E$. Lower part: Daily mean values of absorption taken from the time spans ± 18 min around the time of $\cos \chi = 0.2$ in the morning and in the afternoon. — Open circles indicate days of very low reflection heights and high absorption

be remembered that also the excessive values of $L(\cos \chi = 0.2)$ show a tendency to occur preferably in January, while the smaller values show a maximum centered around winter solstice.

The wave-like variation in the n values, as well as in L_0 and $L(\cos \chi = 0.2)$ values, was analysed. The power spectra obtained from a Fourier analysis shows predominant periods occurring simultaneously in the time series of $L(\cos \chi = 0.2)$, L_0 , and n . The periods vary between 84 and 92, 28 and 30, 19 and 22 days. Applying a bandpass digital filtering (Kertz, 1965) using the above mentioned bands, average periods of 88.5, 29.5, and 21.5 days were found. The period of 88.5 days is the most dominant in the n values, and was observed throughout the observational time span. The periods of 29.5 and 21.5 days emerged only during the winter. It is interesting to note that the period of 88 days is the sidereal period of Mercury, that of 29.5 days the synodical period of the Moon. However, this fact may be mentioned here without discussing whether this correlation is merely accidental, or not.

The enhancement of n in winter has to be considered as a distortion of the periodic variation in n , pointing to an additional physical process superimposed on the process causing the wave-like variation.

It should be recalled that exponent n has a physical meaning, while subsolar absorption L_0 is a formalistic factor, which becomes physically meaningful only

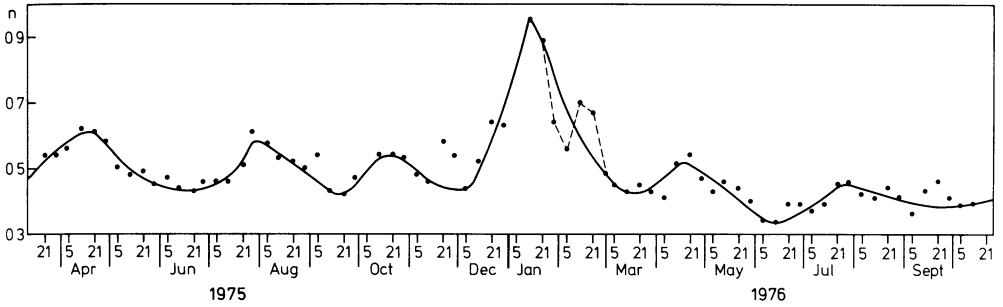


Fig. 3. Seasonal variation of an average value of exponent n . The plotted data were obtained from daily n values; $f = 2.61$ MHz. For every 15 or 16 days, starting with the period 5–21 March 1975, and proceeding in steps of about 8 days, the lower and upper quartile values were determined, and then the mean values of all the n data between the 2 quartile values were calculated. A similar result can be obtained also using the median values of the quoted periods. The curve was drawn tentatively to show the wave-like variation in the seasonal behaviour of exponent n ; the mean period obtained from the plot is about 96 days. Note that the maximum in winter occurs at 15 January, that is about 4 weeks delayed related to the winter solstice

at latitudes where the solar zenith angle becomes 0; this occurs at latitudes between 23.5° North and South to the equator. In this region L_0 is really the measured subsolar absorption. It can be shown that L_0 may be presented as a function only of exponent n . This relationship will be presented and discussed elsewhere.

A comparison of the seasonal variation of $L(\cos \chi = 0.2)$ at 1.73 MHz, 2.23 MHz, and 2.61 MHz (equivalent frequency 1.5 ± 0.25 MHz; heights of reflection varying from 80–140 km) showed that the day-to-day variation is rather similar. The lowest frequency 1.73 MHz, however, reacted most sensitively on winter-anomalous conditions, that is, showed the largest variation in absorption values.

Comparing Figure 1 and Figure 3 the long, weak periods in $L(\cos \chi = 0.2)$ and n appear to be out of phase. An analysis showed that the optimal correlation coefficient ($=0.47$) is obtained when values of $L(\cos \chi = 0.2)$ are shifted by 42 days against the n values. This result is reasonable, for, from plots $\log L$ vs. $-\log \cos \chi$ it is clear that, in general, a small n gives a high $L(\cos \chi = 0.2)$, and vice versa. Using the data obtained from the measurements made at 1.73 and 2.28 MHz, it was studied whether the delay time τ might be correlated with exponent n . The correlation coefficient is 0.04, it is not significant.

A correlation between atmospheric pressure at ground and the behaviour of ionospheric absorption might perhaps emerge. Very probably, it will be significantly observed only every tenth winter, but, in general, does not seem to exist (Schwentek, 1974). Therefore, during winter 1975/76, at Lindau, by means of a micro-barograph (sensitivity 3.75 mm per millibar), also atmospheric pressure at ground was recorded. A significant result did not reveal; this may be due also to the unregular behaviour of atmospheric pressure in winter 1975/76 which shows no particular wave-like variation.

References

- Barke, W., Elling, W., Geisweid, K.H., Heimesaat, G., Loidl, A., Römer, C., Schwentek, H., Zellermann, R.: The southern boundary region of the winter anomaly in ionospheric absorption in winter 1971/72 observed on board a ship between 10° and 55°N, W. Dieminger, G. Pfozter, eds. Mitt. Max-Planck-Institut für Aeronomie, Nr. 51. Berlin-Heidelberg-New York: Springer 1974
- Dickison, P.H.G., Hall, J.E., Bennett, F.D.G.: Rocket measurements of electron concentration in the lower ionosphere at two European locations. *J. Atmospheric Terrest. Phys.* **38**, 163–173, 1976
- Dieminger, W.: Über die Ursache der exzessiven Absorption in der Ionosphäre an Wintertagen. *J. Atmospheric Terrest. Phys.* **2**, 340–349, 1952
- Elling, W., Geisweid, K.H., Schwentek, H.: Shipborne observations of the southern boundary of the winter anomaly in ionospheric absorption. In: *Methods of measurements and results of lower ionosphere structure*, K. Rawer, ed., pp. 313–318. Berlin: Akademie-Verlag 1974
- Kertz, W.: Filterverfahren in der Geophysik. *Gerlands Beitr. Geophysik* **75**, 1–33, 1965
- Rawer, K., ed.: *Manual on ionospheric absorption measurements*. World Data Center A for Solar-Terrestrial Physics. Report UAG-57. NOAA, Boulder, Colorado, June 1976
- Rose, G., Widdel, H.U.: D-region radio-wave propagation experiments, their significance and results during the western European winter-anomaly campaign 1975/76. *J. Geophys.* **44**, 15–26, 1977
- Röttger, J., Schwentek, H.: A numerical description of the winter anomaly in ionospheric absorption for a sunspot cycle. *J. Atmospheric Terrest. Phys.* **36**, 363–366, 1974
- Schwentek, H.: The determination of absorption in the ionosphere by recording the field strength of a distant transmitter. *Ann. Géophys.* **22**, 276–288, 1966
- Schwentek, H.: Ähnlichkeiten im jahreszeitlichen Verhalten der Stratosphäre und der D- und E-Schicht der Ionosphäre. *Z. Geophys.* **34**, 123–146, 1968
- Schwentek, H.: Regular and irregular behaviour of the winter anomaly in ionospheric absorption. *J. Atmospheric Terrest. Phys.* **33**, 1647–1650, 1971a
- Schwentek, H.: The sunspot cycle 1958/70 in ionospheric absorption and stratospheric temperature. *J. Atmospheric Terrest. Phys.* **33**, 1839–1852, 1971b
- Schwentek, H.: Wave-like structures in the variation of ionospheric absorption. *J. Atmospheric Terrest. Phys.* **36**, 1173–1178, 1974
- Schwentek, H.: Some results obtained from the European Cooperation concerning studies of the winter anomaly in ionospheric absorption. In: *Methods of Measurements and results of lower ionosphere structure*, K. Rawer, ed., pp. 293–303. Berlin: Akademie-Verlag 1974
- Schwentek, H.: Ionospheric absorption between 53°N and 53°S observed on board ship. *J. Atmospheric Terrest. Phys.* **38**, 89–92, 1976

Received May 2, 1977

Observations of the Oxygen Green Line Airglow during the Winter Anomaly Campaign 1975/76

H. Lauche

Max-Planck-Institut für Aeronomie, D-3411 Katlenburg-Lindau 3, Federal Republik of Germany

Abstract. Airglow emission of the E-layer has been observed from the ground during the Winter Anomaly Campaign 1975/76. It has been established by earlier *in situ* measurements that the brightness of the oxygen green line is proportional to the second power of the oxygen density. A ground-based photometer was used for monitoring the oxygen density. A relationship between emission rate $B_{\lambda=557.7 \text{ nm}}$ and radio wave absorption was found.

Key words: Airglow – Radio wave absorption.

Red and green oxygen emission from the upper atmosphere was measured from the ground by means of a 4-channel all-sky scanning photometer at Arenosillo, Spain, during the winter anomaly campaign 1975/76. Two of these channels were tuned to the emitted wavelength; the other channels were used to measure simultaneously the background continuum. The line channels and the background channels were matched to give the same response over a wide range of incident photon rate. The photon rate from the background channel was subtracted automatically.

Even when the background brightness was more than 20 times stronger than the line emission, it was possible to measure the line intensity. The sensitivity of this photometer was very stable and checked daily (29 ± 3 counts per Rayleigh). In this way it was possible to make reliable observations even under hazy conditions close to full moon. The great number of measured points in the sky permitted a fairly good approximation to the transmission of the lower atmosphere. The loss of light can be recalculated when the vertical transmission is better than 0.5.

The oxygen green light is emitted from 1S state. This state is produced by the Chapman or the Barth mechanism [Chapman, 1931; Barth et al., 1961]. Both mechanisms give approximately the same production rate of 0 (1S).

Due to the long life time of this state (see Fig. 1) exited atoms are partly quenched by collisions. Recent measurements have shown that atomic oxygen

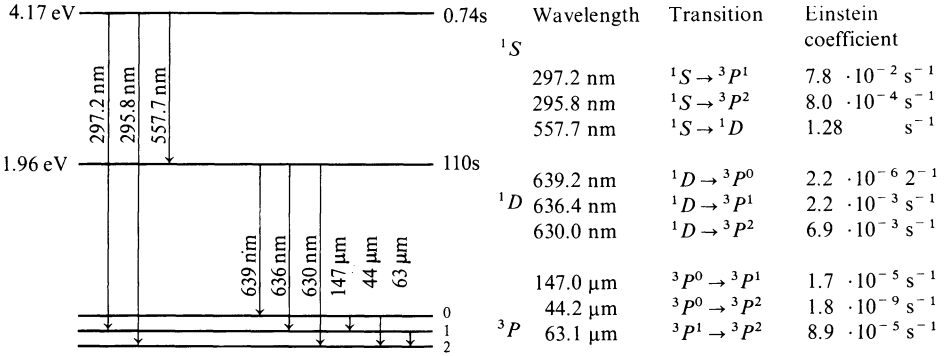


Fig. 1. Excitation terms of Oxygen

is the most important quencher [Offermann and Drescher, 1973; Slinger and Black, 1976]. Quenching by O_2 and N_2 can be neglected.

The rate of emission $I_{\lambda=557.7 \text{ nm}}$ obeys the following equation:

$$I_{\lambda=557.7 \text{ nm}} = \frac{K_1 [0]^3}{1 + K_2 [0]} \quad [\text{Photons cm}^{-3} \text{ s}^{-1}]$$

$$K_1 = 1.4 \times 10^{-30} e^{\left(\frac{-1300}{RT}\right)} \quad [\text{cm}^6 \text{ molecule}^{-2} \text{ s}^{-1}]$$

$$K_2 = 5 \times 10^{-11} e^{\left(\frac{-610}{RT}\right)} \quad [\text{cm}^3 \text{ molecule}^{-2} \text{ s}^{-1}]$$

Variations of the emission rate are caused by changes of either the oxygen density or the neutral gas temperature.

When starting airglow observations at the beginning of the winter anomaly campaign, we expected higher quenching after times of anomalous high absorption, due to heat flux from lower layers.

Upon comparing variations of airglow intensities and of radio wave absorption, correlated periodic variation of about 1 to 2 h were observed with both methods, (see Fig. 2); the correlation coefficient was 0.73 with absorption lagging about 12 h behind the airglow.

The regular behaviour of both effects makes it possible to predict radio wave absorption from the observed nightglow. A typical example is shown in Figure 4.

During the night a strong increase of emitted light was measured and about half a day later strong radio wave absorption was observed.

Changes of oxygen density are probably one important source winter anomaly effects.

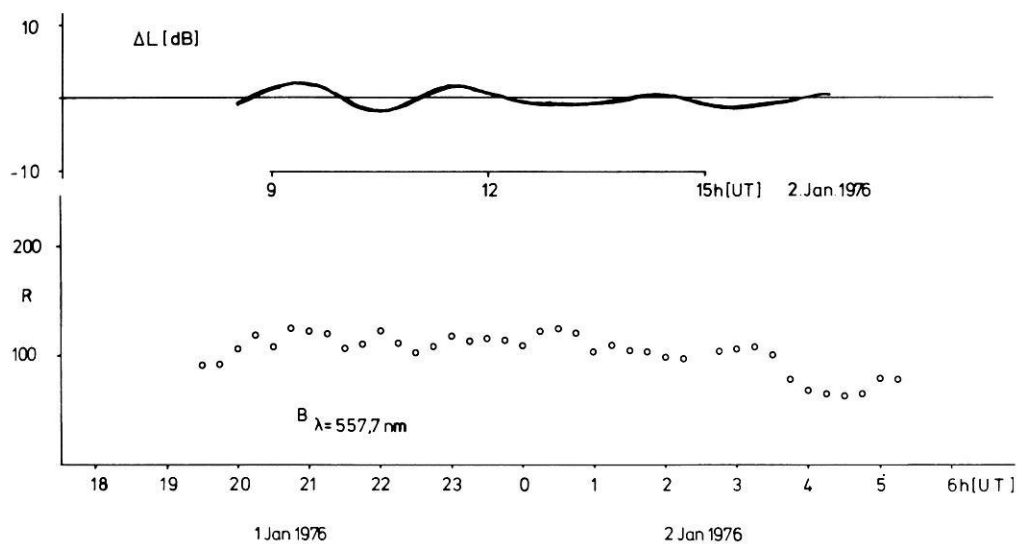


Fig. 2. Periodic variations of airglow and radio wave absorption

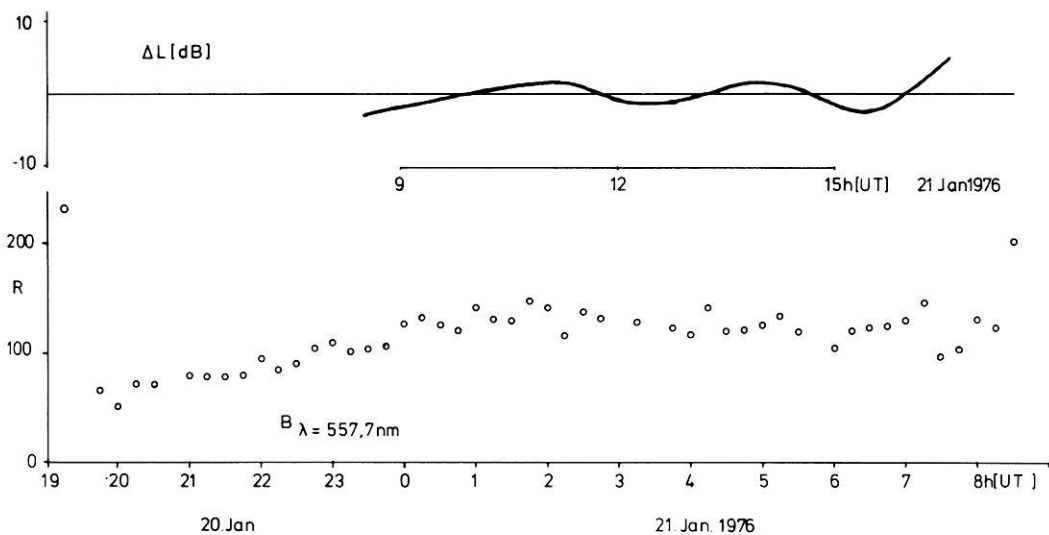


Fig. 3. Variation of radio wave absorption compared with the brightness of the night before

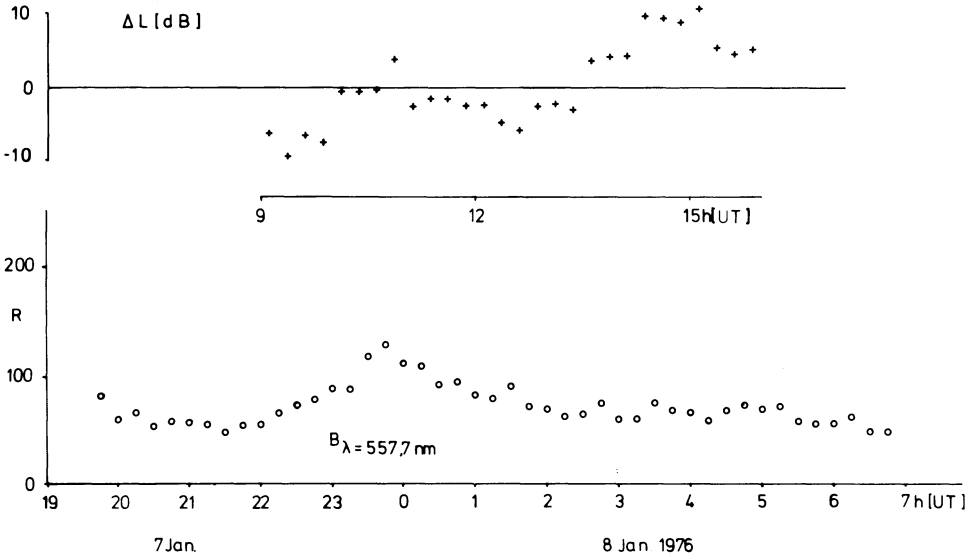


Fig. 4. Strong variation of airglow brightness indicating changes of radio wave absorption during the following day

For future experiments, ground-based equipment capable of determining temperatures in the emitting region would be very helpful.

References

- Chapman, S.: Some phenomena of the upper atmosphere. Proc. Roy. Soc. London Ser. A **132**, 353–374, 1931
- Barth, C.A., Hildebrandt, A.F.: The 5577 Å Airglow Emission Mechanism. J. Geophys. Res. **66**, 985–986, 1961
- Offermann, D., Drescher, A.: Atomic Oxygen Densities in the Lower Thermosphere as Derived from In Situ 5577-Å Night Airglow and Mass Spectrometer Measurements. J. Geophys. Res. **78**, 6690–6700, 1973
- Slinger, Tom G., Black, Graham: O (¹S) quenching by O (³P). The Journal of Chemical Physics, Vol. **64**, Nr. 9, 3763–3766, 1976

Received May 2; Revised Version June 28, 1977

Co-Ordinated Meteor Wind Observations from Sheffield during the January 1976 Winter Anomaly

Heinz G. Muller* and Simon P. Kingsley

Department of Physics, University of Sheffield, Sheffield S3 7RH, United Kingdom

Abstract. Ground based upper atmospheric wind measurements in the 80–110 km region were made at Sheffield on three specific occasions during the El Arenosillo winter anomaly campaign in January, 1976. The radio meteor method employed in this study is described in some detail. Preliminary results indicate that appreciable wave activity was present throughout the duration of the campaign. There is little evidence, though, from the structure of the prevailing winds for significant NS air motions which are currently thought to be responsible for the transport of nitric oxide and other minor constituents from the auroral zone toward mid latitudes during a winter anomaly. Such transport may, however, have been effected by large scale wave motions, with periods of the order of 20 days, whose presence is suggested by the Sheffield data.

Key words: Wind velocity measurement – Wind profiles – Diurnal variations – Periodic variations – Atmospheric circulation – Meridional flow – Ionospheric disturbances.

Introduction

Past investigations of upper atmospheric winds by the radio meteor method have shown that the dominant wind systems have a distinctly periodic character. Apart from the well known diurnal and semidiurnal tidal oscillations variations with periods in excess of one day are quite common (Muller, 1972; Muller and Kingsley, 1974). While at lower altitudes the wind is essentially zonal appreciable meridional components are observed at meteor heights and it has been argued that the meridional flow may be responsible for the transport of nitric oxide (NO) and other minor constituents from the auroral zone to temperate latitudes. NO and other constituents may thus travel considerable distances during their lifetime bringing about the photochemical and electron

* To whom offprint requests should be sent

density changes associated with a winter anomaly. The so called prevailing wind (often no more than an unresolved component of a long period wind oscillation) may also be considered as a means for NS atmospheric transport. It is therefore of paramount importance to examine both the prevailing and periodic wind components over a wide geographic area at such times when the nature of other atmospheric parameters, for example D-region absorption, indicate the development of a winter anomaly.

Such efforts were made in a co-ordinated experiment during the El Arenosillo winter anomaly campaign, January, 1976, involving three meteor wind stations, at Sheffield (U.K.), Garchy (France) and Bologna (Italy), respectively. Although the techniques employed at these stations differ slightly amongst themselves data of identical quality, with similar spatial and temporal resolution, have been obtained over sufficiently long periods of time to allow a good description of neutral winds over a NS baseline of nearly 1000 km. The meteor wind measurements were supplemented by ionospheric drift measurements from Nancy and St. Cassien thus increasing the amount of information available on the general atmospheric circulation in the upper mesosphere and the lower thermosphere.

The present report describes the measurements conducted during three specific periods at Sheffield in January, 1976. Reference is made, in particular, to the presence of meridional wind components as a possible means of transport for minor atmospheric constituents. It is clear that the Sheffield results will become more meaningful when viewed synoptically with those obtained elsewhere. A co-ordinated study of the winter anomaly results is already in progress and will be reported on during the next Cospar meeting at Tel Aviv in June, 1977.

Technique

Measurements of neutral air motions in the region 80–110 km can now be carried out at Sheffield on a routine basis with the use of a 36 MHz coherent pulse Doppler radar. The transmitter has a peak power of 200 kW and is operated in short pulse (25 μ s) mode alternately on two Yagi-Udah aerial arrays directed NW and SW, respectively. Echoes from meteor trains are received by two interferometers, one facing NW, the other SW, and a phase comparison between the transmitted and received signals allows the radial velocity of a meteor train to be measured with an accuracy of ± 2 m s⁻¹. The phase information on the echo wave available from the two interferometers forms the basis, together with the echo range from the pulse delay, for the computation of echo heights in the two preferred directions with a resolution of ± 2 km. It is thus easy to calculate the horizontal wind flow for each echo from the measured radial velocity and by recording echoes sequentially a meaningful vertical wind profile may be established within about 15–20 min. An example of wind data obtained in such a fashion during the January, 1976 winter anomaly campaign is shown in Figure 1. It is seen that individual wind components can be resolved without appreciable data gaps between 80 and 120 km altitude. The apparent

Fig. 1. The variation of meteor wind velocities from Sheffield as a function of height for 2 individual periods of observation, selected at random, during the El Arenosillo winter anomaly campaign. The time indicates the length of recording required to establish a meaningful vertical wind profile

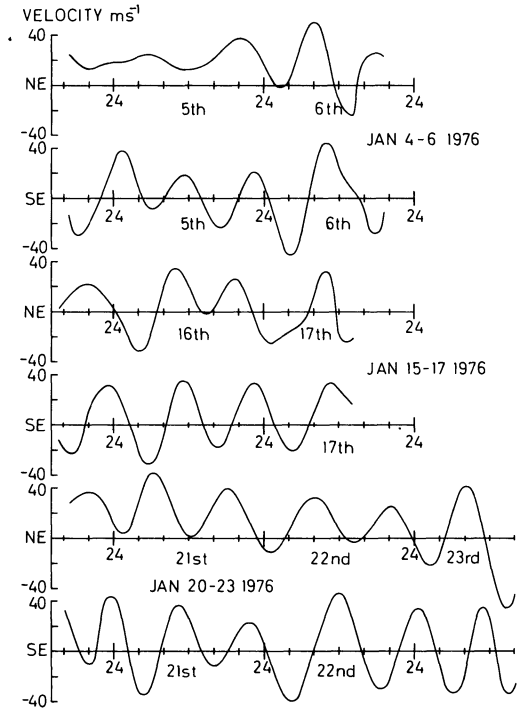
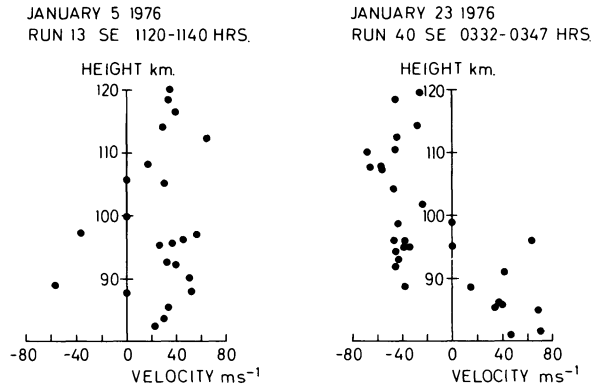


Fig. 2. Average NE and SE meteor wind components from Sheffield for a mean height of 97 km in the form of best fitting polynomials to the raw data

scatter in the data is currently interpreted in terms of the limited height resolution of about 2 km while it is known from rocket vapour trail experiments that wind shears of about 50 m s^{-1} quite commonly occur over a height of about 1 km. It is worth pointing out that the number of available meteor echoes varies appreciably in the course of a day. At times near the maximum (about 06.00 local time) the hourly rate may be 50 times that near the minimum (about 18.00 local time) with a consequent data loss in the hours of the afternoon,

affecting in particular the top and bottom of the meteor region because of the uneven echo number distribution in the vertical. The data profiles shown in Figure 1 relate to times of average meteor activity when a quasi-instantaneous wind profile may be obtained without difficulty. A lower meteor rate would necessitate longer recordings, of up to 1 h, in order to cover smoothly the whole vertical extent of the meteor region. Unfortunately, the wind structure tends to vary appreciably from hour to hour such that recordings have to be limited to a maximum length of about 20 min. It is therefore customary to accept the data loss at certain heights and average within finite height intervals. The present results have thus been grouped into 3 main intervals such that continuous data time series are made available for three average heights. This appears adequate for the description of large scale wind features required in this study.

These time series are harmonically analysed in order to determine tidal components and, when of sufficient length are subjected to spectral analysis involving best fitting polynomial curves to the raw data.

The data at Sheffield are at present displayed on a 24 channel U.V. chart recorder. Information is extracted from the charts manually prior to computer processing which causes considerable delay in the production of the final results. It was therefore impracticable to record continuously during the whole campaign; instead the Sheffield radar was operated on three occasions for limited periods (between 2 and 3 days) while intensive observations were taking place at other stations involved in the winter anomaly campaign.

Results

Recordings of meteor winds from Sheffield took place during the following intervals in January, 1976: (i) from 17.00 on the 4th to 20.00 on the 6th, (ii) from 15.00 on the 15th to 15.00 on the 17th, and (iii) from 17.00 on the 20th to 17.00 on the 23rd. All times quoted in this report are universal time (G.M.T.). The difference between U.T. and local mean time may be neglected for the present purposes since it is only 6 min.

In order to facilitate a general comparison of the data with those obtained elsewhere average winds have been computed for the whole of the meteor region by using all the measurements, regardless of altitude. These correspond to an average altitude of about 97 km, an altitude where the distribution of echo numbers shows a pronounced peak for the Sheffield radar system. Polynomial curves have been fitted to the raw data, using a least square method, and these are shown, for the NE and SE components, respectively, in Fig. 2. All curves indicate a pronounced semidiurnal variation which may be attributed to the effects of the solar tide. Diurnal variations, though not conspicuous in the curves, are resolved by harmonic analysis. Individual trends in the data are well marked and are now understood to be the effect of unresolved oscillations whose periods exceed the lengths of the data series. By averaging all velocities over each period of observation the so called prevailing wind is obtained. Notations in this report conform to the ionospheric convention such that a positive NE amplitude represents a wind blowing toward the NE.

Table 1. The semidiurnal tide during January, 1976

Date	Altitude (km)	NE		SE		U		V	
		Phase (de- grees)	Amp (m s ⁻¹)						
4-6	76-90	165	22	273	20	215	18	131	24
4-6	91-104	133	18	225	41	201	31	68	32
4-6	105-118	139	27	216	34	183	34	79	27
15-17	Av. 97	270	25	333	28	304	32	205	19
20-23	76-90	255	23	354	26	308	22	213	26
20-23	91-104	220	29	307	33	267	32	170	31
20-23	105-118	200	23	279	31	247	29	139	24
20-23	Av. 97	226	24	305	26	267	28	173	24

Table 2. The diurnal tide during January, 1976

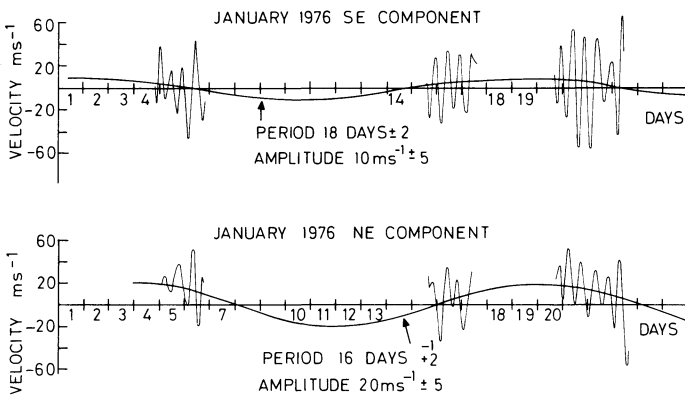
Date	Altitude (km)	SE		NE		U		V	
		Phase (de- grees)	Amp (m s ⁻¹)						
4-6	76-90	262	7	167	14	194	11	321	12
4-6	91-104	196	6	124	9	153	9	265	7
4-6	105-118	284	17	91	4	288	9	281	15
15-17	Av. 97	228	7	249	4	235	8	204	3
20-23	76-90	252	9	209	7	234	11	299	5
20-23	91-104	38	7	247	6	236	3	52	9
20-23	105-118	141	7	287	11	250	5	120	12
20-23	Av. 97	87	7	215	6	273	4	156	7

The data for January 4-6 and 20-23 were recorded while extensive rocket experiments were under way at El Arenosillo. Because of the importance of these particular periods we have conducted data analysis for 3 individual height regions in order to examine the vertical propagation, or their absence, of the periodic wind components. For the middle period, January 15-17, only average wind parameters for a mean height of 97 km have been investigated.

The results of harmonic analysis of the data series for the various periods of observation have been condensed in 3 tables. Table 1 contains information on the semidiurnal tidal oscillation which is the most pronounced at all altitudes. The data show that the tidal wind may be represented by an elliptically rotating vector with an amplitude of about 20-30 m s⁻¹ with the phase of maximum velocity toward N near 06.00 local time. Phase variations in the vertical are

Table 3. The "prevailing" wind during January, 1976

Date	Altitude (km)	NE (m s ⁻¹)	SE (m s ⁻¹)	Total Mag. (m s ⁻¹)	Direction E of N Degrees	U (m s ⁻¹)	V (m s ⁻¹)
4-6	76-90	30	- 5	30	35	17	25
4-6	91-104	34	-13	36	24	14	33
4-6	105-118	24	- 2	24	41	16	18
15-17	Av. 97	-1	6	6	144	4	-5
20-23	76-90	13	6	14	70	13	5
20-23	91-104	12	1	12	50	9	7
20-23	105-118	8	2	8	59	7	4
20-23	Av. 97	13	3	14	58	12	7

**Fig. 3.** Best fitting long periodic sinusoids to three pairs of meteor wind data sets recorded at Sheffield during the El Arenosillo winter anomaly campaign

comparatively small, the steady trend in the data indicating that we are dealing with a propagating mode of large vertical wavelength.

Table 2 shows the results relating to the diurnal tidal wind oscillation. Its amplitude is generally smaller than that of the semidiurnal oscillation and the phase appears to be variable.

The so called prevailing wind components are described by the data shown in Table 3. It is evident that from Sheffield the prevailing wind had an amplitude of about 20 m s^{-1} directed almost due NE during January 4-6, falling to about 6 m s^{-1} to the SE during January 15-17, and rising again to about 14 m s^{-1} , directed NE during January 20-23. There is little vertical structure in the prevailing wind. It is seen that NS winds exist at certain times which is of particular interest with regard to the possible transport of NO and other minor constituents.

In an attempt to resolve oscillations with periods exceeding the length of each individual meteor wind run we have fitted sinusoids to the data which match the trend that is evident in the polynomial curves shown in Figure 1. It was found that sinusoids of constant amplitudes could only be fitted when

their periods had very specific values. Figure 3 illustrates the method used where it is seen that for both the SE and NE wind components sinusoids of comparable amplitude and almost identical period fit the observed wind variation. Although the method is somewhat artificial in using a sinusoid of one particular period instead of a more complex waveform the resulting oscillation is comparable with those caused by the presence of planetary waves during the winter season.

Discussion and Conclusion

Although the measurements of winds from Sheffield during January, 1976 were intermittent it appears fair to draw attention to the general absence of pronounced NS air motions, while the winter anomaly was in progress, which could account for significant transport of minor constituents from the auroral region. The important aspect is the maintenance of such transport over sufficiently large distances during the lifetime of such constituents whose lifetime exceed the order of about one day. Although the prevailing winds were strong at times they generally blew into unfavourable directions as far as the meridional transport is concerned. Tidal oscillations, though represented by large amplitude winds, have insufficiently long time scales to effect coherent mean transport over large distances. One would therefore tend to look for the presence of long period wind oscillations of sufficient amplitude, such as associated with planetary waves, as an effective means of transport. There is some evidence that these may have existed during the January, 1976 winter anomaly as seen by the trend in the data shown in Figure 3. An amplitude of about 20 m s^{-1} may be just sufficient to cause meridional displacement over the expected latitudinal range south of the auroral zone. We are conscious though, that a detailed study of planetary wave structure, apart from the need for continuous recordings over long periods, depends on the synoptic analysis of data recorded simultaneously in different locations. It is gratifying to note that such an analysis is already in progress and we are now awaiting its results with considerable interest.

Acknowledgements. The authors are indebted to Mr. L. Nelson for sharing the meteor wind observations and for contributing towards the data analysis; also to Mrs. Lynne Chambers for much of the processing of the meteor recordings. We wish to thank the Science Research Council for their material support and for a Research Fellowship (for S.P.K.).

References

- Muller, H.G.: Long period meteor wind oscillations Phil. Trans. Roy. Soc. London Ser. A **271**, 585–598, 1972
Muller, H.G., Kingsley, S.P.: Long period meteor wind oscillations. J. Atmospheric. Terrest., Phys. **36**, 1933–1943, 1974

Received May 2, 1977

Winter Anomaly – Trace Constituents Sounding Rocket Campaign

Daytime Neutral Wind Measurements in the Mesosphere and Lower Thermosphere

D. Rees*, P. Rounce, and T.L. Killeen

Department of Physics and Astronomy, University College London, Gower Street,
London, WC1E 6BT, Great Britain

Abstract. During the Winter Anomaly project 3 neutral wind profiles were obtained in the upper mesosphere and lower thermosphere, using lithium trails released from Petrel rockets. These daytime profiles, one in the first salvo (Jan. 4, 1976) and two in the second salvo (Jan. 21, 1976), extended the altitude range of neutral wind coverage during the project from 90 to 135 km. The purpose of these measurements was to examine the dynamical behaviour of the higher regions of the atmosphere and ionosphere at time of occurrence of winter anomaly, overlapping, at the lower extreme of the technique, with data obtained from the chaff cloud technique.

The experimental technique of the daytime wind experiment is described in this paper, as are the preliminary wind results of the 3 B VI experiments. Initial assessment of the 3 wind profiles obtained shows that a strong northward shear occurred in the altitude range 90–150 km, with maximum northward winds of 80–120 m s⁻¹ between 100 and 104 km on each occasion. We are examining the possibilities that these features are indicative of either gravity wave or large scale circulation disturbances of the E region (lower thermosphere) associated with the D region winter anomaly condition.

Key words: Daytime mesospheric/thermospheric winds – Lithium trails – Winter anomaly.

Introduction

One of the aspects of the comprehensive studies of the atmosphere and ionosphere conducted during the Winter Anomaly campaign at Arenosillo, Spain, during January and February 1976, was the measurement of the atmospheric dynamics in the mesosphere and lower thermosphere. These studies were carried out to assess the possible role of atmospheric dynamics in generating the circum-

* To whom offprint requests should be sent

stances under which the anomalous atmospheric condition develops, or else to determine the nature of any dynamical or circulation disturbances which may occur as a result of alternative causes of the Winter Anomaly condition.

One example of the possible role of atmospheric dynamics would be the advection of air towards middle latitudes from a high latitude region where its composition might have been significantly modified (i.e. Nitric Oxide enhancement) by prolonged exposure to a region of enhanced auroral electron precipitation.

Alternatively, in a local mechanism of Winter Anomaly generation, an atmospheric disturbance inducing significant thermal or density fluctuations from a normal situation would be likely to generate, by pressure gradient and Coriolis forces, a local dynamical disturbance large enough to be identified as a significant departure from the normal pattern of atmospheric winds.

During the West German Winter Anomaly project, chaff releases (Skua-rockets) and parachute sondes (Loki-darts) provided a synoptic background of atmospheric dynamical behaviour in the stratosphere and mesosphere (up to 90 or 95 km) throughout the duration of the project. To determine the dynamical conditions above 90 km with more precision, and to extend the limit of monitoring of atmospheric dynamics into the lower thermosphere (up to 130–135 km), 3 additional wind measurements were made on the 'salvo' days, one on January 4, two on January 21. These measurements, by the 'daytime lithium trail' technique, will be used, in coordination both with lower altitude synoptic wind data, and with measurements of other atmospheric parameters such as the composition, temperature and density of both ionised and neutral species, to complete the picture of atmospheric dynamics at the time of day of the salvo launches (1600–1800 Local Time), and thus to determine the role of atmospheric dynamics in Winter Anomaly production, and the extent to which any associated atmospheric disturbance propagates upwards, above the D region, where it would not be observable by conventional ground-based techniques.

Experimental Technique

The rocket-borne technique for measuring neutral winds during daytime in the mesosphere and thermosphere is based on the observation of an alkali trail release, illuminated by sunlight, from the ground or aircraft, by means of either scanning photometers or cameras respectively (Best 1970, Bedinger 1970, Rees et al. 1972, Bedinger and Mills 1977) of high spectral and spatial resolution which discriminate the resonance emission of the alkali trail against the bright daytime sky.

Up to the present only about 15 to 20 such daytime wind profiles have been obtained by both techniques, due mainly to the high cost and complexity of the instrumentation required to observe the daytime releases compared with the simple camera systems which are adequate to observe twilight and night-time chemical releases. Lithium has generally been chosen as the alkali atom for daytime wind measurements. This is due to the large Doppler bandwidth of

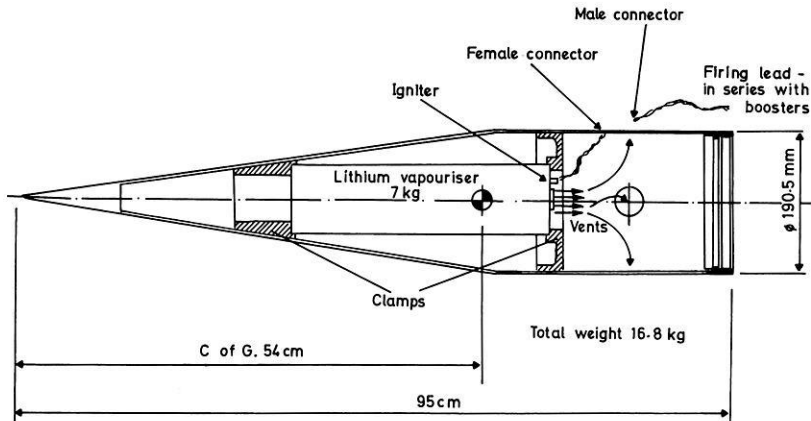


Fig. 1. Lithium vapouriser – Payload B VI (Petrel)

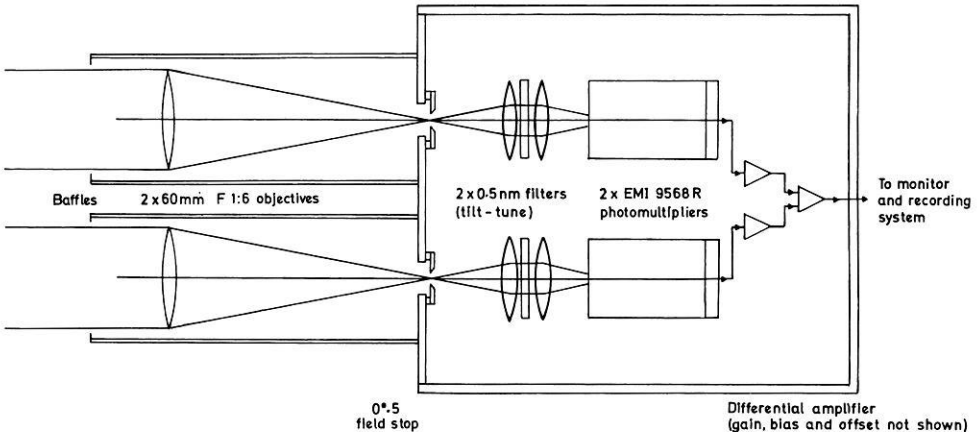


Fig. 2. Schematic diagram of dual channel differential photometer

the lithium atom (low atomic weight) and the high transitional probability of its resonance wavelength (670.8 nm) coupled with the relatively lower intensity of the daytime sky in the extreme red of the spectrum, and the absence of any significant solar or terrestrial Fraunhofer lines at the lithium wavelength which would reduce the available illumination. Other candidate alkalis, such as sodium or barium, compete at their resonance wavelengths with deep Fraunhofer lines and a greater sky brightness, although both are in fact adequately bright for observation under perfect conditions.

The lithium vapour trail is generated by a thermite burner (Fig. 1), mounted for these experiments under a fixed nose-cone on a Petrel rocket. The 7 kg thermite burner produces an optically thick trail over a period well in excess of 120 s. With a release altitude of 80–83 km as for these experiments, a bright trail is then produced over the complete upleg portions of the trajectory, and

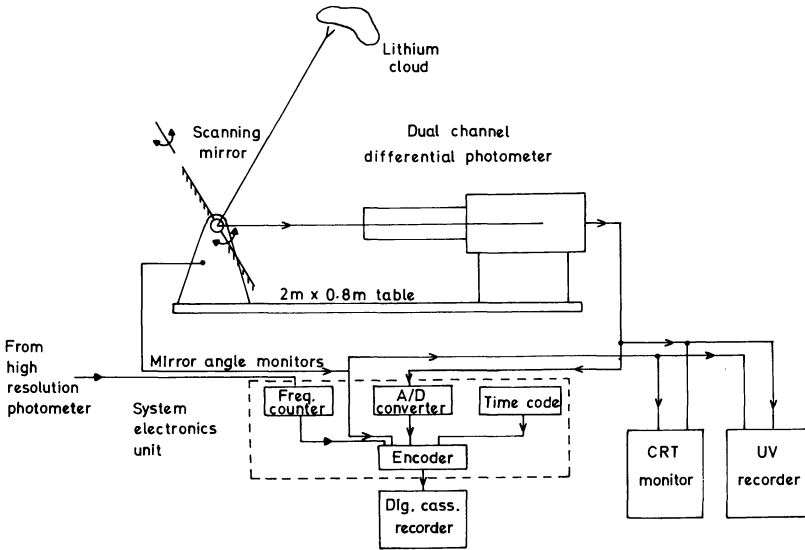


Fig. 3. Schematic diagram of electronics recording and monitoring system

continuing over apogee and downleg, to approximately 110 km altitude. In order to match as accurately as possible, the trajectories of other rockets in the Winter Anomaly project, the payload was ballasted by a heavy nose-cone structure to an all-up weight of 16.8 kg, producing apogees of the order of 130–135 km for the three B VI flights.

The design of the dual channel differential photometers used in the Winter Anomaly Campaign is shown in schematic form in Figure 2. Each channel of the optical system is carefully matched and co-aligned and the analogue outputs of the two photomultipliers are fed to a differential amplifier. One of the interference filters, of 0.3 nm bandwidth (F.W.H.H.) is tuned to the wavelength of the lithium resonance line (670.8 nm) and the second filter is tuned to about 0.5 nm on the short wavelength side of the lithium line (670.3 nm).

When the optical system is matched and the differential amplifiers are balanced to obtain a null when the instrument is looking at the clear daytime sky, observation of a sunlit lithium trail of optical thickness greater than about $\tau=0.05$ will result in a discernible signal if the trail fills the instrument field of view (~ 0.5 arc) defined by the co-aligned apertures of each channel. Alternatively, so also will a trail or cloud of dimensions less than the field of view but of proportionally greater optical thickness.

The instrument itself is rigidly mounted on a 2 m \times 0.8 m table approximately 1 m high, which is aligned in the appropriate direction, with the instrument pointed horizontally, away from the expected viewing direction, looking into a 30 cm \times 25 cm plane scanning mirror which performs a sequential raster scan of selected regions of the sky, approximately $40^\circ \times 40^\circ$ arc in area. The two angles of the scanning mirror are continuously and synchronously scanned to provide one complete picture of the $40^\circ \times 40^\circ$ area every 60 s. The azimuth

scan takes two seconds, providing a resolution in elevation of about $1^{\circ}.3$. The resolution in 'azimuth' is limited by the aperture size ($0^{\circ}.5$ arc) rather than by the data acquisition rate of $160 \text{ samples s}^{-1}$ corresponding to $0^{\circ}.125$ arc.

A block diagram of the data processing and recording electronics is shown in Figure 3. The analogue differential output is converted to a digital signal and recorded in a 60 bit serial format along with time code and azimuth and elevation angle data on the data track of a digital cassette recorder at a rate of $160 \text{ samples s}^{-1}$.

Instrument Performance

The surface brightness of an optically thick lithium trail is of the order of 500 kR, compared with a mean day sky brightness near the zenith (solar elevation 30°) of the order of 10 mR integrated over the spectral transmission bandwidth of the interference filters.

A detailed discussion of instrument response is given in an accompanying paper (Rees, 1977), and only the operational response will be given here. At a fixed location in the sky, in the absence of any haze or cirrus clouds, the typical sky R.M.S. 'noise' is of the order of 20 mV with the system as used for these experiments, while the signal obtainable from the lithium cloud is about 2 Volts peak amplitude (field of view $0^{\circ}.5$, $1/160 \text{ s}$ integration time).

In practice, however, there is always a difficulty caused by the greatly variable sky brightness (primarily a function of elevation and angle with respect to the sun's position). Particularly within 20° of the horizon and about 45° of the sun's position, total sky brightness variations of a factor of 2 to 5 may occur, and even greater variations may occur if any haze or thin, high level clouds are present. The limited common mode rejection of the system – primarily due to imperfect optical matching of the two channels, causes significant fluctuations of the 'background' level, generally in the form of a slow and systematic function of location within the raster system. These variations, which can clearly be seen in Figure 4, and are described in the next section, require limitation of the system gain to keep all the signals within the working range of the amplifiers and analogue to digital converter.

During hazy conditions or in the presence of thin, high level clouds, despite apparently blue skies, the system gain reduction required may be so severe that it would no longer be possible to distinguish clearly the anticipated signal levels due to lithium trails.

In practice, major constraints to the performance of the instrument, apart from the necessity for virtually cloudless skies and haze-free conditions, are set by the logistic problems of location of the photometers and their associated instrumentation. Good physical and telephone communications to the rocket range are essential for coordination of campaign preparations and count-downs. Particularly with relatively remote, coastal rocket ranges, it is usually impossible or impractical to locate the instrumentation in ideal physical sites. Ideally, the optical sites should be located approximately 50–100 km to each side of the range centre line, and approximately 50 km down-range for upleg releases (or 100 km down-range for downleg releases).

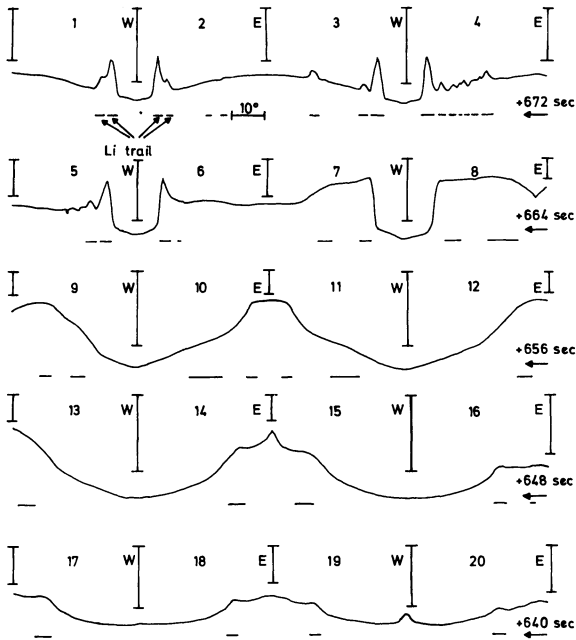


Fig. 4. Raster scan of Lithium trail at 640–680 s after launch

For the El Arenosillo experiments, the San Fernando Observatory, near Cadiz, was physically a very good location, although a little remote (three hours by road via Seville). It also suffered highly changeable local weather conditions due to its proximity to the Straits of Gibraltar and the Mediterranean. Ideally, the second site should have been to the west and south of El Arenosillo, 50 km south of the Portuguese coastline. Other considerations, however, dictated that the instrumentation should be close to El Arenosillo, and a hotel rooftop in Mazagon was eventually chosen, about 10 km NW by W of the range. The major difficulty raised by using a site so close to the rocket range is that the lithium trail on the upleg of the trajectory is released virtually along a line of sight between 80 and 120 km. It is thus often impossible to resolve the tight convolutions of the trail caused by the small scale wind variations in this height region during the first few minutes after trail release, due to overlapping of portions of the trail at different altitudes.

For this particular project, winds in the 80–110 km region were clearly of very great interest. This altitude region is at the lower limit of the lithium trail technique due to two factors. First, at altitudes below about 90 km the lithium metal (as with other metal alkali releases such as sodium, aluminium and barium) is rapidly changed into a stable chemical compound from which the atoms can no longer emit the resonance line. Below 80–83 km, no resonance emission is observed even immediately following the release. Secondly, the diameter of the trail at lower altitudes is quite narrow at release and (subject to molecular and eddy diffusion) grows rather slowly with time. Typical figures are shown in Table 1. At the time of release the apparent angular diameter

Table 1. Trail diameters due to molecular and turbulent diffusion

Altitude (km)	80	85	90	95	100	105	110
'Initial' radius (m)	20	30	50	80	100	150	200
Molecular diffusion coefficient ($\text{m}^2 \text{s}^{-1}$)	2	5	12	30	80	150	400
Radius after:							
10 s	22	35	52	85	120	170	230
100 s	35	55	85	140	200	270	440
1000 s	65	105	170	250	420	560	920
Angular diam. (mrad) after:							
10 s	0.03	0.04	0.06	0.10	0.12	0.16	0.22
100 s	0.04	0.06	0.10	0.16	0.22	0.30	0.44
1000 s	0.08	0.12	0.22	0.30	0.44	0.58	0.88
With maximum turbulence ($\text{m}^2 \text{s}^{-1}$)		100			200		500
Angular diam. (mrad) after:							
10 s		0.12			0.24		0.60
100 s		0.22			0.44		1.00
1000 s		0.44			0.88		2.20
Depletion time constant exponent	~ 5	~ 50 (s)	~ 200	≥ 10 (min)			? (~ h)

of the trail is considerably smaller than the $0^\circ.5$ field of view set by the aperture stop of the instrument, reducing the signal level considerably. Although this angular diameter grows with time, the lower altitudes suffer severe depletion of the lithium content and, below about 85 km, the trail is probably always unobservable in daytime with the standard differential photometers.

A special photometer of novel design was built and used in the Winter Anomaly project to try to overcome the difficulties with wind measurements in the 80–100 km region. Its design and some experimental results are described in an accompanying paper (Rees, 1977).

Calibration

To obtain a successful triangulation of trail and cloud features with a standard deviation of the order of 300–500 m, the scanned field of view of the photometer at both observation sites must be known to within about $\pm 0^\circ.1$ or $0^\circ.2$. It is generally impractical to set up the instruments this precisely and, following installation to a precision of $\pm 1^\circ$ or 2° , the angular residuals are calibrated by means of transits of the sun, moon or bright stars across the scanned field of view of the photometers. For the El Arenosillo experiment, the moon was most useful, covering, particularly at Mazagon, virtually the entire field of view over a period of a few days near first quarter. For these experiments the angular residuals were of the order of $0^\circ.15$ at Mazagon and $0^\circ.25$ at San Fernando, where the moon only entered the edge of the field of view.

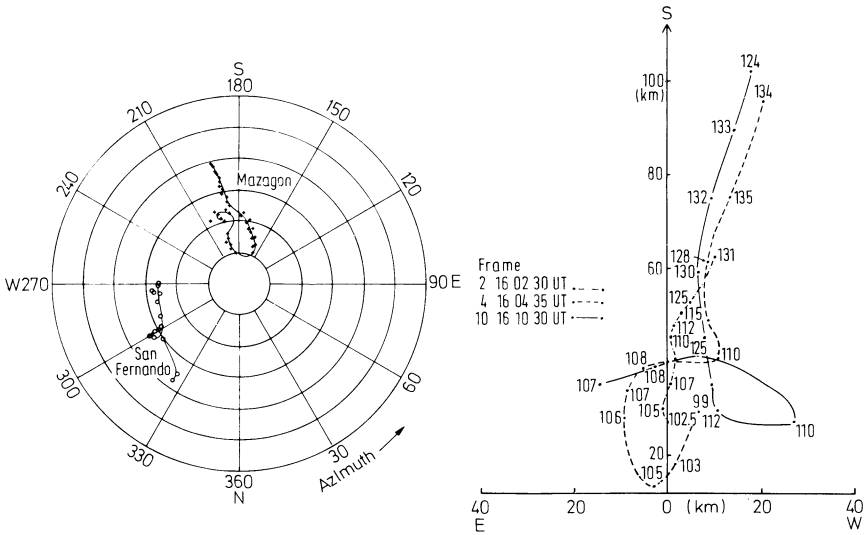


Fig. 5. (a) Raster scans at 160435 from Mazagon and San Fernando (275 s). (b) Ground track of B VI/1 launch, Jan 4, 1976, 1600 UT

Normally, a further improvement in precision can be made using the radar tracking of the rocket to provide precise initial angular coordinates of the trail release position. Thus far, however, it has not been possible to obtain a fully consistent match of optical and radar data on any of the B VI experiments (R.M.S. discrepancies between radar and optical trajectories are about 5 to 10 km).

Experimental Results

The launch conditions of the three B VI lithium wind experiments of the Winter Anomaly project are shown in Table 2. All three rockets and their payloads performed perfectly and each was successfully observed over the full altitude range from 85 km to apogee (130–135 km) from the observation sites at Mazagon ($37^{\circ} 08'N$, $6^{\circ} 49'W$) and the San Fernando Observatory ($36^{\circ} 28'N$, $6^{\circ} 44'W$). Selections of raw experimental results from B VI/1 are shown in Figure 4, for various altitudes and times from release. The variation of the background level with location within the raster is due to the imperfect optical matching and limited common mode rejection of the photometer/electronics system (the

Launch	Date	Local time	Solar elevation
B VI/1	4 Jan. 1976	1700	15°
B VI/2	21 Jan. 1976	1655	15°
B VI/3	21 Jan. 1976	1913	-6°

Table 2. Launch conditions for B VI payloads

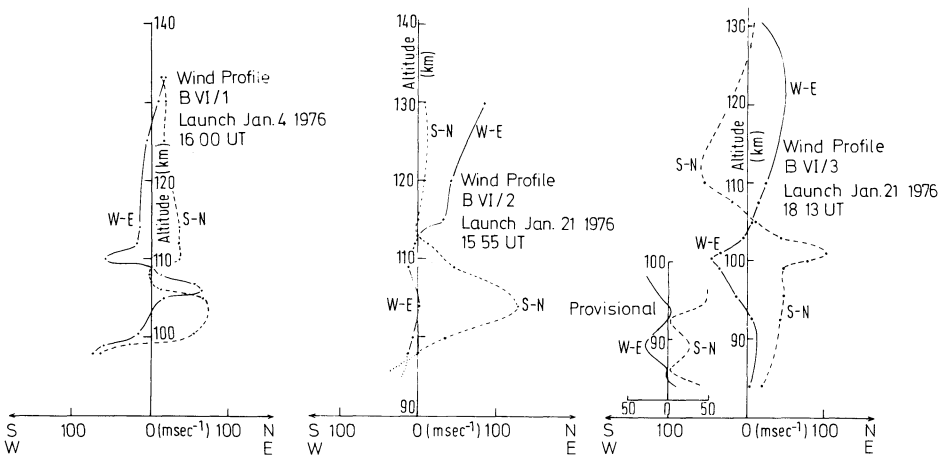


Fig. 6. Wind profiles of B VI/1, B VI/2 and B VI/3

effective common mode rejection being of the order of 60 dB for the transmission bandwidths of the interface filters, or 120 dB in 'white light').

The processed results are reconstituted by computer to obtain complete raster 'pictures' of the trails from both observation sites, as shown in Figure 5a, at a time of 275 s after launch of B VI/1. A 'manual' triangulation of these data sets is then carried out, using a Texas Instruments SR 52/PC 100 calculator/printer. This rough analysis removes spurious data points and checks the general validity of the experimental data and angular calibration of the photometers, and provides an approximate trajectory ($\pm 1-2$ km), and a crude wind profile (± 10 m s⁻¹, $\pm 1-2$ km altitude).

A sophisticated computer analysis then utilizes this 'first-order' hand analysis as initial data and iteratively attempts to make a best fit of all the experimental data from both sites, and a radar trajectory (if available) of the initial trail location. Normally this iterative analysis will reduce the wind errors to less than 5 m s⁻¹ and the height assignments to ± 500 m s⁻¹ or better.

The first order wind analysis for each of the rocket flights is obtained from the ground tracks of the lithium trails which are shown in Figure 5b. The resulting wind profiles are shown in Figure 6.

Discussion

It is not the intention of this paper to examine in detail the aeronomic implications of the wind results described in the last section, or to compare the data from the lithium trails with that of any other wind measuring technique used in the project, or with data on other aeronomic parameters.

Despite considerable apprehension during project planning that it would prove extremely difficult, if not impossible, to obtain interesting scientific conditions for the project (i.e. presence of severe winter anomaly) while also obtaining

favourable weather conditions at Mazagon and San Fernando for the lithium experiment, in practice no such difficulties occurred although, clearly, the ease of obtaining simultaneously all the correct launch conditions was fortuitous. Complete wind profiles have been obtained above 95 km for the two 'daytime' trails and above 85 km for the twilight trail. It will prove possible to extend the 'daytime' profiles down to 85 km if a good radar trajectory can eventually be obtained, thus providing an accurate location of the initial trail release so that the first few minutes of data obtained on the trails below 95 km altitude can be utilized.

Each of the wind profiles showed a strong northward feature in the altitude range 90–105 km, and an indication of complex small-scale wind structure below about 95 km, shown in detail for B VI/3 in Figure 6. We are presently examining the possibilities that some of these features are correlated with the widespread atmospheric disturbance associated with the winter anomaly conditions present during the period of the rocket experiments.

Acknowledgments. The Petrel rockets used for the lithium trail experiments were provided by the DFVLR, funded by the West German Ministry of Science, and launched with the assistance of INTA. Financial support for the UCL payloads and participation in the campaign was provided by the U.K. Science Research Council under Grant No. SG/D/00451. Particular thanks for assistance in carrying out the project go to Mr. J. Satrustegui and Mr. Vilches of INTA, Mr. G.E. Todd of DFVLR and, for the essential cooperation in providing facilities to operate at the San Fernando site, to Professor Catelan of the San Fernando Naval Observatory. We also appreciate the assistance of Miss B. Waters and Miss J. Norman with analysis of the experimental data and preparation of the manuscript and diagrams.

References

- Bedinger, J.F.: Detector for Observation of High Altitude Winds during the Daytime. *Rev. Sci. Instr.* **41**, 1234–1235, 1970
- Bedinger, J.F., Mills, M.T.: Thermospheric Wind Measurements during Project Aladdin, 1974. Space Research XVII. Awaiting confirmation (Presented at COSPAR, Philadelphia, 1976)
- Best, G.T.: Daytime Tracking of a High-Altitude Vapor Trail. *J. Atmospheric Sci.* **27**, 979–980, 1970
- Rees, D.: Winter Anomaly—Trace Constituents Sounding Rocket Campaign. A High Resolution Photometer for Observing Daytime Lithium Releases. *J. Geophysics* **44**, 57–63, 1977
- Rees, D., Neal, M.P., Low, C.H., Hind, A.D., Burrows, K., Fitchew, R.S.: Neutral Wind Measurement during Daytime in the Thermosphere. *Nature, London*, **240**, 32–33, 1972

Received May 2, 1977

Winter Anomaly – Trace Constituents Sounding Rocket Campaign

A High Resolution Photometer for Observing Daytime Lithium Releases

D. Rees

Department of Physics and Astronomy, University College London, Gower Street,
London, WC1E6BT, United Kingdom

Abstract. Differential photometer instruments which have been used to observe rocket-borne lithium trails in daytime have a limited resolution (about 0.5 – 1° arc) with which it is difficult to observe trails at the lowest altitudes (80–95 km) and to make observations of turbulence and diffusion within the trails at altitudes up to about 110 km. A novel instrument which was built for, and used during, the Winter Anomaly project is described in this paper; it has a 0.1 arc resolution, retaining the sensitivity of the conventional differential photometers. The instrument is based on a piezoelectrically-scanned Fabry-Perot interferometer of 0.05 nm spectral resolution.

Key words: Daytime neutral winds, thermosphere – Lithium trails – New high resolution photometer.

Introduction

The anticipated role of neutral wind measurements in the mesosphere and lower thermosphere in describing the atmospheric disturbances associated with Winter Anomaly conditions has been described in an accompanying paper (Rees et al., 1977). Reliable synoptic wind measurements up to about 90 km altitude were made throughout the Winter Anomaly project using chaff releases from Petrel rockets. These measurements were supplemented on the salvo days by lithium trail releases which, as described in Rees et al. 1977, provided reliable daytime measurements above 95 or 100 km. The height interval between 90 and 95–100 km was expected to be quite crucial to the completeness of the Winter Anomaly investigation, but it poses many difficult experimental problems. For the chaff release technique, due to low atmospheric density, the cloud falls very rapidly, and may thus not follow in detail the fluctuations of the wind field. On the other hand, for the lithium trail technique, the sensitivity and angular resolution of the conventional photometers, which are used to track the daytime trails, is adequate to properly detect and resolve the trail below about 95 km. In particular, these photometers cannot

provide any significant information on the turbulent diffusion of low altitude trails below the 'turbopause' at about 105 km. Since an enhancement or reduction of the eddy or turbulent diffusion coefficient would significantly modify the rate of vertical transport of minor constituents into and out of the atmospheric region where Winter Anomaly effects are observed, and since a useful overlap of the altitude ranges of the chaff release and lithium trail techniques would improve the significance of the measurement of atmospheric dynamics and also allow some redundancy of measurement, it was decided to investigate the possibilities of extending the tracking of the daytime lithium trails to the lowest possible altitude.

Of the various instruments which have been used to observe daytime lithium releases (Best, 1970; Bedinger, 1970; Rees et al., 1972; Bedinger and Mills, 1977), only the airborne photographic technique of Bedinger and Mills 1977, with its accompanying problem of a requirement for a high flying jet aircraft (12 km +), can provide adequate spatial resolution to see small-scale structures (turbulence) within lithium trails up to 110 km (the conventional 'turbo-pause'), or actually to detect trails at the lowest levels, 83–90 km. The difficulties are shown diagrammatically in Figure 1, where the nominal trail expansion as a function of time after release is shown for various altitudes for molecular diffusion alone. The enhancement of trail expansion due to various rates of turbulent diffusion ($k = 100, 200, 500 \text{ m}^2 \text{ s}^{-1}$) is also shown. At 90 km, the lithium released decays rather rapidly so that, although after about 100 s the trail radius would exceed the sensitivity limit of the standard differential photometers, there may be insufficient metal vapour remaining for the trail to be visible.

A novel high resolution photometer was designed to attempt to overcome some of the shortcomings of spatial resolution, to attempt to push observations of the lithium trails to the lowest possible altitudes and to look for small-scale structures and turbulence within the trails. This instrument was utilized for the first time in the Winter Anomaly project from the Mazagon station (Rees et al., 1977) to supplement the observations made of three lithium trail releases by conventional dual-channel differential photometers.

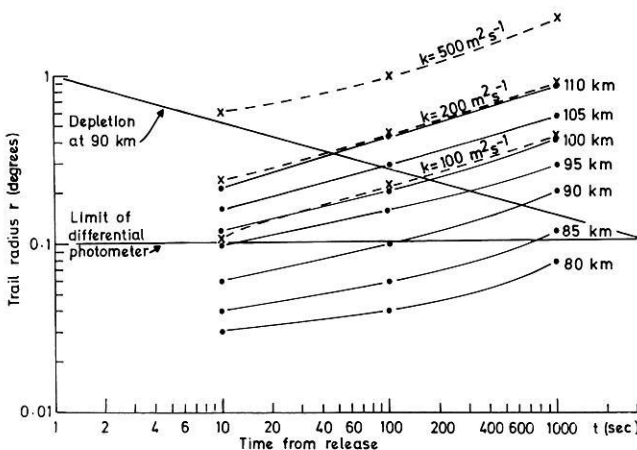


Fig. 1. Trail radius (degrees) as a function of time from release

Instrument Design Concept

The major design driving factors of a photometer for observing rocket-borne chemical trails in daytime are:

1. to obtain the highest possible spectral resolution to reduce the level of transmitted daytime sky brightness,
2. to obtain the highest possible spatial resolution to resolve the chemical trails and
3. to obtain the highest possible throughput with respect to emission from the lithium trail.

In a conventional differential photometer the instrument transmission can be written as:

$$F_S = \frac{1}{4\pi} \cdot Q \cdot \Omega \cdot A \left[(R \cdot k_1 \cdot k_2) t_1 \cdot t_2 + \int_0^{\infty} S(\lambda) \cdot t_S(\lambda) \cdot t_2 \cdot d\lambda \right] \quad (1)$$

where F_S = the detected flux (photons s^{-1})
 Q = the quantum efficiency of the detector
 Ω = the solid angle of the instrument
 A = the usable area of the interference filter in general
 R = the surface brightness of the chemical trail (optically thick)
 k_1 = the proportion of the field of view filled by a trail or cloud
 k_2 = the optical thickness of the trail
 t_1 = the sky transmission at the resonance wavelength
 t_2 = the instrument transmission at the resonance wavelength
 $S(\lambda)$ = the sky brightness as a function of wavelength
 $t_S(\lambda)$ = the instrument transmission as a function of wavelength.

A typical solution for a differential photometer is shown in Table 1, using state of the art interference filters and 5 cm aperture optics. In the design of the differential photometer throughput has been sacrificed, to obtain a $0^\circ.5$ angular resolution, by a factor of about 25, without any corresponding gain in spectral rejection, to improve the contrast of the lithium trail against the daytime sky.

The novel design was intended to provide improved spatial resolution while compensating for the decreased field of view and thus throughput with improved spectral rejection, by using a 100μ gap scanning Fabry-Perot etalon as the wavelength selective device. A 15 cm aperture Cassegrain telescope was used to improve the field of view matching to regain some of the throughput which would otherwise have been lost.

Table 1 shows the specification of the high resolution photometer for comparison.

While the two instruments perform similarly in terms of signal to noise ratio for an optically thick trail larger than $0^\circ.5$ in diameter, thus filling the field of view of both instruments, there is a major difference in the performance both with narrow trails and optically thin trails. For a $0^\circ.1$ trail diameter, and again a 0.005 s integration time, with an optically thick trail the signal to noise ratio of the high resolution photometer is about six times better than the differential photometer,

Table 1. Comparative performance of differential photometer and high resolution photometer

	Differential photometer		High resolution photometer
<i>a. Specification</i>			
Solid angle (Ω , sterad)	10^{-4}		3×10^{-5}
Area (cm^2)	20		26
$\int t_S(\lambda) d\lambda$ (nm)	0.4		0.025
Field of view ($^\circ$)	0.5		0.1
Quantum efficiency		0.05	
Lithium trail brightness (Rayleighs)		0.5×10^6	
$k_1 = k_2$		1	
t_1		0.5	
t_2		0.8	
<i>b. Performance</i>			
Trail diameter ($^\circ$)	2°	$0^\circ.1$	$0^\circ.05$
Optical density (τ)	1	1	0.2
Differential photometer:			
Signal due to lithium (cts.s^{-1})	1.5×10^6	3×10^5	3×10^4
Background due to sky (cts.s^{-1})	1.5×10^7	1.5×10^7	1.5×10^7
In 0.005 s:			
Signal	7×10^3	1.5×10^3	1.5×10^2
Background	7×10^4	7×10^4	7×10^4
Signal (S) to Noise (N) ratio ^a	20:1	5:1	0.5:1
High resolution photometer			
Signal due to lithium (cts.s^{-1})	6×10^5	6×10^5	6×10^4
Background due to sky (cts.s^{-1})	4×10^5	4×10^5	4×10^5
In 0.005 s:			
Signal	3×10^3	3×10^3	3×10^2
Background	2×10^3	2×10^3	2×10^3
Signal (S) to Noise (N) ratio ^a	30:1	30:1	6:1

$$^a N = (\text{Background} + \text{Signal})^{\frac{1}{2}}$$

while the high resolution photometer has a $\times 10$ advantage with a trail $0^\circ.05$ in diameter and an optical thickness $\tau=0.2$.

From experience, it is rather difficult to observe clearly a trail where the signal to noise ratio for a 0.005 s sample falls below 5:1. Under ‘perfect’ skies (rarely obtained at sea level) the differential photometer thus fails to observe a cloud less than about $0^\circ.1$ or $0^\circ.2$ in diameter, which degrades to $0^\circ.5$ in the presence of even thin haze or traces of high cirrus cloud.

The high resolution photometer, however, is capable of resolving an optically thin trail ($\tau=0.2$) $0^\circ.05$ in diameter, or an optically thick trail $0^\circ.01$ in diameter.

Referring to Figure 1, it can be seen that, allowing for metal depletion, the normal differential photometer will never see a trail below about 90 km except under ‘perfect’ conditions, while the high resolution photometer is capable of resolving trails down to about 80 km if an adequate vapour pressure of the free metal is stable in the atmosphere.

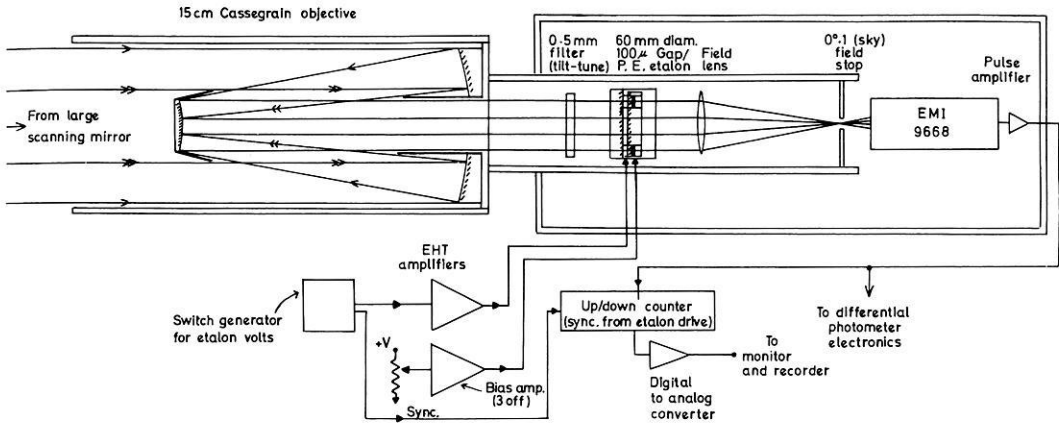


Fig. 2. Schematic design of high resolution photometer system

The realisation of a practical high resolution photometer is based on combining a scanning piezoelectric etalon of 60 mm aperture and $100\ \mu$ gap and finesse ~ 25 with a 1 nm band-pass filter tuned to the lithium 670.8 nm resonance line. A 15 cm Cassegrain telescope matches the etalon field of view for a 0.05 nm 'resolution', to obtain a $0^\circ.1$ field of view in the sky. The instrument is shown schematically in Figure 2. In practice, the piezoelectric etalon is switched between two wavelengths, one of which is the lithium resonance line. The photon count output is taken to feed an up/down counter which is synchronised with the etalon wavelength switching, and the output recorded on a digital magnetic cassette recorder, along with time code and azimuth and elevation information.

Instrument Performance

The high resolution photometer was used during all three of the BVI experiments on January 4 and 21, 1976, during the Winter Anomaly project, and appears to have performed very close to its specification. A section of the quick-look record obtained during the BVI/2 experiment is shown in Figure 3 (this is the direct data output taken from a rate meter in parallel with the input to the up/down counter). The departure from a rectangular wave-form is due to hysteresis of the piezoelectric crystals driving the etalon.

The approximate scale of this record section is shown underneath the data. For comparison, the same section of trail scanned by the differential photometer is also shown in the Figure. The altitudes of the 3 portions scanned (A, B, C) are approximately 115, 120 and 115 km respectively. During these experiments a relatively slow switching rate of the etalon was used, equivalent to a $0^\circ.3$ arc sample at the angular scanning rates which were used. The signal to noise ratio of the records indicates, however, that the switching rate could be increased by at least a

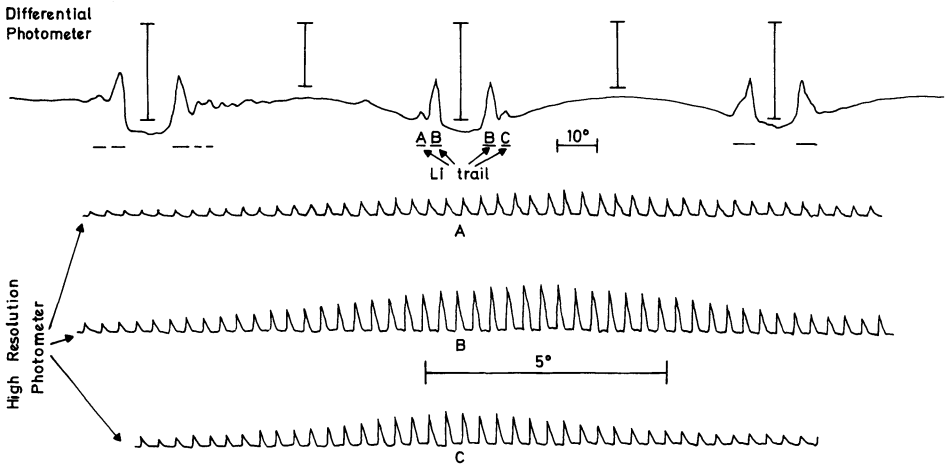


Fig. 3. Experimental data from high resolution photometer

factor of three to match the $0^{\circ}.1$ angular resolution of the optical system. For example, the lower portions of the trail (A and C), which are approximately $1^{\circ}.5$ in diameter, are barely resolved by the standard differential photometer, as can be deduced from the much lower amplitude of signals A and C relative to B (which is nearly 3° in diameter) in the differential photometer record compared with the relative amplitudes in the high resolution photometer record.

Conclusion

A high resolution photometer, built for, and used during, the Winter Anomaly project appears to be capable of observing daytime lithium trails at altitudes below about 85 km, and of obtaining useful measurements (turbulent eddies etc.) within trails and cloud releases under most conditions at altitudes greater than about 90 km.

Experimental data obtained during the B VI project is presently being analysed, in particular to examine the small-scale wind and turbulence features of the lowest altitude regions of each of the three lithium trail releases.

Acknowledgments. The Petrel rockets used for the lithium trail experiments were provided by the DFVLR, funded by the West German Ministry of Science, and launched with the assistance of INTA. Financial support for the UCL payloads and participation in the campaign was provided by the U.K. Science Research Council under Grant No. SG/D/00451. Particular thanks for assistance in carrying out the project go to Mr. J. Satrustegui and Mr. Vilches of INTA, Mr. G.E. Todd of DFVLR and, for the essential cooperation in providing facilities to operate at the San Fernando site, to Professor Catelan of the San Fernando Naval Observatory. I also appreciate the assistance of Miss B. Waters and Miss J. Norman with analysis of the experimental data and preparation of the manuscript and diagrams.

References

- Bedinger, J.F.: Detector for observation of high altitude winds during the daytime. *Rev. Sci. Instr.* **41**, 1234–1235, 1970
- Bedinger, J.F., Mills, M.T.: Thermospheric wind measurements during project Aladdin, 1974. *Space Res.* XVII. (Presented at COSPAR, Philadelphia, 1976)
- Best, G.T.: Daytime tracking of a high-altitude vapor trail. *J. Atmospheric Sci.* **27**, 979–980, 1970
- Rees, D., Neal, M.P., Low, C.H., Hind, A.D., Burrows, K., Fitchew, R.S.: Neutral wind measurement during daytime in the thermosphere. *Nature, London* **240**, 32–33, 1972
- Rees, D., Rounce, P., Killeen, T.L.: Winter anomaly – trace constituents sounding rocket campaign. Daytime neutral wind measurements in the mesosphere and lower thermosphere. *J. Geophys.* **44**, 47–56, 1977

Received May 2, 1977

Payload BI: A Compact and Economic D-Region Experiment Package for Use on Small Sounding Rockets

G. Rose and H.U. Widdel

Max-Planck-Institut für Aeronomie, D-3411 Katlenburg-Lindau 3, Federal Republic of Germany

Abstract. A payload is described consisting of a foil cloud experiment and a guard ring probe. Winds, wind shears and turbulent motions are derived from the spatial movement of the cloud during fall and density and temperature of the neutral air from the fall rates of the cloud, as observed by radar respectively. Electron and ion densities are measured by a guard ring probe of special design. The probe is calibrated by comparison with the results of simultaneous ground based measurements of radio wave absorption applying the Sen-Wyller formula. The set up of the payload and its operation are described and some results are given.

Key words: D-region – Winter anomaly – Wind – Air density – Electron ion density – Falling foil cloud – Guard ring probe.

Concept of BI Payload

Payload BI was designed to gather an overview over the time history of changes of atmospheric parameters in the D-region which comprise both changes in the ionized components and of neutral air (meteorological) parameters.

A fairly large number of individual experiments are required for such a project in order to achieve a significant result. Cost-effectiveness and reliability of the payload are of utmost importance but not at the expense of scientific value or accuracy of measurement. A careful consideration about parameters to be measured is mandatory. The payload to be described here contains two experiments, one for the measurement of neutral air parameters, the other for the measurement of the ionized component of the atmosphere.

The payload was flown successfully a number of times before it was used in the Aeronomy Program (Rose and Widdel, 1972b; Rose et al., 1974; Dieminger et al., 1974).

1. Neutral Atmosphere Parameters: The Foil Cloud Experiment

1.1. Winds, Wind Shears, Turbulent Motions. Winds, wind shears, density and average air temperature can be measured in the simplest way by free-falling, reflective objects which are ejected from the vehicle at or near apogee of the rocket's trajectory and tracked from the ground by suitable means, e.g. radars. Such an experiment has the "all-weather" capability desired for this type of investigation.

Wind measurements allow within certain limits the estimate of large-scale pressure gradients, and, by this, the position of high- and low pressure systems. When temperature measurements are available, wind shears can be used to prove the existence of turbulent layers (Zimmerman and Narcisi, 1970).

For wind measurements, falling spheres of various kinds (Jones, 1959; Otterman, 1961) are not very well suited to greater heights because they are too heavy and their descend velocity is too large to follow the wind shears sufficiently fast (Fig. 1). A more suitable target is a cloud of radar-reflective dipole elements ("CHAFF" or "WINDOW"). Experiments of this kind have been used in the upper atmosphere (D-region heights) by several authors (e.g. Webb, 1961; Smith, 1960; Pachomov, 1969) and also on a routine basis. Rapp (1960) gave an estimate about the accuracy of such experiments.

The main disadvantage of "CHAFF" measurements is the limited height range over which useful measurements can be performed because the cloud spreads out under the influence of diffusion and the initial momentum received during deployment from the spinning rocket. Further, spreading in strong wind shears causes the radar to "hunt". Attempts to overcome this difficulty by using more than one "CHAFF" ejection over the rocket's trajectory have been made by several authors (e.g. Pachomov, 1969). We flew an experimental payload of this kind in 1973 in order to test the feasibility of increasing the height range over which density measurements can be made.

Ordinary "CHAFF" has also a very strong tendency to form clumps because the very thin, hair-like dipole elements do not separate well. This tendency is almost impossible to avoid as our own tests and those of other experimenters have shown. This makes the derivation of air densities and air temperatures from fall rates of "ordinary" CHAFF clouds almost impossible (very rare cases excepted).

However, when elements of proper shape and suitable size and wing load area to have little tendency to form clumps are chosen (Rose and Widdel, 1972, 1973) and means are taken to deploy the cloud in such a (controlled) way that the elements are all separated from each other and that their number density increases toward the center of the cloud (Azcarraga, et al., 1970; Rose, et al., 1972), the situation is different and a larger height interval can be covered with reliable measurements provided that no excessive windshears and turbulences are present: These distort the shape of the cloud to such a extent that a reasonably accurate radar track is no longer possible after the cloud has passed the shear (see Fig. 2). This happens with preference at height levels from which so-called "DEEP ECHOES" (Dieminger and Hoffmann-Heyden, 1952; Gregory, 1961; Thitheridge, 1962) are received. A connection between

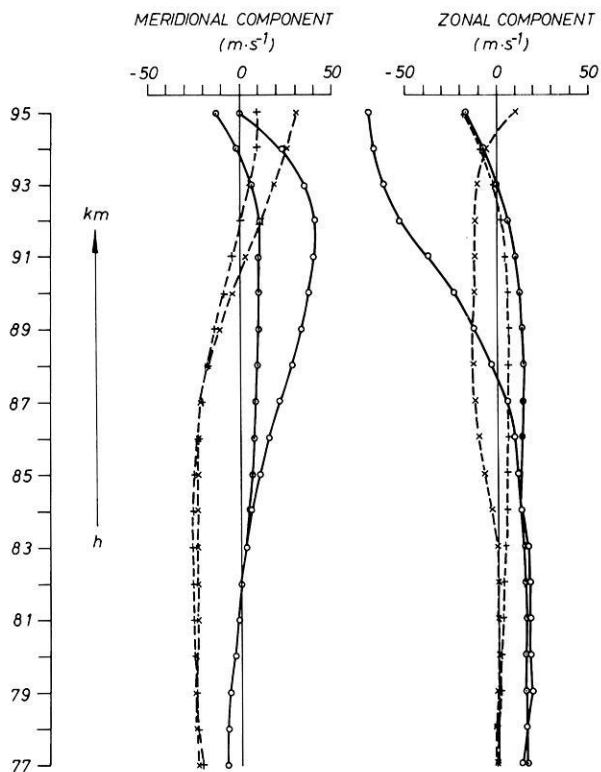


Fig. 1. Response of a falling sphere to winds. Results of tracking by two independent radars

○—○ R 354 17.04.74 1830Z
 ○—○ R 112
 +--+ R 113 10.04.74 1850Z
 ×—× R 354

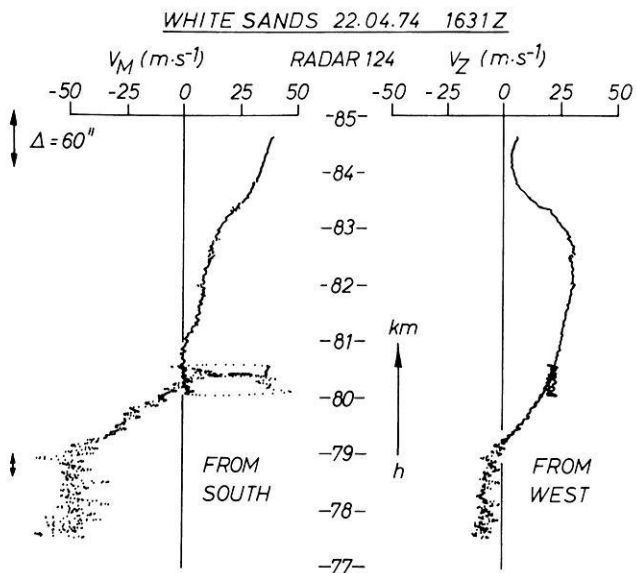


Fig. 2. Results of tracking of a foil cloud passing through a wind shear

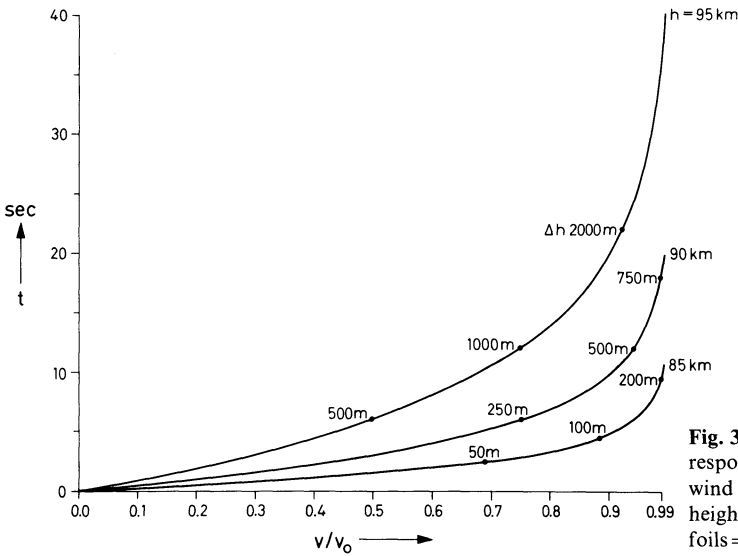


Fig. 3. Calculated response of foil cloud to wind velocity in different heights (initial velocity of foils = 0)

these gradient-induced partial reflections and wind shears seems to be evident though not fully proven by experiments so far.

Even small-scale vertical movements can be observed directly with properly designed foil clouds (Rose and Widdel, 1969) but because these movements are associated with a rapid dissolution of the foil cloud inside the turbulence cell, a fairly sensitive radar is required for tracking. The situation may change when active transponder elements rather than passive reflectors can be used as targets. More detailed investigations of turbulent motions besides wind and density measurements are then possible.

The upper height limit for wind measurement is set by the weight-to-area-ratio of the dipole elements. We use foils, $2.5 \cdot 10^{-6}$ m thick, $9 \cdot 10^{-3}$ m wide, their length cut to be in resonance with the wave length of the radar tracking system. The foils are aluminized from all sides, the weight-to-area-ratio is $3.4 \cdot 10^{-3}$ kg \cdot m $^{-1}$. These foils have less tendency for "bird's nesting". They allow reliable wind measurements from about 95 km downwards. The foil clouds are deployed near apogee of the rocket's trajectory in the direction opposite to flight. This allows a certain amount of compensation of the trajectory speed. Experience has shown that the clouds deployed this way follow almost immediately the direction of the wind with no discernible "ballistic" component. The theoretical response of the cloud to winds is shown in Figure 3.

One weak point however has to be mentioned. In-situ measurements (of any kind whatsoever) can provide only a momentary picture of the state of the wind field even though it takes 20–25 min for the foil cloud to travel down from 95 km to 80 km. Therefore, tides and waves cannot be separated from the prevailing wind except for the case when a whole series of rocket launches is performed over the day (Azcarraga et al., 1971). In our special case however,

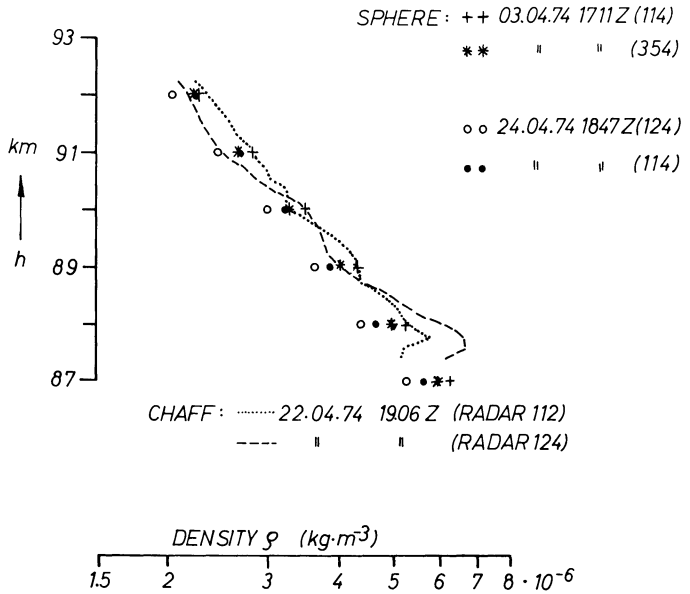


Fig. 4. Density measurement. Comparison between the results attained with falling spheres and with the foil cloud experiment. Each experiment was tracked by two independent radars

in which the winter anomaly is to be investigated, this deficiency is of no significant importance.

1.2. Air Density and Temperature. Air density can be derived from the fall rates of the foil cloud when accurate tracking data are available (Rose and Widdel, 1972) but only over the height range for which the dimensions of the sensor elements (area load and width) are matched to yield low Reynolds numbers and their width is small compared with the mean free path. When the transition region is reached, the increase in density nearly compensates for the decrease of effective drag coefficient and the descend speed of the elements varies then only slowly with height. To restore the flow conditions under which it is possible to derive density one has to match the physical properties of the sensor elements to the relevant height region. Below about 65–60 km the useful height range over which density measurements can be made with “CHAFF” becomes so small that it is of no more practical use, and the method finds its natural limitation (Rose and Widdel, 1972).

This method is sensitive enough to follow diurnal changes of density. From these, even slow vertical movements of the atmosphere can be derived (Azcaraga, et al., 1971; Rose et al., 1972a). Reasonably good agreement between densities derived from falling sphere experiments and foil cloud experiments (Rose et al., 1976) was attained (Fig. 4).

Temperature values can also be derived from the data but only as averages. The second derivative of the data necessary for temperature determination introduces a comparatively large error bar for the temperatures and does not allow at present a finer analysis.

2. Ionized Constituents: The Guard Ring Probe

For the measurement of the ionized component of the D-region atmosphere we used a guard ring probe at the tip of the rocket (Rose et al., 1972b). This probe allows us to distinguish between ions and electrons. Probes of similar design have been used in the past on rockets by several authors, L.G. Smith (1967, 1969) being the first.

While the technical design of the probe itself can be held rather simple, the direct interpretation of the results in terms of absolute values poses a lot of problems. To circumvent these, it has become standard (Thrane, 1974) to calibrate the probe readings against the results of an independent wave propagation experiment flown on the same payload as was first done by Mechtly (Mechtly et al., 1967; Mechtly and Shirke, 1968; Sechrist et al., 1969; Mechtly, 1974). Mechtly found that the "Langmuir" probe readings are proportional to electron concentration up to about 85 km, and tend to deviate from proportionality above this region.

Instead of flying simultaneously an independent wave propagation experiment on each payload for calibration purposes, we used a different approach to convert the probe data into ambient electron densities. We used the results of the ground-based absolute absorption measurements and ionosonde data and results of our in-situ density measurements which have to be performed anyway when such investigations are made.

Our variant of the probe was based upon experience gained during the development of a parachute Gerdien-type experiment (Widdel, et al., 1971; Borchers, 1971; Widdel et al., 1977). We found that insulator surfaces can have an important detrimental effect upon the stability of the zero point especially when the probe potential is changed, because these surfaces collect charges preferably of one polarity because the accommodation coefficients are different. This effect disappears when the insulator is kept as small as possible and recessed.

The insulator of our probe is recessed by about 5 mm in a gap between body and probe tip, only 0.5 to 1 mm wide. The corresponding increase in capacity was compensated by a rather large guard ring section held always on the same potential as the measuring nose tip. The current/voltage characteristics were then what one would expect from the mobility concept. Electrons are easily distinguished from ions because their mobility is so much higher. The probe resembles more an "open" Gerdien mobility probe aspiration system than a "Langmuir" probe. The regime in which the probe operates is easily seen because a time-linear, triangle-shaped waveform and linear amplifiers are used.

Because wake effects can play an important role (as was outlined by Smith) a stable flight behaviour of the rocket is mandatory. This condition was met by selecting a suitable rocket (SK UA II) and each payload was carefully balanced before flight by moment and couple.

2.1. Probe Calibration Procedure. The ground-based data yield the total absorption L_{TOT} measured on an absolute scale over an A_3 absorption path which is always propagated via the $1 \times E$ hop mode during daytime. (Rose and Widdel,

1977a). The reflection height $h'_E(f)$ is taken from ionograms produced on the range. The foil cloud experiment flown on the same rocket yields the air pressure from which the electron collisional frequency is derived (Phelps and Pack, 1959).

The electron currents I of the probe are assumed to be proportional to the ambient electron densities ($N_e = C \cdot I$, $h < h_0$) up to a height h_0 where the mean free path equals the (mean) diameter of the probe. Above that height h_0 a correction factor $\exp(\alpha(h - h_0))$ is assumed ($N_e = C \cdot I \exp \alpha(h - h_0)$) which is replaced by 1 below h_0 . The transmission curve technique is applied to the relevant ionograms taken before, during and after the rocket flight with regard to distance and frequency to determine the angle of incidence ϕ_0 into the ionosphere for the A_3 transmission path to the receiver at the launch site. Some well-known approximations are accepted for a moment. The constants C and α which relate the probe currents to the electron densities are then computed in the following way: Starting with the given angle of incidence and an initial pair of constants C and α , a ray-tracing is performed to adjust α in a way that the ray is "homed in" (it just spans then the distance from the transmitter to the receiver). The absorption of the measured ordinary ray is then integrated along this ray path, taking now into account the magnetic field of the earth and using the full Sen-Wyller formulas with the electron collisional frequencies derived from the air pressures. If the absorption thus integrated does not yet fit the experimental A_3 measurements, the constant C is changed a little into the required direction and the calculation is repeated from the very beginning until transmission path and absorption satisfy the experimental data. It should be mentioned that the experimental electron current profiles were replaced close to the (final) reflection level by an equivalent exponential profile (or they were extrapolated exponentially where necessary) in order to determine analytically the curvature of the ray path necessary for the estimations in the vicinity of the reflection level. Experience gained during the aeronomy program has shown that profiles derived in this way from guard ring probe measurements agree reasonably well with those measured by wave propagation experiments.

3. The Payload

Both experiments, the foil cloud experiment and the guard ring probe were matched together in a single payload. Figure 5a shows what the payload looks like and Figure 5b shows a cross section through it. The cylindrical part of the payload contains the foil cloud experiment and the telemetry antennas for data transmission on 235 MHz. The antennas are of the "traveling-wave" type. The transmitter is located in a bay of the upper part of the payload structure, not far away from the subcarrier oscillators and from the electrometer for the guard ring probe. The latter is housed in a separate cylindrical box for electrical shielding and thermal protection.

Transfer of aerodynamic heat into the payload can be a serious problem. It is more difficult to prevent on small vehicles than on large ones. We solved this problem by avoiding mechanical contact between the inner surface of the nose cone section and the payload structure. The only connection to the metallic

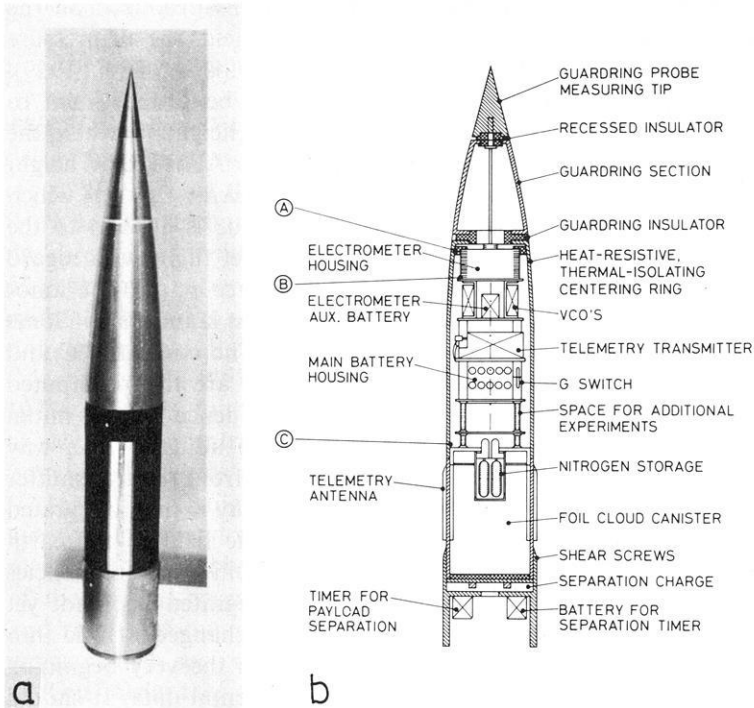


Fig. 5a and b. Actual design of payload B I left: photograph, right: schematic cross section (not to scale). Encircled letters refer to points where temperature measurements were taken

nose cone was at the bottom and through a temperature-insulating, thermal-resistant plastic centering ring at the top of the payload structure.

In order to suppress heat transfer by thermal convection, a number of small ventilating holes were drilled into the nose cone at its end. This ensured a rapid escape of air from the nose cone section during ascent.

The aerodynamic heating was however welcomed and used to advantage as a means of "natural" cleaning of the guard ring probe surface during ascent, especially of the nose tip. The nose tip was made as sharp as possible to assure attachment of the shockwave and to avoid any detachment which might otherwise cause problems in data interpretation.

Photocurrents were of no importance because their maximum value was for the worst case (the lowest heights) estimated to be of the order of one or two magnitudes less than the currents drawn from the environs.

A bay near the end of the ogival section of the nose cone was kept clear to provide space for experiments to be added in later projects (for example, Lyman- α and other radiation counters). On some flights, the space was used to house a modified Henderson probe (Henderson and Shiff, 1970) but despite very promising laboratory results, the probe behaved quite ambiguously during

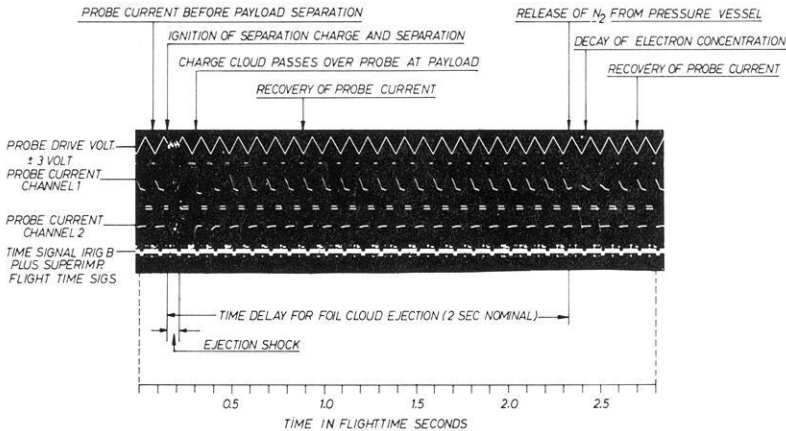


Fig. 6. Copy from telemetry record made on 35 mm film (photographic positive), which shows time interval between separation and foil expulsion. Data transmission for the guard ring probe is made over two separate subcarrier channels which transmit direct output of electrometer and output amplified by a factor of 10. Sensitivity of electrometer is alternatively changed by a factor of 100 at the peaks of the triangular probing waveform. By this, four orders of magnitude in current can be transmitted

flights. It was concluded that this approach to the measurement of atomic oxygen was not a reliable one and the probe was later abandoned.

The front end of the payload rested in a separation section to which it was tightly screwed on with shear screws. A flat, annular charge of explosive was fixed to the bottom of the ejection bay. It was fired at the apogee of the rocket's trajectory and separated the payload front end from the motor in order to expose the back end of the foil cloud canister. The explosive charge was 15 g of a stoichiometric mixture of potassium permanganate and magnesium powder. This composition had turned out to be superior in its characteristics and handling qualities in this special kind of application to conventional black-powder or double based grain powder charges.

1.8–2.2 s after separation pyrotechnic valves were opened for the release of compressed nitrogen which pushed out the foils, separated them, removed from the foils a considerable amount of centrifugal force and created the desired distribution inside the foil cloud. Separation of payload and ejection of foils is observable in the telemetry records of the guard ring probe as is shown in Figure 6: First, the ejection shock causes an interruption of the telemetry transmission which recovers after 80 ms. The cloud of combustion products and unburnt particles from the separation charge passes over the probe environment and causes a transient increase of electron concentration which is produced by photoemission of particles from the cloud. The moment of foil ejection is seen as a decrease in the electron concentration when the nitrogen cloud passes over the probe. These two events serve as simple housekeeping information about proper functioning of separation and foil cloud ejection.

Because the electronics of the payload is designed to stabilize within a few tenths of a second, no umbilical connector is required. Electric power to the payload electronics is applied when a simple inertia switch is actuated by the launch shock (motor ignition and initial acceleration). By this, the aerodynamic configuration of the rocket was kept clean, the design of the payload was simplified and hazards connected with the use of umbilicals on small rockets were avoided. The delay in response of the g-switch contributed to payload reliability because it is a common experience that electronic circuits can survive large shock loads when no power is applied. They often fail in the other case because transient short circuits and transient changes in component values that can occur under heavy g-load conditions may cause fatal overloads. The response time of the g-switch is set to such a value that it closes when the initial launch shock has passed.

Because the SKUA rocket is launched from a tubular launcher, there was some concern at the beginning that the probe surface might be contaminated by combustion products of the boost and sustainer propellant during the initial launch phase. Prototype flights and later experience have shown that this is not the case. The results of the prototype flights stressed however the necessity for a careful balancing of the payloads and led to some improvements of the final design too detailed to be described in this paper.

4. Some Results

Figure 7 illustrates how the circulation pattern of winds changes from winter to summer. High winter-anomalous absorption was observed only when westerlies are present in the whole height regime between 80 and 90 km. This indicates that this state is linked to a low-pressure system which has its center located north of the location where the measurements were made. Because we made our observations rather close to the time-variable southern border of the existence of winter-anomalous conditions, we saw more clearly than in more northern latitudes that the winter-anomaly effect splits up into more than one period of high absorption. Between these events, extremely low absorption is observed in most cases. This raises the question how to define a "normal" and a "winter-anomalous" day. We tried to circumvent these difficulties by referring to electron concentration profiles which were measured at a time when both the wind field is calm and the absorption has little variation from day to day. This is mostly the case in the spring/early summer season.

Like Mechtly we found the maximum enhancement of electron concentration around 82 km (Dieminger et al., 1974). Since then more winter profiles of electron concentration became available. All were measured around local noon.

It takes no effort to classify these profiles either after similarity or after amount of absorption: in both cases, the profiles which sort into a group are the same. There are, however, some slight but significant differences between profiles belonging to the same group: Some of them have a higher electron concentration below about 78 km than others. This difference is related to the diurnal variation of absorption. The profile which has a higher electron

7 JUN 1975 11.00 Z

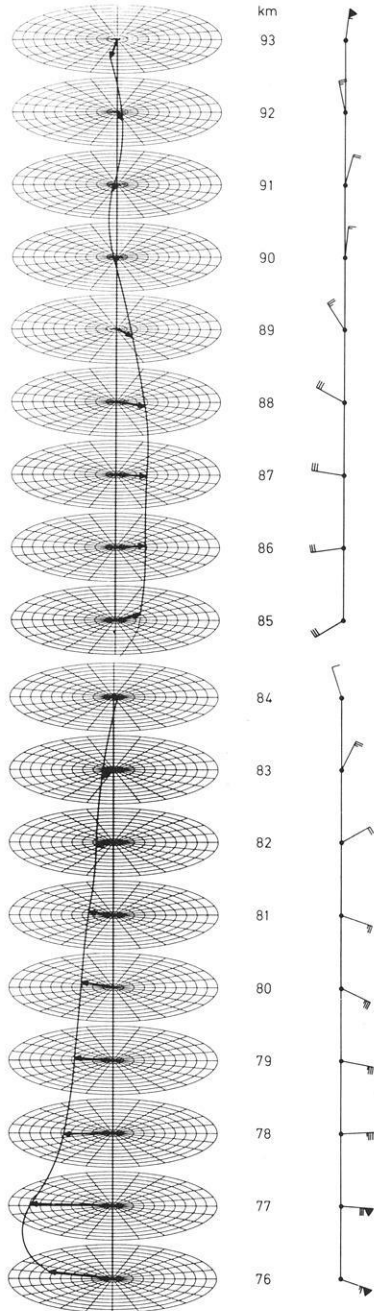
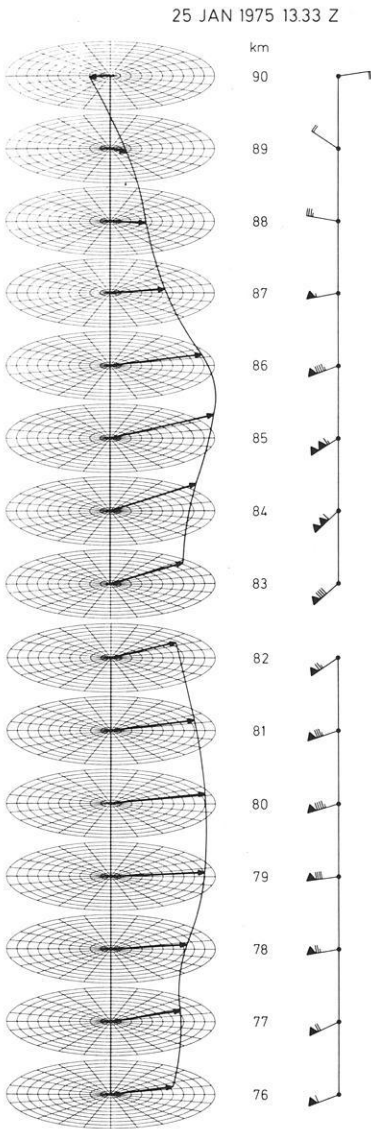


Fig. 7. Two Examples for wind measurements around noon time: Seasonal variation. *Left:* quasi-three dimensional “wind-band” presentation on compass cards. (North: top, west: left, east: right.) Each division: 10m/s. *Right:* meteorological “arrow” notation with barbs. The arrow is flying from where the wind is coming; speed indicated by barbs. One full triangular barb: 50 m/s; one light barb: 10 m/s, short barb: 5 m/s. Note the differences in speed and direction: Wind velocities in the 80–88 km region are much higher during winter

concentration in lower levels corresponds to a day for which the description of the diurnal variation of absorption by the $\cos^n \chi$ -law is given by an “ n ” of the order of 1, while “ n ” is lower for the other profile. This difference is more clearly seen when the corresponding profiles of differential contribution to total absorption along the ray path $dL/dl \cdot \frac{1}{\cos \varphi}$ are considered. This is more closely related to the actual absorption measurement because it contains the electron collision frequency also. It is determined during the evaluation process of the guard ring probe results. For a comparison of different groups of absorption it is convenient to normalize the profiles of differential contribution to total absorption to the relevant amount of total absorption. When “ n ” has a high value (in the order of 1) a maximum contribution to absorption stems from the height region centered around 75 km (see Fig. 8). For lower “ n ” this maximum is shifted to greater heights above 78–80 km. This shift becomes pronounced when “ n ” is small (0.5 or less). This result can at least be qualitatively understood and related to composition changes in the D-region when model calculations made long time ago by Rawer (1943) are considered. He used a simplified model and assumed “thin” and “thick” absorbing layers (in the sense that their scale height was smaller than or equal to that of the environmental gas). He found that the diurnal variation of absorption is proportional to $\cos^{1/2} \chi$ when the layer is “thin” and the electron loss process is recombination. For attachment as the loss process, he arrived at $\cos \chi$. The corresponding values for a “thick” layers were $\cos^{1.5} \chi$ (recombination) and $\cos^2 \chi$ (attachment). The simplifications made in this theory prevented its practical application in the past, but taking it as a guide and considering the results of our in-situ measurements, we can distinguish fairly clearly between at least two height levels which contribute to absorption. One level is below 78 km in which the electron loss process is, as is well known, the formation of negative ions. Above 80 km, the prevailing loss process during winter is recombination.

This level becomes more important when strong winter-anomalous conditions are present. However, there are exceptions in which both levels (above 80 and around 75 km) contribute about equally to total absorption and produce high winter-anomalous absorption. On such days, attachment in the lower level (or a loss process equivalent to attachment) governs the diurnal variation and yields a high “ n ” for the $\cos^n \chi$ -approximation of the diurnal variation. Because the electron/ion ratio is extremely temperature-sensitive in these lower levels (Cipriano, Hale and Mitchell, 1974) one is tempted to relate these events to temperature increases (stratospheric warmings) but this has to be further investigated more closely.

Mass spectrometer results reported by Arnold and Krankowski (1971) and by Arnold, Kissel, Krankowski, Wieder and Zaehring (1971) who found negative ions below 80 km but not in greater heights while Narcisi and co-workers (1972) did find them in heights between about 82 and 87 km but with a different composition fit well into this picture. These two results have been considered to be in conflict with each other but are less controversial if one considers the actual season and not the calendar date on which the two measurements were made and assumes that a depletion of water content in the D-region during winter is one of the main causes of winter anomaly.

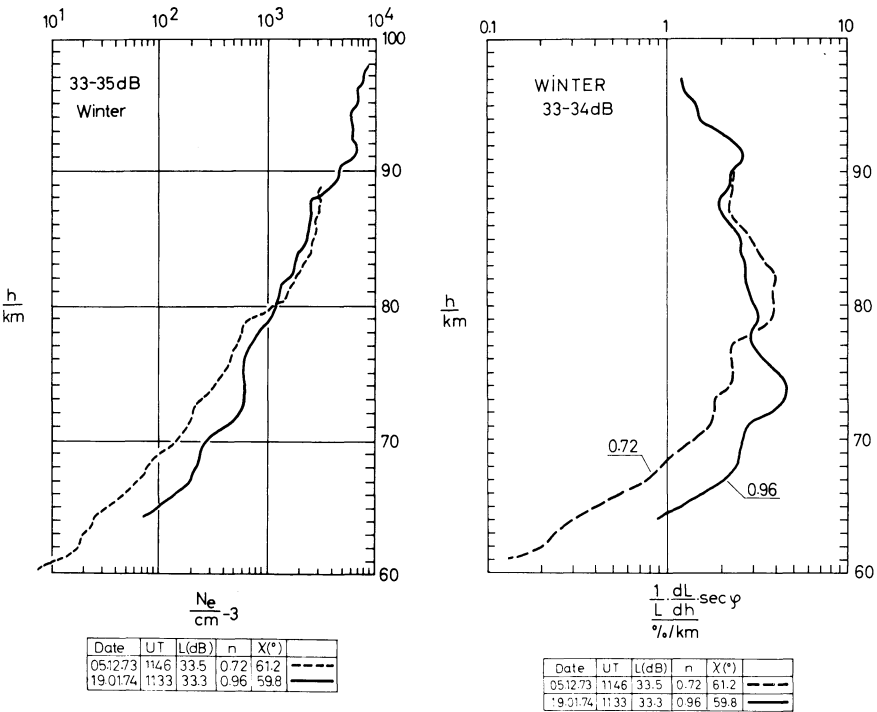


Fig. 8. An example for the relation between “n” of the \cos^{χ} approximation of the diurnal variation of absorption and electron concentration profile resp. profile of differential contribution to total absorption along the ray path (the latter normalized to the relevant absorption value): When “n” is large, a maximum of contribution is found around 75 km (winter profiles)

Therefore, one of the things (amongst others) we want to learn from the results of other measurements taken in the Aeronomy Program is if there is a seasonal change in water vapor content and in the content of nitric oxide in the D-region, preferably between 78 and 88 km, because this would explain the disappearance or reduction of the ledge in electron concentration during winter conditions and the formation of the “bulge” of electron concentration found when high winter anomalous absorption is present.

Acknowledgement. The work was sponsored by the Bundesminister für Wissenschaft und Forschung (WRK 90) and, in part, by GRANT DAERO – 75-G-076.

Our sincere thanks go to our colleague Dr. A. Loidl who developed the probe electrometer and its associated circuitry.

References

Arnold, F., Kissel, J., Krankowski, D., Wieder, H., Zaehring, J.: Negative ions in the lower ionosphere: A mass-spectrometric measurement. *J. Atmospheric. Terrest. Phys.* **33**, pp. 1169–1175, 1971

- Arnold, F., Krankowski, D.: Negative ions in the lower ionosphere: A comparison of model computation and a mass-spectrometer measurement. *J. Atmospheric. Terrest. Phys.* **33**, pp. 1693–1702, 1971
- Azcarraga, A., Sanchez, L., Rose, G., Widdel, H.U.: An evaluation of the scale of mesospheric wind disturbances. In: *Space Research, XII*, pp. 613–614. Berlin: Akademie-Verlag 1972
- Azcarraga, A., Sanchez, L., Widdel, H.U.: On the structure of mesospheric wind. In: *Space Research, X*, pp. 174–179. Amsterdam: North Holland Publ. Comp. 1970
- Azcarraga, A., Sanchez, L., Widdel, H.U.: Measured wind oscillations at mesospheric levels. In: *Space Research, XI*, pp. 835–840. Berlin: Akademie-Verlag 1971
- Borchers, R.: Untersuchungen der Eigenschaften einer Aspiration-Sonde (Gerdiem-Kondensator) zur Bestimmung der Konzentrationen und Beweglichkeiten von Ladungsträgern beiderlei Vorzeichens im Höhenbereich zwischen 80 und 40 km. Forschungsbericht BMBW-FBW71–39, Bundesministerium für Bildung und Wissenschaften, 1971
- Cipriano, J.P., Hale, L.C., Mitchell, H.D.: Relations among low ionosphere parameters and A₃ radio wave absorption. *J. Geophys. Res.* **79**, 2260–2265, 1974
- Dieminger, W., Hoffman-Heyden, A.E.: Reflexionen von Kurzwellen aus Höhen unter 100 km. *Naturwissenschaften* **39**, 1, 1952
- Dieminger, W., Rose, G., Widdel, H.U.: In situ measurements of electron concentration, neutral wind and air pressure compared with the winter anomaly. In: *Lower ionosphere structure*, K. Rawer, ed., pp. 341–348. Berlin: Akademie-Verlag 1974
- Gregory, J.B.: Radio wave reflections from the mesosphere. I. Height of occurrence. *J. Geophys. Res.* **66**, 429–445, 1961
- Henderson, W.R., Schiff, H.I.: A simple sensor for the measurement of atomic oxygen height profiles in the upper atmosphere. *Planetary Space Sci.* **18**, 1527–1534, 1970
- Jones, L.M.: Upper air densities and temperatures from eight IGY rocket flights by the falling sphere method. WDC A, IGY R. Rep. No. 5, 1959
- Mechtly, E.A.: Accuracy of rocket measurements of lower ionosphere electron concentrations. *Radio Sci.* **9**, 373–378, 1974
- Mechtly, E.A., Shirke, J.S.: Rocket electron concentration measurements on winter days of normal and anomalous absorption. *J. Geophys. Res.* **73**, 6243–6247, 1968
- Mechtly, E.A., Bowhill, S.A., Smith, L.G., Knoebel, H.W.: Lower ionosphere electron concentration and collision frequency from rocket measurements of Faraday rotation, differential absorption and probe current. *J. Geophys. Res.* **72**, 5239–5247, 1967
- Narcisi, R.S., Bailey, A.D., Wlodyka, L.E., Philbrick, C.R.: Ion composition measurements in the lower ionosphere during November 1966 and March 1970 solar eclipses. *J. Atmospheric. Terrest. Phys.* **34**, 647–658, 1972
- NASA-Sp-219: Status of passive inflatable falling-sphere technology for an atmospheric sensing to 100 km. Symposium Langley Res. Center, Hampton, Va. 23–24.9.1969. Office of Technology and Utilisation, NASA, Washington, D.C.
- Otterman, J.: Analysis of a falling-sphere experiment for measurement of upper atmosphere density and wind velocity. *J. Geophys. Res.* **66**, 819–822, 1961
- Pachomov, S.V.: Technique of obtaining data about winds in the mesosphere by small meteorological rockets. In: *Small rocket instrumentation techniques*, K.I. Maeda, ed., pp. 135–137. Amsterdam: North Holland Publ. Comp. 1969
- Phelps, A.V., Pack, J.L.: Electron collision frequencies in nitrogen and in the lower ionosphere, *Phys. Rev. Letters* **3**, 240–242, 1959
- Rapp, R.R.: The accuracy of wind derived by the tracking of chaff at high altitudes. *J. Meteorol.* **17**, 507–514, 1960
- Rawer, K.: Der Einfluß der Dämpfung auf die Kurzwellenausbreitung. ZWBM Berlin-Adlershof, FB Nr. 1872, 1943
- Rose, G., Weber, J., Widdel, H.U., Galdon, P.: Experimental results of radio wave absorption measurements in Southwest-Europe. In: *Lower ionospheric structure*, K. Rawer, ed., p. 331–339, Berlin: Akademie-Verlag 1974
- Rose, G., Widdel, H.U.: Zur Möglichkeit des direkten Nachweises vertikaler Luftbewegungen in Höhenbereich 75–80 km. *Z. Geophys.* **35**, 211–212, 1969
- Rose, G., Widdel, H.U.: On the possibility of a simultaneous measurement of wind speed, wind direction, air density and air temperatures at heights which correspond to the upper D-region (max 95 km) with chaff cloud sensors. *Planetary Space Sci.* **20**, 877–889, 1972

- Rose, G., Widdel, H.U.: Results of air temperature, density and pressure measurements obtained with the aid of foil cloud sensors in the height region between 80 and 95 km. *Planetary Space Sci.* **21**, 1131–1140, 1973
- Rose, G., Widdel, H.U.: D-region radio wave propagation experiments, their significance, and results during the Western European winter anomaly campaign 1975/76. *J. Geophys.* **44**, 15–2, 1977
- Rose, G., Widdel, H.U., Azcarraga, A., Sanchez, L.: A payload for small sounding rockets for wind finding and density measurements in the height region between 95 and 75 km. *Phil. Trans. Roy. Soc. London, A* **271**, 509–528, 1972a
- Rose, G., Widdel, H.U., Azcarraga, A., Sanchez, L.: Experimental evidences for a transient ion layer formation in connection with sudden ionospheric disturbances in the height range 20–50 km. *Planetary Space Sci.* **20**, 871–876, 1972b
- Rose, G., Widdel, H.U., Olsen, R.O., Kennedy, B.: Project “Limpas” ein Vergleich zwischen den Ergebnissen von Wind- und Dichtemessungen, gewonnen mit dem Verfahren „fallende Kugel“ und dem Lindauer Folienwolken-Experiment. *Kleinheubacher Berichte* **19**, 471–482, 1976
- Sechrist, C.F., Mechtly, E.A., Shirke, J.S., Theon, J.S.: Coordinated rocket measurements on the D-region winter anomaly – I. Experimental results. *J. Atmospheric Terrest. Phys.* **31**, 145–153, 1969
- Smith, L.G.: The measurement of winds between 100.000 and 300.000 ft. by use of chaff rockets. *J. Meteorol.* **17**, 296–310, 1960
- Smith, L.G.: Langmuir probes for measurements in the ionosphere. In: *Electron density and temperature measurements in the ionosphere*, K.I. Maeda, ed., pp. 2–31. revised edition, COSPAR Techniques Manual Series, 1967
- Smith, L.G.: Langmuir probes in the ionosphere. In: *Small rocket instrumentation techniques*, K.I. Maeda, ed., pp. 1–15. Amsterdam: North Holland Publ. Comp. 1969
- Thrane, E.V.: Ionospheric profiles up to 160 km – A review of techniques and profiles. In: *COSPAR methods of measurement and results of lower ionosphere structure*, K. Rawer, ed., pp. 3–21. Berlin: Akademie-Verlag 1974
- Tiheridge, J.E.: The stratification of the lower ionosphere. *J. Atmospheric. Terrest. Phys.* **24**, 283–296, 1962
- Webb, W.L.: The first meteorological rocket network. *Bull. Am. Meteorol. Soc.* **42**, 482–494, 1961
- Widdel, H.U., Rose, G., Borchers, R.: Results of concentration and mobility measurements of positively and negatively charged particles taken by a rocket-borne parachuted aspiration (Gerdien) probe in the height region from 72 to 39 km. *Pageoph* **84**, p. 154–160, 1971
- Widdel, H.U., Rose, G., Borchers, R.: Payload B III – an instrument package for the measurement of conductivity, concentration and mobility of positive and negative ions in the mesosphere. *J. Geophys.* **43**, 179–188, 1977
- Zimmerman, S.P., Narcisi, R.S.: The winter anomaly and related transport phenomena. *J. Atmospheric. Terrest. Phys.* **32**, 1305–1308, 1970

Received May 2, 1977; Revised Version June 6, 1977

Plasma Measurements during the Western European Winteranomaly Campaign

K. Spenner, W. Ott, and H.J. Bradenstein

Institut für Physikalische Weltraumforschung der FhG,
D-7800 Freiburg, Federal Republic of Germany

Abstract. During the Western European Winteranomaly Campaign two planar Retarding Potential Analyzers were successfully launched on January 4 and 21, 1976 from El Arenosillo, Spain. The experiment on board the B II payload which carried two sensor heads is described. The payload had an active attitude control system with Freon gas as propellant. Its influence upon the plasma measurements is investigated. In the height range 95 to 115 km measured profiles of electron density, temperature and suprathermal electron flux are presented.

Key words. Retarding potential analyzer – Winteranomaly – Electron density – Electron temperature – Suprathermal electron flux – Disturbances by attitude control system.

Introduction

The Western European Sounding Rocket Campaign took place in January 1976 at “El Arenosillo”, Spain (37°6′N, 6°44′W) with a large number of different measurements. The scientific purpose of this combined effort of ground based and rocket carried experiments was to investigate the ionospheric D-region during a winteranomaly. A typical indicator for a winteranomaly condition is unusually great radio wave absorption during a couple of days in a large geographic area. The phenomenon is supposed to be caused by increased electron density in the lower ionosphere through the regular seasonal variation of the state of mesosphere and lower thermosphere (Schwentek, 1971). The not well known relations between ionospheric plasma parameters and neutral composition, and the rather complex processes involved in the D-region can only be studied in more detail when a large number of significant parameters are simultaneously measured. As a part of such a combined study two Retarding Potential Analyzers (RPA) were successfully flown aboard a Skylark rocket in the afternoon of January 4 and 21, 1976. The main thermal plasma parameters viz

electron density and temperature, and the suprathermal electron flux were derived from the measured characteristics. The electron density profile shows the altitude, where the anomaly occurs and how strong it is. Electron temperature and flux may be influenced by the neutral atmosphere and could respond to major changes in the neutral composition.

Instrumentation

We used a planar RPA, similar to an instrument which was flown on earlier rockets and satellites (Spenner et al., 1974). The sensor has a wide entrance grid and a small collector plate as shown in Figure 1. The large first grid and the guard ring surrounding the collector provide for radially uniform particle flux about the sensor axis. The collector samples only electrons or ions from this uniform central region. The sensor has 5 insulated, highly transparent grids. With suitable potentials of these any desired kind of charged particles may be selected and analyzed. In the electron mode the front grids G1, G2, G3 are connected and obtain a staircase retarding voltage; with three grids a most uniform retarding field is achieved. Only electrons with a higher energy than the applied grid voltage can pass through to the collector. Grids G4 and G5 are biased in such a way that ambient ions and secondary electrons produced at the collector are almost completely suppressed. The gold plated grids have 30 wires/cm, the transparency is 86%.

The experiment automatically performs three different modes. Electron temperature and relative density are derived from a 'temperature mode', the suprathermal energy distribution from a 'photoelectron mode' and the ion density from an 'ion mode'. Table 1 summarizes the voltages applied to the sensor grids for the different modes. Each electron mode makes a sequence of 128 steps of 40 mV each. The photoelectron mode executes 28 steps of 1.1 V each. The stepping time is 2 ms. We use a RPA with two identical sensor heads fastened on short booms at the top of the payload (Fig. 2). One sensor is programmed to measure electron temperature and photoelectrons, the other one to determine the ion density with good local resolution. A logarithmic electrometer integrated in the sensor box measures the collector current between the limits 10^{-5} A and 10^{-12} A. Zero level and gain are automatically controlled

Table 1

Symbol	Element	Temperature Mode	Ion density Mode	Photoelectron Mode
G 1	Entrance grid	3 → -1.5	0	4
G 2	Retarding grid 1	3 → -1.5	-6.2	0 → -30
G 3	Retarding grid 2	3 → -1.5	-6.2	0 → -30
G 4	Shielding grid	30	0	30
G 5	Electron suppressor grid	15	-15	15
C, CR	Collector, Guardring	30	0	30

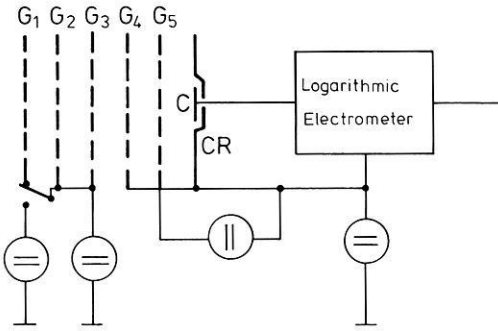


Fig. 1. Sensor schematic of the RPA

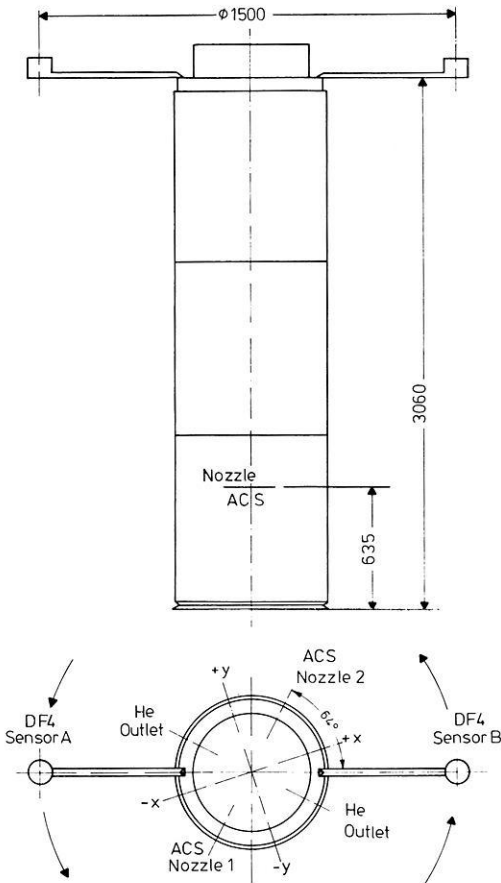


Fig. 2. Position of the RPA and the gas nozzles of the ACS

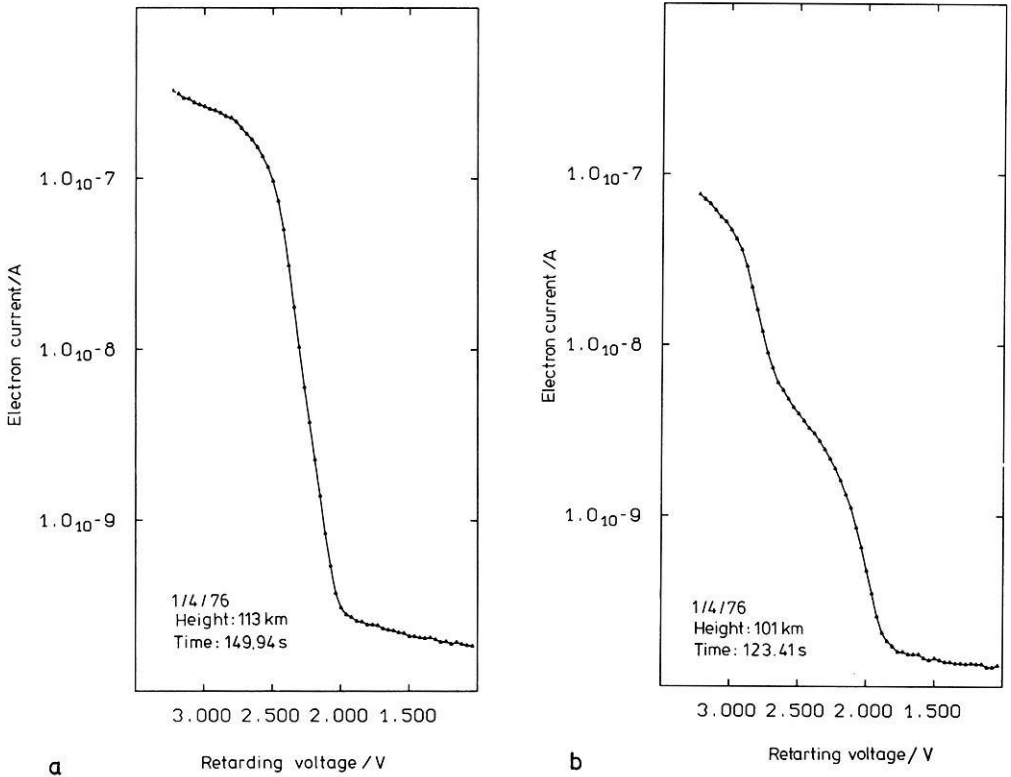


Fig. 3. **a** Measured Langmuir characteristic showing a Maxwellian energy distribution of the thermal electrons. **b** Langmuir characteristic of negative particles with two different energy distributions

and adjusted. Including the bit failure of the 10 bit telemetry the overall accuracy is about 2%. For currents larger than 10^{-11} A the electrometer rise time (99%) is 2 ms. The additional electronics needed to provide the sensor grid voltages, as well as power supply and telemetry interface are installed in a separate box. The achieved stability of the retarding voltages is 0.5 mV. Design and calibration of the instrument are such that electron density and temperature can be measured with an accuracy better than 10%.

Because of the needs of the mass spectrometer the B II payload had an active attitude control system (ACS) so as to point the rocket axis always in the direction of the velocity vector. Thus, the RPA axis was always oriented to optimum ram direction, during ascent and descent. The payload control was achieved by a pulsed Freon gas beam, which was fired about once a spin period (0.5 s). As a consequence the natural environment near the rocket was influenced by a Freon cloud. Its influence to the plasma measurements will be discussed in the following section. The position of the Freon outlets (Nozzle 1 and 2) relative to the RPA sensors is shown in Figure 2. In addition to this there was a Helium outlet of the cooling system of the cryomass-Spectrometer.

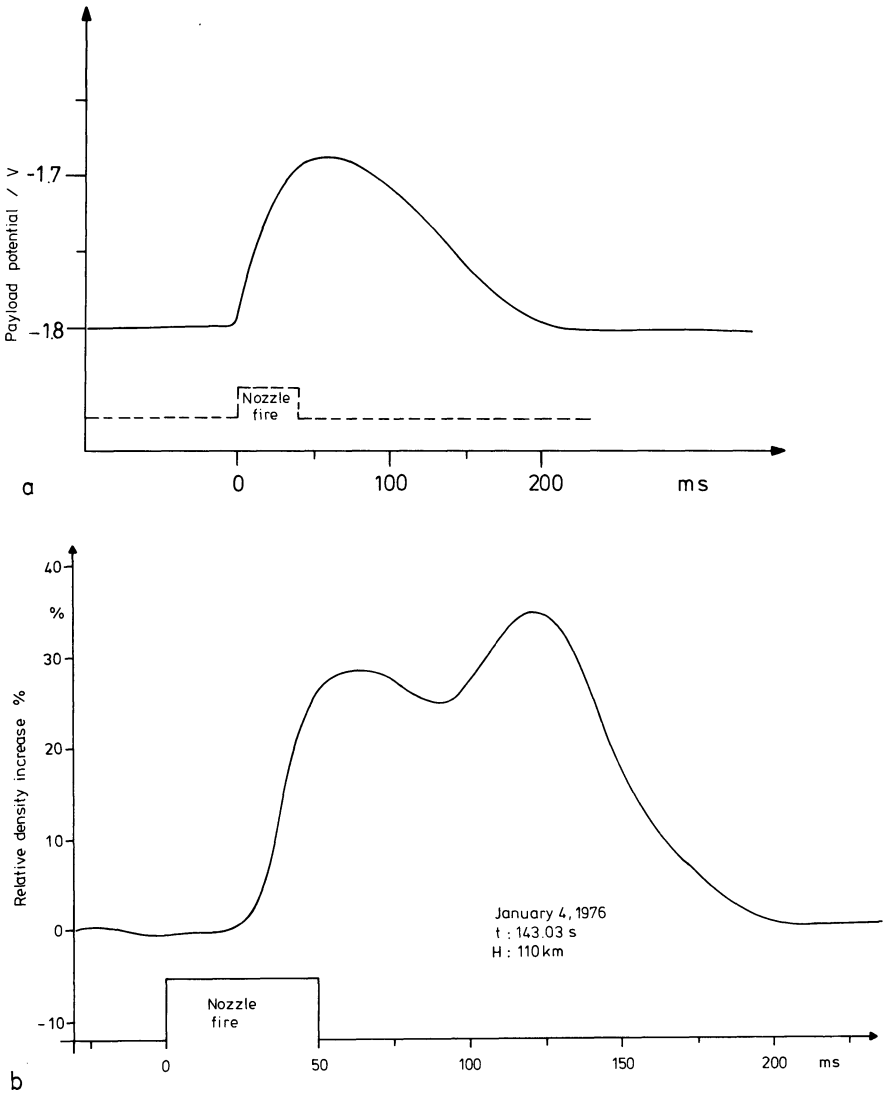


Fig. 4. a Time dependent potential variation of the payload after Freon gas release. **b** Relative plasma density increase after nozzle fire

Results

The transmitted RPA data are of excellent quality for both flights. After boom deployment at 90 km altitude the Langmuir current-voltage characteristic appeared at Sensor A and the ion saturation current at Sensor B. In Figure 3a an example of such a half-logarithmic current-voltage curve is shown. The most important part of the curve is linear with a decrease by about 2 orders of magnitude. Such curve is expected for a Maxwellian energy distribution of the electrons. The maximum slope of this curve determines the electron

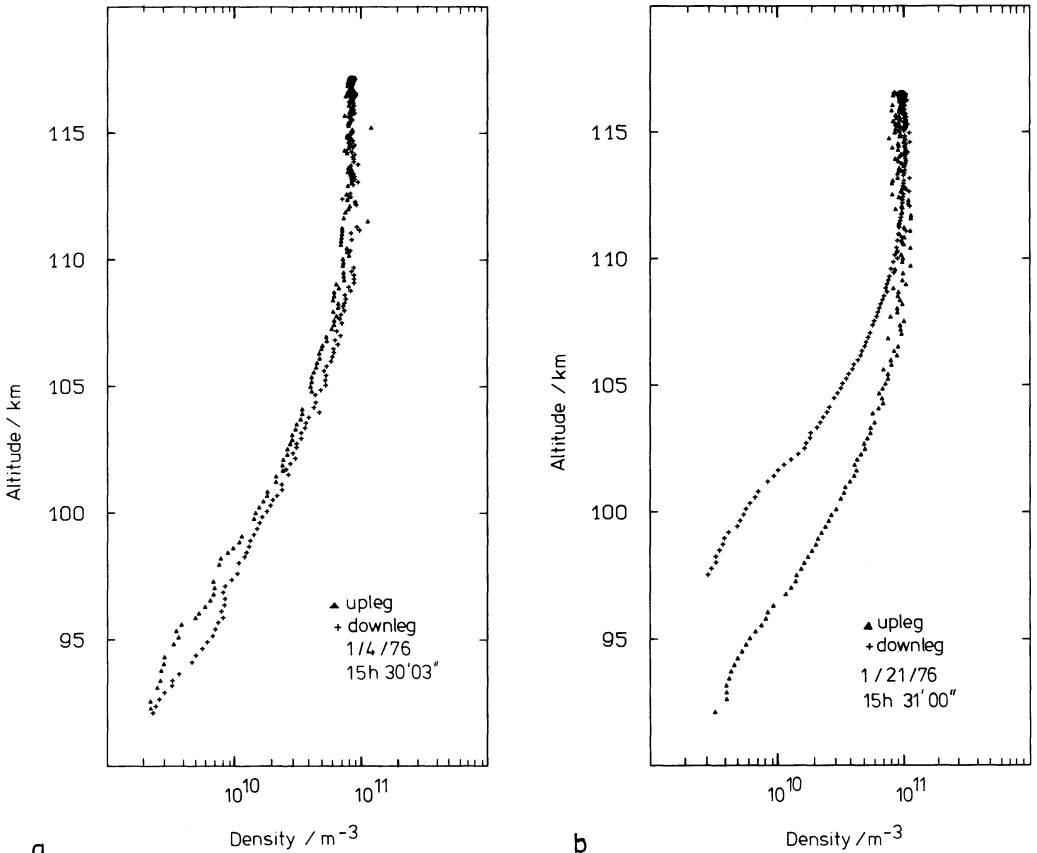


Fig. 5 a Electron density profile for January 4. **b** Electron density profile for January 21

temperature. All current-voltage curves were analyzed. During ascent we found at 100 km altitude an unexpected hump in the lower part of the characteristics as shown in Figure 3b. This proves that a second negative particle population is present with higher than thermal energy. The hump is increased after a nozzle fire. During descent no hump was observed in the same height region. This leads us to suppose that the observed particles are not of natural ionospheric origin. We assume that outgasing, may be in connection with the Freon release, produces negative ions. A rough analysis shows that the hypothesis of negative ions with a mass number greater than 50 μ and a temperature below 300 K is agreeable with the observed curve. At altitudes where these particles are present the true electron temperature can not be obtained by the usual automatic program such that individual analysis is needed.

During each nozzle firing of the ACS the payload is surrounded by a Freon cloud expanding into space. We try to point out how this gas release effects the thermal plasma measurements. The first serious effect is that the payload potential which uses to be always negative in the ionosphere becomes more positive. A corresponding voltage shift in the Langmuir curves is observed after every nozzle fire. The potential increase is between 120 and 200 mV.

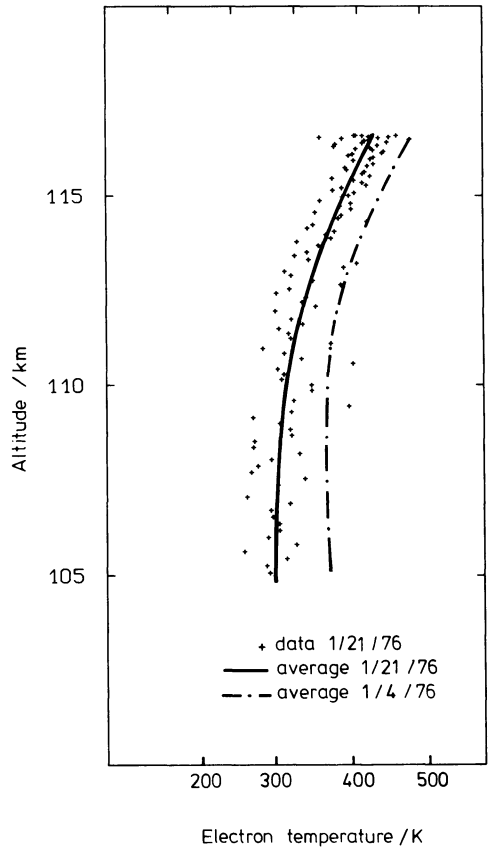


Fig. 6. Electron temperature profiles for January 4 and January 21

The time delay between the gas release and the potential change is probably less than 10 ms, which is the time resolution of the nozzle fire signal. Figure 4a shows the variation of the payload potential during firing of a nozzle (this is an observation of an earlier rocket flight with the same propellant gas). A short gas release leads to a potential change lasting about 200 ms. During that period the plasma density in the neighbourhood of the payload is changed and the ratio between the positive ion and the negative particle flux to the rocket is increased. Secondly we observe an increase of the measured ion current by up to 30% and more as shown in Figure 4b. A first current peak is observed between 20 and 70 ms after the nozzle fire followed by a more pronounced second peak. The observed minimum between the peaks is consistent with the assumption that the plasma density has a minimum at the side opposite to the firing nozzle due to the shadow of payload. This rarefied area is crossed by the spinning sensor B always 90 ms after a nozzle-1-fire (see Fig. 2). Within 200 ms the electron current measured by sensor A was also increased. This confirms that the plasma density is usually enlarged by ionization of the gas released from the ACS. For sensor B the density enhancement is more pronounced when the closer nozzle 2 is activated. The described effects are observed quite generally with only one exception namely at the apogee of the second

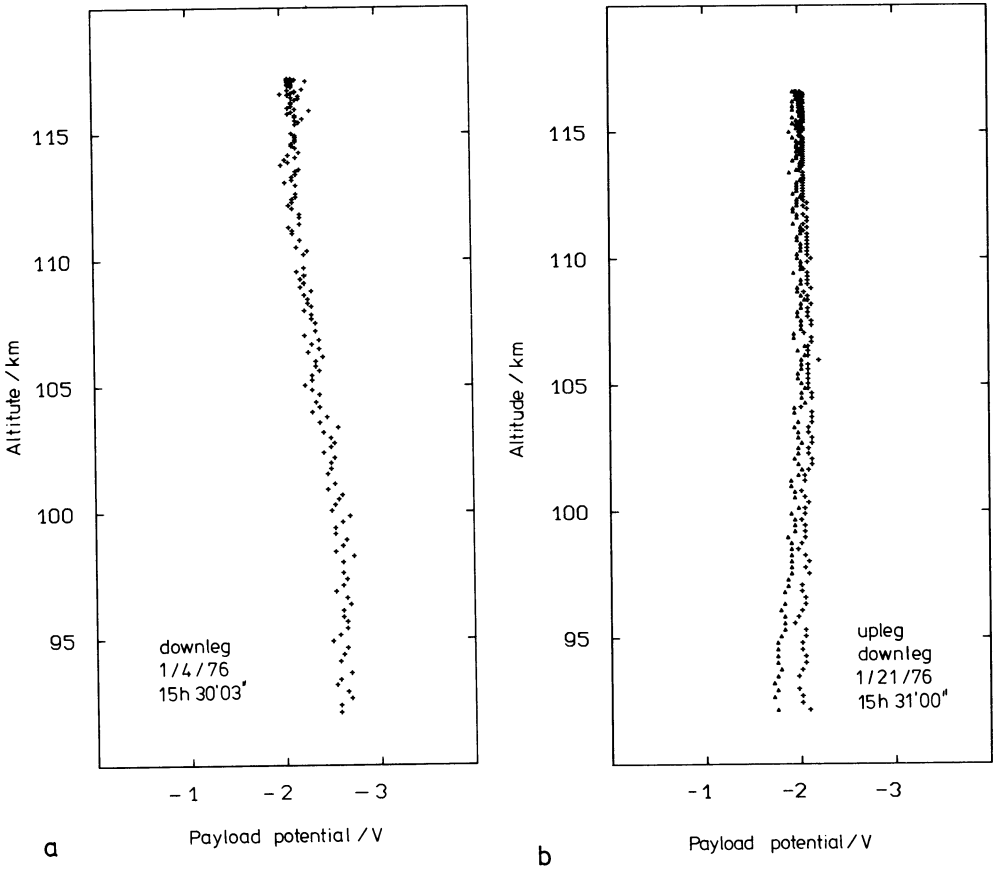


Fig. 7 **a** Payload potential for January 4. **b** Payload potential for January 21

flight. When there for about 10 s a large amount of gas was released the plasma density did not increase, but decreased.

We determined the ion density from the current of Sensor B according to the equation

$$n = \frac{I}{qFTv \cos \vartheta} \quad (1)$$

I is the current averaged over 0.3 s, F the effective area of the collector, q the elementary charge, T the grid transparency, v the rocket velocity and ϑ the angle between rocket velocity vector and sensor axis. Equation (1) is a good approximation for the saturation current as long as $v \cos \vartheta$ is much greater than the thermal ion velocity. This is true during the whole flight pass because the apogee velocity was greater than 800 ms^{-1} . The density profiles of both flights are shown in Figures 5a and b. (These data are not yet corrected for the density increase due to the ACS. Up and downleg of the January 4 density profile fit well together. As for January 21 the apparent discrepancy between

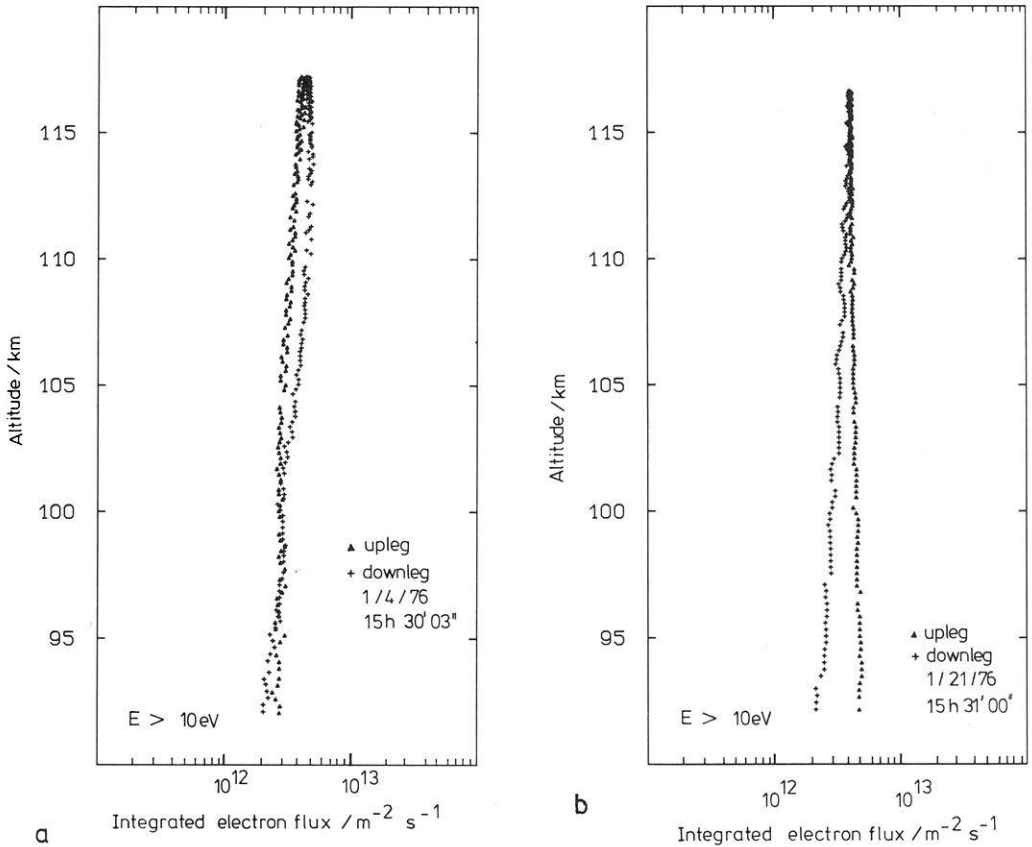


Fig. 8. **a** Integrated electron flux for January 4. **b** Integrated electron flux for January 21

ascent and descent could still be due to incorrect orbit calculation. Upleg and downleg profile can be matched together when the computed apogee height is reduced). Both profiles show a maximum density of $9 \cdot 10^{10} \text{ m}^{-3}$; there is no significant deviation from an expected E-region profile under daylight conditions.

Because of the earlier mentioned not Maxwellian Langmuir characteristic during ascent, we could readily deduce the electron temperature only with the downleg data. The density change and the potential shift caused by the ACS deform the slope of the current-voltage curves to higher and lower values depending on the time after nozzle fire. As a consequence we get some scatter between the individual data points and an averaged more significant temperature profile. Figure 6 shows the individual data points and the averaged temperature for January 21 and for the smoothed temperature profile of January 4, with clearly higher temperature.

The potential of the payload is determined from the highest slope of the semilogarithmic current-voltage curve. We get a rather negative charge as shown in Figures 7a and b. Compared with other rocket flights the rocket potential

of $-2V$ or more is quite important. This could be the result of the rather small ratio of the effective ion collecting area in ram position and the total surface of the payload (which collects the faster electrons).

In the last Figures 8a and b the integral electron flux above 10 eV is shown. The flux profile of the first flight has no significant difference between up and downleg, which indicates nearly isotropic flux. During the second flight the data show that the downcoming flux measured during ascent is higher and almost independent of the altitude. However, since we had attitude control with increasing height the sensor points more and more horizontally so that a vertical flux which might grow slowly with height may not be recognized.

5. Conclusions

The data presented are not yet corrected for the disturbance caused by the gas release of the ACS and must therefore be considered as preliminary. The calculated height of the second flight may be in error by one or two km. All that, however, does not effect seriously the more general results. During these anomalous winter days in the height range 100–115 km we could not observe a significant deviation of the electron density profile from normal E-region behaviour. The strong radio wave absorption observed by ground based measurements is only due to a strong density enhancement in the D-region. The downward directed suprathermal electron flux was smaller for January 4. Assuming that the total production of photoelectrons was equal on both days (as it is measured for the upward flux) we may argue that the downward flux was more absorbed on January 4. At the same time the electron temperature was increased. Now it is well known that the slowing-down process of photoelectrons depends on the neutral atmosphere. An increased atomic oxygen density, for example, on January 4 could absorb a larger amount of the photoelectrons produced at a higher altitude range. (Dalgarno et al., 1971). A part of the photoelectron energy is always transferred to the thermal electrons. The increased electron temperature and atomic oxygen density as measured by the mass spectrometer are in agreement with these considerations. A more complete picture may later be determined when the whole set of simultaneous measurements becomes available.

Acknowledgements. We thank the BMFT for sponsoring this project funded unter Kapitel 3006, titel 68501.

We appreciate the support we had from the DFVLR/BPT. We wish to thank the project scientist of this Western European Winteranomaly Campaign, Prof. Offermann for great encouragement and fruitful cooperation.

References

- Dalgarno, A., Lejeune, G.: The absorption of electrons in atomic oxygen, *Planetary Space Sci.* **19**, 1653–1667, 1971
- Schwentek, H.: Regular and irregular behaviour of the winteranomaly in ionospheric absorption. *J. Atmospheric Terrest. Phys.* **33**, 1647–1650, 1971
- Spenner, K., Dumbs, A.: The retarding potential analyzer on AEROS-B, *J. Geophys.* **40**, 585–592, 1974

Received May 2, 1977

A Rocket Borne Experiment to Measure Plasma Densities in the *D*-Region

M. Friedrich¹, K. Torkar², and S. Ulrich¹

¹ Department of Communications and Wave Propagation, Technical University Graz, Inffeldgasse 12, A-8010 Graz, Austria

² Space Research Institute of the Austrian Academy of Sciences, c/o Technical University Graz, Austria

Abstract. A description of two experiments is presented which, combined on the same rocket payload, can possibly provide the most accurate plasma density measurement in the lower ionosphere.

Key words: *D*-region – Winter anomaly – Plasma density – Faraday rotation – Differential absorption – Electrostatic probe.

1. Introduction

One of the most important parameters of any *D*-region study is the density of free, thermal electrons and ions. Not only is a considerable part of the solar energy converted at these altitudes used to create free electrons, the electron density in this region of the ionosphere also controls the radio wave absorption, hence also the anomalous HF absorption observed in Winter. The experiment consists of two independent instruments: A radio wave propagation method (Faraday rotation and differential absorption), and an electrostatic probe. The results of both instruments supplement each other yielding very accurate absolute densities of electrons, the probe, once normalised to the Faraday data, can provide good height resolution. Furthermore, an *in-situ* measurement has advantages when measuring under unstable conditions. In contrast to a propagation experiment, it is uninfluenced by changes of the plasma underneath, which could be interpreted as the effect of the height layer under consideration. The use of a probe in addition to a propagation experiment is therefore always advisable whenever plasma densities are to be measured which are more or less constant (above ca. 100 km).

Hence, a propagation experiment alone should only be employed at heights of steadily increasing densities (*D*-region). A combination of both experiments was therefore flown on both B IV payloads (Nike Apache) with nominal apogees around 130 km.

2. Faraday Rotation and Differential Absorption

A magneto-plasma, such as the ionosphere, exhibits a dual, complex refractive index for left and right hand sense of circular polarisation, respectively. Both indices are functions of the electron density, N_e , the collision frequency, ν , the signal frequency, f , and the (Earth's) magnetic field, B . The refractive index ($\mu_0 + j\chi_0$) of the wave polarisation which also exists in absence of a magnetic field, is referred to as that of the ordinary wave (in the Northern hemisphere: left hand circular for frequencies above the gyro frequency, f_g). The other index ($\mu_x + j\chi_x$), controlling the other polarisation sense, is called the extraordinary and only exists in presence of a magnetic field (c.f. e.g. Budden, 1966). A linearly polarised HF wave transmitted from the ground to a rocket payload, can be considered as the superpositioning of a right and left hand circularly polarised wave. In absence of a magneto-plasma, the resulting polarisation will be a linear one parallel to the original polarisation, since both waves having the same velocities arrive simultaneously with the same amplitude at the receiving aerial (at the rocket payload). The difference in the real parts of the refractive indices leads to different arrival times of the two partial waves. Their superpositioning results in an elliptical polarisation whose major axis will be rotated by an angle, Ψ , against the original linear polarisation (Faraday rotation):

$$d\Psi = \frac{\pi f}{c} (\mu_0 - \mu_x) ds, \quad \text{rad} \quad (1)$$

ds = element of the propagation path

c = velocity of light.

Similarly, from the difference of the imaginary parts of the two refractive indices, the differential absorption (DA) can be derived:

$$dDA = \frac{2\pi f}{c} (\chi_0 - \chi_x) 20 \log e ds, \quad \text{dB} \quad (2)$$

In the observed elliptical polarisation, the major axis, A_{\max} , is the sum, and the minor axis, A_{\min} , the difference between the two partial wave amplitudes (ordinary and extraordinary).

Hence, the differential absorption can be deduced from:

$$DA = 20 \log \left\{ (10^{M/20} - 1) / (10^{M/20} + 1) \right\}, \quad \text{dB} \quad (3)$$

$$M = A_{\max} / A_{\min} \quad \text{modulation in dB.}$$

The most general formulation of the refractive indices is given by Sen and Wyller (1960). Particularly if investigations in presence of high collision frequencies are made (D -region), the rather complicated Sen and Wyller theory has to be employed. This is especially true for the computation of the collision frequency itself. The observed Faraday rotation and differential absorption, as well as the height to which a sounding frequency can yield usable data, are functions of that frequency.

Figure 1 shows the dependence of Ψ and DA (per kilometre of height) as a function of frequency for a given set of parameters expected at 75 km for a

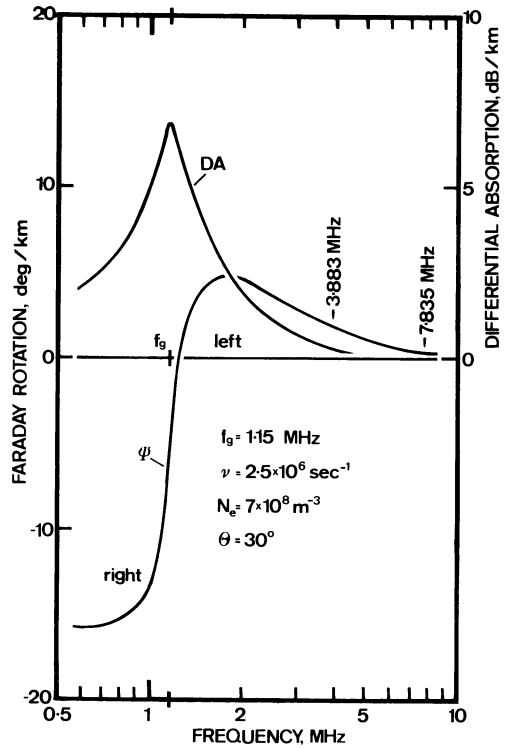


Fig. 1. Faraday rotation, Ψ , differential absorption, DA, (per kilometre) for a set of parameters expected at 75 km above “El Arenosillo” (θ : angle between magnetic field and propagation direction)

launch from “El Arenosillo”. The frequencies 3.883, 7.835 and 15.011 MHz were chosen to ensure that once a frequency is absorbed, a higher one will provide data. This figure also demonstrates that frequencies below the gyro frequency can yield useful data, particularly at lower altitudes (high collision frequencies). At the latitude of Southern Spain this would, however, mean a frequency of less than 1 MHz, which for practical purposes was not considered (interference with broadcast stations).

For each of the three sounding frequencies there was a transmitter of 500 to 800 W output feeding $\lambda/2$ aerials, $\lambda/4$ above ground radiating with linear polarisation. The payload side consists of a receiver for each frequency fed from a common, linearly polarised (dipole) aerial (2 spikes of app. 30 cm). The outputs, representing the momentary field strengths measured by the scanning dipole (spinning rocket), are telemetered by analogue words.

3. Electrostatic Probe

A sphere inside a spherical grid (at rocket potential) is biased to collect charged particles of one polarity (here: positive ions). The bias is chosen high enough to safely repel the unwanted species even if the rocket potential changes during the flight, but low enough to avoid secondary emission on the inner sphere (22.5 V

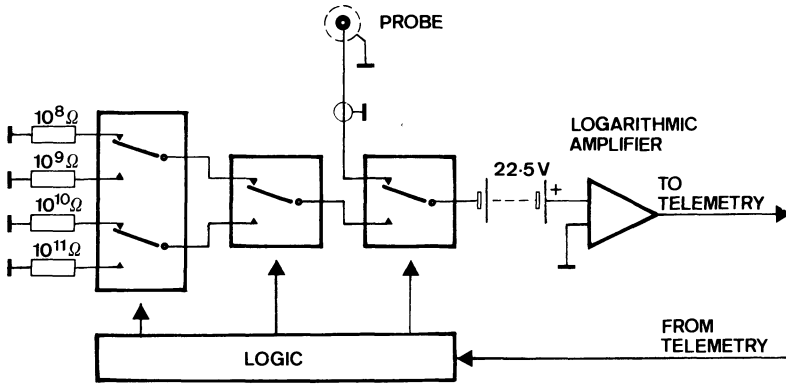


Fig. 2. Block diagramme of electrostatic probe

were chosen). The current thus detected is given by Sagalyn et al. (1963)

$$I = I_0 f(v_T, v) \quad (4)$$

where $I_0 = \pi r^2 e N v_T$ denotes the current to the stationary sphere (sphere radius, r , electron charge, e , density, N and the probe/rocket velocity, v).

$$v_T = \sqrt{8kT/\pi m} \quad (5)$$

describes the particles' thermal velocity (Boltzmann constant, k , temperature, T and species mass, m). Numerical values of D and E -region conditions and typical sounding rocket velocities (100 to 150 km apogee) show that for electrons the rocket velocity is negligible compared to the thermal velocity (stationary current I_0). In the case of ions, however, they can almost be considered as stationary, the probe simply samples a volume defined by the sphere's diameter and the rocket velocity vector (c.f. e.g. Folkestad, 1970).

Therefore, collecting positive ions makes the measurement much less dependent on a good ion temperature model. The mass of the dominant species also hardly influences the result for a large part of the flight. Since on the other hand, the rocket velocity must always be known accurately anyhow, the probe was biased to measure positive ions. The current thus collected by the deployable probe was amplified in a logarithmic amplifier whose input was switched to four calibration resistors ranging from 10^8 to $10^{11} \Omega$ (currents from 2×10^{-7} to 2×10^{-10} A, Fig. 2). Because of the different response times, the lower calibration currents were switched on longer than higher ones; to facilitate data processing the calibration cycle was controlled by the PCM telemetry (every 8160 frames or app. 8.4 s, Ulrich et al., 1976).

4. Results

Due to interference from outside the payload, not all frequencies yielded data, electron densities could, however, be derived up to apogee from both B IV flights of the two salvoes. The raw data were processed to yield absorption and Faraday rotation by a correlation programme described by Torkar and Fried-

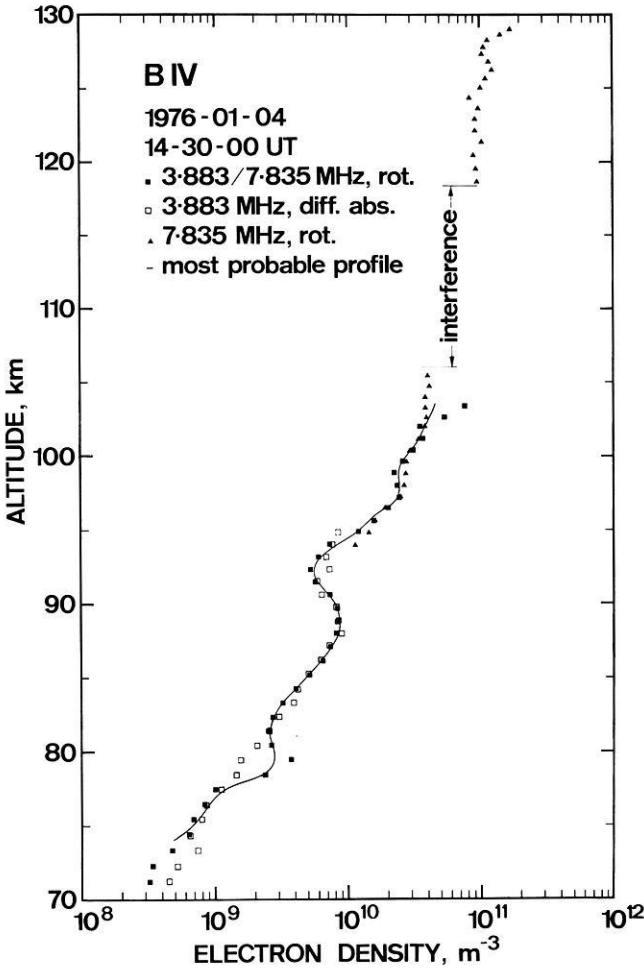


Fig. 3. Electron density profile derived from wave propagation experiment

rich (1976, the Earth's magnetic field model used is the one given by Chain et al. (1965) and the semiconductor integrals required in the Sen and Wyller formulation were computed according to Hara (1963). First the collision frequency, ν , was determined from the first B IV of January 4th, 1976. Best agreement between Faraday rotation (3.883/7.835 MHz) and differential absorption (3.883 MHz) was obtained with a height dependent proportionality factor, $K = \nu/p$, to the CIRA (1972), pressure, p , of the form:

$$K = 1.95 \times 10^5 \exp(0.0205 \times h), \quad \text{m}^2/\text{N s} \tag{6}$$

h in kilometres

p in N/m^2

similar to a study by Mechtly (1974).

Figure 3 shows the electron density profile derived from the same flight using

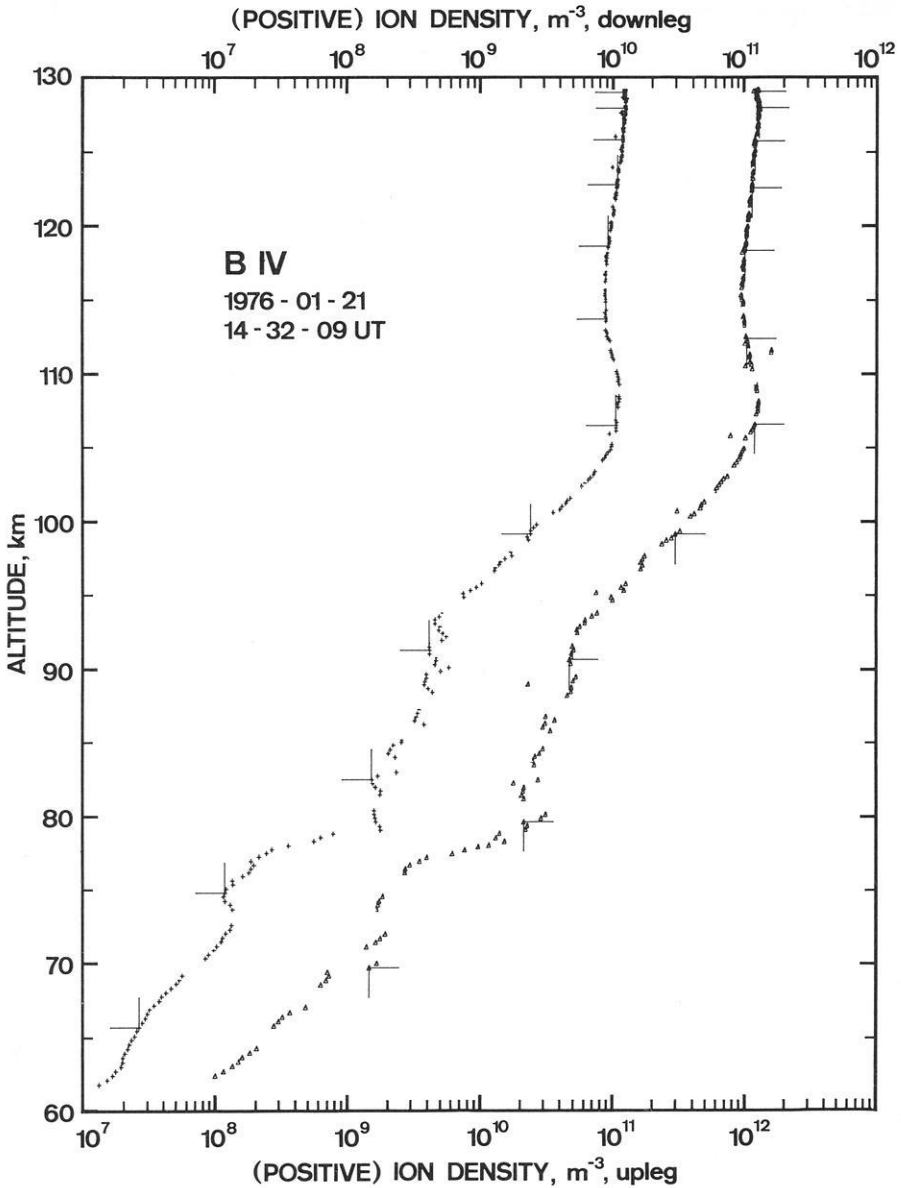


Fig. 4. Density profile of positive ions normalised to the electron density derived from the wave propagation experiment (up and downleg data separated by one decade)

the collision model of Equation (6). The line labelled “most probable profile” was obtained by simulating Faraday rotation and differential absorption until best agreement with the raw data was achieved as described by Friedrich and Jacobsen (1975). The data gap around 110 km which also appeared on the flight of the second B IV (January 21st, 1976) is due to interference from an unwanted transmitter, disappearing above that height and also be seen on the downleg.

Unfortunately, due to mechanical reasons, only the probe of the second B IV deployed and provided data. Because of the supersonic velocity of the rocket, the probe which stands out some 30 cm to the side of the payload will move in and out of the shock cone. The current thus spin-modulated, can be considered to represent the true, unperturbed value whenever the probe is outside the shock front (maximum of the current observed in each spin period). The position of this maximum relative to an aspect sensor should only change slowly during the flight with the angle of attack to the payload. In the data reduction, the rocket rotation sectors where the maxima occur are first plotted versus flight time. Only from this (smoothed) angular range of some $\pm 20^\circ$ the averaged values are considered to represent the “true” ion densities. The current values obtained by this method (one per spin period) are then converted to ion density using Equation (4) by Sagalyn et al. (1963), with an ion temperature profile similar to CIRA (1972) neutral temperatures and ion mass, m , of 16 and 32 which show only a few percent difference in the result. Figure 4 shows the profile of the density of positive ions, above 80 km normalised to the electron density derived by the wave propagation experiment. This procedure is justified, since the mass spectrometer on the same payload measured the last negative ions much below that altitude (Arnold, private communication).

The gaps in the profile are at the times of the mass spectrometer’s neutral gas mode which interfered with the measurement, the angles indicate in-flight calibration. The good agreement between up and downleg demonstrates that:

- The computed trajectory is correct.
- The plasma density remained stable during the flight.
- The assumption of the maximum current observed in a spin period representing the true value is a realistic one.

5. Conclusions

It seems fair to say that the combination of the two described instruments is ideal for the measurements in the *D* and *E*-region. For rocket flights outside the auroral zone where commercial radio stations are heavily absorbed, perhaps more than three sounding frequencies should be employed since one cannot predict all interference from other stations by monitoring the frequencies on the ground.

Acknowledgements. The participation in this project was made possible by Grant 2671 of the Austrian Council for Scientific Research and by support of the Space Research Institute of the Austrian Academy of Sciences. The numerical computations were carried out at the Graz Computer Centre (RZG), and the probe mechanics were fabricated by the Chr. Michelsen’s Institutt, Bergen, Norway.

References

- Budden, K.G.: Radio waves in the ionosphere. Cambridge University Press 1966
 Cain, J.C., Daniels, W.E., Hendricks, S.J.. An evaluation of the main geomagnetic field 1940–1962. *J. Geophys. Res.* **70**, 3647–3674, 1965

- CIRA: Cospar International Reference Atmosphere. Akademie Verlag Berlin 1972
- Folkestad, K.: Ionospheric studies by in-situ measurements in sounding rockets. NDRE report 59, Norwegian Defence Research Establishment 1970
- Friedrich, M., Jacobsen, T.A.: On the accuracy of the determination of electron density and collision frequency with the Faraday experiment. *Kleinheubacher Berichte*, **18**, 333–342, 1975
- Hara, E.H.: Approximation to the semiconductor integrals $C_p(x)$ and $D_p(x)$ for use with the generalized Appleton-Hartree magneto-ionic formulas. *J. Geophys. Res.*, **68**, 4388–4389, 1963
- Mechtly, E.A.: Accuracy of rocket measurements of lower ionosphere electron concentration. *Radio Sci.*, **19**, 373–378, 1974
- Sagalyn, R.C., Smiddy, M., Wisnia, J.: Measurement and interpretation of ion density distributions in the daytime F-region. *J. Geophys. Res.*, **68**, 199–211, 1963
- Sen, H.K., Wyller, A.A.: On the generalization of the Appleton-Hartree magnetoionic formulas. *J. Geophys. Res.*, **65**, 3931–3950, 1960
- Torkar, K., Friedrich, M.: A computer programme to evaluate Faraday rotation and absorption. INW 7602, Techn. Univ. Graz, 1976
- Ulrich, S., Friedrich, M.: An electrostatic ion probe and the method to process its data. INW 7605, Techn. Univ. Graz, 1976

Received May 2, 1977

Measurements of Lyman- α Extinction and Energetic Charged Particle Precipitation during the European Winter Anomaly Campaign 1975–76

E.V. Thrane, B. Grandal, O. Hagen, and F. Ugletveit

Norwegian Defence Research Establishment, P.O. Box 25, Kjeller, Norway

Abstract. The paper deals with two different experiments, both designed to measure mesospheric parameters of importance for the understanding of the winter anomaly in ionospheric absorption. Solar Lyman- α is absorbed in the atmosphere mainly by molecular oxygen, and from measurements of its intensity variation with height, density, pressure and temperature may be derived. The results indicate temperatures significantly above the standard atmosphere values in the height range 70–90 km, during winter anomaly conditions, as measured on two Nike-Apache sounding rockets. The same rockets carried GM tubes and a solid state spectrometer to measure the flux of energetic charged particles penetrating into the mesosphere. The results clearly show that ion production from such particles could not have caused enhanced electron densities during the winter anomaly events studied in this campaign.

Key words: Solar Lyman- α – Mesospheric temperature – Energetic charged particles – Ion production – Solid state detector.

1. Introduction

Throughout the years since its discovery many mechanisms have been proposed to explain the winter anomaly in ionospheric absorption. The experiments to be described in this paper were designed to test 2 of the hypotheses put forward, a) that the increase in absorption was associated with changes in the state of the neutral atmosphere and b) that increased ion production from precipitation of energetic particles causes enhanced ionization densities (Mæhlum, 1967).

Measurements of the extinction of solar H-Lyman- α radiation have been a successful means of deriving neutral gas temperature, density and pressure, (Hall, 1972; Thrane and Johannessen, 1975). The experiment consists of a simple ionization chamber, sensitive to the solar radiation at 121.56 nm. The particle fluxes were measured by Geiger Müller tubes and a solid state telescope recently developed at NDRE (Hagen, 1976).

Both experiments were mounted on the rockets code-named BIVI and BIVII, flown from Arenosillo on January 4th, 1976 at 14:30 UT and January 21st, 1976 at 14:32 UT, respectively. Both rockets reached an altitude of about 130 km. The experiments were partially successful.

2. The Lyman- α Experiment

2.1. Principle of Method

The experiment is based on the fact that H-Lyman- α radiation at 121.6 nm is a very intense line in the solar spectrum, and that this radiation is absorbed in the atmosphere almost exclusively by molecular oxygen, O₂. Consider radiation of intensity I incident at an angle x upon an atmospheric layer of thickness dh with oxygen density [O₂]. Then the radiation absorbed in this layer is

$$dI(h) = I(h) \sigma [\text{O}_2](h) \sec x dh \quad (1)$$

where σ is the absorption cross section of the radiation. From this equation the density [O₂] may be derived as a function of height h if σ is known and the relative change of intensity with height is measured

$$[\text{O}_2](h) = \frac{1}{I(h)} \frac{dI(h)}{dh} \frac{\cos x}{\sigma}.$$

Assuming that the intensity outside the atmosphere, I_∞ , is known, the atmospheric pressure is found by integration which yields:

$$p(h) = -K \frac{\cos x}{\sigma} \ln \frac{I(h)}{I_\infty}$$

where K is a constant if the atmospheric gases are completely mixed and σ is assumed to be constant.

A more complete theory including a variation of intensity as well as absorption as a function of wavelength across the width of the solar H-Lyman α line has been described by Hall (1972).

Finally the temperature may be determined from the equation of state

$$T(h) = \frac{\bar{m} g}{k} \frac{p(h)}{[\text{O}_2](h)} \cdot \frac{1}{K}$$

where k is Boltzmann's constant, \bar{m} the mean molecular mass and g the acceleration of gravity.

2.2. Experimental Technique

The apparatus of the Lyman- α experiment consisted of four parts. These were the detector set, a linear electrometer, a bias voltage supply and an auto-ranging device.

The detector set consisted of two unity gain vacuum-ultraviolet photoionization chambers manufactured by Artech Corporation. The chambers had a copper housing, a lithium-fluoride window and a tungsten centre electrode and were filled with nitric oxide at a pressure of 20 torr. This combination made the chambers sensitive to radiation between 105.0 nm to 135.0 nm. The quantum efficiencies, estimated by the manufacturer, were about 60% at 121.6 nm.

The chambers were mounted as shown in Figure 1 in order to have each chamber point towards the sun once every spin period.

One of the chambers in the detector set had a protection cap, which was released 64 s after launch at an altitude of about 66 km. Lithium Fluoride is a hygroscopic material, and the cap was designed to protect one of the windows from possible changes in sensitivity due to atmospheric humidity. A comparison of the results from the pair of chambers on one of the rockets showed no detectable sensitivity change.

The linear electrometer had a dynamic range from 10^{-10} A to $3,2 \times 10^{-8}$ A. The input impedance was 60 M Ω . Internal calibration was performed each 2,2 s during the flight and each calibration lasted 4 ms. Current measurements were made at a sampling rate of 1116 Hz.

An auto-ranging device followed the electrometer. This divided the output swing from the electrometer into eight equal ranges. Between each range was a small amount of hysteresis. Three bits in the telemetry format were used to monitor the range number. With this device the telemetry resolution was expanded from 8 to nearly 11 bits, giving a total current resolution of about 16,5 pA/bit.

A bias voltage of minus 45 V was supplied by a dry charged battery and was applied to the centre electrode of the detector in order to minimize the effects of photoemission.

The angle between the solar rays and the axis of the ionization chambers was determined by an attitude sensor. This sensor consisted of a light-sensitive transistor housed behind two narrow slits forming an angle of 45 degrees. Every spin period the light-sensitive element was triggered twice and the length of the interval between each triggering was measured by counting the PMC-telemetry bit-frequency (250 kbit).

The accuracy of the attitude sensor was estimated to be better than $\pm 1\%$.

2.3. Results

In the rocket BIV I both Lyman- α detectors as well as the solar attitude sensor functioned well. However, the rocket developed a large coning, and for this reason the sun was not within the aperture of the sensors during parts of the flight. In BIV II only the Lyman- α detector, which was protected by a

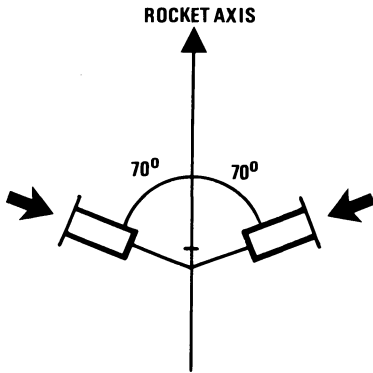


Fig. 1. Orientation of H-Lyman- α detectors

cap, worked and the solar attitude sensor failed. Fortunately this rocket had only moderate coning. The spin rate of both rockets was about 3.5 rps giving about 3 intensity maxima for each detector every second. In order to minimize the effect of noise in the data, the amplitude of each of these maxima was determined by fitting a curve to the data points. Lyman- α intensity as a function of time is shown in Figure 2 for both flights. The intensity corrected for coning is also shown. There is an uncertainty in the determination of I_{∞} , the intensity outside the atmosphere, and the extreme values possible for this parameter are indicated on the figure. For BIV II the coning correction is based on magnetometer data. The atmospheric pressure, density and temperature were derived from the corrected intensities in the manner outlined in section 2.1.

The uncertainties due to random scatter in the data as well as the effect of systematic errors due to coning and uncertainties in I_{∞} were estimated. Figure 3 shows as an example the derived temperatures for BIV II. The derived values are significantly larger than the CIRA (1972) values also indicated in the figure. A detailed discussion of the results will be given elsewhere.

3. The Particle Experiments

3.1. The Particle Detectors

The solid state telescope measured the spectra of precipitating high-energy charged particles. The instrument could resolve electron energies in the range 38–800 keV and distinguish between electrons and protons. The instrument had 4 basic parts. These were the sensor unit, the preamplifier, the pulse height analyzer and the bias voltage supply.

The sensor unit was based on 2 silicon surface barrier detectors manufactured by Ortec Corporation, mounted in a telescopic configuration. The front detector was of the totally depleted type with an active area of 50 mm² and a thickness of 150 microns. The detector was penetrated by incident electrons with energies >185 keV and protons with energies >4 MeV. The rear detector, which had an active area of 150 mm² and a thickness of 1000 microns, was partially

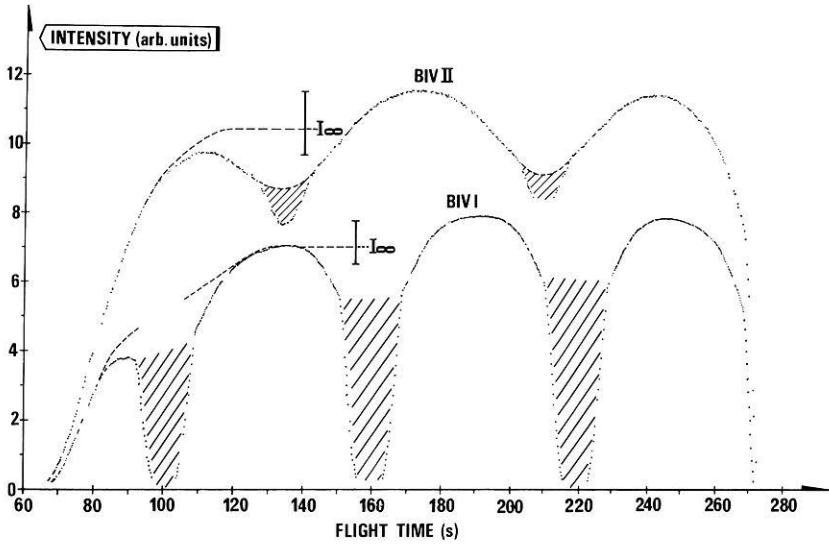


Fig. 2. H-Lyman- α intensity vs. time of flight. *BIV I*: Lower curve. *BIV II*: Upper curve. The hatched regions refer to time intervals when a shadow effect decreased the observed intensity

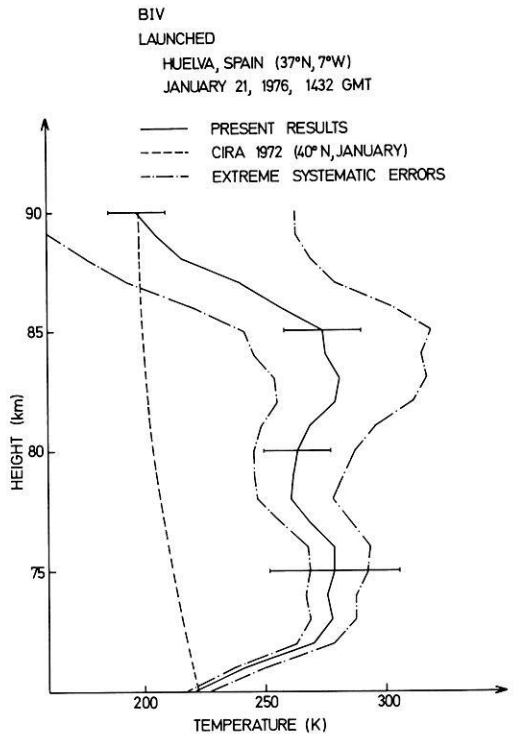


Fig. 3. Temperature vs. height. The temperature profiles are obtained using the different values of I_x from figure 2: — Mean value of I_x ; - - - Extreme values of I_x

depleted. This detector could resolve electron energies up to 800 keV and measure the integral flux of electrons with higher energies. The relation between the incident electron energy and the energy deposited in the rear detector was for incident electrons > 0.25 MeV, according to Katz and Penfold (1952):

$$E_0 = \left(E_1^{1.265} + \frac{\phi}{412} \right)^{0.79}$$

where E_0 is the energy of the incident electron in MeV, E_1 is the remaining energy of the electron after penetration of the first detector in MeV and ϕ is the total density of the front detector in mg/cm^2 .

The telescope housing and collimator were made of aluminium and polyethylene. Several traps in the collimator served to avoid reflection of particles into the detector. The aluminium side of the front detector pointed outwards to make the telescope insensitive to light.

The geometric factor for the telescope was

$$G = 0.14 \text{ cm}^2 \text{ sr.}$$

The preamplifier was of the charge sensitive type. The principle of detection was based on the traditional voltage mode system, where the signal is integrated at the detector to a pulse having a short rise-time followed by a long "tail". The signal was differentiated twice in the two last stages of the amplifier. The sensitivity of the charge sensitive part of the preamplifier was $34 \text{ mV}/\text{MeV}$ and the resolution was 4.8 keV (fwhm, Si) at zero input capacitance with a noise slope of $64 \text{ eV}/\text{pF}$.

The pulse-height analyzer was made of comparators and CMOS logic. The analyzer had eight outputs corresponding to the different energy ranges as shown in Table 1.

The telescope was calibrated by using radioactive sources and an Ortec precision pulse generator, to within an accuracy of 10%.

The bias voltage supply consisted of dry charged batteries embedded in epoxy. The voltage was controlled on-off by a relay and applied to the detectors through an integrating network with a time constant of approximately 2.2 s.

As a supplement to the solid state telescope, two Geiger-Müller counters were flown. The detectors were manufactured by LND, Inc, and were of the type 710. A twelve micron thick mylar sheet was added to one of the detector windows to raise the 50% transmission point (cut-off) from 40 keV to 60 keV. Both detectors were integral counters.

Table 1. Calibration table. All energies in keV

Output	1	2	3	4	5	6	7	8
BIV I	e^- 44-100	100- ∞		210-300	300-400	400-550	550-800	800- ∞
	p 44-100	100-230	230-4000					4600- ∞
BIV II	e^- 38-100	100- ∞		220-300	300-400	400-550	550-800	800- ∞
	p 38-100	100-230	230-4000					4600- ∞

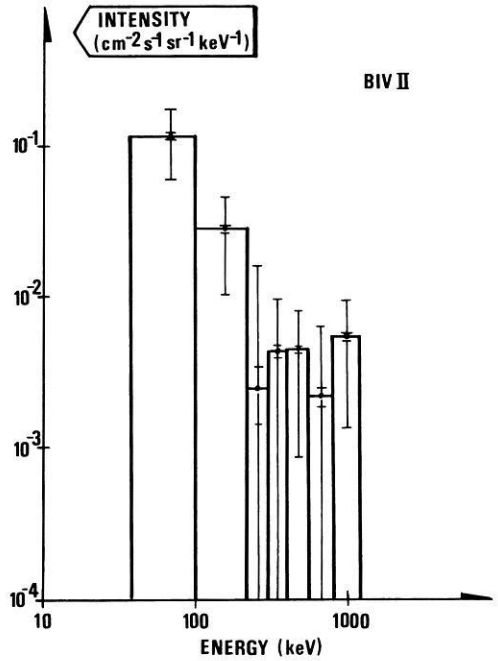


Fig. 4. Differential electron energy spectrum. The error bars indicate the standard deviation and the standard deviation of the mean

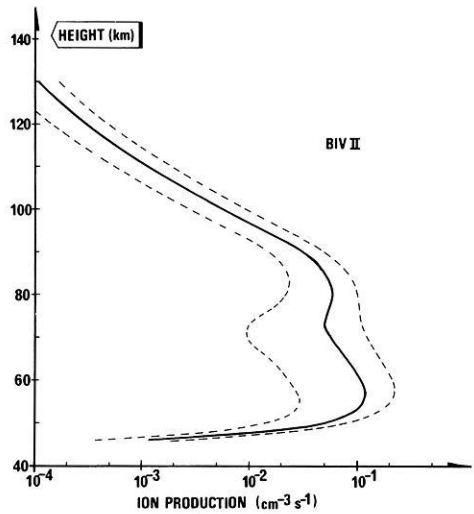


Fig. 5. Ion production vs. height. The dashed curves are obtained using the maximum and minimum values of the error bars in Figure 4

The signal was picked up across a resistor on the groundside of the detector and shaped in a simple network to be compatible to the telemetry. The plateau voltage was supplied from a zener regulated DC-DC converter.

Geometric factors were for both detectors

$$G = 3,24 \times 10^{-2} \text{ cm}^2 \text{ sr.}$$

3.2. Measurements

In rocket BIV I the door in front of the particle detector assembly failed to open during flight. In rocket BIV II the experiment worked satisfactorily, recording electron and proton precipitation for energies above 38 keV. The particle fluxes were very small, nevertheless a differential energy spectrum shown in Figure 4, was derived from the measurements. This spectrum was used to calculate the ion production as a function of height, (Fig. 5), using the method of Rees (1963). The ion production is very small, much too small to make a significant contribution to the total ion production from normal solar radiation at heights above 70 km. Below 70 km the production is of the same magnitude as the production to be expected from galactic cosmic rays.

4. Conclusions

The two experiments outlined in this paper gave information about the state of the lower ionosphere during winter anomaly conditions. Two tentative conclusions may be drawn from the data. a) The neutral gas temperature in the height range 70–90 km was significantly higher than expected from the standard atmosphere (Cira, 1972). b) The ion production due to precipitating energetic electrons and protons was too small to give a significant contribution to the total ion production, except perhaps between 60 and 70 km.

References

- Carver, J.H., Gies, H.P., Hobbs, T.I., Lewis, B.R., McCoy, D.G.: Temperature dependence of the molecular oxygen photo-absorption cross section near the H Lyman- α line. *J. Geophys. Res.* **72**, 1955, 1977
- Cospar International Reference Atmosphere, Berlin: Akademie-Verlag 1972
- Hagen, O.: A solid state telescope for measuring energy spectra of precipitating charged particles in sounding rockets. Technical Note E-805, Norwegian Defence Research Establishment 1976
- Hall, J.E. Atmospheric pressure, density and scale height calculated from H-Lyman- α absorption allowing for the variation of cross section with wavelength. *J. Atmos. Terr. Phys.* **34**, 1337, 1972
- Katz, L., Penford, A.S.: Range-energy relations for electrons and the determination of beta-ray end-point energies by absorption. *Rev. Mod. Phys.* **24**, 28, 1952
- Mæhllum, B.N.: On the "Winter Anomaly" in the midlatitude D-region. *J. Geophys. Res.* **72**, 2287, 1967
- Rees, M.H.: Auroral ionization and excitation by incident energetic electrons. *Planet. Space Sci.* **11**, 1209, 1963
- Thrane, E.V., Johannessen, A.: A measurement of the extinction of solar hydrogen Lyman- α radiation in the arctic mesosphere. **37**, 655, 1975

Received May 2, 1977

Note Added in Proof

New values of the photo absorption cross section of molecular oxygen near the Lyman- α line have been used to derive the results in Figure 3 (Carver et al., 1977)

Mesospheric Molecular Oxygen Density, Pressure and Temperature Profiles Obtained from Measurements of Solar H Lyman- α Radiation

A. Loidl and H. Schwentek

Max-Planck-Institut für Aeronomie, D-3411 Katlenburg-Lindau 3, Federal Republic of Germany

Abstract. The extinction in the mesosphere of hydrogen Lyman- α radiation from the Sun was measured by ionization chambers being part of a complex payload (BII) flown on two rockets of type Skylark. The rockets were launched from El Arenosillo, Spain, (37.10°N; 6.73°W), at 1630 UT on 4 and 21 January 1976. From these measurements molecular oxygen density, pressure, and temperature profiles were determined, and are presented for the height range 70–90 km. The oxygen density and temperature profiles differ considerably from the CIRA 1972, but in a reasonable tendency. We suggest this to be due to the strong winteranomalous conditions during the days of measurement.

Key words: Extinction – Mesosphere – Solar H Lyman- α .

Introduction

From measurement of the absorption in the mesosphere of hydrogen Lyman- α radiation from the Sun the density of molecular oxygen can be determined. The technique of applying ionization chambers for such an experiment is well known, and has been used by many workers (Carver et al., 1964; Hall, 1972; Smith and Miller, 1974). Below heights of about 85 km, the dissoziation of molecular oxygen may be neglected, and the major constituents of the mesosphere are well mixed. Thus, from the molecular-oxygen density-profile, the corresponding mesospheric pressure and temperature profiles can be calculated.

The described experiment was made in the framework of a comprehensive aeronomy programme in order to take advantage of this rare opportunity, that is, to measure simultaneously, and at the same location, a variety of essential parameters of the mesosphere, the same parameters redundantly, and also by different methods.

In this paper only the very experiment and its results are presented. The combination of these results with those from the other experiments will be the subject of another paper.

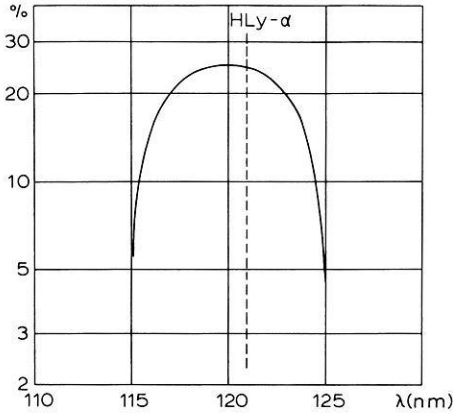


Fig. 1. Relative spectral sensitivity of the ionization chambers (RTC; type CIU 3); λ wavelength of the ultraviolet radiation. The H Lyman- α line is at 121.567 nm (central absorption core; see Bruner and Parker, 1969)

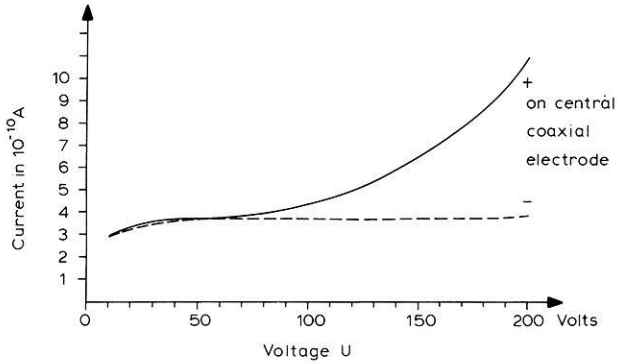


Fig. 2. Quantum efficiency of the ionization chambers as a function of the applied voltage U , in volts, as measured in the laboratory; comparison of sensor with a windowless NBS Diode (Al_2O_3/Al cathode)

Method of Measurement

The solar H Lyman- α radiation was measured redundantly by two ionization chambers (type CIU 4c) with magnesium fluoride end windows and carbondisulfid filling gas under a pressure of 20 millibar. The spectral sensitivity of these sensors, as determined by the material of the window and the filling gas, is shown in Figure 1. An absolut calibration was carried out using a vacuum ultraviolet monochromator and comparing the ionization chambers with a windowless NBS ultraviolet photodiode. For suppressing photoelectric emission from the wall, the shell electrodes of the ionization chambers were operated at a positive potential (about + 50 V; unity gas gain). Figure 2 shows the quantum efficiency of the chambers, as a function of the applied voltage, and Figure 3 their relative sensitivity, as a function of the angle of incidence of the radiation. Particular care was taken to protect the ionization chambers against humidity. Therefore, that section of the rocket where the sensors were mounted was filled with dry nitrogen.

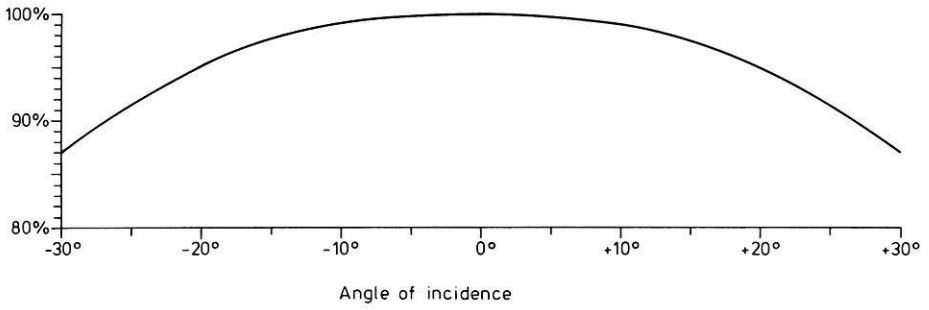


Fig. 3. Relative variation of current of an ionization chamber as a function of the angle of incidence of the H Lyman- α radiation

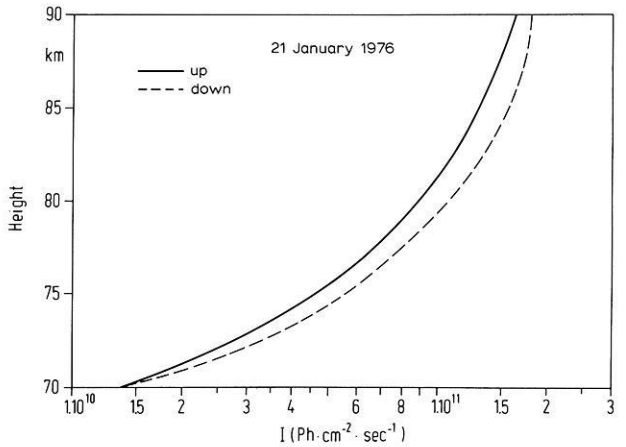
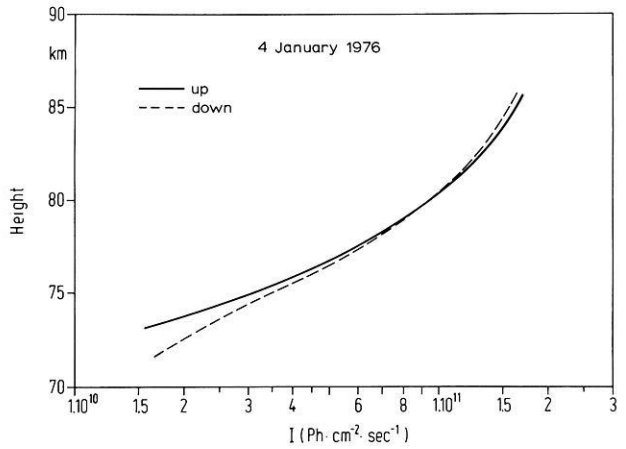


Fig. 4a and b. Solar H Lyman- α intensities measured on 4 and 21 January 1976 at latitude 37.10° N, longitude 6.73° W

Before the rockets were launched, the sensors were turned to definite angles against the axis of the rocket by a remote control, depending on the actual solar zenith angle. Since the rockets were trajectory stabilized, the sensors had to be traversed by means of a programmed timer near the apogee in order to be directed towards the Sun also on the downleg.

The electric currents obtained from the ionizations chambers were amplified; and at each rotation, their peak value was converted into a digital word, and this stored in a memory, from which it was read out by the telemetry system. Triggered by a particular solar sensor, at each rotation of the rocket, two measurements were made, one, when the sensor pointed at the Sun, and the other, when the sensor was opposite to the Sun. By the second measurement the scattered radiation could be found.

The first rocket was launched at 1630 UT on 4 January 1976 at a solar zenith angle of $73^{\circ}22'$, the second at 1631 UT on 21 January 1976 at $70^{\circ}02'$. Both flights were successful. Unfortunately, the real flight trajectories of both rockets deviated considerably from the nominal trajectory for which the experiment was adjusted. Therefore, the sensors did not point at the Sun during the entire part of the trajectory as it was planned.

A detailed description of the experiment is given in a technical report (Loidl and Boogaerts, 1976).

Results

Figure 4 shows the measured solar H Lyman- α intensities of each flight. The absorption profiles are slightly different, crossing at 80 km. Perhaps a cause for the differences in the upleg and downleg curves may be that the distance between up and down trajectory was about 200 km. Due to the deviation of the rocket from the planned trajectory, it was not possible to measure I_{∞} . But it can be extrapolated using the formula

$$I_{\infty} = I_h \exp \frac{\sigma \cdot p(h)}{K \cdot \cos \chi}, \quad (1)$$

where $\sigma = 0.8 \times 10^{-24} \text{ m}^2$, $p(h)$ pressure (taken from CIRA 1972 and introducing some uncertainty) at height h , $K = 2.2 \times 10^{-24} N = g \sum n_i m_i / n(\text{O}_2)$, χ solar zenith angle, $h = 85 \text{ km}$ (flight 4 January 1976), $h = 119 \text{ km}$ (flight 21 January 1976). So it was calculated $I_{\infty} = 2.71 \times 10^{11} \text{ Ph cm}^{-2} \text{ s}^{-1}$ on January 4, and $I_{\infty} = 2.43 \times 10^{11} \text{ Ph cm}^{-2} \text{ s}^{-1}$ on January 21. This value is about 10% lower than the value published by Hinteregger et al. (1965) which is $I_{\infty} = 2.7 \times 10^{11} \text{ Ph cm}^{-2} \text{ s}^{-1}$. An explanation for this may be a decrease in quantum efficiency of the ionization chambers which were calibrated at 30 October 1975 and flown in January 1976. For, three chambers were treated under comparable circumstances but not flown in a rocket, and recalibrated in March 1976. The result was a loss in efficiency up to 50%. For the flight of 21 January 1976, a larger inaccuracy was introduced by uncertainties concerning the real flight trajectory.

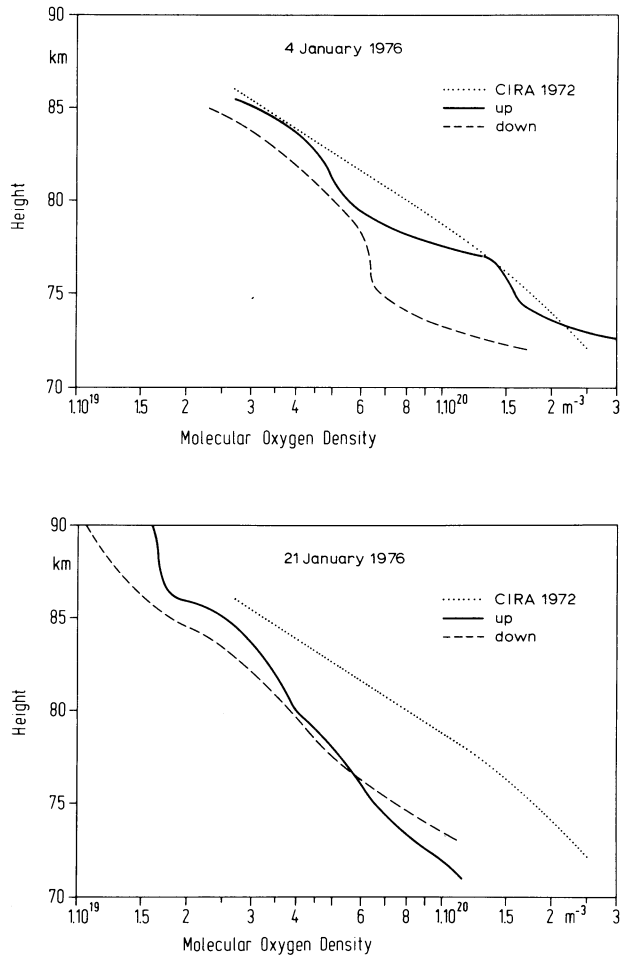


Fig. 5a and b. Measured molecular oxygen densities at latitude 37.10°N on 4 and 21 January 1976 compared with model mesosphere densities adjusted to the same latitude and month (CIRA 1972)

Planning the experiment it was hoped that the US Naval Research Laboratory would start the announced two Solar Radiation (SOLRAD) Satellites in time, so that the solar H Lyman- α intensity could be determined absolutely by satellite. Thus, a comparison of the spot-check measurements by the rockets with the continuous measurements aboard the satellites would have been possible in real time. Unfortunately, the SOLRAD satellites 11a and 11b were not started earlier than on 15 March 1976. Therefore, it is an open question which the absolute intensities of solar H Lyman- α radiation were, and which difference in the intensities really occurred between 4 and 21 January 1976.

Since for the calculation of the molecular oxygen density, pressure and temperature profiles only the *relative* variation in H Lyman- α intensity is important, and thus, a longterm variation in the response of the chambers must not be taken into account, more reliable data should be expected for those profiles.

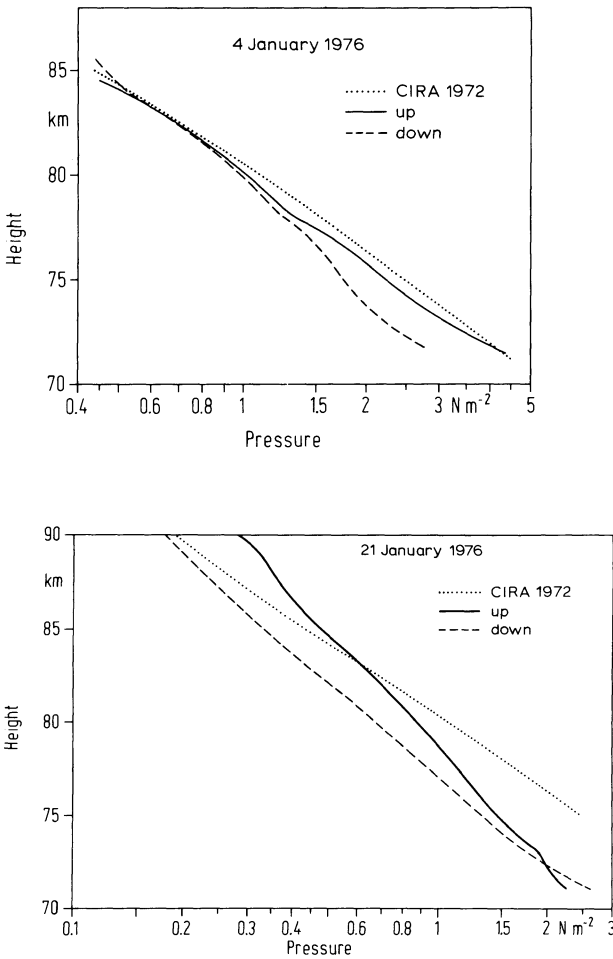


Fig. 6a and b. Calculated mesospheric pressure profiles based on measurement of H Lyman- α intensities at latitude 37.10°N on 4 and 21 January at winteranomalous conditions compared with the CIRA 1972 adjusted to the same latitude and month

The O_2 -density profiles were determined using a fixed absorption cross-section $\sigma = 0.8 \times 10^{-24} \text{ m}^2$ for the entire height range, although a theoretical consideration by Hall (1972) recommends to apply a cross-section varying with height in order to achieve higher accuracy. Smith and Miller (1974), however, showed comparing data obtained from simultaneous measurements using various other techniques, that the assumption of a constant cross section leads to the best agreement with these measurements.

No correction was applied for the effect of dissociation of molecular oxygen, because up to heights of about 85 km this effect seems to be negligible. The molecular oxygen density-profiles are shown in Figure 5. These profiles do not only show smaller densities than the CIRA 1972, up to a factor of two, but also deviations from a steady decrease.

In a discussion of these curves it should be kept in mind that a model atmosphere like the CIRA gives something like a climatic average from which —

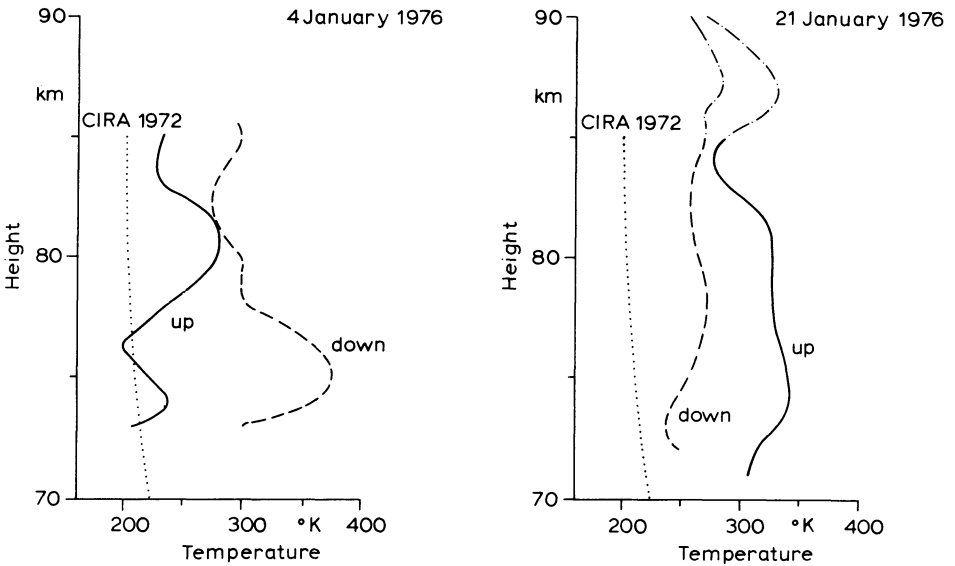


Fig. 7. Calculated mesospheric temperature profiles based on measurement of H Lyman- α intensities at latitude 37.10°N on 4 and 21 January at winteranomalous conditions compared with the CIRA 1972 adjusted to the same latitude and month

particularly during winteranomalous conditions—larger deviations are to be expected. A similar case is found in the stratosphere when a period of stratospheric warming occurs.

The mesospheric pressure and temperature profiles presented in Figure 6 and Figure 7 were calculated using a constant value $K = 2.2 \times 10^{-24}$ N (Hall, 1972).

Estimation of Possible Errors

The extinction of the solar H Lyman- α radiation, and also the windows of the ionization chambers, may be affected by water vapor. In order to avoid at least an influence of water vapor on the windows, up to 60 km, that part of the rocket containing the H Lyman- α sensors was washed round by N_2 . The influence of water vapor on extinction and windows which really occurred in the mesosphere is not yet known and may be a source of error. Perhaps an estimate will be still possible when relevant simultaneous measurements have been evaluated.

A possible increase of the signal produced by other solar radiation than H Lyman- α was reduced as much as possible by use of MgF_2 -windows and a CS_2 gas filling which—combined with each other—give a relative narrow spectral bandwidth of the sensors.

An influence of the Frigen gas which was used for the attitude control system of the rocket can be excluded. An experiment in the laboratory showed no absorption effect on H Lyman- α radiation.

It should be mentioned that the use of H Lyman- α intensity as done in this experiment implies that the intensity does not vary during the flight of the rocket. This is an assumption which is not yet proved. It is known that considerable short-time fluctuations in H Lyman- α intensity are possible. This point should be kept in mind interpreting the results.

An effect on the signal produced by deviation from pointing of the sensors at the Sun was corrected as far as necessary.

Due to an uncertainty in the knowledge of the real trajectory of the rocket, the height scales shown in Figures 4 to 7 perhaps may be wrong by up to ± 5 km on 4 January, and up to ± 10 km on 21 January 1976.

Conclusions

An early synoptic comparison of strato-mesospheric density and temperature profiles obtained from various methods of measurement, separated for summer and winter, showed that, in winter, at middle latitudes, the densities were lower and the temperature above 60 km considerably higher and more variable than in summer (Schwentek, 1968). This situation was considered as a regular atmospheric background for the occurrence of an average winter anomaly in ionospheric absorption. The molecular oxygen, pressure and temperature profiles obtained by calculation from the experiments carried out in January 1976 differ more or less considerably from the CIRA 1972 as valid for January at 40° N, but in the same tendency as mentioned above: The molecular oxygen densities are lower, the temperatures higher than those given by the CIRA 1972. We suggest this result to be due to the strong winter anomalous conditions during the days of measurement. A further, more detailed analysis and discussion on how these results fit with the others obtained simultaneously is beyond the scope of this paper.

Acknowledgements. Both experiments were developed by A. Loidl assisted by W. Boogaerts who also contributed to the data reduction; the rocket payload was instrumented mainly by Messerschmitt-Bölkow-Blohm (MBB). The support concerning calibration of the sensory by G. Schmidtke and F. Fischer, both at the "Institut für physikalische Weltraumforschung", Freiburg i.Br., F.R.G., is acknowledged.

The experiments were mainly funded by the "Bundesministerium für Bildung und Wissenschaft" of the Federal Republic of Germany in the framework of a German Aeronomy Programme carried out at El Arenosillo/Spain.

The authors acknowledge also the various supports of all who contributed to the success of this experiment, and last, not least, they like to mention the encouragement of Prof. Dr. W. Dieminger, the former director of the Max-Planck-Institut für Aeronomie.

References

- Bruner, E.C., Parker, R.W.: Hydrogen Geocorona and Solar Lyman-Alpha Line. — 1. Rocket Measurement of the Solar Line Profile. *J. Geophys. Res.* **74**, 107–113, 1969
- Carver, J.H., Mitchell, P., Murray, E.L., Hunt, B.G.: Molecular Oxygen Density and Lyman- α Absorption in the Upper Atmosphere. *J. Geophys. Res.* **69**, 3755–3756, 1964

- Hall, J.E.: Atmospheric pressure, density and scale height calculated from H-Lyman- α absorption allowing for the variation in cross-section with wavelength. *J. Atmospheric Terrest. Phys.* **34**, 1337–1348, 1972
- Hinteregger, H.E., Hall, L.A., Schmidtke, G.: Solar XUV Radiation and Neutral Particle Distribution in July 1963 Thermosphere. *Space Research XII*, S.A. Bowhill, L.D., Jaffe, M.J., Rycroft, eds., p.p. 1175–1190. Amsterdam: North-Holland Publ. Co. 1965
- Loidl, A., Boogaerts, W.: Internal Report. Experiment DL4. HLy α -Photometer. Max-Planck-Institut für Aeronomie. Lindau 1976
- Schwentek, H.: Zum Auftreten der Winteranomalie der ionosphärischen Absorption von Kurzwellen. *Nachrichtentechn. Z.* **21**, 32–39, 1968
- Smith, L.G., Miller, K.L.: Measurements of O₂ Number Density by Absorption of Lyman α . *J. Geophys. Res.* **79**, 1965–1968, 1974

Received May 2, 1977

Intensity of Solar X-rays in the E Region Measured by Proportional Counters Carried on Rockets

A. Loidl and H. Schwentek

Max-Planck-Institut für Aeronomie, D-3411 Katlenburg-Lindau 3, Federal Republic of Germany

Abstract. The attenuation in the lower thermosphere of the solar X-ray spectrum from 0.1 to 10 keV (6 to 0.2 nm) was measured by Skylark rockets launched from El Arenosillo, Spain (37.10°N; 6.73°W), on 4 and 21 January 1976, at 16.30 UT. The X-ray spectrometers consisted of three proportional counters different in window material and filling gas. They were part of a complex rocket payload (BII).

The solar X-ray spectra and the electron-production rate obtained from the solar X-ray spectrum of 4 January 1976 are presented.

Key words: Attenuation – E region – Proportional counter experiment – Solar X-ray spectrum.

Introduction

In general, the electron- and ion-density profiles in the D-E region may be considered as a product of the attenuation in the lower thermosphere and mesosphere of hydrogen Lyman- α radiation and the X-ray flux from the Sun. In winter, however, also other important influences on the electron-density profiles have to be taken into account. This is suggested from the occurrence of the well known winter anomaly in radio-wave absorption which, in its particular features, cannot be explained by variations in the solar radiation, although its degree, in the average, depends on the solar cycle (Schwentek, 1971; Röttger and Schwentek, 1974). Nevertheless the solar X-ray spectrum should be observed simultaneously when measurements of essential parameters of the D-E region are made, because the solar X-ray flux is one of the main sources of electron production, and the hard component may be very much enhanced during solar flares.

Therefore, measurements were made of the 0.1 to 10 keV solar X-ray spectrum by X-ray spectrometers carried on two Skylark rockets, both launched

from El Arenosillo, Spain, (37.10°N; 6.73°W), on 4 and 21 January 1976, at 16.30 UT. The X-ray spectrometer was part of a complex payload (B II).

Since the solar radiation and the Earth's atmosphere are always varying in space and time, such an observation can give only a spot check. But as a part of a complex experiment, and within a comprehensive aeronomy program, a simultaneous measurement of the solar spectrum at the same location was expected to give an useful contribution to the whole.

When planning the experiment it was hoped that the US Naval Research Laboratory would start the announced two Solar-Radiation Satellites in time, so that absolute solar X-ray data would also be available from satellites. Thus, a comparison and calibration of the spot-check measurements made by rockets with the continuous measurements on board satellites would have been possible in real time. Unfortunately, the SOLRAD Satellites 11a and 11b were not started earlier than 15 March 1976.

Equipment and Measurements

The X-ray spectrometers consisted of three proportional counters different in window material and gas filling (Table 1), and thus in sensitivity. The transmittivity of the window materials, and the sensitivity of the detectors were determined by means of a simple Bragg-crystal vacuum-monochromator which was constructed particularly for this calibration. The output pulses of the counters, which are proportional to the applied photon energies, were amplified by a charge sensitive amplifier, converted to voltage pulses, these separated by a 5-level pulse-height discriminator, then counted in 8-bit quasi-logarithmic counters for each period of measurement, and finally, stored in registers for the read out by the telemetry. The adjustment of the energy channels is shown in Table 2.

Before the rockets were launched, the detectors were turned to definite angles against the axis of the rocket by a remote control, depending on the actual solar zenith angle at the time of launching. Since the rockets were trajectory stabilized, the detectors had to be reversed near the apogee using a programmed timer in order to be directed towards the Sun also on the downleg. Triggered by a particular solar sensor (aperture 40°), at each rotation of the rocket, two measurements were made, one when the sensor pointed at the Sun, the other, when the sensor was opposite to the Sun. By the second measurement the scattered radiation from the background could be found and recorded. For both measurements, the solar sensor determined the (same) counting time of the detectors which was also telemetered.

A detailed description of the equipment is given in a technical report (Loidl and Boogaarts, 1976).

The first Skylark rocket was launched at 16.30 on 4 January 1976 at a solar zenith angle of 73°22', the second at 16.31 UT on 21 January at 70°02'. The real flight trajectories of both rockets deviated considerably from the nominal trajectory for which the experiment was adjusted. The rockets did not reach the projected apogee, and the windows were ejected at heights which

Table 1. Characteristics of the detectors in the X-ray spectrometer

Number of X-ray detector	Energy band (keV)	Window material and thickness (mm)	Gas filling and pressure (Bar)	Wire \varnothing (mm)	Window area (mm ²)
1	0.1–0.5	Hostaphan 0.005 Alu; 0.00012	Ne; 0.72 CH ₄ , 0.08	0.15	2
2	0.4–2.0	Alu; 0.0064	P 10; 0.8	0.15	4.5
3	2.0–10	Be; 0.0508	Xe; 0.88 CH ₄ ; 0.04	0.04	350

Table 2. Adjustment (by a suitable choice of the discriminator levels) of the energy channels used for the three X-ray detectors. The upper energy level of channel 5 of detector 1 was not defined; this channel was only used to detect a possible disturbance of the detector by electrons during the rocket flight

Channel	Detector 1 keV (nm)	Detector 2 keV (nm)	Detector 3 keV (nm)
5	–0.42 –2.94)	2.0–1.68 (0.62–0.73)	10.0–8.40 (0.12–0.15)
4	0.42–0.34 (2.94–3.63)	1.68–1.36 (0.73–0.91)	8.40–6.80 (0.15–0.18)
3	0.34–0.26 (3.63–4.75)	1.36–1.04 (0.91–1.19)	6.80–5.20 (0.18–0.24)
2	0.26–0.18 (4.75–6.86)	1.04–0.72 (1.19–1.71)	5.20–3.60 (0.24–0.74)
1	0.18–0.10 (6.86–12.34)	0.72–0.40 (1.71–3.09)	3.60–2.0 (0.74–0.62)

were lower than planned. Thus, at the first flight, the thin window of the low-energy detector 1 was destroyed. At the second flight, unfortunately, one of the high-voltage converters failed, and detector 3 (2–10 keV) did not produce data.

Results

The measured solar X-ray spectrum, as a function of height, is presented in Figures 1–3.

On 4 January 1976 detector 1 failed; measurable fluxes were obtained from channel 1 of detector 3, and channels 1 to 4 of detector 2. Measurements were made on the upleg and downleg of the rocket, but on both legs not at each height. At heights where two values were obtained, these values were equal within the limits of accuracy, and a mean value was calculated on January 21, 1976 detector 3 failed.

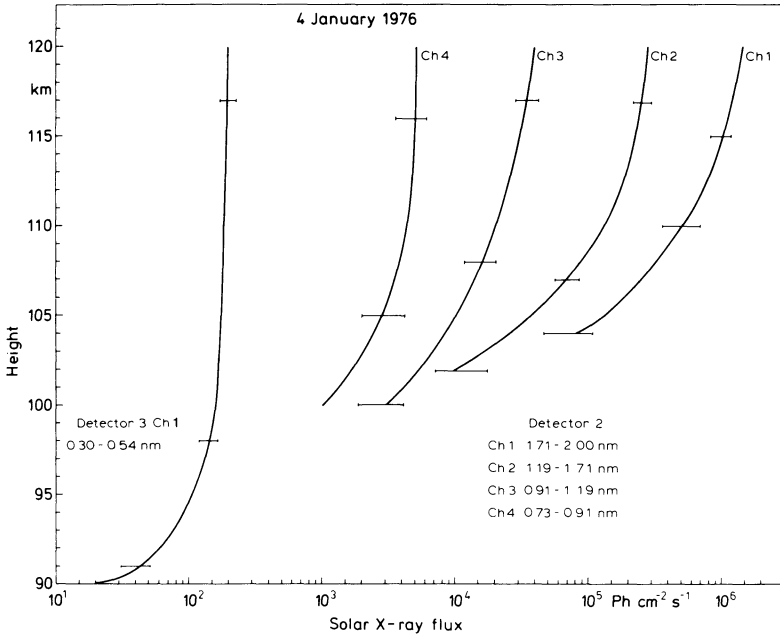


Fig. 1. Measured X-ray flux in channel 1 of detector 3 and in channels 1–4 of detector 2 on 4 January 1976 (the deviation from the wavelengths given in Table 2 are due to a change in gas gain) (channel 1, at wavelengths >2 nm, no signal was obtained due to the window material); (1 nm = 10 \AA ; 1 keV = 1.234 nm)

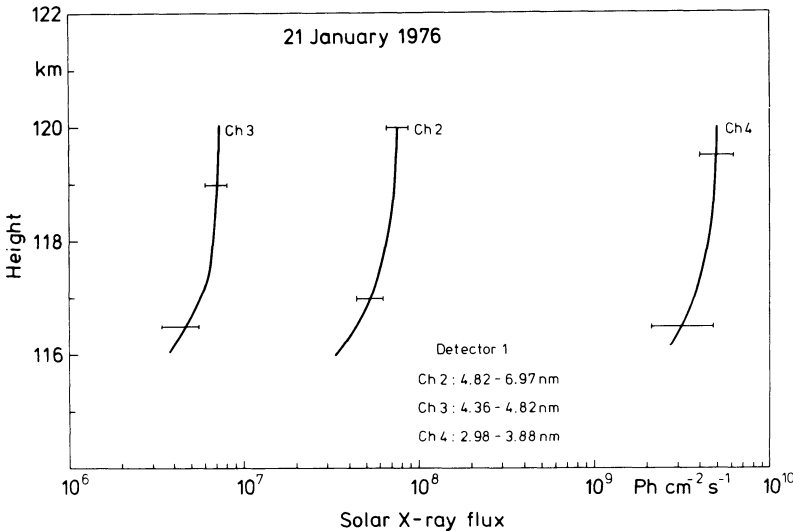


Fig. 2. Measured X-ray flux in channels 2–4 of detector 1 on 21 January 1976. Channel 1, at wavelengths >2 nm, no signal was obtained due to the material of the window. Channel 5 was only used to detect electrons which possibly could penetrate the windows; the result was that electrons did not disturb the measurement by the other channels

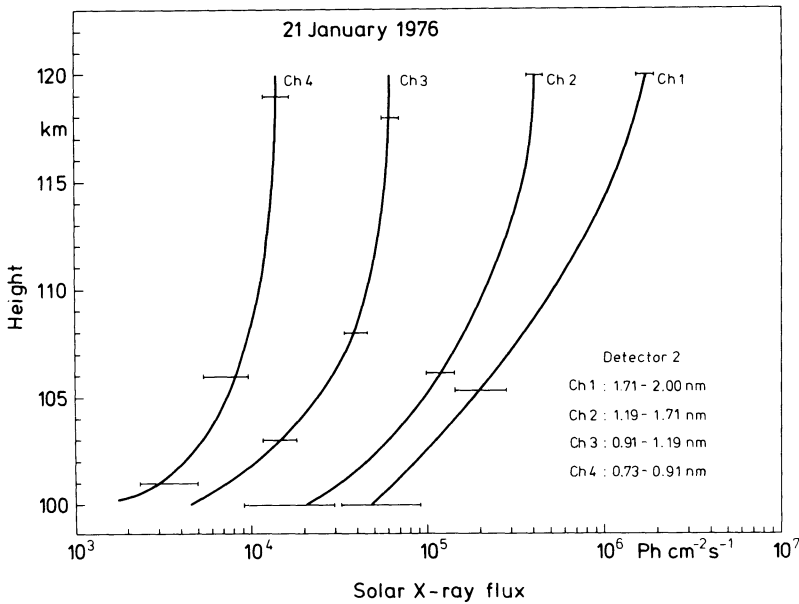


Fig. 3. Measured X-ray flux in channels 1-4 of detector 2 on 21 January 1976. Concerning channels 1 and 5 see legend of Figure 2

On January 1976 Detector 3 Failed

During both flights the solar activity was low, but slightly increased on 21 January 1976, as can be seen by comparing Figures 1 and 3.

Based on the fluxes measured at the apogees, *the solar X-ray spectrum beyond the Earth's atmosphere* was calculated by numerical integration using a model with a number of thin layers of 1 km thickness, and assuming for the small region of concern constant atmospheric density. The atmosphere density data were taken from the CIRA 1972 reference atmosphere, the absorption coefficients from Henke et al. (1967). The results obtained from the calculation are presented in Figure 4. For comparison, the dashed lines indicate the solar fluxes determined by Hinteregger (1965). The agreement is rather good, and reasonable since both measurements were made near sunspot-minimum conditions, those by Hinteregger in July 1963 (sunspot minimum in 1964), and those presented in this paper, in January 1976 (sunspot minimum in 1977).

A main purpose of the described experiment was to find the *ionization production rate*, q , due to solar X-rays, for comparison with the production due to other ionization sources during winter-anomalous conditions. This was done by measuring the attenuation of the X-ray flux as it is absorbed in the lower thermosphere, calculating the effective spectrum as a function of height, and from that calculating electron production.

Solar X-rays with wave-lengths up to 10 nm can produce electrons in the lower thermosphere, and thus contribute to the electron-density distribution of the E region. Since there are no window materials being transparent for

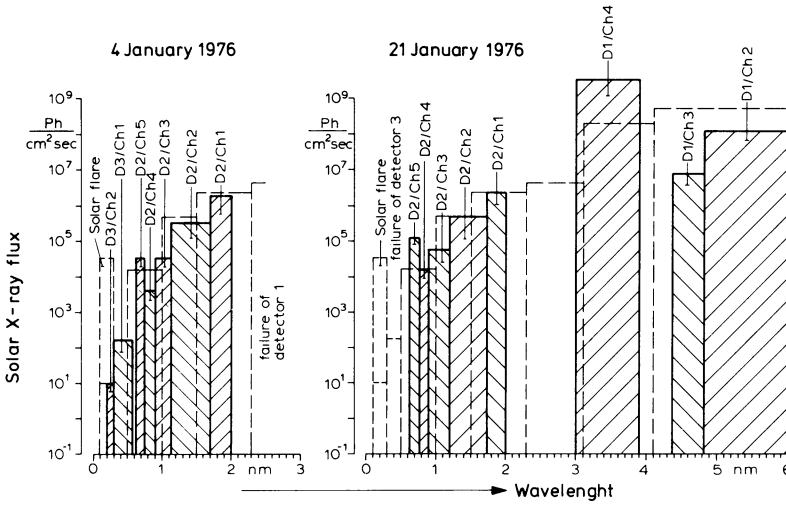


Fig. 4. Comparison of solar X-ray spectrum calculated from the measurement in the apogee on 4 and 21 January 1976 for conditions outside the Earth's atmosphere (solid lines) and the solar X-ray spectrum given by Hinteregger et al. (1965) which is valid for essentially quiet solar conditions (dashed lines)

X-rays above 7 nm, a measurement of the whole solar X-ray spectrum would only be possible beyond the Earth's atmosphere by use of windowless detectors. Therefore, in order to calculate the electron-production rate, it was necessary to complete the measured curves of solar X-ray flux vs. height (range 0.2 to 2 nm) by curves obtained from measurements outside the Earth's atmosphere made by other authors (range 2 to 10 nm) (Hinteregger et al., 1965).

The calculation of the electron-production rate as a function of height was also based on the CIRA 1972 reference atmosphere, and on absorption coefficients published by Henke et al. (1967).

The X-ray spectrum was divided into energy ranges, and for each of these, the effect of the radiation on N_2 and O_2 was calculated from the ratio $n(N_2)\sigma(N_2):n(O_2)\sigma(O_2)$, where σ is the absorption coefficient.

From the set of curves of X-ray flux vs. height, the differential attenuation of flux was determined. This differential attenuation was splitted up according to the ratio given above. From the average energy per wavelength range, the energy of the threshold of ionization was subtracted taking the threshold energies of the K and L edges into account, and the energy thus calculated was divided by 35 eV, because 35 eV were assumed to produce an electron ion pair (Valentine and Curran, 1958; Nicolet and Aikin, 1960). Since the product of absorbing cross-section and atmospheric density of the other atmospheric constituents is small, only N_2 and O_2 were considered.

The result of the calculations is presented in Figure 5. Curve 1 was determined only from the values in the range 0.2–2 nm, measured on 4 January 1976; curve 2 shows the electron production by the entire range 0.2–10.2 nm where

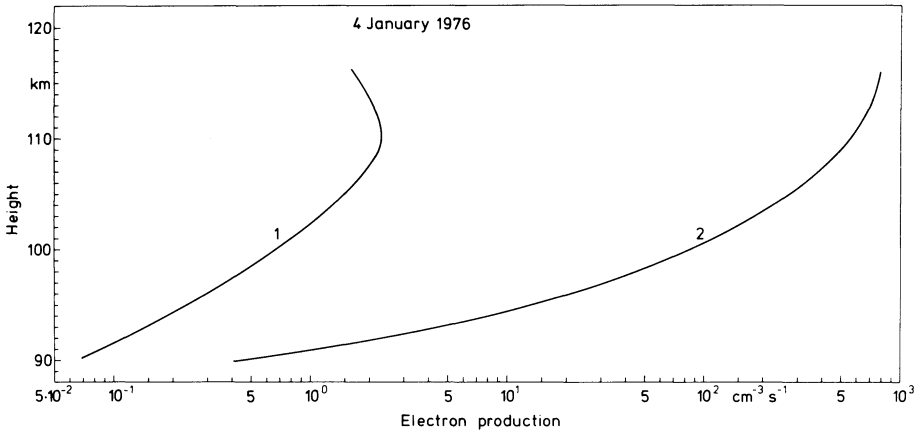


Fig. 5. Electron production from measurement of solar X-ray flux on 4 January 1976 (1), and including data from Hinteregger et al. (1965) of the spectral range 0.2–10.2 nm (2). The curves are for a solar zenith angle of 73°

the part 0.2 to 2 nm is based on our curves of X-ray flux vs. height, and the part 2 to 10.2 nm on calculations using data taken from Hinteregger (1965).

Acknowledgements. Both experiments were developed by A. Loidl assisted by W. Boogaerts who also contributed to the data reduction. The experiments were mainly funded by the "Bundesministerium für Bildung und Wissenschaft" of the Federal Republic of Germany in the framework of a German Aeronomy Programme carried out in 1976 at El Arenosillo/Spain.

The authors acknowledge also the various supports of all who contributed to the success of this experiment, particularly, Dr. A.J.F. den Boggende, Laboratorium voor Ruimteonderzoek, Utrecht (The Netherlands), Mr. A.S. Rate, University of Leicester (England); last, not least, they like to mention the encouragement obtained from Prof. W. Dieminger, the former director of the Max-Planck-Institut für Aeronomie.

References

- CIRA 1972, COSPAR International Reference Atmosphere 1972, Akademie-Verlag, Berlin, 1972.
- Henke, B.L., Elgin, R.L., Lent, R.E., Ledingham, R.B.: X-ray Absorption in the 2 to 200 Å-Region. *Norelco Reporter* **XIV**, 112–134, 1967
- Hinteregger, H.E., Hall, L.A., Schmidtke, G.: Solar XUV Radiation and Neutral Particle Distribution in July 1963 Thermosphere. *Space Research XII*, S.A. Bowhill, L.D. Jaffe, M.J. Rycroft, eds., pp. 1175–1190. Amsterdam: North-Holland Publ. Co., 1965
- Loidl, A., Boogaerts, W.: Internal Report. Experiment DL5. Röntgenspektrometer. Max-Planck-Institut für Aeronomie. Lindau 1976
- Nicolet, M., Aikin, A.C.: The formation of the D-region of the ionosphere. *J. Geophys. Res.* **65**, 1469–1482, 1960
- Röttger, J., Schwentek, H.: A numerical description of the winter anomaly in ionospheric absorption for a sunspot cycle. *J. Atmospheric Terrest. Phys.* **36**, 363–366, 1974
- Schwentek, H.: The sunspot cycle 1958/70 in ionospheric absorption and stratospheric temperature. *J. Atmospheric Terrest. Phys.* **33**, 1839–1852, 1971
- Valentine, J.M., Curran, S.C.: Average energy expenditure per ion pair in gases and gas mixtures. *Reports on progress in physics*, Vol. **XXI**, A.C. Stickland, ed., pp. 1–29. London: The Physical Society, 1958

Received May 2, 1977

A Mass Spectrometer Probe for Composition and Structure Analysis of the Middle Atmosphere Plasma and Neutral Gas

F. Arnold, D. Krankowsky, K.H. Marien, and W. Joos

Max-Planck-Institut für Kernphysik, D-6900 Heidelberg,
Federal Republic of Germany

Abstract. An instrument for composition and structure analysis of the atmospheric plasma and neutral gas at altitudes below 130 km is described. The probe consists of a quadrupole mass filter which can be operated in three modes allowing composition analysis of atmospheric positive ions, negative ions, and neutral gases. The pressure in the spectrometer is kept low by a liquid helium-cooled cryopump. An electrostatic probe for the measurement of total positive ion densities and an ionization gauge for the measurement of the total gas density and thereby also the gas temperature are also integrated in the instrument. Some results obtained by two flights of the instrument during the Western Europe Winter Anomaly Campaign 1975/76 are presented. The measurements indicate drastic enhancements of plasma densities in the *D*-region as well as characteristic changes compared to normal conditions of the positive ion composition namely low fractional abundances of cluster ions and high fractional abundances of molecular and atomic ions.

Key words: Mass spectrometer – Ion composition – Neutral composition – *D*-region – Mesosphere – Middle atmosphere – Winter anomaly.

Introduction

Our current understanding of the physical and chemical processes governing the neutral and ionized gas in the middle atmosphere (<100 km) is still very limited mainly due to the relatively high gas densities which cause complex photochemical and dynamical processes and which complicate in situ measurements. Associated with the complex nature of atmospheric processes is a pronounced variability of the plasma and the neutral trace gases. A striking example for the complexity of these phenomena is the variability of plasma densities in the ionospheric *D*- and lower *E*-regions. From ground-based observations it was

found that the mid-latitude *D*-region exhibits anomalously high radio wave absorption during winter (Appleton, 1937). This phenomenon, termed winter anomaly in the *D*-region was attributed to enhanced electron densities at altitudes below 90 km (e.g. Dieminger, 1952). Further observations revealed a strong short-term variability of the absorption characterized by time scales of days (e.g. Lange-Hesse, 1953; Schwentek, 1974). Because of the complexity and temporal as well as spatial variability of the winter anomaly it is important to measure as many as possible relevant atmospheric parameters at the same time and location. These observations have to be complemented by synoptic measurements to study the spatial extent and temporal development of the event. A detailed description of the campaign strategy is given by Offermann (1977). The scientific objective within the campaign of the instrumentation to be discussed in this paper has been to measure composition and structure of the plasma and the neutral atmosphere in order to help identifying the causes for the anomalous enhancement of the plasma densities in the *D*- and lower *E*-region. The instrumentation has evolved from many years of research in the middle atmosphere. It comprises an instrument package deliberately designed for use on small rockets delivering measurements of composition and density of ionized and major neutral species as well as densities of several neutral trace gas and atmospheric temperature.

Instrumentation

Mass Spectrometer: Ion Mode

A mass spectrometer has to be operated at low pressure in order to avoid collisions of ions with neutral molecules or atoms. Taking a typical ion path length of 10 cm a pressure below $5 \cdot 10^{-4}$ torr is required. This value corresponds to an altitude of about 120 km in the atmosphere. Consequently, mass spectrometric in situ studies of the atmospheric plasma and neutral gas composition at heights below 120 km require differential pumping. This implies that the mass spectrometer has to be mounted inside a vacuum tank into which ions enter through a small inlet orifice. The neutral gas which also enters the tank has to be pumped by a high speed pumping system. In a first approximation the sensitivity of the instrument is mainly determined by the pumping speed, as this limits the diameter of the inlet orifice and thereby the flux of ambient species into the mass spectrometer. A schematic representation of the instrument is given in Figure 1. The mass analyzer is a quadrupole mass filter *MF* of small length because then it can be operated at somewhat higher pressures than most other types of mass spectrometers. This is mainly due to the focussing effect of the quadrupole field which makes the mass filter less sensitive to changes in ion injection parameters and to ion scattering. Aside from the *MF* the vacuum tank *VT* also contains a liquid helium-cooled cryopump consisting of the helium dewar *HD* and the cold pumping surfaces *CS* which both are gold plated. In order to reduce the input of heat radiated from the warm vacuum tank to the dewar, the latter is surrounded by a radiation shield *RS* which is cooled by cold

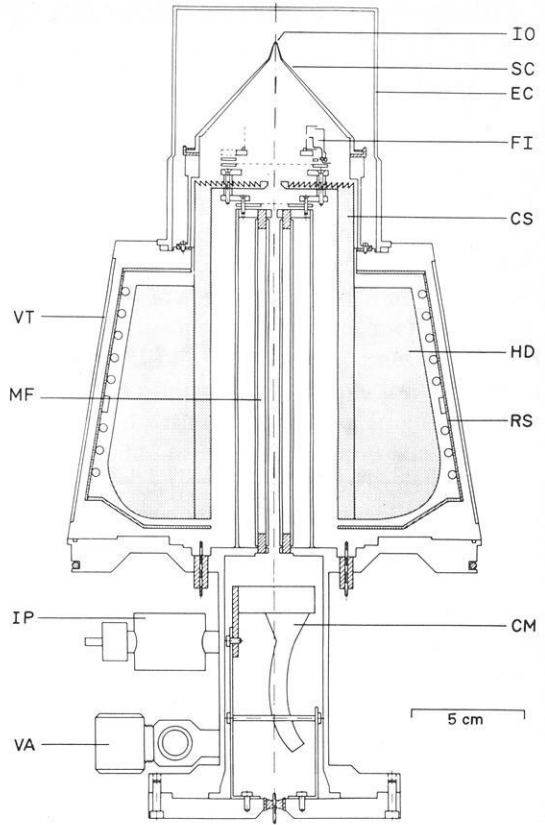


Fig. 1. Configuration of the mass spectrometer probe. *IO* inlet orifice, *SC* sampling cone, *EC* ejectable cap, *FI* filament, *CS* cold surface, *VT* vacuum tank, *MF* mass filter, *HD* Helium dewar, *RS* radiation shield, *IP* ion getter pump, *VA* valve, *CM* channel multiplier

helium gas evaporating from the dewar. On top of the vacuum tank a sampling cone *SC* is mounted bearing the knife-edged orifice *IO* with 1 mm diameter at its center. The purpose of the *SC* is to attach the shock wave which forms upstream the instrument when it traverses the atmosphere at supersonic speeds. The ejectable cap *EC* covering the sampling cone and released at 55 km on the upleg, seals the probe after bake-out and calibration in the laboratory. The inside pressure is maintained below 10^{-6} torr by a small ion getter pump *IP* with a pumping speed of 0.51 s^{-1} . On most of the ascent part of the rocket trajectory the flow approaches the instrument under an angle of attack α which is close to zero. By attaching the shock to the edges of the orifice atmospheric constituents can be sampled without being disturbed by flow effects. It should be noted, however, that an attached shock only forms under conditions of laminar flow below 65 km and that a modestly detached shock has to be expected in the transition flow regime between 65 km to 90 km. Here the effect of the sampling cone is to considerably decrease the distance between the shock wave and the orifice. Thus possible disturbances of the sampling efficiency and of the sample's composition are minimized. Downstream the inlet orifice ions, either ambient or formed from neutrals in the ion source, are extracted from the gas beam and

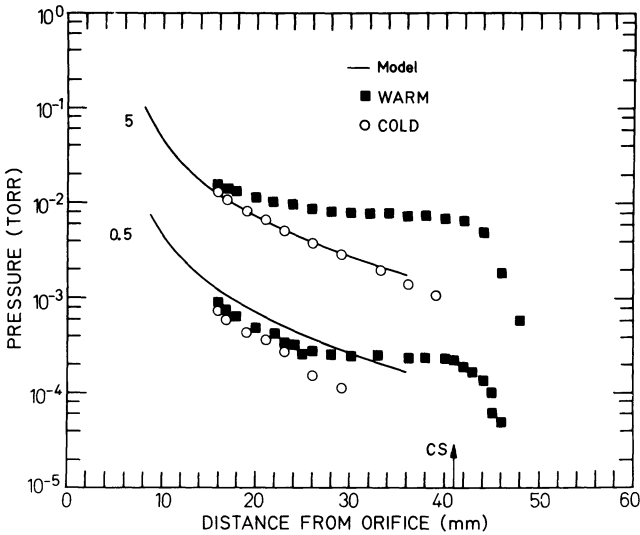


Fig. 2. Axial pressure distribution within the sampling cone for two ambient pressures (0.5 torr and 5 torr) as function of distance from the inlet orifice as measured under stationary conditions. For details see text

focussed onto the entrance hole of the mass filter by use of a simple ion optical system. It consists of one cylindrical and two planar grid electrodes which are located above and below the planar part of the cold surface. The latter freezes out most of the gas beam. Only neutral particles contained in the central part of the beam reach the interior of the mass analyzer where they are scattered by warm walls and finally pumped by the cylindrical part of the cold surface.

In order to investigate the efficiency of the pumping system, the pressure distribution along the beam axis was measured by use of a miniaturized ionization gauge under stationary conditions in the laboratory. As seen from Figure 2 the pressure decreases steeply from its value upstream the inlet orifice towards the planar cold surface and continues to decrease further downstream to a constant value. When compared with a theoretical profile considering no obstacle downstream the SC which is also shown in Figure 2, the data points agree reasonable well. When the cold surface is kept at room temperature and the VT is pumped by a high speed oil diffusion pump, a region of enhanced pressure forms upstream the planar cold surface due to particle reflections and scattering. At an outside pressure of 0.5 torr the region of enhanced pressure extends over a distance of 2.5 cm upstream the CS. Under conditions of a rocket flight the gas beam is more concentrated towards the axis as a result of the relative velocity between the gas and the instrument which is superimposed on the Maxwell-Boltzmann velocity distribution of the gas particles. Detailed computations for typical flight conditions at 90 km altitude indicate an increase of the axial pressure by about a factor of 3 when compared with the stationary case. This implies that the curve for 0.5 torr roughly corresponds to a flight situation at about 60 km altitude. Here collisions of ions with neutral particles in the beam are only important on the first centimeter downstream the orifice and beyond this point effective extraction and focussing is possible. After passing through the mass filter MF the mass analyzed ion current is detected by a

channel multiplier *CM* operated in a pulse counting mode. A mass range from 1 amu to 250 amu is swept in about 2s. Mass spectra of positive and negative ions and of neutrals are measured sequentially (see Table 1). For this purpose the electrical potentials applied for extraction, focussing, mass analysis, and ion detection are changed between subsequent mass scans. A summary of characteristic parameters of the instrument is given in Table 1.

The fragmentation of fragile cluster ions found in the *D*-region during sampling is a problem that deserved special attention in the design of the present instrument. Dissociation energies of cluster ions which are held together by weak dipole interaction forces can be as low as a tenth of one eV. Such complexes may become dissociated upon collisions with neutral molecules. As soon as the relative kinetic energy of the collision partners becomes enhanced with respect to the value in the undisturbed atmosphere, a depletion of fragile ions may occur which, of course, is associated with an increase of fragment ions. The kinetic energy may be increased either due to high temperatures associated with the shock wave or by acceleration of cluster ions in electric fields. Since collisions are not very important downstream the inlet orifice collisional dissociation, if at all, only occurs upstream the inlet orifice. If the shock is attached to the *SC*, no shock-induced composition of cluster ions has to be expected. Electric field-induced decomposition of cluster ions may occur upstream the sampling cone which is kept at a bias potential in order to extract ions from the plasma. Previously typical potential of 10V were applied (c.f. Narcisi, 1970; Aikin et al., 1977). Laboratory studies which we have carried out (Marien and Arnold, 1973), however, revealed severe decomposition of

Table 1

Total Mass	11 kg
Overall Length	49.5 cm
Volume of He-Dewar	0.5 l
Pumping Capacity	$\sim 5 \cdot 10^{20}$ N ₂ -molecules
Pumping Speed	~ 5000 l s ⁻¹
Liquid He Evaporation Rate without Gas Load	~ 0.28 cm ³ s ⁻¹
Quadrupole Rod Diameter	0.48 cm
Quadrupole Rod Length	11.5 cm
Mass Filter High Frequency	2 MHz
Maximum Count Rate	5 MHz
Ion Probe Electrometer	10 ⁻¹² – 10 ⁻⁶ A
Ionization Gauge Electrometer	10 ⁻¹¹ – 10 ⁻⁵ A
Mass Range	1–250 amu
Mass Resolution	100
Scan Time	1 s
Altitude Resolution	2 km
MS Detection Limit Ions	≥ 0.1 cm ⁻³
MS Detection Limit Neutrals	$\geq 10^9$ cm ⁻³
MS Altitude Range Ions	≥ 20 km
MS Altitude Neutrals	≥ 60 km
IP Altitude Range	≥ 60 km
IG Altitude Range	≥ 60 km
IP Detection Limit	10 cm ⁻³
IG Detection Limit	$\sim 3 \cdot 10^9$ cm ⁻³

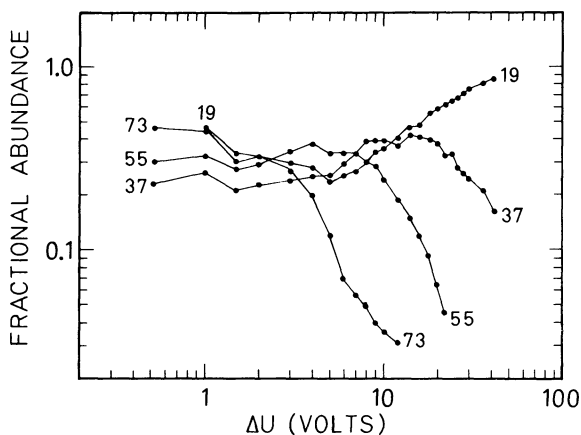


Fig. 3. Fractional abundance of hydrated protons $H^+(H_2O)_n$ as function of drawn-in potential measured under stationary conditions at a pressure of $3 \cdot 10^{-2}$ torr

$H^+(H_2O)_n$, $n=1, 2, 3, 4$ cluster ions when 10 V are used (Fig. 3). Based upon these results, we use bias potentials of 2.5 V which are just sufficient to overcompensate a possible charge-up of the rocket. The benefits of a sampling cone and the use of low sampling potential became obvious when the instrument was flown for the first time (Arnold and Krankowsky, 1974) and a great number of weakly bound atmospheric cluster ion species was observed. The fact that from these measurements reaction cross sections for the formation of such species in the atmosphere could be quantitatively derived (Arnold and Krankowsky, 1977), which were confirmed by laboratory measurements afterwards, can be regarded as a strong argument in favour of the reliability of modern ion composition measurements in the lower ionosphere.

Mass Spectrometer: Neutral Gas Mode

For the mass analysis of neutral atmospheric gases an ion source mounted inside the sampling cone is used. Electrons are produced from a heated tungsten-rhenium filament Fi and injected into the region inside the cylindrical grid electrode. Here they are accelerated towards the inner walls of the front part of the sampling cone. The potential field between the upper planar grid electrode and the sampling cone is adjusted such that the electrons reach an energy of about 16 eV at a potential surface located 2 cm downstream the orifice and gain another 2 eV until they hit the sampling cone. As the ion production rate is proportional to the gas density and to the cross section for electron impact ionization, which strongly increases with energy around 16 eV for most gases of interest here, the downstream boundary of the ionization region is sharply defined. This is true because both the gas density and the electron energy decrease steeply with increasing distance downstream from the sampling cone orifice. As the probability for focussing ions into the mass filter strongly decreases with increasing radial distance from the sampling cone, the effective ionization region is a small volume rather closely confined to this axis. Thus it is

possible to keep the fractional abundance of particles which have undergone wall collisions smaller than 30% of the total number of particles populating the effective ionization volume. This arrangement largely avoids the depletion by wall-reactions of reactive gases, such as for example oxygen atoms, relative to unreactive gases. Another problem associated with mass spectrometric measurements of atomic oxygen below 100 km where O/O_2 is small comes from the production of O^+ ions by dissociative ionization of O_2 . As the cross section for the latter process decreases much faster with decreasing electron energy than does the ionization cross section for the other gases of interest, the problem can be tackled by using low electron energies. However, electron energies much lower than about 18 eV are hardly acceptable because of loss of sensitivity. Thus, atomic oxygen measurements are only possible at altitudes above about 80 km. Another limitation comes from the pressure inside the effective ionization volume which should be sufficiently low in order to avoid ion-neutral collisions. This height limit is about 60 km. Characteristic instrument parameters are given in the Table 1. A full duty cycle of the mass spectrometer includes three mass spectra, one for positive ions, one for negative ions, and one for neutrals. Between subsequent spectra the voltages are switched. No electrons are emitted from the filament in the ion modes.

Positive Ion Probe

The ion probe *IP* (Fig. 4) which measures the relative total positive ion density consists of a cylindrical grid and of an axial cylindrical collector with a diameter of 3 mm which is small compared to the 32 mm diameter of the cylindrical grid. While the grid is on rocket potential, a voltage of -10 V is applied to the ion collector via a fast floating electrometer. The probe is mounted on a small boom which is housed under the ejectable vacuum cap *EC* of the mass spectrometer. The probe is deployed upon cap ejection. Thus contamination of the probe prior to deployment is excluded. As the axis of the cylindrical grid is parallel to the rocket axis, the gas flow is assumed to be only weakly disturbed by the edges of the probe. Therefore the collector current I_C should be related to the total

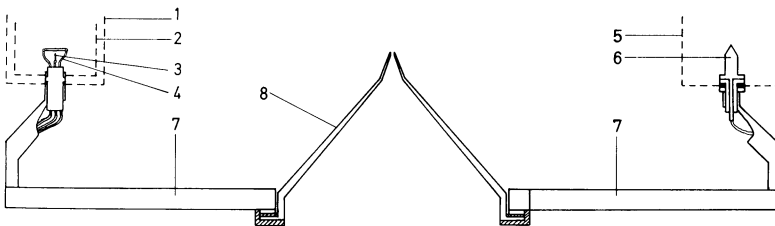


Fig. 4. Flight configuration of mass spectrometer sampling cone, ion probe (right), and ion gauge (left). 1 and 5 shielding grids, 2 ion collector grid, 3 filament, 4 electron collector, 6 ion collector, 7 booms, 8 sampling cone

positive ion density n_+ by:

$$I_C = D e_0 F_G \quad (1)$$

where F_G = flux of positive ions through top circular area of the cylindrical grid

e_0 = unit charge

D = coefficient describing the fraction of collected ions with respect to incoming ions.

Under molecular flow conditions $D = 1$ and

$$F_G = \frac{A_{\text{eff}} \bar{V} F(S) n_+}{4} \quad (2)$$

where A_{eff} = effective top circular sampling area of the cylindrical grid.

$$\bar{V} = \left(\frac{8KT}{\pi m} \right)^{\frac{1}{2}}$$

$$F(S) = \exp(-S^2) + S\pi^{\frac{1}{2}}(1 + \text{erf}(S))$$

$$V_R = \text{rocket velocity}$$

$$S = V_R \cos \alpha / (2KT/m)^{\frac{1}{2}}$$

erf = error function

α = angle of attack

K = Boltzmann's constant

m = ion mass.

In an intermittant mode of operation the potential of the ion collector is varied from +15 to -15 V in 2.5 V steps. Thereby a probe characteristic is obtained which allows to judge whether D is one. The measurements indicate that D becomes smaller than one at altitudes below about 60 km. Here the time required for an ion to drift from the grid to the axial collector becomes larger than the residence time of the ion inside the cylindrical grid which is $\tau_{\text{res}} = L/V_R$ where L is the length of the cylindrical grid and V_R is the rocket velocity. At these altitudes the *IP* is not considered to provide meaningful data.

Ionization Gauge

The ionization gauge *IG* (Fig. 4) measures the absolute total gas density. It consists of a tungsten-rhenium filament from which electrons are emitted and accelerated to a circular wire electrode at +70 V. Positive ions produced by electron bombardment ionization are collected by a cylindrical grid electrode to which a potential of -10 V is applied via a fast floating electrometer. Another cylindrical grid electrode which is at rocket potential is used in order to shield the sampling area of the mass spectrometer from the ion gauge potentials. The geometry of the ionization gauge is designed in such a way that the ambient gas flow reaching the ionizing volume is likely almost undisturbed.

The dimensions of the ion gauge are small so that collisions of ions produced and neutral particles become important only at pressures above about 10^{-2} torr. However, laboratory measurements (Hettmannsperger, 1976; Arnold et al., 1975) indicated that the collected ion current remains almost proportional to the gas density even up to pressures of 0.1 torr. This corresponds to an altitude of about 63 km. The upper height limit for obtaining useful measurements is determined by the density of ambient positive ions which also contribute to total positive ion current measured by the ion gauge. This contribution can be determined when the filament of the ion gauge is switched off. This occurs during the ion modes of the mass spectrometer. Under quiet daytime conditions ionospheric ions contribute 50% to the total collector current at an altitude of about 100 km. The absolute sensitivity of the ion gauge is calibrated in laboratory. The gauge is mounted on a small boom which before cap ejection is housed under the vacuum tight cap of the mass spectrometer. The boom is deployed upon cap ejection. Thus contamination of the ion gauge is avoided. Absolute number densities of the atmospheric gas are obtained by use of the laboratory calibration. The contribution of ionospheric positive ions to the collector current determined as described above is corrected for up to altitudes where it becomes 50%. Above this height the method is not considered to be applicable anymore. As the sampling of ions produced in the ionisation region becomes severely affected by collisions below about 60 km, the method cannot provide relative data below this altitude.

Mass Spectrometer Data Analysis

Ion Measurements

Relative partial ion densities are obtained from the measured partial count rates. The count rate $C(X)$ of an ion species X is related to the flux through the inlet orifice $F_0(X)$ by

$$C(X) = T(X)F_0(X) \quad (3)$$

where $T(X)$ is the transmission factor of the ion optics and the mass analyzer. $T(X)$ is calibrated in the laboratory for various ion species including He^+ , CH_4^+ , H_2O^+ , Ne^+ , N_2^+ , O_2^+ , A^+ , CO_2^+ , Kr^+ , and Xe^+ . Under flight conditions $F_0(X)$ is related to the number density $[X]$ by

$$F_0(X) = \frac{1}{4}A_{\text{eff}}\bar{V}F(S)[X]$$

where A_{eff} = effective orifice area.

The other quantities are the same as in Equation (2). The relation applies only for molecular flow conditions (>90 km) and assumes that ions are sampled like neutral particles except for an enrichment upstream the orifice due to the application of a draw-in potential at the sampling cone. This leads to an effective orifice area. If we assume A_{eff} to be mass independent, it does not enter into the evaluation of relative partial densities. It may also be noted that for a

small α and $V_R \gg \bar{V}$ which occurs below 90 km on ascent, the expression simplifies to

$$F_0 \approx A_{\text{eff}} V_R [X]. \quad (5)$$

In a first approximation no mass dependance of F_0 is expected at these altitudes. Provided all ions can be extracted from the expanding gas beam and focussed into the mass filter, mass discrimination due to flow effects downstream the sampling orifice should not be important. Absolute partial ion densities are obtained by normalizing the sum of the relative partial densities to the total ion density at one altitude. Usually the total ion density is obtained by independent methods such as electrostatic probes, Faraday rotation and ionosonds. The latter two methods give the electron density which above about 70 km should equal to the total positive ion density. At altitudes below about 60 km $F_0(X)$ and $T(X)$ become pressure- and thereby altitude-dependant and the normalization has to be done for each data point.

Neutral Gas Measurements

The channeltron count rate $C(X)$ of a species X is related to the rate of production of ions X^+ in the effective ionization region $P(X^+)$ by:

$$C(X) = P(X^+) T_N(X) \quad (6)$$

where $T_N(X^+)$ is a transmission factor for ion optics and the mass filter. $P(X^+)$ is determined by the ionization cross section $\sigma(X)$, the flux of ionizing electrons F_E and the density of X which all depend on the location inside the effective ionization volume. In the laboratory $C(X)$ is determined as a function of $[X]$ for stationary conditions ($V_R = 0$) and for various gases including CH_4 , H_2O , N_2 , O_2 , A , CO_2 and Kr . The mass discrimination due to flow effects occurring under flight conditions ($V_R \neq 0$) is computed as a function of V_R and atmospheric gas temperature.

For atomic oxygen which was not calibrated in the laboratory $P(O^+)$ was determined from measures $P(X^+)$ values by

$$P(O^+) = \frac{\sigma(O^+)}{\sigma(X^+)} P(X^+). \quad (7)$$

The transmission factor $T_N(X)$ which is essentially a function of mass was determined for O from the measured relation $T_N(M_X)$. Absolute partial densities are determined by normalization of the sum of relative partial densities to the absolute total gas density measured by the ionization gauge. Regarding a possible depletion of reactive gases as for example atomic oxygen the computations indicate that less than 30% of the incoming oxygen atoms undergo wall collisions upstream the effective ionization volume. This method of analyzing neutral gas data as well as the experimental approach outlined above has been checked against a different experimental technique for atomic oxygen

which certainly is the constituent most difficult to measure by mass spectrometer. Atomic oxygen number densities obtained from a mass spectrometer identical to the instrument described here and a resonance fluorescence and absorption experiment (Dickinson, private communication) flown about 30 min after the mass spectrometer showed an excellent agreement of the relative number densities within an altitude region between 83 and 113 km altitude. The average ratio of the resonance fluorescence to the mass spectrometer number densities compared for 26 data points in the height range indicated above was 2.1 with a standard deviation of 0.5.

Results and Discussions

Two instruments B4-1 and B4-2 were flown within the campaign (cf. Offermann, 1977) on January 4 and January 21, 1976 at 1431 UT and 1433 UT, respectively. Both days were characterized by high radio wave absorption in the *D*-region.

The instruments performed as expected and data were obtained on the upleg part of the trajectory from 60 km to apogee at 130 km. On the downleg portion useful measurements were made down to 60 km and 35 km for B4-1 and B4-2, respectively.

The N_2 and O_2 number densities measured on both days are shown in Figure 5 along with the total gas density measured by the ionization gauge on January 21. When compared with N_2 and O_2 profiles of the CIRA 1972 reference atmosphere deviations up to about $\pm 50\%$ are observed. Total positive ion densities as measured by the ion probes with relative probe densities normalized to ionosonde values (Rose and Widdel, private communication) at 109 km are shown in Figure 6. When compared with each other both profiles are very similar. They are characterized by pronounced relative maxima around 88 km and around 79 km. When compared with average winter conditions at

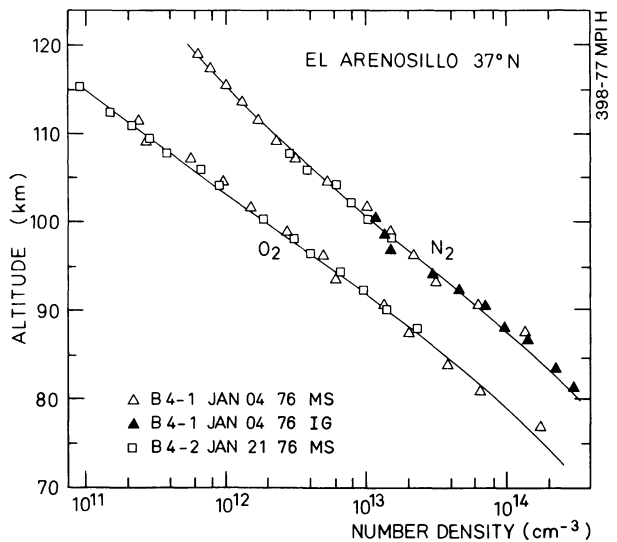


Fig. 5. Height profiles of N_2 and O_2 number densities. Lines represent CIRA 1972 model densities

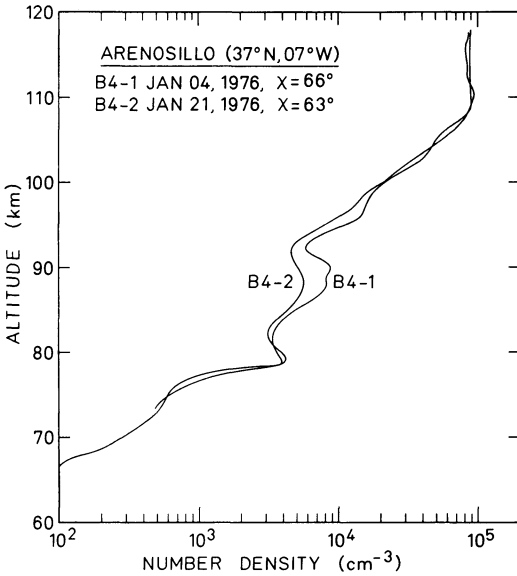


Fig. 6. Total positive ion number densities obtained from the ion probe

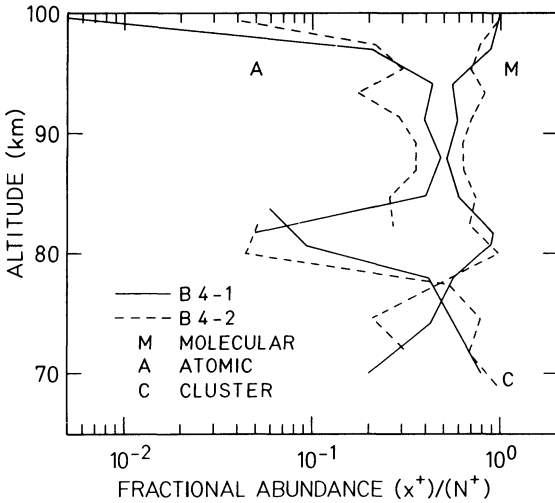


Fig. 7. Fractional abundance of molecular ions, atomic metal ions, and cluster ions versus height

37° N the plasma densities are enhanced between about 75 km and 90 km by factors up to 4.

The enhancement is strongest at the heights of the conspicuous structures mentioned above. The fractional abundance of positively charged molecular ions, atomic metal ions and cluster ions as measured by the positive ion mode of the mass spectrometer is shown in Figure 7. Again the data sets of both days reveal a high degree of similarity when compared with each other. Molecular ions dominate above 76 km (B4-1) and 77 km (B4-2) and cluster ions below.

Atomic metal ions reach high fractional abundance up to 40% in the altitude range 85–90 km. This altitude range coincides with the upper structure shown by the total positive ion density profiles (Fig. 6). Two extraordinary features are obvious when compared to a normal midlatitude situation (Narcisi, 1976).

First, a lowering of the height by about 3 to 4 km is observed at which molecular ions and cluster ions become equally abundant. Second, atomic metal ions appear in high relative abundance below 90 km. When compared with the two previous positive ion composition measurements carried out under winter anomaly conditions (Zbinden et al., 1975; Arnold and Krankowsky, 1977) the present results are rather similar to those reported by Zbinden et al., 1975. But they are much different from those obtained at high middle latitudes (Arnold and Krankowsky, 1977). The preliminary results presented here indicate at least three causes of the winter anomalous plasma density enhancements: (1) an increase in the production of molecular ions; (2) a decrease of the bulk recombination coefficient for positive ions and electrons due to low fractional abundances of rapidly recombining cluster ions above 76 km and 77 km, respectively; (3) a decrease of the bulk recombination coefficient for positive ions and electrons due to high fractional abundances of very slowly recombining atomic metal ions around 85–90 km.

Summary

A mass spectrometer probe experiment for use on small rockets has been developed for studying the plasma and neutral gas in the middle atmosphere. The mass spectrometric measurements are supplemented by an electrostatic ion probe and an ion gauge which both are integral parts of the mass spectrometer. Thus mass spectrometric composition data can be converted to absolute number densities of ions and neutral gas species. In addition, from the data of the ion gauge neutral atmospheric temperatures are derived.

When compared to previous instruments utilized below 100 km the, mass spectrometer sampling technique has been vastly improved. Shock effects and disturbances of the flow field are largely avoided. The absence of shock effects and the use of low draw-in potentials enables the measurement of fragile cluster ions with low bond energies. Reactive neutral gases as e.g. atomic oxygen can be measured without severe depletion due to an appropriate design of the ion source. Therefore, the measured ion and neutral gas composition closely resembles the atmospheric composition.

The mass spectrometer probe delivers ion and neutral gas number density profiles independent from additional observations. To some extent ion and neutral gas data complement each other and allow a check of the internal consistency. Neutral gas temperature derived from the ion gauge data can be compared to the temperature obtained from the ion composition considering the temperature dependent ion-neutral reaction rate coefficients. Number densities of certain neutral gases like NO, H₂O, H₂O₂, and O can indirectly be determined from the ion composition and complement the direct neutral measurements.

Acknowledgment. This work was supported by the Bundesminister für Forschung and Technologie through grant B115/73 – BIV/DH2.

References

- Aikin, A.C., Goldberg, R.A., Jones, W., Kane, J.A.: Observations of the Mid-Latitude Lower Ionosphere in Winter. *J. Geophys. Res.* **82**, 1869, 1977
- Appleton, E.V.: Regularities and Irregularities in the Ionosphere, I. *Proc. Roy. Soc., Ser. A* **162**, 451, 1937
- Arnold, F., Böhringer, H., Hettmannsperger, E., Krankowsky, D., Stanislawski, J., Zettwitz, E.: Annual Report of the Max-Planck-Institute for Nuclear Physics, Heidelberg, Germany, 1975
- Arnold, F., Krankowsky, D.: A New Concept for D-Region Chemistry as Inferred from a Mass Spectrometer Measurement. Paper presented at International Symposium on Solar-Terrestrial Physics, COSPAR, Sao Paulo, June 1974
- Arnold, F., Krankowsky, D.: Ion Composition and Ion- and Electron Loss Processes in the Earth's Atmosphere. In: "Dynamical and Chemical Coupling of the Neutral and Ionized Atmosphere", Reidel Publ. Comp. Dordrecht-Holland, Boston-USA, 1977
- Dieminger, W.: Über die Ursache der exzessiven Absorption in der Ionosphäre an Wintertagen. *J. Atmospheric Terrest. Phys.* **2**, 340, 1952
- Hettmannsperger, E.: Entwicklung einer Sonde zur Messung der Neutralgasdichte in der Mesosphäre und unteren Thermosphäre. Diplomarbeit, Max-Planck-Institut für Kernphysik, Heidelberg, Germany, 1976
- Lange-Hesse, G.: 27-tägige Variationen in der D-Schicht-Absorption der Ionosphäre über Singapore und Slough. *J. Atmospheric Terrest. Phys.* **3**, 153, 1953
- Marien, K.H., Arnold, F.: Annual Report of the Max-Planck-Institute for Nuclear Physics, Heidelberg, Germany, 232, 1973
- Narcisi, R.S.: Physics of Composition Studies of the Lower Ionosphere. In: *Physics of the Atmosphere* (Franco Verniani, ed.) Editrici Compositori Bologna, Italy 1971
- Narcisi, R.S.: Mass Spectrometer Measurements in the Ionosphere, in *Physics and Chemistry of Upper Atmospheres*. Reidel Publ. Comp., Dordrecht-Holland, Boston-USA, 171, 171, 1974
- Offermann, D.: Study of the D-Region Winter Anomaly in Western Europe 1975/76. *J. Geophys.* **44**, 1 13, 1977
- Schwentek, H.: Wave-like Structures in the Variation of Ionospheric Absorption. *J. Atmospheric Terrest. Phys.* **36**, 1173, 1974
- Zbinden, P.A., Hidalgo, M.A., Eberhardt, P., Geiss, J.: Mass Spectrometer Measurements of the Positive Ion Composition in the D- and E-Regions of the Ionosphere. *Planetary Space Sci.* **23**, 1621, 1975

Received August 16, 1977 | Accepted August 17, 1977

The Cryo Mass Spectrometer in the Winter Anomaly Campaign

V.H. Friedrich*, D. Offermann**, H. Trinks**, and U. von Zahn

¹ Physikalisches Institut der Universität Bonn, Nussallee 12, D-5300 Bonn 1,
Federal Republic of Germany

Abstract. On January 4 and 21, 1976, at 1630 CET two rockets were launched as part of the winter anomaly campaign, both carrying amongst other experiments a cryo mass spectrometer. The mass spectrometers performed measurements of the neutral gas composition in the altitude range from about 80 to 117 km.

Scientific goals, design, and operation of the instruments are described in detail. Preliminary results of the data reduction are presented for the flight of January 4. Number density profiles of N₂, O₂, and Ar show a pronounced wave-like structure.

Key words: Winter anomaly — Mass spectrometer — Mattauch-Herzog geometry — Helium-cooled ion-source — Neutral composition — Trace constituents.

Introduction

On January 4 and 21, 1976, at 1630 CET and 1631 CET, respectively, two rocket-borne mass spectrometers with helium-cooled ion sources were flown above El Arenosillo (Spain) as part of the winter anomaly campaign. The mass spectrometers employed “closed” ion-sources, the walls of which were cooled to about 8 K by means of supercritical helium. As all atmospheric species (except He and H₂) condense on the walls at these temperatures, the formation of background gases within the ion-source is largely suppressed. Moreover, the bow-shock ahead of the instrument is removed down to altitudes below 80 km, the instrument forming the front part of the payload.

The scientific goal of the campaign was the investigation of the meteorological type of the mid-latitude winter anomaly. Several suggestions have been made so far to explain the processes leading to an enhancement of the electron density in the D-layer, e.g. atmospheric circulations and/or wave motions causing

* To whom offprint requests should be sent

** Now at: University of Wuppertal, D-5600 Wuppertal, Federal Republic of Germany

changes in the temperature field and in the concentration of minor constituents, which may influence the ion- and neutral-chemistry.

The contribution of the mass spectrometers to this goal was the measurement of the composition of the neutral atmosphere down to about 80 km under shock free conditions and with a good height resolution. Special emphasis was on the determination of atomic oxygen and on specific atmospheric trace constituents which are of importance for the neutral- and ion-chemistry of the D-region. The measurement of inert gases (N_2 , Ar) is of interest for the investigation of turbulent and diffusive processes.

A number of atmospheric parameters was measured by redundant experiments during the campaign. Therefore comparison and combination of the data obtained by these different instruments yields a valuable check on the reliability of the measured data. The mass spectrometer measurements described here may thus be especially compared to the data obtained by two other mass spectrometers which were flown on two other rockets with a time shift of about 1 h, and with pitot tube measurements on the same rockets. The Pitot probes were mounted in the payload directly adjacent to the cryo mass spectrometers. The total density derived from the Pitot data allows a check on the sensitivity of the mass spectrometers. On the other hand the height profiles of the N_2 number density measured by the mass spectrometers will complement the total density profiles of the Pitot probes.

Instrument Configuration

A sketch of the instrument is given in Figure 1. Its essential parts are the helium-cooled ion-source, the mass analyzer, and the helium supply system including the storage dewar, valves, and pipes. The instrument was mounted axially in the uppermost part of the payload looking into the flight direction.

During the flight the angle between payload axis and the velocity vector (angle of attack) should be as small as possible to allow the ambient particles to form a properly shaped molecular beam in the ion-source. For this purpose the payload included an attitude control system which kept the angle of attack below $\sim 10^\circ$ (at all altitudes above 80 km). If the ion-source protection cap is ejected at too low altitudes (i.e. around 80 km) the sensitivity of the instrument could be changed because of large amounts of gas condensing on the ion-source walls. Therefore this cap was ejected not earlier than 110 km on the upleg of the flight. Low altitude data were obtained on the downleg thanks to the attitude control of the payload.

Ion Source and Cooling System

The design of the ion source (Fig. 2) was similar to that described by Trinks and Hellenbroich (1973). The ambient atmospheric particles entered the ion source through two circular holes in both the front-plate and the so-called ion-box. Inside the ion-box the particles crossed an electron sheet, emitted

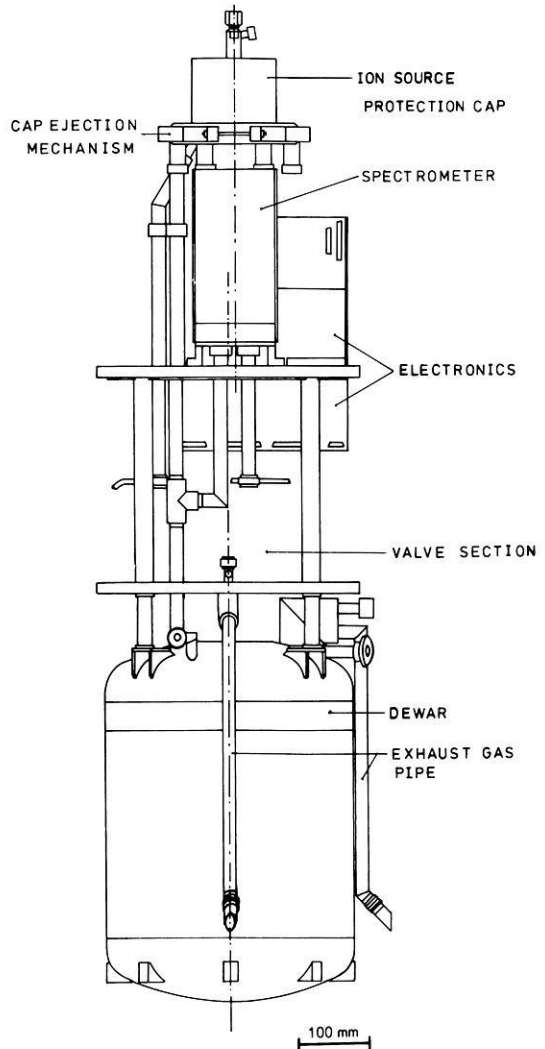


Fig. 1. The cryo mass spectrometer (schematically)

from a hot tungsten-rhenium filament, ionizing part of them. The energy of the ionizing electrons was about 90 eV. The ions were focussed by the ion-lens and a pair of focussing plates onto the "object-slit" of the spectrometer.

The inner parts of the ion source were made of copper with high thermal conductance. Ion-box, ion-lens, and focussing plates were thermally coupled to the heat-exchanger 1 to keep them at temperatures as low as possible during the measurement. This will assure a high sticking probability for gas particles hitting the wall. The wall-temperature normally did not exceed 8 K.

The electron-beam generation system and radiation shield were coupled to the heat-exchanger 3. Their temperature was about 12 K.

In order to avoid the formation of a shock front ahead of the ion-source

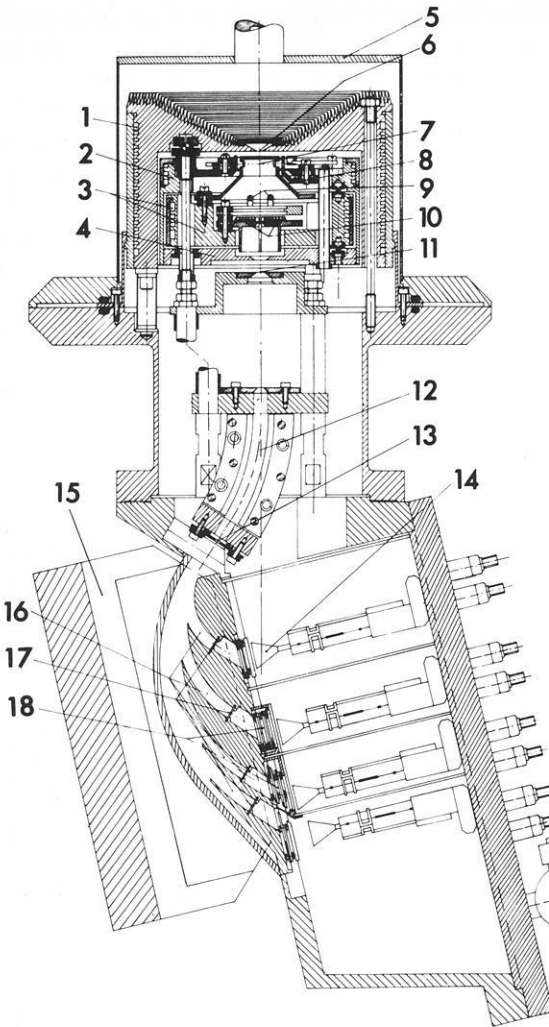


Fig. 2. Cross section of the mass spectrometer. *Legend:* 1 heat exchanger 2 (front plate); 2 heat exchanger 3; 3 heat exchanger 1; 4 radiation shield; 5 ion-source cover; 6 entrance aperture; 7 electron beam; 8 ion-box; 9 ion-lens; 10 focussing plates; 11 object slit; 12 electric field; 13 total ion-current collector; 14 spiraltron; 15 magnet; 16 ion channel; 17 exit slit; 18 ion current collector grid

the temperature of the conical, indented front-plate (heat exchanger 2) should not exceed 20 K (Offermann and Tatarczyk, 1973). A typical value during normal flight operations was about 15 K. To guarantee a high thermal conductance in the front plate it was made from very pure silver.

The heating of the ion source, looking into the flight direction, mainly depends on the solar radiation, the kinetic energy of the impinging particles due to the payload velocity, and on the gas condensation heat. Above about 110 km the heat load mainly consists of the solar input of 0.14 W/cm^2 . As the ambient density and payload velocity increase, the heat caused by the impinging particles becomes dominant at lower heights.

Because of the very different heat loads on the front-plate and on the inner ion source two different helium cooling circuits were used for heat exchangers

1 + 3 and 2, respectively. The cryogen was taken from a 15 liter storage dewar which was filled with liquid helium some time before launch. A few minutes before lift-off the helium was made supercritical (6 K at 5 bars). The flow-rate of the cryogen and thus the ion source temperatures were controlled by several valves and throttles in the exhaust gas pipes. Because of the rapid variation of the heat-loads during the flight, electric feedback circuits were used to control the ion source temperatures and the dewar pressure. These control circuits were blocked during the first part of the flight to avoid accidental cryogen losses.

Mass Spectrometer

Ions which passed the object-slit entered the double focussing Mattauch-Herzog spectrometer which employed a 0.34 T magnetic field (Fig. 2). After mass separation the ions were detected in 4 channels simultaneously by means of 4 spiraltron multipliers operated in the pulse-counting mode. The use of 4 channels allowed a high sampling frequency for the detection of the mass numbers of interest. The dynamical range of the spiraltrons was limited to about 10^6 counts/s which did not allow to measure simultaneously the main atmospheric constituents and the trace gases. The solution to the problem was to determine the main constituents by measuring doubly ionized or isotopic species instead of singly ionized parent molecules.

To further increase the dynamical range, two of the channels were equipped with "ion collector grids". The ion currents intercepted by these grids were fed into logarithmic electrometers.

The mass spectrometer could be operated in two different modes: In the *stepping mode* the acceleration voltage U_a applied to the ion-box was controlled by a programmer selecting 16 fixed voltage steps of a duration of 100 ms each. Thus in 1.6 s—the duration of one measurement cycle—up to 16 different mass lines could be detected per channel. The height resolution for the important constituents, measured twice per cycle, was less than 1 km in the 80 km region and about 100 m near apogee.

In the *scanning mode* U_a was varied continuously from high to low values. The main purpose of this mode was to check whether in the stepping mode U_a was always adjusted to the maximum intensity of the different mass lines. The mass range covered in the scanning mode is given in the following Table 1 for channel 1–4:

Table 1.

Channel	Mass range (amu)
1	1 ... 2
2	7 ... 16
3	14 ... 32
4	28 ... 64

During flight every 4 stepping spectra were followed by 1 scanned spectrum.

Table 2. Flight events

	4 Jan 76	21. Jan 76
Ejection of the protection cap	110.3 km (upleg)	114.1 km (upleg)
Apogee	117.6 km	116.5 km
Deblocking of temperature and helium flow regulation systems	106.5 km (downleg)	105.4 km (downleg)
End of reliable operation of the ion-source	85 km (downleg)	80 km (downleg)

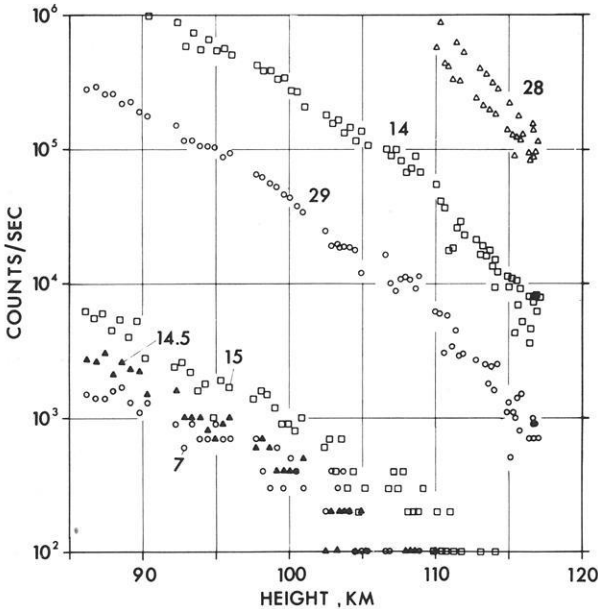


Fig. 3. Ion-counting rates stemming from nitrogen for the flight of January 4, 1976. The numbers labelling the profiles are the respective atomic mass numbers

The Rocket Flights

The essential flight events are summarized in Table 2. To avoid the condensation of large amounts of gas on the ion-source walls, in both flights the protection cap was ejected at heights above 110 km (see above). Therefore low altitude data were taken during the downleg parts of the trajectories. Reliable operation of the instruments on the downleg ceased at altitudes of 85 and 80 km, respectively.

Data Reduction

Typical altitude profiles of the measured ion counting rates are shown in Figure 3. These uncorrected raw data indicate the altitude resolution obtained. The picture also shows how a large dynamical range is obtained by use of

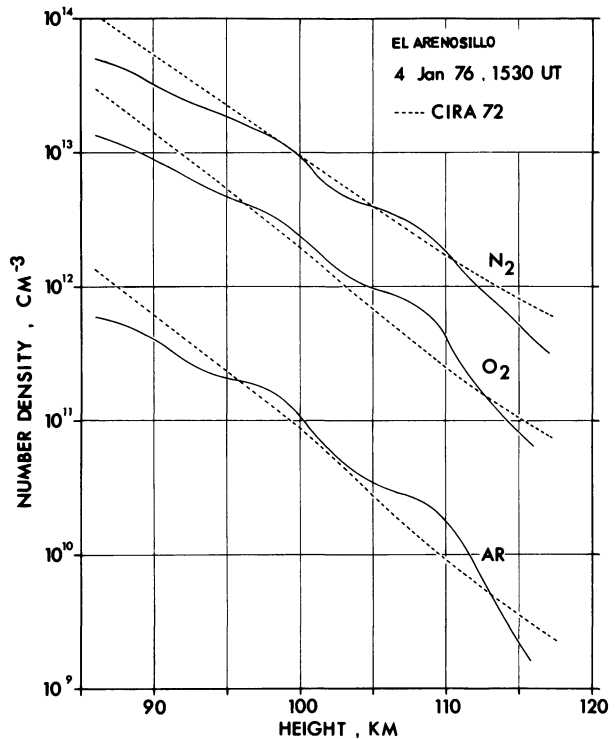


Fig. 4. Preliminary number density profiles of N_2 , O_2 , and Ar for the flight of January 4, 1976

multiply ionized and/or isotopic molecules. Presented are all measured counting rates versus altitude stemming from nitrogen (averaged over one program step). Molecular nitrogen can be determined by mass number 28 ($^{14}N^{14}N^+$) down to 110 km only. Below 110 km the detection is achieved by the mass numbers 29 and 44 ($^{14}N^{15}N$ singly and doubly ionized). The dissociation products of masses 28 and 29 at 14 amu and 15 amu ($^{14}N^+$ and $^{15}N^+$), respectively, and at 7 amu ($^{14}N^{++}$) may also be used.

The altitude profiles in part show large intensity variations. These are mostly due to rocket spin modulation. Below about 10^3 counts/s the statistical scatter becomes considerable.

The ambient atmospheric density N_a is calculated from the ion-counting rate C by the equation:

$$N_a(M) = E(M)^{-1} \cdot T_f^{-1} \cdot C(M)$$

where

M = atmospheric species.

$E(M)$ = spectrometer sensitivity for the constituent M as determined during the calibration procedure (Offermann et al., 1972).

T_f = function which takes account of the flight dynamics, i.e. attitude and velocity of the payload.

To obtain T_f an extensive numerical integration method has to be applied (Grossmann und Offermann, 1972; Friedrich, 1975).

Preliminary altitude profiles were obtained in this way for N_2 , O_2 , Ar, CO_2 , and O for the flight of January 4, 1976. Furthermore, signals were observed on mass numbers 18 and 30 corresponding to H_2O and NO, respectively. It is doubtful, however, whether these are due to atmospheric species because both mass lines appear to be contaminated by degassing from the payload. In addition, the isotopes ^{18}O and $^{30}N_2$ were measured on mass numbers 18 and 30, respectively. Therefore further studies will be necessary to clarify whether ambient H_2O and NO-number densities can be obtained.

Figure 4 shows preliminary number densities of N_2 , O_2 , and Ar versus altitude for the flight of January 4. The N_2 -profile was normalized at one point (95 km) to the total density obtained by the pitot tubes mentioned above.

The most striking feature of all curves shown in Figure 4 is a pronounced wave-like structure with a vertical wave-length of about 10 km. Deviations of up to a factor of 2 from the CIRA 72 model are found. Wavelike structures were also found by a number of other experiments during the campaign in atmospheric wind, temperature, and density data. Further studies are needed to determine the nature of these waves.

Acknowledgement. This experiment was supported by the Bundesministerium für Forschung und Technologie through BPT/DFVLR.

References

- Friedrich, V.: Ein Raketenexperiment zur Messung von Spurengasen in der unteren Thermosphäre, Diplomarbeit, Universität Bonn, 1975
- Grossmann, K.U., Offermann, D.: Eine Bestimmung der Neutralgas-Partialdichten in der unteren Thermosphäre durch ein Massenspektrometer mit heliumgekühlter Ionenquelle, FB W72-34, Bundesm. für Bildung und Wissenschaft, Bonn, 1972
- Offermann, D., Scholz, T.G., Gerhard, H.: Eichung eines Massenspektrometers mit modifizierter Kryo-Ionenquelle unter besonderer Berücksichtigung von Ozon, FB W72-32, Bundesm. für Bildung und Wissenschaft, Bonn, 1972
- Offermann, D., Tatarczyk, H.: A cryo-cooled mass spectrometer ion source for atmospheric composition measurements at supersonic rocket velocities, Rev. Sci. Instr., **44**, 1569-1572, 1973
- Trinks, H., Hellenbroich, T.: Ein doppelfokussierendes magnetisches Massenspektrometer mit heliumgekühlter Ionenquelle zur Messung der Neutralgasdichte und -zusammensetzung in der unteren Thermosphäre, FB W73-15, Bundesm. für Forschung und Technologie, Bonn, 1973

Received May 2, 1977

Pitot Pressure Measurements for Atmospheric Density Determination between 50 and 120 km (Western Europe Winter Anomaly Campaign, January 1976)

J. Bäte, M. Becker, U. Niederlöhner, and D.G. Papanikas

DFVLR, Institut für Angewandte Gasdynamik, D-5000 Köln 90, Federal Republic of Germany

Abstract. Within the Westeuropean Winter Anomaly Campaign (December 75/January 1976) this experiment was set up to furnish from pitot pressure measurements total neutral densities and temperatures. The data were taken by two pressure measuring instruments, a strain gage transducer for pressures higher than 10 N/m^2 and an ionization vacuummeter for pressures lower than 10 N/m^2 .

For data analysis a computer program was written which contains the following elements

- systematic pressure correction for viscous and thermomolecular effects in the probe
- determination of densities from pitot pressures for continuum flow and free molecular flow conditions
- transport properties (viscosities, mean free paths)
- determination of temperatures by integration of density gradients.

The results show that there is an agreement in order of magnitude between data and CIRA-model atmosphere. However, a detailed inspection of the temperature profile shows substantial deviations from CIRA. The data suggest a wave character which should be considered in the context of winter anomalous behavior of the atmosphere.

Key words: Winter anomaly — Pitot pressures — Densities — Temperatures — Pressure transducer — Ionization vacuummeter.

Objectives of Investigation

The Western Europe winter anomaly campaign 1975/1976 was an effort to gather in a well coordinated way many forms of information concerning this effect. Our activities were related to the investigation of the total neutral atmosphere, specifically the mesosphere and lower thermosphere. Our experiment (DP 1) was

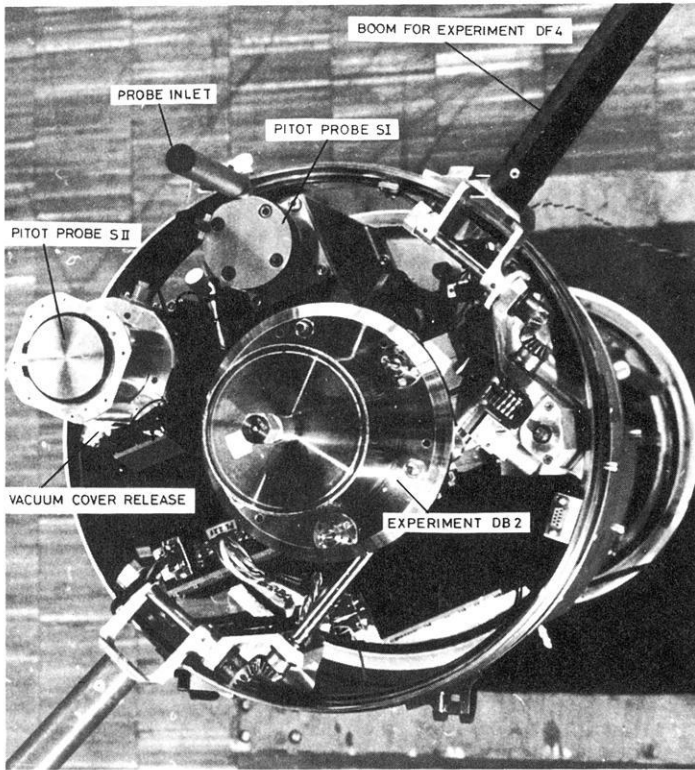


Fig. 1. Arrangement of experiments of payload B II on the front platform

applied to the measurement of pitot pressures, as outlined by Papanikas and Baete, for which our group had a broad spectrum of experiences from wind tunnel investigations under rarefied flow conditions.

In the design phase a few wind tunnel tests were performed to simulate the most critical conditions of heat transfer, shock interaction and angle of attack behavior in altitudes near 80 km for the forward facing experiments of payload B II on a Skylark-rocket. The investigation of a dummy probe gave important hints concerning geometries and optimization of flight requirements (see Papanikas and Becker). The front view of the actual version is shown in Figure 1.

The measurements in flight were taken between 50 and 120 km by two different types of instruments, a strain gage transducer (Probe S I) and an ionization gage (Probe S II). The informations determined from the data gathered by these instruments were geared to serve as standards for other classes of experiments of which the objectives were to find out the compositions and concentrations of atmosphere.

To deduce from pitot pressures the densities the procedure is a continuum flow and free molecular flow approach in lower and higher altitudes respectively and a linearization in the transition regime. Taking into account the probe geometries the

transition (outer probe diameter/mean free path=0(1)) occurs between 78 and 90 km. The flight velocities of the Skylark-rocket were known from radar tracking.

The relation between pitot pressure and density, then, is given for continuum flow condition by

$$\rho = f_1(M; \gamma) p_{2,0}/U^2. \quad (1)$$

The Mach number M is dependent on temperature and ratio of specific heats γ , which is weakly influenced (in these altitudes) by gas composition. So the factor $f_1(M; \gamma)$ changes for the Mach number range in question here (3.98 – 4.15) between 1.062 and 1.065. Then the inaccuracy of density determination is less than 0.1 %.

For free molecular flow the relation between pitot pressure and static pressure is from kinetic theory in the form of Becker:

$$\frac{p_{2,0}}{p} = \left(\sqrt{\frac{\gamma}{2\pi}} M + \frac{1}{2} \sqrt{\frac{T_w}{T}} \right) e^{-\frac{\gamma}{2} M^2} \cdot \left[\sqrt{\frac{\gamma}{2}} M^2 + \frac{1}{2} + \sqrt{\frac{\gamma \pi T_w}{8T}} M \right] \left(1 + \operatorname{erf} \sqrt{\frac{\gamma}{2}} M \right), \quad (2)$$

which gives basically

$$\rho = f_2(M; \gamma) p_{2,0}/U^2. \quad (3)$$

This factor f_2 changes from 0.65 to 0.75 for Mach number from 2.4 to 3.98 and results in an inaccuracy of density determination of ca. 1 %.

The inaccuracies quoted here deal with the procedure of calculating γ from the CIRA-gas composition which is a topic of investigation for other experiments in the campaign. From those results under anomalous conditions an improvement of our results will stem in the near future.

Experimental Set Up

Since the pitot pressures to be measured covered the range from $3.5 \cdot 10^3$ to $1 \cdot 10^{-3}$ N/m² two probes with different methods were used. For the higher pressures from $3.5 \cdot 10^3$ to $3 \cdot 10^0$ N/m² corresponding to altitudes from 50 to 90 km pitot probe SI was operated. The measuring system is a strain gage absolute pressure transducer. For the lower pressures from $3 \cdot 10$ to $1 \cdot 10^{-3}$ N/m² pitot probe SII was applied. The measuring system is an ionization vacuummeter with an ion source which was developed on the basis of a University Bonn design (U.v. Zahn).

Both probes were mounted together with instruments for experiments DB 2 (mass spectrometer, University Bonn) and DF 4 (Retarding Potential Analyzer, MPI Freiburg) on the front platform of payload B II with inlets of probes facing exactly forward. Figure 2 shows the schematic set up with pitot tubes on top, measuring system, and electronic equipment in the bottom portion.

The measuring system of probe SI is composed of an absolute pressure transducer, an installation for nulling the transducer, power supply and electronics

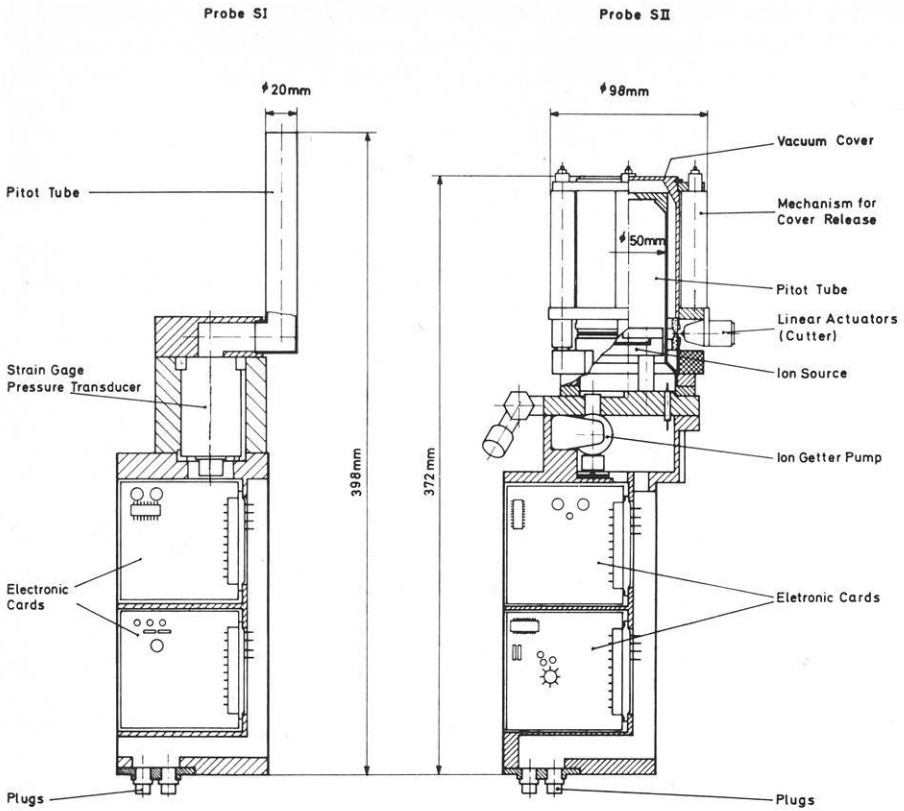


Fig. 2. Schematic view of pitot probes including gages and electronic equipment

for data acquisition. The cranked pitot tube leads to a rigid aluminium tank in which all other components are assembled.

The transducer (type Bell and Howell 4-353) consists of a full bridge with unbounded strain gages. This instrument is extremely rugged with respect to accelerations and shocks because it is designed for airborne application. Pressure measurements can be performed in a temperature range from -35°C to $+135^{\circ}\text{C}$.

The electronic unit of probe SI has as shown in Figure 3

- power supply and null balance for the strain gage transducer
- bridge signal amplifier (error $\leq \pm 0.3\%$ F.S.) with automatic calibration program
- thermo voltage amplifier including power supply
- resistance network for thermistors.

All units have insert cards with printed circuits and are separately mounted in the lower section of the tank. This arrangement provides a perfect shielding of cards under each other and guards against accelerations during start and vibrations in flight.

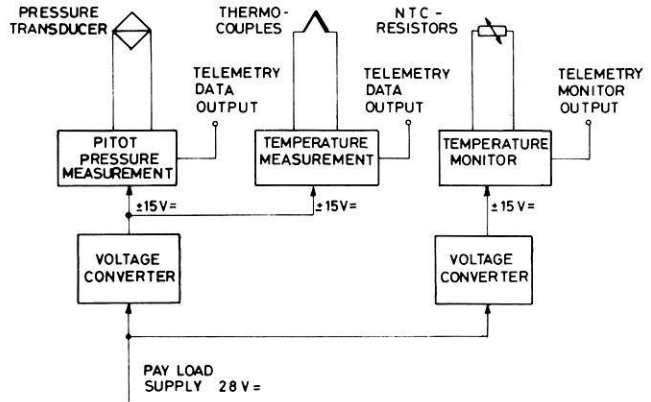


Fig. 3. Electronics block diagram of pressure transducer probe S I

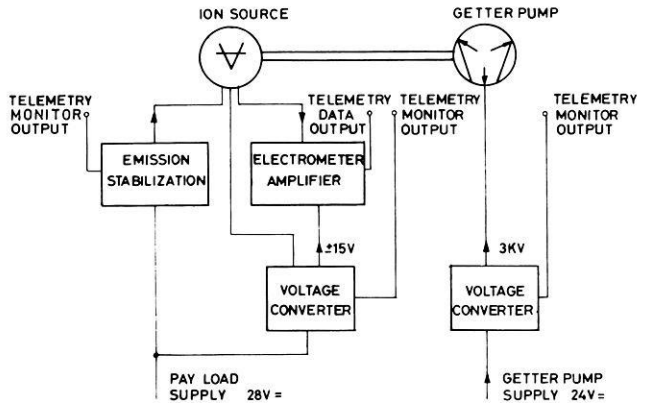


Fig. 4. Electronics block diagram of ionization vacuummeter probe S II

The measuring system of pitot probe S II has an ion source, power supply, and electronics for data acquisition (Fig. 4).

In the probe the incoming molecules are ionized by an ion source. In the calibration procedure the ion current was measured as a function of pressure for fixed cavity temperatures. The temperatures measured in flight were in the range used during calibration.

For operation of the ionization vacuummeter the following electronic units are used:

- emission stabilization of the ion source cathode
- linear electrometer amplifier (error $\leq \pm 0.3\%$ F.S. $\pm 1 \cdot 10^{-14}$ A)
- power supply for ion source and amplifier
- high voltage supply for ion getter pump.

Otherwise the mechanical layout of the electronic tank is similar to that of probe S I.

The ionization process is initiated by electrons emitted from a cathode. The electrons become accelerated and focused by magnets to ionize the gas molecules

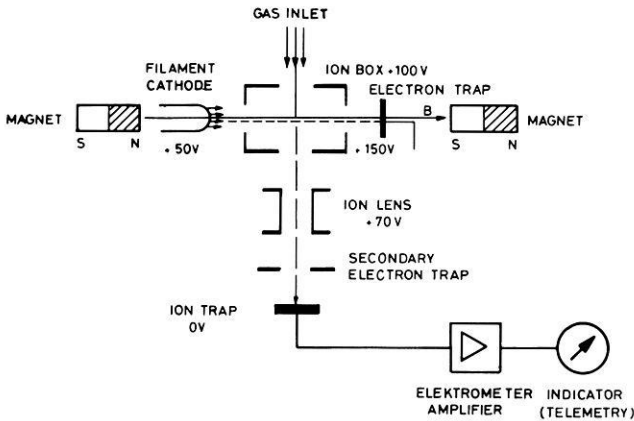


Fig. 5. Functional description of ionization vacuummeter

within the ion box. The generated ions travel through an ion lens and a trap for secondary electrons upon the ion trap (see Fig. 5). Here the ion current is measured by a linear electrometer amplifier. This unit is equipped with an automatic ranging between 10^{-12} A and 10^{-4} A F.S. An automatic nulling correction avoids temperature drifting. An inflight calibration program provides the monitoring of the probe functions.

The ion source is in the first part of upleg protected by a vacuum cover which is released at ca. 80 km altitude. The evacuation is ensured by an ion getter pump which operates until rocket lift off.

All measured data were transmitted by telemetry with a scanning rate of 100 s^{-1} , the house keeping informations were sampled with a rate of 6 s^{-1} .

Computations

On the basis of the procedure described in the introductory chapter a computer program was set up following the schematic flow field calculations performed for a hypersonic free jet by Papanikas. This program contains the following elements:

- systematic pressure correction due to viscous and thermomolecular effects in the probe under supersonic, rarefied flow conditions
- determination of densities from pitot pressures for continuum and free molecular flow conditions including calculating pitot pressure values for CIRA atmosphere and given flight velocities
- transport properties (momentarily used: viscosities and mean free paths derived from these)
- determination of temperatures by integration of density gradients over altitude increments of 1 km by

$$T_2 = \frac{\rho_1 R_1}{\rho_2 R_2} T_1 + \frac{1}{\rho_2 R_2} \int_2^1 \rho g dH. \quad (4)$$

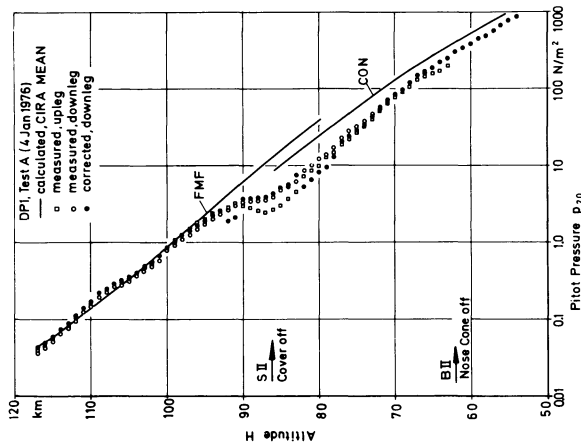
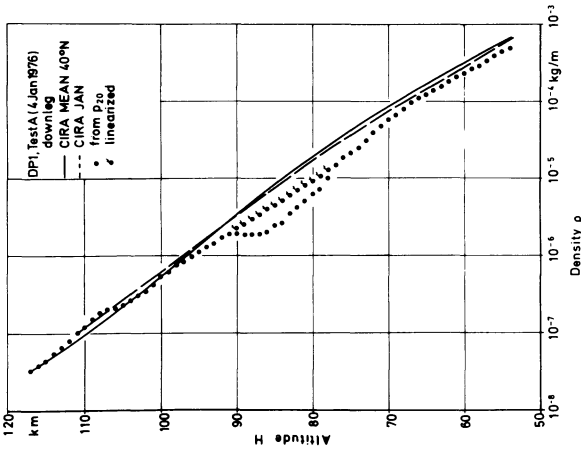
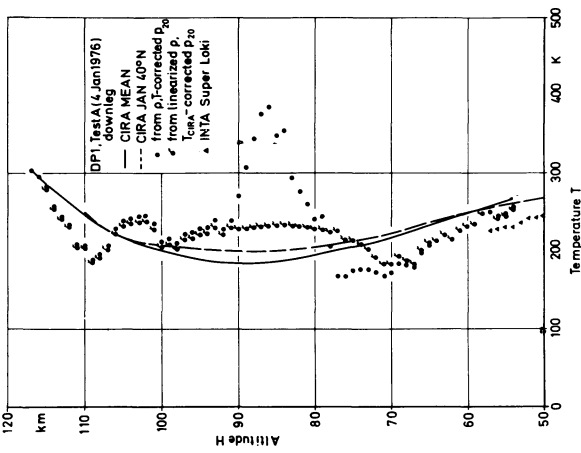


Fig. 6. Measured pitot pressures in up- and downleg; correction for downleg; comparison with CIRA-data

Fig. 7. Densities in downleg derived from pitot pressures in comparison with CIRA-data

Fig. 8. Temperatures in downleg determined from density gradients in comparison with CIRA-data

Results

Coordinated flights of all experiments in the campaign were performed on Jan. 4th and 21st 1976 in Arenosillo, Spain. In the Figures 6–8 some results of the first flight are shown representatively. Figure 6 gives the pitot pressures as raw data representation for up- and downleg. The good correlation between both sets of data justifies the measured flight path. The whole analysis, however, is applied to the downleg since here were clean measuring conditions, i.e. no cover releases, no interactions with other experiment activities.

The influence of pressure correction in Figure 6 is only apparent at higher altitudes.

Figures 7 and 8 show the computed densities and temperatures in comparison to CIRA-model atmosphere data. The temperature profile shows a marked wave structure which possibly stems from chemical events (anomalous behavior) and which is transported into the inner parts of the atmosphere. Damping of amplitude and wavelength is not clearly observable.

In conclusion it can be pointed out that the measurement and determination of total neutral gas data seems to be necessary under anomalous conditions as described. The information thus obtained is not just a steady state atmospheric model but also shows energy transport effects.

References

- Becker, M.: Die ebene Platte in hypersonischer Strömung geringer Dichte – experimentelle Untersuchungen im Stoßformierungs- und Übergangsgebiet. DLR-FB 70–79, 1970
- Papanikas, D.G.: Untersuchungen von axialsymmetrischen Hyperschallfreistrahlen in Windkanalmeßstrecken hoher Gesamtenthalpie. DLR-FB 74–52, 1974
- Papanikas, D.G., Bäte, J.: Pitot Pressure Measurements for Atmospheric Density Determination. In: Winteranomaly/Trace Constituents, Campaign Handbook, Part 2: Science, D. Offermann, ed.: pp. 57–60, 1975
- Papanikas, D.G., Becker, M.: Measurement Techniques in the Continuous DFVLR-Hypersonic, Low-Density, High-Enthalpy Facilities. In: ICIASF '75 Record, IEEE Publication 75 CHO 993-6 AES, 1975, pp. 254–263

Received May 2, 1977; Revised Version August 5, 1977

Intensity Measurement of the (1,0) γ -Band of NO at 2150 Å with a Polarizing Nitric Oxide Photometer

Dieter Beran and Egon Suckfüll

Deutsche Forschungs- und Versuchsanstalt für Luft- und Raumfahrt, Institut für Optoelektronik,
D-8031 Oberpfaffenhofen, Federal Republic of Germany

Abstract. As a possible reason of the winter anomaly an enhancement of nitric oxide can be considered. Therefore, a polarizing nitric oxide photometer was inserted into the Western Europe Winter Anomaly Campaign 1975/76. The experiment was a filter photometer with a sapphire plate at Brewster's angle as a polarizer. This polarizer was necessary because of the Rayleigh scattering background. The calibration procedure and the data evaluation is described shortly. Finally, the height profiles of the (1,0) γ -band intensity of NO is given for two winter anomalous days.

Key words: D-region – Winteranomaly – Nitric oxid – Polarizing photometer.

1. Introduction

Several processes are discussed as possible reasons for the winter anomaly. These processes must essentially either increase the electron production rate or decrease the electron loss rate. One of these possible processes may be a downward transport of NO from higher atmospheric layers by, for instance, eddy diffusion due to a local increase of temperature. This warming also effects the NO chemistry to increase the concentration of nitric oxide. Therefore, besides recording winds, temperature and ions, the accurate measurement of the minor neutral constituents like NO is of major importance.

Nitric oxide has been a subject of aeronomy since Nicolet 1955 proposed, that the D-region of the ionosphere is the result of photoionization of NO by solar Lyman- α radiation. However, the distribution of the neutral nitric oxide, as a function of height, is not well-known and up to date it has not been possible to establish a general model for the electron production in the D-region of the ionosphere.

Up to now information on the distribution of nitric oxide in the mesosphere and lower thermosphere has been obtained in three different ways: from photo-

chemical considerations, from changes in the D-region electron density profiles with variation of solar radiation, and from rocket measurements of the NO dayglow in the ultraviolet γ -bands. The nitric oxide γ -bands are electron transitions between the level $A^2\Sigma^+$ excited by sunlight and the ground level $X^2\Pi$. The strongest band of these γ -transitions is the (1,0)-band at 2150 Å.

The polarizing nitric oxide photometer, to be described here, is one of a group of rocket borne experiments, developed for the Western Europe Winter Anomaly Campaign 1975/76. This experiment has strong interrelation to other experiments like the cryogenic mass spectrometer, the $O_2(^1\Delta)$ photometer, and the solar Lyman- α photometer.

2. Instrumentation

The NO-photometer is a classical filter photometer which records the resonance re-emission of the ultraviolet (1,0) γ -band of NO around 2150 Å (Beran, 1974a). Especially at lower heights a high quantity of atmospheric Rayleigh background reaches the photometer. Because of the linear polarization of this Rayleigh radiation it is possible to eliminate it by computation. The degree of polarization of the Rayleigh radiation is a function of the angle between the direction of incoming solar radiation and the direction of observation and is a maximum of about 93% at an angle of 90°.

Figure 1 shows a schematic drawing of the nitric oxide photometer. The optical part of the experiment consists of a stray light baffle, a polarizer, an interference filter and imaging optics. The stray light baffle protects the detector from direct solar light. The polarizer is a sapphire plate used in reflection at Brewster's angle where the degree of polarization is theoretically 99.2% if the angle of view is $\pm 4^\circ$. Since the refractive index of sapphire at a wavelength of 2150 Å is 1.88 the Brewster angle becomes 62°. The reflection is about 16% at the front plane and 7% at the back surface of the sapphire plate. The interference filter has a half bandwidth of approx. 90 Å.

A second source of background in the measurement of NO γ -bands may be a radiation scattered at possible aerosol layers in the upper atmosphere. Like the resonance or fluorescence emission of the nitric oxide γ -bands this radiation is not polarized. To record this background the intensity, passing through the sapphire plate, was measured in a wavelength region around 2860 Å which is free of airglow emissions. With the additional polarizing filter it is possible to differentiate between Rayleigh scattering and aerosol scattering.

The detectors are two 18-stage EMR side window photomultipliers with a solar-blind photocathode. To get a good dynamic resolution at low intensities pulse counting technique is used. Figure 2 shows the block diagram of the experiment. Each pulse from the photomultiplier output is amplified by a fast low sensitive pulse amplifier. The gain as well as the discriminator threshold of this pulse amplifier are adjustable. A monostable multivibrator gives a constant width of 40 ns for the outgoing pulses.

For optimum performance much care is taken with the grounding concept of the experiment. The output signal and its ground from the pulse amplifier are

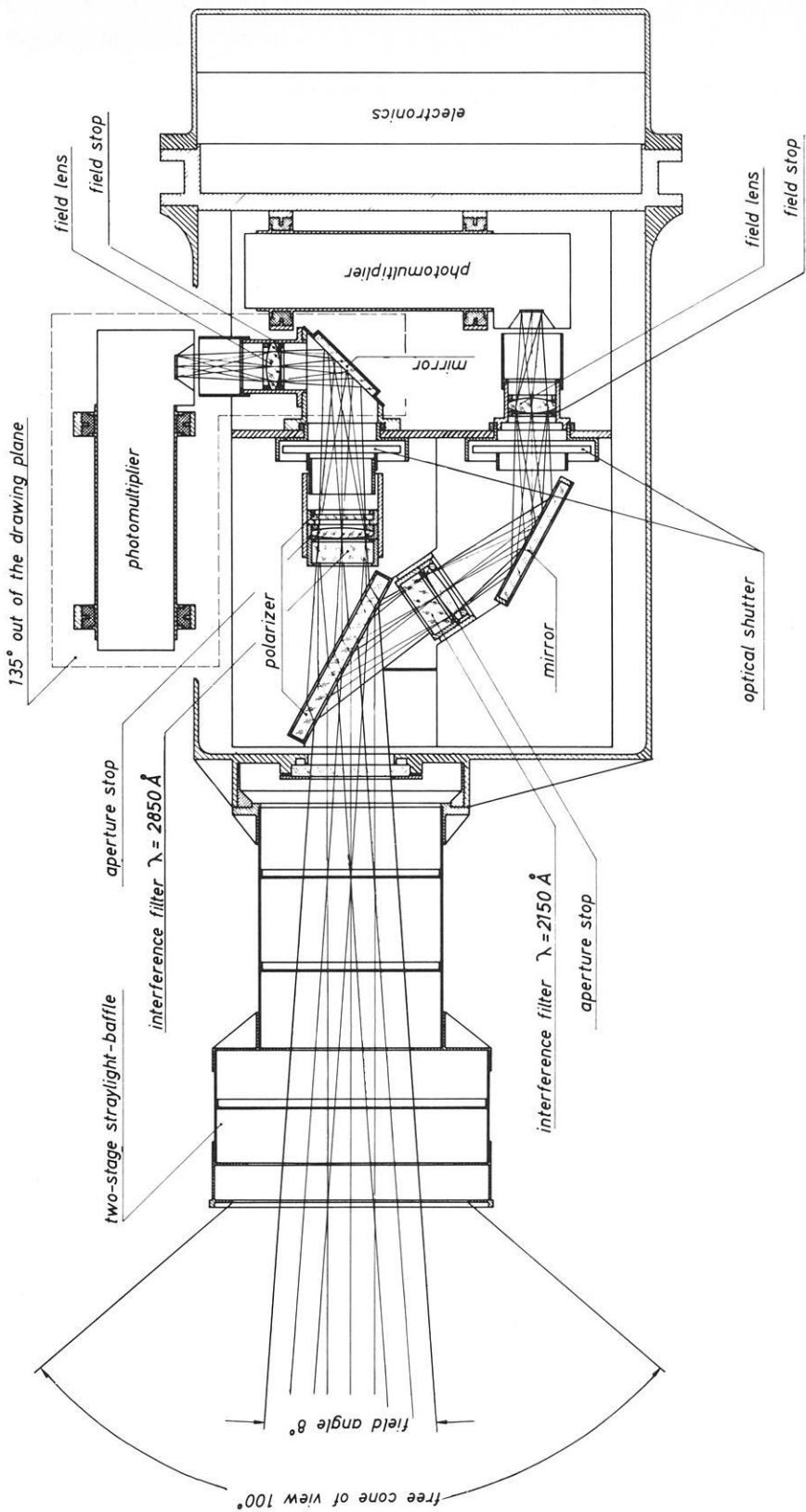


Fig. 1. Schematic drawing of the nitric oxide photometer

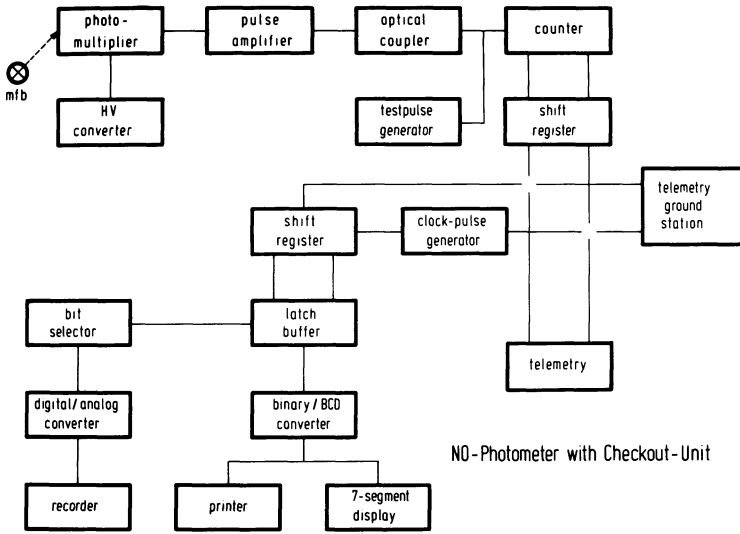


Fig. 2. Block diagram of the nitric oxide photometer

isolated from the following logic circuit by a high speed 20 M bit optical coupler; the high voltage common and the photomultiplier shield are connected to the amplifier ground case. The outgoing pulse from the optical coupler is fed to a 16 bit binary counter. A shift register takes over this 16 bit parallel information and the telemetry interrogates these data serially from the shift register 100 times per second.

The photomultiplier high voltage supply is a self-oscillating dc-dc converter with an adjustable output between 1500 to 3200 Volts depending on the desired amplification of the photomultiplier. A small test lamp can be switched on to illuminate the photomultiplier cathode to give a certain signal at the data output. Alternatively a testpulse generator can be switched on which gives a constant pulse rate to the data unit.

For check-out and data quick-look a test unit was constructed which clocks out the data from the telemetry ground station into a storage register. A binary to BCD converter yields a decimal information to a printer and an optical 7-segment LED display. In addition a digital to analog converter gives the signal to a recorder.

3. Calibration

Within the calibration procedure for the experiment (Beran, 1974b) at first the dependence of sensitivity from the angle of incidence was measured. The half width of this sensitivity curve is defined as the angle of view.

As a next step the dependence of the pulse rate from the number of incident photons was determined. At high photon intensities the number of the regis-

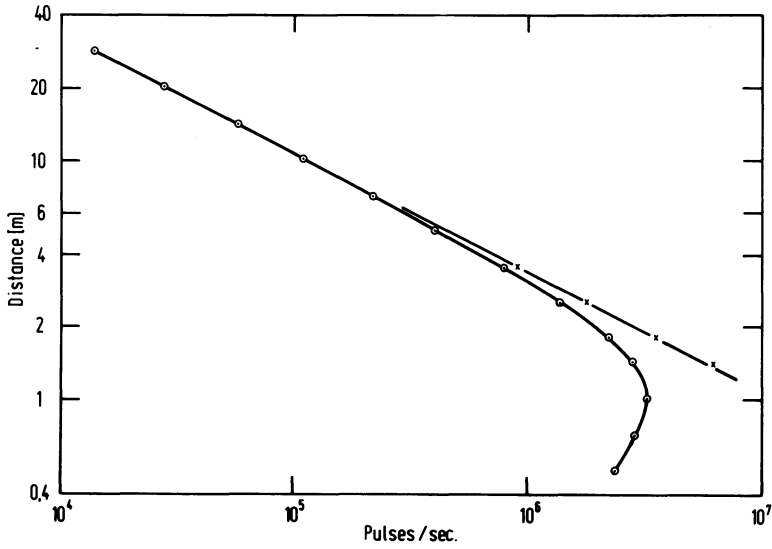


Fig. 3. Dependence of pulses per second from the illumination intensity given by the distance of the light source. \circ = registered number of pulses P_r ; \times = computed number of primary pulses P_0

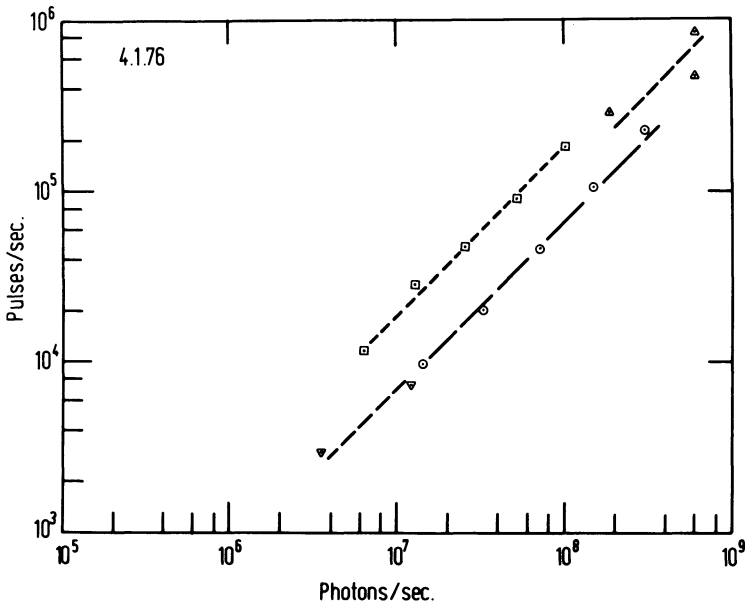


Fig. 4. Absolute calibration factor for the NO photometer of the first flight on January 4; the calibration is performed by: \square = tungsten ribbon lamp; \triangle = vacuum diode; ∇ = vacuum diode and BaSO₄-screen; \circ = Rayleigh scattering background

trated pulses P_g is not proportional to the number of incident photons, but is given by the following equation:

$$P_g = \frac{P_o}{(1 + P_o t_o)(1 + P_o/P_V)} \quad (1)$$

whereas P_o is the number of primary pulses from the photomultiplier, t_o is the width of these pulses, and P_V is the limiting frequency of the pulse amplifier. Figure 3 shows an example for this dependence from the incident intensity given by the varying distance between the light source and the experiment.

For data evaluation the knowledge of the instrumental degree of polarization q is very important. The calibration of this was performed with a quartz plate at Brewster's angle as a polarizer in front of the experiment. Then the photometer was revolved. For the experiment we launched in the first flight the degree of polarization was 98.3% and for the photometer of the second flight 99.3%.

At last the absolute calibration factor was measured with a calibrated tungsten ribbon lamp and independently with a calibrated vacuum diode. Figure 4 shows the results for the photometer launched in the first flight. In this figure we also inserted results given by the Rayleigh scattering during the flight.

4. Rayleigh Scattering Background

Because of the small scattering optical depth of the mesosphere in this wavelength region, only single scattering of direct sunlight needs to be considered. On the assumption of an ideal molecular atmosphere the amount of Rayleigh scattered light at a certain altitude can be predicted theoretically. The cross-section for Rayleigh scattering per molecule is a function of the wavelength λ .

$$\sigma(\lambda) = \frac{32\pi^3 (n-1)^2}{\lambda^4} \frac{2+\Delta}{\rho^2} \frac{2+\Delta}{6-7\Delta} \quad (2)$$

where n represents the refractive index and ρ the number density of the gas, whereas Δ is a depolarizing factor. This factor is a consequence of the asymmetry of the air molecules and has an average of 0.0303 for the earth's atmosphere (Gucker et al., 1969).

The degree of polarization for the plane-polarized Rayleigh scattered light is given by:

$$\rho(\theta) = \frac{(1-\Delta)\sin^2\theta}{1+\Delta+(1-\Delta)\cos^2\theta} \quad (3)$$

The degree of polarization is only a function of the scattering angle θ and remains constant with altitude.

5. Results

Two nitric oxide photometers were launched with Skylark rockets on the winter anomalous days of January 4 and 21. Since the cryogenic mass spectrometer

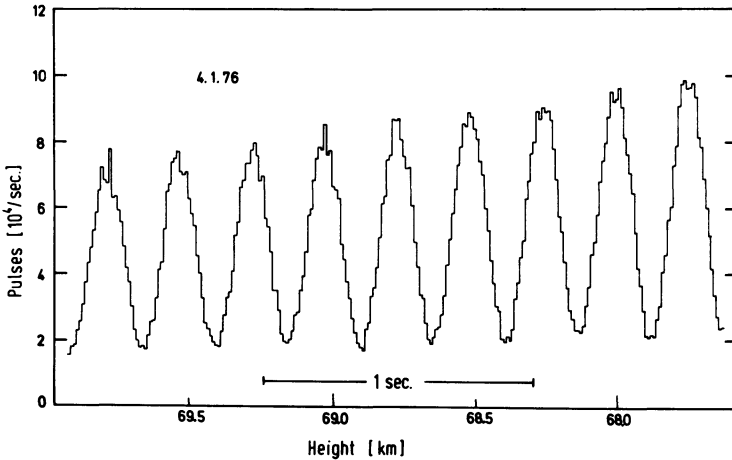


Fig. 5. Analogue data registration from the first flight

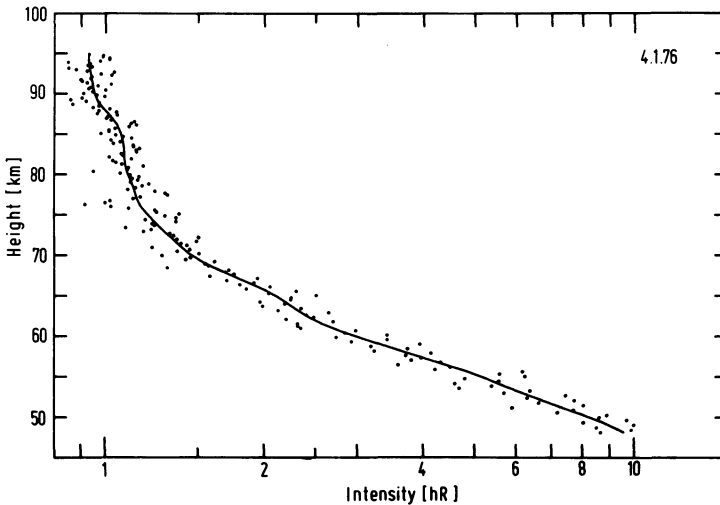


Fig. 6. Intensity of the (1,0) γ -band of nitric oxide from the first flight

which was on the same rocket occupied almost the whole space at the top of the payload and also required that the spin axis followed the tangent of trajectory, the NO photometer viewed rearward and measured only during the descent. In addition the scattering angle θ between the direction of solar incidence and the direction of observation was measured by a solar sensor integrated into the payload.

Good data were received for both flights. From the first flight on January 4 a short recorder registration of the sinusoidally varying data is shown in Figure 5.

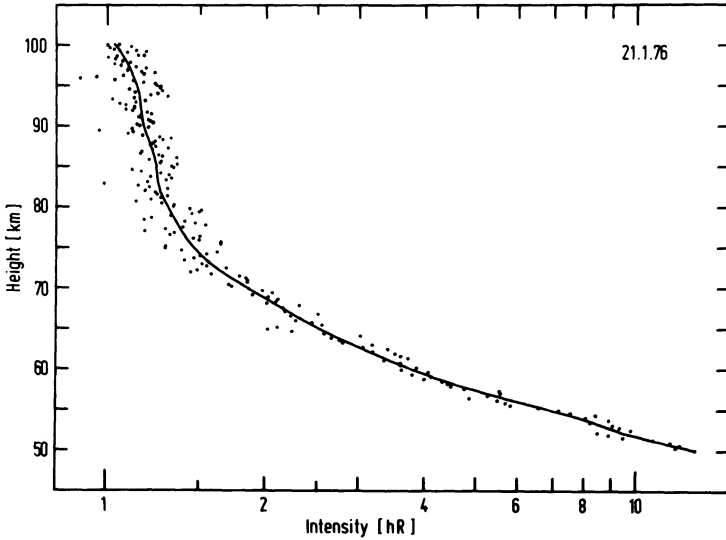


Fig. 7. Intensity of the (1,0) γ -band of nitric oxide from the second flight

With a smoothing sinus

$$y = (a + b \cos \omega \tau + c \sin \omega t) e^{dt} \quad (4)$$

drawn through 70 data points, the minimum I_i and the maximum I_a in the middle of each interval was determined at the "Rechenzentrum Graz" (Torkar and Friedrich, 1976). From these extrema the nitric oxide intensity I_{NO} was computed by the following equation (Beran, 1974a):

$$I_{NO} = \frac{(1 + pq) I_i - (1 - pq) I_a}{2 pq} \cos \phi \quad (5)$$

whereas ϕ is the zenith angle of the direction of observation. Figure 6 shows the nitric oxide intensity I_{NO} as a function of height. The smoothing curve through the intensity values is computed by spline functions. The same diagram for the second flight on January 21 is shown in Figure 7.

6. Conclusions

The polarizing nitric oxide photometer, developed novelly, is a reliable instrument for measuring the ultraviolet γ -bands of NO. The results between 50 and 95 km are reasonable, whereas the result above 95 km need some further correction due to the big zenith angle of the direction of observation. With a rocket only spin-stabilized and with the optical axis perpendicular to the direction of the sun the results would be much more reliable.

Acknowledgements. The development and the measuring flight of the nitric oxide photometer was possible by support of the German Ministry of Research and Technology. The mechanical design of the instrument was carried out by W. Mooshuber.

References

- Beran, D.: A Polarizing Photometer for Measuring the γ -Bands of Nitric Oxide in the Atmosphere between 50 and 140 km, DFVLR-Internal Report 557-74/2, 1974 a
- Beran, D.: Spezifikation zur Eichung des NO-Photometers, DFVLR-Internal Report 557-74/3, 1974 b
- Gucker, F. T., S. Basu, A. A. Pulido, G. Chin: Intensity and Polarization of Light Scattered by Some Permanent Gases and Vapors, J. Chem. Phys. **50**, 2526-2535, 1969
- Nicolet, M.: The Aeronomic Problem of Nitric Oxides, J. Atmospheric Terrest. Phys. **7**, 152, 1955
- Torkar, K., Friedrich, M.: A computer programme to evaluate Faraday rotation and absorption, INW 7602, Techn. Univ. Graz, 1976

Received Mai 2, 1977

Measurement of the $O_2(^1\Delta_g)$ Height Profile during a Winter Anomaly Event

W. Bangert¹ and V. Amann²

¹ Meteorologisches Institut der Universität München, Abteilung für Atmosphärische Strahlung und Satellitenmeteorologie, Barbarastr. 16, D-8000 München 40, Federal Republic of Germany

² Deutsche Forschungs- und Versuchsanstalt für Luft- und Raumfahrt, Institut für Nachrichtentechnik, D-8031 Oberpfaffenhofen, Federal Republic of Germany

Abstract. The emission height profile of the Infrared Atmospheric Band of oxygen at $1.27\ \mu\text{m}$ has been measured at Arenosillo, Spain on January 4, 1976 during a winter anomaly event. The instrument as well as the method of data evaluation are described. Preliminary results for the derived $O_2(^1\Delta_g)$ and O_3 profiles between 40 and 100 km are presented. They show largely enhanced concentrations below 52 km which are assumed to be related to the observed stratospheric warming. Distinct structures at 72, 93, and 100 km are attributed to respective structures in the temperature profile.

Key words: Airglow – Infrared atmospheric bands – $O_2(^1\Delta_g)$ profile – Ozone profile – Winter anomaly.

1. Introduction

Oxygen in the first electronically excited state $^1\Delta_g$ is one of the most abundant minor constituents throughout the mesosphere and lower thermosphere. With an excitation energy of 0.98 eV it is capable of participating in many processes which are important for the photochemistry of the neutral and ionized atmosphere. The measurement of the $O_2(^1\Delta_g)$ concentration height profile may therefore yield a lot of information about the composition of the atmosphere especially when combined with measurements of other constituents like atomic and molecular oxygen and of the temperature profile.

The radiative transition from the $^1\Delta_g$ to the ground state $^3\Sigma_g^-$ gives rise to the emission of the Infrared Atmospheric Band System of oxygen. The strongest band of this system under atmospheric conditions is the vibrational (0,0) transition at $1.27\ \mu\text{m}$. This emission represents the most prominent feature of the day airglow. Despite this fact it is not easily observed from the ground because of very strong self-absorption in the lower atmosphere. The first observations of the Infrared Atmospheric Band System were therefore those of the (0,1) transition at $1.58\ \mu\text{m}$ reported by Vallance Jones and Harrison (1958).

Subsequent measurements of the 1.27 μm band from balloons and rockets revealed the principal behavior of this emission. During the day there is a strong layer centred near 50 km sloping off nearly exponentially with altitude. Most observations show a secondary peak between 80 and 90 km. The total overhead intensity is typically 25 to 30 MR. After sunset the main and the secondary layers decay except for a remaining intensity of roughly 100 kR centred in one or even two layers around 90 km.

The photochemical reaction scheme capable of explaining the twilight and dayglow observations was first proposed by Gattinger and Vallance Jones (1966). $O_2(^1\Delta_g)$ is produced predominantly by photolysis of ozone by solar radiation in the Hartley continuum:



the dissociation coefficient being $J_3 = 9.6 \cdot 10^{-3} \text{ s}^{-1}$ (Ackerman, 1971). Deactivation occurs via spontaneous emission:



with an Einstein transition probability coefficient $A = 2.58 \cdot 10^{-4} \text{ s}^{-1}$ (Badger et al., 1965) and collisional quenching by air molecules:



with a coefficient $k_1 = 4.4 \cdot 10^{-19} \text{ cm}^3 \text{ s}^{-1}$ (Clark and Wayne, 1969). The time constant for this mechanism $\tau = (A + k_1 M)^{-1}$ is smaller than 1 h especially at heights below 75 km where quenching becomes dominant. Thus, photochemical equilibrium can be assumed which means that time dependent as well as flux terms in the continuity equation can be neglected. The processes (1), (2), and (3) therefore lead to the simple equation:

$$(A + k_1[M]) [O_2(^1\Delta_g)] = J_3[O_3]. \quad (4)$$

Using Eq. (4) the O_3 concentration profile can easily be calculated from a measured profile of the $O_2(^1\Delta_g)$ concentration taking the atmospheric density profile from a model atmosphere or from a simultaneous measurement. This scheme has been shown by Evans et al. (1968) to give quite reasonable agreement with O_3 profiles measured by different methods for heights below the mesopause. For higher altitudes there are discrepancies which lead to the conclusion that further production processes besides ozone photolysis must be operating. These might be at least partly the same as those producing the nightglow emission of appr. 100 kR but have not been identified as yet. Therefore O_3 profiles inferred from $O_2(^1\Delta_g)$ measurements should be considered with caution above 85 km.

An example of the interaction of $O_2(^1\Delta_g)$ with the ionized atmosphere is its ionization by solar radiation in the wavelength region between 1027 and 1118 \AA the ionization thresholds of $O_2(^3\Sigma_g^-)$ and $O_2(^1\Delta_g)$ respectively. Combining the ionization coefficients as given by Paulsen et al. (1972) with the actual values of the optical thickness and the $O_2(^1\Delta_g)$ concentration the O_2^+ production rate due to $O_2(^1\Delta_g)$ ionization can be derived. Besides the *NO* photoionization

by Ly- α radiation this is believed to be the most important source of ions in the 70 to 90 km region.

Since the $O_2(^1\Delta_g)$ profile is strongly correlated to the O_3 profile it reflects not only the processes involving $O_2(^1\Delta_g)$ as one of the reactants but also those affecting the ozone concentration. The reaction



is the only known source of O_3 . Hence changes of the O concentration will directly influence the O_3 production rate. The reaction rate coefficient for (5) is according to Davis (1974) $k_2 = 1.1 \cdot 10^{-34} \exp(510/T) \text{ cm}^6 \text{ s}^{-1}$. This means that a temperature change of -50 K which is not unrealistic at mesopause levels will enhance the O_3 production rate by a factor of 2.3 whereas the main destruction process for O_3 i.e. the photolysis remains unaffected. Anomalous structures in the temperature profile will therefore clearly show up in the O_3 and due to reaction (1) also in the $O_2(^1\Delta_g)$ profiles. Since the calculation of O_3 concentrations from Eq. (4) does not include the coefficient k_2 only poor knowledge of the temperature profile will nevertheless yield a relatively accurate O_3 profile. Therefore $O_2(^1\Delta_g)$ is a good indicator of both compositional and structural changes in the upper atmosphere especially for anomalous conditions such as winter anomaly events. While O_3 concentrations are not easily measured by other methods measurements of the emission height profile of the (0,0) band of $O_2(^1\Delta_g)$ is a simple and elegant way for determining the ozone content between 40 and at least 85 km. From this height on the O_3 values start to become less certain due to a lack of knowledge of the photochemistry involved but not due to the quality of the measured data.

2. Experiment

The experiment *DM2* for measuring the $O_2(^1\Delta_g)$ height profile was integrated in the payloads *B II* of the German Winter Anomaly and Trace Constituents Campaign.

The instrumentation comprised a simple filter radiometer and an electronic control and amplification unit. The principles of the radiometer are shown schematically in Figure 1. The bigger part of the instrument is a baffle system mounted in front of the actual radiometer housing. The radiation has to be thought to enter from the right. The optical layout is such that the entrance aperture at C which has a area of 3.14 cm^2 is imaged by the system of the three lenses L_1, L_2, L_3 on the detector *D* the field of view being 0.314 sr or 5.7° half cone angle. The detector is a *PbS* element mounted upon a five-stage thermoelectric cooler which controls the temperature of the flake electronically to approximately -30° C within a few hundredths of a degree, thus ensuring constant sensitivity and improved signal-to-noise ratio. A rotating chopper C just behind the entrance aperture generates a 107 Hz ac-voltage at the detector output. This signal is first ac amplified before it is rectified in a phase sensitive stage and then fed to three *dc*-amplifiers in parallel having amplification factors of 1, 10, and 100 respectively, thus giving a dynamical range of 2000 above

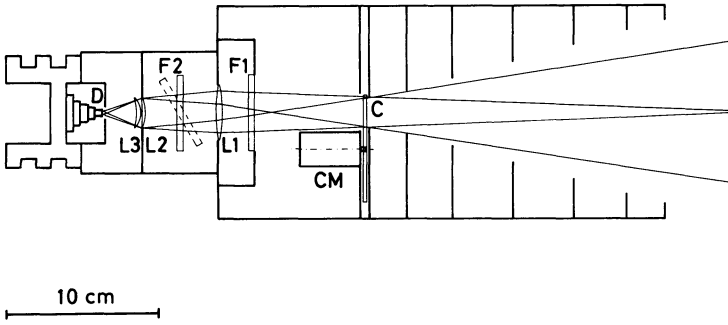


Fig. 1. Schematic drawing of the radiometer DM 2

noise levels. The noise equivalent radiance is $\pm 1.2 \cdot 10^{-9} \text{ W cm}^{-2} \text{ sr}^{-1}$ or $\pm 100 \text{ kR}$ as taken peak to peak. However, by smoothing the data noise can be reduced considerably.

The electronics includes further the control units for the chopper motor *CM* and the filter mechanism which tilts the filter F_2 once every second by means of two rotating magnets operating in turn in opposite directions. F_2 is an interference filter of 110 Å half bandwidth. In the two positions normal and tilted to the optical axis the centre wavelengths are $1.266 \mu\text{m}$ and $1.244 \mu\text{m}$ respectively. The transmission efficiency for the $O_2(^1\Delta_g)$ band is 0.75 and 0.01 respectively. Thus, discrimination of band emission against background radiation is possible. F_1 is an additional blocking filter for suppressing short wavelength radiation produced by Rayleigh scattering of sunlight.

In order to derive $O_2(^1\Delta_g)$ number densities it is necessary to measure the emission in absolute units. Therefore the instruments were calibrated in the laboratory. Neither recalibration prior to launch nor inflight checks of the sensitivity of the radiometer were considered to be necessary since changes of the calibration with time had shown to be beyond detectable limits. The calibration was done in two steps. First the relative response of the radiometer as a whole was measured in the two filter passbands using a monochromator as a source and a thermopile for comparison. Assuming the spectral response of the thermopile to be independent of wavelength between 1.1 and $1.4 \mu\text{m}$ it is possible to calculate the spectral response of the radiometer. The second step was the absolute calibration against a blackbody. The emissivity from the viewpoint of geometry of the source and the emissivity of wall painting used should be better than 0.99. The temperature of the cavity was controlled by an electronic unit by means of three separate electric heating circuits within $\pm 0.1 \text{ K}$ at a preset value which in turn was monitored by a calibrated Pt thermometer. Hence the overall blackbody calibration should be accurate to a few percent.

The radiometer was installed in the rocket looking from the aft end parallel to the payload axis. After motor separation an attitude control system was to turn the payload over and to control its attitude in a way that the axis was closely aligned to the tangent of the trajectory on the downleg portion of

the flight. Soon after apogee an optical shutter inside the radiometer was opened by a timer signal and the instrument started measuring down to approximately 40 km where the payload began to tumble in an uncontrolled manner. Since the rockets were fired to the southwest late in the afternoon the sun was off the optical axis of the radiometer more than 90° for the whole time of the measurement.

There were actually two flights of the instrumentation from Arenosillo, Spain on January 4, 1976 15:30 UT and on January 21, 1976 15:30 UT. Both flights took place during winter anomalous conditions. Due to a failure of an electronic part shortly after take-off on the second launch evaluable data could only be gathered during the first flight.

3. Results

As an example of the data obtained during the flight on January 4, 1976 Figure 2 shows the signal vs. height as measured in the filter channel at $1.266 \mu\text{m}$. The profiles of both signal channels were submitted to a smoothing procedure using cubic spline functions. The $O_2(^1\Delta_g)$ band emission and the background radiation

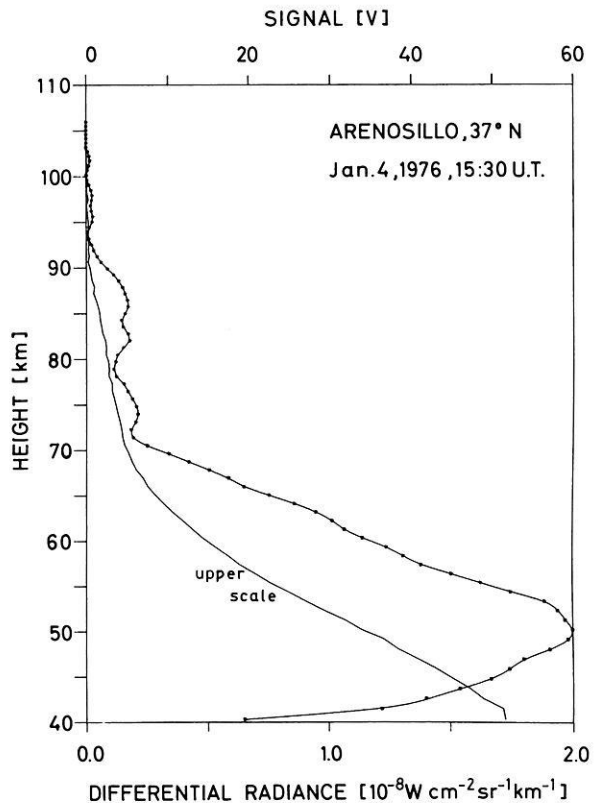


Fig. 2. Unsmoothed signal as measured in the $1.266 \mu\text{m}$ channel versus height (upper scale) and $O_2(^1\Delta_g)$ differential radiance profile (lower scale)

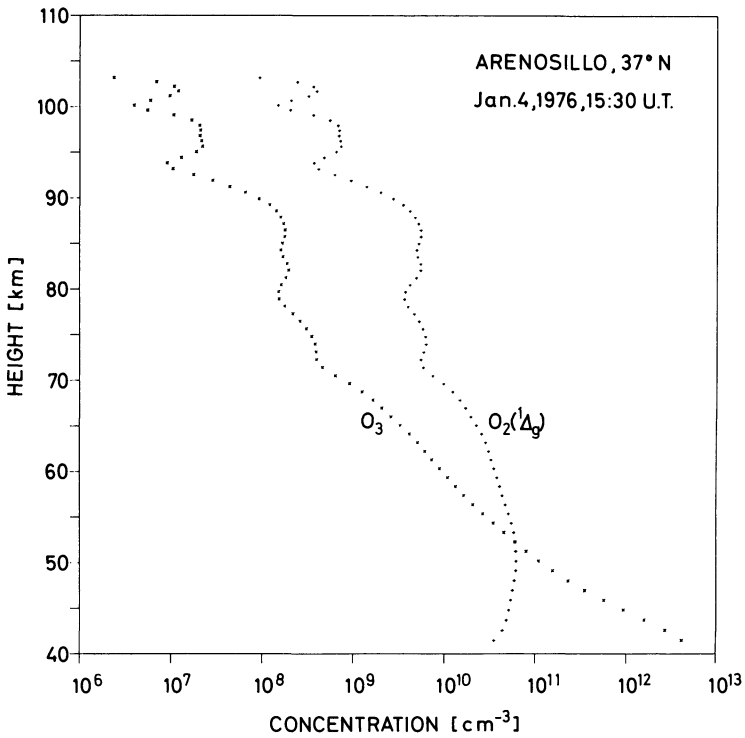


Fig. 3. Concentration height profiles of $O_2(^1\Delta_g)$ and O_3

were separated by solving the set of two equations for each set of data points. For this purpose the actual transmission of the filters for the lines of the band have to be calculated at each of the height levels using the temperature of the emitting layers weighted by the number densities of $O_2(^1\Delta_g)$ in it. This was achieved in a couple of iterations starting from some model profile for $O_2(^1\Delta_g)$ and then using the calculated $O_2(^1\Delta_g)$ values for the next run. The temperature data used here were in part those deduced from the scale heights of the N_2 density profile measured by experiment *DH 2* flown in payload B IV 1 h in advance of *B II*. For altitudes below 57 km the data were taken from the measurement of a Spanish INTA rocket launched 10 min after *B II*. The obtained values of the integrated radiance of the band were then corrected to zenith and differentiated with respect to height to give the differential radiance or volume emission rate profile shown also in Figure 2. The concentration or number density profile was obtained by dividing the volume emission rates given in photon units by the Einstein transition factor. The ozone profile was then calculated according to Eq. (4) using the data of experiment *DH 2* above 80 km and CIRA 1972 data below for the atmospheric density. The two profiles of $O_2(^1\Delta_g)$ and O_3 are given in Figure 3.

There are some remarkable differences in comparison to results of other experiments. The total overhead intensity of the $O_2(^1\Delta_g)$ band of 34 *MR* as

well as the volume emission rate of 1.6 MR/km at 50 km are considerable higher than the values reported by Evans et al. (1968) and Evans and Llewellyn (1970). Besides, there are distinct secondary minima at 72, 93, and 100 km. As pointed out earlier both the $O_2(^1\Delta_g)$ and the O_3 densities should reflect structures in the temperature profile. There were in fact extraordinary deviations from the CIRA 1972 temperature profile for January 40° N. At the time of the flight there was a stratospheric warming over southwest Europe. In the mesosphere, however, the combined data of INTA and experiment *DH2* seem to indicate a wavelike structure in the temperature profile showing minima near 60, 85, and 98 km and maxima near 72 and 92 km the deviations being 30 to 50 K either way. The correlation between the temperature profile on one side and the $O_2(^1\Delta_g)$ and O_3 profiles on the other is striking. But also the magnitude of the deviations seems to be reasonable. For example, the decrease of nearly 50 K around 85 km can well explain the observed enhancement by a factor of 2 in the O_3 content as compared to the observation of Miller and Ryder (1973). However, according to theoretical studies by Fukuyama (1974) and Koshelev (1976) differences of this order could also be attributed to the different latitude and season at which the measurements were conducted.

Below 52 km the scale height of the O_3 profile changes drastically from the normal 4.4 km to 2.0 km indicating a marked increase of the O_3 content in the stratosphere. This increase seems to be related to the observed stratospheric warming which might at least partially be produced by enhanced absorption of solar radiation in the Hartley band of ozone. It should be pointed out that the temperature data used here are not to be considered as final at present. Hence, the presented results are also preliminary although only minor changes are to be expected for the $O_2(^1\Delta_g)$ and O_3 profiles.

Acknowledgment: This research was sponsored by the Bundesministerium für Forschung und Technologie under contract RV 14-B 103/73-B II/DM2. The radiometer was built at the Meteorologisches Institut der Universität München. The electronics was developed by the Institut für Nachrichtentechnik der Deutschen Forschungs- und Versuchsanstalt für Luft- und Raumfahrt, Oberpfaffenhofen. The authors are grateful to Prof. H.-J. Bolle for his support of the project.

References

- Ackerman, M.: Ultraviolet solar radiation related to mesospheric processes. In: Mesospheric models and related experiments, G. Fiocco, ed., pp. 149–159. Dordrecht-Holland: Reidel 1971
- Badger, R.M., Wright, A.C., Whitlock, R.F.: Absolute intensities of the discrete and continuous absorption bands of oxygen gas at 1.26 μ and 1.065 μ and the radiative lifetime of the $^1\Delta_g$ state of oxygen. *J. Chem. Phys.* **43**, 4345–4350, 1965
- CIRA 1972: COSPAR International Reference Atmosphere 1972, Berlin: Akademie-Verlag 1972
- Clark, I.D., Wayne, R.P.: Collisional quenching of $O_2(^1\Delta_g)$. *Proc. Roy. Soc. London A* **314**, 111–127, 1969
- Davis, D.D.: A kinetics review of atmospheric reactions involving H_xO_y compounds. *Can. J. Chem.* **52**, 1405–1414, 1974
- Evans, W.J., Hunten, D.M., Llewellyn, E.J., Vallance Jones, A.: Altitude profile of the Infrared Atmospheric System of oxygen in the dayglow. *J. Geophys. Res.* **73**, 2885–2896, 1968
- Evans, W.J., Llewellyn, E.J.: Molecular oxygen emissions in the airglow. *Ann. Géophys.* **26**, 167–178, 1970

- Fukuyama, K.: Latitudinal distribution of minor neutral hydrogen-oxygen constituents in the winter mesosphere and lower thermosphere. *J. Atmospheric Terrest. Phys.* **36**, 1297-1320, 1974
- Gattinger, R.L., Vallance Jones, A.: The ${}^1\Delta_g - {}^3\Sigma_g^- O_2$ bands in the twilight and day airglow. *Planetary Space Sci.* **14**, 1-10, 1966
- Koshelev, V.V.: Diurnal and seasonal variations of oxygen, hydrogen, and nitrogen components at heights of mesosphere and lower thermosphere. *J. Atmospheric Terrest. Phys.* **38**, 991-998, 1976
- Miller, D.E., Ryder, P.: Measurement of ozone concentration from 55 to 95 km at sunset. *Planetary Space Sci.* **21**, 963-970, 1973
- Paulsen, D.E., Huffman, R.E., Larrabee, J.C.: Improved photoionization rates of $O_2({}^1\Delta_g)$ in the *D* region. *Radio Sci.* **7**, 51-55, 1972
- Vallance Jones, A., Harrison, A.W.: ${}^1\Delta_g - {}^3\Sigma_g^- - O_2$ infrared emission band in the twilight airglow spectrum. *J. Atmospheric Terrest. Phys.* **13**, 45-60, 1958

Received May 2, 1977

A Two Channel Rocket Photometer for 5577 Å OI Nightglow Measurements

Armin Drescher

DFVLR-Institut für Optoelektronik, D-8031 Oberpfaffenhofen, Federal Republic of Germany

Abstract. A Description of a Two Channel Multiplex-Type Photometer for Small Rockets is given.¹

Key words: Winteranomaly – OI 5577 Å Nightglow – Two channel rocket photometer.

1. Introduction

Rocket measurements of the atomic oxygen green line emission during nighttime showed a considerable variability of the emission layer in intensity, half width and height above sea level. Summaries were made by Greer and Best, 1967; Offermann and Drescher, 1973; Shefov and Kropotkina, 1975. Purpose of the rocket experiment was to detect variations in the nighttime emission layer, to correlate them with ground based observations of the spacial and temporal variations of the total green light intensity and to examine correlations to other parameters as the daytime winter anomaly events.

Further it was intended to calculate nighttime oxygen height profiles from the measured volume emission rate by the Chapman and/or the Barth excitation mechanism and to compare these calculated profiles with the daytime mass-spectrometric measurements of atomic oxygen.

The last comparison mentioned above can only be done with all the uncertainties in the knowledge of the excitation processes of the 5577 Å nightglow as discussed most recently by Slinger and Black, 1977.

The OI photometer had to be flown on a Skua IV rocket, as used by the Max Planck Institut für Aeronomie. The photometer had to be small, cheap, and rather rugged. The basic idea was to use two optical channels,

¹ Tests and calibration are described, and preliminary data of 5 flights are communicated

one direct and one chopped, and to give both signals simultaneously on the same photomultiplier, thus needing only one unit for reception and processing of the signal.

The use of two optical channels was thought to be essential to determine background and its variations as caused by continuum emission and rocket coning. Both optical channels are upward-looking, parallel to the rocket axis with the same field of view.

2. Instrument Description

Both optical channels consist of field of view defining baffling entrance apertures A, one inch diameter interference filters I and focusing lenses as shown in Figure 1. In front of the filters are field of view widening lenses to reduce the importance of single stars in the background radiation. The etendue of each channel is 0.04 cm^2 steradian. The upper ray path is reflected by two mirrors, 1 and 2, nearly on the same region of the multiplier-photocathode as illuminated by the lower channel.

The upper channel is chopped by a hollow, sideward semiopen cylinder C. This cylinder is driven by a micromotor with gear M at a chopping frequency of 1.5 cps.

The photomultiplier *P* and the micromotor *M* are mounted each within cylinders of aluminum. The HV power supply and the single photon counter-discriminator are mounted alongside the two aluminum cylinders and not shown in Figure 1. All the other electrical system is contained within the cylindrical box E. The optical part of the photometer with the deflecting mirrors, and the electrical part with the chopping cylinder are each mounted separately and directly into the nosecone. This was done in a vacuum tight way to avoid high voltage break down during flight.

Mounted in front of the photometer is a split nose cone which was separated by a pyroelectric cablecutter in 70–75 km height. The optics had to be protected against oil and dust from the cablecutter.

The photomultiplier was an EMR 541 with high temperature alkali photocathode, operated at $5 \cdot 10^6$ gain. High voltage power supply and pulse amplifier discriminator were from Spacom Electronics. All other electronic system was developed at the DFVLR Institut für Nachrichtentechnik. The TTL compatible output signal of the pulse amplifier is fed into a 16 bit binary counter with reset and parallel data transfer into a shift register every 32 ms. After impedance conversion and frequency filtering the signal is transmitted as 16 bit binary words in PCM format 32 times per second on FM-FM telemetry.

One data frame consists of 128 words, the last word being a synchronization signal. Bit synchronization is realized by use of a modified RZ-Code.

The following housekeeping values were telemetered as time multiplexed analog signal to the ground station: The pressure measured within the pressurized part of the photometer in the range from 20 to 800 Torr, the temperature in the vicinity of the photocathode, the temperature of one of the interference filters, each with a dynamic range from 10–70° C. The position of the chopper

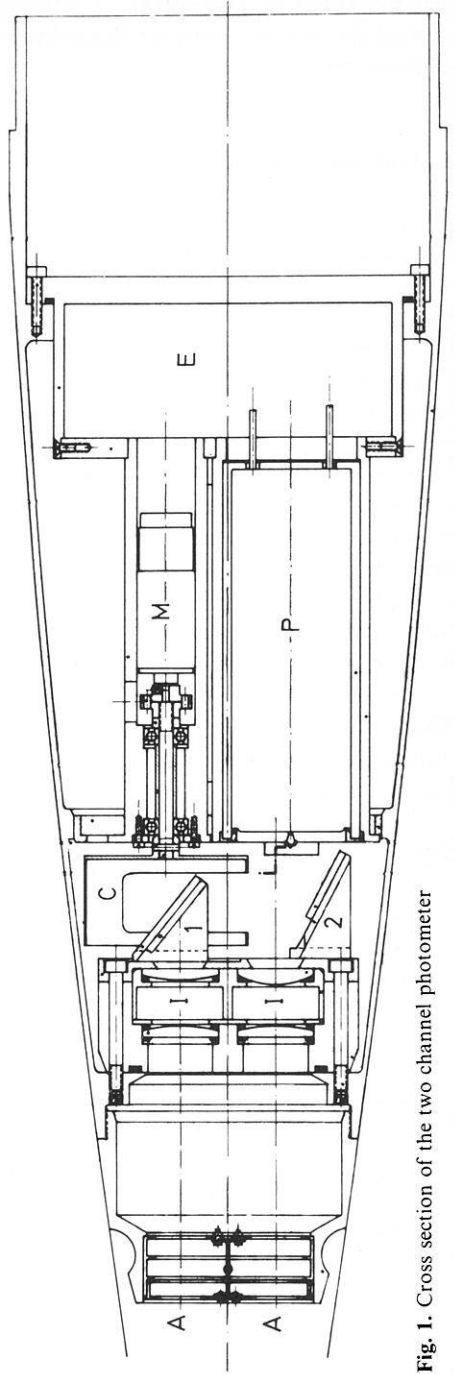


Fig. 1. Cross section of the two channel photometer

was measured by an optical IR reflex sensor and two small mirrors of different size on the cylinder bottom. This signal was telemetered in realtime on a FM-FM channel of its own.

3. Test and Calibration

All testing of components and the whole instrument was done at DFVLR. Instrument tests have been made for vibration, temperature and vacuum. The chopper mechanism had been qualified separately before. Interference filters had been tested for absolute transmission curve and their relative dependency on temperature and angle of incidence. Photomultipliers have been tested for quantum-efficiency, gain, dark current and noise in signal. In comparison with such measurements made for earlier missions at DFVLR no severe discrepancies between producers data and our measurements were found this time.

Optimal performance of the multipliers in pulse counting mode had been found at about 60–70% pulse counting efficiency as compared to the dc-signal. Higher values of the pulse counting efficiency generated excessive noise in signal and strongly enhanced dark counting rates.

Calibration of the instrument was performed over two decades of intensity by using two different calibrated tungsten ribbon lamps projected by a focusing lens upon a Barium-sulphate white standard. Further we used neutral density metal filters and a small bandwidth 5577 Å filter for emission line simulation. The characteristics of the filters had been measured before and were crosschecked during the photometer calibration process. The tungsten ribbon lamps have also been measured with a calibrated detector and controlled interference filters.

The two channels of each photometer were calibrated separately and together. The characteristic curve of intensity with time for the chopped operation of the photometer was determined at low chopper speed with a digital to analog converter for every photometer.

During calibrations lasting for two months, the photometers showed good stability in the ratio of the two channels but up to more than 5% drift in total responsivity, different for the individual instruments.

4. Preliminary Results

To allow van Rhijn correction of the photometer data, a simple, small horizon sensor was developed for the BV payload at DFVLR-Institut für Nachrichtentechnik in cooperation with Bonn university. The horizon sensor consisted of a 1'' germanium lens, a Molecron 4 mm² pyroelectric detector followed by a FET-amplifier in source follower connection. The field of view of the sensor was ± 20 mrad.

The first OI photometer was flown on January 4, 1976 at 22.58 U.T. The apogee of 95.8 km was too low according to a weak rocket motor. The rocket did not penetrate the emission layer. As this flight showed excessive payload heating the interference filters in the other photometers were interchanged so

Table 1.

Date	U.T.	Apogee.	$\Delta\lambda_{5577} \text{ \AA}$	background		horizon sensor applied
				λ	$\Delta\lambda$	
4.1.76	22.58	95.8	20.3	5468	44	+
21.1.76	22.30	109.1	20.1	5641	25	-
5.2.76	22.30	103.1	22.1	5468	44	+
4.5.76	21.30	109.3	23.2	5645	21	-
5.5.76	21.30	104.4	19.8	5644	21	+

Fig. 2. Intensity versus time on downleg below the emission layer at January 21, 1976. The dotted curve is the characteristic curve of the chopped signal as determined in the calibration process

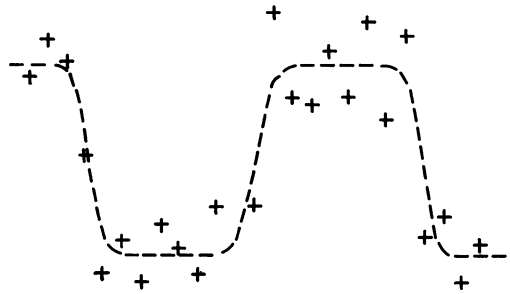
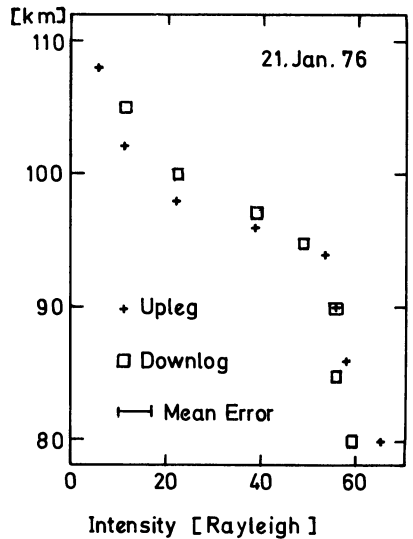


Fig. 3. Relative intensity for upleg and downleg of the flight of January 21, 1976 as determined in a handprocedure by use of half of the data rate and without correction for background variation. The probable error is nearly the same for all data points shown



that the 5577 Å filter was incorporated in the chopped channel and the background filter in the direct channel. Before and after this filter interchange the photometers were calibrated with a radioactivated phosphor to determine the new calibration factors. These measured values were in accordance with the old calibration values and our measured filter and mirror characteristics.

The second flight was in the night of January 21, 1976, at 22.20 U.T. A better rocket motor and lack of the horizon sensor brought an apogee of 109.1 km. Data on all launches are given in the following table.

In all five launches no technical failures occurred. The data were rather noisy according to the high payload temperatures. An example is given in Figure 2. Digital tapes have been constructed from the analog telemetry data. A computer program to minimize noise effects and to determine background signal variations caused by rocket attitude variations is not yet finished. So only some handdata can be presented in Figure 3.

Acknowledgements. The development of the OI photometer was sponsored by Bundesministerium für Forschung und Technologie under Grant No. RV 14-B110/73-BIII/D02. The development of the mechanical and the electrical system was done at DFVLR-Institut für Physik der Atmosphäre and DFVLR-Institut für Nachrichtentechnik.

Under the many persons, who made it possible by their personal engagement, that this photometer could be developed and qualified in time, I want to thank especially Dr. Rossbach, Dr. Hommel, Mr. Leitner, Mr. Müller and Mr. Ziegler of DFVLR and Mr. Sommer of MPI für Aeronomie. I am also indebted to Mr. Widdel, who offered the opportunity to fly the OI photometer on rockets of the MPI für Aeronomie.

References

- Greer, R.G.H., Best, G.T.: A Rocket-Borne Photometric Measurement of the Oxygen Lines at 5577 Å and 6300 Å, the Sodium D-Lines and the Continuum at 5300 Å in the Nightglow. *Planetary Space Sci.* **15**, 1857–1881, 1967
- Offermann, D., Drescher, A.: Atomic Oxygen Densities in the Lower Thermosphere as Derived from In Situ 5577 Å Night Airglow and Mass Spectrometer Measurements. *J. Geophys. Res.* **28**, 6690–670, 1973
- Shefov, N.N., Kropotkina, E.P.: The Variations in the Height of the 5577 Å Emission Layer, *Cosmic Research*, **13**, 765–770, 1975 (in Russian)
- Slanger, T.G., Black, G.: O(¹S) in the Lower Thermosphere—Chapman vs Barth. *Planetary Space Sci.* **25**, 79–88 (1977)

Received May 2, 1977

Payload B III – an Instrument Package for the Measurement of Conductivity, Concentration and Mobility of Positive and Negative Ions in the Mesosphere

H.U. Widdel, G. Rose, R. Borchers

Max-Planck-Institut für Aeronomie, D-3411 Katlenburg-Lindau 3, Federal Republic of Germany

Abstract. Payload BIII was a rocket-borne parachuted, self-tracking Gerdien-type aspiration analyzer designed for the measurement of concentration and mobility of positive and negative ions, electron concentration and polar conductivity in the height range below 80–85 km.

The goal of this instrument was to gather information about the height distribution of charged particles, especially negative and positive ions, their relative size and their seasonal variation in this range.

The instrument is described and results are communicated. The steep increase of conductivity found during the winter season above 43 km was caused by an increase of number density of charged particles and not by a change of carrier mobility. Following model calculations made by Mohnen (1971) the most abundant positive carriers have a particle radius of $3.5\text{--}4 \cdot 10^{-10}$ m. This value corresponds to the size expected for small cluster ions. Below 40 km, little variation of conductivity with season was found. It did not exceed a factor of two in certain height levels. One observation made in summer suggests that an increase of conductivity (also caused by an increase of number density of ions) can occur occasionally also during the summer season.

Key words: Rocket experiments – Gerdien condenser – Lower D-region – Mobility – Seasonal changes.

The role of large particles in the stratosphere, mesosphere and D-region has been discussed in the literature from time to time in an attempt to explain certain peculiarities of atmospheric behaviour observed either by ground-based facilities or by space-borne experiments (e.g. Reid, 1967, 1971; Farlow and Ferry, 1972; Ferry and Farlow, 1972; Rauser and Fechtig, 1972; Roessler, 1972, 1974; Fiocco and Visconti, 1973; Witt, 1974; Hughes, 1974; Fiocco, Grams and Visconti, 1975). Such particles affect heat balance, infrared radiation loss and atmospheric composition and can be, directly or indirectly, source of addi-

tional ionization too. There is no doubt that such large particles exist and that their presence is subject to seasonal changes as is proven by the existence of noctilucent clouds. Their measurement, however, is difficult. A first approach to get information about such particles is the measurement of the concentration and the mobility of charged species of both signs. An instrument package for this purpose was developed and flown in certain numbers.

The Instrument Package

1.1. The Gerdien-Probe

A suitable tool to measure mobilities and concentration of charged particles is a cylindrical condenser through which an airstream is drawn. When a time-variable voltage is applied to the electrodes, the charged particles inside the airstream are forced to move perpendicular to the direction of the axial air flow and cause a current. When the voltage is high enough the probe current saturates on a certain level which is proportional to concentration and flow velocity. From the shape of the current-voltage characteristics and from the saturation current, mobilities, polar conductivities and concentrations can be derived provided the flow velocity through the condenser is known. This kind of instrument was first proposed by H. Gerdien in 1905 and has since then found a wide application in the field of atmospheric electricity.

A first practical attempt to use Gerdien condensers for ionospheric D-region research was made by A. Pedersen (1966). Our own development of a Gerdien-type aspiration analyzer started in 1963 and was flown for the first time in 1968 (Widdel, Rose, Borchers, 1971) after being thoroughly tested in the laboratory under equivalent environmental conditions (Borchers, 1971). A cross section of the instrument is shown in Figure 1. A double-guard ring arrangement was used which helps to solve the problem of confining the front and back end stray field of the cylindrical condenser. Further, it allows to define a reliable reference potential. The Gerdien-analyzer was therefore double-walled. The outer shell was used as the reference for the driving potential and for the probe current measurements. The inner conductor was connected to reference ground through the current measuring device and to a guard ring at the front of the analyzer. The latter confined the front end stray field of the capacitor to the interior of the analyzer in order to prevent mobility discrimination outside of the instrument. A small stray field however was left in order to prevent electrons from entering the analyzer and to guide them to the outside reference shell where their contribution to probe current is then not measured. Ions are not affected by this stray field because their mobility is very much lower than the mobilities of electrons.

When different ion mobilities are present, a serious "grounding" problem exists because not all ions are intercepted inside the analyzer by the time-variable probe voltage during the analyzing process. As the result of this imbalance in charge collection, the probe assumes a charge against the environment which distorts the charge distribution of the environment and disturbs the condition

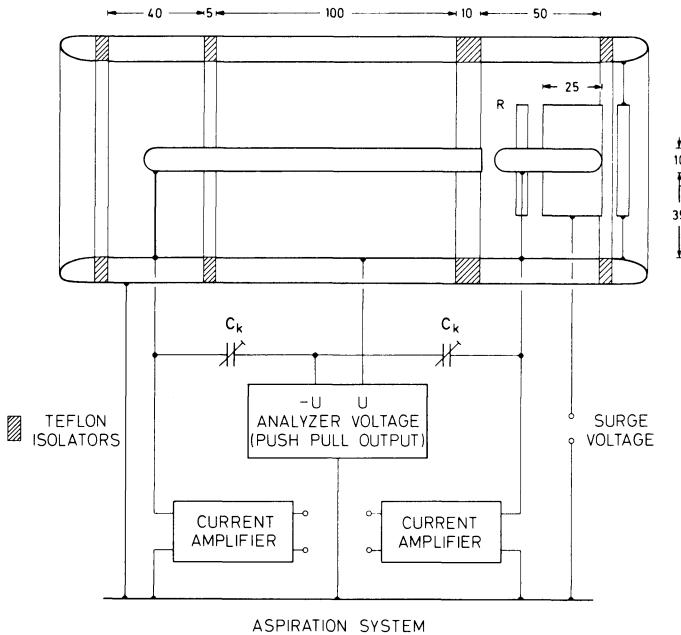


Fig. 1. Semi-quantitative cross section through the Gerdien aspiration instrument. Dimensions are given in millimetres. The capacitors C_k are compensation capacitors for the displacement current generated by the probe sweep. They are adjusted to yield zero output of the current meters when no ionization current is present

of quasi-neutrality. This problem is avoided when a second Gerdien section is used which follows the analyzer. Its electrodes are kept to a constant potential high enough to intercept all charged particles which otherwise might leave the analyzer section. This section is called the “neutralizer”. The probe current of the “neutralizer” is inverse to that of the analyzer and can be used to check the proper function of the instrument.

In order to keep the length of the instrument as short as possible, the neutralizer is folded. Guard rings confine the stray field of the neutralizer potential.

The analyzer voltage is of triangular waveform. Its amplitude is matched to the different height regions in which measurements are taken. It varies from 5 Volt applied for 80 s after deployment of the probe at apogee, then it is changed to 15 Volt from flight second 80 to 160, switched to 30 Volt from second 160 to 240 and then to 60 Volt for the rest of the flight.

1.2. The Flow Meter

The accuracy of the Gerdien measurements depends upon the accuracy which can be attained for the measurement of air flow through the Gerdien system.

It can be assumed that the flow through the tube is the same as the flow in the environment for most parts of the probe trajectory. By this, radar tracking data could in principle be used to determine the flow velocity, but, because one cannot exclude the possibility that the probe is not properly orientated along its descend path and that the actual flow velocity through the Gerdien is then different from the ambient flow, it was decided to supplement the Gerdien analyzer by a second separate system. This flow meter was nearly identical in its mechanical details but operated in a different mode to obtain the flow by modulating the plasma inside the Gerdien tube with square waves of different frequencies and measuring the output in the neutralizer section (Rose and Widdel, 1967). Laboratory measurements made under conditions equivalent to actual flight conditions yielded a fairly good accuracy of the flow measurement (5% was achieved).

1.3. The Radio Altimeter System

The radar tracking of probes which are ejected from rockets during flight poses a lot of problems which are worst during the initial phase of ejection when the two targets are not separated by a distance large enough to allow discrimination. Cases are not too rare in which the wrong target was picked up by the radar for tracking and the right object was lost because it is almost impossible for conventional narrow-beam radars to pick up again the wanted object. The situation becomes aggravated when the tracked target splits up into more than two objects during a separation or expulsion process. Finding the right target in the multitude of objects may become very difficult and needs considerable experience. This problem does not exist when the payload is equipped with a self-tracking device which supplies trajectory data and operates independently from any radar track. Such a device was developed (Widdel, 1964; Rose, Widdel, 1971) and was used to advantage in the payloads. It allows automatic and continuous tracking of the payload on command from a ground station. Its working principle is displayed in Figure 2.

1.3.1. Working Principle

A short (10 μ sec.) pulse is emitted from a ground station on VHF frequencies and is received in the payload. The payload receiver is set to a fairly low sensitivity in order to minimize response to foreign emissions and to electrostatic discharges which are often observed to be generated in large cumulus clouds. The received pulse is re-emitted from the probe on the same frequency. After the emission of the pulse, the receiver in the probe is set to a higher sensitivity which increases linearly with time and waits for the direct return pulse from the ground. Because the return pulse is (to a very good approximation) a true reflexion from the ground and not a radar scatter signal, very low transmitter power is sufficient to achieve a useful signal-to noise-ratio (100 milliwatts suffice when no external noise sources are present). The ground return pulse

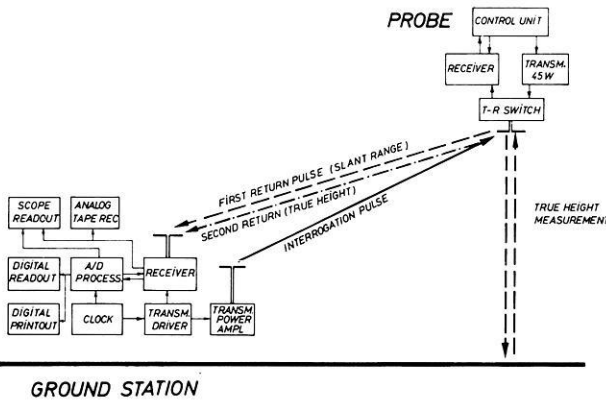


Fig. 2. Working principle of the radio altimeter

is re-transmitted and the receiver is then set to a very low sensitivity in order to suppress multiple response to ground echoes.

1.3.2. Data Evaluation and Display

When the interrogation pulse is emitted from the ground station, a counting device is started. It is stopped by the first return pulse (which corresponds to slant range to the probe) and is started again at its end. At the first stop, the slant range is edited and stored. The second stop of the counting device is provided by the second response pulse from the probe which corresponds to true height. If no second pulse is received, the counting is stopped at a preset time and a fixed value is edited. In the counting process, corrections for receiver and transmitter phase lag are added to achieve true values for slant range and true height above ground.

The results of the measurements are printed out on paper together with real time, flight time and a code which describes the operation mode. These data are also stored on magnetic tape and displayed both on digital readouts and on an oscilloscope. All ground equipment is housed in a small rack which is easily transportable. Simple dipole antennas are sufficient for operation. This radiolocation unit proved to be very useful especially in cases when no radar tracking of the probe was available. It is especially helpful for tracking objects from moving bases (for example, from a ship) which do not allow the installation of elaborate radar or other tracking systems. An example for an actual tracking of a small probe is given in Figure 3.

1.4. The Pressure Probe

Because mobility is a function of pressure, the payload package was supplemented by a Pirani—type pressure gauge which was developed by modification of an available commercial unit.

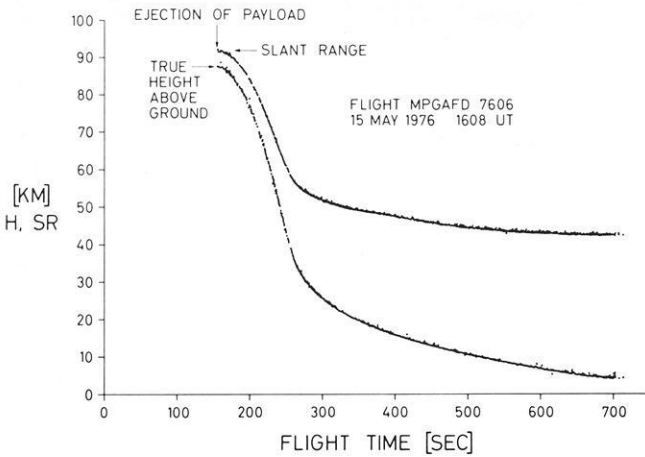


Fig. 3. Example for a probe tracking with the altimeter system. Actual plot of data

2. Probe Arrangement and Deployment

All instruments were designed into a parachuted package which contained the batteries, telemetry systems (IRIG FM/FM) and antennas. The two cylindrical probes (Gerdien condenser and flow meter) were mounted on spring-loaded latching pivots which folded out when the probe was ejected. The probe was mounted in a tube which was fixed to the package plate between the two cylindrical probes.

A conical parachute with very long shroud lines was used to limit the descend velocity and to stabilize the probe. An inflatable torus was provided to open the parachute. The probe was deployed near apogee of the rocket's trajectory backwards into the opposite direction of flight. This is advantageous to the conventional way of ejection in which the probe is thrown out into the forward direction because probe and parachute are put into flight position from the very beginning. Some amount of compensation of the trajectory speed is achieved also in the "backwards" mode. A modified "Petrel I" rocket carried the payload to an apogee of not more than 85 km. To achieve this, the payload was made quite heavy (34.5 kg) and drag buttons (5 mm long) were attached to each of the six fins of the "Petrel" to reduce performance.

To assure stable flight of the deployed probe, de-spinning of the rocket before ejection is mandatory. If this is not done, the probe shall produce precession movements which may render data evaluation of the Gerdien probe almost impossible. Also, the motor has to be jettisoned from the payload as early as possible in order to provide a good separation between payload and burnt-out motor. This is necessary to avoid collision between payload and motor and to minimize the possibility of contamination of the measurements which might occur when the probe crosses the cloud of combustion products of the outgassing motor. The sequence of motor separation and payload deployment is shown in Figure 4.

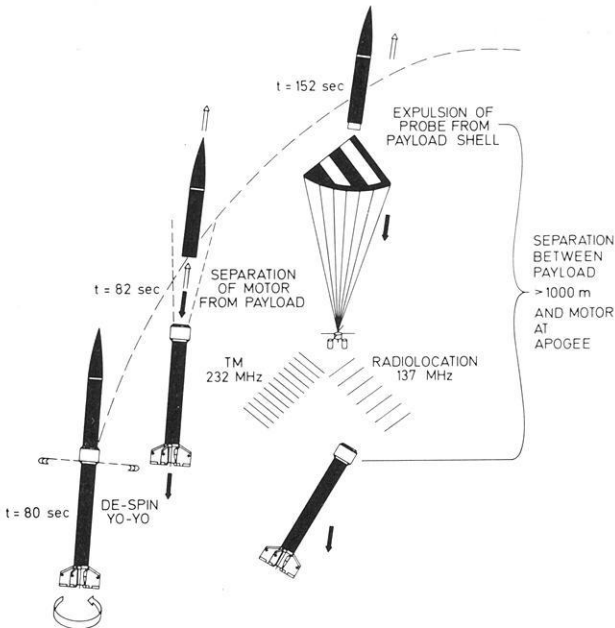


Fig. 4. Payload separation sequence: At flight second 80, the rocket is de-spun by a yoyo-device. Two seconds later, payload and motor are separated by release of compressed nitrogen. Near apogee, the payload and parachute are thrown out of the payload with a piston driven by compressed nitrogen (the piston serves as the gas reservoir). The piston jams into a conical taper serving as a brake shoe. The parachute is opened by a toroidal inflation aid. As soon as the probe leaves the payload shell it is activated and starts to work

3. Results

Some results which we obtained during the flights are shown in Figures 5 to 7. We found a rather good agreement of the mobility measurements for the most abundant species of positive ions on different flights (see Fig. 5). There seems to be no dramatic change for this ion species. Our mobility measurements agreed also well with those communicated by Conley (1972, 1974). He flew his Gerdien system on a supersonic rocket. As expected, we found that the ledge of conductivity increase is in lower heights during winter than in summer (see Figs. 6 and 7). We can also say that this increase in conductivity is not primarily caused by a change in the mobilities of ions but by a significant increase in the number densities of carriers (Fig. 8). Below 40 km there is not much difference in conductivity between summer and winter conditions. Above 40 km however, it looks as if the summer atmosphere can occasionally turn into a state similar to that found in winter (Widdel, Rose, Borchers, 1976). The reason for this effect is not known yet. Extrapolating mobility calculations made by Mohnen (1971), we found that the particle radius of the positively charged carriers was $3.5\text{--}4 \cdot 10^{-10}$ m which is approximately the size to be expected for small cluster ions. Good agreement was found with earlier data.

The development of this experiment was supported by grant WRK 85 and WRK 90 of the Bundesministerium für Wissenschaft und Technologie.

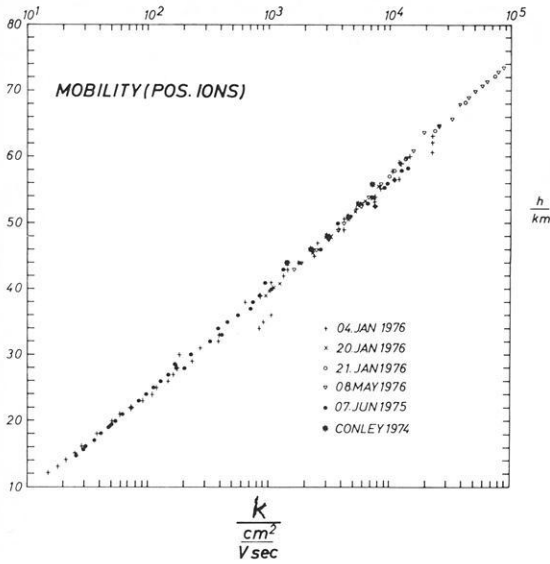


Fig. 5. Results of mobility measurements (positive ions). Below about 50 km, differences in mobility of positive and negative ions cannot be resolved by the instrument. Therefore, the mobilities shown for this height region correspond to negative ions as well. The mobility corresponds to small molecular ions

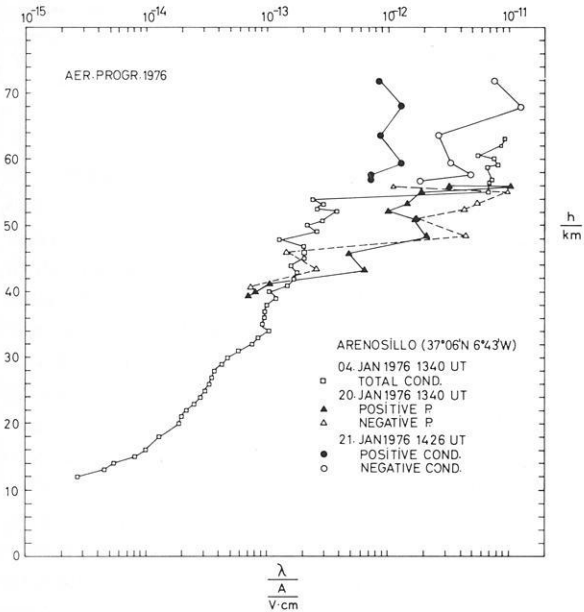


Fig. 6. Height variation of conductivity measured under winter conditions

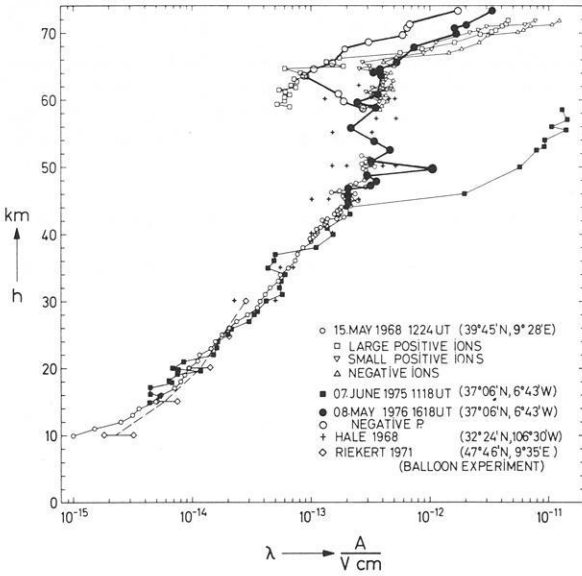


Fig. 7. Height variation of conductivity measured under summer conditions. The cause for the low-level ledge in conductivity observed on 7, June, 1975, is unknown

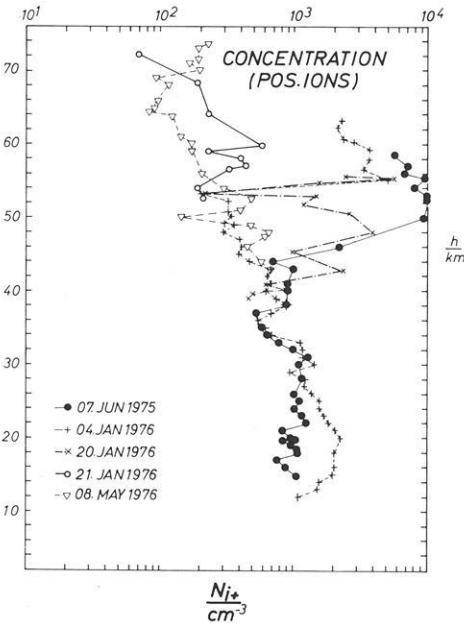


Fig. 8. Height profile of ion concentration

References

- Borchers, R.: Untersuchungen der Eigenschaften einer Aspirationssonde (Gerdien-Kondensator) zur Bestimmung der Konzentration und Beweglichkeiten von Ladungsträgern beiderlei Vorzeichens im Höhenbereich zwischen 80 und 40 km. Forschungsbericht BMBW-FB W71-39, 1971
- Conley, T.D.: Positive ion concentrations in the lower D-region during the November 1969 solar particle event measured by a rocket-borne Gerdien chamber. Spec. Rep. 144, Air Force Cambridge Res. Lab. Bedford, Mass, 1972
- Conley, T.D.: Mesospheric positive ion concentrations, mobilities, and loss rates obtained from rocket-borne Gerdien condenser measurements. *Radio Sci.* **9**, (6) 575–595, 1974
- Farlow, N.H., Ferry, G.V.: Cosmic dust in the mesosphere. In: *Space Res. XII*, 369–380. Berlin: Akademie-Verlag 1972
- Ferry, G.V., Farlow, N.H.: Upper atmospheric dust concentrations in polar regions. In: *Space Res. XII*, pp. 381–390, 1972
- Fiocco, G., Visconti, G.: On the seasonal variation of upper atmospheric sodium. *J. Atmospheric Terrest. Phys.* **35**, 165–171, 1973
- Fiocco, G., Grams, G., Visconti, G.: Equilibrium temperatures of small particles in the earth's upper atmosphere (50–110 km). *J. Atmospheric Terrest. Phys.* **37**, 1327–1337, 1975
- Hughes, D.W.: Cosmic dust influx to the upper atmosphere during the major meteor showers. In: *Space Res. XIX*, pp. 709–713 Berlin: Akademie-Verlag 1974
- Mohnen, V.: The formation of major positive and negative ions up to the 50 km level. In: *Mesospheric models and related experiments*, G. Fiocco ed., pp. 210–218. Dordrecht: D. Reidel Publ. 1971
- Pedersen, A.: Measurements of ion concentration in the D-region of the ionosphere. *Uppsala Ionosferobserv. Rep.* 15, pp. 9–32, Uppsala/Schweden, 1966
- Rausser, P., Fechtig, H.: Combined dust collection and detection experiment during a noctilucent cloud display above Kiruna, Sweden. In: *Space Res. XII*, pp. 391–402 Berlin: Akademie-Verlag 1972
- Reid, G.C.: Ionospheric implications of minor constituents. In: *Space Res. VII*. pp. 197–210. Amsterdam: North Holland 1967
- Reid, G.C.: The roles of water vapor and nitric oxide in determining electron densities in the D-region. In: *Mesospheric models and related experiments*, G. Fiocco, ed., p. 198–209. Holland: D. Reidel Publ. Comp. Dordrecht 1971
- Roessler, F.: Aerosol layers in the atmosphere. In: *Space Res. XII*, pp. 423–431. Berlin: Akademie-Verlag 1972
- Roessler, F.: Optical measurements on noctilucent clouds by rockets. In: *Space Res. XIV*. pp. 695–699. Berlin: Akademie-Verlag 1974
- Rose, G., Widdel, H.U.: Ein Meßgerät zur Bestimmung der Strömungsgeschwindigkeit in kurzen Röhren (Ionenzählern) bei niedrigem Gasdruck. *Mitteilungen aus dem Max-Planck-Institut für Aeronomie*, Nr. 30. Berlin-Heidelberg-New York: Springer 1967
- Rose, G., Widdel, H.U.: An Altimeter/Telemetry System for small sounding rockets. *J. Brit. Interplan. Soc.* **24**, 209–213, 1971
- Widdel, H.U., Rose, G., Borchers, R.: Results of concentration and mobility measurements of positively and negatively charged particles taken by a rocket-borne parachuted aspiration (Gerdien) probe in the height region from 72 to 39 km. *Pure Appl. Geophys.* **84**, 154–160, 1971
- Widdel, H.U., Rose, G., Borchers, R.: Experimental results on the variation of electric conductivity and ion mobility in the mesosphere. *J. Geophys. Res.* **81**, 6217–6220, 1976
- Widdel, H.U.: Suggestion for an active rocket-borne radio altimeter system for sounding probes. *Internal Rep. Max-Planck-Institut für Aeronomie, Lindau/Harz*, 1964
- Witt, G.: Solid particles at the mesopause. In: *Space Res. XIV*, p. 691. Berlin: Akademie-Verlag 1974

Received May 2, 1977

Review Article

Die Einheiten des internationalen Systems in der Geomagnetik

A. Hahn

Niedersächsisches Landesamt für Bodenforschung, Postfach 5101 53,
F-3000 Hannover 51, Federal Republic of Germany

SI Units in the Field of Geomagnetism

Abstract. In the field of Geomagnetism only electromagnetic cgs units were used in the past. In September 1973, however, the International Association of Geomagnetism and Aeronomy recommended the adoption of SI Units. Thereby it was specified that values of the geomagnetic field should be expressed in terms of the magnetic induction B , values of intensity of magnetization in terms of magnetization M and values of susceptibility as the ratio between M and the magnetic field H .

The paper presents guidelines for the adaptation to SI of the fundamental relations and common formulas used in geomagnetism particularly in the field of interpreting magnetostatic anomalies.

Key words: Geomagnetism – Units.

1. Situation

Gemäß dem „Gesetz über Einheiten im Meßwesen“ und der „Ausführungsverordnung zum Gesetz über Einheiten im Meßwesen“, beide von 1970, sind zur Messung physikalischer Größen die SI-Einheiten (SI = Système Internationale d'Unités, internationales Einheitensystem) zu verwenden. Damit fallen die bisher in der Geomagnetik üblichen Einheiten Gauß (G, Γ), Oerstedt (Oe), Gamma (γ ; $1\gamma = 10^{-5}$ Oe) und „elektromagnetische cgs-Einheit“ (für die magnetische Suszeptibilität) weg.

In der Geomagnetik braucht man Einheiten für folgende Größen:

I. das Meßergebnis einer geomagnetischen Geländemessung mit den Instrumenten Feldwaage, Torsionsmagnetometer, Förstersonde, Protonenmagnetometer oder optisch gepumpte Magnetometer u.ä.,

II. die remanente und/oder induzierte Magnetisierung von Probekörpern (meist Gesteine oder Minerale),

III. die physikalische Größe, die in Probekörpern eine Magnetisierung erzeugt,

IV. die Proportionalitätskonstante, die zwischen III. und der induzierten Magnetisierung vermittelt (magnetische Suszeptibilität).

Das SI sieht für diese 4 Größen keine eindeutig bestimmten Einheiten vor. Die Geomagnetiker haben daher in einer Sitzung der Internationalen Assoziation für Geomagnetismus und Aeronomie (IAGA) am 21. Sept. 1973 in Kyoto als Resolution 3 folgendes beschlossen (Melchior, 1974, S. 36):

”IAGA, considering that SI Units are achieving international recognition as a single standard for worldwide use, recommends adoption of SI Units in the field of geomagnetism.

Specifically IAGA recommends that:

1. (a) Values of the geomagnetic field be expressed in terms of the magnetic induction B (SI Unit tesla = weber/metre²).

(b) If it is desired to express values in gamma, a note should be added stating that “one gamma is equal to one nanotesla”.

2. (a) Values of intensity of magnetization be expressed in terms of magnetization M (SI Unit ampere/metre).

(b) If it is desired to express values in e.m.u., a note should be added stating that “one e.m.u. is equal to 10³ ampere/metre”.

3. (a) Values of susceptibility be expressed as the ratio between magnetization M and the magnetic field H .

(b) If, during the transitional period, it is desired to use values of susceptibility in e.m.u., a note should be added stating that “ χ_{SI} is equal to $4\pi\chi_{e.m.u.}$ ”.

Zu 2. (b): Unter der Bezeichnung e.m.u. versteht man in diesem Zusammenhang gewöhnlich 1G.

Zu 3.(b): In diesem Fall bedeutet e.m.u., daß man das (dimensionslose) Verhältnis von induzierter Magnetisierung zu dem Feld Oe, das sie erzeugt, aus den Einheiten G und Oe gebildet hat, die ja im cgs-System dimensionsgleich sind.

Es erscheint auf den ersten Blick unpassend, daß das Ergebnis von Geländemessungen (I.) nicht mit der Einheit des Magnetfeldes H , $A\ m^{-1}$, gemessen werden soll, sondern mit der Einheit der magnetischen Kraftflußdichte oder Induktion B , Tesla; jedoch ist dazu folgendes zu bemerken:

1. Die Beziehung

$$B = \mu_0 H$$

ist in Luft bis auf einen Fehler erfüllt, der bei jeder in der Geophysik noch sinnvollen Präzisionsforderung vernachlässigt werden kann.

2. Der Unterschied zwischen dem Magnetfeld H und der magnetischen Kraftflußdichte B besteht in der Magnetostatik darin, daß H den wirbelfreien und B den quellenfreien Teil des Gesamtphänomens darstellt:

$$\text{rot } \mathbf{H} = 0$$

$$\text{div } \mathbf{B} = 0$$

Dementsprechend findet man an Grenzflächen zwischen zwei Medien unterschiedlicher Permeabilität, daß bezüglich dieser Fläche die Tangentialkomponente von \mathbf{H} und die Normalkomponente von \mathbf{B} stetig von dem einen Medium in das andere übergehen. Diesen Unterschied veranschaulicht ein Gedankenexperiment (z.B. Sommerfeld, 1948, S. 90), bei dem im Innern eines Mediums mit der Permeabilität μ im homogenen Magnetfeld einerseits in einer feldparallelen dünnen Bohrung und andererseits in einem quer zum Feld flächenhaft ausgehenden dünnen Schlitz eine Feldstärkemessung durchgeführt wird. Das Ergebnis der Messung in der feldparallelen Bohrung repräsentiert H , dasjenige im Querschlitz $B = \mu \cdot \mu_0 H$.

Die Frage, ob eine Meßsonde B oder H mißt, hat Lowes (1974) für die z.Z. gängigen Apparaturen untersucht. Er fand in allen Fällen, daß das Meßergebnis in ziemlich komplizierter Weise vom äußeren Feld – sei es nun das Magnetfeld H oder die magnetische Induktion B – und von der Suszeptibilität des umgebenden Mediums Luft oder Wasser sowie von der Gestalt und der Suszeptibilität der Meßsonde abhängt. Es besteht also weder von der Meßpraxis noch vom Verständnis des Meßvorgangs her ein gewichtiger Grund, eine der beiden Größen, B oder H , zur Beschreibung der Ergebnisse von Geländemessungen zu bevorzugen.

Hingegen sprechen zwei praktische Gründe für die in der Resolution getroffene Zuordnung:

1. Es entsprechen sich

$$1 \gamma \cong 1 \text{ nT (nanoTesla)}$$

beim Feld bzw. der Induktion und

$$100 \gamma \cong 1 \text{ A m}^{-1} \quad (4)$$

bei der Magnetisierung. Lediglich bei der Umstellung der abgeleiteten Größe „Suszeptibilität“ tritt der Faktor 4π auf.

2. Die magnetische Induktion, also das gewöhnlich auf Karten oder Diagrammen dargestellte Ergebnis von Geländemessungen, hat nun eine andere Dimension als die Magnetisierung, also die Eigenschaft von Gesteinsproben. Letztere hat zudem eine anschauliche Bedeutung bekommen: Die Magnetisierungskomponente einer z.B. würfelförmigen Gesteinsprobe parallel zu einer Würfelfkante ist in ihrer Wirkung außerhalb der Probe äquivalent der Wirkung einer Drahtwicklung um die Probe, deren Achse parallel zu dieser Kante liegt und die von einem so bemessenen Strom durchflossen ist, daß derselbe Wert in A m^{-1} entsteht, der auch die Magnetisierung kennzeichnet.

Andererseits wird mancher Geophysiker mit Bedauern sehen, daß das Wort „Magnetfeld“, das ja das H -Feld bezeichnet, nun eigentlich nicht mehr auf den Gegenstand der geomagnetischen Vermessungen angewandt werden darf; auch muß bezweifelt werden, daß sich hierfür im Sprachgebrauch der Geophysiker die Worte „(magnetische) Induktion“ oder „(magnetische) Kraftflußdichte“ durchsetzen werden.

2. Gegenüberstellung der Einheiten

Für diese Gegenüberstellung werden im folgenden meist Größengleichungen verwendet. Wenn darin oder in einem anderen Ausdruck die Einheit einer

cgs-System

SI

Größe angegeben werden soll, so wird die betreffende Größe als Produkt aus Zahlenwert und Einheit dargestellt. Dabei werden unbestimmte Zahlenwerte durch das in geschweifte Klammern gesetzte Formelzeichen dargestellt. Solche Größen sind also z.B. $\{H\} \text{ A m}^{-1}$, $\{B\} \text{ T}$. Selbstverständlich stellt das eingeklammerte Formelzeichen denjenigen Zahlenwert dar, der bei Verwendung der dahinterstehenden Einheit erhalten wird (DIN 1313).

Faktoren für die Umrechnung der Zahlenwerte beim Übergang vom cgs-System zum SI sind am Schluß der Arbeit zusammengestellt.

2.1. Magnetfeld, magnetische Induktion

Gebräuchliche Symbole für die zu messenden Größen sind:

H für das Magnetfeld

B für die magnetische Induktion

Aus der Theorie werden diese Größen gekennzeichnet durch

$$\text{rot } \mathbf{H} = 0$$

$$\text{div } \mathbf{B} = 0.$$

Die Einheiten sind:

Für H : Oerstedt (Oe)

H : Ampère pro Meter (A m^{-1})

Für B : Gauss (G)

B : Tesla (T)

(1)

Im Vakuum gilt $B = H$

$B = \mu_0 H$; $\mu_0 = 4\pi \cdot 10^{-7} \text{ T/A m}^{-1}$

Zwischen den Einheiten der beiden Systeme, welche zur Messung derselben Größe dienen, bestehen die Beziehungen:

$$1 \text{ Oe} \cong 10^3/4\pi \text{ A m}^{-1}, \quad (2)$$

$$1 \text{ G} \cong 10^{-4} \text{ T}. \quad (3)$$

Für diese Vergleiche seien hier die entsprechenden Abschnitte aus Kohlrausch (1943) zitiert; die verwendete Schreibweise ist am Anfang des Kapitels erläutert:

„In der folgenden Zusammenstellung ist neben der üblichen Buchstabenbezeichnung (Symbol) die Dimension der Größe in einer eckigen Klammer angegeben. Die der Größe zugehörige Maßeinheit im cgs-System wird, falls kein von 1 verschiedener Faktor hinzutritt, dadurch dargestellt, daß in dem Ausdruck für die Dimension die Größen l (Länge), m (Masse), t (Zeit) durch cm , g , s ersetzt sind.“

„Magnetische Feldstärke. $H = [l^{-1/2} m^{1/2} t^{-1}]$. Sie kann bestimmt werden durch Vergleich mit derjenigen magnetischen Feldstärke, die im Inneren einer von dem Strom I durchflossenen Spule erzeugt wird. Besitzt die gegen ihren Durchmesser lange Spule z Windungen je cm, so ist $[H]_m = 4\pi \cdot z \cdot [I]_m$; $H = z \cdot I$; $[H]_m$ wird gemessen in Örsted (Ø), H in Amperewindungen pro cm (A/cm). In Rücksicht auf den verschiedenen Zahlenwert von $[I]_m$ und I (vgl. Stromstärke) ist

$$H = 10/4\pi [H]_m; \quad [\text{cm}^{-1/2} \text{g}^{1/2} \text{s}^{-1}] = 1 \text{ Ø} = 10/4\pi \text{ A cm}^{-1}.$$

Beim Stichwort „Stromstärke“ ist vermerkt, daß die Einheit der Stromstärke im cgs-System $1 [\text{cm}^{1/2} \text{g}^{1/2} \text{s}^{-1}] = 10 \text{ A}$ ist.

Magnetische Induktion. $B = [l^{-1/2} m^{1/2} t^{-1}]$. Sie kann ermittelt werden aus dem Zeitintegral $\int_{t_1}^{t_2} U \cdot dt$ der elektromotorischen Kraft, die in einer Drahtschleife von der Fläche dF induziert wird, wenn die Drahtschleife während der Zeit $t_2 - t_1$ in einem magnetischen Feld von dem Ort, an dem die Induktion B bestimmt werden soll, bis in praktisch unendliche Entfernung ($B=0$) geführt wird. Unter der Voraussetzung, daß die Drahtschleife homogen von den magnetischen Induktionslinien ausgefüllt wird, gewinnt man die Induktion selbst, wenn man das genannte Zeitintegral durch die Windungsfläche dividiert. Die entsprechende Differentialgleichung lautet: $U = -\frac{d}{dt} \int (B, dF)$. Absolutes Maß: die cgs-Einheit heißt 1 Gauß (G); praktisches Maß:

$$\text{Vs/cm}^2; \quad [\text{cm}^{-1/2} \text{g}^{1/2} \text{s}^{-1}] = 1 \text{ G} = 10^{-8} \text{ Vs/cm}^2.$$

Oder $1 \text{ G} = 10^{-4} \text{ Vs/m}^2 = 10^{-4} \text{ T}$.

Die bisher in der Geomagnetik übliche Einheit $1 \gamma = 10^{-5} \text{ Oe}$, für die man bei Messungen im Vakuum oder in Luft auch unbedenklich schreiben kann $1 \gamma = 10^{-5} \text{ G}$, entspricht also im SI $10^{-9} \text{ T} = 1 \text{ nT}$:

$$1 \gamma \cong 1 \text{ nT}. \quad (4)$$

2.2. Magnetisierung

Zur Betrachtung dieser Größen sei zunächst Stille (1955) zitiert:

„Eine gewisse Sonderstellung nehmen die Größenarten magnetisches Moment, Magnetisierung und magnetische Polstärke ein, für die nebeneinander zwei verschiedene Definitionsarten üblich sind.

In beiden Fällen wird das magnetische Moment m , beispielsweise eines Magneten, über das mechanische Drehmoment eingeführt, das auf den Magneten in einem äußeren Magnetfeld ausgeübt wird. Die beiden Auffassungen unterscheiden sich durch den magnetischen Feldvektor, der zur Charakterisierung des äußeren Magnetfeldes bei der Definition des magnetischen Momentes benutzt wird: magnetische Feldstärke oder magnetische Induktion.“

cgs-System

SI

IAGA hat sich in der zitierten Resolution für die letztere Möglichkeit entschieden. Es sei daher nur die entsprechende Passage aus Stille (l.c.) wiedergegeben:

„Zum anderen wird das magnetische Moment mit der Leerinduktion $B_0 = \mu_0 H$ durch die Gleichung

$$T = m_B \times B_0$$

definiert. Dient m_B zur Beschreibung des in einem magnetisierten Körper hervorgerufenen Magnetismus, so nennt man den Grenzwert ($\tau \rightarrow 0$; τ Volumen des Körpers) des Quotienten m_B/τ „Magnetisierung M “. Der Vektor M wird über den Vektor m_B durch die Gleichung

$$m_B = \int M d\tau$$

definiert.“

Das Wort Leerinduktion deutet an, daß das mechanische Drehmoment T eines magnetisierten Körpers im Vakuum bestimmt sein soll. Die der Magnetisierung entsprechende, über das Magnetfeld H definierte Größe heißt „magnetische Polarisierung“; ihr Formelzeichen ist J . Im cgs-System benutzt man gewöhnlich das Wort „Magnetisierung“ zusammen mit dem Formelzeichen J .

Zwischen den Magnetisierungsgrößen und den Feldgrößen bestehen folgende Zusammenhänge:

$$\operatorname{div} \mathbf{H} = -4\pi \operatorname{div} \mathbf{J}.$$

$$\operatorname{div} \mathbf{H} = -\operatorname{div} \mathbf{M}. \quad (5)$$

Da die Einheit für H : Oe und diejenige für J : G dieselbe Dimension haben, braucht hier auch zwischen J und M nicht unterschieden zu werden.

Hier sind die Größen J und M zu unterscheiden: Im Fall homogener Felder gilt:

$$B = \mu_0(H + M)$$

$$\text{und} \quad (6)$$

$$B = \mu_0 H + J.$$

Also

$$J = \mu_0 M \quad (7)$$

Dementsprechend ist die Einheit für J : Tesla und für M : A m^{-1} .

Zwischen den Systemen entsprechen sich hier

$$\begin{aligned} 1 \text{ G} &\cong 10^3 \text{ A m}^{-1} \\ 10^{-3} \text{ G} = 100 \gamma &\cong 1 \text{ A m}^{-1} \\ 10^{-6} \text{ G} &\cong 1 \text{ mA m}^{-1}. \end{aligned} \quad (8)$$

cgs-System

SI

Diese hinsichtlich der Magnetisierung gültige Beziehung zwischen G und $A\ m^{-1}$ ist sorgfältig zu unterscheiden von der in 2.1 formulierten (Gl. (2) und (3)), die für Feld- bzw. Induktionsmessungen gilt.

2.3. Suszeptibilität

Gebräuchliches Symbol der Suszeptibilität ist χ . Die Größe selbst ist dimensionslos als Quotient zweier Größen gleicher Dimension. Dieser Quotient ist allerdings in den beiden Systemen unterschiedlich

$$\chi_{\text{cgs}} = \left\{ \frac{J}{H} \right\} \frac{G}{\text{Oe}} \qquad \chi_{\text{SI}} = \left\{ \frac{M}{H} \right\} \frac{A\ m^{-1}}{A\ m^{-1}}. \quad (6)$$

Beim Übergang von einem System in das andere muß man den Zähler nach 2.2 und den Nenner nach 2.1 transformieren.

In den Zählern sind Magnetisierungsgrößen zu vergleichen (Gl. 8):

$$1\ \text{G} (= 1\ \text{Oe}) \qquad \cong 10^3\ \text{A}\ m^{-1}.$$

In den Nennern hat man es mit Feldgrößen zu tun (Gl. 2):

$$1\ \text{Oe} \qquad \cong 10^3/4\pi\ \text{A}\ m^{-1}.$$

Der Vergleich ergibt daher:

$$\frac{1\ \text{Oe}_{\text{Magnet.}}}{1\ \text{Oe}_{\text{Feld}}} \qquad \cong \frac{10^3\ \text{A}\ m^{-1}}{(10^3/4\pi)\ \text{A}\ m^{-1}} = 4\pi \frac{\text{A}\ m^{-1}}{\text{A}\ m^{-1}}.$$

Hieraus sieht man, daß die Einheit der Suszeptibilität im cgs-System um den Faktor 4π größer ist als die Einheit im SI-System. Wenn also eine Messung im cgs-System den Wert 1 ergab, erhält man aus derselben Messung im SI-System den Wert 4π :

$$\chi_{\text{cgs}} = 1 \qquad \cong \chi_{\text{SI}} = 4\pi. \quad (10)$$

Wegen der fehlenden Dimension ist es dringend zu empfehlen, bei der Angabe von Werten der Suszeptibilität das verwendete Einheitensystem zu vermerken.

2.4. Induzierte Magnetisierung

Die Suszeptibilität ist bei den meisten Gesteinskörpern so klein, daß ihre im erdmagnetischen Feld induzierte Magnetisierung ohne Berücksichtigung des Entmagnetisierungsfaktors berechnet werden kann. In emcgs-Einheiten lautet die entsprechende Beziehung:

$$\{J_{\text{ind}}\} G = \chi \cdot \{H\} \text{Oe}. \quad (11)$$

cgs-System

SI

Da „Gauß“ und „Oersted“ in der Dimension übereinstimmen, entstehen bei dieser Gleichsetzung keine Probleme. In SI-Einheiten kann man für die Magnetisierung M entsprechend formulieren:

$$\{M_{\text{ind}}\} \text{ A m}^{-1} = \chi_{\text{SI}} \cdot \{H\} \text{ A m}^{-1}. \quad (12)$$

Diese Gleichung ist zwar ebenso einfach wie die Gleichung (11), doch braucht man für die Praxis auch die Beziehung zwischen der induzierten Magnetisierung und der magnetischen Kraftflußdichte B . Sie lautet offenbar (s. Gl. (1)):

$$\{M_{\text{ind}}\} \text{ A m}^{-1} = \chi_{\text{SI}} \frac{\{B\} \text{ T}}{\{\mu_0\} \text{ T/A m}^{-1}}. \quad (13)$$

Wenn man den Wert von B in nT aufschreibt, erhält man unter Berücksichtigung des Wertes von $\mu_0 = 4\pi \cdot 10^{-7} \text{ T/A m}^{-1} = 4\pi \cdot 100 \text{ nT/A m}^{-1}$

$$\begin{aligned} & \{M_{\text{ind}}\} \text{ A m}^{-1} \\ &= \chi_{\text{SI}} \frac{\{B\}' \text{ nT}}{4\pi \cdot 100 \text{ nT/A m}^{-1}} \end{aligned} \quad (14)$$

wobei $\{B\}' = 10^9 \cdot \{B\}$.

An dieser Stelle tritt also im SI-System der unvermeidliche Faktor 4π auf.

Wenn man auf mA m^{-1} übergeht und dementsprechend für M den 1000-fachen Zahlenwert aufschreibt ($\{M_{\text{ind}}\}' = 10^3 \cdot \{M_{\text{ind}}\}$), hat man

$$\begin{aligned} & \{M_{\text{ind}}\}' \text{ mA m}^{-1} \\ &= \chi_{\text{SI}} \cdot (10/4\pi) \cdot \{B\}' \text{ nT} \\ &\approx \chi_{\text{SI}} \cdot 0,8 \{B\}' \text{ nT}. \end{aligned}$$

Da $10/4\pi$ die Größenordnung 1 hat, kann man für Abschätzungen festhalten: Man bekommt durch Multiplikation des B -Feldes in nT mit dem SI-Wert der Suszeptibilität die Größenordnung der induzierten Magnetisierung in mA m^{-1} .

Es sei hier vermerkt, daß die Feldstärke von Feldern, die – meist im Labor – von stromdurchflossenen Spulen erzeugt werden, in A m^{-1} anzugeben ist. Dies gilt insbesondere für die Aufnahme von Hysterese-Schleifen, für die Coerzitivkraft, für Auf- und Abmagnetisierungsversuche im Gleich- oder Wechselfeld bei variabler oder konstanter Temperatur u.ä. Auszunehmen hiervon sind selbstverständlich die Felder von Spezialspulen zur Kalibrierung von Geländemagnetometern.

Gemäß Gleichung (2) hat man

$$\begin{aligned} 10 \text{ Oe} & \cong (10^4/4\pi) \text{ A m}^{-1} \approx 0,8 \text{ kA m}^{-1} \\ 100 \text{ Oe} & \cong (10^5/4\pi) \text{ A m}^{-1} \approx 8 \text{ kA m}^{-1}. \end{aligned} \quad (15)$$

usw.

cgs-System

SI

Ohne Herleitung sei hier noch folgendes notiert:

Das Feld im Innern einer langen Spule beträgt

$$\{H\}_{\text{cgs}} \text{ Oe} = 4\pi \cdot 10^{-3} \cdot n \cdot I$$

$$\{H\}_{\text{SI}} \text{ A m}^{-1} = n \cdot I$$

dabei bedeuten:

 I Spulenstrom in A n Zahl der Windungen pro m Spulenlänge.Die Helmholtzspule mit dem Radius $\{r\}$ m und der Windungszahl n in jeder der beiden Schleifen hat mit dem Spulenstrom $\{I\}$ A in Zentrum die Feldstärke

$$\{H\}_{\text{cgs}} \text{ Oe} = (0,286217 \cdot \pi / (r \text{ 100})) \cdot n \cdot I$$

$$\{H\}_{\text{SI}} \text{ A m}^{-1} = 0,715542 \cdot n \cdot I / r.$$

Der Faktor 100 im Nenner der Formel auf der cgs-Seite kommt daher, daß r hier in m und nicht – wie sonst üblich – in cm gemessen sein soll. Die Formel auf der SI-Seite ergibt sich unmittelbar durch Einsetzen von (2) für Oe.

2.5. Der magnetische Dipol

2.5.1. *Das Dipolmoment (und die Polstärke).* Das Dipolmoment m eines magnetisierten Körpers ist proportional dem Drehmoment, das dieser Körper in einem homogenen äußeren Feld erfährt. Man faßt es auf als Produkt aus dem Volumen des Körpers V und seiner in diesem Sinne gemittelten Magnetisierung J bzw. M

$$m = \{J\} \cdot \{V\} \text{ G cm}^3$$

$$m = \{M\} \cdot \{V\} \text{ A m}^2. \quad (16)$$

Da die Magnetisierungseinheit $1 \text{ G} \triangleq 10^3 \text{ A m}^{-1}$ entspricht und $1 \text{ cm}^3 = 10^{-6} \text{ m}^3$, gilt für die Einheiten

$$1 \text{ G cm}^3 \triangleq 10^{-3} \text{ A m}^2 = 1 \text{ mA m}^2. \quad (17)$$

Die seltener gebrauchten Einheiten der Polstärke sind

G cm²

und A m.

Dabei gilt wegen $1 \text{ cm}^2 = 10^{-4} \text{ m}^2$

$$1 \text{ G cm}^2 \triangleq 10^{-1} \text{ A m}. \quad (18)$$

Das Drehmoment eines Dipols im Feld ist in den Gleichungen (33) und (34) formuliert.

In den folgenden Abschnitten 2.5.2 und 2.5.3 ist in den SI-Gleichungen von (21) ab die Dimension von μ_0 nicht notiert.

2.5.2. *Das Feld des Dipols.* Das Potential $P(H)$ des H -Feldes eines Dipols \mathbf{m} ist gegeben durch

cgs-System

SI

$$P(H) = (\mathbf{m}, \mathbf{r})/r^3$$

$$P(H) = (1/4\pi) \cdot (\mathbf{m}, \mathbf{r})/r^3. \quad (19)$$

Der Faktor 4π tritt hier im SI-System auf, weil er in Gleichung (5) fehlt. Das Potential des B -Feldes lautet entsprechend

$$P(B) = (1/4\pi) \cdot \mu_0 (\mathbf{m}, \mathbf{r})/r^3. \quad (20)$$

Setzt man den Zahlenwert von μ_0 ein und notiert die Dimensionen, so hat man

$$\begin{aligned} & \{P(B)\} \text{ T m} \\ &= \frac{4\pi \cdot 10^{-7} \text{ T}}{4\pi} \frac{(\{\mathbf{m}\} \text{ A m}^2, \{\mathbf{r}\} \text{ m})}{\text{A m}^{-1} \{r^3\} \text{ m}^3}, \\ & \{P(B)\} \text{ nT m} = 10^2 (\{\mathbf{m}\} \text{ A m}^2, \mathbf{r})/r^3. \end{aligned} \quad (21)$$

Man sieht daraus: Das Potential der magnetischen Induktion, die zu einem Dipol $\{\mathbf{m}\} \text{ A m}^2$ gehört, bekommt man in nT m, indem man das innere Produkt aus Dipolmoment \mathbf{m} und Fahrstrahl \mathbf{r} zum Aufpunkt, geteilt durch r^3 mit dem Faktor 100 multipliziert. Es ist dies sozusagen derselbe Faktor 100, der uns schon beim Vergleich der Einheiten der Magnetisierung G und A m^{-1} begegnete (Gl. (8)). Alle daraus abzuleitenden Formeln für die Feldkomponenten gehen nach dieser einfachen Regel vom cgs-System in das SI-System über:

Feld des Dipols

Auf der Achse, achsenparallele Feldkomponente:

$$\mathbf{H} = 2\mathbf{m}/r^3 \quad \{\mathbf{B}\} \text{ nT} = 100 \cdot 2 \{\mathbf{m}\} \text{ A m}^2/r^3. \quad (22)$$

Am Äquator, achsenparallele Feldkomponente:

$$\mathbf{H} = -\mathbf{m}/r^3 \quad \{B\} \text{ nT} = -100 \cdot \{\mathbf{m}\} \text{ A m}^2/r^3. \quad (23)$$

Bei der homogen magnetisierten Kugel ist

$$\begin{aligned} \mathbf{m} &= V \cdot \mathbf{J} & \mathbf{m} &= V \cdot \mathbf{M}, \\ \mathbf{m} &= (4\pi/3) \cdot R^3 \cdot \mathbf{J} & \mathbf{m} &= (4\pi/3) \cdot R^3 \cdot \mathbf{M} \end{aligned} \quad (24)$$

R = Radius der Kugel.

Dementsprechend ist das Feld auf der Achse

$$\begin{aligned} \mathbf{H} &= (8\pi/3) \cdot (R^3/r^3) \cdot \mathbf{J} & \{\mathbf{B}\} \text{ nT} &= (8\pi/3) \cdot (R^3/r^3) \\ & & & \cdot 100 \cdot \{\mathbf{M}\} \text{ A m}^{-1} \end{aligned} \quad (25)$$

und das Feld in der Äquatorebene

$$\begin{aligned} \mathbf{H} &= -(4\pi/3) \cdot (R^3/r^3) \cdot \mathbf{J} & \{\mathbf{B}\} \text{ nT} &= -(4\pi/3) \cdot (R^3/r^3) \\ & & & \cdot 100 \cdot \{\mathbf{M}\} \text{ A m}^{-1}. \end{aligned} \quad (26)$$

cgs-System

SI

2.5.3. *Die Felder von zweidimensionalen Körpern.* Hier werden als Beispiele die wohlbekannten Formeln für die Vertikalkomponente Z des Magnetfeldes eines horizontalen Zylinders und einer dünnen Platte, beide in horizontaler Richtung unendlich ausgedehnt, aufgeschrieben.

Das Feld des Zylinders:

$$\{Z\} \gamma = 2(j_{\perp}/r^2) \cos(2\rho - \vartheta) \qquad \{Z\} \text{ nT} = 200 \cdot (\mu_{\perp}/r^2) \cos(2\rho - \vartheta) \quad (27)$$

j_{\perp}, μ_{\perp} : Magnetisches Moment pro Längeneinheit des Zylinders, Komponente senkrecht zur Zylinderachse in
G cm² A m

ρ : Winkel des Fahrstrahls vom Zylinder zum Aufpunkt,
 ϑ : Winkel der Magnetisierung, beide gemessen vom Lot,
 r : Länge des Fahrstrahls.

Feld der dünnen Platte

$$\{Z\} \gamma = -(2Jb/r) \cos(\rho - \beta) \qquad \{Z\} \text{ nT} = -(200 Mb/r) \cos(\rho - \beta) \quad (28)$$

J, M : Magnetisierung der Platte, gemessen in

G A m⁻¹,

b : Mächtigkeit der Platte,
 r : Länge des Fahrstrahls von der Plattenoberkante zum Aufpunkt,
 ρ : Winkel des Fahrstrahls, gemessen vom Lot,
 β : Winkel zwischen Magnetisierung und Einfallen der Platte.

2.5.4. *Die Eigenfelder von schwach permeablen Körpern im äußeren Feld.* Bisweilen möchte man in diesen Formeln die Suszeptibilität und das induzierende Feld H_a bzw. B_a anstelle der Magnetisierung anschreiben. Zur besseren Unterscheidung bezeichnet in den folgenden Formeln H_K bzw. B_K das Eigenfeld des betrachteten Körpers. Unter Vernachlässigung des Entmagnetisierungsfaktors hat man dann:

Feld der Kugel auf der feldparallelen Achse

$$\mathbf{H}_K = (8\pi/3) \cdot (R^3/r^3) \cdot \chi_{\text{cgs}} \cdot \mathbf{H}_a \quad (29)$$

Im SI-System muß man für die Magnetisierung \mathbf{M} in Gleichung (25) den Wert einsetzen, der in Gleichung (14) formuliert ist

$$\{\mathbf{M}\} \text{ A m}^{-1} = \chi_{\text{SI}}/(4\pi \cdot 100) \cdot \{\mathbf{B}\} \text{ nT}, \quad (14)$$

und erhält

cgs-System

SI

$$\begin{aligned}
 \{\mathbf{B}_K\} \text{ nT} &= (8\pi/3) \cdot (R^3/r^3) \\
 &\cdot (\chi_{\text{SI}} \cdot 100)/(4\pi \cdot 100) \cdot \{\mathbf{B}_a\} \text{ nT} \\
 \{\mathbf{B}_K\} \text{ nT} &= (8\pi/3) \cdot (R^3/r^3) \\
 &\cdot \chi_{\text{SI}}/4\pi \cdot \{\mathbf{B}_a\} \text{ nT.}
 \end{aligned} \tag{30}$$

Man hat also – wie nicht anders zu erwarten – nur das H -Feld der Kugel und das äußere H -Feld durch die magnetische Induktion der Kugel und die äußere magnetische Induktion zu ersetzen und statt χ_{cgs} $\chi_{\text{SI}}/4\pi$ zu schreiben.

Die Formeln für die übrigen Körper lauten:

Feld des Zylinders:

$$\begin{aligned}
 Z_K &= (2\chi FH'_a/r^2) \cos(2\rho - \vartheta) & Z_K &= (\chi_{\text{SI}}/2\pi) \cdot (F \cdot B'_a/r^2) \\
 & & & \cdot \cos(2\rho - \vartheta)
 \end{aligned} \tag{31}$$

χ, χ_{SI} : Suszeptibilität des Zylinders

F : Querschnittsfläche des Zylinders

ρ : Winkel des Fahrstrahls von der Zylinderachse zum Aufpunkt

ϑ : Winkel der Feldkomponente H'_a, B'_a in der Ebene senkrecht zur Zylinderachse, gemessen vom Lot.

Feld der dünnen Platte:

$$\begin{aligned}
 Z_K &= (2\chi \cdot H'_a \cdot b/r) \cdot \cos(\rho - \beta) & Z_K &= (\chi_{\text{SI}} \cdot B'_a \cdot b/(2\pi r)) \\
 & & & \cdot \cos(\rho - \beta)
 \end{aligned} \tag{32}$$

b : Mächtigkeit der Platte

β : Winkel zwischen der Richtung des in die Ebene senkrecht zum Streichen der Platte projizierten äußeren Feldes H'_a, B'_a und dem Einfallen der Platte, sonstige Symbole wie bei Gleichung (31).

In den Formeln für die Felder von anderen einfachen Körpern ist stets die Magnetisierung J (in G) durch $100 \cdot M$ (in A m^{-1}) bzw. die Suszeptibilität χ durch $\chi_{\text{SI}}/4\pi$ zu ersetzen.

2.5.5. Das Drehmoment eines Dipols im Feld. Im cgs-System multipliziert man das H -Feld mit dem Dipolmoment vektoriell und erhält das Drehmoment \mathbf{D}

$$\{\mathbf{H}\} \text{ Oe} \times \{\mathbf{m}\} \cdot \Gamma \text{ cm}^3 = \{\mathbf{D}\} \text{ dyn} \cdot \text{cm.} \tag{33}$$

Im SI-System hat man das B -Feld mit dem Dipolmoment vektoriell zu multiplizieren und erhält das Drehmoment in $\text{N} \cdot \text{m}$

$$\{\mathbf{B}\} \text{ T} \times \{\mathbf{m}\}_{\text{SI}} \text{ A m}^2 = \{\mathbf{D}\}_{\text{SI}} \text{ N} \cdot \text{m.} \tag{34}$$

Man überzeugt sich leicht, daß die Dimensionen im SI-System zusammenpassen. Mit $1 \text{ T} = 1 \text{ V} \cdot \text{sec} \cdot \text{m}^{-2}$ hat man auf der linken Seite

$$\text{V} \cdot \text{sec} \cdot \text{m}^{-2} \cdot \text{A} \cdot \text{m}^2 = \text{W} \cdot \text{sec} = \text{N} \cdot \text{m} \cdot \text{sec}^{-1} \cdot \text{sec} = \text{N m.}$$

2.6. Zusammenfassung für die Anwendung

2.6.1. *Einheiten.* Für die am Anfang genannten vier Größen sind also im SI-System in Verbindung mit dem Beschluß der IAGA folgende Einheiten zu verwenden:

I. Für das Meßergebnis von Geländemessungen: T, nT.

II. Für die Magnetisierung von Gesteinen:

$$\text{A m}^{-1}, \quad \text{mA m}^{-1}.$$

III. Für die Größe, die in Probekörpern eine Magnetisierung erzeugt, z.B. bei Bestimmungen der Suszeptibilität und bei Abmagnetisierungen:

$$\text{A m}^{-1}.$$

IVa. Für die Proportionalitätskonstante zwischen III. und der induzierten Magnetisierung:

$$1 \text{ (dimensionslos).}$$

IVb. Falls man die induzierte Magnetisierung zur magnetischen Induktion proportional setzen will, ist die betreffende Konstante χ_{SI}/μ_0 und hat dementsprechend die Dimension:

$$\text{A m}^{-1} \text{ T}^{-1}.$$

2.6.2. *Umrechnungsfaktoren für die Zahlenwerte beim Übergang vom cgs-System zum SI.* In der folgenden Tabelle sind die Faktoren aufgelistet, mit denen man die Zahlenwerte, die bei Verwendung der cgs-Einheiten auftreten, multiplizieren muß, um die Zahlenwerte zu erhalten, die bei den entsprechenden SI-Einheiten stehen müssen.

Größe, Nr. der entsprechenden Gleichung	Aus dem Zahlenwert bei Verwendung der cgs-Einheit	erhält man durch Multiplikation mit dem Faktor	den Zahlenwert bei Verwendung der SI-Einheit
1 Magnetfeld (2)	Oe	$10^3/4\pi = 79,57747$	A m^{-1}
2 Magnetische Induktion (3), (4)	G γ	10^{-4} 1	T nT
3 Magnetisierung (8)	G γ	10^3 $\left\{ \begin{array}{l} 10^{-2} \\ 10 \end{array} \right.$	A m^{-1} A m^{-1} mA m^{-1}
4 Suszeptibilität (10)	G/Oe	$4\pi = 12,56637$	$\text{A m}^{-1}/(\text{A m}^{-1})$
5 Magnetisierung hervor- gerufen durch magnetische Induktion	$\left. \begin{array}{l} \text{G/G} \\ \gamma/\gamma \end{array} \right\}$	10^{-2}	$\text{A m}^{-1}/\text{nT}$
6 Magnetisches Dipolmoment (17)	G cm^3	10^{-3}	A m^2
7 Magnetische Polstärke (18)	G cm^2	10^{-1}	A m

Bei den Zeilen 3, 4 und 5 ist zu beachten, daß man hier von der magnetischen Polarisation J im cgs-System zur Magnetisierung M im SI übergeht.

3. Danksagung

Wertvolle Hinweise zu diesem Thema erhielt ich von den Herren Professor Dr. G. Angenheister und Professor Dr. O. Rosenbach. Die Herren Dr. W. Bosum, Dr. G. Brass und Dr. J. Pohl haben in mündlichen Diskussionen den Gang der Arbeit gefördert. Ihnen allen gilt mein herzlicher Dank.

Literatur

- Kohlrausch, F.: Praktische Physik, Bd. 1, Leipzig (Teubner), 1943
Lowes, F.J.: Do Magnetometers Measure B or H? – Geophys. J. **37**, 151–155 (1974)
Melchior, P. (Hrsg.): I.U.G.G. Chronicle no. 96 – Juin 1974, Paris (IUGG Publ. Office), 1974
Sommerfeld, A.: Vorlesungen über Theoretische Physik, Wiesbaden (Dieterich), 1948
Stille, U.: Messen und Rechnen in der Physik, Braunschweig (Friedr. Vieweg & Sohn), 1955
Deutsche Normen (Bentz-Vertrieb; Berlin, Köln, Frankfurt a.M.) DIN 1313 Schreibweise physikalische Gleichungen in Naturwissenschaft und Technik

Eingegangen am 16. Dezember 1976; Revidierte Fassung am 14. Oktober 1977

Original Investigations

The Romanian Earthquake of March 4, 1977

I. Rupture Process Inferred From Fault-Plane Solution and Multiple-Event Analysis*

G. Müller, K.-P. Bonjer, H. Stöckl, and D. Enescu¹

Geophysical Institute, University of Karlsruhe,
Hertzstr. 16, D-7500 Karlsruhe, Federal Republic of Germany

¹ Center of the Physics of the Earth and Seismology, Com. Magurele,
Platforma Magurele, Bucharest, Sect. 6, Romania

Abstract. The Romanian earthquake of March 4, 1977, was a multiple event, consisting of a foreshock and at least 3 main shocks. A fault-plane solution is given for the first main shock. It is of thrust type and similar to the solution for the earthquake of November 10, 1940. The locations of the main shocks relative to the foreshock are determined by the master-event technique. Rupture propagated mainly towards SW. The third main shock, which was the strongest shock of the earthquake, occurred 19 s after and at a horizontal distance of 62 km from the foreshock. This agrees well with the reported distribution of intensities and damages and with the aftershock distribution. P-wave polarities for the third main shock are opposite to those for the first and second main shock. This can be explained by (1) strong bending of the rupture surface, (2) reversal of the motions on the rupture plane due to a strongly inhomogeneous tectonic stress field, or (3) abrupt termination of rupture producing strong stopping signals. The third explanation appears most plausible. The rupture plane dips about NW with a dip angle of 70°, and the apparent average rupture velocity is close to the S-wave velocity.

Key words: Earthquakes – Fault-plane solutions – Rupture Process.

Introduction

The earthquakes of intermediate depth in the Vrancea region of Romania form an isolated cluster of events, similar to the clusters beneath the Hindukush and beneath Bucaramanga, Colombia. The distribution of epicenters and depths of the Vrancea earthquakes has been studied extensively (see, e.g., Karnik, 1969; and Iosif and Iosif, 1975), and a large number of fault-plane solutions have been determined (Constantinescu and Enescu, 1964; Constantinescu et al., 1966; Ritsema, 1969, 1974; Radu, 1974). So far, however, no clear picture of the

* Paper of the Romanian-German Seismological Working Group which was formed after the earthquake of March 4 and consists of scientists of the above-mentioned institutes and the Institute of Hydroelectric Studies and Design at Bucharest. Contribution No. 149, Geophysical Institute, University of Karlsruhe

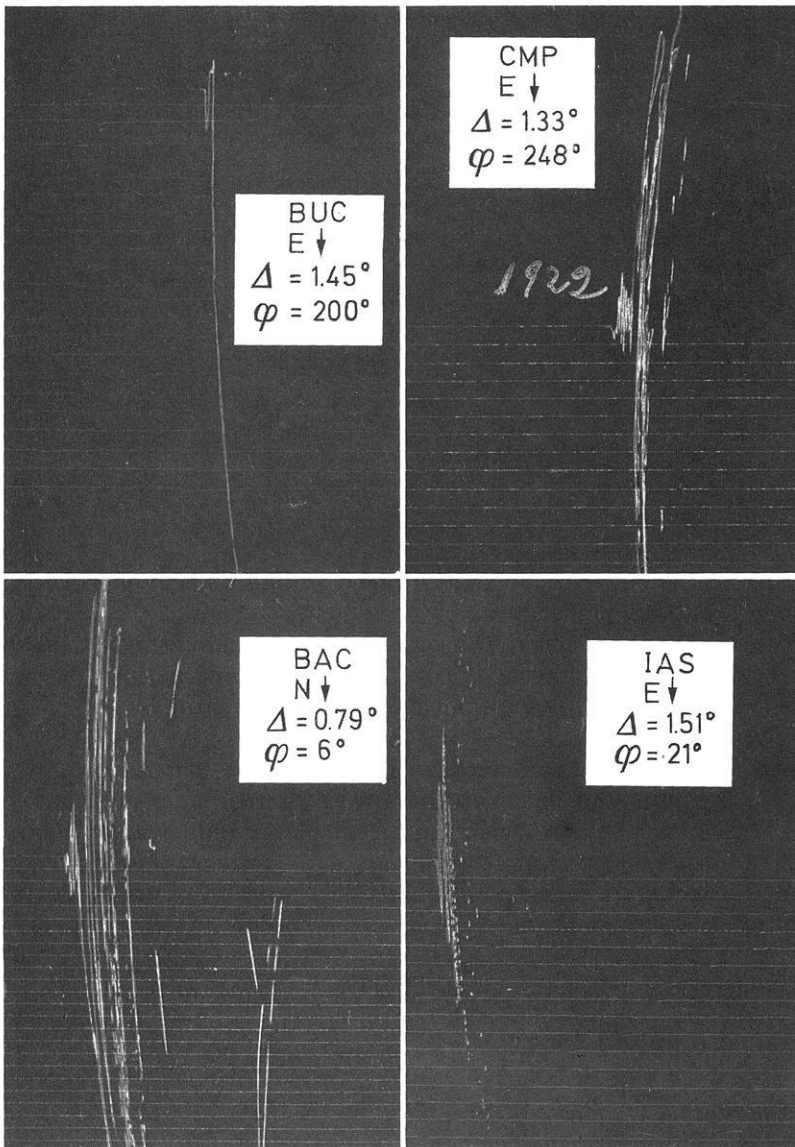


Fig. 1. Mainka pendulum seismograms from the Romanian stations BUC, CMP, BAC and IAS, showing the P-wave arrivals of the foreshock and shock 1. Δ is epicentral distance and φ azimuth. The time scales are different

tectonic causes of these earthquakes has resulted. The current view is that they are produced by underthrusting motions along a fault zone which dips steeply about WNW. In spite of the small dimensions of the earthquake zone and the complicated geometry of the Carpathians with their sharp bend in the Vrancea region simple plate-tectonics concepts have tentatively been used for expla-

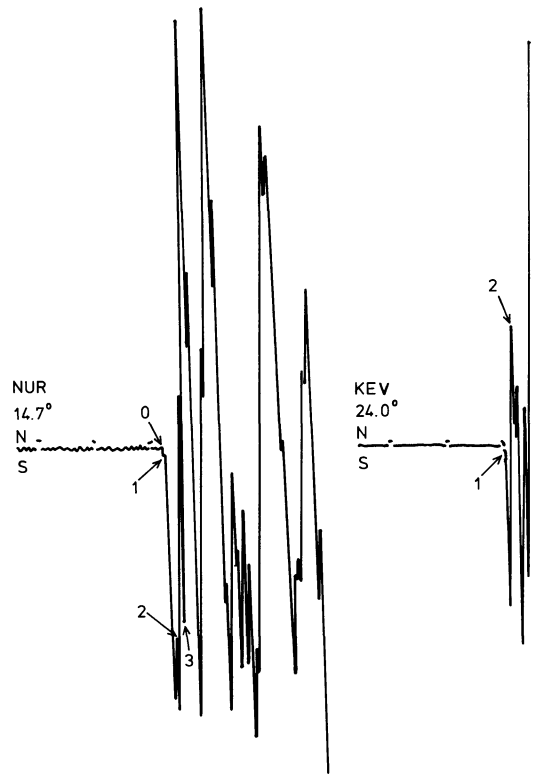


Fig. 2. Long-period WWNSS seismograms containing P-wave arrivals (copies drawn by hand). Numbers below station codes are epicentral distances. Arrows indicate P phases for the different shocks (0=foreshock, 1, 2, 3=shock 1, 2, 3)

nation, leading to the idea that a slab-like continuation of the Black-Sea plate is subducted under the Eurasian plate (Roman, 1971; McKenzie, 1972; Constantinescu et al., 1973; Radu, 1974; Iosif and Iosif, 1975). Further observational studies are necessary to substantiate or change these ideas. Among them investigations of the strong earthquake of March 4, 1977, will certainly be of special importance. Such studies can also help to estimate the seismic risk in the rather densely populated area to the SW of Vrancea, including Bucharest.

In this paper, we investigate the focal process of the earthquake of March 4, 1977. First we describe the data which show that the earthquake was a multiple rupture, consisting of a foreshock and at least 3 main shocks. (These main shocks will be called shock 1, 2 and 3, respectively, in the following.) Then the fault-plane solution for shock 1 will be given, and the nature of shock 3 will be discussed. In a further section, the master-event technique is applied to locate the 3 main shocks relative to the foreshock. Finally, a description in time and space of the rupture process is given for the first 20–25 s, including the selection of the rupture plane from the nodal planes of the fault-plane solution, a comparison with reports on the distribution of damages and intensities in the epicentral region, and a comparison with the area of aftershocks of March 1977.

Data and Identification of Shocks

We have used the following data: (1) Mainka pendulum records on smoked paper of the Romanian stations BUC (Bucharest), CMP (Campulung), BAC (Bacau) and IAS (Iasi). Seismogram examples are given in Figure 1. They clearly show the foreshock and shock 1 and were used for the relative localisation of these shocks.

(2) Long-period seismograms from about 60 stations mainly in the Worldwide Network of Standardized Seismographs (WWNSS). They were used for the fault-plane solution of shock 1 and for the relative localisation of shocks 2 and 3 with respect to shock 1. Seismogram examples are shown in Figures 2–4.

(3) Broadband seismograms from the digitally recording station GRF (Gräfenberg, F.R. Germany). The seismometers of this station are Sprengnether High Performance S-5100 with a natural period of 20 s. Digital simulation by recursive filtering produced the broadband seismogram for ground velocity, corresponding to a natural period of 100 s, and the WWNSS record shown in Figure 5. These seismograms played a key role in the identification of shock 3.

The foreshock and shocks 1 and 2 are easily identified, as the reader can verify by himself from Figures 1–5 where all stations are shown that have been

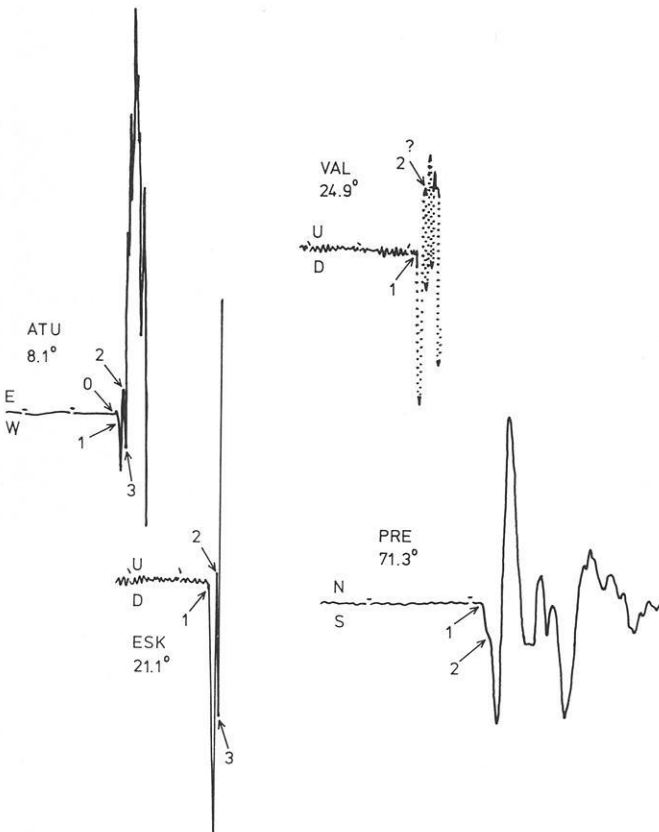


Fig. 3. Same as Figure 2 for 4 more WWNSS stations

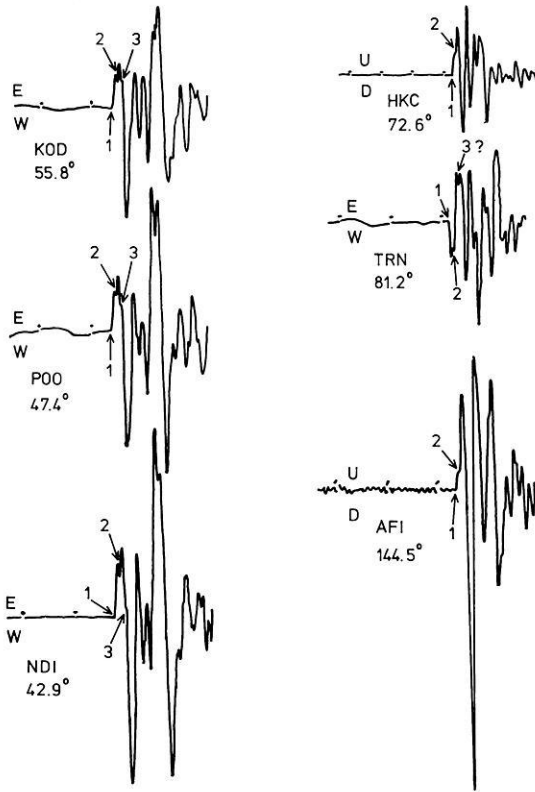


Fig. 4. Same as Figure 2 for 6 more WWNSS stations

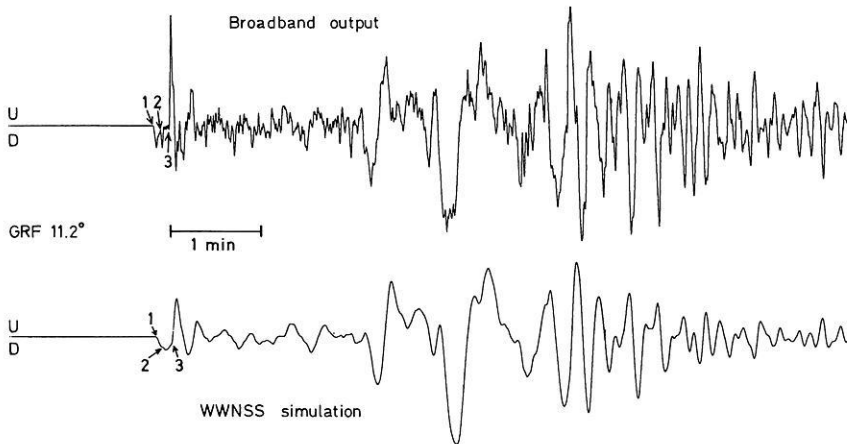


Fig. 5. Vertical-component seismograms of the digitally recording station GRF (digital simulation of broadband ground velocity and of a WWNSS record; courtesy of Dr. Dieter Seidl, Seismologisches Zentralobservatorium Gräfenberg). Meaning of arrows as in Figure 2. Magnified versions of the broadband record also show the foreshock

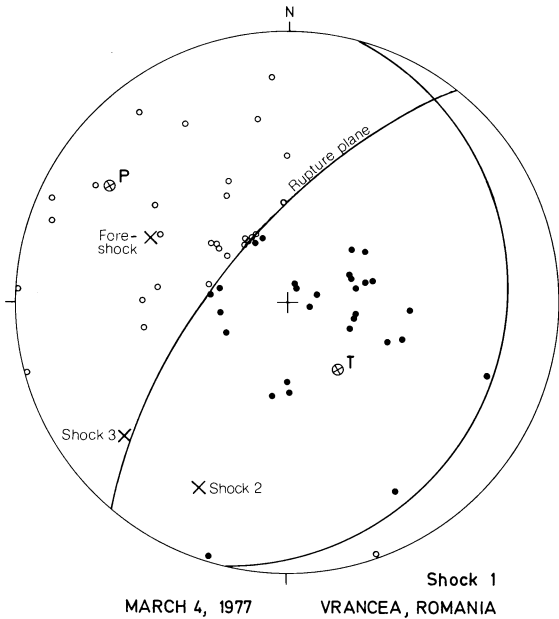


Fig. 6. Fault-plane solution for shock 1. Equal-area projection of the lower focal hemisphere. Open (closed) circles denote first P-wave motions towards (away from) the focus of shock 1. The P-wave velocity at the focus is assumed to be 8.3 km/s. The compressional axis is labelled *P*, the tensional axis *T*. The thick lines are the nodal planes. The symbols \times give the directions from shock 1 to the foreshock, shock 2 and shock 3

used in the multiple-event analysis. The situation is not that obvious with shock 3. At first the corresponding arrival in the broadband record of GRF (upper trace in Fig. 5) was interpreted as a reflection from the earth's surface of the type PP or pP because of its opposite sign, compared with the arrivals due to shocks 1 and 2. This interpretation, however, had to be abandoned since for a focal depth of about 100 km PP and pP are observed only close to and beyond the epicentral distance 18° where the cusp of their traveltimes curves is located. At GRF (distance 11.2°) one would at most expect a diffracted phase as a backward continuation of PP and pP with corresponding weak amplitudes and emergent onset; both is in disagreement with the observation. Another argument is that in the case of a surface reflection (or a reflection from an interface inside the earth such as the Moho) a second pulse of about the same amplitude and polarity, corresponding to shock 2, should be observed; however, such a pulse is not seen. The interpretation of arrival 3 at GRF as the surface reflection sP has to be rejected because sP would arrive 10 to 15 s later. The only remaining hypothesis is that of a third main shock, much stronger than shocks 1 and 2 and producing P waves of opposite polarity. If this hypothesis is correct, this shock should also be visible at other stations. Since these are WWNSS stations, we used the WWNSS simulation of GRF in order to find the characteristics of the beginning of this shock in WWNSS records. They are (see Fig. 5) a clear change in slope with a strong excursion afterwards whose direction is opposite to that of shock 1. With these guidelines it was possible to find the beginning of shock 3 at a number of stations which is sufficient for application of the master-event technique. At other stations only the strong excursion is visible, but its onset cannot be determined (see, e.g., the seismogram for PRE in Fig. 3).

The P-wavegroup in the broadband record of GRF in Figure 5 contains some more peaks after the peak of shock 3. They could correspond to further shocks or represent multiple reflections from shocks 1–3 which begin to build up the leaking mode PL in the waveguide, formed by the crust and the lower lithosphere. Thus, our investigation possibly covers only part of the timespan during which rupturing took place. We are, however, sure that it includes the strongest shock of the earthquake, namely shock 3.

Fault-Plane Solution of Shock 1

The fault-plane solution of shock 1 is given in Figure 6. Its nodal planes could be determined from the polarity distribution of P waves alone. The nodal plane which dips steeply towards NW is very well determined since it runs through North and Middle America where the station density is high. The other nodal plane can also be shifted only very little because of the 3 compressions close to it (stations ATU, JER and TAB). The parameters of the fault-plane solution are:

	Azimuth (deg)	Dip angle (deg)
Pole of first nodal plane	130	20
Pole of second nodal plane	287	68
<i>P</i> -axis	303	23
<i>T</i> -axis	144	65

This solution represents essentially a thrust-type mechanism, in agreement with the mechanisms of other earthquakes of intermediate depth in the Vrancea zone. The similarity with the fault-plane solution of the strong earthquake of November 10, 1940, is remarkable (Constantinescu and Enescu, 1964, Table 1). From the multiple-event analysis, given in a later section, we identify the first nodal plane as rupture plane. In this case the slip vector of the underthrusting block has an azimuth of 287° and a dip angle of 68° .

Nature of Shock 3

P-wave polarity diagrams for shocks 2 and 3 are given in Figure 7. Whereas the polarities of shock 2 agree with those of shock 1, those of shock 3 are reversed. There are 3 different explanations of this reversal: (1) The rupture surface bent abruptly at the origin time of shock 3 and was roughly horizontal afterwards. Motions below this part of the rupture surface were from SE towards NW. However, no indication for such a bending is found in the aftershock distribution.

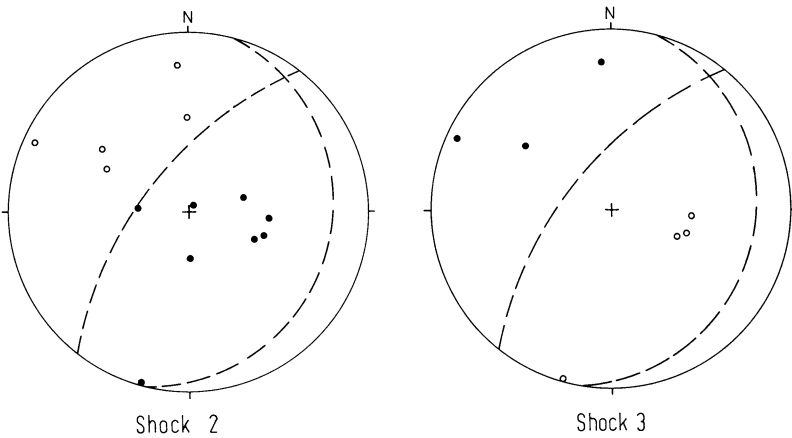


Fig. 7. P-wave polarity distributions for shocks 2 and 3. Open and closed circles have the same meaning as in Figure 6. The dashed lines are the nodal planes of the fault-plane solution of shock 1. In the diagram for shock 3, only those stations are included where the onset of the corresponding P-wave is visible

(2) The rupture surface remained essentially plane, but the motions on it reversed sign, i.e., after the origin time of shock 3 they were upwards on the SE block of the rupture plane as opposed to downwards before. The cause of such a reversal would have been a strongly inhomogeneous stress field in the focal region prior to the earthquake. However, we can offer no idea about the spatial character of the stress inhomogeneity and its generation.

(3) Shock 3 was the abrupt termination of rupture, producing a strong stopping signal. Stöckl (1977) has shown by numerical calculations for idealized stress-relaxation earthquake models that stopping signals can be as strong as and even stronger than the phases from the initiation of rupture. Furthermore, from the ground-velocity seismogram of GRF in Figure 5 we can approximately derive the acceleration close to the foci of the 3 shocks by applying the rule (which is strictly correct for point sources) that a field quantity in the far field is proportional to the time derivative of the same quantity in the near field. Thus, the near-field acceleration is approximately proportional to the far-field ground velocity, and the initial parts of the broadband record of GRF give a rough idea of the accelerations in the source region. We derive 2 acceleration pulses, corresponding to shocks 1 and 2, followed by a strong pulse of opposite sign which corresponds to shock 3. A plausible cause of this deceleration is abrupt termination of rupture or at least of its main part.

The first 2 models require more extreme assumptions than the third model. Even more important, they imply that the main shocks were complete and separate events for which only the starting signals can be seen, at least in the case of shocks 1 and 2. However, it seems more plausible to consider the 3 shocks as prominent episodes during one and the same rupture process. Therefore, we prefer the third explanation of shock 3.

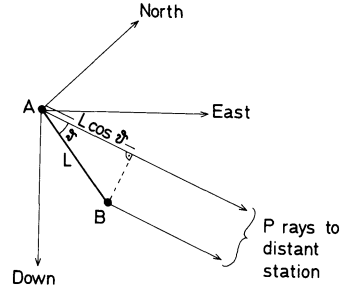


Fig. 8. Sketch of 2 foci, A and B, whose relative location and origin-time difference are determined by the master-event technique

Multiple-Event Analysis

The master-event technique has been applied for localisation of the 3 main shocks relative to the foreshock. For the latter we have taken the coordinates determined by the Centre Séismologique Européo-Méditerranéen (CSEM) soon after the earthquake, assuming that the P-wave recordings reported correspond to the foreshock:

Latitude = 45.78 N Longitude = 26.78 E Depth = 93 km.

A later determination by CSEM with stations at distances less than 11° and our own determinations show that the epicentral coordinates are probably correct within 10–20km, but that the depth can extend to almost 120km. A depth of 110km is suggested by a pP–P time of 27s at OGD (distance 68.6°), but only under the unproven assumption that pP is due to the foreshock and not due to shock 1. Thus, with current knowledge the foreshock depth can be anywhere between 90 and 120km. Several tests showed that the remaining uncertainties in the foreshock coordinates have only very little influence on the results of the multiple-event analysis. If the foreshock is moved, the 3 main shocks practically move in the same way.

The master-event technique (see Fig. 8) assumes a reference focus A and a second focus B at the distance L from A. The time difference between the P-wave arrivals from these foci at a sufficiently distant station is

$$T = \tau - \frac{L}{\alpha} \cos \vartheta, \tag{1}$$

where τ is the difference in origin time of the 2 shocks, α the P-wave velocity in the focal region (in the present case 8.3 km/s), and ϑ the angle between the direction from A to B and the direction of the P-wave rays. Equation (1) is a linear relation between T and $\cos \vartheta$ whose coefficients τ and L/α can be determined from observations at N stations by the method of least squares. The quality of the linear approximation is best judged from the residual

$$R = \left[\frac{1}{N} \sum_{i=1}^N (T_o^{(i)} - T_c^{(c)})^2 \right]^{1/2},$$

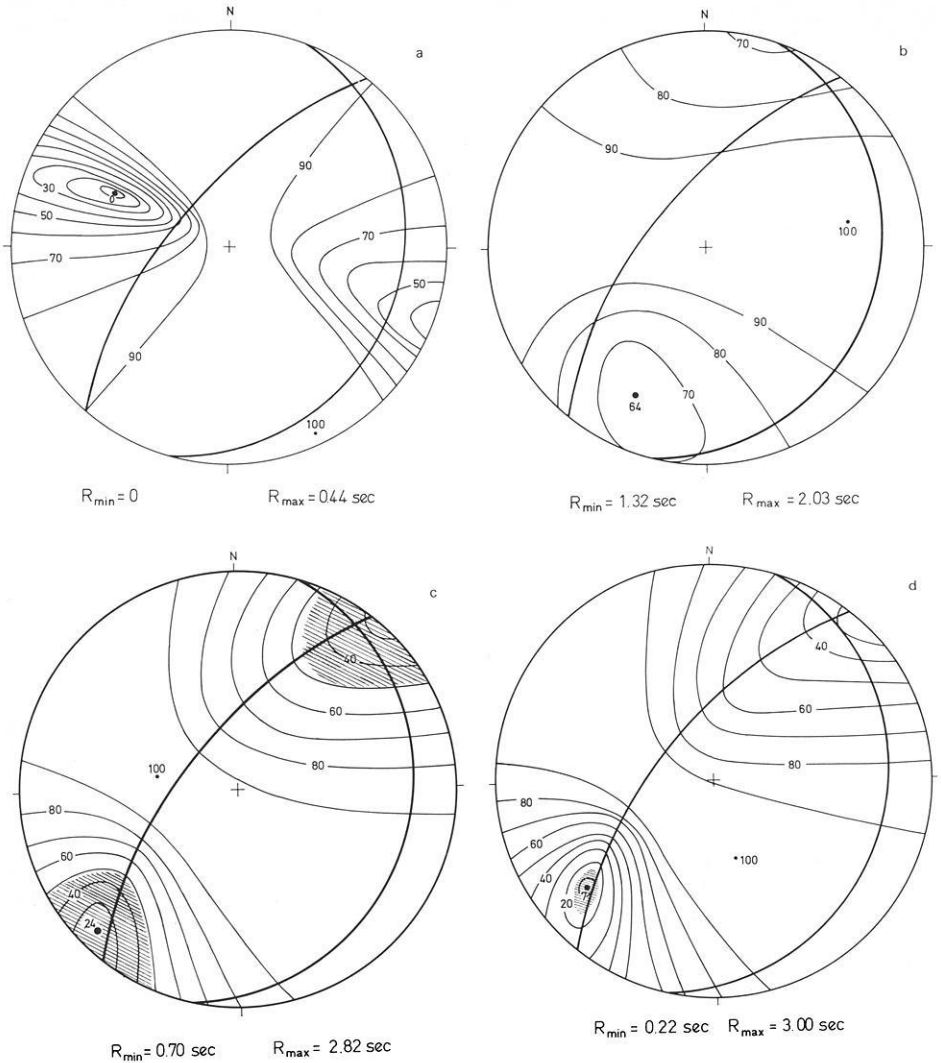


Fig. 9a–d. Plots of residual R (normalized to maximum value 100), superposed on the fault-plane solution of shock 1, for **a** the foreshock, **b** shock 2, **c** shock 3 (including station TRN), and **d** shock 3 (without TRN). The most probable direction from shock 1 to the respective shock corresponds to the minimum of R . The shaded areas, defined by $R \leq 2R_{\min}$, are subjective estimates of the uncertainties in these directions. In the case of **c** the area extends to the upper focal hemisphere and is projected on the lower hemisphere through the center

where $T_o^{(i)}$ is the observed time difference at the i -th station and $T_c^{(i)}$ the time difference computed according to (1). R is determined as a function of the direction from A to B, and the direction with minimum value of R is chosen as the true direction. Plotting R on the focal sphere of shock A allows to assess qualitatively how well this direction is determined. (Actually, a hemisphere is sufficient because of the symmetry properties of R .) From the coefficients of the

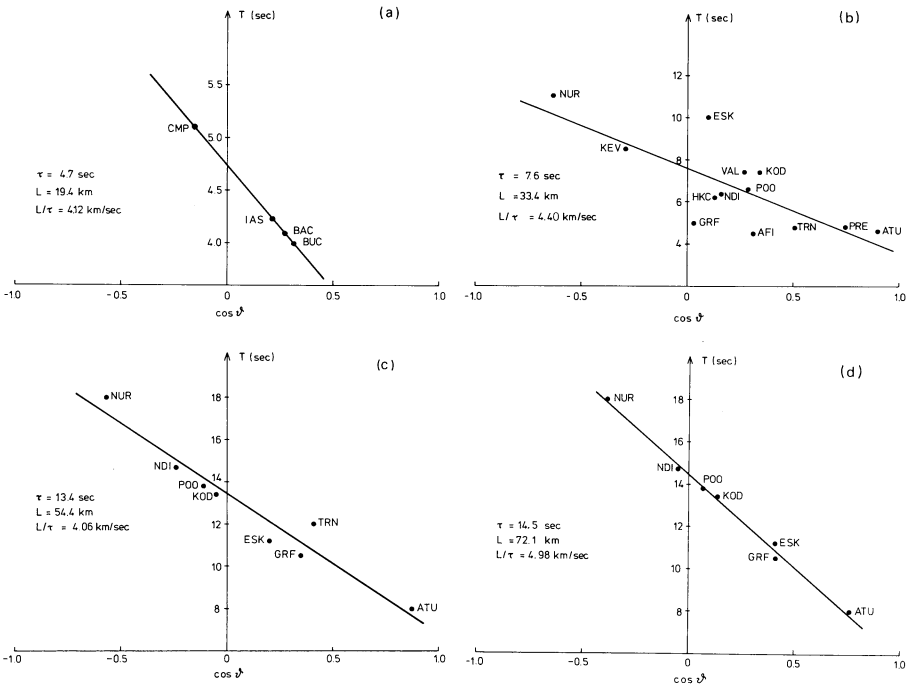


Fig. 10a–d. Time difference T versus $\cos \theta$ for the pairs **a** foreshock – shock 1, **b** shock 1 – shock 2, **c** shock 1 – shock 3 (including station TRN), and **d** shock 1 – shock 3 (without TRN). Dots are observed time differences and the straight lines least-squares approximations for the optimum orientation of the 2 shocks with respect to each other. τ is origin-time difference, L distance between the 2 shocks, and L/τ apparent average rupture velocity

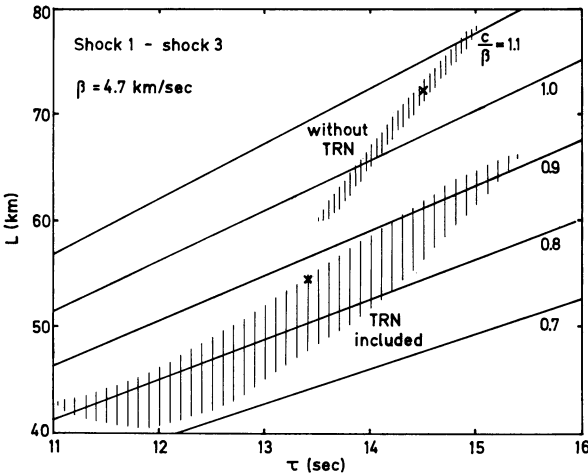
least-squares straight line (1) at the minimum of R the time difference τ and the distance L of the 2 shocks follow.

The results of the master-event technique, applied to the pairs foreshock – shock 1, shock 1 – shock 2 and shock 1 – shock 3, are shown in Figure 9 (plots of R on the lower focal hemisphere of shock 1), Figure 10 (diagrams for T versus $\cos \theta$), Table 1 (coordinates of foreshock and main shocks) and Figure 12 (epicenter map). Some details of the derivation and a discussion of these results are given in the following.

A first attempt to locate shock 1 relative to the foreshock was made with all stations where the foreshock could be identified. Besides the 4 Romanian stations BUC, CMP, BAC and IAS, whose seismograms are shown in Figure 1, 7 more stations were used, giving a rather good coverage of azimuths. However, the data came from 4 different types of instruments: (mechanical) Mainka pendulums, short and long-period WWNSS instruments, and a broadband seismograph. This heterogeneity and the difficulties in reading the time differences from the long-period WWNSS records probably are the reason why no meaningful result was obtained: the optimum solution had a minimum value of R which was 95% of the maximum. We therefore had to restrict the data set and did this by taking only the 4 Romanian stations with identical instruments

Table 1. Coordinates of the foreshock and the main shocks of the Romanian earthquake of March 4, 1977 (foreshock coordinates according to CSEM)

Event	Latitude (deg)	Longitude (deg)	Depth (km)	Origin time (GMT)	Time difference with respect to foreshock (s)
Foreshock	45.78	26.78	93	19:21:56.2	0
Shock 1	45.72	26.94	79	19:22:00.9	4.7
Shock 2	45.48	26.78	93	19:22:08.5	12.3
Shock 3	45.34	26.30	109	19:22:15.4	19.2

**Fig. 11.** Uncertainties in L and τ for the pair shock 1–shock 3, corresponding to the assumed uncertainties in the direction from shock 1 to shock 3 (shaded areas in Fig. 9c and d). Crosses correspond to the most probable directions. Along the straight lines the ratio of apparent average rupture velocity, $c=L/\tau$, and S-wave velocity, β , is constant

which recorded the foreshock and shock 1 very clearly (Fig. 1). Time differences could be read with an accuracy of about ± 0.2 s. In the case of 4 stations an exact solution is obtained, i.e., the minimum value of R vanishes (Fig. 9a) and the T versus $\cos\theta$ relation is exactly linear (Fig. 10a). The time difference of shock 1 and the foreshock is 4.7s and the distance between them 19.4 km.

We mention in passing that the distance between the 2 shocks is sufficiently small, compared with the slant distances to the stations (130–200 km), such that the basic assumptions of the master-event technique are not yet violated. Furthermore, the results are influenced only very little by changing the upper-mantle P-wave velocity from our preferred value 8.3 km/s to 8.1 km/s, a value which is more compatible with the Herrin traveltime tables.

As Figure 9b shows, the minimum of R is rather broad for shock 2, and hence the direction from shock 1 to shock 2 is not as well determined as, for example, the direction to the foreshock. The time difference between shock 1 and shock 2 is 7.6s and the distance 33.4 km.

For shock 3 we have 2 solutions, one with the station TRN (Trinidad) included in the analysis and one without this station (Figs. 9 and 10, c and d). In the first case, the arrival labelled 3 in the seismogram of TRN (Fig. 4) is

interpreted as being due to shock 3. In the second case we assume that it is due to a later shock and that the P-wave from shock 3 arrives somewhere along the preceding steep pulse flank, similar as in all other seismograms used for shock 3, but without visible onset. We prefer the second interpretation which gives a very well determined direction to shock 3. The corresponding time difference between shock 1 and shock 3 is 14.5 s and the distance 72.1 km. Rough estimates of the uncertainties of these quantities can be taken from Figure 11. For this figure we have considered all those directions from shock 1 to shock 3 for which $R \leq 2R_{\min}$ (shaded areas in Fig. 9c and d). The representation chosen is similar to the one used by Strelitz (1975).

Rupture Process

From the distribution of the epicenters of foreshock and main shocks in Figure 12 we derive as main feature of the rupture process the propagation from the region of the foreshock and shock 1 towards SW, leading to the severest shock 19 s after and at a horizontal distance of 62 km from the foreshock. This result is in good agreement with the fact that the zone of greatest intensities and damages extended to the SW of the Vrancea region, with only little damages to the NE. This fact had puzzled seismologists soon after the earthquake, since it differs in this respect from the earthquake of November 10, 1940.

As another result, Figure 12 shows that the rupture zone and the area, covered by the epicenters of located aftershocks, partly overlap. Most aftershocks in the region of overlap have similar depths as foreshock and main shocks. The aftershocks south and southeast of the rupture zone are shallower.

The rupture plane of the earthquake can be selected between the nodal planes of the fault-plane solution of shock 1 by comparison with the directions to the foreshock and shocks 2 and 3 (Fig. 6). Shock 3 whose direction is most accurate is located very close and the foreshock rather close to the steeply dipping (first) nodal plane. Shock 2 which is least well determined is located halfway in between the 2 nodal planes. Taken together, these results point to the first nodal plane as the rupture plane.

From the fault-plane solution and the results of the multiple-event analysis we arrive at the following more detailed description in time and space of the rupture process during the first 20–25 s of the earthquake. Rupture started at the focus of the foreshock at a depth of 93 km and in an initial weak phase spread mainly E and S with an apparent average rupture velocity of 4.12 km/s. Rupture propagated uphill along the rupture plane towards ESE, and after 4.7 s it reached the focus of shock 1 at a depth of 79 km. In the neighborhood of this focus the motions on the rupture plane were strongly accelerated, leading to efficient radiation of seismic waves. We consider this focus as the starting point of the main phase of rupture; hence, the origin-time differences and rupture velocities for shocks 2 and 3, as given in the following, refer to this point. From shock 1 the rupture propagated towards SW and obliquely downhill along the rupture plane, the motions being of underthrust type. The focus of shock 2 at a depth of 93 km was reached after 7.6 s, corresponding to an apparent average

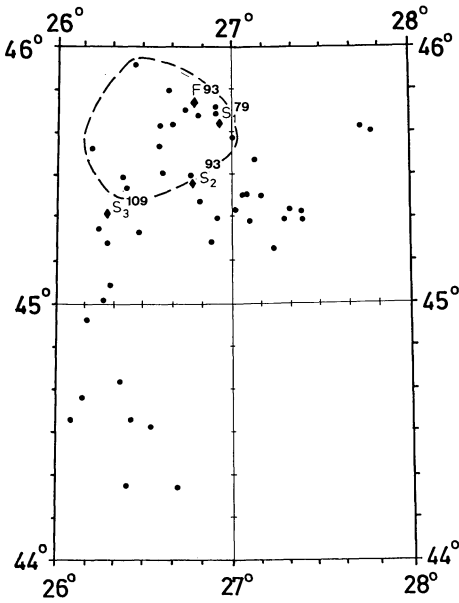


Fig. 12. Epicenter map of foreshock (F), main shocks (S_1 , S_2 , S_3) and aftershocks during March 1977 (dots). Numbers are focal depths in km. The dashed line separates aftershocks with depths greater than 70 km from shallower aftershocks (depths less than 40 km). There were a few shallow aftershocks within the dashed line, but they could not be located reliably

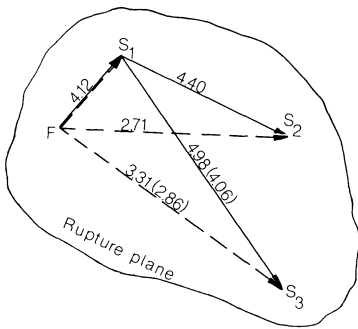


Fig. 13. Apparent average rupture velocities (in km/s) between the foreshock (F) and the main shocks (S_1 , S_2 , S_3). Solid arrows correspond to a rupture model in which S_1 is triggered by F and S_2 and S_3 by S_1 . Dashed arrows illustrate a model in which all main shocks are triggered by F . The rupture velocities in brackets are for the second solution of the master-event technique for shock 3 (Figs. 9c and 10c). The figure is not drawn to scale

rupture velocity of 4.40 km/s. Close to this focus the underthrusting motions were accelerated again. The focus of shock 3 at the depth 109 km was reached after 14.5 s which means an apparent average rupture velocity of 4.98 km/s. In the region of this point rupture stopped quite abruptly, and the moving rock masses were strongly decelerated. Again, this was connected with efficient radiation of seismic waves. The distribution of the epicenters of foreshock and main shocks in Figure 12 indicates that rupture propagation was essentially unilateral. Whether rupture continued on parts of the rupture plane after shock 3, could not be resolved.

Figure 13 shows the apparent average rupture velocities on a schematic view of the rupture plane from NW. The rupture model just described is represented by solid arrows. The apparent average rupture velocities are close to, in one case even larger than the S-wave velocity which in the focal zone is probably between 4.5 and 4.8 km/s. An alternative model, in which the foreshock triggers not only shock 1 but also shock 2 and shock 3, is indicated by dashed arrows. The corresponding apparent average rupture velocities are lower than those for our preferred model. The uncertainties in L and τ normally imply relatively large uncertainties in the apparent average rupture velocity L/τ . Even for our best value, 4.98 km/s, the interval is from about 4.5 to 5.2 km/s, according to our subjective estimates (Fig. 11, shaded area labelled “without TRN”).

Conclusions

The Romanian earthquake of March 4, 1977, was a multiple event with gradually increasing energy release which culminated 19 s after the first rupture. Similar results have been reported in a few other cases (e.g. Wyss and Brune, 1967; Wu and Kanamori, 1973; Fukao and Furumoto, 1975; Chung and Kanamori, 1976; Furumoto, 1977), but they may actually be more common. Corresponding studies are greatly facilitated by broadband seismographs, as the seismogram examples for the station GRF in Figure 5 show.

Broadband data for other earthquakes probably will show whether our observation of a pronounced stopping phase is singular or not. The prevailing assumption that stopping phases are rarely seen may be biased by the lack in resolving power of currently used instruments such as WWNSS seismographs.

The cause of the abrupt termination of rupture is either a significant increase in strength of the rocks, such that they could not be broken, or a stress inhomogeneity. In both cases stresses have been left over after the earthquake close to the focus of shock 3. This may be significant for the future development of seismicity in Vrancea, especially if detailed intensity studies should confirm the first impression, that the rupture zone of the 1977 earthquake has moved towards SW with respect to the rupture zone of the 1940 earthquake.

Finally, our study confirms present assumptions about the stress field and the tectonically active fault system in the Vrancea zone. Therefore, it seems possible to apply plate-tectonics concepts to this region, but different tectonic models might explain these observations as well. The spatial distribution of aftershocks may give additional information on the tectonically significant structures. Detailed description of the recording of aftershocks with a network of fixed and mobile stations, their localisation and distribution will be given in a separate paper.

Acknowledgements. We have obtained seismogram copies of the following (mainly WWNSS) stations: ADE, AFI, ALQ, AQU, ATU, BAC, BKS, BLA, BOG, BUC, CMP, COL, COP, DAG, DBN, DUG, ESK, GDH, GOL, GRF, GRM, GSC, HFS, HKC, HNR, IAS, IST, JER, KEV, KOD, KON, KTG, LEM, LON, LPA, LPB, MAL, MAT, MSO, MUN, NDI, NUR, NWAQ, OGD, PDA, PMG, POO, PRE, PTO, RAB, RAR, SCP, SEO, SHA, SJG, STU, TAB, TRI, TRN, TUC, UPP, VAL, VIE, WIN. We are grateful to the directors and staff of these stations for their cooperation.

Special support from the computing center, University of Karlsruhe, is acknowledged. We thank Dieter Seidl (Seismologisches Zentralobservatorium Gräfenberg) for the broadband and WWNS simulations of station GRF which were of great importance for this work, and Günther Bock, Jürgen Fertig and Karl Fuchs for discussions and reading the manuscript.

References

- Chung, W.Y., Kanamori, H.: Source process and tectonic implications of the Spanish deep-focus earthquake of March 29, 1954. *Phys. Earth Planet. Inter.* **13**, 85–96, 1976
- Constantinescu, L., Cornea, I., Lazarescu, V.: An approach to the seismotectonics of the Romanian Eastern Carpathians. *Rev. Roum. Géol., Géophys. et Géogr., Sér. Géophys.* **17**, 133–143, 1973
- Constantinescu, L., Enescu, D.: Fault-plane solutions for some Roumanian earthquakes and their seismotectonic implications. *J. Geophys. Res.* **69**, 667–674, 1964
- Constantinescu, L., Ruprechtova, L., Enescu, D.: Mediterranean-Alpine earthquake mechanisms and their seismotectonic implications. *Geophys. J. R.A.S.* **10**, 347–368, 1966
- Fukao, Y., Furumoto, M.: Foreshocks and multiple shocks of large earthquakes. *Phys. Earth Planet. Inter.* **10**, 355–368, 1975
- Furumoto, M.: Spacio-temporal history of the deep Colombia earthquake of 1970. *Phys. Earth Planet. Inter.* **15**, 1–12, 1977
- Iosif, T., Iosif, S.: Some tectonic aspects of Vrancea region (Roumania). *Proc. XIVth Gen. Ass. Europ. Seism. Comm. at Trieste*, 417–426, 1975
- Karnik, V.: Seismicity of the European area, Part 1. D. Reidel Publ. Comp., Dordrecht-Holland, 364pp., 1969
- McKenzie, D.: Active tectonics of the Mediterranean region. *Geophys. J. R.A.S.* **30**, 109–185, 1972
- Radu, C.: Contribution à l'étude de la séismicité de la Roumanie et comparaison avec la séismicité du Bassin Méditerranéen et en particulier avec la séismicité du sud-est de la France. Thèse Dr. Sci., Université de Strasbourg, 472pp., 1974
- Ritsema, A.R.: Seismotectonic implications of a review of European earthquake mechanisms. *Geol. Rundschau* **59**, 37–55, 1969
- Ritsema, A.R.: The earthquake mechanisms of the Balkan region. UNDP Project REM/70/172, UNESCO, 1974
- Roman, C.: Plate tectonics in the Carpathians: a case in development. *Proc. XIIth Gen. Ass. Europ. Seism. Comm. at Luxembourg*, 37–40, 1971
- Stöckl, H.: Accelerograms calculated for stress-relaxation earthquake models. Paper at the IASPEI/IAVCEI General Assembly at Durham, August 9–19, 1977
- Strelitz, R.: The September 5, 1970 Sea of Okhotsk earthquake: a multiple event with evidence of triggering. *Geophys. Res. Lett.* **2**, 124–127, 1975
- Wu, F.T., Kanamori, H.: Source mechanism of February 4, 1965, Rat Island earthquake. *J. Geophys. Res.* **78**, 6082–6092, 1973
- Wyss, M., Brune, J.N.: The Alaska earthquake of 28 March 1964: a complex multiple rupture. *Bull. Seism. Soc. Am.* **57**, 1017–1023, 1967

Received September 28, 1977/Revised Version October 28, 1977

Interpretation of Wide-Angle Reflection Travel-Times in Realistic Crust-Mantle Structures

D. Bamford

Department of Geophysics, University of Edinburgh, James Clerk Maxwell Building,
Mayfield Road, Edinburgh EH9 3JZ, Great Britain

Abstract. A method for the interpretation of wide-angle reflection travel-times in laterally varying crust-mantle structures is formulated. A datum correction is first carried out by ray-tracing to remove the effects of refraction above the reflector. The resulting time-distance data may be then expressed in a form which permits, given multiple coverage of the sub-surface, the independent determination of velocity and reflector topography.

The method has been tested on model data and found to be effective.

Key words: Explosion seismology — Wide-angle reflections — Lateral variations.

1. Introduction

Wide-angle reflections (WAR) from intra- and sub-crustal horizons are now routinely observed in high-resolution explosion seismic studies. The review of such studies in central Europe, edited by Giese, Stein and Prodehl (1976), contains many excellent examples and indeed, in this author's experience (Bamford et al., 1976; Bamford, 1973, 1977), wide-angle reflections from the Moho ($P_M P$) are observed more consistently than the corresponding head-wave (P_n).

It is unfortunate therefore that the problem of the interpretation of WAR travel-times in realistic, that is laterally varying, structures has received relatively little attention. Apart from the various techniques used by Russian workers (e.g. Pavlenkova, 1973) and trial-and-error approaches based on ray-tracing (Červený et al., 1974; Clee et al., 1974), few methods are available, certainly nothing to compare with the time-term approach for the interpretation of *refraction* travel-times (Willmore and Bancroft, 1960; Bamford, 1971, 1973, 1976, 1977). In this paper I suggest a comparable technique for the interpretation of WAR travel-times.

2. WAR Time-Distance Relationships

WAR time-distance relationships become rather complex in realistic structures. The well known $T^2 - X^2$ relationship for reflections is strictly applicable only in the case of a single plane horizontal reflector with uniform velocity above. In a multi-

layer situation, refraction effects cause the $T^2 - X^2$ relationship to be approximately true only close to normal incidence. Towards critical and larger angles, the time-distance relationships for a multi-plane-horizontal-layer structure can be derived as follows (Brown, 1969; Robinson, 1970):

The subsurface is specified by n homogeneous layers (numbered 1 to n from the surface), the i^{th} layer having velocity v_i and thickness z_i . A ray leaves the surface at an angle θ_1 to the vertical, traverses the n layers, is reflected at the bottom of the n^{th} layer and re-traverses the n layers, eventually emerging at the surface at a distance $X(n, \theta_1)$ from its starting point, where

$$X(n, \theta_1) = 2 \sin \theta_1 \sum_{i=1}^n z_i v_i / S_i, \quad (1)$$

with a travel-time of $T(n, \theta_1)$ where

$$T(n, \theta_1) = 2 v_1 \sum_{i=1}^n z_i / (v_i S_i), \quad (2)$$

where

$$S_i = [v_1^2 - (v_i \sin \theta_1)^2]^{\frac{1}{2}}.$$

From (1) and (2), T and X are related by a series expansion, the first three terms of which are

$$T(\tau_0, X) \simeq \tau_0 [1 + \frac{1}{2}(X/\tau_0 \sqrt{v^2})^2 - \frac{1}{8}(v^4/v^2)(X/\tau_0 \sqrt{v^2})^4 + \text{etc.}]. \quad (3)$$

The m^{th} power of velocity is a function of τ_0 ($\equiv T(n, 0)$, the two-way normal incidence reflection time) given by

$$\overline{v^m(\tau_0)} = (2/\tau_0) \sum_{i=1}^n z_i v_i^{m-1} \quad (4)$$

the τ_0 notation having been omitted in (3) for simplicity.

In the simple $T^2 - X^2$ relationship, the term containing the velocity information (X^2/v^2) is *independent* from the τ_0^2 term and hence $1/v^2$ and τ_0^2 can be estimated independently from a $T^2 - X^2$ plot. In contrast, the coefficients of the series expansion for the simplest multi-layer case involve complex velocity/layer thickness relationships ((3) and (4)). If variable dip on interfaces and inhomogeneity within layers is considered, ray-path equations analogous to (1) and (2) can be generated but any resulting $T - X$ expansion would certainly *not* be suitable for independent determination of velocity and layer thickness.

In summary, the effects of refraction in a realistic multi-layer situation can be dealt with by ray-tracing (Červený et al., 1974). However these effects frustrate attempts to partition surface-to-surface WAR travel-times for the independent determination of velocities and depths as may be achieved in the simple $T^2 - X^2$ case.

This problem can be overcome by correcting the surface-to-surface times to a horizontal datum within the layer immediately above the reflector. $T^2 - X^2$ methods can then be applied to the datum-datum travel-times. In practice this

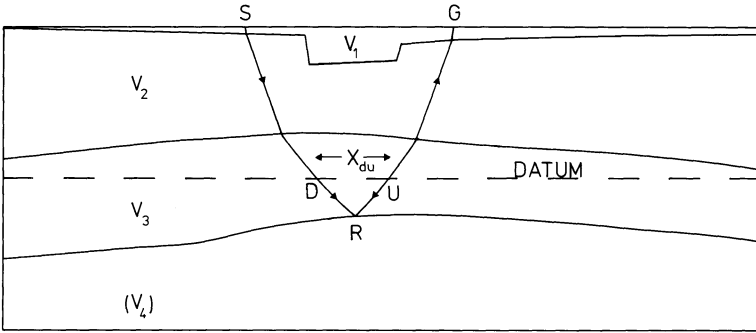


Fig. 1. Reflection, and datum correction, in a multi-layer structure

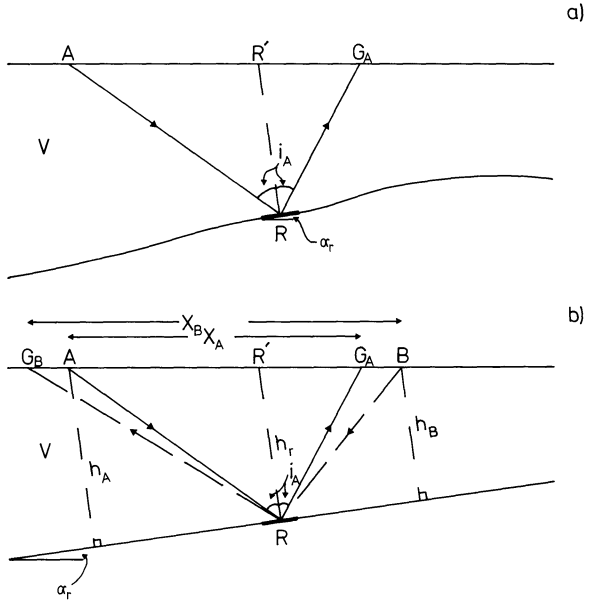


Fig. 2a and b. Reflecting element R in reflector of variable topography (a), and corresponding plane-dipping layer situation (b)

involves having reliable information on structures above the datum and a preliminary idea of those below it. A particular surface-to-surface reflection may then be ray-traced through the model so as to obtain the surface-datum and datum-surface travel-times, and the horizontal offset along the datum. Thus (Fig. 1) a reflection at R with surface-to-surface travel-time T_{SG} has a datum-datum travel-time T_r given by

$$T_r = T_{SG} - t_d - t_u$$

where t_d and t_u are the surface-datum and datum-surface travel-times respectively. The horizontal offset along the datum is X_{du} and the problem has been reduced to that of defining the relationship between T_r and X_{du} in the case of a single reflector of variable topography.

In Figure 2a, a small reflecting element R with dip α_r , forms part of a reflector of variable topography, with uniform velocity V above. Reflection travel-times from

R depend only on R – reflector topography elsewhere has no effect – and so only the equivalent plane-dipping layer (Fig. 2b), for which time-distance relationships are available (e.g. Heiland, 1940, p. 262), need be considered.

The *up-dip* travel-time T_A between A and G_A is given by

$$V^2 T_A^2 = X_A^2 + 4h_A^2 - 4h_A X_A \sin \alpha_r. \quad (5)$$

If the normal from R cuts AG_A at R' ($h_r = R'R$), then for *small dips*, $AR' = X_A/2$ and

$$h_A = h_r + \frac{X_A}{2} \sin \alpha_r$$

and, inserting this into (5), eventually

$$T_A^2 = \frac{4h_r^2}{V^2} + \frac{X_A^2 \cos^2 \alpha_r}{V^2}.$$

Likewise, the *down-dip* travel-time T_B from B to G_B is given by

$$V^2 T_B^2 = X_B^2 + 4h_B^2 + 4h_B X_B \sin \alpha_r,$$

$$h_B = h_r - \frac{X_B}{2} \sin \alpha_r$$

and

$$T_B^2 = \frac{4h_r^2}{V^2} + \frac{X_B^2 \cos^2 \alpha_r}{V^2}.$$

Thus, for small dips, the datum-datum travel-times for a reflection from R are independent of the dip direction and take the form

$$T_r^2 = \tau_r^2 + \frac{X_{du}^2 \cos^2 \alpha_r}{V^2} \quad (6)$$

with $\tau_r = \frac{2h_r}{V}$, the normal incidence reflection time.

For the k^{th} datum-datum observation from R , (6) may be re-written as

$$T_{rk}^2 = \tau_r^2 + \frac{X_{rk}^2 \cos^2 \alpha_r}{V^2}.$$

After ray-tracing to determine the datum-datum T – X data the α_r appropriate to the reflection point may be estimated from the starting model and used to form

$$D_{rk} = X_{rk} \cos \alpha_r$$

leaving T_{rk} and D_{rk} related by

$$T_{rk}^2 = \tau_r^2 + \frac{D_{rk}^2}{V^2}.$$

In this equation, the terms involving reflector topography are separated from those involving velocity and several analytical approaches are possible for their independent determination.

However, before considering these various approaches, it is necessary to consider the significance of the assumption of small dip. It is assumed that

$$AR' = R'G_A = \frac{X_A}{2}$$

whereas in fact

$$AR' = \frac{h_r \sin i_A}{\cos(i_A + \alpha_r)} \quad \text{and} \quad R'G_A = \frac{h_r \sin i_A}{\cos(i_A - \alpha_r)}$$

i.e. $\frac{AR'}{R'G_A} = \frac{\cos(i_A - \alpha_r)}{\cos(i_A + \alpha_r)}$, a ratio which tends to one when the angle of incidence (i_A) is very much greater than the dip angle (α_r), a condition that will often be fulfilled by wide-angle reflections. If the ratio $AR'/R'G_A$ does depart significantly from one, additional second-order corrections must be made to the D_{rk} values to compensate. This ratio can be examined and, if necessary, the appropriate corrections calculated during the ray-tracing stage. Thus, although the models to be discussed later contain only shallow dips and do not require these second-order corrections to be made, the assumption of small dip is not in fact necessary for the following analytical approaches to be applicable.

3. Travel-Time Analysis

The degree of multi-fold coverage necessary for the application of a separate velocity determination for every common reflection point is rarely available in crust/mantle studies. Hence accurate velocity determinations will be possible only if observations from several reflection points are combined. In practice the common reflection elements for the datum-datum reflections will be apparent only after ray-tracing and the method of combining them will depend on the degree of coverage available.

(a) Pairs of Observations

If two observations are available at each reflecting element, then the corresponding time-distance relationships are

$$T_{r1}^2 = \tau_r^2 + \frac{D_{r1}^2}{V^2},$$

$$T_{r2}^2 = \tau_r^2 + \frac{D_{r2}^2}{V^2}.$$

By subtraction

$$\Delta T_r^2 = T_{r1}^2 - T_{r2}^2 = \frac{1}{V^2} (D_{r1}^2 - D_{r2}^2) = \frac{1}{V^2} \Delta D_r^2$$

and thus a plot of ΔT_r^2 against ΔD_r^2 for all available reflection elements yields a straight line of slope $\frac{1}{V^2}$.

By addition

$$\tau_r^2 = \frac{1}{2} \left[T_{r1}^2 + T_{r2}^2 - \frac{1}{V^2} (D_{r1}^2 + D_{r2}^2) \right]$$

for each reflector element.

Some parallels with the “plus-minus” refraction interpretation method (Hagedoorn, 1959) will be recognized.

(b) Multiple Observations

If the r^{th} reflector element has $N(r)$ reflections associated with it ($N(r) \geq 2$) and there are M such elements, the family of theoretical time-distance equations is summarized by

$$t_{rn}^2 = \tau_r^2 + \frac{D_{rn}^2}{V^2} \tag{7}$$

where $r = 1, \dots, M$ (and $n = 1, \dots, N(r)$ for any r). Estimates of $\frac{1}{V^2}$ and every τ_r^2 result from forming from the observations T_{rn} and D_{rn} the sum of squared residuals I , where

$$I = \sum_{r=1}^M \sum_{n=1}^{N(r)} (T_{rn}^2 - t_{rn}^2)^2,$$

and reducing I to a minimum by setting

$$\frac{\delta I}{\delta \left(\frac{1}{V^2} \right)} = 0 \quad \text{and} \quad \frac{\delta I}{\delta (\tau_r^2)} = 0 \quad (r = 1, \dots, M).$$

This gives

$$\left. \begin{aligned} \tau_r^2 &= A_r - \frac{1}{V^2} B_r \\ \text{where} \\ A_r &= \frac{1}{N(r)} \sum_{n=1}^{N(r)} T_{rn}^2 \quad \text{and} \quad B_r = \frac{1}{N(r)} \sum_{n=1}^{N(r)} D_{rn}^2 \end{aligned} \right\} r = 1, \dots, M$$

and

$$V^2 = \frac{\sum_{r=1}^M \sum_{n=1}^{N(r)} (D_{rn}^2 - B_{rn})^2}{\sum_{r=1}^M \sum_{n=1}^{N(r)} (T_{rn}^2 - A_{rn})(D_{rn}^2 - B_{rn})}$$

and also allows simple estimation of uncertainties.

The above formulation is similar to that in the time-term approach and a further parallel is that just as refractor velocity can be allowed to vary in that method (e.g. with direction; Bamford, 1973, 1976, 1977), the velocity in Equation (7) need not be uniform. Thus a small vertical velocity gradient above the reflector could be represented by

$$V^2 = V_0^2 + k D_{rn}^2 \quad (k D_{rn}^2 \ll V_0^2)$$

leading to

$$t_{rn}^2 = \tau_r^2 + \frac{D_{rn}^2}{V_0^2} - \frac{k}{V_0^4} D_{rn}^4.$$

(c) *Resumé*

Problems of surface-to-surface WAR travel-time interpretation can be reduced to $T^2 - D^2$ space by ray-tracing and correction to a datum. The degree of reflection coverage then controls the way in which both the velocity below the datum and the reflector topography can be independently determined.

This is an Iterative Process. The initial guess at structure below the datum can, after the first solution, be replaced by computed values, the iteration then continuing until a stable structure is achieved.

4. Model Studies

The approach described in 2. and 3. above has been tested on both model and real data. The interpretation of data from the 1974 LISPB seismic experiment (Bamford et al., 1976) will be presented elsewhere. Here the results of tests carried out on the model situation shown in Figure 3 are considered.

The crust-mantle model (Fig. 3a) incorporates a fault-bounded sedimentary basin underlain by a regionally uplifted intra-crustal interface and Moho. In the observation scheme (Fig. 3b) stations are placed every $2\frac{1}{2}$ kms along the 220 kms long recording profile, for the shotpoints shown. Theoretical Moho reflection ($P_M P$) travel-times computed by raytracing for observations in the distance range 80 to 220 kms are made more realistic by the introduction of random errors drawn from a population with zero mean, 0.1 secs standard deviation.

The sub-surface coverage offered by this observation scheme (Fig. 3b) varies from two-to five-fold, permitting both analytic approaches (3. above) to be tested. Common reflecting elements average approximately 1 km in length.

(a) *Observation Pairs*

Three of the several suitable groupings are considered here. These are (Fig. 3b)

- pair *E*, shots *E1* and *E2* (180/230 kms),
- pair *C*, shots *C1* and *C2* (230/270 kms),
- and pair *W*, shots *W1* and *W2* (270/320 kms),

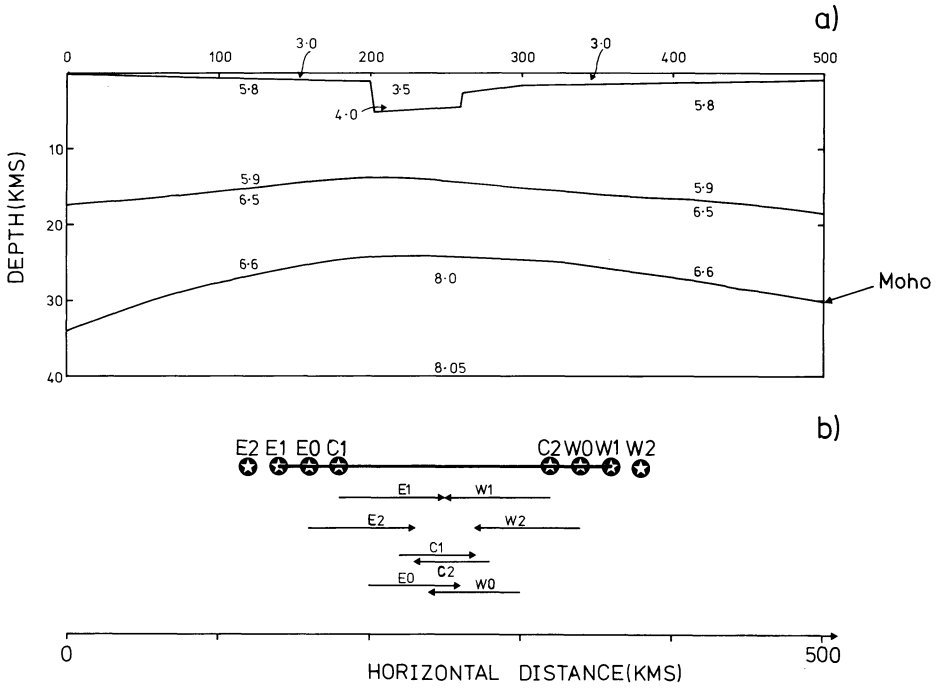


Fig. 3. a Model crust-mantle structure (velocities in km/s), and **b** hypothetical observation scheme and sub-surface coverage for Moho reflections. **KEY:** ● shotpoint; — recording profile (stations every 2½ kms); —*E*²→ sub-surface coverage for each shotpoint

the figures in brackets indicating the horizontal position in the model of the corresponding sub-surface coverage.

The datum is at 20 kms depth. The structure above is assumed to be known exactly, the velocity of the layer immediately above Moho is assumed to be 6.5 km/s throughout (as compared to the actual increase from 6.5 to 6.6 km/s with depth) and to start the iteration Moho depth is assumed to be 30 kms everywhere: thus in the first iteration the dip is assumed to be zero.

After ray-tracing and datum correction, the following velocities result

- pair *E* 6.63 ± 0.05 km/s,
- pair *C* 6.58 ± 0.02 km/s,
- pair *W* 6.65 ± 0.06 km/s.

The estimate for pair *C* is close to the actual root-mean-square value of 6.57 km/s for wide-angle reflections through the structure whereas those for pairs *E* and *W* are slightly too high. This demonstrates an important point. Equation (6)

$$T_r^2 = \tau_r^2 + \frac{X_{du}^2 \cos^2 \alpha_r}{V^2}$$

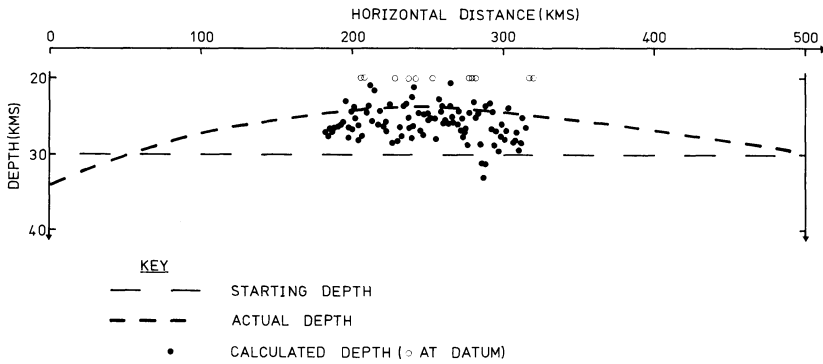


Fig. 4. Depths computed after third iteration of pairs analysis; in comparison with starting and actual models. Occasionally, a zero (or even negative) datum-corrected travel-time may result if the corresponding (introduced) random error happens to have a relatively large value. A zero (or negative) depth may then be computed – for convenience, all such values are shown as lying at the datum depth

is independent of the dip direction, and hence it seems unimportant whether the observation pairs consist of two up-dip, two down-dip or one up-dip and one down-dip observations. However, if the dip estimate in the model is in error then $D_r (= X_{du} \cos \alpha_r)$ will be also. If both observations are made with increasing distance up-dip (pairs *E* and *W*) then, for both, the error in D_r increases as the depth (i.e. τ_r) decreases and the velocity will be overestimated. On the other hand, if distance increases up-dip for one observation and down-dip for the other (pair *C*), then the error in D_r increases as τ_r decreases in one direction but as τ_r increases in the other. The net result will be a balance and a correct velocity calculation. This effect is likely to disappear the closer the actual model is approached and thus after the 3rd iteration, these velocities result

$$\text{pair } E \quad 6.60 \pm 0.04 \text{ km/s,}$$

$$\text{pair } C \quad 6.59 \pm 0.03 \text{ km/s,}$$

$$\text{pair } W \quad 6.60 \pm 0.07 \text{ km/s}$$

with the depths shown in Figure 4.

Clearly the computed reflector position has moved considerably from the starting assumption towards the actual position. However, there is considerable scatter on the depths and the velocity uncertainty is rather large, and this is common to all other observation pairs considered (e.g. *E0* and *E1*, *E1* and *C2*). The problem is that the combination of only observation pairs does not take full advantage of the statistical improvements actually offered by the multiple coverage available. One important consequence of this is that progress towards a final model tends to be slow, and thus three more iterations were required before the structure stabilized correctly.

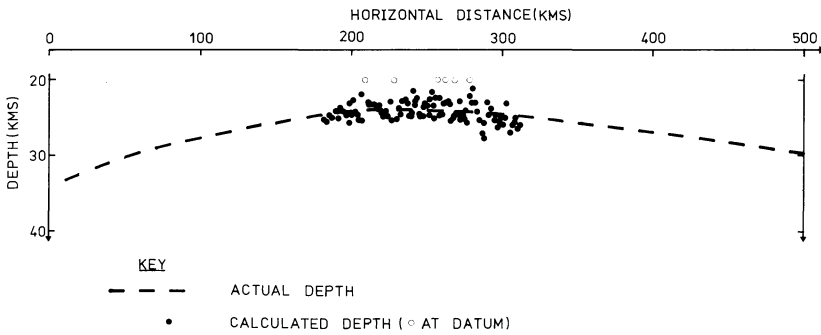


Fig. 5. Depths computed after simultaneous analysis of all data; in comparison with actual model

(b) Multiple Observations

The analytical approach defined for multiple observations allows the simultaneous use of all available travel-times (Fig. 3b). To facilitate comparisons with the analysis of observation pairs, the same starting model was used as for the 3rd iteration in the pairs analysis.

The uniform and increasing velocity options can be compared via their solution variances. In addition, any travel-time that generates an excessive residual (larger than three standard deviations) may be regarded as systematically inconsistent and removed. The resulting "clean" data give variances of $3.24 (\text{sec}^2)^2$ and $3.25 (\text{sec}^2)^2$ for the uniform and increasing velocity cases respectively. Thus, in the presence of introduced errors (0.1 secs. standard deviation), the slight velocity gradient above the Moho cannot be detected and the uniform velocity estimate of $6.58 \pm 0.01 \text{ km/s}$ is preferred. The resulting depth profile is shown in Figure 5; the original reflector topography has been recovered. In comparison with the analysis of pairs, this approach is rather more effective, only one iteration being required and this resulting in a better velocity estimate and less scatter of depths (Figs. 4, 5).

5. Error Propagation

A particular problem with this method is that it concentrates any error that arises anywhere on the whole travel-path into the final set of data, the datum-datum time-distance values. Thus in the foregoing model studies the measurement errors built into the travel-times eventually show up in the final stage of modelling, for example as scatter in the Moho depth estimates (Fig. 5).

In real problems, there will be two main sources of such errors:

(i) Travel-time measurement errors. Even relatively modest errors (0.1 secs standard deviation) can induce considerable scatter into the final model (Fig. 5) and so a great effort must be put into obtaining accurate initial travel-time measurements for these secondary arrivals.

(ii) Errors due to inaccuracies in the starting model. It has been found in tests that errors in the starting model *below* datum are not especially serious – they simply slow down the iterative process. However, errors in the model *above* datum will always generate similar errors in the final model below datum. In particular, systematic inaccuracies above datum will tend to skew deeper results. Further tests show that the normal random uncertainties in the velocities and depths computed in seismic studies (a few per cent) are acceptable limits for the starting model.

Other sources of error relate mainly to a failure of the assumptions of the method. In fact, there are few such assumptions. The assumption of small dip for example is one that leads to particularly simple arithmetic but it is not a necessary one. The same is true for the assumption of uniform velocity; velocity anisotropy, for example, believed to be present in the lower crust/upper mantle (Bamford, 1977) can be introduced via extra terms in Equation (6).

6. Conclusion

Model studies, and experience with real data, indicate that given multicoverage of the reflector of interest and reliable knowledge of structure above it, the approaches described can be used to interpret surface-to-surface WAR travel-times in laterally varying structures. Of the two approaches for the analysis of datum-datum times, the analysis of observation pairs with common reflection points is the simplest to carry out but the simultaneous analysis of all multi-coverage data is ultimately the most effective. A rational interpretation procedure for real problems is to begin with an approximation to the reflector topography (e.g. from refraction interpretation), iterate quickly through several pairs analyses so as to move reasonably close to the actual structure and then carry out one or two simultaneous solutions for final models.

Finally, although the concept of *reversed* profiles is of no ultimate significance in WAR studies, the combination of up- with down-dip observations does yield more reliable models in the early stages of iteration and hence quicker progress toward final models.

References

- Bamford, D.: An interpretation of first-arrival data from the Continental Margin Refraction Experiment, *Geophys. J.* **24**, 213–229, 1971
- Bamford, D.: Refraction data in Western Germany – a time-term interpretation. *Z. Geophys.* **39**, 907–927, 1973
- Bamford, D.: MOZAIK time-term analysis. *Geophys. J.* **44**, 433–446, 1976
- Bamford, D.: P_n velocity anisotropy in a continental upper mantle. *Geophys. J.* **49**, 29–48, 1977
- Bamford, D., Faber, S., Jacob, B., Kaminski, W., Nunn, K., Prodehl, C., Fuchs, K., King, R., Willmore, P.: A lithospheric seismic profile in Britain – I. Preliminary results. *Geophys. J.* **44**, 145–160, 1976
- Brown, R.J.S.: Normal-moveout and velocity relations for flat and dipping beds and for long offsets. *Geophysics* **34**, 180–195, 1969
- Červený, V., Langer, J., Pšenčík, I.: Computation of geometric spreading of seismic body waves in laterally inhomogeneous media with curved interfaces, *Geophys. J.* **38**, 9–20, 1974

- Clee, T.E., Barr, K.G., Berry, M.J.: Fine structure of the crust near Yellowknife. *Can. J. Earth. Sci.* **11**, 1534–1549, 1974
- Giese, P., Stein, A., Prodehl, C. (editors): *Explosion seismology in central Europe – Data and Results*, 429 p. Berlin-Heidelberg-New York: Springer-Verlag, 1976
- Hagedoorn, J.G.: The plus-minus method of interpreting seismic refraction sections. *Geophys. Prospecting* **7**, 158–182, 1959
- Heiland, C.A.: *Geophysical exploration*, 1013 p. New York: Prentice-Hall, 1940
- Pavlenkova, N.I.: Interpretation of refracted waves by the reduced travel-time curve method. *Phys. Solid Earth* **8**, 544–550, 1973
- Robinson, J.C.: An investigation of the relative accuracy of the most common normal-moveout expressions in velocity analyses. *Geophys. Prospect.* **18**, 352–363, 1970
- Willmore, P.L., Bancroft, A.M.: The time-term approach to refraction seismology. *Geophys. J.* **3**, 419–432, 1960

Received June 22, 1977/Revised Version August 29, 1977

Stress and Viscosity in the Asthenosphere

U.R. Vetter

Institut für Geophysik der Universität Kiel, Neue Universität, D-2300 Kiel,
Federal Republic of Germany

Abstract. Stresses and effective viscosities in the asthenosphere down to a depth of 400 km are calculated on the basis of the “temperature method”. Oceanic and continental geotherms and two melting point-depth curves, the dry pyrolite solidus, and the Forsterite₉₀ melting curve are used for a conversion of temperature to viscosity. The dry pyrolite model results in high homologous temperatures in the asthenosphere (>0.9 below oceans), very low stresses (a few bar and lower), and a 300 km thick low viscosity zone. The Fo₉₀ model has lower homologous temperatures; stresses in the asthenosphere are in the range of 5–100 bar, and the asthenosphere itself is not limited to a certain depth interval but extends to great depths.

Key words: Continental and oceanic asthenosphere – Melting-depth curves
– Stresses – Effective viscosities.

1. Introduction

During the last 15 years progress has been made in laboratory study of the creep behavior of rocks. A number of experiments were conducted on the mineral olivine and olivine bearing rocks. It is the opinion of Goetze (in preparation), among others, that the orthorhombic mineral olivine of the approximate composition $(Mg_{0.91}Fe_{0.09})SiO_4$ is the dominant phase to about 350 km depth, where the transition to a spinel structure begins. Accordingly, it seems justified to ascribe tectonic movements in the depth range of 40–400 km to creep in olivine. This is certainly the case, since the other minerals (20–50%) which are found in the material of the uppermost mantle (pyroxene, spinel etc.) show a creep behavior in laboratory experiments which is not significantly different from that of olivine (Green and Radcliffe, 1972; Carter et al., 1972).

The results of laboratory measurements on olivine are described in papers by Carter and AvéLallemant (1970), Goetze and Brace (1972), Kirby and Raleigh

(1973), Post and Griggs (1973), Goetze and Kohlstedt (1973), Kohlstedt and Goetze (1974), Kohlstedt et al. (1976), and others. In the range of stresses (differential stresses $\sigma_1 - \sigma_3$) from 50 bar to about 10 kb and in a temperature field above $0.5 T_m$ (T_m = melting temperature) the experimental data can be approximated by a power creep law of the general form

$$\dot{\epsilon} = K \sigma^n \exp[(-Q + pV)/RT] \quad (1)$$

(Kohlstedt et al., 1976)

with $\dot{\epsilon}$ = creep rate
 K = constant
 σ = shear stress (diff. stress)
 Q = activation energy (for self diffusion of the slowest moving species)
 V = the corresponding activation volume
 p = lithostatic pressure
 R = gas constant
 T = temperature (in K).

The exponent n of the shear stress increases with increasing stress. For the stress range between 50 bar and about 2 kb a power creep law with an exponent $n=3$ fits the data best. Creep in materials at very low stresses, i.e. about 1 bar and less, and at high temperatures ($>0.75 T_m$) is apparently transitional between that described by a power law (= PL) and Nabarro-Herring creep (= NH , with $n=1$), which is a function of the grain size (Herring, 1950; Weertman, 1970; Kirby and Raleigh, 1973; Stocker and Ashby, 1973; Carter, 1976). Coble creep ($n=1-2$) which has gained more acceptance recently (Twiss, 1976; Schwenn and Goetze, 1977) is not treated in this study.

Comparisons between experimentally and naturally deformed rock samples, by means of electron microscope observations, lead to the conclusion that the samples come from depths, where stresses from ca. 50 bar to 1–2 kb existed (Raleigh and Kirby, 1970; Nicolas et al., 1971; Phakey et al., 1972; Goetze and Kohlstedt, 1973; Carter, 1976; Nicolas, 1976). As pointed out by Meissner and Vetter (1976, in the following referred to as paper 1) regions from which these samples came may not be representative of the mantle in general, since some mechanism was operating there bringing up the samples to the surface, a process which is not common in the rest of the mantle. However, since stresses from 1 bar and smaller (in the middle of the asthenosphere) to a few kb (in the lithosphere) seem to cover the whole range of tectonic processes of creep and fracture (Vetter and Meissner, 1977; hereafter referred to as paper 2) the data obtained on laboratory and natural samples mentioned above should be applicable to the problem.

The creep rates in laboratory experiments are in general 8–10 orders of magnitude larger than geologic creep rates. An application of experimental data to in situ conditions requires an extrapolation to much lower creep rates (Kohlstedt et al., 1976; Goetze, in preparation). Moreover, the confining pressures in laboratory studies reach only 15 kb which corresponds to the upper

50 km. It has not yet been possible to detect any transition from *PL* to *NH* creep in rocks, neither under laboratory conditions nor in naturally deformed specimens.

Little is known about the exact composition of the silicate mixture which constitutes the upper mantle. Hence, melting point-depth relations are model dependent although the creep behavior of many mantle minerals seem to be similar as mentioned before. A further problem is the possible presence of fluid phases (water, carbon dioxide) which strongly suppress the melting point (Green and Liebermann, 1976). Because of the uncertainty in our knowledge of the fluid phases their effect on the melting point will not be considered in this study.

While in papers 1 and 2 some observational evidence for the transition from *PL* to *NH* creep was presented on the basis of uplift data, the present study attempts to define the range of conditions in which the different creep laws are valid. Hence, two models with different melting curves will be presented which are assumed to be the limiting cases for in situ conditions.

2. Models and Formulas Used

A plate tectonic model with an oceanic plate and a continental plate and their substructures to a depth of 400 km is considered (Fig. 1). Theoretical computations of the stress-depth distribution are performed for the model.

In Equation (1) the exponential term can be substituted for by a term including the diffusion coefficient. The influence of increasing pressure on the creep rate is taken into account by the increase of the melting temperature with pressure (Sherby and Simnad, 1961; Goetze and Brace, 1972; Kirby and Raleigh, 1973; and others). This substitution results in the following formulas:

$$\dot{\epsilon} = C_1 \sigma \exp(-g^* T_m/T) \quad (2)$$

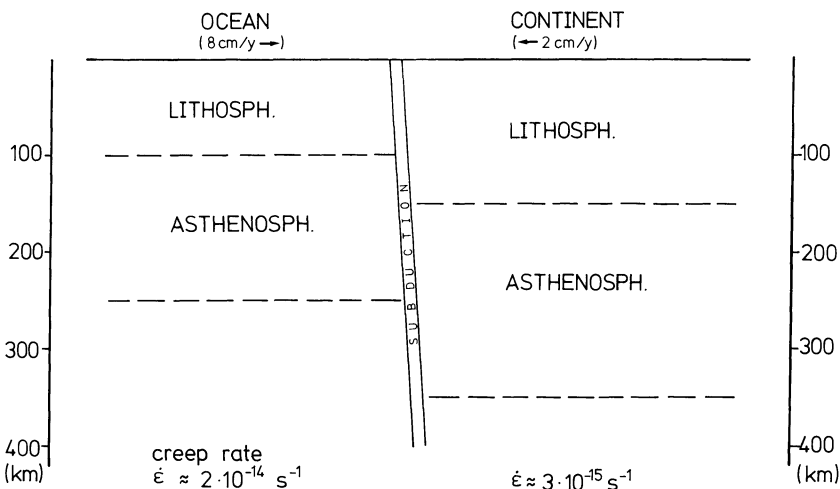


Fig. 1. Plate tectonic model (exaggeration 1:10)

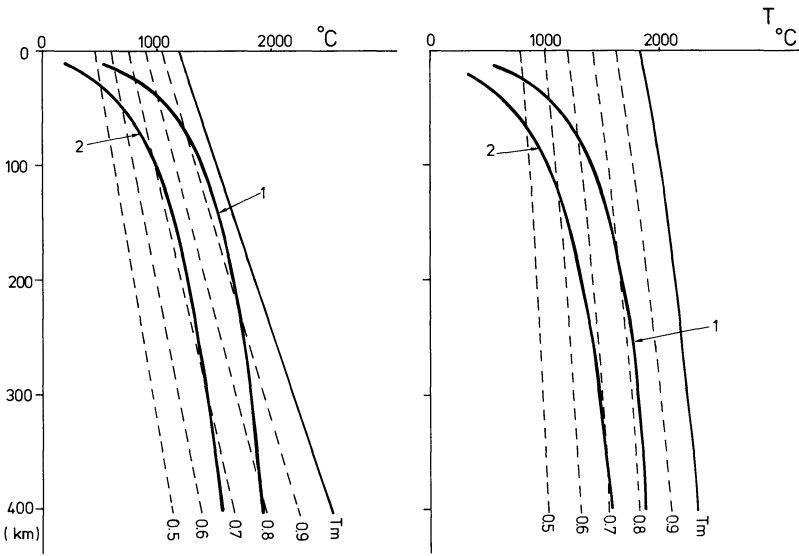


Fig. 2. Temperatures and melting points in the upper 400 km of the earth; *left:* T_m =dry pyrolite solidus (Stocker and Ashby, 1975); *right:* T_m =Forsterite₉₀ melting curve (Carter, 1976); 1: hot oceanic geotherm (Griggs, 1972); 2: continental shield geotherm (Clark and Ringwood, 1964); *dashed lines:* fractions of melting point

with

$$C_1 = \alpha_1 \Omega D_0 / r^2 kT \tag{3}$$

- and $\alpha_1 = \text{constant}$
- $k = \text{Boltzmann's constant}$
- $r = \text{grain size}$
- $\Omega = \text{atomic volume}$
- $D_0 = \text{diffusion constant}$
- $g = \text{constant}$

which are valid for grain size dependent *NH* creep and

$$\dot{\epsilon} = C_3 \sigma^3 \exp(-g^* T_m / T) \tag{4}$$

with

$$C_3 = \alpha_3 \Omega D_0 / \mu^2 kT \tag{5}$$

- and $\alpha_3 = \text{constant}$
- $\mu = \text{shear modulus}$

which are valid for dislocation (=PL, $n=3$) creep. For detailed explanations and derivations of these equations see Weertman (1970) and papers 1 and 2.

From a comparison of Equations (2) and (4) it is seen that power law creep with $\dot{\epsilon} \sim \sigma^3$ is much more sensitive to changes in stress than is *NH* creep. Using

Equations (2–5) and the relation

$$\eta = \sigma / \dot{\epsilon} \quad (6)$$

the effective viscosity can be determined on the basis of the “temperature method”. That creep process will dominate which gives the highest creep rate in each stress level. In the transition from one creep process to the other, both processes contribute about equally to the resulting creep rate. The transition from *PL* to *NH* creep occurs at ever decreasing stress as the temperature increases and as the grain size decreases (see paper 1, Fig. 4 and paper 2, Fig. 6).

Two different melting point-depth curves will be considered: (a) the dry pyrolite solidus curve, taken from Stocker and Ashby (1973, Fig. 9) and (b) the dry Forsterite₉₀ melting curve, taken from Carter (1976, Fig. 39). These two melting curves differ by about 600°C at a pressure of 1 bar and come together in a pressure range of about 100 kb. In Figure 2a and b both melting curves are plotted with the geotherm of a hot oceanic region (Griggs, 1972) and of a continental shield (Clark and Ringwood, 1964). The restriction $T/T_m > 0.5$ for high temperature steady state creep is fulfilled in both cases for depths greater than the crust-mantle boundary.

3. Numerical Values of the Constants Used in the Calculations

As in paper 2, the following numerical values were used in Equations (2–5):

1. The grain size r was taken to be 5 mm according to the observations of mantle specimens, in which most grains lie between 1 and 10 mm. Also indications from the uplift data, as mentioned in paper 2, Figures 4 and 5, give evidence of a grain size around 5 mm. This grain size is taken as constant in the following calculations. Certainly this treatment is a rough approximation because it is well known that grain sizes vary not only with temperature and pressure but also with tectonic stress (Kohlstedt et al., 1976; Mercier, 1977).

2. The constant g^* was examined by Kohlstedt and Goetze (1974) in their laboratory creep experiments on dry olivine; they obtained a best value of $g^* = 29$, which is used here. The experimental values of g^* in olivine creep studies of other authors vary between 26.4 and 31.8 with a mean of 29 (Weertman and Weertman, 1975). Since $g^* \approx 10^3 Q/RT_m$, one finds an activation energy of $Q \approx 125$ kcal/mol at the melting point $T_m = 2170$ K of Fo_{90} at 1 bar. This Q value is also a mean obtained from a number of measurements by different authors (see Goetze, in preparation, Fig. 10) and is nearly constant in the temperature interval from $0.5T_m$ to T_m .

If one takes the dry pyrolite solidus temperature T_m (1 bar) = 1470 K, and $g^* = 29$, an activation energy of $Q \approx 85$ kcal/mol results. Schwenn and Goetze (1977) obtained this value as a mean for Coble creep in olivine during hot pressing.

3. The following numbers were used for the constants C_1 and C_3 in Equations (2 and 4): $C_1 = 2 \cdot 10^{-4}$ cm s g^{-1} for T_m , a grain size $r = 5$ mm and $\alpha_1 = 10$ (Weertman, 1970); included in C_1 is the diffusion constant $C_0 = 3 \cdot 10^4$ cm² s⁻¹

(Goetze and Kohlstedt, 1973). $C_3 = 4.2 \cdot 10^{11} \text{ kb}^{-3} \text{ s}^{-1}$, as experimentally determined by Kohlstedt and Goetze (1974) at the olivine melting point. If $\alpha_3 = 2.26 \cdot 10^{12} \text{ dyn cm}^{-2}$, then the diffusion constant will be $D_0 \approx 10^6 \text{ cm}^2 \text{ s}^{-1}$.

The constants differ from those in paper 1 where a value of $g^* = 18$ was used. This g^* was based on hot creep experiments with different metals (Weertman, 1970) and resulted in a $C_3 = 8.2 \cdot 10^4 \text{ kb}^{-3} \text{ s}^{-1}$. The g^* and C_3 values from Kohlstedt and Goetze's (1974) experiments on dry olivine crystals seem to be more realistic for the mantle conditions. The difference in the resulting effective viscosity on the base of both mentioned sets of constants is small for temperatures around $0.7 T_m$, but reaches about one order of magnitude for $0.5 T_m$ and for T_m .

Introducing the constants in Equations (2), (4), and (6), stresses and effective viscosities for the models are obtained.

4. Results

Figures 3 and 4 show so called deformation maps (=stress-depth curves with the strain rate as a parameter) for the oceanic and continental geotherms from Figure 2. The subduction zone in these figures is considered only as a separating feature and is not specifically investigated in this study. Figures 3a and b are based on the dry pyrolite solidus curve and are taken from paper 2, Figures 7 and 8. Figures 4a and b show the analogous maps based on the Fo_{90} melting curve, maps which are similar to those of Kirby and Raleigh (1973). Using the pyrolite solidus curve one obtains high homologous temperatures T/T_m , especially for the oceanic case; they reach nearly 0.95 below oceans and 0.72 below continents. *NH* creep seems to play an important role below oceans for geologic strain rates, because stresses in this particular model are in general very small. In the deformation map based on the Fo_{90} melting curve (Figs. 4a and b) homologous temperatures reach a maximum of 0.83 for a "hot" oceanic asthenosphere and 0.7 for the continental shield, but at much greater depth than in the case discussed above. Under these conditions, *NH* creep only plays a minor role. Stresses are about a factor of 10 higher than for the dry pyrolite model. These stress values are in good accord with those given by Kirby and Raleigh (1973).

Neugebauer and Breitmayer (1975) also calculated a deformation map for the oceanic mantle to a depth of 1100 km and under the assumption of a power creep law ($n=3$). They adjusted the strain rates to a sinking rate of the plate of 8 cm/y to avoid the use of problematic constants. Their stress values are about 2 orders of magnitude higher than the stresses in this consideration calculated on the base of the Fo_{90} melting curve.

The power creep law ($n=3$) leads to a relation between σ and $\dot{\epsilon}$ in the form of $\sigma \sim \dot{\epsilon}^{1/3}$. Therefore stresses could change up to a factor of about 3 if the strain rate changes by about one order of magnitude in a depth range of 400 km. A larger variation of the creep rate does not seem to occur in zones of quiescence, i.e. away from plate boundaries. If one treats *NH* creep as the dominant

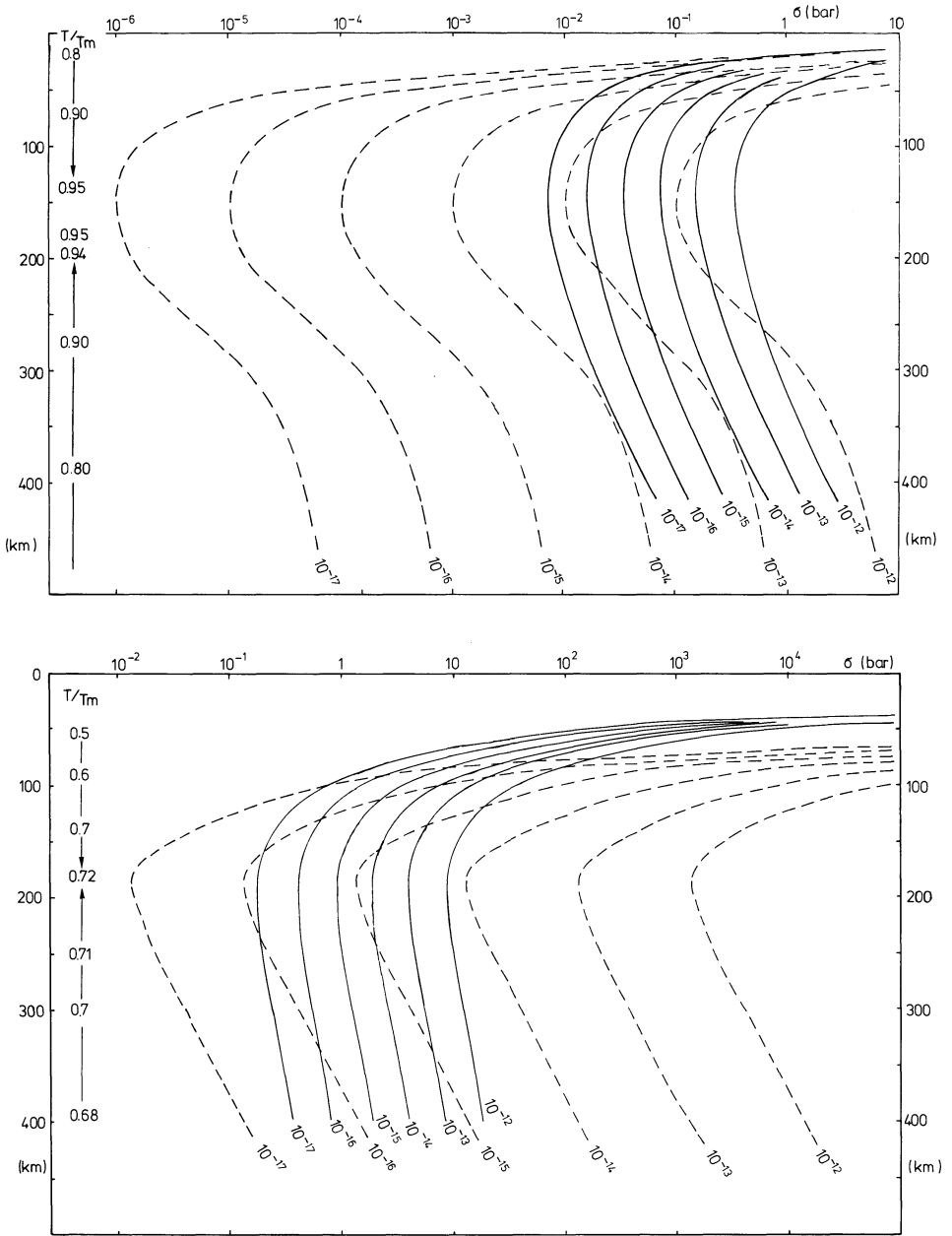


Fig. 3. Stress-depth curves with the strain rate $\dot{\epsilon}$ as a parameter on the basis of the dry pyrolite solidus curve for an hot ocean (above) and a continental shield (below). Full lines: PL creep; dashed lines: NH creep; on the left side: the corresponding homologous temperatures

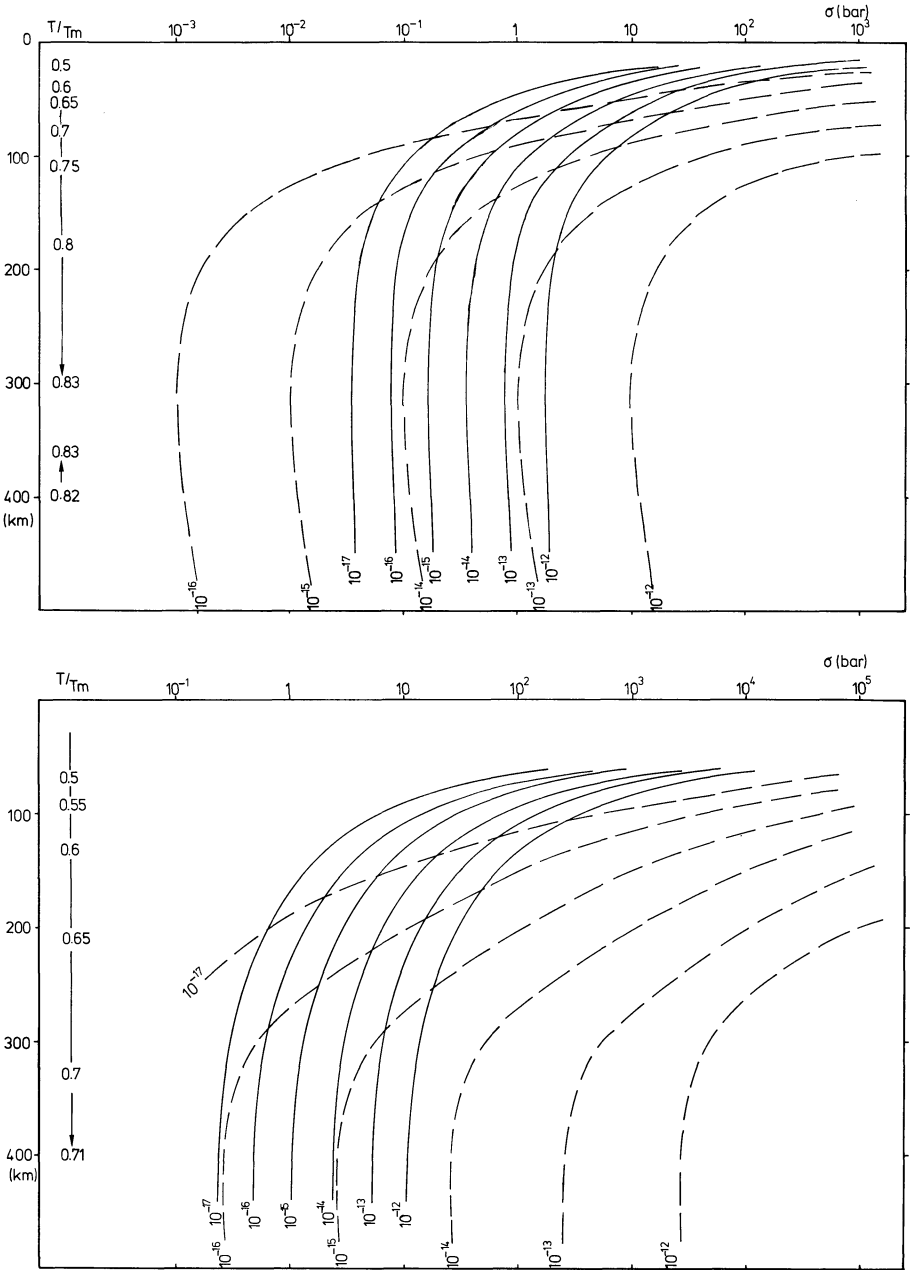


Fig. 4. As Figure 2, but on the basis of the F_{090} melting curve

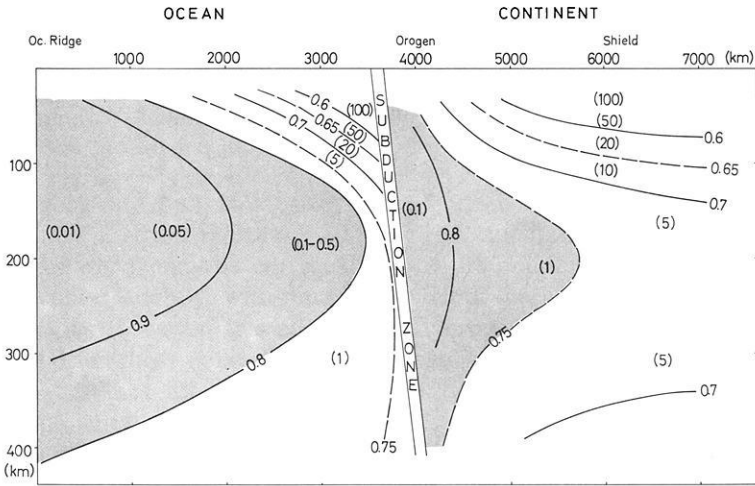


Fig. 5. Average stress distribution and lines of equal homologous temperatures on the basis of the dry pyrolite solidus for the plate tectonic model (Fig. 1). Figures in parentheses: stress values in bar hatched areas: zones of dominating NH creep

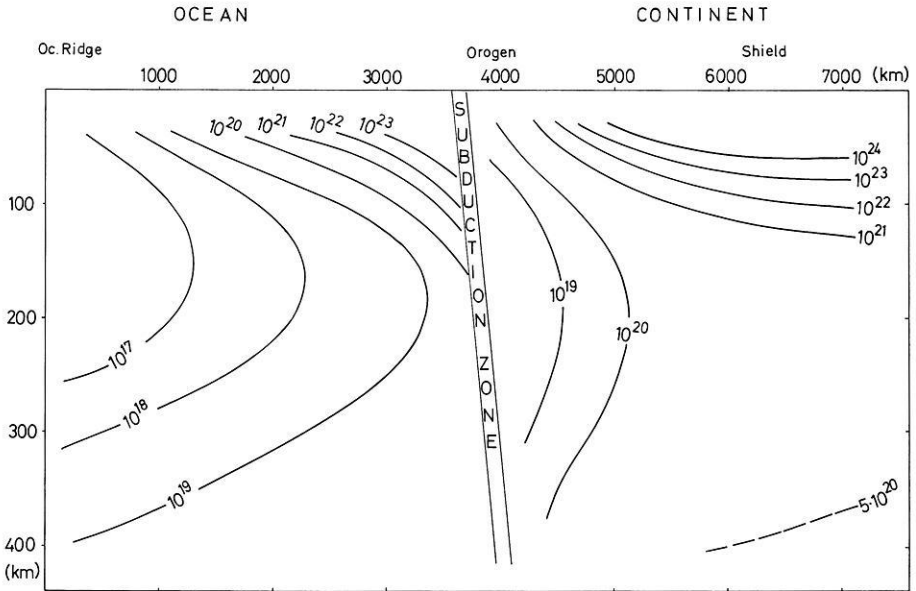


Fig. 6. Viscosity isolines for the case of Figure 5

mechanism stresses will change with the same order of magnitude as the creep rate does.

Figures 5–8 show stresses, homologous temperatures, and effective viscosities for the special plate tectonic model mentioned below. Additional geotherms were used (for instance the Basin and Range temperature distribution, represent-

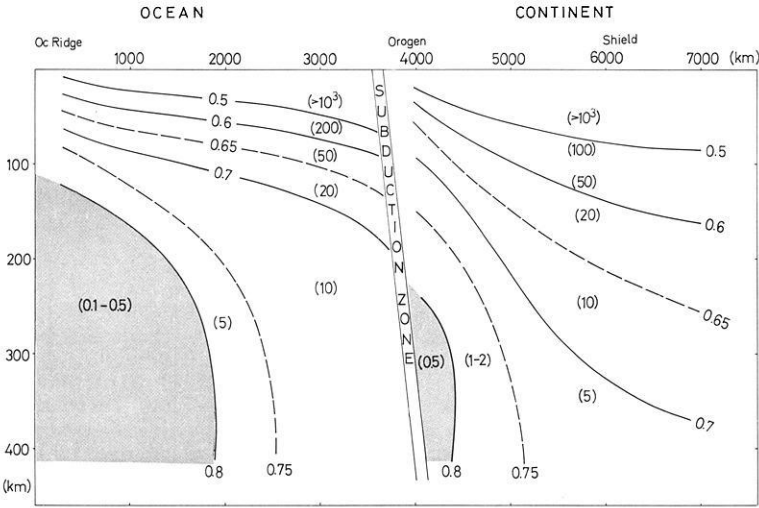


Fig. 7. Average stress distribution and lines of equal homologous temperatures on the basis of the $F_{0.90}$ melting curve; for further legend: see Figure 5

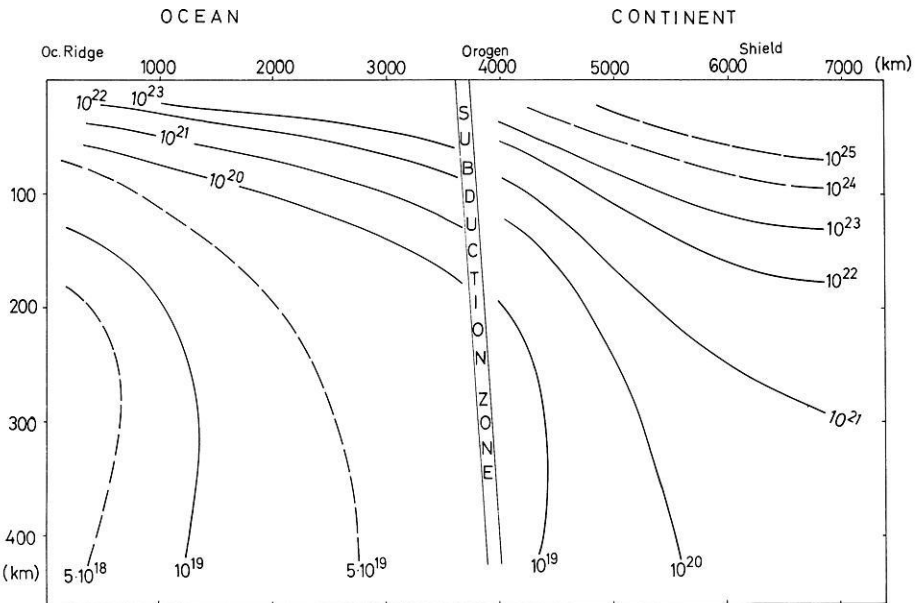


Fig. 8. Viscosity isolines for the case of Figure 7

ing an orogen (Herrin, 1972), and a few oceanic temperature curves of Clark and Ringwood (1974) and Forsyth and Press (1971).

In the plate tectonic model (Fig. 1) the oceanic plate is assumed to be moving with a speed of 8 cm/y. The differential movement may be concentrated in a

layer 100–200 km thick (asthenosphere). From the relationship

$$\dot{\epsilon} = \partial v / \partial h \approx v/h \quad (7)$$

where h = gliding thickness

and v = drift velocity

a creep rate $\dot{\epsilon} \approx 2 \cdot 10^{-14} \text{ s}^{-1}$ results. For the continental plate which is drifting at 2 cm/y a strain rate $\dot{\epsilon} \approx 3 \cdot 10^{-15} \text{ s}^{-1}$ is calculated. They represent mean creep rates which may be correct down to the middle of the asthenosphere and will decrease slightly with increasing depth because of increasing pressure (see Eq. (1)). However, this effect is not considered here. The calculated stresses are valid for those zones in the asthenosphere which do not show tectonic activity, for instance for the asthenosphere beneath the deep sea floor and beneath continental shield regions.

In Figures 5 and 7 those zones are indicated in which *NH* creep yields the higher creep rate for a given stress. This is the case in wide regions of the asthenosphere below oceans and also in the region around an orogen below continents for the first case which is based on the dry pyrolite solidus. In the second model, based on the $F_{O_{90}}$ melting curve, *NH* creep plays only a minor role, locally confined to the vicinity of oceanic ridges (or plumes) and perhaps in small zones below continental orogens. The important difference between the two T_m -models is clearly visible in the stress-depth distribution. Whereas the first model is characterized by very low stresses (below 1 bar in most parts of the oceanic and below 5 bar in most parts of the continental asthenosphere), stresses resulting in the $F_{O_{90}}$ melting model are higher by one order of magnitude. However, they reach their minimum values at greater depths than in the first model. This stress level (10–100 bar in the upper part of the asthenosphere and 1–2 kb in the lithosphere) is favoured by most authors who have carried out laboratory experiments or electron microscope observations.

A further difference between the models is the “shape” of the asthenosphere. Characteristic of the first model is a pronounced high temperature channel at a depth of 80–250 km under oceans and 130–350 km under continents. In the second model, a pronounced asthenospheric channel is not indicated; on the contrary, there seems to exist a region of more or less constant temperature from about 200 km down to great depths. Upper mantle models derived from seismic observations indicate the existence of a more or less limited asthenospheric channel, at least below oceans (e.g. Smith, 1972; Forsyth, 1975; Froidevaux et al., 1977). They support the result of model 1 whereas O’Connell (1977) derived a mantle model with a relatively uniform temperature structure in the whole upper mantle without a pronounced asthenospheric channel from glacial rebound data and gravity anomalies. His ideas are in better agreement with the result of model 2. Both these models may limit the realistic mantle temperature variation, if the assumption “dry” is correct.

Figures 6 and 8 show the corresponding viscosity profiles. The calculations were made for *NH* creep with a grain size of 5 mm and for *PL* creep with the stress distribution from Figures 5 and 7. Both melting temperature models show effective viscosity values not very different from each other. The remarkable

difference again is shown in the shape of the viscosity isolines. They delineate the asthenosphere as a 150–300 km broad low viscosity channel in the first model.

In the second model, however, the low viscosity asthenosphere covers the depth range from 150–200 km to at least 400 km, and no indication of a viscosity decrease with increasing depth is seen. A low velocity “channel” which is shown by numerous seismic measurements to be in the depth range of 80 km (ocean) to 300 km (Precambrian shield) must be caused by the existence of minor amounts of water (or other fluid phases) in the upper mantle material, if the Fo_{90} melting temperature model is the realistic one. Obviously, this water content must be more significant below oceans. The dry melting curve may then be partially replaced by a wet melting curve. Green and Liebermann (1976) suggest the existence of a zone of incipient melting ($<2\%$) with an abrupt beginning at about 80–90 km depth below oceans because of amphibole break down connected with a water content $<0.4\%$. Their considerations are based on the pyrolite melting curve. Such a sharp boundary is not confirmed so far by any seismic measurements. Nor is the recording of P_n -velocities larger than 8.5 km s^{-1} at depths of 50–100 km in agreement with a wet pyrolite model. Also Wyllie (1971) has shown the influence of the presence of 0.1% water on the peridotite melting curve. Both investigations show a depression of the melting point by about 500°C at a depth greater than about 100 km. It seems probable that even a smaller water content will change the creep mechanism strongly.

5. Conclusions

Based on the assumption that the lithosphere and asthenosphere are dry, two rheologic models were calculated which provide boundary conditions for creep processes:

Model 1 (based on the dry pyrolite solidus melting-depth curve) indicates that the asthenosphere begins at rather shallow depths and terminates between 300 and 400 km. In model 2 (based on the Fo_{90} melting-depth curve) the asthenosphere begins at a deeper level and extends to greater depths than in model 1, i.e. no changes in the physical parameters are indicated to a depth of 400 km. In general the viscosity values (i.e. the mean effective viscosity of the asthenosphere) are similar in both models. They both show a viscosity difference of about $1^{1/2}$ orders of magnitude between the continental and oceanic asthenospheres.

If there is a relation between seismic Q -values and effective viscosity η as suspected by McConnell (1965) and Meissner (1977), seismic investigations should reveal the differences between the asthenospheres below shields and oceans in more detail. Also a discrimination between the dry pyrolite and the Fo_{90} model should be attempted by seismic as well as by mineralogical investigations.

Acknowledgements. I grateful thank Prof. R. Meissner for his stimulating discussions and Dr. A. Binder for correcting my English.

References

- Carter, N.L.: Steady state flow of rocks. *Rev. Geophys. Space Phys.* **14**, 301–360, 1976
- Carter, N.L., AvéLallemant, H.G.: High-temperature flow of dunite and peridotite. *Bull. Geol. Soc. Am.* **81**, 2181–2202, 1970
- Carter, N.L., Baker, D.W., George, R.P. Jr.: Seismic anisotropy, flow, and constitution of the upper mantle. In: *Flow and Fracture of Rocks*, H.C. Heard et al., eds.: AGU, Monogr. **16**, 167–190, 1972
- Clark, S.P. Jr., Ringwood, A.E.: Density distribution and constitution of the mantle. *Rev. Geophys. Space Phys.* **2**, 35–68, 1964
- Forsyth, D.W.: The early structural evolution and anisotropy of the oceanic upper mantle. *Geophys. J.* **43**, 103–162, 1975
- Forsyth, D.W., Press, F.: Geophysical tests of petrological models of the spreading lithosphere. *J. Geophys. Res.* **76**, 7963–7979, 1971
- Froidevaux, C., Schubert, G., Yuen, D.A.: Thermal and mechanical structure of the upper mantle: comparison between continental and oceanic models. *Tectonophysics* **37**, 233–246, 1977
- Goetze, C., Brace, W.F.: Laboratory observations of high-temperature rheology of rocks. *Tectonophysics* **13**, 583–600, 1972
- Goetze, C., Kohlstedt, D.L.: Laboratory study of dislocation climb and diffusion in olivine. *J. Geophys. Res.* **78**, 5961–5971, 1973
- Green, D.H., Liebermann, R.C.: Phase equilibria and elastic properties of a pyrolyte model for the oceanic upper mantle. *Tectonophysics* **32**, 61–92, 1976
- Green, H.W., Radcliffe, S.V.: Deformation processes in the upper mantle. In: *Flow and Fracture of Rocks*, H.C. Heard et al., eds.: AGU, Geoph. Monogr. **16**, 139–156, 1972
- Griggs, D.T.: The sinking lithosphere and the focal mechanism of deep earthquakes. In: *Nature of the Solid Earth*, E.C. Robertson, ed., pp. 361–384. New York: McGraw Hill 1972
- Herring, E.: A comparative study of upper mantle models: Canadian shield and Basin and Range provinces. In: *Nature of the Solid Earth*, E.C. Robertson, ed., pp. 216–231. New York: McGraw Hill 1972
- Herrin, C.: Diffusional viscosity of a polycrystalline solid. *J. Appl. Phys.* **21**, 437–445, 1950
- Kirby, St.H., Raleigh, C.B.: Mechanism of high-temperature, solid state flow in minerals and ceramics and their bearing on the creep behavior of the mantle. *Tectonophysics* **19**, 165–194, 1973
- Kohlstedt, D.L., Goetze, C.: Low-stress high-temperature creep in olivine single crystals. *J. Geophys. Res.* **79**, 2045–2051, 1974
- Kohlstedt, D.L., Goetze, C., Durham, W.B.: Experimental deformation of single crystal olivine with application to flow in the mantle. In: *The Physics and Chemistry of Minerals and Rocks*, S.K. Runcorn, ed., pp. 35–49. London: J. Wiley & Sons Ltd. 1976
- McConnell Jr., R.K.: Isostatic adjustment in a layered earth. *J. Geophys. Res.* **70**, 5171–5191, 1965
- Meissner, R.: Lunar viscosity models. *Phil. Trans. Roy. Soc. London, Ser. A*, **285**, 463–467, 1977
- Meissner, R.O., Vetter, U.R.: Isostatic and dynamic processes and their relation to viscosity. *Tectonophysics* **35**, 137–148, 1976
- Mercier, J.C., Anderson, D.A., Carter, N.L.: Stress in the lithosphere: inferences from steady state flow of rocks. *Pure Appl. Geophys.* **115**, 199–226, 1977
- Neugebauer, H.J., Breitmayer, G.: Dominant creep mechanism and the descending lithosphere. *Geophys. J.* **43**, 873–895, 1975
- Nicolas, A.: Flow in upper mantle rocks: some geophysical and geodynamic consequences. *Tectonophysics* **32**, 93–106, 1976
- Nicolas, A., Bouchez, J.L., Boudier, F., Mercier, J.C.: Textures, structures, and fabrics due to solid state flow in some European lherzolites. *Tectonophysics* **12**, 55–86, 1971
- O'Connell, R.J.: On the scale of mantle convection. *Tectonophysics* **38**, 119–136, 1977
- Phakey, P., Dollinger, G., Christie, J.: Transmission electron microscopy of experimentally deformed olivine crystals. In: *Flow and Fracture of Rocks*, H.C. Heard et al., eds. AGU, Geophys. Monogr. **16**, 117–138, 1972
- Post, R.L. Jr., Griggs, D.T.: The earth's mantle: evidence of non-Newtonian flow. *Science* **181**, 1242–1244, 1973
- Raleigh, C.B., Kirby, S.H.: Creep in the upper mantle. *Mineral. Soc. Am., Spec. Papers* **3**, 113–121, 1970

- Schwenn, M.B., Goetze, C.: Creep of olivine during hot-pressing. *Tectonophysics*, in press, 1977
- Sherby, O.D., Simnad, M.T.: Prediction of atomic mobility in metallic systems. *Trans. Am. Soc. Metals*, **54**, 227–240, 1961
- Smith, S.W.: The anelasticity of the mantle. *Tectonophysics* **13**, 601–622, 1972
- Stocker, R.L., Ashby, M.F.: On the rheology of the upper mantle. *Rev. Geophys. Space Phys.* **11**, 391–426, 1973
- Twiss, R.J.: Structural superplastic creep and linear viscosity in the earth's mantle. *Earth Planet. Sci. Lett.* **33**, 86–100, 1976
- Vetter, U.R., Meissner, R.O.: Creep in geodynamic processes. *Tectonophysics*, **42**, 37–54, 1977
- Weertman, J.: The creep strength of the earth's mantle. *Rev. Geophys. Space Phys.* **8**, 145–168, 1970
- Weertman, J., Weertman, J.R.: High temperature creep of rock and mantle viscosity. *Ann. Rev. of Earth and Plan. Sci.*, **3**, 293–315, 1975
- Wyllie, J.P.: Role of water in magma generation and initiation of diapiric uprise in the mantle. *J. Geophys. Res.* **76**, 1328–1338, 1971

Received June 1, 1977/Revised Version October 7, 1977

The Theoretical Investigation of Resistivity Methods for Geoelectrical Prospecting in Marine Areas

J. Sebulke

Technische Universität Berlin, Institut für Angewandte Geophysik,
Petrologie und Lagerstättenforschung, Straße des 17. Juni 135, EB 15, 1000 Berlin 12

Abstract. The applicability of the geoelectrical resistivity method in marine areas is studied by model calculations. For a simplified three-layer-model assuming homogeneous and isotropic conditions together with parallel boundaries the apparent resistivity is calculated for three different electrode configurations. It is concluded that for two of the configurations the thickness of layer 2 (sediments) can be determined with a sufficient accuracy.

Key words: Marine geoelectrical sounding – Computed apparent resistivity – Marine Geophysical survey.

1. Introduction

As the demand for mineral raw materials and the geoscientific interest in the oceans have increased, methods primarily used for measurements on land were modified for an application in the marine areas or even totally new techniques were developed. Thus important progresses have been obtained in seismics, gravimetry, geothermics and magnetics which also led to new developments in some sub-branches of marine geophysics.

In geoelectrics comparatively few experiments have been published which examine methods for an application at the sea. Sovietic and Dutch authors (Volker and Dijkstra, 1955; Terekhin, 1962; Van' Yan, 1956) have reported about the application of the resistivity methods hitherto used on land.

This article informs about activities to develop special geoelectric resistivity methods suitable for the special conditions at sea. The preferred prospecting object is thin clastic sea floor sediments which, at the present time, cannot be examined neither by seismic nor ultrasonic methods with a sufficient precision.

The experiment shows that one can draw conclusions about the structure of ocean floor sediments at arbitrary water depths from some of the investigated geoelectrical arrays.

2. Potential of a Point Source in a Three – Layer Halfspace at Arbitrary Depths

A very simple model is used for the following observations with different resistivities (Fig. 1). A sediment layer lies on top of an unlimited half-space, here called bedrock, and is covered with water.

The following assumptions have been made to simplify the calculations:

Each layer is homogeneous and isotropic.

The boundaries of the layers are parallel to each other.

The following considerations have been made at the planning of the electrode configurations:

The source point of the potential field shall be near to that part of the ground which is of interest for the measurements. Therefore the current electrodes are placed either in the water layer or in the sediment.

The potential electrodes are always situated in the water layer, preferably on the sea floor.

Three different configurations will be presented for which model calculations have been carried out.

The one-electrode configuration (Fig. 2): The first current electrode is inserted into the sediment, the second one is located at a – from the physical point of view – infinite distance from the array. The two electrodes for the measurement of the potential difference will be separated so that the distance r between E_1 (current electrode) and S_1 (potential electrode) and between S_1 and S_2 always remains the same.

The asymmetrical two-electrode configuration (Fig. 3a): The current electrodes E_1 and E_2 are inserted either into the sediment or into the water layer (a is the horizontal distance between E_1 and E_2). The electrodes are placed asymmetrically with respect to the centre of the current electrodes as in the preceding configuration.

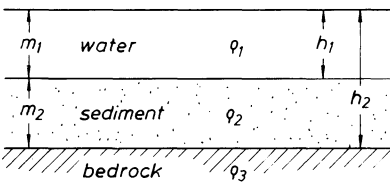


Fig. 1. The model assumed

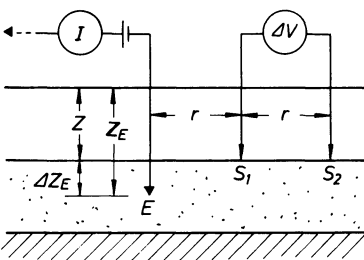


Fig. 2. The one-electrode configuration

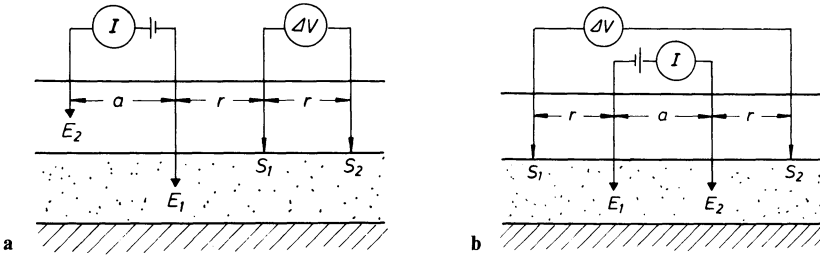


Fig. 3. a The asymmetrical two-electrode configuration. b The symmetrical two-electrode configuration

The symmetrical two-electrode configuration (Fig.3b): The two current electrodes are put at the same depth either into the water layer or on the sea floor, the potential electrodes on the sea floor symmetrically to the current electrodes ($S_1 E_1 = S_2 E_2 = r$). The potential of arbitrary coordinates of a point source in the half-space has to be known for the calculation of the apparent resistivity $\rho_s(r)$ for each of the described configurations. Each single potential can be calculated by the complementary solution of the Laplace's equation in cylindrical coordinates:

$$V(r, z) = \int_0^\infty [A(\lambda) e^{-\lambda z} + B(\lambda) e^{\lambda z}] J_0(\lambda r) d\lambda. \tag{1}$$

The following expressions are obtained for each potential in the different layers n (E_1 and E_2 in layer j):

$$\begin{aligned} V_1 &= V_p + q_j \int_0^\infty (\theta_1(\lambda) e^{-\lambda z} + \psi_1(\lambda) e^{\lambda z}) J_0(\lambda r) d\lambda \\ V_2 &= V_p + q_j \int_0^\infty (\theta_2(\lambda) e^{-\lambda z} + \psi_2(\lambda) e^{\lambda z}) J_0(\lambda r) d\lambda \\ V_3 &= V_p + q_j \int_0^\infty (\theta_3(\lambda) e^{-\lambda z} + \psi_3(\lambda) e^{\lambda z}) J_0(\lambda r) d\lambda \end{aligned} \tag{2}$$

V_p is the primary potential for which the following is valid:

$$V_p = \begin{cases} 0 & \text{for } j \neq n \\ q_j \int_0^\infty e^{-\lambda(z_E - z)} \cdot J_0(\lambda r) d\lambda & \text{for } j = n \text{ and } z_E > z \\ q_j \int_0^\infty e^{-\lambda(z - z_E)} \cdot J_0(\lambda r) d\lambda & \text{for } j = n \text{ and } z_E < z \end{cases} \tag{3}$$

with:

$$q_j = \frac{\rho_j \cdot I}{4\pi}. \tag{4}$$

The symbols of the parameters are the same as previously used by Flathe (1955). On the condition that the current across the surface of the halfspace is zero we get:

$$\theta_1(\lambda) = \begin{cases} \psi_1(\lambda) + e^{-\lambda z} & \text{for } j=1 \\ \psi_1(\lambda) & \text{for } j \neq 1. \end{cases} \quad (5)$$

The condition

$$\psi_3(\lambda) = 0 \quad (6)$$

results from the claim that the potential has to disappear at an infinite distance.

The boundary conditions of the stationary electrical field, applied to the generally formulated potentials yield a system of 2 $(n-1)$ equations which determines the same number of initially arbitrary chosen functions $\theta_n(\lambda)$ and $\Psi_n(\lambda)$.

The potentials of an electrode in the different layers j for a point in the layer 1 are as follows:

$j=1$:

$$V(r, z) = q_1 \left[\frac{1}{(r^2 + (z - z_E)^2)^{1/2}} + \frac{1}{(r^2 + (z + z_E)^2)^{1/2}} + \int_0^\infty \frac{k_1(e^{-\lambda(2h_1 - z_E)} + e^{-\lambda(2h_1 + z_E)}) + k_2(e^{-\lambda(2h_2 - z_E)} + e^{-\lambda(2h_2 + z_E)})}{1 - k_1 e^{-2\lambda h_1} - k_2 e^{-2\lambda h_2} + k_1 k_2 e^{-2\lambda(h_2 - h_1)}} \cdot (e^{-\lambda z} + e^{\lambda z}) J_0(\lambda r) d\lambda \right] \quad (7a)$$

$j=2$:

$$V(r, z) = q_2(1 - k_1) \int_0^\infty \frac{(e^{-\lambda z_E} + k_2 e^{-\lambda(2h_2 - z_E)})(e^{-\lambda z} + e^{\lambda z})}{1 - k_1 e^{-2\lambda h_1} - k_2 e^{-2\lambda h_2} + k_1 k_2 e^{-2\lambda(h_2 - h_1)}} J_0(\lambda r) d\lambda \quad (7b)$$

$j=3$:

$$V(r, z) = q_3(1 - k_1)(1 - k_2) \cdot \int_0^\infty \frac{e^{-\lambda z_E}(e^{-\lambda z} + e^{\lambda z})}{1 - k_1 e^{-2\lambda h_1} - k_2 e^{-2\lambda h_2} + k_1 k_2 e^{-2\lambda(h_2 - h_1)}} J_0(\lambda r) d\lambda \quad (7c)$$

where

$$k_n = \frac{\rho_{n+1} - \rho_n}{\rho_{n+1} + \rho_n}$$

k_n is called the resistivity contrast between neighbouring layers.

These results correspond to those of other authors who examined the potentials of burried current electrodes (Alfano, 1962; Merkel, 1971). All potentials can be written as:

$$V(r, z) = q_j \left(A_j + C_j \int_0^\infty \frac{\sum_i g_i e^{-2\lambda b_i}}{1 - k_i e^{-2\lambda h_1} - k_2 e^{-2\lambda h_2} + k_1 k_2 e^{-2\lambda(h_2 - h_1)}} J_0(\lambda r) d\lambda \right). \quad (8)$$

Substituting $u = e^{-2\lambda h_0}$ and $b_i = m_i \cdot h_0$, where h_0 is the unit length, the integrand of each expression for the potentials (7a-7c) can be transformed into the product of a

rational function and the Bessel function of zero order when only integer multiples of the unit length h_0 are permitted:

$$V(r, z) = q_j \left(A_j + C_j \int_0^\infty \frac{\sum_i g_i u^{m_i}}{P(u)} J_0(\lambda r) d\lambda \right) \tag{9}$$

where

$$P(u) = 1 - k_1 u^\alpha - k_2 u^\beta + k_1 k_2 u^{\beta - \alpha} \tag{10}$$

and

$$\alpha = \frac{h_1}{h_0}, \beta = \frac{h_2}{h_0}. \tag{11}$$

Each rational function can be expressed as power series following the increasing powers of its argument. Consequently the improper integrals can be transformed into infinite convergent series by means of the Weber-Lipschitz formula:

$$\int_0^\infty e^{-b\lambda} J_0(a\lambda) d\lambda = \frac{1}{(a^2 + b^2)^{1/2}} \quad (b > 0). \tag{12}$$

The general expression for the potentials (9) is:

$$V(r, z) = q_j \left(A_j + C_j \sum_{n=1}^\infty \frac{B_n}{(r^2 + (2n h_0)^2)^{1/2}} \right) \tag{13}$$

where

$$\frac{\sum_i g_i u^{m_i}}{P(u)} = \sum_{n=1}^\infty B_n u^{n-1}. \tag{14}$$

3. The Apparent Resistivity

The apparent resistivity of the arrays described above is given by

$$\rho_s = K \frac{\Delta V}{I} \tag{15}$$

where K is the configuration factor which depends only on the geometrical part of the array. K has the dimension of m . It is defined in such a way that $\rho_s(r)$ corresponds to the true specific resistivity when Equation (15) has been applied for the homogeneous half-space. To find K , the potential difference ΔV is evaluated for the described array in the homogeneous half-space. Generally the potential of a point source is:

$$V_{pq} = \frac{\rho \cdot I}{4\pi} \cdot \frac{1}{R_{pq}} + \frac{\rho \cdot I \cdot k_0}{4\pi} \cdot \frac{1}{R_{pq}^*} \tag{16}$$

where: p = index of the current electrode

q = index of the potential probe

R_{pq} = distance between the current and the potential electrodes

R_{pq}^* = distance between the current electrode p (reflected with respect to the boundary of the half-space) and the potential probe q

k_0 = resistivity contrast between the conducting and the non-conducting half-space.

Using Equation (15) for a two-electrode configuration we get:

$$K = \frac{4\pi}{(1/R_{11} + 1/R_{11}^* - 1/R_{12} - 1/R_{12}^* - 1/R_{21} - 1/R_{21}^* + 1/R_{22} + 1/R_{22}^*)}. \quad (17)$$

ΔV has to be evaluated by the expressions of the potential (13) and put into Equation (15) for the calculation of the model graphs of the apparent resistivity. For example the apparent resistivity for an asymmetrical configuration is (provided that E_1 is placed in layer 2 and E_2 in layer 1 ($h_1 < z_{E1} < h_2$; $z_{E2} < h_1$)):

$$\begin{aligned} \rho_s = & \rho_2(1 - k_1) K^* \left[\sum_{n=1}^{\infty} \frac{B_{2n}}{(1 + (2n h_0/r)^2)^{1/2}} - \sum_{n=1}^{\infty} \frac{B_{2n}}{(4 + (2n h_0/r)^2)^{1/2}} \right] \\ & - \rho_1 K^* \left[A_1^* + \sum_{n=1}^{\infty} \frac{B_{1n}}{((1 + a/r)^2 + (2n h_0/r)^2)^{1/2}} \right. \\ & \left. - \sum_{n=1}^{\infty} \frac{B_{1n}}{((2 + a/r)^2 + (2n h_0/r)^2)^{1/2}} \right] \end{aligned} \quad (18)$$

where

$$K^* = K/4\pi r$$

and

$$A_1^* = \frac{r}{(1/R_{21} + 1/R_{21}^* - 1/R_{22} - 1/R_{22}^*)}.$$

Those expressions, calculable by a digital computer, have been derived for each of the considered configurations. The computer was of the type CD 6400. The programming language was FORTRAN IV. A detailed description of the mathematical derivation and the computer programs can be found in Sebulke (1973).

4. Results of the Model Calculations

A large number of model graphs has been computed and apparent resistivity curves have been plotted in one diagramm by changing m_2 . Only a limited number of results will be presented here. Figure 4a shows the results for a one-electrode configuration (water depth: 10 m, penetration depth of the electrode into the sediment: 10 m). In this case ρ_2 is double as high as ρ_1 . The graph shows that it is possible to determine m_2 of up to 20 m with a good accuracy, especially in the region

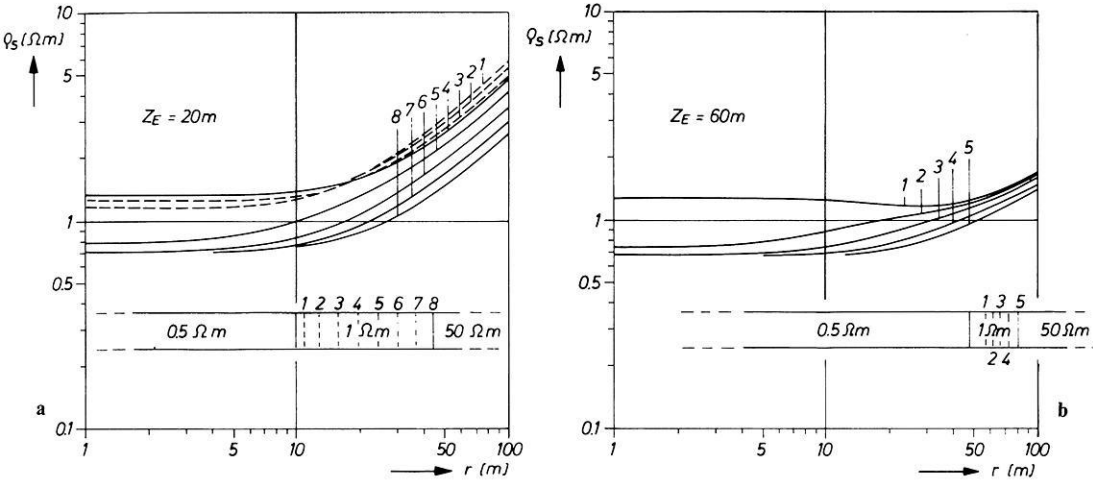


Fig. 4a and b. Computed apparent resistivity for the one-electrode configuration. a shallow water; b deep water

near the current electrode. The resolving power is made considerably worse with the increase of m_2 . It is possible to determine ρ_2 by the curves $\rho_s(r)$ for small r when m_2 is sufficiently large and provided that ρ_1 is known. This value is easily determined. The choice of the ratio ρ_1/ρ_2 is based on practical field measurements in the Mediterranean.

The next Figure 4b shows the results for deeper water both with the same resistivity ratio. In this case m_1 is 50 m. The source of the electrical field is placed 10 m inside the sediment. The increase in m_1 aggravates only slightly the resolving power. The surface of the water has no influence on the measurements beyond a water depth largely compared with the dimensions of the array. The accuracy of the determination of m_2 is bad when the potential electrodes are on the level of the water surface.

The two-electrode configuration has advantages because the very long supply-line for the second electrode at “infinity” is omitted. A peculiarity of the model graphs for the asymmetrical two-electrode configuration has to be mentioned in this context. K (17) shows a singularity, because the potential difference for this special configuration in the homogeneous half-space disappears for a special distance r . K as a function of the distance r is shown in Figure 5. This behaviour of K determines largely the form of the curves $\rho_s(r)$.

The symmetrical two-electrode configuration (Fig. 3b) gives a slightly improved resolving power for the same ground model (case 1: one-electrode configuration, Fig. 4a). The results are shown in Figure 6. A comparison with results of the one-electrode configuration (Fig. 4a) shows that the gradient of the curves $\rho_s(r)$ with the same parameter differs for large distances r . The resolving power does not change, but as mentioned before, the two-electrode configuration has some advantages with respect to the measuring procedure. A towed multiple conductor cable with electrodes at fixed distances r and an apparatus adapted to

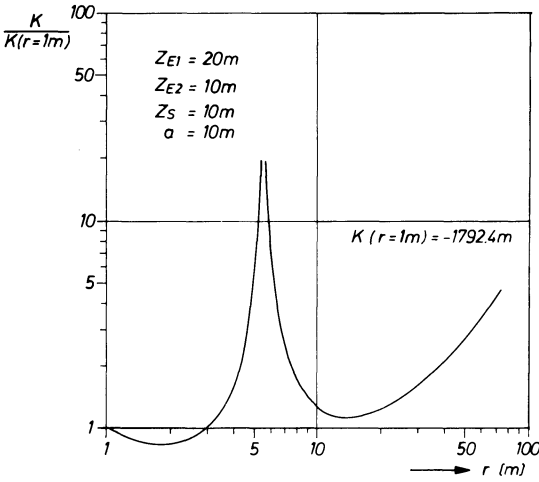


Fig. 5. The configuration factor for the asymmetrical two-electrode configuration

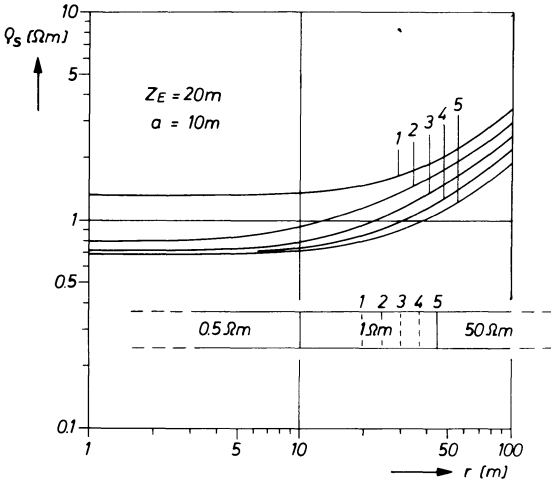


Fig. 6. Computed apparent resistivity for the symmetrical two-electrode configuration

the particular measurement conditions at sea have been constructed. It will be described by Bischoff in a later publication.

The asymmetrical two-electrode configuration has some measuring advantages, e.g. only one electrode cable, and at the same time a high resolving power may be expected.

The same model as before is considered for the first example of calculation (Fig. 7a). The current electrodes have a horizontal separation of $a = 10$ m. The electrode E_1 (see Fig. 3a) is inserted into the sediment, electrode E_2 is situated in the water layer. The singularity of the curve is caused by K . The model calculation shows strong variations between the $\rho_s(r)$ -curves for different thicknesses of m_2 . Figure 7a shows that in this special case h_2 can be determined up to a thickness $m_2 = 40$ m with an accuracy of ± 1 m. Even a relative reduction of ρ , does not impair the

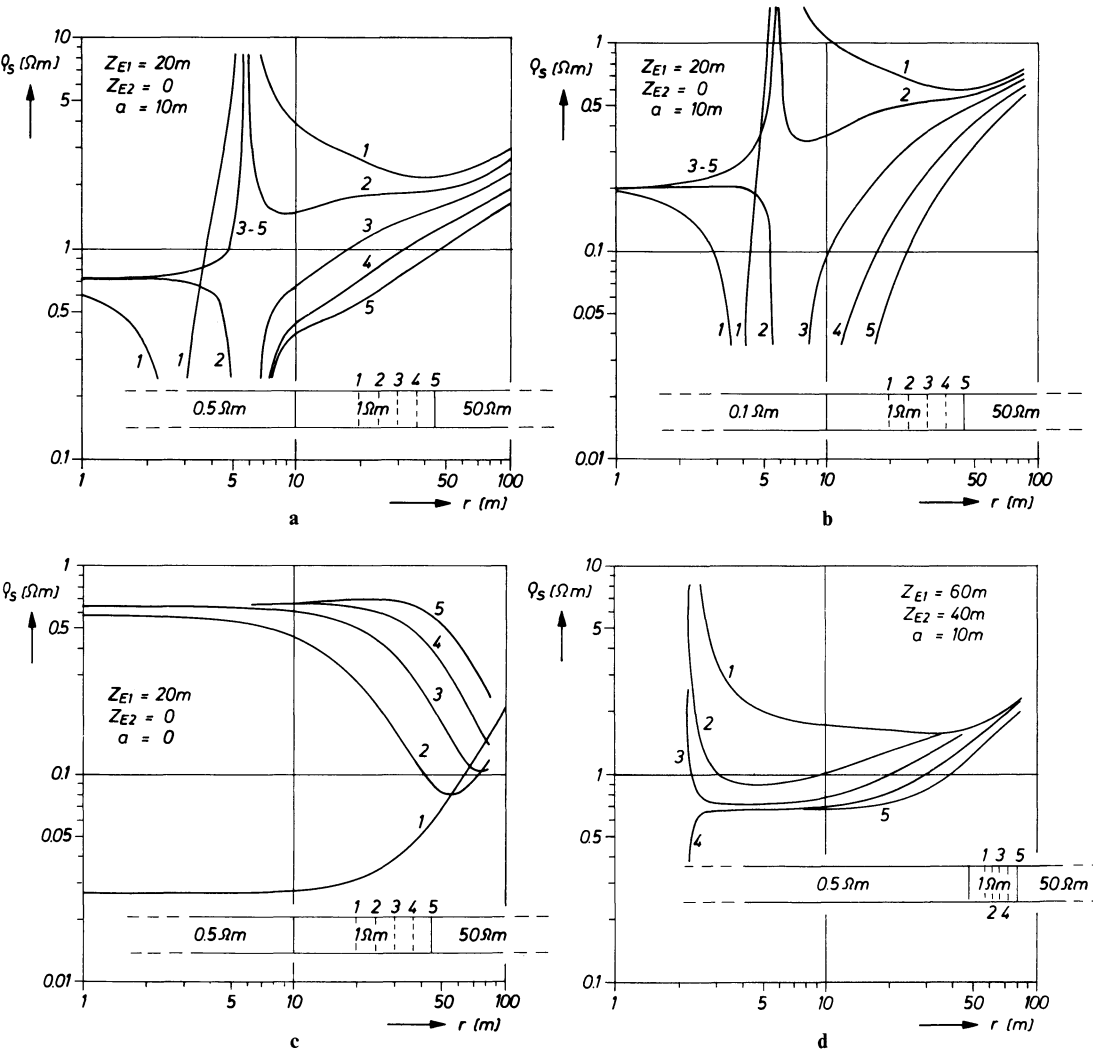


Fig. 7a – d. Computed apparent resistivity for the asymmetrical two-electrode configuration (Electrodes in different layers). **a** shallow water; **b** shallow water, $\rho_1/\rho_2=0,1$; **c** current electrodes perpendicular one upon another; **d** deep water

interpretation accuracy (Fig. 7b). These model calculations have been made for the same configuration but with a ratio of $\rho_1/\rho_2=0,1$.

A high efficiency will be obtained when the two sources are perpendicular to each other. The results of this geometrical array are shown in Figure 7c. Again the hitherto most frequent physical model is used. But measuring problems will arise for this version of the asymmetrical configuration because the potential differences between the electrodes at a current of $I = 1 \text{ A}$ go down to $\Delta V = 4 \mu\text{V}$ ($m_2 = 15 \text{ m}$). The calculations for this special array were checked by the aid of model measurements

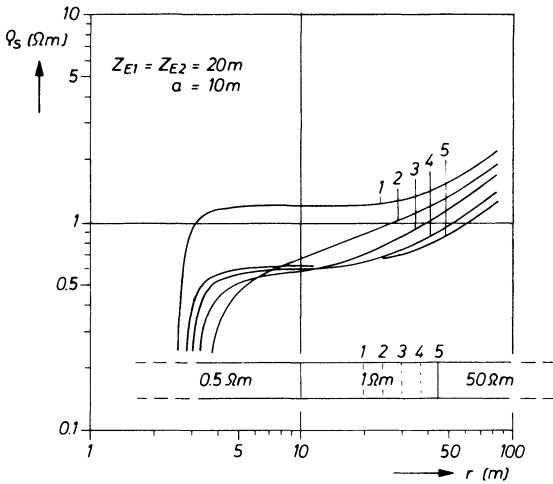


Fig. 8. Computed apparent resistivity for the asymmetrical two-electrode configuration (Both electrodes in the second layer)

in an electrolytical trough (Bischoff, 1973), and a good conformity has been observed.

A removal of the whole array deeper into the water layer aggravates the resolving power in relation to changes of m_2 . Figure 7d shows the model graphs for $h_1 = 50$ m. But the curves differ well enough to determine m_2 up to 30 m with a sufficient accuracy. The change of the position of electrode E_2 from the water layer into the layer 2 does not improve the interpretation accuracy and even aggravates the resolving power (Fig. 8).

5. Conclusion

Each of the three configurations examined is suitable for marine geophysical prospecting, but the one-electrode configuration will be excluded because of additional technical expenses. In spite of the small values of ρ_1 , the curves $\rho_s(r)$ are sensitive enough to changes of m_2 and ρ_2 , so that h_2 can be determined with a sufficient accuracy.

Each method gives useful results even for large water depths. ρ_1 and ρ_2 can be determined by additional measurements and by the behaviour of the sounding curves for small distances r . m_1 can be measured and the problem to determine m_2 is conditionally unique, provided that the prospected object can be described by a three-layer model.

Acknowledgements. I would like to thank Prof. Dr. J. Behrens and Prof. Dr. A. Wilke for some useful discussions and their interest in this problems. Thanks are due to all my colleagues who helped with the measuring in the Mediterranean.

References

- Alfano, L.: Geoelectrical prospecting with underground electrodes. *Geophys. Prospecting* **10**, 290–303, 1962
- Bischoff, J.: Eine Apparatur für die Durchführung modellgeoelektrischer Arbeiten nach der Widerstandsmethode zur Simulierung von geoelektrischen Messungen im marinen Bereich. Diplomarbeit, Berlin 1973
- Flathe, H.: A practical method of calculation geoelectrical model graphs for horizontal stratified media. *Geophys. Prospecting* **3**, 268–294, 1955
- Merkel, R. H.: Resistivity analysis for plane-layer-half-space models with burried current sources. *Geophys. Prospecting* **19**, 626–639, 1971
- Sebulke, J.: Entwicklung und Untersuchung einer Widerstandsmethodik zur geoelektrischen Prospektion im marinen Bereich. Dissertationschrift D 83, Technische Universität, Berlin 1973
- Terekhin, E. I.: Theoretical bases of electrical probing with an apparatus immersed in water. In: *Applied Geophysics U.S.S.R.* p. 169–195, Oxford: Pergamon Press 1962
- Van'Yan, L. L.: Theoretical curves for electrical sea probing with a sea-bottom apparatus. *Applied Geophysics* Nr. 50, Gostoptekhizdat 1956
- Volker, E., Dijkstra, J.: Determination des salinites des eaux dans le sous-sol du Zuiderzee par prospection geophysique. *Geophys. Prospecting* **3**, 111–125, 1955

Received January 6, 1977/Revised Version October 3, 1977

Interpretation of Magnetic Anomalies With Fourier Transforms, Employing End Corrections

B.S.R. Rao, I.V. Radhakrishna Murthy, and
D. Bhaskara Rao

Department of Geophysics, Andhra University, Waltair (India)

Abstract. The method of Fourier transforms has been extended to interpret the magnetic anomalies of arbitrarily magnetised horizontal circular cylinders, dykes and faults. The Fourier transforms of the magnetic anomalies are derived without any apriori assumption of the position of the source and its magnetisation. They are usually evaluated by numerical integration of the available anomalies along the finite length of the profile. ‘End corrections’, which account for the contributions of the unknown anomalies outside the length of the profile, have been suggested to improve the reliability of these functions. It is also shown that without these corrections, the derived functions tend to be highly oscillatory and no useful interpretation can be arrived at.

Formulae useful in actual interpretation are derived for the three models mentioned above, making use of the amplitude spectrum and some auxiliary functions derived from them. These new functions are found to be dependent on the shape of the body.

Key words: Fourier transforms – Magnetic interpretation – End corrections.

Introduction

Many articles have appeared in the recent literature on the use of Fourier transforms for interpreting gravity and magnetic anomalies. In this method, the anomalies in the space domain are transformed into the frequency domain and the various body parameters of the model are derived from the characteristic properties of the amplitude spectrum. Odegard and Berg (1965) derived expressions for the amplitude spectrum of the gravity anomalies of spheres, horizontal circular cylinders and vertical steps. Bhattacharya (1966), and Spector and Grant (1970) studied the continuous spectrum of the total field anomalies of prismatic bodies. Sharma and Geldart (1968) applied the method of Fourier transforms to interpret the gravity anomalies of two-dimensional faults. Rao and

Avasthi (1973) could determine all the body parameters of a symmetrical anticline from the amplitude spectrum of its gravity anomalies for a given density contrast.

Many authors (eg. Collins et al., 1974; Regan and Hinze, 1976) have recognised that the calculated spectra from the gravity and magnetic anomalies differ substantially from the true spectra so as to arrive at useful interpretation. The basic reason is that the anomalies are available only on a finite length of the profile, whereas the numerical integrations involved in the transformation require the data from $-\infty$ to $+\infty$ on the profile. During the course of the calculations, it is assumed or taken for granted that the data beyond the available length of the profile take zero values. In the present paper, corrections known as 'end corrections' are suggested for anomalies of two-dimensional bodies to improve the reliability of the spectrum calculated from them, when available over a finite length of the profile. The discussion is with special reference to the vertical magnetic anomalies of arbitrarily magnetised and arbitrarily striking cylinders, dykes and thick faults, but the same rules will apply to their total field anomalies also.

In the majority of papers published to date in this field it is assumed that the magnetisation is caused by induction. It is also assumed that the origin, with respect to which the anomaly expression is written, is known. In practice, the origin is not known and the magnetisation is not always caused by induction. Thus, in this paper, the anomaly expressions are written with reference to an arbitrary reference and methods are suggested to determine not only the body parameters of the model under question, but also the direction of magnetisation and the exact position of the body. Both the sine and cosine transforms are derived and used in interpretation. It is also found out that the shape of the body can be decided directly from the spectrum.

Derivation of Analytical Expressions

The Fourier transform $f^*(\omega)$ of a function $f(x)$ is defined by the relation

$$f^*(\omega) = \int_{-\infty}^{\infty} f(x) \exp(-i\omega x) dx$$

which is a complex quantity. $f(x)$ is the known geophysical data, and can be numerically integrated to give $f^*(\omega)$ for any given value of the spatial wave number ω . But the Fourier cosine and Fourier sine transforms are real quantities defined by the relations,

$$\text{FCOS}(\omega) = \int_{-\infty}^{\infty} f(x) \cos \omega x dx \quad \text{and} \quad \text{FSIN}(\omega) = \int_{-\infty}^{\infty} f(x) \sin \omega x dx.$$

The amplitude spectrum of $f(x)$ is defined as

$$\text{FT}(\omega) = \sqrt{\text{FCOS}^2(\omega) + \text{FSIN}^2(\omega)}.$$

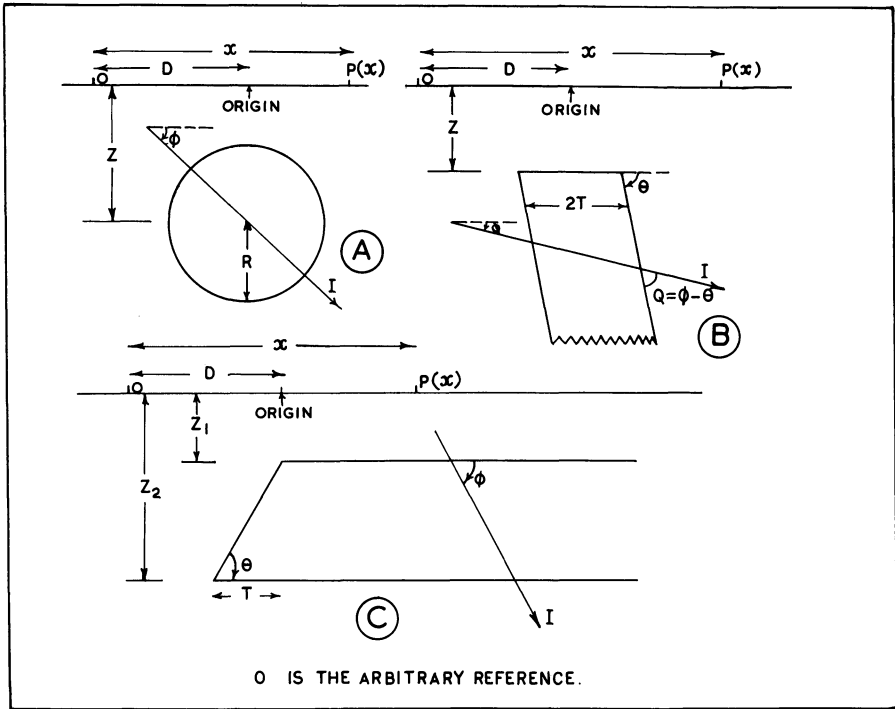


Fig. 1. Illustration of the various parameters. (A) Horizontal circular cylinder (B) Inclined dyke, and (C) Fault

i) Horizontal Circular Cylinder

The vertical magnetic anomaly over a horizontal circular cylinder is given by

$$\Delta V(x) = C_1(I_1 \sin \Phi - I_2 \cos \Phi) \tag{1}$$

where $I_1 = [Z^2 - (x - D)^2] / [(x - D)^2 + Z^2]^2$

$$I_2 = 2Z(x - D) / [(x - D)^2 + Z^2]^2$$

$$C_1 = 2\pi R^2 I$$

and the other parameters are as shown in Figure 1(A). Since the exact position of the cylinder is not known, the magnetic anomalies may be plotted from an arbitrary reference 0 on the profile. Thus C_1 , D , Φ and Z are the parameters to be obtained from the Fourier amplitude spectrum. To evaluate the transform of Equation (1), we may first evaluate the transforms of I_1 and I_2 separately, letting $D=0$ and finally employing the translation theorem. Accordingly I_1 and I_2 exhibit even and odd symmetry respectively, so that the sine transform of I_1 and cosine transform of I_2 are zero. Following from the Tables of integrals by Erdelyi et al. (1954), we have

$$\int_{-\infty}^{\infty} [1/(x^2 + Z^2)] \cos \omega x dx = (\pi/Z) \exp(-Z\omega)$$

and

$$\int_{-\infty}^{\infty} [x/(x^2 + Z^2)] \sin \omega x \, dx = \pi \exp(-Z\omega).$$

Differentiating the above with respect to Z we can deduce that

$$\int_{-\infty}^{\infty} [(Z^2 - x^2)/(x^2 + Z^2)^2] \cos \omega x \, dx = \pi \omega \exp(-Z\omega)$$

and

$$\int_{-\infty}^{\infty} [2Zx/(x^2 + Z^2)^2] \sin \omega x \, dx = \pi \omega \exp(-Z\omega).$$

Using the translation theorem i.e., the Fourier transform of $f(x-D)$ is $f^*(\omega) \exp(-iD\omega)$, we can finally obtain that

$$FCOS(\omega) = \pi C_1 \omega \exp(-Z\omega) \sin(\Phi + D\omega)$$

and

$$FSIN(\omega) = -\pi C_1 \omega \exp(-Z\omega) \cos(\Phi + D\omega) \tag{2}$$

ii) *Dipping Dyke*

Measuring the distance x from an arbitrary reference point 0 on the profile, the expression for the vertical magnetic anomaly of a dipping dyke can be written as

$$\Delta V(x) = C_2(I_3 \cos Q + I_4 \sin Q) \tag{3}$$

where $C_2 = 2I \sin Q$ $Q = \Phi - \theta$

$$I_3 = \arctan(\overline{x - D + T/Z}) - \arctan(\overline{x - D - T/Z})$$

$$I_4 = \frac{1}{2} \{ \ln[(x - D + T)^2 + Z^2] - \ln[(x - D - T)^2 + Z^2] \}$$

and the various other parameters are defined as in Figure 1(B). When $D=0$, I_3 and I_4 show even and odd symmetry respectively. To obtain the transforms of these functions, we may start from the following equations (Erdelyi et al., 1954)

$$\int_{-\infty}^{\infty} \left[\frac{T+x}{Z^2 + (T+x)^2} + \frac{T-x}{Z^2 + (T-x)^2} \right] \cos \omega x \, dx = -2\pi \sin T\omega \exp(-Z\omega)$$

and

$$\int_{-\infty}^{\infty} \left[\frac{Z}{Z^2 + (T+x)^2} - \frac{Z}{Z^2 + (T-x)^2} \right] \sin \omega x \, dx = -2\pi \sin T\omega \exp(-Z\omega).$$

Integrating the above with respect to Z , we have

$$\begin{aligned} & \int_{-\infty}^{\infty} [\arctan(\overline{x + T/Z}) - \arctan(\overline{x - T/Z})] \cos \omega x \, dx \\ & = 2\pi(\sin T\omega/\omega) \exp(-Z\omega) + \lambda_1 \end{aligned}$$

and

$$\frac{1}{2} \int_{-\infty}^{\infty} [\ln((x+T)^2 + Z^2) - \ln((x-T)^2 + Z^2)] \sin \omega x \, dx$$

$$= 2\pi(\sin T\omega/\omega) \exp(-Z\omega) + \lambda_2$$

where λ_1 and λ_2 are integration constants. The quantity

$$\arctan \overline{(x+T/Z)} - \arctan \overline{(x-T/Z)}$$

is actually the angle subtended by the top of the dyke at the point of observation. If $T=0$, the above quantity is zero for all values of x , so that the transform is also zero. Thus λ_1 is zero. Similarly it can be shown that λ_2 is also zero. Using translation theorem we can finally show that

$$\text{FCOS}(\omega) = (2\pi C_2/\omega) \exp(-Z\omega) \sin T\omega \cos(Q+D\omega)$$

and

$$\text{FSIN}(\omega) = (2\pi C_2/\omega) \exp(-Z\omega) \sin T\omega \sin(Q+D\omega) \quad (4)$$

for an infinite dyke.

iii) Fault

The vertical magnetic anomaly due to an arbitrarily magnetised fault model is given by

$$\Delta V(x) = C_3 \left[\frac{1}{2} \sin Q \ln \frac{Z_2^2 + (x-D+T)^2}{Z_1^2 + (x-D)^2} \right. \\ \left. + \cos Q \left(\arctan \frac{x-D+T}{Z_2} - \arctan \frac{x-D}{Z_1} \right) \right] \quad (5)$$

where $C_3 = 2I \sin \theta$, $Q = \Phi + \theta$, and the other parameters carry the meanings shown in Figure 1(C). Following the analysis similar to that of the dyke, we can finally deduce that

$$\text{FCOS}(\omega) = (\pi C_3/\omega) [\exp(-Z_1\omega) \sin(Q+D\omega) \\ - \exp(-Z_2\omega) \sin(Q+\overline{D-T\omega})]$$

and

$$\text{FSIN}(\omega) = -(\pi C_3/\omega) [\exp(-Z_1\omega) \cos(Q+D\omega) \\ - \exp(-Z_2\omega) \cos(Q+\overline{D-T\omega})] \quad (6)$$

when the distances are measured from an arbitrary reference point.

End Corrections

Evaluation of the sine and cosine transformation is essentially a technique of numerical integration, and many methods exist in this direction. But the method

used in evaluation of the integrals in the various examples cited in this paper is based on the method of Filon (1928–29). In any method, the integration is performed on the anomalies available on the finite length of the profile by writing, for example,

$$FCOS(\omega) = \int_{x_1}^{x_{2N+1}} f(x) \cos \omega x \, dx,$$

where x_1 and x_{2N+1} are the initial and final values of x in the profile containing $2N + 1$ observations. The arbitrary reference with which the values of x are measured may be anywhere, but can be selected as close to the origin as possible.

We will observe at a later stage that these ‘finite transforms’ tend to be highly oscillatory and that correct interpretation can not be obtained from them. These transforms can however be improved by applying corrections by calculating the contributions of the missing anomalies outside the length of the profile. The basis of this correction is as follows: A simple analytical expression can be fitted to the last few anomaly points, showing the trend or variation of the anomaly over this distance. This trend is assumed to prevail from the last anomaly point to infinity also. Knowing these expressions, one for each end of the profile, their Fourier transforms can be arrived at in a closed form. These may be called the correction terms and will represent the effects of the missing anomalies from $-\infty$ to x_1 and from x_{2N+1} to ∞ . They may be added to finite $FCOS(\omega)$ and finite $FSIN(\omega)$ worked out above.

i) Horizontal Circular Cylinder

At sufficiently large values of x , we can neglect D and Z^2 in comparison with x and x^2 respectively in Equation (1). Thus,

$$\Delta V(x) = C_1(-\sin \Phi/x^2) - (2 C_1 Z \cos \Phi/x^3)$$

and the magnetic anomaly may be assumed to obey the equation $\Delta V(x) = A_1/x^2 + A_2/x^3$ from $x = -\infty$ to $x = x_2$, and $\Delta V(x) = A_3/x^2 + A_4/x^3$ from $x = x_{2N}$ to $x = \infty$. A_1 and A_2 can be solved from the magnetic anomalies $\Delta V(1)$ and $\Delta V(2)$, and A_3 and A_4 from $\Delta V(2N)$ and $\Delta V(2N + 1)$. Knowing A_1, A_2, A_3 and A_4 , the correction can be worked out as follows:

C_{FCOS} = correction for Fourier cosine transform

$$\begin{aligned} &= \int_{-\infty}^{x_1} (A_1/x^2 + A_2/x^3) \cos \omega x \, dx + \int_{x_{2N+1}}^{\infty} (A_3/x^2 + A_4/x^3) \cos \omega x \, dx \\ &= A_1[C(1) + SI(1)] + A_3[C(N) + SI(N)] + A_2[-C(1)/2 |x_1| \\ &\quad + \omega S(1)/2 - (\omega/2) CI(1)] + A_4[C(N)/2x_{2N+1} - \omega S(N)/2 \\ &\quad + (\omega/2) CI(N)] \end{aligned}$$

C_{FSIN} = correction for Fourier sine transform

$$\begin{aligned} &= \int_{-\infty}^{x_1} (A_1/x^2 + A_2/x^3) \sin \omega x \, dx + \int_{x_{2N+1}}^{\infty} (A_3/x^2 + A_4/x^3) \sin \omega x \, dx \\ &= A_1[-S(1) + \text{CI}(1)] + A_3[S(N) - \text{CI}(N)] + A_2[S(1)/2|x_1| \\ &\quad + \omega C(1)/2 + (\omega/2) \text{SI}(1)] + A_4[S(N)/2x_{2N+1} + \omega C(N)/2 \\ &\quad + (\omega/2) \text{SI}(N)] \end{aligned}$$

where

$S(1) = \sin(\omega x_1)/ x_1 $	$C(1) = \cos(\omega x_1)/ x_1 $
$S(N) = \sin(\omega x_{2N+1})/x_{2N+1}$	$C(N) = \cos(\omega x_{2N+1})/x_{2N+1}$
$\text{SI}(1) = \omega \text{Si}(\omega x_1)$	$\text{CI}(1) = \omega \text{Ci}(\omega x_1)$
$\text{SI}(N) = \omega \text{Si}(\omega x_{2N+1})$	$\text{CI}(N) = \omega \text{Ci}(\omega x_{2N+1})$

ii) *Dipping Dyke*

At large values of x , we can write that,

$$\begin{aligned} &\arctan [(x - D + T)/Z] - \arctan [(x - D - T)/Z] \\ &= \arctan [2TZ/(Z^2 + (x - D)^2 + T^2)] \\ &= \arctan (2TZ/x^2) = 2TZ/x^2 \end{aligned}$$

and

$$\ln \frac{(x - D + T)^2 + Z^2}{(x - D - T)^2 + Z^2} = 2 \ln \frac{(x + T)}{(x - T)} = 2 \ln \frac{(x/T + 1)}{(x/T - 1)} = \frac{4T}{x}.$$

Substituting these in Equation (3), we may show that the magnetic anomaly due to a dyke varies according to the equation

$$\Delta V(x) = A_1/x + A_2/x^2 \quad \text{from } x = -\infty \text{ to } x = x_2,$$

and

$$\Delta V(x) = A_3/x + A_4/x^2 \quad \text{from } x = x_{2N} \text{ to } x = \infty.$$

Based on the first two and the last two anomalies on the profile, A_1 to A_4 can be solved. Then,

$$\begin{aligned} C_{\text{FCOS}} &= A_1 \text{CI}(1)/\omega - A_3 \text{CI}(N)/\omega + A_2 [C(1) + \text{SI}(1)] + A_4 [C(N) + \text{SI}(N)] \\ C_{\text{FSIN}} &= -A_1 \text{SI}(1)/\omega - A_3 \text{SI}(N)/\omega + A_2 [-S(1) + \text{CI}(1)] + A_4 [S(N) \\ &\quad - \text{CI}(N)] \end{aligned}$$

iii) *Fault*

For the fault model, it can be shown that the anomaly varies according to the equation

$$\begin{aligned} \Delta V(x) &= A_1/x + A_2/x^3 \quad \text{from } x = -\infty \text{ to } x = x_2, \text{ and} \\ \Delta V(x) &= A_3/x + A_4/x^3 \quad \text{from } x = x_{2N} \text{ to } x = \infty. \end{aligned}$$

The corrections can be finally worked out as:

$$C_{\text{FCOS}} = A_1 \text{CI}(1)/\omega - A_3 \text{CI}(N)/\omega \\ + A_2 [-C(1)/2 |x_1| + \omega S(1)/2 - (\omega/2) \text{CI}(1)] \\ + A_4 [C(N)/2x_{2N+1} - \omega S(N)/2 + (\omega/2) \text{CI}(N)]$$

$$C_{\text{FSIN}} = -A_1 \text{SI}(1)/\omega - A_3 \text{SI}(N)/\omega \\ + A_2 [-S(1)/2 |x_1| + \omega C(1)/2 + (\omega/2) \text{SI}(1)] \\ + A_4 [S(N)/2x_{2N+1} + \omega C(N)/2 + (\omega/2) \text{SI}(N)]$$

Method of Analysis and Examples

For any given magnetic profile, the Fourier transforms FCOS(ω) and FSIN(ω) can be calculated by numerical integration for different values of ω . From these data we can determine the various parameters of the model.

i) Horizontal Circular Cylinder

The amplitude spectrum for this model can be obtained from Equation (2) as

$$FT(\omega) = \sqrt{\text{FCOS}^2(\omega) + \text{FSIN}^2(\omega)} = \pi C_1 \omega \exp(-Z\omega). \quad (7)$$

The amplitude spectrum $FT(\omega)$ shows a maximum at $\omega = \omega_{\text{max}}$ given by $Z = 1/\omega_{\text{max}}$ from which the depth can be found out. If ω is expressed in radians per station spacing, Z is obtained in units of station spacing. The value of C_1 is then solved from any one value of $FT(\omega)$ by substituting the value of Z thus obtained in Equation (7). Alternatively, a new function $F(\omega)$ can be worked out from the amplitude spectrum as defined below:

$$F(\omega) = FT(\omega)/\omega = \pi C_1 \exp(-Z\omega).$$

This, when drawn on a semi-logarithmic paper, appears as a straight line having a slope of $-Z$ and cutting the ordinate at πC_1 . Φ may be determined from the relation, $\Phi = \arctan[-\text{FCOS}(0)/\text{FSIN}(0)]$. An alternative procedure may also be followed to calculate D and Φ . The ratio $-\text{FCOS}(\omega)/\text{FSIN}(\omega)$ is calculated for different values of ω . Then the quantity $\arctan[-\text{FCOS}(\omega)/\text{FSIN}(\omega)]$ when plotted against ω gives a straight line defined by $\Phi + D\omega$. This straight line has a slope of D and cuts the ordinate at Φ . Φ in the correct quadrant may be finally worked out from the signs of FCOS(ω) and FSIN(ω).

Figure 2 shows as an example the interpretation of magnetic anomalies over a cylinder. The magnetic profile, the transforms FCOS(ω) and FSIN(ω) along with the Fourier spectrum $FT(\omega)$ and the function $F(\omega)$ are also indicated in the figure. The theoretical values of these functions over the range of ω considered, coincide with the corrected transforms and consequently are not shown. The various parameters calculated from these functions are as follows: Depth=5

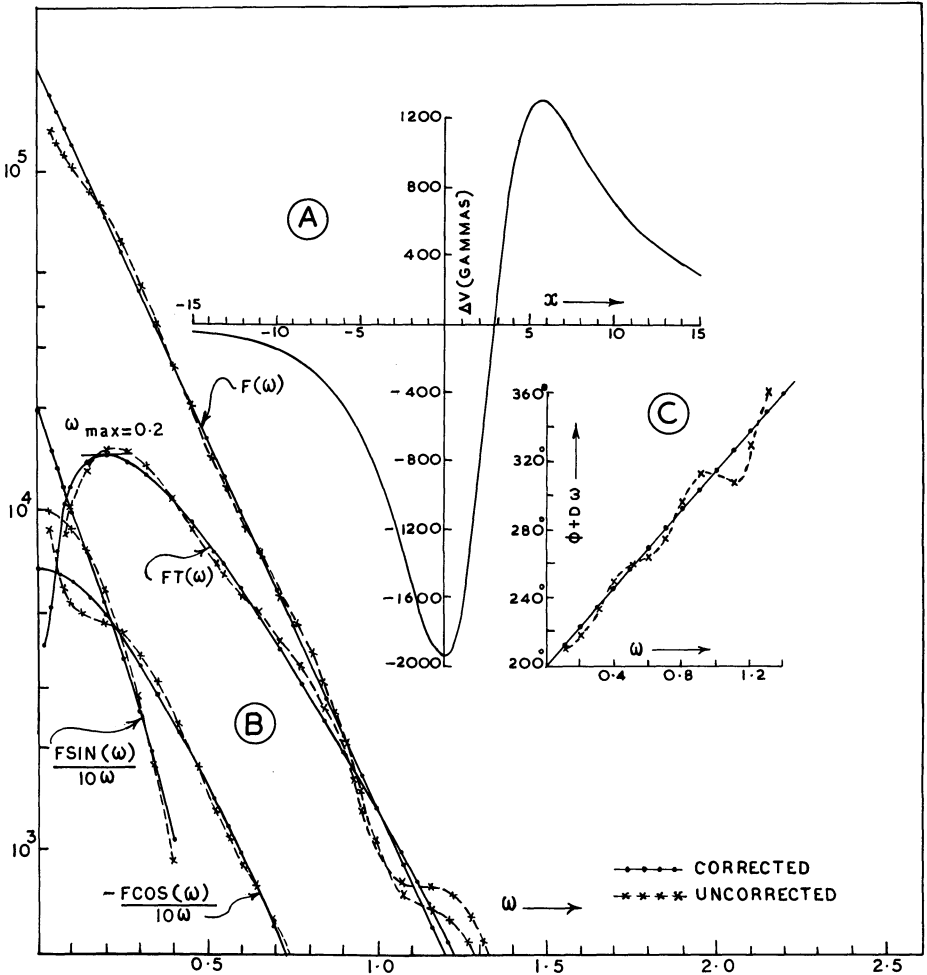


Fig. 2. Interpretation of a theoretical vertical magnetic anomaly profile over an arbitrarily magnetised horizontal circular cylinder. (A) Magnetic profile (B) Variation of $FSIN(\omega)$, $FCOS(\omega)$ and $F(\omega)$ against ω , and (C) Diagram for calculation of Φ and D

units (assumed value = 5 units), $\Phi = 199$ degrees (assumed value = 200 degrees) origin = 1.98 units (assumed value = 2.00 units).

ii) Dipping Dyke

For the dyke model, the amplitude spectrum is given by

$$FT(\omega) = (2\pi C_2 / \omega) \exp(-Z\omega) |\sin(T\omega)|. \tag{8}$$

A new function $F(\omega)$ can be calculated as follows:

$$F(\omega) = FT(\omega) \times \omega = 2\pi C_2 \exp(-Z\omega) |\sin(T\omega)|. \tag{9}$$

The function $F(\omega)$ is zero at points defined by $T\omega_0 = n\pi$ ($n=0, 1, 2, \dots$). In practice the zero points will not be brought out on the $F(\omega)$ curve because this function can never be negative and thus has no cross-overs. However, the zero-points will appear as 'sharp minima' on the $F(\omega)$ curve and can therefore be easily identified. Figure 3 shows the functions $F(\omega)$, $\text{FCOS}(\omega)$ and $\text{FSIN}(\omega)$ calculated for a theoretical anomaly profile over a dyke having $2T=4$ times the station spacing and $Z=2$ times the station spacing. The anomaly profile used for numerical integration is shown in Figure 3(A). In Figure 3(B), the functions $F(\omega)$, $\text{FCOS}(\omega)$ and $\text{FSIN}(\omega)$ for this profile are shown. The function $F(\omega)$ is calculated both from the corrected and uncorrected values of $\text{FCOS}(\omega)$ and $\text{FSIN}(\omega)$ and is plotted separately. The function $F(\omega)$ is also calculated theoretically by substituting $Z=2$ and $T=2$ in Equation (9), and shown as open circles in the same figure. It can be observed from this figure that the $F(\omega) - \omega$ curve as derived from the uncorrected values of $\text{FCOS}(\omega)$ and $\text{FSIN}(\omega)$ is highly oscillatory and does not give any useful information. Also the uncorrected values of $F(\omega)$ deviate too much from the theoretical values for all values of ω greater than one radian per station spacing. In contrast to this, the corrected values of $F(\omega)$ show a consistent trend. They also agree closely in magnitude to the theoretical values upto $\omega=3.2$ radians per grid spacing. Figure 3 thus brings out the importance and need of applying the correction to the numerically evaluated transforms, and shows the extent to which the evaluated transforms are improved.

To determine T , we can use any one of the values of ω_0 , at which the function $F(\omega)$ vanishes. If ω_0 is the position of the first zero-point, then,

$$T = \pi / \omega_0. \quad (10)$$

If ω_0 is expressed in radians per station spacing, T will be given in station spacings. Alternatively, two consecutive values of ω_0 ($=\omega_{01}$ and ω_{02} say) can be located to find out T by the formula, $T = \pi / (\omega_{02} - \omega_{01})$. The use of this formula may however be avoided because $F(\omega)$ cannot be calculated very accurately at higher values of ω . Either of the two formulae determines T independent of Z , D and C_2 . Z can be determined from the position of the maximum value of $F(\omega)$. This is maximum or minimum if

$$Z = T \cot(T\omega_{\max}). \quad (11)$$

Actually $F(\omega)$ shows many turning points and any value of ω_{\max} corresponding to any one of these turning points may be used in the above equation to find out Z . Because the function $F(\omega)$ is obtained more accurately at lower values of ω , it is preferable to use the location of the first turning point only for more accurate values of Z . Z is thus determined independent of C_2 , D and Q .

C_2 may be determined by substituting the values of T and Z thus obtained in Equation (9), knowing $F(\omega)$ for any given value of ω . Q and C_2 may also be determined from the values of $\text{FCOS}(0)$ and $\text{FSIN}(0)$ because, from Equation (4) it can be shown that, $\text{FCOS}(0) = 2\pi C_2 T \cos Q$ and $\text{FSIN}(0) = 2\pi C_2 T \sin Q$. Alternatively, the relation $\arctan[\text{FSIN}(\omega)/\text{FCOS}(\omega)] = Q + D\omega$ is a straight line having a slope D and intersecting the ordinate at Q . Although this prop-

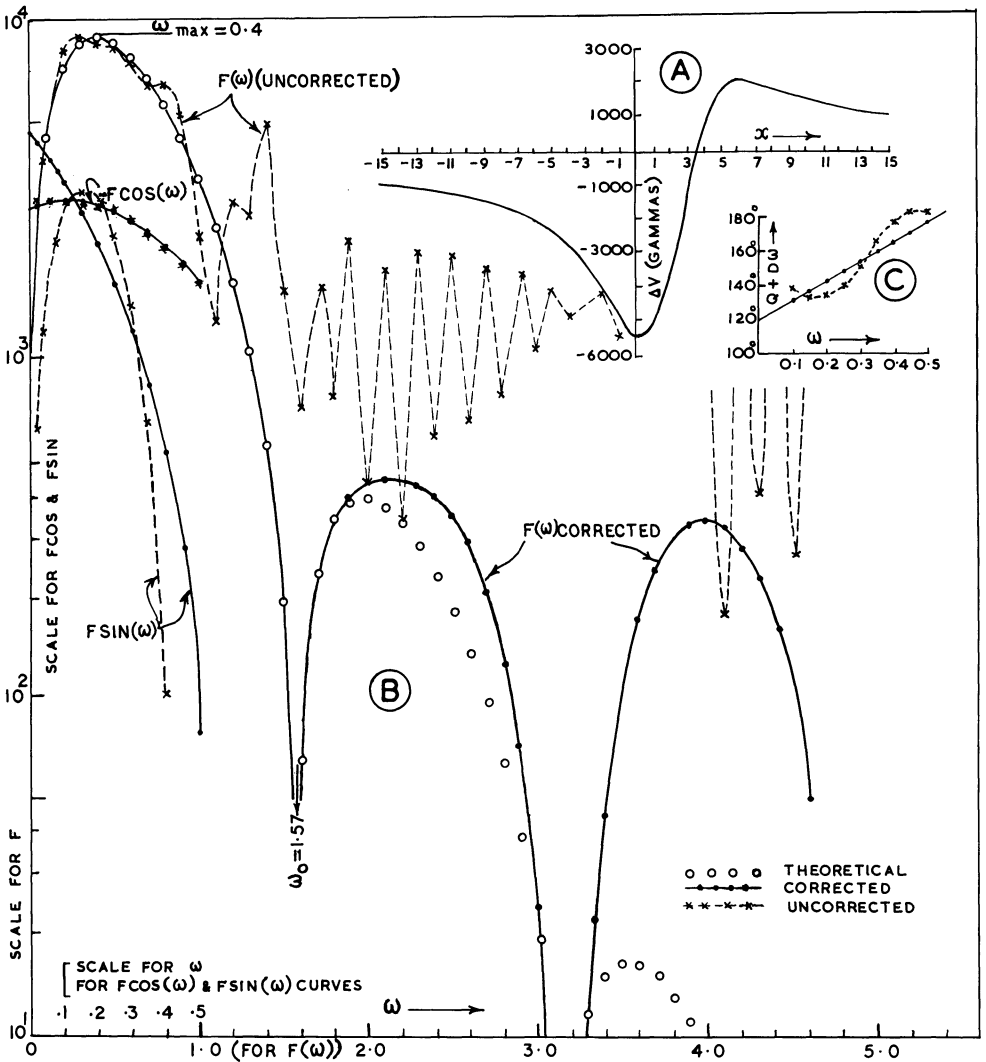


Fig. 3. Interpretation of a theoretical vertical magnetic anomaly profile over an arbitrarily magnetised dyke. (A) Magnetic profile (B) Variation of $FSIN(\omega)$, $FCOS(\omega)$ and $F(\omega)$ against ω , and (C) Diagram for calculation of Q and D

erty is valid for all values of ω , calculation of the quantity $\arctan[FSIN(\omega)/FCOS(\omega)]$ shall be limited to small values of ω , particularly in the interpretation of field profiles. This is because the functions $FSIN(\omega)$ and $FCOS(\omega)$ are not very accurate at higher values of ω , as we have already noted above. Also geological bodies do not fit perfectly to a dyke model and do not have a uniform magnetisation throughout their volume.

The values of Z , T , Q and D as calculated from the above rules of interpretation for the profile shown in Figure 3(A) are as follows: Thickness

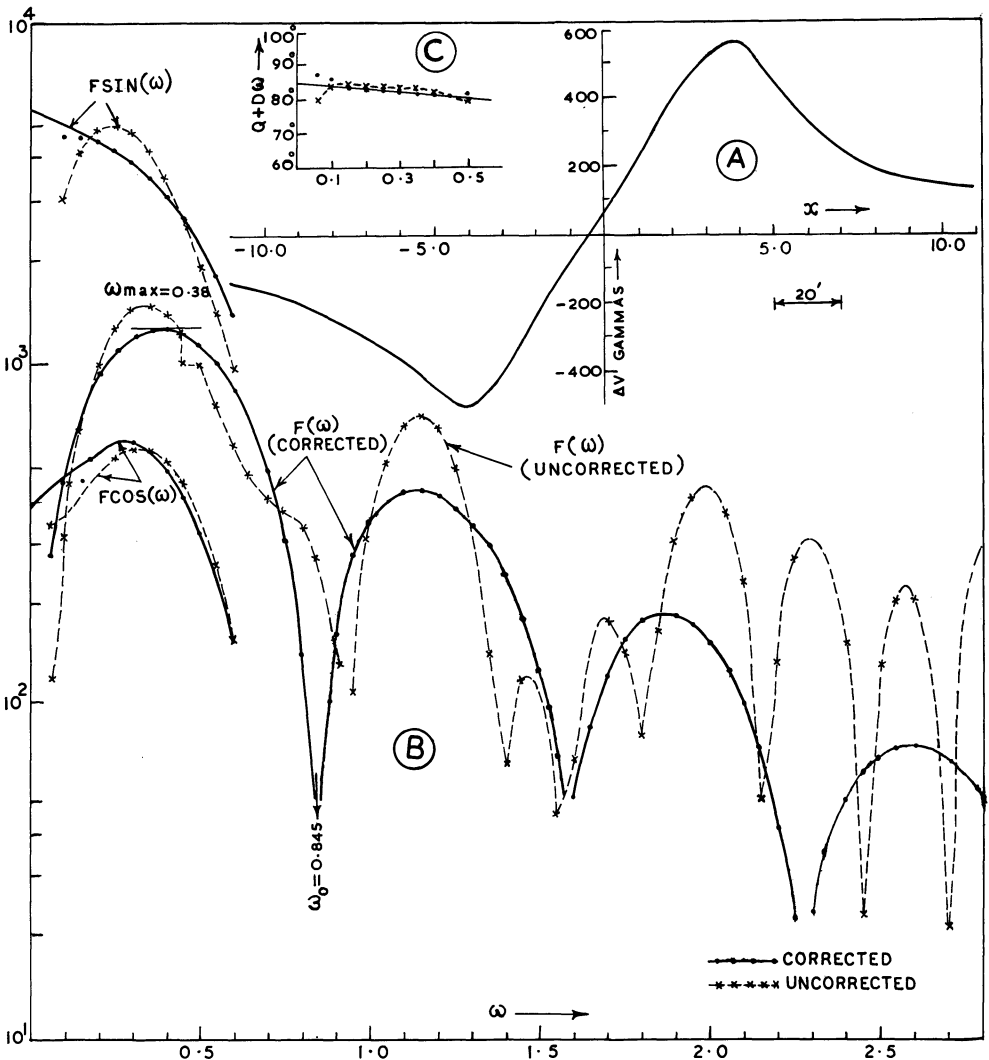


Fig. 4. Interpretation of a vertical magnetic anomaly profile over an outcropping quartz-magnetite dyke-like body, Karimnagar area, Andhra Pradesh. (A) Magnetic Profile (B) Variation of $FSIN(\omega)$, $FCOS(\omega)$ and $F(\omega)$ against ω , and (C) Diagram for calculation of Q and D

=4.0 units (assumed value=4.0 units), Depth = 1.94 units (assumed value=2.00 units), $Q=120$ degrees (assumed value=120 degrees), and $D=2.01$ units (assumed value=2.00 units).

Figure 4 shows the interpretation of a field example of vertical magnetic anomalies observed over a dyke-like body by the method of Fourier transforms. Figure 4(A) is a magnetic anomaly profile taken over an outcropping quartz-magnetite dyke-like body of thickness 80 ft in Karimnagar area, Andhra Pradesh (Subba Rao, 1974). The transformed anomalies of this profile, both corrected and uncorrected, and the function $F(\omega)$ are also shown in the figure.

The corrected transforms are interpreted by the application of the rules cited above. The profile is also interpreted on the computer by the method of iteration of Rao and Radhakrishna Murthy (1973). The values obtained for various parameters are as follows: Thickness = 74 ft (by iteration 75 ft), Depth = 6 ft (by iteration 9 ft), $Q = 86$ degrees (by iteration 85 degrees), and $D = -1.8$ ft (by iteration -2.3 ft). It may be observed that the results obtained by Fourier transformation and also by the method of iteration mentioned above are close to each other.

iii) Fault

The expressions for the Fourier cosine and sine transforms of the magnetic anomalies over faults are given in Equation (6). To calculate the various parameters, we evolve a new function $F(\omega)$ defined as

$$\begin{aligned} F(\omega) &= \omega FT(\omega) = \omega [\text{FCOS}^2(\omega) + \text{FSIN}^2(\omega)]^{1/2} \\ &= \pi C_3 [\exp(-2Z_2\omega) + \exp(-2Z_1\omega) \\ &\quad - 2\exp(-\overline{Z_1 + Z_2}\omega) \cos(T\omega)]^{1/2}. \end{aligned}$$

At large values of ω , this becomes, $F(\omega) = \pi C_3 \exp(-Z_1\omega)$, showing that the $F(\omega)$ versus ω curve, when drawn on a semi-logarithmic paper, degenerates into a straight line. The slope of this straight line gives $-Z_1$. The intercept of this straight line on the ordinate is equal to πC_3 and hence C_3 can be calculated. The relation

$$\arctan [-\text{FCOS}(\omega)/\text{FSIN}(\omega)] = Q + D\omega$$

is a straight line at large values of ω , corresponding to the straight line portion of the function $F(\omega)$. From this straight line, Q and D can be calculated. To find out the other parameters, we may determine the values of $\text{FCOS}(0)$ and $\text{FSIN}(0)$, which are given by

$$\text{FCOS}(0) = \pi C_3 [T \cos Q + (Z_2 - Z_1) \sin Q] = \pi C_3 (Z_2 - Z_1) \text{cosec } \theta \cos \phi$$

$$\text{FSIN}(0) = \pi C_3 [T \sin Q - (Z_2 - Z_1) \cos Q] = \pi C_3 (Z_2 - Z_1) \text{cosec } \theta \sin \phi.$$

From these, the parameters ϕ , θ and Z_2 can be worked out by the relations

$$\Phi = \arctan [\text{FSIN}(0)/\text{FCOS}(0)], \quad \theta = Q - \Phi$$

and

$$Z_2 = (\sin \theta / \pi C_3) \sqrt{\text{FCOS}^2(0) + \text{FSIN}^2(0)} + Z_1.$$

Figure 5 shows an actual example of magnetic fault interpretation worked out by the method of Fourier transforms. The function $F(\omega)$ as obtained from the uncorrected values of $\text{FCOS}(\omega)$ and $\text{FSIN}(\omega)$ is also plotted to bring out again the need of applying the 'end corrections'. The values of the various parameters interpreted from the corrected transforms along with the assumed

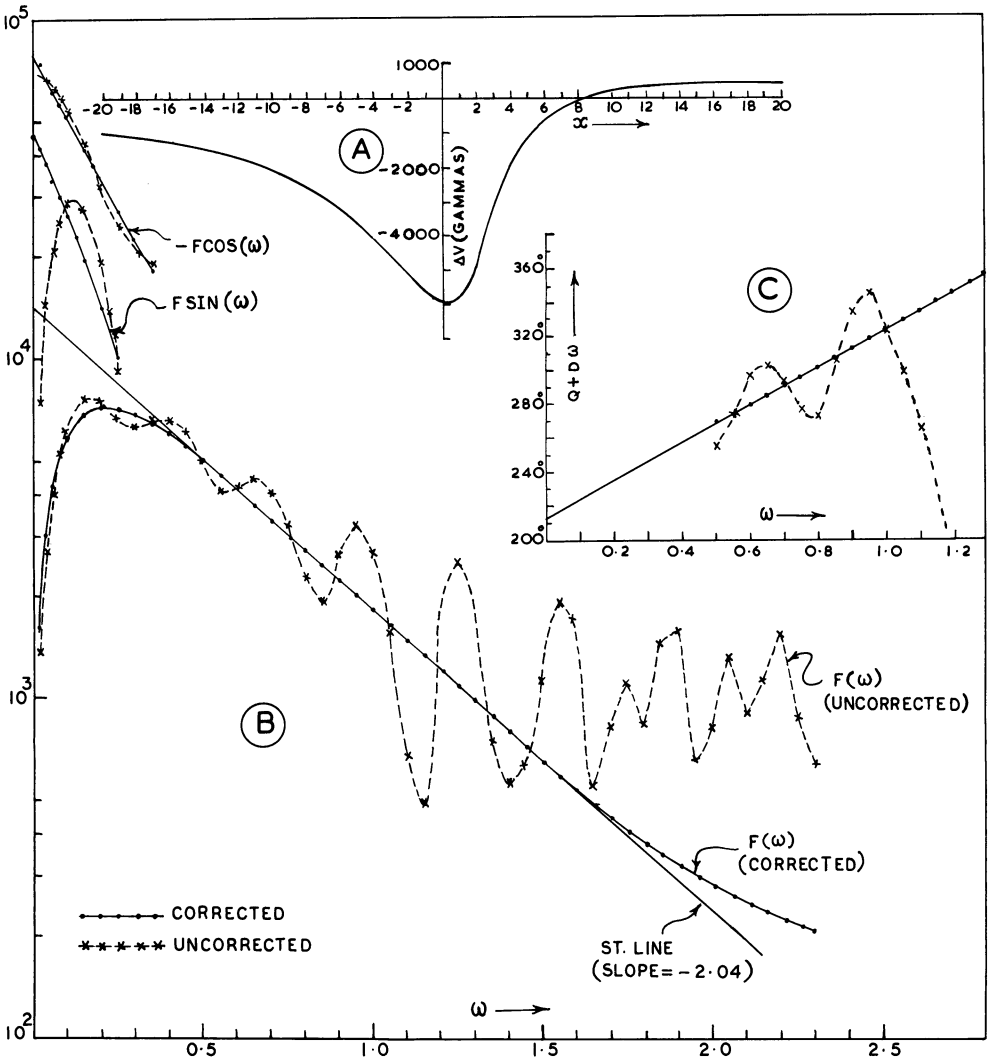


Fig. 5. Interpretation of a theoretical vertical magnetic anomaly profile over an arbitrarily magnetised fault. (A) Magnetic profile (B) Variation of $FSIN(\omega)$, $FCOS(\omega)$ and $F(\omega)$ against ω , and (C) Diagram for calculation of Q and D

values are as follows: $Z_1 = 2.04$ units (assumed value = 2.00 units), $Z_2 = 7.90$ units (assumed value = 8.00 units), $D = 1.92$ units (assumed value = 2.00 units), $\Phi = 149.8$ degrees (assumed value = 150 degrees), and $\theta = 62.7$ degrees (assumed value = 60 degrees).

Discussion

This paper does not advocate any superiority of the method of Fourier transforms over the other methods of interpretation of magnetic anomalies of simple

geometric models. It only studies the possibility of interpreting these anomalies in a generalised case where the magnetisation is not by induction and when the position of the body is not known. By deriving both the sine and cosine transforms, it is shown that both the direction of magnetisation and the position of the body can be easily determined. 'End corrections' are suggested, probably for the first time, to improve the sine and cosine transforms obtained by numerical integration of the anomalies over a limited length of the profile. It is observed that without application of these corrections, the derived transforms tend to be highly oscillatory and any information obtained, there from may not be reliable. It is also observed in this analysis that even the corrected transforms tend to deviate from true transforms for $\omega > 2.0$. However, this will not affect the interpretation because all body parameters are deduced at lower frequencies. The validity of the expressions, representing the anomalies outside the length of the profile is verified by calculating a few anomalies from these expressions and comparing them with those by the exact formulae. Further, the constants A_1 to A_4 were determined from the edge anomalies, with and without application of the procedure of least-squares, and it was found that the application of the least-square procedure does not improve the values of these constants.

The following advantages are usually mentioned for the method of Fourier transforms: (a) All anomalous field values are taken into consideration during analysis, (b) calculations of derivatives and continuation to different levels are easily carried out in the frequency domain than in the space domain. In addition to the above, we observe in this paper two interesting applications of the method of Fourier transforms. The first is that the shape of the function $F(\omega)$ depends on the shape of the body, and consequently it can be determined. $F(\omega)$, when plotted, against ω on semi-logarithmic paper is a straight line for the cylinder, a curve showing a series of maxima for the dyke, and a curve showing a maximum and then degenerating into a straight line for a fault. The second relates to the interpretation of magnetic anomalies of faults. We are not aware of any simple and standardised method of interpreting the magnetic anomalies of arbitrarily magnetised faults. The difficulty is due to the large number of parameters to be obtained from the anomalies. In contrast to this, all the parameters of the model can be solved very easily, at least theoretically, by the method of Fourier transforms.

Acknowledgements. Research work reported here is supported by financial assistance from the Council of Scientific and Industrial Research, India. Thanks are due to Prof. V. Bhaskara Rao, Head of the Department of Geophysics, Andhra University, Waltair for providing all facilities during the progress of the work. The computations for the construction of the various diagrams have been made on the IBM 1130 Computer available at the Andhra University.

References

- Bhattacharya, B.K.: Continuous spectrum of the total magnetic field anomaly due to a rectangular prismatic body. *Geophysics* **31**, 97–121, 1966
Collins, S.J., Dodds, A.R., Johnson, B.D.: Gravity profile interpretation using the Fourier transforms. *Geophysics* **39**, 862–866, 1974

- Erdelyi, Arthur, et al.: Tables of Integral transforms. New York: McGraw-Hill Book Company, Inc., 1954
- Filon, L.N.G.: On a quadrature formula for trigonometric integrals. Proc. Roy. Soc. Edinburgh **49**, 38–47, 1928–1929
- Odegard, M.E., Berg, Jr. J.W.: Gravity interpretation using the Fourier integral. Geophysics **30**, 424–438, 1965
- Rao, B.S.R., Radhakrishna Murthy, I.V., Visweswara Rao, C.: Two methods for computer interpretation of magnetic anomalies of dikes. Geophysics **38**, 710–718, 1973
- Rao, K.G.C., Avasthi, D.N.: Analysis of the Fourier spectrum of the gravity effect due to two-dimensional triangular prism. Geophys. Prospecting **21**, 526–542, 1973
- Regan, R.D., Hinze, W.J.: The effect of finite data length in the spectral analysis of ideal gravity anomalies, Geophysics **41**, 44–55, 1976
- Sharma, B., Geldart, L.P.: Analysis of gravity anomalies using Fourier transforms. Geophys. Prospecting **16**, 77–93, 1968
- Spector, A., Grant, S.: Statistical models for interpreting aeromagnetic data. Geophysics **35**, 293–302, 1970

Received January 12, 1977/Revised Version June 15, 1977

Short Communication

Extreme Models From the Maximum Entropy Formulation of Inverse Problems

E. Rietsch

Deutsche Texaco Aktiengesellschaft, Hauptlaboratorium für Erdölgewinnung, D-3101 Wietze, Federal Republic of Germany

Key words: Extreme model – Maximum entropy – Density – Earth.

In geophysics an Earth model is usually understood to mean a finite number of functions of the position vector \mathbf{r} representing the distribution of some physical properties within the Earth. In 1972, Parker proposed that a kind of “extreme model” might be the type of information that should be extracted from data (observations) too limited to allow inversion to a meaningful Earth model by the Backus-Gilbert inversion technique (Backus, Gilbert, 1967, 1968). Such a model is extreme in the sense that it places bounds on the properties of all Earth models complying with a set of given data. In this way Parker showed, for instance, that no Earth model with mean density $\bar{\rho}$ and ratio

$$y = 5I/(2MR^2)$$

(where I , M , and R denote moment of inertia, mass, and radius of the Earth, respectively) can have a maximum density lower than

$$\rho_0 = \bar{\rho} y^{-3/2}. \tag{1}$$

It is the purpose of this note to show, via the example of the density distribution within the Earth, that this idea of handling inverse problems can also be implemented by means of the maximum entropy method (Rietsch, 1977).

According to this latter paper (Eq. (57) with $N \rightarrow \infty$) the expectation value of the density has the form (with slightly modified notation)

$$\bar{\rho}(x) = \rho_l + 1/h(x) - \Delta\rho / \{\exp[\Delta\rho h(x)] - 1\} \tag{2}$$

where $x = r/R$. The abbreviation $h(x)$ stands for

$$h(x) = \lambda_1 + \lambda_2 X^2. \tag{3}$$

The Lagrange multipliers λ_1 and λ_2 are to be determined in such a way that $\bar{\rho}(x)$ satisfies

$$\int_0^1 \bar{\rho}(x) x^2 dx = \bar{\rho}/3$$

$$\int_0^1 \bar{\rho}(x) x^4 dx = y \bar{\rho}/5. \quad (4)$$

It is a particular feature of this expectation value of the density that it has been derived with the assumption, that all possible density values within the Earth are bounded by a lower density limit ρ_l and an upper density limit $\rho_u = \rho_l + \Delta\rho$. In general, the range of possible values of the density extends from zero to some maximum density which is usually high enough to make $\Delta\rho h(x) \gg 1$ and hence render the last term on the right hand side of Equation (2) negligible.

The density distribution computed from Equation (2) with this assumption and $\rho_l = 0$ and 1 g/cm^3 , respectively, turned out to be in good agreement with established density distributions employing additional information.

This is, however, just one way of using Equation (2). An alternative application of this equation is to ask for the lowest possible value of ρ_u for a given ρ_l . Apparently ρ_u attains this lowest possible value if

$$\bar{\rho}(x) = \rho_u \quad \text{for some } x, \quad (5)$$

i.e., if the expectation value actually reaches the upper density limit. If in this case $\bar{\rho}(x)$ still allows Equations (4) to be satisfied, it is the density distribution with the lowest upper density limit that complies with the given data.

Explicitly, condition (5) reads

$$\Delta\rho = 1/h(x) - \Delta\rho/\{\exp[\Delta\rho h(x)] - 1\}. \quad (6)$$

It is satisfied for

$$1/h(x) \rightarrow 0, \quad \exp[\Delta\rho h(x)] \rightarrow 0, \quad (7)$$

and, since $\bar{\rho}(x)$ is a monotonic function of $h(x)$, this is the only solution.

Let

$$\lambda_1 = -\lambda \cos \varphi, \quad \lambda_2 = \lambda \sin \varphi, \quad \lambda = (\lambda_1^2 + \lambda_2^2)^{1/2}. \quad (8)$$

Then $h(x)$ can be written as

$$h(x) = -\lambda(\cos \varphi - x^2 \sin \varphi),$$

and, for $\lambda \rightarrow \infty$, we get

$$\bar{\rho}(x) = \begin{cases} \rho_l & \text{for } \cos \varphi - x^2 \sin \varphi < 0 \\ \rho_u & \text{for } \cos \varphi - x^2 \sin \varphi > 0. \end{cases} \quad (9)$$

This means $\bar{\rho}(x)$ is discontinuous at some $x_0 = \sqrt{\cot \varphi}$. Confining our attention to the case

$$\bar{\rho}(x) = \begin{cases} \rho_u & 0 \leq x < x_0 \\ \rho_l & x_0 < x \leq 1 \end{cases} \quad (10)$$

we get by substituting (10) for $\bar{\rho}(x)$ in Equations (4)

$$\begin{aligned} x_0^3 \rho_u + (1 - x_0^3) \rho_l &= \bar{\rho} \\ x_0^5 \rho_u + (1 - x_0^5) \rho_l &= y \bar{\rho}. \end{aligned} \quad (11)$$

Elimination of x_0 from these equations leads to

$$\rho_u = \rho_l + (\bar{\rho} - \rho_l)^{5/2} / (y \bar{\rho} - \rho_l)^{3/2} \quad (12)$$

which reduces to Equation (1) for $\rho_l = 0$.

Though demonstrated for this particular example only, the method is, of course, applicable to any other inverse problem of this kind. It is perhaps also appropriate to point out that extreme models obtained in this way are independent of the particular prior probability distribution provided it does not vanish at the upper and/or lower limits of the admitted function values.

Acknowledgement. I am indebted to Deutsche Texaco Aktiengesellschaft for the permission to publish this paper.

References

- Backus, G., Gilbert, F.: Numerical applications of a formalism for geophysical inverse problems, *Geophys. J.*, **13**, 247–276, 1967
 Backus, G., Gilbert, F.: The resolving power of gross Earth data, *Geophys. J.*, **16**, 169–205, 1968
 Parker, R.L.: Inverse theory with grossly inadequate data, *Geophys. J.*, **29**, 123–138, 1972
 Rietsch, E.: The maximum entropy approach to inverse problems, *J. Geophys.*, **42**, 489–506, 1977

Received July 21, 1977

Short Communication

**Macroseismic Intensity Map
of the Federal Republic of Germany
for the Friuli Earthquake of May 6, 1976**

E. Schmedes¹ and G. Leydecker²

¹ Institut für Allgemeine und Angewandte Geophysik,
Theresienstr. 41, D-8000 München 2, Federal Republic of Germany

² Seismologisches Zentralobservatorium Gräfenberg,
Krankenhausstr. 1–3, D-8520 Erlangen, Federal Republic of Germany

Key words: Macroseismic observations – Friuli earthquake.

The earthquake of May 6, 1976 in Friuli, Northern Italy, with magnitude $M_s = 6.5$ and $m_b = 6.0$ (US Geological Survey, Colorado) and macroseismic intensity $I_0 = X$ was felt over a large area in Central Europe (Karnik et al., 1976; Karnik et al., 1977). The macroseismic map of the FRG (Fig. 1) shows only a small part of the whole shaken area, but gives detailed information on observations.

These observations are not as complete and well distributed as they could be, since at the time of the earthquake only few newspapers were available for some days due to a strike. Therefore people could not be asked this way to send us their observations; only the knowledge about the effects north of Hannover results from a call in a small regional newspaper. Most data from Bavaria ensue from letters to the Geophysical Observatory in Fürstenfeldbruck after an announcement in the regional Bavarian television. The rest of the observations are from people who had been disturbed and than had called by telephone a police-station or a geophysical observatory. Inaccurate reports had been reexamined by macroseismic lists of queries.

The observed effects are classified according to the macroseismic scale MSK 1964. Because of strong long-period waves, resonances of multi-story buildings have been observed, which cannot be classified in MSK values. Therefore only reports from first and second floor were used.

At larger distances – and even in towns North of Hannover – free suspended objects like lustres oscillated for up to some minutes. It can roughly be supposed that these last effects have been observed in most parts of Germany. If only these oscillations were reported, the intensity value II was attached.

According to Figure 1, the area near the southern border of Germany was shaken with an intensity of V and nearly the whole Molasse basin with an intensity of IV. Due to missing data the change from intensity III to II cannot be established very accurately and for the same reason an effect of geological structures upon macroseismic intensities cannot be attached. Roughly one can

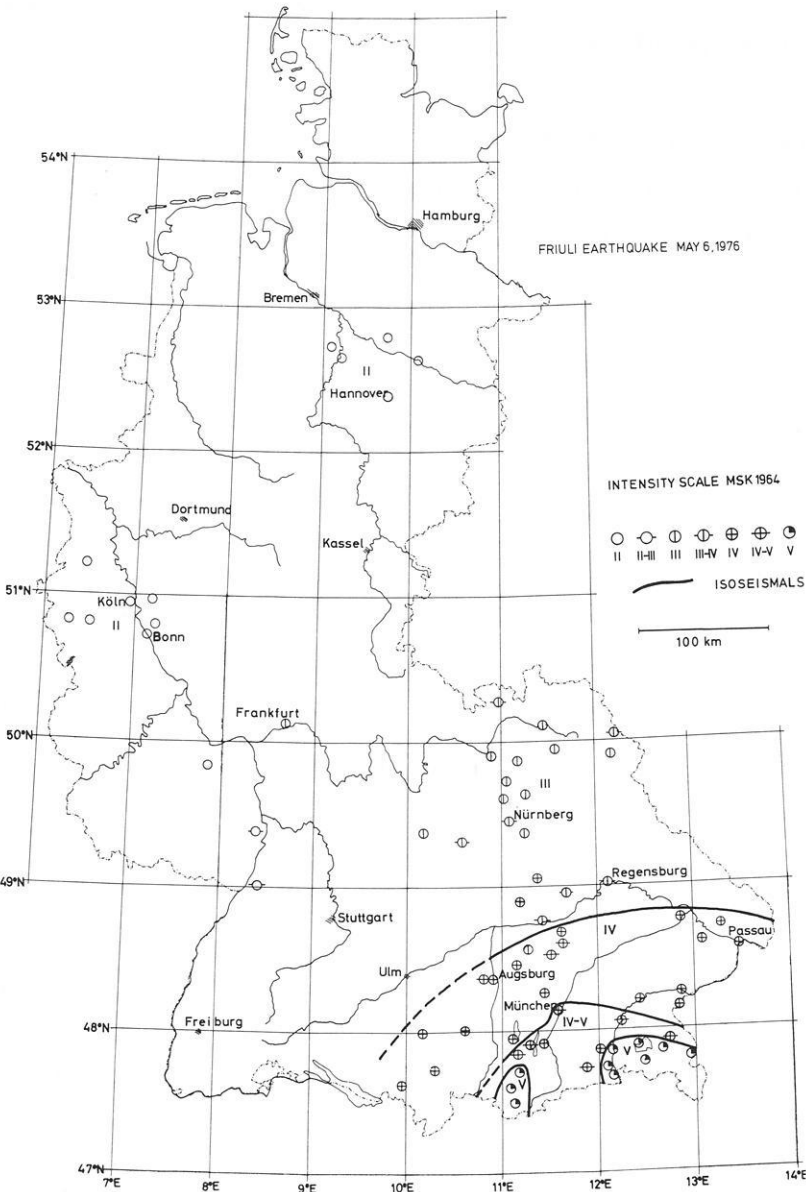


Fig. 1. Macroseismic map of the Federal Republic of Germany for the Friuli earthquake of May 6, 1976

say that between the rivers Danube and Main an intensity of III was observed, while North of the river Main only intensity II was reached.

Acknowledgements. We thank L. Ahorner, Bensberg, providing us with a list of macroseismic reports and all persons who contributed with their observations to this investigation

References

- Kárník, V., Procházková, D., Ruprechtová, L., Schenková, Z., Dudek, A., Drimmel, J., Schmedes, E., Leydecker, G., Rothé, J.P., Guterch, B., Lewandowska, H., Mayer-Rosa, D., Cvijanovič, D.: Macroseismic effects of the Friuli earthquake of May 6, 1976 in Austria, Czechoslovakia, F.G.R., France, Poland and Yugoslavia. Proc. Intern. Meet. Friuli Earthqu., Udine, Dec. 4–5, 1976. *Boll. Geofis. Teor. Appl.*, **19**, part 1, 729–737, 1976
- Kárník, V., Procházková, D., Schenková, Z., Ruprechtová, L., Dudek, A., Drimmel, J., Schmedes, E., Leydecker, G., Rothé, J.P., Guterch, B., Lewandowska, H., Mayer-Rosa, D., Cvijanovič, D., Kuk, V., Giorgetti, F., Grünthal, G., Hurtig, E.: Map of isoseismals of the main Friuli earthquake of May 6, 1976. *Pure Appl. Geophys.*, 1977 (in press)

Received April 22, 1977 / Accepted December 9, 1977

In Memoriam Ulrich Fleischer

Am 4. 7. 77 verstarb Ulrich Fleischer, Leiter der Abteilung „Marine Geophysik“ am Deutschen Hydrographischen Institut, Hamburg, an einer Herzattacke. Jeder, der ihn kannte, wußte, daß er seit seiner Nierenerkrankung nur unter schweren gesundheitlichen Belastungen seinen Dienst versehen konnte. Alle Kollegen und Freunde bewunderten ihn wegen seiner dennoch ungebrochenen Schaffenskraft. Noch am Tage seines Todes hat er im Institut normal gearbeitet.

Ulrich Fleischer wurde am 12. 9. 1927 in Neuglobsow in der Mark Brandenburg geboren. In Brandenburg besuchte er die von-Saldern-Oberschule bis kurz vor dem Abitur. Wie so viele seines Jahrganges wurde er noch in der letzten Phase des Krieges zum Dienst verpflichtet. Bevor er nach dem Krieg in Göttingen mit dem Studium begann, mußte er die Abiturprüfung nachholen.

Sein Interesse für die Naturwissenschaften hatte sich schon sehr früh gezeigt. Von Freunden wissen wir, daß er schon während seiner Schulzeit in Brandenburg selber ein Fernrohr baute und daß er in der Schulzeit astronomische Fragen behandelte. So schwankte er auch während der ersten Semester in Göttingen zwischen Astronomie und Geophysik. 1954 promovierte er bei Julius Bartels mit einer Arbeit über erdmagnetische Tiefensonderungen. Er schloß zum ersten Mal aus charakteristischen erdmagnetischen Baystörungen auf die Existenz eines Erdstromes im tieferen Untergrund Norddeutschlands, woraus er eine Leitfähigkeitsanomalie im Raum südlich Bremen folgerte. Ulrich Fleischer war einer der ersten, der bei diesen Arbeiten mit dem damals neu entwickelten Askania Variograph auf mobilen Stationen im Raum zwischen Göttingen und Wingst arbeitete. Nach einer kurzen Tätigkeit am Amt für Bodenforschung in Hannover war er von 1955 an (im In- und Ausland) Leiter einer Meßgruppe der Firma Seismos.

1959 ging er zum Deutschen Hydrographischen Institut und war zuletzt Leiter der Abteilung „Marine Geophysik“. Während dieser für ihn wissenschaftlich so fruchtbaren Zeit war er maßgeblich an der Entwicklung der seegravimetrischen Methoden beteiligt. Er war einer der Pioniere der antiparallelen Anordnung der Askania Gss2 Gravimeter zum Eliminieren des Cross-Coupling-Effekts. Unter seiner Leitung wurde das erste Gss3 Gravimeter getestet, das seitdem

allgemein in der Meßtechnik benutzt wird. Ulrich Fleischer nahm an zahlreichen Forschungsfahrten im Mittelmeer, dem Roten Meer, der Nordsee, dem Atlantik und der Labrador See teil, die er zum Teil selbst vorbereitet hatte. Seine Arbeiten reflektieren diese Unternehmungen. Sie befassen sich mit den großen Anomalien unserer Erde. Seine Beiträge über das Gebiet um Island und den Reykjanesrücken, die untermeerischen Tafelberge der großen Meteorbank südlich der Azoren und über die Schwerestörungen im Mittelmeer tragen wesentlich zur Kenntnis dieser aktiven Zonen unserer Erde bei.

Ulrich Fleischer war mit Annelies, geborene Brauer, verheiratet. Er verstarb wenige Tage vor seiner Silberhochzeit und hinterläßt einen Sohn und zwei Töchter.

Wir alle verlieren in Ulrich Fleischer einen immer aktiven, stets einsatzbereiten und menschlich sympathischen Kollegen und Freund. Ulrich Fleischer war Mitglied der DGG, des Forschungskollegiums Physik des Erdkörpers, der EAEG und der Internationalen Gravimetrischen Kommission.

Hannover, Dezember 1977

H. Dürschner

Weak Earthquakes in the Northern Part of the Rift Zone of Iceland

S.M. Zverev, S.A. Boldyrev, V.Yu. Bourmin, and V.I. Mironova

Institute Physics of the Earth, Bolshaya Gruzinskaya 10, Moscow B242, USSR

Abstract. More than 900 microearthquakes were recorded during 2.5 months in the summers of 1972–73 by a network of 7 automatic seismic stations in the northern part of the rift zone of Iceland.

The more permanent activity was found in the rift zone near the shore of Axarfiördur and on the oblique Husavik fault zone, as well as under the sea north-west of the land rift zone. The focal depths range from 3 to 8–13 km under the land rift zone and Husavik fault and increase to 20–30 km under the sea. Most of the foci in the rift zone are situated within the blocks between the vast fissure swarms. The focal solutions here reveal the dominance of horizontal compressive stresses oriented E–W.

These results are discussed together with other data from Iceland. In particular, the focal solution is given for the strong earthquake ($M=6.4$) which took place in the region of our investigation in January 1976. The orientation of compression for this and other strong earthquakes is approximately perpendicular to that of the microearthquakes of this study and coincides with the stress orientation measured by Hast (1969) in rocks in shallow boreholes. The compressive stresses are oriented in general perpendicular to the isolines of the Bouguer anomaly (Einarsson, 1954). This probably shows some interrelation between the origin of the gravity field and that of the stresses, which are released through strong earthquakes. The discharge of the main stress occurred in weak places and is often accompanied by the revival of the fissure swarms. The weak seismicity during the time between the strong shocks is probably connected with the redistribution of the stresses in smaller areas. In particular, our results in the north of Iceland could be explained by the development of the depression on the shelf between the shore and the continuation of the submerged Kolbeinsey ridge.

Key words: Iceland rift – Foci – Section mechanism structure.

Introduction

Iceland and the North Atlantic have lately become vast geodynamic test areas, where the key problems of modern geology are being unfolded. Recent hopes

that Iceland is just an uplifted part of the Mid-Atlantic Ridge were, however, not justified, and it is now generally acknowledged that Iceland and the adjacent regions have a specific, anomalous structure. As the problems of plate tectonics are elaborated in and around Iceland in variants and the details grow in complexity (see e.g., Kristjansson, 1974), it becomes evident that it is necessary to break through the limitations of the standard set of experimental data and to pass over to a new and higher level of geological-geophysical observation. An effort in this direction has been made by the Geodynamic Expedition of the Academy of Sciences of the USSR, which has been working in and around Iceland since 1971 (Belousov and Milanovsky, 1976).

The processing of observed material, obtained by extensive and complex geological-geophysical methods, is still incomplete and, therefore, as yet not available to the greater part of the scientific community.

The present paper discusses the basic results of seismological studies carried out by the Geodynamic Expedition of the Academy of Sciences of the USSR in Iceland in 1971–73. The choice fell on Northern Iceland as the major subject of research because here we can see clear evidence of modern volcanism and rifting, and a very complicated interrelation between the rift zone of the island and the oceanic Kolbeinsey ridge. Northern Iceland is scarcely studied compared to the southern and south-western part of the island, where extensive seismological researches were undertaken by Icelandic and American scientists. (e.g. Klein et al., 1973.)

Some Geophysical Data on Iceland

Extensive multidisciplinary studies were carried out in Iceland during the last few years. Here we mention some of them as they deal with the earth's crust and mantle and with seismicity.

The Bouguer gravity map is shown in Figure 1. This map is taken from an old paper (T. Einarsson, 1954), but more recent surveys generally confirm it (G. Palmason, personal communication 1975). The axial symmetry and the Bouguer minimum in the centre of Iceland have been explained as being caused by the low density mantle column existing to depths of 200 km (Long and Mitchell, 1970). Deep seismic sounding shows a thick crust under north-eastern Iceland (Zverev et al., 1976), and combined interpretation of seismic and gravity data led us to the conclusion that the Bouguer minimum is connected with the depression of normal density mantle under Iceland to depths of 50–60 km (Zverev et al., in press). A somewhat different interpretation has been advanced by Bott (in Kristjansson, 1974).

The map of the earthquake epicenters with $m_b \geq 4.0$, determined by the world wide standard seismograph network is shown in Figure 1. Open circles represent foci between 1954 and 1963 (Sykes, 1965); shaded circles show ISC and NEIS data for 1964–1976.

Data summaries of the seismicity of Iceland were published by Sykes (1965), Ward et al. (1969), Ward and Björnsson (1971), Ward (1971), Palmason and Saemundsson (1974), Björnsson and Einarsson (1974), Einarsson (1976). The

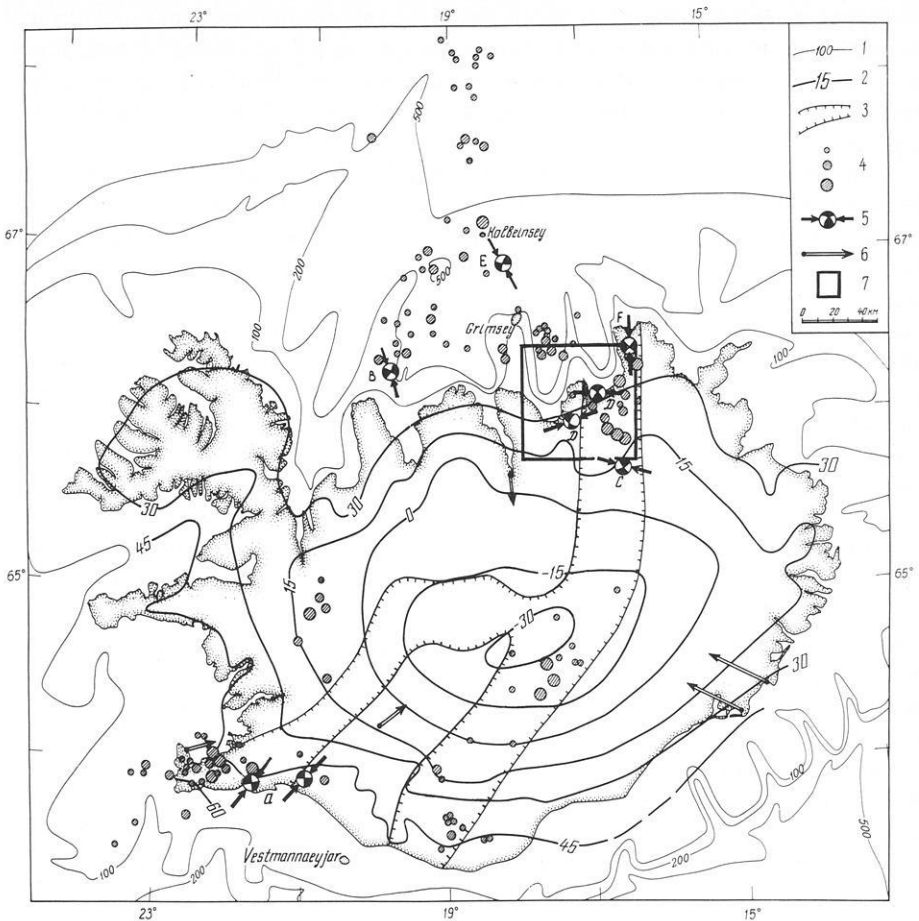


Fig. 1. Some geophysical data for the region of Iceland. 1: depth contours (m); 2: gravity Bouguer anomaly (mgal) (Einarsson, 1954); 3: active zones of rifting and volcanism (Palmason and Sæmundsson, 1974); 4: epicenters of earthquakes recorded by the world network for 1954–1976: $m_b < 4.5$; $4.5 \leq m_b \leq 5.5$; $m_b > 5.5$; 5: focal mechanism solutions; the arrows indicate the directions of the principal compressive stresses: A: $m_b \sim 3.5\text{--}4.0$ (Ward, 1971); B: $m_b = 6.8$ (Sykes, 1967); C: $m_b \sim 1.0$ (Ward et al., 1969); D: $m_b \sim -0.5\text{--}1.5$ (this paper); E: $m_b = 5.2$ (Einarsson, 1976) F: $m_b = 6.4$ (this paper); 6: the vectors of the compressive stresses measured in rocks (Hast, 1969); 7: region of detailed investigations of the Soviet expedition in 1972–73

geographical distribution of earthquake foci and their deviation from the general strike of the Mid-Atlantic Ridge was an important reason for the suggestion of the presence of two transverse (transform) faults south and north of Iceland (Sykes, 1967; Ward, 1971).

The analysis of epicenters indicates that transverse faults in the southwest of the island and along the northern coast are lacking the distinction of transform faults. We prefer to suggest the existence of two seismoactive zones on the island approximately corresponding to two branches of rifting. These two zones

are joined north of Iceland in the Kolbeinsey region, and continue northward along the submerged ridge. The data collected on the seismicity during more than 20 years (see Fig. 1) testify that the seismoactive zones are traced across Iceland with significant gaps, and this distinguishes the island from the adjacent parts of the Mid-Atlantic ridge.

The microseismicity of Iceland was studied by Icelandic and American scientists. Thirteen local zones of microearthquakes were established, all of them situated within the modern rift zone (Ward et al., 1969). These data can be compared with the results of bottom seismic observations in the rift valleys of submarine mid-ocean ridges. Such observations were carried out in 1971 off the coasts of Iceland on the submarine Reykjanes and Kolbeinsey ridges by the staff of the Soviet Geodynamic Expedition on the research vessel "Akademik Kurchatov". Weak local earthquakes, specific for rift valleys or their slopes, were discovered everywhere on submarine ridges. Observations on Carlsberg Ridge in the Indian Ocean (Neprochnov et al., 1969) and on the Mid-Atlantic Ridge in two regions (Francis and Porter, 1972; Spindel et al., 1974) were similar. On the other hand, seismicity studies in Iceland revealed that micro-earthquake occurrence is not universal but local, which in general indicates a weaker manifestation of seismic activity on the island than on submarine ridges.

The available mechanism solutions for some of the earthquakes and for groups of microearthquakes are also presented in Figure 1. The solid arrows indicate the direction of the principal compressive stresses. These compressive stresses are always close to horizontal. For the two strongest earthquakes on the north shore of Iceland ($M > 6.0$) it is possible to observe the same feature. For the earthquake in the western branch of the seismoactive zone (B see Fig. 1) (Sykes, 1967), one of the nodal planes is with good accuracy parallel to the strike of this branch (N 25°). For the earthquake of 1976, situated in the eastern branch (F, Fig. 1), the nodal planes are well concordant to the strike of this eastern branch (N 315°). For the weaker earthquake north of the eastern branch (E, Fig. 1) (Einarsson, 1976), the distribution of the signs of *P*-wave arrivals does not contradict such a feature.

The data on the orientation of compressive stresses in the foci of strong earthquakes agree comparatively well with stress vectors measured in rocks (Hast, 1969) (see Fig. 1). The compressive stresses at depth (from earthquakes data) and at the surface (Hast, 1969) are approximately perpendicular to the Bouguer isolines and they are oriented toward the center of Iceland. Exceptions are two examples of microearthquakes: C (Ward et al., 1969) and D (this paper) (see Fig. 1).

Region of Research Purpose and System of Observations

In 1971 our expedition carried out a reconnaissance survey of seismicity of Northern Iceland, as the result of which a high seismicity region was determined near the Tjörnes peninsula where a network of stations was set up for temporary observations (Fig. 2).

It was the purpose of the observations to determine the peculiarities of the

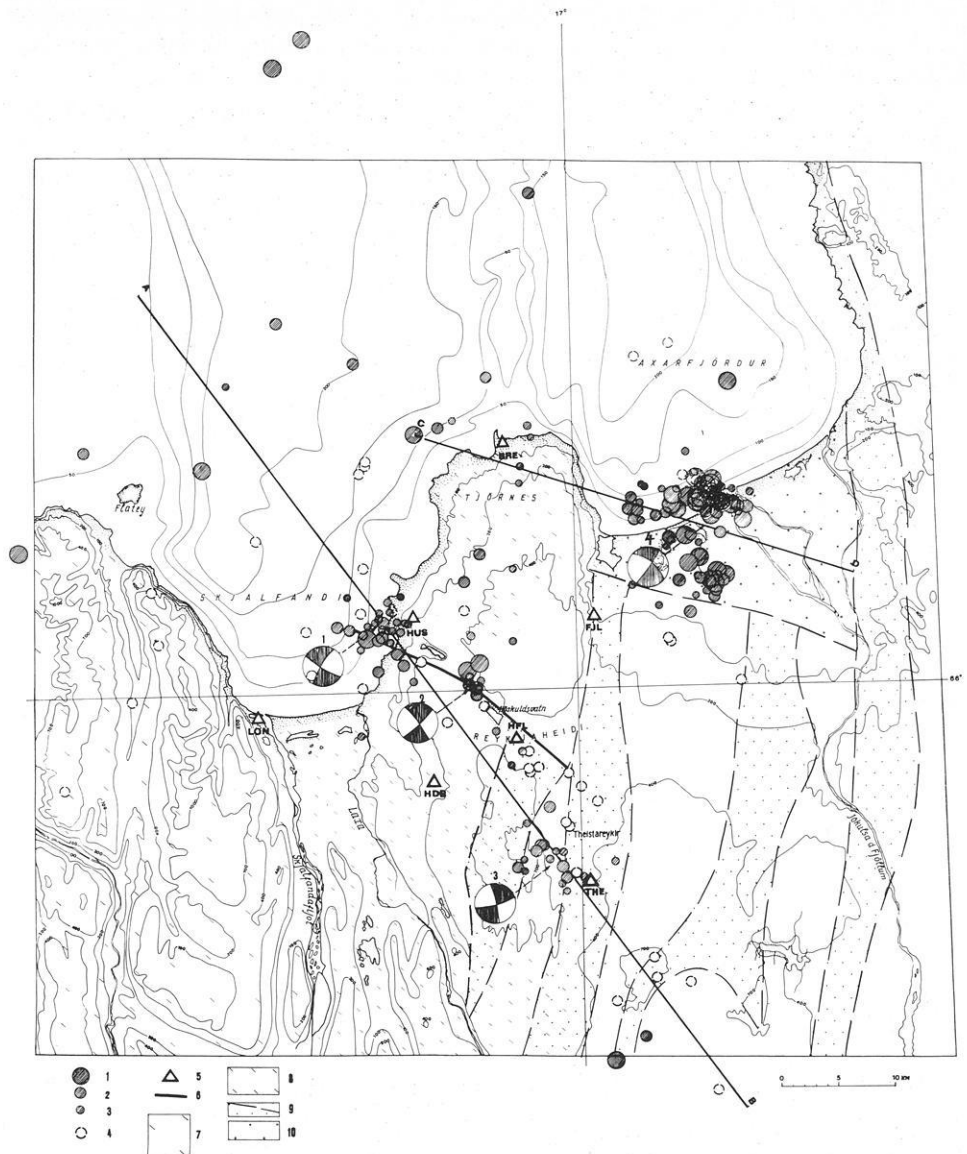


Fig. 2. Map of earthquake epicentres located by our stations in 1972–1973. 1: $m_{SH} \geq 0.9$ ($K_{SH} \geq 6.0$) 1973; 2: $0.3 \leq m_{SH} \leq 0.9$ ($5.0 \leq K_{SH} \leq 6.0$) 1973; 3: $m_{SH} \leq 0.3$ ($K_{SH} \leq 5.0$) 1973; 4: earthquakes 1972; 5: recording stations; 6: Husavik fault zone, 7 and 8: Tertiary and Quaternary flood basalts respectively; 9: fissure swarms, 10: Jökulsá river gravel plain. 6 to 9: according to Saemundsson (1974)

seismic activity in space and time, i.e. to determinate the focal coordinates, the energy characteristics, focal mechanisms and, finally, to establish the relationships between modern seismicity and tectonics and to compile the distribution model of elastic stresses in the region studied.

The Tjörnes peninsula and its environs were the major object of seismological research. As stated above, this region is located on the eastern branch of the seismoactive zone (see Fig. 1) associated with the Mid-Atlantic Ridge.

According to geoclaical data, Tjörnes peninsula is a block of the Tertiary and Quaternary basalts, joined to the western edge of the rift zone of Iceland and bounded in the south by the large Husavik fault (Saemundsson, 1974). The structures of the peninsula, as those of the adjoining bays Skjalfandi and Axarfjörður in the west and east, can be traced northward below sea level and are then cut off by the shelf edge.

During the reconnaissance in 1971 the larger part of the epicenters was fixed in the Husavik fault area and, therefore, in 1972 the network of stations was set up in view of the best determination of the focal parameters of these earthquakes (see Fig. 2). In 1973 the area of study was extended and the network of stations had the form of a triangle 30×40 km.

Equipment

Seismic observations in Iceland and at sea around Iceland were carried out with the aid of automatic seismic stations, designed at the Institute of Physics of the Earth, Academy of Sciences of the USSR (Zverev et al., 1971). In 1972 and 1973 the three-component stations had identical instruments; the seismograph NSP-3 with $T_0 = 0.7$ s was used as the detector. The signals were automatically recorded on magnetic tape. A tape lasts 5–7 days. The speed of the tape was 0.47 mm/s and the frequency band of the recording channel was 5–13 Hz. The lower sensitivity level of the band was given by the microseismic background of displacement, on the average, $\sim 0.8 \cdot 10^{-9}$ m; the upper limit of undistorted recording was determined by the dynamic range of the recording channel being $\sim 70 \cdot 10^{-9}$ m for $f = 10$ Hz. Beside the three seismic channels, the magnetic tape also recorded the coded signals of quartz clocks, thus allowing the absolute arrival time of the earthquake waves to be established with an accuracy of a few hundredths of a second. Sensitivity control was achieved with the aid of the calibrating generator, transmitted to the input of the recording amplifiers, while time control was obtained by recording the signals of the British radiostation “Rugby” when switching on and off the automatic stations.

General Description of Observation Material

The conditions of installation and the microseismic background allowed us to record a large number of shocks. The most favourable conditions were at stations HFL and HDB (see Fig. 2), which recorded up to 80 earthquakes per diem, and more than 300 earthquakes in total during 1.5 months of observation in 1973. The least favourable conditions were at station LON, which recorded only 20 events. The bulk of earthquake records had $t_{s-p} = 0.7$ –5.0 s. The lag time t_{s-p} of the transverse wave relative to the longitudinal *P*-wave is in this case the most convenient and objective function of distance. Since for most of the seven

stations of 1973 the distribution of t_{s-p} records was approximately the same, the recording might be presumed to be optimal.

For most earthquake records the times of arrivals of P - and S -waves were determined, as well as the maximum amplitude and the dominant oscillation period for longitudinal and transverse waves and the sign of the first P -wave displacement and the direction to the epicenter. However, not all earthquakes were recorded by the entire station network. Rather often very weak oscillations close to the level of the noise background were observed. Therefore, the coordinates and the source depths were determined for only 41 earthquakes of 1972 and for 167 earthquakes of 1973.

Processing Technique of Observation Material

In the first stage, the coordinates of the earthquake foci were determined with the aid of a computer program based only on t_{s-p} times recorded by three and more stations. In this case the velocity model was used, which was obtained for the surrounding region by explosion seismology (Palmason, 1971). This cross-section was transformed into an apparent velocity $V_{s-p} = \frac{V_p}{\frac{V_p}{V_s} - 1}$ (Table 1). The

coefficient $K = V_p/V_s$ was determined by the sum of records of many earthquakes at our stations with a precision of up to ± 0.02 .

Table 1. Velocity section assumed for determination of hypocenters of Icelandic earthquakes

H (km)	V_p (km/s)	V_p/V_s	V_{s-p} (km/s)
0-1.0	2.5	1.72	3.5
1.0-3.5	4.6	1.72	6.4
more than 3.5	6.4	1.72	8.9

The standard error of the instrumental hypocenter determinations within the perimeter of the station network is 0.1-0.6 km; for remote earthquakes it increases to 1.0-3.0 km.

The magnitude of the earthquakes m_{SH} was evaluated on the basis of the body waves SH according to the relationship $m_{SH} = \lg(A/T)_{\max} + \sigma(R)$. As the calibrating function $\sigma(R)$ we took the one for European earthquakes at small epicentral distances (Christoskov, 1969). For our purposes this function was approximated by logarithmic curves:

$$\sigma(R) = 1.98 \cdot \lg R - 1.05.$$

Instead of the epicentral distances Δ in degrees we used R in kilometers. The standard deviation of the experimental points from the approximating curve is about 0.1. The accuracy of magnitude determination is evaluated to be 0.3. Beside the magnitudes the energy classes K (energy $E = 10^K$ joules) were determined by means of nomograms (Fedotov, 1972) for the longitudinal (K_p) and shear (K_s) waves.

Map of Epicenters and Cross-Sections

The positions of the instrumental hypocenters are shown on the map (Fig. 2) and on two cross-sections (Fig. 3). Figure 2 shows that there are two groups of epicenters. One of them, in the form of a band, follows the Husavik fault and its continuation in the rift zone. Here the most stable manifestation of seismicity has been noted during the two observation seasons in 1972 and 1973. Within the band the greatest concentration of epicenters was observed in the region of the HUS station. The second group of epicenters is compact; it is located on the coast of Axarfjörður. This group lies on the continuation of the northern branch of the rift zone. Here the activity is quite variable with time; in the summer of 1972 only a few single foci were observed, while in 1973 it was a dense group of epicenters. Other earthquakes are scattered mostly in the sea area. A few single epicenters were detected on the Tjörnes peninsula and on land west of Skjal-fandi Bay.

The focal depths distributed along the Husavik fault, are from 2–3 to 10–12 km (Fig. 3). Submarine earthquakes in the Skjal-fandi Bay are much deeper: (up to 20–25 km). Such depths were confirmed here by additional observations in 1975, when one of the recording stations was placed on Grimsey island. The maximum focal depth in general obviously increases in the north-western direction. In the region of Axarfjörður (Fig. 3) the earthquakes occur mainly at the depth interval from 3–5 to 17–20 km. Here the focal depths also appear to increase toward N–W. On the eastern shore of Axarfjörður where the swarm of strong earthquakes took place in late 1975 – early 1976, no event of $m_{SH} > -1.0$ was fixed during our observations in the summers 1972, 73 and 75.

The positions of the fissure swarms are shown in Figure 3 after K. Sae-mundsson (1974). These fissures trace vast tension zones. Most of the foci are located outside of fissure swarms, within blocks between them.

All foci are located in the seismic layer with the P -wave velocity of 6.4 km/s.

Earthquake Mechanisms

From the signs of the P -wave arrivals the mechanisms active in the foci have been determined for various groups of earthquakes. The entire epicentral zone was divided into four regions according to the temporal stability of the signs of the first arrivals. For each of these regions a single mechanism for a group of epicenters has been defined. The distribution of signs of the P -wave arrivals is presented in Figure 4. The most reliable nodal planes could be drawn for the first three regions along the Husavik faults. In the fourth region corresponding to the group of foci at Axarfjörður the one-sided location of the stations prevents a reliable determination of one of the nodal planes. On the whole, the good correlation of data for different earthquakes indicates the stable character of the focal mechanisms of the selected groups of earthquakes. In all cases the main compressive stresses are close to horizontal mainly in the E–W direction. The schematic focal spheres presented in Figure 2 show a gradual turning of one of the nodal planes along the Husavik fault from west-north-west in the north to

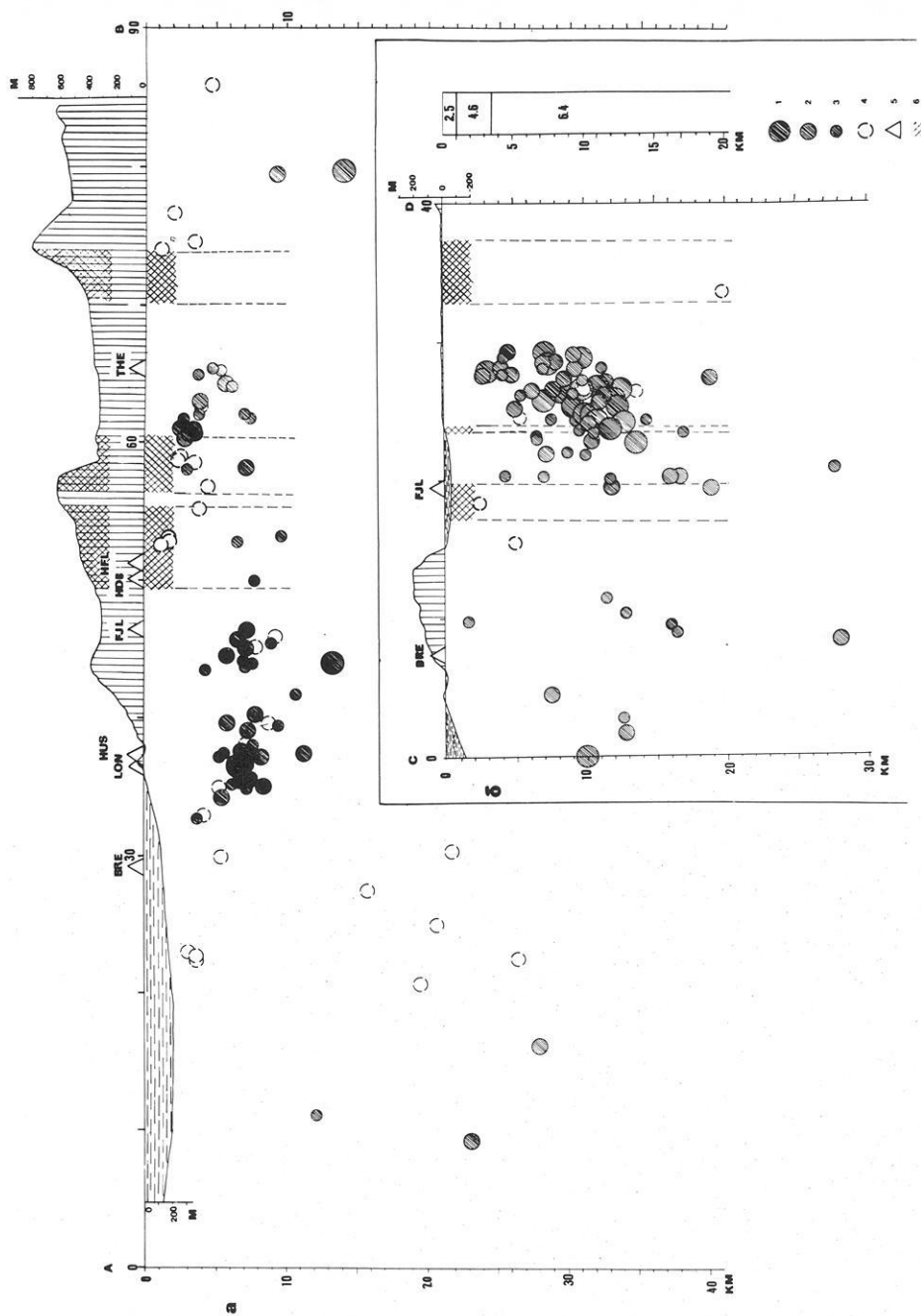


Fig. 3. Seismic cross-sections along the lines AB and CD (see Fig. 2) and the velocity model adopted for locating the earthquakes. Legend 1-5 identical to that of Figure 2. 6-fissure zones (Saemundsson, 1974)

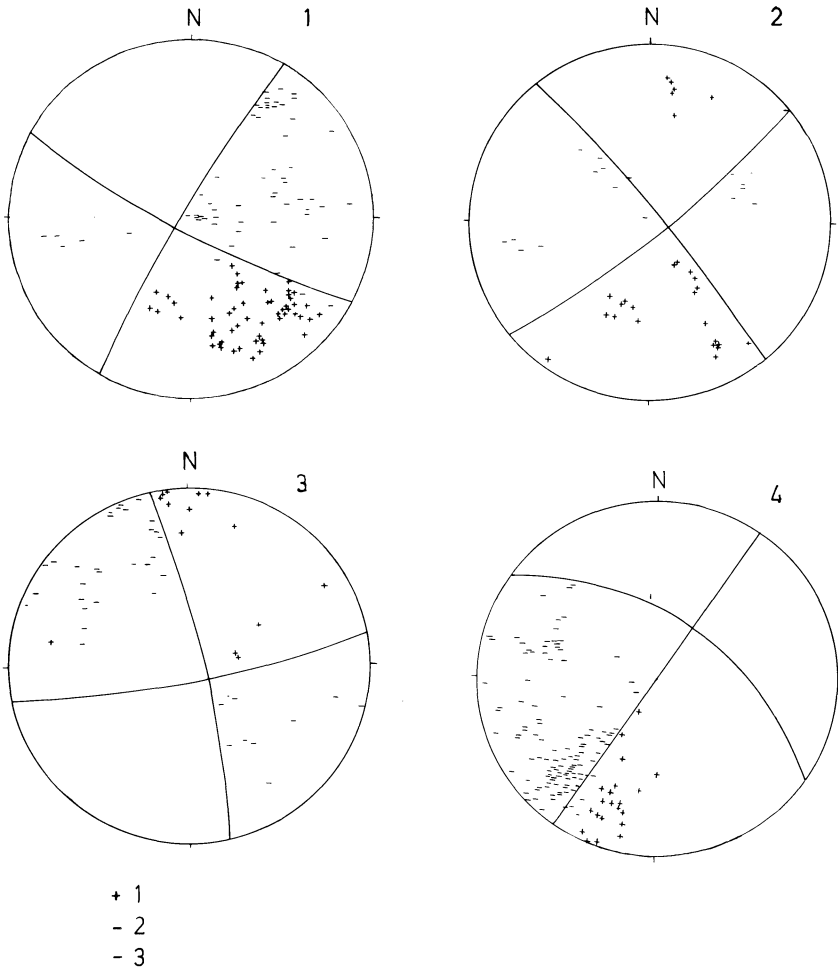


Fig. 4. Distribution of signs of first motion of *P*-wave onsets on the Wulff grid (upper hemisphere) for four epicentral regions (see Fig. 2); 1: compression; 2: dilatation; 3: nodal lines

north-north-west in the south. This tendency seems likely to continue further to the south to the Krafla region, where according to the data by Ward et al. (1969), the strike of one of the nodal planes is almost north-south (see Fig. 1).

The maximum compression axes for the microearthquakes are approximately perpendicular to the strike of the tension fissures (see Fig. 2) and to the directions of the compressive stress in the foci of the strong earthquakes (see Fig. 1), in particular, the earthquakes of 13 January 1976. In Figure 5 the distribution of the signs of the *P*-wave onsets for these earthquakes is shown on the lower hemisphere. The data of more than 100 of the world network stations were used. The main compressive axis is horizontal and has an azimuth of 355° . If we suppose that the slip plane follows the strike of the eastern branch of the seismoactive zone, the displacement is north for the western side of the fault. It

13.01.76 13^h29^m
 $\varphi = 66,2^\circ \text{N}$ $\lambda = 16,6 \text{W}$.
 $m_B = 6,4$

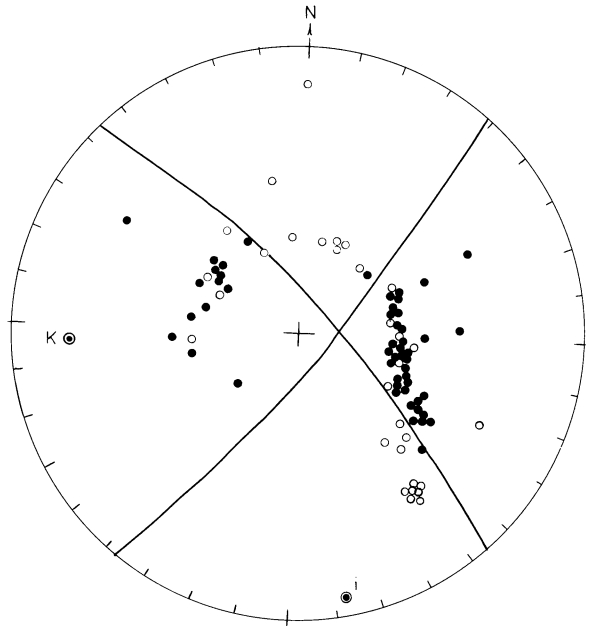


Fig. 5. Distribution of signs of first motion of *P*-wave onsets the Wulff grid (lower hemisphere) for the earthquake of 13 January 1976, $m_b = 6.4$. Solid circles denote compression; open circles dilatation

may be mentioned that the swarm of strong ($m_b = 4.0-6.4$) shocks 1975-76 on the eastern part of the neovolcanic zone took place in the vicinity of Kopasker village. These shocks reveal the revival of the known fissure swarms in the rift zone.

Seismic Regime of the Area

The analysis of the time variations of activity for the given area (Fig. 6) demonstrates that on particular days the number of recorded earthquakes with $m_{SH} \geq 0.5$ changes from 0 to 10 and more. These variations are even stronger for weaker earthquakes ($m_{SH} \geq -0.3$) which reach 40 per day.

Activation covered the entire research area simultaneously. Figure 6 represents the accumulated and released energy (more exactly; ΣK_{SH} in earthquakes with $K_{SH} \geq 4.0$, i.e. $m_{SH} \geq -0.3$). These plots show that in the two most active sites, the Axarfjörður region (a) and the Husavik fault zone (b), the activation periods are displaced by 1-3 days, but they invariably have the same succession with stable, quiescent periods in between. The shocks started always in the Husavik fault zone and then continued in the Axarfjörður region. For the group

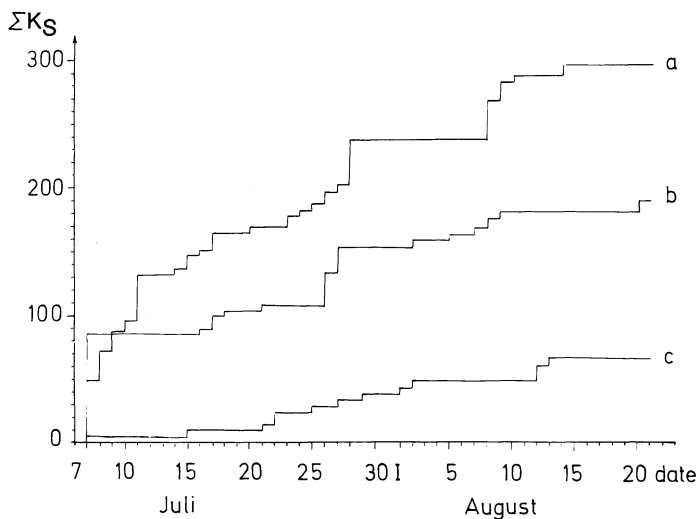


Fig. 6. Plots of ΣK_S accumulation for earthquakes with $K_S \geq 4.0$ ($m_{SH} \geq -0.3$) for the Axarfjörður region (a), the Husavik fault region (b), and the north-western marine region (c)

of submarine earthquakes (c), where the probability of omissions is high, the accumulation curve ΣK does not have such a good correlation with the first two regions. Apparently, the earthquakes of the most active regions, where 90% of all shocks occurred, separated by an aseismic block, are to a considerable extent connected with each other. The similarity of focal mechanisms for both regions and for the adjacent Krafla region supports this supposition.

Discussion of Results

The seismic activity in Iceland considerably differs from most of the submarine regions of mid-ocean ridges. In the area of Iceland far fewer earthquakes are recorded than on the ridges to the south and to the north of Iceland, and besides, the earthquakes themselves are much weaker. The microearthquakes are also located only in small zones.

Most of the strong earthquakes in Iceland were observed near south-western and northern shores. The largest number of earthquakes both strong and weak occurred as a result of the release of the near horizontal compressive stresses. In all the strongest earthquakes and part of the microearthquakes these compressive stresses are oriented approximately toward the centre of Iceland. Their directions agree with the orientation of the stress axes in rocks determined by overcoring (Hast, 1969) and they are approximately perpendicular to the Bouguer anomaly isolines.

The focal depths under Iceland do not exceed 10–12 km, but reach 17–20 km under the northern shore and sometimes 20–25 km under the shelf. It may be mentioned that some deep foci at 20–30 km depth were observed on the southern side of Iceland by Björnsson and Einarsson (1974).

We think that all the above data reflect large scale geophysical phenomena in Iceland. Probably the shape of Iceland and its shelf, the gravity anomalies, the generation and accumulation of the compressive stresses, revealed in the rocks and in the earthquake focal mechanisms have a common origin at depth.

The stresses are first released in strong earthquakes in the weakest places, i.e. in the rift zones. The submerged rift zone runs from the north toward Iceland as the single Kolbeinsey ridge. The seismic zone follows the ridge, but south of Kolbeinsey it forks into two branches. The two seismoactive branches in Iceland generally coincide with the modern and ancient zones of rifting and volcanism. The nodal planes for the strongest shocks coincide with the strike of these two branches.

The attenuation of the rate of seismicity from the borders toward the middle of Iceland should be discussed together with the crustal thickness. The interpretation of explosion seismology investigations (Zverev et al., 1976) shows that in northeastern Iceland the normal mantle dips to depths of more than 40–50 km toward the centre of the island, and the combined interpretation of seismic and gravity data led us to suggest a cap shaped depression of the mantle under Iceland filled by the low density crust (Zverev et al., 1977). Taking this into account, we can tie the attenuation of seismicity in with the growing thickness of the crust and its absorption properties.

The weak earthquakes give us another more local scale of geophysical phenomena. In northern Iceland most of the microearthquakes fall in between the vast tension zones of the fissure swarms (see Fig. 3). The vast fissures were absolutely inactive in seismically quiet periods. The compressive stresses in the foci were oriented normally to the strike of the fissures, i.e. the blocks were compressed between the tension zones. The orientation of one of the nodal planes for the different groups of foci very closely follows the variable strike of the Husavik fault zone.

The above observations of focal depths increasing toward N–W, the surface and bottom relief, the gravity and magnetic anomalies (Johnsson, 1974) could be most easily understood by supposing an important role of the depression of the shelf between the shore of Iceland and Kolbeinsey. The shape of this depression is triangular with Kolbeinsey at the top and the base following the north shore of Iceland. Its sides may be traced from the epicentres of the strong earthquakes from positive magnetic anomalies, from outcrops of fresh basalts, and from some bathymetric contours (Johnsson, 1974).

The base of the triangle is characterized by a large step in surface and bottom relief, and by a local negative gravity anomaly (Palmason, 1974). The active modern development of this depression, probably bordered by large fault zones, can explain the above phenomena better than the suppositions of transform faulting and large scale horizontal movement in this region (Sæmundsson, 1974).

Acknowledgements. These investigations were carried out by the staff of the Soviet Geodynamic Expedition in Iceland arranged and supervised by Professor V.V. Belousov. A.N. Fursov and G.N. Akimov provided field observations.

Our results were discussed in parts with the Icelandic scientists Drs. S. Björnsson, K. Sæmundsson and P. Einarsson.

The help of S. Hermansson made the Soviet scientific investigations in Iceland possible.

The invariable and kind attention of Dr. G. Palmason made our work in Iceland very pleasant.

References

- Belousov, V.V., Milanovsky, Ye. Ye.: On the tectonic and tectonic position of Iceland. In: "Greinar V", pp. 96–120, Reykjavik, 1976
- Bjornsson, S., Einarsson, P.: Seismicity of Iceland. In: "Geodynamics of Iceland and North Atlantic Area" pp. 225–239. D. Reidel Publishing Company, Dordrecht-Holland 1974
- Christoskov, L.: On the Standardization (Equalization) of Magnitude Determination of small Epicentric Distances. *Bull. Intern. Inst. Seism. Earth* **6**, 1–10, 1969
- Einarsson, T.: A survey of gravity in Iceland. *Reykjavik Soc. Sci. Iceland*, **30**, 1954
- Einarsson, P.: Relative location of earthquakes in the Tjörnes fracture zone. "Greinar V", pp. 45–60, Reykjavik, 1976
- Fedotov, S.A.: Energy classification of the Kuril-Kamchatka earthquakes and the problem of magnitude (in Russian). M., Nauka 1972
- Francis, T.J.G., Porter, I.T.: Microearthquake survey of the Mid-Atlantic Ridge. *Nature* **240**, 5383, 547–549, 1972
- Hast, N.: The state of stress in the upper part of the earth's crust. *Tectonophysics* **8**, 169–211, 1969
- Johnson, G.L.: Morphology of the mid-oceanic ridge between Iceland and Arctic. In: "Geodynamics of Iceland and the North Atlantic Area" pp. 49–62. D. Reidel Publishing Company, Dordrecht-Holland, 1974
- Klein, F.W., Einarsson, P., Wyss, M.: Microearthquakes on the Mid-Atlantic plate boundary, the Reykjanes peninsula in Iceland. *J. Geophys. Res.* **78**, 5084–5099, 1973
- Kristjánsson, L.: Geodynamics of Iceland and North Atlantic Area. D. Reidel Publishing Company, Dordrecht-Holland, 1974
- Long, R.E., Mitchell, M.G.: Teleseismic *P*-wave delay time in Iceland. *Geophys. J. Roy. Astron. Soc.* **20**, 1, 1970
- Neprochnov, Yu.P., Kovylin, V.V., Yelnikov, I.N., Rykounov, L.N., Zverev, S.M.: Deep seismic sounding in the Indian Ocean by the joint Expedition of the research vessels "Akademik Kurchatov" and "Vityaz" (in Russian). *DAN SSSR*, **185** (4), 917–920, 1969
- Palmason, G.: Crustal structure of Iceland from explosion seismology. *Soc. Sci. Islandica* **40**, 1971
- Palmason, G.: The insular margin of Iceland. *The Geology of continental margin*. Berlin-Heidelberg-New York: Springer 1974
- Palmason, G., Saemundsson, K.: Iceland in relation to the Mid-Atlantic Ridge. *Ann. Rev. Earth Planet. Sci.* **2**, 25–50 1974
- Saemundsson, K.: Evolution of the axial rift zone in Northern Iceland and Tjörnes Fracture zone. *Bull. Geol. Soc. Am.* **85**, 4, 495–504, 1974
- Spindel, R.C., Davis, S.B., Macdonald, K.C., Porter, B.P., Phillips, J.D.: Microearthquake survey of median valley of the Mid-Atlantic Ridge at 36° 30' N. *Nature* **248**, 577–579, 1974
- Sykes, L.R.: The seismicity of the Arctic. *Bull. Seism. Soc. Am.* **55**, 501–516, 1965
- Sykes, L.R.: Mechanism of earthquakes and nature of faulting on the Mid-Oceanic ridges. *J. Geophys. Res.* **72**, 2131–2154, 1967
- Ward, P.L.: A new interpretation of the geology of Iceland (a detailed study of a boundary between lithospheric plates). *Bull. Geol. Soc. Am.* **82**, 2991–3012, 1971
- Ward, P.L., Bjornsson, S.: Microearthquakes, swarms and the geothermal area of Iceland. *J. Geophys. Res.* **76**, 3953–3982, 1971
- Ward, P.L., Palmason, G., Drake, C.: Microearthquake survey and the Mid-Atlantic Ridge in Iceland. *J. Geophys. Res.* **74**, 665–684, 1969
- Zverev, S.M., Kosminskaya, I.P., Krasilschikova, G.A., Mikhota, G.G.: The crustal structure of Iceland and of the Icelandic-Faeroes-Scotland region. In: "Greinar V", pp. 74–96, Reykjavik, 1976
- Zverev, S.M., Kosminskaya, I.P., Mikhota, G.G., Krasilschikova, G.A.: Deep structure of Iceland by geophysical data complex (in Russian). In: *Iceland and Mid-Ocean Ridge. Deep structure, seismicity, geothermy*, pp. 170–188. Moscow: Nauka 1977
- Zverev, S.M., Novikov, V.S., Akimov, G.N., Afanasiev, Yu.M., Kastorsky, S.A., Shablitsky, V.M.: Autonomous buoy seismic station (in Russian). *Izv. AN SSSR, Fizika zemli*, **5**, 102–113, 1971

Characteristics of VRM in Oceanic Basalts*

W. Lowrie¹ and D.V. Kent²

¹ Institut für Geophysik, ETH Hönggerberg, 8093 Zürich, Switzerland

² Lamont-Doherty Geological Observatory, Palisades, New York 10964, USA

Abstract. Laboratory experiments, each lasting several weeks, have been conducted to establish the characteristics of viscous remanent magnetization (VRM) in oceanic basalts from many sites of the Deep Sea Drilling Program (DSDP). VRM is most pronounced in low-coercivity basalts whose natural remanences (NRM) have low median destructive fields, less than 100 Oe. A simple logarithmic acquisition law is rarely obeyed, but two or three distinct stages are instead observed, in each of which a logarithmic dependence of VRM intensity on acquisition time may be assumed. This observation leads to a simple interpretational model for the nature of VRM in DSDP basalts, but also implies that extrapolation of laboratory observations to geological times is not meaningful. Instead, the ratio of laboratory VRM (acquired in a 1 Oe field during 1000 h) to NRM is used as a minimum indicator of the potential seriousness of VRM. Experiments show that VRM acquired in the presence of NRM is more serious than VRM acquired in alternating field (AF) demagnetized samples. As most published VRM data in DSDP basalts were obtained after AF demagnetization, these are regarded also as minimum estimates of the significance of VRM acquired by oceanic basalts in situ. The consequences of the common occurrence of such an unstable component of magnetization in the oceanic basalt layer are considered in relation to the nature and distribution of oceanic magnetic quiet zones. The Cretaceous, and possibly the Jurassic, magnetic quiet zones are considered adequately explained by constant paleomagnetic field polarity. However, if VRM is a substantial and widespread magnetization component in the oceanic crust, it may not always be appropriate to interpret oceanic magnetic anomalies (or their absence) as an exact record of paleomagnetic field behavior. Remagnetization of the oceanic crust by VRM acquisition may be a viable alternative explanation of the origin of the marginal magnetic quiet zones.

* Institut für Geophysik, ETH Zürich, Contribution No. 200 Lamont-Doherty Geological Observatory, Contribution No. 2635

Key words: VRM—DSDP—Oceanic basalts—Magnetic quiet zones—Oceanic magnetic anomalies.

Introduction

Sea floor spreading studies are based upon interpretation of marine magnetic anomalies which are thought to derive chiefly from magnetization contrasts in Layer 2 of the oceanic crust. The principal sources are usually ascribed to the extrusive basalts in the uppermost 500 m (Layer 2A) (Talwani et al., 1971; Atwater and Mudie, 1973) although it is probable that a substantial part of the signal has sources deeper in Layer 2 (Harrison, 1976; Lowrie, 1974, 1977) and perhaps even in Layer 3 (Cande and Kent, 1976). The Koenigsberger ratios of most oceanic basalts whose magnetic properties have been studied are generally greater than unity; that is the remanent magnetizations dominate the magnetizations that can be induced by the present magnetic field. This condition fulfills one of the requirements of the Vine and Matthews (1963) hypothesis, that the oceanic magnetic anomalies result from remanent magnetization contrasts.

The rocks additionally must pass the usual paleomagnetic requirement that they have high magnetic stability in order to preserve original remanent magnetization directions over geologically long periods of time. The remanences of many investigated oceanic basalts are in fact stable in the sense that they show only minor intensity or directional variation when measured repeatedly over laboratory experimental times, and also are resistive to alternating field (AF) demagnetization.

Not all oceanic basalts display this high stability. Whereas the median destructive fields of stable basalts commonly lie within the range 100–1000 Oe, a large proportion of the samples that have been investigated have median destructive fields lower than 100 Oe (Lowrie, 1974). These unstable basalts show a pronounced tendency during laboratory investigation to remagnetize in the presence of a constant magnetic field by acquisition of viscous remanent magnetization (VRM). If this can happen in the laboratory it can happen also to the basalt in situ. For this reason it has been proposed that a possible explanation for some oceanic magnetic quiet (or smooth) zones lies in the remagnetization of the oceanic crust in these areas by acquisition of VRM (Lowrie, 1973).

In light of the possible importance of VRM as a component of magnetization of the oceanic crust it is desirable to establish the characteristics of this remanence in oceanic basalts, and to understand what limitations are placed on the VRM mechanism as a possible explanation of magnetic quiet zones.

VRM Characteristics in Oceanic Basalts

Since it was first suggested that VRM might be an important magnetization component of the oceanic crust in some areas (Lowrie, 1973), many studies of VRM acquisition have been carried out on oceanic basalts recovered on

the different legs of the Deep Sea Drilling Project (DSDP). The main interest in VRM has been to estimate its seriousness and most of the experiments carried out have been similar in type. A select number of samples are left at room temperature in a constant magnetic field of intensity usually in the range 0.5 Oe to 1 Oe, and the measurement of remanent magnetization is repeated at intervals over a period of generally 500 to 2000 h.

Simple Logarithmic Acquisition of VRM

The properties of the natural remanent magnetization (NRM) of the basalts, including their stability, have usually been of primary interest, and, as a result, most VRM experiments on DSDP basalts have been initiated after AF demagnetization has virtually eliminated the original NRM in the samples. Whether the VRM is acquired by multidomain or by very fine, near-superparamagnetic grains, the expected growth is logarithmic with time. Over intervals of time (t) lasting several minutes to several tens of hours, the VRM grows according to a law of the form

$$J(t) - J(0) = S \log t$$

where S , the magnetic viscosity coefficient, depends on the magnetic field and ambient temperature for a given sample. $J(0)$ and $J(t)$ are the initial remanence and that after time t , respectively.

There is usually a fairly large amount of scatter in VRM acquisition data. This may be due to uncontrolled temperature effects; a variation of a few degrees can influence S by several percent. Moreover, the VRM is an extremely unstable magnetization and it is possible that removing the sample from the acquisition field to make a measurement can affect the remanence.

Another source of scatter is the effect of stress on the magnetization. A high speed spinner magnetometer of the Princeton Applied Research (PAR) type exerts quite high stresses on the sample: at a distance of 1 cm from the axis of rotation the centrifugal force is equivalent to 9 g at 15 Hz (g =force of mean gravity), and to 440 g at 105 Hz. The first reported observation of VRM in DSDP basalts consisted of a dramatic decay of remanent intensity during the measurement of NRM with a 105 Hz PAR spinner in Leg 15 basalts from the Caribbean Sea (Lowrie and Opdyke, 1973). The sensitivity to stress of VRM in oceanic basalts was emphasized by Peirce et al. (1974) who recorded an abnormal change in VRM on lightly tapping a sample. It is therefore to be expected that in such unstable samples the DSDP drilling process itself may have a strong effect on the magnetization that is first recorded and analyzed as NRM.

Because of the data scatter, and also because data are gathered at rather infrequent intervals, a straight line is often fitted through all the points on a semi-logarithmic plot so as to determine an average value of S for the period of observation (Peirce et al., 1974). This value of S has been used to extrapolate to much longer times, specifically to 700,000 years, the present duration of the Brunhes period of normal geomagnetic polarity, in order to estimate the VRM that could be acquired in that interval (Lowrie, 1973; Tarasiewicz et

al., 1976). This method makes the assumption that the VRM acquisition is a single-phase process and that observations made within laboratory experiments can be simply extrapolated to geologic periods. This assumption is usually unwarranted but the seriousness of VRM in many samples can often be demonstrated without it.

Multi-Stage VRM Acquisition and Decay

VRM observations in which closely spaced data have been acquired over a long period of time indicate that in most DSDP basalts a multi-stage acquisition process is involved. It is frequently possible to observe more than one of these stages during an acquisition experiment in 1 Oe lasting 2000 h or less. In Leg 28 basalts, the semi-logarithmic plot was clearly non-linear (Lowrie and Hayes, 1975). We have fitted many data sets with higher order polynomials up to 5th order but this has proved to be a rather fruitless exercise as it leads one into the temptation of overinterpreting the acquisition curves. The data are frequently well-satisfied by dividing them into three separate sections (Fig. 1 b), to each of which a straight line is fitted. The slopes of the straight line segments have been calculated for a number of such experiments and it is found that the slopes of segments 1 and 3 are approximately equal (Lowrie, 1974, Table 4).

A three-stage process is often not observed during the period of a normal laboratory experiment, but in most cases a 2-stage VRM acquisition curve is observed (Fig. 1 a), with the slope in the second segment about two to three times that in the first (Fig. 2). It is possible that the same situation exists here as in the three-stage case; if the experiment could be continued for a sufficient length of time the third stage might be observed. The logarithmic nature of the acquisition process limits the deductions that can be made to those observable within a practical length of time, and the possibility of additional stages at longer times can not be excluded. Although the process can be speeded up by using higher fields or temperatures, additional assumptions have to be made that the results are still applicable under the ambient conditions in the oceanic crust.

In contrast to the acquisition of VRM in a constant field, viscous relaxation behaviour is also displayed by oceanic basalts under zero-field conditions. Samples which have been given a VRM in a 1.0 Oe field over a period of 1000 h were placed in a zero-field space created by Helmholtz coils. Their magnetizations, observed over several hundred hours (Fig. 3), decayed in a manner also involving several stages. Too few experiments have been carried out and data are too sparsely distributed to establish whether the slopes of the different parts of the VRM decay curves are correlated with the corresponding slopes of the VRM acquisition curves. On theoretical grounds it is expected that the viscosity coefficient for VRM decay is the same as that for VRM acquisition starting from the AF demagnetized state (Dunlop, 1973).

Comparison of VRM and NRM

It is evident from the above that, even if a simple semi-logarithmic relationship is observed in the course of a laboratory VRM experiment extrapolation to

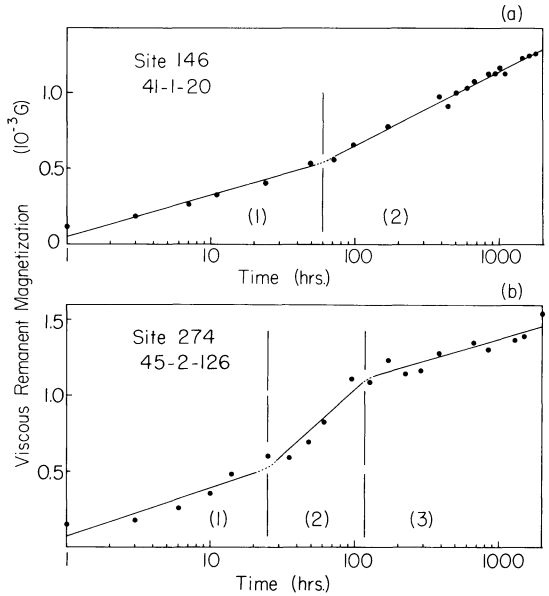


Fig. 1. a Two-stage and **b** three-stage acquisition of viscous remanent magnetization in a constant field of 1.0 Oe in DSDP basalt samples (from Lowrie, 1974)

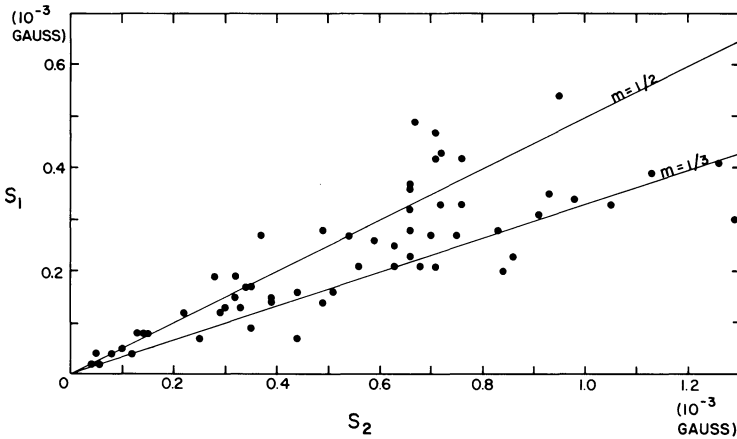


Fig. 2. Comparison of VRM acquisition coefficients in 60 DSDP basalt samples. S_1 and S_2 are the slopes of the straight lines in stages 1 and 2, respectively, in Figure 1. Lines (solid) of constant ratio (S_1/S_2) are shown for reference

geological periods of time is highly uncertain. Thus predictions of the amount of VRM that may be acquired since the beginning of the Brunhes are entirely speculative.

Frequently, however, DSDP basalts are so susceptible to VRM acquisition that the NRM intensity is exceeded within the duration of a laboratory experiment. For example, basalts from site 319A of Leg 34 acquired VRM intensities equivalent to their NRM in times of only 9 to 490 h in a 1 Oe field (Lowrie and Kent, 1976).

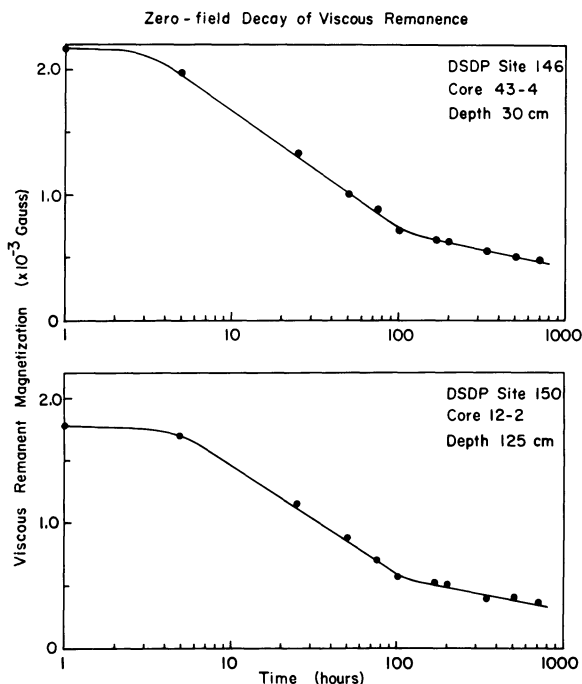


Fig. 3. Zero-field decay of VRM acquired in a 1.0 Oe field over a period of 1000 h in two DSDP basalt samples

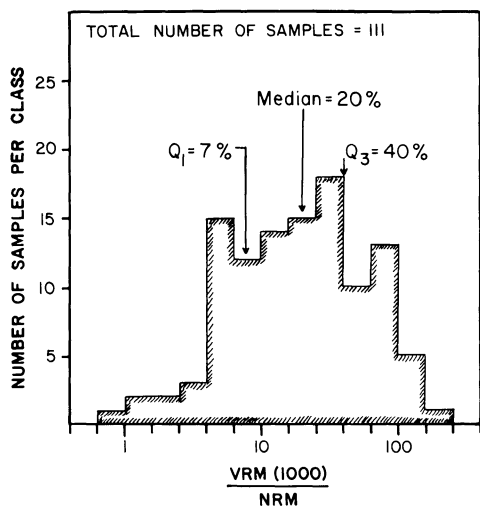


Fig. 4. Histogram of the ratio VRM(1000)/NRM in 111 DSDP basalt samples. VRM(1000) was acquired after AF demagnetization of NRM in most cases in a constant field of 1 Oe over 1000 h. The values of the first quartile (Q_1), median, and third quartile (Q_3) of the distribution are indicated

An effective method of comparing the VRM acquisition in a sample to its NRM intensity is to use a standard field for a standard length of time. Most observers of VRM have continued their observations for at least 1000 h. Fields used have been in the range 0.5 to 1.0 Oe, in which the viscosity coefficient presumably varies linearly with applied field. It is, however, unsafe to correct

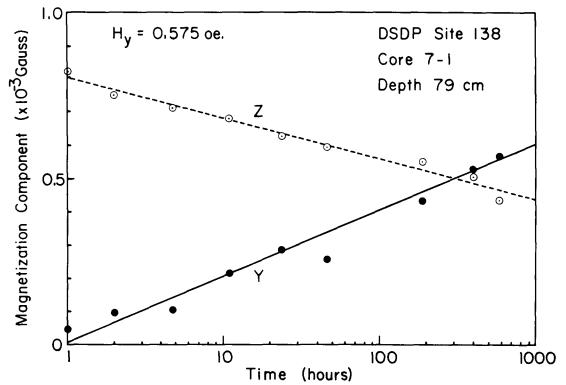


Fig. 5. Acquisition of VRM in the presence of NRM in a DSDP basalt sample. Sample was aligned so the magnetic field ($H=0.575$ Oe) was parallel to Y -axis and the NRM lay in the X - Z plane

for this field variation (for the same reasons that acquisition curves cannot be extrapolated) and data from authors who have not used a 1.0 Oe field (Peirce et al., 1974; Tarasiewicz et al., 1976) are incorporated without correction in compiling a histogram of VRM (1000)/NRM values for 111 basalt samples representing 30 DSDP sites (Fig. 4). The median value of the distribution is 20%. The distribution is probably not truly representative of all DSDP basalts since VRM investigations are usually carried out deliberately on those basalts which display unstable characteristics during measurement of NRM properties. Nevertheless the histogram indicates that in $1/4$ of the samples studied the VRM acquired in a few weeks in the laboratory exceeded 40% of the original NRM intensity. Moreover, these 30 sites represent 40% of all DSDP sites up to Leg 41 for which basalt magnetic properties have been published. Their age range from a few million years (site 332B) to 150 million years (site 100).

VRM Acquisition in the Presence of NRM

The VRM data described above were acquired after the NRM properties of the basalts had been studied and after the NRM had been effectively eliminated (or reduced to a very low value) by AF demagnetization. The conditions prepared for acquisition of VRM are, therefore, artificial when compared to the conditions in nature, where VRM is not acquired from a demagnetized state but in the presence of an NRM component (presumed to be TRM). It is questionable if deductions on the importance of VRM made on the basis of laboratory acquisition in demagnetized basalts are directly applicable to VRM acquisition in the oceanic crust. Laboratory experiments indicate, however, that VRM in nature is likely to be even more serious than indicated by the above laboratory data.

An undemagnetized basalt sample was oriented so that its NRM direction was exactly perpendicular to the geomagnetic field in the laboratory. The sample axes were defined so that the Y -axis was parallel to the field direction and the NRM lay in the Z - X plane. The acquisition of VRM over a period of 500 h was practically logarithmic and was accompanied by a corresponding

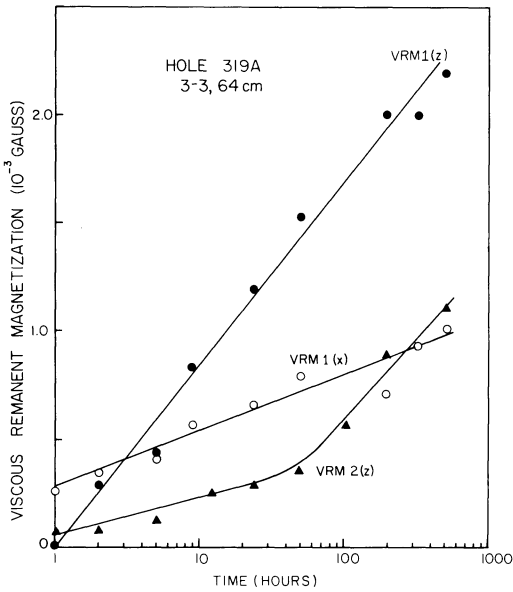


Fig. 6. Acquisition of VRM in presence of NRM (VRM 1) and after AF demagnetization (VRM 2) in a DSDP basalt sample

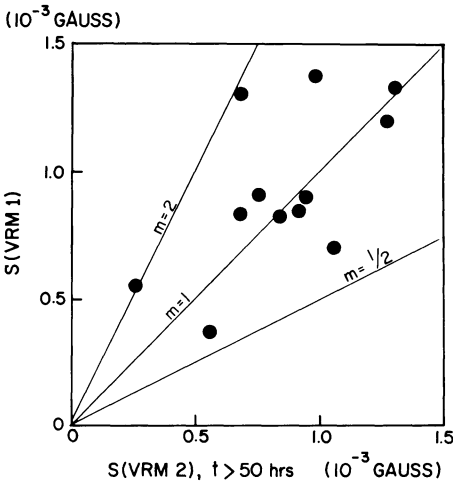


Fig. 7. Comparison of the viscosity coefficient characterizing VRM growth in the presence of NRM ($S(\text{VRM } 1)$) and the viscosity coefficient for the second segment of VRM growth after AF demagnetization ($S(\text{VRM } 2)$, $t > 50$ h) in DSDP Leg 34 basalt samples. Lines (solid) of constant ratio are shown for reference

decay of the Z-component (Fig. 5). The X-component was much stronger than the Y or Z-components; variation in this component could not be distinguished from the error of measurement. Possibly part of the growth of VRM along the Y-axis is enhanced by the decay of NRM along the Z-axis as the unstable (soft) component rearranges itself. In this case the VRM acquisition was not multistage.

In VRM experiments on basalts from DSDP Leg 34 (Fig. 6) Lowrie and Kent (1976) also reported simple logarithmic growth of VRM prior to AF demagnetization (VRM1(z)). This was again accompanied by a change in the remanence component normal to the VRM. After AF demagnetization the

Table 1.

Site	Sample	NRM (10^{-3} Gauss)	VRM (10^{-3} Gauss)	VRM/NRM (%)
100	11-1-20	16.0	1.83	11
	11-1-100	23.7	1.51	6
	11-1-125	6.18	2.49	40
105	42-2-5	3.53	0.68	19
	42-2-38	1.07	1.34	124
	42-2-71	3.09	1.18	38
	42-2-105	3.21	0.98	31
	42-2-121	1.43	1.55	108
	42-2-147	3.27	0.91	28
146	41-1-20	2.65	1.13	43
	41-2-2	1.21	1.13	93
	42-2-70	2.81	1.75	62
	42-3-148	2.78	1.72	62
	43-2-123	5.93	1.39	23
	43-3-73	3.79	1.75	46
	43-4-130	4.98	1.76	35
	150	11-2-65	3.92	1.39
12-1-132	6.64	1.40	21	
12-2-125	4.69	1.46	31	
151	14-1-118	5.84	0.56	10
	15-1-148	1.96	0.39	20
152	23-1-112	2.38	0.75	31
	24-1-68	1.68	0.58	35
	24-2-75	8.32	0.57	7
153	19-1-118	8.81	1.53	17
	20-1-147	5.88	1.39	24
	20-2-82	3.52	1.55	44
274	44-1-cc	2.74	1.32	48
	44-3-cc	2.22	1.78	84
	45-1-cc	12.3	0.94	8
	45-2-2	12.2	1.37	11
367	38-2-76	5.36	0.014 (3.39)	0.3 (63)
	38-3-2	3.84	0.25 (3.65)	7 (96)
	38-3-129	2.59	0.022 (2.83)	0.8 (109)
	39-2-35	2.78	0.26 (1.47)	9 (53)
	39-2-122	1.39	0.040 (2.10)	3 (66)
	40-1-87	4.06	0.20 (2.71)	5 (67)

entire character of the VRM acquisition curve changed (VRM2(z)); two distinct segments were now discernible and there were no changes in the orthogonal directions. When plotted against each other the slope of the steeper second segment and the slope of the single stage VRM acquisition prior to demagnetization (Fig. 7) are scattered but are positively and significantly correlated ($r=0.614$) and do not differ by more than a factor of 2.

The character of VRM acquisition observed before and after AF demagnetization differed also in experiments conducted for 500 h on basalts from site 367

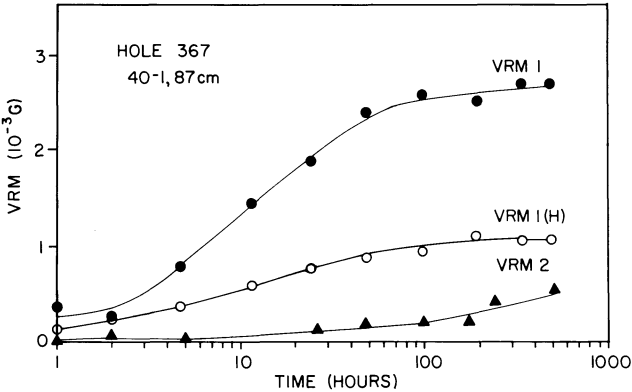


Fig. 8. Acquisition of VRM in presence of NRM (VRM 1) and after AF demagnetization (VRM 2) in a DSDP basalt sample from a site in the Jurassic Quiet Zone in the eastern North Atlantic. VRM 1 (H) represents the change in remanence in the plane perpendicular to the applied field of 1 Oe

(Kent and Tsai, 1977). Before demagnetization the VRM acquired in this short period amounted to a large fraction (53% to 109%) of the initial NRM intensity (Table 1). In this case also the growth of VRM is accompanied by a change in the component normal to the acquisition field, which shows a 3 stage relaxation exactly matching the VRM acquisition. In contrast, the VRM observed after AF demagnetization was much less pronounced. Whereas prior to AF demagnetization 3-stage acquisition was exhibited, this was not observed after demagnetization, although the slope of the logarithmic plot appears to increase after 100 h (Fig. 8). The marked difference in VRM acquisition as a function of the initial remanence state was similar to that noted in Leg 34 basalts (Fig. 6, and Lowrie and Kent, 1976).

From these few data it cannot be established if the same physical process is involved in both cases (i.e. before and after AF demagnetization). It appears that the AF demagnetization stabilized the short activation-time component that participated previously in the VRM acquisition. The important paleomagnetic observation is that the rate of VRM acquisition in the presence of NRM is at least equivalent to the most rapid acquisition from the AF demagnetized state. Since the laboratory VRM acquisition experiments made in the presence of NRM are likely to be more representative of the viscous behavior exhibited by the basalts in situ, we feel that a significant portion of the NRM of these site 367 and Leg 34 basalts can be attributed to recently acquired viscous components.

Summary of VRM Acquisition Experiments

The experimentally established characteristics of VRM in oceanic basalts may be summarized as follows:

1. The tendency of DSDP basalt to acquire VRM varies approximately

inversely with the median destructive field and is especially high in basalts with MDF less than 100 Oe (Kent and Lowrie, 1977).

2. A long term simple logarithmic law is rarely obeyed during acquisition of VRM in oceanic basalts. Two or three stages are usually observed, in each of which a simple logarithmic relationship can be assumed.

3. For this reason it is not meaningful to try to extrapolate quantitatively from the results of laboratory VRM experiments in an attempt to account for the NRM intensity of the basalts. Instead we prefer to consider the VRM acquired during the course of a laboratory experiment as a minimum indicator of the seriousness of VRM in situ. If a large fraction of NRM can be accounted for by VRM acquisition during a period of only a few weeks it is reasonable to assume that an equivalent or larger fraction of the remanence of the basalt in situ must be viscous.

4. Contrary to expectation, the VRM acquired under laboratory conditions in the presence of NRM is apparently more serious than that acquired in the demagnetized basalts. Since the overwhelming majority of published VRM results (Lowrie, 1974; Peirce et al., 1974; Tarasiewicz et al., 1976) have been obtained after demagnetization, most of these data must be interpreted as minimum estimates of the significance of VRM acquired by DSDP basalts in situ (that is, in the presence of NRM).

Origin of VRM in Oceanic Basalts

Magnetic Domain State

The remanent magnetic properties of oceanic basalts are due to fine grains of titanomagnetite or titanomaghemite with titanium compositional parameters in the range $x=0.4$ to $x=0.6$. Formulae that allow computation of the critical grain size for transitions between the different magnetic domain states are summarized and their limitations discussed, by Stacey and Banerjee (1974). Although they probably are qualitatively correct, they are rather inexact quantitatively because of simplifying assumptions that are involved.

For the compositional range found in oceanic basalts the transition from superparamagnetism to single domain behavior occurs at grain sizes of 0.04–0.07 μm ; the thickness of a domain wall is 0.1–0.2 μm , and the critical upper grain size for single domain behavior is 0.2–0.6 μm . Pseudo-single domain behavior is displayed until grain sizes of 20–40 μm , above which multidomain behavior is found.

The only direct optical evidence of magnetic domain states in titanomagnetites was obtained by the Bitter technique on a titanomagnetite with compositional parameter $x=0.65$ by Soffel (1971). He observed that particles up to several microns in size contained only two domains, and by extrapolating the plotted relation between number of domains and particle size, he inferred a critical maximum diameter of about 1 μm for single domains.

Commonly oceanic basalts belong to deuteritic oxidation class 1 according to the scheme of Wilson and Watkins (1967), but occasionally classes 2, 3

or 4 have been reported (Ade-Hall et al., 1976). Systematic measurement of magnetic grain sizes and correlation with stable or unstable remanent magnetic properties unfortunately have not been made. Most DSDP basalts investigated have contained grains from a few microns in size down to the limit of optical resolution, while some have occasionally contained grains coarse enough to permit optical classification of the deuteric oxidation state. Very coarse grains up to 100 μm in size were observed in DSDP basalts from size 57 in the North Pacific Ocean (Lowrie et al., 1973) while electron microscope investigation of oceanic basalts dredged from the North mid-Atlantic ridge revealed grain sizes finer than 0.1 μm (Evans and Wayman, 1972).

Although VRM has been observed in a wide range of basalt grain sizes, it is most serious in comparison to NRM in coarse-grained basalts and dolerites. It therefore seems reasonable to associate stable remanence in oceanic basalts with single domain grains, and viscous behavior with pseudo-single-domain (PSD) and multidomain (MD) grain sizes.

This conclusion is supported by the properties of NRM in a number of DSDP sites (Lowrie, 1974, 1977). Königsberger ratios (Q_n) are high in basalts with stable NRM, and even in unstable basalts rarely are much lower than unity. Viscous remanent magnetization is often observed in basalts with low median destructive fields and Q_n values around unity; sometimes a strong NRM intensity is compensated by correspondingly large susceptibility. The NRM contains a low-coercivity fraction usually accompanied by a small hard component which is hard to isolate in the presence of the larger soft component. The soft component of NRM and the sample susceptibility are possibly multidomain effects, while the hardest part of NRM arises from PSD moments. Support for this rather generalized statement also comes from the VRM characteristics.

Theory of VRM in Oceanic Basalts

The current status of the theory of VRM in SD, PSD and MD materials has been reviewed and discussed critically by Dunlop (1973). The following phenomenological interpretation of our VRM observations is based on his article, which should be consulted for details and a stricter analysis.

Without specifying the domain state or nature of the magnetization a phenomenological model may be set up in which a relaxation time (T) is associated with each magnetic moment. If the spectrum of $\log T$ is open ended and uniform (Fig. 9a), a simple logarithmic VRM acquisition law will be obeyed for all experimental times. For this situation it would be possible to extrapolate the results from experimental times to geological periods. Dunlop (1973) has shown that a uniform $\log T$ distribution can result from a wide range of grain sizes and coercivities.

Non-uniformity of the $\log T$ distribution gives rise to non-logarithmic acquisition of VRM. In particular, if the $\log T$ spectrum is bounded by relaxation times T_1 and T_2 , both of which lie within the period of experimental observation, a VRM acquisition curve similar to that shown in Fig. 9b results. For observation times $t \ll T_1$ and $t \gg T_2$ there is no activation; for $T_1 < t < T_2$ a logarithmic

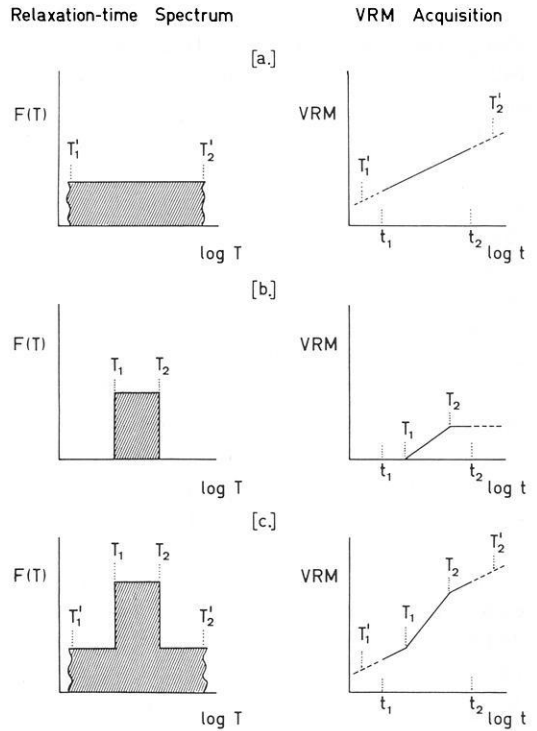


Fig. 9 a-c. Illustration of VRM acquisition curves in materials with three different distributions of magnetization relaxation times T . **a** VRM grows logarithmically when the distribution of $\log T$ is uniform over a wide range, **b** VRM grows logarithmically over a certain time range, representing the limits of a discrete range of relaxation times. **c** Three-stage VRM growth results from the combination of effects **a** and **b**

mic growth of VRM is observed. In fact the onset and termination of VRM growth due to activation of this discrete range of relaxation times need not coincide with T_1 or T_2 , and the acquisition curve will have tails.

We envisage the 3-stage VRM acquisition curves in AF demagnetized DSDP basalts to be represented by the sum of these two effects; a discrete range of relaxation times is superposed on a broader background (Fig. 9c). In view of the known magnetic mineralogy of oceanic basalts, the background VRM growth is probably due to multidomain grains, on which is superposed a discrete fraction possibly representing SD or PSD grains. The coexistence of two disparate grain size generations among titanomagnetites in the same basalt sample is supported by observation. Ade-Hall et al. (1976) describe massive basalts containing anhedral grains up to 100 μm in size and skeletal grains from 10 μm down to the limit of visibility.

Creer et al. (1970) and Petherbridge (1977) heated Rauher Kulm basalt samples at 400° C to produce a ‘daughter’ magnetic mineralogical phase whose interaction with the ‘mother’ phase led to partial self-reversal, and also to a change in the character of viscous magnetization acquisition. Heated (two-phase) samples showed 2-stage acquisition (as in Fig. 1a) whereas natural unheated samples did not.

Production of a ‘daughter’ phase in the laboratory by heating can be achieved in nature at lower temperatures over longer time intervals. Abundant optical evidence has been reported of oceanic basalts containing otherwise homogeneous

titanomagnetites that displayed the characteristic whitening of maghemitization along internal cracks and on grain rims (see, for example, Ade-Hall et al., 1976). Strong-field thermomagnetic curves occasionally also show an initial increase of induced magnetization on heating (see, for example, Lowrie et al., 1973, Fig. 2), possibly indicating partial self-reversal.

Petherbridge (1977) attributed viscous behaviour of the 'daughter' mineralogical phase to ultra-fine, unstable grains whose sizes were intermediate between the ranges for superparamagnetism and stable SD magnetization. However, the viscosity coefficient for this SD-type VRM ought to be more than an order of magnitude greater than that for MD-type (Dunlop, 1973), whereas the observed ratio of viscosity coefficients in stages 1 and 2 is only around 2 or 3 (Fig. 2). We attribute stage 2 rather to a PSD fraction.

Some of the experimental evidence suggests that a single stage VRM growth observed before AF demagnetization changes to multi-stage acquisition after AF demagnetization (Fig. 6) with the original viscosity coefficient matched by the viscosity coefficient in stage 2 (Fig. 7). This implies that AF demagnetization resulted in partial stabilization of the spectrum of relaxation times, preventing their participation in further VRM growth. For this model the AF demagnetized state is taken to be equivalent to an anhysteretic remanent magnetization (ARM) acquired in a constant field of zero intensity. ARM can possess quite high stability, and we envision this to be imparted to a fraction of the magnetization spectrum that originally participated in the VRM process. However, we can offer no exact mechanism by which this took place or by which it can be quantitatively explained. In the hole 367 basalts 3-stage VRM acquisition was greatly altered by AF demagnetization, to the extent that the magnetic viscosity was almost entirely stabilized (Fig. 8).

Discussion

Dunlop and Hale (1976) report strong VRM in DSDP Leg 37 basalts that contain stoichiometric titanomagnetites and weaker, more variable VRM in basalts with cation-deficient oxidized titanomagnetites and attribute the difference primarily to a difference in effective magnetic grain size. However, from our investigations of VRM in a large number of geographically distributed DSDP sites we do not observe a simple relationship between extent of VRM, grain size and degree of maghemitization. Strong VRM has been observed in fresh coarse-grained basalts elsewhere, for example at site 57 (Lowrie, 1973) and at site 319A (Lowrie and Kent, 1976), in apparent agreement with Dunlop and Hale's findings, but strong VRM has been observed as well in some fine-grained, altered basalts. For example, basalts from site 367 have elevated Curie temperatures near to 400° C that suggest cation-deficient oxidized titanomagnetites and give a fine-grained pattern in the test according to Johnson et al. (1975) of dominant magnetic domain state (Kent and Tsai, 1977; Fig. 10a). These properties are in contrast to the coarse-grained basalts from site 319A which have low Curie temperatures conforming to near stoichiometric titanomagnetites (Lowrie and Kent, 1975) and which give a coarse-grained indication in a test of domain state (Fig. 10b). However, both the site 367 and site 319A

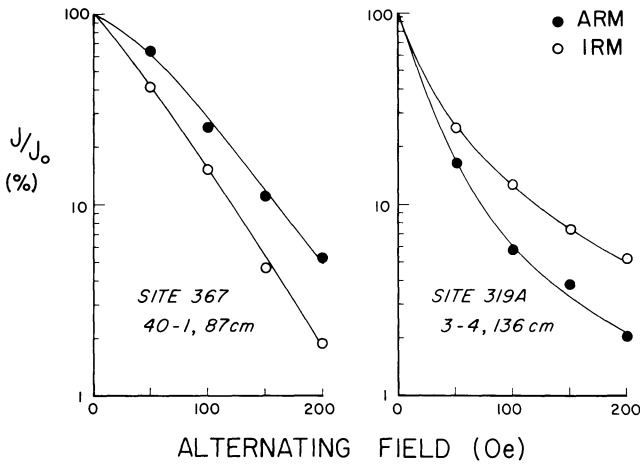


Fig. 10. Comparison of stability against AF demagnetization of anhysteretic (*ARM*) and isothermal (*IRM*) remanent magnetizations in two DSDP basalt samples. The sample from site 367 gives a single-domain indication while the sample from site 319 A gives a multidomain indication. However, both samples have viscous remanent magnetic properties

basalts were able to acquire large VRM components in laboratory experiments (compare Figs. 6 and 8; Table 1). We conclude from this that while it is possible that strong VRM may be a characteristic of fresh coarse-grained oceanic basalts, it does not necessarily appear to be confined to them.

The potential seriousness of VRM in oceanic basalts is therefore difficult to predict. The relatively few studies of VRM and the bias of these studies towards those basalts which display unstable characteristics (i.e., low median destructive fields) during measurement of NRM properties do not enable us to categorically state the extent of VRM in the magnetization of the oceanic crust. However, it is possible that VRM is more prevalent in oceanic basalts than is indicated by these VRM studies. The average median destructive field (MDF) of DSDP basalts from 51 sites averaged only 120 Oe (Lowrie, 1977). In basalts with MDF less than 100 Oe VRM can account for a large fraction of the NRM. Moreover, VRM can be important, at least theoretically, even in basalts with high MDF. This is because VRM is a thermally activated process and under certain conditions may not be strongly related to coercivity (Pullaiah, et al., 1977).

A fundamental assumption in the Vine and Matthews (1963) hypothesis is that the remanent magnetization of the ocean crust is preserved from the time of crustal formation at the sea floor spreading axis. If the oceanic basalts recovered by the Deep Sea Drilling Project are considered representative of the source of marine magnetic anomalies, the occurrence of strong VRM of recent origin in many of these rocks suggests that this assumption is not uniformly applicable and it may not always be appropriate to interpret marine magnetic anomalies (or their absence) as a precise record of paleomagnetic field behavior.

We note that the acquisition of a secondary magnetization in oceanic basalts does not necessarily result in reduced anomaly amplitudes. For example, if

a secondary (or an induced) magnetization component is acquired in a uniform direction and in equal amounts by adjacent source blocks with opposite remanent polarities, the magnetization contrast is unaltered and hence the magnitude (and the shape) of the magnetic anomaly does not change provided the original remanent magnetization is not affected. All other factors the same, a decrease in the amplitude of marine magnetic anomalies will only result from a reduction in the original basalt remanent magnetization that carries the record of field reversals.

Our data indicate that VRM acquisition is accompanied by erosion of another component of NRM (Fig. 5, 6 and 8). It is not certain what the "NRM" in this case represents. The large soft component of most basalts studied for VRM purposes obscures unambiguous identification of the original remanence. In many cases AF demagnetization of unstable DSDP basalts beyond only 100 Oe results in scattered directions, and a stable inclination is difficult or impossible to isolate. Although a thermoremanence must have been acquired during initial cooling of the basalts, subsequent modification by VRM, by chemical alteration, by the stresses of sampling, and by other secondary processes, are very likely. For example, the dramatic effect on the remanence observed after lightly tapping an unstable DSDP basalt (Peirce et al., 1974), emphasizes the possibility that drilling with a magnetic drill collar and core barrel can induce a secondary remanent magnetization (Ade-Hall and Johnson, 1976). The apparent decay of NRM during VRM acquisition may merely represent relocation of a secondary unstable component acquired just prior to the laboratory investigation.

It is also possible, however, that the original TRM of unstable basalts has been at least partly lost. If the original TRM is carried by grains whose magnetization relaxation times at ambient sea-floor temperatures are shorter than a few hundred thousand years, a part of the original TRM will be eroded and participate in a VRM acquisition process. Magnetization contrasts between adjacent, oppositely magnetized crustal blocks will consequently be reduced and the associated magnetic anomalies will be reduced in amplitude or absent.

Of interest in this context are marine magnetic quiet zones, regions in which magnetic anomalies are either poorly developed or not lineated. The interpretation of the Cretaceous quiet zone as representing sea-floor spreading during an interval of predominantly normal geomagnetic polarity is supported by independent paleomagnetic data (e.g., Helsley and Steiner, 1968; Lowrie and Alvarez, 1977). In contrast, the available land paleomagnetic record does not independently require an interval of constant geomagnetic polarity for the interval of time corresponding to the Jurassic quiet zones (Irving and Pullaiah, 1973) and apparently conflicting interpretations of paleomagnetic field behavior during this interval have been given (i.e., dominantly normal polarity: Larson and Pitman (1972), Larson and Hilde (1975); dominantly reversed polarity: Steiner and Helsley (1975); rapidly reversing field polarity: Cande et al. (1977). It is possible that a single explanation does not suffice for the Jurassic quiet zone. However, the fact that the Jurassic quiet zone boundary appears to cut across magnetic lineations in the eastern North Atlantic (Hayes and Rabinowitz, 1975) indicates that it is not an isochron, but is a feature of variation in the rock

magnetic properties of the oceanic crust. This, in addition to the unstable magnetic properties of the only DSDP basalts recovered from the Jurassic quiet zone (Site 100 and perhaps Site 105 in western, Site 367 in eastern, North Atlantic) and the current lack of independent paleomagnetic data suggest that viscous remagnetization of the crust may contribute to the observed smooth magnetic field over the Jurassic quiet zones.

Magnetic quiet zones are also found adjacent to the margin of certain continents, such as southern Australia (Weissel and Hayes, 1972). Irving (1970) pointed out that a local geological cause is probably responsible for marginal quiet zones and suggested the probable difference in conditions for submarine basalt formation at the time of initial rifting compared to later steady sea-floor spreading. An example at present is to be seen in the Red Sea; although a well-defined axial anomaly exists, oceanic magnetic anomaly amplitudes in the adjacent areas are subdued (Girdler, 1969). Irving assumed that conditions at initial rifting would favor development of coarse grain sizes in basalts, and expected these to have low NRM intensities and stabilities. The concurrence of high VRM in coarse-grained DSDP basalts observed by Dunlop and Hale (1976) and in this study indicates that viscous remagnetization may be an important process in the production of marginal quiet zones.

Lineated magnetic anomalies are not always absent in magnetic quiet zones although their amplitudes are greatly reduced. There is frequently good correlation between topography and positive anomalies, but reversely magnetized zones have also been interpreted as in the Jurassic quiet zone in the eastern North Atlantic (Barrett and Keen, 1976). These observations indicate that the quiet zone crust is acting as a poor recorder of reversals, and are compatible with the VRM model hypothesized above.

Acknowledgements. We are grateful to Drs. S. Cande, J.E.T. Channell and F. Heller for constructive criticism of the manuscript. Partial financial support was provided by NSF grant OCE 76-21962.

References

- Ade-Hall, J.M., Johnson, H.P.: Review of magnetic properties of basalts and sediments, Leg 34. In: Initial Reports of the Deep Sea Drilling Project, Volume XXXIV, R.S. Yeats and S.R. Hart, eds.: pp. 769–778. Washington: U.S. Government Printing Office 1976
- Ade-Hall, J.M., Fink, I.C., Johnson, H.P.: Petrography of opaque minerals, Leg 34. In: Initial Reports of the Deep Sea Drilling Project, Volume XXXIV, R.S. Yeats and S.R. Hart, eds.: pp. 349–362. Washington: U.S. Government Printing Office 1976
- Atwater, T., Mudie, J.D.: Detailed near-bottom study of the Gorda Rise. *J. Geophys. Res.* **78**, 8665–8689, 1973
- Barrett, D.L., Keen, C.E.: Mesozoic magnetic lineations, the magnetic quiet zone, and sea-floor spreading in the northwest Atlantic. *J. Geophys. Res.* **81**, 4875–4884, 1976
- Cande, S.C., Kent, D.V.: Constraints imposed by the shape of marine magnetic anomalies on the magnetic source. *J. Geophys. Res.* **81**, 4157–4162, 1976
- Cande, S.C., LaBrecque, J.L., Larson, R.L.: Marine magnetic anomaly data from the Jurassic and Cretaceous quiet zones: Implications for long period intensity variations of the paleomagnetic field (abs.). *EOS* **58**, 740, 1977
- Creer, K.M., Petersen, N., Petherbridge, J.: Partial self-reversal of remanent magnetization and anisotropy of viscous magnetization in basalts. *Geophys. J. Roy. Astron. Soc.* **21**, 471–483, 1970

- Dunlop, D.J.: Theory of the magnetic viscosity of lunar and terrestrial rocks. *Rev. Geophys. Space Phys.* **11**, 855-901, 1973
- Dunlop, D.J., Hale, C.J.: Simulation of long-term changes in the magnetic signal of the oceanic crust. *Can. J. Earth Sci.* **14**, 716-744, 1977
- Evans, M.E., Wayman, M.L.: The mid-Atlantic Ridge near 45° N: XIX. An electron microscope investigation of the magnetic minerals in basalt samples. *Can. J. Earth Sci.* **9**, 671-678, 1972
- Girdler, R.W.: The Red Sea—a geophysical background. In: *Hot brines and recent heavy metal deposits in the Red Sea*, pp. 38-58. E.T. Degen and D.A. Ross, eds.: New York: Springer, 1969
- Harrison, C.G.A.: Magnetization of the oceanic crust. *Geophys. J. Roy. Astron. Soc.* **47**, 257-283, 1976
- Hayes, D.E., Rabinowitz, P.D.: Mesozoic magnetic lineations and the magnetic quiet zone off northwest Africa. *Earth Planet. Sci. Lett.* **28**, 105-115, 1975
- Helsley, C.E., Steiner, M.C.: Evidence for long intervals of normal polarity during the Cretaceous period. *Earth Planet. Sci. Lett.* **5**, 325-332, 1968
- Irving, E.: The mid-Atlantic ridge at 45° N: XIV. Oxidation and magnetic properties of basalt; review and discussion. *Can. J. Earth. Sci.* **7**, 1528-1538, 1970
- Irving, E., Pullaiah, G.: Reversals of the geomagnetic field, magnetostratigraphy, and relative magnitude of paleosecular variation in the Phanerozoic. *Earth-Sci. Rev.* **12**, 35-64, 1976
- Kent, D.V., Lowrie, W.: Magnetic properties of igneous rock samples from Leg 37. In: *Initial Reports of the Deep Sea Drilling Project, Vol. XXXVII*, in press. F. Aumento and W.G. Melson, eds.: Washington: U.S. Government Printing Office, 1977
- Kent, D.V., Tsai, L.P.: Paleomagnetism and rock magnetism of Upper Jurassic limestone and basalt from Site 367. In: *Initial Reports of the Deep Sea Drilling Project, Vol. XXXXI*, in press. Y. Lancelot and E. Seibold, eds.: Washington: U.S. Government Printing Office, 1977
- Larson, R.L., Hilde, T.W.C.: A revised time scale of magnetic reversals for the Early Cretaceous and Late Jurassic. *J. Geophys. Res.* **80**, 2586-2594, 1975
- Larson, R.L., Pitman III, W.C.: Worldwide correlation of Mesozoic magnetic anomalies, and its implications. *Bull. Geol. Soc. Am.* **83**, 3645-3662, 1972
- Lowrie, W.: Viscous remanent magnetization in oceanic basalts. *Nature* **243**, 27-30, 1973
- Lowrie, W.: Oceanic basalt magnetic properties and the Vine and Matthews hypothesis. *J. Geophys.* **40**, 513-536, 1974
- Lowrie, W.: Intensity and direction of magnetization in oceanic basalts. *J. Geol. Soc.* **133**, 61-82, 1977
- Lowrie, W., Alvarez, W.: Upper Cretaceous-Paleocene magnetic stratigraphy at Gubbio, Italy. III. Upper Cretaceous magnetic stratigraphy. *Geol. Soc. Am. Bull.* **88**, 374-377, 1977
- Lowrie, W., Hayes, D.E.: Magnetic properties of oceanic basalt samples. In: *Initial Reports of the Deep Sea Drilling Project, Vol. XXVIII*, pp. 869-878. D.E. Hayes and L.A. Frakes, eds.: Washington: U.S. Government Printing Office, 1975
- Lowrie, W., Kent, D.V.: Viscous remanent magnetization in basalt samples. In: *Initial Reports of the Deep Sea Drilling Project, Vol. XXXIV*, pp. 479-484. S.R. Hart, and R.S. Yeats, eds.: Washington: U.S. Government Printing Office, 1976
- Lowrie, W., Løvlie, R., Opdyke, N.D.: Magnetic properties of Deep Sea Drilling Project basalts from the North Pacific Ocean. *J. Geophys. Res.* **78**, 7647-7660, 1973
- Lowrie, W., Opdyke, N.D.: Paleomagnetism of igneous and sedimentary samples. In: *Initial Reports of the Deep Sea Drilling Project, Vol. XV*, pp. 1017-1022. N.T. Edgar and J.B. Saunders, eds.: Washington: U.S. Government Printing Office, 1976
- Peirce, J.W., Denham, C.R., Luyendyk, B.P.: Paleomagnetic results of basalt samples from DSDP Leg 26, Southern Indian Ocean. In: *Initial Reports of the Deep Sea Drilling Project, Vol. XXVI*, pp. 517-527. T.A. Davies and B.P. Luyendyk, eds.: Washington: U.S. Government Printing Office, 1974
- Petherbridge, J.: A magnetic coupling occurring in partial self-reversal of magnetism and its association with increased magnetic viscosity in basalts. *Geophys. J. Roy. Astron. Soc.* **50**, 395-406, 1977
- Soffel, H.: The single domain-multidomain transition in natural intermediate titanomagnetites. *Z. Geophysik* **37**, 451-470, 1971
- Stacey, F.D., Banerjee, S.K.: *The physical principles of rock magnetism*, pp. 190. Elsevier 1974

- Steiner, M.B., Helsley, C.E.: Magnetic field polarity during the Late Jurassic (abs.) EOS **56**, 354, 1975
- Talwani, M., Windisch, C.C., Langseth, Jr., M.G.: Rekjanes Ridge Crest: a detailed geophysical study. J. Geophys. Res. **76**, 473–517, 1971
- Tarasiewicz, G., Tarasiewicz, E., Harrison, C.G.A.: Some magnetic properties of Leg 34 rocks. In: Initial Reports of the Deep Sea Drilling Project, Vol. XXXIV, pp. 473–478. S.R. Hart and R.S. Yeats, eds.: Washington: U.S. Government Printing Office, 1976
- Taylor, P.T., Watkins, N.D., Greenewalt, D.: Magnetic property analysis of basalt beneath the quiet zone. EOS **54**, 1030–1032, 1973
- Vine, F.J., Matthews, D.H.: Magnetic anomalies over oceanic ridges. Nature **199**, 947–949, 1963
- Vogt, P.R., Anderson, C.N., Bracey, D.R.: Mesozoic magnetic anomalies, sea-floor spreading and geomagnetic reversals in the southwestern North Atlantic. J. Geophys. Res. **76**, 4796–4823, 1971
- Weissel, J.K., Hayes, D.E.: Magnetic anomalies in the Southeast Indian Ocean. In: Antarctic Oceanology II: The Australian-New Zealand Sector. D.E. Hayes, ed.: Series **19**, 165–196. Washington: D.C., AGU Antarctic Research, 1972
- Wilson, R.L., Watkins, N.D.: Correlation of petrology and natural magnetic polarity in Columbia plateau basalt. Geophys. J. **12**, 405–424, 1967

Received November 4, 1977 / Revised Version March 3, 1978

Magnetic Discordance in Gran Canaria/Tenerife and Its Possible Relevance to the Formation of the NW. African Continental Margin

K.M. Storetvedt, S. Svalestad, K. Thomassen, Aa. Langlie, A. Nergård, and
A. Gidskehaug

Department of Geophysics, University of Bergen, Allégt. 70, 5014 Bergen, Norway

Abstract. The palaeomagnetic stratigraphy of Gran Canaria and Tenerife suggests that these islands have been built up during two major volcanic ‘pulses’, i.e. in Mesozoic (probably late Cretaceous) and Upper Tertiary/Quaternary times. The palaeomagnetic implications are compared with other evidences from the NW. African shelf and margin such as geological data from drill holes in coastal basins, Deep Sea Drilling Project results and information from various marine geophysical surveys. The combined evidence favours a continental origin of a crustal belt (including the Canary Islands) extending seaward into water depths of at least 4500 m.

Key words: Palaeomagnetism – Marine geology/geophysics – Formation of Canary Islands and adjacent oceanic tracts.

1. Introduction

The origin of the Canarian Archipelago has been a matter of much speculation and a continental as well as an oceanic sub-stratum for the islands have been proposed. The oldest stage of development of the islands appears to have produced a basal complex of mostly mafic and ultramafic plutonics, but submarine volcanics and various types of sediments occur also. This basement complex, which appears to underlie the entire island group, is exposed in La Palma, Gomera and Fuerteventura (Cendrero, 1971; Fúster et al., 1968a–d; Hausen, 1956, 1958, 1959, 1962; Ibarrola, 1970) and it is likely to be represented as inclusions in the younger basalts of Lanzarote (Fúster et al., 1970). According to Fúster et al. (1970) the chemical composition of the basement plutonics differs from that of the overlying volcanic rocks and there is an erosional discordance between the two series. The thick section of marine sedimentary rocks in the basal complex of Fuerteventura is strongly folded and fossil evidence points towards a Mesozoic origin of these strata (Rothe, 1968; Rothe and Schmincke, 1968). On the other hand, the major column of subaerial volcanics of the islands have generally been assigned to the middle or late Tertiary on

the basis of palaeontologic and radiometric dating (Fúster et al., 1968a–d; Abdel-Monem et al., 1971). There seems to be no doubt that a marked peak of volcanic activity swept the islands in Miocene-Pliocene time but one may be sceptical as to whether the outpouring of all the older volcanics actually represents this time interval. Thus, the oldest series, at least in some areas, are extremely weathered (having turned into red soil in places) compared to the overlying, rather fresh rocks for which a Miocene-Pliocene age seems well established. In Gran Canaria, for example, an erosional discordance is found between the two groups of subaerial lavas as well as between the various petrographically different units of the older series (Fúster et al., 1968d). Consequently, one of the fundamental problems of the volcanologic evolution of the Canary Islands is the question of whether there are major time gaps between and within the older subaerial lava sequences of the islands.

For marine geophysical studies, the Canarian archipelago, together with the Cape Verde Islands and Madeira, hold a key position in the Atlantic, as they are situated either within or close to the border zone of the 'quiet' magnetic anomaly field. At present, the favoured explanation of the 'quiet' zone seems to be in terms of sea-floor spreading during a constant geomagnetic polarity epoch sometime in the Mesozoic. Another, but less accepted, way of explaining quiet magnetic zones is through the mechanism of continental crust conversion into a transitional/oceanic structure by the processes of subsidence and sub-crustal erosion (Van Bemmelen, 1966). Unfortunately, standard crustal structure studies seem to be of little help in choosing between the two alternatives (sea floor spreading versus continental oceanization); probably only very young subsidence structures can in some cases be distinguished from a true oceanic crust by the presence of low upper mantle seismic velocities and the absence or suppression of seismic wave propagation along the Moho. In support of an oceanization process, Rona and Nalwalk (1970) and Dietz and Sproll (1970) have given evidence for a sialic substratum under the Canary Islands based on postulated predrift reconstructions of N. America and NW. Africa. Palaeomagnetism of regions like the Cape Verde and Canary Islands may provide important information relevant to these problems. It cannot, unfortunately, be said that there are complete palaeomagnetic analysis of these islands. At present, there exist some palaeomagnetic results by Carracedo and Talavera (1971) of the Anaga peninsula of Tenerife and numerous reconnaissance data by Watkins (1973) and Watkins et al. (1966, 1968) of the Canary Islands/Madeira and the Cape Verde Islands respectively.

In an attempt to provide further information on the abovementioned aspects a detailed experimental study of the palaeomagnetic record of the Canary Islands is at present being undertaken by this department. The present synthesis is based upon the analysis of palaeomagnetic data obtained from Gran Canaria and Tenerife and by consideration of available marine geological and geophysical structures of the adjacent oceanic tracts.

2. Palaeomagnetic Discordance in Gran Canaria and Tenerife

The present palaeomagnetic study of Gran Canaria and Tenerife is based on a total of 305 oriented hand samples from altogether 63 sites (lavas or intrusives).

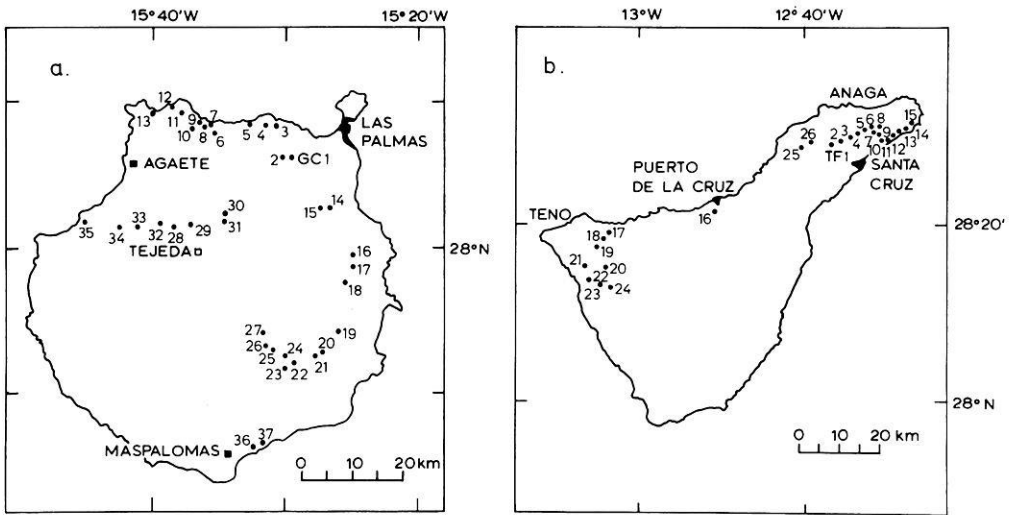


Fig. 1 a and b. Distribution of collecting sites on Gran Canaria (a) and Tenerife (b)

In Gran Canaria the collected sites are concentrated in the northeastern half of the island and span all the major rock units. In stratigraphic order (from 'bottom') these are: Basalt Series 1, Trachyte, Phonolite, Pre-Roque Nublo, Roque Nublo, Ordanchitica Series, Basalt Series 2, and Basalt Series 3 and 4 (Fúster et al., 1968 d). In Tenerife the lavas of Series 1 in the Anaga peninsula as well as dikes cutting through this lava sequence were collected in addition to Basalt Series 3 and 4 from various parts of the island. At the collecting sites post-emplacement tectonics seem too small to be of importance for the present study. For orientation both magnetic and sun compasses were used. Figure 1 shows the distribution of sampling sites. It is not known to which extent these sampling localities may duplicate those of earlier studies.

All collected material has been subjected to detailed thermal and/or alternating field (AF) demagnetization. A test of the entire stability spectrum has been aimed at, i.e. the progressive demagnetization was in general continued until the remanence either became too weak for reliable measurements (this occurred in particular on thermal demagnetization above 500°C) or came into a stage where the remanence parameters initiated an erratic behaviour. All phonolite specimens exploded when heated above 500°C . A large proportion of the rocks had a fairly high resistance to alternating field demagnetization, having a rather high percentage of their remanence intensity left after treatment in the highest available field (1500 Oe).

In general, the Pre-Roque Nublo and younger rocks are easy to deal with in the laboratory, giving mostly stable and consistent within-site directions of magnetization. The palaeomagnetic axis of the Quaternary volcanics (Series 3 and 4) corresponds extremely well with the late Tertiary axis as defined by data from Pre-Roque Nublo, Roque Nublo, Ordanchitica and Basalt Series 2 (cf. Fig. 2a and b and Table 1). Also, as shown in Figure 5, the overall palaeomagnetic pole is in close agreement with middle-late Tertiary poles for Africa.

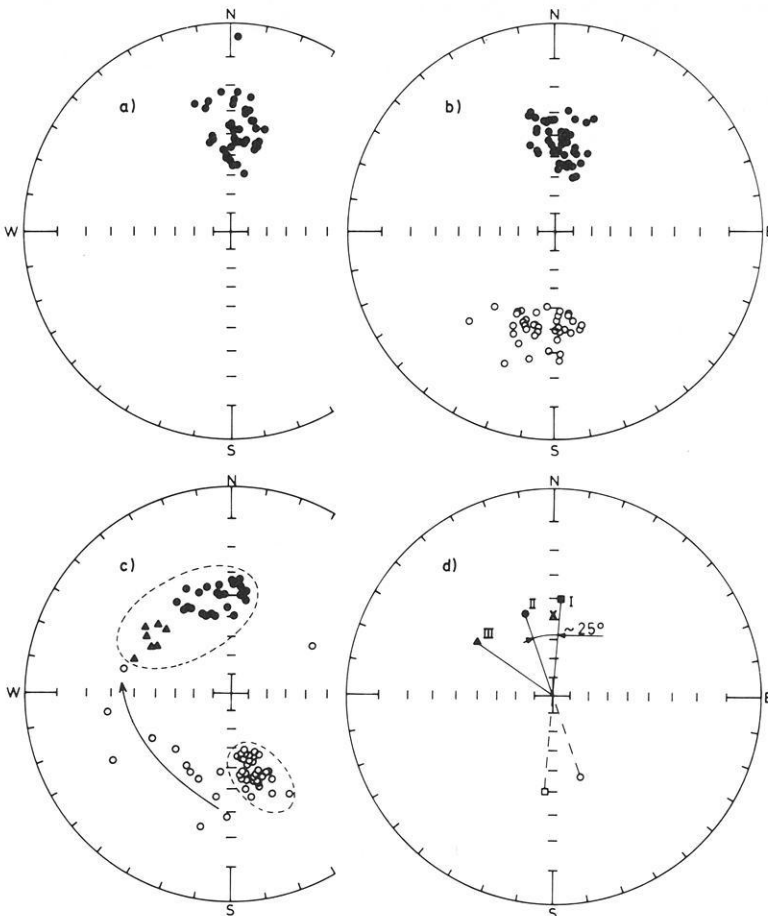


Fig. 2a-d. Palaeomagnetic directions from Gran Canaria and Tenerife; (a) Basalt Series 3 and 4 (Quaternary) (b) Upper Tertiary formations and (c) Basalt Series 1, Trachyte and Phonolite (triangles). Axis I (d) gives the estimated time-average palaeomagnetic direction for the Upper Tertiary-Quaternary and axis II represents the overall directions of the older formations (Series 1, Trachyte and Phonolite). Axis III is the mean directions for the Phonolite rocks taken separately. The cross is the present axial geocentric dipole field relative to the Canary Islands. Full symbols are downward inclinations and open symbols upward inclination

The corresponding field direction from Gran Canaria/Tenerife, is however, significantly different (at the 95% level of confidence) from that of an axial geocentric dipole model (cf. Fig. 2d and Table 1); the somewhat shallower inclination of the observed field lines up with recent ideas (Wilson, 1971; Wilson and McElhinny, 1974) of the dipole source being axial but slightly displaced north of the equatorial plane.

Rocks older than Pre-Roque Nublo in Gran Canaria (i.e. Basalt Series 1, Trachyte and Phonolite) and the Series 1 rocks from the Anaga peninsula of Tenerife show a more complex magnetization than the younger sequences. The

Table 1. Mean palaeomagnetic data from Gran Canaria and Tenerife

Formation		<i>N</i>	<i>R</i>	<i>K</i>	α_{95}	\bar{D}	\bar{I}	Pole location	Remarks
Quaternary basalts; series 3 and 4	a	43	41.9	39.4	3.5	003.7	+38.2	317.9E 82.2S	a: unit weight on speci- men b: unit weight on site
	b	11	10.9	102.4	4.5	004.1	+34.7	316.2E 81.8S	
Late Tertiary formations; Pre-Roque Nublo (-), Roque Nublo (-), Bas. Series 2 (\pm) and Ordanchitica Series (+)	a	85	83.1	43.9	2.3	186.0	-41.6	293.2E 82.9S	
	b	13	12.8	65.6	5.2	184.1	-41.0	306.8E 83.8S	
Quaternary and late Tertiary formations combined	a	128	125	41.7	2	185.2	-40.4	302.1E 82.8S	
	b	24	23.7	79.2	3.4	184.1	-39.5	311.9E 82.9S	
Older lavas: Bas. Series (\pm) Trachyte (\pm) and Phonolite (+)	a	70	68.1	35.6	2.9	162.8	-45.1	071.2E 74.7S	
	b	12	11.6	30.7	8.0	159.9	-44.5	071.2E 72.0S	

N=number of unit vectors (specimens or sites); *R*=length of resultant; *K*=precision parameter; α_{95} =radius of circle of confidence at 5% significance level; \bar{D} , \bar{I} =declination and inclination of mean vector

increased complexity is in part shown by more irregular within-site (and within-sample) distribution of magnetization and in part by the occurrence of an increased number of systematic directional trends on demagnetization for which stable end-points could not be achieved. The dikes gave considerably more scattered results than all the other formations studied—because of the greater uncertainties in the palaeomagnetic parameters of these rocks they have been excluded from the present analysis.

All stable specimen directions (AF or thermal treatment) from Series 1, Trachyte and Phonolite are shown in Figure 2c. Basalt Series 1 rocks from Tenerife are reversely magnetized while Series 1 lavas and Phonolites of Gran Canaria are normally magnetized. The Trachyte lavas show both polarities. The remanence parameters of many of these older rocks were followed to temperatures well above 600° C (see Fig. 3) suggesting haematite as a relatively important magnetic carrier. This evidence is in line with the generally much more altered state of the older strata compared with the younger series. It is not surprising therefore that evidence of multicomponent magnetization (of high magnetic stability) within individual specimens is relatively important in the older strata while such features are practically absent in the more recent ones (Pre-Roque Nublo and younger).

The linear spread of apparently stable directions in the SW-quadrant of Figure 2c is confined to the Series 1 lavas of Tenerife. This pattern appears to be best interpreted in terms of partial remagnetization: a variable normal

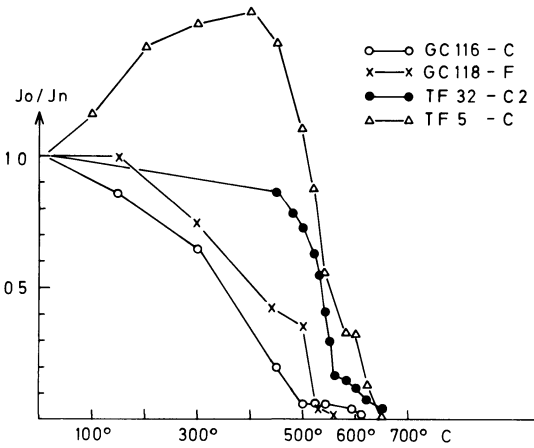


Fig. 3. Examples of thermal decay patterns from the older basalt sequences. *TF* Tenerife specimens; *GC* Gran Canaria specimens

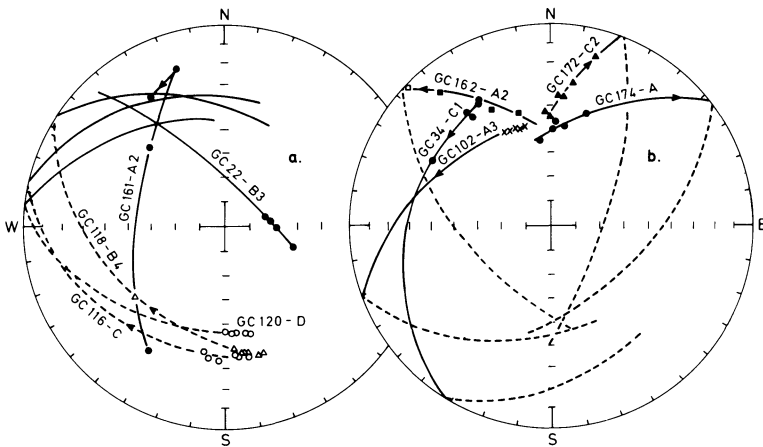


Fig. 4a and b. Examples of directional variation vs. demagnetization along with the extended great circle (remagnetization) paths and their convergence points. Full (open) symbols are downward (upward) inclinations

component of high magnetic stability (probably of chemical origin) having been added to a supposed original reversed magnetization of south-southeasterly declination causing deviating directions of the resultants. This explanation is further supported by the fact that the linear directional spread agrees with great circle paths of the older Series as defined for individual specimens through stepwise demagnetization. Figure 4 gives a number of examples where the resultant remanence directions move along well defined great circles (Halls, 1976) suggesting an interplay between two components of magnetization. Specimens of this type do not qualify to be included in the groups of stable end point data though magnetic stability alone does not prove that one actually is dealing with a single-component remanence. The extended remagnetization circles define intersection points that are either in agreement with the majority of stable end points for the older lavas (cf. Fig. 4a) or are in line with stable directions

for the younger rocks (axis I, cf. Fig. 2d). This component variability merely implies that remagnetization of the older rock sequences continued into axis I time. The important consequence of this prolonged magnetization history is that the original axis will have a tendency of being deflected towards the younger axis. However, as illustrated in Figure 4a, the same deflection effect can certainly be accomplished through remagnetization in the opposite field polarity, axis remaining constant. The encircled reversed group of Figure 2c is considered to represent an actual palaeomagnetic direction to a reasonable approximation but based on the experimental evidence it appears very likely that this reversed group had a slightly more easterly declination originally than that shown at present.

The series 1 lavas as well as the Phonolites of Gran Canaria are of normal polarity, but the combined directional data exhibit a certain smeared distribution which needs further consideration. Firstly, some of the Series 1 sites concerned tend to have become at least partially remagnetized in the normal direction of the late Tertiary/Quaternary field (axis I of Fig. 2d). This suggestion appears properly demonstrated in the collection of 3 sites from the southeastern part of Gran Canaria. One of these sites, which was located close to a thick Series 2 lava gave directions of magnetization in excellent agreement with the inferred late Tertiary axis. The remaining two sites, which probably have not been in immediate proximity to late Tertiary igneous activity, show more westerly declinations (330° – 340°) and are in nearly perfect alignment with the axis based on the reversed group (cf. Fig. 2c). Another reason for the smeared normal distribution is that the Phonolites tend to have a characteristic magnetization with more westerly declination. Two of the three sites collected were closely grouped having declinations between about 290° and 315° (cf. triangles of Fig. 2c), while the third site, having north-northwesterly NRM directions, tends to have a composite magnetization. Demagnetization of the latter site suggests that the relatively stable NRM directions are deflected away from the position of the other two sites by a superposition of a middle-late Tertiary normal component. It is possible, therefore, that the Phonolite Series represent a palaeomagnetic axis which is different from that of the investigated Trachytes and Series 1 lavas, but they could also represent a polyphase remanence caused by partial remagnetization. Owing to the limited number of Phonolite data presently at hand the 'safest' way of estimating mean palaeomagnetic directions for the older series would be to combine all the normal directions of Figure 2c with those of the encircled reversed group. By doing so, the strong westerly directions of the Phonolites would at least in part compensate the demonstrable remagnetization effect of some of the Series 1 samples of Gran Canaria into the more recent field axis.

In Table 1 mean directions of magnetization, statistical parameters (Fisher, 1953) and pole locations have been calculated both with unit weight on specimen (a) and with unit weight on site (b).

It may be argued that the observed magnetic discordance here concerned is merely the result of the older lavas representing a shortlived excursion of the geomagnetic field. However, the observed erosional discordances as well as the more advanced state of mineral alteration in these strata (compared to the younger ones) are not in favour of such an idea. In fact, the probable

involvement of a chemical remanence in these rocks suggest that the total time span covered by axis II (Fig. 2d) may be considerably longer than the actual duration of extrusive activity (and may even exceed that of axis I). Also, the lava sequences of Fuerteventura, for which the detailed palaeomagnetic structures will be dealt with in a following paper, define the same general palaeomagnetic discordance as found in Gran Canaria/Tenerife. It is therefore contended that unlike Pre-Roque Nublo and younger rocks the older volcanics (at least Series I and the Trachytes) did not acquire their original magnetization in the late Tertiary geomagnetic field.

Before considering the geophysical and geological implications of the data it is of some importance to compare our results with those of Watkins (1973). It may be pointed out here that the procedure of the two studies are different: the present analysis includes both extensive thermal as well as alternating field demagnetization (involving a large number of demagnetization steps), whereas Watkins used a more restrictive procedure of alternating field treatment (100, 200 and 300 Oe). It is clear from a comparison that, as far as the Pliocene and younger volcanics are concerned, the overall data agree very well. This agreement is thought to be due to the fact that these rocks basically appear to possess a simple remanence structure (a small soft secondary component added to a primary component of high stability) so that the final results are not critically dependent upon the extent of the experimental analysis. There are, however, discrepancies between the two studies as regards the older lava series. This is due to the fact that here we are dealing with a more complex magnetization which requires more extensive laboratory analysis. In this regard it is contended that the present results must supersede those of Watkins (it may be remarked that Watkins' data do in fact also demonstrate the higher magnetic complexity of the older lava series: his Table 2(b) shows drastic reductions in the precision parameters, K , along with corresponding increases in the respective circles of confidence, α_{95} , for these rocks compared to the younger ones). Also, in a study of the Anaga peninsula of Tenerife, Carracedo and Talavera (1971) obtained directional data in close agreement with those of the present study.

As expected, the late Tertiary–Quaternary pole for the Canary Islands presented here is in good agreement with corresponding poles for continental Africa (see Fig. 5). The most interesting observation, however, is that the relative pole location for the older Gran Canaria/Tenerife strata corresponds very well with those for the Mesozoic of Africa. Based on magnetization axis II (Fig. 2d) the inferred pole is situated at a slightly higher palaeolatitude than the African Mesozoic poles, but an anticlockwise adjustment of axis II by only 5° (this is justified by the experimental evidence which suggests that a partial remagnetization has imposed a slight clockwise rotation of the original time-average magnetic vector) is sufficient to bring the pole into the major Mesozoic polar group. Recent evidence suggests that in the earliest Cretaceous the African palaeomagnetic pole underwent an excursion to a lower palaeolatitude (Bardon et al., 1973; Gidskehaug et al., 1975: poles 6 and 11 of Fig. 5) but returned to the previous position before Middle Cretaceous times (Gidskehaug et al., 1975). Further information in support of this polar behaviour is provided by

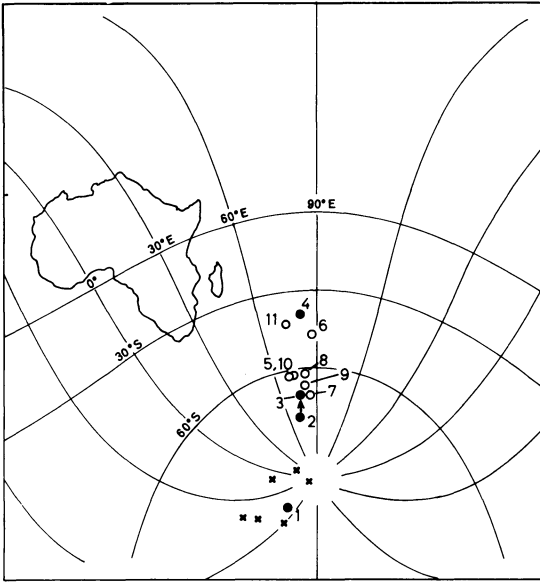


Fig. 5. Estimated pole locations for Gran Canaria/Tenerife basalts (poles 1–4) in comparison with relevant polar estimates from Africa. Pole 1 is the Upper Tertiary/Quaternary pole, poles 2 and 3 represents the older series (axis II of Fig. 1) before and after a 5° anticlockwise adjustment of the mean declination (cf. text) respectively, and 4 is the Phonolite pole. Crosses are African Tertiary poles. The other poles are as follows: 5, Hoachanas 161–173 (Gidskehaug et al., 1975); 6, Kaoko 110–128 (Gidskehaug et al., 1975); 7, Mlanje (Gough and Opdyke, 1963; Briden, 1967) (suggested to be post-Kaoko by Gidskehaug et al., 1975); 9, mean Mesozoic SE. African (Hailwood and Mitchell, 1971); 10, mean Mesozoic NW. African (Hailwood and Mitchell, 1971); Lower Cretaceous, Atlas Mountains (Bardon et al., 1973)

contemporaneous poles from South America. When the two continents are re-assembled in the manner proposed by Bullard et al. (1965) it is seen that the Serra Geral pole of Lower Cretaceous age exhibits a nearly identical excursion from the Mesozoic group as do the Kaoko pole (pole 6 of Fig. 5) of SW. Africa which is of similar age. As seen from Figure 5 the Phonolite pole of Gran Canaria (pole 4) is situated close to the Kaoko pole and the Lower Cretaceous pole for Morocco. This agreement may, however, be purely coincidental as pole 4 is only based on two sites and may therefore be biased either by geomagnetic secular variation or, perhaps more likely in this case, by partial remagnetization. In the following the Phonolites will therefore not be considered as representing a palaeomagnetic marker horizon.

For assessing an upward age limit of axis II it is very unfortunate that there are practically no palaeomagnetic data available for the Lower Tertiary of Africa. However, the Ethiopian traps which have K/Ar ages ranging between 69 m.y. and 30 m.y. give an estimated pole in good agreement with the Upper Tertiary poles for Africa suggesting that also the Lower Tertiary geomagnetic field was significantly different from that of the Mesozoic. It is therefore concluded that based on palaeomagnetism the minimum age of the oldest volcanic series in Gran Canaria/Tenerife is Upper Cretaceous.

3. Geology of NW. African Continental Margin

On the coasts of Morocco and Spanish Sahara data from petroleum exploration wells suggest that the sedimentary strata of the Essaouira and Aaiun basins are distributed in a 'down-to-basin' flexuring and normal fault pattern paralleling the coast and related to seaward subsidence (Martinis and Visintin, 1966; Querol, 1966; Seibold and Hinz, 1974). This fault system (having a NE-NNE trend) may be an important tectonic feature even several hundred kilometres from the NW. African shelf edge. For example, Dash and Bosshard (1969) and Bosshard and McFarlane (1970), through gravity and seismic refraction work, have suggested a major fault west of Gran Canaria as well as one passing through the islands of Tenerife, Gomera and Hierro. Similar faults have also been traced by Rona (1970) in seismic reflection profiles west and northwest of Cap Blanc.

In both the Essaouira and Aaiun basins late Triassic continental sediments (redbeds and evaporites) are interbedded with great amounts of basaltic lavas (Dillon and Sougy, 1974; Martinis and Visintin, 1966; Querol, 1966). The great importance of Triassic/Jurassic volcanism in W. Africa is further manifested by extensive outpouring of basic lavas in Algeria, Mauritania, Senegal, Guinea, Sierra Leone and Ivory Coast (Dillon and Sougy, 1974).

The coastal basin geology suggests that on the slope and shelf the Lower Mesozoic through Lower Cenozoic sediments are thickening seaward (Dillon and Sougy, 1974; Rona, 1970). Though the younger strata have terminations at the slope (due to erosion) the pre-Upper Cretaceous sediments appear to continue further seaward at least across the upper continental rise (Rona, 1970; Seibold and Hinz, 1974). The latter strata may however be vertically offset when crossing the general NE-NNE trending fault pattern. Except for a general transgression in Jurassic times the Lower Mesozoic to Tertiary depositional environment (at least beneath the coastal plain) was continental/shallow water marine, implying a more or less continuous crustal subsidence since late Triassic (Dillon and Sougy, 1974; Rona, 1970). Based on evidence for deep sea diapirism, Rona (1970) has suggested that the late Triassic salt layer may extend at least 1000 km west of Cap Blanc. Similarly, Schneider (1969) has reported deep sea diapiric features in the vicinity of the Cape Verde Islands though Pitman and Talwani (1972) have suggested that these may be of volcanic origin. However, more important information in favour of a salt layer extending seaward far from the continental shelf comes from DSDP holes 139 and 140 (cf. Fig. 6). Site 139 is situated at the middle continental rise at a water depth of around 3000 m and site 140 at the lower continental rise at depths of about 4500 m (Hayes et al., 1971). At site 139 the drill did not penetrate below Miocene strata but at site 140 the Upper Cretaceous sequence was reached though sonobuoy data suggest that beneath the cored Upper Cretaceous there is at least 1 km of sediments above the suggested basement. Furthermore, in the two DSDP sites a pronounced increase in salinity with depth takes place, suggesting the existence of a pre-Upper Cretaceous evaporite horizon at a greater depth.

From a seismic survey around the western Canary Islands Dash and Bosshard (1969) suggested a four-layered crustal structure comprising unconsolidated sedi-

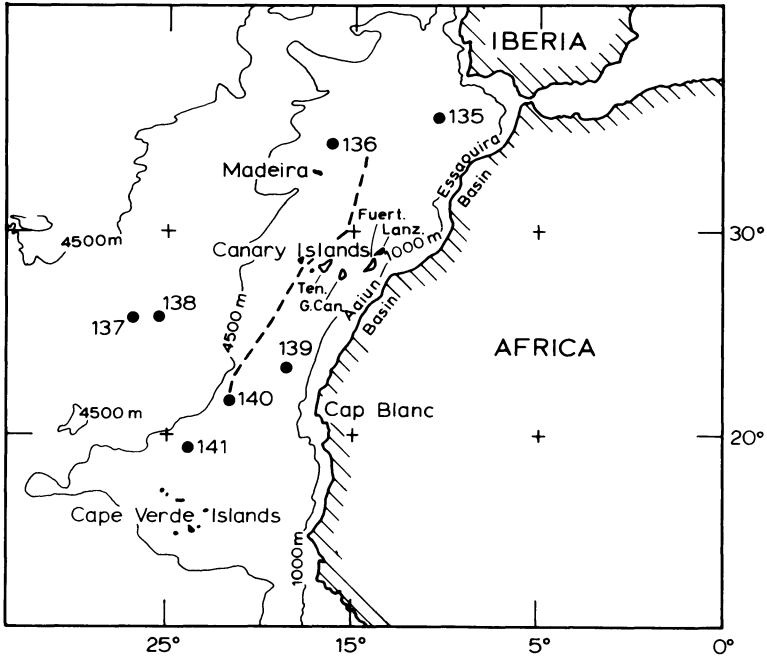


Fig. 6. Sketch map of coastal NW. Africa and adjacent oceanic areas. Numbers refer to drill sites explored by DSDP. Dashed line represents part of the westward boundary of the quiet magnetic zone

ments (a top layer of tuff and clastic material), consolidated sediments, basalt and oceanic layer, respectively. Special attention should be paid to the second layer, which in the seismic profiles has a thickness ranging between 2.2 km and 3.7 km, and for which Dash and Bosshard (1969) found no satisfactory explanation. If the geological interpretation of this layer in terms of consolidated sediments (1969) is the corrected one, a considerable time span must have elapsed between the first volcanic period (forming the basalts of layer 3) and the more recent volcanism forming the top layer of unconsolidated tuffs and other clastics. This upper crustal layering agrees very well with the palaeomagnetic structure from Gran Canaria and Tenerife (cf. Table 2) and represents further support in favour of a major gap between the two major subaerial volcanic sequences. However, based on the inferred episodic nature of the older volcanism of Gran Canaria the suggested consolidated sediments of layer 2 are likely to contain some tuff horizons at least in its lower stratigraphic levels. Further evidence of extreme importance for the present problem is that the crustal layer 2 (consolidated sediments) of Dash and Bosshard is thickening westward. This is in complete agreement with the sedimentary thickness distribution below the shelf and slope of West Africa. This combined evidence not only supports the Dash and Bosshard interpretation of their layer 2 but it also suggests a continental origin of the oceanic crust in the western Canaries region. If one had been dealing with a true oceanic crust formed by sea-floor spreading one

Table 2. Suggested correlation of upper crustal oceanic layering in the western Canaries region (Dash and Bosshard, 1969) with subaerial volcanic features of Gran Canaria/Tenerife

	Oceanic structure	Subaerial activity
layer 1:	Unconsolidated tuffs and clastics ($V = 3.00\text{--}3.35$ km/s)	Miocene – recent volcanism
layer 2:	Probably consolidated sediments ($V = 3.90\text{--}4.75$ km/s)	Long period (probable time span: Mesozoic – Miocene) of basically weathering and erosion
layer 3:	Basalts ($V = 5.63\text{--}6.00$ km/s)	Formation of Series 1 plateau basalts in the Mesozoic, probably in the Upper Cretaceous
layer 4:	Lower crustal layer	

would have thought that on the whole the greater accumulations of sediments would be concentrated closer to the continental slope and with decreasing thicknesses seaward. A pronounced sediment distribution in the opposite sense even at large distances from the continent is in line with the well-established and marked down-to-basin faulting off NW. Africa as well as off eastern N. America, forming an extensive graben structure as the first stage in the separation process between the two continental blocks. The evidence from DSDP drilling of a salt layer beneath deep water (holes 139 and 140) may strengthen this idea, particularly if the salt is of Triassic/Jurassic age (i.e. correlatable with the adjacent continental deposits) but salt can certainly also form on an oceanic crust in a system of intermittent spreading.

4. Conclusions on Formation of the Canary Islands and the Adjacent Oceanic Terrain

According to the available palaeomagnetic results Gran Canaria and Tenerife were principally build up during two distinctly different periods of volcanicity of which the older one at least dates back to the Upper Cretaceous, but it may well have covered a broad time span within the Mesozoic. After culmination of the first magmatic period there appears to have been volcanic quiescence until late Tertiary times when another major period of outbursts swept the islands. While the first period of activity most likely reflects early phases of rifting between Africa and North America the second major period of volcanicity in the Canaries was probably related to the Miocene deformation of the Atlas Mountains (Bosshard and McFarlane, 1970).

Based on marine geophysical and geological evidence it can be inferred that considerable crustal subsidence took place in the area during the second half of the Mesozoic. The subaerial basalts of Gran Canaria/Tenerife of suggested Upper Mesozoic age are likely to have taken part in this subsidence.

In regions which were not subjected to substantial upwarping and erosion prior to the Miocene (unlikely the Cape Verde and Canary Islands) one would expect to find a major succession of sediments intercalated between the two major volcanic 'horizons'. This is exactly what can be inferred from studies of the upper crustal layering northwest of Tenerife. Thus, there appears to be a very good correspondence between the marine geophysical evidence and the palaeomagnetic data as far as a major time gap in volcanic activity is concerned. The time span of volcanic quiescence within the region of Gran Canaria/Tenerife may at least have been of the order of 50 m.y. A late Cretaceous age for the older volcanic strata does not contradict palaeontologic evidence from Fuerteventura where the earlier plutonics seem to intrude Albian to Upper Cretaceous sediments (Rothe, 1968).

As regards the older basalts sequences the present results apparently diverge from available K/Ar age determinations (Abdel-Monem et al., 1971, 1972; Watkins, 1973). The present authors, naturally enough, rely on their palaeomagnetic data and are inclined to explain the discrepancy in terms of incomplete retention of the radiogenic argon in the older lavas, possibly caused both by the fairly extensive mineral alteration in these rocks as well as by the extensive magmatic activity in late Tertiary times. The authors attach considerably weight to the evidence for remagnetization (probably of chemical/thermochemical origin) within the older sequences and suggest that this evidence throws doubt on the reliability of the K/Ar ages for these rocks. Also, the K/Ar data themselves may pose severe problems of interpretation. For example, in Tenerife Abdel-Monem et al. (1972) have deduced radiometric ages from the old basalts in four different areas of the Island (Anaga, Teno, Ladera de Guimar and Tiagaia) obtaining ages ranging from 15.7 m.y. to 0.67 m.y. which are conflicting with geological observations by Hausen (1956) and Fúster et al. (1968) that the sequences concerned are time equivalent units. More alarming, however, is the occurrence of internal inconsistencies of stratigraphically controlled sections. In fact, these results indicate that argon loss may be an important problem. In the present situation one finds it hard to believe that any of the estimated dates from the older lavas represent true rock ages. We therefore fully agree with Abdel-Monem et al. (1972) that 'the final resolution of these stratigraphic and radiometric age inconsistencies require further study'.

The marked crustal subsidence of the continental shelf and rise of NW. Africa along with corresponding sedimentary thicknesses increasing seaward (at distances several hundred kilometers from the seaboard) and the evidence for a salt layer beneath water depths of around 4500 m (probably the Triassic/Jurassic evaporite horizon as found beneath the coastal plain) indicate that portions of the deep oceanic crust of NW. Africa may be of continental origin. For the area under consideration this conclusion applies at least to the region of the quiet magnetic anomaly field—the existence of some more marked magnetic lineations here and there inside the quiet zone (with a NE-NNE trend) would be a natural consequence of magmatic infill along the prevailing fault pattern of the region during the stages of foundering. This idea is supported by recent seismic evidence (Wissman et al., 1977) which shows that off Morocco and

Mauritania a true oceanic crust can only be found west of the quiet magnetic zone.

By invoking a sea-floor spreading origin for the quiet magnetic zone there are obvious problems in fitting Central America in pre-drift reconstructions. Also, one has to envisage an asymmetric (Mesozoic) spreading between N. America and Africa in the initial stages of continental separation. On the other hand, if the quiet zones (or perhaps even wider belts) represent original continental crust having turned into oceanic-like structures in situ (as suggested by the present authors) such anomalies may virtually disappear. This suggestion is opposed neither by the DSDP leg 11 results (Hollister et al., 1972) from sites 100 and 105 (off eastern N. America) nor from the recent DSDP drilling in the Cape Verde Basin (Lancelot et al., 1975). In both areas a basaltic 'basement' was uncovered below apparently unbaked Middle-Upper Jurassic sediments. However, so far, no proper evidence in favour of a sea-floor spreading origin of these basalts has been given: it is at least equally plausible that they were formed during a process of rifting and subsidence of a continental to sub-continental basement. Recalling the existence of erosional discordances within the older lava sequence of Gran Canaria there are in fact reasons to suggest that rifting and lava extrusion may have taken place intermittently (within a subsiding continental belt between Africa and N. America) over a time span covering at least a greater part of the Mesozoic. Therefore, when sea-floor spreading between Africa and North America started, an ocean basin, formed by foundering of a zone of continental basement, seems to have been in existence at these latitudes in the Atlantic.

Acknowledgements. The extensive support during field work provided by Professor J.M. Fúster and other members of Departamento de Petrología y Geoquímica, University of Madrid, is gratefully acknowledged. We thank Professor J. Hospers and Dr. R. Løvlie for critically reading this paper and for offering a number of constructive comments. The palaeomagnetic investigations of the Canary Islands are supported by the Norwegian Research Council for Science and the Humanities.

References

- Abdel-Monem, A., Watkins, N.D., Gast, P.W.: Potassium-argon ages, volcanic stratigraphy and geomagnetic polarity history of the Canary Islands: Lanzarote, Fuerteventura, Gran Canaria and La Gomera. *Am. J. Sci.*, **271**, 490–521, 1971
- Abdel-Monem, A., Watkins, N.D., Gast, P.W.: Potassium-argon ages, volcanic stratigraphy, and geomagnetic polarity history of the Canary Islands: Tenerife, La Palma and Hierro. *Am. J. Sci.* **272**, 805–825, 1972
- Bardon, C., Bossert, R., Hamzeh, R., Rolley, J-P., Westphal, M.: Etude paléomagnétique de formations volcaniques de Crétacé inférieur dans l'Atlas de Beni Mellal (Maroc). *C.R. Acad. Sci., Paris* **277**, 2141–2144, 1973
- Basshard, E., McFarlane, D.J.: Crustal structure of the western Canary Islands from seismic refraction and gravity data. *J. Geophys. Res.* **75**, 4901–4918, 1970
- Briden, J.C.: A new palaeomagnetic result from the Lower Cretaceous of East Central Africa. *Geophys. J. Roy. Astron. Soc.* **12**, 375–380, 1967
- Bullard, E.C., Everitt, J.E., Smith, A.G.: The fit of the continents around the Atlantic. *Phil. Trans. Roy. Soc. London, Ser. A*, **258**, 41–51, 1965
- Carracedo, J.C., Talavera, F.G.: Estudio palaeomagnético de la serie antigua de Tenerife. *Estud. Geol.*, **27**, 341–353, 1971

- Cendrero, A.: The volcano-plutonic complex of La Gomero (Canary Islands). *Bull. Volcanol.* **34**, 537–561, 1971
- Dash, B.P., Bossard, E.: Seismic and gravity investigations around the western Canary Islands. *Earth Planet. Sci. Lett.* **7**, 169–177, 1969
- Dietz, R.S., Sproll, W.P.: East Canary Islands as a microcontinent within the Africa–North America continental drift fit. *Nature* **266**, 1043–1045, 1970
- Dillon, W.W., Sougy, J.M.A.: Geology of West Africa and Canary and Cape Verde Islands. In: *The Ocean basins and margins*, Vol. 2, A.E.M. Nairn and F.G. Stehli, ed.: pp. 315, 367. New York: Plenum Press, 1974
- Fisher, R.: Dispersion on a sphere. *Proc. Roy. Soc., London*, **217**, 295–305, 1953
- Fúster, J.M., Arána, V., Brandle, J.L., Navarro, M., Alonso, U., Aparicio, A.: Geología y volcanología de las Islas Canarias-Tenerife. Consejo Sup. Investig. Cient., Madrid, 218 pp, 1968a
- Fúster, J.A., Cendrero, A., Gastesi, E., Lopez Ruiz, J.: Geología y volcanología de las Islas Canarias – Fuerteventura. Consejo Sup. Investig. Cient., Madrid, 239 pp, 1968b
- Fúster, J.A., Fernandez Santin, A., Sagredo, J.: Geología y volcanología de las Islas Canarias – Lanzarote, Consejo Syp. Investig. Cient., Madrid, 177 pp, 1968c
- Fúster, J.M., Hernandez-Pacheco, A., Hunnoz, H., Peoriques Badiola, E., Garcia Cacho, L.: Geología y volcanología de las Islas Canarias – Gran Canaria. Consejo Sup. Investig. Cient. Madrid, 243 pp, 1968d
- Fúster, J.M., Paez, A., Sagredo, J.: Significance of basic and ultramafic rock inclusions in the basalts of the Canary Islands. *Bull. Volcanol.* **33**, 665–691, 1970
- Gidskehaug, A., Creer, K.M., Mitchell, J.G.: Palaeomagnetism and K-Ar ages of the South-West African basalts and their bearing on the time of initial rifting of the South Atlantic Ocean. *Geophys. J. Roy. Astron. Soc.* **42**, 1–20, 1975
- Gough, D.J., Opdyke, N.D.: The palaeomagnetism of the Lupata Alkaline volcanics. *Geophys. J. Roy. Astron. Soc.* **7**, 457–468, 1963
- Hailwood, E.A., Mitchell, J.G.: Palaeomagnetic and radiometric dating results from Jurassic intrusions in South Morocco. *Geophys. J. Roy. Astron. Soc.* **24**, 351–364, 1971
- Halls, H.C.: A least-squares method to find a remanence direction from converging remagnetization circles. *Geophys. J. Roy. Astron. Soc.* **45**, 297–304, 1976
- Hausen, H.: Contribution to the geology of Tenerife (Canary Islands). *Soc. Sci. Finnica. Comment. Phys.-Math.* **18**, No. 1, 271 pp, 1956
- Hausen, H.: On the geology of Fuerteventura (Canary Islands). *Soc. Sci. Finnica, Comment. Phys.-Math.* **22**, No. 1, 211 pp, 1958
- Hausen, H.: On The geology of Lanzarote, Graciosa and the Isletas (Canarian Archipelago). *Soc. Sci. Finnica. Comment. Phys.-Math.* **23**, No. 4, 116 pp, 1959
- Hausen, H.: New contributions to the geology of Gran Canary (Gran Canaria, Canary Islands). *Soc. Sci. Finnica. Comment. Phys.-Math.* **27**, No. 1, 418 pp, 1962
- Hayes, D.E., Pimm, A.C., Benson, W.E., Berger, W.H., von Rad, U., Supko, P.R., Beckmann, J.P., Roth, P.H., Musich, L.F.: The Deep Sea Drilling Project, Leg 14. *Geotimes* **16** (2), 14–17, 1971
- Hollister, C.D., Ewing, J.I., Habib, D., Hathaway, J.C., Lancelot, Y., Luterbacher, H., Paulus, F.J., Wylie Poag, C., Wilcoxon, J.A., Worstell, P.: Initial reports of the Deep Sea Drilling Project, Vol. **XI**, Washington, 1977 pp., 1972
- Ibarrola, E.: Variation trends in basaltic rocks of the Canary Islands. *Bull. Volcanol.* **33**, 729–775, 1970
- Lancelot, Y., Seibold, E., Cepek, P., Dean, W.E., Eremeev, V., Gardner, J.V., Jansa, L.F., Johnson, D., Krashennikov, V., Pflaumann, U., Rankin, J.G., Trabant, P.: Deep Sea Drilling Project, Leg 41. *Geotimes*, **20** (11), 18–21, 1975
- Martinis, B., Visintin, V.: Données Géologiques sur le bassin sédimentaire côtier de Tarfaya (Maroc méridional). In: *Bassins sédimentaires du littoral africain*, D. Reyre, ed., pp. 13–26, Assoc. Serv. Géol. Afr., Paris 1966
- Pitman, W.C., Talwani, M.: Sea-floor spreading in the North Atlantic. *Geol. Soc. Am. Bull.* **83**, 619–646, 1972
- Querol, R.: Regional geology of the Spanish Sahara. In: *Bassins sédimentaires du littoral africain*, D. Reyre, ed.: pp. 27–38, Assoc. Serv. Géol. Afr., Paris 1966
- Rona, P.: Comparison of continental margins of eastern North America at Cape Hatteras and northwestern Africa at Cap Blanc. *Assoc. Petrol. Geol. Bull.* **54**, 129–157, 1970

- Rona, P., Nalwalk, A.J.: Post-early Pliocene unconformity on Fuerteventura, Canary Islands. *Geol. Soc. Am. Bull.* **81**, 2117–2122, 1970
- Rothe, P.: Mesozoische Flysch-Ablagerungen auf der Kanariensinsel Fuerteventura. *Geol. Rundschau* **58**, 314–322, 1968
- Rothe, P., Schmincke, H-U.: Contrasting origins of the eastern and western islands of the Canarian Archipelago. *Nature* **218**, 1152–1154, 1968
- Schneider, E.D.: The deep sea—a habit for petroleum? *Under Sea Technology*, **10**, 32–41, 1969
- Seibold, E., Hinz, K.: Continental slope construction and destruction, West Africa. In: *Geology of continental margins*, C.A. Burke and C.L. Drake, ed.: pp. 179–196, Berlin: Springer 1974
- Van Bemmelen, R.W.: On mega-undations: a new model for the earth's evolution. *Tectonophysics* **3**, 83–127, 1966
- Watkins, N.D.: Palaeomagnetism of the Canary Islands and Madeira. *Geophys. J. Roy. Astron. Soc.* **32**, 249–267, 1973
- Watkins, N.D., Richardson, A., Mason, R.G.: Palaeomagnetism of the Macaronesian insular region: The Canary Islands. *Earth Planet. Sci. Lett.* **1**, 225–231, 1966
- Watkins, N.D., Richardson, A., Mason, R.G.: Palaeomagnetism of the Macaronesian insular region: The Cape Verde Islands. *Geophys. J. Roy. Astron. Soc.*, **16**, 119–140, 1968
- Wilson, R.L.: Dipole offset—the time-average palaeomagnetic field over the past 25 million years. *Geophys. J. Roy. Astron. Soc.* **22**, 491–504, 1971
- Wilson, R.L., McElhinny, M.W.: Investigation of the large scale palaeomagnetic field over the past 25 million years. Eastward shift of the Icelandic spreading ridge. *Geophys. J. Roy. Astron. Soc.* **39**, 571–586, 1974
- Wissman, G., Hinz, K., Weigel, W.: Geophysical evidence for the nature of the continent-ocean boundary off northwest Africa. Abstract, Royal Society meeting 19–20 Oct. 1977, London

Received July 9, 1976; Revised Version October 12, 1977

Note Added in Proof

Some recent K/Ar dates of younger Gran Canaria lavas by Lietz and Schmincke (*Palaeogeography, Palaeochin. Palaeoecology*, **18**, 1975) have no implications for the ideas presented in the present paper.

Palaeomagnetism of Cretaceous Nubian Sandstone, Egypt

A. Schult¹, H.C. Soffel¹, and A. Gouda Hussain²

¹ Institut für Allgemeine und Angewandte Geophysik, Universität München,
Theresienstraße 41, 8000 München 2, Federal Republic of Germany

² Helwan Institute of Astronomy and Geophysics, Helwan, Cairo, Egypt

Abstract. From Upper Cretaceous Nubian Sandstone and iron ores in the Aswan area (25° N, 33° E) about 200 cores from 19 sites were collected. After thermal demagnetization the remanent magnetization of 18 sites showed stable components. Giving unit weight to each site direction (secular variation is probably not averaged out in the individual sites) the overall mean direction is $D=178^\circ$, $I=-29.3^\circ$ with $\alpha_{95}=5.8^\circ$ (6 sites have normal and 12 sites reversed polarity). This yields a pole at 80° N, 227° E ($d_p=3.7^\circ$, $d_m=6.3^\circ$). This pole is nearer to the present geographic pole than most of the other Cretaceous poles for Africa but in view of only few known Cretaceous poles the agreement is fairly good.

The mean direction of magnetization of 7 sites of Baharia Oasis iron ores (28° N, 29° E) is $D=8.1^\circ$, $I=+41.6^\circ$ with $\alpha_{95}=7.0^\circ$ (2 normal, 5 reversed polarities). The pole position (81.5° N, 145° E) is consistent with the probable Tertiary age of this formation.

Key words: Palaeomagnetism – Cretaceous sediments – Africa.

1. Introduction

Previous palaeomagnetic investigations have been carried out on Nubian Sandstone near Aswan and also on Upper Cretaceous volcanic rocks of Wadi Natash (about 150 km ENE of Aswan) by El Shazly and Krs (1973). In this paper palaeomagnetic results from the Nubian Sandstone in the Eastern desert of Egypt and in the Baharia Oasis are presented (Fig. 1).

Nubian Sandstone consisting of brownish, almost horizontal sandstone beds, often rich in iron ores and with interlayers of iron ore, is widely distributed in Egypt. The Nubian Sandstone was deposited in tropical and subtropical climates in shallow water (marine and non-marine) environments (El Shazly and Krs, 1973).

Generally an Upper Cretaceous age is attributed to the Nubian Sandstone

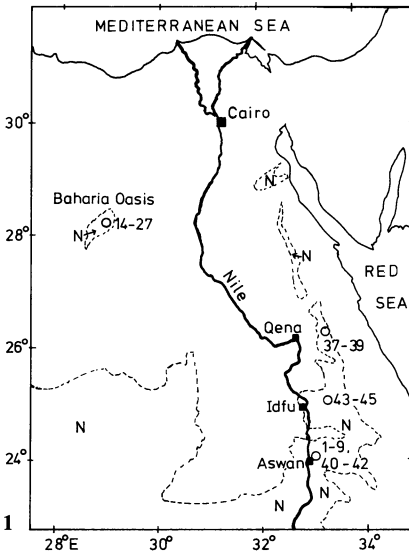


Fig. 1. Map showing sampling sites and distribution of Nubian Sandstone (*N*)

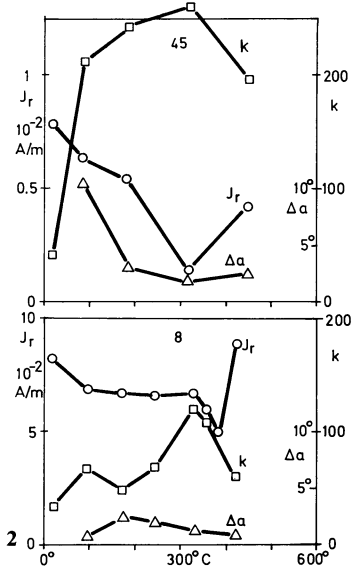


Fig. 2. Intensity of magnetization J_r , precision parameter k , and change of direction of magnetization (change of azimuth Δa) as a function of increasing stepwise thermal demagnetization for typical cases (No. 8: iron ore, No. 45: sandstone)

according to fossils, at least in the South of Egypt (Said, 1962). The interlayers of iron ores occurring along the Nile valley have been formed together with the surrounding rocks and are therefore also of Upper Cretaceous age (El Shazly and Krs, 1973). The ore consists nearly completely of haematite (Gheith, 1955). The origin of the ore deposits in Baharia Oasis is not so clear. Probably the ore was formed by replacement during hydrothermal activities in Tertiary (post Eocene according to Attia (1955), or in Oligocene-Miocene according to Said (1962)). This Tertiary age is consistent with the palaeomagnetic results as shown later. The ore in the Baharia Oasis shows great variation with regard to its composition. It consists mainly of goethite, some haematite, and magnetite in minor amounts (Gheith, 1955).

2. Sampling and Measurements

In Figure 1 the location of the 34 sites sampled are shown. A total of about 330 cores (2.5 cm diameter) has been collected from the Nubian Sandstone and from the iron ore with a portable drilling machine (see Tables 1 and 2). Specimens (2.5 cm long) were cut from the cores. The natural remanent magnetization (NRM) was measured with a "Digico" spinner magnetometer or with a "Förster" flux gate magnetometer. Because alternating field demagnetization up to 2000 Oe peak field had no significant influence on the intensity or the direction of magnetization the specimens were subjected to thermal demagnetization.

Table 1. Site mean palaeomagnetic results from Aswan, Quena and Idfu

Site	Classi- fication	Location		N	J _r (10 ⁻² A/m)	NRM		Cleaning (°C)	N	J _r (10 ⁻² A/m)	CARM		α ₉₅ (°)	k	Pole position	
		° N	° E			D(°)	I(°)				D(°)	I(°)			° N	° E
1	iron ore	24.1	33.0	4	6.7	177.5	-42.9	400	4	5.9	176.0	-36.5	8.0	134	84.7	259
2	iron ore	24.1	33.0	8	5.6	179.7	-14.0	400	8	3.7	169.3	-12.9	10.0	32	69.7	245
3	iron ore	24.1	33.0	3	not measured			400	3	0.8	189.3	+6.9	27.9	21	61.0	193
4/1	iron ore	24.1	33.0	9	6.3	181.6	-28.1	400	9	5.2	179.4	-27.7	3.9	180	80.6	217
4/10	iron ore	24.1	33.0	9	8.1	180.0	-24.1	400	9	6.3	179.8	-22.9	2.6	406	77.9	214
5	iron ore	24.1	33.0	5	6.5	183.4	-28.4	400	5	5.1	182.9	-35.3	3.5	476	84.7	181
6	sandstone	24.1	33.0	12	1.4	177.8	-47.9	400	11	1.1	179.4	-34.2	2.7	285	84.7	219
7	iron ore	24.1	33.0	14	6.5	180.0	-22.1	400	12	6.0	176.2	-21.3	5.8	57	76.5	229
8	iron ore	24.1	33.0	12	7.0	175.0	-29.2	360	12	6.2	177.0	-29.7	4.2	107	81.4	233
9(-)	sandstone	24.1	33.0	5	1.1	183.8	-50.1	360	6	1.0	187.0	-48.9	11.0	38	81.4	78
9(+)	sandstone	24.1	33.0	6	0.8	359.6	+20.2	360	7	0.8	355.0	+29.7	7.5	66	80.6	244
40	sandstone	24.1	33.0	21	no consistent result											
41	sandstone	24.1	33.0	21	0.8	24.9	+18.0	350	13	0.6	353.4	+24.0	9.6	20	76.0	243
42	sandstone	24.1	33.0	15	0.7	19.1	+35.0	350	7	0.15	10.7	+31.8	19.0	11	77.8	155
37	sandstone	26.4	33.3		no consistent result											
38	sandstone	26.4	33.3	9	0.7	349.0	+37.4	300	10	0.35	346.2	+37.9	8.6	32	76.3	283
39	sandstone	26.4	33.3	3	0.7	346.0	+20.1	350	5	0.1	350.8	+25.7	15.4	26	74.5	249
43	sandstone	25.1	33.3	18	0.45	179.0	-32.8	300	11	0.25	172.4	-31.6	7.1	41	79.3	256
44	sandstone	25.0	33.6	10	0.34	193.4	-32.1	300	10	0.13	178.4	-41.9	4.7	107	88.3	273
45	sandstone	25.0	33.6	21	0.77	359.3	+44.3	300	13	0.10	357.9	+37.2	7.7	30	85.3	238
Mean of site means, 6 sites normal, 12 sites reversed																
Mean of site means (this paper plus El Shazly and Krs, 1973)																
(7 sites normal, 15 reversed)																
d _p =3.7°, d _m =6.3°, A ₉₅ =4.1°																
d _p =3.6°, d _m =6.2°, A ₉₅ =4.0°																

N = number of samples, J_r = remanent magnetization, D = declination, I = inclination, α₉₅ or A₉₅ = radius of the 95% circle of confidence, k = precision parameter, CARM = characteristic remanence (after thermal cleaning)

Table 2. Site mean palaeomagnetic results from Baharia Oasis (mean location 28.2° N, 28.9° E). For legend see Table 1

Site	Classification	N	J_r (10^{-2} A/m)	$\frac{\text{NRM}}{D(^{\circ})}$	$\frac{I(^{\circ})}{D(^{\circ})}$	α_{95} ($^{\circ}$)	k	Cleaning ($^{\circ}$ C)	N	J_r (10^{-2} A/m)	$\frac{\text{CARM}}{D(^{\circ})}$	$\frac{I(^{\circ})}{D(^{\circ})}$	α_{95} ($^{\circ}$)	k	Pole position °N °E	
14	iron ore deposit	2	12.0	193.8	-33.5	13.0	373	thermal cleaning not possible							79.5	189
15	Nubian Sandstone	15	no consistent result	no consistent result												
16	Nubian Sandstone	12	no consistent result	no consistent result												
17	Limestone with iron oxides	12	1.6	359.9	+39.1	6.6	44	500	10	0.7	358.0	+38.5	8.3	35	83.2	225
19	iron ore		no consistent result	no consistent result				480	4	10.5	186.5	-36.2	7.4	154	80.0	171
20	iron ore	6	13.5	187.1	-40.6	6.4	112	480	5	8.6	184.1	-39.6	7.8	98	83.2	175
21	iron ore		no consistent result	no consistent result												
22	(goethite)	15	no consistent result	no consistent result												
23	iron ore	10	no consistent result	no consistent result												
23	iron ore	5	11.5	217.2	-37.5	18.7	18	350	5	3.8	207.5	-46.7	22.8	12	65.8	113
24	ferruginous sandstone	5	1.8	9.8	+45.8	27.8	9	500	5	1.5	3.4	+48.3	23.0	12	86.8	96
26	iron ore		no consistent result	no consistent result												
27	iron ore	15	15.5	196.9	-45.9	5.2	56	thermal cleaning not possible	7	-	8.1	+41.6	7.0	75	81.5	145.2

Mean of site means (2 sites normal, 5 reversed)

$$d_p = 5.2^{\circ}, d_m = 8.6^{\circ}, A_{95} = 7.6^{\circ}$$

In Figure 2 typical thermal demagnetization results for sandstone and iron ore are shown. There is only a slight reduction of the within site scatter (increase of precision parameter) of the directions in most cases accompanied by a slight drop of intensity of NRM. The total change of mean directions generally is also small. Above 300° to 400° an increase of intensity was observed in most cases together with an increase of scatter of the directions. Depending on the results of 3 or 4 pilot samples for each site the most appropriate thermal demagnetization temperature was chosen for all samples (see Tables 1 and 2). In some cases however thermal cleaning was not possible because the samples disintegrated during heating.

3. Discussion

3.1. Nubian Sandstone and Iron Ore of the Eastern Desert

Site mean directions with the respective circles of confidence before and after thermal cleaning are shown in Figure 3 for Nubian Sandstone and for iron ore. Sites from the Nubian Sandstone have mixed polarity, sites from iron have only reversed polarity. After inverting different polarities to one polarity in the usual way, there is no significant difference in the mean direction between normal and reversed sites or between sandstones and iron ores (see Fig. 4).

For the magnetic latitude of Egypt the angular standard deviation s for the direction due to palaeosecular variation should be about 17° with lower and upper limits of 10° and 25° respectively (e.g. Brock, 1971) yielding a precision parameter k of about 23 with the respective limits $k=66$ and $k=11$ ($s \approx 81(k)^{-0.5}$). Half of the sites have $k \geq 66$ (see Table 1). It can therefore be assumed that the directions of magnetization of samples from one particular site contain only a relatively short interval of palaeosecular variation. The smaller k (larger angular standard deviation) for the other sites may at least partly be due to unstable magnetic properties of the samples and not due to palaeosecular variation. Therefore the best estimation of the overall mean is probably

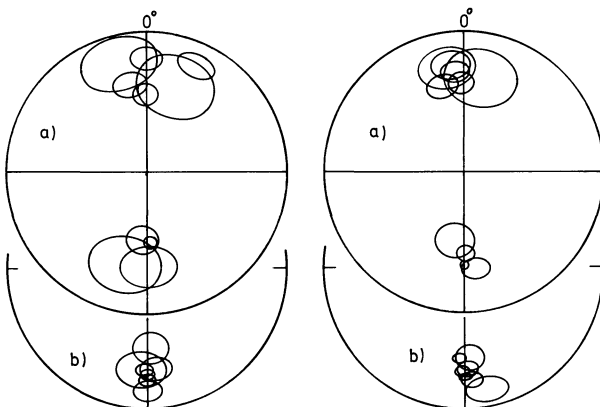


Fig. 3a and b. Equal area projection of site means (only the respective circles of confidence are shown) for sandstone (a) and iron ore (b) before (left side) and after (right side) thermal demagnetization

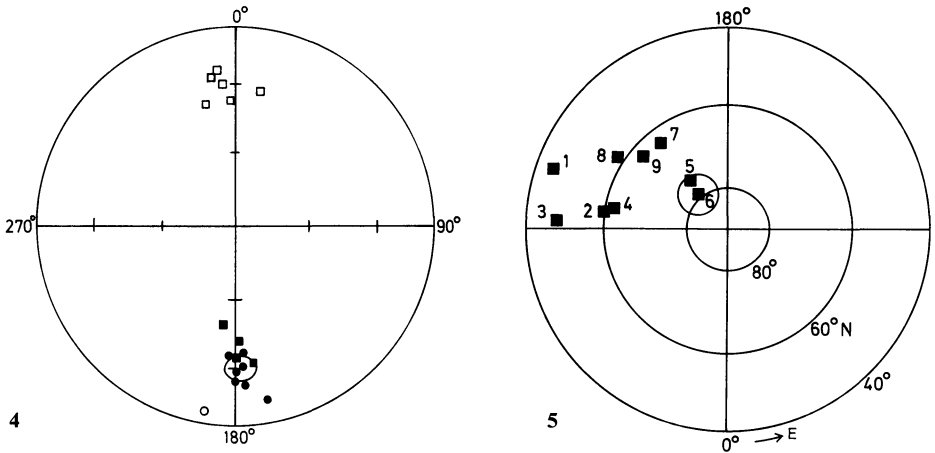


Fig. 4. Site means and overall mean circle of confidence for the Aswan area after thermal demagnetization. Squares denote the sandstone, circles the iron ore. *Open symbols*: oositive inclination. *Closed symbols*: negative inclination

Fig. 5. Cretaceous pole positions for Africa. For details see Table 3. Pole No. 6 with circle of confidence is from this paper

the average of the site mean direction giving unit weight to each site. The result $D=178^\circ$, $I=-29.3^\circ$, $\alpha_{95}=5.8^\circ$ is in agreement with the previous one given by El Shazly and Krs (1973): $D=183^\circ$, $I=-18.2^\circ$, $\alpha_{95}=11^\circ$. For further discussion the combination of the results of the two collections is used (see Table 1).

In Table 3 and Figure 5 Cretaceous pole positions for Africa are compiled including a pole position for South East Sicily which may be regarded as part of the African plate (e.g. Schult, 1973). Considering that the data represent a time span of about 70 My all Cretaceous pole positions for Africa are in fairly good agreement.

3.2. Baharia Oasis

The results are given in Table 2. From 12 investigated sites only 7 sites consisting of iron ores or iron ore rich sediments turned out to be suitable for palaeomagnetic measurements (5 normal, 2 reversed polarity). In the calculation of the mean two additional sites were included from which the samples could not be demagnetized thermally. This seems to be justified as the influence of thermal demagnetization on the directions was in most cases quite small.

The palaeopole for the Baharia Oasis sites is at 81.5° N, 145° E. This pole is significantly different from the pole for the Nubian Sandstone and iron

Table 3. Summary of African Cretaceous pole positions

No.	Age (My)	Formation	Site location	Pole position		$A_{95}(d_p, d_m)$	Reference
				° N	° E		
1	K_1	Moroccan volcanics	32° N, 354° E	44	251	10	Bardon et al. (1973)
2	116–128	Mljanje Massif	16° S, 36° E	60	262	12	Briden (1967)
3	110–128	Koaka lavas	20° S, 14° E	48	267	(2.5; 3.9)	Gidskehaug et al. (1975)
4	106–111	Lupata volcanics	17° S, 34° E	62	260	3.5	Gough et al. (1963)
5	K_1	Moroccan sediments	32° N, 353° E	75	217	5.5	Hailwood (1975)
6	K_u	Nubian sandstone, iron ores	25° N, 33° E	79	220	4.0	This paper
7	81–90	Wadi Natash volcanics	24° N, 34° E	64	218	(2.8; 5.6) ^a	El Shazly and Krs (1973)
8	83–89	Kimberlite pipes	29° S, 25° E	58	237	15.3	McFadden et al. (1977)
9	71–81	Volcanics, SE-Sicily	37° N, 15° E	63	229	3.8	Schult (1973)

^a d_p, d_m was calculated from the sample means and not from the site means

ores of the Eastern desert and is in good agreement with Tertiary poles for Africa (e.g. Schult, 1974). This finding confirms the probably Tertiary age of the iron ores in the Baharia Oasis.

Acknowledgement. We thank Professor M. Fahim, Helwan Institute of Astronomy and Geophysics, Cairo, for his generous help and advice. We are grateful to all members of the palaeomagnetism group of our Institute for many helpful discussions. The financial support of the Deutsche Forschungsgemeinschaft is also gratefully acknowledged.

References

- Attia, M.I.: The Geology of the Iron Ore Deposits of Egypt. 18th Intern. Geol. Congr., London **13**, 6–13, 1950
- Bardon, C., Bossert, A., Hamzeh, R., Rolley, J.P., Westphal, M.: Etude Paleomagnetique de Formations Volcaniques du Cretace Inferieur dans l'Atlas de Beni Mellal (Maroc). C.R. Acad. Sci., Paris **277 D**, 2141–2144, 1973
- Briden, J.C.: A New Palaeomagnetic Result from the Lower Cretaceous of East-Central Africa. Geophys. J. **12**, 375–380, 1967
- Brock, A.: An Experimental Study of Palaeosecular Variation. Geophys. J. **24**, 303–317, 1971
- El Shazly, E.M., Krs, M.: Palaeogeography and Palaeomagnetism of the Nubian Sandstone, Eastern Desert of Egypt. Geol. Rundschau **62**, 212–225, 1973

- Gheith, M.A.: Classification and Review of Egyptian Iron Ore Deposits. Symposium Appl. Geol. Near East, Unesco, Ankara 1955
- Gidskehaug, A., Creer, K.M., Mitchell, J.G.: Palaeomagnetism and K-Ar Ages of the South-West African Basalts and their Bearing on the Time of Initial Rifting of the South Atlantic Ocean. *Geophys. J.* **42**, 1–20, 1975
- Gough, D.I., Opdyke, N.O.: The Palaeomagnetism of the Lupata Alkaline Volcanics. *Geophys. J.* **7**, 457–468, 1963
- Hailwood, E.A.: The Palaeomagnetism of Triassic and Cretaceous Rocks from Morocco. *Geophys. J.* **41**, 219–235, 1975
- McFadden, P.L., Jones, D.L.: The Palaeomagnetism of some Upper Cretaceous Kimberlite Occurrences in South Africa. *Earth Planet. Sci. Lett.* **34**, 125–135, 1977
- Said, R.: The Geology of Egypt. Amsterdam: Elsevier Publ. Comp. 1962
- Schult, A.: Palaeomagnetism of Upper Cretaceous Volcanic Rocks in Sicily. *Earth Planet. Sci. Lett.* **19**, 97–100, 1973
- Schult, A.: Palaeomagnetism of Tertiary Volcanic Rocks from the Ethiopian Southern and the Danakil Block. *J. Geophys.* **40**, 203–212, 1974

Received November 18, 1977 / Revised Version January 26, 1978

Measurements of Anisotropy of Magnetic Susceptibility Using Inductive Magnetometers *

H. Scriba and F. Heller

Institut für Geophysik, ETH Zürich, CH-8093 Zürich, Switzerland

Abstract. At present the instruments most commonly used for sensitive measurement of remanent and induced magnetization of rocks are spinner magnetometers and cryogenic magnetometers. The analysis of magnetic susceptibility anisotropy with these instruments is described in this paper with special emphasis on measurements with the cryogenic magnetometer. Problems arising from finite specimen size are discussed. It is shown that the optimum length-to-diameter ratio for a cylindrical specimen is 0.90 ± 0.02 for the spinner magnetometer used and 0.86 ± 0.02 for the cryogenic magnetometer. Comparative measurements of magnetic anisotropy obtained from the two instruments yield good agreement. In order to demonstrate the performance of the cryogenic magnetometer in measuring magnetic susceptibility anisotropy, a regional investigation has been carried out. The main plane of anisotropy is observed to be consistent with the macroscopic rock fabric.

Key words: Magnetic susceptibility anisotropy – Cryogenic magnetometer – Spinner magnetometer.

1. Introduction

Rock magnetism has become a very important branch of geophysics during the last two decades. This is mainly due to the observation that rocks containing ferromagnetic minerals are able to conserve the magnitude and direction of the magnetic field in which they cooled down or were deposited. This is the basis for studying the history of the Earth's magnetic field and associated phenomena such as continental drift and polar wandering.

One of the principal assumptions of palaeomagnetism is that the direction of magnetization is parallel to the magnetizing field. This is only true as long as the material is magnetically isotropic, i.e. the magnetic susceptibility is a scalar. However, many rocks are anisotropic and the susceptibility must be represented

* Contribution No. 199, Institut für Geophysik, ETH Zürich

by a symmetrical tensor of second order. The corresponding geometrical body is an ellipsoid. Thus, for palaeomagnetic investigations of strongly anisotropic rocks, the direction of magnetization has to be corrected for anisotropy. Moreover, the observed anisotropy is closely related to rock fabric and can be used as a tool in structural analysis of rocks.

Magnetic anisotropy was first observed in sediments by Ising (1943). It has been shown that this anisotropy is mostly caused by mechanical forces acting during deposition (e.g. Granar, 1958; Rees, 1961), the minimum axis of susceptibility being aligned perpendicular to the bedding plane. The structure of igneous rocks can also be determined by anisotropy measurements (cf. e.g. Heller, 1973). In these rocks the macroscopic schistosity planes usually coincide with the main anisotropy plane which is defined as the plane containing the maximum and intermediate principal axes of anisotropy. A comprehensive review on magnetic anisotropy is given by Bhathal (1971).

In principle the anisotropy of magnetic susceptibility can be observed using any instrument which measures the bulk susceptibility in a certain direction, e.g. the transformer bridge (cf. Fuller, 1960; Kubli, 1967). Of course, anisotropy can also be studied with instruments measuring only the difference between the maximum and minimum susceptibility (in the plane of measurement) and its phase, e.g. the torque meter (Stone, 1967; Scriba, 1967) or the spinner magnetometer (cf. Kent and Lowrie, 1975). Most early investigations were carried out using the torque meter. In this instrument the rock sample is suspended from a thin wire. When a horizontal field is applied, the specimen is deflected by a small angle due to its remanence and anisotropy of susceptibility. The effect of remanence, of course, can be avoided by using AC fields. Either low fields (cf. Granar, 1958; King and Rees, 1962; Scriba, 1967) or high fields have been used (cf. Stacey, 1960). The other instrument commonly used now is the spinner magnetometer (cf. Noltimier, 1967; Berset, 1968; Heller, 1973). This paper adds the cryogenic magnetometer to the instruments measuring magnetic susceptibility anisotropy.

2. Method of Measurement

The measurements were carried out using a Digico spinner magnetometer with anisotropy head and a ScT cryogenic magnetometer. These instruments are called inductive magnetometers in this paper because the signal induced by the field of a magnetized rock sample is analysed.

2.1. Spinner Magnetometer

Only a brief outline of the method of measurement will be given here. In principle the method is identical to that when measuring remanent magnetization with the only difference that a magnetic field is applied which causes an induced magnetization in the specimen. If the rotating specimen has a susceptibility difference in the plane of measurement, it produces a signal in the sensor coils the frequency of which is twice the frequency of rotation; the amplitude

and phase of the anisotropy signal depend upon the susceptibility tensor elements in the measurement plane. Measurements in three perpendicular planes of a specimen provide the complete susceptibility matrix. Its eigenvalues and eigenvectors can be found by transforming to principal axes.

The Digico anisotropy meter uses two orthogonally arranged coils one of which is excited at an audio frequency. A signal is only detected in the sensor coil, if the sample is anisotropic in the plane of measurement (cf. Eq. (8b)). The corresponding elements of the susceptibility matrix are computed on line by harmonic analysis. The coils of our Digico anisotropy meter are very close to the sample. There is a new version on the market now which has a slightly larger detector distance.

2.2. Cryogenic Magnetometer

Essentially this instrument is a modern version of the ballistic magnetometer. The instrument we have in use consists of three pairs of Helmholtz pickup coils which are kept in a superconducting state. If a magnetized sample is inserted into the coils a persistent current is initiated in each coil pair which is proportional to the component of magnetization of the sample along the corresponding coil axis (for details see Goree and Fuller, 1976).

Besides of remanence measurements the cryogenic magnetometer can also be used for measuring bulk susceptibility and its anisotropy. The method is very simple. A field of a few Oersteds—we have used $H=1.01$ Oe—is applied to the sensor coils. After cooling below the critical temperature for superconductivity, this field is permanently retained in the system. A sample inserted into the coils will now produce a signal S which is the sum of the induced (I_i) and the remanent component (R_i) of magnetization multiplied by the volume (V) of the specimen

$$S_i = (R_i + I_i) \cdot V \quad (1)$$

with $i = \xi, \eta, \zeta$ (coordinate system of the specimen). This can also be written in vector form

$$\mathbf{S} = (\mathbf{R} + \mathbf{I}) \cdot V \quad (2)$$

where the induced magnetization is proportional to the applied field H

$$\mathbf{I} = K \cdot \mathbf{H} \quad (3)$$

with K = magnetic susceptibility tensor. This tensor is symmetrical and of second order

$$K = \begin{pmatrix} k_{\xi\xi} & k_{\xi\eta} & k_{\xi\zeta} \\ k_{\eta\xi} & k_{\eta\eta} & k_{\eta\zeta} \\ k_{\zeta\xi} & k_{\zeta\eta} & k_{\zeta\zeta} \end{pmatrix}. \quad (4)$$

In our measuring procedure a field is applied parallel to the x -axis of the instrument with the ζ -axis of the specimen coinciding with the z -axis of the

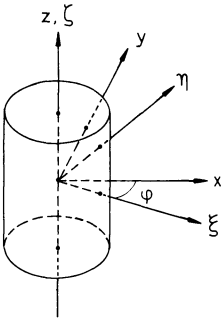


Fig. 1. Orientation of the specimen with the coordinates ξ, η, ζ with respect to the instrument's coordinates x, y, z

instrument. The specimen will now be rotated around this axis such that ξ and η lie in the plane of measurement (Fig. 1). For any position the components of the magnetic field H in coordinates of the specimen are given by

$$H_{\xi} = H \cdot \cos \varphi \quad \text{and} \quad H_{\eta} = H \cdot \sin \varphi. \quad (5)$$

Inserting into (3) we obtain for the components of the induced magnetization

$$I_{\xi} = H(k_{\xi\xi} \cos \varphi + k_{\xi\eta} \sin \varphi) \quad (6)$$

$$I_{\eta} = H(k_{\xi\eta} \cos \varphi + k_{\eta\eta} \sin \varphi).$$

The corresponding expressions in the coordinate system of the instrument are

$$I_x = I_{\xi} \cos \varphi + I_{\eta} \sin \varphi \quad (7)$$

$$I_y = -I_{\xi} \sin \varphi + I_{\eta} \cos \varphi.$$

Inserting (6) into (7) yields

$$I_x = H \left[\frac{1}{2}(k_{\xi\xi} + k_{\eta\eta}) + \frac{1}{2}(k_{\xi\xi} - k_{\eta\eta}) \cos 2\varphi + k_{\xi\eta} \sin 2\varphi \right] \quad (8a)$$

$$I_y = H \left[\frac{1}{2}(k_{\eta\eta} - k_{\xi\xi}) \sin 2\varphi + k_{\xi\eta} \cos 2\varphi \right]. \quad (8b)$$

We now turn the specimen such that ξ and η , respectively, are parallel to z . The corresponding expressions are easily derived from (8) by cyclic exchange.

As can be seen from (8) it would be sufficient to make two measurements at an angle $\varphi = 0^\circ$ and $\varphi = 90^\circ$ in order to determine the k_{ik} . In practice, however, the specimen has a remanent magnetization which has to be eliminated. Moreover, there is instrumental drift. The first problem can be solved by repeating the measurements at 180° and 270° , taking advantage of the different periodicities of the remanent magnetization R and the induced magnetization I , i.e. 2π and π , respectively. Thus by taking the arithmetic mean of two readings with a phase shift of π , the influence of remanence is cancelled. On the other hand the remanence can be determined by taking the difference of the readings. Actually we have taken readings in steps of 45° from 0° to 360° in order to improve the quality of data which are later used for the computation of the anisotropy ellipsoid. Instrumental drift is taken into account by comparing the readings at

0° and 360° and correcting the values measured in between by linear interpolation of the difference. Instrumental drift is of the order of $1 \cdot 10^{-8}$ G equivalent magnetization during the measurements in one plane which take about 40s. This value is well below the errors introduced by instability of remanence which are of the order of $1 \cdot 10^{-7}$ G for the specimens measured.

The measurements are repeated for the $\eta\zeta$ - and the $\zeta\xi$ -plane, respectively. Then the susceptibility ellipsoid can be computed by a transformation to the principal axes (Granar, 1958; Scriba, 1967).

As the susceptibility matrix K is real and symmetrical, the transformation to principal axes can easily be carried out using the Jacobi method (cf. e.g. Sperner, 1961). A FORTRAN program for this computation can be obtained from the authors upon request. The program uses the data from the cryogenic magnetometer as input. Remanent magnetization and instrumental drift have already been eliminated according to the procedure described previously. The program can also be used for any other kind of anisotropy measurements by simply adapting the input. It also serves as the fundamental program for the Digico anisotropy meter.

3. Effects of Specimen Shape and Size

For practical convenience cylindrical rock specimens are used for magnetic investigations. Ideally a specimen should have spherical shape. Then, even for finite distances between sample and sensor, it would act like a dipole at its centre provided that the magnetization is uniform. However, as we are working with cylindrical specimens, even for isotropic rocks an apparent anisotropy results which is caused by the shape of the specimen and the finite distance to the sensor.

3.1. Effect of Specimen Shape

This effect is caused by the different demagnetization factors along the axes of the specimen. It is given by Rees (1965)

$$\frac{\Delta k}{k} = k \cdot \frac{N_z - N_r}{(1 + N_z k)(1 + N_r k)} \quad (9)$$

where N_z is the demagnetizing factor along the axis of the cylinder and N_r is the demagnetizing factor in the radial plane. Shape induced anisotropy will be zero if $N_z = N_r$. The demagnetizing factors for cylinders with different ratios of length to diameter have been computed by Sharma (1966). N_z and N_r have been plotted against the ratio of length to diameter in Figure 2. They are equal for $l/d = 0.9185$. However, as can be seen from Equation (9) and Figure 2 the influence of an error of 10% in the length to diameter ratio will be negligible $\left(\frac{\Delta k}{k} < 10^{-3}\right)$

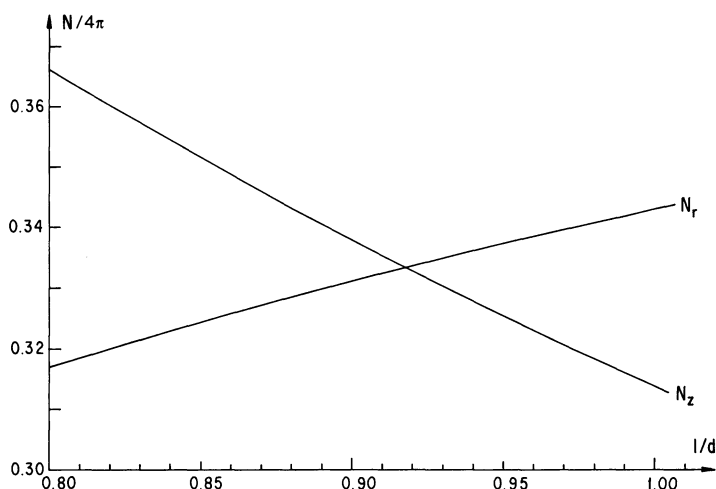


Fig. 2. Axial (N_z) and radial (N_r) demagnetizing factors as a function of length-to-diameter ratio l/d for cylindrical specimens

if the bulk susceptibility does not exceed $10^{-3} G/Oe$ (see also Kent and Lowrie, 1975). Higher bulk susceptibilities are very unusual in rocks (Sharma, 1976) and therefore the specimen *shape* effect can generally be neglected.

3.2. Effect of Specimen Size

The other effect that may cause errors in anisotropy measurements comes from the finite specimen size. It applies only when using inductive magnetometers such as spinner magnetometers where the field produced by a rotating sample is measured by a sensor at a finite distance from the sample. However, when using other instruments, e.g. a torque meter where the torsion caused by the interaction of the applied field with the magnetized sample is measured, the specimen size is unimportant. Of course, this is only true if the field is homogeneous in the region of the sample.

In order to obtain a high sensitivity with inductive magnetometers a relatively small specimen-sensor distance is required. Therefore the specimen no longer can be treated as an infinitesimal dipole. The corresponding formulae have been derived by Sharma (1964) and a brief summary will be given here. Only two planes of measurement need to be considered because of the axial symmetry of a cylindrical specimen. The axial field of a uniformly magnetized cylinder of length l , radius r at a distance a from its centre is given by

$$H_z = 2\pi \cdot I_z \left[\frac{a+l/2}{\sqrt{r^2 + (a+l/2)^2}} - \frac{a-l/2}{\sqrt{r^2 + (a-l/2)^2}} \right] \quad (10)$$

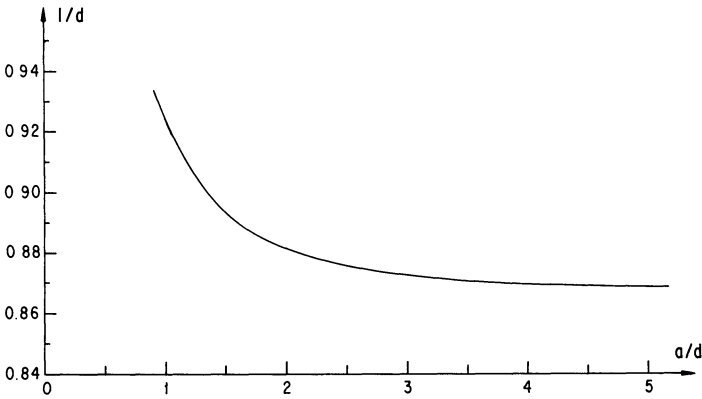


Fig. 3. Optimum length-to-diameter ratio l/d as a function of sensor-distance-to-diameter ratio a/d

where I_z is the axial component of magnetization. The corresponding field of a dipole is

$$H_{z,D} = 2\pi \cdot I_z \cdot \frac{r^2 l}{a^3}. \tag{11}$$

The radial field is given by the integral (using cylindrical coordinates)

$$H_r = 2r l I_r \int_0^\pi \frac{(a - r \cos \theta) \cdot \cos \theta d\theta}{(r^2 + a^2 - 2ra \cos \theta) \sqrt{(l/2)^2 + r^2 + a^2 - 2ra \cos \theta}} \tag{12}$$

where I_r is the radial component of the magnetization. For every ratio a/d – where d is the diameter of the specimen – an optimum ratio l/d can be found where $H_r = H_z$. In this case no apparent anisotropy is observed although the specimen dimensions are comparable to the sample-detector separation. The optimum value of l/d according to formulae (10) and (12) is plotted as a function of a/d in Figure 3. As can be recognized, the optimum l/d ratio decreases with increasing a/d ratio. The anisotropy produced by a deviation from the optimum l/d value, of course, depends on the distance to the sensor. For a 5% error in l/d which is equal to a 1.1 mm change in length for a specimen with a diameter of 25.4 mm, some resulting anisotropy errors are given in Table 1. The change in

Table 1. Percentage anisotropy $\Delta k/k$ arising from a 5% error in l/d as a function of a/d

a/d	1.5	3	5
$\frac{\Delta(l/d)}{l/d}$	5%	5%	5%
$\frac{\Delta k}{k}$	1.4%	0.3%	0.1%

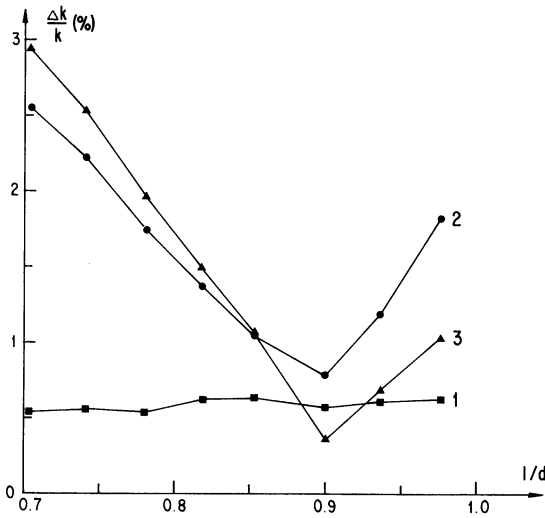


Fig. 4. Relative anisotropy values $\Delta k/k$ of a basalt specimen as a function of the length-to-diameter ratio l/d for the three planes of measurement: $\xi\eta$ (1), $\eta\zeta$ (2), $\zeta\xi$ (3). Instrument used: Digico anisotropy meter

anisotropy due to errors in l/d is of the correct order of magnitude to explain the observed anomalous behaviour of magnetic anisotropy in weakly anisotropic deep sea sediments which has been measured by means of a spinner magnetometer (Kent and Lowrie, 1975).

When the magnetic anisotropy of a specimen is measured using an inductive magnetometer the specimen size given by the ratio l/d has to be optimized, as the sensor distance is fixed by the given detector geometry. In order to find out the optimum size experimentally, we have sliced up some rock samples into sets of thin discs (each disc approximately 1 mm thick) which enabled us to measure the anisotropy as a function of l/d . It should be pointed out that the actual detecting coil geometries of both instruments are very complex or unknown to us in detail. Therefore it was not possible to measure or to calculate the effective a/d ratios.

Using the Digico anisotropy meter first, two tests have been carried out in order to determine the optimum l/d ratio for this instrument experimentally. Firstly, we have observed the change of percentage anisotropy $\Delta k/k$ as a function of l/d in each of the three measuring planes of a basalt sample which has a bulk susceptibility of $9.4 \cdot 10^{-4} \text{ G} \cdot \text{Oe}^{-1}$. As basalts are very weakly anisotropic, $\Delta k/k$ should depend to a large extent on l/d when measuring in the $\zeta\xi$ - or $\eta\zeta$ -plane, respectively, and $\Delta k/k$ should be a minimum at the optimum l/d ratio. When measuring in the $\xi\eta$ -plane $\Delta k/k$ should not be influenced by varying l/d ratios. The percentage anisotropy in each measuring plane is plotted in Figure 4. For the radial $\xi\eta$ -plane $\Delta k/k$, as expected, does not change whereas a distinct minimum is found in the other two measuring planes for a ratio of $l/d = 0.9$. The anisotropy within the latter two planes decreases from about 3% at $l/d = 0.7$ to less than 1% at $l/d = 0.9$. It increases again above $l/d = 0.9$ with increasing l/d .

There is another possibility of determining the optimum l/d ratio. Not only

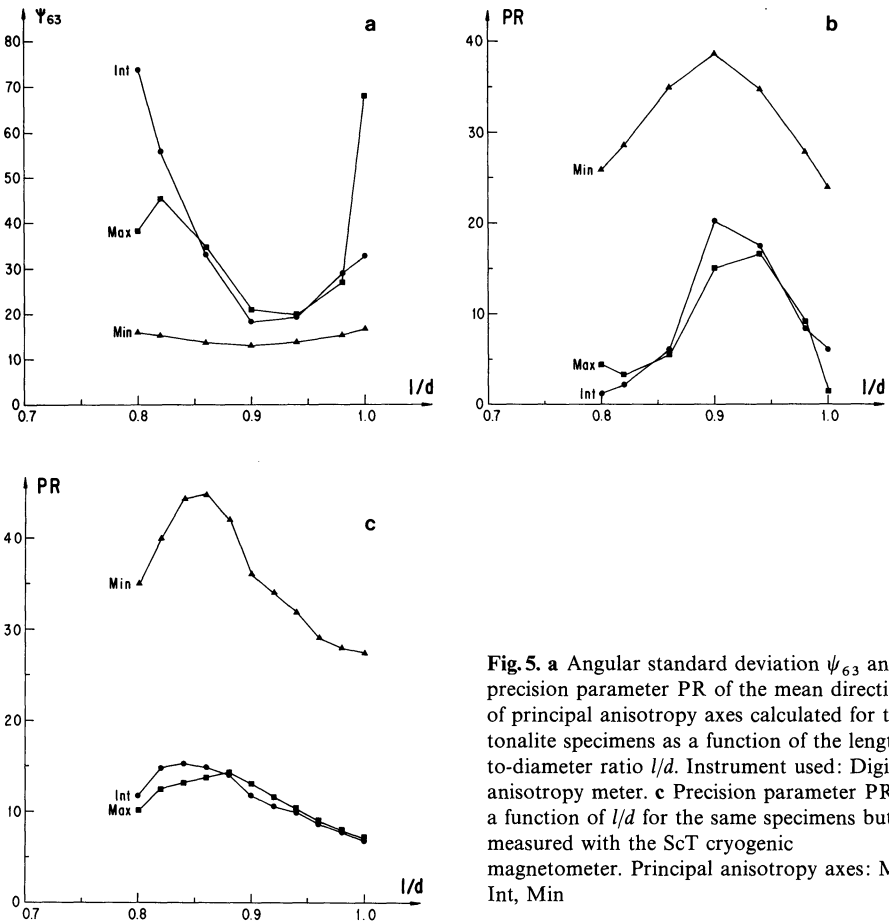


Fig. 5. a Angular standard deviation ψ_{63} and b precision parameter PR of the mean directions of principal anisotropy axes calculated for three tonalite specimens as a function of the length-to-diameter ratio l/d . Instrument used: Digico anisotropy meter. c Precision parameter PR as a function of l/d for the same specimens but measured with the ScT cryogenic magnetometer. Principal anisotropy axes: Max, Int, Min

the intensities but also the directions of the principal anisotropy axes depend on l/d . The dispersion of corresponding axes of different samples must pass through a minimum for the optimum l/d ratio. Two conditions have to be fulfilled for the validity of this test. Firstly the samples must have a macroscopic structure which is consistent throughout the region of investigation, and secondly they have to be oriented with respect to the macroscopic structure in different directions. Three tonalite specimens from Val Nambro (Adamello massif, Northern Italy) having a mean bulk susceptibility of $2.7 \cdot 10^{-5} \text{ G} \cdot \text{Oe}^{-1}$ showed adequate properties in the above sense. The dispersion of their principal susceptibility axes expressed by the angular standard deviation ψ_{63} indicates a minimum for a l/d ratio of 0.90 ± 0.02 (Fig. 5a). The effect is especially pronounced for the maximum and intermediate axes, whereas the dispersion of the minimum axes is less affected. This is due to the fact that these rocks show a clearly visible schistosity which magnetically is reflected by a predominant oblate anisotropy ellipsoid. The computed precision parameter (Fisher, 1953) shows a corresponding maximum for the three principal axes for a value of $l/d = 0.90 \pm 0.02$ (Fig. 5b).

The dispersion test was applied to the cryogenic magnetometer, too (Fig. 5c). The precision parameter shows a less well defined but nevertheless distinct maximum for all three principal anisotropy axes at a ratio of $l/d=0.86\pm 0.02$. The same quality of results was obtained before and after AF cleaning, although the remanence intensity observed before cleaning exceeded the differences of the induced magnetization ($H=1.01$ Oe) by one to two orders of magnitude.

We conclude from our measurements that the optimum values of l/d for the two instruments are slightly different due to varying pickup coil geometries. For our Digico anisotropy meter the optimum specimen length ($d=25.4$ mm) has been found to be $l=22.9\pm 0.5$ mm, whereas for the ScT cryogenic magnetometer (3-axis-instrument with 38 mm access) the optimum length is a bit shorter with $l=21.8\pm 0.5$ mm.

4. Instrumental Performance

In order to demonstrate the performance of the cryogenic magnetometer for the measurement of magnetic susceptibility anisotropy, a small scale regional investigation has been carried out in the Val Nambrone (Eastern Adamello massif, Northern Italy). As shown in Figure 6, the mean directions of the principal axes of the site susceptibility ellipsoids are fairly consistent throughout the whole area of investigation. They are in good agreement with the available data on the macroscopic structure (Callegari and Dal Piaz, 1973). The geological map presented by these authors shows a SW-NE trending schistosity in the area

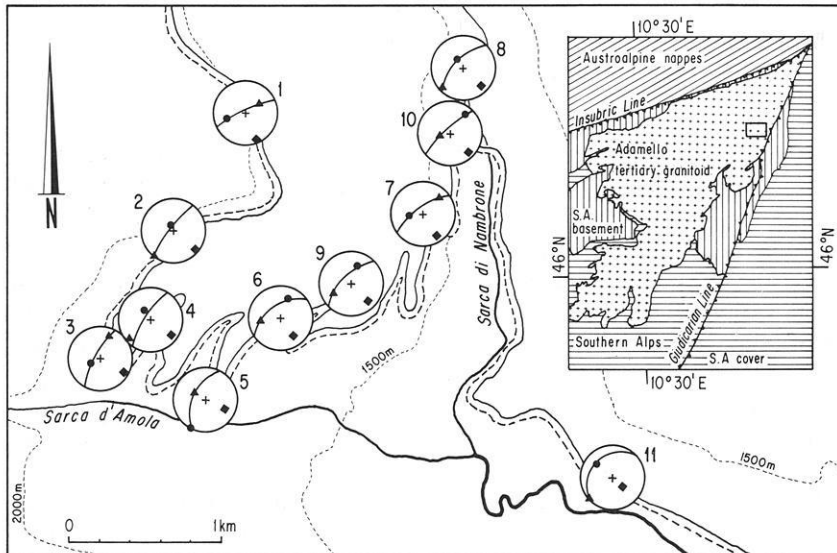


Fig. 6. Sketch map of the Val Nambrone area, eastern Adamello massif, with site mean directions of the principal anisotropy axes: maximum (●), intermediate (▲), minimum (◆). The great circle indicates the position of the main anisotropy plane

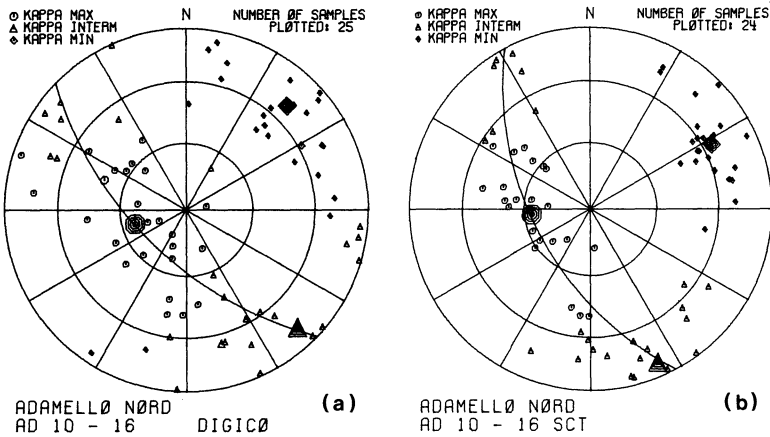


Fig. 7a and b. Lower hemisphere equal area projection of the directions of principal anisotropy axes for another sampling area in the northern Adamello massif (Italy) measured with the Digico anisotropy meter (a) and the ScT cryogenic magnetometer (b). The corresponding numerical mean values are listed in Table 2

Table 2. Mean directions of principal axes with precision parameter PR of a set of specimens from the northern Adamello massif as measured with the Digico and the ScT magnetometer. *N* denotes number of specimens

	k_{\max}			k_{int}			k_{\min}			<i>N</i>
	Az.	Dip	PR	Az.	Dip	PR	Az.	Dip	PR	
Digico	254.3	66.2	6.7	136.7	12.0	5.0	44.1	21.5	9.5	25
ScT	264.5	63.7	10.5	156.4	8.6	8.1	62.0	25.5	20.5	24

adjoining to the *E* of our sampling region. The very consistent alignment of the minimum axes of the sampling sites along a SE-NW direction—the minimum being perpendicular to the main anisotropy plane which obviously parallels the schistosity plane—indicates that the macroscopic structural features found at the eastern margin of the massif continue westward into the more central parts. The bulk susceptibility of the rocks has a well defined mean value of $2.66 \pm 0.24 \cdot 10^{-5} \text{ G} \cdot \text{Oe}^{-1}$ (number of specimens $N = 56$) which is in good agreement with the uniform tonalite petrology of the sampling area.

In order to compare results obtained from the cryogenic magnetometer and the Digico anisotropy meter, very weakly anisotropic samples have been measured on both instruments (cf. Fig. 7 and Table 2). Although the directions of the principal anisotropy axes are scattered to some extent, their mean directions coincide fairly well when comparing the results of both instruments. The mean directions and their precision parameters have been calculated independently for each axis. Both instruments show the best grouping of directions for the minimum axes, whereas the maximum and intermediate axes are distributed along a great circle.

Acknowledgements. We would like to thank Dr. J. Ansoerge and Professor Dr. W. Lowrie for valuable discussions and critical reading of the manuscript. The suggestions of the unknown referees also are gratefully acknowledged.

References

- Berset, G.: Eine Apparatur zur Messung kleiner remanenter Magnetisierungen an Gesteinen (Rockgenerator). *Pageoph* **69**, 205–228, 1968
- Bhathal, R.S.: Magnetic anisotropy in rocks. *Earth-Sci. Rev.* **7**, 227–253, 1971
- Callegari, E., Dal Piaz, G.: Field relationships between the main igneous masses of the Adamello intrusive massif (Northern Italy). *Mem. Ist. Geol. Min. Univ. Padova* **29**, 38, 1973
- Fisher, R.A.: Dispersion on a sphere. *Proc. Roy. Soc., London, Ser. A* **217**, 295–305, 1953
- Fuller, M.D.: Anisotropy of susceptibility and the natural remanent magnetisation of some Welsh slates. *Nature* **186**, 791–792, 1960
- Goree, W.S., Fuller, M.: Magnetometers using RF-driven squids and their application in rock magnetism and paleomagnetism. *Rev. Geophys. Space Phys.* **14**, 591–608, 1976
- Granar, L.: Magnetic measurements on Swedish varved sediments. *Ark. Geofys.* **3**, 1–40, 1958
- Heller, F.: Magnetic anisotropy of granitic rocks of the Bergell massif (Switzerland). *Earth Planet. Sci. Lett.* **20**, 180–188, 1973
- Ising, G.: On the magnetic properties of varved clay. *Ark. Mat. Astr. Phys.* **29A**, 1–37, 1943
- Kent, D.V., Lowrie, W.: On the magnetic susceptibility anisotropy of deep-sea sediment. *Earth Planet. Sci. Lett.* **28**, 1–12, 1975
- King, R.F., Rees, A.I.: Measurement of the anisotropy of magnetic susceptibility of rocks by the torque method. *J. Geophys. Res.* **67**, 1565–1572, 1962
- Kubli, F.: Bau einer Apparatur zur Messung der magnetischen Suszeptibilität von Gesteinen. Diplomarbeit Inst. Geophysik ETH Zürich, unpublished, 1967
- Noltimier, H.C.: Use of the spinner magnetometer for anisotropy measurements. In: *Methods in palaeomagnetism*, D.W. Collinson et al., eds.: pp. 399–402. Amsterdam: Elsevier 1967
- Rees, A.I.: The effects of water currents in the magnetic remanence and anisotropy of susceptibility of some sediments. *Geophys. J. Roy. Astron. Soc.* **66**, 235–251, 1961
- Rees, A.I.: The use of anisotropy of magnetic susceptibility in the estimation of sedimentary fabric. *Sedimentology* **4**, 257–271, 1965
- Scriba, H.: Zusammenbau und Eichung einer Torsionswaage zur Messung der Anisotropie der Suszeptibilität von Gesteinen – Programmierung der Auswertung der Messungen. Diplomarbeit Inst. Geophysik ETH Zürich, unpublished, 1967
- Sharma, P.V.: On the point dipole representation of a uniformly magnetised cylinder. *Helv. Phys. Acta* **38**, 234–240, 1965
- Sharma, P.V.: Digital computation of gravitational and magnetic anomalies and their derivatives for two-dimensional bodies of arbitrary shape. *Pageoph* **64**, 14–18, 1966
- Sharma, P.V.: *Geophysical methods in geology*, Amsterdam-Oxford-New York: Elsevier 1976
- Sperner, E.: *Einführung in die analytische Geometrie und Algebra*, **2**, 4th ed. Göttingen: 1961
- Stacey, F.D.: Magnetic anisotropy of igneous rocks. *J. Geophys. Res.* **65**, 2429–2442, 1960
- Stone, D.B.: Torsion balance method of measuring anisotropic susceptibility, In: *Methods in Palaeomagnetism*, D.W. Collinson et al., eds.: pp. 381–386. Amsterdam: Elsevier 1967

Received December 12, 1977; Revised Version February 15, 1978

Petro-Physical Properties (Density and Magnetic-Susceptibility) and Lithologic Composition of Some Dolerite Dykes of Andhra Pradesh, India

S.M. Varaprasada Rao, B.V. Satyanarayana Murty,
and V.L.S. Bhimasankaram

Centre of Exploration Geophysics, Osmania University, Hyderabad 500007, India

Abstract. The density and magnetic susceptibility of 40 samples from dolerite dykes have been measured. They occur in the Peninsular granites of South India and belong to tholeiitic and alkali types. It is observed that the dolerites could be classified into two groups based on their density and susceptibility values. While one group with lower values was found to correspond with the tholeiitic type, the other group with higher values possibly signifies the alkali type dolerites.

Key words: Rockmagnetism – Dolerites – Correlation of density and magnetic susceptibility.

The basic dykes of Peninsular India possess diversified trends of structural, physical and chemical characters. Analyses of structural, petro-chemical and palaeomagnetic data on dyke rocks from selected places in India, as attempted by earlier workers (Sitaramayya and Appajee, 1972; Murty, 1968; Verma et al., 1968; Divakara Rao et al., 1970 and Iqbal Hasnain and Qureshy, 1970) revealed very interesting results. Briefly, while the emplacement of dykes was controlled by the prevailing tectonic features (Appajee, 1970 and Sitaramayya and Appajee, 1972), the dykes could possibly belong to two lithological groups viz., alkali and tholeiitic and that both these types might have originated during Precambrian as well as Cretaceous and Tertiary periods (Divakara Rao et al., 1970; Verma et al., 1968 and Iqbal Hasnain and Qureshy, 1970).

With a view to substantiate the field geophysical anomalies from certain parts of Andhra Pradesh by the present authors, a set of about 40 dolerite dykes were sampled from the Districts of Hyderabad, Nalgonda and Khammam. The results and analysis of the study of the bulk density and magnetic susceptibility of the samples are discussed in the following.

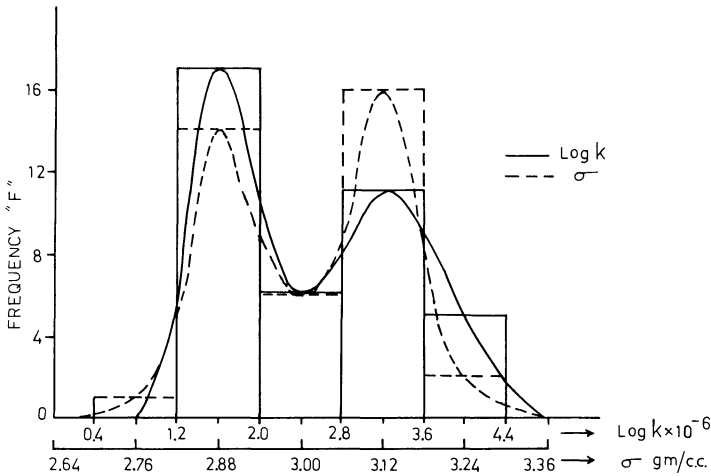


Fig. 1. Histograms and frequency curves for density and magnetic susceptibility of dolerites

These dykes of varying sizes trend in E-W, NW-SE, N-S and NE-SW directions and appear in the midst of Peninsular granitic country. A minimum of two samples from each dyke were studied in the laboratory using a densitometer (accuracy 0.02 gm/cc) and a magnetic susceptibility meter (value measured upto $\pm 5 \times 10^{-6}$ cgs unit in earth's field). Both the density (σ) and susceptibility (k) values showed wide ranges of variation (2.81 to 3.22 gm/cc for σ and 10×10^{-6} to $10,000 \times 10^{-6}$ cgs for k). Evidently this variation could not alone be due to the effect of weathering. Hence a statistical approach was adapted to study the variation phenomenon of these widely scattered values. It was observed that while the density values obey the law of normal distribution the magnetic susceptibility values follow the log-normal distribution.

In Figure 1 are presented the histograms and frequency curves with the r.m.s. deviation as the class interval. The two peaks and central low of the frequency curves are corresponding in both the parameters σ and $\log k$ in the present case. As these two parameters obey normal distribution law, the two parts of the curves on either side of the central low were treated here as two separate normal curves showing the different groups of dolerites with approximate average values 2.88 gm/cc and 1.6 ($k = 40 \times 10^{-6}$ cgs) and 3.12 gm/cc and 3.2 ($1,600 \times 10^{-6}$ cgs) respectively in each group.

The above classification of the dolerites was further verified by statistical probability study by adapting Kalmogorov's test (Kapur and Saxena, 1976). The probabilities that σ and 'log k ' of the whole set of samples follow normal distribution were obtained as 0.02 and 0 respectively. The same test, however, when adapted on the two groups separately for the two parameters σ and $\log k$ respectively showed the probability as 0.992 and 0.997 for group I and 0.997 and 0.632 for group II.

The dolerite samples with smaller σ and $\log k$ values fall in group I while those with higher values fall in group II. However, it was observed that a few (about 3 or 4) samples with lower density (group I) showed higher susceptibility values (group II) and vice versa. Perhaps this indicates the scatter phenomenon

Table 1.

1	2	3	4	5	6	7	8	9
Whole set of samples	39	$\frac{2.81-3.22}{3.03}$	0.12	3.89	39	$\frac{1.30-3.72}{2.44}$	0.80	31.12
Group I	20	$\frac{2.81-3.00}{2.932}$	0.06	1.86	18	$\frac{1.30-2.18}{1.81}$	0.25	13.81
Group II	19	$\frac{3.05-3.22}{3.13}$	0.05	1.49	21	$\frac{2.65-3.72}{3.23}$	0.43	13.32

Columns 2 to 5: Statistics of Bulk density (σ)

Columns 6 to 9: Statistics of Magnetic susceptibility ($\log k$)

Columns 2 and 6: No. of samples

Columns 3 and 7: Range and average

Columns 4 and 8: r.m.s. deviation

Columns 5 and 9: Coefficient of variation

in the samples. For such samples and also for samples with border line values additional data from chemical analysis or petrographic studies are necessary for their identification.

In Table 1 are given the number of samples, average value, r.m.s. deviation and the coefficient of variation¹ for the two physical characters studied for the whole set of samples as well as for each group separately. One can find from this table that the r.m.s. deviation and the coefficient of variation for the individual groups are very low when compared to those values for the whole set, thus justifying the two fold classification of the samples.

Correlation coefficient obtained for σ and $\log k$ values for the entire set is positive and equal to about 0.84. This is in good agreement as the increase in mafic content increases both density as well as magnetic susceptibility of the dolerites.

Petro-chemical and palaeomagnetic studies by Iqbal Hasnain and Qureshy (1970) suggest that some of the basic dykes of Peninsular India do belong to Precambrian alkali basalts while most of the dykes are of tholeiitic type equivalent to Deccan Traps. Manson (1967) reported that the average chemical composition of tholeiitic dolerites shows slightly higher values of SiO_2 (51.20%) and CaO (10.10%) and lower values of Na_2O (2.20%), K_2O (0.90%) and TiO_2 (1.50%) over those of the alkalic dolerites (SiO_2 —48.30%, CaO—2.80%, Na_2O —3.30%, K_2O —1.30% and TiO_2 —1.80%) while the percentages of the minerals are almost identical for both types. The ultimate deduction may be that the tholeiitic dykes could be expected to show smaller values of σ and k due to high silica and less mafic content. Thus the two groups of dolerites identified from their σ and k values might be representing the tholeiitic and alkali types of dolerites.

The authors acknowledge the assistance received from Mr. B. Chakrapani Sastry in collecting the field samples. A part of the work was financed by C.S.I.R.

¹ Coefficient of variation is the percentage ratio of the r.m.s. deviation to the arithmetic mean value of the set. It represents the variability of the given property of rock samples (Kreiter, 1968)

References

- Divakara Rao, V.: Iqbal Hasnain and Madoom Hussain, S., Petrochemical studies on a dyke near Nasaram. *Bull. Nat. Geophys. Res. Inst.* **8**, 27–37, 1970
- Hargraves, R.B., Petersen, N.R.: Notes on correlation between petrology and magnetic properties of basaltic rocks, *Z. Geophys.* **37**, 367, 1971
- Iqbal Hasnain, Qureshy, M.N.: Palaeomagnetic and Geochemical correlation of basic dykes of Mysore State, India. Proceedings of the Second Symposium of Upper Mantle Project, Hyderabad, 463–477, 1970
- Kapur, J.N., Saxena, H.C.: *Mathematical Statistics*, S. Chand publishing Co., New Delhi, India, 516–540, 1976
- Kreiter, V.M.: Geological prospecting and exploration, Mir Publishers, Moscow, 169, 1968
- Manson, V.: *Geochemistry of Basaltic Rocks*, Major Elements in 'Basalts'—Poldervaart volume. New York: Inter Science Publishers 1967
- Murty, S.R.N.: Studies on the dyke rocks around Hyderabad, Andhra Pradesh. Abstracts, Seminar on Plutonic Complexes of India, Geology Department; Osmania University, Hyderabad, 40–46, 1968
- Sitaramayya, S., Appajee, Y.: Trends of dolerite dykes and quartz reefs in the Northern parts of Andhra Pradesh *J. Ind. Acad. Geosci.* **15**, 39–46, 1972
- Verma, R.K., Pullaiah, G., Iqbal Hasnain: Palaeomagnetic study of a dyke near Hyderabad, *Bull. Nat. Geophys. Res. Inst.* **6**, 79, 1968

Received March 30, 1977; Revised Version October 7, 1977

Detection of Meridional Currents in the Equatorial Ionosphere

G. Musmann¹ and E. Seiler²

¹ Institut für Geophysik und Meteorologie der Technischen Universität Carolo-Wilhelmina, Mendelssohnstraße 1A, 3300 Braunschweig, Federal Republic of Germany

² Physikalisch-Technische Bundesanstalt, Bundesallee 100, 3300 Braunschweig, Federal Republic of Germany

Abstract. Theoretical investigations predict meridional currents in the dynamo region of the ionosphere a few degrees north and south of the magnetic equator as a consequence of the equatorial electrojet. The magnetic fields of these currents are perpendicular to the permanent magnetic field of the earth and cause a height variation of the magnetic declination. It was the aim of six rocket launches performed in 1970 near noon at Natal, Brazil, to detect these currents. To reach this objective, identical payloads each consisting of two flux-gate magnetometers, a solar aspect sensor, an experiment to measure the angle between the magnetic field and the direction to the sun, and an impedance probe to determine the electron density were launched under different magnetic conditions. The predicted variation of the declination has been observed but with considerably higher amplitude than was expected. On the other hand, the measured height integrated current density in the west-east direction was smaller than deduced from ground based magnetic H-variations.

These discrepancies can be explained by currents flowing at 5 degrees off the magnetic equator, on both sides, with intensities of about 0.3 of the electrojet intensity at the same height but in reversed direction. Such reversed currents have recently been observed from ground based magnetic observations by others and have also been interpreted theoretically by ionospheric wind effects.

Key words: Equatorial electrojet – Meridional currents – Rocket experiments.

Introduction

Untiedt (1967) has shown that the primary eastward electric field responsible for the equatorial electrojet also gives rise to a meridional current flow perpendicular to the equator. This flow constitutes an infinite solenoid which generates a

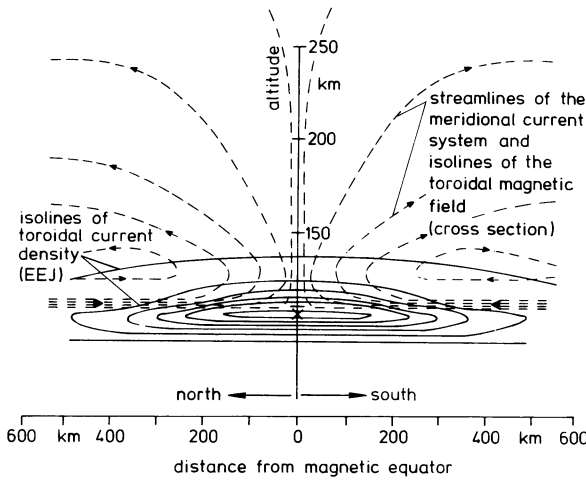


Fig. 1. Schematic drawing of the equatorial electrojet (EEJ, toroidal current system) flowing perpendicular to the plane of the figure, the meridional current system (dashed lines) and the corresponding toroidal magnetic field. Streamlines of the meridional current systems represent also isolines of the toroidal magnetic field

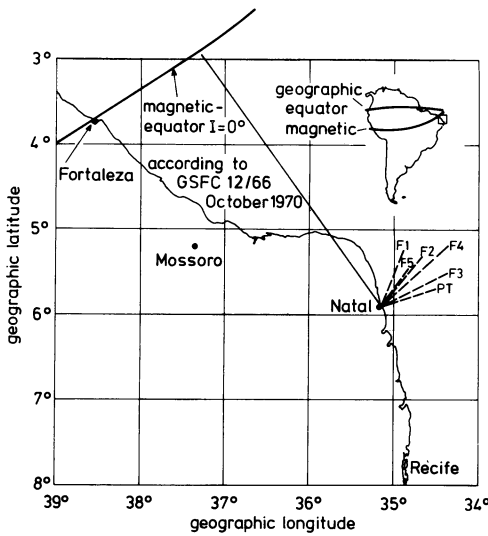


Fig. 2. Launch site Natal and horizontal projection of trajectories of the rocket flights (dashed lines). The magnetic equator is indicated. Ground based measurements of the magnetic field variations were recorded at Fortaleza, Mossoro and Natal by Askania-Variographs

toroidal east-west or west-east directed magnetic field within the ionosphere. A schematical representation of the meridional current flow and of the equatorial electrojet is shown in Figure 1.

According to calculations by Untiedt (1967), Sugiura and Poros (1969) and Richmond (1973) the two maximum absolute values of the toroidal magnetic field ΔY_M which changes sign above the magnetic equator are to be expected at about 300 to 400 km off the magnetic equator and at an altitude of about 120 km. The magnitude of these values should be about the same as that one of the magnetic variations on the ground caused by the electrojet at the magnetic equator.

Assuming a value of 160 nT for such a variation on the ground, representing a moderately developed electrojet, the toroidal magnetic field should change the

declination of the total earth's magnetic field by as much as 0.5 degrees at 120 km altitude and at the flanks of the jet. The contribution to the total field intensity at this height should be less than 1 nT because the direction of the disturbing toroidal magnetic field is nearly perpendicular to the permanent field F ($F \approx 25,000$ nT).

Because the toroidal field is confined to the ionospheric E - and F -regions it is not observable on the ground and can only be detected by means of rocket-borne vector magnetic measurements.

The present paper reports on the results of six such rocket experiments that were performed at Natal (Brazil) in October 1970. Day and time of each launch may be taken from Figure 8. Natal was selected as the launch site because it is situated about 380 km off the magnetic equator (Fig. 2), approximately below the maximum of the toroidal field strength (Fig. 1).

Description of Instrumentation

A detailed description of the instrumentation is given by Musmann (1971), therefore only some particulars of the payload will be reported on here.

On board the rocket the electron density was measured using an impedance probe developed by Melzner and Rabben (1970). The components of the magnetic field parallel and perpendicular to the spin axis of the rocket were determined by flux gate magnetometers (Förstersonde). The spin modulations of the magnetometer outputs were eliminated on board by filtering. It was therefore possible to limit the measuring range for the component R perpendicular to the spin axis to 8,000 nT with a constant offset of 20,000 nT while the measurement range of the longitudinal component L was 0 to 13,000 nT. Using a fast 12 bit A/D -converter a resolution of about ± 1 nT for the radial (R) and ± 1.5 nT for the longitudinal component (L) was obtained.

The sampling rate for all sensors was triggered by a precision differential sun slit sensor giving one pulse per rotation of the rocket. For each rotation (spin frequency approximately 10 Hz) the field magnitude F and the angle α between the figure axis of the rocket and the field vector were calculated according to $F = (R^2 + L^2)^{1/2}$ or $\tan \alpha = R/L$ respectively. The resolution of α is about one minute of arc.

The angle ψ between sun direction and figure axis (see Fig. 3) was measured with a high accuracy solar aspect sensor developed by Ernst Leitz GmbH, Optische Werke, Wetzlar, Germany. The resolution of this sensor was 1.8 min of arc.

From the rocket data the variation of declination is seen in the variation of the azimuth angle ν between the sun meridian indicated by the sun slit sensor and the direction of the magnetic field detected by a search coil. This angle ν was determined as the time difference between both signals. The time resolution was 1 μ s corresponding to a resolution of 0.4 min of arc.

In addition the spin period of the rocket was measured with the same precision slit sensor with a resolution of 4 μ s. Four payloads operated successfully ($F1$, $F3$, $F4$, and PT). One failed partially, and for one flight the solar aspect sensor was out of range.

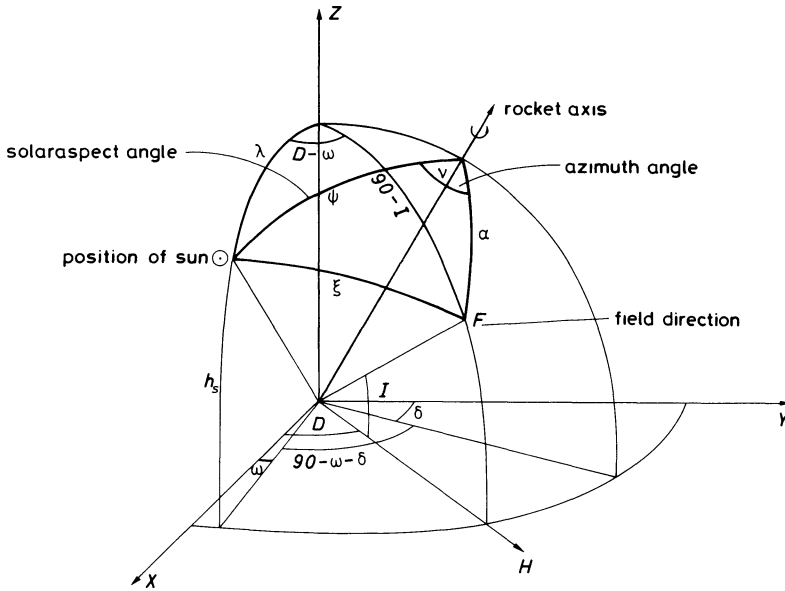


Fig. 3. Coordinate system defining the measured angles α, ψ, ν . x, y geographical north and west direction; D, I, H magnetic declination, inclination, and horizontal component, respectively

Identification of the Toroidal Field

In Figure 3 the sun is represented by its coordinates λ (distance from zenith) and ω (azimuth). These values can be calculated for each flight using the geographical coordinates of Natal, the launch time, data from the Nautical Yearbook 1970, and the tracked trajectory of the rocket. The flight altitude of the rocket is negligible when compared to the distance of the sun. The direction of the magnetic field vector \mathbf{F} is characterized by the inclination I and the declination D .

The spherical triangle given by the direction towards the sun, the field vector \mathbf{F} and the rocket figure axis (Fig. 3), is determined by the measured solar aspect angle ψ , the field direction angle α , and the azimuthal angle ν . From these measured quantities the angle ξ between sun and magnetic field direction, here named ξ_1 can be calculated according to the equation

$$\cos \xi_1 = \cos \psi \cos \alpha + \sin \psi \sin \alpha \cos \nu \tag{1}$$

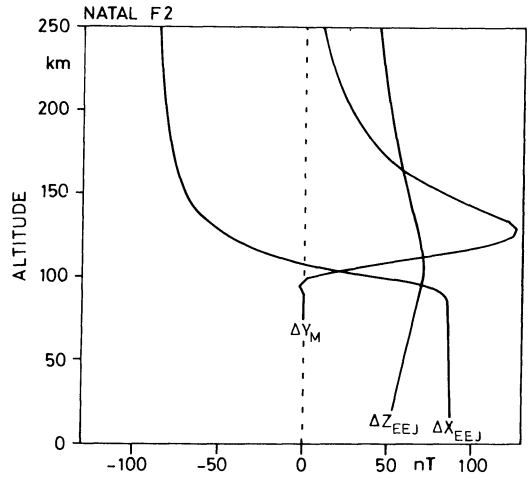
with an error of a few minutes of arc.

The orientation of the spherical triangle in space is not considered because it is of no interest for the subject in question. ξ_1 is the "measured value" of ξ .

On the other hand a second value for ξ (named ξ_2) can be calculated using the triangle represented by the sun's direction, the field vector \mathbf{F} , and the vertical axis Z , from calculated values of λ, ω, I , and D :

$$\cos \xi_2 = \cos \lambda \sin I + \sin \lambda \cos I \cos (D - \omega) \tag{2}$$

Fig. 4. Vertical (ΔZ_{EEJ}) and northward (ΔX_{EEJ}) components of magnetic variation produced by the equatorial electrojet as function of height at Natal. ΔY_M is the magnetic variation in east direction expected from the meridional currents. Calculations by Rippen (1975) according to Untiedt's (1967) model for rocket experiment F2 conditions



I and D , respectively, are the undisturbed values for inclination and declination of the earth's magnetic field along the trajectories. The variations of the inclination and declination produced by the main electrojet without meridional currents can be neglected. Therefore ξ_2 is a "calculated value" of ξ , neglecting the influence of the meridional currents.

Figure 4 shows the predicted variations with height of the field components ΔX_{EEJ} , ΔZ_{EEJ} , and ΔY_M as produced by the main electrojet (index EEJ) and by the meridional current system (index M), respectively.

It is assumed that the difference between the measured and the calculated values ξ , namely between ξ_1 and ξ_2 , must be caused by the meridional current system via ΔD_M , the variation in declination caused by the meridional current system. According to Untiedt's (1967) model significant values of ΔD_M are to be expected in the region $90 \text{ km} \leq h \leq 130 \text{ km}$ only. Therefore ξ_1 and ξ_2 should be identical with the exception of this region where the meridional currents are flowing.

However there can be a systematic deviation between the two curves $\xi_1(h)$ and $\xi_2(h)$ due to differences between the actual values of D and I and those calculated from spherical harmonic expansions, which are used to determine $\xi_2(h)$. However, this difference is not critical as will be shown later. If the influence of the meridional current system (ΔD_M) is taken into account, $D - \omega$ has to be replaced by $D - \omega + \Delta D_M$ in Equation (2), and also ξ_2 has to be replaced by ξ_1 . This yields the relation

$$\begin{aligned} \cos \xi_1 = & \cos \lambda \sin I + \sin \lambda \cos I \cos(D - \omega) \cos \Delta D_M \\ & - \sin \lambda \cos I \sin(D - \omega) \sin \Delta D_M. \end{aligned} \quad (3)$$

ΔD_M is expected to be $< 1^\circ$, that means $\cos \Delta D_M \geq 0.9998$. Therefore we use $\cos \Delta D_M = 1$. ΔI_M is assumed to be zero because the meridional currents produce no vertical magnetic disturbance.

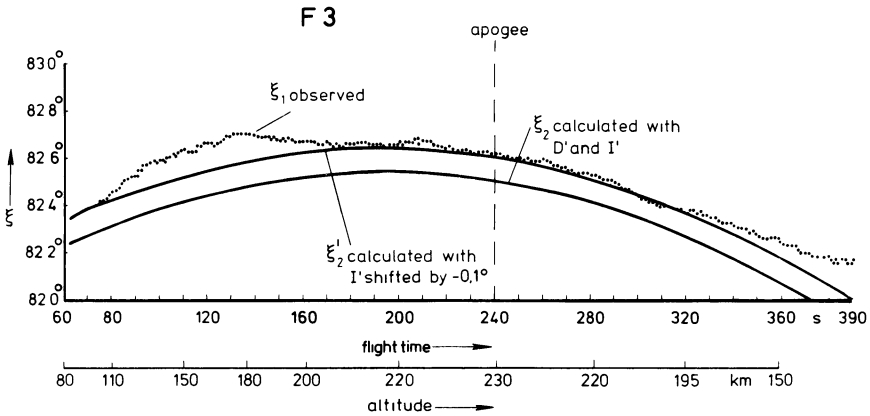


Fig. 5. Example (experiment *F 3*) of observations of ξ_1 and calculations of ξ_2 as function of flight time. For exact definition of the angles (cf. Fig. 3) ξ_1 and ξ_2 see text. ξ'_2 shows the influence of a constant shift in inclination I by -0.1° which gives the best approximation to ξ_1 in the regions where the influence of the meridional current systems should be negligible

Now, the combination of Equations (2) and (3) yields

$$\sin \Delta D_M = \frac{\cos \xi_2 - \cos \xi_1}{\sin \lambda \cos I \sin (D - \omega)} \tag{4}$$

The values of D and I can be calculated according to Cain et al. (1968) using the spherical harmonic expansion of the earth's magnetic field and the NASA GSFC 12/66 set of coefficients with deviations (actual main magnetic field minus computed field) of about $\pm 0.2^\circ$ for the flight area.

Due to the uncertainties in the spherical harmonic expansion a small but nearly constant deviation between $\xi_1(t)$ and $\xi_2(t)$ may be expected. This deviation may be eliminated by including a constant shift of D and I in the calculation of $\xi_2(t)$. Figure 5 shows the effect of such a shift in I (as an example). Apparently, only by including such a constant shift it is possible to match ξ_1 and ξ_2 below and above the height region of meridional currents. The finally adopted shift of $I - 0.1^\circ$ represents the best fit between ξ_1 and ξ_2 for $h < 90$ km and $h > 200$ km. For all flights the curves $\xi_2(t)$ were adjusted in the same manner.

Observational Results

All impedance probe measurements show a fairly smooth increase of the electron density with height and are similar in character. Therefore only the results of flight *F 5* are shown in Figure 6 as an example. More details about these measurements are given by Mühlhausen (1974). The results also agree with other observations of electron densities in the equatorial ionosphere, e.g. (Aikin and Blumle, 1968), (Jacobs and Rawer, 1966), (Jacobs and Rawer, 1965), and (Maynard, 1967).

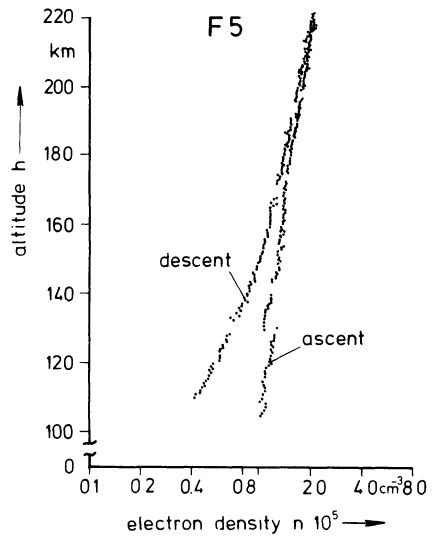


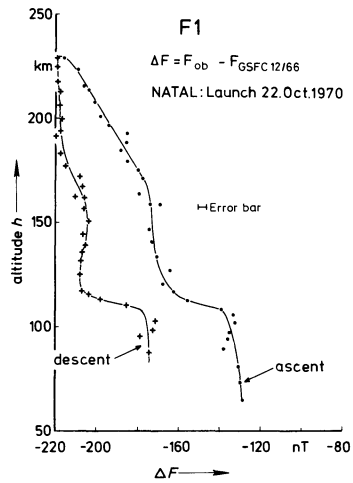
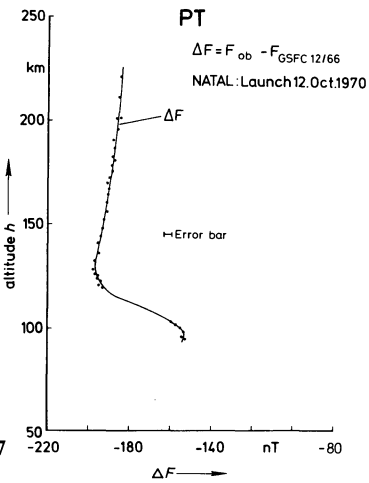
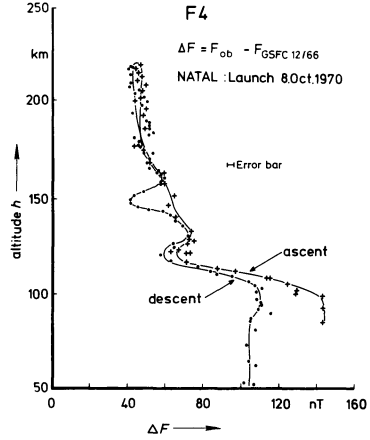
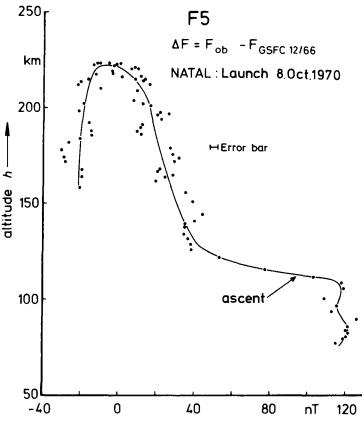
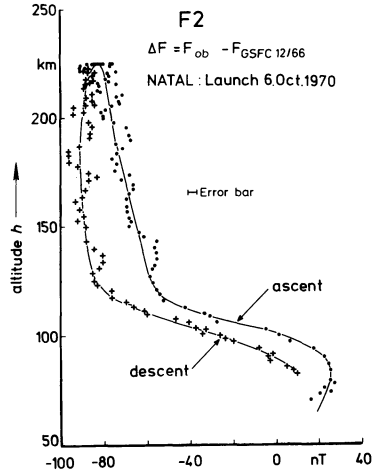
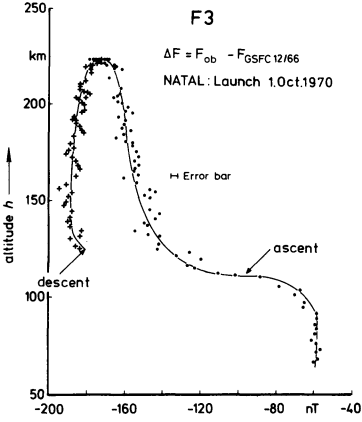
Fig. 6. Observed electron density profile for flight *F 5*

From the two magnetometer outputs R and L the field magnitude F_{ob} was calculated according to $F_{ob} = (R^2 + L^2)^{1/2}$. A field magnitude F_{GSFC} computed according to Cain et al. (1968) using the NASA GSFC 12/66 set of coefficients was subtracted from the observed field F_{ob} to get the observed field intensity difference ΔF . These values of ΔF are shown as a function of height in Figure 7 for the different rocket experiments. Only differences of ΔF are meaningful, because no zero adjustment has been made in all these cases. The remarkably nearly parallel shifts in ascent and descent curves for flights F_1 , F_3 , and F_5 are mainly due to uncertainties in the determination of the rocket trajectories. This is due to the fact that only skin tracking radar observations for limited time intervals after launch were available.

During all the flights a steep decrease in ΔF is to be seen beginning at altitudes of 100 km for flights, F_3 , F_4 , and PT , at about 110 km for F_1 and F_5 , and at 90 km for F_2 . A second but not as well defined change in slope is to be seen at 125 km for F_2 , F_4 , PT , at 130 km for F_3 , and F_5 , and at 120 km for F_1 . If we assume that the observed slope is due to the main electrojet current a variation in thickness of the current layer from about 15 to 35 km may be derived.

A close correlation between the magnitude of the magnetic variation in the horizontal component H on the ground and the total variation of ΔF with height is to be expected. Figure 8 shows the H traces as observed at Natal for all six rocket launches, taken from Musmann et al. (1971). If we define ΔH as the difference between the H component during rocket flight and the H level of the two nights before and afterwards, it may be seen (Table 1) that ΔH is nearly equal to ΔF_{total} . On the other hand, the relation $\Delta F_{total} \approx 2 \cdot \Delta H$ when passing the current layer should hold, if the internal part within ΔH is being neglected. A possible explanation for this apparent discrepancy will be given below.

During the flights F_1 and F_4 some special features are to be seen in the ΔF



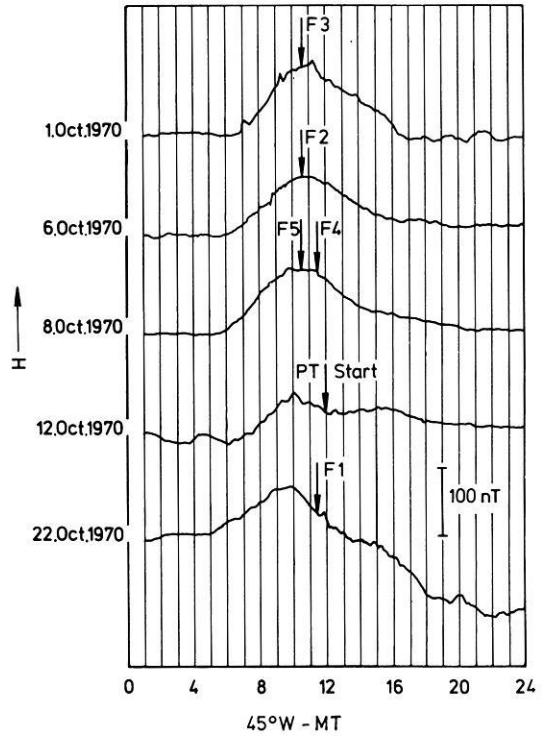


Fig. 8. Horizontal magnetic field variations H observed on the ground at Natal during launch days. Actual launch times are marked by arrows

Table 1. The measured total ΔF variation during flight and the ground observation of ΔH at Natal for the flight time

	ΔF (flight)		ΔH Natal
	ascent (nT)	descent (nT)	ground (nT)
F 1	45	45	≈ 30 (disturbed)
F 2	80	80	80
F 3	100		100
F 4	100	60	88 (decreasing to 80)
F 5	100		92
PT	40		≈ 30 (disturbed)

Fig. 7. Differences ΔF between observed (F_{ob}) and calculated (F_{GSFC}) field magnitudes versus altitude, for the different rocket experiments. Only every tenth measured value has been plotted. Differences between ascent and descent are due to uncertainties in trajectory determination and in spherical harmonic representation of the actual permanent magnetic field. The abscissa values are not corrected for absolute numbers, because only the variations of magnitude are of interest. The small periodical variations in the representations for F 2, F 3 and F 5 are due to the influence of the on board spin demodulation on the nutation modulation of the magnetometer outputs

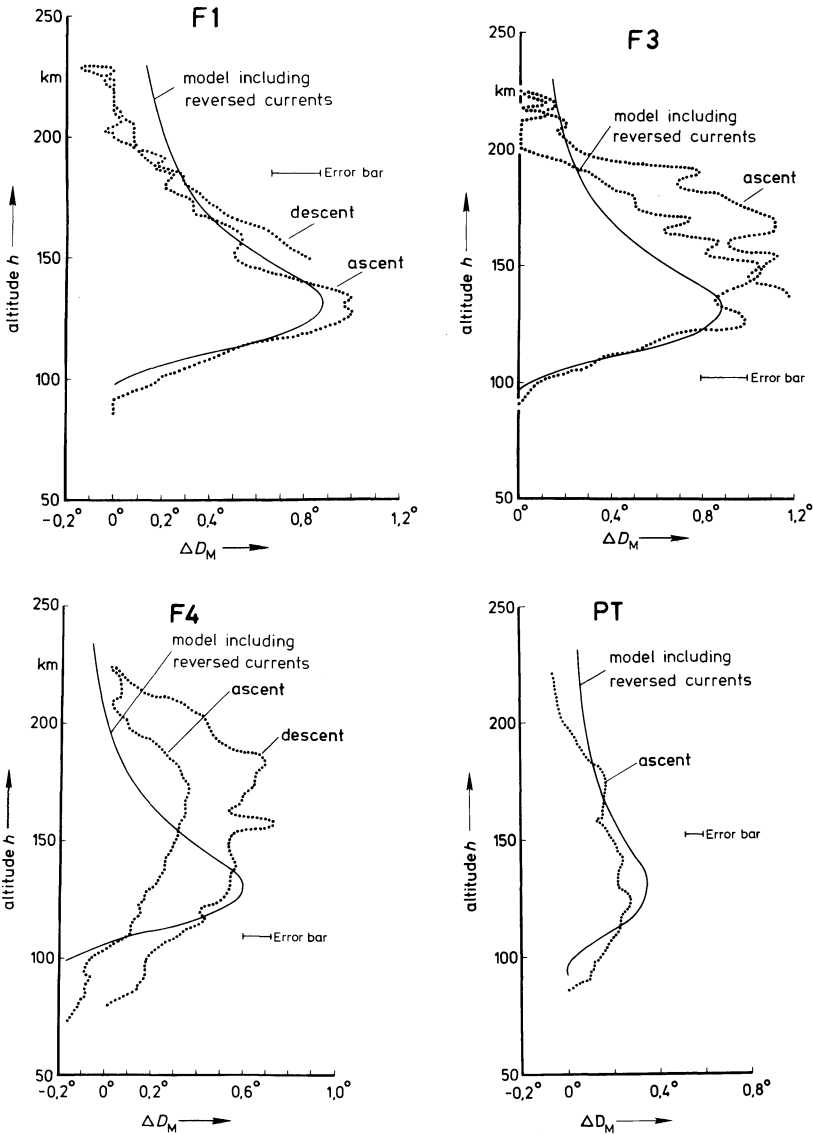


Fig. 9. The existence of meridional currents is seen in the measured variation ΔD_M of the declination with altitude. Each point of the dotted lines represents an average of 10 measured values. The solid lines represent model calculations including currents on both sides of the equator with intensities of 0.3 of the electrojet but in reversed direction

curves: For flight *F1* a change in ΔF occurred when the ground observations showed a small positive change in the decreasing phase of H indicating also a temporary increase of the current density. The ΔF curve for flight *F4* showed two significant extreme values at about 150 km and 125 km during the descent. These variations were not seen in the ground data, which only showed a steep

Table 2.

Flight	Max. value of ΔD_M degrees	ΔH (magn. Equator) (nT)	ΔY_M (nT)	ΔH_E (nT)
<i>F 1</i>	≈ 1	(disturbed)	≈ 430	?
<i>F 3</i>	≈ 1	185	≈ 430	346
<i>F 4</i>	0.7	170	300	284
<i>PT</i>	0.3	80	130	121

decrease in H of nearly 10 nT during the flight time. Therefore the variations during this flight must be due to locally enhanced current densities.

While the effect of the electrojet is seen in ΔF , the disturbance of the meridional current is observed as a variation ΔD_M of the declination D . To get this variation ξ_1 was calculated according to Equation (1). This was possible for the four successful flights *F 1*, *F 3*, *F 4*, and *PT*. The computed curves of ξ_2 were shifted as discussed above in connection with Figure 5 to get a good agreement between the curves $\xi_1(h)$ and $\xi_2(h)$ above 200 km as expected although the corrections are only made for $h \leq 90$ km altitude. A deviation between both curves can clearly be seen in Figure 5, as an example, between 100 km and 200 km altitude. This deviation is considered to be due to the effect of the meridional currents of the electrojet system.

To get ΔD_M Equation (4) is used. The term $(\sin \lambda \cos I \sin(D - \omega))^{-1}$ is of the order of 7 to 10 for all flights and varies only slightly during a special flight. It can be determined with a possible error of $\pm 10\%$. The ΔD_M results for the four flights are shown in Figure 9. Each point of the dotted lines in Figure 9 represents an average of 10 measured values. As expected from the electrojet model the maxima of ΔD_M occur at higher levels than the main electrojet and are much broader.

The measured maximum values of ΔD_M are given in Table 2 for the four flights, together with the instantaneous values of ΔH at the magnetic equator (station Fortaleza) and values of ΔY_M which is the toroidal field strength from the given ΔD_M . The meaning of ΔH_E will be explained later.

Although there seems to exist some correlation between ΔH and ΔY_M within Table 2 the observed $\Delta Y_M/\Delta H$ amounting to about 2 is larger than has to be expected from Untiedt's (1967) model. According to this model the ΔY_M maximum value should be comparable to the equatorial ΔH variation at the ground.

Possible Explanation of the Observations

Although the equatorial electrojet and the toroidal magnetic fields of the predicted meridional currents have been observed within our rocket experiments there seem to exist two discrepancies:

1. The measured total ΔF variation with height is considerably smaller than expected from the ground ΔH measurements via calculations according to Untiedt's (1967) model.

2. The observed toroidal magnetic field ΔY_M is larger than predicted by Untiedt's (1967) model by about a factor of 2.

In addition to recent results from ground based magnetic observations (Fambitakoye and Mayaud, 1976a and b; Hesse, 1977, private communication) our results indicate that the influence of other currents has to be taken into account.

The ground based observations mentioned clearly have shown the existence of two secondary current ribbons flowing at about 500 km distance from the magnetic equator in a direction which is opposite to the direction of the main electrojet. Richmond (1973) has shown that an electrojet model including the effects of height-dependent ionospheric east-west winds is able to generate such secondary current ribbons. His model has been applied by Fambitakoye et al. (1976c) to explain the recent observations of Fambitakoye and Mayaud (1976a and b). Accordingly, we assume that the observed magnetic variations ΔH on the ground are a superposition of the effects of the following currents: the equatorial electrojet, the reversed currents north and south of the equator, the normal Sq-current system, and their induced currents.

For each rocket flight the ΔH variation on ground was measured at the three stations Fortaleza ($d=0$ km, d =distance from the magnetic equator), Mossoro ($d=180$ km) and Natal ($d=370$ km) [Musmann et al., 1971].

For the simplified model three equivalent line currents were selected: a line current at an altitude of 500 km above the magnetic equator and two reversed line currents at an altitude of 400 km at a distance of 500 km north and south from the magnetic equator with 0.3 the current intensity of the main electrojet. These equivalent line currents representing the main electrojet and the reversed currents, respectively, are producing the same magnetic variations on the ground as the measured quantities. The heights and distances of the line currents from the magnetic equator were selected to match the observed latitudinal field distribution on ground while the ratio of the current densities was chosen to give a best fit to the H -observations at Natal and Fortaleza.

For adaptation of the model there are still three variables free: The current intensity I of the electrojet line current, a part of ΔH which is independent of d (representing the contribution from the Sq current system) and the depth T of an infinitely conductive layer for modelling the induced currents.

A value of $T=200$ km was selected which gives maximum influence of the induced currents, according to observations reported by Sastry (1973), Davis et al. (1967), and Hesse (1977, private communication). On the other hand, Fambitakoye and Mayaud (1976a) have shown that the effective depth for image earth currents must be greater than 1200 km for regular variations. Therefore in Figure 10 also the $\Delta H(d)$ profile including no effects from induced currents, i.e. for the case $T=\infty$, are shown to demonstrate all possible values between maximum and zero influence. To $\Delta H(d)$ in Figure 10 one possible profile of Sq as observed in Brazil (Hesse, private communication) was added. The absolute value of the electrojet current intensity I was selected to match the observations of ΔH in Natal. Using this simplified model it is possible to calculate the influence in the observed H values of the reversed currents for the station Fortaleza (magnetic equator). In Table 2 the value ΔH_E is representing this corrected ΔH value.

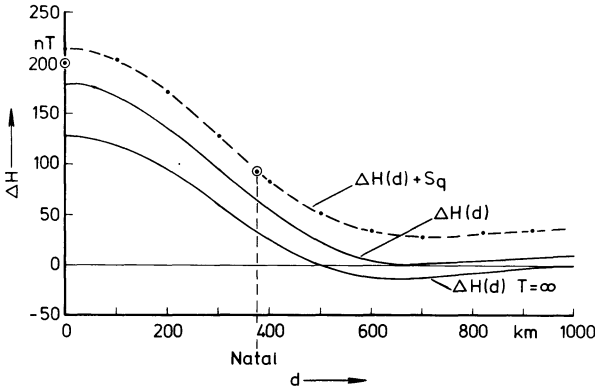


Fig. 10. Model calculations for $\Delta H(d)$ on the ground for the electrojet and two reversed currents at a distance of $d=500$ km north and south of the equator with a current intensity of 0.35 each with respect to the electrojet. The induced currents assuming a perfect conductor at a depth of $T=200$ km are included in the curves of $\Delta H(d)$ and $\Delta H(d)+S_q$. One possible S_q profile taken from ground based observations (Hesse, private communication) is added to $H(d)$ to get $\Delta H(d)+S_q$. (S_q is about 30 nT for Natal). For comparison a profile neglecting induced currents ($T=\infty$) is also shown. The magnitude of the electrojet current was chosen to get the best agreement at $d=0$ km (Fortaleza) and $d=370$ km (Natal) with ground observations for flight *F 3*. The observations of H on the ground at Fortaleza and Natal are marked (\odot)

According to Untiedt’s model this value ΔH_E would be comparable with the maximum value of ΔY_M of the toroidal field. As can be seen in Table 2 this is now in good agreement so that the second discrepancy cited above has been removed. In Figure 9 the solid lines represent calculations of $\Delta D(h)$ including the influence of reversed currents of 0.3 the strength of the electrojet. The agreement with observations is fairly good for *F 1* and *PT*, whereas the results for *F 3* and *F 4* differ significantly in the shapes of the curves but not so much in amplitudes. This may be due to meridional currents with other current distributions.

In order to predict $\Delta F(h)$ the variation with height for Natal ($d=370$ km) from this simple model, an equivalent current density $J(d)$ at 100 km height has been calculated under the condition that it produces the same magnetic field as the three line currents mentioned above between this height and the ground. For heights greater than 100 km the magnetic field is assumed to be that of the current layer $J(d)$ with zero thickness. Therefore there is a jump in $\Delta H(h)$ at 100 km. If one includes also the field of the induced currents, one obtains $\Delta H(h)$ profiles for any distance d which can be compared with the measured flight profile, approximately.

Figure 11 shows the calculated profile $\Delta H(h)$ for $d=0$ (magnetic equator) and $d=370$ km (Natal). The asymmetry with respect to the line $\Delta H = \Delta F = 0$ nT results from the fact that the magnetic field of the induced currents does not change sign at the height of the electrojet. In addition to the theoretical curves (solid line) the observed values ΔF_{ob} for flight *F 3* as an example are shown (dashed line) together with a curve ΔH_u calculated from Untiedt’s (1967) model without reversed currents. The observational results are in good agreement with

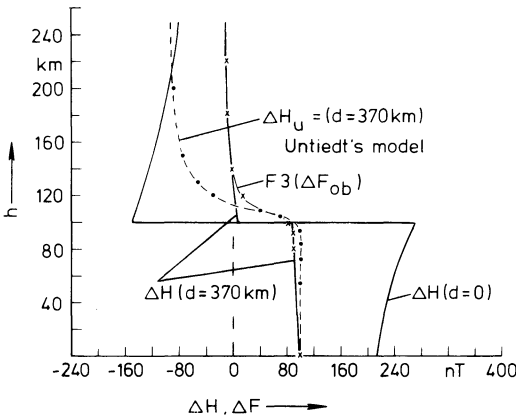


Fig. 11. Model calculations of the ΔH variation with height for $d = 370$ km (Natal) and $d = 0$ (Fortaleza) including reversed currents. $d =$ distance from the magnetic equator. The observed ΔF_{ob} variation for flight F 3 is added to show how well the calculations and the observations agree. Also included is the field variation $\Delta H_U(h)$ for $d = 370$ km as calculated by Rippen (1975) according to Untiedt's (1967) model

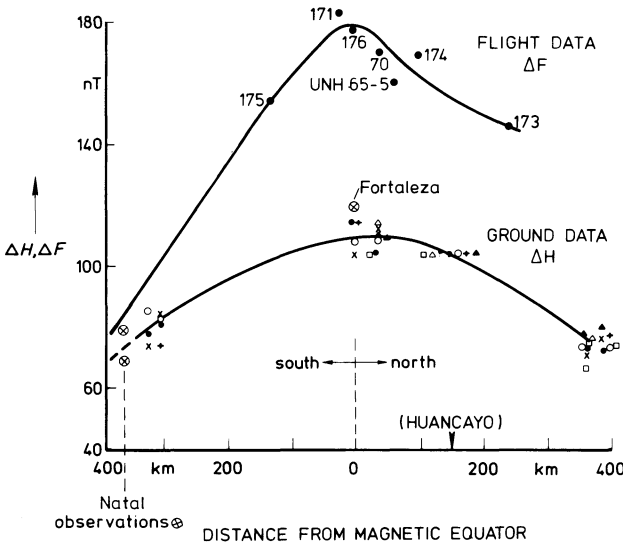


Fig. 12. Ground observations of ΔH and flight observations of ΔF in Peru for various distances from the magnetic equator as presented by Davis et al. (1967). Included are the measurements of ΔH on ground in Natal and Fortaleza (normalized to the scale selected by Davis et al.) as well as the flight data of ΔF above Natal

the simple model calculations also for the other flights, so that the introduction of reversed currents also removes the first discrepancy.

Using this model it is also possible to explain the rocket flight results of Davis et al. (1967) in more detail. At Natal a ratio of 1:1 for $\Delta H : \Delta F_{ob}$ was observed for all flights under regular magnetic conditions (see Table 1). But as can be seen from Figure 11 this ratio is a function of the distance d from the magnetic equator, reaching a value of 1:2 for $d = 0$ km. This is in agreement with observations of Davis et al. (1967) who measured ΔF (flight) and ΔH (ground) as a function of latitude. For comparison their results are shown in Figure 12 together with our results. Thus it seems that with the model described above not only the amount of the ΔF variation but also its latitudinal dependence as observed by Davis et al. (1967) can be explained.

Conclusions

It was the aim of the rocket experiments to verify the existence of meridional currents in the equatorial ionosphere. The results obtained clearly indicate such currents, but the measured values of ΔF and ΔD_M (in Tables 1 and 2) can be explained only by taking into account reversed currents. The strengths of these reversed currents giving the best fit to the observed results were calculated. Similar values were deduced from ground-based measurements. With the assumption of reversed currents the observed variation of ΔF with latitude can also be explained. Although not all details of the observations can be explained by this simple model, some understanding of the observed ΔF and ΔD_M variations seems possible. However, up to now there are no simultaneous measurements in the ionosphere of the electrojet and its reversed currents. To get a better picture of the electrojet phenomena simultaneous rocket measurements at at least three different distances from the magnetic equator should be carried out: At the equator to get the maximum effect of the electrojet, at the center of the reversed currents which is at about 500 km north respectively south of the magnetic equator, and at about half this distance. In addition to the rocket borne measurements ground based observations of the earth's magnetic field on a profile perpendicular to the magnetic equator should be carried out also. The influence of the Sq-currents can only be calculated if there are observations at a distance far enough from the magnetic equator. Therefore ground stations at 3,000 to 4,000 km off the equator should be included. With actual values of magnetic variations along a groundbased profile of some thousand kilometers and ionospheric observations at three different distances one should be able to distinguish between the different current systems. Besides some minor changes the payload described here seems to be suitable for ionospheric measurements, and especially for the observation of meridional currents.

Acknowledgements. We are grateful to Professor Dr. W. Kertz, Director of the Institut für Geophysik und Meteorologie der Technischen Universität Carolo-Wilhelmina, Braunschweig, for his support, advice and the computations of model current systems. Thanks are also due to Mr. D. Hesse, also Braunschweig, and Professor J. Untiedt, Münster, for valuable discussions.

This work was supported financially by the Bundesministerium für Forschung und Technologie.

References

- Aikin, A.C., Blumle, L.I.: Rocket measurements of the E-region electron concentration in the vicinity of the geomagnetic equator, *J. Geophys. Res.* **73**, 1619–1626, 1968
- Cain, J.C., Hendriks, W.E., Jensen, D.C.: Computation of the main geomagnetic field from spherical harmonic expansions. Data Users Note NSSDC 68–11. National Space Science Data Center, Greenbelt, 1968
- Davis, T.N., Burrows, K., Stolarik, J.D.: A latitude survey of the equatorial electrojet with rocket-borne magnetometers. *J. Geophys. Res.* **72**, 1845–1861, 1967
- Fambitakoye, O., Mayaud, P.N.: Equatorial electrojet and regular daily variation S_R . I. A determination of the equatorial electrojet parameters. *J. Atmos. Terr. Phys.*, **38**, 1–17, 1976
- Fambitakoye, O., Mayaud, P.N.: Equatorial electrojet and regular daily variation S_R . II. The center of the equatorial electrojet. *J. Atmos. Terr. Phys.*, **38**, 19–26, 1976

- Fambitakoye, O., Mayaud, P.N., Richmond, A.D.: Equatorial electrojet and regular daily variation S_R . III. Comparison of observations with a physical model. *J. Atmos. Terr. Phys.*, **38**, 113–121, 1976
- Jacobs, K.G., Rawer, K.: Electron density measurements in the ionosphere over the sahara with a variable frequency impedance probe, *Space Res.* **5**, 706–718, 1965
- Jacobs, K.G., Rawer, K.: Raketenmessungen mit einer Hochfrequenz-Impedanzsonde, *Jahrbuch 1966 der WGLR*, 378–384, 1966
- Maynard, N.C.: Measurements of ionospheric currents off the coast of Peru, *J. Geophys. Res.*, **72**, 1863–1875, 1967
- Melzner, F., Rabben, H.H.: Elektronendichte-Messungen in der Ionosphäre mit einer neuartigen HF-Impedanzsonde. *Z. Geophys.* **36**, 135–150, 1970
- Mühlhausen, K.H.: Elektronendichtemessungen in der Ionosphäre, Auswertung des Impedanzsondenexperiments der EEJ-Raketen. Diplom-Arbeit, Institut für Geophysik und Meteorologie der Technischen Universität Braunschweig, Braunschweig, 1974
- Musmann, G.: Verfahren zur Lagemessung von Raketen. *GAMMA 15*, Institut für Geophysik und Meteorologie der Technischen Universität Braunschweig, Braunschweig, 1971
- Musmann, G., Seiler, E., Hansel, J.: Bodenmessungen während der EEJ-Raketenkampagne in Brasilien, Oktober 1970. *GAMMA 19*, Institut für Geophysik und Meteorologie der Technischen Universität Braunschweig, Braunschweig, 1971
- Richmond, A.D.: Equatorial electrojet. I. Development of a model including winds and instabilities. *J. Atmos. Terr. Phys.*, **35**, 1083–1103, 1973
- Rippen, H.: Anwendung eines meridionale Ströme berücksichtigenden Modells auf den äquatorialen Elektrojet in Brasilien. Diplom-Arbeit, Institut für Geophysik und Meteorologie der Technischen Universität Braunschweig, Braunschweig, 1975
- Sastry, T.S.G.: Daily Variation of Geomagnetic Field at the Indian Stations under the Electrojet during Period of the July 1966 Proton Flare. *J. Geophys. Res.*, **78**, 1692–1698, 1973
- Sugiura, M., Poros, D.J.: An improved model equatorial electrojet with a meridional current system. *J. Geophys. Res.*, **74**, 4025–4034, 1969
- Untiedt, J.: A model of the equatorial electrojet involving meridional currents. *J. Geophys. Res.*, **72**, 5799–5810, 1967

Received June 24, 1977; Revised Version December 23, 1977

Joint Magnetometer Array and Radar Backscatter Observations of Auroral Currents in Northern Scandinavia

W. Baumjohann¹, R.A. Greenwald², and F. Küppers¹

¹ Institut für Geophysik, Universität Münster, Gievenbecker Weg 61, D-4400 Münster, Federal Republic of Germany

² Max-Planck-Institut für Aeronomie, Postfach 60, D-3411 Katlenburg-Lindau 3, Federal Republic of Germany

Abstract. As a contribution to the International Magnetospheric Study the University of Münster has installed an array of 32 Gough-Reitzel type magnetometers located mostly in Northern Scandinavia. Also for the IMS, the Max-Planck-Institut für Aeronomie at Lindau is operating the Scandinavian Twin Auroral Radar Experiment (STARE) which consists of two nearly identical backscatter radars located near Trondheim (Norway) and Sauvamaeki (Finland). For a weak isolated substorm on October 7, 1976 the spatial structure of the electron density irregularities observed by the Trondheim-radar and the equivalent current distribution derived from the magnetic measurements have been compared. A good correspondence has been found between the location and magnitude of the maxima of the horizontal magnetic disturbance and the radar backscatter amplitude for an eastward electrojet. For most of the comparison there appeared also to be good agreement between the direction of the equivalent current and the direction antiparallel to the line-of-sight irregularity drift. This supports the idea that the backscatter irregularities are caused by current driven plasma instabilities and that it is possible to determine auroral ionospheric currents with the backscatter radar technique. However, during periods of enhanced electron precipitation, differences between the drift directions given by the two methods were observed.

Key words: Auroral electrojets — Scandinavian magnetometer array — STARE-radar.

Introduction

As a result of the International Magnetospheric Study (IMS), extensive new arrays of ground based geophysical instrumentation have been installed in northern Scandinavia. Two of these new systems are a two-dimensional array of 32 magnetometers (Küppers et al., 1978) of an improved Gough-Reitzel type (Gough and Reitzel, 1967) and a two station radar auroral experiment — STARE (Greenwald et al., 1977).

The magnetometers are sensitive to current flows in the polar region. These include horizontal ionospheric currents which are commonly referred to as auroral electrojets and magnetic field aligned currents which are associated with these electrojets. The STARE-radars are sensitive to electrostatic ion waves in the auroral E-region. These waves, often called irregularities, are produced by the combined effect of the two stream (Buneman, 1963; Farley, 1963) and gradient drift (Rogister and D'Angelo, 1970) plasma instabilities. Both of these instabilities require a sufficiently large relative drift between the Hall drifting electrons and the collision dominated ion species. Hence, these instabilities occur within the regions of the auroral electrojets.

During the past several years a number of studies have shown a close correspondence between the location of radar aurora and the location of electrojet currents. Some of these studies have used ground-based magnetometers to locate the currents, (e.g. Greenwald et al., 1973, 1975; Tsunoda et al., 1976), whereas others have used the Chatanika incoherent scatter radar to determine the E-region current density (Siren et al., 1977). In both cases a curious linear relationship has, at times, been observed between the electrojet current strength and the intensity of radar auroral backscatter. This relationship has, as yet, not been explained.

In this paper we report the results of a similar study using the 32 magnetometer array and the STARE radar located near Trondheim, Norway. The comparison was done for a three hour period of a substorm on 7 October 1976. We have found, consistent with previous studies, that radar auroral irregularities are collocated with the eastward electrojet currents and that, within our experimental error, the amplitude of radar auroral irregularities associated with the eastward auroral electrojet appears to be linearly related to the intensity of this current.

We have also been able to use the Doppler capabilities of the Trondheim radar to determine if the Doppler shifts of the backscattered signals were consistent with the electrojet current directions obtained from an equivalent current analysis. Since linear plasma theory indicates that radar auroral irregularities have a mean drift in the electron drift direction (e.g. Buneman, 1963; Rogister and D'Angelo, 1970) one would expect the mean drift of the irregularities to be opposite to the Hall-current direction. Having only the Trondheim radar it has not been possible to determine the precise irregularity drift direction. However, we were able to determine if the sign of the Doppler shift was consistent with the current direction. In general eastward electrojet associated irregularities and irregularities in the region of the Harang-discontinuity (Harang, 1946) had Doppler shifts consistent with the electrojet current direction. However, irregularities observed in conjunction with the westward electrojet near the maximum phase of the substorm were found to have drifts inconsistent with the concurrently derived equivalent current directions.

Description of the Instrumentation

The locations of the magnetometers used for this study are shown in Figure 1. Basically, they are located along 5 roughly parallel north-south profiles. The spacing between magnetometers within these profiles varies from 100–150 km.

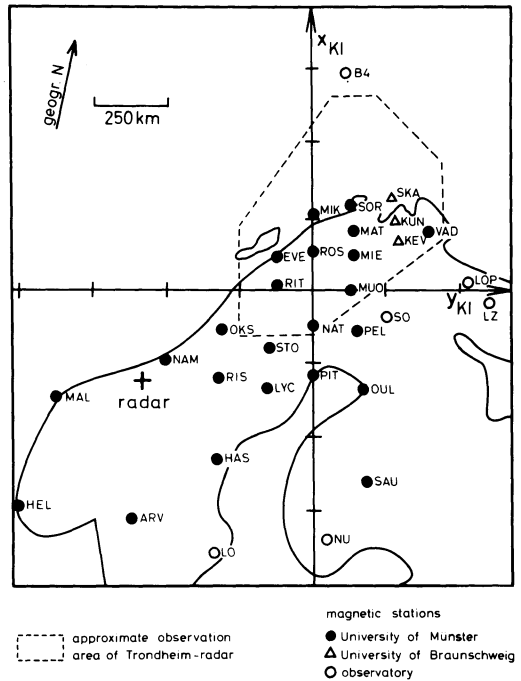


Fig. 1. Locations of magnetic stations used in this study and approximate observation area of Trondheim-radar in the Kiruna-system representation. For explanation of the Kiruna-system see text

A number of additional magnetometers have also been used and are also plotted in the figure. Recently, a more complete description of this magnetometer network has been given by Küppers et al. (1978)

The coordinate system used in Figure 1 has been denoted as the Kiruna-system (Küppers et al., 1978). It is a cartesian system obtained from a stereographic projection of the globe onto a tangential plane centered on Kiruna, Sweden (67.8° N, 20.4° E). The y_{KI} -axis has been chosen so that it is tangential to the projection of the $\phi_c(KI) = 64.8^\circ$ line with ϕ_c being the revised corrected geomagnetic latitude given by Gustafsson (1970). The x_{KI} -axis is parallel to the revised corrected geomagnetic meridian and is directed approximately 12° west of geographic north.

Again referring to Figure 1, the area enclosed by the dashed lines is the region examined by the central eight beams of the receiving array of the STARE radar near Trondheim. Within this area, the spatial resolution of the radar is approximately 20 km by 35 km by the vertical thickness of the scattering region. Normally, the last dimension is approximately 20 km. The temporal resolution of the radar was set at 60 s during this event.

The STARE radar is designed to measure the intensity and radial Doppler velocity of the radar auroral irregularities within each resolution cell of the scattering volume during each integration period.

The intensity data is corrected for antenna pattern variations, range dependence, and aspect angle dependence. All of these corrections and the methods by which the intensity and Doppler velocity information are obtained are described in detail by Greenwald et al. (1977).

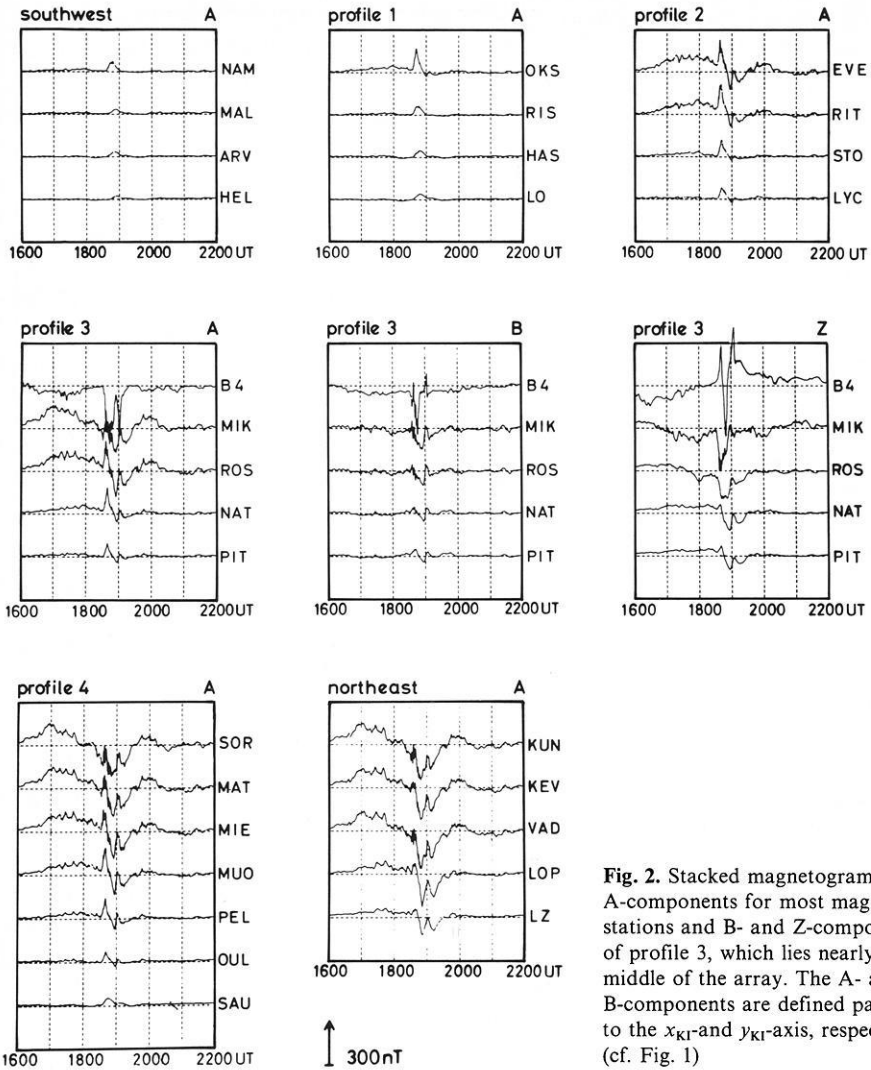


Fig. 2. Stacked magnetograms of A-components for most magnetic stations and B- and Z-components of profile 3, which lies nearly in the middle of the array. The A- and B-components are defined parallel to the x_{KI} - and y_{KI} -axis, respectively (cf. Fig. 1)

Overview of the 76-10-07 Substorm

On 7 October 1976, an isolated, weak substorm ($K_p=3$) occurred between 1600 and 2200 UT (1830–0030 MLT). The magnetic effects observed in the Scandinavian sector in conjunction with this substorm are summarized in Figure 2. Here we show the A-components (magnetic deflection parallel to x_{KI}) for four profiles and the northeast and southwest stations. We also show the B-components (magnetic deflection parallel y_{KI}) and the vertical Z-components for profile 3. The components are obtained by conformal mapping of the spherical magnetic components.

One can see that, between 1600 and 1800 UT, the A-components of all stations except the northernmost (B4-Bear Island) were positive, thereby indicating an eastward electrojet over northern Scandinavia. Between 1800 and 1900 UT these features change dramatically. In particular the stations to the south continue to indicate positive disturbances for most of the hour, whereas the stations to the north begin to show negative disturbances indicative of a westward electrojet. The most dramatic changes take place shortly after 1830 UT. This current configuration with westward currents to the north and eastward currents to the south is a feature that occurs, on the average, shortly before magnetic midnight. It has become known as the Harang discontinuity (Harang, 1946).

The B and Z components on profile 3 also show dramatic variations after 1830 UT. The B-variations may be interpreted as north-south directed currents or the effects of field-aligned currents.

After 1900 UT, nearly all magnetometers have negative deflections indicative of a westward electrojet. This condition slowly weakens and eventually the current reverses. After 1930 UT most magnetometers again show a positive magnetic deflection suggesting an eastward electrojet.

On this day, the STARE radar near Trondheim recorded nearly continuous backscatter after 1430 UT. After 1600 UT, the region moved southward over northern Scandinavia. Until 1812 UT, only positive Doppler velocities were observed. These Doppler shifts could be interpreted as being due to westward moving irregularities. Hence, they are associated with an eastward electrojet.

After 1812 UT, negative Doppler velocities were, at times, observed in a second scattering region located well to the north of the eastward electrojet associated irregularities. These Doppler shifts could be interpreted as being associated with eastward moving irregularities (westward electrojet). During two periods, 1812–1912 and 2015–2045, the poleward scattering region underwent interesting Doppler variations, in which the Doppler velocity changed from positive to negative and then back to positive. These variations could be interpreted as rotations in the direction of the poleward current system. The equatorward scattering region either weakened or moved equatorward of the STARE viewing area during these periods.

Comparison of Magnetic and Radar Observations

In Figure 3 we present several comparisons of the magnetic and radar data during the period from 1700–2015 UT. The upper curve in this figure shows the variation in the ratio of the maximum horizontal magnetic disturbance ($H_{\max} = (\sqrt{A^2 + B^2})_{\max}$) to the maximum corrected backscatter amplitude (R_{\max}) observed in the common area of both measurements. The amplitude is simply the square root of the backscatter intensity. Both the radar and magnetic data represent 1 min averages taken every 5 min. The radar data are averaged over a $100 \times 100 \text{ km}^2$ area. These areas were chosen as being more comparable with the spatial resolution of the magnetometers. The ratios have been normalized so that their average value over the entire period is unity.

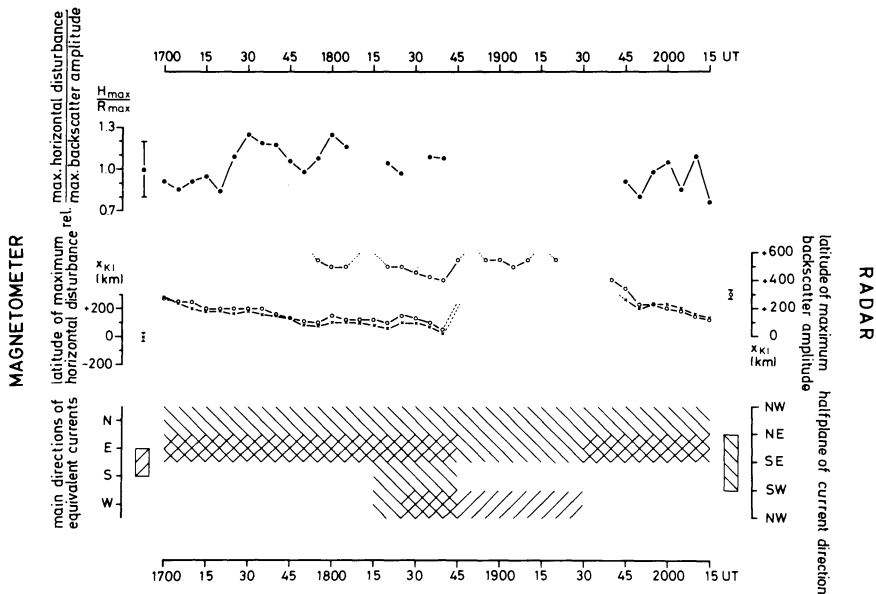


Fig. 3. Comparison of magnetic and radar data during the period from 1700–2015 UT. The upper curve shows the variation in the ratio of the maximum horizontal disturbance to the maximum corrected backscatter amplitude while the middle set of curves shows the latitudinal locations of these two maxima. The lower comparison relates the main direction of the magnetic equivalent current with the halfplane of allowable current direction consistent with the Doppler velocities

One can see that over the entire period of the measurement the ratio never varies outside of the range 0.7–1.3, even though there have been appreciable variations (up to a factor of 5) in both the horizontal magnetic disturbance and the backscatter intensity. This near constancy is more impressive when one considers that the probable errors in this comparison are of the order of $\pm 20\%$. They are due to uncertainties in interpolating the correct maximum amplitude between the observed values. Additionally, we have not considered the effects of field-aligned currents on the horizontal components or the effects of changes in the induced currents as the ionospheric current layer moves from being over water to being over land. For the radar measurements, variations in backscatter power could result from cross section changes produced by rotations of the current direction or changes in the height of the irregularity layer. None of the problems is, as yet, completely understood.

The middle set of curves in Figure 3 illustrates a comparison of the latitudinal locations of the maximum magnetic disturbance and the maximum backscatter amplitudes as a function of time. The magnetic data are represented by the small crosses and the radar data is denoted by circles. The latitudinal error for each set of measurements is shown by the error bars near each axis. One can see that between 1700 and 1840 UT the maxima of the magnetic disturbance and radar backscatter amplitude are at virtually the same latitudes. The same behaviour is true after 1945 UT when both techniques again observe maxima. Although the figure only displays a latitudinal comparison, we have found

longitudinal variations of both maxima, but the spatial collocation was also observed. That is, the strongest backscatter is observed in the E-region above the magnetometer that observes the largest magnetic disturbance.

From the latitudinal comparison of disturbance maxima, we see that the radar observes a second maximum between 1755 UT and 1920 UT. However, as the current appears to be located well north of the Scandinavian coast, the magnetometers were unable to see the maximum.

Finally, the lower comparison in Figure 3 relates the main direction of the equivalent current derived from the magnetic A- and B-variations in the area of common observations with the halfplane of allowable current directions consistent with the observed Doppler velocities. The two measurements are differentiated by the direction of the hatching. We see that whenever the magnetometers observe an eastward current, the radar observes Doppler shifts implying this current direction (see also below). Furthermore, we see that it is an eastward current that yielded in the interesting relationships in the upper two curves of this figure. We also note that between 1825 UT and 1845 UT when the magnetometers observe the effects of a westward electrojet, the radar also observes westward electrojet associated irregularity drifts. A similar explanation can possibly hold for the period from 1815 UT to 1825 UT. It is possible that a westward electrojet was flowing in the north at this time, but it is too far north and was not strong enough to be observed by the magnetometers. The only time interval in which the magnetic and radar observed current directions are not consistent, extends from 1845 UT until 1930 UT. During this period the magnetometers indicate the presence of a westward current, whereas the radar would predict an eastward or northward current. One should note that during this period the disturbance maximum is well north of the northern coast of Scandinavia and only observable with the radar.

In order to examine the relationship between the current directions derived by both methods more carefully, we present in Figure 4 a more detailed comparison of equivalent currents obtained with the magnetometers and radial current direction component implied by the radar data. The current direction component implied by the radar data is opposite to the observed irregularity drift velocity component. Again, both data sets represent 1 min averages and the radar data is averaged over $100 \times 100 \text{ km}^2$ areas.

The equivalent current vector analysis assumes that all current producing a disturbance on any given magnetometer flows horizontally above that magnetometer. The effects of field aligned currents or distant horizontal ionospheric currents are not considered. The equivalent current vector is obtained from the magnetic disturbance vector by rotating the vector 90° clockwise.

There are several important differences to keep in mind when looking at Figure 4. The length of the equivalent current vector is proportional to the horizontal magnetic disturbance and has its origin at the observing magnetometer's site whereas the length of the radar determined radial current direction arrow is equal and opposite to the radial irregularity velocity. The small box at the base of each radial current direction arrow has sides proportional to the intensity of the backscatter from that region.

In Figure 4a, we have compared the magnetic and radar data at 1700 UT.

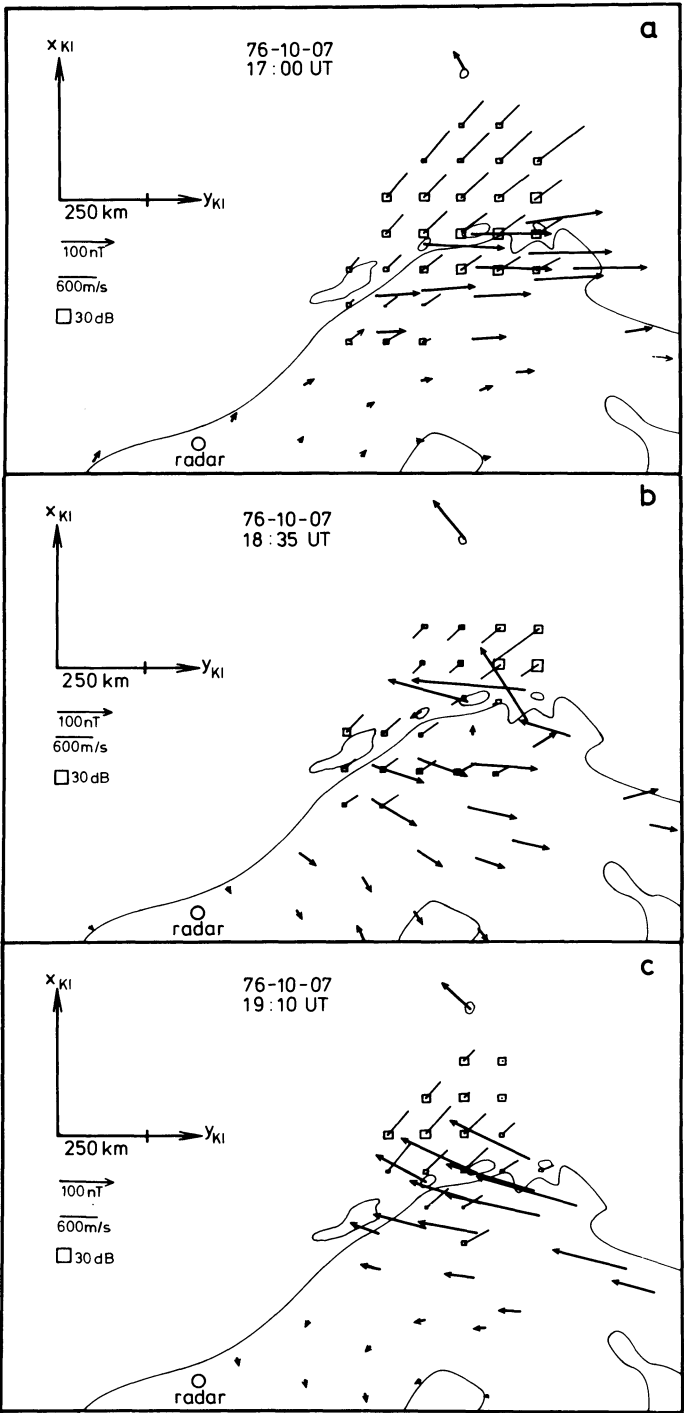


Fig. 4a-c. Comparison of magnetic equivalent current given by the equivalent current vectors at each station with irregularity strength and reversed Doppler velocity component on a 100×100 km grid for three different times. The current arrows have their origin at the station, where they have been recorded. The side of the boxes is proportional to the intensity of the backscatter signal (irregularity strength)

At this time the disturbance maxima in Figure 3 were collocated. One comes to the same conclusion by comparing the equivalent current vectors and box sizes in Figure 4a. Furthermore, all of the radar current direction components in Figure 4a are consistent with the eastward equivalent current vectors. Similar good agreement between the two data sets is observed at 1835 UT, shown in Figure 4b. At this time an eastward equivalent current was observed by the more southerly magnetometers and a westward equivalent current was observed by the magnetometers on the northern coast. Again the radar implied current directions are consistent with the equivalent current directions. One can also see that the radar shows the maximum westward-electrojet-associated irregularity intensity to occur just north of the Scandinavian coast and hence just beyond the latitude where the magnetometers could detect a disturbance maximum.

Finally, in Figure 4c, one can more clearly observe the disagreement in the data sets that occurred between 1845 UT and 1930 UT. Here, at 1910 UT, the radar locates the maximum disturbance about 200 km north of the coast and shows it to be associated with an eastward or northward current. The magnetometers show a westward equivalent current with a slight tendency for the vectors to turn northward on the coastal stations.

Discussion

As we have mentioned earlier in this paper, one would expect radar auroral irregularities to be located within the auroral electrojets and previous studies have shown this to be true. This study, however, has literally added another dimension to this association. The Scandinavian magnetometer array is the first closely packed two dimensional magnetometer network that has been set into operation at high latitudes for observations over several years. Used in conjunction with a multibeam backscatter radar, it has been possible to compare in both latitude and longitude the location of the most intense equivalent current with that of the most intense backscatter. This comparison has shown that the two are collocated to within the uncertainties of the analysis. Furthermore, the ratio of the equivalent current density to the backscatter amplitude, in the region where these two quantities maximize, remains approximately constant throughout the measurement.

The near constancy of the current density to backscatter amplitude ratio implies that the above mentioned possible reasons for non-constancy have either not occurred or had a weak influence. In particular, it appears that the equivalent current density was either dominated by horizontal currents or the ratio of field-aligned to horizontal currents remained constant during most of the comparison. Furthermore, it appears as if the height of the irregularity layer and the direction of the mean irregularity drift must have remained approximately constant, thereby not appreciably changing the irregularity cross-section.

Since the backscatter regions used for this comparison were associated with an eastward electrojet one can ask whether variations in the drift direction or height of the irregularities might have been expected to occur. From an examination of the variations in the direction of the eastward equivalent current,

we have found that the current direction and, hence, the electron drift direction generally was within $\pm 10^\circ$ of the y_{KI} -axis. An example of these current vector configurations can be seen in Figure 4a. Moreover, Kamide and Brekke (1977) have shown that the eastward auroral electrojet does not undergo large altitude variations and that it is enhanced primarily by intensifications of the northward electric field. Therefore, it would seem, that the irregularities are located in a relatively constant altitude range and that the variations in backscatter intensity are associated with variations of the northward ionospheric E-field. This conclusion was suggested earlier by Greenwald et al. (1975) on the grounds that modulation in the magnitude of the electric field would produce an associated modulation in the electron drift velocity and, hence, in the driving term of the plasma instability.

The relationship of mean radar auroral irregularity drift directions with ionospheric current directions is still a much debated topic. Recently, there has been an increasing amount of evidence that irregularity mean drift velocities can be used to determine the velocity of the Hall drifting electrons. For example, Ecklund et al. (1977) have shown that there is good agreement between the Hall drift of the F-region plasma as measured with the Chatanika incoherent scatter radar and the E-region irregularity drift. Also, Greenwald et al. (1977) have recently presented evidence that the mean irregularity drift direction is approximately that of the Hall-drifting electrons.

From the magnetic viewpoint, Fukushima (1976) has presented a theorem which states that no ground magnetic effect is produced by a combination of vertical currents into and out of the ionosphere and Pedersen closure currents within the ionosphere, if the height integrated ionospheric conductivity is uniform. Since field-aligned currents are nearly vertical in the auroral ionosphere, at times when the ionospheric conductivity is nearly uniform, ground magnetometers will see predominantly the effect of the ionospheric Hall current.

During the period of this comparison 30 MHz riometer data was available from Tromsø and Bear Island (Stauning and Christensen, 1977). This data indicates that prior to 1840 UT and after 1915 UT very little 20–40 keV electron precipitation was apparent. If we interpret the absence of energetic electron precipitation as indicative of a relatively uniform ionospheric conductivity, then we would expect the ground magnetic perturbations to be due to Hall currents. This would explain the good agreement between the current directions derived from the two techniques.

In contrast, between 1840 UT and 1915 UT, strong keV electron precipitation was observed at Bear Island while moderate precipitation was observed at Tromsø. It is during this period, that the uniform conductivity assumption is no longer valid and significant disagreements are noted between the two data sets. Presumably, the equivalent currents no longer represent only Hall currents, but are also due to field aligned currents and/or Pedersen currents. The analysis of the problem under these circumstances becomes extremely difficult. We plan in the future to use the completed STARE radar system, with which full electron drift velocity vectors can be estimated, in conjunction with the Scandinavian magnetometer array to make a more detailed analysis of this problem.

Acknowledgements. We are indebted to Dr. E. Nielsen for his great help in the processing of the STARE-data and B. Inhester for his help in the calculations for this comparison.

We thank all people at the Max-Planck-Institut für Aeronomie and the University of Trondheim, who helped in building and maintaining the radar. We also thank all members of the magnetometer group at the University of Münster and especially Professor J. Untiedt, without whose efforts the magnetometer array observations would have been impossible.

Finally we would like to thank H. Maurer and Drs. G.A. Loginov, Ch. Sucksdorff, S. Berger, F. Eleman, P. Stauning, and B. Christensen, who made additional magnetic and riometer data available for this study. The magnetometer array observations were made possible by a grant of the Deutsche Forschungsgemeinschaft.

References

- Bunemann, O.: Excitation of field-aligned sound waves by electron streams. *Phys. Rev. Letters* **10**, 285, 1963
- Ecklund, W.L., Balsley, B.B., Carter, D.A.: A preliminary comparison of F region plasma drifts and E region irregularity drifts in the auroral zone. *J. Geophys. Res.* **82**, 195-197, 1977
- Farley, D.J.: A plasma instability resulting in field-aligned irregularities in the ionosphere. *J. Geophys. Res.* **68**, 6083-6097, 1963
- Fukushima, N.: Generalized theorem for no ground magnetic effect of vertical currents connected with Pedersen currents in the uniform conductivity ionosphere. *Rept. Ionos. Space Res. Japan* **30**, 35-40, 1976
- Gough, D.I., Reitzel, J.S.: A portable three component magnetic variometer. *J. Geomag. Geoelectr.* **19**, 203-215, 1967
- Greenwald, R.A., Ecklund, W.L., Balsley, B.B.: Auroral currents, irregularities, and luminosity. *J. Geophys. Res.* **78**, 8193-8203, 1973
- Greenwald, R.A., Ecklund, W.L., Balsley, B.B.: Radar observations of auroral currents. *J. Geophys. Res.* **80**, 3635-3641, 1975
- Gustafsson, G.: A revised corrected geomagnetic coordinate system. *Ark. Geofys.* **5**, 595-617, 1970
- Harang, L.: The mean field of disturbance of polar geomagnetic storms. *Terr. Magn. Atmos. Elec.* **51**, 353-380, 1946
- Kamide, Y., Brekke, A.: Altitude of the eastward and westward auroral electrojets. *J. Geophys. Res.* **82**, 2851-2853, 1977
- Küppers, F., Untiedt, J., Baumjohann, W.: A two-dimensional array for ground-based observations of auroral zone electric currents during the IMS. Submitted to *J. Geophys.* 1978
- Register, A., D'Angelo, N.: Type II irregularities in the equatorial electrojet. *J. Geophys. Res.* **75**, 3879-3887, 1970
- Siren, J.C., Douppnik, J.R., Ecklund, W.L.: Comparison of auroral currents measured by the Chatanika radar with 50 MHz backscatter observed from Anchorage
- Stauning, P., Christensen, B.: Compilation of Ionlab riometer data for IMS-Workshop in Hanka-salmi. *Ionlab Rep. R 41*, Lyngby (Denmark), 1977
- Tsunoda, R.T., Presnell, R.L., Kamide, Y., Akasofu, S.-I.: Relationship of radar aurora, visual aurora, and auroral electrojets in the evening sector. *J. Geophys. Res.* **81**, 6005-6015, 1976

Received December 20, 1977 / Revised Version January 25, 1978

New Methods of Separating F Region Absorption From the Cosmic Radio Noise Absorption

S.B.S.S. Sarma and M.C. Sharma

Radio Science Division, National Physical Laboratory, New Delhi -12, India

Abstract. A comparison of cosmic noise absorption data with pulse absorption and the absorption derived by using CW transmitters has given some interesting results. New techniques have been suggested to separate out the absorption contribution of the F region from the total cosmic noise absorption. A comparison of the F region contribution thus derived by the above techniques is fairly consistent with other classical techniques of separation. The electron temperature derived from the above F region absorption compare well with the temperature obtained from more sophisticated techniques. Further the electron density profile (in the lower ionosphere) derived from the lower region absorption using the above technique has given comparable values with rocket and other theoretical profiles.

Key words: Cosmic radio noise – Riometer absorption – Pulse reflection technique – C.W. waves – Solar cycle – Sunspot number – Magnetic storm – Window effect – Electron temperature – Electron density.

1. Introduction

In the present investigation the authors have realised the importance of comparing riometer absorption (A_2) with pulse technique (A_1) and with the absorption derived from CW waves from commercial transmitters (A_3). Simultaneous use of any of the above two techniques with sunspot number has led us in developing a new technique of separating the F region contribution from the total riometer absorption. Riometer absorption is an integrated effect on the radio wave passing through the whole ionosphere. With proper separation techniques, valuable information can be derived regarding the various regions of the ionosphere. Mitra and Shain (1953) have developed a method of separating the relative contributions of the F and D regions. This involves a fundamental assumption, namely, the shape of the curve relating to absorption and f_oF_2 remains the same irrespective of the time of the day. Later Lusignan (1960) extended this technique by correlating the absorption with f_{\min} and thus separated the D region contribution. However, by these techniques the D and E (lower) region contribution is overestimated by underestimating the contribution from the

F region and above. Krishnamurthi and Sarma (1967) modified the above method to get more dependable results. This is discussed quite elaborately by Sarma and Sharma (1972).

Another approach of separating the F region absorption is to compare the simultaneous observations of riometer and pulse technique at the same station as reported by Taubenheim et al. (1966) during solar eclipse. When this technique was tried for the station Neustrelitz, even though there is a linear relationship between the (A_2) and (A_1) absorption we landed in difficulties as there remained a residual absorption on A_1 when the A_2 absorption is zero for which no plausible justification could be put forward.

To avoid this difficulty we extended this technique by comparing A_3 (oblique incidence method) with A_2 (riometer) for the same station and obtained fruitful results which will be explained in later sections. It was shown earlier by Sarma et al. (1970) and Mitra et al. (1970) that riometer and pulse absorptions behave differently with sunspot number. This fact was utilized in the present investigation in separating the F region contribution from the total absorption. The main limitation of this method is that one needs observations on both techniques over a complete solar cycle or at least a substantial part of it.

2. Data Analysis and Selection

In order to separate the F region contribution from the total cosmic radio noise absorption we have used the riometer, pulse and oblique incidence absorption (A_2 , A_1 and A_3 techniques respectively) data for three stations Delhi, Ahmedabad and Neustrelitz to cover the period of IGY, IQSY and IASY. In all the cases the monthly mean values are used as the raw data by any two techniques for the analysis at different stations. The authors have eliminated directly the data taken during anomalous winter days, during magnetic storms and disturbed days and any other unreliable conditions. While considering the A_1 absorption data the frequency selection was such that the pulse is reflected back from around 100 km so that the absorption suffered by the pulse is mainly due to D region where the electron collision frequency exceeds the observing radio frequency of the pulse. Also care is taken to remove the deviative component of absorption when it occurs at certain time intervals. It was also observed for Delhi that in the case of riometer absorption (A_2) the window effect is almost non-existing during 95% of the time and during the rest of the period (especially during IGY) the effect is almost negligible as this is within the experimental accuracies and when it exists appropriate corrections were applied for Ahmedabad and Neustrelitz data.

Earlier it was shown by Sarma et al. (1970) that the relationship between the F region absorption (by A_2 technique) and f_oF_2 is the same for all the hours of the day and season. Further we could not establish any definite relationship between the absorption and the thickness of F region with our data and as such it was presumed that the layer thickness does not play a significant role in the F region contribution of absorption even though we expect the F region absorption to vary in proportion to the product of f_oF_2 raised to a power (exponent n) and the thickness of the F region. Earlier, Mitra and

Shain (1953) also reported that there is no correlation of F-layer thickness with the observed absorption. As we have observed that this exponent value differs from station to station and also with solar epoch conditions we feel that the F region thickness at any particular station may be taken care by the value of the exponent that is observed at different stations as it is invariably quoted by many investigators which is not equal to the expected value of the fourth power. With these selection criteria and observation we report our results below.

3. Experimental Results and Discussion

We have plotted A_2 absorption against sunspot number in the Figure 1. In the same plot the A_1 absorption converted to A_2 frequency by using the inverse square relationship (Sarma and Sharma, 1972) is also plotted and is normalized to zero sunspot number. The line depicting the A_1 absorption is mainly due to the D region and that of A_2 absorption is due to the entire ionosphere. The difference between these two lines gives the F region contribution corresponding to that sunspot number. So one can get a set of values of F region absorption against sunspot number which can be directly related to f_oF_2 values. For this we plot in Figure 2 the difference between the A_2 and A_1 absorption (scaled upto A_2 frequency) as a function of sunspot number, as well as average f_oF_2 values. The f_oF_2 values can be read out from this curve and thus establish a relationship between AF and f_oF_2 . A similar type of analysis was carried out for Ahmedabad and the results are in good agreement as obtained for the station Delhi. However, for Neustrelitz this method did not give encouraging results.

After establishing the relation between F region absorption and f_oF_2 our next step was to use this F region absorption in deriving some physical parameters like electron temperature and electron density. We have calculated the

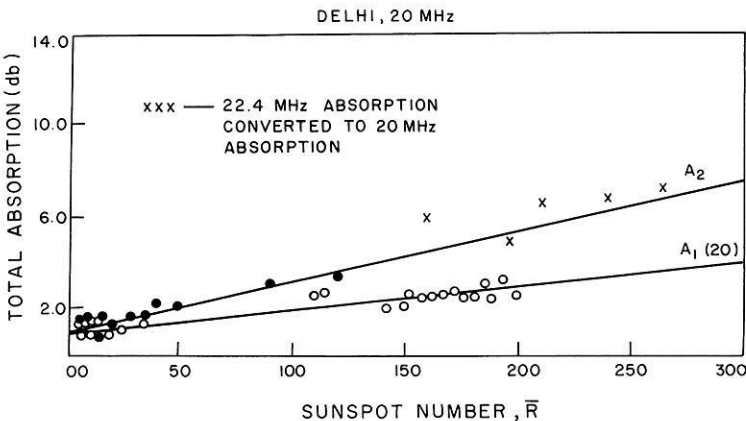


Fig. 1. Comparison of riometer (A_2) and pulse (A_1) absorption (scaled up to the riometer frequency) with sunspot number for Delhi

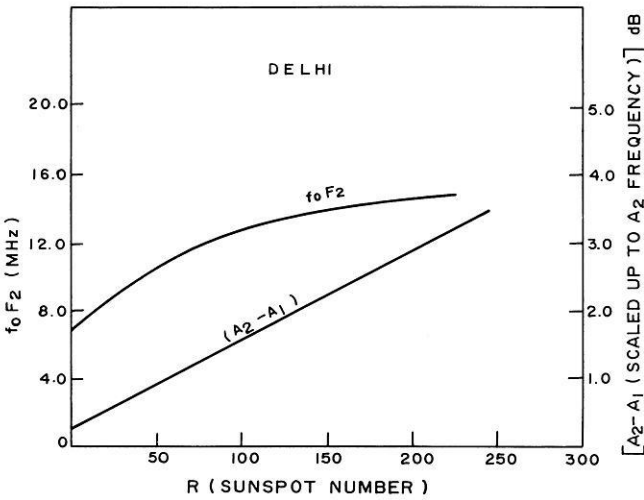


Fig. 2. Comparison of the difference in absorption (by riometer and pulse techniques) and foF2 with sunspot number for Delhi

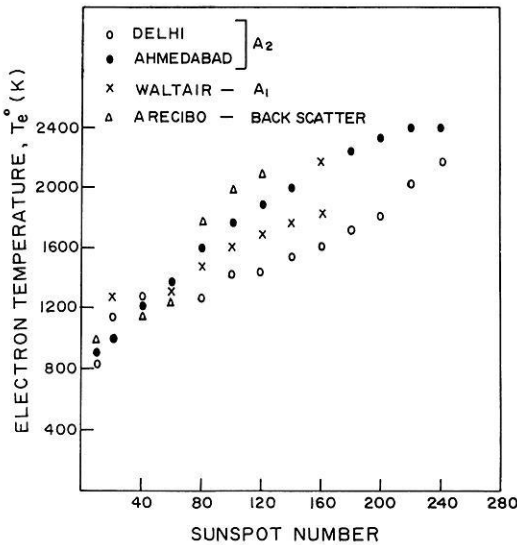


Fig. 3. Comparison of the derived electron temperature from riometer data with other insitu techniques at various sunspot numbers

electron temperature at the height of peak electron densities in F region under certain assumptions as reported by Sarma and Sharma (1972). The derived electron temperature against sunspot numbers are shown in Figure 3. In the same figure the electron temperature reported by Reddy et al. (1972) and the temperature measured by incoherent scatter technique at Arecibo is also shown. We see from the figure that the electron temperature derived by F region absorption is consistent with the temperatures derived by other techniques. This shows that F region absorption thus separated is dependable and reliable.

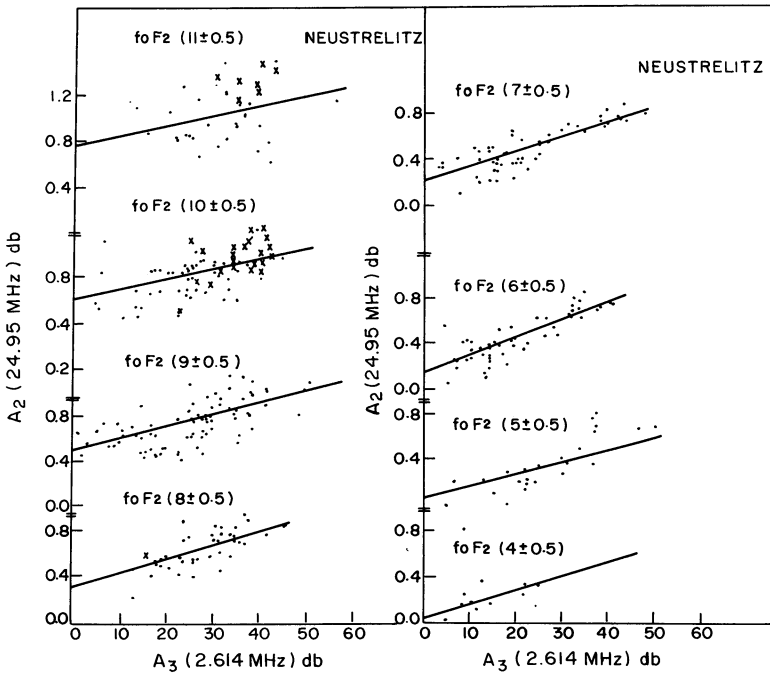


Fig. 4. Comparison of riometer absorption (A_2) with the absorption derived from CW transmissions (A_3) at various f_oF_2 values for Neustrelitz

Another attempt has been made to separate the F region absorption by comparing A_2 and A_3 absorption as the A_3 method essentially measures the absorption from D region. For Neustrelitz the absorption data are available for all the three techniques A_1 , A_2 and A_3 . So we have compared the A_2 absorption with A_1 and A_3 absorption separately. There is a very good correlation between A_1 and A_3 absorption as reported by Mitra (1970) and this is expected as these two techniques essentially measure lower region absorptions. Hence by comparing A_2 absorption with either of A_1 and A_3 will enable us to separate the F region absorption from total absorption. The A_2 absorption is plotted against A_3 absorption for different slabs of f_oF_2 in Figure 4. As seen from the figure that when A_3 is zero, A_2 is not zero. This residual A_2 absorption is mainly due to the F region determined by the corresponding values of f_oF_2 . It is also clear from the figure that the intercept on the A_2 axis goes on increasing with increasing values of f_oF_2 . Hence a relation is established between absorption and f_oF_2 . From the values of f_oF_2 one can directly get the F region absorption.

The lower region A_2 absorption is utilized in deriving the electron density distribution in the lower ionosphere. To do this we have chosen an appropriate reference electron density profile from Mechtly et al. (1972) from rocket measurements and the collision frequency is calculated from the pressure data given in CIRA (1965). The absorption is calculated from 60 km to h_mE and compared with the observed absorption. The reference electron density profile is shifted

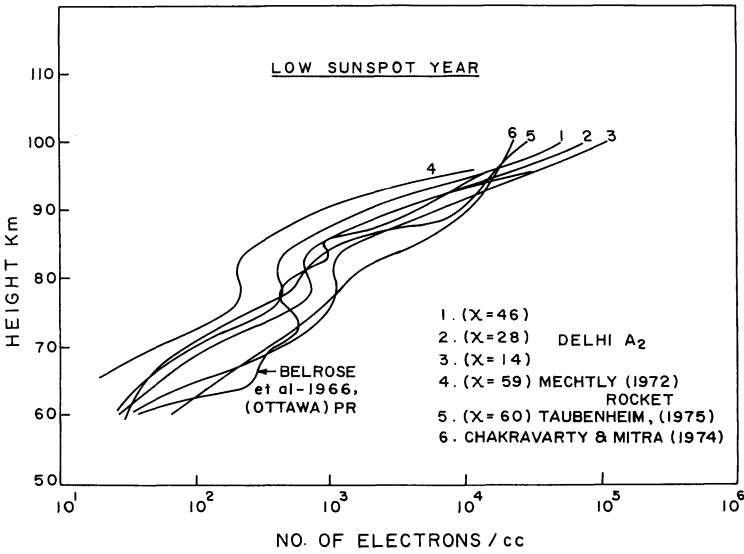


Fig. 5. Intercomparison of the electron density profile derived from the riometer absorption during low sunspot period for Delhi with other techniques

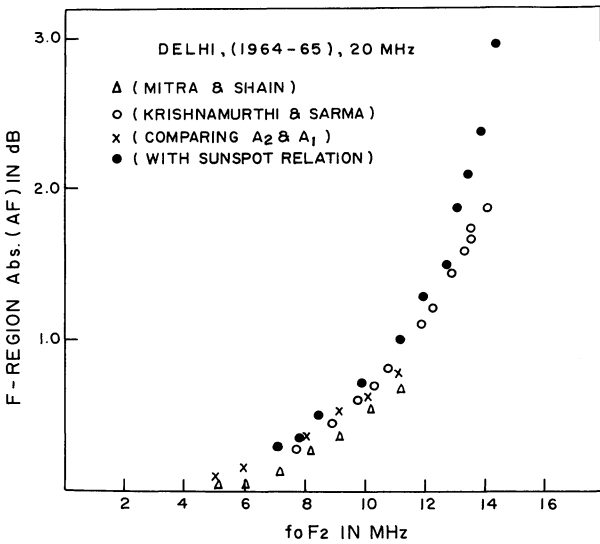


Fig. 6. Intercomparison of various methods of separating the F region absorption from riometer data

iteratively till the observed and calculated absorptions match. Such a profile consistent with the observed absorption is shown in Figure 5. In this figure the theoretical model of Mitra and Chakrabarty (1974) is also shown. In the same figure the profile by Mechtly et al. (1972) from rocket measurements is also shown. From the figure we see that the profile by A_2 absorption is consistent with that obtained by other sophisticated techniques. This shows

that the lower region absorption can be used as a check point on models or to derive the day-to-day variation in electron density in the lower ionosphere. The F region absorption thus separated by these techniques is compared with other methods of separation as shown in Figure 6. It is evident from the above figure that the Mitra and Shain method shows a lower value of F region contribution (for the same f_oF_2 as expected). The other methods give comparable values essentially the same value within the experimental accuracies which seem to be more dependable.

3. Conclusions

Simultaneous use of riometer absorption (A_2) and any absorption measurement like pulse reflection technique (A_1) or use of c.w. waves from commercial transmitters (A_3) has given new methods of successful separation of the F region absorption from the riometer data. The F region contribution derived by the above techniques is shown to be dependable, as the electron temperature derived from F region absorption and the electron density derived from the lower region absorption are in consonance with those obtained by more sophisticated techniques.

Acknowledgements. The authors are grateful to Dr. A.P. Mitra for giving many valuable suggestions in preparing this paper.

References

- Chakrabarty, D.K., Mitra, A.P.: Theoretical models of D-region electron density profiles under different conditions. *Ind. J. Radio Space Phys.* **3**, 76–86, 1974
- CIRA: COSPAR International Reference Ionosphere, Amsterdam: North Holland Publishing Co. 1965
- Lusignan, B.: Cosmic noise absorption measurements at Stanford, California and Pullman, Washington. *J. Geophys. Res.* **65**, 3895–3902, 1960
- Krishnamurthi, M., Sarma, S.B.S.S.: Ionospheric absorption studies based on cosmic noise data at 28.6 MHz at Bangalore. *Austral. J. Phys.* **20**, 455–462, 1967
- Mechtly, E.A., Bowhill, S.A., Smith, L.G.: Changes of lower ionosphere electron concentrations with solar activity. *J. Atmos. Terr. Phys.* **34**, 1899–1907, 1972
- Mitra, A.P., Shain, C.A.: The measurement of ionospheric absorption using observations of 18.3 Mc/s cosmic noise. *J. Atmos. Terr. Phys.* **4**, 204–218, 1953
- Mitra, A.P., Sarma, S.B.S.S., Sharma, M.C., Sudesh Kumari: Comments on A_2 method of measuring absorption. *URSI Manual on absorption*, 1970
- Reddy, B.M., Lakshmi, D.R., Ramanadham, R.: Variation of F_2 -region electron temperature with solar activity as deduced from collision frequency measurements. *Ind. J. Radio Space Phys.* **1**, 138–140, 1972
- Sarma, S.B.S.S., Sharma, M.C., Juneja, S.L.: Cosmic noise absorption measurements in Delhi. *Indian J. Pure Appl. Phys.* **8**, 529–532, 1970
- Sarma, S.B.S.S., Sharma, M.C.: Cosmic noise absorption studies at Delhi over a solar cycle. *Planet. Space Sci.* **20**, 253–259, 1972
- Sarma, S.B.S.S., Sharma, M.C.: Electron temperature measurements from cosmic radio noise absorption. *Ind. J. Radio Space Phys.* **1**, 175–177, 1972
- Taubenheim, J., Hense, V., Lippert, W.: *Ann. Geophys.* **22**, 320, 1966

Short Communication

Evidence for Partial Reflection of VHF Radar Signals From the Troposphere

J. Röttger

Max-Planck-Institut für Aeronomie, D-3411 Katlenburg-Lindau 3, Federal Republic of Germany

Key words: Partial reflection – Scattering radar – Troposphere.

Recently powerful VHF radar systems were introduced to investigate the dynamics of the lower and middle atmosphere (Woodman and Guillen, 1974; Green et al., 1975; Czechowsky et al., 1976; Rastogi and Bowhill, 1976). The mechanism responsible for the radar echoes was assumed to be scattering from refractive index variations caused by atmospheric turbulence.

The purpose of this letter is to stress that besides of pure turbulence scattering also specular (partial) reflection from stratified atmospheric layers has to be taken into account as a cause of these radar echoes. This considerably influences the evaluation and interpretation of data from VHF radars.

Experimental evidence, supporting the role of partial reflection to explain the radar echoes from the troposphere, was found during the first operation of the SOUSY-VHF-Radar of the Max-Planck-Institut für Aeronomie (Röttger and Czechowsky, 1978; Röttger and Liu, 1978):

1. Assuming pure volume scattering, it is deduced from the observed high radar echo power that the mean refractive index structure constant C_n^2 in several cases must be 1–2 orders of magnitude larger than currently accepted values (e.g. Gossard, 1977), or another mechanism than scattering has to be considered.

2. The correlation times of radar signals often are up to minutes in contrary to expected correlation times of a few seconds when assuming turbulence scattering (Woodman and Guillen, 1974).

3. The radar echo power is proportional to the correlation time which is just opposite to turbulence theory (Tatarskii, 1971).

4. The intensity variations of radar echoes often are quasi-periodic (periods of some ten seconds). This can be explained by interference or focussing due to reflection at thin layers or patches of enhanced humidity or temperature variations which are influenced by atmospheric waves.

5. Peak radar echoes are much weaker (up to 20 dB) and not as structured when swinging the radar beam from the vertical to off-vertical (12.5° zenith angle). This points to reflection at vertical incidence into rough, horizontally stratified layers (Röttger and Liu, 1978).

The layers are estimated not to exceed a few ten meters in vertical extent. The vertical gradient of refractive index has to be about 10^{-7} m^{-1} . The horizontal dimension of the stratified layers must be at least several 100 m.

6. The amplitude distributions of strong tropospheric radar echoes cannot be fitted to a Rayleigh distribution which would be expected for turbulence scattering. A better fit is possible when assuming that the signals contain a constant, partially reflected part. Phase distributions are not random (i.e. phases equally distributed between 0 and 2π), but also indicate consistent contributions from partial reflection.

7. Doppler spectra of strong radar echoes do not fit to a Gaussian shape which is anticipated if one assumes turbulence velocities to be normally distributed. High resolution spectra indicate strong spikes superimposed on Gaussian shaped spectra which must be caused by partial reflection.

It appears reasonable that partial reflection also should be considered to explain VHF radar signals (at quasi-vertical beam pointing) from the stratosphere and mesosphere. According to considerations on transhorizon propagation (Beckman and Spizzichino, 1963), the most appropriate mechanism responsible for VHF radar echoes from the troposphere, stratosphere and mesosphere is proposed to be a composition of (1) specular (partial) reflection at rather stable stratified layers, (2) diffusive reflection at rough layers and (3) scattering from turbulence. It seems to be a serious task to clearly separate in observations these three contributions.

Since partial or diffusive reflection often appears to occur, VHF radar systems, due to the longer wavelengths; are more favorable than higher frequency radars to detect these layers in the atmosphere and to make use of the strong radar echoes to investigate the dynamics of the lower and middle atmosphere.

References

- Beckman, P., Spizzichino, A.: "The Scattering of Electromagnetic Waves from Rough Surfaces". Pergamon Press, 1963
- Czechowsky, P., Klostermeyer, J., Röttger, J., Rüster, R., Schmidt, G., Woodman, R.F.: "The SOUSY-VHF-Radar for tropo-, strato- and mesospheric sounding", Proc. 17th Conf. Radar Meteor., pp. 349-353, Boston: Am. Meteor. Soc. 1976
- Gossard, E.E.: "Refractive index variance and its height distribution in different air masses", Radio Science **12**, 89-105, 1977
- Green, J.L., Warnock, J.M., Winkler, R.H., VanZandt, T.E.: "A sensitive VHF radar for the study of winds, waves and turbulence in the troposphere, stratosphere and mesosphere", Proc. 16th Conf. Radar Meteor., 313-315, Boston: Am. Meteor. Soc., 1975
- Rastogi, P.K., Bowhill, S.A.: "Gravity waves in the equatorial mesosphere", J. Atmospheric Terrest. Phys., **38**, 51-60, 1976
- Röttger, J., Czechowsky, P.: "VHF-radar echoes from the troposphere and stratosphere", Kleinheubacher Berichte **21**, 1978 (in press)
- Röttger, J., Liu, C.H.: "Partial reflection and scattering of VHF radar signals from the clear atmosphere", submitted to Geophys. Res. Letters, 1978
- Tatarskii, V.I.: "The effects of the turbulent atmosphere on wave propagation", Report TT-68-50464, Springfield, Va.: Nat. Techn. Inform. Service, U.S. Dept. of Commerce, 1971
- Woodman, R.F., Guillen, A.: "Radar observations of winds and turbulence in the stratosphere and mesosphere", J. Atmospheric Sci., **31**, 493-505, 1974

Letter to the Editor

Scale Factor Determinations of a LaCoste and Romberg Gravimeter Model D

Peter Steinhauser

Institut für Meteorologie und Geophysik, Universität Wien, Hohe Warte 38, A-1190 Vienna, Austria

Key words: Gravimetry – LCR model D “microgal” gravimeter – Non-linearity of scale factor.

LCR gravimeters model D have a resolution in the microgal-range, which exceeds the resolution of usual field gravimeters almost by one order or magnitude. The model D has only a scale range of 200,000 units, with 1,000 unit being equivalent to approximately 1 mgal. The scale ranges of less sensitive gravimeters cover some times many thousands of mgals. In the later case the scale factors are often not linear within these broad scale ranges. For the model D gravimeter the manufacturer claims that the scale factor is constant for the complete scale range, which seems to be reasonable because of its small size. However, this assumption should not be generalized. When, during field work resetting of the D-9 gravimeter was required, systematic deviations from the gravity differences which have been measured previously with other scale ranges occurred. Because this seemed to indicate a nonlinearity of the scale factor, systematic tests were performed between two gravity stations situated in the departmental building Hohe Warte, Vienna, and at the top of the Kahlenberg (near Vienna) respectively. A series of measurements at five different range settings was carried out. At each station at least three readings were taken. After eliminating drift and tidal effects the following scale values resulted:

Reading Hohe Warte	Reading Kahlenberg	Difference
57,186	20,188	36,998
90,332	53,323	37,009
120,018	82,989	37,029
150,175	113,135	37,040
174,837	137,785	37,052

(All values are given in scale units)

Obviously the scale factor of the gravimeter decreases when the reading increases within the scale range. The following equation is obtained by least square fitting:

$$F = 1,12356 \frac{1}{1 + 6,3595 \cdot 10^{-6} \cdot S}$$

(F = Scale factor [mgal/scale unit], S = Scale value.)

In comparison with the non-linear scale factor the use of a constant one would cause errors up to 72 μ gal. Thus, the nonlinearity of the scale factor of the LCR-D 9 is rather large, compared to an equivalent range of LCR gravimeters model G. Therefore LCR gravimeters model D should be checked for nonlinearities when high precision measurements have to be performed.

Acknowledgement. This investigation was sponsored by the Austrian Academy of Sciences, Geophysical Commission.

Received December 23, 1977; Revised Version February 3, 1978

Book Reviews

J. Coulomb, G. Jobert (Herausgeber): **Traité de géophysique interne. Teil II: Magnétisme et géodynamique.** Paris-New York-Barcelona-Mailand: Masson, 1976. 600 Seiten, 206 Abbildungen. ffr 295. —

Die hier zu besprechende Veröffentlichung bildet den zweiten Band einer umfassenden Einführung in die Physik des Erdkörpers. Während der erste Band unter dem Motto „Seismologie und Schwere“ steht, ist der zweite Band den Themen „Magnetismus und Geodynamik“ gewidmet. Wie schon beim ersten Band ist der Themenkreis wesentlich weiter gespannt, als es die stichwortartige Charakterisierung vermuten läßt. Das Gesamtwerk ist ein „Vielmännerbuch“, an dem Wissenschaftler aus Forschung und Praxis mitgewirkt haben. Beide Bände sind durchgehend in 41 Kapitel gegliedert. Die ersten acht Kapitel des zweiten Bandes befassen sich mit den elektromagnetischen Phänomenen des Erdkörpers. Am Beginn steht die klassische Analyse des erdmagnetischen Feldes. Die Kartendarstellungen des Gesamtfeldes beziehen sich auf den Zeitraum 1965. Es folgt eine Darstellung des Gesteins-, Archäo- und Paläomagnetismus, also einer klassischen Domäne der französischen Geophysik. Die Entstehung der äußeren und der inneren Anteile des Feldes wird in getrennten Kapiteln behandelt. Für den „Nicht-Magnetiker“ ist vor allem die zusammenfassende Darstellung der unterschiedlichen Dynamotheorien hilfreich. Abschließend werden Interpretationsverfahren, die der Auffindung von Untergrundstrukturen dienen, kurz umrissen.

Der Mittelteil des Bandes macht den Geophysiker in sehr knapper Form mit den Forschungsergebnissen der Nachbardisziplinen (Mineralogie, Petrologie, Stratigraphie, Tektonik, Vulkanologie, absolute Altersbestimmung) bekannt. Als Basis des sehr willkürlich abgegrenzten Gebietes der „Geodynamik“ dient im dritten Teil des Bandes eine Beschreibung des physikalischen Zustandes von Mantel und Kern. Die eigentliche Geodynamik besteht aus Kapiteln über Plattentektonik und Erdwärme.

Der „Traité“ ist wesentlich mehr als ein Standardlehrbuch der Physik des Erdkörpers. Er ist vor allem auch ein zuverlässiges Nachschlagewerk für die zahlreichen Gebiete unserer Wissenschaft. Für den Geophysiker, der das Französische nicht als Muttersprache beherrscht, bieten die beiden Bände eine gute Möglichkeit, sich in relativ kurzer Zeit französische Fachausdrücke und wissenschaftliche Redewendungen anzueignen.

G. Schneider, Stuttgart

D.F. Merriam (Herausgeber): **Random Processes in Geology.** Berlin-Heidelberg-New York: Springer, 1976. 168 Seiten, 64 Abbildungen, 16 Tabellen. DM 34,50 — US \$ 15.20.

Die Veröffentlichung enthält 11 Vorträge, die im Rahmen eines Kolloquiums über Zufallsprozesse in der Geologie September 1972 in Montreal (Kanada) gehalten worden sind. Den Geophysiker dürften vor allem die beiden Beiträge über statistische Modelle vulkanischer Tätigkeit interessieren. Dabei werden in einem Artikel verschiedene Abläufe der Aktivität mit MARKOW-Modellen verglichen. Die zweite Arbeit beschäftigt sich mit vulkanischer Bebenaktivität. Die bei der tektonischen Seismizität zu beobachtende Konzentration der Aktivität in Raum und Zeit wird hier bei den vulkanischen Beben durch die Abweichung von einem POISSON-Prozeß verdeutlicht. Die übrigen Vorträge behandeln die statistische Anordnung von Entwässerungssystemen, Fragen der Sedimentation und allgemeine Probleme bei der Behandlung geologischer Fragestellungen mit Methoden der mathematischen Statistik. Das Gebiet der Zufallsprozesse ist innerhalb der angewandten Statistik ein noch relativ junger Arbeitsbereich. In den verschiedenen Aufsätzen wird gezeigt, daß man mit Zufallsprozessen häufig eine bessere Modellanpassung erreichen kann als mit zeit- bzw. ortsunabhängigen Verteilungen.

G. Schneider, Stuttgart

R. Meissner und L. Stegena: Praxis der seismischen Feldmessung und Auswertung. Studienhefte zur Angewandten Geophysik 1, Berlin-Stuttgart: Gebrüder Borntraeger, 1977. 275 Seiten mit 197 Abbildungen und 7 Tabellen. DM 58,60.

Mit vorliegendem Buch erschien nunmehr der erste Band einer Reihe „Studienhefte zur Angewandten Geophysik“. War die Praxis der seismischen Feldmessung und ihre Auswertung bedauerlicherweise bis in die jüngste Zeit hinein an vielen Hochschulinstituten ein „Stiefkind“ – vielleicht, weil es an geeignetem Lehrmaterial fehlte – so findet man hier nun eine lückenlose Darbietung dieses Stoffgebietes. Daß hier ein ganz aktuelles Buch zur Verfügung steht, mag auch dem Bestreben, Hochschulforschung und Industriegeophysik einander zu sinnvoller Ergänzung näherzubringen, sehr nützlich sein.

Durch seine klare Gliederung und durch didaktisches Geschick der Autoren, eine moderne „Angewandte Geophysik“ darzustellen, ohne Spezialkenntnisse vorauszusetzen, eignet sich das Buch für Vorlesung und Selbststudium gleichermaßen ideal. Der Rezensent empfand es glücklich gelungen, daß keinerlei Thematik, die in der jetzigen seismischen Forschung und Exploration aktuell ist, fehlt; obwohl manche Abschnitte z.B. über Migration knapp gefaßt sind – dies aber mit voller Berechtigung, denn in Ausführlichkeit gehört es in eines der von den Herausgebern für die Zukunft angekündigten Bände („Theoretische Grundlagen der Angewandten Seismik“).

Beginnend von den einfachen physikalischen Grundlagen der Feldseismik werden z.B. die Schußtechniken und Geophonbündelungen, das Stapeln, statische und dynamische Korrekturen und die Geschwindigkeitsbestimmung behandelt. Dies aber nicht, ohne die dem Praktiker begegnenden Störungen verschiedenster Art (Bodenunruhe, Oberflächenwellen, Schall, Multiple Reflexionen u.s.f.) zu diskutieren.

Dann wird der Leser an die aktuellen Auswertetechniken, die die Einführung der Digitaleismik mit sich brachte, von Grund auf vertraut gemacht: digitale Filter, Konvolution und Dekonvolution seien nur einige Stichworte hierzu.

Schließlich sei erwähnt, daß nicht nur die Reflexionsseismik, sondern gleichermaßen auch die Refraktionsseismik abgehandelt werden.

Bedauerlich bleibt jedoch, daß die zahlreichen, didaktisch gut ausgewählten Seismogrammeispiele nur von einem einzigen der deutschen Unternehmen, die solche Beispiele hätten liefern können, verwendet wurden. Gerade für ein Buch, welches bevorzugt für die Hand des Studenten gedacht ist, hätte man sich „Firmenneutralität“ gewünscht – oder man hätte die Firmenherkunft an der einzelnen Abbildung fortlassen sollen; es wird ja bereits im Vorwort der Herausgeber auf die Quelle des Bildmaterials verwiesen. Leider ist auch der Preis des Buches auf einem Niveau, der vielleicht manchen Studenten vor dem eigenen Erwerb des Buches zurückschrecken lassen mag.

L. Engelhard, Braunschweig

Horst Falke: Anlegung und Ausdeutung einer geologischen Karte, VIII, ISBN 3 11 001624 9 Berlin-New York: Walter de Gruyter, 1975, 224 Seiten, 157 Abbildungen und 7 farbige Karten. DM 48,—.

Das vorliegende Buch ist aus der Sicht des Geophysikers, der oftmals keine oder nur geringe geologische Kenntnisse hat, eine erfreuliche Bereicherung: Als Benutzer geologischer Karten fehlt ihm oft das Gefühl, welche Aussagekraft er der Karte im Hinblick auf seine Messungen zubilligen darf. Gerade hier wird diese Lücke geschlossen, weil Falke es glänzend versteht, die Entstehung einer geologischen Karte und die möglichen geologischen Strukturen des Untergrundes, wie sie sich auf der „Bildfläche“, also der Erdoberfläche zeigen, darzustellen. Weder werden größere geologische noch sonstige Spezialkenntnisse vorausgesetzt – stattdessen wird auf reichhaltige Beispiele Wert gelegt. So zeigt dies Buch – welches sich bestens zum Selbststudium eignet (jeder Abschnitt schließt mit einem Katalog von Übungsfragen) – wie eine geologische Karte tektonische und geologische Geschichte gleichermaßen widerspiegeln kann, wenn man sie nur zu lesen versteht.

Der Hauptteil des Buches behandelt „Die geologische Karte 1:25000 (GK 25) und ihre Ausdeutung“ und hier liegt das Hauptinteresse des Geophysikers. Daneben wird aber auch das „Erstellen einer geologischen Karte“ durch den Feldgeologen dargestellt – geschrieben mit zahlreichen praktischen Hinweisen, die dem Geophysiker als Benutzer einer geologischen Karte vielleicht nicht direkt betreffen, ihm aber mindestens einen guten Einblick in die Arbeit des Kollegen der Nachbardisziplin geben.

L. Engelhard, Braunschweig

Norman H. Ricker: Transient Waves in Visco-Elastic Media. Developments in Solid Earth Geophysics; 10. Amsterdam: Elsevier Scientific Publishing Company, 1977, pp. X+278, 121 figures, 7 pages graphs. US \$ 48.95/Dfl. 120.00.

Beim ersten Durchlesen von gut zwei Dritteln dieser Monographie ist man versucht zu fragen, warum im Jahre 1977 ein Buch gedruckt wurde, das sich im wesentlichen mit der Lösung von reflexionsseismischen Problemen der 40er Jahre beschäftigt. Spätestens aber bei den letzten sieben Seiten des Hauptteils, eines mit „Epilogue“ überschriebenen Kapitels, blättert man zurück und beginnt, die Darstellung ein wenig mit anderen Augen zu sehen. Der Buchtitel sollte den an die heute übliche rheologische Terminologie gewöhnten Leser nicht irreführen: Tatsächlich werden Wellen in *firmoviskosen* Medien behandelt, die dem Kelvin-Körper entsprechen, und nicht solche in Maxwell- oder Burgers-Körpern, was der Titel nahelegen könnte. Doch ist leider der Sprachgebrauch in der Literatur nicht ganz einheitlich.

Angesichts der Beobachtung, daß seismische Wellen mit zunehmender Frequenz zunehmend stark absorbiert werden, wird Ricker die Unzulänglichkeit der klassischen Theorie elastischer Wellen zur Beschreibung tatsächlicher Wellenformen bewußt; er wendet sich der Wellengleichung von Stokes zu, die Energiedissipationen aufgrund innerer Reibung des viskosen Typs einschließt. Anlaß war die Aufgabe der 40er Jahre, die Qualität der Reflexions-Seismogramme zu verbessern. Ricker ging konsequent vor: Um willkürliches Experimentieren zu vermeiden, stellte er die Frage nach der physikalischen Natur der Wellenausbreitung und berechnete die Form der Wellenimpulse als Funktion der Zeit bzw. Entfernung vom Schußpunkt aufgrund von Lösungen der Stokes'schen Wellengleichung; keine leichte Aufgabe bei einer Differentialgleichung dritter Ordnung. Diese „wavelet-Theorie“ bewährte sich erstaunlich gut bei den anschließenden Feldexperimenten im Pierre shale im östlichen Colorado.

Man wird zunächst einige Fragen stellen, z.B. ob die Stokessche Wellengleichung, d.h. der Kelvin-Körper, die Eigenschaften der Gesteine als Wellenleiter tatsächlich zutreffend beschreibt. Sagt doch Bullen in seiner „Introduction to the Theory of Seismology“ dem Sinne nach, daß die dem Kelvin-Körper entsprechende Differentialgleichung nicht ausreicht, eher die erweiterte Differentialgleichung für die elastische Nachwirkung. Letztere führt jedoch auf Wellen mit stets scharfem Einsatz im Gegensatz zu den Ricker-wavelets, die übereinstimmend in Beobachtung und Theorie weich einsetzen. Die von Bullen bevorzugte Reihenanzordnung von Kelvin- und Hooke-Körper müßte hohe Frequenzen gut durchlassen, wogegen damalige und heutige Beobachtungen, insbesondere der Reflexionsseismik, sprechen. Das Rickersche Buch regt somit zum erneuten Nachdenken über ein adäquates rheologisches Modell an, zumindest für Sedimentgesteine; die exzellente Übereinstimmung von Messung und Theorie gibt jedenfalls der Stokesschen Wellengleichung und damit dem Kelvin-Körper den Vorzug. Dabei möchte Ricker diese Gleichung nicht auf die Seismik beschränkt sehen, sondern betont dezidiert ihre seiner Meinung nach nicht genügend beachtete Bedeutung für Wellenausbreitungsprozesse in anderen Festkörpern, Flüssigkeiten und Gasen mit einem interessanten Beispiel im Kapitel „Epilogue“, wo es ihm gelingt, durch eine statistisch-theoretische Behandlung der Schallausbreitung im einatomigen Gas im Nachhinein die Stokessche Wellengleichung zu verifizieren.

Die wavelet-Theorie führte Ricker Ende der 40er Jahre zur Entwicklung seines wavelet-Kontraktors; er hatte damit frühzeitig die Bedeutung der Inversen Filterung bei der Verbesserung der Reflexionsseismogramme erkannt, wenn auch die Beschreibung der mit damaligen elektronischen Hilfsmitteln gebauten Geräte und der hiermit erzielten Ergebnisse nur noch von historischem Interesse sein dürften. Doch wenn auch die heutige Digitaltechnik und die vor allem auf Norbert Wiener zurückgehenden Verfahren mit jenen frühen Versuchen nicht verglichen werden können: Ricker hat seinerzeit wesentliche Impulse gegeben und vor allem auch die damals viel diskutierte Frage nach dem bevorzugten Auftreten des Frequenzbandes von ca. 30–60 Hz in der Reflexionsseismik klären können, ebenso die schlechte Energieabstrahlung beim Schießen im Sand, die er, wie auch seine Laborexperimente an einer Sandpresse bestätigten, auf die Zertrümmerungsarbeit der Sandkörner zurückführte. Interessant ist ferner das Kapitel über die Natur der inneren Reibung. Die theoretisch berechnete Verbreiterung der wavelets als Funktion der Entfernung erlaubt die Bestimmung der Absorption; der Vergleich mit den Geländebeobachtungen ergibt, daß sie mit der zweiten Potenz der Frequenz erfolgt im Gegensatz zu Ergebnissen anderer Autoren, die eine Proportionalität der Dämpfungskonstanten mit der ersten Potenz der Frequenz angeben. Zur Klärung dieser Diskrepanz kann Ricker mittels sorgfältig durchgeführter Laboruntersuchungen an einem Torsionsvibrator zeigen, daß die Schwingungsdämpfung bei großen Amplituden mit der

ersten Potenz, jedoch bei sehr kleinen Amplituden wie in der Seismik mit der zweiten Potenz der Frequenz erfolgt.

Das Buch enthält im Anhang Computerausdrucke von Tafeln und dazugehörige Kurvendarstellungen der Ricker-wavelets für verschiedene Entfernungen von der Impulsquelle als Grundlage für vergleichende Untersuchungen der Wellenausbreitung in realen Medien.

Ricker behandelt in seiner Monographie ausschließlich eigene Arbeiten; auf die neuere Entwicklung wird nicht eingegangen. Wer die Materie nicht voll überblickt, könnte meinen, daß seit dem Ende der 50er Jahre nichts wesentliches mehr geschehen sei, ein Eindruck, der sich beim Lesen des einleitenden Kapitels noch verstärkt.

K. Strobach, Stuttgart

W.D. Means: Stress and Strain, Basic Concepts of Continuum Mechanics for Geologists. New York-Heidelberg-Berlin: Springer, 1976. 339 Seiten, 223 Abbildungen. DM 36,20 – US \$ 14,80.

Als Hans Cloos im Jahre 1936 seine international bekanntgewordene „Einführung in die Geologie“ veröffentlichte, bedeutete die Einschaltung eines Kapitels über die mechanischen Grundlagen der Erdkrustenbewegungen noch eine Besonderheit für ein Lehrbuch der allgemeinen Geologie. Heute hat sich dagegen die Einsicht sehr weitgehend durchgesetzt, daß man bei der Behandlung von Fragen der Gesteinsmechanik kaum noch einer quantitativen Analyse ausweichen kann. Das gilt nicht nur für die wissenschaftlichen Probleme der allgemeinen Geologie sondern auch für die Anwendungsbereiche der Geologie. Die Darstellung des Stoffes erfolgt in vier Teilen und 23 Abschnitten. Der erste Teil ist der Hinführung zum Problembereich „Deformationsarten in der Geologie“ gewidmet. Im Teil II wird der Spannungstensor als Ursache von Gesteinsdeformationen behandelt. Teil III beschäftigt sich mit der Wirkung mechanischer Spannungen auf Gesteine, wie sie sich in den unterschiedlichen Deformationsarten ausdrückt. Neben den elastischen Deformationen finden vor allem auch die für Veränderungen in der Erdkruste wichtigen „endlichen“ Deformationen entsprechende Berücksichtigung. Im Teil IV wird das zwischen Spannung und Deformation stehende Materialverhalten behandelt. Das letzte Kapitel ist der Energiefrage bei Deformationen gewidmet.

Die Darstellung ist klar und übersichtlich, was durch einen heute kaum noch anzutreffenden Aufwand im Satz erreicht wird. Das Werk ist als Übungsbuch besonders wertvoll, da es in einem 50 Seiten umfassenden Anhang die Lösungen aller gestellten Aufgaben bringt. Dem Geophysiker bietet das Buch die Möglichkeit geologische Fragen unter einem physikalischen Aspekt zu betrachten.

G. Schneider, Stuttgart

B. Le Méhauté: An Introduction to Hydrodynamics and Water Waves. Springer Study Edition, Berlin-Heidelberg-New York: Springer, 1976. 323 Seiten, 231 Abbildungen, 12 Tabellen, DM 60,60 – US \$ 24,80.

Die Darstellung, als Einführungstext für Studenten gedacht, besticht durch ihre Klarheit. Das bezieht sich einmal auf die Gliederung des Textes und auf die Qualität der Abbildungen, zum anderen aber auch auf die physikalische Interpretation der vor allem bei Strömungsproblemen recht umfangreichen Gleichungssysteme. Der Autor ergänzt die Gleichungen durch eine physikalische Interpretation ihrer einzelnen Bestandteile. Das in drei Teile und 18 Kapitel eingeteilte Werk bietet am Ende eines jeden Kapitels Übungsaufgaben an, für die man zu einem guten Teil Antworten und Lösungen in einem gesonderten Anhang findet.

Teil I beschäftigt sich mit der Aufstellung von Gleichungen, die der Beschreibung von Strömungen dienen. Dabei wird sowohl die Bewegung von Flüssigkeiten in offenen Gerinnen wie auch die in porösen Medien berücksichtigt. Im Teil II wendet sich der Autor der Anwendung der Strömungsgleichungen auf praktische Probleme zu. Die eingehende Behandlung von Grenzschichtproblemen dürfte für viele Geophysiker besonders interessant sein. Im Teil III werden die Wasserwellen und damit ein wichtiges geophysikalisches Aufgabengebiet behandelt. Die verschiedenen Ansätze der theoretischen Behandlung von Wellenproblemen werden in tabellarischer Form übersichtlich vorgestellt. Im einzelnen wird auf die unterschiedlichen Lösungswege, die gegenüber dem allgemeinen Ansatz eine durch Einschränkungen bedingte erleichterte Behandlung erlauben, eingegangen: Wellen kleiner Amplitude, Wellen mit endlicher Amplitude, lange Wellen. Das Buch ist in Druck- und Herstellungstechnik hervorragend.

G. Schneider, Stuttgart

Variations in the Auroral Spectrum at the Latitude of the Polar Cleft

K. Henriksen¹, B. Holback², and G. Witt³

¹ Nordlysobservatoriet, Tromsø, Norway

² Uppsala Ionospheric Observatory, Uppsala, Sweden

³ Department of Meteorology, University of Stockholm, Stockholm, Sweden

Abstract. During the period November 23 to December 7, 1975 simultaneous photometric and spectrometric auroral measurements were performed for 250 h on the latitude of the polar cleft from Ny-Aalesund. The auroral green and red lines were observed all the time. During certain periods around local geomagnetic noon the intensity of the red line increased even when the intensity of the green line decreased. This was taken as an optical signature of the polar cleft. In the spectral range between the auroral green line and the hydrogen Balmer line H_{β} the NI doublet at 5200 Å was the dominating emission, occurring in 65% of the spectra, especially strong within the polar cleft. The peak 5200 Å intensity of averaged spectra seldom exceeded 100 R whereas the peak of 6300 Å was several kR.

The H_{β} was found in 30% of the averaged spectra. Its intensity was mostly below 20R, and showed a weak correlation with the degree of “completeness” of the cleft. The 5200 Å and 6300 Å emissions are generated mainly by low-energy electron precipitation at high altitudes where the emission rate can be comparable with the quenching rate of the long-lived, metastable emitting states. Low-energy protons have a low efficiency for generating H_{β} photons which is believed to be the main reason for the low H_{β} intensity.

Key words: NI 5200 Å emission – Intensity ratios – Production and quenching rates – Dayside aurora – Polar cleft.

1. Introduction

The only accessible site where the sky is dark during the winter and yet near the locus of the daytime aurora is found on Svalbard. There Norway operates an auroral research station in Ny-Aalesund (78.9° N, 11.9° E, geographic, and 75.9° N, 114.7° E corr. geomagnetic coordinates) (Fig. 1). Ny-Aalesund is supposed to traverse the polar cleft at low and moderate magnetic activity (Feldstein,

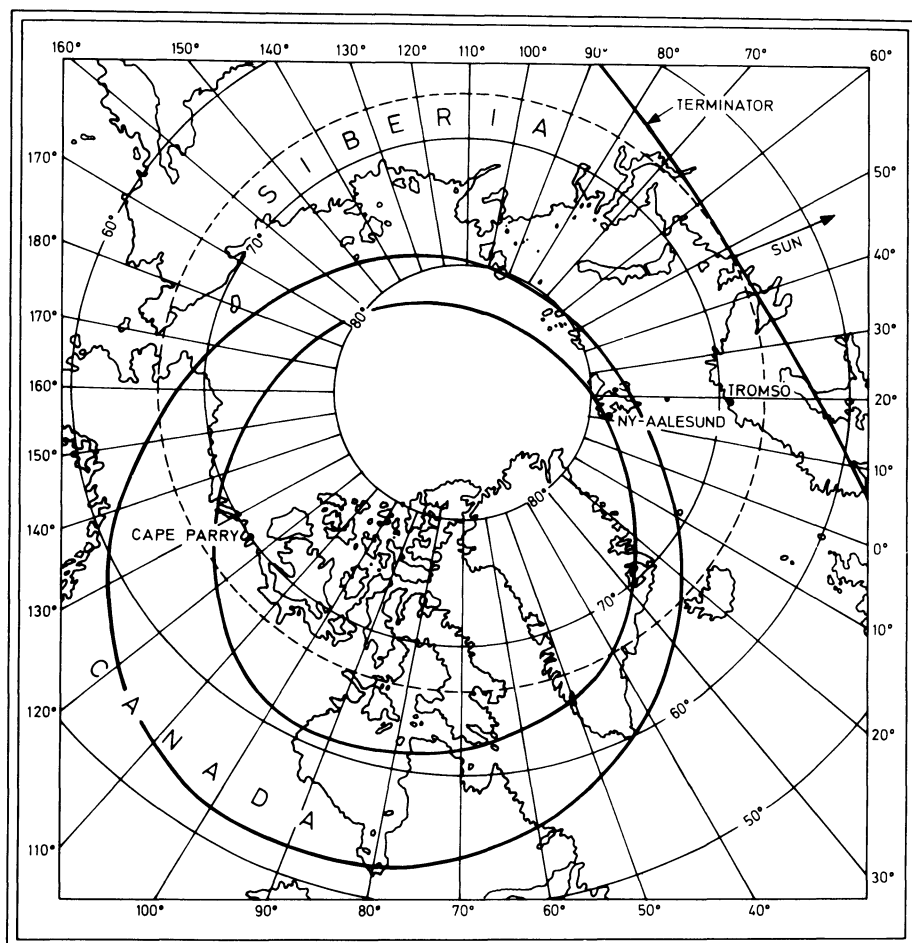


Fig. 1. The north polar region showing the sunrise-sunset line (terminator) at winter-solstice with respect to Ny-Aalesund at local geomagnetic noon and an approximate location of the auroral oval for a moderately disturbed period (Feldstein, 1966)

1966; Starkov and Feldstein, 1968). Local magnetic noon is at 0845 UT. With southward interplanetary magnetic field the latitudinal extent of the cleft region can be relatively long, $\Delta\lambda \sim 12$ h (Zaitzeva and Pudovkin, 1976), and Ny-Aalesund is expected to be within the cleft for several hours per day, depending on the level of geomagnetic activity.

In conjunction with the International Magnetospheric Study an expedition to Ny-Aalesund was undertaken during the period November 20 to December 12, 1975. Auroral optical and radio drift measurements were coordinated with passes of ISIS-2, and the purpose of the campaign was to study the daytime aurora by simultaneous ground-based and space observations (Berkey and Harang, 1976). A complete data analysis is underway.

Ground-based photometric and spectrometric measurements were performed from November 23 to December 8. In this report characteristic auroral features obtained from analysis of photo- and spectrometer data will be given.

2. Measurements and Analysis

The instruments used in this work were one scanning spectrometer and five fixed interference filter photometers. The spectrometer, called SP4 and described elsewhere (Stoffregen et al., 1971), had a spectral resolution of 30 Å and made in 4 min one wavelength scan between 4800 Å and 5800 Å. The photometers were constructed to measure the auroral emissions at 4861 Å (H_{β}), 5577 Å, 6300 Å, and the continuum around 5400 Å, where the FWHM of the interference filters was 30 Å. The sensitivity threshold of SP4 and the photometers were 10 R and 1 R, respectively. The photometers had a circular field of view with a full angle of 5°, whereas the spectrometer had a rectangular field of view $\sim 0.3^{\circ} \times 3^{\circ}$. The measurements were performed towards zenith. The instruments were calibrated in absolute units, and the data stored on digital tape.

During this campaign the solar depression angle, S_d , was always greater than 9°, which allowed continuous measurements in the zenith direction. Local noon shifted from 1104 UT to 1109 UT during the period of observations, and then, especially in November, the shorter wavelength observations were disturbed by sunlight, multiply scattered by air molecules and aerosol particles in the lower atmosphere (Henriksen et al., 1977).

The sky background, originating from airglow, scattered sunlight and extraterrestrial sources, was estimated from the photometric measurements. Around local noon the contribution from multiply scattered sunlight dominated. The baseline of the recorded radiance was estimated for each quarter of an hour by taking the lowest value within that interval. The sampling rate of the radiance was one per second. This method of obtaining the sky background intensity on the wavelengths of the auroral green and red lines at 5577 Å and 6300 Å was less reliable since at Ny-Aalesund there was an almost continuous auroral activity during daytime. The obvious improvement here is the use of a polarizing filter which, however, was not available for the present expedition.

The sky background estimated for the day of November 24 is shown in Figure 2. Since S_d is less than 15°, the intensity maximum around local noon is due to multiply scattered sunlight. The deviations from a smooth curve are most probably caused by auroral enhancements. During the afternoon the intensity drops to a few R/Å, which is the estimated sky background value. The relatively high intensity before noon is explained by a misty sky in combination with weak moonlight.

A better estimate of the sky background as a function of S_d is obtained from a statistic analysis of all the data during the period (Henriksen et al., 1977). This is used in the present study to find the auroral intensities at 4861 Å, 5200 Å, 5577 Å, and 6300 Å.

A sample SP4 scan taken close to local noon is shown in Figure 3, showing the increase of the scattered light intensity towards shorter wavelengths. A

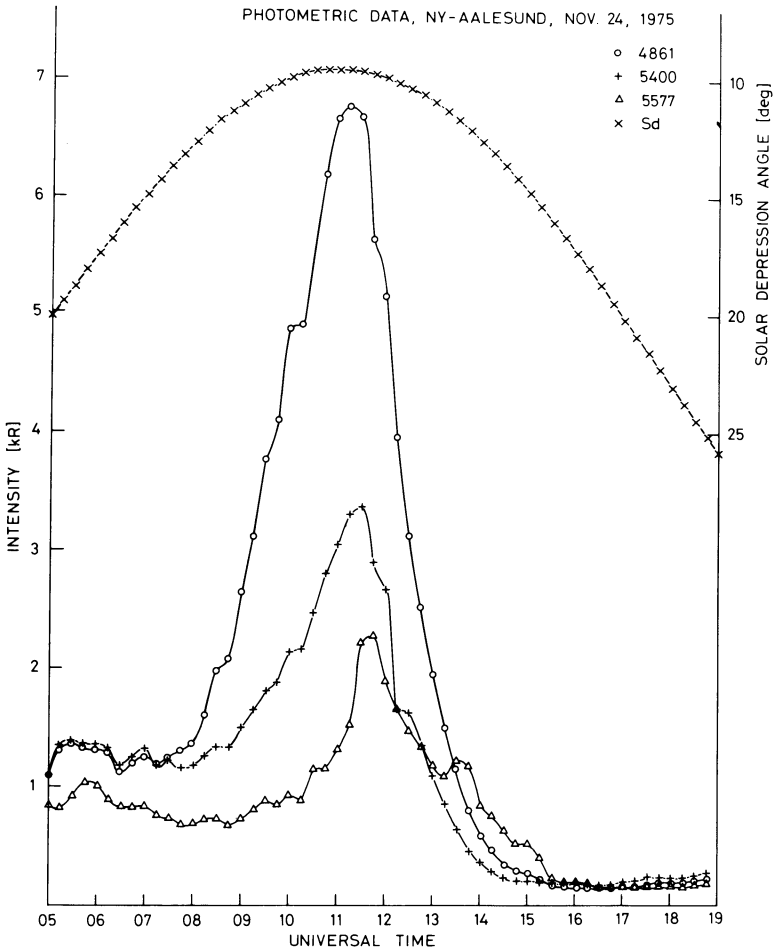


Fig. 2. The minimum intensity measured by photometers and calculations of Sd during daytime. The moon was low, and before 10 UT the sky was misty, clearing up later

small enhancement is seen at 5200 \AA , but from this example it is hard to decide its significance as a real spectral feature. Signal averaging has accordingly been performed adding eight scans together, giving one spectrum each 32 min, and then a significant emission appears at 5200 \AA . An example of the averaged data is shown in Figure 4. The strongest emissions between OI 5577 \AA and H_{β} 4861 \AA is then one at 5200 \AA , which is likely to be the $\text{NI}({}^4\text{S}-{}^2\text{D})$ doublet. This is supported by recent spectrometric measurements in Alaska by Sivjee and Romick (1976), which show that the only emission within 30 \AA of 5200 \AA is the N_2^+ first negative band (0,3) with P-bandhead at 5228 \AA . Preliminary spectrometric measurements in Tromsø give further evidence that the $\text{NI}({}^2\text{D})$ 5200 \AA emission with the doublet lines at 5198.5 \AA and 5200.7 \AA is a dominating auroral feature around 5200 \AA . In Figure 5 an example of these new measure-

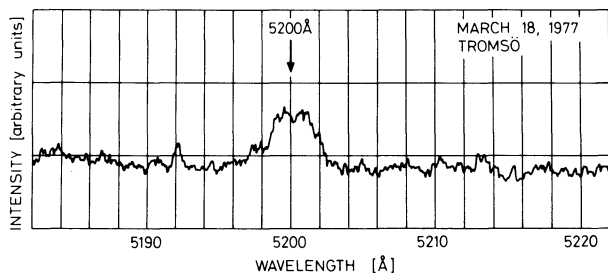


Fig. 5. Preliminary observation of spectral range around 5200 Å with a resolving power of 2 Å/cm. The NI 5200 Å doublet is on the point of being resolved. This observation is made with an improved spectrometer used in the January 78 campaign

ments is given. This recording is obtained at local geomagnetic midnight with the spectrometer at an elevation angle of 20°, pointing towards north into a diffuse auroral glow. Since the bulk of the 5200 Å emission originates from altitudes above 200 km, it is likely that the main emission region in this case was located within the polar cap, and therefore related to similar ionospheric conditions as in Ny-Aalesund.

The intensities of the auroral emissions at 4861 Å, 5200 Å, and 5577 Å are obtained from the averaged spectra, and the intensity of the 6300 Å emission is derived from the photometric measurements. The resulting averaged auroral intensities are presented and discussed below.

3. The Observational Results

A total of 467 averaged scans are analyzed, and the 5577 Å emission is clearly seen in every one. The averaged 5577 Å and 6300 Å intensities are plotted in Figures 6 and 7. For most of the time the 6300 Å emission is the strongest feature which is specific for high latitude aurora. Especially during intensity enhancements around local geomagnetic noon the 6300 Å line shows the strongest increase with maximum averaged intensities around 4 kR. The 6300 Å emission is regarded as an optical polar cleft signature (Shepherd et al., 1976). In several cases the 5577 Å intensity exceeds the 6300 Å intensity and must be due to bursts of more energetic electrons than those ~100 eV characteristic of the polar cleft (Doering et al., 1976). At lower latitudes, in the auroral zone, the 5577 Å emission is normally stronger than the 6300 Å emission, and the reversal of this intensity ratio seems to be inherent with the aurora in the polar cleft and the polar cap.

The NI 5200 Å emission is found to be a significant feature of the auroral spectrum of the polar cleft and within the polar cap. It is clearly identified in 302 averaged spectra. The 5200 Å intensity of the spectra has been plotted in Figures 8 and 9. Only in rare cases does the intensity exceed 100 R. The intensity variations of 5200 Å are similar to those of 6300 Å, but the intensities are more than ten times lower. On the basis of the similarity of the intensity

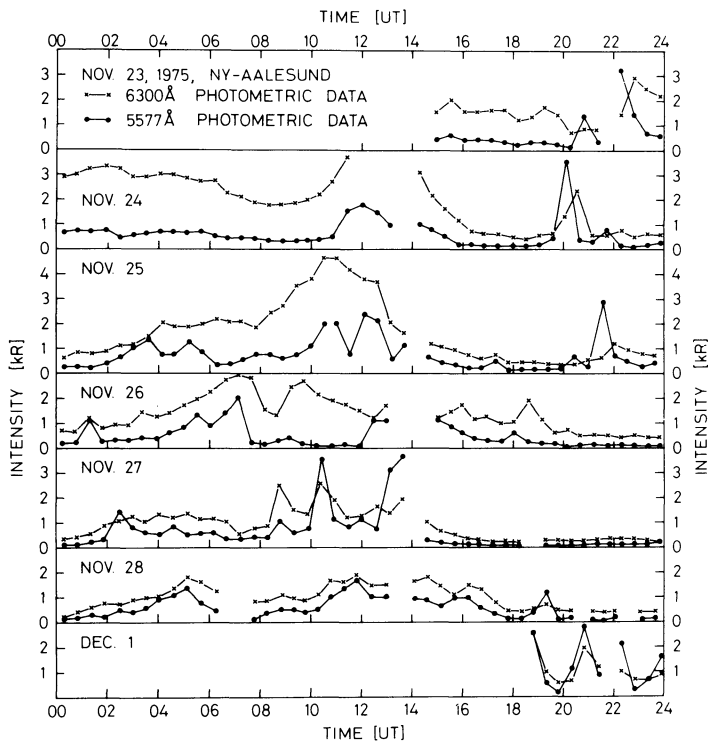


Fig. 6. Intensity of 5577 Å and 6300 Å obtained from spectrometer and photometer data for the period from Nov. 23 to Dec. 1, 1975 at Ny-Aalesund. The marks are at the start of each interval

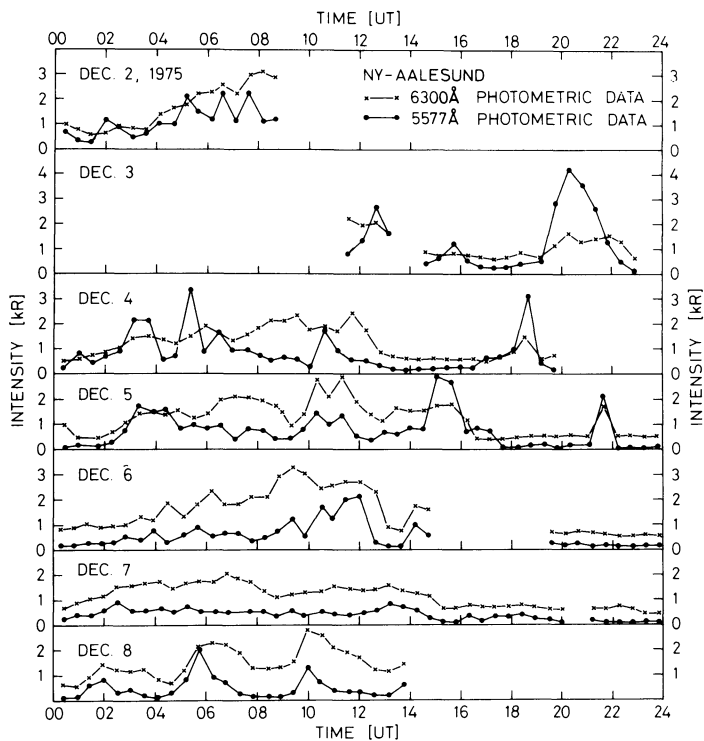


Fig. 7. Intensity of 5577 Å and 6300 Å obtained from spectrometer and photometer data for the period from Dec. 2 to Dec. 8, 1975 at Ny-Aalesund

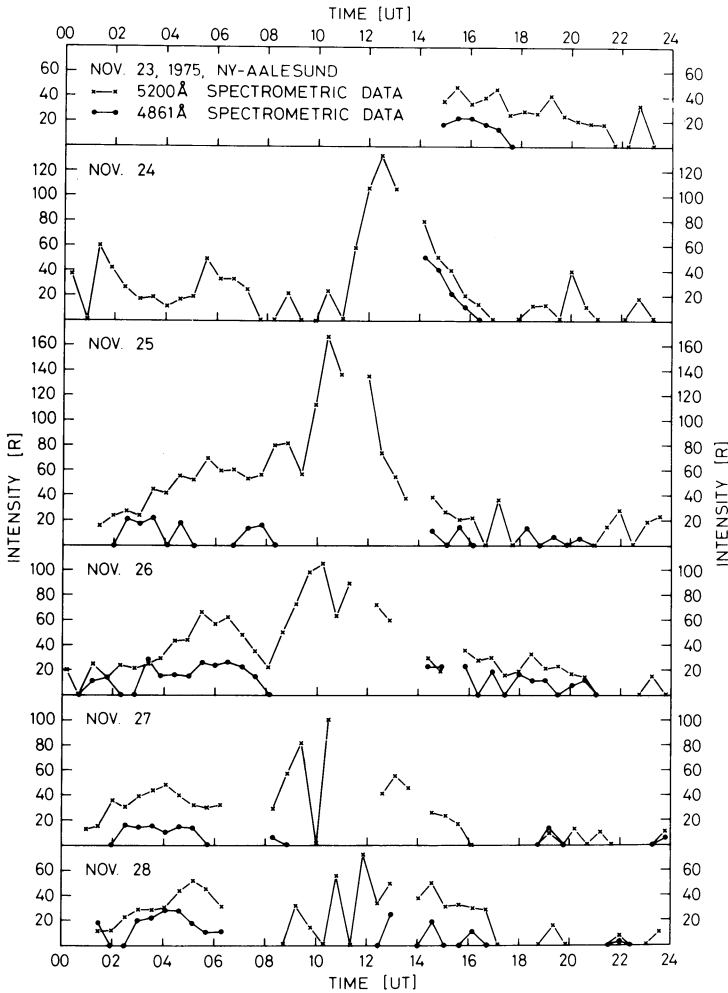


Fig. 8. Intensity of 5200 Å and 4861 Å obtained from averaged spectra for the period from Nov. 23 to Nov. 28, 1975. The observations were performed at Ny-Aalesund, using the SP4 spectrometer

variations and the quenching characteristics, the former can be regarded as another optical signature of the polar cleft.

The averaged H_{β} intensity is plotted in Figures 8 and 9 together with the 5200 Å measurements. From these diagrams it can be seen that the H_{β} in general is weaker than the 5200 Å emission. The averaged H_{β} intensity is mostly below 20 R and exceeds only a few times the 5200 Å intensity. The H_{β} emission can be identified in 140 of the averaged spectra. It occurs most frequently in the morning sector, and is therefore considered a less good indicator of the completeness of the polar cleft which is expected to be centered around geomagnetic noon. However, the increased background around local noon, at least in November, makes it difficult to detect H_{β} intensities of about 20 R.

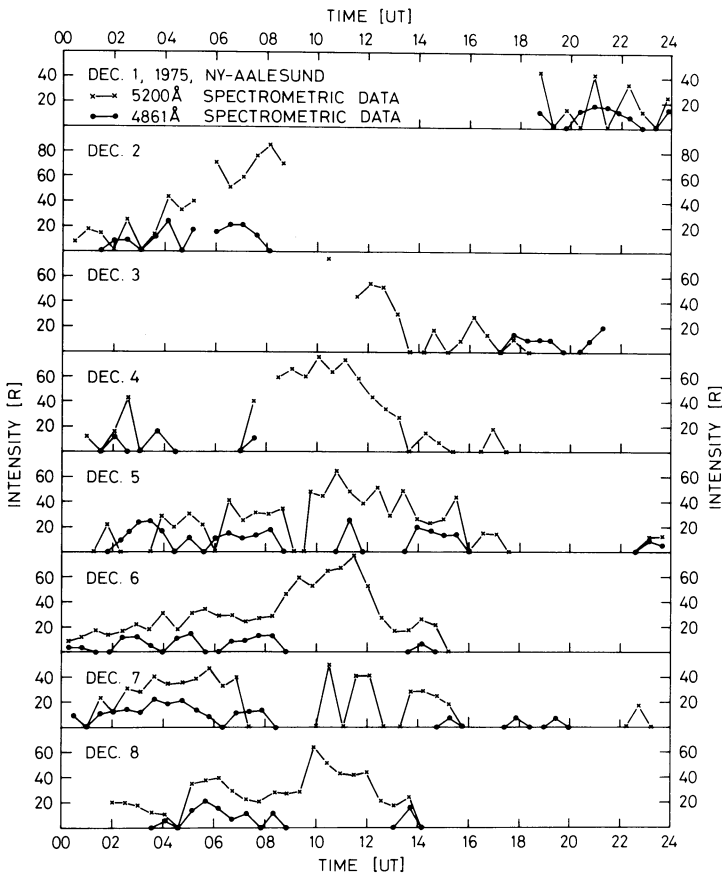


Fig. 9. Intensity of 5200 Å and 4861 Å obtained from averaged spectra for the period from Dec. 1 to Dec. 8, 1975 at Ny-Aalesund

The occurrence frequencies of this emission can accordingly be higher than our measurements show.

4. Excitation and Temporal Variations of the Observed Emissions

The H_{β} emission is due to an allowed transition in the neutral hydrogen atom. Within aurora the excited H atoms are mainly produced by neutralization of precipitated protons and collisional excitation of energetic neutral hydrogen atoms as the particles penetrate into the atmosphere (Omholt, 1971). Additional processes like dissociative excitation of hydrogen atoms by electron impact on H_2 and H_2O (Vroom and de Heer, 1969) are of minor importance. Therefore the H_{β} emission can be used as a monitor of proton precipitation.

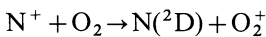
Using satellites, high fluxes of low energy protons with characteristic energy below 1 keV have been detected and interpreted as a signature of the polar

cleft (Heikkila et al., 1972; Doering et al., 1976). However, the efficiency of these protons to produce H_{β} is very low, less than 0.1 photon per proton (Eather, 1967). Therefore observed fluxes around 10^8 protons/(cm² sr keV s) (Sivjee and Hultqvist, 1975) may generate less than 10 R of H_{β} , indicating that the H_{β} output due to the characteristic polar cleft protons is small, and frequently escaped detection by our instruments.

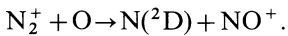
The auroral emissions at 5577 Å and 6300 Å are due to forbidden transitions in the oxygen atom, $O(^1D-^1S)$ and $O(^3P-^1D)$. The auroral excitation of the $O(^1D)$ atoms is probably a superposition of several direct and indirect processes, and because of its low excitation energy of 1.96 eV, the same and additional sources as for the $O(^1S)$ atoms (Henriksen, 1974) can contribute. The most important additional process can be dissociative recombination of NO^+ ions, and it may account for the dominating 6300 Å intensity.

In the twilight $O(^1D)$ atoms are also produced by photodissociation of O_2 in the Schumann-Runge continuum (Noxon and Johanson, 1972). During our campaign the photodissociative contribution to the observed 6300 Å intensity was of minor importance since Sd remained $>9^\circ$. The maximum photodissociative contribution is about 100 R, and therefore this excitation source can not account for the enhanced intensities around local noon.

The 5200 Å emission is due to the forbidden transition $N(^4S-^2D)$. The excitation energy of the 2D state is 2.38 eV, and a number of indirect processes can contribute (Strobel et al., 1976; Frederick and Rusch, 1977). These processes comprise dissociative excitation of N_2 by photons and fast electrons, dissociative recombination of NO^+ , and the reactions



and



The indirect excitation processes can be initiated both by electron and proton precipitation, and the observed 5200 Å, 5577 Å, and 6300 Å intensities may in principle also be partly generated by low-energy proton precipitation, but is considered to be of minor importance. A detailed analysis of the excitation sources is underway.

Examining the individual spectrometer scans which lasted for 4 min, one can frequently find intensity variations greater than 90% from scan to scan. These variations which are considered real indicate that the effective lifetime of the $N(^2D)$ atoms can be shorter than 4 min. The photometric records of 6300 Å contain 90% intensity variation within a few seconds, reflecting the magnitude of the effective $O(^1D)$ lifetime. The natural lifetime of the upper states of the 5200 Å, 5577 Å, and 6300 Å emissions are 26 h (Wiese et al., 1966), 0.8 s (Sinanoglu, 1970), and 110 s (Garstang, 1951), respectively.

In comparison the 5577 Å line can be considered as an instantaneous emission. When the effective lifetime is drastically shortened, the effect is due to collisional quenching which is analysed below.

5. Production Rate and Collisional Deactivation

When the atmospheric number density is sufficiently high, collisional deactivation, or quenching, is the main loss mechanism of the excited species. This mechanism is particularly important for ^2D and ^1D metastable states.

The height variation of the ratio between the emission and the quenching rates of excited atoms can be given by the expression

$$r_j = A_j / \sum_x d_f(x) n(x, h),$$

where $d_f(x)$ is the quenching coefficient for excited state j by species x with density $n(x, h)$ at height h . A_j is the sum of the radiative probabilities from state j .

Molecular nitrogen is regarded to be the dominating quenching agent of the $\text{O}(^1\text{D})$ state (Zipf, 1969). Using the N_2 number density $n(\text{N}_2, h)$ versus altitude from the CIRA mean atmosphere (1972), $A = 0.0091 \text{ s}^{-1}$ (Garstang, 1951), and $d(\text{N}_2) = 6 \cdot 10^{-11} \text{ cm}^3/\text{s}$ (Zipf, 1969), the ^1D effective lifetime altitude profile is calculated and illustrated in Figure 10. This figure demonstrates that around 200 km 95% of the excited $\text{O}(^1\text{D})$ atoms are quenched, and an effective lifetime of a few seconds appears.

The energy of the auroral electrons penetrating down to 200 km is estimated to be a few hundred eV (Rees, 1963; Banks et al., 1974), typical energies of polar cleft electrons. As the diurnal variation of the 6300 Å emission differs considerably from the behaviour of H_β , it gives further evidence that the main part of the $\text{O}(^1\text{D})$ excitation is due to low-energy electron precipitation. The collisional quenching of the $\text{O}(^1\text{S})$ atoms is below 10% above 150 km (Henriksen, 1975), and therefore the excitation rate of the $\text{O}(^1\text{D})$ atoms generally exceeds the excitation rate of the $\text{O}(^1\text{S})$ atoms by at least an order of magnitude within the polar cleft.

Recent investigations find that for the $\text{N}(^2\text{D})$ atoms, atomic oxygen is the major quenching agent between 140 km and 220 km with a rate coefficient of $1 \cdot 10^{-12} \text{ cm}^3 \text{ s}^{-1}$ (Strobel et al., 1976). Below 140 km collision with O_2 is the main loss process with rate coefficient of $7 \cdot 10^{-12} \text{ cm}^3 \text{ s}^{-1}$, and above 220 km the quenching rate due to thermal electrons becomes the dominating loss mechanism. Using the quenching rate $5 \cdot 10^{-10} (T_e/300)^{1/2} \text{ cm}^3 \text{ s}^{-1}$, the steady-state electron densities, and electron temperatures obtained by Frederick and Rusch (1977), the calculated electron quenching does not exceed the other loss mechanisms below 300 km. The effective lifetime τ and the emission to quenching ratio r have been calculated, using O , and O_2 number densities of the CIRA mean atmosphere (1972). The results are illustrated in Figure 11. The spectrometric records of 5200 Å infer that the effective lifetime can be at least as short as 4 min, a value which is obtained at 220 km. At this altitude less than 1% of the $\text{N}(^2\text{D})$ excitation leads to 5200 Å radiation.

Using our data, we estimate that in the cleft the production of the $\text{N}(^2\text{D})$ atoms generally is of the same order of magnitude as the production of the

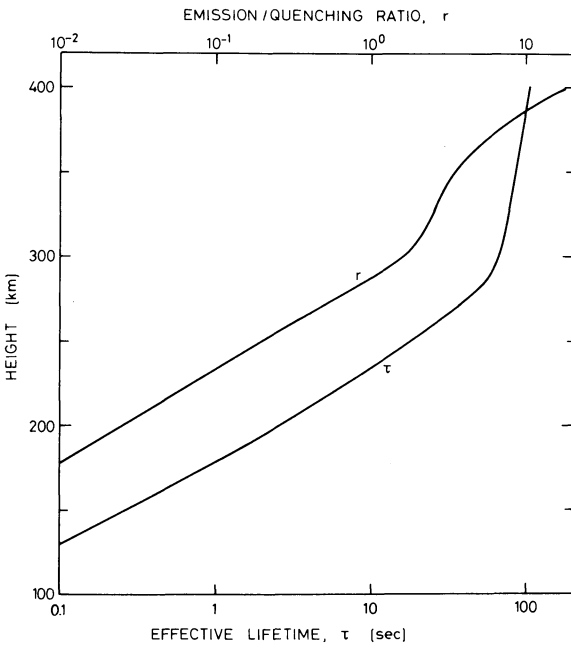


Fig. 10. The effective lifetime τ of the $O(^1D)$ atoms and the ratio of emission to quenching r versus height

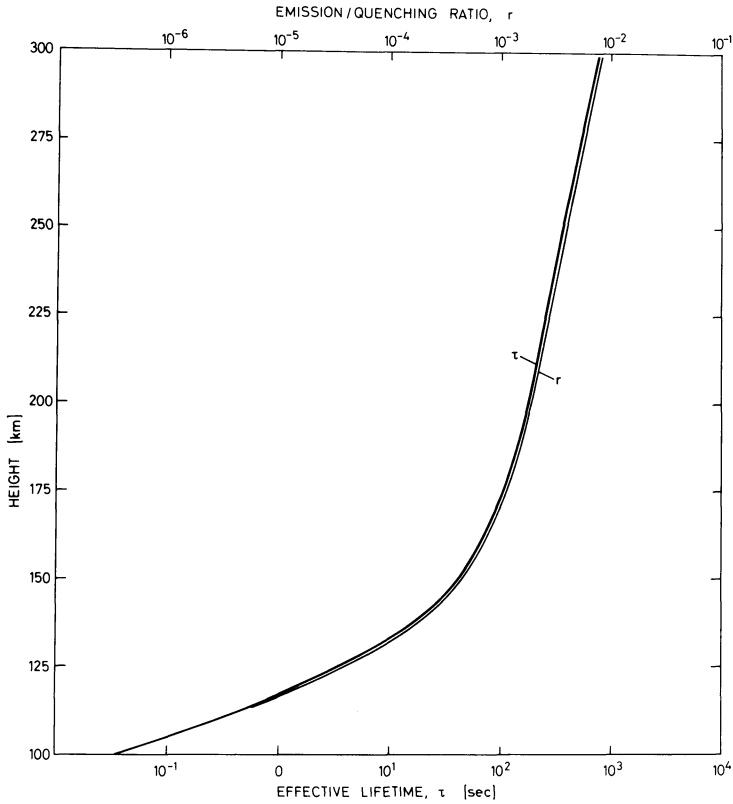


Fig. 11. The effective lifetime τ of the $N(^2D)$ atoms and the ratio of emission to quenching r versus height

O(¹S) atoms. The diurnal variation of the 5200 Å emission indicates that the main part of the production is due to low-energy electrons as for the O(¹D) species.

Direct rocket-measurements in the polar cleft show that the emission height of 6300 Å can be found between 200 km and 235 km, and 5200 Å is emitted from altitudes above 235 km (Shepherd et al., 1976). The results of these experiments are in accord with the present work.

6. Conclusions and Future Work

The above discussed enhancements of the 5200 Å and 6300 Å features lead to the conclusion that the [NI] emission is another optical signature of the polar cleft aurora. The H_β intensity is relatively low, and it does not seem to be correlated with the 5200 Å and 6300 Å emissions, and remains low around local geomagnetic noon when Ny-Aalesund is expected to be within the polar cleft. Satellite particle measurements indicate that the particle precipitation is dominated by low-energy protons and electrons, probably of direct-entry origin. The enhanced intensity of the 6300 Å line is due to low-energy electron precipitation, and the low-energy protons may give only minor contributions to both 5200 Å and 6300 Å intensities.

The present set of data is not sufficient to predict adequately the location of the auroral oval at various levels of geomagnetic activity. Improved spectrometric observations, however, can be used to map the location of the dayside auroral oval, the polar cleft, and to identify the coupling mechanisms between the ionosphere and the magnetosphere.

A new campaign to Ny-Aalesund took place during January 1978, with an extended spectrometric observation programme. An improved spectrometer with a spectral resolution of 2 Å was included for the purpose of identifying the possible HeI 5876 Å emission from zenith and its expected Doppler shift of a few Ångströms towards shorter wavelengths. The wavelength region 5876 Å ± 10 Å was systematically explored, and weak intensity enhancements identified.

Acknowledgements. The authors gratefully acknowledge the support of the Norwegian Polar Institute in setting the facilities at Ny-Aalesund to the disposal of the expedition, Dr. R. Armstrong for calculations of the solar depression angle, and Mr. R. Espenes for computer codes.

References

- Banks, P.M., Chappell, C.R., Nagy, A.F.: A new model for the interaction of auroral electrons with the atmosphere: Spectral degradation, backscatter, optical emission, and ionization. *J. Geophys. Res.* **79**, 1459–1470, 1974
- Berkey, F.T., Harang, O.E.: Norwegian-Canadian Svalbard expedition, winter 1975. *Polar Record* **113**, 171–173, 1976
- CIRA: COSPAR International Reference Atmosphere 1972. Berlin: Akademie-Verlag 1972
- Doering, J.P., Potemra, T.A., Peterson, W.K., Boström, C.O.: Characteristic energy spectra of 1- to 500-eV electrons observed in the high latitude ionosphere from Atmosphere Explorer C. *J. Geophys. Res.* **81**, 5507–5516, 1976

- Eather, R.H.: Auroral proton precipitation and hydrogen emissions. *Rev. Geophys.* **5**, 207–285, 1967
- Feldstein, Y.I.: Peculiarities in the auroral distribution and magnetic disturbance distribution in high latitudes caused by the asymmetrical form of the magnetosphere. *Planet. Space Sci.* **14**, 121–130, 1966
- Frederick, J.E., Rusch, D.W.: On the chemistry of metastable atomic nitrogen in the F-region deduced from simultaneous satellite measurements of the 5200 Å airglow and atmospheric composition. *J. Geophys. Res.* 1977 (accepted for publication)
- Garstang, R.H.: Energy levels transition probabilities in p^2 and p^4 configurations. *Monthly Notices Roy. Astron. Soc.* **111**, 115–124, 1951
- Heikkilä, W.J., Winningham, J.D., Eather, R.H., Akasofu, S.-I.: Auroral emissions and particle precipitation in the noon sector. *J. Geophys. Res.* **77**, 4100–4115, 1972
- Henriksen, K.: Studies of the auroral green line. Electron excitation mechanisms. Ph. D. Thesis, The Auroral Observatory, Tromsø, Norway 1974
- Henriksen, K.: The effective lifetime profiles of the $O(^1S)$ and $N_2^+(B^2\Sigma_u^+, v=0)$ excited species. *J. Atmos. Terr. Phys.* **37**, 1491–1495, 1975
- Henriksen, K., Holback, B., Witt, G.: Sky background measurements on the wavelength region from 4800 Å to 5800 Å at the altitude of the polar cleft. Report no. 39–77, The Auroral Observatory, Tromsø, Norway 1977
- Noxon, J.F., Johanson, A.E.: Changes of thermospheric molecular oxygen abundance inferred from twilight 6300 Å airglow. *Planet. Space Sci.* **20**, 2125, 2151, 1972
- Omholt, A.: *The Optical Aurora*. Berlin-Heidelberg-New York: Springer 1971
- Rees, M.D.: Auroral ionization and excitation by incident energetic electrons. *Planet. Space Sci.* **11**, 1209–1218, 1963
- Shepherd, G.G., Picau, J.F., Creutzberg, F., McNamara, A.G., Gerard, J.-C., McEwen, D.J., Delana, B., Whitteker, J.H.: Rocket and ground-based measurements of the dayside magnetospheric cleft from Cape Perry, N.W.T. *Geophys. Res. Lett.* **3**, 69–72, 1976
- Sinanoglu, O.: Oxygen auroral lines: New theory and experiment on forbidden transition probabilities. *Comments Atomic Molecular Phys.* **2**, 79–84, 1970
- Sivjee, G.G., Hultqvist, B.: Particle and optical measurements in the magnetic noon sector of the auroral oval. *Planet. Space Sci.* **23**, 1597–1601, 1975
- Sivjee, G.G., Romick, R.J.: Studies of N_2 vibrational distribution in the auroral F region. Geophysical Institute report, University of Alaska, Fairbanks, Alaska 1976
- Starkov, G.V., Feldstein, Ya.I.: Auroral oval and its dependence on magnetic disturbance. Results of Researches of the International Geophys. Projects Pub. House 'NAUK', Moscow, Articles, *Polar Aurora* **17**, 22–23, 1968
- Stoffregen, W., Derblom, H., Ladell, L., Gunnarsson, H.: The chemistry of artificial clouds in the upper atmosphere and their response to winds and fields. Report 17B, Uppsala Ionospheric Observatory, Uppsala, Sweden 1971
- Strobel, D.F., Oran, E.S., Feldman, P.H.: The aeronomy of odd nitrogen in the thermosphere, 2. Twilight emissions. *J. Geophys. Res.* **81**, 3745–3752, 1976
- Vroom, V.A., de Heer, F.J.: Production of excited hydrogen atoms by impact of fast electrons on water vapour. *J. Chem. Phys.* **50**, 1883–1888, 1969
- Wiese, W.L., Smith, M.W., Glennon, B.M.: *Atomic Transition Probabilities*. Volume 1, pp. 55. Washington: National Bureau of Standards 1966
- Zaitzeva, S.A., Pudovkin, M.I.: On the longitudinal extent of the polar cusp. *Planet. Space Sci.* **24**, 518–519, 1976
- Zipf, E.C.: The collisional deactivation of metastable atoms and molecules in the upper atmosphere. *Can. J. Phys.* **47**, 1863–1877, 1969

Parameters of the Auroral Electrojet From Magnetic Variations Along a Meridian

H. Maurer and B. Theile

Institut für Geophysik und Meteorologie der Technischen Universität Braunschweig,
Mendelssohnstraße 1 A, 3300 Braunschweig, Federal Republic of Germany

Abstract. The parameters of the auroral electrojet are described by using an ionospheric sheet current model. Data from a line of magnetometers between 62 and 67 degrees magnetic latitude are the input for the computation of the parameters during electrojet activity. The parameters are depicted in the parameter-time diagram which furnishes mainly the following information:

1. Applicability of the two dimensional current model.
2. Latitudinal extent of the electrojets as a function of time.
3. Location of centre of the current as a function of time.
4. Current flow direction.

Two case studies are carried out. The first comprises DMSP (*Defense Meteorological Satellite Program*) data, the second makes use of data collected simultaneously by the *Scandinavian Twin Auroral Radar Experiment* (STARE). The results of the parameter-time diagram and the DMSP as well as the STARE data are in good agreement.

Key words: Substorm – Auroral electrojet – Ionospheric currents – Magnetic field observation – IMS.

1. Introduction

Six magnetometer stations are installed in Finland and Norway between 66 and 71 degrees northern geographic latitude in order to measure the magnetic variations of auroral electrojet activity. The proper locations of the stations are shown in Figure 1. The project is carried out as part of the *International Magnetospheric Study* (IMS). The european magnetometer network is dedicated to the IMS. It consists of the Braunschweig magnetometer chain on which is reported here only, and the Münster network (Küppers et al., 1978). Table 1 contains the geographical and geomagnetic coordinates of our line of stations.

The auroral electrojet has to be regarded as the ionospheric component of a dynamical magnetospheric process called the magnetospheric substorm (Akasofu, 1968). Thus the quantitative knowledge of the electrojet's properties

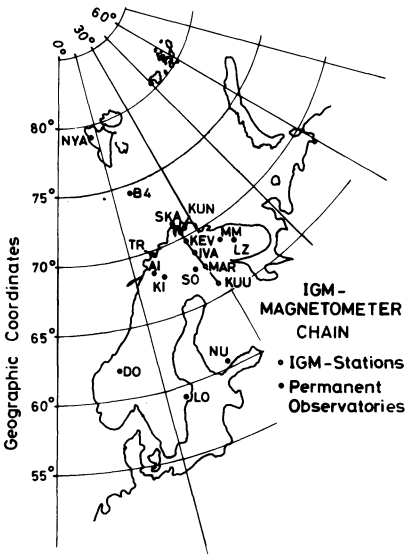


Fig. 1. The IMS-Magnetometer Chain in Scandinavia of the Technical University Braunschweig. Observatories are indicated by two-letter codes

Table 1. Coordinates of the magnetometer stations used in this study

Name	Code	Geographic coordinates		Geomagnetic coordinates ^a		CGM ^b [UT]
		Latitude [Deg]	Longitude [Deg]	Latitude [Deg]	Longitude [Deg]	
Skårsvag	SKA	71.11 N	25.83 E	67.61 N	111.04 E	21:17
Kunes	KUN	70.35 N	26.51 E	66.84 N	110.79 E	21:18
Kevo	KEV	69.75 N	27.03 E	66.23 N	110.61 E	21:19
Ivalo	IVA	68.60 N	27.47 E	65.05 N	109.94 E	21:22
Martti	MAR	67.47 N	28.28 E	63.90 N	109.76 E	21:23
Kuusamo	KUU	65.91 N	29.05 E	62.37 N	109.24 E	21:25

^a Revised corrected geomagnetic coordinates calculated after Gustafsson (1970)

^b Corrected Geomagnetic Midnight calculated for January 19, 1977 (Montbriand, 1970)

is a prerequisite for the understanding of the physics of the substorm. The observation along a meridian enables us to resolve temporal and spatial variations along the profile. Heinrich et al. (1970) and Hanser et al. (1973) used north-south magnetometer lines to determine parameters of the auroral electrojet in conjunction with sounding rocket launches. Czechowsky (1970) calculated equivalent E-region currents from four magnetic ground recordings for comparison with VHF backscatter data. Significant advances were achieved by the North American line of Rostoker and his coworkers. Kisabeth and Rostoker (1971) were the first to publish data collected from their meridian line of magnetometers in North America. In a series of papers (Kisabeth and Rostoker, 1973; Rostoker and Kisabeth, 1973; Kisabeth and Rostoker, 1974; Rostoker et al., 1975; Wiens and

Rostoker, 1975) they analysed the structural and temporal behaviour of auroral electrojets.

The purpose of this paper is to show how the data of the magnetometer chain can be used to obtain a synoptic survey of the electrojet activity along a meridian. It is shown how the simultaneous observation by six stations can be converted into a concise representation for subsequent physical interpretation. The temporal and spatial behaviour of the electrojet can be studied by means of a parameter-time diagram. This diagram is based on a method of data presentation first published by Zaitzev and Boström (1970). Two examples demonstrate under what circumstances the data from the magnetometer chain can be used to give quantitative information on the electrojet. For instance, if the current flow becomes too complex, it is difficult to interpret the magnetic field data using the technique presented in this paper.

2. Data Collection

The six stations are of identical design: A three component flux gate magnetometer measures the variation of the horizontal component H , of the magnetic east component D and of the vertical component Z of the earth's magnetic field. Each component may vary within ± 1000 nT with respect to the baseline value. The analogue magnetometer output signal is digitised by a 12 bit analogue to digital converter (ADC) with an accuracy of 0.5 nT. A quartz controlled time base generator provides the time code and controls data recording on a magnetic tape compatible with a digital computer. The normal sampling rate is 10 s, aliasing filters suppress frequencies above the Nyquist frequency in the original signal. The subsequent data processing procedure includes error detection routines and conversion of the field components from the magnetic system H - D - Z into the geographic system X (= North), Y (= East) and Z (= Down). By this the geographic north direction is used as directional reference rather than the magnetic declination which varies from one location to another.

3. Parameters of the Electrojet

Simultaneous observations by backscatter techniques and magnetometers show that the auroral electrojet can be described in terms of a sheet current flowing in 115 km altitude (Brekke et al., 1974; Greenwald et al., 1977). We will use x , y , and z to denote the geographic directions north, east and down. The corresponding magnetic field components are X , Y , and Z . Figure 2 shows the resulting X and Z field components at the earth's surface for a model westward flowing sheet current with infinite extent in the east-west direction, positioned at a height of 115 km. The north-south extent of the sheet is 4 degrees centered at 68 degrees with a uniform surface current density of 1.5 Am^{-1} .

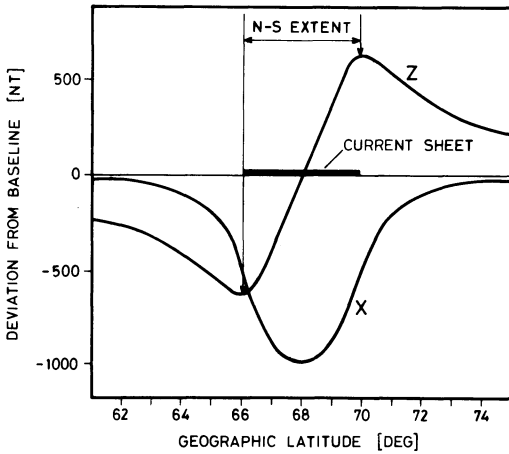


Fig. 2. Sheet current model for the auroral electrojet and resulting magnetic field components measured on the ground

This figure also may illustrate the parameters we use for the description of the current (cf. Figs. 6 and 9):

X_{\min} or X_{\max} = indicates latitude where the centre of the current is located, from minimum or maximum in X

Z_{zero} = indicates same latitude from $Z=0$

Z_{\min} , Z_{\max} = indicates latitudes of the Z extrema as a measure of the north-south extent of the current flow

X_a = X value at the latitude indicated by X_{\min} or X_{\max} as a measure of the current density and the flow direction (west or east)

Z_g = gives the gradient of Z at the latitude where $Z=0$.

If the latitudes indicated by the symbols Z_{zero} and X_{\min} , X_{\max} , derived from measurements along our station line, coincide, the actual current can be approximated using this model.

The gradient Z_g together with the amplitude value X_a will be used to compute the north-south extent of the current for those cases where the extrema of Z (cf. Fig. 2) are outside the range of the magnetometer chain.

As shown by Kertz (1954) the magnetic field of a line current I at height h_l can be expressed in terms of an infinitely broad sheet current at height $h < h_l$ with the current density:

$$j_H(x) = \frac{I}{\pi} \frac{h_l - h}{x^2 + (h_l - h)^2} \quad 0 \leq h < h_l \quad (1)$$

h_l = height of the line current

h = height of the sheet current

I = line current strength.

For a line current of infinite east-west extent, flowing at the height h_l above the earth's surface in east-west direction we have the well known equations:

$$\begin{aligned}
 X(x) &= \frac{\mu_o}{2\pi} \frac{I \cdot h_i}{x^2 + h_i^2} \\
 Y(x) &= 0 \\
 Z(x) &= \frac{-\mu_o}{2\pi} \frac{I \cdot x}{x^2 + h_i^2}.
 \end{aligned}
 \tag{2}$$

Assuming that the measured magnetic field variations at the earth's surface are due to a line current we obtain expressions for the current I and the height h_i in terms of the measured quantities Z_g and X_a :

$$\begin{aligned}
 I &= \frac{2\pi}{\mu_o} \frac{X_a^2}{Z_g} \\
 h_i &= \frac{X_a}{Z_g}.
 \end{aligned}
 \tag{3}$$

With the result of (3) and the assumption that the ionospheric sheet current flows at 115 km altitude ($h = 115 \text{ km} < h_i$) we can determine the current distribution by using Equation (1). This in turn allows us to determine the north-south extent of the electrojet which is chosen to be the half width of the current distribution. In Section 4.1 a comparison is made between the directly measured extrema of Z and the indirectly computed north-south extent. These show good agreement.

This simple model cannot account for east-west fields. The Y -component may be due to field-aligned currents first reported by Zmuda et al. (1966) and/or an x -component of the ionospheric current (cf. Brekke et al., 1974).

Earth induction effects are neglected. Investigations using simplifying assumptions for the conductivity within the earth and the temporal behaviour of the current are previously reported in the pioneering work by McNish (1938) and Forbush and Casaverde (1961). Recent results are given by Boström (1971) and Mareschal (1976). The result is an increase of the magnetic field amplitude by the earth-induced current which in turn means that current densities derived from ground-based magnetic recordings may appear to be larger than they are in nature.

If we plot the latitudes X_{\min} or X_{\max} as well as the Z_{zero} as a function of time, we are able to judge how well this model describes the actual current. The current flow is symmetrical relative to our station line and satisfies also the model assumptions as long as the X_{\min} , X_{\max} , and Z_{zero} are measured simultaneously at the same latitude.

4. Case Studies

4.1. January 19, 1977

Figure 3 shows the magnetic field components as recorded by the six stations between 18:00 and 21:00 UT. Upper, middle and lower panel contain X , Y , and Z

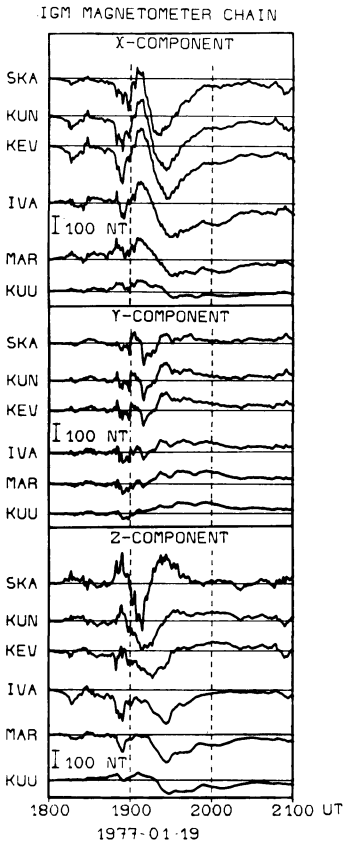


Fig. 3. Traces of magnetic field components recorded along a north-south line. For station codes refer to Table 1. Corrected geomagnetic midnight occurs at 21:18 UT. Upper panel: X or Northward Component, middle panel: Y or Eastward Component, lower panel: Z or Downward Component

respectively. The magnetic field was very quiet until 18:00 UT. Therefore the magnitudes of the field components as measured before 18:00 UT were chosen as baselines. Corrected geomagnetic midnight (Montbriand, 1970) occurs between 21:17 UT and 21:25 UT at the different station latitudes (cf. Table 1). Each trace in Figure 3 reflects temporal and spatial variations of the ionospheric current. We separate temporal and spatial effects by computing latitude profiles from our station line for selected times. The profiles are obtained by joining the six field values given at the six station latitudes by means of a Spline interpolation. The result is shown in Figure 4 with the time increasing from bottom to top.

Until about 19:20 UT X is positive in the south and negative in the north. From this we conclude that there is an eastward current in the south and at the same time a westward electrojet north of it. After this time there is a well developed negative X , this means a westward electrojet.

Hughes and Rostoker (1977) as well as Yasuhara et al. (1975) have shown that field-aligned currents may be observed on the ground by changes of the east-west component of the magnetic field. As Y (Fig. 4) is just slightly positive and fairly constant after 19:20 UT, we assume that there is no strong field-aligned current flow during that time along our line.

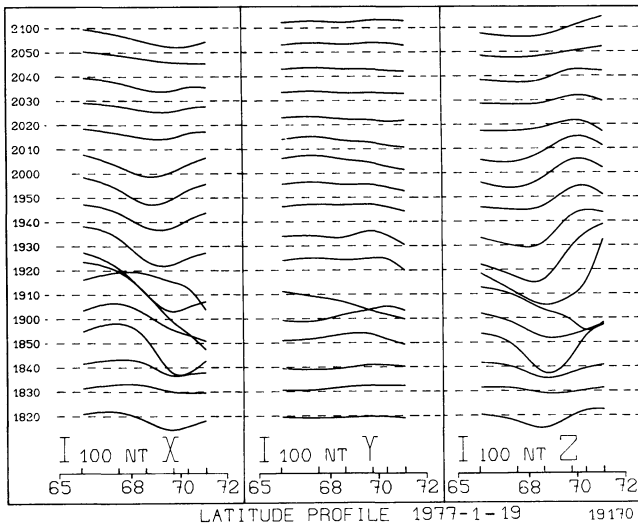


Fig. 4. Latitude profile of magnetic field variations on January 19, 1977 between 18:20 and 21:00 UT. The six ticks on the abscissas indicate the station latitudes. Refer to text for further explanation. $Kp = 3-$

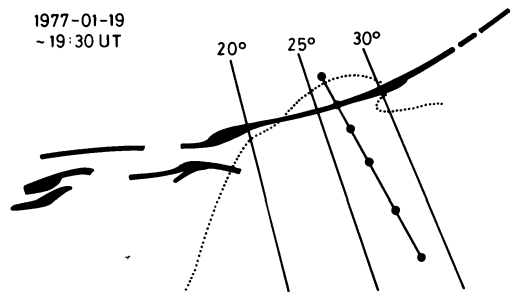


Fig. 5. Auroral emissions taken by a DMSP satellite. The dotted line indicates the scandinavian coastline. The magnetometer chain is between the 25° and 30° meridians

After 19:30 UT both extrema of Z are within the range of the chain. The actual locations of the maximum and the minimum (i.e., the north-south extent) coincides with the values obtained by computation using Equations (1) through (3).

Figure 5 shows auroral structures photographed by a DMSP satellite (*Defense Meteorological Satellite Program*). The Scandinavian coast is indicated by a dotted line, the station line is between 25 and 30 degrees geographic longitude. The picture was taken at about 19:30 UT corresponding to 22:11 corrected geomagnetic time. The aurora is located over Kunes. The latitude profile (Fig. 4) indicates a westward electrojet to the south of Kunes.

A comprehensive description of the development between 18:00 and 21:00 UT is given in the parameter-time diagram (Fig. 6). The upper panel shows the latitude variations of the parameters Z_{zero} , Z_{max} , Z_{min} , X_{max} , X_{min} versus time. The middle panel shows – as far as it can be calculated by the method described in Chapter 3 – the north-south extent of the current versus time. The lower panel gives the direc-

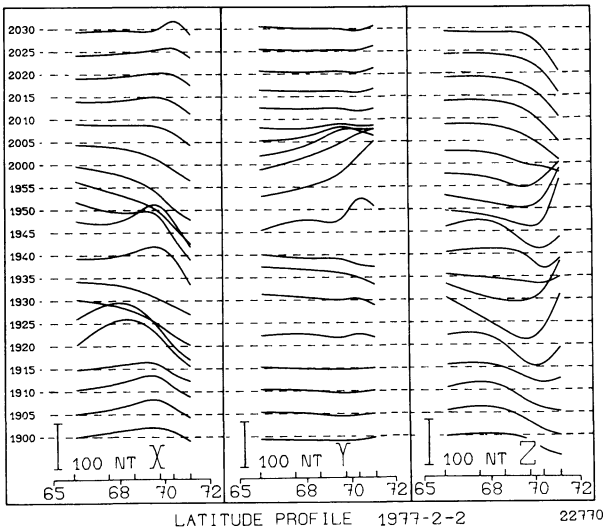


Fig. 7. Latitude profile of magnetic field variations on February 2, 1977 between 19:00 and 21:00 UT. $Kp=3-$. Refer to Figure 4 and text for explanation

the centre of the current is at 69 degrees geographical latitude. The horizontal field is rather homogeneous and directed mainly to the south with as slight deviation to the east as one can see in the lower panel of Figure 6.

The parameter-time diagram allows the following summary: Between 18:00 and 19:20 UT we find strongly varying currents which cannot be explained by a simple model. After 19:20 UT until about 21:00 UT the current becomes a westward sheet current. The counterflowing currents before 19:20 UT indicate that a Harang discontinuity (Heppner, 1972) moved over the magnetometer line. The substorm onset occurred at about 18:45 UT followed by the main phase and recovery phase.

4.2. February 2, 1977

Figure 7 shows the three magnetic components in a latitude profile plot for the time between 19:00 and 20:30 UT. The X-component shows an eastward electrojet at 19:00 UT. Later on, from 19:15 UT onwards X becomes negative in the north, which means that a westward current develops in the north. After some time the eastward current in the south disappears. The variations in the Y-component from 19:40 UT onwards suggest either field-aligned currents or a north-south component in the ionospheric current.

Figure 8 depicts four selected STARE (Scandinavian Twin Auroral Radar Experiment) observations (courtesy of R.A. Greenwald). STARE measures the horizontal Hall-currents in the ionosphere. At 19:05 UT STARE shows an eastward electrojet between 69 and 70 degrees geographic latitude (panel a in Fig. 8). The parameter-time diagram for the same time interval is shown in Figure 9.

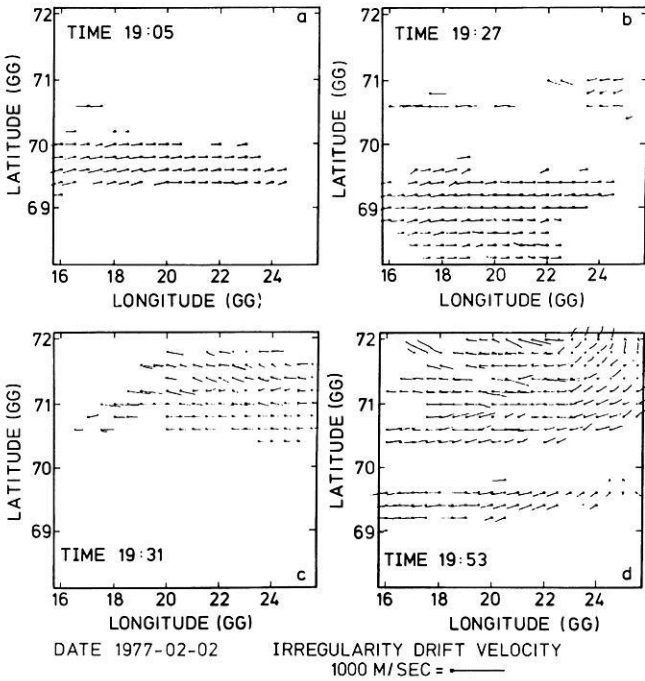


Fig. 8. Current flow measured by the STARE on February 2, 1977. The current is opposite to the drift velocity and shows only the Hall current. (Courtesy of R.A. Greenwald)

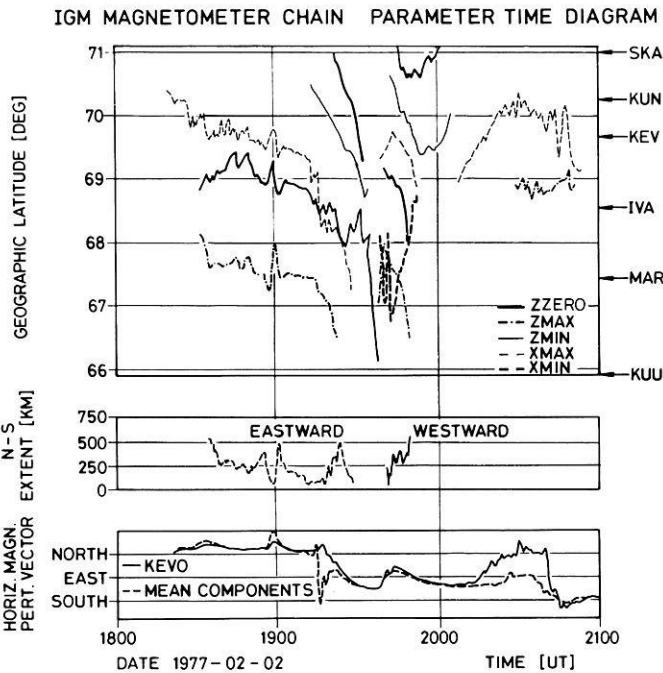


Fig. 9. Parameter-time diagram for February 2, 1977. Until about 19:30 UT an eastward electrojet centered at 69° latitude dominates. After that time there are at least two currents of opposite direction

The X_{\max} curve in the parameter-time diagram indicates the same position of the electrojet as well. X_{\max} and Z_{zero} do not coincide too well, but the locations are not more than 40 km apart. The next STARE observation at 19:27 UT (panel b in Fig. 8) shows an eastward current between 68 and 69.5 degrees and a westward current between 70.5 and 71 degrees latitude. For this time we find two Z_{zero} curves in the parameter-time diagram indicating the proper locations of the current flow. A few minutes later, at 19:31 UT (panel c in Fig. 8) the current in the south has vanished, only a westward flow between 71 and 72 degrees latitude is observed. The parameter-time diagram shows rather confusing patterns. This is due to two effects: 1. The STARE observation shows the high temporal variability of the current, which results in highly variable magnetic fields. 2. There are currents of opposite direction. The superposed magnetic fields lead to erroneous results in the parameter-time diagram.

The last STARE observation at 19:53 UT (panel d in Fig. 8) shows a westward electrojet with a southward component north of 70 degrees latitude. Only 100 km to the south there is an eastward current. It appears quite natural that this current flow cannot be derived from the parameter-time diagram. The latitude profile of the Y-component in Figure 7 becomes positive in the northern part after 19:40 UT. By comparison with the STARE data we can explain this by the southward current (panel d in Fig. 9).

5. Conclusions

Magnetic field observations can only be interpreted in terms of electric currents when some geometrical properties of the currents are known. By means of an ionospheric sheet current model the parameters Z_{zero} , Z_{min} , Z_{max} , X_{min} , and X_{max} are computed and plotted in the parameter-time diagram. As long as the electrojet behaves as assumed in the model, the parameter-time diagram is a good tool to study the behaviour of the current. Magnetic data and auroral emissions as well as auroral radar data are consistent. As soon as the ionospheric current flow becomes so complex that the model assumption is strongly violated, the parameter-time diagram becomes a confusing line pattern, telling us that the situation cannot be analysed only by magnetic observations along the profile. Simultaneous measurements by auroral radar technique and the ground based magnetometer chains show how difficult it is to solve complex current structures by ground based measurements. However, it is considered to be an important result of the parameter-time diagram that it immediately delivers information on the simplicity or complexity of the prevailing ionospheric current at a certain time.

Acknowledgements. The authors are indebted to Professor Dr. W. Kertz for the steady support of this project. We greatly acknowledge the help of Drs. Sucksdorff, Helsinki and Boström, Uppsala, through which the observation in Scandinavia became possible. Mr. Kataja and Mr. Mustonen from the Geophysical Observatory in Sodankylä supported greatly the operation of the chain, as well as Mr. Berger in Tromsø. We appreciate the valuable software and hardware contribution by Mr. Hähnsen and Mr. Stoll. We are indebted to Drs. Greenwald and Nielsen, MPAe Lindau, for relaying DMSP data and supplying us with STARE data. The authors are grateful to the DFG who financed the project.

References

- Akasofu, S.-I.: Polar and magnetospheric substorms. Dordrecht, Holland: D. Reidel Publishing Comp. 1968
- Boström, R.: The magnetic field of three-dimensional magnetospheric model current systems and currents induced in the ground. Acta Polytechnica Scandinavica, PH 77. The Royal Swedish Academy of Engineering Sciences, Stockholm 1971
- Brekke, A., Doupnik, J.R., Banks, P.M.: Incoherent scatter measurements of E region conductivities and currents in the auroral zone. J. Geophys. Res. **79**, 3773–3790, 1974
- Czechowsky, P.: Calculation of an equivalent current system in the polar E-region. Radio Sci. **6**, 247–253, 1971
- Forbush, S.E., Casaverde, M.: Equatorial Electrojet in Peru, Publication 620, Department of Terrestrial Magnetism. Carnegie Inst. Washington D.C. 1961
- Greenwald, R.A., Weiss, W., Nielsen, E., Thomson, N.R.: STARE: A new radar auroral backscatter experiment in northern Scandinavia, submitted to Radio Sci. 1977
- Gustafsson, G.: A revised corrected geomagnetic coordinate system. Ark. Geofys. **5**, 595–617, 1970
- Hanser, F.A., Sellers, B., Vancour, R.P.: The real-time determination of ionospheric current parameters during a substorm. J. Geomag. Geoelectr. **25**, 339–348, 1973
- Heinrich, H., Reimer, D., Siemann, H.: Investigation of the auroral electrojet. Z. Geophys. **36**, 399–420, 1970
- Hepner, J.P.: The Harang discontinuity in auroral belt ionospheric currents. Geofysiske Publikasjoner **29**, 105–120, 1972
- Kertz, W.: Modelle für erdmagnetisch induzierte elektrische Ströme im Untergrund. Nachr. Akad. Wiss. Göttingen, Math.-phys. Kl. IIa, 101–110, 1954
- Kisabeth, J.L., Rostoker, G.: Development of the polar electrojet during polar magnetic substorms. J. Geophys. Res. **76**, 6815–6828, 1971
- Kisabeth, J.L., Rostoker, G.: Current flow in auroral loops and surges inferred from ground-based magnetic observations. J. Geophys. Res. **78**, 5573–5584, 1973
- Kisabeth, J.L., Rostoker, G.: The expansive phase of magneto-spheric substorms: 1. Development of the auroral electrojets and auroral arc configuration during a substorm. J. Geophys. Res. **79**, 972–984, 1974
- Küppers, F., Untiedt, J., Baumjohann, W.: A two-dimensional array for ground-based observations of auroral zone electric currents during the IMS, submitted to J. Geophys. 1978
- Mareschal, M.: On the problem of simulating the earth's induction effects in modeling polar magnetic substorms. Rev. Geophys. Space Phys. **14**, 403–409, 1976
- McNish, A.G.: Heights of electric currents near the auroral zone, Terr. Magn. Atmos. Electr. **43**, 67–75, 1938
- Montbriand, L.E.: A simple method for calculating the local time of corrected geomagnetic midnight. J. Geophys. Res. **75**, 5634–5636, 1970
- Rostoker, G., Kisabeth, J.L.: Response of the polar electrojets in the evening sector to polar magnetic substorms. J. Geophys. Res. **78**, 5559–5584, 1973
- Rostoker, G., Kisabeth, J.L., Sharp, R.D., Shelley, E.G.: The expansive phase of magnetospheric substorms: 2. The response at synchronous altitude of particles of different energy ranges. J. Geophys. Res. **80**, 3557–3570, 1975
- Wiens, R.G., Rostoker, G.: Characteristics of the development of the westward electrojet during the expansive phase of magnetospheric substorms. J. Geophys. Res. **80**, 2109–2128, 1975
- Zaitzev, A.N., Boström, R.: On methods of graphical displaying of polar magnetic disturbances. Planet. Space Sci. **19**, 643–649, 1971
- Zmuda, A.J., Martin, J.H., Heuring, F.T.: Transverse magnetic disturbances at 1100 kilometers in the auroral region. J. Geophys. Res. **71**, 5033–5045, 1966

The Recurrence Tendency of Geomagnetic Activity During Solar Cycle 20

J. Meyer

Troppauer Str. 28, 1000 Berlin 45

Abstract. The equivalent recurrence number $\omega(n)$ of geomagnetic activity introduced by Bartels (1960) is a quantitative measure of the recurrence tendency during n consecutive solar rotations. Tabulated values of $\omega(n)$, for n equal to 2, 4, 8, 16, and 32, are given for the years 1971–1976 supplementing former tables (Meyer, 1965, 1973) comprising the years 1884–1970. A musical diagram of $\omega(n)$ for the years 1965–1976 provides a detailed picture of the recurrence tendency during the entire solar cycle 20.

The general course of the recurrence tendency variation, apart from superimposed arbitrary fluctuations, follows the one noticed for previous solar cycles and is especially well pronounced for the higher values of n : The recurrence tendency is lowest in the years immediately following the preceding sunspot minimum till sunspot maximum (1965–1968), it is increasing in the years after sunspot maximum (1969–1973), and is strongest in the two years before the final sunspot minimum (1974–1975), remaining still relatively high throughout 1976. In a physical interpretation the equivalent recurrence numbers $\omega(n)$ are reflecting the stability of the large-scale solar wind structure or, more specifically, of high-speed solar wind streams.

Key words: Geomagnetic activity – Recurrence tendency – Equivalent recurrence numbers.

1. Introduction

For geomagnetic activity a great variety of measures exist, the most customary ones being derived from Bartels' three-hour range index K . They usually underly studies of both time variations of activity and correlation with other solar or interplanetary data. Special investigations on the 27-days recurrence tendency with any of these measures have previously been carried out mainly by applying the method of superposed epochs (synchronization or Chree method), thus yielding only average results for long periods. A higher resolution of time

variations requires a quantitative measure of the recurrence tendency itself. For this purpose J. Bartels initiated an extensive study to express the recurrence tendency numerically by means of equivalent recurrence numbers, based on the continuous series of daily character figures $C8$ extending back to 1884. Preliminary results were presented by Bartels (1960) at the Helsinki Meeting of IAGA. A complete table of recurrence numbers for each solar rotation from 1884–1963/64 was published by Meyer (1965), together with a first evaluation of the calculated indices. In the same paper musical diagrams similar to those for Kp provided a comprehensive picture of the recurrence tendency in the course of more than seven sunspot cycles. The diagram for the years 1954–1964 (solar cycle 19) has also been shown in another paper (Meyer, 1966). Supplementary tables and diagrams for 1964–1970, 1971 have been given by Meyer (1973). The present paper contains additional data for the years 1971–1976, completing the recurrence tendency picture for the entire sunspot cycle 20.

2. The Equivalent Recurrence Number $\omega(n)$

The original concept of recurrence scaling has already been put forward by Bartels (1935; see also Chapman and Bartels, 1940) by generalizing the fundamental law of propagation of errors. The *equivalent recurrence number* $\omega(n)$ (equivalent number of repeated sets) is defined by

$$\omega(n) = m^2(n)/(m^2/n), \quad (1)$$

where m is the average standard deviation for n (long) individual sets of single values, and $m(n)$ is the standard deviation for the average set. A detailed treatment of the morphology of geophysical time series with conservation and recurrence tendencies, including the deduction of all formulas, can be found in the treatise of Meyer (1965).

For geomagnetic data, arranged as usual in lines according to solar rotations of exactly 27 days, the equivalent recurrence number $\omega(n)$ indicates how many times (among n of such consecutive sets) statistically independent sets are repeated: $\omega(n)$ being 1 means arbitrary succession without any recurrence tendency at all; $\omega(n)$ being n means perfect repetition, i.e., all n rotations show an identical day-to-day variation of activity. Thus the highest possible value for the index $\omega(n)$ is always the number n itself. Values of $\omega(n)$ between 1 and n denote positive recurrence tendency, those smaller than 1 denote negative (opposite) recurrence tendency. Starting from the daily character figures $C8$ (Bartels, 1951, 1958, and supplementary tables), the equivalent recurrence numbers $\omega(n)$, for n equal to 2, 4, 8, 16, and 32, have been calculated separately for each mean (or associated) solar rotation number. The first day of the mean solar rotation is the central day of all n rotations concerned. The $\omega(n)$ data in Table 1 supplements the former tables making available a continuous series of equivalent recurrence numbers for the years 1884–1976.

Table 1. Equivalent recurrence numbers $\omega(n)$ for geomagnetic activity during 1971–1976

Year	Assoc. Rot.-No.	Rot.-No.	$\omega(2)$	Rot.-No.	$\omega(4)$	Rot.-No.	$\omega(8)$	Rot.-No.	$\omega(16)$	Rot.-No.	$\omega(32)$
1971	1880	1879+80	1.15	1878-81	1.56	1876-83	1.42	1872-87	1.67	1864-95	2.18
	1881	1880+81	1.69	1879-82	1.79	1877-84	1.68	1873-88	1.60	1865-96	1.94
	1882	1881+82	1.37	1880-83	2.14	1878-85	2.64	1874-89	1.86	1866-97	1.95
	1883	1882+83	1.48	1881-84	1.94	1879-86	2.60	1875-90	1.67	1867-98	1.96
	1884	1883+84	1.14	1882-85	1.81	1880-87	2.67	1876-91	1.96	1868-99	1.79
	1885	1884+85	1.08	1883-86	1.57	1881-88	2.06	1877-92	1.75	1869-00	1.81
	1886	1885+86	1.21	1884-87	1.29	1882-89	1.65	1878-93	2.12	1870-01	1.84
	1887	1886+87	1.10	1885-88	1.32	1883-90	1.27	1879-94	2.02	1871-02	1.81
	1888	1887+88	1.42	1886-89	1.58	1884-91	1.58	1880-95	1.90	1872-03	1.92
	1889	1888+89	1.30	1887-90	1.58	1885-92	1.75	1881-96	1.39	1873-04	1.65
1890	1889+90	1.19	1888-91	1.54	1886-93	2.18	1882-97	1.24	1874-05	1.54	
1891	1890+91	1.16	1889-92	1.45	1887-94	2.46	1883-98	1.32	1875-06	1.51	
1892	1891+92	1.27	1890-93	1.67	1888-95	2.20	1884-99	1.23	1876-07	1.43	
1893	1892+93	1.07	1891-94	1.68	1889-96	1.40	1885-00	1.30	1877-08	1.51	
1972	1894	1893+94	1.26	1892-95	1.39	1890-97	1.35	1886-01	1.39	1878-09	1.66
	1895	1894+95	1.12	1893-96	0.89	1891-98	1.44	1887-02	1.61	1879-10	1.62
	1896	1895+96	1.04	1894-97	1.03	1892-99	1.12	1888-03	1.71	1880-11	1.87
	1897	1896+97	1.34	1895-98	1.69	1893-00	1.12	1889-04	1.52	1881-12	1.91
	1898	1897+98	1.50	1896-99	1.36	1894-01	1.07	1890-05	1.41	1882-13	1.87
	1899	1898+99	0.84	1897-00	0.93	1895-02	1.17	1891-06	1.28	1883-14	1.74
	1900	1899+00	0.67	1898-01	0.79	1896-03	1.02	1892-07	1.11	1884-15	1.80
	1901	1900+01	1.35	1899-02	0.75	1897-04	0.84	1893-08	1.28	1885-16	1.65
	1902	1901+02	0.96	1900-03	1.84	1898-05	0.98	1894-09	1.18	1886-17	1.57
	1903	1902+03	1.47	1901-04	1.49	1899-06	1.11	1895-10	1.13	1887-18	1.69
1904	1903+04	0.91	1902-05	1.26	1900-07	1.42	1896-11	1.23	1888-19	1.54	
1905	1904+05	1.19	1903-06	1.23	1901-08	1.38	1897-12	1.52	1889-20	1.42	
1906	1905+06	1.41	1904-07	1.38	1902-09	1.27	1898-13	1.88	1890-21	1.37	
1973	1907	1906+07	1.29	1905-08	1.56	1903-10	1.33	1899-14	1.84	1891-22	1.19
	1908	1907+08	1.37	1906-09	1.56	1904-11	1.82	1900-15	2.02	1892-23	1.13
	1909	1908+09	1.44	1907-10	2.07	1905-12	2.01	1901-16	1.90	1893-24	0.99
	1910	1909+10	1.49	1908-11	2.36	1906-13	2.53	1902-17	1.72	1894-25	1.05
	1911	1910+11	1.64	1909-12	2.27	1907-14	2.33	1903-18	1.32	1895-26	1.09
	1912	1911+12	1.41	1910-13	1.91	1908-15	2.19	1904-19	1.30	1896-27	0.99
	1913	1912+13	1.54	1911-14	1.56	1909-16	1.80	1905-20	1.17	1897-28	1.22
	1914	1913+14	1.09	1912-15	1.53	1910-17	1.37	1906-21	1.24	1898-29	1.56
	1915	1914+15	1.23	1913-16	1.65	1911-18	1.03	1907-22	1.24	1899-30	1.72
	1916	1915+16	1.48	1914-17	1.91	1912-19	1.29	1908-23	1.12	1900-31	1.84
1917	1916+17	1.37	1915-18	1.58	1913-20	1.18	1909-24	1.35	1901-32	1.96	
1918	1917+18	1.29	1916-19	1.73	1914-21	1.52	1910-25	1.53	1902-33	1.70	
1919	1918+19	1.41	1917-20	1.81	1915-22	1.67	1911-26	1.98	1903-34	1.97	
1920	1919+20	1.17	1918-21	1.93	1916-23	1.72	1912-27	2.38	1904-35	2.25	
1974	1921	1920+21	1.53	1919-22	2.04	1917-24	2.47	1913-28	2.73	1905-36	2.26
	1922	1921+22	1.39	1920-23	2.05	1918-25	2.73	1914-29	3.22	1906-37	2.43
	1923	1922+23	1.36	1921-24	1.90	1919-26	3.39	1915-30	3.31	1907-38	2.88
	1924	1923+24	1.09	1922-25	2.42	1920-27	3.39	1916-31	3.99	1908-39	3.50
	1925	1924+25	1.76	1923-26	2.20	1921-28	3.55	1917-32	4.85	1909-40	3.94
	1926	1925+26	1.48	1924-27	2.08	1922-29	3.41	1918-33	5.14	1910-41	4.15
	1927	1926+27	1.51	1925-28	2.32	1923-30	3.09	1919-34	5.48	1911-42	4.65

Table 1 (Continued)

Year	Assoc. Rot.-No.	Rot.-No.	$\omega(2)$	Rot.-No.	$\omega(4)$	Rot.-No.	$\omega(8)$	Rot.-No.	$\omega(16)$	Rot.-No.	$\omega(32)$
		1928	1.60	1926-29	2.91	1924-31	3.37	1920-35	5.40	1912-43	4.94
		1929	1.74	1927-30	2.69	1925-32	3.77	1921-36	4.95	1913-44	4.74
		1930	1.49	1928-31	2.65	1926-33	4.13	1922-37	4.52	1914-45	4.65
		1931	1.52	1929-32	2.54	1927-34	4.03	1923-38	4.75	1915-46	4.75
		1932	1.47	1930-33	2.46	1928-35	3.95	1924-39	5.00	1916-47	4.84
		1933	1.37	1931-34	2.69	1929-36	3.25	1925-40	4.74	1917-48	5.09
		1934	1.80	1932-35	2.40	1930-37	3.14	1926-41	4.55	1918-49	4.91
1975		1935	1.50	1933-36	1.98	1931-38	3.33	1927-42	4.54	1919-50	4.78
		1936	1.44	1934-37	2.10	1932-39	3.11	1928-43	4.39	1920-51	4.47
		1937	1.43	1935-38	2.39	1933-40	2.94	1929-44	4.08	1921-52	4.07
		1938	1.56	1936-39	2.05	1934-41	2.85	1930-45	3.70	1922-53	3.61
		1939	1.24	1937-40	1.91	1935-42	2.89	1931-46	3.56	1923-54	3.47
		1940	1.37	1938-41	1.75	1936-43	2.30	1932-47	3.15	1924-55	3.43
		1941	1.57	1939-42	1.89	1937-44	1.87	1933-48	2.83	1925-56	3.60
		1942	0.96	1940-43	1.36	1938-45	1.80	1934-49	2.73	1926-57	3.73
		1943	1.25	1941-44	1.45	1939-46	2.41	1935-50	2.84	1927-58	3.49
		1944	1.56	1942-45	1.85	1940-47	2.20	1936-51	2.71	1928-59	3.31
		1945	1.34	1943-46	2.07	1941-48	2.48	1937-52	2.55	1929-60	3.47
		1946	1.10	1944-47	1.67	1942-49	2.61	1938-53	2.46	1930-61	3.11
		1947	1.27	1945-48	1.79	1943-50	2.37	1939-54	2.43	1931-62	2.84
1976		1948	1.42	1946-49	2.14	1944-51	2.16	1940-55	2.27	1932-63	2.73
		1949	1.54	1947-50	2.14	1945-52	2.20	1941-56	2.42	1933-64	2.79
		1950	1.52	1948-51	2.34	1946-53	2.45	1942-57	2.41	1934-65	2.60
		1951	1.59	1949-52	2.30	1947-54	2.04	1943-58	2.41	1935-66	2.64
		1952	1.36	1950-53	1.86	1948-55	2.23	1944-59	2.51	1936-67	2.49
		1953	0.97	1951-54	1.52	1949-56	1.93	1945-60	2.64	1937-68	2.26
		1954	1.70	1952-55	1.32	1950-57	1.80	1946-61	2.46	1938-69	2.17
		1955	1.07	1953-56	1.88	1951-58	1.81	1947-62	2.18		
		1956	1.41	1954-57	1.84	1952-59	2.18	1948-63	2.18		
		1957	1.36	1955-58	1.96	1953-60	3.02	1949-64	2.13		
		1958	1.22	1956-59	1.78	1954-61	2.63	1950-65	2.03		
		1959	1.29	1957-60	2.01	1955-62	2.45	1951-66	1.91		
		1960	1.45	1958-61	1.57	1956-63	1.92	1952-67	2.13		
		1961	1.15	1959-62	1.52	1957-64	1.98	1953-68	2.13		

The physical significance of the equivalent recurrence number $\omega(n)$ can easily be derived from its relation to the mean correlation coefficients r_τ ($\tau=1, 2, \dots, n-1$) between the n solar rotations:

$$\omega(n) = 1 + 2 \frac{n-1}{n} r_1 + 2 \frac{n-2}{n} r_2 + \dots + \frac{2}{n} r_{n-1}. \quad (2)$$

It shows that, for a higher value of n , e.g., n equal to 16 or 32, $\omega(n)$ is determined to a considerable amount by the number of non-vanishing correlation coefficients: $\omega(n)$ increases with increasing number of solar rotations connected

by positive correlation, and vice-versa. Thus the indices $\omega(16)$ and $\omega(32)$ are essentially determined by the mean duration of the activity sequences in the time-pattern of geomagnetic activity. They can be interpreted as a relative measure of the *average life-time* of all disturbance-causing solar *M*-regions within the 16 or 32 rotations considered. Since the solar wind is the transmitting medium for the geomagnetic activity originating primarily from solar activity, the equivalent recurrence numbers may also be conceived as a measure for the degree of *stability* of the large-scale solar wind structure.

The latter interpretation can also be applied to $\omega(8)$. However, regarding $\omega(2)$ and $\omega(4)$ attention has to be paid to the superimposed semiannual wave (Meyer, 1965, 1966, 1973) which clearly is an effect of terrestrial or magnetospheric modulation (see also Damaske, 1977). The appearance of a semiannual wave also in the recurrence tendency, i.e., in the persistence of geomagnetic activity sets, is probably due to the method of calculating $\omega(n)$, using linear deviations from quasi-logarithmic character figures. If $\omega(2)$ and $\omega(4)$ are to indicate the stability of the solar wind structure, the semiannual wave has to be eliminated in a way analogous to the one suggested already for activity indices (Roosen, 1966; Meyer, 1973).

The equivalent recurrence numbers $\omega(n)$ have proved to be a useful tool for recurrence studies of geomagnetic activity (e.g., see Siebert, 1971). Beyond, they are regarded as an adequate basis for detailed correlation studies with solar wind and interplanetary field data.

3. Results for Solar Cycle 20

The musical diagram for $\omega(n)$ ($n=2, 4, 8, 16,$ and 32) shown in Figure 1, supplementing also former diagrams (Meyer, 1965, 1966, and 1973) gives a synoptic picture of the recurrence tendency variations during solar cycle 20 (years 1965–1976). The first index in a year is always associated with the first rotation belonging fully to that year. It refers to the period from $n/2$ rotations before to $(n/2)-1$ rotations after the associated (mean) rotation number. In practice, the associated rotation number can be read either from the table of $\omega(n)$ or from the semi-graphic table of *C9*. Sunspot minimum and maximum are particularly marked by the triangles above the musical charts. In order to facilitate the recognition of recurrence tendency decrease at or soon after sunspot minimum, the beginning of solar cycle 21, beyond the minimum of March 1976, is also shown. The base line for the single indices meets the value of $\omega(n)=1$, corresponding to the absence of any recurrence tendency (accidental sequences of solar rotations). Indices plotted upward denote positive, those plotted downward denote negative (opposite) recurrence tendency. The key shows values at intervals of 0.5. The scale itself is continuous.

As is immediately apparent from the diagram, the recurrence tendency was strongest in 1974 and 1975, i.e., in the two years preceding sunspot minimum, remaining relatively high throughout 1976. But it is also perceptible, with varying intensity, in the years immediately following the sunspot maximum year of 1968. In the interval from 1965 to about 1968 (i.e., the years after the 1964

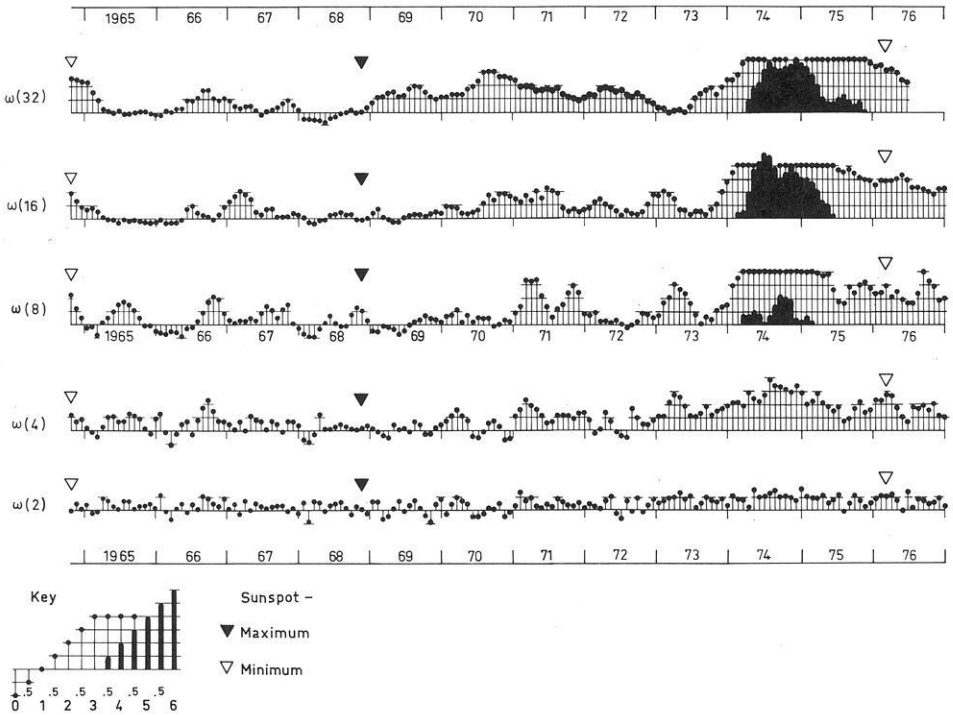


Fig. 1. Equivalent recurrence numbers $\omega(n)$ for the years 1965–1976 (solar rotations 1796–1961)

minimum till sunspot maximum) the recurrence tendency was less pronounced, though still existing on the average.

In its essential characteristics the systematic variation of the recurrence indices $\omega(n)$ during solar cycle 20 corresponds to the average variation of recurrence tendency in the course of a sunspot cycle found, for example, using the superposed epochs method (Bartels, 1948). On the other hand, quite an unusual aspect of solar cycle 20 has been noted concerning variations of geomagnetic activity itself (e.g., Gosling et al., 1977). The maximum activity occurred exceptionally late, not earlier than 1973–1975: i.e., 5–7 years after sunspot maximum, whereas the usual lag is 1–2 years. Furthermore, the activity maximum nearly coincided with the period of extremely high recurrence tendency, while the maximum recurrence tendency usually appears for declining or even minimum activity. This suggests that geomagnetic activity and its recurrence tendency are not as closely correlated as previously supposed by the results from other solar cycles.

As solar cycle 20 is the first cycle for which direct solar wind measurements for longer periods are available, some of the inferences from geomagnetic activity analysis can immediately be related to results of interplanetary data evaluation, though still tentatively in many respects. Recurrence tendencies in the earth passage of interplanetary magnetic sector boundaries as well as in well-defined high-speed wind streams have been reported by Sawyer (1976). Comparing

both he finds that the recurrence interval for the latter has a clearly narrower frequency distribution centered at 27.0 days, i.e., at exactly the same period obtained on the average for geomagnetic activity recurrences. (For sector boundaries the average recurrence interval turns out to be half a day longer). Thus the results of Sawyer are quite in favour of a close correlation between recurrent geomagnetic activity and high-speed solar wind streams.

Further evidence for this view has been given by Gosling et al. (1976) who have plotted the occurrence of all high-speed streams observed from 1962 to 1974 in a 27-day format to emphasize recurrent features. A merely qualitative judgement already shows the distinct difference in the recurrence pattern of different years, i.e.: a rather poor stability in years of high solar activity (1965–1967), an increasing stability on the declining branch of the solar cycle (1970–1973), and the most stable streams appearing in 1974. This is in good agreement with a corresponding variation of the recurrence tendency of geomagnetic activity. Gosling et al. (1976) confirm their results in a more quantitative manner by means of yearly and half-yearly autocorrelation curves. The resolution, however, is not nearly as high as it is for the equivalent recurrence numbers $\omega(n)$. A definite relation between geomagnetic activity and high-speed solar wind streams would, at the same time, identify Bartels' hypothetic M-regions as the coronal holes in which the streams most probably originate (for a review see Zirker, 1977). A detailed analysis of this relation will have to imply systematic correlations between individual streams and activity sequences after eliminating any effects of superimposed magnetospheric modulation. An investigation on this topic is being planned.

References

- Bartels, J.: Erdmagnetismus. In: Naturforschung und Medizin in Deutschland 1939–1946 (FIAT-Review of German Science), Bd. 17 (Geophysik I), J. Bartels, ed.: pp. 27–91. Wiesbaden: Dieterichsche Verlagsbuchh. 1948
- Bartels, J.: Tägliche erdmagnetische Charakterzahlen 1884–1950 und Planetarische dreistündliche erdmagnetische Kennziffern K_p 1932/33 und 1940–1950. Abh. Akad. Wiss. Göttingen, Math.-Phys. Kl., Sonderheft. Göttingen: Vandenhoeck u. Ruprecht 1951
- Bartels, J.: Planetary geomagnetic activity in graphic representation: daily C_p , 1937–1958; three-hourly K_p , 1937–1939, 1950–1958. Abh. Akad. Wiss. Göttingen, Math.-Phys. Kl.; Beitr. Intern. Geophys. Jahr, Heft 3. Göttingen: Vandenhoeck u. Ruprecht 1958
- Bartels, J.: Random fluctuations, persistence, and quasi-persistence in geophysical and cosmical periodicities. Terr. Mag. Atm. El. **40**, 1–60, 1935 (reprinted by Carnegie Institution of Washington, 1959)
- Bartels, J.: Report of Committee No. 9 (Activity). IAGA Meeting of Helsinki 1960
- Chapman, S., Bartels, J.: Geomagnetism, Vol. II. Oxford: Clarendon Press 1940
- Damaske, D.: Magnetospheric modulation of geomagnetic activity, I. Harmonic analysis of quasi-logarithmic indices K_m , K_n , and K_s . Ann. Géophys. **33**, 461–478, 1977
- Gosling, J.T., Asbridge, J.R., Bame, S.J.: An unusual aspect of solar wind speed variations during solar cycle 20. J. Geophys. Res. **82**, 3311–3314, 1977
- Gosling, J.T., Asbridge, J.R., Bame, S.J., Feldman, W.C.: Solar wind speed variations: 1962–1974. J. Geophys. Res. **81**, 5061–5070, 1976
- Meyer, J.: Zur 27täglichen Wiederholungsneigung der erdmagnetischen Aktivität, erschlossen aus den täglichen Charakterzahlen C_8 von 1884–1964. Mitt. Max-Planck-Inst. Aeronomie, Nr. 22. Berlin Heidelberg New York: Springer 1965

- Meyer, J.: A semiannual wave in the recurrence tendency of geomagnetic activity. *J. Geophys. Res.* **71**, 2397–2400, 1966
- Meyer, J.: Zur Modulation der erdmagnetischen Aktivität. *Geophys. Abh., Inst. Geophys. FU Berlin*, Heft 3. Berlin: Reimer 1973
- Roosen, J.: The seasonal variation of geomagnetic disturbance amplitudes. *Bull. Astron. Inst. Netherlands* **18**, 295–305, 1966
- Sawyer, C.: High-speed streams and sector boundaries. *J. Geophys. Res.* **81**, 2437–2441, 1976
- Siebert, M.: Maßzahlen der erdmagnetischen Aktivität. In: *Encyclopedia of Physics*, Vol. XLIX/3, K. Rawer, ed.: pp. 206–275. Berlin Heidelberg New York: Springer 1971
- Zirker, J.B.: Coronal holes and high-speed wind streams. *Rev. Geophys. Space Phys.* **15**, 257–269, 1977

Received October 31, 1977 / Revised Version April 10, 1978

Upper Mantle Structure and Global Earth Tides

H. Wilhelm

Institut für Geophysik, Universität Göttingen, Herzberger Landstraße 180, 3400 Göttingen,
Federal Republic of Germany

Abstract. Static earth tide characteristic numbers are calculated for seismic earth models differing with respect to upper mantle structure. The results confirm that global earth tides are rather insensitive to variations of upper mantle structure. The values of the static numbers obtained for a European continental structure are within the limits $h=0.611 \pm 0.002$, $k=0.301 \pm 0.001$, $l=0.0844 \pm 0.0006$, $\delta=1.161 \pm 0.002$, $\gamma=0.689 \pm 0.002$.

Key words: Earth tides – Upper mantle structure – Love numbers.

Introduction

Model calculations of the response of the earth to tidal accelerations have led to the conviction that the structure of the earth's upper mantle has only a minor influence on earth tides. Alsop and Kuo (1964) concluded from their calculations that different seismic velocities in the upper mantle do not significantly modify the earth tide parameters and that a change of the density distribution may cause a slight variation of the Love numbers. Kuo and Ewing (1966) obtained differences of 3% between the Love numbers h and k for a Gutenberg-Bullen A earth model with a low velocity channel centered at 140 km and a corresponding model with a structure of the New York-Pennsylvania area. Farrell (1972) calculated the M_2 -tide Love numbers for a Gutenberg-Bullen A earth model and two corresponding models in which the top 1000 km were replaced by an oceanic and a continental shield mantle. The differences between the corresponding characteristic numbers were about 1%, and Farrell (1973) concluded that global earth tides are quite insensitive to the earth's structure. Calculations of Wilhelm (1976, 1978) contradicted these results as differences up to 10% between corresponding Love numbers appeared for some of the considered earth models. But, as Denis (1978) pointed out, it is physically quite unlikely that a change of properties in any part of the mantle could produce such large variations of the Love numbers. An examination of the referred calculations has confirmed this objection. As Denis supposed the differences are due to an inadequate computational procedure used for the numerical differentiation of the parameters for the model of Wang (1972) and the models

UTD124A' and UTD124B' of Dziewonski and Gilbert (1972). In the upper mantle of these models there are second order discontinuities with high gradients where the numerical differentiation procedure introduced large errors. If these discontinuities are replaced by first order discontinuities with the corresponding boundary conditions the surprisingly large differences between the results (Wilhelm, 1976, 1978) disappear and a good agreement is obtained.

Results

The transformations used to obtain a set of six first order linear differential equations determining the tidal induced deformation and gravity disturbance differ from the corresponding transformations of Alterman et al. (1959). In order to solve the set of equations (9.38) of Wilhelm (1976) it is therefore necessary to compute the derivatives of density, gravity and Lamé's parameters. In the computation a rigidity of 1 kbar was assumed for the outer core. A diminution of the rigidity generally yields only negligible changes of the results but according to Denis (1978), the calculated static Love numbers can be different according to whether the outer core is assumed to be fluid or not. In case of a nonvanishing rigidity in the outer core the Jeffreys-Vicente conjecture (Pekeris and Accad, 1972) holds whereas for a fluid outer core this conjecture may not be valid. However, if the Jeffreys-Vicente conjecture applies the static Love numbers calculated for core models with vanishing or small nonvanishing rigidity should agree. The determination of the static deformation of an earth model with a fluid core is still a matter of discussion (for references see (Denis, 1978)).

The tidal characteristic numbers were calculated for the model of Wang (1972), the models UTD124A' and UTD124B' of Dziewonski and Gilbert (1972), the models B497 and C198 of Gilbert et al. (1973) tabulated in (Dziewonski and Gilbert, 1973), the models 1066A and 1066B of Gilbert and Dziewonski (1975), the model B1 of Jordan and Anderson (1974), and the model C2 of Anderson and Hart (1976). The results are shown in Table 1. The model of Wang is slightly modified in the crust in order to avoid a negative Poisson's number. Model C2 has an ocean of 3 km depth, therefore the characteristic numbers refer to the ocean bottom. The values of h , k , $\delta-1$ and γ agree to within about 2% and l to within 3% with each other. These calculations confirm the result that global earth tides are rather insensitive to the structure of the upper mantle and contrary assertions of Wilhelm (1976, 1978) are disproved.

Reference values of the earth tide parameters for European stations can be obtained by substituting a common upper mantle for the different upper mantles of the models of Table 1. Investigations of the dispersion of surface waves (Seidl, 1971; Seidl et al., 1971) have led to the model KA-100 for the upper mantle structure in western Europe. If the substitution is performed with this upper mantle model the characteristic numbers of Table 2 are obtained. Now there are only small differences in the third significant digit between corresponding values. The last two lines show the centered values and bounds for each column. They represent undisturbed static tidal parameters which can be expected for western Europe.

Table 1. Static characteristic numbers for the considered earth models

	h	k	l	δ	γ
WANG	0.612	0.302	0.0846	1.159	0.690
UTD124A'	0.609	0.301	0.0861	1.158	0.691
UTD124B'	0.609	0.301	0.0861	1.158	0.691
B497	0.610	0.301	0.0850	1.159	0.691
C198	0.610	0.301	0.0851	1.159	0.691
1066A	0.611	0.301	0.0845	1.159	0.690
1066B	0.611	0.301	0.0842	1.159	0.690
B1	0.608	0.301	0.0856	1.158	0.692
C2	0.618	0.303	0.0841	1.163	0.685

Table 2. Static characteristic numbers for the models of Table 1 with KA-100 upper mantle structure (cf. text)

	h	k	l	δ	γ
WANGKA	0.612	0.300	0.0840	1.162	0.688
124A'KA } 124B'KA }	0.610	0.300	0.0850	1.160	0.690
B497KA } C198KA }	0.612	0.301	0.0842	1.161	0.689
1066AKA	0.610	0.300	0.0844	1.160	0.690
1066BKA	0.611	0.301	0.0842	1.160	0.690
B1KA	0.611	0.301	0.0845	1.159	0.690
C2KA	0.613	0.301	0.0838	1.161	0.688
	0.611 ± 0.002	0.301 ± 0.001	0.0844 ± 0.0006	1.161 ± 0.002	0.689 ± 0.002

Table 3. Static characteristic numbers for model B497 with upper mantle structure of W-, SW-, and SE-Europe (cf. text)

	h	k	l	δ	γ
B497KA	0.612	0.301	0.0842	1.161	0.689
B497SW	0.611	0.300	0.0834	1.160	0.690
B497SE	0.610	0.300	0.0835	1.160	0.690

For SE-Europe and for SW-Europe a slightly different structure of the upper mantle has to be assumed. The body wave velocities of these models were taken from (Mayer-Rosa, 1969) and (Mayer-Rosa and Müller, 1973), the density is tabulated in (Müller, 1971). In order to examine how much the differences of the upper mantle structure of W-Europe, SW-Europe and SE-Europe can affect the tidal parameters, the upper mantle of model B497 was replaced by the upper mantle models for SW- and SE-Europe. From the results shown in Table 3 it is evident that there are no significant variations of the values of h , k , δ -1, and γ for these models of the upper mantle in Europe.

Comparison With Earth Tide Measurements

A comparison with characteristic numbers resulting from earth tide measurements is only possible for the tide O_1 which in the European area is not so much disturbed by the indirect effect of ocean tides or by meteorological disturbances. From measurements over a period of altogether about 16,000 days at European stations Melchior (1974) obtains

$$\delta(O_1) = 1.164 \pm 0.001 \quad \gamma(O_1) = 0.674 \pm 0.005 \quad (1)$$

from which follows

$$h(O_1) = 0.638 \pm 0.017 \quad k(O_1) = 0.317 \pm 0.011. \quad (2)$$

$\delta(O_1)$ is somewhat greater and $\gamma(O_1)$ is distinctly smaller than the corresponding values of Table 2. The difference between the values of γ indicates that systematic disturbing influences are still affecting the mean value (1) of $\gamma(O_1)$. Since about 70% of the original data were obtained at earth tide stations in Belgium and Luxembourg (Melchior, 1973) a systematic disturbance may be caused by the indirect effect of ocean tides. A map of the regional distribution of $\delta(O_1)$ in Europe (Melchior et al., 1976) shows a continuous decrease of $\delta(O_1)$ from the Belgian coast (Ostende) via Bruxelles to Luxembourg (Walferdange). However, it is doubtful if the indirect effect is responsible for the deviation from the theoretically calculated values, as model calculations of the influence of the indirect effect on the M_2 -tide lead to even greater discrepancies. On the other hand the recently published values (Melchior, 1978)

$$\delta(O_1) = 1.1608 \pm 0.0086 \quad \gamma(O_1) = 0.6788 \pm 0.0056 \quad (3)$$

are approaching the corresponding values of Table 2.

Conclusions

The present investigation confirms that global earth tides are not significantly influenced by the structure of the upper mantle. The differences between the characteristic numbers calculated for earth models with various upper mantle structures are about 2%. Only the differences between the corresponding Shida numbers l attain 3%.

There are discrepancies left between the mean values of $\gamma(O_1)$ obtained from measurements at European stations and the corresponding static values calculated for a European continental structure. The reason for these discrepancies should be examined.

Acknowledgements. I am grateful to Carlo Denis for critical discussions and convincing argumentation in favour of the smallness of the influence of the upper mantle structure on earth tides, and I am thankful to Professor St. Müller for communicating to me the upper mantle model KA-100 and to the referees for their comments. The numerical calculations have been done at the Univac 1108 of the Gesellschaft für Wissenschaftliche Datenverarbeitung mbH Göttingen.

References

- Alsop, L.E., Kuo, J.T.: Semi-diurnal tidal components for various earth models, *Comm. Obs. Roy. Belgique* 236, sér. géophys. **69**, 93–107, 1964
- Alterman, Z., Jarosch, H., Pekeris, C.L.: Oscillations of the earth, *Proc. Roy. Soc. London, Ser. A* **252**, 80–95, 1959
- Anderson, D.L., Hart, R.S.: An earth model based on free oscillations and body waves, *J. Geophys. Res.* **81**, 1461–1475, 1976
- Denis, C.: Static and dynamic effects in theoretical Love numbers, *Proceedings 8th Symp. Earth Tides*, M. Bonatz, ed. Bonn: 1978 (accepted for publication)
- Dziewonski, A.M., Gilbert, F.: Observations of normal modes from 84 recordings of the Alaskan earthquake of 1964 March 28, *Geophys. J.* **27**, 393–446, 1972
- Dziewonski, A.M., Gilbert, F.: Observations of normal modes from 84 recordings of the Alaskan earthquake of 1964 March 28-II. Further remarks based on new spheroidal overtone data, *Geophys. J.* **35**, 401–437, 1973
- Farrell, W.E.: Deformation of the earth by surface loads, *Rev. Geophys. Space Phys.* **10**, 761–797, 1972
- Farrell, W.E.: Earth tides, ocean tides and tidal loading, *Phil. Trans. Roy. Soc. London, Ser. A* **274**, 253–259, 1973
- Gilbert, F., Dziewonski, A.M., Brune, J.: An informative solution to a seismological inverse problem, *Proc. Natl. Acad. Sci.* **70**, 1410–1413, 1973
- Gilbert, F., Dziewonski, A.M.: An application of normal mode theory to the retrieval of structural parameters and source mechanisms for seismic spectra, *Phil. Trans. Roy. Soc. London, Ser. A* **278**, 187–269, 1975
- Jordan, T.H., Anderson, D.L.: Earth structure from free oscillations and travel times, *Geophys. J.* **36**, 411–459, 1974
- Kuo, J.T., Ewing, M.: Spatial variations of tidal gravity, in the Earth beneath the Continents, J.S. Steinhart, T.J. Smith, eds., *Am. Geophys. Monograph* **10**, 595–610, 1966
- Mayer-Rosa, D.: Die Geschwindigkeitsverteilung seismischer Wellen im oberen Erdmantel Europas, Dissertation, Fak. f. Natur- u. Geisteswiss., Univ. Stuttgart, 1969
- Mayer-Rosa, D., Müller, St.: The gross velocity-depth distribution of P- and S-waves in the upper mantle of Europe from earthquake observations, *Z. Geophys.* **39**, 395–410, 1973
- Melchior, P.: Some problems of tilt and strain measurements, *Phil. Trans. Roy. Soc. London, Ser. A* **274**, 203–208, 1973
- Melchior, P.: Earth tides, *Geophys. Surv.* **1**, 275–303, 1974
- Melchior, P.: Report on the activities of the International Centre for Earth Tides (ICEI), *Proceedings 8th Int. Symp. Earth Tides*, M. Bonatz, ed. Bonn: 1978 (accepted for publication)
- Melchior, P., Kuo, J.T., Ducarme, B.: Earth tide gravity maps for western Europe, *Physics Earth Planet. Inter.* **13**, 184–196, 1976
- Müller, G.: Approximate treatment of elastic body waves in media with spherical symmetry, *Geophys. J.* **23**, 435–449, 1971
- Pekeris, C.L., Accad, Y.: Dynamics of the liquid core of the earth, *Phil. Trans. Roy. Soc. London, Ser. A* **273**, 237–260, 1972
- Seidl, D.: Spezielle Probleme der Ausbreitung seismischer Oberflächenwellen mit Beobachtungsbeispielen aus Europa, Dissertation, Fak. f. Physik, Univ. Karlsruhe, 1971
- Seidl, D., Müller, St., Reichenbach, H.: Dispersion and absorption of seismic surface waves and the structure of the upper mantle based on observations in Europe, *Comm. Obs. Roy. Belgique, A* 13, sér. géophys. **101**, 198–199, 1971
- Wang, C.Y.: A simple earth model, *J. Geophys. Res.* **77**, 4318–4329, 1972
- Wilhelm, H.: Bestimmung elastischer Parameter des Erdinnern durch Erdzeiten, *Deutsche Geodät. Komm.*, C **222**, 1976
- Wilhelm, H.: Influence of upper mantle structure on earth tides, *Proceedings 8th Symp. Earth Tides*, M. Bonatz, ed. Bonn: 1978 (accepted for publication)

Simple Plate Models of Mantle Convection

F. Richter¹ and D. McKenzie²

¹Department of the Geophysical Sciences, The University of Chicago, Chicago, Ill, 60637, USA

²Department of Geodesy and Geophysics, Cambridge University, Madingley Rise,
Madingley Road, Cambridge CB3 0EZ, England

Abstract. A simple convective model that can maintain observed plate motions consists of a viscous upper mantle of uniform density overlain by denser rigid plates. In the absence of density differences within the upper mantle the viscous stresses exerted by the flow are easily obtained and demonstrate that the buoyancy forces associated with plate creation and destruction can maintain plate motions. A model having a uniform viscosity upper mantle is, however, unsatisfactory because it predicts gravity and residual depth anomalies two orders of magnitude larger than those observed. This problem can be overcome by introducing a thin low viscosity layer beneath the plates. The resulting model is then similar to that proposed by Forsyth and Uyeda and by Chapple and Tullis despite a very different approach. This agreement suggests that the energetics of plate motion are now understood in outline. The model cannot, however, account for the existence of the longwavelength gravity anomalies which are not associated with plate motions.

Key words: Plate dynamics – Mantle convection – Mantle viscosity.

1. Introduction

Though the kinetic description of the earth's surface motion has been generally accepted, there is much less agreement about how the motions are maintained. The dynamic problem consists of two separate but related questions: How does the mantle convert heat into mechanical work to maintain the observed plate motions, and why is the large-scale flow of which the plate motions form part stable to smaller scale motions? The first of these two questions is the simpler, and it is with it that this paper will be principally concerned. All the forces which we will consider arise from thermal convection: Heat is transported upward by hot, less dense, material rising to replace denser, colder material. However, the form the motion takes does not resemble Rayleigh-Benard con-

vection. The dimensions and relative velocities of the plates are known by direct observation, and simple models for the thermal structure of ridges and sinking slabs account for a considerable variety of geophysical observations. If all other buoyancy forces are ignored it is straightforward to use this information to calculate the work supplied by the rigid plate motions themselves. This is the simple model we consider below. Though it is likely that the buoyancy forces near ridges and trenches provide an important part of the energy required to maintain the flow, exactly how important a part is not yet clear. It seems unlikely that the only buoyancy forces in the mantle are those which result from the temperature contrast between the sinking slabs and the surrounding mantle, and the corresponding forces at ridges. For a variety of reasons (Richter, 1973b; McKenzie et al., 1974; McKenzie and Weiss, 1975; Richter and Parsons, 1975) some form of flow in the mantle with a length scale of 700 km or less seems difficult to avoid, though as yet we have no observations about the form such flow takes. But if it occurs it must be driven by buoyancy forces which are not the direct result of plate production or destruction. Here we will assume that the only effect of the small scale on the large occurs through the mean temperature gradient. The small-scale flow must maintain a temperature gradient close to the adiabatic in most parts of the mantle and hence a reasonable approximation is to ignore all buoyancy effects outside the plates when considering the energetics of the large-scale flow. This approximation enormously simplifies the discussion because the equations governing the flow of material beneath the plates no longer explicitly involve the convection of heat. Whether such an approximation is justified is uncertain. Both scales of convection are strongly non-linear and can interact, but until more knowledge is forthcoming from laboratory or numerical experiments it seems sensible to ignore such possible complications.

Perhaps a more important difficulty is the probable existence of large-scale vertical motions unrelated to that associated with ridges and trenches. That such flows exist is strongly suggested by the long wavelength gravity anomalies determined from satellite motions. Many major anomalies are not obviously related to any present day plate boundaries, and the implied mantle flow may well be partly responsible for maintaining plate motions (see Section 5).

We will assume that the deformation of mantle materials can be described by a Newtonian viscosity, and allow the viscosity to be only a function of position. The equations are then linear and easily solved numerically. Such an approach is still basically kinematic, since the mantle motions are driven by motions of the boundaries. It does, however, allow a discussion of the forces which resist plate motion in terms of a possible fluid mechanical model, and in this respect is superior to the models used by Forsyth and Uyeda (1975) and by Chapple and Tullis (1977). They attempted to use the observed plate motions to determine the force balance on the major plates but did not explicitly consider the fluid dynamical forces resulting from the surface motions.

A most important feature of our model is that the motions are confined to the upper 700 km of the earth's mantle. Recently various authors (O'Connell, 1977; Davies, 1977a and b) have argued that convection associated with plate motions extends throughout the mantle. However, they have not put forward a

detailed model to account for the focal mechanisms within sinking slabs (Fig. 11). The state of stress indicated by the focal mechanisms is most easily explained by the inability of the slabs to penetrate deeper than 700 km. The observed mechanisms have always been and still are most difficult to account for by convection throughout the mantle, and none of the authors who favor such a flow have done so. No corresponding difficulty arises with the model used here.

In Section 4 the model is required to satisfy four observational constraints that are not in dispute. Three of these provide upper limits and one provides a lower limit on the mantle viscosity. These limits do not overlap for models having uniform viscosity, but it appears possible to construct a self-consistent model in which the mantle viscosity increases with depth.

2. The Model

In the absence of buoyancy forces the equations governing the motion of an incompressible fluid may be written:

$$\eta \nabla^2 \mathbf{u} = -\rho \nabla U + \nabla p \quad (1)$$

$$\nabla \cdot \mathbf{u} = 0 \quad (2)$$

where η is the viscosity, ρ the density, \mathbf{u} the fluid velocity, U the gravitational potential and p the pressure. Both the density and the viscosity are taken to be constant. If the flow is two-dimensional in the x, z plane, \mathbf{u} can be written in terms of a stream function

$$\mathbf{u} = \left(\frac{\partial \psi}{\partial z}, 0, -\frac{\partial \psi}{\partial x} \right) \quad (3)$$

and the curl of (1) becomes

$$\nabla^4 \psi = 0. \quad (4)$$

It is convenient to rewrite (4) as

$$\nabla^2 \zeta = 0 \quad (5)$$

$$\nabla^2 \psi = \zeta \quad (6)$$

where ζ is the vorticity, because fast subroutines are available for solving Poisson's and Laplace's equations. Though conversion of (1) and (2) into (5) and (6) is a convenient method of solving Stokes flow problems, it somewhat obscures the nature of the driving force. (1) shows that the flow is driven by the difference between the gravitational and pressure forces. In many fluid mechanical problems it is not necessary to determine the pressure, and a solution to (5) and (6) is sufficient. This is not the case here because we need to know the work done by rigid boundaries moving into the fluid. In the absence of flow (1) reduces to

$$\rho \nabla U_0 = \nabla p_0 \quad (7)$$

where U_0 and p_0 are the hydrostatic values for the gravitational potential and the pressure. When $\mathbf{u} \neq 0$

$$\begin{aligned} U &= U_0 + U_1 \\ p &= p_0 + p_1 \end{aligned} \quad (8)$$

and (1) becomes

$$\eta \nabla^2 \mathbf{u} = -\rho \nabla U_1 + \nabla p_1 \quad (9)$$

The term $-\rho \nabla U_1$ describes the influence of the gravity perturbation resulting from the flow on the fluid motions themselves, and is somewhat complicated to evaluate. Provided $\rho \nabla U_1 \ll \nabla p_1$ we may neglect the contribution of $\rho \nabla U_1$ to \mathbf{u} , even though we later need to obtain ∇U_1 for comparison with the observations. The resulting error may be estimated from the expressions obtained by McKenzie (1968, Appendix D) and by Pekeris (1935) for the surface deformation and gravity field produced by low Rayleigh number thermal convection in a uniform viscous sphere. These expressions show that, when the wavelength of the circulation is 10^4 km, the gravity anomaly is underestimated by about 30%, if $\rho \nabla U_1$ is neglected in (9), and the surface deformation by about 10%, decreasing to 15% and 5%, respectively, when the wavelength is 4000 km. Since we are only concerned with the order of magnitude of these two quantities, we may therefore neglect $\rho \nabla U_1$ in (9), which may be then written as

$$\eta \left(\frac{\partial \zeta}{\partial z}, 0, -\frac{\partial \zeta}{\partial x} \right) = \left(\frac{\partial p_1}{\partial x}, 0, \frac{\partial p_1}{\partial z} \right) \quad (10)$$

and hence p_1 is easily obtained. Since only ∇p_1 enters (9), any arbitrary constant may be added to p_1 . This indeterminacy allows us to choose an arbitrary origin for p_1 .

In all cases we will consider, the motion will be driven by a rigid plate of thickness t moving with a velocity V and the layer in which the motion is occurring will have a depth d (Fig. 1). It is therefore convenient to write

$$\begin{aligned} \mathbf{u} &= V \mathbf{u}', \quad \zeta = \frac{V}{d} \zeta', \quad x = dx' \\ p_1 &= \frac{\eta V}{d} p_1', \quad \psi = V d \psi', \quad z = dz' \end{aligned} \quad (11)$$

$$F = -\int p_1 dx, = -\eta V \int p_1' dx'$$

where the primed quantities are dimensionless, and F is the force/unit length. (10) then reduces to

$$\left(\frac{\partial \zeta'}{\partial z'}, 0, -\frac{\partial \zeta'}{\partial x'} \right) = \left(\frac{\partial p_1'}{\partial x'}, 0, \frac{\partial p_1'}{\partial z'} \right) \quad (12)$$

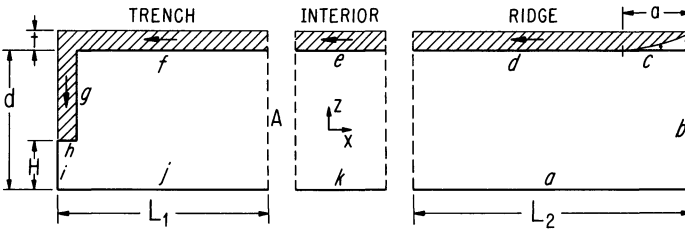


Fig. 1. Typical model for the large-scale flow, driven by dimensionless velocities imposed on the boundaries. Both components of the velocity vanish on a , j , and k . The normal component vanishes, but the tangential component is set to -1 on d , e , f , and g . On b and i the normal component of the velocity and the tangential stress vanish. On h the tangential velocity is zero and the normal component is -1 . On c the normal velocity is given by (20). This model imposes reflection symmetry across both left and right hand edges, and was used to calculate the forces in Figures 4–6, and 8. Those in Figure 7 were obtained from a model with a more realistic boundary condition on the left

It is clear from the dimensionless forms of (5) and (6) that the solutions do not depend on V . Similarly the dimensionless values of the forces/unit length are independent of V , and the true forces F can be obtained simply by multiplying by ηV . This simplicity and generality is a consequence of the neglect of buoyancy forces in the fluid, and the assumption that η is constant.

It is convenient to divide the circulation into three regions shown in Figure 1: The trench, the interior, and the ridge. This division resembles that made by Schubert and Turcotte (1972), who were concerned with the flow in the interior region. Sufficiently far from both ridge and trench regions, the stream lines must be horizontal and expressions for ψ' , ζ' , and dp'_1/dx' may be obtained analytically

$$\begin{aligned}
 \psi' &= (3t' + 1)z'^2 - (2t' + 1)z'^3 \\
 \zeta' &= 2\{(3t' + 1) - 3(2t' + 1)z'\} \\
 \frac{\partial p'_1}{\partial x'} &= -6(2t' + 1)
 \end{aligned}
 \tag{13}$$

where $t' = t/d$ is the dimensionless plate thickness, the surface velocity is unity, and the total mass flux across any vertical plane is zero. The principal test we use to discover how far we need to be from the ridge and trench regions before (13) applies depends on the independence of dp'_1/dx' on z' in the interior. The interior solution for ψ' is imposed as a boundary condition on the dashed line of either the ridge or the trench region (Fig. 1). For ζ' and p' given by (13) to apply on the boundary, dp'_1/dx' and hence p'_1 , must be found to be independent of z' . Various cases are given in Figure 4, and show that the greatest variation of p'_1 with depth is less than 1%.

We will also need the corresponding expressions when the shear stress vanishes on the upper surface of the viscous layer;

$$\psi' = \frac{t'}{2} (3z'^2 - z'^3)$$

$$\zeta' = 3t'(1 - z')$$

$$\frac{dp'_1}{dx'} = -3t' \quad (\text{see also Appendix}).$$
(14)

Since the lateral extent of large plates is much greater than their thickness, the horizontal variation in p'_1 cannot be maintained by elastic forces within the plate but must be compensated isostatically. Therefore the appropriate boundary condition to apply at the surface is that the normal stress vanishes, and that dp'_1/dx' is maintained by a surface slope de'/dx' where $e'd$ is the change in elevation above a level surface due to the flow.

$$\frac{de}{dx} = \frac{1}{(\rho_m - \rho_w)g} \frac{dp_1}{dx} = \frac{\eta V}{(\rho_m - \rho_w)d^2g} \frac{dp'_1}{dx'} \quad (15)$$

where ρ_m is the density of the mantle, ρ_w that of sea water. The gradient of the gravity anomaly corresponding to the surface slope is

$$\frac{d\Delta g}{dx} \approx 0.42 \frac{\eta V}{g d^2} \frac{dp'_1}{dx'} \quad (16)$$

when Δg is measured in mms^{-2} . Since ρ is affected by the thermal structure of the plate, whereas the long wavelength components of Δg are not, (16) is generally a more useful result than (15). This argument assumes that the lower boundary of the convecting region near 700 km is not deformed by the horizontal variation in p'_1 . If deformation is possible (15) remains unchanged but the long wavelength components of the gravity field are removed by compensation (McKenzie, 1977). Under these conditions (15) is more useful. An additional complication occurs if the lower boundary results from a phase change. It may then be shown (McKenzie, in preparation) that (16) underestimates the size of $d\Delta g/dx$. Since it is not yet clear what is the nature of the boundary at a depth of 700 km, we use both (15) and (16) to estimate η .

The interior flow produces a viscous stress on the base of the plate, and the surface tilting causes a sliding force to act in the same direction. Both these forces therefore oppose the motion. The first of these gives a force/unit length

$$f_V = \frac{\eta V}{d} \zeta' \Big|_{z'=1} \quad (17)$$

whereas the sliding force/unit length f_s

$$f_s = -\frac{\eta V}{d} t' \frac{dp'_1}{dx'} \quad (18)$$

In the trench region the boundary conditions used are indicated in the captions to Figures 1 and 2. In some models a velocity of -2 was used on g to discover whether a rapidly sinking slab could drag the surface plate towards the

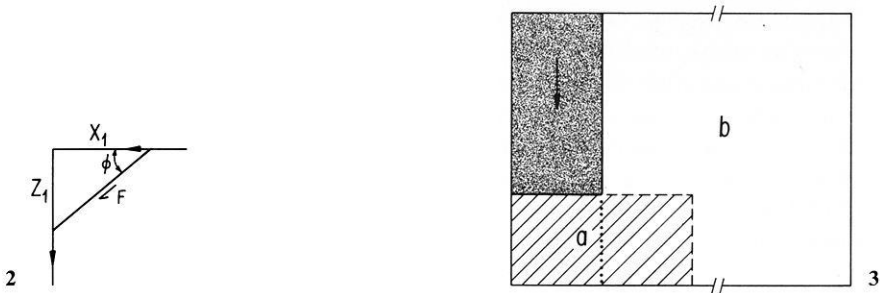


Fig. 2. The corner region at the trench. Because the velocity gradient is singular at the corner the stress is infinite. This region was excluded from the force balance calculations by neglecting the forces on x_1 and z_1 , where $x_1=0.125$, $z_1=0.185$. The force F on the oblique boundary was obtained from both the finite difference calculation and from a (singular) similarity solution

Fig. 3. Sketch to illustrate how the biharmonic equation was solved in the region beneath the slab tip. The equation was first solved in b with $\psi'=\zeta'=0$ on the dotted boundary, then this solution used to provide boundary conditions on the dashed boundary of a , and the process repeated by b . This iterative method converged rapidly

trench. The least realistic of the boundary conditions is that imposed on i . This boundary is only stress free if the flow has reflection symmetry about the left edge of the figure, and clearly this is a poor approximation: Real trenches are strongly asymmetric. We therefore also carried out calculations on a more realistic asymmetric model.

The basic numerical method used to solve (5) and (6) in the presence of rigid boundaries was described by Richter (1973a). All the calculations described below used 32 vertical mesh points and square elements. However, certain difficulties arise in applying finite difference schemes to the trench region. Because the position of the boundary A in Figure 1 is arbitrary, the value of L_1 should not affect the solution. If, however, (13) is imposed as a boundary condition on A and L_1 is small, the flow will be strongly affected by the value chosen, whereas if L_1 is made large, computer time will be wasted since a large part of the solution will be indistinguishable from (13). It is undesirable to increase the mesh spacing since in places the vorticity varies rapidly. A convenient test was the constancy of p'_1 on A . Since the pressure in the interior flow should only be a function of x' , too small a value of L_1 produced some variation with z' . This and other simple tests showed that a value of 1.5 was a good compromise.

The most obvious objection to the boundary conditions imposed in Figure 1 in the trench region is that they require a singularity in the vorticity in the upper left hand corner. The singularity occurs because the velocity is not continuous, and it is not obvious that the numerical scheme will model this region accurately. Furthermore, the similarity solution for the flow in this corner (Hewitt et al., 1975) shows that the shear forces acting on the horizontal and vertical boundaries are infinite. The mathematical cause of this singularity is that the velocity is not continuous and hence the stress, which depends on the gradient of the velocity, is infinite. Such singularities commonly arise in fluid mechanics

when the equations used to describe the physical behavior of the system locally no longer do so. In this example the relationship between stress and strain rate ceases to be linear when the stress exceeds a particular value. Unless solutions to the non-linear equations are obtained we must exclude the corner region from the calculations of force balance. We did this by cutting off the region with an oblique surface at an angle ϕ to the horizontal (Fig. 2), and calculating the force F' which the flow exerted on this surface. When $\phi = \pi/4$, the value of F' is easily obtained from the similarity solution:

$$F' = 2\sqrt{2} \left/ \left(1 + \frac{\pi}{2} \right) \right. \doteq 1.10 \quad (19)$$

It must be independent of the position of the surface because there are no length scales in the similarity solution. The corresponding value from the numerical solution was 1.07 when the surface intersected 4 grid points from the corner. Such good agreement is somewhat surprising, and shows that the singularity in the vorticity does not produce undesirable numerical effects.

The last difficulty in the trench region results from the geometry of the fluid. The numerical schemes we used can only solve the equations in rectangular regions. We overcame this problem by using two overlapping regions shown in Figure 3, and iterating between the two. The first step consisted in solving for ψ' and ζ' in region b with $\zeta' = \psi' = 0$ on the dotted part of the boundary. The resulting solution was then used as a boundary condition on the dashed part of the boundary of region a . This solution was in turn used for boundary conditions for region b . Ten such iterations were used, and the maximum difference in ψ' in the overlapping region was 1 part in 10^4 . The accuracy of this numerical procedure was tested by carrying out a simple experiment, described in detail elsewhere (Richter, 1977). A buoyant rectangular rod was allowed to rise through a layer of glycerine. Since the buoyancy force depends only on the cross sectional area of the rod and the density contrast between the rod and the glycerine, the driving force is known. The calculated and observed velocities showed excellent agreement, and therefore confirm the accuracy of the iterative scheme.

The ridge region contains no features not present in the trench region. A simpler model would not possess the boundary c , and d would continue to meet b . However, such a model would possess a vorticity singularity and would also have no boundary where material could flow out of the region. Both difficulties may be avoided by introducing a free boundary c of width $a = da'$ on which the normal velocity is specified:

$$U'_z = \frac{2t'}{a'^2} (x' - L_2 + a'). \quad (20)$$

Such a boundary seems reasonable beneath a ridge, where the partial melting and the elevated temperature are likely to decouple the surface plate motions from those of the mantle below. Since d is a rigid boundary and c is not, there is a discontinuity in vorticity where they meet. The same arguments as before apply to the choice of L_2 , which was taken to be 2.

Though the model outlined above is obviously an approximation to the full mantle circulation problem it is nonetheless a self-consistent convective model (except in the corner region near the trench where the singularity is present). Hence within the limitations of our model we take full account of all fluid dynamical forces. The unusual form which some of these forces take arises because of mass transfer across boundaries h and c in Figure 1 and the work done by other moving boundaries. It is important to emphasize that these forces are not artifacts of our particular model and that exactly the same forces are found in a continuously deforming material if one isolates particular parts of the system.

3. Forces

Resistive Forces

The results of the calculations using the model in Figure 1 are shown in Figures 4–8. The ridge models in Figure 4 have a variable width of boundary on which the vertical velocity is non-zero and given by (20). Since the plate thickness is small compared to the thickness of the layer, flow which is driven by the mass flux across the boundary is weak compared with that driven by the

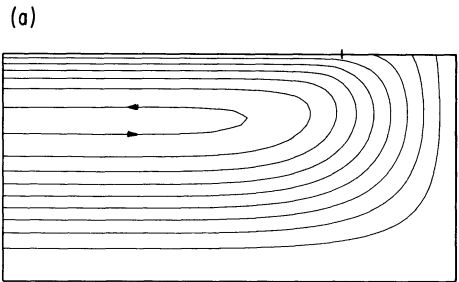
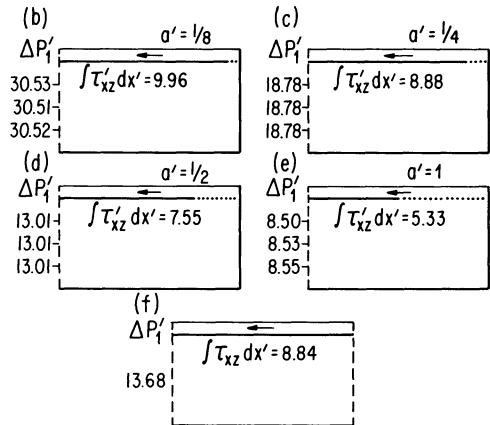
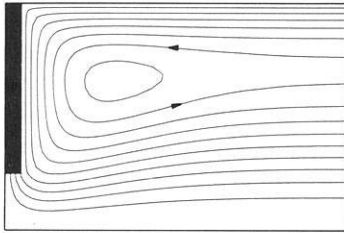


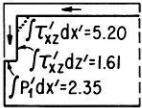
Fig. 4a-f. Ridge models with a plate moving to the left with $u'_x = -1$ for various values of a' . The width of the region is twice the depth. $\int \tau'_{xz} dx'$ is the dimensionless force/unit width which resists the motion of the plate. $\Delta p'_1$ is the dimensionless pressure difference between points at depths of $\frac{1}{4}$, $\frac{1}{2}$, and $\frac{3}{4}$, and the ridge axis at the top right. (f) shows the resistive force and pressure drop of the corresponding interior solution. The vertical velocity imposed on the dotted boundary is given by (20). The contour interval for ψ' in (a) is 0.022 and $t' = 4.5/32$



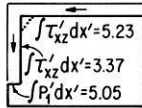
(a)



(b)



(c)



(d)

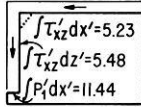


Fig. 5a-d. Trench models, symmetric about the left hand boundary, with a sinking slab moving vertically with $u'_z = -1$ and the plate moving horizontally with $u'_x = -1$. The region extends a distance of 1.5. The mass flux through the tip of the slab and through the right hand boundary is $Vt/2$. $\int \tau'_{xz} dx'$ is the force/unit width resisting the plate motion, excluding the part to the left of the dotted line within $9/64$ of the corner singularity. $\int \tau'_{xz} dz'$ is the force/unit width acting on one side of the sinking slab, excluding the part above the dotted line. $\int p'_1 dx'$ is the force/unit width due to the pressure difference between the right hand edge of the region and the tip of the slab. The force/unit width acting on the dotted line is 1.10 and is a driving, not a resistive, force. It is not included in the force balance calculations. The contour intervals for stream lines in (1) is 0.022, and the slab extends to a depth of $\frac{1}{2}$ in (b), $\frac{3}{4}$ in (c), and $\frac{7}{8}$ in (d)

horizontal plate motion. Hence the major upwelling does not occur beneath the ridge axis but where the boundary condition changes to fixed horizontal velocity. The various models for a ridge in Figure 4 should be compared with the corresponding interior solution (Fig. 4f). Only those models with a total width of prescribed upwelling smaller than $\frac{1}{4}$ have significantly greater resistive forces than those of the corresponding interior solution. There is at present no information about the half width of the region below the ridge axis where the viscosity is strongly reduced. It is not even known whether this region is limited to the ridge axis or extends beneath all plates and decouples their motion from that of the mantle below (see section 4). This ignorance suggests that it is at present unnecessary to use anything more sophisticated than the interior solution when calculating the resistive forces near ridges.

The forces near trenches are considerably more complicated. The simplest model consists of a slab sinking vertically with velocity -1 (Fig. 5). The resistive force $\int \tau'_{xz} dx'$ which acts on the horizontal plate is infinite if evaluated from the point in contact with the sinking slab. As explained in the last section, this corner region was excluded from the calculations (Fig. 2). The remaining force is slightly less than the corresponding interior solution for a plate of width 1.5. The force acting on the dotted line in Figure 5 is a driving force of small magnitude (1.10). It was not included in the force balances because it is not a true source of work, but results from the exclusion of the singularity. The force acting on the side of the sinking slab $\int \tau'_{xz} dz'$ also is infinite if integrated from the corner, but once again this region is excluded. Since large velocity gradients occur when the

tip of the sinking slab approaches the lower boundary of the layer, the magnitude of this force depends strongly on the length of the sinking slab.

The most important force F'_p acts on the tip of the sinking slab and involves the perturbed pressure p'_1 .

$$F'_p = \int_0^{l'} p'_1 dx'$$

The origin of p'_1 was chosen to be the ridge axis. It is convenient to divide p'_1 into three contributions: the first due to the flow in Figure 4, the second due to the interior flow and the third due to the flow near the trench. Only the third contribution is shown in Figure 5. If the plate width is greater than 1.5, a term due to the interior flow must be added. F'_p represents the work that must be done to transfer mass from the tip of the slab to the ridge axis. It is not present if the slab and plate have no thickness. It is clear from the numbers in Figure 5 that, even without the contribution from the interior, F'_p is greater than the shear force on the vertical boundary of the sinking slab. Within a convecting fluid the same result holds: the pressure considerably exceeds the shear stress (McKenzie, 1977). This result is only apparent if p'_1 is calculated, which it rarely is.

Besides the fluid dynamical forces acting on the bases and edges of plates, forces act on the faults which form plate boundaries. These forces can be divided into two components, one in the plane of the fault and one normal to it. The first component is involved in the generation of earthquakes, and most of the information about its magnitude has been obtained from detailed investigations of the radiated seismic waves. Studies of a number of large earthquakes (Kanamori, 1970a, 1971; Wu and Kanamori, 1973; Fukao, 1973) have shown that the difference between the initial and final stress is between 2×10^6 and 5×10^6 newtons m^{-2} . There is at present no evidence that either the stress or the stress drop depend on the type of plate boundary involved. On ridges the earthquakes produced by motion on both normal and strike slip faults are shallower than 10 km (Weidner and Aki, 1973; Prothero et al., 1976). Also on rapidly spreading ridges, with plate separation rates of 60 mm yr^{-1} or more, earthquakes are rare and small, and large normal faults are also absent. We will therefore ignore frictional resistance between separating plates.

The importance of transform faults is less clear. They are generally almost vertical, and those that have been studied in detail release little seismic energy below 12 km. If the resistive forces were zero below this depth their contribution to the force balance could be ignored. Since, however, plates are more than 80 km thick the absence of earthquakes is unlikely to result from the absence of stresses, but is more likely to be due to a change in the behaviour of deforming rocks. If the stress on transform faults is 10^7 newtons m^{-2} and extends to a depth of 100 km it could strongly influence plate motions. Chapple and Tullis (1977) included a resistive force due to transform faults in their analysis of the forces controlling plate motions, but found that its magnitude was too small to be determined. We chose to ignore this contribution to the plate motions principally because it can only be introduced into a two-dimensional force balance model in an arbitrary way.

In contrast to the forces from ridges and transform faults, those acting on the thrusts beneath island arcs are probably an order of magnitude greater because the dip on the faults is small. If a shear stress σ acts on the fault whose dip is θ , the resulting horizontal force F on the plate of thickness t is $\sigma t/\tan\theta$ in a direction normal to the strike of the fault. Taking $t=85$ km and $\sigma=10^7$ newtons m^{-2} gives $F=4.8 \times 10^{12}$ newtons m^{-1} when $\theta=10^\circ$ and $F=2.3 \times 10^{12}$ newtons m^{-1} when $\theta=20^\circ$. The magnitude of this force is independent of the plate velocity and should be included in any force balance. This is easily done because the density variations near ridges produce a driving force F_R of 2×10^{12} newtons m^{-1} (see below) which balances the resistive force at trenches within the uncertainty of both calculations. Hence neither need be explicitly included. This convenient equality may, however, conceal the importance of these forces, since both are large compared with those in the two layer model considered in section 4, and the uncertainty in the value of $F-F_R$ is large. Since F_R acts near ridges and F on the thrust plane beneath island arcs together they keep plates in compression. For the same reason plates surrounded by ridges must also be in compression. Such a stress state agrees with the limited observations available concerning the stress state within plates (Sbar and Sykes, 1973; Rayleigh et al., 1972).

No information about the normal component of the force acting on faults can be obtained from earthquakes, and nothing is yet known about its magnitude and importance, or even whether this component acts as a driving or resistive force. Despite this ignorance there is some evidence (see Molnar and Tapponnier, 1975) that normal forces acting in some continental regions do control the motion of some large plates. Despite this evidence we chose to ignore such forces everywhere, partly because their magnitude is unknown, and partly because their importance depends on the shape of individual plates.

In Figure 5 the plate and the slab move with the same velocity. This is a sensible model to use if the slab and plate are connected and stress can be transmitted from one to the other. However, recent work on earthquakes produced by normal faulting within the plate and slab strongly suggests that the faults extend through the plate (see McKenzie and Weiss, 1975). If all plates are broken in this way, any stress transmission that occurs must do so either by frictional forces within the plate and slab or by viscous forces acting on their boundaries. In the absence of the sinking slab the resistive force on the plate of length 1.5 would be 6.63 (Fig. 4f) and it is clear from Figure 5 that a slab sinking with velocity -1 has little effect on this force. If viscous forces are to transmit the force, the slab must sink faster than -1 . Since the mass flux is fixed, the slab can only sink faster if its thickness is less than t . Figure 6 shows the forces acting when the slab sinks at -2 and is half the thickness of the surface plate. The force resisting the plate motion is reduced but it not negative, even though the width of the plate in Figure 6 is only 1000 km. Clearly considerably larger sinking velocities are needed if plates the size of the Pacific are to be moved by viscous forces. Because mass must be conserved, larger velocities require thinner slabs, and it is not obvious how a plate can become a thin rapidly moving slab at shallow depths beneath a trench.

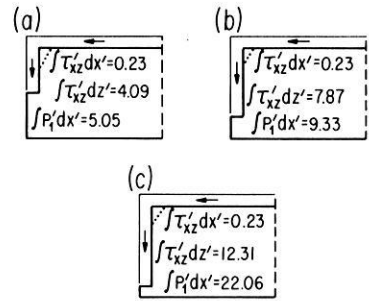


Fig. 6a c. As for Figure 5 but with the slab sinking with $u'_z = -2$. The driving force/unit width on the dotted line is 1.36 and is omitted in the force balance calculations. The mass flux through the tip of the slab and the right hand boundary is Vt

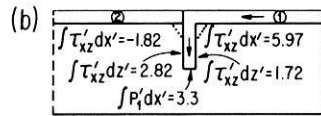
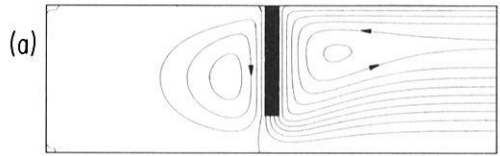
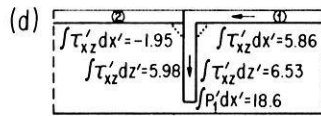
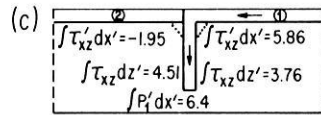


Fig. 7a d. Model for an asymmetric trench with the slab sinking with $u'_z = -1$, plate 1 moving to the left with velocity -1 and plate 2 stationary. The integrals are taken over the same boundaries as in Figure 5. The forces on the base of plate 2 act to the right. The forces on the base of plate 1 act to the left. The mass flux through the right hand boundary is Vt , that through the left hand zero. The contour intervals for ψ' in (a) are 0.02866, the slab extends to a depth of $\frac{1}{2}$ in (b), $\frac{3}{4}$ in (c) and $\frac{7}{8}$ in (d). The perturbed pressure on the right hand boundary is taken to be zero



Driving Forces

Since the oceanic crust is produced by partial melting of the mantle, large scale differences in density can only be produced by differences in temperature. Hence all the driving forces are convective in origin. Horizontal temperature variations beneath ridges produce both the shallow bathymetry and a driving force F_R , whose magnitude may be obtained from any thermal model of a spreading ridge. A simple model consists of isothermal hot material of density ρ_m upwelling at the ridge axis, then cooling as it moves away until the temperature gradient is constant across the plate of thickness t . The density at the base of the plate is everywhere ρ_m . If the elevation difference between the ridge axis and the

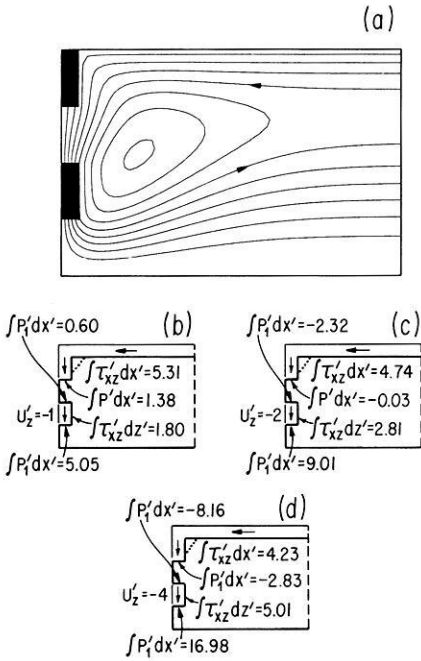


Fig. 8a-d. As for Figure 5, but with a piece of slab detached, and sinking with various different velocities. The contour interval for ψ' in (a) is 0.0308, and the flow corresponds to (c). A negative pressure integral corresponds to a resistive force on the upper boundary of the sinking block. The length of both the slab and the block is $\frac{1}{4}$

cooled plate is e , the density of sea water is ρ_w , then the pressure P_1 beneath the ridge axis at a distance z above the base of the plate is

$$P_1 = (\rho_m - \rho_w) g(t + e - z) \tag{21}$$

When the plate has cooled and a linear temperature gradient has become established between the mantle and the sea floor, the density within the plate ρ_p increases linearly with z :

$$\rho_p = \rho_m - \rho_w + \beta z \tag{22}$$

where β depends on the thermal expansion coefficient. Integration gives P_2 , the pressure beneath old sea floor

$$P_2 = g(\rho_m - \rho_w)(t - z) + \frac{g\beta}{2}(t^2 - z^2). \tag{23}$$

Since the ridge is taken to be in hydrostatic equilibrium $P_1 = P_2$ when $z = 0$. Thus

$$\beta = 2(\rho_m - \rho_w) e/t^2. \tag{24}$$

We can now obtain the driving force due to ridge pushing by integration

$$\begin{aligned}
 F_R &= \int_0^{t+e} P_1 dz - \int_0^t P_2 dz \\
 &= g e (\rho_m - \rho_w) \left(\frac{t}{3} + \frac{e}{2} \right).
 \end{aligned} \tag{25}$$

Only a small part of this force arises from the tendency of the plate to slide down the sides of the ridge. If the uplift of the upper surface is prevented by applying normal forces, the pressure still exerts a force F_2 where

$$F_2 = \int_0^t P_1 dz - \int_0^t P_2 dz = g e (\rho_m - \rho_w) \frac{t}{3}. \tag{26}$$

F_2 originates from ridge pushing and $F_R - F_2$ from plate sliding. Substitution from table 1 gives $F_R = 2 \times 10^{12} \text{ nm}^{-1}$ and $F_R - F_2 = 10^{11} \text{ nm}^{-1}$, and therefore most of the force is due to ridge pushing. The estimate of F_R is probably accurate to within a factor of 2, and corresponds to a shear stress of $1.2 \times 10^7 \text{ nm}^{-2}$. Except in rare cases oceanic plates do not fail under this stress, which therefore places a lower limit on the shear strength of the oceanic lithosphere.

Table 1

$t = 85 \text{ km}$	$T_1 = 1200^\circ \text{C}$
$e = 3 \text{ km}$	$\alpha = 3 \times 10^{-5} \text{ }^\circ\text{C}^{-1}$
$\rho_m = 3.3 \text{ Mg m}^{-3}$	$C_p = 1.2 \times 10^3 \text{ J kg}^{-1} \text{ }^\circ\text{C}^{-1}$
$\rho_w = 1.0 \text{ Mg m}^{-3}$	$k = 3.1 \text{ W m}^{-2} \text{ }^\circ\text{C}^{-1}$
$g = 9.8 \text{ m s}^{-2}$	$d = 615 \text{ km}$

The other source of convective energy results from density contrasts associated with trenches. The most important is undoubtedly the density contrast between the sinking slab and the surrounding mantle, and its magnitude may be estimated from the thermal structure (McKenzie, 1969).

$$F_t(z) = \frac{8 g \alpha \rho_m T_1 t^2}{\pi^4} R \left\{ \exp\left(-\frac{\pi^2 z}{2 R t}\right) - \exp\left(-\frac{\pi d}{2 R t}\right) \right\} \tag{27}$$

where

$$R = \frac{\rho_m C_p V t}{2 k} \tag{28}$$

α is the coefficient of thermal expansion, T_1 the temperature difference between the bottom of the ocean and the mantle, z the depth below the base of the plate, k the thermal conductivity and C_p the specific heat. Substitution gives $R = 1.7 V$ where V is in mm yr^{-1} . Assuming that the slab sinks vertically, the total driving force $F_t(0)$ is plotted as a function of V in Figure 9. When V is small

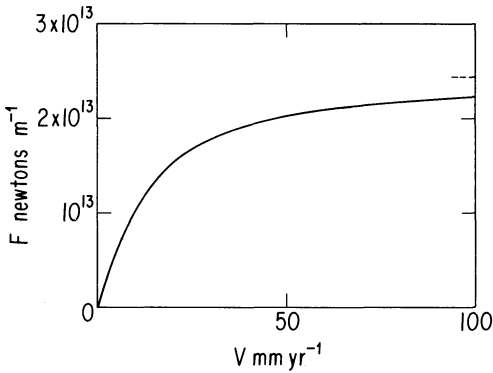


Fig. 9. Available driving force from subducted slab as a function of the consumption velocity V , obtained from (27). The horizontal dashed line shows the asymptotic limit as $V \rightarrow \infty$

($\approx 10\ mm\ yr^{-1}$) the last term in (27) may be neglected, and $F_t(0)$ increases linearly with V . Under such conditions the temperature of the slab's interior has become approximately T_1 when it reaches the base of the upper mantle. If, however, V is large then (27) may be written

$$F_t = \frac{4g\alpha\rho_m T_1 t}{2}(d-z) \quad (29)$$

and is independent of V . The expression is appropriate when $V \gtrsim 40\ mm\ yr^{-1}$ and the slab sinks with little increase in temperature. Figure 9 shows the maximum force available from a sinking slab. When the slab reaches the base of the upper mantle at a depth of 700 km, we are assuming that the cold material must flow horizontally and does not contribute to F_t . The force actually exerted will be less because the slab does not remain intact as it descends, but breaks up into blocks. The motion between these blocks produces intermediate and deep focus earthquakes. Studies of the stress involved in such shocks (Wyss, 1970; Wyss and Molnar, 1972; Fukao, 1972; Mikumo, 1972) have found some evidence that intermediate shocks may involve somewhat larger stress drops than either shallow or deep earthquakes. However, we are only concerned with the force which can be transmitted to the plates, and hence with the stress within the shallow part of the slab beneath the front of the island arc. We will therefore impose an upper limit of 2×10^7 newtons m^{-2} on the stress within this part of the slab. In the absence of resistive forces it is clear from Figure 9 that this stress will be exceeded in slabs sinking faster than about $3\ mm\ yr^{-1}$. The consumption rate in all major trench systems is greater than this limit, and therefore failure of the sinking slabs may occur. Whether or not it does so depends on how the buoyancy forces are balanced by resistive forces.

These two contributions to the driving forces are generally recognized and easily calculated. Two others are not. Probably the most important of these results from large-scale flow which is not driven by plate motions. At present the only evidence for the existence of such flow comes from long-wavelength gravity anomalies determined from satellite motions (Gaposchkin, 1974; Lerch et al., 1974). As explained above, flow associated with these anomalies may make a large contribution to the perturbed pressure field and the viscous

stresses. The other driving force which could help maintain the motions results from the topography of trenches. A driving force may arise in the same way as that at ridges. Because mantle rock is replaced by water the lithostatic pressure at all depths is reduced by $(\rho_m - \rho_w)gH$ where H is the depth of the trench. However, unlike ridges, trenches are not isostatically compensated and must be maintained by elastic forces. Unfortunately, very little is yet known about the distribution of these stresses. It is not even clear whether any of the pressure reduction is available to drive the plates. Therefore this possible energy source or sink is also neglected.

4. Observational Constraints and Force Balance

Gravity

If the model discussed in section 2 is to provide a useful description of the large-scale flow it must be compatible with relevant geophysical observations. Since the only major uncertainties are the value of the viscosity and its variation with depth we use the observational constraints to impose constraints on the viscosity.

The simplest constraint to apply depends on the absence of large long wavelength gravity anomalies. The gravity anomaly produced by the flow in Figure 1 is complicated and difficult to calculate near the ridge and trench regions where large horizontal density contrasts must exist and elastic forces are important. In the interior region, however, the gravity anomaly should increase linearly towards the trench, and is produced by the horizontal pressure gradient (see Eq. (16)). Hence we can impose a bound on the viscosity by considering the horizontal gradient of the gravity field across interior regions of plates remote from their boundaries. The long wavelength pressure gradient will "tilt" the sea floor because the plates are thin and flexible. The observed difference in gravity between trenches and ridges is less than about 0.3 mm s^{-2} and is positive over trenches. Since the return flow should produce an anomaly which varies linearly between trenches and ridges, whereas the observed field consists of a positive anomaly centered on the trenches whose extent is only a fraction of that of the plate (Gaposchkin, 1974; Lerch et al., 1974), this value is probably an upper limit. To obtain the magnitude of the gravity anomaly from the expression in section 2 we need the horizontal extent and velocity of the plate. In the discussion below we will consider two plates. The first, plate *A*, moves at 100 mm yr^{-1} and has a lateral extent of 10^4 km . These values are comparable to those of the Pacific plate. The second, plate *B*, moves at 50 mm yr^{-1} and has an extent 6000 km . These values resemble those for the Indian-Australian plate. If the viscosity of the mantle below the plates is constant, then the upper limit on the viscosity and stress on the base for the two plates is

$$\begin{aligned} \eta_A &\gtrsim 10^{19} \text{ kg s}^{-1} \text{ m}^{-1}, & \sigma_A &\gtrsim 2.6 \times 10^5 \text{ newtons m}^{-2} \\ \eta_B &\gtrsim 3.3 \times 10^{19} \text{ kg s}^{-1} \text{ m}^{-1}, & \sigma_B &\gtrsim 5.2 \times 10^5 \text{ newtons m}^{-2}. \end{aligned} \quad (30)$$

If, however, there is a thin layer of very low viscosity material beneath the plates (Appendix) then the horizontal pressure gradient required to drive the return flow is much reduced and the corresponding expressions are

$$\eta_A \gtrsim 1.9 \times 10^{20}, \quad \eta_B \gtrsim 6.4 \times 10^{20} \text{ (kg s}^{-1} \text{ m}^{-1}) \quad (31)$$

from (14) and (16). The shear stress on the base of the plates is also greatly reduced in both cases.

There are several objections to using the gravity field from our simple model to obtain an upper limit on the allowable viscosity. The most obvious is that the sign of the gravity anomaly obtained in section 2 is opposite to that obtained by McKenzie et al. (1974). Since the model we use here contains no buoyancy forces within the fluid whereas the numerical models used by McKenzie et al. do, the disagreement in sign could be due to such forces. If this were the case no limits such as (30) and (31) could be obtained. Fortunately this is not true. Recent convective calculations by McKenzie (1977), using a temperature dependent viscosity, have shown that the sign of gravity anomaly over a rising region changes from positive to negative when the viscosity variation is sufficiently large. This change in sign results from a change in sign of the horizontal gradient of p_1 . The model used here contains a plate at the surface, rather than a high viscosity region, but is otherwise similar to the convective models. There is therefore no reason to suppose that buoyancy forces and density variations in the mantle invalidate the limits (30) and (31).

The argument above depends on the mechanical behavior of the lower boundary of the convecting region. This question has been discussed above in section 2. If the lower boundary cannot be deformed vertically or is a phase change, then (31) applies. If, however, the lower boundary is deformable, then the long wavelength gravity anomalies are compensated (McKenzie, 1977) and only the elevation differences limit η . Unfortunately most of the variations in bathymetry are produced by variations in the temperature of the plates and thus a large and uncertain correction must be applied to obtain the dynamic variation produced by dp_1/dx (Parsons and Sclater, 1977). Though the thermal models fit the observed variation of age with depth to within the observational errors, the models were constructed to do so. Since Parsons and Sclater could fit the observations from all major ocean basins with a single curve of depth as a function of age, it seems unlikely that the return flow can produce more than about 1 km variations in depth not associated with gravity anomalies. If this rather uncertain limit is used to obtain estimates of the viscosities from (15) we obtain

$$\begin{aligned} \eta_A &\gtrsim 3.5 \times 10^{19} \text{ kg s}^{-1} \text{ m}^{-1}, & \sigma_A &\gtrsim 8.7 \times 10^5 \text{ nm}^{-2} \\ \eta_B &\gtrsim 1.2 \times 10^{20} \text{ kg s}^{-1} \text{ m}^{-1}, & \sigma_B &\gtrsim 1.5 \times 10^6 \text{ nm}^{-2} \end{aligned} \quad (32)$$

if there is a single layer, and

$$\eta_A \gtrsim 6.1 \times 10^{20}, \quad \eta_B \gtrsim 2.1 \times 10^{21} \text{ kg s}^{-1} \text{ m}^{-1} \quad (33)$$

if there is a low viscosity layer beneath the plates.

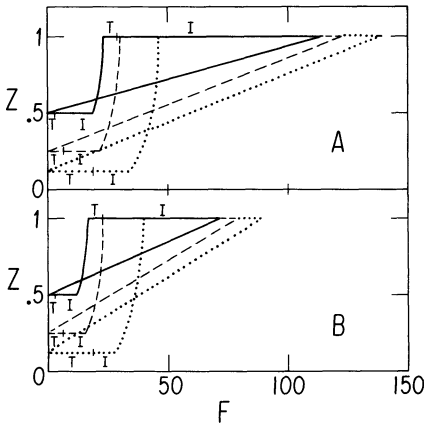


Fig. 10 A and B. Force balance diagrams for plate A, 10,000 km long (A), and plate B, 6000 km long (B) in units of ηV , all for the asymmetric models in Figure 7 and constant viscosity. The vertical scale on the left shows the dimensionless depth to which the slab reaches beneath the trench. The horizontal line extending to the right from the tip shows the resistive force due to the local pressure field within a distance of 1.5 from the trench, marked *T*, and that due to the interior pressure, marked *I*. The curved line drawn from the tip of the slab to the surface indicates the shear force exerted on the sides of the sinking slab integrated upwards from their base. Their magnitude is correct but the depth dependence is sketched. The horizontal lines at $z'=0$ show the total horizontal resistive force acting on the base of the plates due to both the region near the trench and the interior. The interior force includes both f_v and f_s (Eqs. (17) and (18)). For the two cases where the tip extends to $z'=0.5$ these two contributions are marked *T* and *I*. The gravity force due to the slope of the surface has been included in *I*. The oblique straight lines show the integrated buoyancy and must close the diagrams. The reciprocal of their slopes correspond to the buoyancy force in units of ηV exerted by a constant density contrast between the sinking slab and the surrounding mantle which are necessary to maintain the plate motions. The slab will be subject to extensional stress at those depths where the integrated buoyancy is greater than the cumulative resistive force up to that depth. When the integrated buoyancy is less than the cumulative resistive forces, the slab will be in down-dip compression. The continuous line shows the forces for $z'=0.5$, dashed for $z'=0.75$ and dotted for $z'=0.875$

Force Balances

All other constraints we impose depend on the balance between resistive and driving forces, and are most easily understood using a force balance diagram (Fig. 10). Since forces due to the inertia of the mantle material are extremely small compared with the viscous forces, the forces driving the plate and slab must exactly balance the resistive forces. Figure 10 shows the cumulative resistive forces and the integrated driving force (buoyancy force) starting from the bottom of the downgoing slab. Since the total resistive and driving forces must be equal in magnitude, the two curves for each case must form a figure closing at $z'=1$. Furthermore, where the cumulative resistance exceeds the integrated buoyancy, (near the bottom of downgoing slab) the slab will be in compression. Where the opposite is true (nearer the surface) the slab is in tension. These terms are somewhat misleading. Since all principal stresses are everywhere negative the failure is always a shear failure. When the slab is in

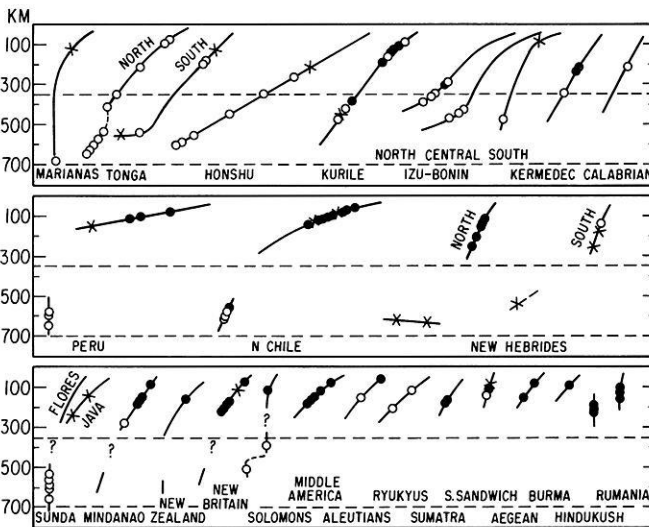


Fig. 11. Summary of the stress state within sinking slabs (Isacks and Molnar, 1971). Open (closed) circles represent zones where the $P(T)$ axis of the fault plane solutions is approximately coincident with the dip of the sinking slab, described as compression (tension). Crosses mark solutions which showed no simple relationship between the stress state and the slab geometry. Continuous curved lines represent the shape of the seismic zone. The upper horizontal dashed line at a depth of 350 km marks the approximate depth below which the slabs are in compression; no earthquakes have been recorded at a depth greater than that of the lower dashed line

tension shear failure permits it to lengthen, whereas when it is in compression it must shorten if a shear failure occurs. Most models of island arcs assume that the slabs move with the same velocity as that of the plate being consumed, despite the existence of intermediate and deep focus shocks. It is, however, hard to exclude major variations in velocity associated with slab deformation, and we have therefore considered models in which part or all of the sinking slab sinks with greater velocity.

The pressure forces acting on the slab tip consists of two parts. The first, marked T in Figure 10, results from the local flow near the trench. The second, marked I , is due to the interior flow. Since the second contribution is independent of the depth to which the slab extends, and depends only on the distance between the trench and the ridge, the lower part of the slab must always be in compression. When the slab approaches the base of the layer the local contribution becomes very large and may exceed the buoyancy force of the entire slab. Under these conditions the plate will be in compression at all depths.

Fortunately it is possible to use fault plane solutions of earthquakes within the sinking slabs to discover whether they are in tension or compression. Figure 11, from Isacks and Molnar (1971), shows the extent and the stress state of most known slabs. It shows that slabs whose tips do not reach below a depth of 350 km are in tension throughout most of their length. Though few mechanisms are available from close to the tips of these slabs (Fig. 11), they must always be in compression. If the tip of the slab extends deeper than 350 km, but

less than 600 km, then the part above 350 km is in tension, that below in compression, whereas if the tip extends below 600 km the slab is in compression throughout its length. The force balance diagram must satisfy these constraints. The observations from the Kermadec and Kurile Arcs (Fig. 11) suggest that the lower 150 km of the slab are in compression. This value will be used for plate *A*, since the return flow from these two arcs must extend to great distances. Other arcs, such as Middle America where all the solutions are tensional, have correspondingly shorter return paths. Other arcs with slabs, such as those beneath the Aleutian and Ryukyu Islands, extending to a similar depth to that beneath Middle America have longer portions of the slab in compression, suggesting that the difference is not due to depth of penetration alone. One further condition we impose is that pieces of the slab should be able to fall through 600 km driven by their own buoyancy. In all but one case the existence of detached blocks gives little information because the consumption rate in the past is unknown. The sole exception is New Zealand, where the consumption rate is known from the magnetic anomalies on the Pacific-Antarctic and Southeast Indian Rises. The mean rate over the last 10 My is about 10% less than the present rate (Molnar et al., 1975). Beneath the North Island of New Zealand the sinking slab is continuous to a depth of about 300 km, then there is a gap, followed by a few shocks spread over 50 km at a depth of about 600 km (Fig. 11). It is only possible to form such a structure with little variation in consumption rate if small blocks can sink through the mantle below a depth of 300 km at velocities greater than the rate of 30 mm/yr at which the slab has been sinking (Christoffel and Calhaem, 1973).

A One-Layer Mantle

If the sinking slab extends to a depth of 630 km and the buoyancy forces (from Fig. 9) are balanced by viscous forces, then the viscosity can be obtained from the force balance diagrams in Figure 10. That for plate *A* gives

$$\eta_A \simeq 5 \times 10^{19} \text{ kg s}^{-1} \text{ m}^{-1}$$

and plate *B*

$$\eta_B \simeq 1.6 \times 10^{20} \text{ kg s}^{-1} \text{ m}^{-1}$$

The mean stress σ acting on the sides of the sinking slabs is

$$\sigma_A \simeq 2.8 \times 10^6 \text{ newtons m}^{-2}$$

$$\sigma_B \simeq 4.4 \times 10^6 \text{ newtons m}^{-2}$$

and that on the base of the plates is

$$\sigma_A \simeq 1.3 \times 10^6 \text{ newtons m}^{-2}$$

$$\sigma_B \simeq 2.0 \times 10^6 \text{ newtons m}^{-2}$$

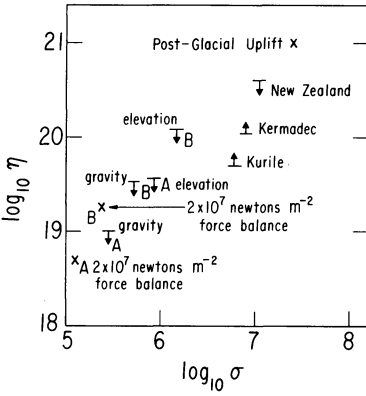


Fig. 12. Estimates of viscosity ($\text{kg s}^{-1} \text{m}^{-1}$) of and stress (newtons m^{-2}) within a one layer mantle of constant viscosity (see text). Crosses mark estimated values, horizontal lines with arrows mark bounds; upper bounds if the arrow points downwards, lower if it points upward. *A* and *B* refer to the two plate models

It is, however, improbable that these values are sensible. The model requires large forces to be transmitted through the lithosphere beneath the trench. The stress involved is easily obtained from Figure 10, and is about 1.8×10^8 newtons m^{-2} . Since the lithosphere appears to be broken by normal faults in the region where it bends beneath the island arcs, this stress must be transmitted by friction. Since there is little evidence in favour of such large stresses being involved in earthquakes (see section 3) it seems more sensible to limit the stress to some value, and we choose 2×10^7 newtons m^{-2} and then use the scaled dimensionless forces in Figures 4a and 7 to obtain the value of the viscosity which will allow the plate to move. This balance gives

$$\begin{aligned} \eta_A &\approx 5.5 \times 10^{18} \text{ kg s}^{-1} \text{ m}^{-1} & \sigma_A &\approx 1.4 \times 10^5 \text{ newtons m}^{-2} \\ \eta_B &\approx 1.8 \times 10^{19} \text{ kg s}^{-1} \text{ m}^{-1} & \sigma_B &\approx 2.4 \times 10^5 \text{ newtons m}^{-2} \end{aligned}$$

which are shown in Figure 12. Since the total force on the plates must be zero these are estimates, not upper or lower bounds. Since the slab is broken and does not move with a uniform velocity we can no longer use the simple models to examine the total force balance. Under these conditions the buoyancy of the sinking slabs must be balanced locally by the pressure and shearing forces but these resistive forces cannot be estimated unless the velocity variation is known.

Figure 11 shows that the bottom 150 km of the slabs beneath the Kermadec and the Kurile arcs is in compression. The consumption rates are both around 80 mm yr^{-1} , and their bases are at 550 km and 620 km respectively. If we assume that the sinking rate is equal to the consumption rate we can use Figure 10 to obtain

$$\eta \approx 1.1 \times 10^{20} \text{ kg s}^{-1} \text{ m}^{-1}, \quad \sigma \approx 8 \times 10^6 \text{ newtons m}^{-2}$$

for the Kermadec Arc and

$$\eta \approx 5 \times 10^{19} \text{ kg s}^{-1} \text{ m}^{-1}, \quad \sigma \approx 6 \times 10^6 \text{ newtons m}^{-2}$$

for the Kurile Arc, where the stresses refer to the mean shear stress on the sides of the lower 150 km of the plate.

The last limits come from the existence of detached blocks. If we use the $u'_z = -2$ case with $V = 15 \text{ mm yr}^{-1}$ and require a block 150 km long to fall with a velocity of at least 30 mm yr^{-1} (see above and Fig. 8), we require:

$$\eta \gtrsim 4 \times 10^{20} \text{ kg s}^{-1} \text{ m}^{-1}, \quad \sigma \gtrsim 1.1 \times 10^7 \text{ newtons m}^{-2}$$

This value of the viscosity is considerably greater than that obtained by Christoffel and Calhaem (1973) for New Zealand because they required the block to sink at 100 mm yr^{-1} and be only 60 km in length.

The limits shown in Figure 12 are quite obviously incompatible. The viscosity required varies by two orders of magnitude. If the creep rate is a non-linear function of stress when the stress exceeds a certain value, estimated to be about $10 \text{ newtons m}^{-2}$ (Stocker and Ashby, 1973; Weertman, 1970) the problem becomes worse, since the effective viscosity is a decreasing function of shear stress, whereas Figure 12 requires the opposite. The only reasonable explanation for the failure of the model is that the viscosity of the mantle is not constant but increases with depth. The simplest model is then one which contains two layers, an upper layer with low viscosity which allows the plates to slide and a lower one of higher viscosity. Unfortunately two parameters are required to describe such a model, and for this reason it is no longer possible to obtain dimensionless forces valid for all viscosities as was done for the one layer model. Instead of carrying out extensive calculations with a wide variety of two layer models we chose to obtain approximate expressions for the forces on sinking slabs from the one layer calculations and only carry out a complete two layer calculation for the interior flow, where analytic expressions can be obtained. The estimates of the forces acting on the sinking slabs are little affected by the presence of a thin low viscosity layer.

Two-Layer Models

We consider two models, model *C* has an upper layer 85 km thick, and in model *D* it is 8.5 km thick. Both can satisfy the observational constraints, though a model similar to *C* seems to us more plausible. We first estimate the viscosity η_2 of the lower layer assuming that no stress is transmitted through its upper surface, and then discuss the likely range of the viscosity of the upper layer.

Models of this type with thin low viscosity zones beneath the plates have been suggested by several authors (Anderson, 1962; Green, 1972; Wyllie, 1971) who believe the uppermost mantle to be partly molten. The existence of a fluid phase insufficient by itself to lower the viscosity. If, however, the liquid phase is in equilibrium with the solid, mass transfer may occur through the fluid and in this way dramatically lower the viscosity.

If the resistive forces are required to balance a total buoyancy of order $2 \times 10^{13} \text{ newtons m}^{-1}$ (Fig. 9), then

$$\eta \gtrsim 5 \times 10^{20} \text{ kg s}^{-1} \text{ m}^{-1} \quad \sigma \gtrsim 1.1 \times 10^7 \text{ newtons m}^{-2}$$

for the Kermadec slab and

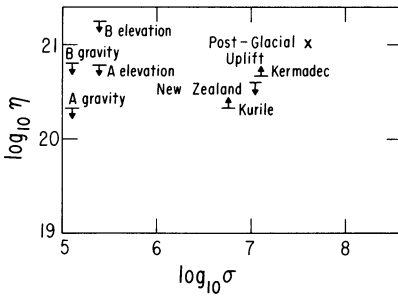


Fig. 13. Estimates of viscosity ($\text{kg s}^{-1} \text{m}^{-1}$) and stress (newtons m^{-2}) within the lower layer of a two layer model, *C* for the mantle. The symbols have the same meanings as in Figure 12. The estimates marked *A* and *B* are uncertain, and could be increased or decreased by at least a factor of 3

$$\eta \approx 2.2 \times 10^{20} \text{ kg s}^{-1} \text{ m}^{-1} \quad \sigma \approx 6.6 \times 10^6 \text{ newtons m}^{-2}$$

for the Kurile slab. The values of η are somewhat larger than the one layer values principally because of the stress free condition which causes the contribution of the interior flow to p_1 to be small. The falling block gives values which are little affected by the free upper surface. These values are plotted in Figure 13 and are in substantial agreement with the value obtained from post-glacial uplift. It is not at once obvious why these values should agree. Clearly if the viscosity of the upper layer is sufficiently small the ice load will be compensated by movement of material within the upper layer (see Appendix) and produce a peripheral bulge around the load. If this is not to occur then $\eta_2/\eta_1 \approx 10^4$ for model *C* and $\approx 10^6$ for model *D*. If, however, the above conditions are satisfied the low viscosity layer may become extremely hard to detect, especially when it is overlain by an elastic plate (Peltier, personal communication). The only effect of the upper layer is to alter the boundary condition on the upper surface of the lower layer. In the absence of a low viscosity layer the tangential velocity due to the ice load must vanish at the base of the plate, whereas when a low viscosity layer is present the shear stress vanishes instead. However, if the lower layer is a half space, both boundary conditions are satisfied by a stream function

$$\psi = c(kz - 1)e^{kz} \sin kx$$

where c is a constant, and k is the wavenumber, and therefore post-glacial uplift cannot distinguish between the two boundary conditions, and in both cases determines the viscosity of the lower layer.

The other apparent difficulty involves the rigid boundary imposed at a depth of 700 km. Peltier and Andrews (1976) could not account for the post-glacial uplift without permitting flow to occur below this depth. If, however, the rigid region is as thin as McKenzie and Weiss (1975) believed, it would not influence the surface motion but would still prevent the return flow penetrating the lower mantle.

The Upper Layer

We wish the upper layer to decouple the plate motions from the motions below, but it must not channel the horizontal flow. If it did so this would be apparent

in the post-glacial uplift observations. Another observation which excludes this possibility is the observed correlation between the depth of the ocean and gravity anomalies (Sclater et al., 1975). If normal stresses could not be transmitted to the base of the plate then its upper surface would be an equipotential after the age corrections had been made. Since the ocean surface is an equipotential, the corrected depth would be constant (McKenzie, 1977). This is not the case. Therefore the viscosity of the upper layer must be sufficiently small to decouple the plate motions from the lower layer, but large enough to prevent large horizontal mass fluxes within it. These conditions cannot be satisfied if the layer is much thicker than 85 km. The limits for model *C* are

$$2 \times 10^2 \gtrsim \eta_2/\eta_1 \gtrsim 10^3$$

and for *D*

$$10^3 \gtrsim \eta_2/\eta_1 \gtrsim 10^5.$$

If we take η_2 to be $2.5 \times 10^{20} \text{ kg m}^{-1} \text{ s}^{-1}$ and $\eta_1 = 5 \times 10^{17}$, 2.5×10^{17} for models *C* and *D*, respectively, we satisfy these two constraints. Using the expressions in the Appendix, and including the sliding force we find that the force required to maintain the surface plate motions corresponds to stresses within the plates at island arcs of

$$\sigma_A \simeq 2.6 \times 10^7 \text{ newtons m}^{-2}$$

$$\sigma_B \simeq 7.9 \times 10^6 \text{ newtons m}^{-2}$$

in model *C* for the two plates and

$$\sigma_A \simeq 3.2 \times 10^7 \text{ newtons m}^{-2}$$

$$\sigma_B \simeq 9.7 \times 10^6 \text{ newtons m}^{-2}$$

for model *D*. It is therefore possible to maintain the plate motions by frictional forces transmitted across faults, and also to provide enough resistance to permit the upper part of some sinking slabs to be in tension. One further condition must be satisfied. There is no evidence that the heat flow through old parts of plates depends on the spreading rate, and therefore shear stress heating should not make an important contribution to the surface heat flux. The total contribution from this source for plate *A* using model *C* is about $8 \times 10^{-4} \text{ Watts m}^{-2}$, and for model *D* is about $7 \times 10^{-4} \text{ Watts m}^{-2}$. Both are less than 2% of the surface heat flux. It is clear from this discussion that the difficulties faced by a one-layer model are removed if a thin low viscosity layer is present beneath the plates.

5. The Driving Force for Plate Motions

In the last section we have argued that geophysical observations require a large contrast in viscosity within the mantle. A high viscosity lower layer is required to account for the post-glacial uplift data and for the fault plane solutions for deep earthquakes. However, unless the surface motions are decoupled from this

lower layer by a low viscosity region, long wavelength gravity anomalies or residual depth variations are produced whose magnitude is about two orders of magnitude larger than those observed. We argued that a model with a thin low viscosity layer beneath the plates could reconcile the differences between the different estimates of viscosity, but it is also important to discuss whether the model is compatible with the extensive knowledge of plate motions.

The two plate models considered above both contain sinking slabs, and therefore buoyancy forces from density contrasts beneath trenches are available to maintain the motions. For this reason these models closely resemble that of Elsasser (1969), who suggested that this buoyancy force could drive all observed motions. One of the principal objections to this idea was that many large plates, such as Eurasia, America, Africa and Antarctica are in relative motion (McKenzie, 1969). At first sight this objection is overcome by the convective forces available from ridge pushing. Unfortunately such forces are available only if spreading is already taking place, and therefore they cannot break an existing plate. Since it seems likely that the separation of both North America and Eurasia and of South America and Africa started when no large sinking slabs were attached to any of these plates, another source of work is required. One possibility is that the decoupling layer is absent beneath shield regions, and hence that continents are strongly coupled to flows in the mantle. Another is the sliding force discussed in section 2, given by Eq. (18). This force exists because convection in the lower layer lifts the plate on top. Sclater et al. (1975) showed that parts of the North Atlantic were up to 1 km shallower than expected from their age. Even when shear stresses do not act on the base of the plates, such an elevation produces a stress of about 2.3×10^7 newtons m^{-2} which is comparable to that expected from a sinking slab. Large positive elevations exist in the North Atlantic and South West Indian Ocean which could maintain the relative motions of North America, Eurasia, Africa and Antarctica, but it is less easy to understand why the South Atlantic is spreading faster than any of the other ridges between non-subducting plates. Either mechanism can account for the formation of new plate boundaries, since the stress involved is comparable to that involved in earthquakes.

It is encouraging that there do not appear to be any major conflicts between the simple models considered above and the geophysical observations. One of the few obvious problems is in the Eastern Pacific, with the Cocos plate. The distance between the two ridges and the Middle America trench is only about 1000 km, and therefore the pressure difference required to drive the return flow is much less than that for large plates such as the Pacific. Probably for this reason the sinking slab beneath Central America is in tension. Despite the lack of resistive forces the Cocos plate does not appear to be accelerating as the length of the sinking slab increases. Any such acceleration would show clearly on the magnetic profiles across the Galapagos Rift. Perhaps the explanation is that the buoyancy of the sinking slab is smaller than elsewhere because the plate now being consumed is relatively young and warm.

The two-layer model implies that the velocities of plate motion are considerably greater than those within the lower layer. If melting spots are the surface expression of structures in the lower layer then their relative motion should be slow compared to the plate velocities, as Minster et al. (1974) have demon-

strated. Therefore this model is consistent with the observations that Morgan (1971, 1972) has argued require the existence of plumes of hot rising material extending to greater depths.

Our models have various important shortcomings which prevent them from being used for detailed calculations using the observed plate geometries. We have assumed that all the motions are two dimensional, and obviously the observed motions are strongly three dimensional. We have taken all slabs to be vertical and to be stationary with respect to the lower boundary of the fluid layer. Since the buoyancy force normal to a dipping slab must be balanced by a pressure difference across the slab, non-vertical slabs make a large contribution to the pressure field. Relative motion between the slab and the lower boundary must also make an important contribution to the pressure field. Perhaps realistic calculations will be possible, though they will not be straightforward because of resolution problems. Hager and O'Connell (1977) have recently calculated the three-dimensional flow in the earth's interior which is consistent with the observed surface velocities, but they take no account of the contribution that the sinking slabs make to the flow through their rigidity and their buoyancy. It seems likely that both effects are important.

Conclusions

The most important result we have obtained is that several uncontroversial geophysical observations combined with an idealized model of plate dynamics, impose important constraints on the form of mantle convection. In particular a constant viscosity mantle is ruled out by the magnitude of the long wavelength gravity and residual depth anomalies and the stress state within the sinking slabs. However, a model with two layers of widely different viscosity can satisfy these and other observations, but only if the viscosity of the upper layer is a factor of about 500 less than that of the lower. Furthermore, the thickness of the upper layer cannot be greater than about 100 km, and may be thinner. Despite the decoupling which such a low viscosity region produces, mantle convection can maintain plate motions and form new plate boundaries. Provided the upper layer is thin, such a two-layer model does not appear to be in conflict with other observations such as post-glacial uplift, and has been in fact already proposed to account for isostasy (Fisher, 1881) and the attenuation of seismic waves (Anderson, 1962). The low viscosity may be produced by a very small fraction of partial melt believed to be present in the low velocity layer beneath the plates (Green, 1972).

Our investigation has demonstrated the importance of the pressure perturbation due to the flow. The pressure contribution controls the stress state within the sinking slabs, the surface deformation and the gravity anomaly associated with the return flow from trenches to ridges. More information can be obtained about this pressure field from focal mechanisms of earthquakes within slabs which extend to depths of 400 km or less (McKenzie, 1976).

Our model is consistent with the existence of two scales of flow within the mantle. Because the plate motions are decoupled from most of the mantle

below, the small-scale flow is more likely to consist of three-dimensional time dependent motions than two-dimensional rolls. We have principally discussed that part of the large-scale flow which is associated with plate motions, but it is not possible to maintain the observed long wavelength gravity anomalies by such flow. A large-scale circulation not directly associated with the mass fluxes generated by plate motions must also exist. The energetics and stability of this flow are not yet understood, and can only be investigated by a model which takes account of buoyancy forces within the fluid.

Our model is also consistent with the results of Forsyth and Uyeda (1975) and of Chapple and Tullis (1977) who used the observed plate motions to estimate the importance of a variety of forces driving and resisting plate motions. Both pairs of authors found similar results: The large driving forces due to the sinking slabs are resisted locally and are not communicated to the plate which is being consumed. The form that this resistance takes differs in the two models because the authors formulate the problem in slightly different ways. Forsyth and Uyeda find that most of the buoyancy force is balanced by stresses on sides and ends of the slabs. Chapple and Tullis do not allow for such forces and find that the buoyancy force is balanced by forces between the converging plates, and they then balance the reaction on the island arc by a local driving force. All the other forces in both models are considerably smaller, a result which requires decoupling of the plate motions from those of the mantle below. However, neither model was concerned with the physical processes which produced the resistive forces. The agreement between our results and the two models is very encouraging, especially because our approach is so different.

Acknowledgements. We thank Barry Parsons for many helpful suggestions. This work forms part of a general investigation of mantle convection at Cambridge, supported by the Natural Environmental Research Council. It was also in part supported by a National Science Foundation Grant, NSF EAR-75 17170.

F. Richter thanks the John Simon Guggenheim Foundation for a fellowship which supported his visit to Cambridge.

Appendix

The interior solution to the two-layer model shown in Figure 14 is easily obtained, though the algebra is tedious. If d_2 and η_2 are used to reduce the equations to dimensionless form and

$$M = \eta_2/\eta_1, \quad r = d_1/d_2, \quad t' = t/d_2$$

then

$$\frac{dp'_1}{dx'} = -\frac{6\{2t'(1+Mr) + (1+2r+Mr^2)\}}{1+4Mr+6Mr^2+4Mr^3+M^2r^4}. \quad (\text{A.1})$$

When $M \rightarrow \infty$ (A.1) becomes

$$\frac{dp'_1}{dx'} = -\frac{6(2t'+r)}{Mr^3}.$$

Hence

$$\frac{dp_1}{dx} = -\eta_1 V \frac{6(2t+d_1)}{d_1^3} \quad (\text{A.2})$$

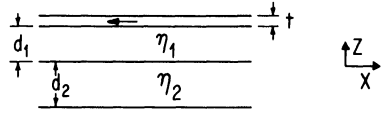


Fig. 14. Two-layer model with different viscosity η in each layer

Thus dp_1/dx is independent of both η_2 and d_2 and hence the properties of the lower layer. This behaviour occurs because the return flow occurs entirely within the upper layer, as can be seen either by examining the mass flux or by comparing (A.2) with (13). Hence this is not the limit corresponding to (14) which allows the motion of the plate to decouple from that of the lower layer. To obtain this limit we require $M \rightarrow \infty$ and $r \rightarrow 0$, while $Mr \rightarrow \infty$ and $Mr^2 \rightarrow 0$ giving

$$\frac{dp_1'}{dx'} \rightarrow -3t' \tag{A.3}$$

In this limit no stress is transmitted across the upper layer, but the return flow is restricted to the lower layer.

The expression for the dimensionless shear stress σ' on the base of the plate may be obtained from (A.1)

$$\sigma' = \left\{ 1 - \frac{1}{2} \frac{dp_1'}{dx'} (Mr^2 + 2r + 1) \right\} / (1 + Mr) \tag{A.4}$$

The fraction f of the return flow taking place in the upper layer is

$$f = \frac{r}{2t(1 + Mr)} \left\{ 2 + Mr + \frac{1}{6} \frac{dp_1'}{dx'} Mr(3 + 4r + Mr^2) \right\} \tag{A.5}$$

The average dimensionless viscous dissipation Φ'_1 in the upper layer is

$$\Phi'_1 = M \left\{ B^3 - \left(B - \frac{dp_1'}{dx'} \right)^3 \right\} / 3r \frac{dp_1'}{dx'} \tag{A.6}$$

and in the lower layer

$$\Phi'_2 = \left\{ \left(B + \frac{dp_1'}{dx'} \right)^3 - B^3 \right\} / 3 \frac{dp_1'}{dx'} \tag{A.7}$$

where

$$B = \left\{ 1 - \frac{1}{2} \frac{dp_1'}{dx'} (1 - Mr^2) \right\} / (1 + Mr) \tag{A.8}$$

The dimensionless velocity u'_x at the interface is

$$u'_x = \left\{ 1 + \frac{1}{2} \frac{dp_1'}{dx'} Mr(1 + r) \right\} / (1 + Mr) \tag{A.9}$$

References

Anderson, D.L.: The plastic layer of the earth's mantle. *Sci. Amer.* July 1962, pp. 52–59, 1962
 Chapple, W.M., Tullis, T.E.: Evaluation of the forces that drive the plates. *J. Geophys. Res.* **82**, 1967–1984, 1977
 Christoffel, D.A., Calhaem, I.M.: Upper mantle viscosity determined from Stokes' Law. *Nature Phys. Sci.* **243**, 51–52, 1973

- Davies, G.F.: Whole mantle convection and plate tectonics. *Geophys. J. Roy. Astron. Soc.* **49**, 459–486, 1977a
- Davies, G.F.: Viscous mantle flow under moving lithospheric plates and under subduction zones. *Geophys. J. Roy. Astron. Soc.* **49**, 557–563, 1977
- Elsasser, W.M.: Convection and stress propagation in the upper mantle. In: *The Application of Modern Physics to the Earth and Planetary Interiors*, S.K.: Runcorn, ed.: pp. 223–246. New York: Interscience 1969
- Fisher, O.: *Physics of the Earth's Crust*. London: MacMillan 1881
- Forsyth, D., Uyeda, S.: On the relative importance of the driving forces of plate motion. *Geophys. J. Roy. Astron. Soc.* **43**, 163–200, 1975
- Fukao, Y.: Source process of a large deep-focus earthquake and its tectonic implications.—The western Brazil earthquake of 1963. *Phys. Earth Planet. Inter.* **5**, 61–76, 1972
- Fukao, Y.: Thrust faulting at a lithospheric plate boundary: The Portugal earthquake of 1969. *Earth Planet. Sci. Lett.* **18**, 205–216, 1973
- Gaposchkin, E.M.: Earth's gravity field to the eighteenth degree and geocentric coordinates for 204 stations from satellite and terrestrial data, *J. Geophys. Res.* **79**, 5377–5411, 1974
- Green, D.H.: Magmatic activity as the major process in the chemical evolution of the earth's crust and mantle. In: *The Upper Mantle*, A.R. Ritsema, ed. pp. 47–71, Amsterdam: Elsevier 1972
- Hager, B.H., O'Connell, R.J.: Benioff zone dip angles and flow driven by moving planes. *Trans. Am. Geophys. Union* **58**, 499 (abstract), 1977
- Hewitt, J.M., McKenzie, D.P., Weiss, N.O.: Dissipative heating in convective flows. *J. Fluid Mech.* **68**, 721–738, 1975
- Isacks, B.L., Molnar, P.: Distribution of stresses in the descending lithosphere from a global survey of focal-mechanism solutions of mantle earthquakes. *Rev. Geophys. Space Phys.* **9**, 103–174, 1971
- Isacks, B.L., Oliver, J., Sykes, L.R.: Seismology and the new global tectonics. *J. Geophys. Res.* **73**, 5855–5899, 1968
- Kanamori, H.: Synthesis of long-period surface waves and its application to earthquake source studies.—Kurile Islands earthquake of October 13, 1963. *J. Geophys. Res.* **75**, 5011–5027, 1970a
- Kanamori, H.: The Alaskan earthquake of 1964: radiation of longperiod surface waves and source mechanism. *J. Geophys. Res.* **75**, 5029–5040, 1970b
- Kanamori, H.: Focal mechanism of the Takachi-Oki earthquake of May 16, 1968: contortion of the lithosphere at a junction between two trenches, *Tectonophysics* **12**, 1–13, 1971
- Lerch, F.J., Wagner, C.A., Richardson, J.A., Brown, J.E.: Goddard earth models (5 and 6). Goddard Space Flight Centre report no. x-921-74.145, 1974
- McKenzie, D.P.: The influence of the boundary conditions and rotation on convection in the earth's mantle. *Geophys. J. Roy. Astron. Soc.* **15**, 457–500
- McKenzie, D.P.: Speculations of the causes and consequences of plate motions. *Geophys. J. Roy. Astron. Soc.* **18**, 1–32, 1969
- McKenzie, D.P.: The orientation of the stress within sinking slabs. *Earth Planet. Sci. Lett.* **31**, 305–307, 1976
- McKenzie, D.P.: Surface deformation, gravity anomalies and convection. *Geophys. J. Roy. Astron. Soc.* **48**, 211–238, 1977
- McKenzie, D.P., Roberts, J.M., Weiss, N.O.: Convection in the earth's mantle: towards a numerical simulation. *J. Fluid Mech.* **62**, 465–538, 1974
- McKenzie, D.P., Weiss, N.O.: Speculations on the thermal and tectonic history of the earth. *Geophys. J. Roy. Astron. Soc.* **42**, 131–174, 1975
- Mikumo, T.: Focal process of deep and intermediate earthquakes around Japan as inferred from long-period *P* and *S* waveforms. *Phys. Earth Planet. Inter.* **6**, 293–299, 1972
- Minister, J.B., Jordan, T.H., Molnar, P., Haines, E.: Numerical modelling of instantaneous plate tectonics. *Geophys. J. Roy. Astron. Soc.* **36**, 541–576, 1974
- Molnar, P., Atwater, T., Mammerickx, J., Smith, S.M.: Magnetic anomalies, bathymetry and the tectonic evolution of the South Pacific since the late Cretaceous. *Geophys. J. Roy. Astron. Soc.* **40**, 383–420, 1975
- Molnar, P., Tapponnier, P.: Cenozoic tectonics of Asia: effects of a continental collision. *Science* **189**, 419–426, 1975
- Morgan, W.J.: Convection plumes in the lower mantle. *Nature* **230**, 42–43, 1971

- Morgan, W.J.: Deep mantle convection plumes and plate motions. *Bull. Amer. Ass. Petrol. Geol. Bull.* **56**, 203–213, 1972
- O'Connell, R.J.: On the scale of mantle convection. *Tectonophysics* **38**, 119–136, 1977
- Parsons, B., Sclater, J.G.: An analysis of the variation of ocean floor bathymetry and heat flow with age. *J. Geophys. Res.* **82**, 803–827, 1977
- Pekeris, C.L.: Thermal convection in the interior of the earth, *Monthly Notices Roy. Astron. Soc. Geophys. Suppl.* **3**, 343–367, 1935
- Peltier, W.R., Andrews, J.T.: Glacial-isostatic adjustment I: the forward problem. *Geophys. J. Roy. Astron. Soc.* **46**, 605–646, 1976
- Prothero, W.A., Reid, I., Reickle, M.S., Brune, J.N.: Ocean bottom seismic measurements on the East Pacific Rise and Rivera Fracture Zone. *Nature* **262**, 121–124, 1976
- Rayleigh, C.B., Healy, J.H., Bredehoeft, J.D.: Faulting and crustal stress at Rangely, Colorado. In: *Flow and Fracture of Rocks*, H.C. Heard et al., ed.: A.G.U. monograph **16**, pp. 275–284, 1972
- Richter, F.M.: Dynamical models for sea-floor spreading. *Rev. Geophys. Space Phys.* **11**, 223–287, 1973a
- Richter, F.M.: Convection and the large scale circulation of the mantle. *J. Geophys. Res.* **78**, 8735–8745, 1973b
- Richter, F.M.: On the driving mechanism of plate tectonics. *Tectonophysics* **38**, 61–88, 1977
- Richter, F.M., Parsons, B.: On the interaction of two scales of convection in the mantle. *J. Geophys. Res.* **80**, 2529–2541, 1975
- Sbar, M.L., Sykes, L.R.: Contemporary compressive stress and seismicity in eastern North America: an example of intra-plate tectonics. *Bull. Geol. Soc. Am.* **84**, 1861–1882, 1973
- Schubert, G., Turcotte, D.L.: One-dimensional model of shallow-mantle convection. *J. Geophys. Res.* **77**, 945–951, 1972
- Sclater, J.G., Lawver, L.A., Parsons, B.: Comparison of long-wavelength residual elevation and free air gravity anomalies in the North Atlantic and possible implications for the thickness of the lithospheric plate. *J. Geophys. Res.* **80**, 1031–1052, 1975
- Stocker, R.L., Ashby, M.F.: On the rheology of the upper mantle, *Rev. Geophys. Space Phys.* **11**, 391–426, 1973
- Weertman, J.: The creep strength of the earth's mantle. *Rev. Geophys. Space Phys.* **8**, 145–168, 1970
- Weidner, D.J., Aki, K.: Focal depth and mechanism of mid-ocean ridge earthquakes. *J. Geophys. Res.* **78**, 1818–1831, 1973
- Wu, F., Kanamori, H.: Source mechanism of February 4, 1965, Rat Island earthquake. *J. Geophys. Res.* **78**, 6082–6092, 1973
- Wyllie, P.J.: *The Dynamic Earth*. New York: J. Wiley & Sons 1971
- Wyss, M.: Apparent stresses of earthquakes on ridges compared to apparent stress of earthquakes in trenches. *Geophys. J. Roy. Astron. Soc.* **19**, 479–484, 1970
- Wyss, M., Molnar, P.: Source parameters of intermediate and deep focus earthquakes in the Tonga Arc. *Phys. Earth Planet. Inter.* **6**, 279–292, 1972

Received August 1, 1977 / Revised Version February 10, 1978

Tonga-Lau System: Deep Collision of Subducted Lithospheric Plates

V. Hanuš and J. Vaněk

Geological Institute and Geophysical Institute, Czechoslovak Academy of Sciences,
141 31 Praha 4 – Spořilov, Boční II, 1401 Czechoslovakia

Abstract. Deep collision of the presently subducted Pacific plate with activated remaining parts of the buried Lau paleoplates was found on the basis of a detailed investigation of the morphology of the Wadati-Benioff zone in the Tonga region. The position of two centres of deep collision was determined and the extent of activation of the Lau paleoplates was delineated.

Key words: Seismicity – Plate tectonics – Tonga island arc – Lau Ridge.

Introduction

The plate tectonic interpretation of the distribution of earthquake foci in the Tonga region implies a complicated pattern of subducted lithospheric plates (Hanuš and Vaněk, 1978a). In this aspect the most remarkable feature seems to be the deep collision of the recently subducted Pacific plate with buried remnants of Lau paleoplates causing the highest deep seismicity in the world. The aim of the present paper is to give a description of this new phenomenon based on a detailed investigation into the morphology of the Wadati-Benioff zone in the interacting Tonga and Lau systems of subduction.

Tonga System

For studying the morphology of the Wadati-Benioff zone in the Tonga region the ISC data (Regional Catalogue of Earthquakes) for the seven years' period 1967–73 were used. In some areas with low intermediate and deep seismicity the ISC data for selected shocks from 1964–66 were also included. The Tonga region (14°–27.5° S, 170° W–178° E) was covered by a system of 22 sections approximately perpendicular to the axis of the Tonga-Kermadec trench, the scheme of which is given in Figure 1, see also Hanuš and Vaněk (1978a).

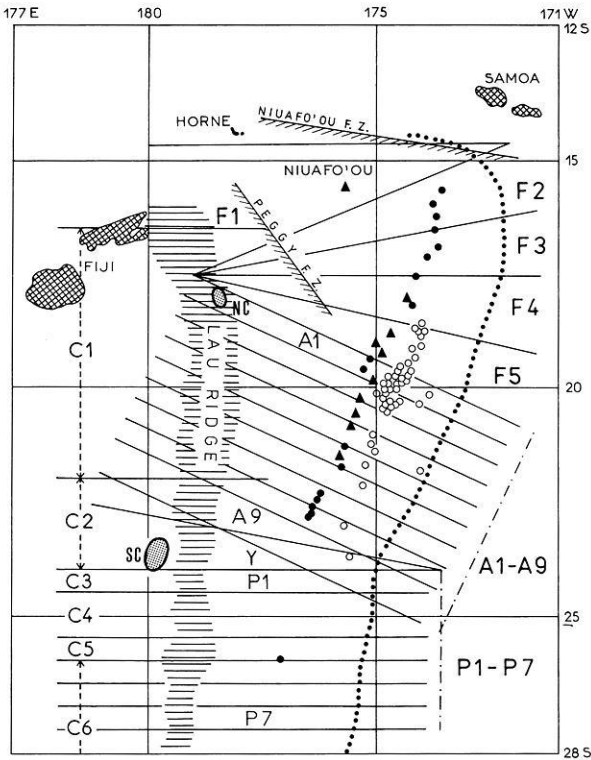


Fig. 1. Geographic scheme and position of sections used for the study of the Tonga-Lau deep collision; the Tonga-Kermadec trench is denoted by a dotted line, active volcanoes by full triangles, islands and submarine elevations associated with active volcanic chain by full circles, coral islands and reefs with associated submarine elevations by open circles, centres NC and SC of deep collision by dotted areas. Scheme compiled on the basis of Cullen (1970) and World Map (1968)

From the sequence of the vertical sections, showing the depth distribution of earthquake foci in dependence on the distance from the trench, four sections F5, A1, Y, and P1 are selected in Figures 2 and 3. The analysis of the complete set of vertical sections (Hanuš and Vaněk, 1978a) reveals that the complicated geometry of the earthquake foci distribution is caused by an interplay of different systems of lithospheric plates. If we omit the northern closure of the Tonga subduction zone, two different systems can be delineated: the presently subducted Tonga system including the plates T 1 and T 2 in the east, and the remnant Lau system composed of plates L 1 and L 2 in the west.

The well-defined Wadati-Benioff zone T 1, representing the presently active subduction of the Pacific plate, begins in the vicinity of the Tonga-Kermadec trench and is divided by an intermediate aseismic gap into two distinct seismically active parts (see Figs. 2 and 3). The gap appears to be spatially connected, similarly as in the Andean region (Hanuš and Vaněk, 1976), with the occurrence of active andesitic volcanism and can be interpreted as a zone of partial melting in the subducted plate. The depth penetration of the zone T 1 changes along the trench in a considerable range between 185 and 565 km.

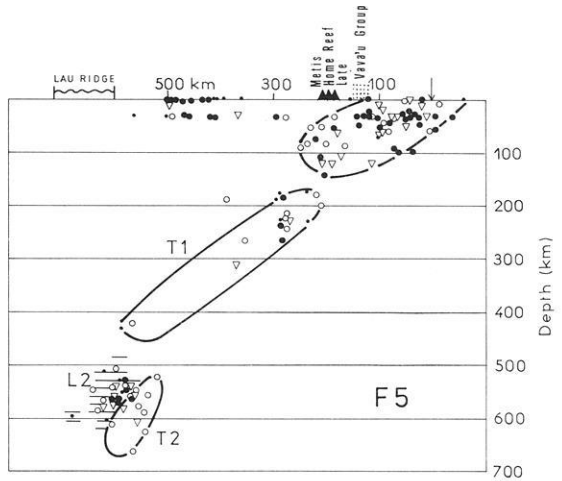
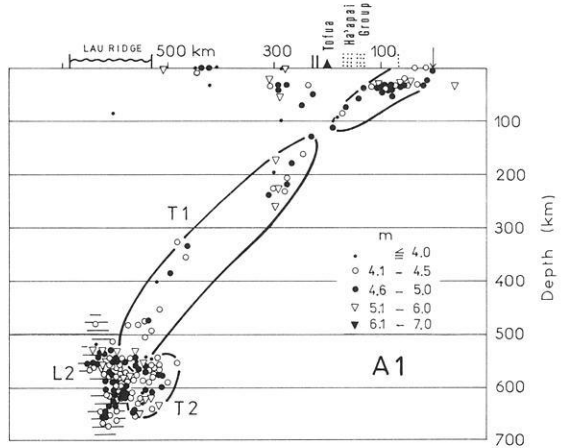


Fig. 2. Vertical sections F5 and A1 giving the distribution of earthquake foci in dependence on the distance from the Tonga-Kermadec trench; *m*: ISC magnitude; active volcanoes are denoted by full triangles, islands and submarine elevations associated with active volcanic chain by short vertical lines, coral islands and reefs with associated submarine elevations by short dotted lines, position of the trench by arrows, the Lau Ridge by a wave-line, Wadati-Benioff zones T 1 and T 2 by full-line contours, zones L 1 and L 2 by vertical and horizontal hatching. For position of sections see Figure 1



In most vertical sections a clearly separated group of deep earthquakes, shifted eastwards in relation to the zone T 1, can be observed. In analogy with our interpretation of deep Andean shocks (Hanuš and Vaněk, 1978c) this zone, denoted as T 2, is interpreted as the remaining active part of the foregoing cycle of subduction. The shape of T 2 itself and the existence of isolated intermediate shocks (see, e.g., Fig. 3) show that the zone T 2 runs in an approximately parallel strip below the present Wadati-Benioff zone T 1. The bottom of T 2 reaches the depths between 495 and 690 km. The interpretation of the zone T 2 as a remaining active part of the foregoing cycle of subduction is strongly supported by the position of the extinct volcanic line appearing now as a chain of coral islands, reefs and submarine elevations in the Tonga island arc (Hanuš and Vaněk, 1978b).

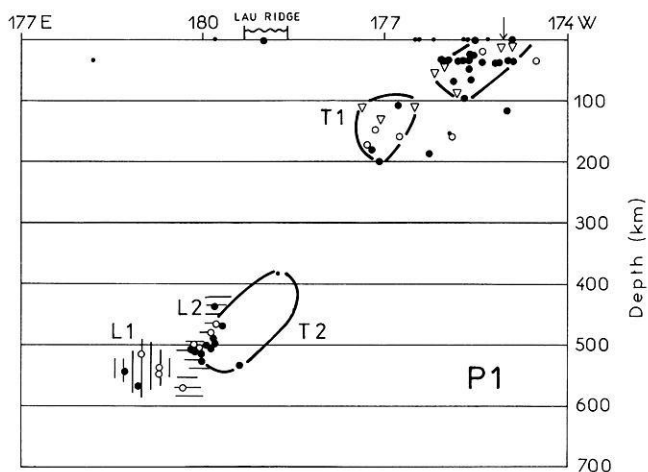
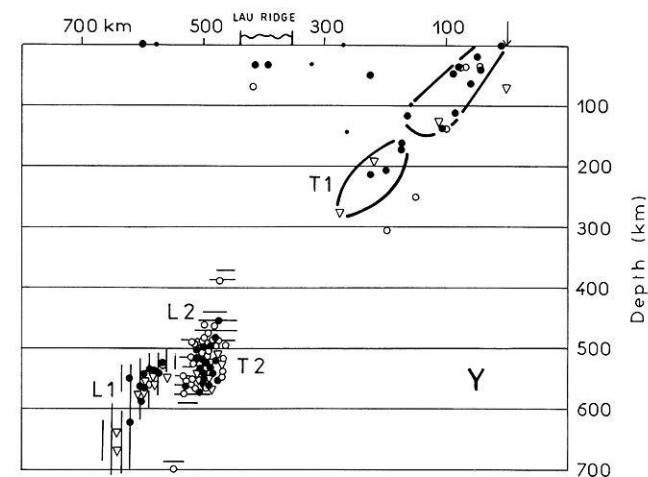


Fig. 3. Vertical sections *Y* and *P1*. For key see Figure 2 and for position of sections see Figure 1

Lau System

In the western part of the region investigated numerous deep earthquakes occur, which can be simply associated neither with the Tonga zone T 1, nor with the zone T 2 (see Figs. 2 and 3; Hanuš and Vaněk, 1978a). They are interpreted as a contorted part of the Tonga slab by Oliver et al. (1973). However, the epicenters of these deep earthquakes are arranged into a meridional belt, the course of which substantially differs from that of the Tonga-Kermadec trench. These earthquakes may be coordinated to the Lau Ridge, a remnant arc according to Milsom (1970) and Karig (1972), which has the same meridional strike and is situated above the belt of deep earthquakes in question.

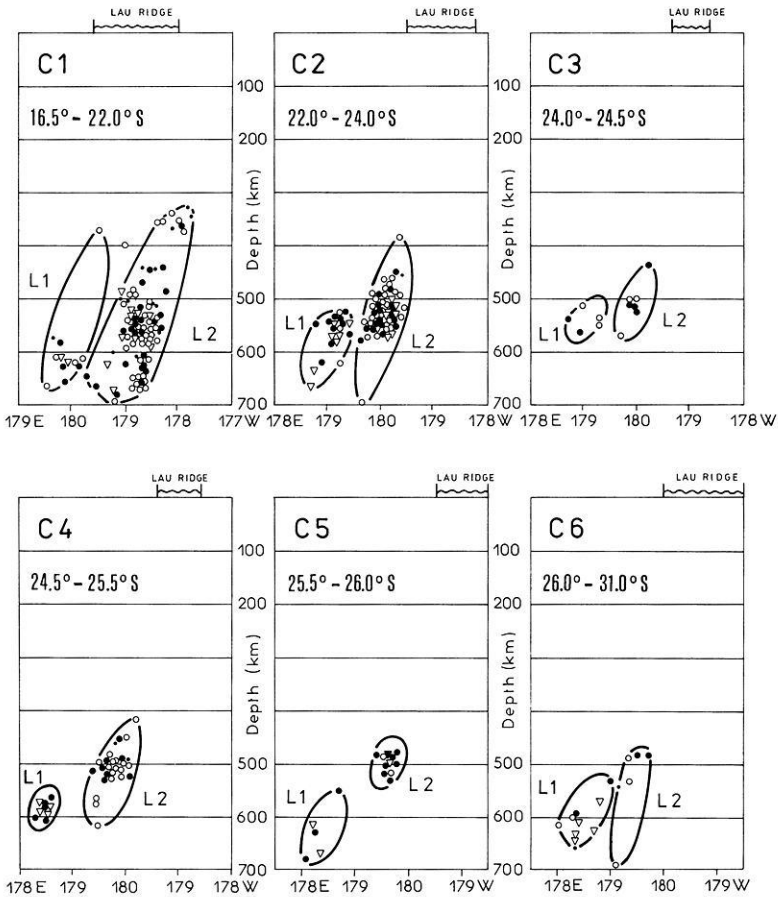


Fig. 4. Vertical sections C1–C6 for the Lau system giving the distribution of earthquake foci in dependence on longitude; symbols as in Figure 2, zones L1 and L2 are denoted by full-line contours. For position of sections see Figure 1

In order to demonstrate the reality of this interpretation, the depth distribution of the above foci was constructed and plotted together with the position of the Lau Ridge in a system of six parallel sections (see C1–C6 in Fig. 1). The resulting vertical sections, given in Figure 4, show that the earthquakes can be divided into two separated zones denoted arbitrarily as L1 and L2. They are very steeply dipping, the present average dip appearing to be about 70° to the west. It seems that the zones L1 and L2 represent two buried paleoplates activated by a deep collision with the recently subducting zones T1 and T2.

The top of the activated zone L1 ranges from 370 to 565 km (sections C1, C4), the bottom of L1 reaching depths between 565 and 685 km (sections

C3, C5). The thickness of the active part of L 1, measured perpendicularly to the dip, varies from 50 to 75 km with the prevailing value of 70 km. The corresponding parameters for L 2 are as follows: depth of the top between 325 and 485 km (sections C1, C6), depth of the bottom between 535 and 695 km (sections C5 and C1, C2, C6), thickness variable between 50 and 100 km.

Deep Collision and Activation of Buried Paleoplates

Deep collision of subducted lithospheric plates is a new phenomenon in the plate tectonic hypothesis. It is characterized by an anomalous clustering of deep earthquake foci in a relatively limited space, which cannot be interpreted by a simple model of one subducted plate. The geometry of the earthquake distribution gives an impression that smoothly downgoing slabs of recent subduction meet an obstacle during their penetration through the upper mantle. An analysis of the geometry of earthquake distribution and the position of remnant island arcs reveals that these obstacles can be interpreted as activated remaining parts of buried paleoplates belonging to ancient zones of subduction.

The above phenomenon is demonstrated in Figures 2 and 3, where the deep collision of the recently subducting Pacific plate with buried remnants of Lau paleoplates is shown. In the Tonga region two main centers of collision can be identified: the northern centre, appearing in the vertical section A1 (see Fig. 2), is produced by the collision of the Tonga zones T 1, T 2 with the Lau zone L 2; in the southern centre, which can be observed in the vertical section Y (see Fig. 3), the Tonga zone T 2 and the Lau zones L 1 and L 2 take part in the collision. In the southern centre T 1 is not involved in the collision because its depth of penetration is not sufficient to reach the Lau zone L 2 (for details see the complete sequence of vertical sections in Hanuš and Vaněk, 1978a).

The clustering of earthquake foci in the northern centre of collision is very intensive; therefore an enlarged picture of this region is shown in Figure 5, where we attempt to coordinate the individual earthquake foci to the interacting zones assuming that all the zones preserve their simple plate-like shape: zone T 1 is delineated by full-line contour, zones T 2 and L 2 are denoted by vertical and horizontal hatching, respectively, and the centre of collision by cross-hatching. The position of the centre of gravity of the northern collision is at 18.0° S and 178.4° W, its depth is at 600 km. The corresponding parameters of the southern collision are 23.6° S, 179.8° W, and 540 km depth. Both centres of collision are also shown in the geographic scheme of the Tonga region given in Figure 1.

By the deep collision with the Tonga zones T 1 and T 2 the buried Lau paleoplates L 1 and L 2 were activated not only in the centres of collision. The activation takes place also between both centres of collision and the earthquake foci belonging to L 1 can be observed up to the latitude of 31° S southwards of the southern centre and those belonging to L 2 up to the latitude of 16.5° S northwards of the northern centre of collision. This means that the Lau system of paleoplates is activated for a length of about 1600 km.

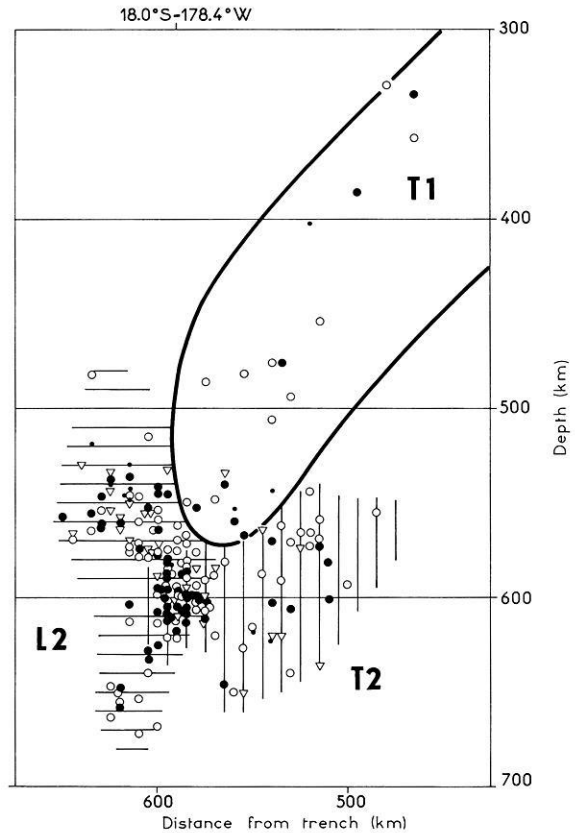


Fig. 5. Detailed picture of the northern centre of the Tonga-Lau deep collision; zone T 1 is denoted by full-line contour, zones T 2 and L 2 by vertical and horizontal hatching, centre of collision by cross-hatching

It appears that the earthquake foci are not distributed randomly in the paleo-plates but that they are arranged in an orthogonal system with a specific orientation with respect to the possible direction of subduction. A detailed discussion of this phenomenon will be published in a separate paper. It must be also noted that the present dip of the zones L 1 and L 2 need not correspond to the original dip of the Lau subduction and can be substantially influenced by the deep collision with the zones T 1 and T 2.

One of the most specific features of the Tonga region is the highest deep seismicity in the world. The deep collision of lithospheric plates may be the decisive factor in explaining this phenomenon.

References

- Cullen, D.J.: Tectonic map of the South-west Pacific (1:10000000). New Zealand Oceanogr. Inst. Chart, Miscellaneous Series 20, 1970
- Hanuš, V., Vaněk, J.: Intermediate aseismicity of the Andean subduction zone and recent andesitic volcanism. *J. Geophys.* **42**, 219–223, 1976

- Hanuš, V., Vaněk, J.: Structure of the Wadati-Benioff zone in the Tonga region. *Čas. Mineral. Geol. (Prague)* **23**, 5–23, 1978a
- Hanuš, V., Vaněk, J.: Time sequence of volcanism and subduction in the Tonga island arc. *Čas. Mineral. Geol. (Prague)* **23**, No. **4**, 1978b
- Hanuš, V., Vaněk, J.: Morphology of the Andean Wadati-Benioff zone, andesitic volcanism, and tectonic features of the Nazca plate. *Tectonophysics* **44**, 65–77, 1978c
- Karig, D.E.: Remnant arcs. *Geol. Soc. Am. Bull.* **83**, 1057–1068, 1972
- Milsom, J.S.: The evolution of the Lau Ridge, Fiji Islands. *Earth Planet. Sci. Lett.* **8**, 258–260, 1970
- Oliver, J., Isacks, B., Barazangi, M., Mitronovas, W.: Dynamics of the down-going lithosphere. *Tectonophysics* **19**, 133–147, 1973
- Regional Catalogue of Earthquakes, Vol. 1–10. Edinburgh: Intern. Seismol. Centre, 1964–1973
- World Map (1:2500000): Samoa Islands. Moscow: Main Admin. Geod. Cartogr., 1968; Kermadec Islands. Prague: Central Office Geod. Cartogr., 1968

Received November 15, 1977/Revised Version April 1, 1978

Seismic Risk Evaluation for the Upper Rhine Graben and Its Vicinity

L. Ahorner¹ and W. Rosenhauer²

¹ Erdbebenstation der Universität Köln, Vinzenz-Pallotti-Straße 26,
5060 Bergisch Gladbach 1 (Bensberg), Federal Republic of Germany

² INTERATOM, Internationale Atomreaktorbau GmbH,
Postfach, 5060 Bergisch Gladbach 1 (Bensberg), Federal Republic of Germany

Abstract. A probabilistic large-scale seismicity model for the Upper Rhine graben and adjoining regions has been developed considering all available seismological and geological information. With this model the probability distribution of macroseismic intensities (MSK-scale) was calculated for 208 sites regularly covering the region under investigation with a grid width of 25 km. Four maps with intensity isolines are presented according to exceedance probabilities 63 %, 10 %, 1 % and 0,1 % for a period of 50 years (corresponding to annual occurrence rates $2 \cdot 10^{-2}$, $2 \cdot 10^{-3}$, $2 \cdot 10^{-4}$, and $2 \cdot 10^{-5}$). The intensities given reflect the regional seismicity level with respect to quantitative risk values, which might be modified by local particularities (soil conditions, nearby seismoactive fault lines, etc.) for a special site. The risk for an average site in the Upper Rhine graben is characterized by an annual occurrence rate of about 10^{-4} for intensity VIII. On a statistical basis, the exceedance of intensity IX cannot be excluded, but could only occur at a very low probability level.

Key words: Earthquake Risk – Upper Rhine graben – Central Europe.

1. Introduction

At the present state of seismological research the occurrence of major earthquakes in seismoactive regions cannot be predetermined on a deterministic basis on the one hand and cannot be excluded on the other one. The seismic risk is therefore best described by probabilities for certain earthquake effects at given sites. It is assessed in terms of exceedance probabilities for intensities, peak acceleration, or other quantities during a given period of time.

Analytical methods to determine the site dependent risk have been developed by Cornell (1968) and Esteva (1969) and applied to a great number of seismic regions all over the world. For Europe probabilistic studies have been performed, e.g., by Lilwall (1976) for Great Britain, and very recently by Sägesser et al. (1977), Sägesser et al. (1978), and Mayer-Rosa (1978) for Switzerland.

Ahorner and Rosenhauer (1975) developed a probabilistic seismicity model using Gumbel's extreme value statistics for the Northern Rhine area. In the present paper this method is used with slight modifications to evaluate the seismic risk in the Southern Rhine area with special emphasis on the Upper Rhine graben. Instead of probability distributions of earthquake accelerations the exceedance of earthquake intensities at given sites is considered, since in Central Europe the attenuation law for macroseismic intensity is much better known than for peak acceleration.

2. Seismicity of the Upper Rhine Graben and Its Vicinity

The Upper Rhine graben (Fig. 1), which cuts through the earth's crust of Central Europe from Basel in the South to Frankfurt in the North, is a classical example of a continental rift valley and by this a favoured research object for geoscientists since many decades. A review of the latest results of geological, geophysical and geodetical investigations has been published in two monographs edited by Illies and Müller (1970), and Illies and Fuchs (1974).

Taphrogenesis started in the Middle Eocene, i.e., about 45 million years ago, and is continuing up to recent time. The neotectonic activity in and around the graben zone is indicated by Quaternary faults with dislocations up to several 100 m (Bartz, 1974), geodetically observed vertical crustal movements in the order of 0.5 mm/year (Mälzer, 1967; Prinz and Schwarz, 1970; Schwarz, 1974), structural damage to buildings founded immediately above the main faults (Müller and Prinz, 1966), and by a remarkable seismicity with damaging earthquakes up to moderate magnitudes (Ahorner et al., 1970).

The seismicity of the Upper Rhine graben and its vicinity has been studied in detail by Hiller et al. (1967), Schneider (1968, 1971), Ahorner (1970, 1975), Ahorner et al. (1972), Bonjer and Fuchs (1974), and others. Original data of historical events are available from earthquake catalogues of Sieberg (1940), Sponheuer (1952), Fiedler (1954), and Rothé and Schneider (1968).

The seismotectonic zone of the Upper Rhine graben and its bordering mountain ranges (Black Forest, Vosges, Odenwald, and Pfälzer Wald) forms the southern part of the Rhenish earthquake zone, which continues farther to the Northwest in the Lower Rhine graben (Ahorner and Rosenhauer, 1975). The Rhenish earthquake zone represents the most conspicuous seismological feature in the northern foreland of the Alps. Earthquakes occurring along this intra-plate zone of crustal weakness have focal depths between several and 25 km as a maximum. The focal mechanisms are as well of dip-slip as of strike-slip type and are clearly controlled by the present-day stress field within the earth's crust of Central Europe (Ahorner, 1975).

The energy release diagram (Fig. 2) gives a general impression of the time distribution of seismic activity in the Upper Rhine graben region. The sum of the square roots of seismic energies, which is under simplifying assumptions proportional to the seismic strain release in the earthquake region, increases relatively uniform with time as may be expected in a highly fractured graben zone with mainly tensional tectonics. Obviously the major part of the stored

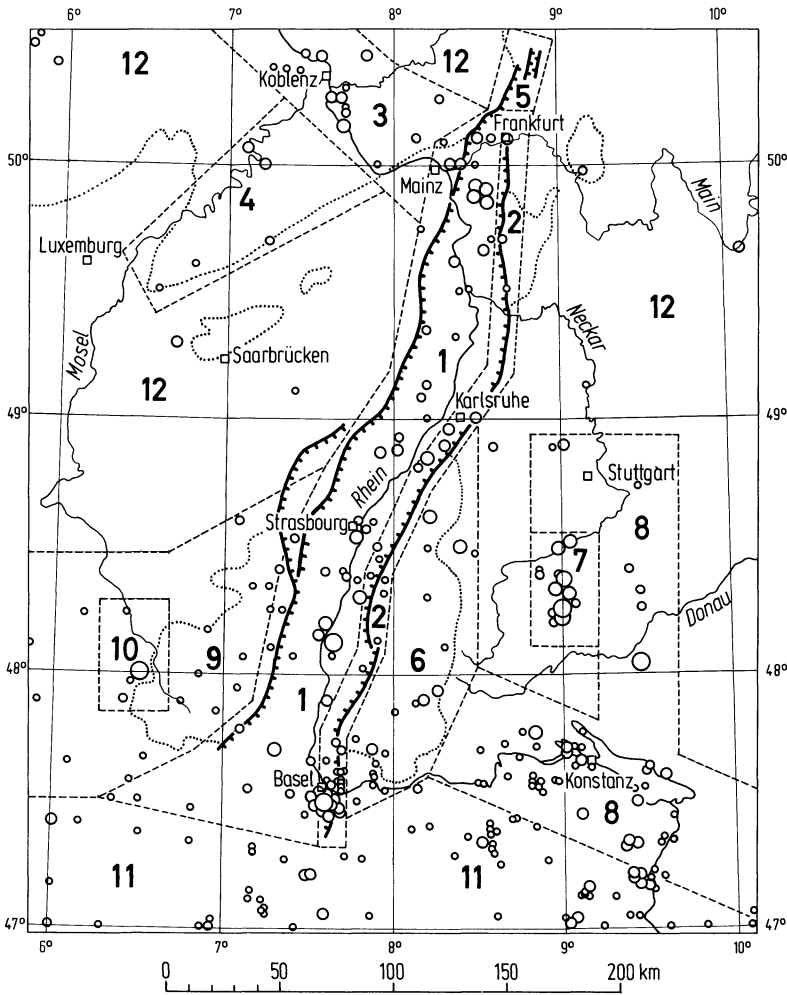


Fig. 1. Seismotectonic regionalization of the Upper Rhine graben region. Numbers refer to regions in Table 1. Circles denote epicenters of historical earthquakes with intensities $I \geq V$ MSK-scale. Dotted lines give the contours of outcropping Hercynian basement rocks

stress energy is released with small and medium earthquakes, whereas stronger shocks are comparatively seldom. Damaging earthquakes with magnitudes $M_m \geq 5$ (Richter-scale) and macroseismic intensities $I_0 \geq VII$ (MSK-scale) occur in the Rhine graben region only 2 to 3 times per century. The strongest shock observed is the famous Basel earthquake 1356, which killed 300 people (Sieberg, 1940). This event was released at the southern end of the graben and has an estimated magnitude $M_m = 6\frac{1}{4}$ and the epicentral intensity $I_0 = VIII-IX$. It is the most catastrophic earthquake felt in Central Europe north of the Alps in historical time.

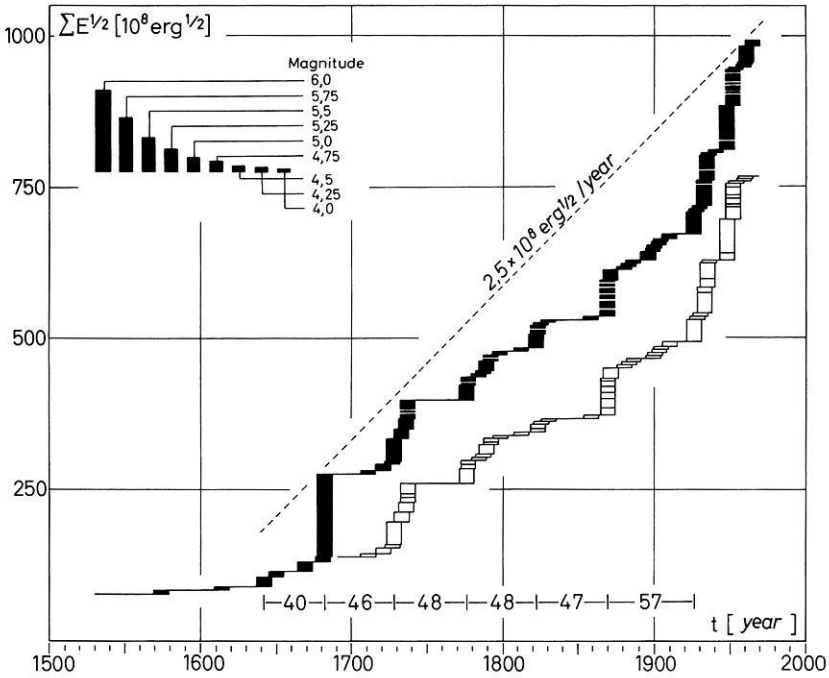


Fig. 2. Accumulated seismic energy release for earthquakes in the Upper Rhine graben zone during the last 300 years. The white diagram is for the graben zone alone, the black diagram for the graben zone and the bordering mountain ranges. Bursts of higher energy release occur with time intervals of 40 to 60 years. Earthquake data prior to 1600 are incomplete

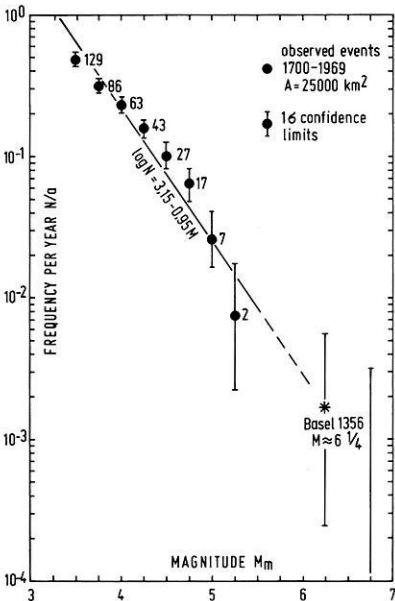


Fig. 3. Cumulative magnitude-frequency diagram for the Upper Rhine graben zone. The least square fit regression line gives $b=0.95$. The uncertainty of b can be judged considering the 1σ confidence limits of observed event numbers

The cumulative magnitude-frequency diagram (Fig. 3) shows how frequently earthquakes in the Upper Rhine graben region occur. The original data were taken from the earthquake catalogues mentioned above, mainly from Rothé and Schneider (1968). M_m is the macroseismic magnitude determined from the epicentral intensity I_0 (MSK-scale) and the focal depth h with the formula of Karnik (1969)

$$M_m = 0.5 I_0 + \log_{10}(h/\text{km}) + 0.35. \quad (1)$$

For shocks with unknown or uncertain intensity or focal depth the mean radius of perceptibility R_m was used to get the magnitude with the empirical relationship proposed by Sponheuer (1962),

$$M_m = 0.52 I + 1.56 \log_{10}(R_m/\text{km}) + 0.7 \alpha R_m \quad (2)$$

with the macroseismic intensity I at the limit of perceptibility (usually taken as II) and the absorption coefficient α (normally $2.5 \cdot 10^{-3}/\text{km}$). The validity of Equation (2) for the Rhine area has been checked by us evaluating well observed earthquakes with known instrumental magnitudes.

The general trend of the observed frequencies in Figure 3 follows the linear Gutenberg-Richter (1949) relation and is closely fitted by the regression line

$$\log_{10}(N \cdot T) = a_{GR}(A, T) - bM_m = 3.15 - 0.95 M_m \quad (3)$$

with $T=1$ year and $A=2.5 \cdot 10^4 \text{ km}^2$. The b value in Equation (3) differs only slightly from the average b values for shallow earthquakes in other regions. Wohlenberg (1968) for instance found $b=0.84$ for the East African rift zones, Karnik (1969) $b=0.94$ for the whole European region, and Gutenberg and Richter (1949) $b=0.90$ for the world.

It is of special interest that the regression line of Figure 3, derived from events between 1700 and 1969 in the magnitude range $3.5 \leq M_m \leq 5.3$, meets the isolated value of the Basel earthquake 1356. This suggests the conclusion (see Sect. 4, too), that the Basel event is not as exceptional for the seismotectonic regime of the Upper Rhine graben as is often assumed.

The linearity assumption of the magnitude – frequency relation for shocks up to $M_m \approx 6^{1/4}$ seems reasonable at least in some parts of the Upper Rhine graben, bearing in mind that in other continental rift zones with comparable geological conditions similar or even higher magnitudes have been observed, e.g., $M=6^{1/4}$ for the Jordan graben (Arieh, 1967) and $M=7.1$ for the East African graben zones (Wohlenberg, 1968).

A pessimistic seismotectonic estimate for the maximum possible earthquake along a preexisting geological fault line often used in the USA would lead to an upper bound magnitude $M_{\max}=7$ to 8 for the Upper Rhine graben if a total length $L=300$ km of the fracture zone is assumed and an active fault-plane length of $0.2 L$ to $0.5 L$ for the largest possible earthquake (Bonilla, 1970). These values, however, seem to be extremely conservative and thus cannot serve as a basis for a realistic risk assessment.

Considering all available seismological and geological information $M_{\max}=6^{1/2}$ is assumed for the eastern border faults (Fig. 1, region 2) and $M_{\max}=5^{3/4}$

Table 1. Seismological subdivision of the area under investigation and source specifications. Gumbel parameters a and u_0 are normalized to $T=10$ years and $A=10^4$ km². Values in parenthesis are estimated or uncertain

Region	Area $A/10^4$ km ²	Gumbel parameters (normalized)		Maximum magnitude	
		a	u_0	M observed	M_{\max} assumed for the model
1 Upper Rhine graben except eastern border zone	1.30	0.51 ± 0.12	3.82 ± 0.20	$5\frac{1}{4}$	$5\frac{3}{4}$
2 Eastern border zone of the Upper Rhine graben	0.30	0.51 ± 0.12	3.82 ± 0.20	$6\frac{1}{4}$	$6\frac{1}{2}$
3 Middle Rhine zone	0.51	0.60 ± 0.12	3.29 ± 0.21	5	$5\frac{3}{4}$
4 Hunsrück zone	0.48	(0.60)	(2.70)	$4\frac{1}{2}$	$5\frac{3}{4}$
5 Wetterau	0.08	(0.60)	(2.70)	4	$5\frac{3}{4}$
6 Black Forest	0.54	0.78 ± 0.15	3.47 ± 0.25	5	$5\frac{3}{4}$
7 Western Swabian Alb	0.15	0.58 ± 0.15	5.78 ± 0.25	6	$6\frac{1}{2}$
8 Eastern Swabian Alb, Upper Swabia, Lake Constance, Hegau	1.30	0.72 ± 0.15	3.53 ± 0.25	$5\frac{1}{2}$	$5\frac{3}{4}$
9 Vosges mountains and Eastern France	1.13	(0.60)	(3.00)	—	$5\frac{3}{4}$
10 Epinal-Remiremont zone	0.15	(0.60)	(4.00)	6	$6\frac{1}{2}$
11 Northern Switzerland	2.04	(0.60)	(3.30)	—	$5\frac{3}{4}$
12 Regions with very low seismicity (outside regions 1–11)	6.74	(0.48)	(1.95)	$4\frac{1}{2}$	$5\frac{3}{4}$

along the western border faults and in the graben interior (Fig. 1, region 1) in our seismicity model.

Outside of the seismotectonic unit of the Upper Rhine graben several seismic source regions exist influencing the seismic risk of the graben area. The specifications of these neighbouring sources and their boundaries were determined using historical seismicity and available geological and tectonical evidence as shown in Figure 1 and Table 1.

The most important focal region southeast of the graben is the Western Swabian Alb (Fig. 1, region 7). This small-sized highly active seismotectonic unit is characterized by strike-slip shocks occurring along a $N-S$ trending crustal fracture zone (Schneider, 1968, 1971). The specific seismicity (earthquake frequency per magnitude class and unit area and time) of the Swabian Alb zone is much higher than in the Upper Rhine graben, but only for the last seven decades (Ahorner, 1975). The period of high activity starts with the major earthquake near Ebingen 1911 (epicentral intensity VIII, magnitude $M_{\text{LGH}}=6.1$; Karnik, 1969). Since that time more than 20 earthquakes with intensities equal or greater VI have been observed. Before 1911 the seismic activity of the Swabian Alb zone was of minor significance for many centuries. This non-uniform time distribution raises the difficulty whether the high activity rate of the present century or a smaller rate averaged over two or more centuries in the past should be used for the risk calculation. Conservatively the higher specifi-

cations derived from the period 1900–1974 were taken for the Swabian Alb region (see Table 1) in our seismicity model.

A seismotectonic pendant to the Swabian Alb zone is the focal region of Epinal-Remiremont (Fig. 1, region 10) on the south-western side of the Upper Rhine graben, where equally damaging earthquakes occur, too. The strongest shock observed is that of 1682 (epicentral intensity VIII–IX, magnitude $M_m \approx 6$; Sieberg, 1940).

From all other neighbouring sources only the Black Forest zone (Fig. 1, region 6) has an essential influence on the seismic risk in the graben area. The focal depths of the Black Forest earthquakes are between 8 km and 25 km, somewhat deeper than in the surrounding seismotectonic units (Ahorner et al., 1970). This implies that in spite of large areas of perceptibility the epicentral intensities are not very high. The maximum observed intensity is $I_0 = \text{VI–VII}$ (Schneider, 1968).

3. Attenuation Law for Macroseismic Intensity

In Ahorner and Rosenhauer (1975) a peak acceleration–distance curve has been used as transfer function between earthquake sources and site. Because sufficient acceleration data for Central European earthquakes are lacking until now, great uncertainties had to be associated with this curve, which were taken into account in the uncertainty analysis of the probability results. In the present paper, an intensity attenuation law based on local observations is derived, which is a better basis for the assessment of earthquake risk at given sites in the region under investigation.

Two well known empirical laws describe the dependence of macroseismic intensity I on hypocentral distance R and magnitude M_m . The first is from Sponheuer (1960):

$$I(R) - I(R') = 3 \log_{10}(R'/R) + 3\alpha \log_{10} e \cdot (R' - R)/\text{km}. \quad (4)$$

The absorption coefficient α varies for most earthquakes in the Rhine area between 0.001 and 0.005. Its uncertainty, however, is not important for hypocentral distances $R < 200$ km relevant for the calculations described in Section 4. The value $\alpha = 0.0025$ was chosen, i.e.

$$3\alpha \log_{10} e = 3.26 \cdot 10^{-3} \approx 3 \cdot 10^{-3}. \quad (5)$$

Choosing $R' = 10$ km as a reference distance one gets

$$\begin{aligned} I - I_{10 \text{ km}} &= I(R) - I(10 \text{ km}) \\ &= 3 - 3 \log_{10}(R/\text{km}) - 3\alpha \log_{10} e (R/\text{km} - 10). \end{aligned} \quad (6)$$

This formula is in good agreement with observed intensity-distance curves for the Rhine area (Fig. 4).

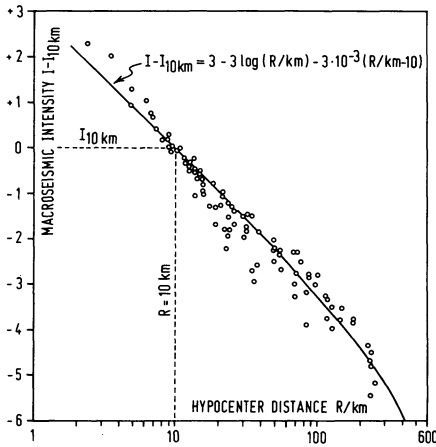


Fig. 4. Attenuation of macroseismic intensity I (MSK-scale) with hypocentral distance R . Points give mean isoseismal radii for 19 earthquakes observed in the Rhine area from 1846 to 1965. The continuous variable $I_{10\text{ km}}$ (at $R = 10\text{ km}$), which serves as reference intensity, has been derived from observed intensity-distance curves graphically

The second law is Equation (1) (Karnik, 1969), which gives the intensity at $R = 10\text{ km}$ by insertion of the focal depth $h = 10\text{ km}$:

$$I_{10\text{ km}} = 2M_m - 2.7. \tag{7}$$

Combination of Equations (5) to (7) yields the desired intensity attenuation law valid for the Upper Rhine graben and adjacent regions:

$$I = 2M_m - 3 \log_{10}(R/\text{km}) - 3 \cdot \alpha \cdot \log_{10} e \cdot (R/\text{km} - 10) + 0.3$$

$$3\alpha \log_{10} e \approx 3 \cdot 10^{-3}. \tag{8}$$

4. Statistical Model and Calculation Methods

The probabilistic description of earthquake occurrence and the calculation of site dependent probability distributions for intensities have been performed using the methods and computer codes presented in detail by Ahorner and Rosenhauer (1975). Therefore, only the main characteristics will be repeated here.

For each of the seismicity zones in Figure 1 Gumbel's extreme value distribution (Gumbel, 1958)

$$G(M) = \exp \left[-\exp \left(-\frac{M-u}{a} \right) \right] \tag{9}$$

is assumed to give the probability that the Richter magnitude of the largest earthquake in the zone with area A in a specified time T does not exceed a value M .

This corresponds to the linear magnitude-frequency relation Equation (3), because the following general relation between the extreme value distribution

$G(M)$ and the mean frequency N holds:

$$G(M) = \exp(-N \cdot T). \tag{10}$$

Insertion of Equation (3) leads to the Gumbel distribution Equation (9) with

$$u = a_{GR}(A, T)/b, \quad a = \log_{10} e/b \approx 1/(2.3b). \tag{11}$$

The Gumbel parameters a and u have been obtained from observed extremes with the INTERATOM computer code GUMBEL using unbiased evaluation methods based on order statistics. For the Upper Rhine graben examples are given in Figures 5 and 6. The evaluation of observed 50-year extremes for the

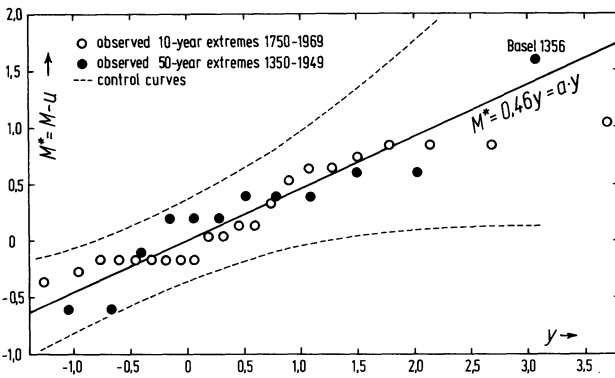


Fig. 5. Gumbel plots of observed magnitude extremes for the Upper Rhine graben ($A = 1.6 \cdot 10^4 \text{ km}^2$). The values for u normalized to $T = 10$ years and $A = 10^4 \text{ km}^2$ are $u_0 = 3.99 \pm 0.20$ for the 10-year extremes and $u_0 = 3.65 \pm 0.25$ for the 50-year extremes. On the abscissa plotting positions y are used calculated with the computer code GUMBEL

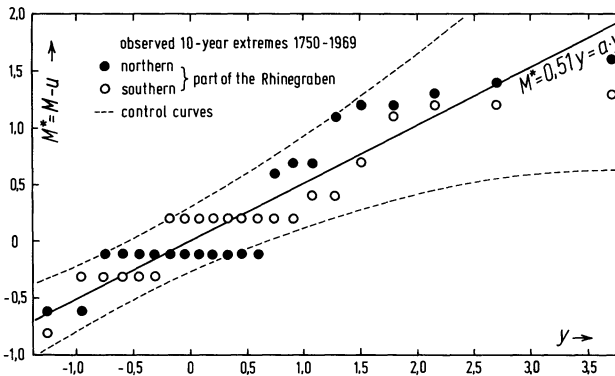


Fig. 6. Gumbel plots of observed magnitude extremes for the northern part (N of Lat. 49° , $A = 0.9 \cdot 10^4 \text{ km}^2$) and the southern part ($A = 0.7 \cdot 10^4 \text{ km}^2$) of the Upper Rhine graben. Normalized values u_0 are very similar for both parts of the graben ($u_0 = 3.86$ and 3.82 respectively)

period 1350–1949 including the Basel earthquake of 1356 shows remarkable agreement with the values based on 10-year extremes for the period 1750–1969, indicating that the Basel event is not extraordinary for the seismic regime of the Upper Rhine graben. Similarly, no significant difference could be found between the southern and northern part of the graben.

The Gumbel parameters a and u can as well be determined from the Gutenberg and Richter parameters $a_{GR}(A, T)$ and b using Equation (11) and the values of Figure 3,

$$u = 3.15/0.95 = 3.32 \quad a = 1/(2.3 \cdot 0.95) = 0.46 \quad (12)$$

referring to $T = 1$ year and $A = 2.5 \cdot 10^4 \text{ km}^2$. Normalizing to 10 years and an area of 10^4 km^2 one gets (Ahorner and Rosenhauer, 1975)

$$\begin{aligned} u_0 &= u + a \cdot \ln \left(\frac{10^4 \text{ km}^2 \cdot 10 \text{ years}}{AT} \right) \\ &= 3.32 + 0.46 \cdot \ln \left(\frac{10^4 \text{ km}^2 \cdot 10 \text{ years}}{2.5 \cdot 10^4 \text{ km}^2 \cdot 1 \text{ year}} \right) = 3.96. \end{aligned} \quad (13)$$

These values for a and u_0 agree well with $a = 0.51 \pm 0.12$ and $u_0 = 3.82 \pm 0.20$ determined by the evaluation of extremes directly (Table 1).

In order to exclude infinite values of M , absolute upper bounds M_{\max} have again been introduced by a correction of Equation (9), which is small in the range of observed extremes:

$$\begin{aligned} G_c(M) &= G(M)/G(M_{\max}) & (M \leq M_{\max}) \\ G_c(M) &= 1 & (M > M_{\max}). \end{aligned} \quad (14)$$

$G_c(M)$ is identical with the bounded magnitude-frequency distribution used by Knopoff and Kagan (1977). Criticism by these authors concerning the application of biased estimators for extreme value statistics to earthquake problems does not cover the methods used by us. Detailed comments defending the procedures of the theory of extremes for risk evaluations against the general objections of Knopoff and Kagan (1977) will be contained in a paper under preparation by the present authors. Methods to obtain reliable estimates for regional values of M_{\max} justifying the assumptions made in our 1975 calculations and in this paper will also be published in this paper. Figure 7 shows the magnitude probability distributions $G_c(M)$ used in the Upper Rhine graben Regions 1 and 2).

For each seismicity zone a focal depth distribution $W(h)$ was used giving the probability that the focal depth of an earthquake is smaller than h . These distributions were found by evaluating observed data (see Ahorner and Rosenhauer, 1975).

The total region under investigation (Fig. 1) has been covered by a regular net of 208 sites with 25 km grid width. For each site, the probability distribution of the intensity has been calculated with the INTERATOM computer code WASEW. WASEW subdivides the environs of a site into elements of volume

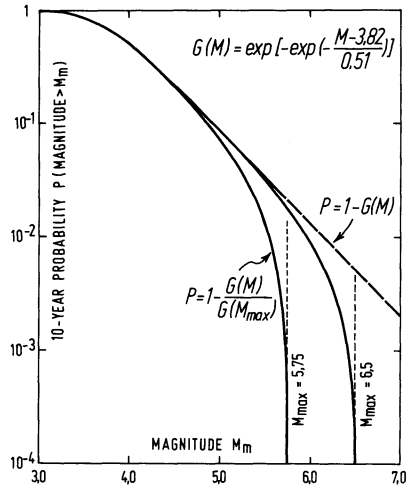


Fig. 7. Magnitude probability distributions used for the Upper Rhine graben model. $M_{max} = 6.5$ was assumed for the eastern border faults and $M_{max} = 5.75$ for the graben interior and the western border faults

ΔV . For a fixed intensity I Equation (8) gives—as a function of the distance between ΔV and the site—the magnitude that has to be exceeded in ΔV in order to get an exceedance of intensity I at the site. The probability of this event is determined from the corresponding magnitude and focal depth distributions $G_c(M)$ and $W(h)$ respectively. Summing up the contributions of all ΔV , the probability for exceedance of I at the site is gained.

5. Results

Figure 8 shows as typical examples three of the 208 probability distributions calculated as described in the preceding section. The whole set of distributions was evaluated in order to draw probabilistic intensity maps. To this purpose, the intensities I for each site were determined corresponding to yearly exceedance probabilities of $2 \cdot 10^{-2}$, $2 \cdot 10^{-3}$, $2 \cdot 10^{-4}$, and $2 \cdot 10^{-5}$ respectively, and drawn into maps (Figs. 9 to 12). Interpreting these values for a reasonable reference time, the maps show the intensity values and isolines with exceedance probabilities of 63%, 10%, 1%, and 0.1% within $T = 50$ years.

The probabilistic intensity maps give a gross quantitative measure of the regional seismic risk level only, because local soil conditions, nearby seismoactive fault lines, and other local features contribute to the actual risk at a site. Local particularities cannot be incorporated into large scale seismicity models, which give averaging results. Because of the limited dimensions of the model the probability values are too small for sites nearer than about 50 km to the map boundaries. This influence disappears with decreasing probability level. Moreover, the far reaching contribution of the Lower Rhine area is not included in the model. Consequently, the intensities calculated for sites in the northwestern part of the maps (NW of the line Saarbrücken-Mainz) are in general too small.

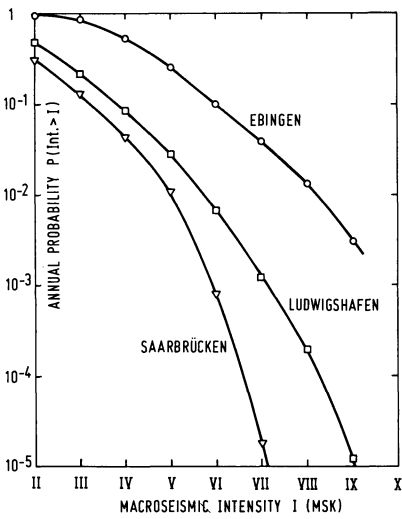


Fig. 8. Annual probability P of exceeding an intensity I at typical localities. Ludwigshafen is a representative site in the graben interior (near the confluence of the river Neckar with the Rhine). Ebingen is near the center of the Swabian Alb focal region. Saarbrücken is situated about 60 km west of the graben

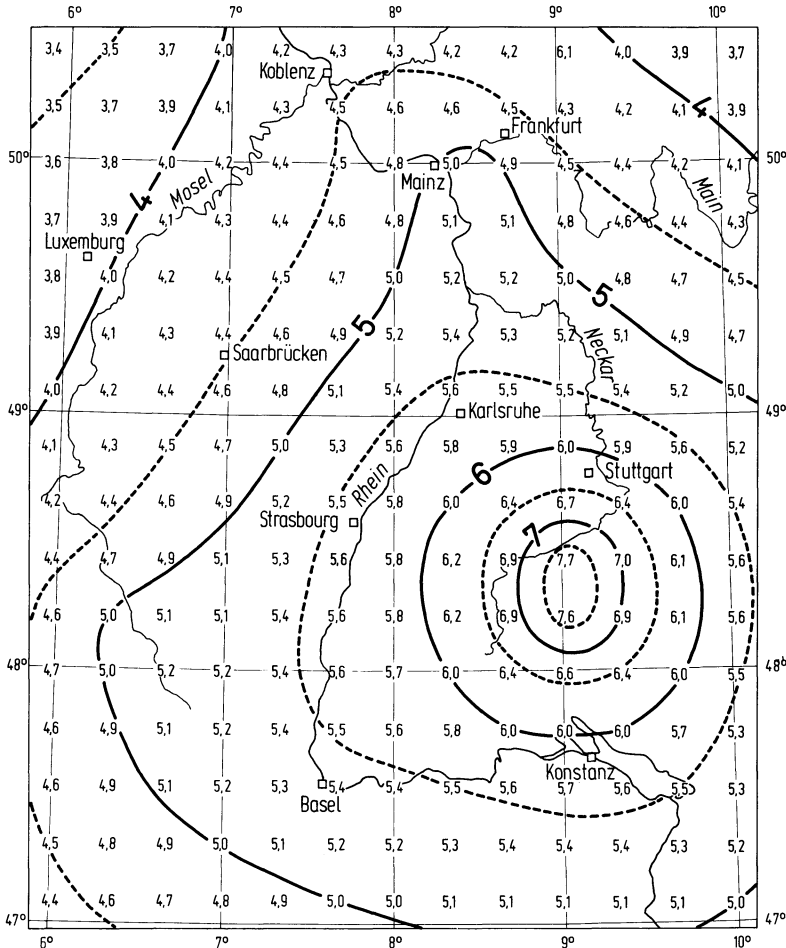


Fig. 9. Seismic risk map for the Upper Rhine graben region showing intensities (MSK-scale) for yearly exceedance probability $P = 2 \cdot 10^{-2}$ corresponding to $P = 63\%$ for $T = 50$ years

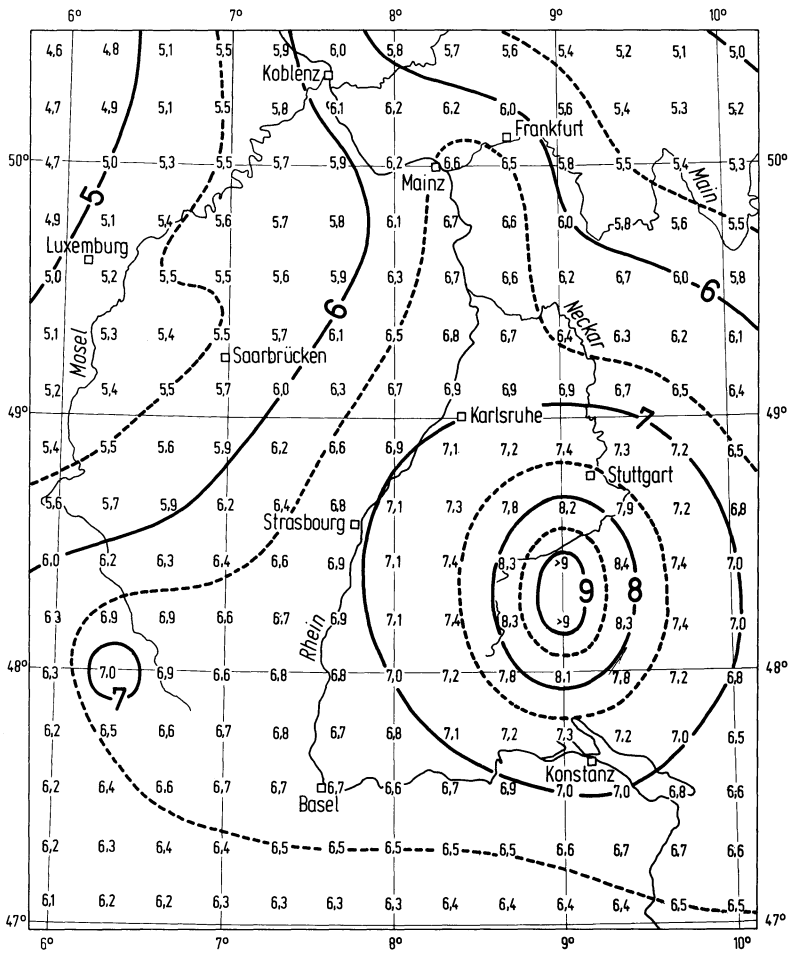


Fig. 10. Seismic risk map for the Upper Rhine graben region showing intensities (MSK-scale) for yearly exceedance probability $P=2 \cdot 10^{-3}$ corresponding to $P=10\%$ for $T=50$ years

Both effects however are not relevant for the Upper Rhine graben itself and its direct environment.

Obviously the earthquake intensity which might be used as a basis for design purposes is strongly controlled by the site dependent occurrence frequency tolerated. For the Upper Rhine graben, for instance, a probability of 10% for exceedance within $T=50$ years corresponds to $I \approx VII$, whereas a value of 1% suggests $I \approx VIII$. For sites in the Swabian Alb seismotectonic region about two units higher intensities would be requested at the same exceedance probability levels.

From the comparison of the four maps it becomes also clear that for intensities with higher occurrence rates the seismic risk in the Upper Rhine graben is influenced distinctly by the Swabian Alb focal region and that for

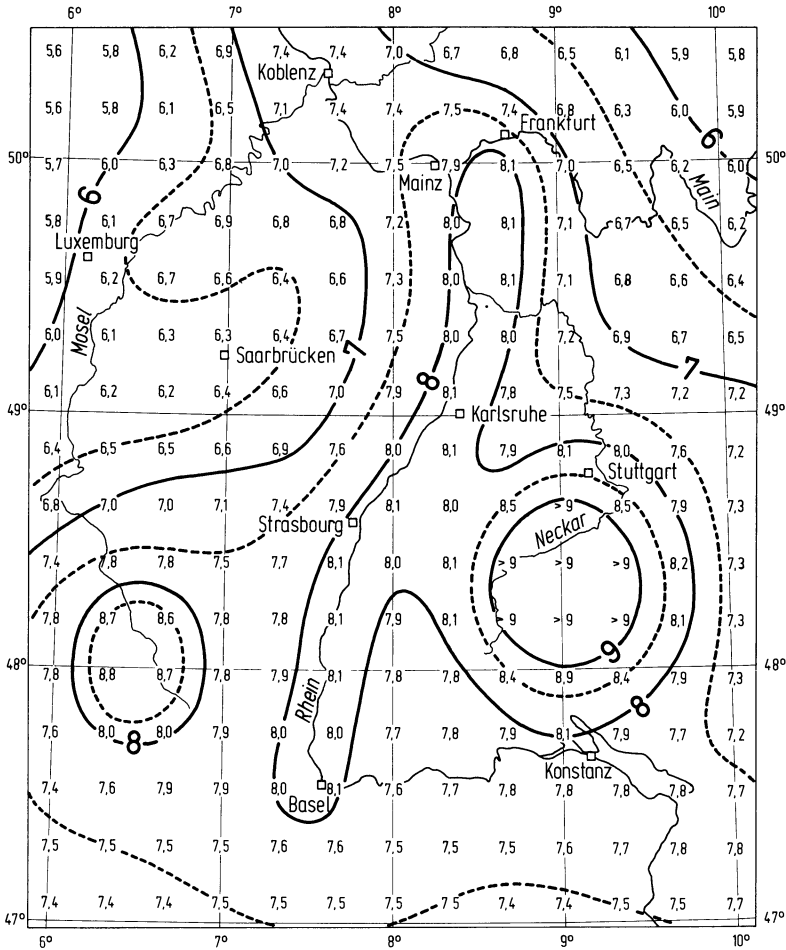


Fig. 11. Seismic risk map for the Upper Rhine graben region showing intensities (MSK-scale) for yearly exceedance probability $P=2 \cdot 10^{-4}$ corresponding to $P=1\%$ for $T=50$ years

lower occurrence rates events in the graben itself give the most important contributions.

The uncertainty analysis in Ahorner and Rosenhauer (1975), which has not been repeated for the Upper Rhine graben, suggests similar resulting uncertainties of the probability numbers, i.e., up to one to two orders for higher intensities, with the typical effect of smaller values for the upper, and greater values for the lower uncertainties.

Nevertheless it must be concluded that, concerning the overall seismic risk of the Upper Rhine graben, intensities up to $I=9$ cannot be excluded on a statistical basis but might occur at very low probability levels.

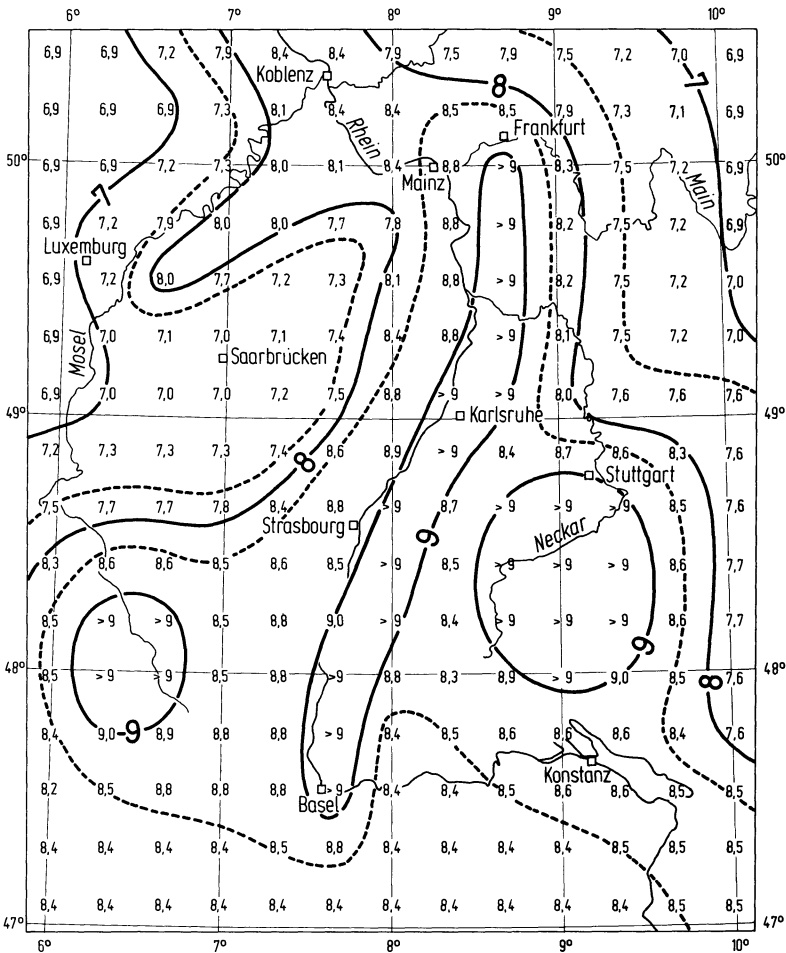


Fig. 12. Seismic risk map for the Upper Rhine graben region showing intensities (MSK-scale) for yearly exceedance probability $P=2 \cdot 10^{-5}$ corresponding to $P=0.1\%$ for $T=50$ years

It is interesting to compare our results for the Upper Rhine area with those of the seismic risk maps for Switzerland recently published by the Eidgenössisches Amt für Energiewirtschaft (Sägesser et al., 1977; Mayer-Rosa, 1978). For high seismicity regions in Switzerland, e.g., the Upper Rhone valley (Valais), the Swiss maps give maximum intensities $I=9.6$ with yearly exceedance probability 10^{-4} comparable with our highest values for the Swabian Alb region. Though the analyses have been carried out independently and are based on different statistical models, the final results for probabilistic intensities in the Swiss-German border region (e.g., near Basel, Table 2) show—considering the uncertainties of both approaches—remarkable agreement.

Table 2. Comparison between probabilistic intensities for the Basel area

Annual probability of exceedance	Intensity (MSK-scale)	
	Swiss risk map 1977	Our risk analysis
$P = 10^{-2}$	$I = 6.1$	$I = 5.8$
$P = 10^{-3}$	$I = 7.4$	$I = 7.0$
$P = 10^{-4}$	$I = 8.8$	$I = 8.5$

References

- Ahorner, L.: Seismo-tectonic relations between the graben zones of the Upper and Lower Rhine valley. In: Graben problems, H. Illies and St. Müller, ed., pp. 155–166. Stuttgart: Schweizerbart 1970
- Ahorner, L.: Present-day stress field and seismotectonic block movements along major fault zones in Central Europe. *Tectonophysics* **29**, 233–249, 1975
- Ahorner, L., Murawski, H., Schneider, G.: Die Verbreitung von schadenverursachenden Erdbeben auf dem Gebiet der Bundesrepublik Deutschland. *Z. Geophys.* **36**, 313–343, 1970
- Ahorner, L., Murawski, H., Schneider, G.: Seismotektonische Traverse von der Nordsee bis zum Apennin. *Geol. Rundschau* **61**, 915–942, 1972
- Ahorner, L., Rosenhauer, W.: Probability distribution of earthquake accelerations with applications to sites in the Northern Rhine area, Central Europe. *J. Geophys.* **41**, 581–594, 1975
- Arieh, E.J.: Seismicity of Israel and adjacent areas. *Geol. Surv. Israel Bull. No. 43*, 14 p. 1967
- Bartz, J.: Die Mächtigkeit des Quartärs im Oberrheingraben. In: Approaches to Taphrogenesis, J.H. Illies and K. Fuchs, eds.: pp. 78–87. Stuttgart: Schweizerbart 1974
- Bonilla, M.G.: Surface faulting and related effects. In: *Earthquake Engineering*, Chapt. 3, R.L. Wiegel, ed.: Englewood Cliffs, N.J.: Prentice-Hall 1970
- Bonjer, K.-P., Fuchs, K.: Microearthquake activity observed by a seismic network in the Rhein-graben region. In: Approaches to Taphrogenesis, H.J. Illies and K. Fuchs, eds.: pp. 99–104. Stuttgart: Schweizerbart 1974
- Cornell, C.A.: Engineering seismic risk analysis. *Bull. Seism. Soc. Am.* **58**, 1583–1606, 1968
- Esteva, L.: Seismicity prediction: A Bayesian approach. *Proc. World Conf. Earthquake Eng.*, 4th, Santiago, Chile, **1**, 172–184, 1969
- Fiedler, G.: Die Erdbebenstätigkeit in Südwestdeutschland in den Jahren 1800–1950. 152 p. Stuttgart: Diss. TH 1954
- Gumbel, E.J.: *Statistics of Extremes*, 375 p. New York and London: Columbia University Press 1958
- Gutenberg, B., Richter, C.F.: *Seismicity of the Earth and associated phenomena*. 273 p. Princeton, N.J.: Princeton University Press 1949
- Hiller, W., Rothé, J.-P., Schneider, G.: La sismicité du Fossé Rhénan. *Abh. geol. Landesamt Baden-Württemberg* **6**, 98–100, 1967
- Illies, J.H., Fuchs, K. (ed.): *Approaches to Taphrogenesis*. 460 p. Stuttgart: Schweizerbart 1974
- Illies, J.H., Müller, St. (ed.): *Graben problems*. 316 p. Stuttgart: Schweizerbart 1970
- Karnik, V.: *Seismicity of the European Area*, part 1. 364 p. Dordrecht: Reidel 1969
- Knopoff, L., Kagan, Y.: Analysis of the theory of extremes as applied to earthquake problems. *J. Geophys. Res.* **82**, 5647–5657, 1977
- Lilwall, R.C.: Seismicity and seismic hazard in Britain. *Seismol. Bull. Inst. Geol. Sci. No. 4*, 9 p., 1976
- Mälzer, H.: Untersuchungen von Präzisionsnivellements im Oberrheingraben von Rastatt bis Basel im Hinblick auf relative Erdkrustenbewegungen. *Dtsch. Geodät. Komm.* **138**, 1–23, 1967
- Mayer-Rosa, D.: Seismizität und seismisches Risiko der Schweiz. Paper presented at the 38. Jahrestagung der Deutschen Geophysikalischen Gesellschaft, March 7–10, 1978, Münster (abstract), 1978

- Müller, K.H., Prinz, H.: Zur Frage rezenter tektonischer Bewegungen am Oberrheingrabenabbruch. Notizbl. hess. L. A. Bodenforschung, **94**, 390–393, 1966
- Prinz, H., Schwarz, E.: Nivellement und rezente tektonische Bewegungen im nördlichen Oberrheingraben. In: Graben problems, H.J. Illies and St. Müller, eds.: pp. 117–183. Stuttgart: Schweizerbart 1970
- Rothé, J.-P., Schneider, G.: Catalogue des tremblements de terre du Fossé Rhéna 1021–1965. Veröff. Landeserdbedienst Baden-Württemberg, 1–91, 1968
- Sägesser, R., Rast, B., Merz, H.: Seismic risk maps of Switzerland. Transact. 4th Int. Conf. Struct. Mech. React. Techn. (SMIRT) San Francisco 15–19 August, 1977, Vol. K. (a) 1/3, 12p. (1977)
- Sägesser, R., Mayer-Rosa, D.: Erdbebengefährdung in der Schweiz. Schweizerische Bauzeitung **96**, 107–123, 1978
- Schneider, G.: Erdbeben und Tektonik in Südwest-Deutschland. Tectonophysis **5**, 459–511 (1968)
- Schneider, G.: Seismizität und Seismotektonik der Schwäbischen Alb. 79p. Stuttgart: Enke 1971
- Schwarz, E.: Levelling results at the northern end of the Rhinegraben. In: Approaches to Taphrogenesis, H.J. Illies and K. Fuchs, eds.: 261–263. Stuttgart: Schweizerbart 1974
- Sieberg, A.: Beiträge zum Erdbebenkatalog Deutschlands und der angrenzenden Gebiete für die Jahre 58–1799. Mitt. deutsch. Reichserdbedienst **2**, 1–11, 1940
- Sponheuer, W.: Erdbebenkatalog Deutschlands und der angrenzenden Gebiete für die Jahre 1800–1899. Mitt. deutsch. Erdbedienst **3**, 1–195, 1952
- Sponheuer, W.: Methoden zur Herdtiefenbestimmung in der Makroseismik. Freiburger Forschungsh., Reihe C **88**, 1–120, 1960
- Sponheuer, W.: Untersuchung zur Seismizität von Deutschland. Veröff. Inst. Bodendyn. Erdbebenforsch. Jena **72**, 23–52, 1962
- Wohlenberg, J.: Seismizität der ostafrikanischen Grabenzone zwischen 4° N und 12° S sowie 23° E und 40° E. Veröff. Bayr. Komm. Intern. Erdmessungen, Heft 23, 95p., 1968

Received February 23, 1978 / Revised Version April 27, 1978

A Comparison of PKP Precursor Data From Several Seismic Arrays

A.P. van den Berg, S.A.P.L. Cloetingh, and D.J. Doornbos

Vening Meinesz Laboratory, Lucas Bolwerk 6, University of Utrecht, Utrecht, The Netherlands

Abstract. Data from the four UKAEA arrays have been analyzed, using methods similar to those applied previously to NORSAR data. This allows a comparison of the different data sets, and such a comparison has been made for PKP phases and their precursors: The precursors are characterized by direction of approach and relative arrival time and spectral content; computational values, based on the interpretation of scattering in the lower mantle or at the core-mantle boundary (CMB), are used as a reference. Precursors at the different arrays have sampled different regions of the lower mantle and CMB. Significant differences between the various data sets, in characteristics like spectral ratio and azimuth deviation from the great circle, suggest large scale lateral variations in the properties of heterogeneous structure sampled by the data. It leads to the mapping of relatively “smooth” regions (beneath the S. Sandwich Islands and Central North America, from YKA data), and “rough” regions (beneath the Fiji Islands and Fennoscandia, from NORSAR data).

Key words: Scattering – Core-mantle boundary – Lower mantle – Lateral variations – Arrays.

1. Introduction

During the last 5 years or so, seismic array data have been used in exploring lateral variations in the lower mantle. The array evidence of large scale variations as inferred mainly from slowness vector anomalies (e.g., Davies and Sheppard, 1972; Kanasewich et al., 1973; Wright and Lyons, 1975), is still subject to debate (Green, 1975; Berteussen, 1976; Vermeulen and Doornbos, 1977). More conclusive has been the evidence of small scale variations as inferred from the characteristics of certain types of precursors to core phases, following their interpretation in terms of scattered waves (Cleary and Haddon, 1972); see, e.g., Doornbos (1976) and Husebye et al. (1976) for precursors to PKP,

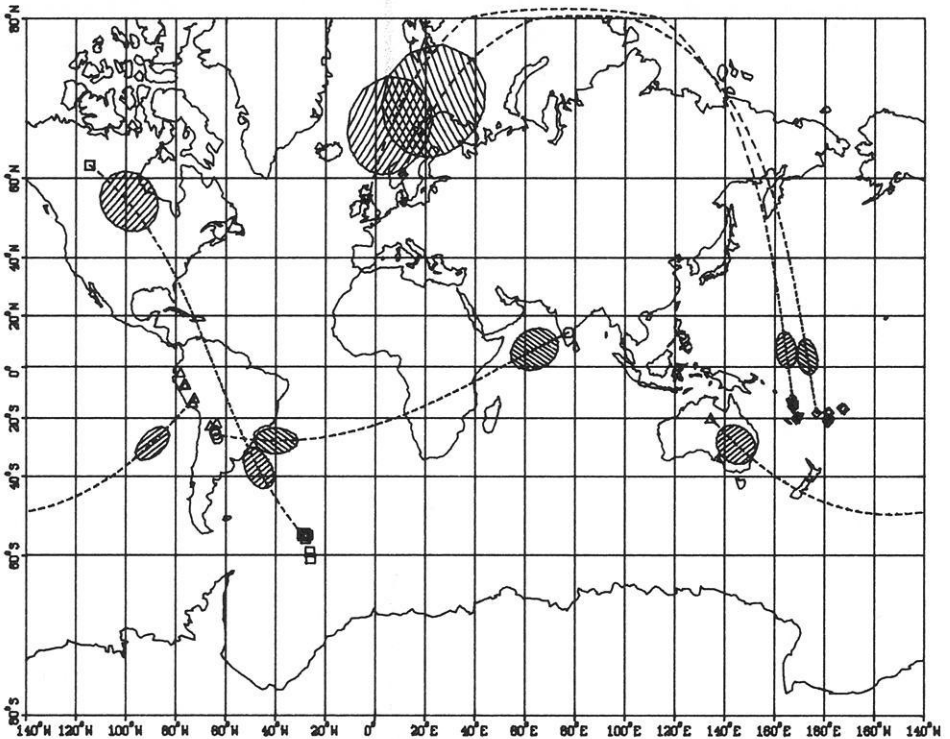


Fig. 1. Mercator projection of the world, with epicentra and array receiver locations, and surface projections of great circle paths and areas sampled on and above CMB; the hatched areas are for one typical source in each source region only. Array symbols: \diamond (NORSAR at 60.82° N, 10.83° E), \square (YKA at 62.49° N, 114.61° W), \circ (GBA at 13.60° N, 77.44° E), ∇ (EKA at 55.33° N, 3.16° W), \triangle (WRA at 19.95° S, 134.35° E). Event symbols according to the receiver array

Doornbos (1974a) for precursors to PKKP, Haddon et al. (1977) for precursors to P'P'. Yet, there are some significant differences in the models of small scale heterogeneity proposed or inferred by different authors. For example, some workers explain the PKP precursor data by a uniform scattering layer of thickness 200 km or less at the base of the mantle (Haddon and Cleary, 1974; Wright, 1975; Husebye et al., 1976); Doornbos (1977) concluded that both a slightly rough core-mantle boundary (hereafter referred to as "CMB") and a slightly heterogeneous lower mantle would explain the observed energy level in most of the PKP precursors, but as was pointed out, the simultaneous explanation of other characteristics like travel time and slowness vector, by scattering in an otherwise standard Earth model, may require scattering regions well above CMB, and/or large scale lateral variations in these regions (c.f., Doornbos, 1976).

Besides differences in source-receiver geometry, thereby sampling different regions of the lower mantle or CMB, some differences in the proposed scattering models may be due to the different array systems and data analysis techniques used. This paper reports on an experiment where we try to avoid introducing

subjective differences by analyzing data from the 4 UKAEA arrays, in comparison with the existing NORSAR data set. The UKAEA analog data were converted to the same digital form as NORSAR data. Thus, although several of these arrays have been employed separately for similar purposes, our aim here is to test the idea of large scale variations in the lower mantle or CMB structure (besides the small scale variations inherent in the scattering interpretation), by a similar analysis of data from different source-receiver combinations. Figure 1 illustrates the source-receiver geometry and the areas thus sampled (these areas are shown for one typical source in each source region only).

In the next section we give a brief summary of the arrays and data processing techniques used. The observational results are parameterized in the form of arrival time, slowness vector and spectral ratio (relative to PKP). The results are presented and discussed along with theoretical results for scattering from a rough CMB and a heterogeneous lower mantle.

2. The Arrays and Data Analysis Techniques

The arrays we use have been extensively documented. Moreover, NORSAR and three of the four UKAEA arrays have been used for similar purposes as in this paper. For discussions of the arrays, their response, etc., we therefore refer to the literature. (For general discussions, see, e.g., Birtill and Whiteway (1965) and Bungum et al. (1971); for discussions in the context of core phase analysis, see, e.g., Doornbos and Husebye (1972), Ram Datt and Varghese (1972), King et al. (1974), Wright (1975). We use the NORSAR data from Doornbos and Vlaar (1973). UKAEA analog data records from events with $m_b > 5.5$ during a period of about 2.5 years from 1-1-1971, have been converted to a 20 Hz sampling rate digital form, in analogy to the NORSAR short period data. Similar processing techniques could thus be employed, and we have adopted those applied previously by, e.g., Doornbos and Husebye (1972) and Doornbos (1974b). Briefly, a rough estimate of the direction of approach of incident wave energy was obtained by Vespa analysis at a number of azimuths at and around the event azimuth; maximum coherent power peaks in slowness and time were then relocated in an iterative beamforming program. The procedure yields the direction of approach and arrival time of relatively coherent energy in a wave train, similar to the BEAMAN analysis described by King et al. (1975). Spectral analysis of the energy maxima was subsequently performed on the final array beams; the analysis involved the concept of so called instantaneous spectra (Dziewonski et al., 1969; Doornbos, 1974b). The procedures were applied to both precursors and PKP, thus allowing the results to be presented in a relative, rather than absolute form (e.g., spectral ratios).

Evidently, identical analysis procedures do not prevent the differences introduced by different array geometry and geological structure. Array geometry determines the array response. At a large array like NORSAR it limits wave interference, and interference tests as described by Doornbos and Vlaar (1973) may be quite useful. The response of the medium aperture UKAEA arrays is much smoother and the possibility of more interference must be admitted,

although slowness measurements with these arrays usually suffice to discriminate between scattering at the source and receiver side of the core (King et al., 1974; Wright, 1975). The effect of structure beneath the arrays should ideally be compensated for, and correction tables for slowness measurements have been used on a routine basis at NORSAR (Berteussen, 1974). Again, for the medium aperture arrays the situation is more difficult. Although consistent slowness measurements may be made for events in the same region (as we have verified by measuring PKP; YKA anomalies were consistently about 0.3 s/deg), it is also known that, in particular for medium and small arrays, the effect of local structure may change rapidly with small changes in the incident wave direction (Berteussen, 1975). Indeed, slowness anomalies at the UKAEA arrays of PKP and those of nearby *P* in the slowness plane from data of Corbishley (1970), were sometimes very different, so it is not clear whether a correction based on interpolation between calibrated points in the slowness plane is justified. Since also the geological structure itself is not known in sufficient detail, we decided to leave the slowness data from the UKAEA arrays uncorrected; such a correction was also omitted by Ram Datt and Varghese (1972) at GBA, by King et al. (1974) at WRA and by Wright (1975) at YKA.

3. Model Calculations

We will present observational along with theoretical results, since it facilitates interpreting trends in the data (e.g., with epicentral distance), and it indicates which observations should be considered anomalous. The choice of a scattering model is somewhat arbitrary. Following the formulation of Doornbos (1976; 1977), we give results for scattering by a rough CMB with average radial variations of 200 m, and by a heterogeneous 400 km thick layer at the base of the mantle, with an average relative density variation of 1%. Similar variations in the elastic properties could have been included, but the resultant amplitude-distance curves would not be much different. The results represent scattering at one side of the core only (either the source or the receiver side, which is consistent with precursor observations at arrays). Scale lengths of variation of 10 and 20 km will be considered in both cases. It has been shown by Doornbos (1977) that both of the above models produce the energy level that is observed in most of the PKP precursors, and that scale lengths of 10–20 km should be considered relevant, except at relatively long epicentral distances where larger scale lengths may become important. The 400 km layer model is akin to the 200 km layer model of Haddon and Cleary (1974).

We emphasize that the computational curves are not intended to fit all observed precursor characteristics. For example, the models are laterally uniform whereas we will present evidence of lateral variations in scattering regions. Relative to the above models, scattering from laterally limited regions will decrease the precursor energy or alternatively, the heterogeneity in this region would have to be increased to maintain the same energy level of the precursors. The array response has a similar effect since it restricts interference to a limited region in the slowness plane. The latter effect is important for NORSAR,

whose response reduces the energy level produced by a laterally uniform scattering model with roughly 3 to 6 dB at 1 Hz (Doornbos, 1977), but for the UKAEA arrays with their much wider response, the effect is unimportant. Ideally, the characteristics of groups of precursor data should be inverted to obtain scattering regions consistent with these data. This strategy has been applied to some groups of precursor data at NORSAR (Doornbos, 1976). However, for data from the UKAEA arrays, such an inversion is not warranted due to the limited resolving power of these arrays, so only the forward approach will be followed here.

4. Results and Discussion

The precursor data from the different arrays were also associated with different source regions (Fig. 1). NORSAR data are from the Solomon and Fiji Islands region, the bulk of the YKA data (around an epicentral distance of 136°) is from the S. Sandwich Islands region, most EKA data are from the New Hebrides, WRA data are from several regions in S. America, whereas GBA gave only two data from Argentina events at relatively long distances (142° – 143°). Typical records with PKP and precursors from each of these arrays are shown in Figure 2. For purposes of comparison, the NORSAR central subarray, rather than the arraybeam, has been used here (not in the remainder of this paper). UKAEA data are given in Table 1; for NORSAR data tabulation we refer to previous work (e.g., Doornbos, 1976). In the Figures to follow, the data will be distinguished according to array type, no further distinction will be made.

The information on arrival time and slowness vector is summarized in Figures 3–5. The theoretical curves in these figures do not bring out the difference between 10 and 20 km scale length, as this difference was not important in these cases. Arrival times of energy maxima in precursors and PKP were measured from the instantaneous spectral envelopes in the frequency range 0.8–1.2 Hz.

The precursor times are plotted in Figure 3, relative to PKIKP. Since measured PKP energy does not only involve PKIKP but also, e.g., PKiKP, we have assumed that, when the energy maxima did not separate (which was always the case for surface focus distances below 138°), the observed maximum is halfway between PKIKP and PKiKP, and applied a time correction accordingly. It should be realized that the CMB curve in Figure 3 lags the minimum time curve (see, e.g., Cleary and Haddon, 1972) by several seconds. Whereas the model curves in Figures 3 indicate the general trend in the data, the relatively poor fit of any of the individual curves to the data may reflect deviations from a uniform scattering model. Indeed, from previous experience with NORSAR data alone it has become clear that large scale lateral variations in scattering properties must be invoked to account for the characteristics of these data.

In plotting $dT/d\Delta$ and azimuth deviations from the great circle (Figs. 4 and 5), it was realized that for the UKAEA arrays, large biases may be introduced by wave interference and by uncorrected effects of near array structure

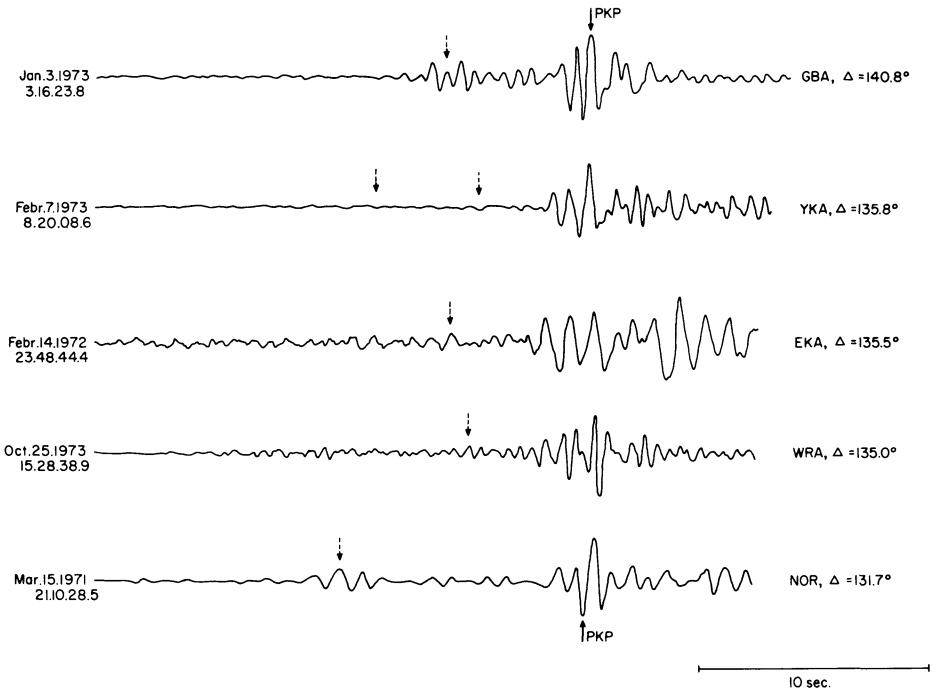


Fig. 2. PKP with precursors at UKAEA arrays (array beams) and at NORSAR (central subarray beam); filtered traces. Dashed arrows indicate precursor detections

(section 2). Some control on the reliability of ($dT/d\Delta$, azimuth) data may be exercised by applying the scattering interpretation and requiring that, within specified limits, measured arrival time, $dT/d\Delta$ and azimuth be consistent with a scattering source on or above CMB. By applying this test we had to reject some of the ($dT/d\Delta$, azimuth) solutions, and these are not reproduced in Figures 4 and 5. Figure 4 clearly shows the separation of $dT/d\Delta$ in precursors due to scattering at the source and receiver side of the core, respectively. Besides, we remark that the $dT/d\Delta$ data in Figure 4 are not necessarily at the same position relative to the model curves, as their corresponding arrival times in Figure 3. The YKA data in Figures 3–5 are generally in agreement with those of Wright (1975). The correspondence of WRA data with those of King et al. (1974) is less clear; this may be partly due to our limited number of good data for this array, which was characterized by many (partial) breaks during our observation period. Most striking in Figure 5 are the large azimuth deviations for NORSAR data groups corresponding to scattering at the receiver side of the core, whereas for the other arrays (in particular YKA) no consistently large deviations are observed.

Spectral information is summarized in Figures 6 and 7. Peak frequencies of PKP and its precursors are generally around 1 Hz (for UKAEA data slightly higher).

Table 1. Events and precursor data at UKAEA arrays

Array	Date	Source region	Depth	Dis- tance	Resid- ual time	$dT/d\Delta$	Azi- muth devia- tion	Spectral ratio peak frequency	Spectral ratio at 1 Hz
			(km)	(°)	(s)	(s/°)	(°)	(Hz)	(dB)
YKA	1972, Jan 8	South Sandwich Isl.	60	135.5	7.10			0.9	32.05
	1973, Feb 2	South Sandwich Isl.	33	136.0	8.05	3.65	4.2	1.5	24.61
					4.25	2.30	0.	1.6	24.80
					10.50	3.50	0.	1.7	27.71
	1973, Feb 7	South Sandwich Isl.	33	135.8	4.60	2.30	0.	1.7	23.13
	1973, Feb 18	South Atlantic Ridge	33	125.1	5.70			1.3	19.13
	1972, Feb 25	South Sandwich Isl.	33	140.1	8.05			1.6	16.01
	1973, Feb 25	Scotia Sea	33	136.2	9.25	3.44	-9.9	1.8	23.02
					3.95			2.1	20.77
	1972, Mar 31	South Sandwich Isl.	33	135.4	9.80	3.86	-8.1	1.1	14.75
	1973, Apr 25	South Sandwich Isl.	67	138.9	8.55	2.75	-0.1	1.1	25.14
					5.55	3.46	-6.6	1.1	14.00
	1973, Nov 25	South Sandwich Isl.	33	135.5	2.05			1.2	24.40
	1972, Dec 22	South Sandwich Isl.	33	135.4	8.50	2.90	3.6	1.5	26.68
					3.40	2.00	3.6	1.5	29.51
1972, Dec 22	South Sandwich Isl.	33	135.4	7.95	3.71	2.1	1.5	23.11	
1972, Dec 28	South Sandwich Isl.	33	135.5	8.65			1.9	30.83	
GBA	1973, Jan 3	Santiago del Estero prov. Argentina	563	140.8	5.40	3.28	0.	1.6	14.89
	1973, Nov 19	Salta prov. Argentina	40	142.6	3.60			1.5	10.76
EKA	1972, Feb 14	Santa Cruz Isl.	102	135.5	8.25			1.3	14.35
	1972, May 4	New Hebrides Isl.	45	140.9	5.75	2.66	5.5	1.4	14.46
					7.25			1.7	10.45
	1971, Sep 14	New Britain	33	127.2	3.80	0.72	-11.5	1.8	16.97
	1971, Oct 27	New Hebrides Isl.	40	139.5	7.45			1.6	9.66
	1973, Nov 30	New Hebrides Isl.	124	139.3	7.50			1.6	7.41
	1973, Dec 9	New Hebrides Isl.	39	142.9	2.65	3.31	15.4	0.7	4.78
1973, Dec 28	New Hebrides Isl.	26	138.5	8.70			1.6	11.51	
WRA	1973, Feb 1	Jujuy Prov. Argentina	229	133.1	11.80			1.0	11.18
	1972, Mar 20	Northern Peru	64	139.4	9.10			1.7	16.29
	1973, Sep 18	Northern Peru	133	139.8	4.90	2.15	-19.7	2.0	17.10
	1971, Oct 15	Peru	54	136.1	10.40				
					3.10	1.50	0.2	0.6	19.22
1973, Oct 25	Southern Bolivia	548	136.0	12.40					
				5.60	1.81	35.6	1.7	10.72	

In Figure 6, peak frequencies of the precursor/PKP spectral ratio are plotted. The PKP spectrum used is representative of PKiKP. Because source and receiver effects are largely eliminated, the spectral ratio is thought to be more representative of the scattering mechanism itself. However, two points must be made. First, for low energy precursors (e.g., YKA data around 136°) the signal to noise ratio is low in particular at the higher frequencies (say above 1.4 Hz), and spectral ratio peaks in this frequency range may become unreliable. Second, if the incident precursor energy is not well concentrated in slowness space

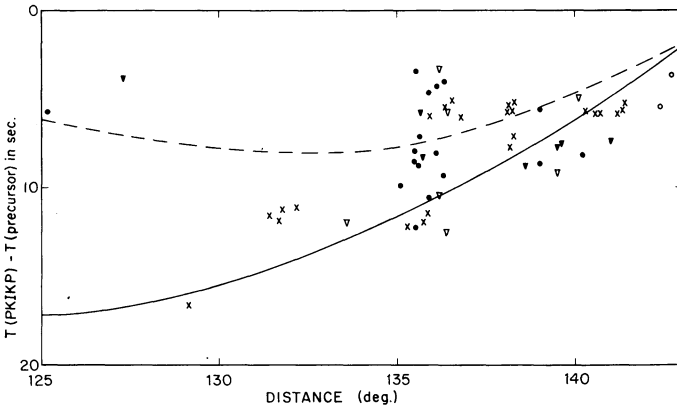


Fig. 3. Residual travel times of precursors, relative to PKIKP. Data and theoretical curves represent energy maxima. Data symbols: x (NORSAR), ● (YKA), ○ (GBA), ▼ (EKA), ▽ (WRA). Model curves: — (rough CMB), --- (density heterogeneity in 400 km thick layer at the base of the mantle)

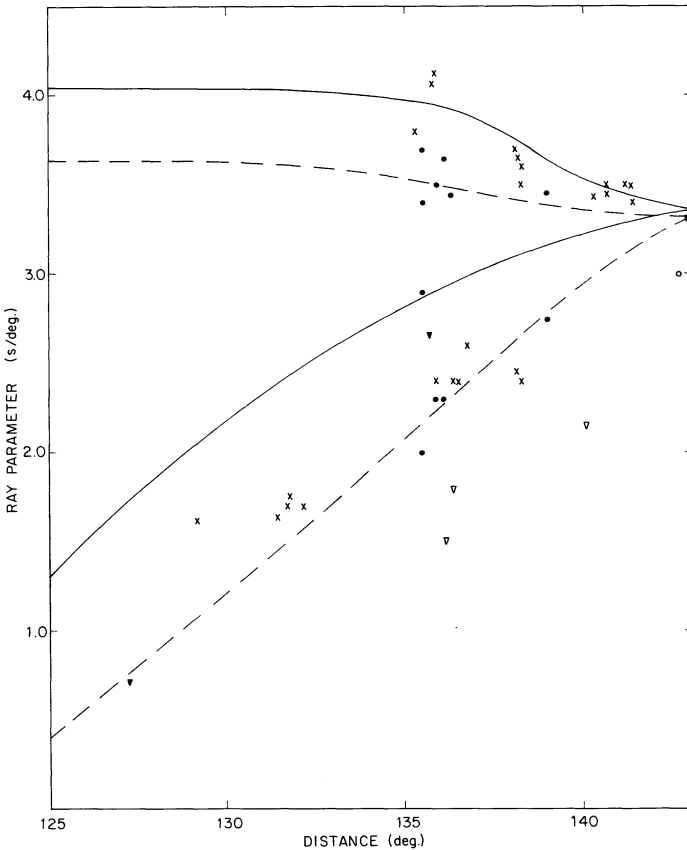


Fig. 4. Ray parameters of precursors. Data symbols and models as in Fig. 3

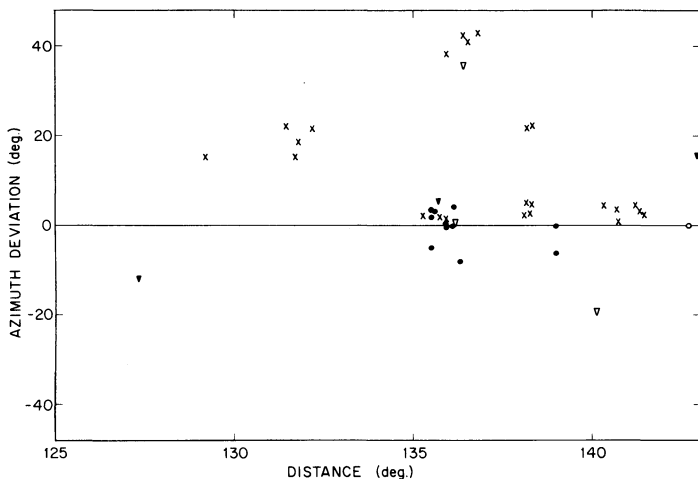


Fig. 5. Azimuth deviation from great circle of precursor direction of approach. Data symbols as in Figure 3

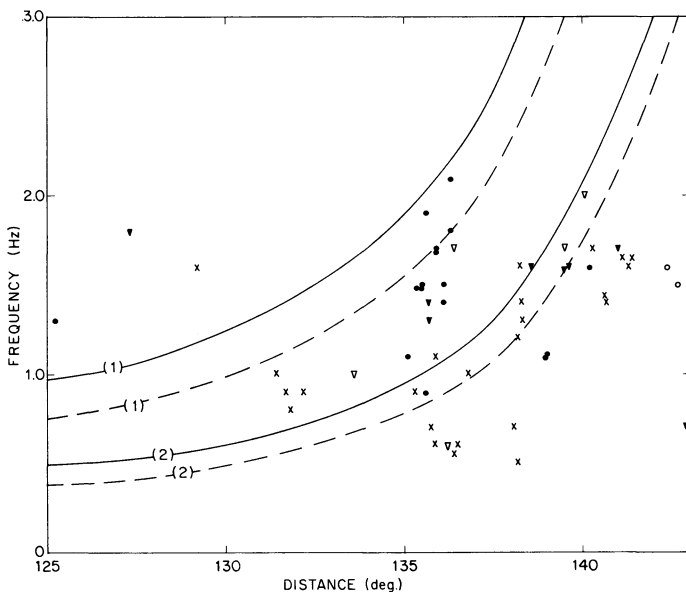


Fig. 6. Dominant frequencies of (precursor/PKiKP) spectral ratios. Data symbols and model curves as in Figure 3. (1): 10 km scale length of variation in radius CMB or in lower mantle structure (for details see text); (2): 20 km scale length

(e.g., if one of the laterally uniform scattering models were valid), the reduction of interfering precursor energy by large array beamforming increases with frequency; as a result the measured peak frequency of spectral ratio may be biased to lower frequencies. These points may explain at least part of the differences in Figure 5 between NORSTAR and YKA data around 136°.

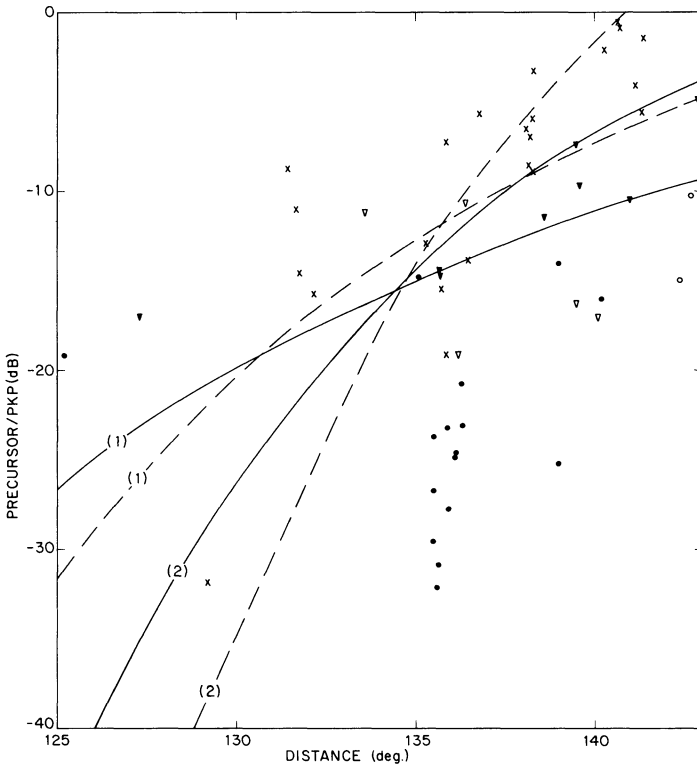


Fig. 7. Maximum precursor energy at 1 Hz, in dB relative to PKiKP. Data symbols and models as in Figures 3 and 6

Figure 7 gives spectral ratios at 1 Hz. As mentioned before, frequencies at or slightly above 1 Hz are representative of our data set. We have also computed the spectral ratios at 1.2 Hz and the results were similar to those in Figure 7. The figure clearly demonstrates the difference in energy level between the NORSAR and YKA data, which we estimate to be of the order of 10–15 dB. The energy level of the NORSAR data is higher than most of the other data and if the afore-mentioned correction for large array beamforming were applied, most NORSAR data would also fall clearly above the theoretical curves. On the other hand, the YKA data fall far below these curves. Data from the other arrays are generally in between those of NORSAR and YKA. NORSAR data have sampled lower mantle and CMB regions beneath the Fiji Islands and beneath Fennoscandia (c.f., Doornbos, 1976); YKA data (around 136°) have sampled regions beneath the S. Sandwich Islands and beneath Central North America. The observed differences may be a manifestation of large scale variations involving these regions. In this respect we also mention that UKAEA precursor wave trains appear to be more complex than many of the NORSAR data, although this difference is difficult to evaluate and may be partly due to different array geometry. Another argument would involve so called negative evidence, e.g., Ram Datt and Varghese (1972) report on an unsuccessful search

for PKP precursors from Nevada explosions recorded at GBA (at a distance of nearly 128°). More quantitative evidence of lateral variations is given by the large azimuth deviations of some groups of precursors at NORSAR whereas for YKA, no consistently large deviations have been observed.

In summary, the characteristics of the YKA data may be well explained by any of the models involving slight lower mantle heterogeneity and/or a slightly rough CMB, whereas some groups of NORSAR data require laterally limited regions of stronger heterogeneity. The implied large scale lateral variations in the amount of heterogeneity seems to be confirmed in this comparison of different array data, sampling different regions of the lower mantle and CMB. The difference in relative energy between YKA and NORSAR precursors is particularly pronounced (10–15 dB) and leads to the mapping of relatively “smooth” regions (beneath the S. Sandwich Islands and Central N. America, from YKA data), and “rough” regions (beneath the Fiji Islands and Fennoscandia, from NORSAR data).

Acknowledgements. We thank various staff members of the UKAEA center in Blacknest, and of the NORSAR array, for making their data facilities available to us.

We wish to acknowledge Drs. J.M. Vermeulen for generous help in various stages of the work especially in the data handling, and Professor N.J. Vlaar for encouragement.

References

- Berteussen, K.A.: NORSAR location calibrations and time delay corrections. NORSAR Sci. Rep. 2–73/74, 1974
- Berteussen, K.A.: Array analysis of lateral inhomogeneities in the deep mantle. Earth Planet. Sci. Lett. **28**, 212–216, 1975
- Berteussen, K.A.: The origin of slowness and azimuth anomalies at large arrays. Bull. Seism. Soc. Am. **66**, 719–741, 1976
- Birtill, J.W., Whiteway, F.E.: The application of phased arrays to the analysis of seismic body waves. Phil. Trans. Roy. Soc., London, Ser. A **258**, 421–493, 1965
- Bungum, H., Husebye, E.S., Ringdal, F.: The NORSAR array and preliminary results of data analysis. Geophys. J. Roy. Astron. Soc. **25**, 115–126, 1971
- Cleary, J.R., Haddon, R.A.W.: Seismic wave scattering near the core-mantle boundary: a new interpretation of precursors to PKIKP. Nature **240**, 549–551, 1972
- Corbishley, D.J.: Structure under seismic arrays. Geophys. J. Roy. Astron. Soc. **21**, 415–425, 1970
- Datt, R., Varghese, T.G.: Array detection and location of core shadow events. Bull. Seism. Soc. Am. **62**, 231–245, 1972
- Davies, D., Sheppard, R.M.: Lateral heterogeneity in the Earth's mantle. Nature **239**, 318–323, 1972
- Doornbos, D.J.: Seismic wave scattering near caustics: observations of PKKP precursors. Nature **247**, 352–353, 1974a
- Doornbos, D.J.: The anelasticity of the inner core. Geophys. J. Roy. Astron. Soc. **38**, 397–415, 1974b
- Doornbos, D.J.: Characteristics of lower mantle inhomogeneities from scattered waves. Geophys. J. Roy. Astron. Soc. **44**, 447–470, 1976
- Doornbos, D.J.: On seismic wave scattering by a rough core-mantle boundary. Geophys. J. Roy. Astron. Soc. **56**, 643–662, 1978
- Doornbos, D.J., Husebye, E.S.: Array analysis of PKP phases and their precursors. Phys. Earth Planet. Inter. **5**, 387–399, 1972

- Doornbos, D.J., Vlaar, N.J.: Regions of seismic wave scattering in the Earth's mantle and precursors to PKP. *Nature Phys. Sci.* **243**, 58–61, 1973
- Dziewonski, A., Bloch, S., Landisman, M.: A technique for the analysis of transient seismic signals. *Bull. Seism. Soc. Am.* **59**, 427–444, 1969
- Green, A.G.: On the postulated Hawaiian Plume with emphasis on the limitations of seismic arrays for detecting deep mantle structure. *J. Geophys. Res.* **80**, 4028–4036, 1975
- Haddon, R.A.W., Cleary, J.R.: Evidence for scattering of seismic PKP waves near the mantle-core boundary. *Phys. Earth Planet. Inter.* **8**, 211–234, 1974
- Haddon, R.A.W., Husebye, E.S., King, D.W.: Origins of precursors to P'P'. *Phys. Earth Planet. Inter.* **14**, 41–70, 1977
- Husebye, E.S., King, D.W., Haddon, R.A.W.: Precursors to PKIKP and seismic wave scattering near the mantle-core boundary. *J. Geophys. Res.* **81**, 1870–1882
- Kanasewich, E.R., Ellis, R.M., Chapman, C.H., Gutowski, P.R.: Seismic array evidence for a core boundary source for the Hawaiian linear volcanic chain. *J. Geophys. Res.* **78**, 1361–1371, 1973
- King, D.W., Haddon, R.A.W., Cleary, J.R.: Array analysis of precursors to PKIKP in the distance range 128° to 142°. *Geophys. J. Roy. Astron. Soc.* **37**, 157–173, 1974
- King, D.W., Haddon, R.A.W., Husebye, E.S.: Precursors to PP. *Phys. Earth Planet. Inter.* **10**, 103–127, 1975
- Vermeulen, J.M., Doornbos, D.J.: Mantle heterogeneity and mislocation patterns for seismic networks. *J. Geophys.* **43**, 545–559, 1977
- Wright, C.: The origin of short period precursors to PKP. *Bull. Seism. Soc. Am.* **65**, 765–786, 1975
- Wright, C., Lyons, J.A.: Seismology, $dT/d\Delta$ and deep mantle conversion. *Geophys. J. Roy. Astron. Soc.* **40**, 115–138, 1975

Received September 19, 1977 / Revised Version February 6, 1978

Digital Recording and Analysis of Broad-Band Seismic Data at the Graefenberg (GRF)-Array

H.-P. Harjes and D. Seidl

Seismologisches Zentralobservatorium Gräfenberg, Krankenhausstraße 1–3, 8520 Erlangen, Federal Republic of Germany

Abstract. An array of 19 broad-band seismometers with flat velocity response between 0.05 Hz and 5 Hz combined with a binary gain-ranging data acquisition system of 138 db dynamic range is being installed in Southern Germany. The array has a maximum extension of 80 km, it consists mainly of three triangular subarrays, the dimensions of which are chosen so as to reduce the microseisms by simple summation. The dynamic range is accomplished by digitizing the output at the seismometer sites and transmitting the digital information on telephone lines to a central control station. Single station data are available since 1975 and continuous recordings of the first subarray exist since 1976. They provide extended information of the fine structure of the seismic wave field in the medium frequency range between 0.5 Hz and 0.05 Hz and allow the quantitative investigation of frequency-dependent seismic phenomena over a wide range of amplitude and frequency. An elementary problem is the numerical analysis of broad-band seismograph systems especially seismometer-galvanometer systems and the determination of the true ground displacement or velocity. This simulation and restitution problem can be solved by digital recursive filters applying the z-form method. The simulation may include high sensitive short-period detection instruments.

Key words: GRF-array — Broad-band seismology — Digital seismogram analysis.

Introduction

A broad-band array is in the process of being installed at the Graefenberg-Observatory (GRF) in Southern Germany, which is the Central Seismological Observatory of the Federal Republic of Germany. This set-up and especially the new array concept is a joint project of the seismological institutions of our country.

The idea of establishing an array was to provide different seismic groups

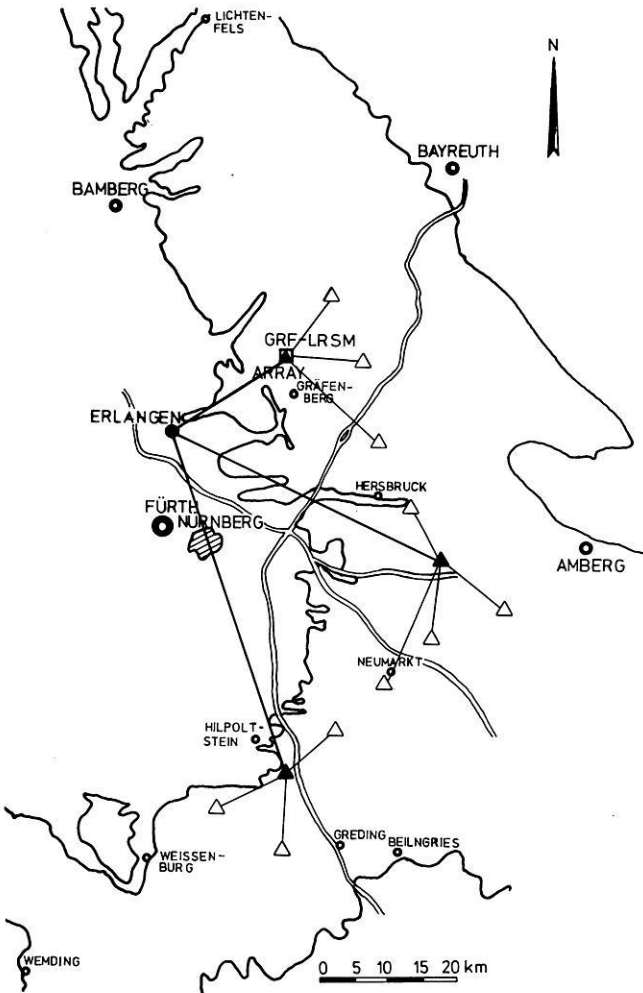


Fig. 1. Map showing the location of GRF broad-band array. \blacktriangle Three-component station and subarray center; \triangle Single-component station (vertical seismometer); \square GRF LRSM-array

with an “optimal” data set for a large variety of research programs including the study of the fine structure of the seismic wave field. Optimal in this respect implies to record the true ground motion over a large amplitude range and a wide frequency band. The best way from a technical point of view to reach this aim is to combine broad-band seismometry with the wavenumber resolving capabilities of arrays (Baker, 1970; Berckhmer, 1971). This concept differs as well from conventional detection arrays like LASA (Green et al., 1965) as from the new SRO-installations (Peterson et al., 1976) both of which only record seismic waves in usual period bands around 1 s and 20 s.

Because of the large dynamic range of earthquake signals broad-band recording represents not only a different technical approach. It also requires a careful study of signal and noise characteristics in the total seismic frequency band.

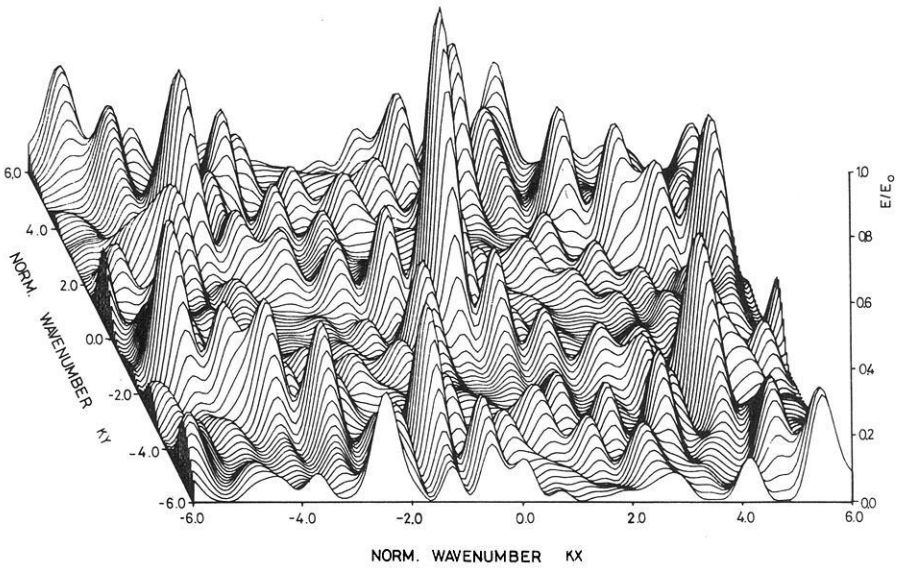
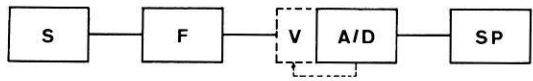


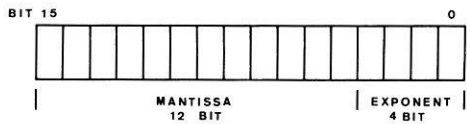
Fig. 2. Wavenumber characteristic of the GRF-array



DIGITAL DATA ACQUISITION

Fig. 3. Digital data aquisition and data format.

- S* Broad-band seismometer;
- F* Antialiasing filter;
- V* Gain-ranging amplifier;
- A/D* Analog-digital converter



PSEUDO-FLOATING POINT DATA CODE

Array Configuration

The purpose of the installation of a broad-band array is not so much to enhance signal to noise ratio rather than to set up a data base for frequency-wavenumber analysis of seismograms. In any case the success of the array concept depends on noise conditions and signal coherence. In a densely settled and highly industrialized country like Germany it is difficult to find a suitable area with homogeneous geological structure. A careful study showed that the formation of the Swabian-Frankonian Jura in Southern Germany fulfilled these conditions best.

Figure 1 shows the configuration of the GRF-array. The approximate L-shape of 80 km extension is given due to geological constraints. The array

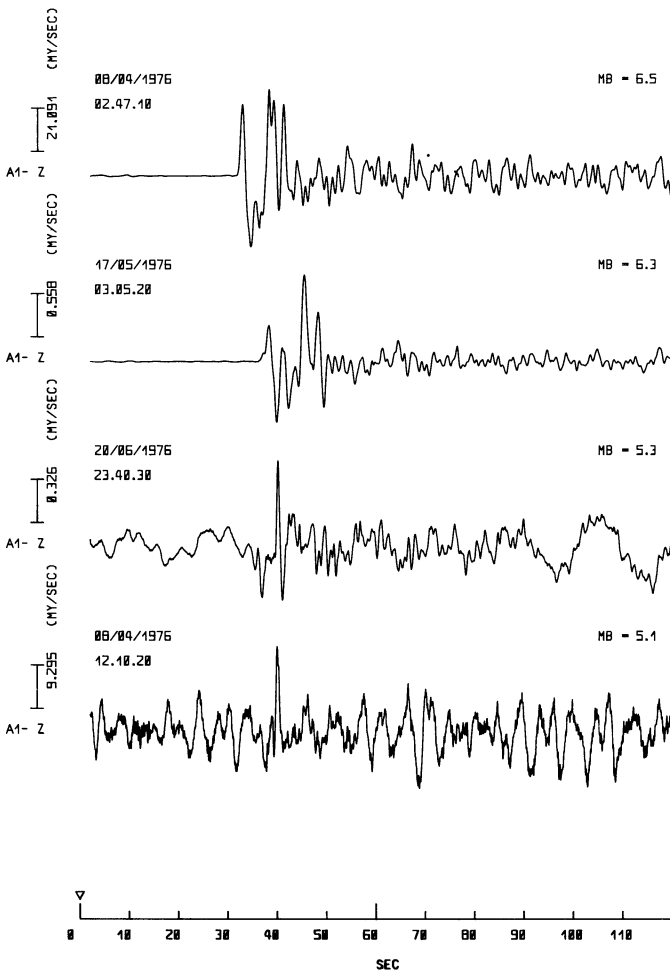


Fig. 4. Seismograms of four Uzbekistan earthquakes recorded with the GRF broad-band system

consists of 13 seismometer sites which form three triangular subarrays and some stations in between to reduce sidelobe effects in the array response. The distances between the seismometers are chosen such that the microseismic noise can be reduced by simple summation of single traces. As has been suggested (Baker, 1970) and later experimentally proven (Henger, 1975) distances of 10–12 km are suitable for broad-band recordings. Figure 2 features the array response for monochromatic signals. This is only slightly changed for broad-band inputs (Kelly, 1967). This three-dimensional wavenumber characteristic shows the rejection capability of the array as a function of wavenumber \vec{k} normalized to the array dimension (\vec{k}_{NORM}). The width of the rejection band between the main lobe at $|\vec{k}_{\text{NORM}}|=0$ and the side lobes at $|\vec{k}_{\text{NORM}}|=6$ depends on the array size. The array shown in Figure 1 is especially designed to suppress coherent seismic noise in the medium frequency range (0.05 to 0.5 Hz) propaga-

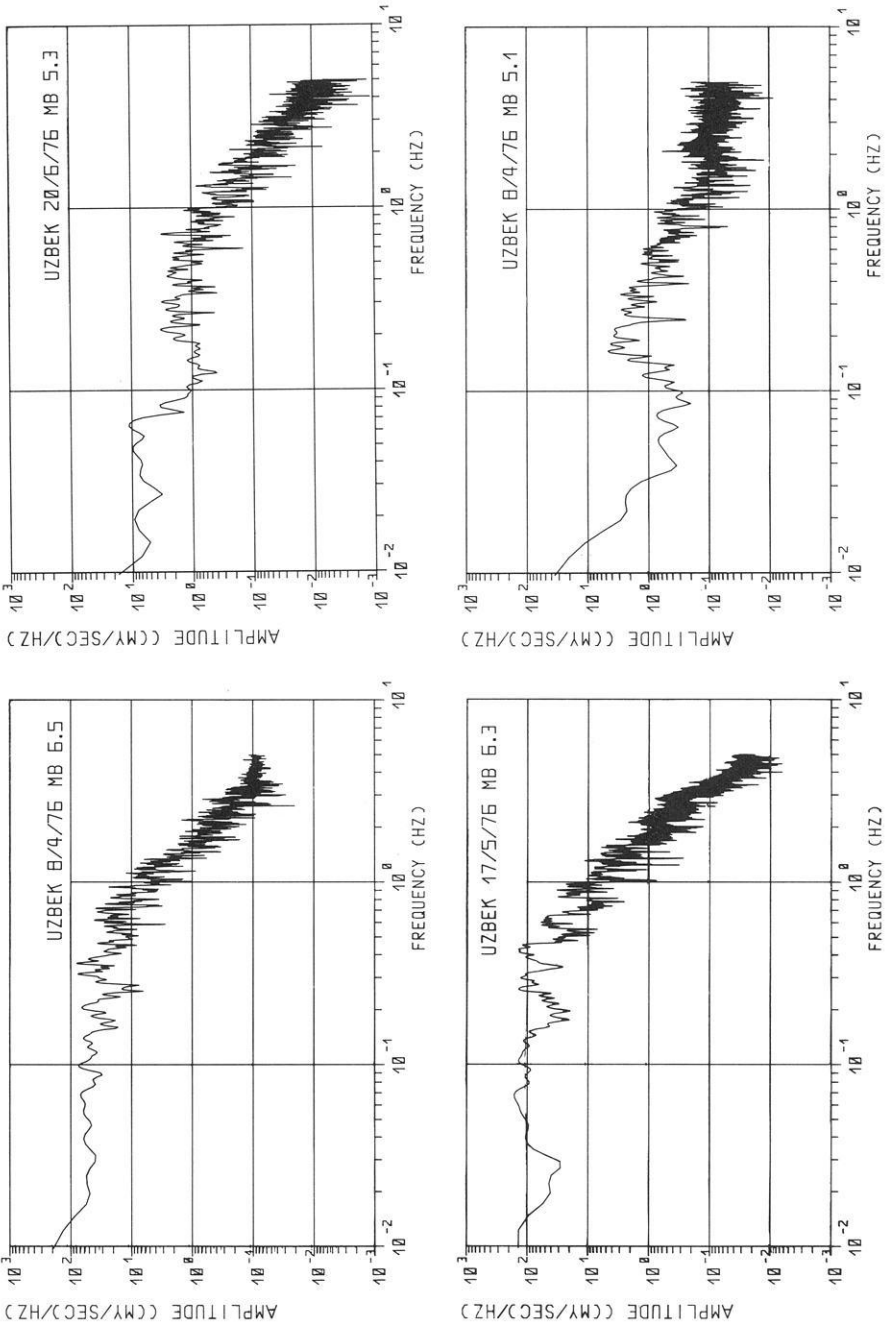


Fig. 5. P-wave spectra of the Uzbekistan earthquakes in Figure 4

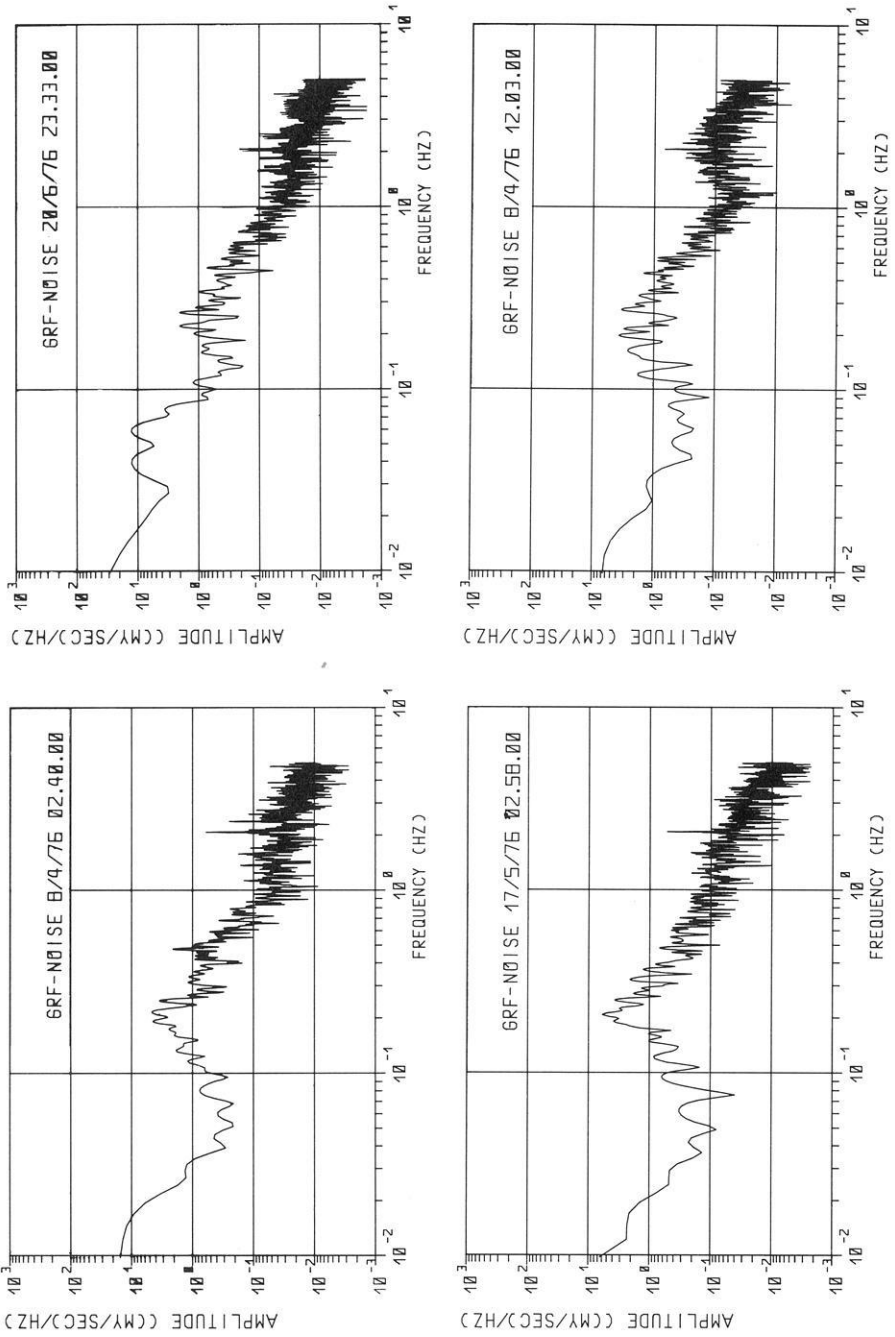


Fig. 6. Spectra of noise preceding the signals in Figure 4

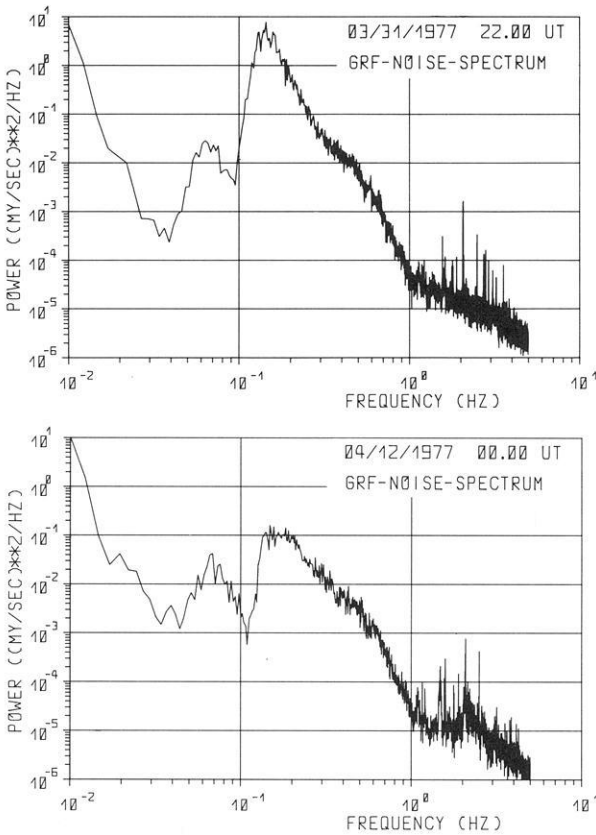


Fig. 7. Noise powerspectra showing the temporal amplitude variations of microseism at GRF

ting at surface wave velocities. The seismometer output is digitized at the site with 20 samples per second. The digital information is transmitted on telephone cables in asynchronous mode to a subarray centre which is a three-component station. The three subarrays are connected with the data centre in Erlangen by 2400 baud synchronous lines. Technical details of the data acquisition and transmission are already published (Harjes et al., 1973), the basic principle is summarized in Figure 3 (upper half). The seismometer output passes an anti-aliasing filter (3db-point at 5 Hz, 42 db/octave slope) and is converted into digital form by a computerized binary gain-ranging system. In the data centre all data are stored on magnetic tapes for about one year to extract event tapes for various scientific purposes. The lower half of Figure 3 shows the data format which is a pseudo-floating point code very similar to the SRO data format (Seismic Research Observatories installed by USGS).

Test data from the first three-component broad-band station at GRF are available since 1974, the northern triangular subarray in Figure 1 is in continuous operation since April 1976 whereas the two other subarrays will be installed in 1978. The seismograms of the following chapters are examples of this data base.

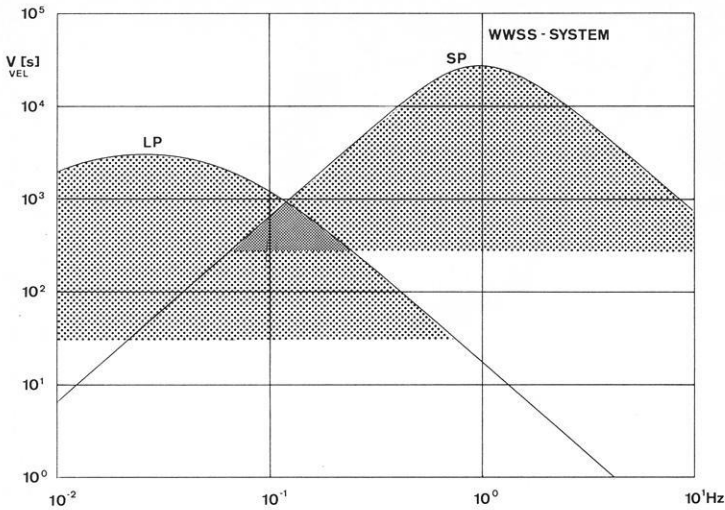


Fig. 8. Velocity response characteristic and dynamic range of short period (maximum magnification 200 k) and long period (maximum magnification 1 k) World-Wide Standard Seismographs

Seismological Implications on Broad-Band Systems

The amplitude range and frequency content of seismic signals and background noise gives very clear constrains to the instrumental realization of broad-band seismographs. Some examples of the GRF recordings will illustrate the importance of the medium frequency range between conventional long-period and short-period instrumental responses. In Figure 4 there is plotted the body wave arrival of four shallow Uzbekistan earthquakes of different magnitudes (PDE-values).

The amplitude spectra of these events are given in Figure 5 which show besides the well known trend a large variability of the maximum compressional energy and a pronounced fine structure between 0.1 Hz and 1 Hz. The quantitative interpretation of the *P*-wave spectrum is the more difficult the weaker the event is because of the influence of the microseismic noise. This is demonstrated by comparison of the noise spectra in Figure 6 computed from a noise sample just before the *P*-onset. The noise problem becomes even more important if we look at the large variability of the microseismic peak (Fig. 7) which differs by 40 db in the two examples. These broad-band noise spectra were computed by the periodogram method using 10 nonoverlapping segments each of 400 seconds length (90% confidence limit is 7 db).

Thus, two factors define the seismological data acquisition system: the dynamic range which gives the saturating point of the system, and the resolution which should be constant over a wide frequency range. Only a digital technique allows recording the total frequency and magnitude range without saturation. A binary gain-ranging concept is then adequate to get constant resolution. High resolution is needed to separate signal and noise components for spectral

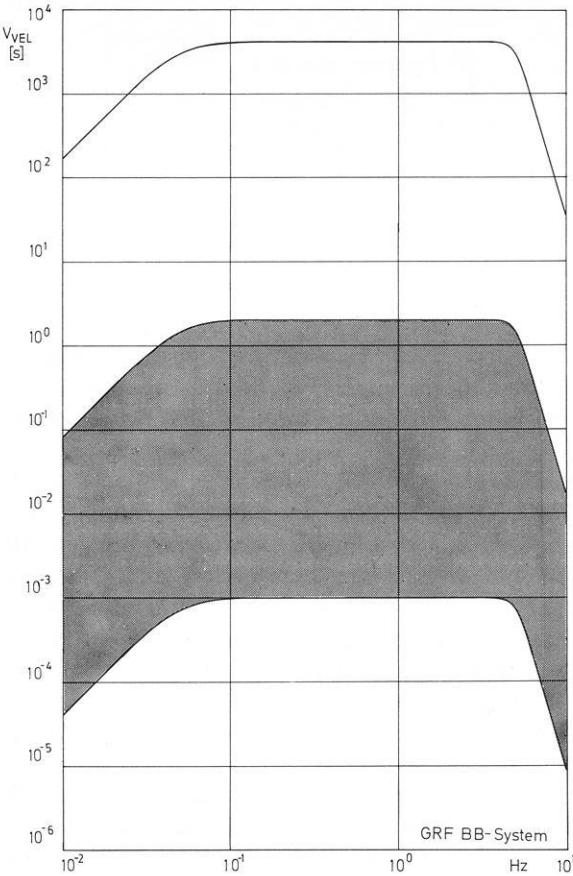


Fig. 9. Velocity response characteristic, dynamic range and resolution (shaded area) of the GRF broad-band system

analysis. In the medium frequency range where signal and noise strongly overlap the separation can only be accomplished by the use of broad-band array data.

To compare the GRF-type digital data acquisition with conventional analog seismographs the velocity response curves of the WWSSN-system are plotted in Figure 8. The corresponding maximum magnifications are 1 k for the long-period and 200 k for the short-period system. The shaded area indicates the dynamic range for direct recording. The low resolution for both systems in the medium frequency range strongly limits the numerical inversion of instrumental filtering effects. In comparison Figure 9 shows the velocity response, dynamic range and resolution for the GRF wide-band system.

During the test phase of the array a Sprengnether S-5100 seismometer was used, in the final version a new leaf-spring seismometer (Wielandt, 1975) will be installed which is of smaller size and higher stability. The seismometer acts as a high-pass filter with corner frequency at 0.05 Hz and 12 db/octave slope for the velocity response, the high frequency limitation of the transfer function is given by the antialiasing filter with a 3 db point at 5 Hz and a 42 db/octave slope.

Table 1. Comparison of GRF and WWSSN-recording systems

Resolution (1 s)		Dynamic range (20 s)	
GRF-BB	WWSSN-SP (200 K)	GRF-BB	WWSSN-LP (1 K)
1 Bit \cong 1,2 nm/s Least significant bit	$\frac{1}{4}$ mm \cong 9 nm/s	22 Bit \cong 8,8 mm/s Most significant bit	15 cm \cong 0.050 mm/s

In Figure 9 the lowest and uppermost curves limit the dynamic range of 138 db while the shaded area shows the resolution of 66 db. Because of the floating-point amplification this resolution remains constant over the whole recording range.

Table 1 compares in a different way the GRF digital system where the magnification of the recording is arbitrary with a conventional analog system with photographic registration. Assuming that in the short-period range the smallest visible amplitude is 0.25 mm and for the long-period film recording the largest amplitude is 15 cm the superiority of one single digital broad-band instrument in both frequency bands can be deduced from Table 1. In the short-period range an amplitude of 0.25 mm is equivalent to a ground velocity of about 9 nm/s. In comparison the least significant bit of the digital broad-band system represents about 1 nm/s which means a higher sensitivity by a factor of 9 than the short-period WWSSN.

Similarly for the long-period band an amplitude of 15 cm gives a saturating point at 0.05 mm/s, which demonstrates the well-known clipping problem of the long-period WWSSN. The digital broad-band system reaches its saturation point at about 1 cm/s (at 20 s).

With digital data acquisition the dynamic range of the recording system is arbitrarily high, hence the transfer function of the seismometer should be as broad as reasonable to record the true ground motion. A special instrumental characteristic which optimizes the signal/noise ratio in small frequency bands is not necessary. Thereby the restitution problem is practically avoided, and arbitrary transfer functions may be simulated by simple digital filters.

Numerical Analysis of Digital Seismic Recordings

A broad-band seismogram is an overall picture of the seismic wave field. The high dynamic range allows to focus upon special features by digital filters. These filters can simulate arbitrary seismographs or reconstitute the true ground motion. Figure 10 shows the mathematical formulation of the simulation for arbitrary seismometer-galvanometer combinations applying the z-form method (Kaiser, 1963). The continuous system with the transfer function $G(s)$ transforms the broad-band seismogram $x(t)$ into the simulated seismogram $u(t)$. A discrete description of this continuous transfer function is obtained by the use of the

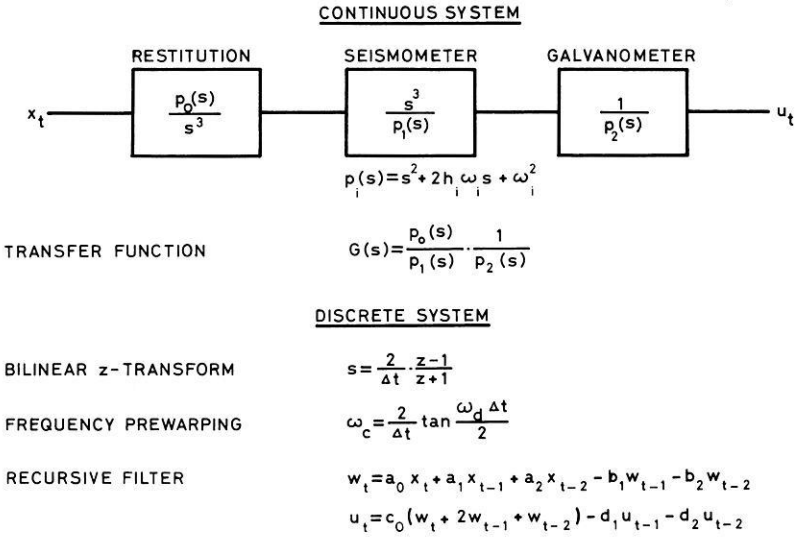


Fig. 10. Block diagram showing the digital simulation of a seismometer-galvanometer system with a double-recursive filter applying the z-form method

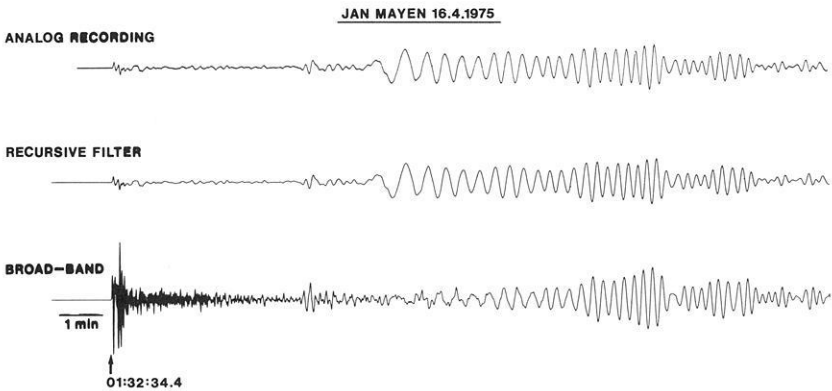


Fig. 11. Analog seismogram recorded by a long-period seismometer-galvanometer system ($T_s=20$ s, $T_g=100$ s, $h_s=h_g=1.0$) and corresponding seismogram filtered from the digital broad-band data (lowermost line) for a Jan-Mayen earthquake on April 16, 1975 (Origin Time 01:27:18.7, latitude 71.5° N, longitude 10.4° W, $m_b=6.1$)

bilinear z-transform which is ideally adapted to digital systems. The inverse transformation into the time domain yields a cascade recursive filter. The filter coefficients depend on the instrumental parameters (free period, damping) of the broad-band seismograph and the simulated seismometer-galvanometer system. A detailed description of the simulation and restitution problem for broad-band seismograms will be published in a subsequent paper.

The accuracy of the filter method is demonstrated in Figure 11. The seismogram on the bottom of this picture shows the digital broad-band recording whilst the uppermost seismogram is an analog record of a long-period seismome-

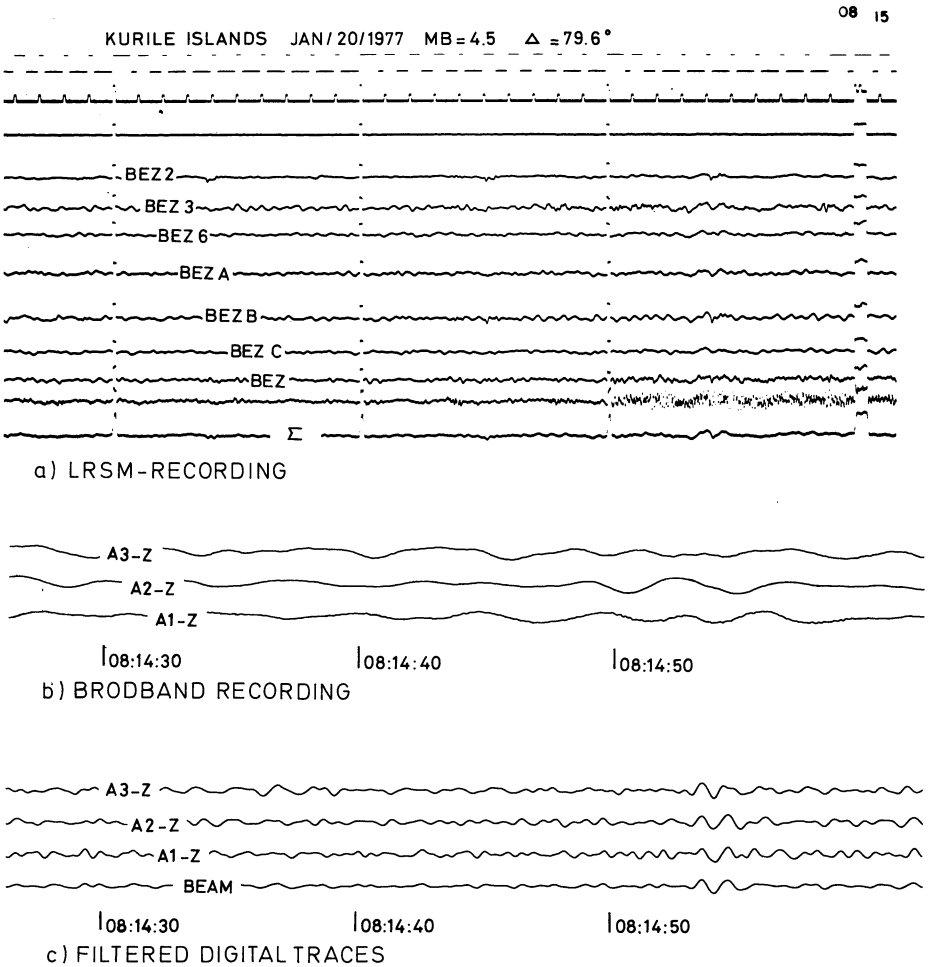


Fig. 12. a LRSM-recording at GRF of a weak teleseismic event; b Digital broad-band recording; c Digital filtered traces and beam

ter-galvanometer system ($T_s = 20\text{s}$, $T_g = 100\text{s}$, $h_s = h_g = 1.0$). This is found to compare precisely with the digitally simulated seismogram in between both recordings.

Filtering digital broad-band seismograms can also help to avoid one particular disadvantage of conventional analog wide-band recordings, namely its poor detection capability. Figure 12a shows a small Kuril-earthquake ($m_b = 4.5$) recorded with the LRSM-array at GRF. The event is near the detection level of this very sensitive instrument (maximum magnification 200 k for 0.3s, seismometer distance about 2 km). Because of the visual coherency of the P -onsets and a signal/noise ratio improvement in the summed trace (Σ) the event is clearly discernible. On the contrary it is hidden in the broad-band recording for the same time interval (Fig. 12b). One can use the filter technique of figure 10 to simulate the LRSM-characteristic. Figure 12c shows the result of an approxi-

mate simulation by simple band-pass filtering. The weak event is easily detected even if it is about 40 db below the noise level. There is a higher signal/noise ratio in the beam of the three instruments (lowermost seismogram) of the northern subarray (see Fig. 1) than in the summed trace of 8 analog short-period seismometers.

This example shows that broad-band instruments with floating-point amplification at least arrive at the same detection level as short-period conventional sensors. Of course the purpose of a broad-band array is to avoid the signal distortion of simple frequency filters by separating the signals with wavenumber filtering techniques. Nevertheless this new data acquisition system has demonstrated a possibility to escape the trade-off between low detection level and wide-band recording.

Conclusion

Digital broad-band data acquisition is the appropriate concept to record a wide spectral and amplitude range of teleseismic signals. The digital data base can be used to simulate arbitrary seismographs and to investigate the frequency dependence of earthquake mechanisms and path effects.

Some basic seismological parameters, like magnitude, will also get a clearer meaning by the evaluation of broad-band recordings.

Acknowledgements. The authors are indebted to their colleagues in the "GRF-Working Group", especially H. Berckhemer, for many valuable discussions. We would also like to thank W. Hanka, M. Henger, and B. Stork for preparing several figures. The GRF-array project is supported by the Deutsche Forschungsgemeinschaft (German Research Council) and the Bundesanstalt für Geowissenschaften und Rohstoffe (Federal Institute for Geosciences and Natural Resources).

References

- Baker, R.G.: Suggested use of a medium-period seismograph array. *Bull. Seism. Soc. Am.* **60**, 1735–1737 (1970)
- Berckhemer, H.: The concept of wide-band seismometry. *Observ. Royal Belgique, Serie Geophys.* No. **101**, 214–220 (1971)
- Green, P.E., Frosch, R.A., Romney, C.F.: Principles of an experimental large aperture seismic array (LASA). *Proc. IEEE* **53**, 1821–1833 (1965)
- Harjes, H.-P., Henger, M.: Array-Seismologie. *Z. Geophys.* **39**, 865–905 (1973)
- Henger, M.: Wavenumber filtering of microseism with triangular arrays. *NATO Advanced Study Institute Series, E: Applied Sciences* No. **11**, 205–210 (1975)
- Kaiser, J.F.: Design methods for sampled data filters. *Proc. 1st Annu. Allerton Conf. Circuit System Theory*, 221–236 (1963)
- Kelly, E.J.: Response of seismic arrays to wide-band signals. *Linc. Lab. Techn. Note* 1967-30 (1967)
- Peterson, J., Butler, H.M., Holcomb, L.G., Hutt, G.R.: The Seismic Research Observatory *Bull. Seism. Soc. Am.* **66**, 2049–2068 (1976)
- Wielandt, E.: Astatic vertical pendulum supported by a leaf spring. *J. Geophys.* **41**, 545–546 (1975)

Rockmagnetic Studies of Upper Jurassic Limestones From Southern Germany*

F. Heller

Eidgenössische Technische Hochschule Zürich, Institut für Geophysik,
ETH Hönggerberg, CH-8093 Zürich, Schweiz

Abstract. Acquisition of isothermal remanent magnetization (IRM) and the behaviour of IRM during high and low temperature treatment indicate that magnetite, goethite and minor quantities of hematite determine the magnetic properties of the Upper Jurassic limestones in Southern Germany. The direction of natural remanent magnetization (NRM) of magnetite is of detrital, syndimentary origin, whereas the goethite, although its NRM is extremely stable against AF cleaning, has been magnetized only partly during the Jurassic. Part of the goethite NRM is interpreted to be of Tertiary (pre-Upper Miocene) age being formed during a period of Karstification in the Lower Tertiary. The apparent polarity sequence described earlier (Heller, 1977) is not of Jurassic age.

Key words: Rockmagnetism – Palaeomagnetism – Limestones.

1. Introduction

Recently the palaeomagnetic record preserved through a 160 m thick Late Jurassic limestone sequence from Southern Germany (Franconia, Swabia: Lat. N: 49°, Long. E: 11°) has been described (Heller, 1977). The well bedded, shallow water marine sediments do not show signs of major sedimentation breaks or essential later folding and seemed therefore to be suitable for the development of a reversal stratigraphy during the Oxfordian to Lower Kimmeridgian (Malm α - δ), the time when the limestones were deposited.

Only normal polarities have been observed in the older part of the section (Oxfordian) and the older portion of the Lower Kimmeridgian (Malm α - γ). Thus a period of normal polarity of the geomagnetic palaeofield could be established which lasted at least about 6 my. The younger part of Lower Kimmeridgian limestones (Malm δ) contained many reversely magnetized

* Contribution No. 202, Institut für Geophysik, ETH Zürich

samples and yielded a polarity stratigraphy which tentatively has been correlated with the Mesozoic oceanic magnetic anomalies M25–M24 (Larson and Hilde, 1975).

During the previous work the interpretation of the stable remanence, and therefore the palaeomagnetic significance of the data, remained ambiguous to a certain extent. The purpose of this paper is to establish the significance of the palaeomagnetic record by rockmagnetic studies as well as optical, electron microprobe and X-ray analysis of the ferromagnetic minerals contained in the limestones. Five characteristics of the magnetic stratigraphy need to be discussed in the light of an improved knowledge of the rockmagnetic properties of the limestones.

1. The palaeopole position of the normal polarity sequence differs from that of the mixed polarity sequence, the latter being very close to European Tertiary palaeopole positions. The statistically significant difference was previously interpreted as possibly resulting from apparent polar wandering, but it could not be ruled out that the type and time of acquisition of the stable remanence were different in the upper and lower part of the section. The magnetization in the higher portion perhaps originated more recently than the time of deposition of the sediments.

2. Occasionally within the mixed polarity sequence normally magnetized as well as reversely magnetized individual specimens have been found in the same sample. What kind of magnetization process caused this curious directional behaviour of the remanence?

3. Two closely neighbouring sections (Heller, 1977, Fig. 6), situated in the mixed polarity zone and exposing exactly the same stratigraphic limestone sequence, do not yield exactly corresponding reversal patterns. There are several limestone beds in the two sections in which different remanence polarity has been observed at nearly the same stratigraphic level within one bed. This, of course, could be ascribed to a high reversal frequency of the palaeofield, but the complexity of the reversal pattern which is generated when plotting a combined polarity profile, casts doubt on whether the stable remanence actually was acquired at the same time in both sections.

4. The initial natural remanent magnetization (NRM) intensities are very weak. They average around 2×10^{-7} Gauss and depend on the stratigraphic position or, what turns out to be equivalent, on the limestone facies. At the bottom of the section which is shown in Figure 1, marls and marl-rich limestones (Malm $\alpha(+\beta)$) are predominant. They have the highest initial NRM intensities of the order of 1×10^{-6} Gauss. Proceeding into higher parts of the profile the limestone facies changes to very pure micritic limestones (Malm $\beta-\gamma$). At the same time the NRM intensity decreases gradually to a value of about 6×10^{-8} Gauss. The youngest portion of the section showing mixed polarities of NRM directions is built up by a sponge facies known as bafflestones (Wilson, 1975). These limestones (Malm δ) have a slightly increased NRM mean intensity of about 2×10^{-7} Gauss. The correlation between facies and NRM intensity is certainly related to varying intrinsic rockmagnetic properties of the limestones, as the formation of the ferromagnetic minerals depends on the syn- or postdepositional environment of these sediments.

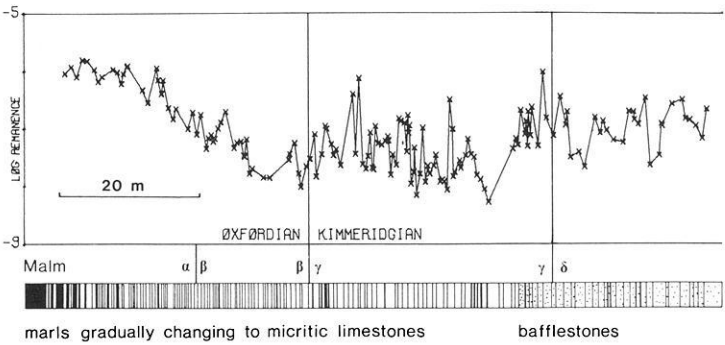


Fig. 1. Correlation of NRM intensity and limestone facies. Thick and thin marl beds are indicated by black shading; marl-rich and pure micritic limestones are the white layers; bafflestone layers are dotted. Bottom of the section to the left. Remanence intensities given in Gauss

5. Within the mixed polarity sequence zones of marl deposition are found especially in Swabia. These marl beds are always normally magnetized, whereas the under- and overlying bafflestones carry mixed polarities of stable remanence. In order to elucidate the problems and questions raised above, the following experiments and investigations have been carried out.

2. Rockmagnetism

2.1. Magnetic Identification of Ferromagnetic Minerals

The limestones contain only very small amounts of ferromagnetic minerals, their weight percentage ranging up to about 0.05%. Dissolution of the limestone matrix by means of diluted formic acid and subsequent heavy liquid separation unfortunately did not yield enough material for thermomagnetic analysis. Therefore all the rockmagnetic studies had to concentrate on the characteristics of remanent magnetization, measured in standard one-inch solid rock specimens. Besides AF demagnetization of natural remanence, acquisition curves of isothermal remanent magnetization (IRM) have been measured at a constant temperature of 0° C in fields up to 50 kOe using a superconducting magnet. Furthermore, the temperature dependence of IRM measured in zero field has been observed by using a modified Digico spinner magnetometer (Heiniger and Heller, 1976). This magnetometer enables continuous measurement of the remanence vector between liquid nitrogen temperature and 700° C. Some additional temperature dependent measurements have been made on IRM acquired at liquid nitrogen temperature. Typical results obtained from the different limestone facies types will be described in the following sections.

Marl-Rich Limestones. Figure 2 presents rockmagnetic data of a marl-rich limestone sample. During AF demagnetization of NRM (Fig. 2a) in fields up to

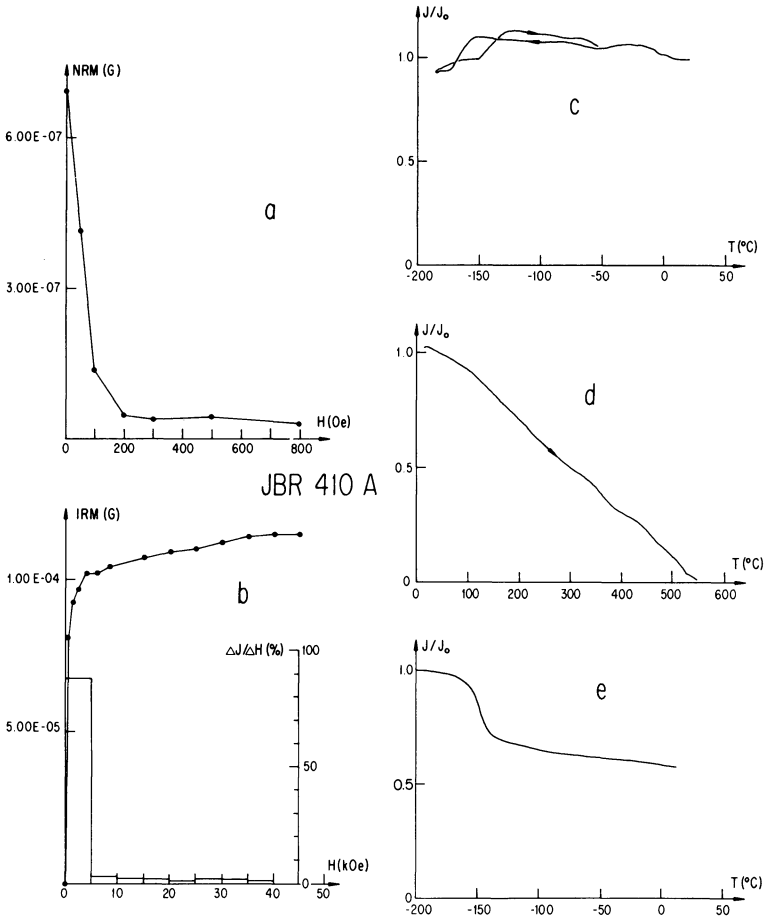


Fig. 2a-e. NRM and IRM characteristics of a marl-rich limestone sample (JBR 410 A) containing magnetite. **a** AF-demagnetization of NRM intensity. **b** IRM acquisition at $T=0^\circ\text{C}$ and resulting coercivity spectrum. **c** Cyclical behaviour of room temperature IRM during low temperature treatment. **d** Continuous thermal demagnetization of IRM during heating. **e** Behaviour of low temperature IRM (given at $T=-196^\circ\text{C}$) on re-warming to room temperature

800 Oe a large soft component is removed by a peak field of 200 Oe. Above this field amplitude a small, but stable component remains. Only minor directional changes of NRM are observed during AF cleaning.

IRM acquired in fields up to 45 kOe (Fig. 2b) increases rapidly up to 4 kOe. Above 4 kOe the curve has a very low gradient and seems to saturate at the highest field amplitudes available. According to Dunlop (1972) this type of curve represents magnetite as the main carrier of IRM with a small additional contribution to the IRM by a high coercivity mineral which usually is suggested to be hematite. As we will see later, it is probable that the high coercivity part of IRM is carried by goethite.

During cooling (Fig. 2c) the IRM intensity increases very slightly until -150°C where about 15% of the magnetization are lost upon further cooling. On re-warming to room temperature the original magnetization is fully recovered showing a sharp increase in intensity which starts around -150°C . The observed thermal hysteresis is caused by the large sample size (volume: 11.4 cm^3). The observed low temperature transition can be attributed to the K_1 zero-transition of almost pure magnetite and agrees with the interpretation of the IRM acquisition curve in which most of the magnetization is acquired below 4 kOe due to the presence of magnetite. The reversibility of the cooling and re-warming cycle as well as the high percentage of magnetization which is not affected by the low temperature treatment may indicate that the magnetite grain size is very small and the IRM is essentially carried by single and pseudosingle domain grains of magnetite (Merrill, 1970).

The same conclusions can be drawn from Figure 2e where the IRM-acquired at liquid nitrogen temperature—of another marl-rich limestone has been plotted as a function of temperature on re-warming to room temperature. Again part of the magnetite magnetization is lost during the K_1 transition at around -150°C . Upon further warming the intensity of magnetization decreases slightly. As the experiment was done in zero field and as the room temperature IRM does not change during cooling (Fig. 2c), the decrease can be attributed mainly to a change from the ferrimagnetic to the superparamagnetic state of a small percentage of magnetite particles contained in the sample. Therefore this experiment confirms that the grain size distribution covers mainly single domain grains, the magnetization of which is not affected by the low temperature treatment, pseudosingle domain grains, which reversibly show the transition effect, and even superparamagnetic grains at room temperature. Subsequent heating of IRM to high temperatures (Fig. 2d) yields an uppermost blocking temperature $T_{b\max} \cong 550^{\circ}\text{C}$ which again can be interpreted as being due to almost pure magnetite. The low and high temperature curves of IRM do not allow the positive identification of the high coercivity magnetic mineral.

Micritic Limestones. Typical data for a micritic pure limestone sample are given in Figure 3. NRM is almost stable against alternating demagnetizing fields up to 800 Oe (Fig. 3a), but the demagnetization curve is zigzagged between 50 Oe and 300 Oe. These intensity fluctuations which are not accompanied by directional variations of the remanence vector, arise from a strong temperature dependence of magnetization (cf. Fig. 3c and d) rather than from spurious magnetization processes during cleaning. Therefore during the various steps of IRM acquisition all the samples were kept at constant temperature $T=0^{\circ}\text{C}$ (ice water) to avoid irregularly shaped magnetization curves.

As demonstrated in Figure 3b, the sample acquires only a very small IRM component in DC fields below 10 kOe which possibly may reside in a negligible amount of magnetite present in the sample. Most of the magnetization is acquired at fields higher than 15 kOe and saturation is not reached even at $H=45\text{ kOe}$. The coercivity spectrum of IRM therefore is dominated by high field components.

The low temperature curve of IRM (Fig. 3c) shows a very peculiar intensity

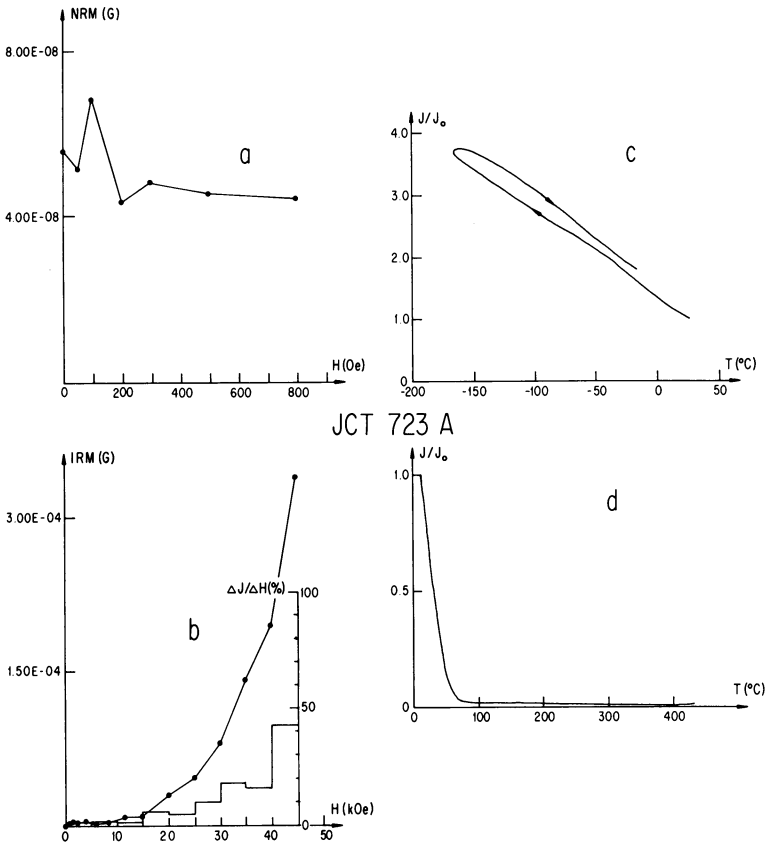


Fig. 3a-d. NRM and IRM characteristics of a micritic, pure limestone sample (JCT 723 A) containing goethite. For the significance of Figure 3a-d see Figure 2a-d

increase during cooling which is reversible on re-warming to room temperature except that again thermal hysteresis is observed. As IRM is acquired at $T=0^{\circ}\text{C}$ and measured in zero field during low temperature treatment, the drastic intensity change (amounting to about 3% per $^{\circ}\text{C}$) must be due to a strong temperature dependence of spontaneous magnetization. Subsequent heating of IRM (Fig. 3d) shows a maximum blocking temperature $T_{b\text{max}} \cong 70^{\circ}\text{C}$. Above this temperature essentially no remanent magnetization is left.

The high stability during AF cleaning, the extremely high coercivity spectrum of IRM and the low maximum blocking temperature suggest that goethite, the α -form of iron oxyhydroxide (FeO OH) is the most important ferromagnetic mineral in the micritic limestones. It should be mentioned that a few micritic limestones have been found which possess maximum blocking temperatures as high as $T_{b\text{max}} \cong 610^{\circ}\text{C}$. They may correspond to the presence of hematite which formed by oxydation from a pre-existing goethite.

Limestones With Reduced Clay-Content. The facies change from marls and marl-rich limestones to pure micritic limestones, which causes a reduction in NRM intensity (Fig. 1), occurs rather gradually. Figure 4 shows the characteristics of the rockmagnetic parameters investigated in a sample originating from this zone of facies transition. As in the previous example of a marl-rich limestone a high percentage of NRM is removed without directional change by AF cleaning up to 300 Oe (Fig. 4a). The remaining component is stable even in a peak field of 3000 Oe. Again intensity fluctuations are observed during the cleaning procedure which are due to the temperature sensitivity of goethite present in the sample. The IRM acquisition curve (Fig. 4b) reveals a significant amount

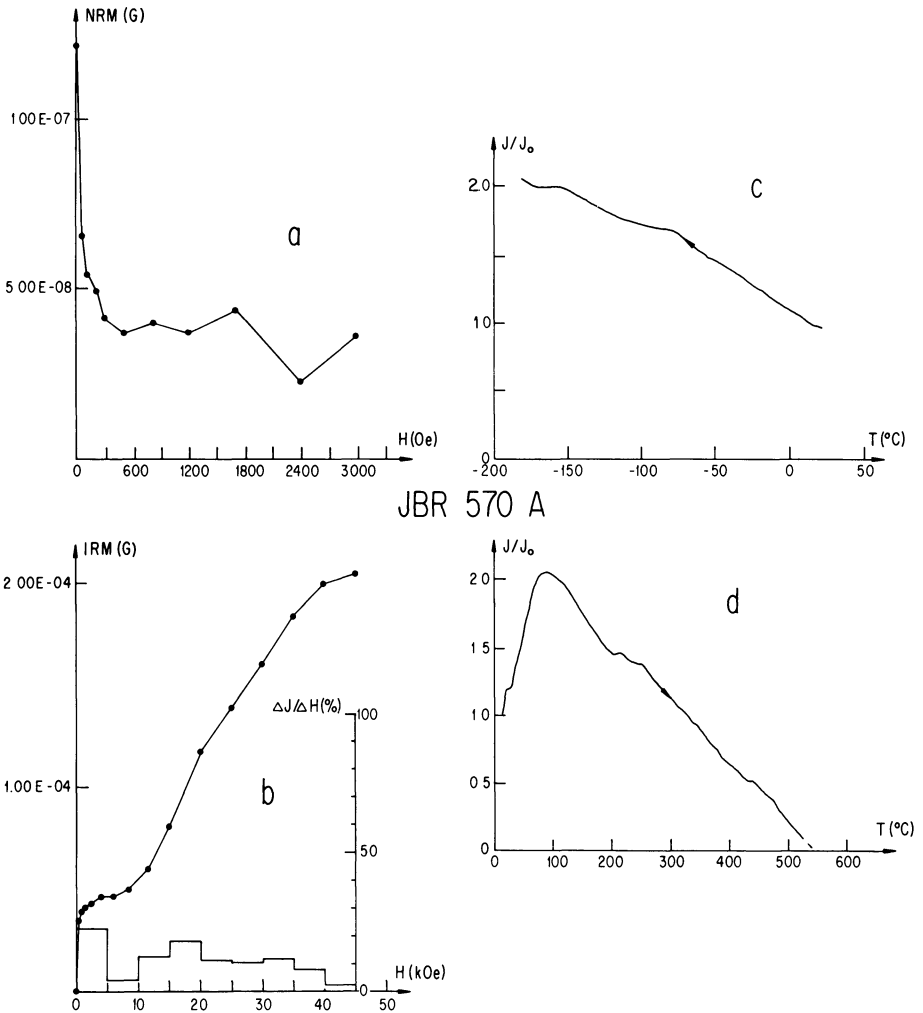


Fig. 4a-d. NRM and IRM characteristics of a limestone sample (JBR 570A) containing both magnetite and goethite. For the significance of Figure 4a-d see Figure 2a-d

of magnetite, indicated by the sharp initial increase and subsequent saturation of magnetization up to 4 kOe. Again between 10 kOe and 15 kOe IRM starts to increase. Saturation is not observed, although the curve gradient flattens off at the highest fields available. Corresponding to these observations the coercivity spectrum of IRM has two peaks, one being situated between 0 kOe and 5 kOe and the other sitting on top of a widely distributed spectrum at 15 kOe to 30 kOe. This broad spectrum probably indicates a large range of grain sizes of goethite and may arise from different degree of crystallization of this mineral.

The presence of goethite is recognized in the increase of IRM intensity during cooling in zero field (Fig. 4c), whereas the magnetite low temperature transition is only vaguely indicated by a flexure in the IRM(T) curve just below -150°C . Before heating (Fig. 4d) the sample was first given an IRM in a field of 45 kOe, and then given an IRM in a 10 kOe field in the antiparallel direction. Thus the maximum blocking temperatures of goethite and magnetite could easily be separated (Fig. 4d). Magnetite has a $T_{b\max} \cong 550^{\circ}\text{C}$ which is very near to that of pure magnetite and the maximum blocking temperature of goethite can be determined to be $T_{b\max} \cong 90^{\circ}\text{C}$.

Bafflestones. The third main type of limestone facies are the bafflestones. Their rockmagnetic parameters are very similar to those of the micritic limestones. The ferromagnetic mineralogy is dominated by goethite, occasionally hematite and minor amounts of magnetite. The NRM intensity (and direction) often does not change during AF cleaning as shown by the sample of Figure 5a. In the course of IRM acquisition only a high coercivity phase is detected in this sample (Fig. 5b). The strong reversible change of IRM intensity during low temperature treatment indicates the presence of goethite only (Fig. 5c), and low temperature transitions due to magnetite or hematite have not been found. During heating (Fig. 5d) we recognize that 70% of the magnetization is carried by goethite whose maximum blocking temperature lies around $T_{b\max} \cong 90^{\circ}\text{C}$. The rest of remanence is due to hematite with $T_{b\max} \cong 635^{\circ}\text{C}$. The Morin transition is not found during low temperature treatment, because either the hematite grain size is too small or the transition is suppressed due to the presence of impurity ions in hematite.

2.2. Thermal Treatment of Goethite

It has been demonstrated by Dunlop (1972) that a remanence coercivity spectrum can be derived from IRM acquisition curves simply by plotting the increment ΔJ of isothermal remanence in intervals ΔH of a certain width of the applied field H . Dunlop also showed how changes of the coercivity spectra obtained during heating can be interpreted in terms of changes in the ferromagnetic mineralogy. This technique has been applied to a bafflestone sample which initially contained goethite as the only ferromagnetic mineral. The coercivity spectra (increment $\Delta H = 5$ kOe, $\Delta H = 1$ kOe for $H \leq 5$ kOe) obtained after heating to stepwise increased maximum temperatures are given in Figure 6. The

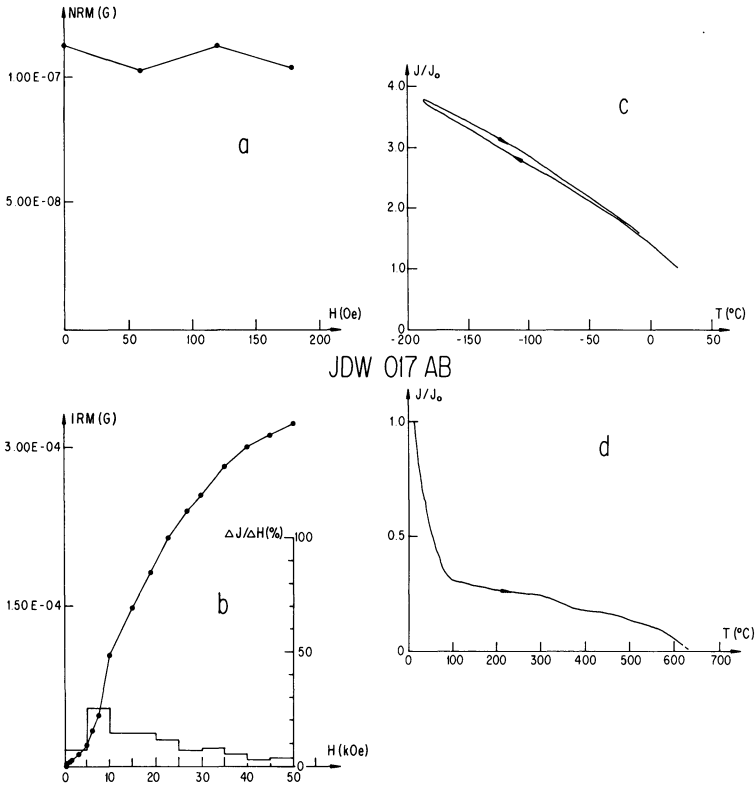


Fig. 5a-d. NRM and IRM characteristics of a bafflestone sample (JDW 017 AB) containing goethite and hematite. For the significance of Figure 5a-d see Figure 2a-d

IRM intensity decay during each heating cycle (heating rate always $dT/dt = 10^\circ \text{C}/\text{min}$) has been measured continuously and plotted in Figure 7. After having attained the maximum heating temperature the sample always was allowed to immediately cool down to room temperature again.

Before heating ($T = 0^\circ \text{C}$) we observe a broad coercivity spectrum which has a maximum between 5 kOe and 20 kOe (Fig. 6a). The maximum blocking temperature is about 60°C (Fig. 7a). After heating to $T_{\text{max}} = 90^\circ \text{C}$ the shape of the coercivity spectrum as well as the maximum blocking temperature change very little (Figs. 6b and 7b), but the intensity of magnetization is increased by about 50% of the initial IRM produced by $H = 50 \text{ kOe}$. The intensity increase possibly is caused by grain size growth of very small (superparamagnetic?) goethite particles dispersed throughout the sample and/or by advancing crystallization of poorly crystalline material due to modest heat treatment. Heating to $T_{\text{max}} = 225^\circ \text{C}$ does not affect the magnetic properties of the sample essentially; also its colour remains white. After heating to $T_{\text{max}} = 310^\circ \text{C}$ major changes occur. They are due to dehydration and decomposition of goethite which starts

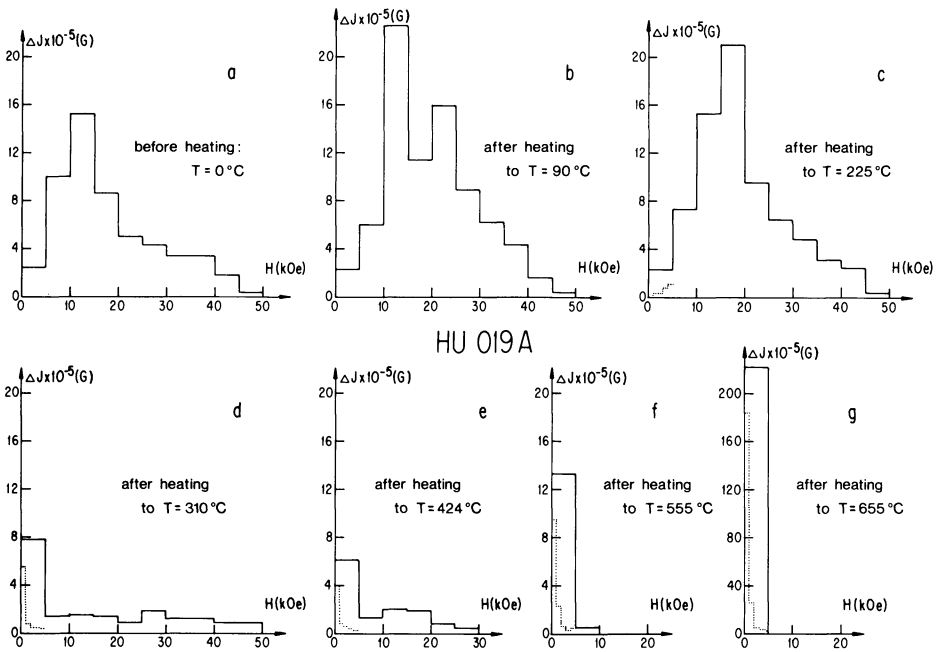


Fig. 6a-g. Coercivity spectra of IRM of a goethite containing bafflestone sample (HU 019 A) obtained after heating to stepwise increased maximum temperature. Note change of scale in Figure 6g

around 290°C (Hedley, 1968). The colour of the limestone begins to redden. The reddish colour is observed only in the bafflestones which before heating obviously contain finely dispersed iron-hydroxides. These are converted during heating to very fine grained hematite which causes the colour change. Thus the suggestion made by Lowrie and Alvarez (1977) that hematite formed by dehydration of goethite in the Scaglia Rossa limestones from Italy, is supported by the observed colour changes. The former coercivity spectrum breaks down having a well developed maximum now at fields $H < 5$ kOe, but fields $5 \text{ kOe} < H < 50 \text{ kOe}$ still contribute about half of the IRM (Fig. 6d). The finer ΔH increments (dotted lines in Fig. 6d-g) show the beginning development of a magnetic mineral phase having a coercivity $H_{cr} \leq 1$ kOe. The IRM intensity is reduced by a factor 5 and therefore, although the sample appears reddish, hematite does not seem to contribute very much to the remanence probably because its grain size is very small. Upon further heating we see a kink in the IRM decay curve around 70°C (Fig. 7d) which indicates that some goethite still has survived, but the main part of IRM is associated with higher blocking temperatures. Heating to $T_{\text{max}} = 424^{\circ}\text{C}$ does not reach the maximum blocking temperature of this IRM, but it turns out that after this heating cycle the IRM intensity decreases even further. The colour of the limestone still is red and the subsequent IRM acquisition curve saturates at $H = 30$ kOe (Fig. 6e). Thus the coercivity spectrum begins to shorten. The magnetization component which has a coercivity $H_{cr} \leq 1$ kOe shows a very slight decrease. Subsequent

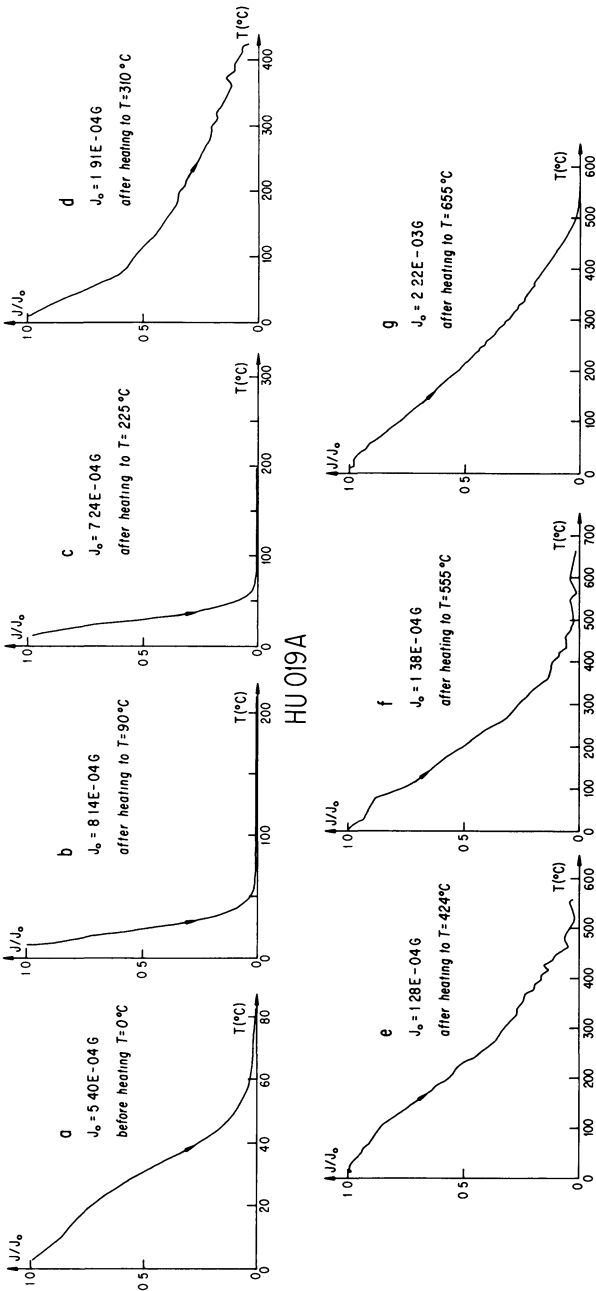


Fig. 7a-g. Continuous thermal demagnetization of IRM up to stepwise increased maximum temperature. J_0 denotes initial IRM intensity before each heating cycle

heating (Fig. 7e) does not show signs of goethite magnetization components, but the uppermost blocking temperatures seem to be reached around 500°C . This heating cycle up to $T_{\text{max}} = 555^\circ\text{C}$ restricts the coercivity spectrum to $0 < H_{\text{cr}} \leq 10$ kOe with a definitely increased low coercivity component (Fig. 6f) which now carries the main portion of IRM. The colour of the sample becomes

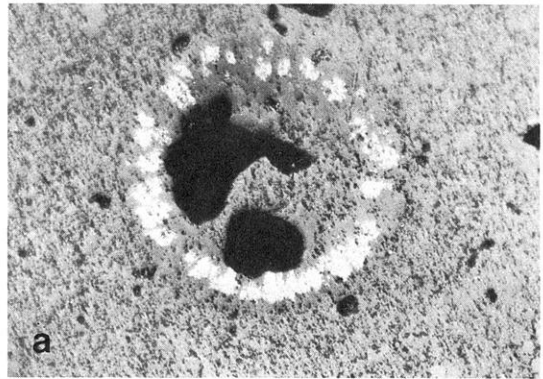
grey with some small patches on the surface still being red. After heating to $T_{\max} = 665^{\circ}\text{C}$ another drastic change of the magnetic properties becomes evident. There is no further colour change, but the IRM intensity has increased by a factor 20 (Fig. 6g; ordinate with enlarged scale!); nearly 100% of the magnetization are held by a magnetic phase which has a coercivity $H_{\text{cr}} \leq 2$ kOe. The maximum blocking temperature is found to be $T_{b_{\max}} \cong 540^{\circ}\text{C}$ (Fig. 7g).

It is evident from these experiments that not only hematite is formed by thermal destruction of goethite. At temperatures below 300°C goethite is the only ferromagnetic mineral present in the limestone sample. Figures 6d and e and 7d and e show that between 300°C and 450°C probably hematite is forming and partly contributing to the IRM, as the component with $10 < H_{\text{cr}} \leq 20$ kOe increases and at least part of the high coercivity component of IRM is due to a magnetically hard mineral with blocking temperatures well above 100°C . The carrier of the low coercivity component formed within this temperature range cannot be positively identified from the measurements. Because heating to 424°C reduces the intensity of this component slightly, possibly maghemite was formed after heating to 310°C and is going to be destroyed upon further heating. Its formation during oxidation of goethite was also noted by Kelly (1956). But it cannot be excluded alternatively that possibly magnetite is responsible for this portion of IRM. Heating to temperatures $> 500^{\circ}\text{C}$ causes magnetite to constitute. Evidence for magnetite comes from the intensity increase of the low coercivity component by one to two orders of magnitude, from the coercivity spectrum reduction to $H_{\text{cr}} \leq 2$ kOe, from the maximum blocking temperature being about $T_{b_{\max}} = 540^{\circ}\text{C}$ and from a faint indication of a low temperature transition at -150°C during low temperature treatment. The formation of magnetite at these relatively low temperatures (beginning around 550°C) is unusual (cf. Dunlop, 1972), but it is probably due to the large amount of organic compounds contained in the bafflestones which decompose upon heating and create reducing conditions in the sample at higher temperature.

3. Non-Magnetic Identification of Ore Minerals

3.1. Ore Microscopy

Ore microscopic studies reveal the presence of several opaque minerals whose occurrence depends on the facies type of the limestones. No ore mineral—especially no magnetite—could be identified in the Oxfordian marl-rich limestones. In the micritic limestones weakly reflecting, grey goethite has been observed. The grains predominantly have idiomorphic to hypidiomorphic (cubic!) shape (Fig. 8b) and it seems that they have replaced pyrite which also is found at places in this part of the section. These goethite grains range in size between $10\ \mu\text{m}$ and $1000\ \mu\text{m}$. Small brightly reflecting patches within the larger goethite grains and red internal reflections along the grain margins indicate that they have been partly altered to hematite. The bafflestones contain very irregularly shaped (Fig. 8a) goethite grains of various size ($10\ \mu\text{m}$ to $100\ \mu\text{m}$) which often



1 mm

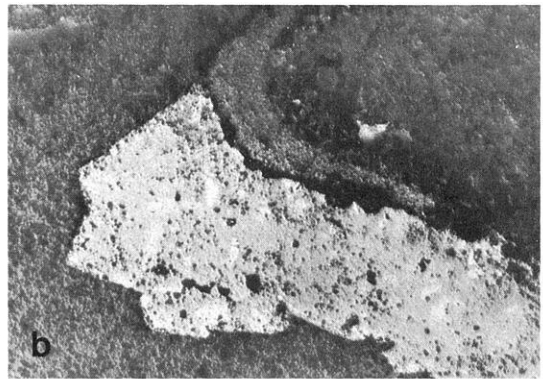


Fig. 8. a Irregularly shaped goethite, probably concentrated around a fossil relict. Bafflestone sample (HU 018 D).
b Regularly shaped goethite (grey) which has replaced pyrite. The brighter patches within goethite indicate oxidation. Micritic limestone sample (JBH 085 AA)

seem to be oxidized to hematite more strongly than in the micritic limestones. Usually these goethites occur in the close neighbourhood of fossil fragments.

3.2. *Electron Microprobe and X-Ray Analysis*

Table 1 gives the results of microprobe analysis. No other cations such as Ni, Cr, Mn, Al, Ca, Mg have been detected. The iron contents of pyrite and “idiomorphic” goethite are very near to stoichiometry for pure FeS_2 , and FeO OH , respectively, whereas the iron content of the irregularly shaped goethite is slightly reduced. All the goethites contain a small amount of silica up to 2 wt% for single point analyses. Sulphur is absent in the “idiomorphic” goethite suggesting a thorough oxidation of pyrite which probably preceded this type of goethite.

Heavy mineral extracts taken from a marl-rich limestone and two bafflestone samples yielded useful X-ray powder photographs only for the bafflestones.

Table 1. Microprobe analysis of ore minerals. Elements analyzed: Fe, Si, S; *N* denotes number of analyses

Limestone facies, mineral	<i>N</i>	Fe wt%	Si wt%	S wt%
Micritic limestone, 'idiomorphic' goethite	33	63.14 ± 1.11	1.65 ± 0.40	—
Micritic limestone, irregular goethite	4	58.77 ± 1.86	1.76 ± 0.08	—
Bafflestone, irregular goethite	30	58.27 ± 2.49	1.70 ± 0.19	—
Bafflestone, pyrite	9	46.40 ± 0.37	0.04 ± 0.03	52.16 ± 1.29

Table 2. Lattice constants of orthorhombic goethite (α -FeOOH)

Sample	a (Å)	b (Å)	c (Å)	Camera	<i>T</i> (°C)
HU 003	4.618 ± 0.002	9.969 ± 0.003	3.020 ± 0.001	Jago	20
JDW 027	4.618 ± 0.004	9.971 ± 0.005	3.019 ± 0.001	Jago	20
JDW 027	4.610 ± 0.007	9.967 ± 0.011	3.019 ± 0.002	Simon	20
JDW 027	4.601 ± 0.005	9.959 ± 0.006	3.017 ± 0.002	Simon	-150

These photographs obtained with a Guinier focussing camera (Jagodzinski type) using Si as internal standard, again showed goethite as the only ferromagnetic mineral to be identified. Broad diffraction lines indicate poor crystallization of the material. The lattice constants are given in Table 2. The table also includes lattice parameters of goethite which have been measured with another Guinier camera (Simon type) at room temperature as well as at low temperature (-150° C) in order to find out if there is a correlation between cell constants and magnetic properties of goethite during low temperature treatment. The data given in Table 2 agree closely with the values published by Sampson (1969) on synthetic goethite and indicate a trend to slightly reduced lattice constants at low temperature.

4. Discussion

4.1. Physical Properties of Goethite

Goethite is known to be antiferromagnetic with a weak ferromagnetism superimposed (Strangway et al., 1968; Forsyth et al., 1968). Hedley (1971) suggested that the ferromagnetism is due to spin imbalance between the antiferromagnetic sublattices caused either by vacancies or faults in the crystal structure or by impurity ions entering the lattice.

The extreme stability of NRM against alternating demagnetizing fields up to 3000 Oe (Fig. 5) as well as the spectra of very high coercivity of IRM observed in the goethite containing limestones support Hedley's idea that the ferromagnetic magnetization shares the strong antiferromagnetic anisotropy. The maximum blocking temperatures range between 55° C and 95° C. If we assume

that the maximum blocking temperatures coincide with the corresponding Néel-temperatures, then these relatively low temperatures point to poorly crystallized material (Hedley, 1971). This is in agreement with the X-ray examination where broad diffraction lines have been observed. We have noted a small amount of Si in our goethites (Table 1). Therefore the goethite ferromagnetism could be caused by imbalance due to Si impurities, but it is not clear how Si enters the lattice non-randomly. We see on the other hand in Table 1 a higher Fe-content (63.1 wt%) which is near to stoichiometry of the pure mineral, in the "idiomorphic" goethite compared to a slightly reduced iron content (58.5 wt%) in the irregular goethite. The NRM and IRM intensities of sediments containing "idiomorphic" goethite generally are reduced by a factor 5 compared to the limestones with irregular goethite, which may imply that vacancies play a rôle in the stronger magnetization of the irregular goethites.

It is difficult to encounter the mechanism which causes the observed ferromagnetism in the goethite because of uncertainties about the degree of crystallization and oxidation state of the material which in small clusters may be altered to hematite. The trend to a lattice contraction at low temperature may account for the strong temperature dependence of spontaneous magnetization (increase of IRM with decreasing temperature in zero field), but a quantitative explanation cannot be given before a better knowledge of the chemical and structural properties of these goethites has been achieved.

4.2. Magnetization Process

We have described in the previous chapters that mainly two phases—magnetite and goethite—dominate the ferromagnetic mineralogy of the limestones. The processes by which these minerals acquired their NRM, are different.

The marls and marl-rich limestones have been deposited during times of increased influx of mud suspensions (v. Freyberg, 1966). Rockmagnetic studies revealed the presence of single- to pseudo-single domain magnetite in these sediments. As the grainsize of magnetite is very small, optical identification and separation methods failed. The fine grainsize on the other hand allowed magnetite to be carried within the mud suspensions and to be aligned during or shortly after deposition so that a detrital remanence (DRM) has been acquired by the magnetite. The mean NRM direction of the marls and marl-rich limestones (Table 3, Malm $\alpha + \beta$) confirms a detrital, synsedimentary origin of natural remanence, because the resulting virtual geomagnetic pole position (VGP: = 68° Lat.N; 130° Long.E) has been found to coincide closely with the European Late Triassic palaeopole (cf. Heller, 1977; Fig. 8). The same close agreement has been observed between Late Triassic and Jurassic palaeopoles in North America (Steiner and Helsley, 1972).

When swells became active in the sedimentation basin, the influx of clastic material stopped to a large extent. Consequently magnetite is of little importance for the magnetic properties of the pure, micritic limestones and the bafflestones.

There are at least two time periods when goethite acquired the natural remanence. From ore microscopic observations we have recognized two goethite

Table 3. Mean directions of stable remanence and virtual geomagnetic pole positions (VGP) derived from the Late Jurassic limestones of Southern Germany (site Lat.N: 49°, Long.E: 11°)

Malm Subdivision	Number of samples	Direction of NRM			VGP position	
		D	I	α_{95}	Lat.N	Long.E
δ	125	13	62	5	79	124
γ	48	31	51	8	62	122
$\alpha + \beta$	79	23	53	5	68	130

types. The first type occurring mainly in the micritic limestones has pseudoidiomorphic shape which suggests formation by alteration from pre-existing pyrite. For the timing of this oxidation process which produces a chemical remanent magnetization (CRM), we may use the same arguments as for the magnetite DRM. The micritic limestones have the same stable mean direction (Table 3; part of Malm β and Malm γ) as the marls and marl-rich limestones. On this basis we conclude that the alteration must have taken place soon after deposition of these sediments and that this CRM may also be of Jurassic age. This on the other hand implies that the redox potential of the sediments changed early during diagenesis into more oxygenated conditions.

The other goethite type found predominantly in the bafflestones is irregularly shaped. Apparently it did not form by alteration from pyrite. But still a Jurassic NRM direction could be expected since goethite could precipitate from iron solutions under certain redox conditions (Schellmann, 1959; Stumm and Morgan, 1970) perhaps dependent on the oxidation of organic matter a lot of which has been available in the bafflestones, and it may form irregularly shaped crystals in the neighbourhood of fossil relicts. But we have noted (Table 3; Malm δ) that the stable mean direction of the bafflestones differs significantly from that of the older members of the limestone sequence. This NRM is aligned very near to a Lower Tertiary European field direction and has been interpreted previously to reflect apparent polar wander setting in with the beginning of the middle Lower Kimmeridgian. This interpretation required a sudden and rapid polar movement starting between Malm γ and Malm δ . In view of the rock magnetic information for these bafflestones this interpretation must be revised.

The NRM of the bafflestones probably has a post-sedimentary, secondary origin, possibly connected to Karst formation and red soil development which started during the Lower Cretaceous and reached its climax during the Eocene and Miocene (Birzer, 1939). During this process goethite, if it existed, and other iron minerals were dissolved, and iron-hydroxide (re)-precipitated from iron solutions which penetrated the bafflestones from the land surface. Such an interpretation would easily solve the problems invoked in the introduction.

We can place a lower limit to the age of NRM of the limestones. We have taken samples from an outcrop situated near to the main fault which separates the limestone basin from the Bohemian massif. The steeply dipping limestone layers are overturned here and a magnetization direction which coin-

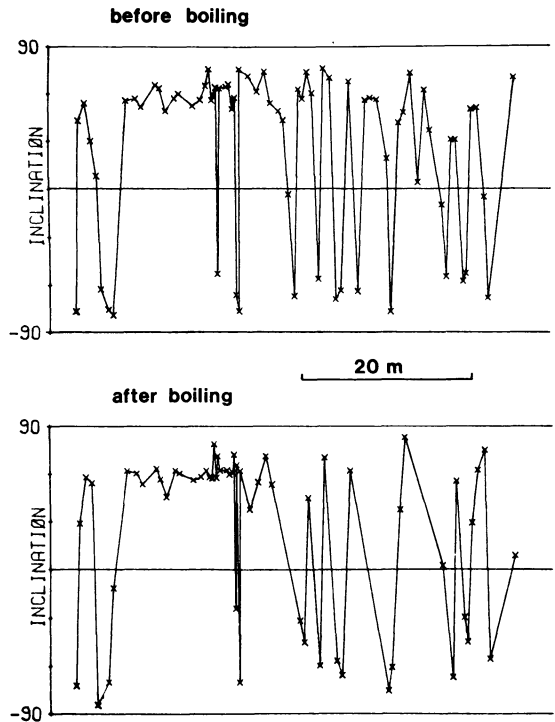


Fig. 9. Inclination of NRM of the Swabian bafflestone section before and after boiling in water

cides with the NRM directions measured elsewhere, can only be obtained by repositioning to the original horizontal position. As the faulting took place certainly before Upper Miocene (Bauberger and Cramer, 1961), the age of NRM must be older than Upper Miocene.

During the period of Karstification the upper parts of the limestones have been eroded and iron contained in the sediments was dissolved when the groundwater level was lowered down (Birzer, 1939). The iron solutions which led to iron ore deposits on the Eocene land surface, also penetrated the underlying limestones where precipitation and, as we see in polished sections, concentration of goethite took place preferentially in the neighbourhood of fossil relicts the remaining organic material of which supported the crystal growth of ironhydroxides. Recipitation and crystal growth of goethite does not necessarily occur contemporaneously throughout a limestone bed, as they depend on factors like porosity, content of organic substances, water content etc. which may vary locally.

This explains readily the observed occurrence of specimens with different NRM polarity within the same sample in the bafflestones. Normal and reversed samples may be found within the same limestone bed at different places, since the goethite crystals may have grown out of the superparamagnetic into the ferromagnetic state at different times in palaeofields of different polarity. The observed polarity sequence then no longer can be attributed to a Jurassic field

reversal sequence, but reflects undatable field reversals of probably Lower Tertiary age. It should be mentioned that the apparent polarity profile is not changed by thermal demagnetization which was carried out by boiling in water. After boiling at 100° C the goethite component of NRM has been removed due to the low maximum blocking temperatures, but where a stable NRM component still was present after boiling, the direction of NRM remained unchanged (Fig. 9). This component is due to hematite the magnetization direction of which is controlled by that of goethite. Thus we find magnetic evidence that hematite has been formed by dehydration and oxidation of goethite.

In the Swabian section the Malm δ bafflestones are intercalated with marls and marl-rich limestones which like the Oxfordian facies equivalents always carry a normal magnetization direction. Whereas the bafflestones themselves have been magnetized during the Tertiary, this normal magnetization of Malm δ marls carrying a synsedimentary DRM probably indicates that the period of normal polarity of the geomagnetic field lasted during the Lower Kimmeridgian, too. Following this argument, we may conclude that the younger portion of the Jurassic quiet zone (Larson and Hilde, 1975) comprises both the Oxfordian and the Lower Kimmeridgian.

Acknowledgements. Thanks are due to Dr. Bachmann, BBC Research Laboratories Baden, for making available the superconducting magnet, to R. Gubser for microprobe analyses, to Mr. Hertz for low temperature X-raying and to Dr. K. Girgis for X-raying and calculation of the lattice constants of goethite. Finally I would like to thank Professor W. Lowrie, Dr. J. Channell, and Dr. I. Hedley for critical reading of the manuscript.

References

- Bauberger, W., Cramer, P.: Erläuterungen zur Geologischen Karte von Bayern 1:25000, Blatt Nr. 6838 Regenstauf, 1961
- Birzer, F.: Verwitterung und Landschaftsentwicklung in der südlichen Frankenalb. Z. Deut. Geol. Ges. **91**, 1–57, 1939
- Dunlop, D.J.: Magnetic mineralogy of unheated and heated red sediments by coercivity spectrum analysis. Geophys. J. Roy. Astron. Soc. **27**, 37–55, 1972
- Forsyth, J.B., Hedley, I.G., Johnson, C.E.: The magnetic structure and hyperfine field of goethite. J. Phys. C Ser. 2, **1**, 179–188, 1968
- Freyberg, B.v.: Der Faziesverband im Unteren Malm Frankens. Erlanger Geol. Abh. **62**, 1966
- Hedley, I.G.: Chemical remanent magnetization of the FeOOH, Fe₂O₃ system. Phys. Earth Planet. Inter. **1**, 103–121, 1968
- Hedley, I.G.: The weak ferromagnetism of goethite (α -FeOOH). Z. Geophys. **37**, 409–420, 1971
- Heiniger, Chr., Heller, F.: A high temperature vector magnetometer. Geophys. J. Roy. Astron. Soc. **44**, 281–287, 1976
- Heller, F.: Palaeomagnetism of Upper Jurassic limestones from Southern Germany. J. Geophys. **42**, 475–488, 1977
- Kelly, W.C.: Application of differential thermal analysis to identification of natural hydrous ferric oxides. Amer. Mineral. **41**, 353–355, 1956
- Larson, R.L., Hilde, T.W.C.: A revised time scale of magnetic reversals for the Early Cretaceous and Late Jurassic. J. Geophys. Res. **80**, 2586–2594, 1975
- Lowrie, W., Alvarez, W.: Late Cretaceous geomagnetic polarity sequence: Detailed rock and palaeomagnetic studies of the Scaglia Rossa limestones at Gubbio, Italy. Geophys. J. Roy. Astron. Soc. **51**, 561–582, 1977
- Merrill, R.T.: Low temperature treatments of magnetite and magnetite-bearing rocks. J. Geophys. Res. **75**, 3343–3349, 1970

- Sampson, C.F.: The lattice parameters of natural single crystal and synthetically produced goethite (α -FeOOH). *Acta Cryst.* **B25**, 1683–1685, 1969
- Schellmann, W.: Experimentelle Untersuchungen über die sedimentäre Bildung von Goethit und Hämatit, *Chemie Erde* **20**, 104–135, 1959
- Steiner, M.B., Helsley, C.E.: Jurassic polar movement relative to North America. *J. Geophys. Res.* **77**, 4981–4993, 1972
- Strangway, D.W., Honea, R.M., McMahon, B.E., Larson, E.E.: The magnetic properties of naturally occurring goethite. *Geophys. J. Roy. Astron. Soc.* **15**, 345–359, 1968
- Stumm, W., Morgan, J.J.: *Aquatic chemistry*. New York: Interscience Publishers 1970
- Wilson, J.L.: *Carbonate facies in geologic history*. Berlin Heidelberg New York: Springer 1975

Received March 7, 1978

Palaeosecular Variation Studies of the Brunhes Epoch in the Volcanic Province of the East-Eifel, Germany

H. Kohnen and H. Westkämper

Institut für Geophysik der Universität Münster,
Gievenbecker Weg 61, 4400 Münster, Federal Republic of Germany

Abstract. In the Quarternary volcanic province of the East-Eifel 46 occurrences were investigated palaeomagnetically. According to radiometric dating, the volcanic activity covered the past 600,000 years more or less uniformly and is adequate to study the palaeosecular variation of the Brunhes epoch. The mean pole position (VGP) of the occurrences investigated follow a Fisherian distribution. Averaging all pole positions yields 87.0° N and 69.2° E ($A_{95} = 4.8^\circ$) which coincides with the north geographic pole within the limits of error. This agreement shows that the area as well as the time interval are large enough in this particular case to confirm the axial dipole hypothesis. The angular dispersion of the VGP: $S_F = 15.1^\circ$ (angular dispersion of the ancient field) is in accordance with the models C, E, and M proposed for the palaeosecular variation of the earth's magnetic field.

Key words: Palaeomagnetic investigations — Quaternary volcanics of the East-Eifel — Palaeosecular variation — Mean pole position — Angular dispersion.

Introduction

The East-Eifel is part of the Rhenian Mass (Rheinisches Schiefergebirge), which consists mainly of quartzites, gray-wakes and slates of the Lower Devonian. The area of young volcanism extends between the rivers Rhine (N, NE), Nette (S, SW) and Brohl (N, NW) (Fig. 1). The onset of the volcanic activity coincided roughly with the beginning of the Pleistocene glaciation.

About 70 volcanic occurrences are known in this volcanic province of which 46 sites were palaeomagnetically investigated during 1976/77. The ages of several sites based on radiometric and stratigraphic dating, are listed in Figure 2. The dominating rock types are alkali basalts and among these mainly basanites, nephelinites, tephrites and phonolites. The time interval of the whole cycle seemed adequate to study the palaeosecular variation of the Brunhes epoch in this region.

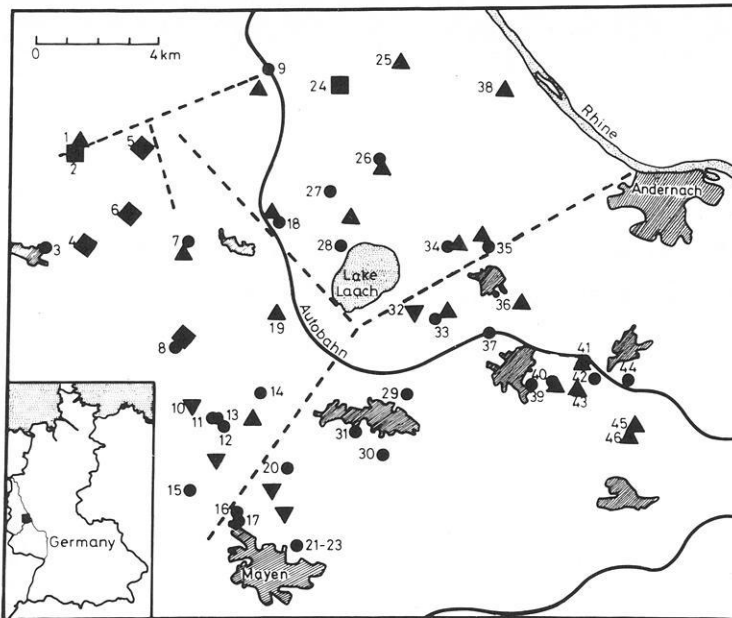


Fig. 1. Sampling sites in the East Eifel. The angular symbols denote volcanoes which are petrologically investigated. \blacktriangle basanite; \blacksquare nephelinite; \blacklozenge phonolite; \blacktriangledown tephrite; the circles indicate additional localities investigated palaeomagnetically during this study. ----- Plio-Pleistocene faults

Of principal interest herein is a comparison of the palaeosecular variation of the Pleistocene or the Brunhes epoch respectively in the East-Eifel with the global palaeosecular variation.

The Models of Palaeosecular Variation

Different models based on historical observations of the geomagnetic field and on theoretical considerations have been developed to describe the global pattern and behaviour of the palaeosecular variation. Any latitudinal dependence of the palaeosecular variation should be manifest in the angular dispersion of the pole positions, which, therefore, is the quantity of basic importance in all models. The principles of the models developed so far are briefly outlined below and presented in Figure 3.

According to model A (Irving and Ward, 1964), the palaeosecular variation is only due to a non-dipole component of random direction but constant intensity. Model B (Creer et al., 1959) postulates a wobble of the main dipole following a Fisherian distribution. Such a latitudinal invariance of the angular standard deviation of the VGPs is not at all confirmed by experimental data. In Model C (Cox, 1962; Creer, 1962), the total angular dispersion is assumed to be a superposition of angular dispersions, due to a dipole wobble (S_D^2) and non-dipole components (S_N^2): $S_T^2 = S_D^2 + S_N^2$.

AGE(a)	VOLCANO	ROCK TYPE	DATING
	EITERKOPF II	BASANITE	* ¹⁴ C
15 000			
20 000			
30 000	KUNKSKOPF NIEDERMENDIG KRUFTER OFEN NICKENICHER GRUPPE KORRETSBERG PLAIDTER HUMMERICH WANNEN GRUPPE	BASANITE TEPHRITE TEPHRITE BASANITE BASANITE BASANITE BASANITE	LOESS STRATIGR. RHINE TERRACE STRATIGRAPHY
50 000	HERCHENBERG WANNEN GRUPPE	NEPHELINITE BASANITE	¹⁴ C
70 000			
100 000	MAUERLEY	BASANITE	K-AR (± 40 000)
140 000	HOHE BUCHE	BASANITE	RHINE TERRACE STRATIGRAPHY
200 000	BAUSENBERG VEITSKOPF	BASANITE BASANITE	K-AR (± 40 000) RHINE TERRACE STRATIGRAPHY
300 000	HOCHSTEIN (J,T)	BASANITE	K-AR (± 80 000)
400 000	HOCHSIMMER PERLER KOPF ENGELNER KOPF SULZBUSCH	TEPHRITE BASANITE PHONOLITE TEPHRITE	K-AR (± 100 000) K-AR (± 30 000) K-AR (± 40 000) K-AR (± 80 000)
2 600 000	OLBRUCK SCHELLKOPF	PHONOLITE PHONOLITE	K-AR (± 30 000) K-AR (± 40 000)

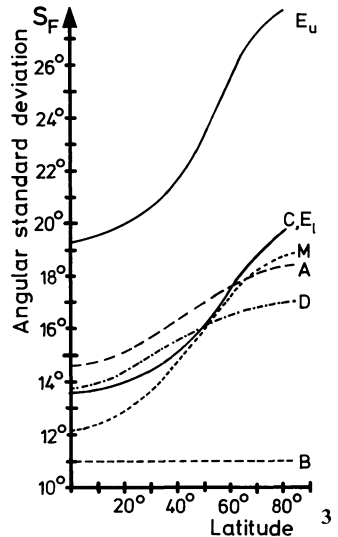


Fig. 2. Radiometric and stratigraphic ages of several quarternary volcanics in the Eifel after Frechen (1976) and *Schmincke (pers. communication).

Fig. 3. Different models proposed for the palaeosecular variation: A (Irving and Ward, 1964); B (Creer et al., 1959); C (Cox, 1962; Creer, 1962); D (Cox, 1970); E (Baag and Helsley, 1974a); E_u: upper limit of model E with r = 1; E₁: lower limit of model E with r = 0; and M (McElhinny and Merrill, 1975). See text for explanation

S_N is deduced by using averaged data from the 1965 International Geomagnetic Reference Field. $S_D = 11^\circ$ is based on palaeomagnetic measurements on the Hawaiian lavas, where non-dipole components are supposed to be absent (Pacific dipole window). Model D (Cox, 1970) is principally similar to model C; S_N , however, is based on theoretical assumptions. In model E (Baag and Helsley, 1974a), a linear coupling between S_D and S_N is proposed: $S_T^2 = S_D^2 + S_N^2 + 2r S_D S_N$ ($0 \leq r \leq 1$). The values for S_D and S_N are taken from model C. C and E are consequently identical for $r = 0$. Model M (McElhinny and Merrill, 1975) is an extension of model D. However, McElhinny, and Merrill propose a non-dipole field consisting of two components due to different mechanisms in the earth's interior. The intensity of the first component is invariant with latitude whereas the intensity of the second component increases with increasing latitude like the intensity of the dipole field. This separation is in accord with the investigations of Yukutake and Tachinaka (1969) splitting the non-dipole field in a standing and

drifting part of similar magnitude. Curve M is calculated from:

$$S_T^2 = S_D^2 + (aW_{DP}^2 + bW_{NF}^2) S_N^2.$$

W_{NF} and W_{DP} are terms describing the latitudinal dependence of the components of the non-dipole field. $S_D = 9^\circ$, $S_N = 8.25^\circ$ (non-dipole component at the equator), $a = 0.25$ and $b = 0.75$ ($a + b = 1$) are taken by the authors to obtain a best model fit to the present as well as to the past non-dipole field.

All models tacitly anticipate an axial geocentric dipole. The time average of VGPs spanning a period, which is large compared with the secular cycles of the geomagnetic field, should consequently yield coincidence between the dipole and the rotational axis. However, a critical review (McElhinny and Merrill, 1975) of all palaeosecular investigations of volcanics younger than two million years shows that 45% of the VGPs give significant differences between the geomagnetic and geographic north pole.

Only comprising various investigation areas of equal latitude yields satisfactory results. Some of the differences may be due to the two sources of the non-dipole field as outlined by Yukutake and Tachinaka (1969). If the magnetic field in the investigation area is mainly controlled by a great standing part, time averaging over long periods might not cancel out the differences entirely. McElhinny and Merrill (1975) argue, that for some areas the period of the volcanic activity might have not been long enough or insufficiently covered with regard to volcanic productivity. The latter point is particularly important because there seem to be cycles of secular variation of about 200,000 years (McElhinny and Merrill, 1975). Thus, the crucial problem also in the present study is, whether the investigation area of only $20 \times 24 \text{ km}^2$ is large enough or the time period of approx. 600,000 years is long enough to fulfil the requirements outlined by McElhinny and Merrill (1975).

Field and Laboratory Procedure

Figure 1 shows the sites investigated palaeomagnetically during 1976 and 1977. The angular symbols denote volcanics with wellknown petrological nature. The circles represent localities, whose relation to distinct centres of eruption are somewhat speculative. From each site, 6 to 17 cores each giving 2 or 3 specimens were taken. A fluxgate spinner magnetometer (Digico) was used to determine intensity and direction of the magnetization of the specimens. The stability of the natural remanent magnetization (NRM) was tested by demagnetizing 2 to 3 pilot specimens from each site in alternating fields up to 56,000 A/m (1 OE \cong 80 A/m). Figure 4 presents typical demagnetization curves, the normalized intensities being plotted against the peak alternating fields. The stability against demagnetization increases from curve A to D. Curve A represents a magnetically unstable, coarse-grained phonolite from a lava flow. The maximum may be caused by ambient fields acting opposite to the direction of the NRM during storage. Some of the samples were able to acquire considerable secondary viscous components when stored for days or weeks in the earth's magnetic field or when subjected for a short time to small artificial fields as will be shown elsewhere (Böhnel and Kohnen, in

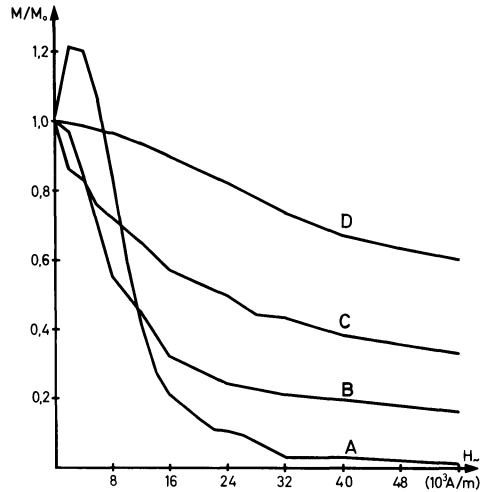


Fig. 4. Normalized NRM intensity versus peak alternating field.
A Phonolite (Olbrück, EEL 5),
B Nephelinite (Herchenberg, EEL 24),
C Basanite (Meirother Kopf, EEL 7),
D Tephrite (Krufter Ofen, EEL 32)

preparation). Curve D is obtained from a fine-grained volcanic scoria. Most results range in between the curves B and C. The differences between the extremes can be attributed to the grain size variation and are not a characteristic feature of the rock types encountered (Böhnel and Kohnen, in preparation). Most of the viscous magnetization was erased in alternating fields of only 8,000 A/m to 16,000 A/m. The directional stability of the remanent magnetization of the pilot specimens was estimated applying the stability index of Symons and Stupavsky (1974): $PSI = |d\mathbf{r}(H)/dH|$ (\mathbf{r} = unit vector of magnetization; H = demagnetizing field). PSI should be zero in the most stable region but minimum values are usually obtained. All other specimens were then demagnetized in alternating fields covering this region. The site mean direction of the characteristic remanent magnetization (CARM) was taken from the stable region at alternating fields yielding minimum α_{95} angles of confidence. Best results were obtained at fields between 8,000 and 24,000 A/m.

Results

1. The Mean Pole Positions (VGP)

Taking into account the above selection criteria, the site mean directions, the pole positions and the precision parameters were calculated from the core means. The results are listed in Table 1.

There is considerable geological and geomorphological evidence that some of the sites investigated result from the same volcanic event. Additional proof was obtained from the site mean directions being identical within the limits of statistical error (*F*-test). These sites were consequently combined and their relevant results averaged as indicated in Table 1 resulting in 31 independent volcanic events.

Table 1. Summary of palaeomagnetic results from the Pleistocene volcanics of the East-Eifel province. N_0 : site number; n : number of cores; M_0 : intensity of the natural remanent magnetization (NRM); H : peak alternating field at which the site mean direction of the characteristic remanent magnetization (CHARM) is taken; Dec , Inc : site mean direction of the CHARM; R : resultant vector; k : precision parameter; s : standard deviation of the within-site angular dispersion; $Long$, Lat : position of the virtual geomagnetic poles; dP , dm : parameters of the 95% ovals of confidence

N_0	n	M_0 (A/m)	H (A/m)	Dec (°)	Inc (°)	R	k	s (°)	d_{95} (°)	$Long$ (°)	Lat (°)	dP (°)	dm (°)
EEL1	6	0.650	12,000	28.8	70.3	5.99106	559	3.4	2.8	73.0	72.1	4.2	4.9
EEL2	12	2.919	16,000	31.8	64.8	11.84619	72	9.6	5.2	94.7	68.8	6.7	8.3
EEL3	6	0.118	8,000	10.3	71.8	5.98846	433	3.9	3.2	47.7	81.3	5.0	5.7
EEL4	8	0.157	32,000	20.5	66.6	7.97692	303	4.7	3.2	94.7	76.8	4.3	5.2
EEL5	6	0.090	16,000	72.3	81.5	5.96908	162	81.5	5.3	33.9	52.6	9.9	10.2
EEL6	10	0.242	4,000	37.0	75.6	9.90526	95	8.3	5.0	51.1	66.6	4.2	9.2
EEL7	7	5.048	28,000	0.5	63.7	6.98189	331	4.5	3.3	183.7	84.9	8.4	5.3
EEL8	10	0.126	6,000	5.3	60.6	9.93968	149	6.6	4.0	162.7	80.4	4.6	6.0
EEL9	14	8.000	16,000	13.6	73.7	13.91352	150	6.6	3.3	42.2	78.0	5.3	5.8
EEL 10-12	22	4.014	24,000	349.5	68.5	21.87559	169	6.3	2.4	293.2	83.3	3.4	4.0
EEL 14+30	20	4.908	8,000	1.3	64.7	19.91925	235	5.3	2.1	173.5	86.2	2.8	3.4
EEL 15-17	18	3.605	24,000	353.4	65.6	17.90038	171	6.2	2.7	250.2	85.0	3.5	4.3
EEL 18	10	2.299	24,000	9.9	63.0	9.98081	469	3.7	2.2	135.0	81.1	2.8	3.5
EEL 19	17	8.576	16,000	8.6	75.8	16.91480	188	5.9	2.6	23.9	76.4	4.4	4.8
EEL 20-23	43	4.355	24,000	339.4	73.6	42.80025	210	5.6	1.5	323.2	75.1	2.4	2.7
EEL 24	15	6.508	16,000	17.7	63.0	14.96795	437	3.9	1.8	117.6	76.6	2.3	2.9
EEL 26	12	5.959	0	3.1	68.7	11.98352	668	3.1	1.7	58.5	87.6	2.4	2.8
EEL 27	8	7.549	12,000	347.8	63.4	7.97132	244	5.2	3.6	248.2	80.1	4.4	5.6
EEL 28	9	3.388	8,000	344.4	54.8	8.99144	934	2.7	1.7	230.1	71.1	1.7	2.4
EEL 29	11	5.228	24,000	6.6	63.3	10.97825	460	3.8	2.1	146.1	82.9	2.7	3.4
EEL 32	10	1.798	24,000	350.3	49.9	9.97344	339	4.4	2.6	211.1	68.9	2.3	3.5
EEL 33+37	21	9.499	32,000	2.7	81.0	20.94700	377	4.2	1.6	9.4	67.9	3.1	3.2
EEL 34	6	10.887	12,000	2.6	72.3	5.99375	800	2.9	2.4	18.4	82.8	3.7	4.2
EEL 35	8	3.707	12,000	21.2	69.8	7.99215	891	2.7	1.9	75.2	76.6	2.7	3.2
EEL 36	11	5.877	20,000	10.4	66.9	10.97183	355	4.3	2.4	100.5	83.3	3.3	4.0
EEL 38	12	4.931	16,000	344.2	64.8	11.95502	245	5.2	2.8	263.4	78.9	3.6	4.5
EEL 39+40	16	3.631	12,000	346.5	71.5	15.96487	427	3.9	1.8	318.1	80.1	2.7	3.1
EEL 41+42	21	4.146	12,000	347.6	48.2	20.82727	116	7.6	3.0	215.9	66.8	2.5	3.9
EEL 43	11	9.615	12,000	27.7	59.4	10.97817	458	3.8	2.1	114.5	68.2	2.4	3.2
EEL 44+45	15	6.189	12,000	338.0	71.3	14.98382	871	2.8	1.3	308.3	75.8	2.0	2.3
EEL 46	9	9.587	0	0.6	65.1	8.97615	336	4.4	2.8	179.5	86.7	3.7	4.5

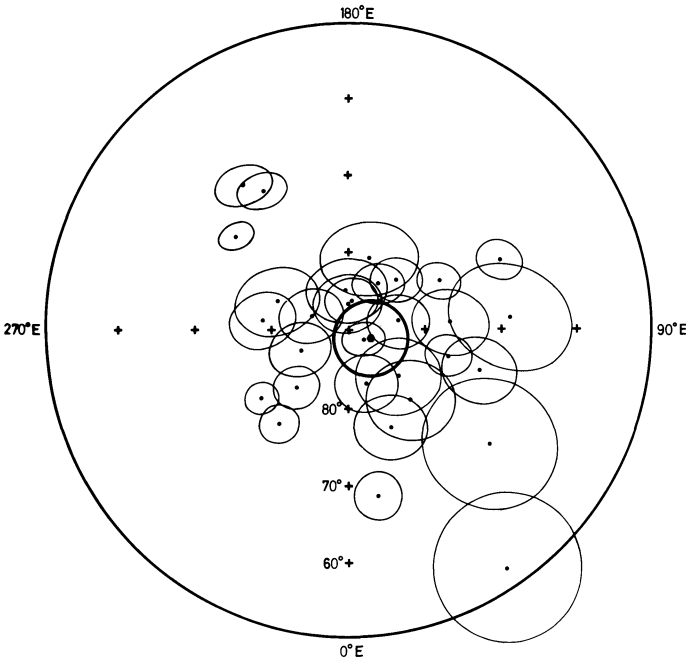


Fig. 5. Mean pole positions (VGP) together with A_{95} -ovals of confidence. The average VGP is indicated by the hexagon

When dealing with palaeosecular variation it is more convenient to use pole positions than directions (Cox, 1962) because the VGPs follow a Fisherian distribution, whereas directions usually follow a non-Fisherian pattern. In Figure 5, the pole positions are plotted together with the ovals of confidence. The pole positions scatter around the north geographic pole with angular separations exceeding rarely 25° to 30° . The distribution appears to be random and can most likely be attributed to palaeosecular variation entirely. Such behaviour could be expected, because the cycles of the non-dipole components ($\approx 10^3$ years) and the dipole wobble ($\approx 10^4$ years) are both shorter than the main volcanic cycle ($6 \cdot 10^5$ years). Averaging all VGPs gives a mean pole at 87.0° N and 69.2° E including with its A_{95} -circle of confidence ($A_{95} = 4.8^\circ$) the north geographic pole. The agreement is significant according to the F -test and is in accord with the hypothesis of an axial dipole.

The distribution of the pole positions around the rotational pole, if uniquely due to palaeosecular variation, should theoretically be Fisherian as pointed out above. In Figure 6 the latitudinal and longitudinal distributions of the pole positions relative to the mean pole and relative to the rotational pole are compared with theoretical distributions. The X^2 -test confirms that the longitudinal distribution is significantly ($P > 0.05$) Fisherian in relation to the mean VGP as well as to the geographic pole. As for the latitudinal values, the agreement is only marginally significant ($P < 0.01$). The total number of 31 independent events might be too small to obtain a reliable information from the X^2 -test with regard to the longitudinal

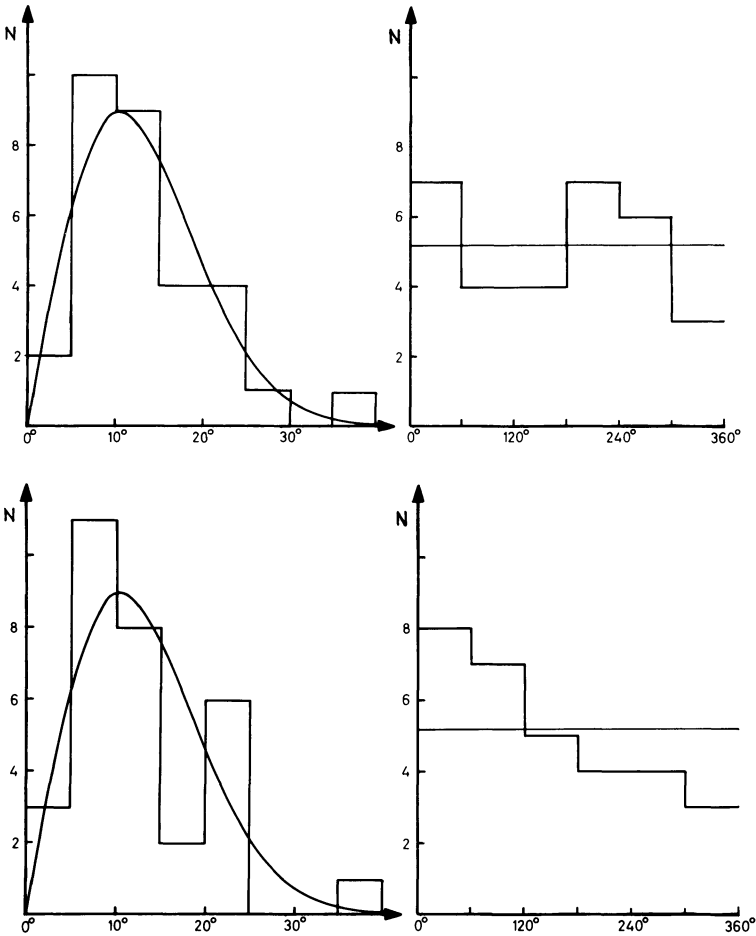


Fig. 6. Latitudinal (*left*) and longitudinal (*right*) distribution of the pole positions (block diagram) compared with the theoretical (Fisherian) distribution in relation to the average VGP (*above*) and the north geographic pole (*below*)

variation (Baag and Helsley, 1974b). Excluding the pole position of the Olbrück lava (EEL 5), located at 52.6° N, 33.9° E, would yield, for instance, significant agreement ($P > 0.05$). We may, therefore, assume that the scatter of the pole positions is not in contradiction to a Fisherian distribution.

2. The Angular Dispersion

The quantity of principal interest in the study of palaeosecular variation is the angular dispersion of the VGPs which can be expressed as total standard deviation S_T or Fisher's precision parameter K_T , being related by $S_T^2 = 2/K_T$; ($K_T = (N - 1)/(N - R)$) for small angular dispersions. K is not used because of the

Table 2. Angular dispersion parameters of VGPs. S_T : total standard deviation; S_W : within-site standard deviation; S_B : between-site standard deviation; S_A : standard deviation due to local magnetic anomalies (estimated according to Doell and Cox, 1963); S_F : standard deviation due to the ancient geomagnetic field; S_{Fu} and S_{F1} : upper and lower confidence limits of S_F (tabulated in Cox, 1969). The experimental error and the errors due to tilting are estimated to be 4.1° and 2.6° respectively, both are included in S_W

	S_T	S_W	S_B	S_A	S_F	S_{Fu}	S_{F1}
rel. to mean VGP	15.1°	8.2°	14.9°	1.8°	14.8°	18.0°	12.6°
rel. to geogr. pole	15.4°	8.2°	15.2°	1.8°	15.1°	18.3°	12.8°

approximate nature of this relation. The total standard deviation is computed from:

$$S_T^2 = \frac{1}{(N-1)} i \sum \delta_i^2$$

($N=31$: number of independent volcanic events, δ_i = angular separation of the i -th VGP from the mean pole position or from the geographic north pole). S_T^2 comprises the between-site dispersion S_B^2 and the within-site dispersion S_W^2 (Cox, 1969):

$$S_T^2 = S_B^2 + S_W^2/\bar{n}.$$

\bar{n} (= 12.9) is the weighted average number of cores per site (Watson and Irving, 1957). S_W^2 is computed from the within-site precision parameter of directions (Watson and Irving, 1957; Cox, 1970). The between-site dispersion results primarily from the ancient secular variation but still includes a small component due to local magnetic anomalies existing when the lava cooled:

$$S_B^2 = S_F^2 + S_A^2$$

(F = ancient field; A = local anomalies). Following Doell's (1972a and b) suggestions and analysis, it is preferable to use S_B and/or S_F which are not affected by the within-site scatter. The quantity S_A is difficult to estimate and usually taken from Doell and Cox (1963). The different dispersion parameters are given in Table 2 together with upper and lower confidence limits (95% level) of S_F . The differences are small and only apparent in the first decimal.

Figure 7 presents a summary of palaeosecular variation studies carried out by various investigators on volcanics of the Brunhes epoch. The values exhibit a strong latitudinal dependence favouring the models which anticipate such behaviour. The result from the East-Eifel is in excellent agreement with the models, C, E_1 , and M as well with the experimental data from comparable latitudes. Doell (1970), for instance, obtained from the investigations of 31 volcanoes in France an angular dispersion $S_F = 15.2^\circ$. Models B, C, and E assume a dipole wobble of 11° whereas curve M is calculated with $S_D = 9^\circ$. Due to the considerable limits of confidence, it cannot be decided from the present experimental data which model is most appropriate to describe the global behaviour of the palaeosecular variation. More data, especially at low and high latitudes are required to obtain reliable informations on the dipole wobble and its relation to the non-dipole field.

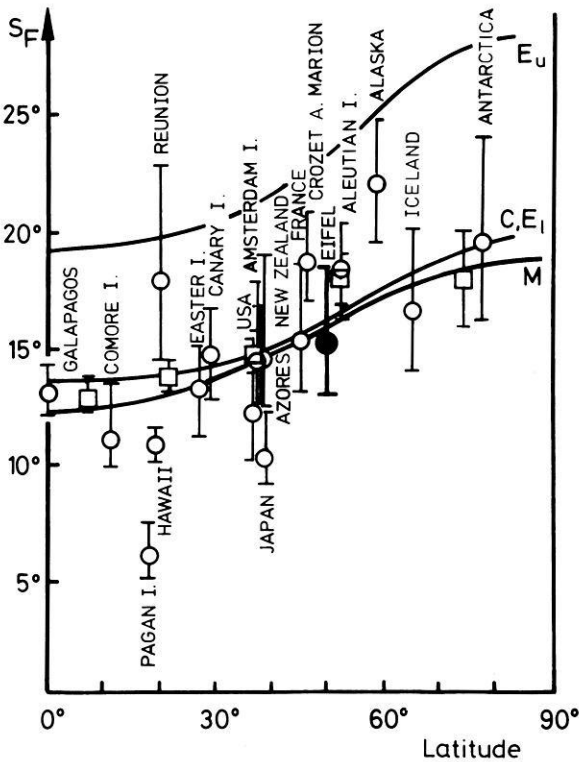


Fig. 7. Angular standard deviation S_F of pole positions with limits of confidence versus latitude on the northern hemisphere (summarised in Isaacson and Heinrichs (1976), and McElhinny and Merrill (1975)). The data of the latter authors (squares) were obtained by averaging VGPs from regions of similar latitudes. Dot: East Eifel result. The curves represent models of palaeosecular variation. Models B, C, and E are calculated assuming a dipole wobble $S_D = 11^\circ$ and model M with $S_D = 9^\circ$.

Conclusions

Although quite a number of measurements have been carried out to investigate the components and the global behaviour of the palaeosecular variation, there is still some uncertainty about the appropriate regional extent and the length of the time interval necessary to evaluate reasonable coincidence between the average dipole axis and the axis of rotation.

The pole positions determined from the Pleistocene volcanics in the East-Eifel follow a Fisherian distribution about the north geographic pole proving that here both, the time span of about 600,000 years and an area of not more than $20 \times 24 \text{ km}^2$ are sufficient to attain the agreement required by the average dipole hypothesis. This result is not in accord, for instance, with the Pacific data for the same epoch reported by Cox and Doell, (1964) yielding a significant difference between the dipole and rotational axis. Also the assumption that only averaging the VGPs over continental areas (McElhinny and Merrill, 1975) would give sufficient agreement, is not approved by the East-Eifel results. This might be due to the fact, that in this particular case the standing part of the non-dipole field is small or oscillates in periods much shorter than 600,000 years.

Acknowledgement. The authors are indebted to H. Böhnel and R. Giesbert for their assistance during the field and laboratory measurements. The help of Drs. U. Bleil and H.-U. Schmincke (both Ruhr-

Universität Bochum) in selecting the volcanic sites is highly appreciated. The authors further acknowledge the critical comments of U. Bleil and H. Böhnel.

References

- Baag, C., Helsley, C.E.: Geomagnetic secular variation model E. *J. Geophys. Res.* **79**, 4918–4922, 1974a
 Baag, C., Helsley, C.E.: Shape analysis of palaeosecular variation data. *J. Geophys. Res.* **79**, 4923–4932, 1974b
- Cox, A.: Analysis of the present geomagnetic field for comparison with palaeomagnetic results. *J. Geomag. Geoelectr.* **13**, 101–112, 1962
- Cox, A.: Confidence limits for the precision parameter k . *Geophys. J.* **18**, 545–549, 1969
- Cox, A.: Latitude dependence of the angular dispersion of the geomagnetic field. *Geophys. J.* **20**, 253–269, 1970
- Cox, A., Doell, R.R.: Long period variations of the geomagnetic field. *Bull. Seism. Soc. Am.* **54**, 2243–2270, 1964
- Creer, K.M.: The dispersion of the geomagnetic field due to secular variation and its determination for remote times from palaeomagnetic data. *J. Geophys. Res.* **67**, 3461–3476, 1962
- Creer, K.M., Irving, E., Nairn, A.E.M.: Palaeomagnetism of the Great Whin Sill. *Geophys. J.* **2**, 306–323, 1959
- Doell, R.R.: Palaeomagnetic secular variation study of lavas from the Massiv Central, France. *Earth Planet. Sci. Lett.* **8**, 352–362, 1970
- Doell, R.R.: Palaeomagnetism of lava flows from Kauai, Hawaii. *J. Geophys. Res.* **77**, 862–867, 1972a
 Doell, R.R.: Palaeomagnetism of volcanic rocks from Niihau, Nihoa and Necker Islands, Hawaii. *J. Geophys. Res.* **77**, 3725–3730, 1972b
- Doell, R.R., Cox, A.: The accuracy of the palaeomagnetic method as evaluated from historic Hawaiian lava flows. *J. Geophys. Res.* **68**, 1997–2009, 1963
- Frechen, J.: Siebengebirge am Rhein, Laacher Vulkangebiet, Maargebiet der Westeifel — Vulkanologisch-petrographische Exkursionen, Sammlung Geologischer Führer, **56**, (3. Auflage). Berlin-Stuttgart: Bornträger 1976
- Irving, E., Ward, M.A.: A statistical model of the geomagnetic field. *Pure Appl. Geophys.* **57**, 47–52, 1964
- Isaacson, L.B., Heinrichs, D.F.: Palaeomagnetism and secular variation of Easter Island basalts. *J. Geophys. Res.* **81**, 1476–1482, 1976
- McElhinny, M.W., Merrill, R.T.: Geomagnetic secular variation over the past 5 m.y. *Rev. Geophys. Space Phys.* **13**, 687–708, 1975
- Symons, D.T.A., Stupavsky, M.: A rational palaeomagnetic stability index. *J. Geophys. Res.* **79**, 1718–1720, 1974
- Watson, G.S., Irving, E.: Statistical methods in rock magnetism, *Monthly Notices Roy. Astron. Soc., Geophys. Suppl.* **7**, 289–300, 1957
- Yukutake, T., Tachinaka, H.: Separation of the earth magnetic field into drifting and standing parts, *Bull. Earthq. Res. Inst.* **47**, 65–97, 1969

Received March 29, 1978 / Revised Version May 12, 1978

Modellversuche zur elektromagnetischen Induktion in langgestreckten Strukturen*

M. Leppin und B. Boldt**

Institut für Geophysikalische Wissenschaften, Freie Universität Berlin,
Rheinbabenallee 49, 1000 Berlin 33

Analogue Model Experiments for Electromagnetic Induction in Elongated Structures

Abstract. By means of an electrolytic tank with an imbedded graphite cylinder, analogue model experiments have been carried out to study the induced electromagnetic field for elongated conductivity anomalies. It is shown that the electric field or current within the solution is in general elliptically polarized, the maximum amplitudes occurring near the ends of the cylinder. However, the results do not infer any systematic concentration or “bundling” of the induction currents through the highly conducting cylinder. When applying the magneto-telluric method to the surface measurements of electric and magnetic fields, the apparent resistivity turns out to be a function of location, with a minimum above the cylinder axis. The induction arrows derived from the total magnetic field at a surface point besides the cylinder for different frequencies are nearly perpendicular to the striking of the imbedded model anomaly. For lower frequencies both real and imaginary components of the complex induction arrow are pointing away from the anomaly, whereas for higher frequencies the latter has changed sign, now pointing into the opposite direction.

Key words: Electromagnetic induction – Analogue model experiments.

1. Einleitung

Seit nunmehr zwei Jahrzehnten werden in zunehmendem Maße die natürlichen Variationen des erdmagnetischen Feldes benutzt zur Erkundung der Leitfähig-

* Nach einem Vortrag, gehalten auf der 37. Jahrestagung der Deutschen Geophysikalischen Gesellschaft vom 29. 3. – 1. 4. 1977 in Braunschweig

** *Gegenwärtige Adresse:* 39 Brunswick Blvd. #308, Dollard des Ormeaux, P. Q. H9B 2K4, Canada

keitsstruktur des tieferen Untergrundes. Um bei der Interpretation der beobachteten anomalen Felder auf Größe, Form und Lage einer Leitfähigkeitsanomalie schließen zu können, werden diese mit bekannten Modellfeldern verglichen, die auf numerischem bzw. analytischem Wege berechnet oder auch durch Messungen an Analog-Modellen gewonnen werden. Räumlich langgestreckte Anomalien erlauben dabei oft eine wesentliche Vereinfachung der Rechnungen. Unter dieser Voraussetzung behandelt beispielsweise Steveling (1973) die Norddeutsche Leitfähigkeitsanomalie als ein zweidimensionales Induktionsmodell. Nach Modellversuchen von Rokityansky (1972) und Boldt (1977) hängt die Länge, von der ab ausgedehnte Leitfähigkeitsanomalien in hinreichender Näherung wie unendlich lange Strukturen behandelt werden können, wesentlich vom betrachteten Periodenbereich sowie von dem Leitfähigkeitsverhältnis zwischen der Einlagerung und dem Nebengestein ab. Ein Störkörper, dessen Leitfähigkeit sehr viel größer ist als diejenige seiner Umgebung, verhält sich im Vergleich zu einem Körper in einem nichtleitenden Medium erst bei einer bedeutend größeren Erstreckung wie ein unendlich langer Leiter. Ist der Leitfähigkeitsunterschied dagegen gering, so können nach Weidelt (1975) bereits bei relativ kurzen Einlagerungen zweidimensionale Verhältnisse angenommen werden.

Es fehlt daneben nicht an Versuchen, begrenzte Induktionsanomalien durch nahezu stationäre Stromverteilungen im Untergrund quantitativ zu interpretieren. Im Falle der Kirovograder Leitfähigkeitsanomalie vergleicht Rokityansky (1974) die Registrierungen mit der Induktion in einem leitfähigen Ellipsoid an der Grenze zwischen Erdkruste und Erdmantel. Da im Gebiet des Ukrainischen Schildes der Induktionsparameter im Normalfall als vergleichsweise klein gegenüber eins angesehen werden kann, führt der Autor das beobachtete anomale Magnetfeld auf eine im Ellipsoid verstärkte Stromdichte zurück, die als gleichstromartige Bündelung der im Nebengestein induzierten Ströme durch die wesentlich besser leitende Einlagerung verstanden wird. Von ähnlichen Vorstellungen geht auch Frischknecht (1973) aus, um das verstärkte anomale Magnetfeld eines leitenden Zylinders in einer leitfähigen Umgebung zu erklären.

In der vorliegenden Arbeit werden die Ergebnisse von Modellexperimenten dargelegt, bei denen das räumliche und zeitliche Verhalten des induzierten elektrischen und magnetischen Feldes in der schwach leitfähigen Umgebung eines gut leitenden Zylinders untersucht wird. An diesem speziellen Beispiel wird insbesondere die Möglichkeit diskutiert, erdmagnetische Induktionsanomalien durch lokal konzentrierte Quasi-Gleichströme zu beschreiben. Daneben wird die Frequenzabhängigkeit des geomagnetischen Induktionspfeiles sowie das Verhalten des nach der magnetotellurischen Methode ermittelten scheinbaren spezifischen Widerstandes für das betrachtete Modell näher untersucht.

2. Das Analog-Modell

In Figur 1 ist der Aufbau der Meßapparatur, mit der erdmagnetische Induktionsvorgänge in mittleren magnetischen Breiten modellhaft untersucht werden können, schematisch angegeben. Ein ebenes Flächenstromsystem mit den Abmessungen $2,9 \text{ m} \times 3,5 \text{ m}$ erzeugt ein horizontales und genähert homogenes induzierendes Magnetfeld im Frequenzbereich zwischen 10^3 Hz und $2,5 \cdot 10^5 \text{ Hz}$. Unterhalb der Stromschicht befindet sich ein elektrolytischer Trog mit einer

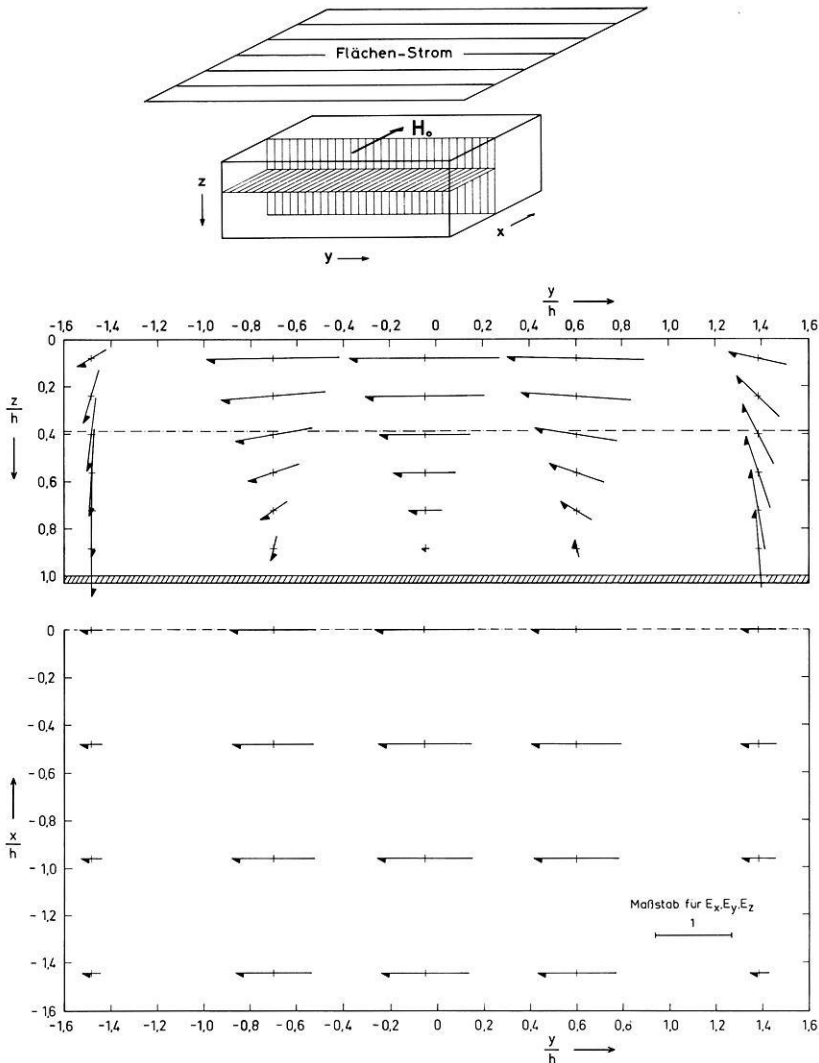


Fig. 1. Projektionen der oszillierenden elektrischen Feld- bzw. Stromvektoren im Innern der elektrolytischen Lösung auf eine Vertikalebene quer zum induzierenden Magnetfeld H_0 (mittleres Bild; schraffiert: die Graphit-Bodenschicht) sowie auf eine Horizontalebene bei $z/h=0,39$ (h = Mächtigkeit der elektrolytischen Lösung). Ganz oben das Versuchsschema. Das elektrische Feld ist durchweg linear polarisiert

Grundfläche von $1\text{ m} \times 1\text{ m}$ und einer Tiefe von $0,31\text{ m}$ als Modell eines leitfähigen Halbraumes. Als Elektrolyt dient eine 7%ige HCl-Lösung, deren Leitfähigkeit bei Zimmertemperatur $39\ \Omega^{-1}\text{m}^{-1}$ beträgt. Um den Trog in seinem Induktionsverhalten besser dem Modell des Halbraumes anzupassen, ist der Boden des Tanks mit Graphitplatten bedeckt (s. auch Dosso, 1966; Leppin, 1977a). Das magnetische Gesamtfeld innerhalb und außerhalb der elektrolytischen Lösung wird mit Hilfe einer kleinen Induktionsspule in allen Komponenten vermessen (Koordinatenursprung in der Mitte des Troges an der Oberfläche der Lö-

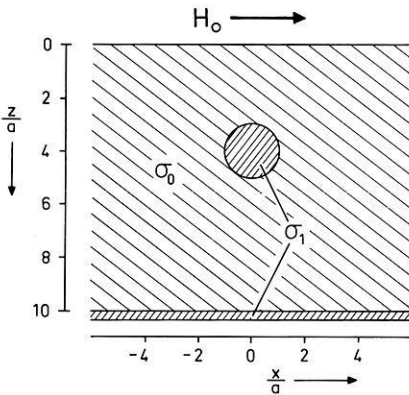


Fig. 2. Querschnitt durch den elektrolytischen Trog mit eingelagertem Zylinder (a = Radius des Zylinders; σ_0 = Leitfähigkeit der elektrolytischen Lösung; σ_1 = Leitfähigkeit des Zylinders und der Bodenplatte)

sung). Das im Elektrolyten induzierte elektrische Feld berechnet sich aus der Spannung zwischen zwei Elektroden, deren gegenseitiger Abstand 0,02 m beträgt.

Eine mögliche Form, das zeitliche Verhalten des induzierten elektrischen Feldes während einer Schwingungsperiode zu veranschaulichen, ist die Darstellung von Amplituden und Phasen zweier zueinander senkrechter Feldstärkekomponenten. Im allgemeinen beschreibt dabei der Endpunkt des elektrischen Feldvektors im Raum eine elliptische Bahn, die sogenannte Feldellipse. Dann und nur dann, wenn die Phasen der beiden Komponenten übereinstimmen bzw. sich um 180° unterscheiden, ist der Feldvektor linear polarisiert mit fester Schwingungsrichtung. Dies ist im reinen Elektrolyten an allen Meßorten der Fall. Das elektrische Feld und damit der Induktionsstrom in der elektrolytischen Lösung ist durchweg linear polarisiert. In Figur 1 ist die Verteilung der elektrischen Feldvektoren in der mittleren Vertikalebene senkrecht zum induzierenden Feld sowie in einer Horizontalebene dargestellt. Bei den Messungen, die bei einer Frequenz von $7 \cdot 10^4$ Hz durchgeführt wurden, stimmt die elektromagnetische Eindringtiefe z_0 des Elektrolyten ($z_0 = \sqrt{2/\sigma_0 \mu_0 \omega}$; σ_0 = Leitfähigkeit der Lösung; μ_0 = Induktionskonstante; ω = Kreisfrequenz) mit der Schichtmächtigkeit h der Lösung überein. Alle Amplituden sind auf das horizontale elektrische Feld in der Mitte des Troges nahe der Oberfläche bei $z/h = 0,06$ bezogen. Die von den Seiten des Troges ausgehenden Störfelder sind in einer Entfernung von ungefähr einer Eindringtiefe nahezu vollständig abgeklungen. Insgesamt bedeuten die Meßergebnisse, daß sich das induzierte elektrische Feld in einem hinreichend großen Raumbereich in der Mitte des Elektrolyten wie bei einem zweifach geschichteten Halbraum mit den gleichen Modellparametern im Sinne der Cagniardschen Theorie verhält (vgl. Leppin, 1977 b).

3. Messungen am eingelagerten Zylinder

Als ein vergleichsweise einfaches Modell einer langgestreckten Leitfähigkeitsanomalie wurde ein Graphitzylinder (Länge = 0,48 m; Radius $a = 0,03$ m; Leitfähigkeit $\sigma_1 = 1,4 \cdot 10^5 \Omega^{-1} \text{m}^{-1}$) mit horizontaler Achse quer zum induzierenden Magnetfeld in die elektrolytische Lösung eingelagert (Fig. 2). Die Zylinderachse befand sich in einer Tiefe von $m = 0,13$ m.

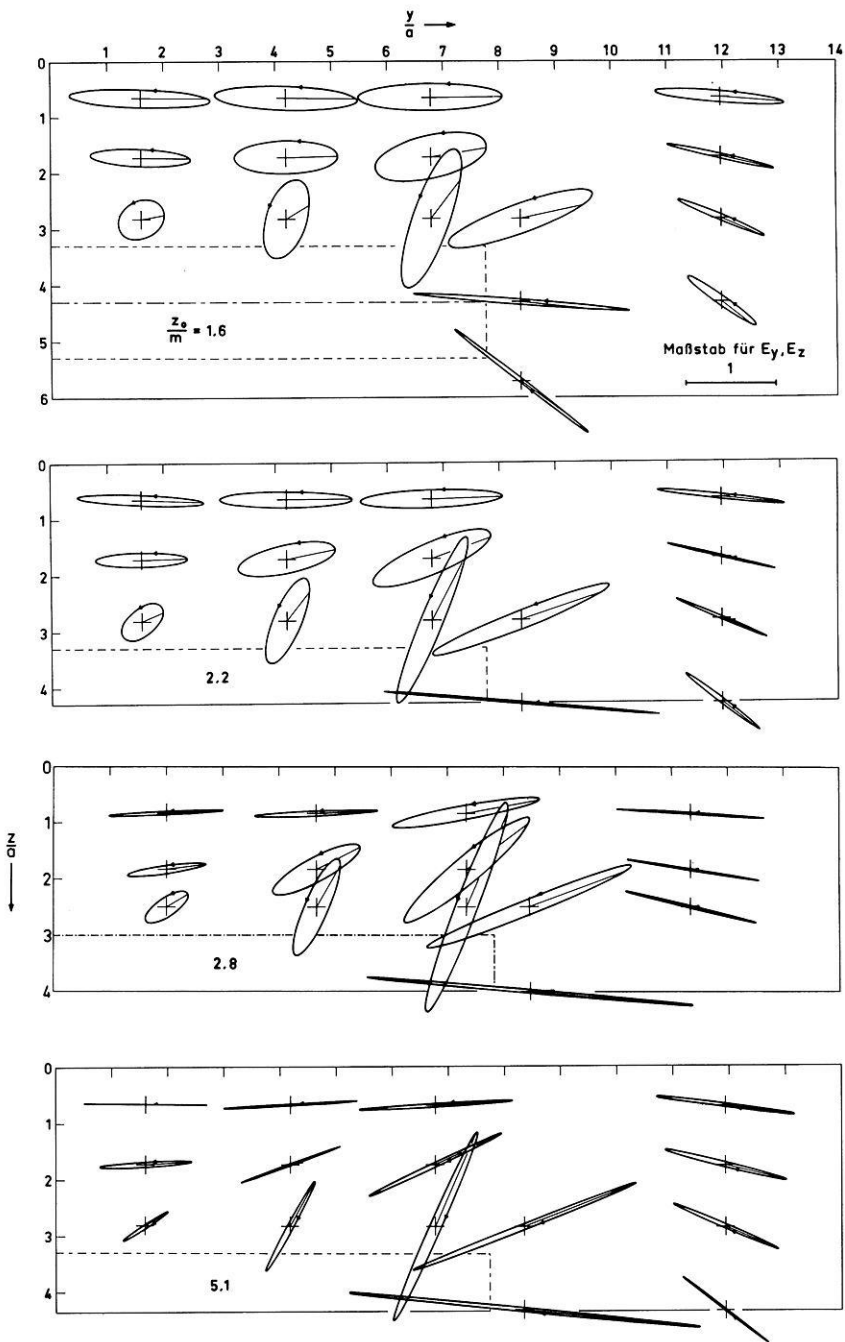


Fig. 3. Feldellipsen des elektrischen Feldes bzw. des Induktionsstromes im Elektrolyten bei eingelagertem Zylinder für verschiedene Frequenzen des induzierenden Magnetfeldes, ausgedrückt durch die relative Eindringtiefe z_0/m (m =Tiefe der Zylinderachse). Vertikalschnitte durch die Zylinderachse. Der Zylindermantel ist gestrichelt mit eingezeichnet. Aus Symmetriegründen ist jeweils nur die rechte Hälfte des Troges dargestellt. Die Amplituden sind angegeben in relativen Einheiten, bezogen auf das ungestörte elektrische Feld im Koordinatenursprung (Mitte der Trogoberfläche). Die eingetragenen Radiusvektoren dienen dem Phasenvergleich. Sie kennzeichnen das elektrische Feld zum Zeitpunkt des Maximums des ungestörten Oberflächenfeldes

Wie die Modellversuche und Induktionsrechnungen verschiedener Autoren zeigen, kann ein leitfähiges Einbettungsmedium zu einer bedeutenden Verstärkung des im Zylinder induzierten anomalen Magnetfeldes führen. Gegen die Vorstellungen von Frischknecht (1973), Ward et al. (1974) und Rokityansky (1976), nach denen eine endlich lange, gut leitende Einlagerung die in der Umgebung induzierten Ströme gleichstromartig bündelt, spricht jedoch die Polarisierung des elektrischen Feldes in der Umgebung des Zylinders. Die gemessene Verteilung des elektrischen Feldes in der mittleren Vertikalebene $x \equiv 0$ ist in Figur 3 dargestellt für die Frequenzen $1,5 \cdot 10^4 \text{ Hz}$, $5 \cdot 10^4 \text{ Hz}$, $8 \cdot 10^4 \text{ Hz}$ und $15 \cdot 10^4 \text{ Hz}$, entsprechend einem Wert des Induktionsparameters $R_a = \sqrt{\sigma_1 \mu_0 \omega a}$ von 3,9; 7,1; 9,0 bzw. 12,3 und einer relativen Eindringtiefe z_0/m von 5,1; 2,8; 2,2 bzw. 1,6.

Im gesamten untersuchten Frequenzbereich ist das elektrische Feld und damit auch der Induktionsstrom fast überall elliptisch polarisiert. Von der Zylindermitte bei $y=0$ ausgehend, wächst dabei die vertikale bzw. radiale Komponente des elektrischen Feldes mit zunehmender Annäherung an die Zylinderenden immer mehr an, bis die Feldellipsen kurz vor den Zylinderenden deutlich eine radiale Vorzugsrichtung besitzen. Ihre absoluten Größtwerte nehmen Feldstärke und Induktionsstrom jedoch erst vor den Stirnflächen des Zylinders, in der Höhe der Zylinderachse an. Lediglich unterhalb dieser Ebene sind Feld und Strom annähernd linear polarisiert.

Betrachtet man in einem vereinfachten Bild nur die Vorzugsrichtungen der Feldellipsen, so entsteht das Bild einer an den Stirnflächen der Einlagerung erhöhten Stromdichte, veranschaulicht etwa durch Stromlinien, die in den Zylinder hineingezogen werden. Aufgrund der ausgeprägten elliptischen Polarisierung des elektrischen Feldes im Elektrolyten drehen sich jedoch in Wirklichkeit die Feldvektoren während jeder Schwingungsperiode einmal im Raum, so daß im strengen Sinne von zeitlich und räumlich festen Stromlinien nicht mehr die Rede sein kann. Die Annahme großräumig angelegter, durch die leitfähige Einlagerung lokal gebündelter Stromsysteme, wie sie der Vorstellung von Quasi-Gleichströmen entspricht, kann in Grenzfällen eine brauchbare Näherung ergeben, die indes den tatsächlichen physikalischen Vorgängen in keinem Fall voll gerecht wird.

Am gleichen Modell des eingelagerten Zylinders wurden in einer weiteren Versuchsreihe die magneto-tellurischen Feldkomponenten an der Oberfläche des Elektrolyten vermessen. Die daraus nach der Cagniardschen Methode ermittelten scheinbaren spezifischen Widerstände auf einem Querprofil über den Zylinder sind in Figur 4 wiedergegeben; Figur 5 zeigt die entsprechenden Phasendifferenzen zwischen elektrischem und magnetischem Feld. Die Größen sind jeweils als Funktion der Frequenz und des relativen Horizontalabstandes von der Zylinderachse in Form von Isolinien dargestellt. Infolge der hohen Leitfähigkeit der Bodenplatte verkleinert sich der scheinbare spezifische Widerstand mit abnehmender Frequenz an allen Beobachtungsorten. Oberhalb des gleichermaßen gut leitenden Zylinders wölben sich die Isolinien zu höheren Frequenzen hin auf und erreichen einen Scheitelpunkt über der Zylinderachse. Im betrachteten Frequenzbereich erscheint der Zylinder in den Isolinien deshalb qualitativ ähnlich wie eine Erhebung der Bodenplatte. In den Isolinien der Phase bildet

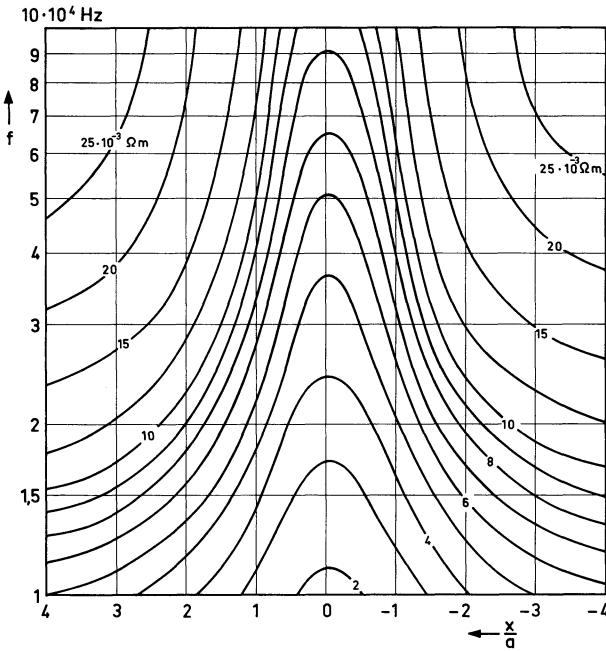


Fig. 4. Linien gleichen scheinbaren spezifischen Widerstandes für das Modell des leitenden horizontalen Zylinders in leitfähiger Umgebung bei transversalem induzierendem Magnetfeld (f =Frequenz)

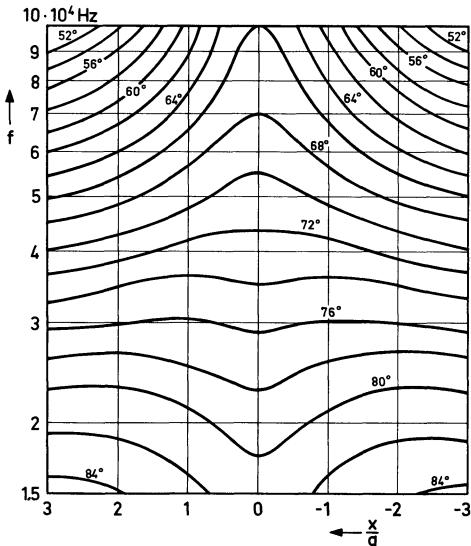


Fig. 5. Linien gleicher Phasendifferenz zwischen elektrischem und magnetischem Feld (sonst wie Fig. 4)

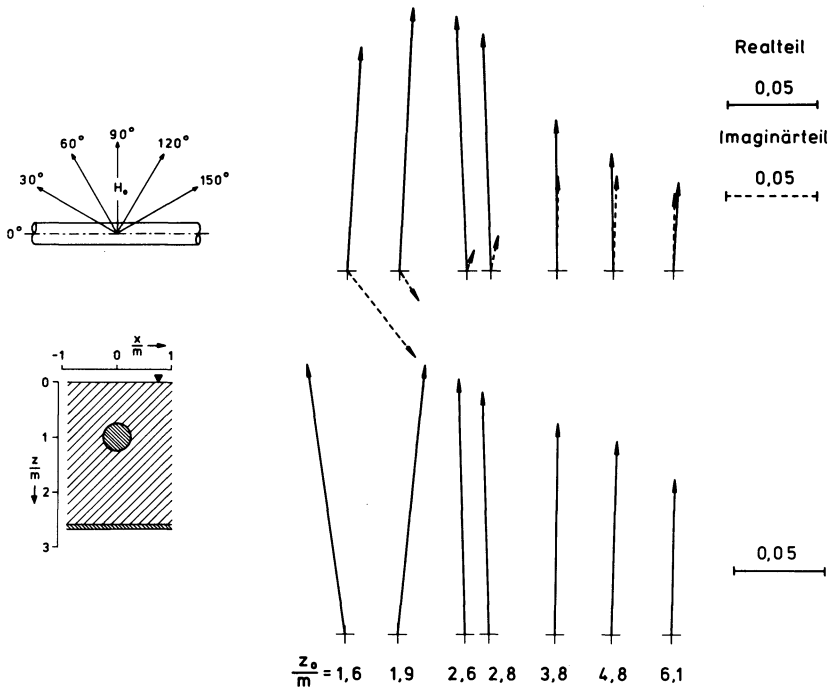


Fig. 6. Geomagnetische Induktionspfeile für das Modell des leitenden horizontalen Zylinders in leitfähiger Umgebung bei verschiedenen Frequenzen, entsprechend unterschiedlicher relativer Eindringtiefe z_0/m (m = Tiefe der Zylinderachse). Rechts oben eine getrennte Darstellung von Real- und Imaginärteil des komplexen Induktionspfeiles. Das Streichen der Modellanomalie ist in der Bildebene waagrecht, wie im Versuchsschema links oben angezeigt, zusammen mit den fünf Orientierungen des induzierenden Magnetfeldes, aus denen die Pfeile hergeleitet sind. Der Meßort an der Oberfläche des Elektrolyten ist in der Lageskizze links unten besonders gekennzeichnet

sich die Leitfähigkeitsanomalie ebenfalls ab. Für höhere Frequenzen als $4 \cdot 10^4$ Hz wölben sie sich oberhalb des Zylinders auf, für niedrigere hingegen satteln sie sich ein. Die Isolinien der Phase können demnach möglicherweise als Interpretationshilfe dienen, um zwischen einem eingelagerten Störkörper und einer Schichtaufwölbung als Ursache einer Induktionsanomalie zu unterscheiden.

Erste Aussagen über die geographische Lage einer Leitfähigkeitsanomalie im Untergrund werden häufig aus der Richtung von geomagnetischen Induktionspfeilen (Wiese, 1965; Schmucker, 1970) gewonnen. Für einige geometrisch einfache Störkörper liegen ebenfalls bereits analytisch bzw. numerisch berechnete Induktionspfeile vor. Am Modell der Kugel in nichtleitender Umgebung untersucht Meyer (1968) die Ausrichtung geomagnetischer Induktionspfeile bei dreidimensionalen Störkörpern. Weidelt (1975) berechnet komplexe Induktionspfeile für einen leitenden Quader in leitfähiger Umgebung. Mit der vorhandenen Modellapparatur ist, wieder am Beispiel des eingelagerten Zylinders, insbesondere die Frequenzabhängigkeit des Induktionspfeiles bei langgestreckten Leitfähigkeitsanomalien nun auch experimentell untersucht worden.

Die in Figur 6 dargestellten Induktionspfeile sind aus dem magnetischen Gesamtfeld an einem Meßort in Zylindernähe ($z=y=0$; $x/m=0,8$) für fünf verschiedene Orientierungen des induzierenden Magnetfeldes abgeleitet (Winkel gegen die Zylinderachse = 30° , 60° , 90° , 120° , 150°). Die Streichrichtung der Modellanomalie liegt dabei in der Bildebene waagrecht. Im Bereich relativ großer elektromagnetischer Eindringtiefe z_0/m , entsprechend niedriger Frequenz, stehen die Pfeile nahezu senkrecht auf der Zylinderachse. Die Abweichungen im Bereich kleinerer Eindringtiefen gehen zurück auf eine apparativ bedingte Verringerung der Meßgenauigkeit bei Frequenzen oberhalb 10^5 Hz. Mit abnehmender Eindringtiefe vergrößert sich jedoch die Länge des geomagnetischen Induktionspfeiles sowie des Realteils des komplexen Induktionspfeiles. Ihr Größtwert wird in diesem Versuch bei einer Eindringtiefe von nahe dem Zweifachen der Tiefe der Zylinderachse erreicht. Ein unterschiedliches Verhalten zeigt lediglich der Imaginärteil des komplexen Induktionspfeiles, der sich mit abnehmender Eindringtiefe des elektromagnetischen Feldes zunächst verkürzt und dann sogar die Richtung wechselt. Der Befund deutet an, daß hinsichtlich der Lage und Ausrichtung einer Leitfähigkeitsanomalie der Realteil des komplexen Induktionspfeiles im allgemeinen aussagekräftiger ist als der Imaginärteil, der theoretisch wie experimentell noch weiterer Untersuchungen bedarf.

Danksagung. Unser besonderer Dank gilt Herrn Professor J. Meyer für sein stetes Interesse am Fortgang der Arbeit. Das Gesamtprojekt der Induktions-Modellversuche wurde von der Deutschen Forschungsgemeinschaft gefördert.

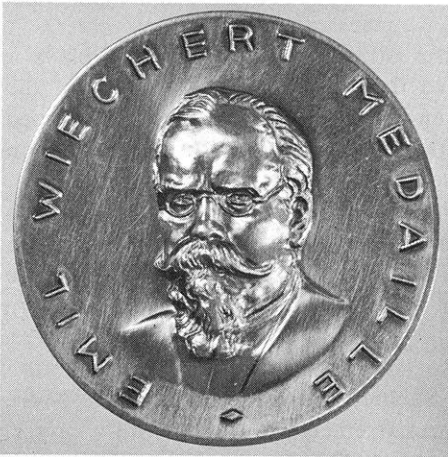
Literatur

- Boldt, B.: Vergleichende Modellversuche zu dem magneto-tellurischen Verfahren nach Cagniard und der magnetischen Tiefensondierung nach der Gradientenmethode. Diplomarbeit, Inst. Geophys., Freie Universität Berlin, 1977
- Dosso, H.W.: A plane-wave analogue model for studying electromagnetic variations. *Can. J. Phys.* **44**, 67–80, 1966
- Frischknecht, F.C.: Electromagnetic scale model study of geophysical methods using a plane wave source. Diss., University of Colorado, Dept. of Electrical Engineering, 1973
- Leppin, M.: Modellversuche zur erdmagnetischen und magneto-tellurischen Tiefensondierung mit Hilfe eines elektrolytischen Troges. *Geophys. Abh., Inst. Geophys., Freie Universität Berlin*, Heft 6, Berlin: Reimer-Verlag 1977 a
- Leppin, M.: Analogue model experiments for electromagnetic induction in three-dimensional conductors. *Acta Geodaet., Geophys. et Montanist. Acad. Sci. Hung.* **12**, 319–326, 1977 b
- Meyer, J.: Über die Richtungsveränderlichkeit des geomagnetischen Induktionspfeiles bei endlicher Leitfähigkeit. *Z. Geophys.* **34**, 195–211, 1968
- Rokityansky, I.I.: Interpretation of electric conductivity anomalies (in Russian). *Geofiz. Sb. Akad. Nauk SSSR*, No. **58**, 1974
- Rokityansky, I.I., Kulik, S.N.: Effect of body length on the MVP anomalous field (in Russian). *Geofiz. Sb. Akad. Nauk Ukrainian SSSR*, No. **47**, 1972
- Rokityansky, I.I., Kulik, S.N., Shuman, V.N.: Theoretical fundamentals of magnetic variation profiling (MVP). In: *Geoelectric and Geothermal Studies*, KAPG Geophysical Monograph, A. Ádám, ed.: pp. 105–123. Budapest: Akadémiai Kiadó 1976
- Schmucker, U.: Anomalies of geomagnetic variations in the southwestern United States. *Bull. Scripps Inst. Oceanogr.* **13**, 1–165, 1970

- Steveling, E.: Erdmagnetische Tiefensondierung mit Variationen und Pulsationen im Einflußbereich der norddeutschen Leitfähigkeitsanomalie. Diss., Math.-Nat. Fak., Univ. Göttingen 1973
- Ward, S.H., Ryu, J., Glenn, W.E., Hohmann, G.W., Dey, A., Smith, B.D.: Electromagnetic methods in conductive terranes. *Geoexploration* **12**, 121–183, 1974
- Weidelt, P.: Electromagnetic induction in three-dimensional structures. *J. Geophys.* **41**, 85–109, 1975
- Wiese, H.: Geomagnetische Tiefentellurik. Dt. Akad. Wiss. Berlin, Geomagn. Inst. Potsdam, Abh. Nr. 36, Berlin: Akademie-Verlag 1965

Eingegangen am 5. Dezember 1977 / Revidierte Fassung 17. April 1978

Presentation of the Emil Wiechert-Medal to Leon Knopoff, Los Angeles, on March 7, 1978 at Münster



“The Earth Has Music for Those Who Listen”

To the physicist, seismologist and musicologist Leon Knopoff the earth has music indeed which however can be appreciated only if its rules are understood.

The Executive Committee of the Deutsche Geophysikalische Gesellschaft has, during its meeting on October 13, 1977, decided to bestow its highest award, the Emil Wiechert-Medal, on Professor Leon Knopoff. The medal bears the name of the first president of the Deutsche Geophysikalische Gesellschaft following its foundation in 1924. Since first awarded in 1955 to Julius Bartels the Emil Wiechert-Medal has been conferred on Beno Gutenberg, Albert Defant, Inge Lehmann, Sydney Chapman and Ludwig Biermann. Today it will be awarded for the seventh time. In this, the 50th year after the death of its first president, the Deutsche Geophysikalische Gesellschaft awards the Emil Wiechert-Medal to a scientist who in his research has penetrated the solid earth in width and depth.

The experiment in the field or in the laboratory was always stimulating and challenging for you as a theoretical physicist. In particular your investigations with long period surface waves produced important new knowledge on the structure of the earth's upper mantle and its regional differences.

During your systematic study of lateral heterogeneities you came to Germany for the first time in 1960 to explore differences in the upper mantle of southern Germany and the Alps—using a network of long period seismometers. Similar expeditions followed to the Mediterranean, South America and Antarctica. Today you are preparing to extend the range of penetration into the lower mantle.

The improved quality of the observations required a corresponding improvement of classical interpretation techniques. The theory of propagation of seismic waves in layered and in laterally inhomogeneous media, as well as their scattering and anelastic attenuation, has been advanced significantly by you. In particular it became necessary to develop inversion methods which permitted the establishment of the multitude of possible models compatible with the observations. The hedgehog-method devised by you and Keilis-Borok is a most powerful search procedure.

The analysis and synthesis of processes at the earthquake focus plays a key role in your research. You established the body force equivalence of the seismic dislocation model. An analogue and numerical model was developed to understand the sequences of earthquakes observed in nature. Finally you advanced a new method of earthquake prediction by pattern recognition.

An appreciable part of your research has been, and is, devoted towards using seismological knowledge to improve models of the state and composition of the earth's interior. Extensive theoretical investigations covered the state of compounds under high pressures, the state and composition of the core and mantle.

Of the many friends cooperating in your work time permits me to mention but a few: Keilis-Borok, Gilbert, Press, Slichter, Burridge and others. More than 180 research papers are witness of an extremely fruitful scientific career.

As a Member of the National Academy of Sciences and as a Fellow of the American Academy of Arts and Sciences your merits have been previously recognized.

We honour also your distinguished role as secretary of the international Upper Mantle Project. This Project remains the most successful international enterprise in the geosciences—it culminated in a scientific revolution which has changed our thinking. It needed men of your wide and profound knowledge and your ability to stimulate.

It is now my duty and pleasure to award the medal. It bears the inscription: *„Die Deutsche Geophysikalische Gesellschaft verleiht die Emil Wiechert-Medaille an Leon Knopoff, Los Angeles, in Anerkennung seines umfassenden Beitrages zur seismologisch-physikalischen Erforschung des Erdinnern“.*

Karl Fuchs

Vorsitzender der
Deutschen Geophysikalischen Gesellschaft

Book Reviews

Physik des Planeten Erde. Ergebnisse geophysikalischer Forschung. R. Lauterbach (Herausgeber), 266 Seiten, 88 Abbildungen und 13 Tabellen. Stuttgart: Ferdinand Enke Verlag 1975.

Es ist sicher kein leichtes Unterfangen, auf 266 Seiten eine Enzyklopädie der Physik des Planeten Erde in Kurzform darzustellen. Die Auswahl und Darbietung des Materials ist notgedrungen subjektiven Kompromissen unterworfen und hängt natürlich ganz stark von dem Leserkreis ab, den man mit dem Buch ansprechen möchte. Eine Aufzählung der Kapitelüberschriften zeigt das breite Gebiet, das in dem Buch von insgesamt 12 Autoren behandelt wird:

1. Kosmogonie und Erdentstehung (von K. Schmidt und H.J. Treder)
2. Fortschritte der Erforschung des Mondes (von M. Reichstein)
3. Paläogeophysik (von R. Lauterbach)
4. Fortschritte der Magnetosphärenphysik (von C.U. Wagner)
5. Physik der Hochatmosphäre (von J. Taubenheim)
6. Entwicklung der Atmosphäre und Stand ihrer Erforschung (von C. Hänsel)
7. Physikalische Ozeanologie (von P. Hupfer)
8. Physik und Chemie des Erdinnern (von H. Kautzleben und H. Stiller)
9. Fortschritte der Seismologie (von S. Grässl)
10. Paläomagnetismus (von K. Rother)
11. Biogeophysik (von R. Lauterbach)

Eine einheitliche Beurteilung des Buches ist nicht möglich. Unbestritten enthält das Buch eine Fülle von Information über die einzelnen Fachgebiete. Eine sehr gute Einführung und ausgezeichneten Überblick über den Stand der Forschung gibt das Kapitel über die Physik der Hochatmosphäre. Über der Abschnitt „Biogeophysik“ enthält Ergebnisse, welche man sonst nur schwer in der Literatur findet. In anderen Kapiteln beschränkt sich der Text jedoch häufig auf eine etwas trockene Aufzählung geophysikalischer Einzelergebnisse. Man vermißt immer wieder eine geschlossene Betrachtung und Diskussion neuerer Forschungsergebnisse, wie es im Vorwort des Buches versprochen wird: „Ziel dieses Buches ist es vielmehr, die Fortschritte bei der geophysikalischen Erforschung von Bau, Struktur, Dynamik und Funktionsmechanismus der Erde insgesamt .. zu kennzeichnen.“ Warum beschränkt sich die Angabe der Geschwindigkeitsverteilung seismischer Wellen im Erdkörper auf die Wiedergabe der gut 20 Jahre alten Kurven von Gutenberg und Jeffreys-Bullen? Kein Wort über moderne Inversionsverfahren oder die mit der Monte-Carlo Methode erzielten Ergebnisse. Ein Diagramm für die Dichteverteilung in der Erde sucht man vergeblich. Auch die Eigenschwingungen der Erde werden nur in wenigen Zeilen erwähnt. Zweifelhaft ist manchmal auch die didaktische Gestaltung der Abbildungen. Ein Fachfremder wird vermutlich an Abbildung 65 (Typen von Erdkrustenmodellen) keine große Freude haben. Auch für die Abbildung 73 angegebene „Rekonstruktion der Lage der Kontinente“ hätte sich sicher eine etwas eindrucksvollere Darstellung finden lassen, z.B. die nach Dietz und Holden. „Das Modell der Plattentektonik“ wird auf weniger als 2 Seiten und ohne Abbildung behandelt, obwohl die Autoren der Meinung sind, daß „die Plattentektonik eine Vielzahl von geologischen und geophysikalischen Erscheinungen auf verblüffend einfache Weise zu erklären vermag“ Und wenn schon aus Platzgründen um jede Zeile gerungen werden muß, warum hat man dann die Kapitel „Paläogeophysik“ und „Paläomagnetismus“ nicht zusammengelegt? Die Beispiele in dieser Art könnten fortgesetzt werden; das Buch vermag deshalb nicht in allen Punkten zu überzeugen.

R. Schick, Stuttgart

Geological Hazards. B.A. Bolt, W.L. Horn, G.A. Macdonald und R.F. Scott. 328 Seiten mit 116 Abbildungen. Berlin-Heidelberg-New York: Springer 1975.

Das Buch beschäftigt sich mit Umwelteinflüssen, welche sich auf den Menschen und die Natur katastrophenartig auswirken können und deren Beschreibung in das Gebiet der Geologie und der Geophysik fällt. In 7 Kapiteln werden die Auswirkungen von Erdbeben (Verf. Bolt), Vulkanen (Verf. Macdonald), Tsunamis (Verf. Bolt), Hangrutschungen, Bodensenkungen, Schneelawinen (Verf. Scott) und Überschwemmungen (Verf. Horn) untersucht. In einem 8. Kapitel werden einige grundsätzliche Fragen zur Risikodarstellung und zur Risikoversicherung bei Elementarschäden behandelt. Ein Anhang enthält Tabellen mit Angaben über bedeutende Erdbeben, Vulkanausbrüche und Hochwasserfluten.

Bei der Behandlung eines derartig breiten Spektrums müssen die Autoren naturgemäß Kompromisse in der Gestaltung des Textes eingehen. Der Inhalt der einzelnen Kapitel ist deshalb auch nicht für den jeweiligen Fachwissenschaftler geschrieben. Der Text ist vielmehr auf einen breiten Leserkreis zugeschnitten, der sich für Naturkatastrophen interessiert. Die Verfasser verzichten auf eine mathematische und quantitative Darstellung und stellen die anschauliche Beschreibung in den Vordergrund, so daß das Buch ohne spezielle Vorkenntnisse gelesen werden kann. Trotzdem ist der Text alles andere als elementar. Die Verfasser geben klar und informativ eine Einführung in die physikalischen und geologischen Grundlagen von Naturkatastrophen. Sie verzichten nicht darauf, offene Fragen und Kontroversen zu diskutieren. Ein großer Teil des Buches befaßt sich mit bekannten und bedeutenden Naturkatastrophen. Die angegebenen Zahlenwerte machen das Buch auch als Nachschlagewerk interessant. Viele ausgezeichnete Abbildungen tragen dazu bei, das Buch lesenswert und anregend zu gestalten.

R. Schick, Stuttgart

S. Warren Carey: The Expanding Earth. Developments in Geotectonics. 10. Amsterdam-Oxford-New York: Elsevier Scientific Publishing Company 1976, 470 Seiten.

Der Gedanke einer Expansion der Erde im Laufe ihrer Entwicklung ist zweifelsohne außerordentlich faszinierend. Könnte man sich doch die Erde mit einer gleichmäßigen, geschichteten (kontinentalen) Kruste entstanden denken, die erst später als Folge einer Expansion aufriß und dadurch zur Bildung ozeanischer Kruste führte. So paßt dann natürlich die zweifelsfrei erwiesene Neubildung von (ozeanischer) Kruste an den mittelozeanischen Rücken ganz ins Bild einer Vergrößerung der Erdkruste, während die Annahme von Subduktionszonen von Carey völlig abgelehnt wird (einige andere, der Erdexpansionshypothese zuneigende Geowissenschaftler fordern lediglich, daß in den Subduktionszonen weniger Erdkruste verschlungen, als an den mittelozeanischen Rücken erzeugt wird). Leider setzt sich Carey nicht intensiv genug mit unbestreitbaren Erkenntnissen der Geophysik über Subduktionszonen (z.B. der Anordnung der Tiefherdbeben) auseinander, sondern er bringt stattdessen eine Fülle von lauter Einzeldetails, die er im Sinne der Expansionshypothese ausdeutet.

Leider ist in dieser Art das gesamte Buch aufgebaut: Der Leser wird mit einer Fülle von Fakten überschüttet und es fällt recht schwer, deren Wichtigkeit oder Bedeutungslosigkeit im einzelnen zu erfassen. Diese Menge des Materials, die Carey präsentiert, macht es nicht leicht, beim Lesen des Buches die Übersicht und das kritische Mitdenken zu behalten.

Der Wert des Buches liegt eben in dieser ausführlichen Stoffsammlung zur Erdexpansionshypothese, die keine geophysikalische Teildisziplin übergeht: global-tektonische Aspekte, Reinterpretation paläomagnetischer Daten hinsichtlich Erdradiusänderungen, Figur und Asymmetrie der Erde, Rotation der Erde, regional-geophysikalische Erscheinungen (wie z.B. Interpretation der San Andreas Verwerfung) und schließlich die Frage nach der Ursache einer Erdexpansion. Gerade bei dieser Frage legt sich Carey nicht fest ("What causes the Earth to expand?: My first answer is I do not know. Empirically I am satisfied that the Earth is expanding"), sondern trägt nur die verschiedenen, in der Literatur diskutierten Möglichkeiten (z.B. Änderung der Gravitationskonstanten, Phasenänderungen an der Kern-Mantelgrenze) zusammen.

Die Auseinandersetzung mit dem von Carey zusammengetragenen Material ist – trotz der oben erwähnten Schwierigkeit beim Lesen des Buches – auch für den von einem unveränderlichen Erdradius überzeugten Geowissenschaftler reizvoll. Schließlich bleibt doch immer die erfreuliche Aussicht, in naher Zukunft z.B. mit Hilfe der Satellitengeodäsie die Erdexpansionshypothese überprüfen zu können.

L. Engelhard, Braunschweig

J.A. Jacobs: The Earth's Core. International Geophysical Series. London: Academic Press Inc. 1975, Vol. 20, 253 pp., 71 figures. £ 8.50/US \$22, —.

Die Erforschung des Aufbaus und Zustands des Erdkerns und der in ihm ablaufenden physikalischen Prozesse ist zum Verständnis zahlreicher geophysikalischer Phänomene von grundlegender Bedeutung. Nicht nur das erdmagnetische Hauptfeld und die Säkularvariation, sondern auch andere Erscheinungen wie die dekadischen Rotationsschwankungen haben ihren Ursprung im Erdkern. Dabei ist man von einem Verständnis dieser Prozesse noch weit entfernt. Dies gilt um so mehr für vermutete Zusammenhänge zwischen einerseits den Rotationsschwankungen und andererseits dem Erdmagnetfeld, der Erdbebenaktivität, dem Vulkanismus, und möglicherweise sogar klimatischen Schwankungen.

Wer sich über den Stand der Erdkern-Forschung umfassender orientieren wollte als es geophysikalische Gesamtdarstellungen bisher boten, war auf viele, weit verstreute Originalarbeiten angewiesen. Jacobs hat sich mit „The Earth's Core“ der Mühe unterzogen, die wesentlichen Ergebnisse von mehr als 700 Arbeiten in komprimierter Form und thematisch gegliedert darzustellen und zu diskutieren. Seine eigenen Vorstellungen treten zumeist zurück; an verschiedenen Stellen bleibt es dem Leser überlassen, kontroverse Hypothesen kennenzulernen und sich selbst ein Urteil zu bilden. Diese sehr objektive Darstellungsweise ist dem schwierigen Gegenstand angemessen: Gesicherte Erkenntnis gibt es wenig, dafür um so mehr Probleme und ein weites Feld zukünftiger Forschung; wurde doch sogar die Möglichkeit von Konvektion im äußeren Kern angezweifelt und u.a. untersucht, ob Erdbebenwellen im Kern das erdmagnetische Feld erzeugen könnten.

Im 1. Kapitel (General Physical Properties of the Earth) wird der Gesamtaufbau der Erde nach Ergebnissen seismischer Methoden und von Eigenschwingungen dargestellt, wobei die Verhältnisse an der Kern-Mantel-Grenze und der Übergangszone vom äußeren zum inneren Kern eingehend behandelt werden. Leider sind einige Figuren der entsprechenden Modelle wegen anders formulierter Tiefenangaben erst nach Umrechnungen mit dem Text vergleichbar.

Das 2. Kapitel (Origin of the Core) behandelt die Problematik der Kernbildung bei der Erdentstehung. Sie muß sehr früh erfolgt sein, weil z.B. alte Gesteine (2,7 Mrd. Jahre) bereits thermoremanente Magnetisierung zeigen. Viel spricht für eine inhomogene Kondensation der Erde, wobei zuerst der metallische Kern entstand. Doch auch Modelle homogener Kondensation und nachfolgender Differenzierung werden diskutiert.

Das 3. Kapitel (The Thermal Regime of the Earth's Core) behandelt Schmelzpunktkurven und adiabatische Temperaturgradienten, wobei die Deutung des festen Zustands des inneren Kerns und des flüssigen Zustands des äußeren Kerns das eigentliche Problem darstellt. Dabei tritt die Problematik der labilen oder stabilen Schichtung des äußeren Kerns auf, mit den entsprechenden u.U. schwerwiegenden Konsequenzen für die Erzeugung des Magnetfelds. Ferner wird das Problem der Wärmequellen im Kern und der Wärmesenken im Mantel behandelt: Ohne ausreichende Abführung der Wärme durch den untersten Mantel wäre Konvektion im Kern unmöglich. Das Kenntnis-Defizit beruht vornehmlich auf der Schwierigkeit, Schmelztemperaturen und adiabatische Temperaturen genügend sicher abschätzen zu können.

Das erdmagnetische Feld mit Säkularvariation und Feldumkehrungen und deren Ursachen (Dynamotheorie) werden im 4. Kapitel (The Earth's Magnetic Field) behandelt. Dabei wird auch auf das Feldverhalten während eines Polaritätswechsels, die Westwärtsdrift und die Zusammenhänge mit den Rotationsschwankungen der Erde eingegangen.

Das 5. Kapitel (The Constitution of the Core) ist, ausgehend von Zustandsgleichungen, u.a. der (k,p)-Hypothese von Bullen, dem chemischen Aufbau des Kerns gewidmet. Der äußere Kern muß neben Eisen ein leichteres Element, vermutlich Schwefel, enthalten wegen der um 8% zu niedrigen Dichte und der zu hohen seismischen Geschwindigkeit. Dadurch würde auch die Schmelztemperatur auf mit anderen Daten verträgliche Werte erniedrigt werden. Ferner wird u.a. die Möglichkeit eines Gehalts von K^{40} als Wärmequelle im äußeren Kern diskutiert.

Im 6. Kapitel (The Cores of Other Planets) werden Vorstellungen über die Zustände und Bestandteile der Kerne des Mondes und der Planeten Mars, Venus und Merkur besprochen.

Die Literaturangaben (insgesamt 711 Titel) finden sich am Ende jedes Kapitels, während am Buchende nochmals ein Autorenverzeichnis und ein etwas zu knapp geratenes Sachregister vorhanden sind.

Dieses schöne, sachlich ausgewogene und komprimiert geschriebene Buch vermittelt den wesentlichen Erkenntnisstand und ist für Geophysiker unentbehrlich.

K. Strobach, Stuttgart

Concepts in Geostatistics. Richard B. McCammon (ed.). Berlin-Heidelberg-New York: Springer, 1975. 168 pp.

There is an ever increasing need for quantification in modern geology, especially in the fields of exploration for economic mineral resources.

Simultaneously the means for fast handling large amounts of data by electronic data processing have been advancing. Not at the same pace however, has the mathematical background and especially the knowledge in statistics, of geologists developed.

The book "Concepts in Geostatistics" provides an excellent remedy against this lack, and bridges the gap between mathematics and geology by a down-to-earth, though exact presentation of subjects of mathematical statistics to non-mathematicians. Especially helpful for geoscientists, the many examples of application to various fields of geology, sedimentology, petrography and geophysics might prove.

The book has evolved from a two-week summer short course for upgrading geology college teachers in the application of statistics to geology, and deals with Probability, Factor Analysis, Time Series Analysis, Markov Models etc.

While certainly not completely covering the already very wide and diversified field of geostatistics, it provides a clear introduction to this field and can be recommended as such to students as well as practical geoscientists.

J.R. Schopper, Clausthal-Zellerfeld

Wladimir Baranov: Potential Fields and Their Transformations in Applied Geophysics, Geoexploration Monographs, R.G. van Nostrand und S. Saxov (Eds.), XVI, 121 pages, 32 figures, 18 tables, 17 × 24 cm, Cloth. Stuttgart: Gebr. Borntraeger 1975. US\$ 25.30, DM 64, —.

Mit diesem Buch setzt der Verlag eine Reihe von Einzeldarstellungen namhafter Autoren zur Angewandten Geophysik fort, die sich durch ihr hohes Niveau und die klare Darstellungsform schnell einen Platz bei Geophysikern gesichert hat. Baranov will nicht — wie man dem Titel nach vermuten könnte — eine umfassende Darstellung der klassischen Potentialtheorie geben, sondern er beschränkt sich auf die Fragen des magnetostatischen Feldes und des Schwerefeldes in der angewandten Geophysik. Dieses Fehlen an Allgemeinheit der Darstellung (z.B. fehlen Kugelfunktionen völlig, Zylinderfunktionen werden sehr knapp abgehandelt) ist bedauerlich.

In der sonst aber klaren Darstellung nimmt natürlich Baranov's Methode der „reduction to the pole“ zur Interpretation magnetischer Anomalien entsprechenden Raum ein. Daneben wird z.B. auch die Feldfortsetzung nach oben und unten und das Filtern von Anomalien (Trennung von klein- und großräumigen Anteilen) behandelt. Der ausführliche Anhang enthält u.a. Rechnerprogramme für die im Hauptteil des Buches abgeleiteten Algorithmen. **L. Engelhard, Braunschweig**

Plasma Instabilities and Nonlinear Effects. A. Hasegawa. 217 p., Physics and Chemistry in Space 8, ISBN-No. 3-540-06947-X. Berlin Heidelberg New York: Springer 1975.

The occurrence of instabilities in plasma configurations in space and in the laboratory is the rule rather than the exception. In spite of the decisive role of instabilities in the understanding of space plasmas there has been a consistent lack of appropriate books which give a reasonably complete and concise overview of instabilities in space. One problem in writing such a book is the difficulty in ordering and evaluating the vast amount of literature on instabilities. This book by A. Hasegawa, an active worker in the field, can be considered as a very useful treatment of the subject of instabilities in space plasmas. In style it is a mixture between an advanced text book and an extended review article. The book is divided in four parts. It starts with an introduction into the field of plasma instabilities with a short treatment of negative energy waves. The second chapter deals with microinstabilities in space plasmas. The treatment is mostly based on analytical expansion techniques. It might have been useful to add some recent results on numerical solutions of the plasma dispersion relations. Nevertheless the treatment is very clear and oriented towards understanding of the physics involved. The third chapter deals with macroinstabilities with subdivisions on drift wave instabilities, Rayleigh-Taylor, Kelvin-Helmholtz and current pinch instabilities. In the fourth chapter nonlinear effects associated with plasma instabilities are treated. Here the selection of the topics to be covered is particularly difficult. Consider the large amount of literature on collisionless shocks, for example. The selection of material is a particularly fortunate one in this chapter, however. The book is concluded by a useful summary of necessary conditions of plasma instabilities. In spite of the high price the book is recommended to all researchers in the field of space plasma physics because of the unique presentation of a difficult subject.

F.M. Neubauer, Braunschweig

Crustal Structure of the Rhenish Massif and Adjacent Areas; a Reinterpretation of Existing Seismic-Refraction Data*

W.D. Mooney**

Geophysical and Polar Research Center, University of Wisconsin, Madison, WI 53706, USA

C. Prodehl

Geophysikalisches Institut der Universität, Hertzstr. 16, D-7500 Karlsruhe 21,
Federal Republic of Germany

Abstract. Most of the existing seismic-refraction profiles in the Rhenish Massif/Rhenohercynian zone of Western Germany have been jointly reinterpreted using traveltime and amplitude information. The general pattern of observed phases can be divided into three types; each type corresponds to a distinct kind of velocity structure.

Type I: Throughout the central Rhenish Massif and the adjacent Hessische Senke a strong P-phase reflection from the crust-mantle boundary is recorded in regions where no major volcanic features are crossed by the lines of seismic observations. The average crustal thickness is 28–29 km, the average crustal velocity (excepting sediments) is 6.2–6.3 km/sec, and the crust is nearly homogeneous. This structure is here referred to as the Rhenohercynian crustal model.

Type II: Beneath the southern part of the Rhenish Massif and two areas in the northeast and southeast some structure within the crust is evident. Both an intracrustal and the Moho discontinuities are evidenced by strong reflected phases, the Moho reflection being the stronger one. Along the profiles crossing major volcanic features such as Vogelsberg and central Westerwald, but not beneath the eastern Eifel, the M-discontinuity is heavily disrupted or “smeared” and an intermediate intracrustal boundary at about 20 km depth forms the main reflector for seismic waves. Beneath this boundary the velocity increases gradually from about 7 km/sec to upper-mantle velocities.

Type III: For profiles crossing the northern Rhine Graben area as well as for a line from the Siebengebirge through the Rhenish Massif to the north, east of the Lower Rhine basin, the observed phases indicate only one major seismic boundary at a depth of about 23 km where the velocity

* Contribution within the priority research program of the Deutsche Forschungsgemeinschaft “The driving mechanism of epirogenic movements: Rhenish shield”

Contribution no. 153 Geophysical Institute, University of Karlsruhe

** also Geophysikalisches Institut der Universität Karlsruhe

increases rapidly to 7.3 km/sec. Below this boundary the velocity increases gradually with depth reaching 8 km/sec at 27–28 km.

The occurrence of types I, II, and III can be roughly correlated with tectonic setting. The P_n phase is recorded with variable success and disappears completely on a profile passing the eastern Eifel volcanics, but is clear on the lines through Vogelsberg and central Westerwald. The petrographic differences between these volcanics appear such to be reflected in the behaviour of the seismic waves. Cross sections and areal views are used to display the variations in crustal and upper mantle velocity structure.

Key words: Seismic-refraction profiles – Crustal structure – Lateral variations – Rhenish Massif – Rhenohercynian zone.

Introduction

The Rhenish Massif is part of the Variscan mountain system of western Europe and as such part of the Rhenohercynian zone being located as a consolidated block between the Upper Rhine Graben in the south, the Lower Rhine Basin in the northwest, and the Hessische Senke in the east. Tertiary to Quarternary volcanism is concentrated in the Westerwald, Eifel and Siebengebirge and the adjacent Hessische Senke to the east. Since the Mesozoic the Rhenish Massif has been undergoing uplift, a movement which seems still to be active today. Within the scope of a priority program, sponsored by the German Research Society, aimed at the investigation of vertical movements and their origin, the

Table 1. Profiles observed in the area of the Rhenohercynian zone and reinterpreted in this report with number of recordings (up to January 1971) and references

N1 = Number of explosions which were used for the corresponding profile. N2 = Number of photographic records. N3 = Number of magnetic-tape records

Profile	N1	N2	N3	
02–165–01	10	52	21	German Research Group, 1964; Fuchs and Landisman, 1966a, b; Ansorge et al., 1970; Wangemann, 1970; Fuchs and Müller, 1971; Giese and Stein, 1971; Bamford, 1973; Mueller et al., 1973; Giese, 1976a, b; Müller and Fuchs, 1976; Mooney and Prodehl, 1977
02–215	04	33	16	Meissner and Berckhemer, 1967; Mueller et al., 1969; Wilde, 1969; Meissner et al., 1970; Giese and Stein, 1971; Bamford, 1973; Mueller et al., 1973; Meissner and Vetter, 1974; Rhine-Graben Research Group 1974; Giese, 1976a, b; Meissner et al., 1976a; Mooney and Prodehl, 1977
02–220–05	02	17	00	Strobach, 1963; German Research Group, 1964; Giese and Stein, 1971; Bamford, 1973; Meissner and Vetter, 1974; Rhine-Graben Research Group, 1974; Giese, 1976a, b; Meissner et al., 1976a; Prodehl et al., 1976; Mooney and Prodehl, 1977

Table 1 (continued)

Profile	N1	N2	N3	
02-265	05	39	00	Behnke, 1961 a; Closs and Behnke, 1961; German Research Group, 1964; Hänel, 1964; Giese and Stein, 1971; Bamford, 1973, 1976 a, b; Giese, 1976 a, b; Mooney and Prodehl, 1977
02-350-06	07	19	22	German Research Group, 1964; Fuchs and Landisman, 1966 a, b; Wangemann, 1970; Giese and Stein, 1971; Bamford, 1973; Giese, 1976 a, b; Mooney and Prodehl, 1977
03-250	02	37	00	Hänel, 1963; German Research Group, 1964; Hänel, 1964; Giese and Stein, 1971, Bamford, 1973; Meissner and Vetter, 1974; Bamford, 1976 a, b; Meissner et al., 1976 b; Giese, 1976 a, Mooney and Prodehl, 1977
06-170-20	04	45	08	German Research Group, 1964; Fuchs and Landisman, 1966 a, b; Wangemann, 1970; Giese and Stein, 1971; Bamford, 1973; Giese, 1976 a, b; Mooney and Prodehl, 1977
06-260	04	23	11	Closs and Behnke, 1961; Plaumann, 1961 a; German Research Group, 1964; Giese and Stein, 1971, Bamford, 1973, 1976 a, b; Giese, 1976 a, b; Mooney and Prodehl, 1977
08-000	01	20	00	Plaumann, 1961 b; Hänel, 1963; German Research Group, 1964; Giese and Stein, 1971, Giese, 1976 a; Prodehl et al., 1976; Mooney and Prodehl, 1977
12-260	03	30	06	Hänel, 1963; German Research Group, 1964; Hänel, 1964; Giese and Stein, 1971; Bamford, 1973; Meissner and Vetter, 1974; Bamford, 1976 a, b; Giese, 1976 a; Meissner et al., 1976 b; Mooney and Prodehl, 1977
13-120-09	05	53	20	Stein, 1963; German Research Group, 1964; Giese and Stein, 1971; Bamford, 1973; Mooney and Prodehl, 1977
13-240-20	03	00	55	Giese and Stein, 1971; Bamford, 1973, 1976 a, b; Mooney and Prodehl, 1977
14-010	05	13	34	Giese and Stein, 1971, Thyssen et al., 1971; Giese, 1976 b; Mooney and Prodehl, 1977
14-090-02	02	36	00	German Research Group, 1964; Giese and Stein, 1971; Bamford, 1973, 1976 a, b; Giese, 1976 a, b; Mooney and Prodehl, 1977
16-080	02	19	09	Meissner and Berckhemer, 1967; Meissner et al., 1970; Giese and Stein, 1971; Bamford, 1973; Meissner and Vetter, 1974; Rhine-Graben Research Group, 1974; Giese, 1976 a; Meissner et al., 1976 b; Prodehl et al., 1976; Mooney and Prodehl, 1977
17-240-20	05	00	95	Giese and Stein, 1971; Giese, 1976 a; Mooney and Prodehl, 1977
20-070-22	05	00	59	Giese and Stein, 1971; Weber, 1973; Giese, 1976 a; Mooney and Prodehl, 1977
22-060-17	02	00	13	Mooney and Prodehl, 1977
240-LO-060	8	00	173	Bartelsen, 1970; Giese and Stein, 1971; Meissner and Vetter, 1974; Giese, 1976 a; Glocke and Meissner, 1976; Meissner et al., 1976 a, b; Mooney and Prodehl, 1977

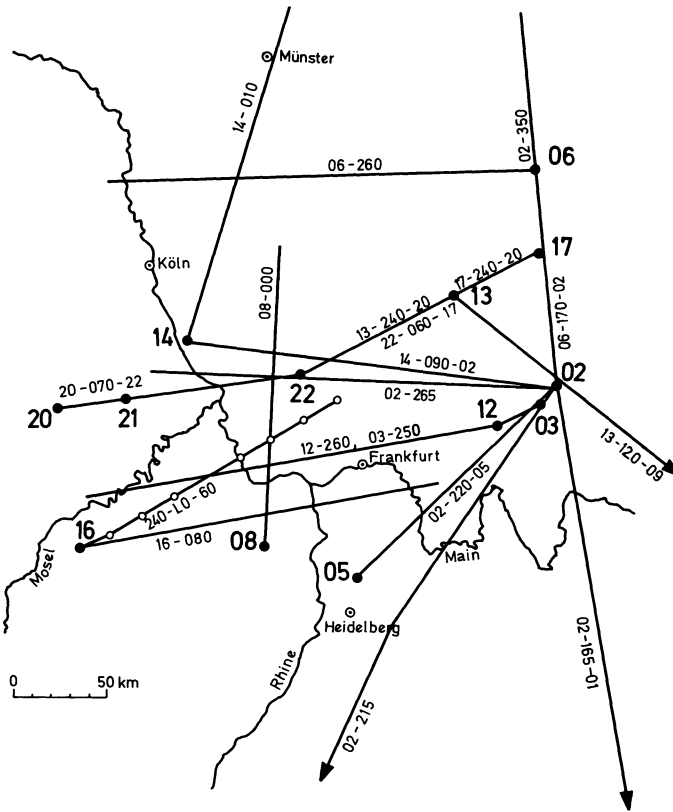


Fig. 1. Location map of seismic-refraction profiles in the Rhenohercynian zone.

Explanation: ●— profiles. 16-080-02 shotpoint code—azimuth—reversed shotpoint code. 12-240 shotpoint code—azimuth—(no reversed shot). ○— common-depth point profile. 240-LO-060 with center near LO=Loreley. Shotpoints: 02 Hilders, 03 Gersfeld, 05 Birkenau, 06 Adelebsen, 08 Kirchheimbolanden, 12 Roms-thal, 13 Dorheim, 14 Mehrberg, 15 Büdingen, 16 Taben Rodt, 17 Bransrode, 20 Birresborn, 21 Bermel, 22 Dorndorf

Rhenish Massif is at present being investigated in detail in a broad-scale geoscientific effort.

Within two former priority programs of the German Research Society: The Deep Structure of Central Europe (1958–1964) and Upper Mantle Project (1965–1974), explosion seismology investigations of central Europe were based mainly on quarry blast observations. A part of these programs covered also the Rhenohercynian zone where numerous quarries firing large explosions are located. These programs are described in general by Giese, Prodehl and Stein (1976); publications dealing with individual profiles are listed in Table 1. This paper concentrates on the reinterpretation of profiles obtained within the area of the Rhenohercynian zone during the two former priority programs mentioned above. Figure 1 shows the quarries used as shotpoints and the corresponding profiles, while Figure 2 shows the geologic position of these quarry blast observa-

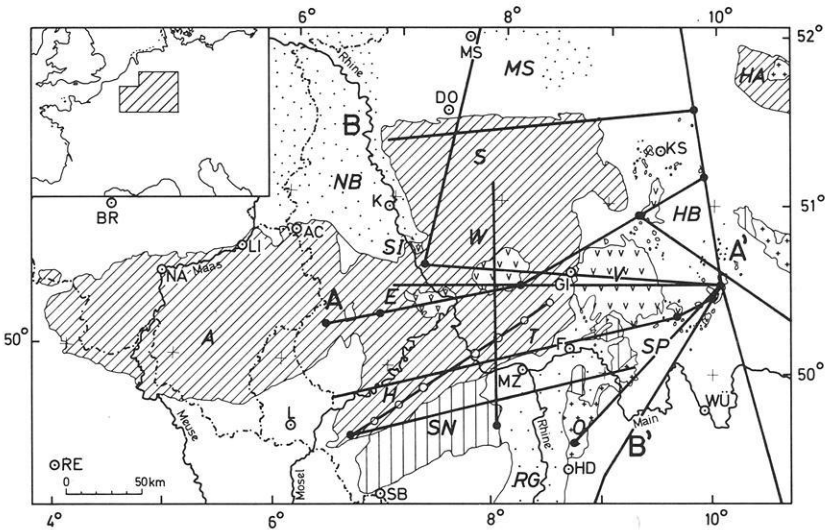


Fig. 2. Location of seismic-refraction profiles on a generalized geologic map of the Rhenohercynian zone and adjacent areas.

Explanation: Quaternary and Tertiary, Mesozoic, Permian, Carboniferous and Devonian, Trachytes and phonolites, Young Tertiary volcanics, Plutonites, Shotpoints and recording lines, Common-depth point profile, **AA'** Location of cross section of Figure 17, **BB'** Location of cross section of Figure 18.

○ Cities: AC Aachen, DO Dortmund, LI Liège, KS Kassel, L Luxembourg, F Frankfurt, BR Bruxelles, K Köln, GI Gießen, SB Saarbrücken, HD Heidelberg, NA Namur, MS Münster, MZ Mainz, WÜ Würzburg.

A Ardennes, *E* Eifel, *H* Hunsrück, *HA* Harz, *HB* Hessische Senke, *MS* Münsterländer Bucht, *N* Neuwieder Becken, *NB* Niederrheinische Bucht, (Lower Rhine Basin), *O* Odenwald, *RG* Rhine Graben, *S* Sauerland, *SI* Siebengebirge, *N* Saar-Nahe trough, *SP* Spessart, *T* Taunus, *V* Vogelsberg, *W* Westerwald

tions. It can be noted that only a few of the profiles run entirely in the Rhenish Massif proper but partly cross the volcanic areas within and east of the Rhenish Massif. As the quarries with usable blasts are spread more or less randomly, the normal requirement of seismic-refraction measurements of having reverse and overlapping profiles could only be fulfilled by one special line running from Birresborn in the Eifel (shotpoint 20 on Figs. 1 and 2) to Bransrode (no. 17) in the Rhön, which was initiated and organized by Stein (1977). Also, the position of the profiles is not always optimal with regard to geologic and tectonic settings of the area.

In spite of these complications the record sections of the numerous profiles exhibit a similar pattern of travelt ime branches which permit a classification of the observed record sections in relation to its geologic and tectonic situation. Conventional flat-layer methods of interpretation using trial and error fitting of traveltimes and amplitudes have been applied with care.

For some profiles the data clearly show that lateral heterogeneities play a major role. We have, however, produced for all profiles flat-layer approximations of the velocity-depth structure. On the other hand, the variable quality

of the available data and the infrequency of reversing and overlapping profiles does not justify the use of a more sophisticated method which would take care of lateral inhomogeneities in particular.

Correlation and Inversion of Phases

As a first step in the correlation we have identified the wave penetrating into the basement, P_g , the Moho reflection, P_mP , and the mantle "head" or diving wave, P_n . In some cases other phases are apparent, while in still other cases P_mP or P_n are either weak or completely missing.

The general patterns of arrivals in the area of investigation can be divided into three types (Figure 3). In type I, we correlate only the P_g , P_mP and P_n arrivals. In type II, in addition to these phases we correlate, beginning at a distance range of 60–90 km, a reflected phase between P_g and P_mP , named here P_iP . Type III, similar to type I, shows only one reflected phase. However, its apparent velocity at the critical distance is much lower than that of the P_mP phase in type I. For this reason we here refer to it as P_iP . The identification of these three types of the pattern of arrivals is important because each type corresponds to a distinct kind of crustal structure. It should be pointed out, however, that the phases P_mP and P_iP are not always true reflections, but often diving waves in a strong gradient zone on top of the corresponding boundary.

Type I: Data and Interpretation

Figures 4–8 show record sections representing type I. The first four profiles (17-240-20, 13-240-20, 22-060-13 and 20-070-22) constitute a reversing and over-

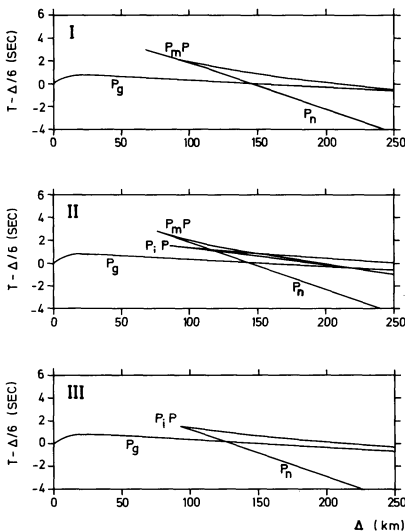


Fig. 3. Three types (I, II, and III) of basic traveltime diagrams identified in the area of investigation (see text for explanation of phases). Each type corresponds to a distinct kind of crustal velocity-depth structure

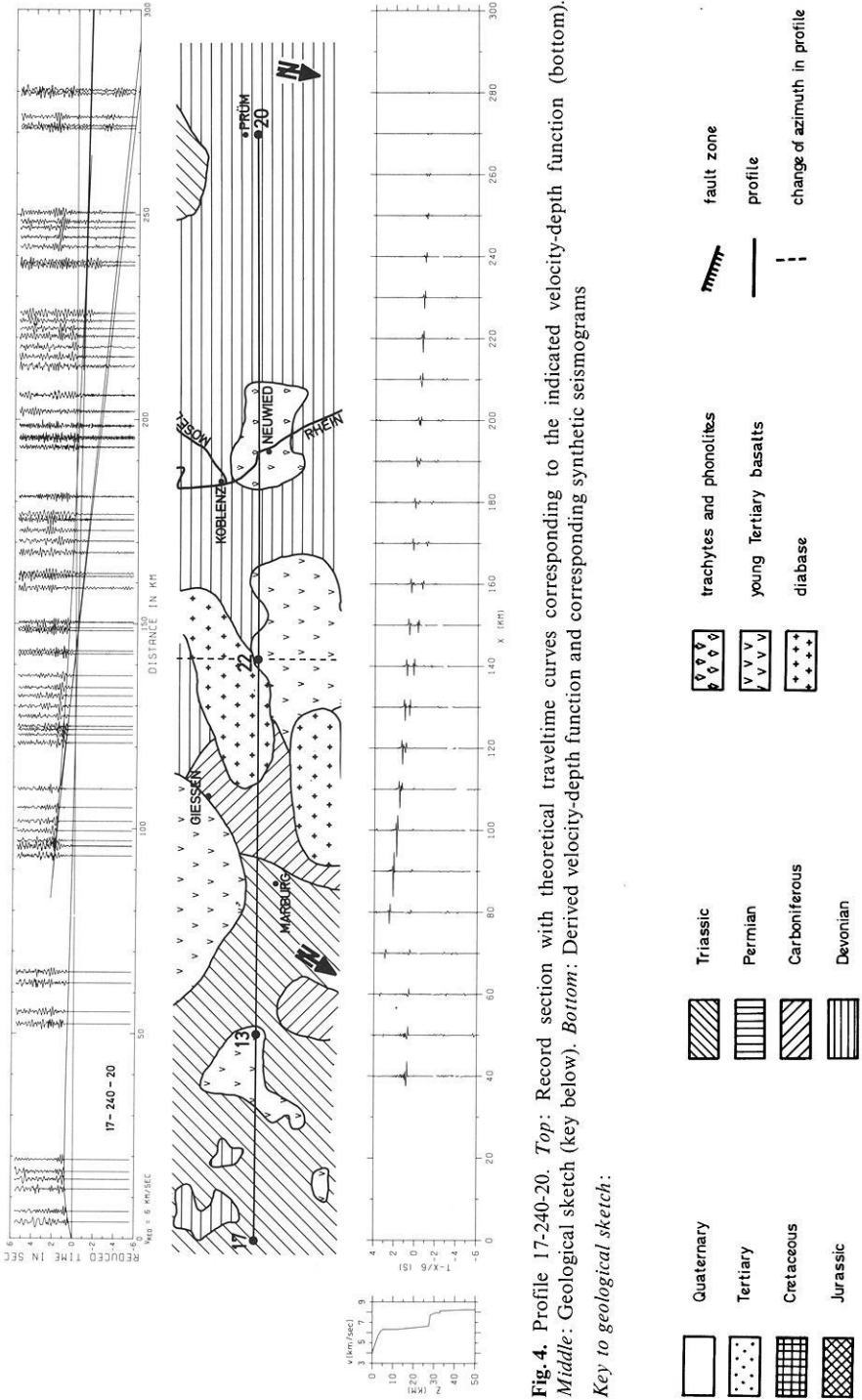


Fig. 4. Profile 17-240-20. *Top:* Record section with theoretical traveltimes curves corresponding to the indicated velocity-depth function (bottom). *Middle:* Geological sketch (key below). *Bottom:* Derived velocity-depth function and corresponding synthetic seismograms

Key to geological sketch:

-  Quaternary
-  Tertiary
-  Cretaceous
-  Jurassic
-  Triassic
-  Permian
-  Carboniferous
-  Devonian
-  trachytes and phonolites
-  young Tertiary basalts
-  diabase
-  fault zone
-  profile
-  change of azimuth in profile

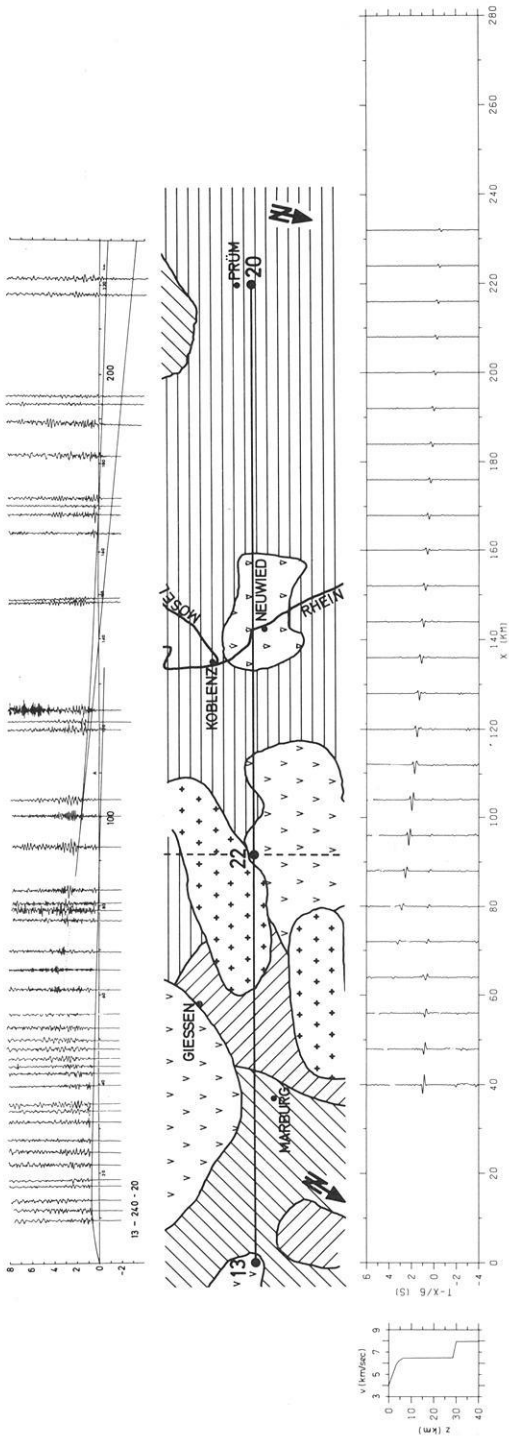


Fig. 5. Profile 13-240-20. *Top*: Record section and theoretical traveltime curves for indicated velocity-depth function. *Middle*: Geological sketch (key given in Fig. 4). *Bottom*: Velocity-depth function and corresponding synthetic seismograms

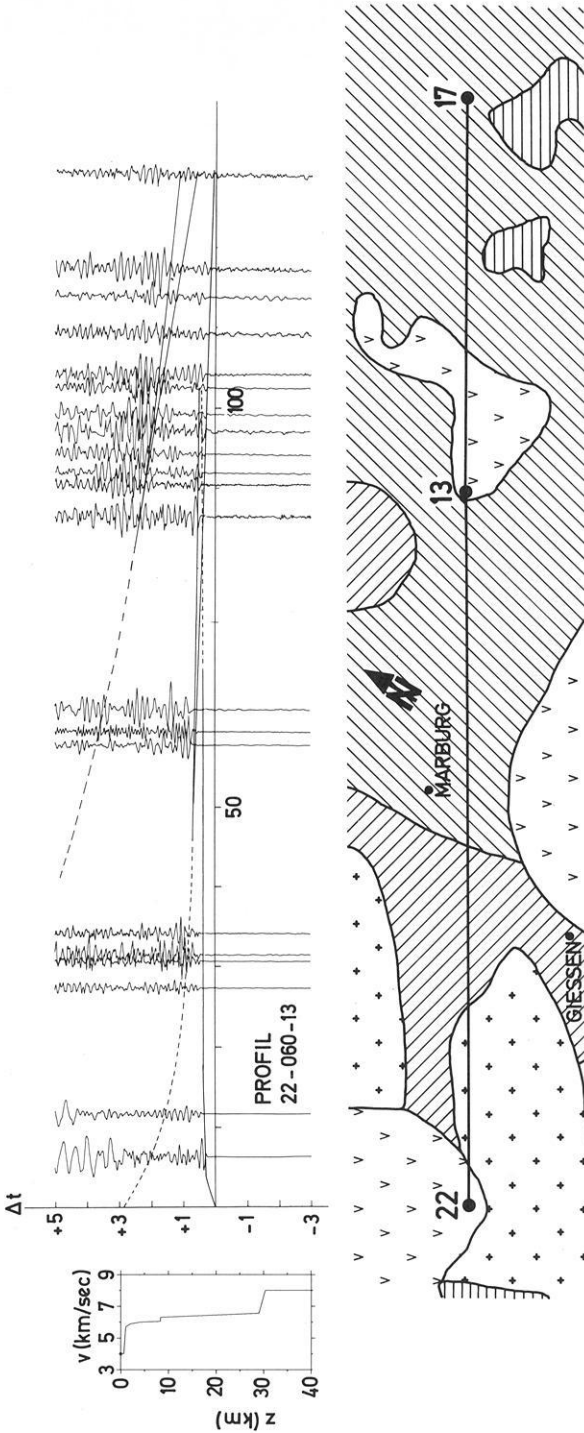


Fig. 6. Profile 22-060-13. Top: Record section with theoretical traveltime curves for indicated velocity-depth function. Broken lines: sub-critical reflections. Bottom: Geological sketch (key given in Fig. 4)

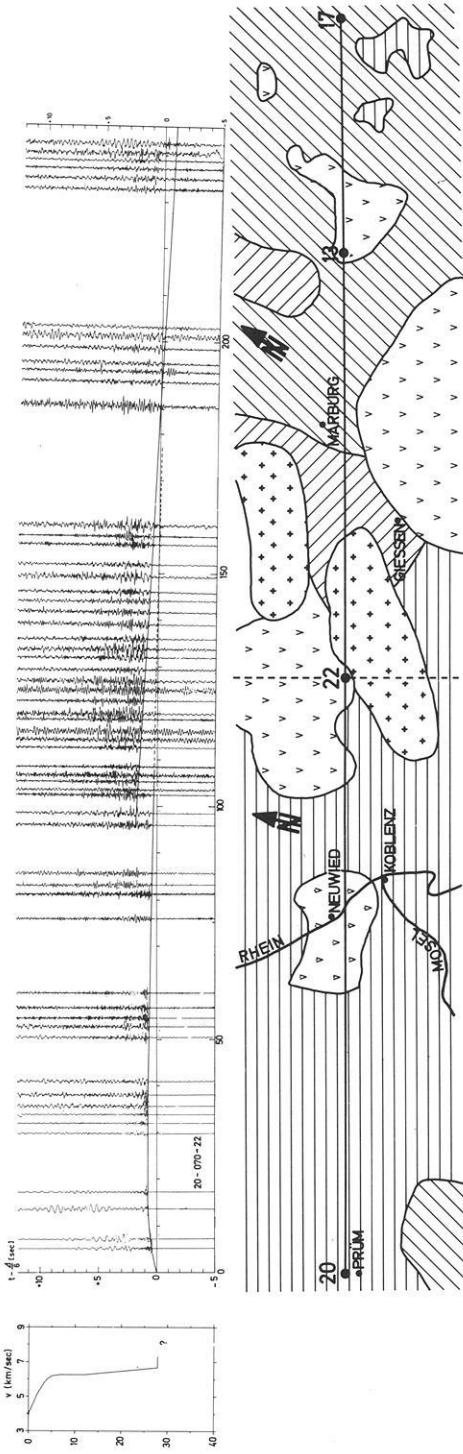


Fig. 7. Profile 20-070-22. *Top*: Record section and theoretical traveltime curves for the indicated velocity-depth function. P_n arrivals are not present. *Bottom*: Geological sketch (key given in Fig. 4)

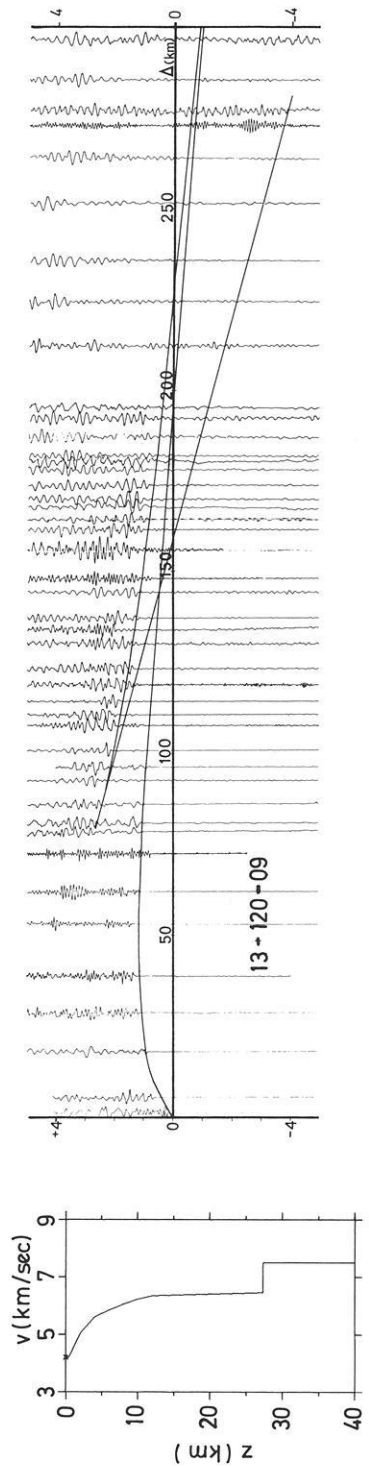


Fig. 8. Profile 13-120-09. Record section and theoretical traveltime curves for the indicated velocity-depth function

Table 2. Velocity-depth models shown in Figure 21. The number of each model refers to the profile shown in Figure 1 from which it is derived

Depth (km)	Velocity (km/s)	Depth (km)	Velocity (km/s)	Depth (km)	Velocity (km/s)	Depth (km)	Velocity (km/s)
02-165-01		02-215		02-220-05		02-265	
0.0	4.0	0.0	4.5	0.0	3.5	0.0	3.5
0.6	4.0	2.0	5.45	0.5	3.5	0.5	3.5
1.3	5.7	4.0	6.0	2.0	5.8	2.0	5.7
4.0	6.0	6.0	6.15	4.0	5.95	3.0	5.8
8.5	6.1	12.0	6.25	8.0	6.28	8.0	6.0
24.0	6.4	13.5	6.25	13.5	6.28	19.8	6.0
27.0	6.8	13.5	5.8	13.5	5.9	19.8	6.5
27.0	7.3	19.7	5.8	20.0	5.9	27.8	7.05
31.0	8.0	19.7	6.75	21.0	6.6	29.8	8.1
34.0	8.0	27.5	6.8	22.0	6.7		
34.0	8.1	28.5	8.3	22.0	6.0		
		33.0	8.48	26.5	6.0		
				26.5	7.0		
				27.5	8.2		
02-350-06		03-250		06-170-02		06-260	
0.0	4.2	0.0	3.1	0.0	4.0	0.0	4.0
0.8	4.2	0.5	3.1	1.3	4.0	1.6	4.0
2.0	5.65	2.0	6.06	3.0	5.6	2.0	5.0
4.0	6.0	4.0	6.15	6.0	6.0	3.3	5.8
6.0	6.2	5.0	6.15	22.2	6.4	6.3	6.0
8.0	6.31	14.8	6.2	22.2	6.8	10.0	6.05
10.0	6.35	14.8	5.5	31.5	8.0	10.0	6.0
28.8	6.35	23.3	5.5			14.0	6.0
30.5	7.9	23.3	7.25			14.0	6.3
		28.0	8.0			27.5	6.6
						28.8	8.0
08-000		12-260		13-120-09		13-240-20	
0.0	4.35	0.0	3.5	0.0	4.2	0.0	4.0
1.8	4.35	2.0	5.5	0.4	4.2	3.4	5.9
2.5	5.35	4.0	5.9	2.0	5.05	4.5	6.2
4.7	6.11	6.0	6.1	4.0	5.6	6.5	6.4
8.0	6.11	8.0	6.2	6.0	5.85	12.0	6.4
8.0	6.0	12.0	6.2	8.0	6.05	28.1	6.5
14.0	6.0	12.0	5.8	10.0	6.2	29.6	7.8
14.0	6.3	18.0	5.8	12.0	6.35		
26.2	6.4	18.0	6.4	27.3	6.45		
27.5	7.9	20.0	6.45	27.3	7.5		
		20.0	5.85				
		24.0	5.85				
		24.0	7.4				
		27.0	8.05				

Table 2 (continued)

Depth (km)	Velocity (km/s)	Depth (km)	Velocity (km/s)	Depth (km)	Velocity (km/s)	Depth (km)	Velocity (km/s)
14-010		14-090-02		16-080		17-240-20	
0.0	4.2	0.0	3.0	0.0	3.0	0.0	4.0
1.0	4.6	0.3	3.0	0.5	3.0	3.0	5.75
4.0	5.8	1.0	5.0	1.5	5.0	4.0	6.1
6.0	5.95	4.0	5.85	4.0	6.1	5.2	6.3
8.0	6.1	6.0	6.0	6.0	6.2	12.0	6.3
12.0	6.15	8.1	6.1	8.0	6.25	27.5	6.6
21.4	6.15	12.0	6.25	28.5	6.6	28.2	7.7
21.4	6.9	12.0	5.8	31.0	8.4	31.0	7.9
(27.0	8.0)	20.0	5.8			33.0	8.08
		20.0	6.6			45.0	8.17
		26.0	6.8				
		32.0	8.1				
20-070-22		22-060-17		240-LO-060			
0.0	4.0	0.0	4.0	0.0	5.25		
3.4	5.8	0.6	4.0	0.3	5.5		
4.0	6.0	1.0	5.7	0.6	5.9		
6.7	6.25	2.0	5.7	2.1	6.35		
12.0	6.25	2.0	5.9	6.0	6.35		
27.8	6.65	4.0	6.0	6.0	6.15		
27.8	7.3	8.3	6.05	15.8	6.15		
(32.0	8.0)	8.3	6.3	15.8	6.65		
		29.0	6.55	17.0	6.65		
		30.3	8.0	17.0	6.45		
				22.2	6.45		
				22.2	6.70		
				23.7	6.70		
				23.7	6.45		
				29.0	6.45		
				30.0	8.1		

lapping system from the Hessische Senke into the Eifel (Figs. 1 and 2). As can be seen on the geologic sketches of Figures 4, 5 and 7, the line avoids significant contact with the young Tertiary basalts of the Vogelsberg and the central Westerwald, but passes through the trachytes and phonolites of the eastern Eifel and adjacent Neuwieder Becken. The fifth profile of type I discussed here, 13-120-09, is located completely outside of the Rhenish Massif.

On all profiles the phases P_g and P_mP are clearly visible, P_mP being always the dominant secondary arrival at distances greater than 90 km. P_n is visible to a varying degree on all profiles of sufficient length (i.e. more than 200 km) except on profile 20-070-22. A slight deviation from the type I-pattern of arrivals is exhibited in profile 22-060-13. Here an additional phase has to be correlated following the P_g phase by about 0.25 seconds.

For all profiles individual velocity-depth functions have been determined (Figs. 4–8). The corresponding computer-produced traveltimes curves have been superimposed on the data. Table 2 lists all velocity-depth functions discussed in this paper. In addition, for profiles 17-240-20 and 13-240-20 synthetic seismograms are shown in Figures 4 and 5. On profiles 17-240-20, 13-240-20 and 20-070-13 the crustal structure is very similar. The velocity increases continuously with depth reaching 6.3 km/s at about 5 km. With further depth it increases only a few tenths of km/s before reaching the crust-mantle boundary. For profiles 22-060-13 and 13-120-09 the velocity-depth functions look similar except for the upper crust.

The structure of the crust-mantle boundary is variable. On profiles 17-240-20, 13-240-20 and 22-060-13 it consists of a thin transition zone at 28–30 km depth with a strong velocity increase from 6.6 to 7.8–8.0 km/s. Profiles 20-070-22 and 13-120-09 show a strong velocity increase up to only 7.3–7.5 km/s; for the former, detailed knowledge of upper-mantle structure is lacking due to the absence of P_n arrivals; for the latter, P_n arrivals indicate that a low velocity of ~ 7.5 km/s seems to continue to greater depths beneath the Moho. For profile 17-240-20 a greater resolution of the structure immediately beneath the Moho can be obtained. Strong P_n arrivals and especially the P_n/P_mP amplitude relationship suggests positive velocity gradients and a velocity step in the uppermost mantle as shown in Figure 4 (see also Table 2).

From the preceding five profiles the following conclusion seems to be justified: the data obtained in the area between shotpoints 20 and 17 define a similar and relatively simple crustal model. In concordance with the geologic province, this model is here referred to as the Rhenohercynian Model (Fig. 9). Basically it is characterized by a rather homogeneous crust between 5 and 28 km depth where the velocity increases only slightly from 6.3 to 6.6 km/s, a thin crust-mantle transition of about one kilometer thickness within which the velocity increases rapidly up to about 7.7 km/s and an additional positive velocity

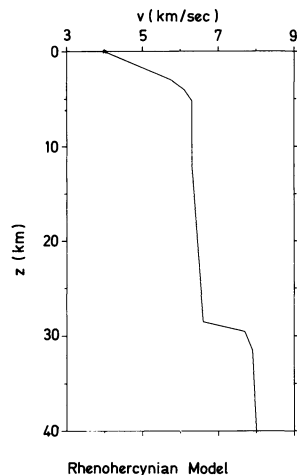


Fig. 9. Rhenohercynian model. Standard crustal model based on the common results of several seismic profiles (see discussion in the text)

gradient beneath the Moho which produces an average upper-mantle velocity of 7.9–8.0 km/s.

Type II: Data and Interpretation

The profiles of type II show greater variability in crustal structure than those of type I. As mentioned above, in addition to the P_mP phase, a second phase, named here P_iP , can be correlated in later arrivals. This phase may be either weaker or stronger than the P_mP phase. The profiles where P_mP is dominant will be discussed first.

The original data of profile 240-LO-060 (Fig. 10), a specially planned wide-angle reflection profile with a common depth point along the strike of Hunsrück and Taunus, are published by Giese et al. (1976, Appendix, Map 3, record section 62) and Meissner et al. (1976a, Fig. 3). Profiles 08-000 (Fig. 11) and 06-260 (Fig. 12) are observed from shotpoints outside the Rhenish Massif. 08-000 crosses the Saar-Nahe-Trough, Taunus and Westerwald in south-north direction, while 06-260 is located at the northern margin of the Rhenish Massif extending westward from the Solling into the Ruhrgebiet. All three profiles show a strong P_mP phase as the dominant feature in the secondary arrivals; however, an additional phase can be correlated indicating an intermediate crustal reflector at about 15 km depth, where the velocity increases from about 6.0 to 6.4 km/s. Similar to the profiles of type I, the presence of clear P_mP arrivals at approximately 80–100 km distance defines a relatively thin crust-mantle transition zone, ~ 1 km thick, with a strong velocity increase. The velocity structure beneath the Moho is rather uncertain because these profiles extend to a maximum range of only 160 to 190 km and show only very weak indications of P_n .

The profiles 14-090-02 and 02-265 (Fig. 13) can also be regarded as belonging to type II. Both profiles cross the young Tertiary volcanics of the Vogelsberg and the central Westerwald. In contrast to the profiles just discussed, the P_mP phase is not the dominant secondary arrival. Rather, the strongest arrivals are formed by a phase reflected from a boundary within the lower crust at about 20 km depth. For these profiles a 6–8 km thick crust-mantle transition is derived by traveltimes and amplitude modelling. Also the observed P_n velocity (~ 8.1 km/s) is greater than on the adjacent profiles.

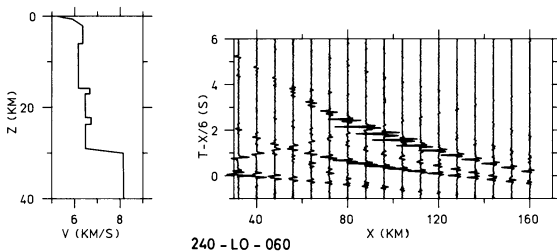


Fig. 10. Profile 240-LO-060. Derived velocity-depth function and synthetic seismograms

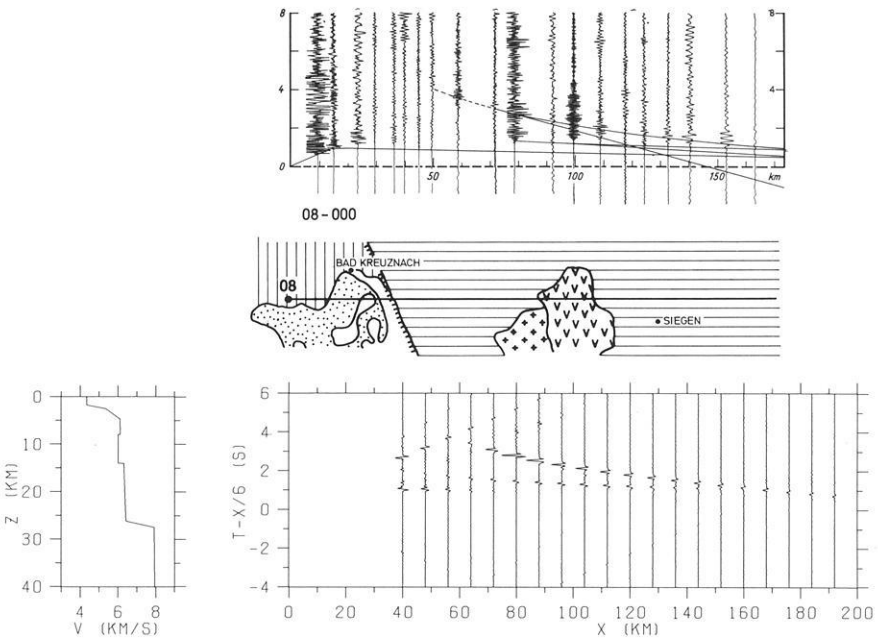


Fig. 11. Profile 08-000. *Top:* Record section with theoretical traveltime curves for the indicated velocity-depth function (bottom left). Broken line: sub-critical reflection. *Middle:* Geological sketch (key given in Fig. 4). *Bottom:* Derived velocity-depth function and synthetic seismograms

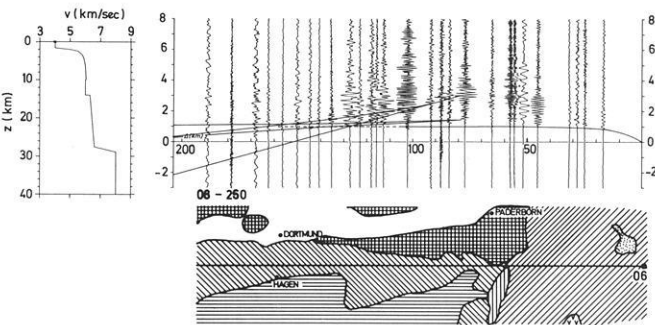


Fig. 12. Profile 06-260. *Top:* Record section with theoretical traveltime curves for the indicated velocity-depth function. *Bottom:* Geological sketch (key given in Fig. 4)

In profile 14-090-02 the close fitting of the traveltimes of the P_g phase (upper part of Figure 13) produces high amplitude P_g arrivals which do not agree with the observed P_g/P_iP amplitude ratio. Consequently in the synthetic-seismogram calculations the upper crust has been simplified to produce amplitude ratios closer to those observed (middle part of Fig. 13). The resulting traveltime deviations are less than 0.2 seconds and may be attributed to lateral inhomogeneities.

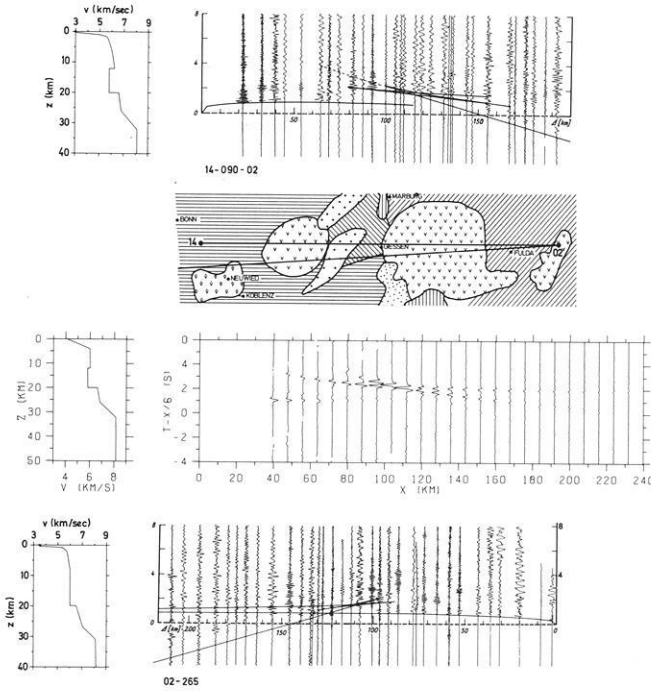


Fig. 13. Profiles 14-090-02 and 02-265. *Top:* Record section for profile 14-090-02 with theoretical traveltim curves for the given velocity-depth function. Broken line: sub-critical reflections. Geological sketch shows the locations of the shotpoints 14 and 20 (key given in Fig. 4). *Middle:* Velocity depth functions and corresponding synthetic seismograms. The best match to the data of profile 14-090-02 is obtained with a zero velocity gradient in the upper crust. *Bottom:* Record section for profile 02-265 with theoretical traveltim curves for the given velocity-depth function

A feature general to all profiles of type II is a lower average velocity (~ 6.0 km/s) in the depth range between 5 and 15–20 km than that observed on most profiles of type I (~ 6.3 km/s).

Type III: Data and Interpretation

Two of the profiles discussed here, 03-250 and 12-260, cross several geological units, and therefore lateral heterogeneities have to be suspected. Both profiles extend from the Hessische Senke through the northern end of the Rhine Graben into the Rhenish Massif. For profile 03-250 (Fig. 14) the later arrivals recorded up to 90 km distance are interpreted as a reflection, here called P_iP , from a boundary within one geological unit, the Hessische Senke. The velocity-depth structure based mainly on these and P_n arrivals is shown in Figure 14. The synthetic seismograms emphasize the indeterminate configuration of the crustal velocity inversion; both adequately model the large-amplitude (P_iP) reflection arrivals which are observed between 65 and 90 km distance. The presence of

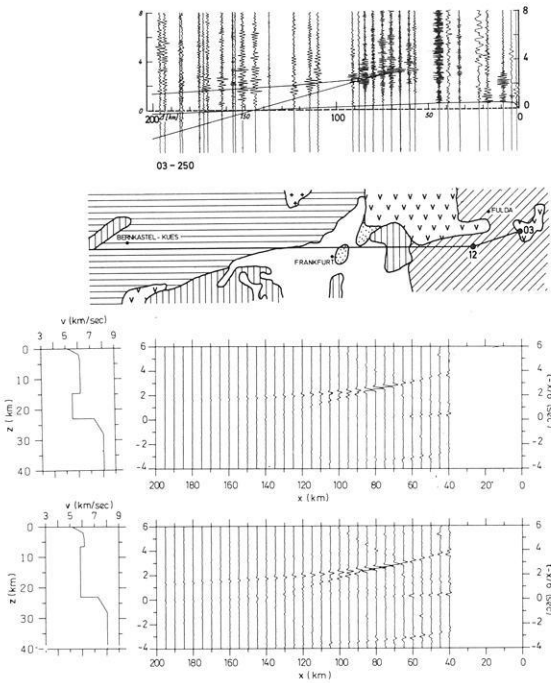


Fig. 14. Profile 03-250. *Top*: Record section with theoretical traveltime curves corresponding to the velocity-depth function given with the first synthetic seismograms. *Middle*: Geologic sketch (key given in Fig. 4). *Bottom*: Velocity-depth functions and synthetic seismograms. The area within the low-velocity zone is the same in the two velocity-depth functions. Both synthetic seismograms are in good agreement with the observed data

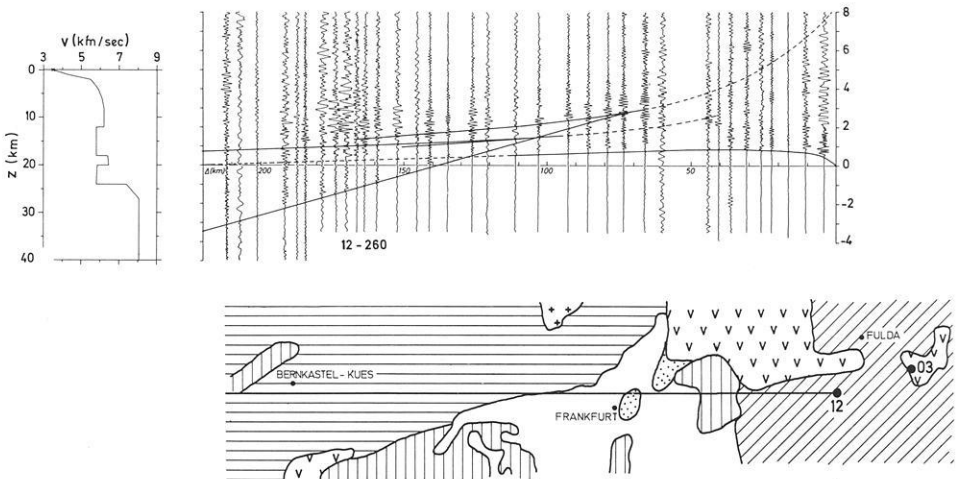


Fig. 15. Profile 12-260. *Top*: Record section and theoretical traveltime curves for the indicated velocity-depth function. Broken lines: subcritical reflections. *Bottom*: Geologic sketch (key given in Fig. 4)

this phase can also be recognized, although less clearly, in profile 12-260 (Fig. 15). For both profiles, the low apparent velocity of the P_iP phase and the well-defined P_n phase are best modelled as shown in Figures 14 and 15. At a depth of 23–24 km the velocity increases rapidly from less than 6 to about 7.3 km/s. The velocity increases then gradually with depth, reaching an upper-mantle velocity of 8.0 km/s at 27–28 km depth. In profile 12-260 we have indicated an additional phase between P_g and P_iP indicative of a complex structure within the region of general velocity decrease. Scattered arrivals between P_g and P_iP are also present in profile 03-250, but have not been modeled.

A similar P_iP phase is observed on profile 14-010 (Fig. 16) extending northward from the Siebengebirge through the Rhenish Massif into the Münsterländer Bucht. At about 100 km distance a phase is weakly indicated in later arrivals which if interpreted as a remnant of a reflected phase would yield a depth of about 30 km. However, because of its uncertainty it is not taken into account for the calculation of the velocity-depth function. The P_n phase is poorly recorded due to the sediments in the Münsterländer Bucht. The derived velocity-depth function shown with synthetic seismograms in Figure 16 is similar to those of profiles 03-250 and 12-260, but does not show a velocity inversion within the crust.

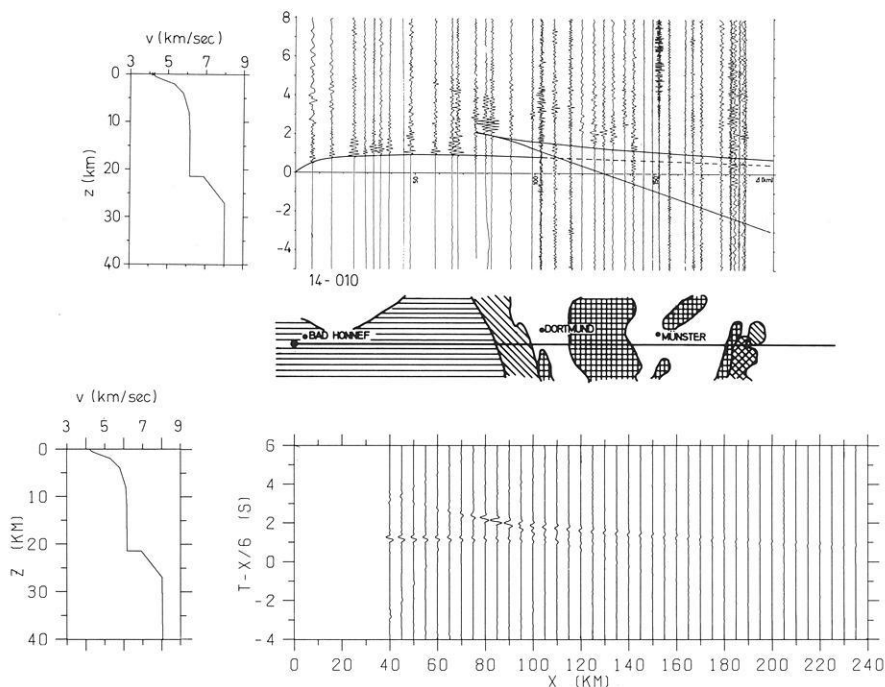


Fig. 16. Profile 14-010. *Top*: Record section and theoretical traveltimes for the indicated velocity-depth function. *Middle*: Geologic sketch (key given in Fig. 4). *Bottom*: Derived velocity-depth function and synthetic seismograms

Crustal Structure of the Rhenish Massif

In Figures 17 and 18 an attempt has been made to compile the main features of crustal structure along two selected lines through the Rhenish Massif. The first line (Fig. 17) crosses the Rhenish Massif in an E-W direction (AA' in Fig. 2). The eastern part of the cross section is located in the Hessische Senke, showing a structure which looks very similar to the Rhenohercynian type: a rather homogeneous crust separated from the upper mantle by a well-defined crust-mantle transition zone. Continuing to the west, beneath the Vogelsberg, the crustal structure gets more complicated. The main features are a seismic discontinuity at a depth of 20 km and the replacement of a clear crust-mantle boundary by a wide transition zone. Entering the Rhenish Massif the Rhenohercynian structure is again encountered. The area of the central Westerwald, covered by young Tertiary basalts, however, shows an anomalous structure similar to the one evident beneath the Vogelsberg. In contrast, the area covered by trachytes and phonolites further to the west in the eastern Eifel and adjacent Neuwieder Becken, while apparently showing an undisturbed Rhenohercynian

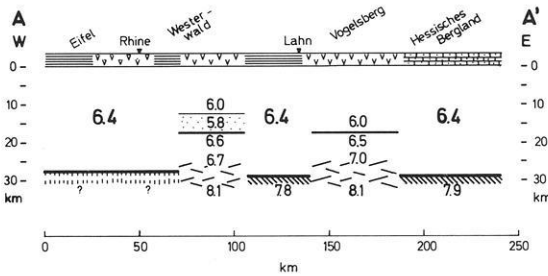


Fig. 17. Cross section through the Rhenohercynian zone (AA' in Fig. 2).

Explanation: Tertiary and Quaternary sediments, Triassic, Devonian, Young Tertiary basalts, Trachyte and Phonolite, strongly reflecting boundary, boundary causing weak or scattered reflected phases, interpolated boundary, positive velocity gradient within the lower crust, upper mantle producing clear P_n arrivals, upper mantle producing weak or no P_n arrivals, crustal velocity inversion, **6.1** average crustal velocity below 3 km depth, **6.1** velocity above or below a boundary

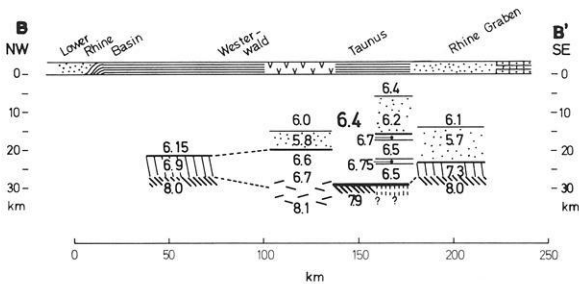


Fig. 18. Cross section through the Rhenohercynian zone (BB' in Fig. 2). Explanation see Fig. 17

crustal structure, shows an anomalous mantle: the clear P_mP arrivals reach an apparent velocity of only 7.3 km/s, and P_n arrivals are not at all visible.

The second line (Fig. 18) crosses the Rhenish Massif in a NW-SE direction (BB' in Fig. 2). The northern part of the section is located at the edge of the Lower Rhine basin. Although it is not evident from its geologic setting, the Rhenish Massif in the region east of Cologne shows an unexpectedly anomalous crustal structure: a seismic discontinuity is apparent at about a 21-kilometer depth followed by an apparently smooth and continuous transition to the upper mantle. Towards the southeast, east of the Siebengebirge, no data are available. The volcanic area of the central Westerwald, whose crustal structure also appears in section AA', also exhibits an intermediate crustal boundary and wide crust-mantle transition zone. Comparing this structure with that observed east of Cologne, it can be suggested that the Rhenish Massif east of the Siebengebirge also consists of a similar anomalous crust. South of this volcanic area the Rhenohercynian crust is encountered. Upon entering the Taunus, the densely-recorded profile (240-LO-060) has revealed a more complex crustal structure whose main features are pronounced discontinuities at about 16 km and 29 km depths. Due

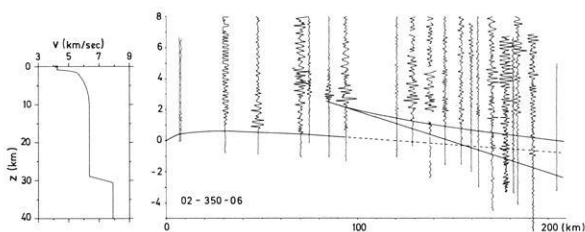


Fig. 19. Profile 02-350-06. Record section and theoretical traveltime curves for the indicated velocity-depth function. Broken line: weak P_g arrivals. The geologic location of the profile is given in Fig. 20

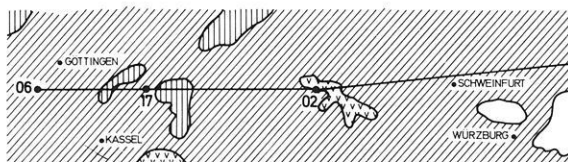
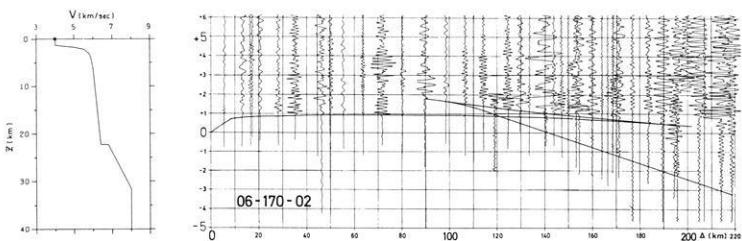


Fig. 20. Profile 06-170-02. *Top*: Record section and theoretical traveltime curves for the indicated velocity-depth function. *Bottom*: Geologic location of profiles 02-350-06 and 06-170-02 (key given in Fig. 4). Strong lateral heterogeneity of crustal structure is evidenced by the differing velocity-depth functions obtained for these reversing profiles (see text)

to the manner of recording and incomplete length of the profile 240-LO-060 it cannot be conclusively stated whether the lack of P_n arrivals is due to mantle velocity structure. Entering the northern end of the Rhinegraben the crustal structure changes yet again: a low-velocity upper crust reaching a discontinuity at 23–24 km is followed by a high-velocity lower crust which gradually reaches upper mantle velocity.

Similar to the two cross-sections just discussed, a rapid change in crustal structure is evident along the line between shotpoints 02 and 06 in the Hessische Senke. The observed data of profiles 02-350-06 and 06-170-02 shown in Figures 19 and 20 evidently do not contain phases representing reflections from the same depth range. The independently derived velocity-depth functions shown with the data are of type I and III, respectively, though they represent crustal structures separated by only 25 km distance. Thus, though it is not evident from the geologic setting, strong lateral heterogeneities are indicated for this region.

Discussion

The results are summarized in Figures 21 and 22. Figure 21 shows the geographic location of the velocity-depth functions obtained for each individual profile, each inlet being placed approximately in the area for which it is representative. Figure 22 summarizes the main features of crustal structure. To a certain extent these maps reflect the features discussed for the individual profiles as type I, II and III. For the major part of the area of investigation a strong reflection from a depth of 28–30 km is found. For the areas of young Tertiary volcanism, this reflection is only weakly indicated, and in three widely separated areas none is observed.

A similar variation is observed for intracrustal reflectors, which some authors refer to as Conrad or/and Sub-Conrad boundaries (e.g. Meissner et al., 1976a).

Such a reflector is notably absent in a large area north and east of the Vogelsberg and in the Eifel west of the Rhine. In contrast, the Hunsrück and Taunus as well as some areas at the northeastern and southeastern edge of the Rhenish Massif do contain intracrustal reflectors. In the areas of young Tertiary volcanism this intracrustal reflector produces by far the dominant phase. Finally, there do exist areas where only a strong reflection from depths within the crust is obtained, while the crust-mantle boundary is only indicated by a gradual transition from crustal to upper-mantle velocities.

The results obtained by the reinterpretation of the profiles discussed in the previous sections differ in detail but in general strengthen and confirm the results published by various authors at earlier stages. Fritsch (1971) discusses in detail results of short-range refraction measurements in the Siegerland. His results for the uppermost crust are confirmed by those presented here for profiles 14-010 and 14-090-02 which cross the neighbouring regions. In the same geographic area, Dürbaum et al. (1971) report the recording of strong reflections with 5–7 seconds two-way traveltime. This may correspond to the strong reflector at about 20 km depth found on both profiles radiating from shotpoint 14 (see Fig. 21), thus supporting the assumption that such a boundary may continue

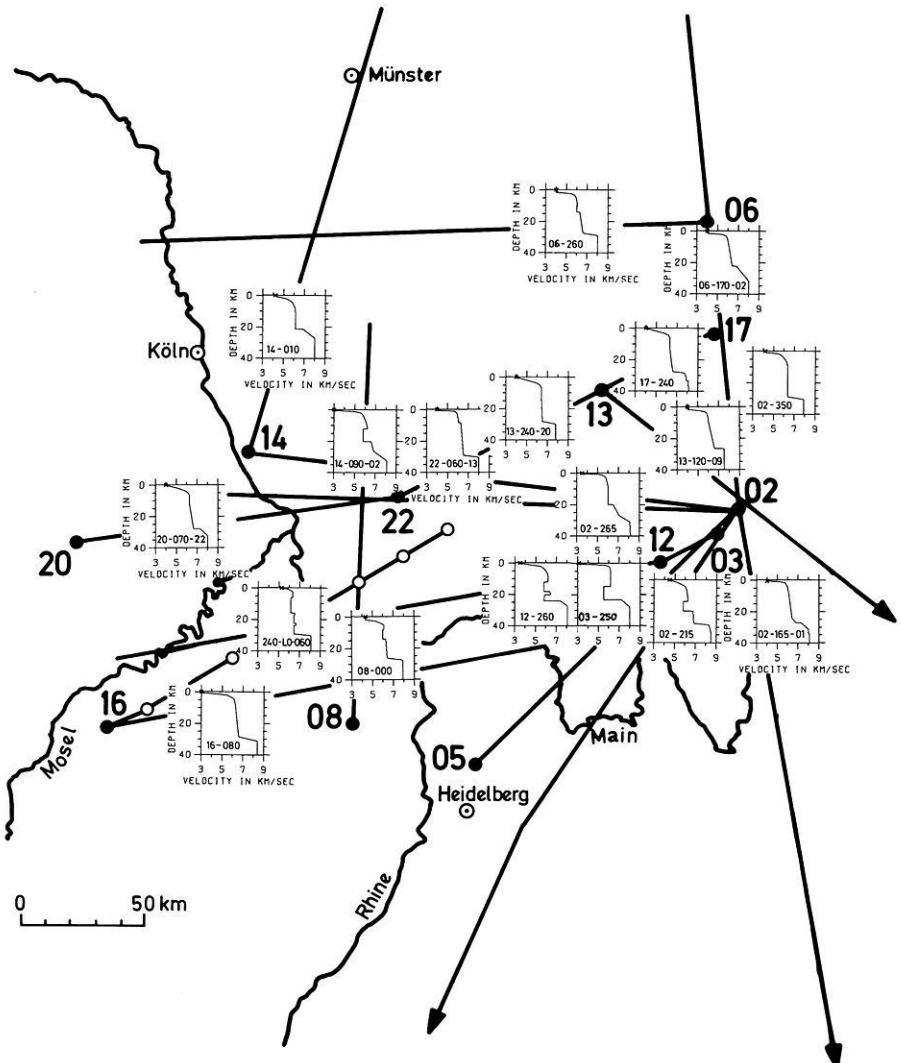


Fig. 21. Map of the areal distribution of the velocity-depth functions derived in the present study. The shot-points are indicated in bold letters. The velocity-depth functions are representative for the area into which they have been placed (see text for discussion)

from the central Westerwald towards the north and northwest, as indicated in Figure 18.

The interpretation of the profile 240-LO-060 is based on our agreement with the phase correlation published by Meissner et al. (1976a). It is therefore not surprising that despite some minor differences the results of depth determination correspond quite well. The major difference is that our M-discontinuity is sharper than that proposed by Meissner et al. (1976a). Though the data of the profile 08-000 are not of good quality, the agreement of the resulting model with the model obtained for profile 240-LO-060 is surprisingly good! As shown by Glocke and Meissner (1976), the interpretation of these

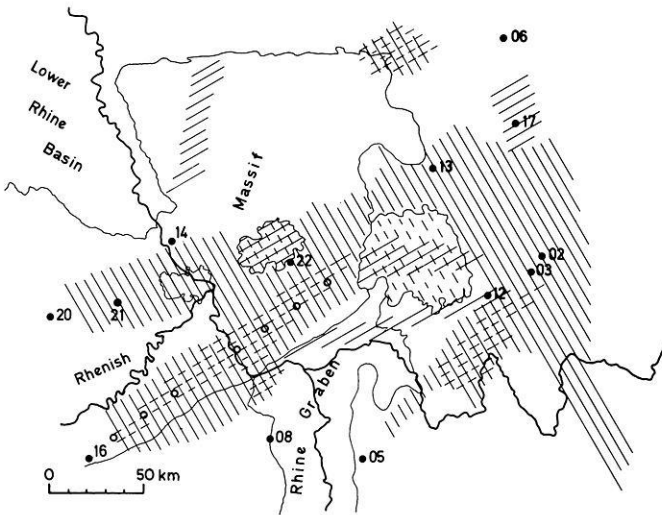


Fig. 22. Map of the area of the Rhenohercynian zone showing main features of crustal structure. Explanation:  strong reflection from a depth of 28-30 km,  weak reflection from a depth of 28-30 km,  strong reflection from a depth between 10 and 22 km,  weak reflection from a depth between 10 and 22 km, ● shotpoints at quarries, ○ shotpoints of wide-angle profile. Profile lines are indicated in Figure 1

wide-angle measurements is in good agreement with that of the near-angle reflection survey carried out along the same line. The first results obtained by Bartelsen et al. (1975) for the seismic-reflection measurements along the geotraverse Rhenoherkynikum, which at its northern end crosses the line 240-LO-060, also indicate a similar depth range of the main reflectors.

Profile 20-070-17 has been interpreted by Weber (1973). The corresponding velocity-depth function given here shows the same average properties of upper and lower crust, but differs in the shape of the crust-mantle boundary. As P_n arrivals have not been recorded on this profile it can neither be decided whether the velocity reaches values of 8 km/s nor to which depth the crust-mantle transition zone extends. The lack of P_n on this profile does, however, argue against strong positive velocity gradients below the crust-mantle discontinuity.

The particular shape of the velocity-depth distribution for the area of the northern end of the Rhine Graben has been discussed by Meissner et al. (1976 b), who also obtain a gradual transition below a reflector at about 22 km depth, below which the velocity increases gradually towards upper-mantle values without forming a distinct crust-mantle boundary. A similar shape of the crust-mantle transition zone is also found for the southern Rhine Graben proper (Edel, 1975; Edel et al., 1975; Prodehl et al., 1976).

The line between shotpoints 02 and 06 and its northward and southward extension has been previously intensively studied (see, e.g., Fuchs and Landisman, 1966 a, b; Wangemann, 1970). Corresponding to the result shown in Figure 20 for profile 06-170-02, Fuchs and Landisman (1966 b) describe a 7.2 km/s refraction line which is also evident in the crustal model which the authors

regard as representative for the South German Triangle. However, in comparing profiles 02-350-06 and 06-170-02, they do not make note of the strong lateral changes which are commented on in the present paper.

The most extensive discussion of the data reinterpreted in this paper has been published by Giese and Stein (1971) and Giese (1976a). These papers summarize all quarry blast data available in Western Germany, and Giese (1976b) discusses them within the corresponding geological framework. Similar to the results shown in Figures 21 and 22, Giese (1976a) shows areas of reduced upper-mantle velocities which, according to his interpretation, are connected with decreased crustal thickness. In our interpretation, we have defined a reflector at about 22 km depth as an intracrustal reflector beneath which the velocity increases gradually to upper-mantle velocity values. Giese's (1976b) conclusion that the existence of a wide crust-mantle transition is connected with areas where young Tertiary volcanism occurred is confirmed by our reinterpretation.

Conclusions

Although there are some gaps in the data in the profiles between shotpoints 17 and 20, it can be stated that the absence of an intermediate phase P_iP is due to crustal structure and not due to insufficient data. The P_n phases also show varying quality, being well recorded on the profile 17-240-20 and apparently absent on profile 20-070-17. This lateral variability may correspond to that which is well known from the results of reflection profiles.

According to the geological situation the Devonian and lower Carboniferous sediments of the Rhenish Massif continue into the Hessische Senke beneath a thin cover of Buntsandstein and Tertiary sediments which at the most are only some hundred meters thick (Henningsen, 1976). This is in agreement with the result described in this paper that in general a "Renohercynian model" can be derived both for the Rhenish Massif and the Hessische Senke, as far as they are not covered by extensive volcanic features. In this context it is to be questioned why the Hessische Senke did not take part in the uplifting process of the Rhenish Massif.

As has been also observed by Giese (1976b), the influence of volcanic events on crustal structure is significant. This is shown in the cross section traversing the Rhenish Massif in an E-W direction (Figure 17). The crustal structure beneath the volcanic area of the eastern Eifel and adjacent Neuwieder Becken (which is covered mainly by phonolites and trachytes) is very different from the structure beneath the central Westerwald and the Vogelsberg where young Tertiary basalts are exposed. The petrologic differences seem to explain the differing seismic wave propagation. The tholeiitic magmas of the Vogelsberg and the central Westerwald may originate within the upper mantle at depths greater than 60 km. During their eruption through the crust the crust-mantle boundary has been heavily disrupted and to a certain extent been replaced by a boundary at intermediate depths of about 20 km. The alcaic volcanism of the eastern Eifel has evidently influenced the upper mantle immediately beneath the Moho, and so attenuates the propagation of P_n waves penetrating

into the uppermost parts of the mantle. There remains, however, a sharp crust-mantle boundary thus giving the strong reflection of seismic energy.

The continuation with depth of surficially visible volcanic and tectonic features is also reflected in the nature of the crustal structure and the crust-mantle transition in other areas. For example, the crustal structure of the central Massif of France changes rapidly when crossing the Limagne Graben and the volcanic areas of the Auvergne as shown by Perrier and Ruegg (1973) and Hirn and Perrier (1974).

As is evident from the cross sections in Figures 17 and 18, and the maps in Figures 21 and 22, in areas where weak or no Moho reflection is found the intracrustal reflector at about a 20–22 km depth produces strong reflected seismic energy. For the southern Rhine Graben Edel et al. (1975) have shown a highly anomalous crust-mantle transition between 20 and 25 km, which may be caused by mass intrusion from the upper mantle or by phase transformations. A similar anomalous structure is also found in that part of the northern Rhine Graben covered by this investigation, and may also be valid for the area east of Cologne and the areas of young Tertiary volcanism. While the crustal structure typical for the Rhine Graben area definitely terminates at the northern end of the Vogelsberg it may be suggested that the Rhine Graben-like crustal structure is also present in the area east of Cologne and the Lower Rhine Basin. While no crustal information is available for the Lower Rhine Basin proper it has been observed (e.g., Ahorner, 1970; Bonjer, 1977) that an earthquake activity similar to that of the Rhine Graben area is observed in parts of the Rhenish Massif and the Lower Rhine Basin.

Concerning the Rhenish Massif proper, the map showing the main features of crustal structure (Figure 22) also indicates a division of the Rhenish Massif parallel to its strike. While the southern part—Hunsrück and Taunus—shows some structure within the crust, the central part—Westerwald and Eifel—is characterized by a more homogeneous crust. This is concordant with the geologic observation that the southern part of the Rhenish Massif has been subjected to a higher grade of metamorphism (Henningsen, 1976). Bonjer (1977) has shown that the areas showing a higher grade of metamorphism such as Hunsrück and Taunus in the south as well as Hohes Venn (northern Eifel) in the northwest are connected with increased microearthquake activity. Also in the northeastern corner of the Rhenish Massif, which is traversed by profile 06-260, slightly increased metamorphism is indicated in the Lippstädter Gewölbe (Hoyer et al., 1974). It does not seem unreasonable to suggest that the areas, where a higher grade of metamorphism and increased seismicity are indicated, have been uplifted versus the adjacent areas and that eventually the intermediate crustal layer found here may be identified with a fossil crust-mantle boundary of pre-Tertiary times.

There remain many open questions which cannot be solved with the data available. Only little can be stated about the Hercynian basement beneath the Devonian and Carboniferous sediments. A special structure of the crust and the upper mantle beneath the Tertiary volcanic areas is clearly indicated by the existing data. However, for a detailed resolution, more data are required. The same is true for the possible differences between the Rhenish Massif and

the Hessische Senke; the structure we have presented here is very similar in these areas. Considering these uncertainties, a contour map of the depth of the crust-mantle boundary has not been constructed.

As only few profiles extend into distances beyond 150 km, the determination of the upper-mantle velocity is rather uncertain. Thus, it is also an open question to what areal extent P_n waves are attenuated when passing the region of Quaternary volcanism of the eastern Eifel. Bamford (1973, 1976a,b) has concluded, on the basis of a larger data set than considered here, that there is significant anisotropy in the upper-mantle P-wave velocity in Germany. As Figure 1 shows, the profiles considered in the present paper are not favorably arranged to detect azimuthal variations in P_n velocity. On the process of preparing this paper the authors did, however, note the indication of another sort of anisotropy, namely anisotropy in the P_n/P_m amplitude ratio. A more complete study of this type of anisotropy seems to be warranted at this time.

The results of this investigation are regarded as the basis for future work in order to fill gaps where necessary and to plan carefully towards the detailed investigation of the crustal structure of selected areas and towards the extension of our knowledge into the lower lithosphere, aiming especially towards the problem of vertical movements in the area of the Rhenish Massif and adjacent areas.

Acknowledgments. The authors are indebted to K. Fuchs for his continuous support and special interest in this investigation. S. Faber, P. Giese, S. Hammer, W. Kaminski and G. Müller supported us with stimulating advice. Helpful discussions with J. Ansorge, D. Bamford, K. Bonjer, R. Emmermann, R. Meißner and A. Stein are gratefully acknowledged. R. Kind kindly provided his revised computer program of the reflectivity method. H. Bartelsen and R. Meissner, Kiel, M. Degutsch, Münster, W. Kaminski, Karlsruhe, A. Stein, Hannover, R. Veas, Clausthal, generously provided largescale record sections.

The research project was made possible by the support of the Deutsche Forschungsgemeinschaft. One of the authors (W.D.M.) was partially supported by NSF grant EAR76-14840 during his stay in Germany. Computation facilities were made available by the Geophysikalisches Institut and the computer center of Karlsruhe University.

References

- Ahorner, L.: Seismo-tectonic relations between the graben zones of the Upper and Lower Rhine valley. In: Illies, H.; Mueller, S. (eds.): Graben problems, Stuttgart: Schweizerbart, 155-166, 1970
- Ansorge, J.; Emster, D.; Fuchs, K.; Lauer, J.P.; Mueller, S.; Peterschmitt, E.: Structure of the crust and upper mantle in the rift system around the Rhinegraben. In: Illies, H., Mueller S. (eds.): Graben problems, Stuttgart: Schweizerbart, 190-197, 1970
- Bamford, D.: Refraction data in western Germany—a timeterm interpretation. *Z. Geophys.* **39**, 907-927, 1973
- Bamford, D.: MOZAIC time-term analysis. *Geophys. J. Roy. Astron. Soc.* **44**, 433-446, 1976a
- Bamford, D.: An updated time-term interpretation of P_n data from quarry blasts and explosions in western Germany. In: Giese, P.; Prodehl, C.; Stein, A.: Explosion seismology in central Europe—data and results. Berlin-Heidelberg-New York: Springer 215-220, 1976b
- Bartelsen, H.: Deutung der seismischen Weitwinkelmessungen in der Rheinischen Masse unter Verwendung neuer Kontroll- und Auswerteverfahren. Diplomarbeit, Univ. Frankfurt, 90 p., 1970

- Bartelsen, H.; Meissner, R.; Murawski, H.: Seismic reflection measurements along the geotraverse Rhenoherynikum. Proc. 14th Ass. Europ. Seismol. Comm. (Trieste 1974), Berlin: Akad. Wiss. DDR, 245–251, 1975
- Behnke, C.: Bericht über die Auswertung refraktionsseismischer Messungen "Westprofil Thaiden". In: Niedersächsisches Landesamt für Bodenforschung (ed.): Kurzfassungen der Vorträge des DFG-Kolloquiums "Erforschung des tieferen Untergrundes in Mitteleuropa" in Frankfurt vom 4.–6.1.1961, NLFH Hannover, 7 p., 1961
- Bonjer, K.: Zusammenhänge zwischen Seismizität und lateralen Variationen der Krustenstruktur im Rheinischen Schild. In: Maronde, D. (ed.): Protokoll über das 2. DFG-Kolloquium im Schwerpunkt "Vertikalbewegungen und ihre Ursachen am Beispiel des Rheinischen Schildes" in Königstein vom 25.–26.11.1977, Deutsche Forschungsgemeinschaft Bonn, 76–79, 1977
- Closs, H.; Behnke, C.: Fortschritte der Anwendung seismischer Methoden in der Erforschung der Erdkruste, Geol. Rundschau **51**, 315–330, 1961
- Dürbaum, H.J.; Fritsch, J.; Nickel, H.: Reflexionsseismik. In: Lang, H.D. (ed.): Geologisch-lagerstättenkundliche und geophysikalische Untersuchungen im Siegerländer – Wieder Spateisenbezirk. Beih. geol. Jb. **90**, 99–124, 1971
- Edel, J.B.: Structure de la croûte terrestre sous le fossé Rhénan et ses bordures. Thèse, Univ. Strasbourg, 207 p., 1975
- Edel, J.B.; Fuchs, K.; Gelbke, C.; Prodehl, C.: Deep structure of the southern Rhinegraben area from seismic refraction investigations. Z. Geophys. **41**, 333–356, 1975
- Fritsch, J.: Refraktionsseismik. In: Lang, H.D. (ed.): Geologisch-lagerstättenkundliche und geophysikalische Untersuchungen im Siegerländer-Wieder Spateisenbezirk. Beih. geol. Jb. **90**, 90–99, 1971
- Fuchs, K.; Landisman, M.: Results of a re-interpretation of the N-S refraction line Adelebsen-Hilders South in West-Germany. Z. Geophys. **32**, 121–123, 1966a
- Fuchs, K.; Landisman, M.: Detailed crustal investigation along a north-south section through the central part of Western Germany. In: Steinhart, J.S.; Smith, T.J. (eds.): The earth beneath the continents, Geophys. Monogr. **10**, Am. Geophys. Un., Washington, D.C., 433–452, 1966b
- Fuchs, K.; Müller, G.: Computation of synthetic seismograms with the reflectivity method and comparison with observations. Geophys. J. Roy. Astron. Soc. **23**, 417–433, 1971
- German Research Group for Explosion Seismology: Crustal structure in western Germany. Z. Geophys. **30**, 209–234, 1964
- Giese, P.: Results of the generalized interpretation of the deep-seismic sounding data. In: Giese, P.; Prodehl, C.; Stein, A. (eds.): Explosion seismology in western Germany—data and results. Berlin-Heidelberg-New York: Springer 201–214, 1976a
- Giese, P.: The basic features of crustal structure in relation to the main geological units. In: Giese, P.; Prodehl, C.; Stein, A. (eds.): Explosion seismology in central Europe—data and results, Berlin-Heidelberg-New York: Springer 221–242, 1976b
- Giese, P.; Hinz, E.; Prodehl, C.; Schröder, H.; Stein, A.: Description of profiles. In: Giese, P.; Prodehl, C.; Stein, A. (eds.): Explosion seismology in central Europe—data and results. Berlin-Heidelberg-New York: Springer 73–112, 1976
- Giese, P.; Prodehl, C.; Stein, A. (eds.): Explosion seismology in central Europe—data and results. Berlin-Heidelberg-New York: Springer 429 p., 1976
- Giese, P.; Stein, A.: Versuch einer einheitlichen Auswertung tiefenseismischer Messungen aus dem Bereich zwischen der Nordsee und den Alpen. Z. Geophys. **37**, 237–272, 1971
- Glocke, A.: Refraktions- und reflexionsseismische Untersuchungen zur Erforschung der Struktur der Erdkruste im Rhein-Main Gebiet, Versuch einer Gesamtdarstellung. Diplomarbeit, Univ. Frankfurt, 1970
- Glocke, A.; Meissner, R.: Near-vertical reflections recorded at the wide-angle profile in the Rhenish Massif. In: Giese, P.; Prodehl, C.; Stein, A. (eds.): Explosion seismology in central Europe—data and results, Berlin-Heidelberg-New York: Springer 252–256, 1976
- Hänel, R.: Ergänzungsmessungen auf dem Profil zwischen Rhön und Hunsrück. In: Mueller S. (ed.): Kurzfassungen der Vorträge des DFG-Kolloquiums "Erforschung des tieferen Untergrundes in Mitteleuropa" in Stuttgart vom 22.–24.4.1963, Universität Stuttgart, 22V5, 2 p., 1963
- Hänel, R.: Ergänzungsmessungen auf einem Profil zwischen Rhön und Ahrgebirge. In: Rosenbach, O. (ed.): Kurzfassungen der Vorträge des DFG-Kolloquiums "Erforschung des tieferen Untergrundes in Mitteleuropa", in Bad Kreuznach vom 9.–12.3.1964, Universität Mainz, 9N5, 2 p., 1964

- Henningsen, D.: Einführung in die Geologie der Bundesrepublik Deutschland. Stuttgart: Enke-Verlag, dtv, Wiss. Reihe 4182. 119 p., 1976
- Hirn, A.; Perrier, G.: Deep seismic sounding in the Limagne graben. In: Illies, H.; Fuchs, K. (eds.): Approaches to taphrogenesis, Stuttgart: Schweizerbart, 329–340, 1974
- Hoyer, P.; Clausen, C.D.; Leuteritz, K.; Teichmüller, R.; Thome, K.N.: Ein Inkohlungsprofil zwischen dem Gelsenkirchener Sattel des Ruhrkohlenbeckens und dem Ostsauerländer Hauptsattel. Fortschr. Geol. Rheinld. u. Westf. **24**, 161–172, 1974
- Meißner, R.; Bartelsen, H.; Glocke, A.; Kaminski, W.: An interpretation of wide angle measurements in the Rhenish Massif. In: Giese, P., Prodehl, C.; Stein, A. (eds.): Explosion seismology in central Europe – data and results. Berlin-Heidelberg-New York: Springer 245–251, 1976 a
- Meißner, R.; Berckhemer, H.: Seismic refraction measurements in the northern Rhinegraben. In: Rothé, J.P.; Sauer, K. (eds.): The Rhinegraben Progress Report 1967. Abh. Geol. Landesamt Baden-Württemberg **6**, 105–108, 1967
- Meißner, R.; Berckhemer, H.; Glocke, A.: Results from deep seismic sounding in the Rhine-Main-area. In: Giese, P.; Prodehl, C.; Stein, A. (eds.): Explosion seismology in central Europe – data and results, Berlin-Heidelberg-New York: Springer 303–312, 1976 b
- Meißner, R.; Berckhemer, H.; Wilde, R.; Poursadeg, M.: Interpretation of seismic refraction measurements in the northern part of the Rhinegraben. In: Illies, H., Mueller, S. (eds.): Graben problems, Stuttgart: Schweizerbart, 184–190, 1970
- Meißner, R.; Vetter, U.: The northern end of the Rhinegraben due to some geophysical measurements. In: Illies, H.; Fuchs, K. (eds.): Approaches to taphrogenesis, Stuttgart: Schweizerbart, 236–243, 1974
- Mooney, W.D.; Prodehl, C.: Crustal and upper-mantle structure in the Rhenohercynian zone of western Germany. Abstract, EOS **58**, 912, 1977
- Müller, G.; Fuchs, K.: Inversion of seismic records with the aid of synthetic seismograms. In: Giese, P.; Prodehl, C.; Stein, A. (eds.): Explosion seismology in central Europe – data and results. Berlin-Heidelberg-New York: Springer 178–188, 1976
- Mueller, S.; Peterschmitt, E.; Fuchs, K.; Emter, D.; Ansoerge, J.: Crustal structure of the Rhinegraben area. In: Mueller, S. (ed.): The structure of the earth's crust based on seismic data. Tectonophysics **20**, 381–392, 1973
- Perrier, G.; Ruegg, J.C.: Structure profonde du Massif Central français. Ann. Géophys. **29**, 435–502, 1973
- Plaumann, S.: Bericht über die Auswertung des refraktionsseismischen Profils Adelebsen. In: Niedersächsisches Landesamt für Bodenforschung (ed.): Kurzfassungen der Vorträge des DFG-Kolloquiums "Erforschung des tieferen Untergrundes in Mitteleuropa" in Frankfurt vom 4.–6.1.1961, NLFH Hannover, 5 p., 1961 a
- Plaumann, S.: Bericht über die Auswertung des seismischen Profils Kirchheimbolanden. In: Niedersächsisches Landesamt für Bodenforschung (ed.): Kurzfassungen der Vorträge des DFG-Kolloquiums "Erforschung des tieferen Untergrundes in Mitteleuropa" in Frankfurt vom 4.–6.1.1961, NLFH Hannover, 9 p., 1961 b
- Prodehl, C., Ansoerge, J., Edel, J.B.; Emter, D., Fuchs, K., Mueller, S.; Peterschmitt, E.: Explosion seismology in the central and southern Rhinegraben – a case history. In: Giese, P.; Prodehl, C., Stein, A. (eds.): Explosion seismology in central Europe – data and results. Berlin-Heidelberg-New York: Springer 313–328, 1976
- Rhinegraben Research Group for Explosion Seismology: The 1972 seismic refraction experiment in the Rhinegraben. – First results. In: Illies, H.; Fuchs, K. (eds.): Approaches to taphrogenesis, Stuttgart: Schweizerbart, 122–137, 1974
- Stein, A.: Ein Gegenschußprofil Kellerwald-Bayrischer Wald. In: Mueller, S. (ed.): Kurzfassungen der Vorträge des DFG-Kolloquiums "Erforschung des tieferen Untergrundes in Mitteleuropa" in Stuttgart vom 22.–24.4.1963, Universität Stuttgart, 22V4, 2 p., 1963
- Stein, A.: Some results of deep seismic sounding in the Rhenish Massif. Report at 33rd JLG Meeting of Working Party on Geodynamics at Walferdange, Luxembourg, May 1977
- Strobach, K.: Ein Gegenschußprofil von der Rhön zum Odenwald. In: Mueller, S. (ed.): Kurzfassungen der Vorträge des DFG-Kolloquiums "Erforschung des tieferen Untergrundes in Mitteleuropa" in Stuttgart vom 22.–24.4.1963, Universität Stuttgart, 22V6, 4 p., 1963

- Thyssen, F.; Allnoch, H.G.; Lüttkebohmer, G.. Einige Ergebnisse geophysikalischer Arbeiten im Bereich der Bramschen Anomalie. *Fortschr. Geol. Rheinld. und Westf.* **18**, 395–410, 1971
- Wangemann, E.-K.. Die Geschwindigkeitsverteilung in der Erdkruste im Gebiet des Süddeutschen Dreiecks, abgeleitet aus refraktionsseismischen Messungen auf einem gestaffelten Nord-Süd-Profil, Diplomarbeit, Univ. Hamburg, 73 p., 1970
- Weber, V.: Zusammenhang zwischen Laufzeit und Form refraktionsseismischer Signale am Beispiel des Profils 20-070 (Birresborn). Diplomarbeit, Techn. Univ. Clausthal, 68 p., 1970
- Wilde, R.: Refraktionsseismische Untersuchungen auf dem Kraichgauprofil. Diplomarbeit, Univ. Frankfurt/Main., 1969

Received April 24, 1978 / Revised version July 10, 1978

The Reflectivity Method for a Buried Source

R. Kind

Seismologisches Zentralobservatorium, Krankenhausstr. 1–3, D-8520 Erlangen,
Federal Republic of Germany

Abstract. The reflectivity method for the computation of theoretical seismograms is extended for the case of a point source buried in a layered medium. Two sources are considered, an explosive source and a vertical single force. Appearing accuracy problems are solved. Poles of Rayleigh waves are shifted away from the real axis of the wavenumber plane by introducing attenuation, in order to allow numerical integration along the real axis. The results of several computations are discussed. This method allows the computation of complete seismograms including surface waves, leaking modes and all body wave phases, including depth phases like pP .

Key words: Theoretical seismograms – Buried source – Thomson-Haskell matrix formalism.

Introduction

The reflectivity method of Fuchs (1968) computes theoretical seismograms for the case of an explosive point source located in a half-space on top of a layered medium. The essential points in this method are the numerical integration over the wavenumber and the application of the Thomson-Haskell matrix formalism. This method has been used extensively in various fields of seismology. It computes complete theoretical seismograms, of course only for the model, for which it was derived. Surface waves and body wave phases, which are due to the depth of the focus in the earth are not computed by this original version of the reflectivity method. The problem of the computation of the displacement at the free surface due to a source buried in a layered medium was solved analytically by Harkrider (1964). In the present paper a method is described, which applies numerical integration to Harkrider's analytical solution. The same accuracy problem, which is well known from the Thomson-Haskell formalism and which was solved by the delta matrix extension (Dunkin, 1965), also appears in the present numerical method. A solution of this problem is given. The numerical

integration is carried out along the real axis in a finite wavenumber window. Rayleigh poles are shifted away from the real axis by the introduction of attenuation. Therefore, theoretical seismograms computed by this method always include the influence of attenuation.

Method

Details of the analytical derivation are given by Harkrider (1964). His results are summarized in the following. He derives the horizontal and vertical surface displacements, u_0 and w_0 , for the case of a layered medium from the matrix equation

$$\begin{pmatrix} \Delta_n \\ \Delta_n \\ \omega_n \\ \omega_n \end{pmatrix} = J \left[\begin{pmatrix} \dot{u}_0/c \\ \dot{w}_0/c \\ 0 \\ 0 \end{pmatrix} + A^{-1} \begin{pmatrix} \Delta_1 \\ \Delta_2 \\ \Delta_3 \\ \Delta_4 \end{pmatrix} \right], \quad (1)$$

where Δ_n and ω_n are the potential coefficients for P - SV waves in the half-space, J is the product of the Haskell matrices (Haskell, 1953) of the half-space and of all layers. A is the product of the Haskell matrices of all layers above the source, and $(\Delta_1, \Delta_2, \Delta_3, \Delta_4)$ is the discontinuous displacement-stress source vector. The homogeneous source layer is divided into two layers at the source level. Only the part of the source layer above the source is contained in A . Rewriting (1) in the form

$$\begin{pmatrix} \Delta_n \\ \Delta_n \\ \omega_n \\ \omega_n \end{pmatrix} = J \begin{pmatrix} W \\ X \\ Y \\ Z \end{pmatrix}$$

and solving for \dot{u}_0/c and \dot{w}_0/c yields (see Harkrider 1964, 1970)

$$\begin{aligned} \dot{u}_0/c &= W - (A_{44} \Delta_1 - A_{34} \Delta_2 + A_{24} \Delta_3 - A_{14} \Delta_4) \\ \dot{w}_0/c &= X - (-A_{43} \Delta_1 + A_{33} \Delta_2 - A_{23} \Delta_3 + A_{13} \Delta_4) \end{aligned}$$

with

$$\begin{aligned} X &= \frac{R_{12} Y + R_{13} Z}{-R_{11}} \\ W &= \frac{R_{14} Y + R_{15} Z}{R_{11}} \end{aligned}$$

and

$$\begin{aligned} Y &= A_{42} \Delta_1 - A_{32} \Delta_2 + A_{22} \Delta_3 - A_{12} \Delta_4 \\ Z &= -A_{41} \Delta_1 + A_{31} \Delta_2 - A_{21} \Delta_3 + A_{11} \Delta_4. \end{aligned}$$

The A_{ij} are obtained from the A_{ij}^{-1} using the relation $A_{ij} = (-1)^{i+j} A_{ij}^{-1}$, which is due to Haskell (1962).

The R_{st} are Dunkin's (1965) delta matrix elements of the J -matrix. Their definition is

$$R_{st} = J \begin{pmatrix} jk \\ lm \end{pmatrix} = J_{jl} J_{km} - J_{jm} J_{kl}$$

where $s = 1, 2, 3, 4, 5, 6$ corresponds to the pairs $jk = 12, 13, 14, 23, 24, 34$ and with the same correspondence of t to lm (see Harkrider (1970)). Or, again in matrix form, one obtains

$$\begin{pmatrix} R_{11} \dot{u}_0/c \\ -R_{11} \dot{w}_0/c \\ 0 \\ 0 \end{pmatrix} = \begin{pmatrix} -R_{11} & 0 & R_{13} & R_{15} \\ 0 & R_{11} & R_{12} & R_{13} \\ 0 & 0 & 0 & 0 \\ 0 & 0 & 0 & 0 \end{pmatrix} A^{-1} \begin{pmatrix} \Delta_1 \\ \Delta_2 \\ \Delta_3 \\ \Delta_4 \end{pmatrix} \tag{2}$$

Symmetry properties of R_{st} and A_{ij} , like $R_{13} = R_{14}$ or $A_{11} = A_{44}$, are used in obtaining (2).

The surface displacements cannot be computed numerically using (2) for lower phase velocities than the velocities of P - and S -waves due to accuracy problems. These are the same problems, which led Dunkin (1965) to introduce in seismology the delta matrices instead of the Haskell matrices. Červený (1974) has proposed to compute Haskell matrix elements from delta matrix elements in order to improve the accuracy. However, attempts to apply this method to avoid numerical problems did not result in great improvements.

For the case of one layer on top of the half-space where the source is on the bottom of the layer, (2) can be written in this form:

$$R_{11} \dot{u}_0/c = (R_{11}^h \ R_{12}^h \ 2R_{13}^h \ R_{15}^h \ R_{16}^h) \begin{pmatrix} -R_{11}^l & 0 & R_{13}^l & R_{15}^l \\ -R_{21}^l & 0 & R_{23}^l & R_{25}^l \\ -R_{31}^l & 0 & R_{33}^l - 0.5 & R_{35}^l \\ -R_{51}^l & 0 & R_{53}^l & R_{55}^l \\ -R_{61}^l & 0 & R_{63}^l & R_{65}^l \end{pmatrix} \cdot (A^l)^{-1} \begin{pmatrix} \Delta_1 \\ \Delta_2 \\ \Delta_3 \\ \Delta_4 \end{pmatrix} \tag{3}$$

$$-R_{11} \dot{w}_0/c = (R_{11}^h \ R_{12}^h \ 2R_{13}^h \ R_{15}^h \ R_{16}^h) \begin{pmatrix} 0 & R_{11}^l & R_{12}^l & R_{13}^l \\ 0 & R_{21}^l & R_{22}^l & R_{23}^l \\ 0 & R_{31}^l & R_{32}^l & R_{33}^l - 0.5 \\ 0 & R_{51}^l & R_{52}^l & R_{53}^l \\ 0 & R_{61}^l & R_{62}^l & R_{63}^l \end{pmatrix} \cdot (A^l)^{-1} \begin{pmatrix} \Delta_1 \\ \Delta_2 \\ \Delta_3 \\ \Delta_4 \end{pmatrix}$$

where h and l stand for half-space and layer, respectively. Watson's (1970) reduced delta matrix extension is used to work with 5×5 matrices instead of 6×6 matrices. Multiplying the two layer matrices first, one obtains

$$\begin{aligned}
 R_{11} \dot{u}_0/c &= (R_{11}^h R_{12}^h R_{13}^h R_{15}^h R_{16}^h) \begin{pmatrix} -A_{22}^l & A_{12}^l & 0 & 0 \\ -A_{32}^l & 0 & A_{12}^l & 0 \\ -A_{42}^l & -A_{33}^l & A_{22}^l & A_{12}^l \\ 0 & -A_{42}^l & 0 & A_{22}^l \\ 0 & 0 & -A_{42}^l & A_{32}^l \end{pmatrix} \begin{pmatrix} \Delta_1 \\ \Delta_2 \\ \Delta_3 \\ \Delta_4 \end{pmatrix} \\
 -R_{11} \dot{w}_0/c &= (R_{11}^h R_{12}^h R_{13}^h R_{15}^h R_{16}^h) \begin{pmatrix} -A_{21}^l & A_{11}^l & 0 & 0 \\ -A_{31}^l & 0 & A_{11}^l & 0 \\ -A_{41}^l & -A_{31}^l & A_{21}^l & A_{11}^l \\ 0 & -A_{41}^l & 0 & A_{21}^l \\ 0 & 0 & -A_{41}^l & A_{31}^l \end{pmatrix} \begin{pmatrix} \Delta_1 \\ \Delta_2 \\ \Delta_3 \\ \Delta_4 \end{pmatrix}. \quad (4)
 \end{aligned}$$

The result of the multiplication of the Haskell layer matrix and the delta layer matrix in (3) is a matrix containing only Haskell elements, and not a new type of elements, as one could expect. If in (4) the Haskell elements for one layer are replaced by elements of the Haskell product matrix of any number of layers, (4) is still true. This was also checked numerically for cases where numerical problems do not appear. In this case the label h means the half space and all layers below the source, and the label l means all layers above the source. Using (4) means doing a (1×5) delta matrix multiplication through the complete model, because R_{11} is needed. When the source level is passed, the elements of the (1×5) product delta matrix must be stored. A (4×4) Haskell matrix multiplication through all layers above the source is also required. Then the first two columns of this Haskell product matrix is used to set up a matrix according to (4). This new matrix is then multiplied with the (1×5) product delta matrix, which contains only layers up the source level. The advantage of using (4) is, that the numerical problems disappeared in all encountered cases. The equations (4) contain much simpler expressions than (2).

Harkrider (1964) has given the displacement-stress source vector for several source types. We will use in the present paper only two of these sources, the vertical single force and the explosive point source. The source vector for the vertical single force is according to Harkrider (1964) $(0, 0, -\bar{L}(\omega)k/(2\pi), 0)$, where \bar{L} is the Fourier transformed force-time function and k the wavenumber. If we express the compressional potential of the wave radiated from the explosive point source as $\bar{L}(\omega) \exp(-ik_x R)/R$, then we obtain for the source vector of the explosive point source, following Harkrider (1964), the expression $(0, -2ik^2 \bar{L}(\omega), 0, 4ik^2 \beta_s^2 \rho_s \bar{L}(\omega))$, where i is the imaginary unit and β_s and ρ_s are the shear velocity and density of the source layer, respectively.

Finally Harkrider (1964) arrives for the considered two sources at the following expressions \bar{u}_0 and \bar{w}_0 for the Fourier transformed surface displacements

$$\begin{aligned}\bar{u}_0 &= - \int_{k_1}^{k_2} \frac{1}{k} \dot{u}_0/c J_1(kr) dk \\ \bar{w}_0 &= -i \int_{k_1}^{k_2} \frac{1}{k} \dot{w}_0/c J_0(kr) dk.\end{aligned}\tag{5}$$

Here the integration is already limited to a finite k -window. J_0 and J_1 are the Bessel functions of order zero and one. The asymptotic approximations of the Bessel functions for large arguments for propagation in positive r -direction is used. Since the integration is carried out along the real axis, attenuation is used to shift the poles away from the real axis. The attenuation is determined by the Q -factor for P - and S -Waves in each layer. The Q -factors are used to determine complex velocities (see Schwab and Knopoff (1972)). The integrals (5) are computed numerically using the trapezoidal rule.

A Test of the Method

In order to test the method, the displacements at the surface of the homogeneous half-space was computed for a vertical single force at a depth close to the surface. This problem is very similar to Lamb's problem (Lamb, 1904). The differences are, that in the original form of Lamb's problem the force is acting at the surface of the half-space, and the effects of attenuation are included in the present solution of the problem. A half-space was chosen with a P velocity of 6.0 km/s, and an S velocity of 4.5 km/s, and a density of 2.5 g/cm³. The attenuation factor Q_α for P waves was 200, and Q_β , the attenuation factor for S waves was chosen to be 4/9 Q_α . The source depth was 1 km. The spectrum $\bar{L}(\omega)$ of the vertical single force $L(t)$ was chosen as follows:

$$\bar{L}(\omega) = \frac{1}{2} \left(1 + \cos \frac{\pi \omega}{\omega_0} \right), \quad -\omega_0 \leq \omega \leq \omega_0\tag{6}$$

where $\omega_0 = 2\pi/T_0$, $T_0 = 1.4$ s (cut-of period). The time function of this spectrum is similar to Lamb's original input signal. The acausality of this input signal is removed by a time shift of half the duration.

In Figure 1 are shown the vertical and horizontal displacements of the Rayleigh wave. The same seismograms are plotted on a 40 times larger amplitude scale in Figure 2, in order to make visible the much smaller P and S waves. The signal forms of all phases are in very good agreement with those obtained by Lamb. Two seismograms from Lamb's paper can be found in Ewing, Jadetzky and Press (1957, Figs.2–18). The same problem was also computed by Müller and Kind (1976) with similar good results, using a different version of the reflectivity method. There are differences to the seismograms obtained by Lamb in the Figure 1 and 2, which result from the somewhat different model. The amplitudes of the Rayleigh waves decay faster than the inverse square root of the distance, which is due to the attenuation. It is also possible to see in

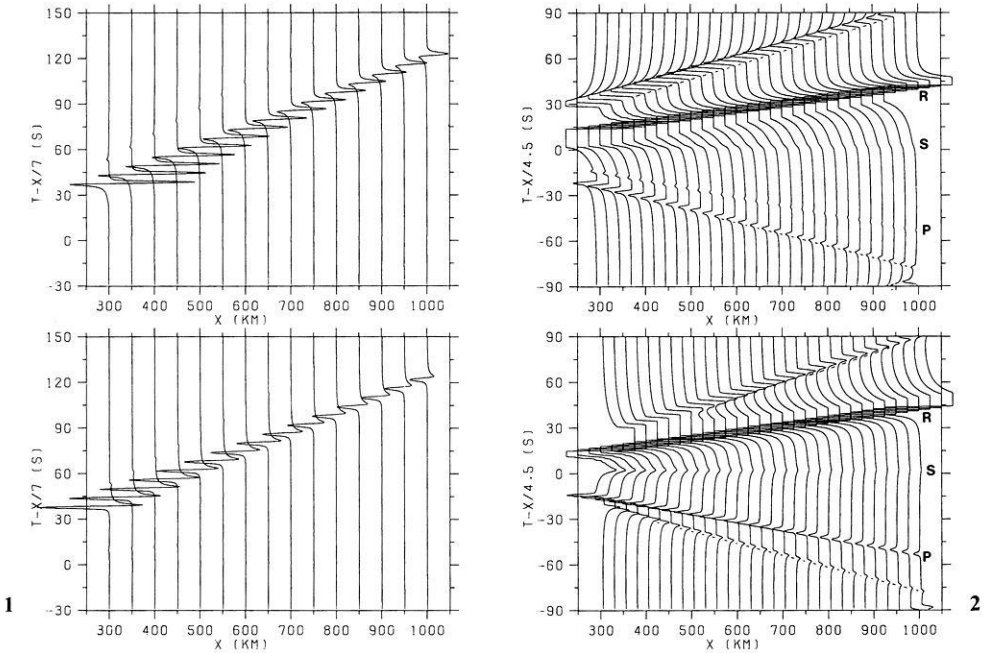


Fig. 1. Theoretical seismograms for Lamb's problem computed with the reflectivity method for a buried source. Top: vertical displacement components (upward motion to the left). Bottom: radial displacement component (motion towards the source to the left). The dominant arrival is the Rayleigh wave

Fig. 2. Same as Figure 1 on a 40 times larger amplitude scale. The Rayleigh wave amplitudes are clipped. Dashed lines mark non-physical phases which are due to the computational method. They are also visible in other figures

Figure 1, that the seismograms at larger distances contain less high frequencies than those at shorter distances, which is also due to the attenuation. Another difference to Lamb's original seismograms can be seen in Figure 2: The sign of the P wave on the horizontal component is reversed. This is due to the location of the receivers at a level above the source, where the first motion of the P wave of the vertical single force is dilation.

Examples

A few examples of computed seismograms will be discussed in this section. The Jeffreys-Bullen earth model was used in all examples. The earth-flattening approximation of Müller (1977) is applied. The P wave attenuation factor Q_α was assumed 50 in the crust, 200 in the uppermost mantle with a gradual increase to 5000 at 800 km depth. The high attenuation in the crust was chosen in order to make the integrand smoother and to save computer time. The choice of Q is no limitation of the method. The S wave attenuation factor was assumed

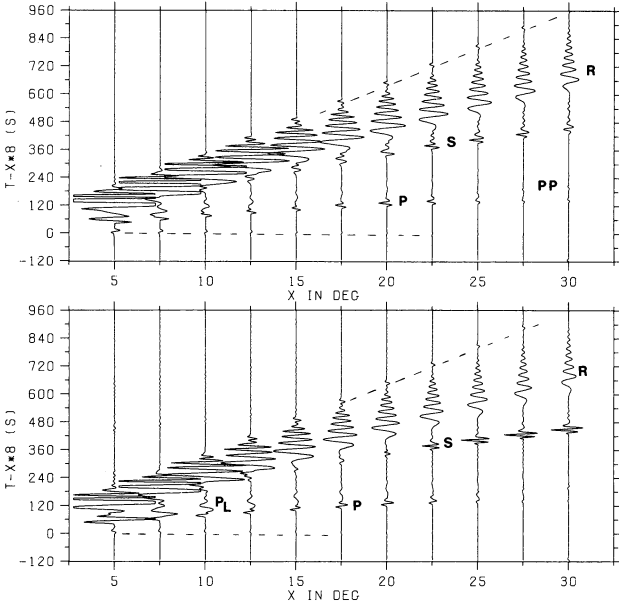


Fig. 3. Vertical (top) and radial (bottom) displacement components due to an explosive source in 300 m depth (Jeffreys-Bullen model). Lower and upper cut-off phase velocities are 2.8 and 15 km/s, respectively, cut-off period is 8.4 s. No amplitude correction due to the earth-flattening approximation is applied in this figure and in Figure 4. The decay of the *P* amplitudes with distance is too fast because the halfspace was assumed at a too shallow depth

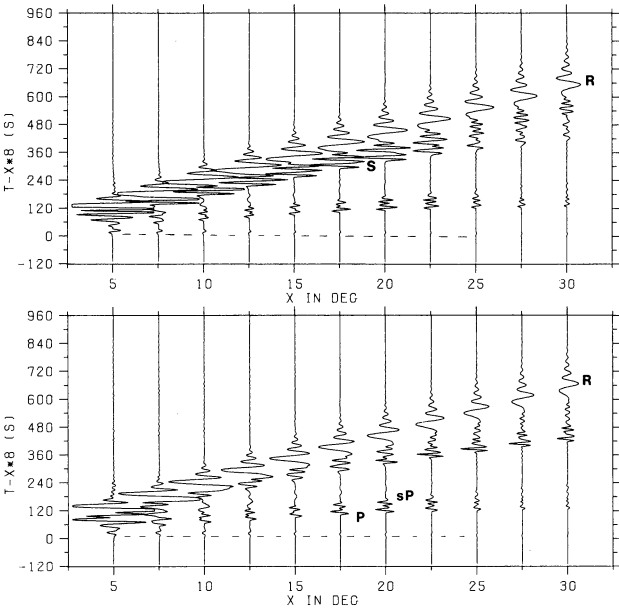


Fig. 4. Vertical (top) and radial (bottom) ground velocity components due to a vertical single force at 100 km depth. All other parameters are identical with those in Figure 3

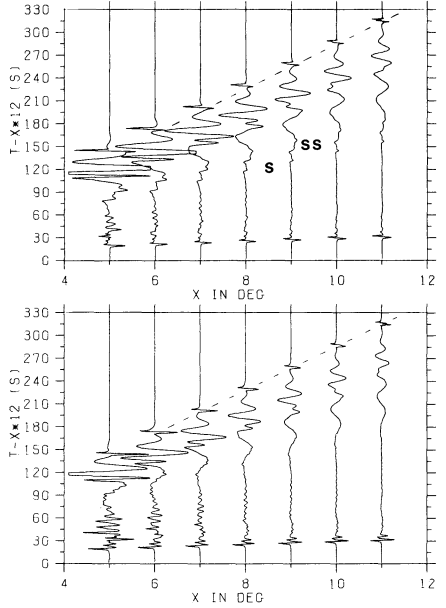
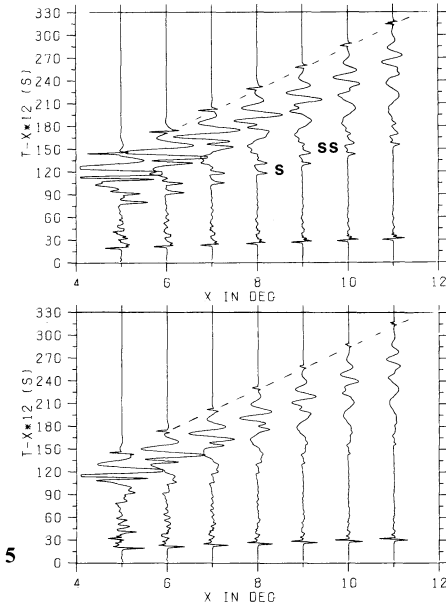


Fig. 5. Vertical (top) and radial (bottom) ground velocity components due to a vertical single force at 300 m depth

Fig. 6. Vertical (top) and radial (bottom) ground displacement components due to an explosive point source at 300 m depth. All other parameters are identical in Figures 5 and 6

to be $4/9 Q_x$. Figure 3 shows complete theoretical seismograms for an explosive source in 300 m depth. Equation (6) was chosen as source spectrum with a short period cut-off at $T_0 = 8.4$ s. The dominant phases are P and S and the Rayleigh waves. The Rayleigh waves show clear regular dispersion, shorter periods, which would show inverse dispersion, are not contained in the source signal. P decays very rapidly beyond about 20° , this is due to the assumption of a homogeneous half-space below 800 km depth in the model. Weak indications of PP are visible. The complication of S on the radial component beyond 20° is probably due to interference with shear coupled P_L -modes. Direct P_L -modes are clearly visible, especially on the radial component. In Figure 4 the ground velocity is displayed due to a single vertical force at a depth of 100 km. All other parameters are identical with those of Figure 3. The dominant phases are essentially the same in Figure 4. The Rayleigh waves are less well developed than in Figure 3, as it is expected for a source at depth. Depth phases appear clearly on both components.

Next the Figure 5 and 6 will be discussed. All parameters are kept identical in both figures, except that the source in Figure 5 is a vertical single force, and in Figure 6 an explosive source. Source depth is 300 m, cut-off period is 1.6 s. The phase-velocity window is from 11 to 2.75 km/s. Figure 5 cannot be compared directly with recordings of nuclear explosions, because of differences in the

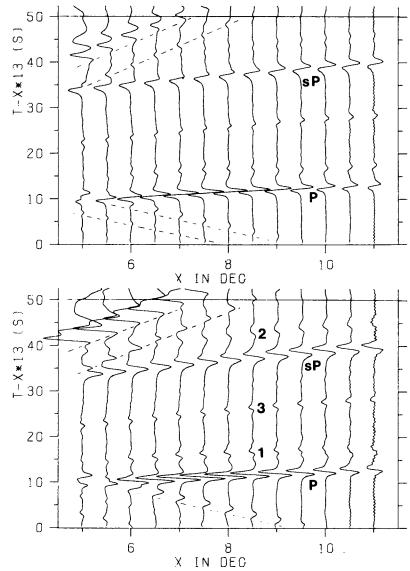


Fig. 7. Vertical (top) and radial (bottom) ground displacement due to a vertical single force at 100 km depth. Major phases are P and sP . The weaker phases are due to conversions and reflections at the Moho. See text for more details

source spectra. A nuclear explosion is radiating less energy at long periods, whereas the source function (6), which is also used in Figure 5 and 6, is more earthquake-like. The dominant phases are the same as in the previous figures. Because of the higher resolution in Figures 5 and 6, the phases S and SS are separated. As it is expected, the seismograms of the two figures, are very similar, except that the seismograms of the single force contain more S energy.

The reflectivity method can easily be used for the computation of individual phases alone. For example, if one is only interested in P waves, then one should choose the proper integration window for that purpose. Figure 7 shows an example for the P waves from a vertical single force at 100 km depth. The cut-off period is 0.6 s, the limits of the integration are 6.4 and 10.5 km/s. The dominant phases in Figure 7 are P and sP . In addition, a number of weaker phases can be recognized on both components. These phases are all due to converted and reflected waves at the crust-mantle boundary. For example, two weak phases, labelled 1 and 2, can be recognized, especially on the horizontal component, about 5 s after P and sP , respectively. These phases are probably S waves, generated at the Moho by the two larger P phases in front. Another weak phase inbetween P and sP , labelled 3, is probably an sP phase, which is reflected at the Moho instead the free surface.

Conclusions

The present extension of the reflectivity method in connection with an earthflattening approximation allows to compute the complete response of a vertically inhomogeneous earth, as far as the earth-flattening approximation can be used.

The location of the source is arbitrary. It is also a method which can easily be adopted to special problems by choosing the proper wavenumber window. A limitation of the method is probably its long computation time.

Acknowledgments. This research was supported by a grant of the Deutsche Forschungsgemeinschaft. Parts of the computations have been carried out at the computer center of the university of Karlsruhe. I wish to thank Vladislav Červený and Gerhard Müller for discussions and suggestions, and Gerhard Müller for reading the manuscript.

References

- Červený, V.: Reflection and transmission coefficients for transition layers. *Studia geophys. geodaet.* **18**, 59–68, 1974
- Dunkin, J.W.: Computation of modal solutions in layered media at high frequencies. *Bull. Seism. Soc. Am.* **55** (2), 335–358, 1965
- Ewing, W.M., Jadetzky, W.S. and Press, F.: *Elastic waves in layered media*, New York: McGraw-Hill, 1957
- Fuchs, K.: The reflection of spherical waves from transition zones with arbitrary depth-dependent elastic moduli and density. *J. Phys. Earth* **16**, Special Issue, 27–41, 1968
- Harkrider, D.G.: Surface waves in multilayered elastic media, 1. Rayleigh and Love waves from buried sources in a multilayered elastic halfspace. *Bull. Seism. Soc. Am.* **54**, 627–679, 1964
- Harkrider, D.G.: Surface waves in multilayered elastic media. Part II. Higher modes spectra and spectral ratios from point sources in plane layered earth models. *Bull. Seism. Soc. Am.* **60**, 1937–1987, 1970
- Haskell, N.A.: Dispersion of surface waves on multilayered media. *Bull. Seism. Soc. Am.* **43**, 17–34, 1953
- Haskell, N.A.: Crustal reflection of plane *P* and *SV* waves, *J. Geophys. Res.* **67**, 4751–4767, 1962.
- Lamb, H.: On the propagation of tremors over the surface of an elastic solid. *Phil. Trans. R. Soc. (London) A*, **203**, 1–42, 1904
- Müller, G.: Earth-flattening approximation for body waves derived from geometric ray theory—improvements, corrections and range of applicability. *J. Geophys.* **42**, 429–436, 1977
- Müller, G., Kind, R.: Observed and computed seismogram sections for the whole earth, *Geophys. J.R. astr. Soc.*, **44**, 699–716, 1976
- Schwab, F.A., Knopoff, L.: Fast surface wave and free mode computations. *Methods in computational physics*, Vol. II, B.A. Bolt, ed. New York: Academic Press 1972
- Watson, T.H.: Fast computation of Rayleigh wave dispersion in a layered halfspace. *Bull. Seism. Soc. Am.* **60**, 161–166, 1970

Received April 24, 1978 / Revised version June 29, 1978

Dual Magnetic Polarity Measured in a Single Bed of Cretaceous Pelagic Limestone From Sicily*

J.E.T. Channell

Institut für Geophysik, ETH Hönggerberg, CH-8093 Zürich, Switzerland

Abstract. A single bed of Cretaceous pelagic limestone from Sicily which varies in colour from red to white gives antiparallel magnetic directions after partial demagnetization. “Reversed” polarities occur in the white portion of the bed whereas almost exactly antiparallel directions of “normal” polarity characterise the red. The remanence in the case of the white variety is due to detrital magnetite, and that in the red is due to haematite. The haematite grew through its critical volume after slumping but before tectonic folding, and was probably derived from a goethitic precursor. The haematite magnetization significantly post-dates the detrital magnetization and the age relationship has important implications not only for magnetic stratigraphy in red beds, but also for the study of diagenesis in iron bearing sediments.

Key words: Palaeomagnetism – Pelagic limestones – Colour variations – Diagenesis.

1. Introduction

The Scaglia-type pelagic limestones are a characteristic Cretaceous facies in the Periadriatic region. They were deposited in basins on the southern margin of the Mesozoic Tethys. The Adriatic continental margin had a characteristic pre-orogenic morphology of carbonate platforms and basins which were elongated more or less parallel to the junction between the continental and oceanic crust (D’Argenio, 1976). The Mesozoic platform and basin carbonates are relatively free of detrital influence partly because the morphology inhibited sediment transport, partly due to the extensive development of shallow water carbonates over potential source areas, and partly due to the arid climate on the southern margin of the Mesozoic Tethys (Bernoulli and Jenkyns, 1974).

In western Sicily, at the village of Terrasini (near Palermo airport), Scaglia limestones of Late Cretaceous age crop out (see Catalano et al., 1973). The

* Contribution No. 212 Institut für Geophysik, ETH Zürich



Fig. 1. The Upper Cretaceous Scaglia limestones of Terrasini (Sicily), showing the relationship between the red and white varieties. The uppermost white bed has an average thickness of about 50 cm



Fig. 2. The single bed which gives the dual polarity, dampened to accentuate the red/white colour contrast

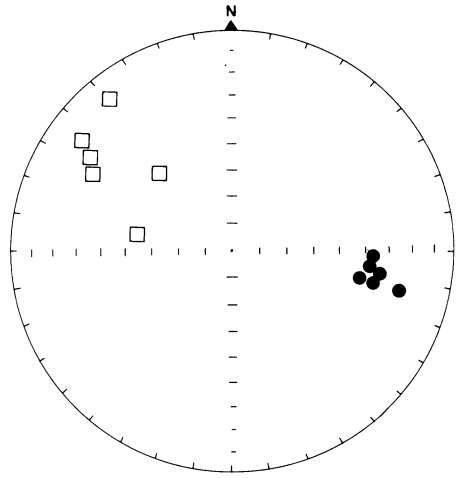


Fig. 3. Stereographic plot of magnetic directions of six samples from the white part (squares) and six from the red part (circles) of the same bed, after thermal demagnetization at 200° C and 600° C respectively. The open symbols represent negative inclinations and the closed symbols positive inclinations

limestones vary in colour from white to red and this colouration is generally tied to bedding, although variations in colour along a single bed occasionally occur (Fig. 1). Palaeomagnetic samples have been collected from one bed of variable colour (Fig. 2). The samples taken from the red portion of the bed yield “normal” polarity and those from the white give “reversed” polarity, the directions being almost exactly antiparallel (Fig. 3) after thermal demagnetization at 200° C for the white and 600° C for the red. Above these demagnetization temperatures, the magnetic intensities are generally too weak for precise measurement, reflecting the variable blocking temperature spectra of the two Scaglia varieties. Assuming that a self-reversal process is not the cause, this dual polarity indicates that one of the two magnetizations significantly post-dates the other. The magnetic properties of this Scaglia are very different to those of a similar Scaglia facies in Umbria (Lowrie and Alvarez, 1975). The declination of the “normal” directions ($\sim 100^\circ$, Fig. 3) is a result of tectonic rotations during the Neogene deformation of the Sicilian continental margin (Catalano et al., 1976).

2. White Scaglia

The magnetic properties characteristic of the white variety of Scaglia are summarised in Figure 4. Blocking temperature spectra (Fig. 4a) were found by monitoring the decay of an isothermal remanent magnetization (IRM) acquired in a 10 KOe. field, using equipment developed by Heiniger and Heller (1976). The instrument is not sensitive enough for the natural remanent magnetization to be treated in this way. The maximum blocking temperature of over 600° C indicates that at least part of the IRM is held by haematite.

The rate of acquisition of IRM in increasing d.c. fields gives a measure of the coercivity spectrum of the magnetic mineralogy. The spectrum associated with the white Scaglia (Fig. 4b) is generally bimodal indicating a low coercivity

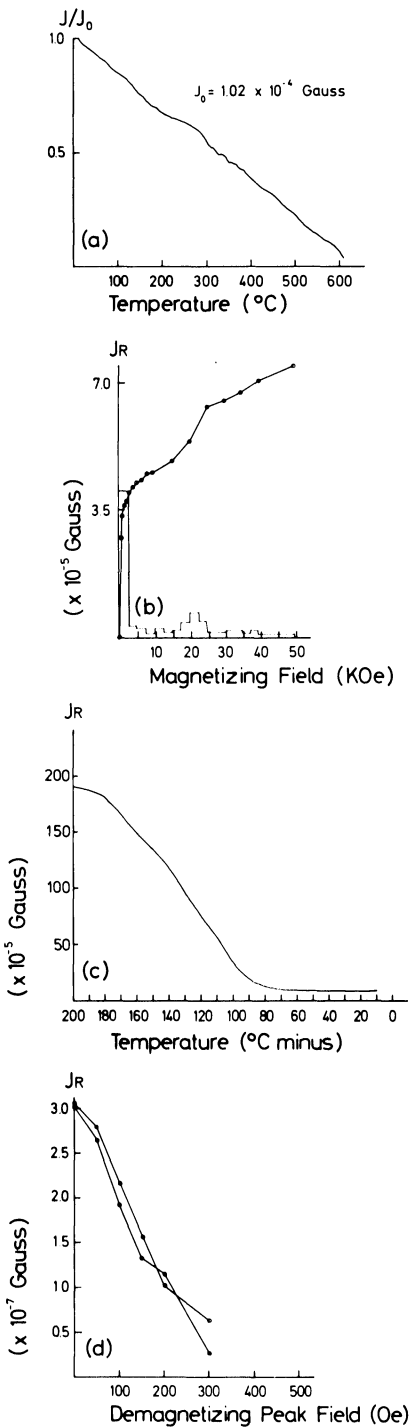


Fig. 4

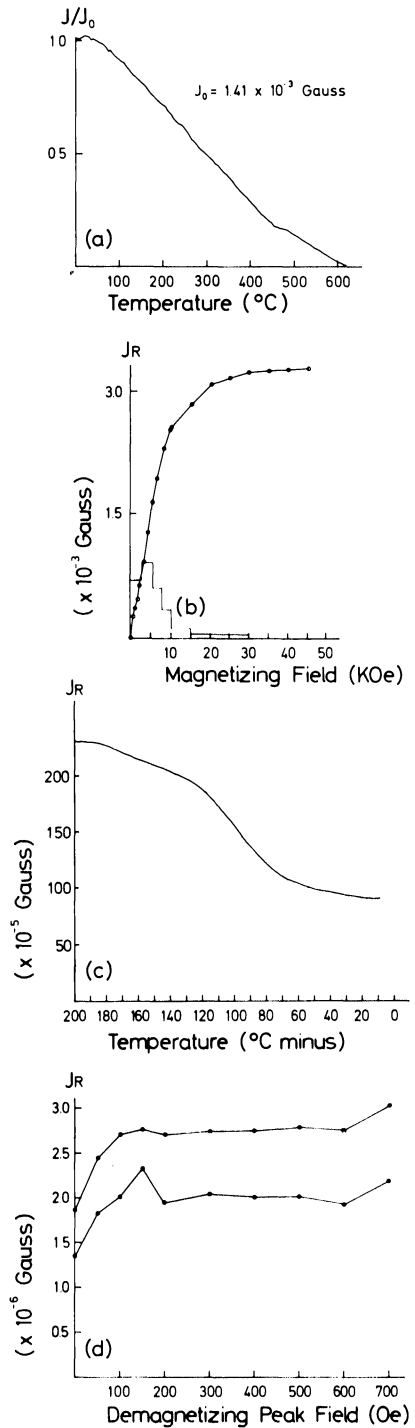


Fig. 5

Fig. 4 a-d. Some magnetic properties of the white Scaglia. **a** Continuously measured blocking temperature curve of IRM. **b** IRM acquisition curve **c** Decay during heating of IRM imposed at liquid nitrogen temperature. **d** Intensity change during alternating field demagnetization

Fig. 5 a d. Some magnetic properties of the red Scaglia (caption for **a**, **b**, **c** and **d** as for Fig. 4)

component together with a variable contribution from a high coercivity component. The low coercivity material is probably magnetite and the higher coercivities may be due to the haematite seen in the blocking temperature spectrum. The samples generally do not attain saturation remanence even after introduction into fields of over 50 KOe. Therefore, if the higher coercivity mineral is haematite, it has unusually high coercivity. However, the anisotropy constants of naturally occurring haematite are poorly known and internal stresses in fine grained haematite may produce these coercivities.

An IRM from a 10 KOe field was given to various samples of white Scaglia at liquid nitrogen temperature. The behaviour of the remanence was then monitored during warming up to room temperature. The isothermal remanence decays to about 5% of its original value (Fig. 4c). An IRM (10 KOe) was then given to the same sample at room temperature and the magnetization of the sample measured continuously down to liquid nitrogen temperature. Negligible change in magnetization intensity occurred indicating that the decay represented by Figure 4c is not due to a change in spontaneous magnetization (J_s) with temperature but is due to low blocking temperatures of superparamagnetic grain sizes. Either haematite or magnetite could be producing this superparamagnetic effect although the large reduction in magnetization (1.4×10^3 G) on heating to room temperature suggests that magnetite, with its much larger spontaneous magnetization, is the superparamagnetic phase. As the spontaneous magnetization of haematite is about 1% that of magnetite, a large concentration of haematite would be necessary to give the same effect, and one might expect the Scaglia to be red in this case.

The natural remanent magnetization (NRM) of the white Scaglia is weak ($\sim 2 \times 10^{-7}$ G) and the median destructive field on alternating field demagnetization is about 150 Oe (Fig. 4d). This suggests that the natural remanence is held by the low coercivity fraction seen in the IRM acquisition curves (Fig. 4b) rather than the higher coercivity material. The low coercivity mineral is probably a magnetite.

3. Comparison With the Red Scaglia Variety

The magnetic properties of the red variety of Scaglia are summarised in Fig. 5. The maximum blocking temperature (Fig. 5a) indicates that haematite contributes to the IRM acquired in a 10 KOe. field, and a slight flexure in the curve may correspond to a magnetite blocking temperature.

The IRM acquired by the red Scaglia is much higher than that acquired by the white variety in the same field. The red variety generally reaches saturation in fields of the order of 30 KOe (Fig. 5b) and has a unimodal coercivity spectrum which may be due to the pigmentary haematite alone or a combination of haematite and a very minor amount of magnetite. The absence of the very high coercivities which are seen in the white Scaglia, suggests that the haematite has larger grain size in the red variety.

An IRM acquired at liquid nitrogen temperature decays to 40% of its original value during heating to room temperature (Fig. 5c) indicating that, compared to the white Scaglia, a smaller fraction of the IRM resides in superparamagnetic

grain sizes. Again, cooling an IRM acquired at room temperature indicates negligible dependence of spontaneous magnetization (J_s) on temperature. The fall in magnetization in the case of the white variety (Fig. 4c) is somewhat greater than that for the red (Fig. 5c). Assuming that the magnetite is detrital, one would expect a similar magnetite concentration and grain size distribution in both red and white varieties, as they are adjacent samples from the same bed. The white variety therefore probably contains more superparamagnetic haematite, which may be the finer-grained part of the same grain-size distribution which gives the high coercivities (Fig. 4b).

The natural remanence of the red Scaglia was so stable against AF demagnetization that the median destructive field could not be measured. During demagnetization to 700 Oe, the intensity showed no significant change between 200 Oe and 700 Oe (Fig. 5d) suggesting that haematite is the principle remanence carrier. The intensities generally *increase* during the early stages of alternating field demagnetization (Fig. 5d) indicating that an antiparallel component is being removed. The subtracted vector is very consistent during alternating field demagnetization for both the red and the white Scaglia (Fig. 6a). This vector is

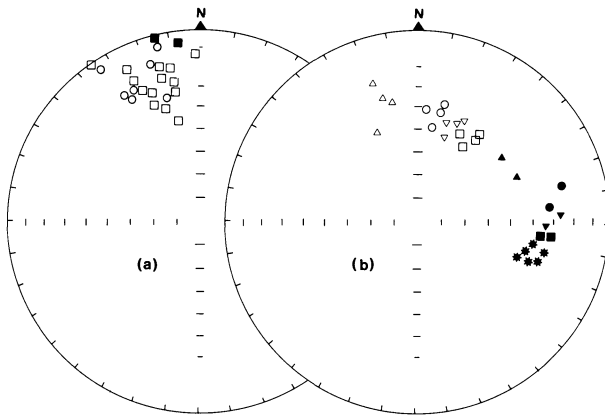


Fig. 6. **a** Subtracted vectors during alternating field demagnetization from 50 Oe to 100 Oe for red (circles) and white (squares) samples. Other demagnetization intervals give similar directions. Open symbols represent negative inclinations and closed symbols positive inclinations
b Directional changes of four white (open symbols) and two red (closed symbols) samples during alternating field demagnetization. Open symbols represent negative inclinations and closed symbols positive inclinations.

White samples	Red samples	Peak field
Negative inclinations	Positive inclinations	
△	▲	NRM
○	●	50 Oe
▽	▼	100 Oe
□	■	150 Oe
	*	200-400 Oe

close to the directions obtained from the white variety after thermal demagnetization at 200° C (Fig. 3). This, together with the directional changes during a.c. demagnetization (Fig. 6b) which tend to follow paths from reversed to normal polarity, indicates that the primary (reversed) magnetite magnetization vector is being removed in both white and red Scaglia varieties during a.c. cleaning leaving a magnetization vector with an increasing secondary component of normal polarity due to haematite. In the case of the red variety, a.c. fields greater than 200 Oe produce the same magnetic directions as thermal demagnetization up to 600° C (Fig. 3). This cleaned direction (Fig. 6b) is probably attributable solely to pigmentary haematite.

4. The Origin of the Magnetic Minerals

The magnetic properties of these Scaglia limestones are related to their colour. Haematite is the dominant natural remanence carrier in the red variety and magnetite is dominant in the white. It is impossible that both minerals could be of detrital origin, not only because of their antiparallel magnetizations, but also because of the physical nature of colour variations within a single bed. The magnetite is probably detrital, and the reversed magnetization of the white Scaglia may well represent the geomagnetic field at the time of deposition. The haematite is secondary and has been derived during diagenesis from a precursor. The colour variations in this Scaglia are maintained around slump folds (a spectacular example is shown in Fig. 7). Therefore, the colour variations cannot be the result of later selective leaching, and the properties of the sediment

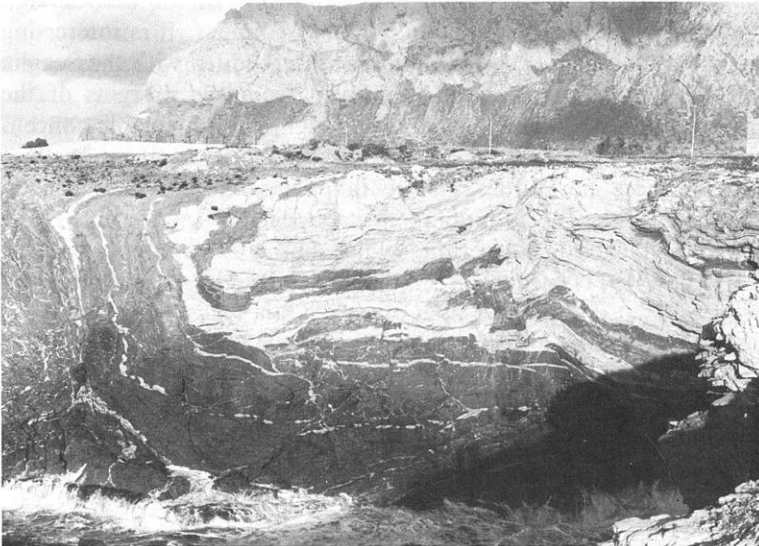


Fig. 7. Large slump fold showing that the colour variations are maintained around the curvature of the fold. The house and lamp-posts at the top of the cliff give the scale

which control the colour variations are an inherent feature of the soft sediment.

The haematite in these Scaglias may have originated in a number of different ways.

(a) Oxidation of magnetite: this seems unlikely as the intensity of remanence of the red Scaglia is about one order of magnitude greater than that of the white variety. This would most probably *not* be the case if magnetite was the precursor of the haematite.

(b) Haematite pigment in red sandstones often occurs as a result of the diagenetic breakdown of iron silicates into iron oxide and clay minerals (Walker, 1967a, 1967b; Walker, Ribbe and Honea, 1967; Turner and Archer, 1975). The oxidation of iron-bearing detrital clay can also produce pigmentary haematite (Walker and Honea, 1969). In the case of the Scaglia, these alteration processes *may* contribute, but it is unlikely that enough iron-bearing detritus has been introduced into these pelagic basins to account for the haematite pigment.

(c) Haematite in sediments can be formed by the dehydration of goethite. The Mesozoic basinal facies of the southern Tethys have been likened to recent abyssal sediments on the ocean floor (Trümpy, 1960; Garrison and Fischer, 1969). The environment of deposition was similar in that these sediments were uninfluenced by sources of terrigenous detritus and the sedimentation rate was very low. Goethite is a common constituent of modern pelagic sediments deposited on the abyssal plain. Therefore, by analogy, goethitic oxy-hydroxides may well have been deposited from sea-water in this Scaglia basin. In addition, a very similar pelagic facies of Jurassic age in Western Sicily contains fossil manganese nodules (Jenkyns, 1970). Goethite is an important constituent of manganese nodules and therefore goethite was deposited in a Jurassic environment analogous and adjacent to this Scaglia basin. Variable organic content in the Scaglia limestones may control either the deposition or the dehydration product of the goethite, and hence the colour of the sediment. It is interesting to note that the turbidites which occasionally occur interbedded with the Scaglia are always white. The turbiditic material is derived from the margins of the basin where sedimentation rates were probably too high for appreciable concentration of goethite. Although it seems likely that goethite was the precursor of the haematite in these limestones, no goethite apparently remains, as it does not manifest itself in the blocking temperature spectra (Fig. 4a, 5a). However, we have some evidence that goethite, which has a Néel temperature at around 110° C (Hedley, 1971), occurs in similar facies Scaglia limestones from the Southern Alps.

Chemical analysis of the red and white Scaglia collected from a varicoloured bed at the same Sicilian locality indicates that the total iron content in the red (0.68%) and in the white (0.65%) is the same within the experimental uncertainty. The concentration of Fe^{3+} varies from 0.55% for the red to 0.40% for the white. As the total iron contents are the same, the differences in colour and magnetic properties are not the result of selective deposition. It is proposed that whereas in the red Scaglia, the goethite reverted to haematite, in the white variety only a small proportion of the goethite altered to haematite, the bulk

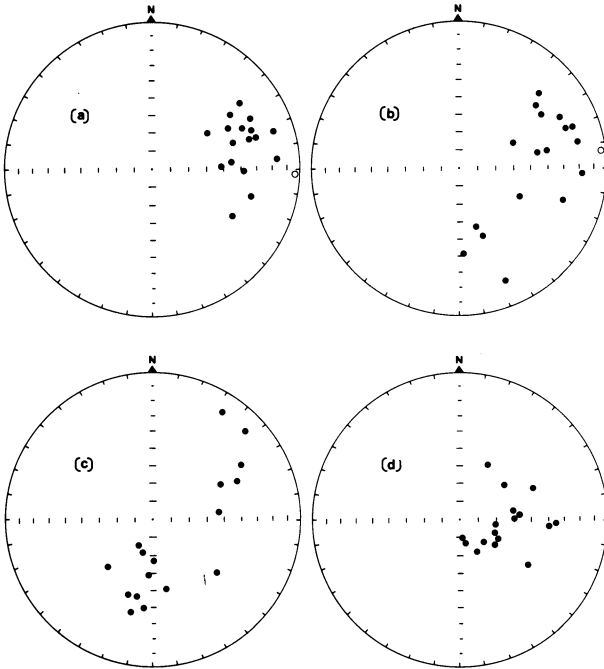


Fig. 8a-d. Thermally cleaned sample directions from a slump fold **a** before and **b** after bedding correction; and from a tectonic fold **c** before and **d** after bedding correction

reverting to a non-ferromagnetic mineral such as pyrite. Pyrite has been observed optically only in the white Scaglia.

The dual polarity indicates that the time interval between fixing of detrital magnetite grains and the growth of haematite through its critical volume was at least the time taken for a polarity inversion. The timing of diagenetic haematite growth can also be limited by the application of a fold test to both a tectonic fold and a soft sediment slump (Fig. 8) which indicates that the remanence was retained by the haematite before Miocene folding but after the Maestrichtian/Paleocene synsedimentary slumping.

Further palaeomagnetic studies of this nature will provide information on the timing of this and other diagenetic processes in iron bearing sediments.

Acknowledgements. Thanks are due to Bill Lowrie and Friedrich Heller for many useful suggestions both in the laboratory and after critical reading of the manuscript. Rob Van der Voo and Roy Kligfield also passed comments on the manuscript.

References

- Bernoulli, D., Jenkyns, H.C.: Alpine, Mediterranean, and Central Atlantic Mesozoic Facies in Relation to the Early Evolution of the Tethys. In: Modern and Ancient Geosynclinal Sedimentation. R.H. Dott & R.H. Shaver (eds.). Society of Economic Paleontologists & Mineralogists, Special Publication No 19. 129-160 (1974)

- Catalano, R., Channell, J.E.T., D'Argenio, B., Napoleone, G.: Mesozoic Palaeogeography of the Southern Apennines and Sicily. *Mem. Soc. Geol. It.* **15**, 95–118 (1976)
- Catalano, R., Maniaci, G., Renda, P., Urso, G.: Un Esempio di Evoluzione Sedimentaria nelle Facies di Bacino dei Monti di Palermo la Successione Mesozoico-Terziaria di Cala Rossa (Terrasini). *Geologica Romana* XII, 151–175 (1973)
- D'Argenio, B.: Le piattaforme Carbonatiche Periadriatiche una Rassegna di Problemi nel Quadro Geodinamico Mesozoico dell'Area Mediterranea. *Mem. Soc. Geol. It.* XIII (2), 1–28 (1976)
- Garrison, R.E., Fischer, A.G.: Deep-water limestones and Radiolarites of the Alpine Jurassic. In: *Depositional environments in carbonate rocks*. G.M. Friedman (ed.), *Soc. Econ. Paleontol. Mineral. Spec. Publ.* **14**, 20–56 (1969)
- Hedley, I.G.: The Weak Ferromagnetism of Goethite (α -FeOOH). *Z. Geophys.* **37**, 409–420 (1971)
- Heiniger, Ch., Heller, F.: A high temperature Vector Magnetometer. *Geophys. J. Roy. Astron. Soc.* **44**, 281–288 (1976)
- Jenkyns, H.C.: Fossil Manganese nodules from the West Sicilian Jurassic. *Eclogae Geol. Helv.* **63/3**, 741–774 (1970)
- Lowrie, W., Alvarez, W.: Paleomagnetic evidence for the Rotation of the Italian peninsula. *J. Geophys. Res.* **80**, 1579–1592 (1975)
- Trümpy, R.: Paleotectonic Evolution of the Central and Western Alps. *Geol. Soc. Am. Bull.* **71**, 843–908 (1960)
- Turner, P., Archer, R.: Magnetisation History of Lower Old Red sandstones from the Gamrie Outlier, Scotland. *Earth Planet. Sci. Lett.* **27**, 240–250 (1975)
- Walker, T.R.: Formation of red beds in modern and ancient deserts. *Geol. Soc. Am. Bull.* **78**, 353–368 (1967a)
- Walker, T.R.: Colour of Recent sediments in tropical Mexico: a contribution to the origin of red beds. *Bull. Geol. Soc. Am.* **78**, 917–920 (1967b)
- Walker, T.R., Honea, R.M.: Iron content of modern deposits in the Sonoran Desert: a contribution to the origin of red beds. *Bull. Geol. Soc. Am.* **80**, 535–544 (1969)
- Walker, T.R., Ribbe, P.H., Honea, R.M.: Geochemistry of hornblende alteration in Pliocene red beds, Baja California, Mexico. *Bull. Geol. Soc. Am.* **78**, 1055–1060 (1967)

Received May 10, 1978 / Revised version July 11, 1978

Palaeomagnetic Data From the Central Part of the Northern Calcareous Alps, Austria

H.J. Mauritsch¹ and W. Frisch²

¹ Institute of Applied Geophysics, Mining University, A-8700 Leoben, Austria

² Institute of Geology, University of Vienna, Universitätsstr. 7, A-1010 Wien, Austria

Abstract. Palaeomagnetic data from the Osterhorngruppe in the Northern Calcareous Alps (NCA) southeast of Salzburg are presented. The investigations were concentrated on the red nodular Adneter Kalk (limestone) of Liassic age which carries a stable natural remanent magnetisation. Rockmagnetic investigations revealed magnetite as the carrier of the remanent magnetization.

The obtained palaeomagnetic results do not contradict a northward shift of the NCA of the order of several hundred kilometres and indicate a clockwise rotation of about 45° of the Northern Calcareous Alps with respect to Eurasia, since the Jurassic. Time of possible shift and rotation are briefly discussed.

Key words: Palaeomagnetism — Rockmagnetism — Adriatic plate — Northern Calcareous Alps — Jurassic — Adneter Kalk.

Introduction

In the last few years, a series of palaeomagnetic data has been published which show an anticlockwise rotation of the Adriatic plate in the Tertiary. The data are based on measurements in several places throughout the Apennine peninsula and the Southern Alps and show rotation angles between 23° and 55° (Hargraves and Fischer, 1959; Van Hilten, 1960; Manzoni, 1970; Soffel, 1972; Zijdeveld and Van der Voo, 1973; Lowrie and Alvarez, 1974; Channell and Tarling, 1975; Channell and Horvath, 1976; Vandenberg and Wonders, 1976; Van der Voo and Zijdeveld, 1969).

The Austroalpine nappe system of the Eastern Alps is considered to have been part of the Adriatic plate which split off from the Eurasian continent due to the opening of the South Penninic ocean. The question arises whether the Austroalpine region rotated with the main part of the Adriatic plate, or whether there was differential movement between these areas during the Alpidic orogeny.

To date very few palaeomagnetic data have been published from the Austroalpine region, and only from the Northern Calcareous Alps (NCA). Hargraves and Fischer (1959) established a 20° clockwise rotation for the Lofer area west of Salzburg.

By far the greatest part of the Mesozoic cover of the Austroalpine basement is found in a large décollement nappe, the Northern Calcareous Alps (NCA), which has been thrust over the Rhenodanubian flysch by gravity gliding in the late Eocene. For geometric reasons, the Northern Calcareous Alps, considered as a whole, cannot have suffered major rotation relative to their basement, during the downgliding process. However, they are dissected into several smaller nappes, slices and blocks (see Tollmann, 1976) which may have rotated individually through larger angles.

Our investigations were carried out in the Osterhorn mountain group which is a flat-lying stable block within the central part of the NCA. Our results, obtained for Jurassic rocks, are in accordance with the Jurassic magnetic direction of Hargraves and Fischer (1959) and the Triassic directions of Soffel (pers. comm.) from other areas of the NCA. Therefore the conclusion seems justified that the data are representative for the NCA throughout their length.

The samples were drilled in the field and oriented in situ with an orientation table and compass. 6 to 8 cores were collected at each site across an area of less than 1 m².

Geological Review of the Osterhorn Mountains

Tectonic Relations

The Osterhorn mountain group is situated in the central part of the Northern Calcareous Alps (Salzkammergut) southeast of Salzburg (Fig. 1). This flat-lying, only marginally distorted block belongs to the "Tirolicum" (Tyrolian nappe).

The borders of the Osterhorn block are tectonic ones (Fig. 1) (Plöching, 1953, 1973; Tollmann, 1976). To the northeast, it has been thrust some distance onto the Schafberg unit which is also attributed to the Tyrolian nappe; along the thrust fault, the Wolfgangsee fault, there are the windows of St. Gilgen and Strobl containing members of the Rhenodanubian flysch and the Ultrahelvetic nappes. To the north, the Tyrolian nappe has been thrust over a very thin nappe slice, the "Bajuvaricum" (Bavarian nappes), which represents the northern margin of the NCA and in turn has been thrust over the Rhenodanubian flysch. To the west, the Salzachtal fault separates the Osterhorn block from the tectonically more complicated Berchtesgaden Alps. To the south, a complex normal and high angle slip fault separates the tectonically highly contorted zone of the Lammer valley. To the east, the tectonically higher Gamsfeld nappe ("Juvavicum" Unit), borders against the Osterhorn block by a normal fault.

The interior of the Osterhorn block is characterized by the horizontally lying Upper Triassic to Upper Jurassic sequence (Fig. 2). Only the margins

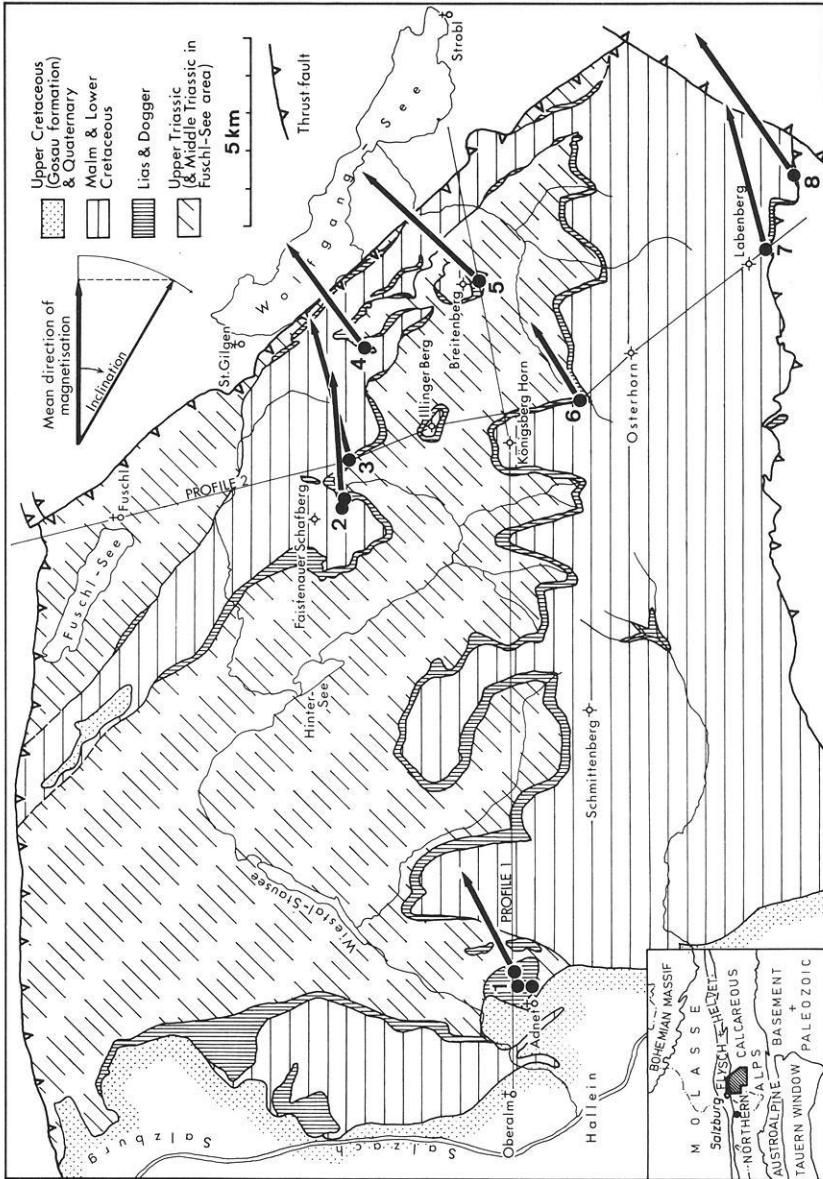


Fig. 1. Geological sketch of the Osterhorn mountains, sample localities and mean directions of magnetisation. Geology after Bittner and Fugger (1907), Mojsisovics and Bittner (1905), Plöching (1953, 1972), and Prey (1969)

have been subjected to stronger deformation: this is in particular true along the northeastern border where accompanying faults to the Wolfgangsee thrust fault are responsible for tectonic complications, and along the southern margin. The interior of the block is only slightly folded; in the sampling areas of the Faistenauer Schafberg (no. 2 and 3) there are north-south trending folds dying out towards the south; approaching the NW-SE striking Wolfgangsee

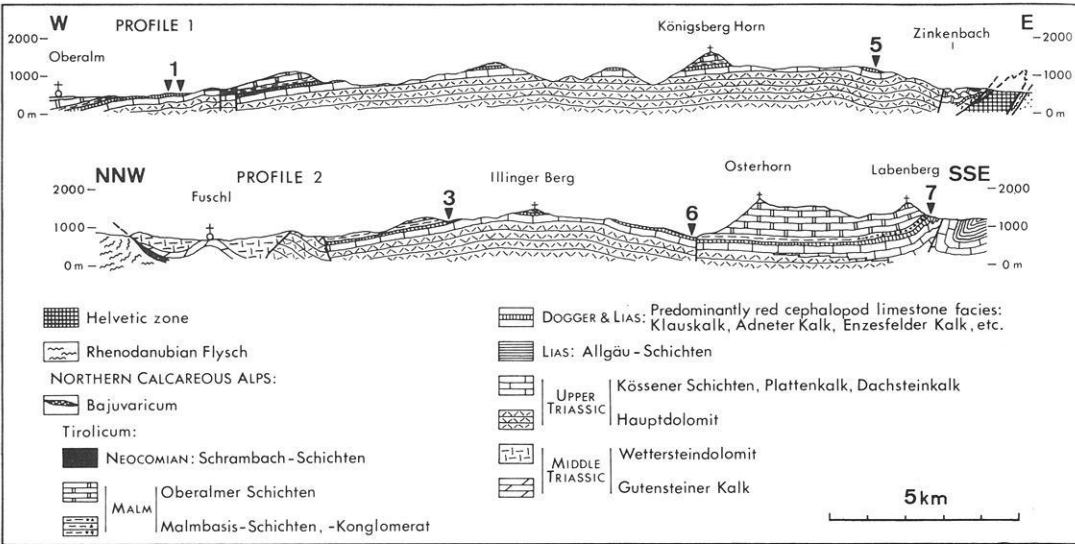


Fig. 2. Geological profiles through the Osterhorn mountains. For location of profiles, see Figure 1

fault, these structures bend parallel to it (Plöchinger, 1973). At the western and eastern margins of the Osterhorn block the rock sequences are downwarped.

Stratigraphy

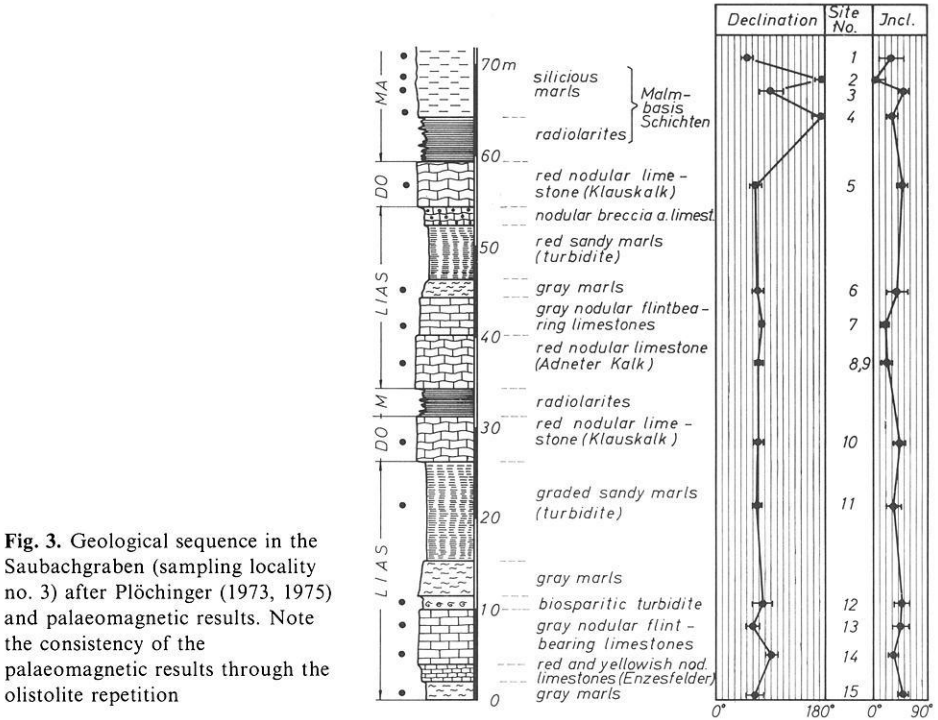
A synoptical description of the stratigraphic sequence of the Osterhorn mountains is given by Plöchinger (1973, 1975) to whom the reader is referred.

The most prominent members of the Osterhorn mountains are the Upper Triassic Hauptdolomit and the Upper Jurassic Oberalmer Schichten. Middle Triassic carbonates are exposed only in the tectonically disturbed Fuschlsee area (Figs. 1 and 2).

The thick Upper Triassic Hauptdolomit sequence indicates a basement steadily subsiding at a rate of 150–200 m/m.y. Towards its top, it gives way to the Plattenkalk and the Rhaetian Kössener Schichten with intercalations of reef buildings.

In the Liassic, the subsidence process continues but becomes inhomogeneous; the Upper Triassic platform decomposes, and becomes faulted and differentiated in basins and swells by tensional processes which are palaeogeographically characteristic throughout the southern domain of the Eastern Alps in the Jurassic.

The Liassic sequence consists of grey and red limestones and marls. The grey facies changes vertically and laterally into the red which is characterized by low sedimentation rates and subsolution (Jurgan, 1969). The Liassic of the Osterhorn mountains does not exceed a few tens of metres. The grey facies includes partly siliceous marls ("Fleckenmergel") and skeletal and nodular limestones, which contain flints in places. The red facies is mainly represented by the nodular cephalopod limestones (Adneter Kalk), also flint-bearing in



places. In the Saubachgraben (locality 3; Fig. 1) turbidites occur in two horizons (Plöchingner, 1973, 1975) (Fig. 3). The relationships in the area of Lofer (black spot in inset of Fig. 1) are well comparable (Hargraves and Fischer, 1959) with the NCA.

Dogger has recently been proved by fossils in the Saubachgraben (loc. 3) by Plöchingner (1975) in the form of red nodular cephalopod limestone rich in Mn-Fe-oxides (Klauskalk). This member is only a few metres thick.

The Malm starts with red radiolarite (Ruhpoldinger Radiolarit) which changes into variegated siliceous marls (“Malmbasis-Schichten” of Plöchingner, (1973)). This facies already reflects a deep-water environment although no absolute figures for the water depth can be given. In the “Malmbasis-Schichten” there are repetitions in the sequence (Fig. 3) which are explained by Plöchingner (1973, 1975) as syndepositional gliding masses (olistolites) (cf. Vortisch, 1937). In the southern Osterhorn mountain group, the “Malmbasis-Schichten” grade laterally into a clastic facies, the Tauglboden-Schichten. These consist of coarse local breccias transported by olistostromes, fluxoturbidites, and turbidity currents from a southerly direction (Schlager and Schlager, 1973).

The “Malmbasis-Schichten” are topped by the mighty Oberalmer Schichten (Kimmeridgian to Portlandian), flint-bearing micritic limestones which dominate in the southern Osterhorn group.

In the Neocomian, the sequence continues with deep-water marls (the Schrambach Schichten) preserved in synclines of the Osterhorn mountains.



Fig. 4. Typical outcrop of red nodular Adneter Kalk. Königsbachtal (loc. No. 6)

Selection of Rock Types for Palaeomagnetic Measurements

Due to its thickness, the Hauptdolomit crops out over a large area in the central, western and northwestern parts of the Osterhorn mountain group. Because the magnetisation is very weak ($< 5 \times 10^{-8}$ G) no reliable measurements and interpretation can be made.

The other prominent member of the Osterhorn mountains, the Oberalmer Schichten, is also weakly magnetised, and outcrops are not easily accessible (with the drilling equipment) as they form the upper parts of the mountain group.

Thus, our investigations were concentrated in the Liassic beds, and there predominantly in the red Adneter Kalk facies which, in general, does not exceed a few metres in thickness. The Adneter Kalk has been preferred for the following reasons: (a) it is the only member between the Triassic and the Ruhpoldinger Radiolarit that is persistent throughout the Osterhorn mountain group; (b) its NRM shows stable components during progressive thermal demagnetization; (c) it is possible to get good drill cores out of these limestones. Disadvantages are errors with the measuring of the bedding plane due to its nodular development (Fig. 4), poor and limited outcrops and landslips at several localities.

At localities 2, 3, and 4 (Fig. 1), siliceous marls of the Lower Malm, Dogger limestone (Klauskalk) and different members of the Liassic were also sampled.

The Lower Malm radiolarites possess satisfying rockmagnetic properties but it was impossible to attain suitable specimens because of the hardness of the rock, and its subsequent disintegration upon drilling.

Depositional Environment of the Red Nodular Limestones

The red nodular limestones of Liassic (Adneter Kalk, Fig. 4; pale yellowish variety: Enzesfelder Kalk) and Dogger (Klauskalk) age are rich in cephalopods which are largely responsible for the nodular appearance of the rock. The

Adneter Kalk is worked in quarries near Adnet (locality 1) as decorative plate "marble". An abandoned quarry is situated near the top of Breitenberg (locality 5).

The red limestones are characterized by low rates of sedimentation (in the order of less than 1 m/m.y.), subsolution and rearrangement of particles and fossil skeletons. In places, the limestone is developed as an intraclastic breccia.

Some of these properties would suggest that the red limestones are not well suited for a palaeomagnetic investigation. However, the directions of stable remanence are fairly consistent (Fig. 3). The tight clustering of stable NRM directions is possibly caused by the low sedimentation rate which allowed concentration and tight orientation of the magnetic particles. If, however, the magnetite, which is definitely the carrier of the characteristic remanent magnetisation (ChRM), was formed by reduction of the primary haematite in a diagenetic stage, good groupings of the directions of the ChRM could also be explained.

The depositional environment of the red limestones is considered to be that of a swell facies rich in bottom currents in an oxygen-rich water; the corresponding basin facies are the grey marls ("Fleckenmergel" or Allgäu Schichten) which are poorly developed in the Osterhorn mountains.

The alternation of the prevailing red and the grey limestone facies, thin marl beds and turbidite layers reflects the unsteady and changing conditions during the Liassic between swells, slopes and local basins. The water depth will have been that of a deeper littoral (50–100 m) for the condensed red limestones according to Wendt (1970) who based his results on the fauna, and a few hundred metres at most for the small local basins.

The Middle Jurassic Klauskalk is extremely condensed (missing in parts?) which is considered to be possibly due to bottom currents. The water depth will have been increasingly deeper thus approaching the deep water environment of the Oxfordian (Ruhpoldingner Radiolarit).

Palaeomagnetic Investigations

The palaeomagnetic investigations started in 1974 with the sampling of two profiles in the Schafbachgraben (locality 2 in Fig. 1, 20 sites) and Saubachgraben (locality 3, 14 sites). The results are presented in Figure 3. The profiles covered the Lias, Dogger and lower Malm, and detailed rockmagnetic studies were carried out to find the carrier of the remanence. For this purpose, high temperature, low temperature and saturation magnetisation experiments were carried out (Fig. 5). As shown in Figure 5a and b, the high temperature experiments establish magnetite (Fe_3O_4) with a maximum blocking temperature of about 540–550° C as the carrier of the NRM.

However there is a remarkable difference in the behaviour of the samples shown in Figure 5a (representing the Malmian) and Figure 5b (representing the Liassic Adneter limestones). Whereas Figure 5a establishes only magnetite with one blocking temperature at about 540° C, Figure 5b shows two blocking temperatures at about 320° C and 540° C. Using the susceptibility curves as an indication of chemical changes we can see that in the Malmian material

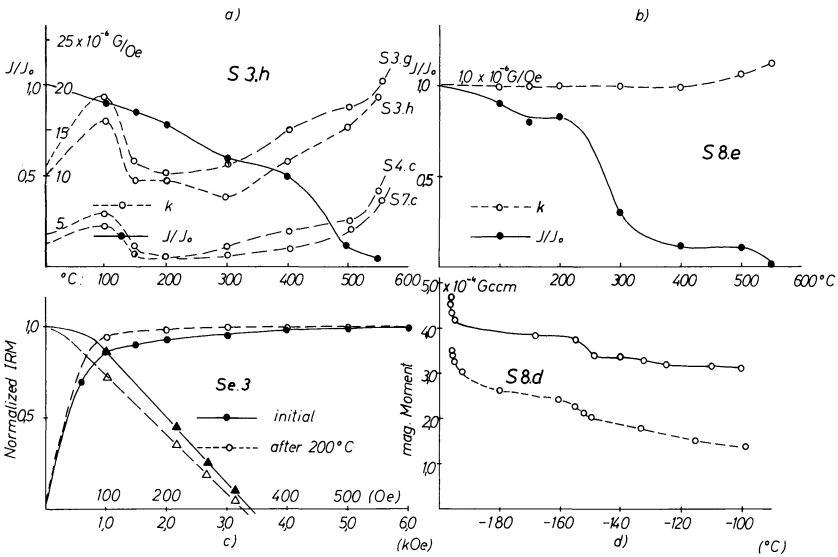


Fig. 5a-d. Results of the rockmagnetic investigations. (a) and (b) show the high temperature behaviour (normalized intensity and volume susceptibility versus temperature) of typical members of the investigated sequence; note in (a) that the characteristic change in susceptibility at 100°C occurs in the majority of the samples. (c) saturation magnetisation and coercive force versus field strength, and (d) low temperature-transition for Fe_3O_4 at $-143^\circ C$

in Figure 5a there seems to be ironhydroxide ($FeOOH$) as a second mineralisation. Limonite is proved by microscope analysis but there is no evidence if it is a mixture of α and γ ironhydroxide in the sense of Millot (1970, p. 22) or if it is pure α - $FeOOH$ or γ - $FeOOH$. In Figure 5b the susceptibility curve shows clearly that no chemical change occurs in the red sediments at about 320°C which shows that there is no other mineralisation besides magnetite. This means that both blocking temperatures are due to magnetite and that the reduced blocking temperature at about 320°C is caused by yet unknown changes in the chemical composition.

In Figure 5c the saturation magnetisation behaviour is presented. It can be seen that in the initial stage the material was saturated at 4 kOe which is a bit high but nevertheless typical for magnetite. Therefore, and for the fact that the susceptibility curve (Fig. 5a) indicates some additional effect from another mineralisation, the samples were heated up to 200°C and the saturation magnetisation behaviour was again tested. The dotted line clearly shows saturation at 2 kOe. This effect is in good agreement with the susceptibility curve in Figure 5a which shows some chemical changes in this temperature range.

In Figure 5d a typical curve for low temperature experiments is presented. The curve shows two remarkable anomalies, one at $-195^\circ C$ and the other at around $-148^\circ C$. The first is due to the fact that a large sample has to be used to get a strong signal, and the temperature gradient between the surface of the sample and the centered thermo couple causes a decrease of the magnetic

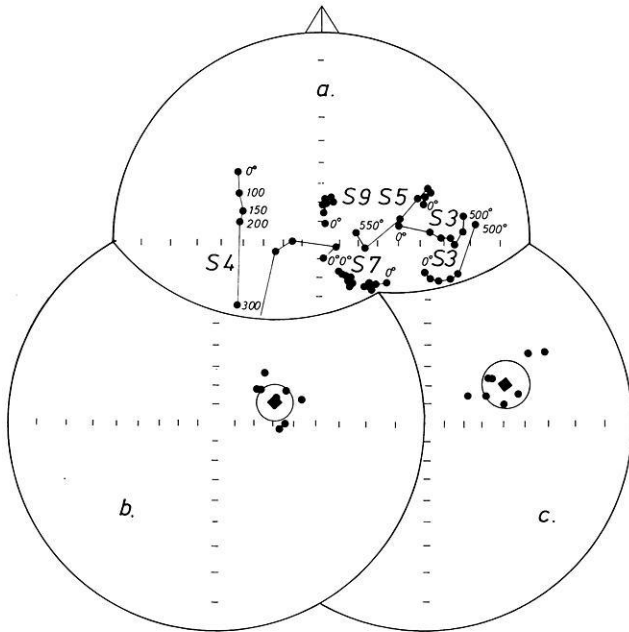


Fig. 6a-c. Stability results. (a) Stability of the direction of NRM during thermal demagnetisation. (b) Mean of the site mean values before and (c) mean of the site mean values after bedding correction

moment (Mauritsch and Turner, 1975). The second is the true low temperature magnetic transition for magnetite.

The tests carried out establish that the main carrier of the NRM is magnetite and there is no clear evidence that any other mineralisation is of importance. Even in the red coloured limestones of the Adnet type there was no magnetic effect caused by haematite. Haematite seems to occur in a superparamagnetic stage at room temperature (Fig. 5d).

We cannot decide whether the remanence (NRM) has been formed by depositional or chemical processes. To test the stability of the direction of NRM, a large number of pilot samples were heated stepwise (0–550°C). The direction was measured after each step with a spinner magnetometer (digico, Molyneux, 1971) and afterwards plotted on a stereogram (Fig. 6a). In this figure the pilots S3 and S4 represent the Malmbasis Schichten. They are extremely unstable. The sample S5 covers the Dogger, S7 (grey, nodular flint bearing limestone) and S9 (Adneter Kalk) the lower Lias and it can be noticed, that the sample S5 remains stable up to 300°C. Above this temperature and up to 550° the direction moves and no other stable direction has been found. Above 550°C the intensity was too low ($< 2 \times 10^{-8}$ G) so that further demagnetisations became impossible. The samples S7 and S9 are very stable over the whole range of thermal cleaning, making it easier to decide which material should be used for further work.

Concluding the rockmagnetic investigations, one observes that above 100°C

of thermal cleaning, the suitable material (Liassic members) remains stable up to 500° C. The Malmbasis Schichten were found to be extremely unstable and were rejected.

Palaeomagnetic Results

At localities 2 and 3, the Jurassic sequence was sampled including various Liassic members, Klauskalk (Dogger), and the Malmbasis Schichten (lower Malm). Figure 3 shows the profile of the Saubachgraben which has been described geologically in detail by Plöchinger (1973, 1975).

The upper half of the profile (Fig. 3) cuts an olistolite (Plöchinger, 1973, 1975) and it is remarkable that the directions of the ChRM are quite uniform throughout the profile, independent of the rock type.

Major disturbance occurs in the Malmbasis-Schichten at the top of the profile. This is probably the top part of the olistolite, and therefore the disturbance is considered to be due to perturbation during the gliding process. The good correspondence of the data of the lower part of the profile and the olistolite suggests that the gliding occurred without any rotation.

Members of the Dogger were sampled only in the Saubachgraben (loc. 3).

Malmbasis Schichten were sampled at localities 2, 3 and 4. At all localities, except loc. 4 because of landslips, the red Adneter Kalk was sampled. In addition at loc. 2 and 3 various Liassic members were also sampled, even turbiditic layers (Fig. 3).

The local mean directions are shown in Figure 1, Figure 7 and Table 1 show the mean directions with the α_{95} cones of confidence for the Liassic members only.

The magnetic intensity (NRM) for the Adneter Kalk varies between 1×10^{-5} and 5×10^{-7} G.

The α_{95} cones of confidence for individual sites vary between 5° and 20°. The relatively large angles are attributable to the inaccuracy of the measurement of the nodulous bedding planes of certain members.

In the locality Breitenberg the results within a site are very consistent (COFC < 10°) but the local mean direction is (more or less) unsuitable. The reason is that sometimes even a statistical determination of the bedding parameters does not give satisfying results as in these sediments. Furthermore, we

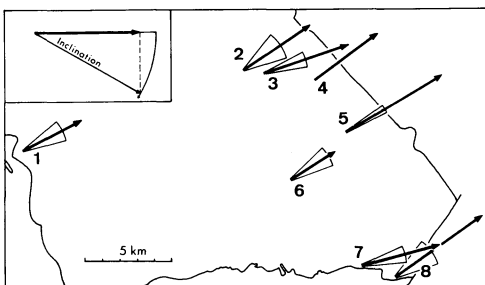


Fig. 7. Distribution of the direction of the characteristic remanent magnetisation for the Liassic sites of the Osterhorn mountain group with the cones of confidence. Loc. 4 shows vector for Malmbasis Schichten, because Liassic members could not be sampled there

Table 1. Palaeomagnetic results from the northern calcareous alps (austria)

Sampling area	Palaeo Data (Bedding corrected)					COFC.	Sampled members
	LOC.	DEC	INC	N(Sites)	k		
Lofer ^a		47.9	50.6	30 cores	70.7	6.5	Radiolarites, Lias
Adnet	1	63.7	56.1	6	26.8	13.1	Adneter Kalk
Schafbachgraben	2	56.4	48.9	6	15.3	17.6	Lias
Saubachgraben	3	71.1	42.3	8	34.1	9.6	Lias
Breitenberg	5	59.3	24.1	6 cores	255.73	4.2	Adneter Kalk
Königsbachtal	6	57.9	63.8	2	417.3	12.2	Adneter Kalk
Ausserlimbach	7	75.7	49.1	2	688.6	9.5	Adneter Kalk
Moosbergalm	8	55.2	30.0	2	228.0	16.6	Adneter Kalk
Mean values		62.5	45.1		29.1	11.3	
Osterhorn Gruppe (7 locations)							
Palaeoposition for Lofer and Osterhorngruppe							
	Sampling area position			Palaeopoleposition			
Lofer ^a	47,37°N;		12,34°E	LAT.: 53°N;		LONG. = 112°E	
Osterhorngruppe:	47,7°N;		13,3°E	LAT.: 37,5°N;		LONG. = 103,4°E	

^a After Hargraves and Fischer (1959)

get the same effect but with lower perturbation for the mean result of the whole area investigated. Figure 6b and c show the mean direction for the Osterhorn mountain group before and after the bedding correction.

Summarizing these details we have found in the area investigated a stable Jurassic magnetisation direction, which is suitable for attempting a geotectonic reconstruction of this part of the NCA.

Conclusions

Our results from Jurassic rocks of the Osterhorn mountain group, which is a stable block within the Northern Calcareous Alps (NCA), are in accordance with those obtained by Hargraves and Fischer (1959) for Jurassic, and Soffel (pers. comm) for Triassic rocks in other areas of the NCA. Therefore, the results are considered to be representative for the NCA throughout their length. To attain coincidence of the computed palaeopole for the Osterhorn mountains with the palaeopoles obtained by Van der Voo and French (1974) for the Jurassic of the European and African continents, it is necessary to rotate and laterally shift the NCA.

Figure 8 shows the Jurassic poles for stable Europe and Africa in their present position, as well as the computed palaeopole (with its cone of confidence) for the Jurassic rocks of the Osterhorn mountains, within the present geographi-

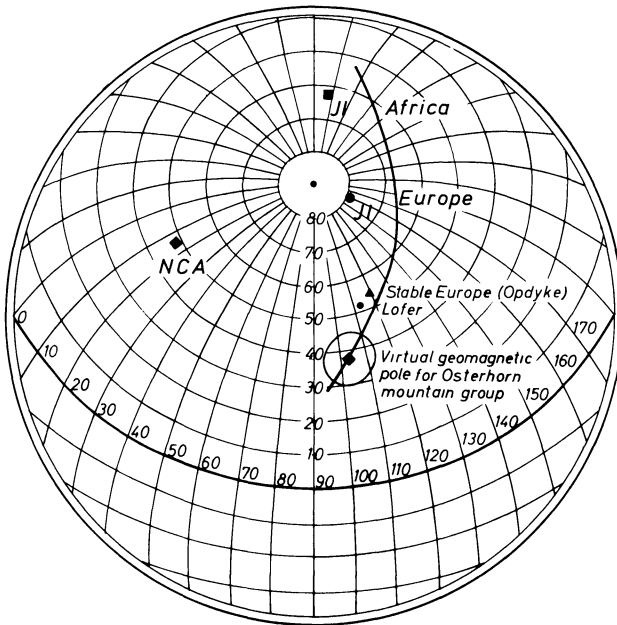


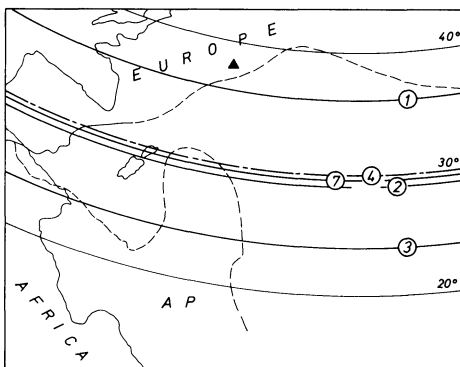
Fig. 8. Positions of lower (J1) Jurassic magnetic poles for Africa and Europe after Van der Voo and French (1974) within the present geographical grid. Abandoned Jurassic pole for Europe after Opdyke (1960), as well as poles for the Lofer area after Hargraves and Fischer (1959) and for the Osterhorn mountains are shown. NCA: present position of the Northern Calcareous Alps. (Polar error: $dm=13,9$; $dp=9,04$)

cal grid. A major clockwise rotation is evident. The magnetic palaeopoles for Africa and Europe on the one hand and for the Osterhorn mountains on the other do not lie on a small circle centered at the present position of the Osterhorn mountains. Therefore the Osterhorn mountains seem to have not only rotated but also moved laterally since the Jurassic. The lateral shift is necessary to attain coincidence in the inclination of the palaeomagnetic vectors.

Coincidence in the inclination for the Jurassic rocks of the Osterhorn mountains on the one hand and of stable Europe and Africa on the other is realized along a small circle (palaeolatitudes) around the Jurassic magnetic pole. Figure 9 shows the position of Europe relative to Africa in the middle Jurassic after Channel and Horvath (1976), based on the results of Van der Voo and French (1974). Palaeolatitudes are shown for the Liassic rocks of localities 1, 2, 3, and 7, and for the lower Malmian rocks of loc. 4. The average of these values is the 30° magnetic palaeolatitude (corresponding to $49,5^\circ$ inclination) which is shown as a broken line. The palaeolatitudes for localities 5, 6, and 8 are situated too far to the north and south and are therefore impossible palaeopositions for the NCA. The reason for this lies in difficulties with the measurements of the bedding plane at these localities. This does not significantly influence the declination and therefore all values were taken into account in Figure 8.

The mean palaeolatitudes (Fig. 9) is computed omitting localities 5, 6, and 8 and is in very good accord with the mean inclination obtained by Hargraves

Fig. 9. Reconstruction of the palaeolatitudes for the different sampling areas in the Osterhorn mountain group with the mean latitude of about 30°N which represents also the mean latitude for Lofer area after Hargraves and Fischer (1959). Black triangle indicates the present position of NCA. A.P.: Adriatic plate in the position of Channell and Horvath (1976)



and Fischer (1959) for the Lofer area. The palaeolatitude for this area also is on the broken line, Figure 9.

Theoretically, the NCA could have been placed at any point along the palaeolatitudes whose mean value runs through the wedge of the western Tethys formed by the Eurasian and African continents in the Jurassic.

The authors consider the NCA as a part of the Adriatic "plate" or "promontory" in the Jurassic comprising the autochthonous Apennines, the Southern Alps, and the Austroalpine domain. The Adriatic region has been separated from the Eurasian continent by the opening of the South Penninic ocean (Frisch, 1977). Tensional faulting of the NCA in the early Jurassic reflects this event. The Adriatic plate may have been separated from the African plate by a transform fault or a small ocean whose period of activity is unknown. Channel and Horvath (1976) considered the Adriatic region as a promontory of northern Africa. Our results are consistent with this interpretation although a slightly different position of the Adriatic region is preferred by Frisch (1977). Evidence for the timing of the separation of the Adriatic region from the African plate is poor; Biju-Duval et al. (1977) put this event near the beginning of the Jurassic implying that the Adriatic plate existed from this time on as a separate plate. Channel and Horvath (1976) let the Adriatic region remain as an African promontory up to the late Tertiary. Frisch (1977) presents evidence for the separation of the Adriatic plate from Africa in the Cretaceous.

The palaeoposition of the NCA (Fig. 9) implies lateral shift of the order of several hundred kilometres with respect to Eurasia. The magnetic vectors show clockwise rotation of about 45° relative to the Eurasian plate, and of about 90–100° relative to the African plate (Fig. 8). Progressively easterly palaeopositions of the NCA would enlarge the rotation angle.

If the Adriatic plate formed a coherent unit from the Jurassic on up to the present, the measured magnetisation directions of the autochthonous Apennine, the Southern Alps and the Northern Alps should correlate. This is definitely not the case. The Apennines and the Southern Alps show anticlockwise rotation of 23° to 55° (depending on the paper and the age of the rocks) relative to Europe. This anticlockwise rotation is in course agreement with the movement of Africa since the Jurassic (Channel and Horvath, 1976). The significant devia-

tion in the magnetic orientation of the Austroalpine realm (NCA) from the major part of the Adriatic plate implies decomposition of the plate at some time. Several theoretical possibilities are discussed:

(a) The separation of the NCA from the major part of the Adriatic region occurred earlier than the separation of the Adriatic plate from Africa. This is not supported geologically.

(b) The separation occurred after a common clockwise rotation of the Adriatic plate; while or after overthrusting welded the Austroalpine domain onto the Eurasian continent, (a process which has been finished by the late Eocene), the southern and major part of the Adriatic plate split off and rotated anticlockwise through an angle enlarged for the amount of the preceding clockwise rotation.

(c) The Adriatic plate remained as a unit without significant anticlockwise rotation up to the Upper Cretaceous. The breakoff of the NCA occurred at some time when the Austroalpine realm first came in contact with microcontinents to the north (Middle Penninic zone; Frisch, 1977). The clockwise rotation commenced at this moment and continued during the consequent overthrusting.

(d) The separation of the NCA from the Adriatic plate occurred at some time during the north- or northwestward drift of the Adriatic plate, prior to the collision to the north.

From our results, we are not able to decide whether the rotation of the NCA occurred at the beginning, during, or at the end of the drift. The decision as to which possibility preference should be given, is therefore delayed until more palaeomagnetic data, in particular for variously aged sequences from both sides of the Periadriatic lineament, are available. Drift and rotation of the NCA, however, can be limited to the period between the middle Jurassic and the collision and overthrust of the Austroalpine realm to the north. Frisch (1977) presents a plate tectonics reconstruction which makes decomposition of the Adriatic plate during the Upper Cretaceous most probable; according to this model, preference should be given to possibility (c).

Acknowledgements. The authors are thankfully obliged to Dr. B. Plöching, Geological Survey of Austria, Vienna, for valuable aid with the selection of the sampling sites and numerous discussions about stratigraphic problems. Dr. H. Heinz, Leoben, has carried out the thermal cleaning of the samples of several sites in Newcastle. We gratefully acknowledge his support. Part of the field work has been financed by the "Österreichischer Fonds zur Förderung der wissenschaftlichen Forschung, Project-No. 2778" which is also thankfully acknowledged.

References

- Biju-Duval, B., Dercourt, J., Le Pichon, X.: From the Tethys ocean to the Mediterranean seas: a plate tectonic model of the evolution of the western Alpine system. In: Structural history of the Mediterranean basins, Biju-Duval and Montadert, eds. Paris: Ed. Techniq 1977
- Bittner, A., Fugger, E.: Hallein und Berchtesgaden, 1:75.000 Geol. Spezialkarte d. Österr. Ungar. Monarchie, Bl. 4950, Geol. Reichsanst. Wien, 1907
- Channell, J.E.T., Horvath, F.: The African/Adriatic Promontory as a Palaeogeographical Premise for Alpine Orogeny and Plate Movements in the Carpatho-Balkan Region. *Tectonophysics* **35**, 71–101 1976

- Channell, J.E.T., Tarling, D.H.: Palaeomagnetism and the Rotation of Italy. *Earth Planet. Sci. Lett.* **25**, 177–188, 1975
- Frisch, W.: Die Alpen im westmediterranen Orogen – eine plattentektonische Rekonstruktion. *Mitt. Ges. Geol. Bergbaustudenten Österr.* **24**, 263–275, 1977
- Hargraves, R.B., Fischer, A.G.: Remanent Magnetism in Jurassic Red Limestones and Radiolarites from the Alps. *Geophys. J. Roy. Astron. Soc.* **2**, 34–41, 1959
- Jenkyns, H.C.: Origin of red modular limestones (Ammonitico Rosso, Knollenkalke) in the Mediterranean Jurassic: a diagenetic model. *Spec. Publ. int. Ass. Sediment* **1**, 249–271, 1974
- Jurgan, H.: Sedimentologie des Lias der Berchtesgadener Kalkalpen. *Geol. Rundschau* **58**, 464–501, 1969
- Lowrie, W., Alvarez, W.: Rotation of the Italian Peninsula. *Nature* **251**, 285–288, 1974
- Manzoni, M.: Palaeomagnetic Data of Middle and Upper Triassic Age from the Dolomites (Eastern Alps, Italy). *Tectonophysics* **10**, 411–424, 1970
- Mauritsch, H.J., Turner, P.: The Identification of Magnetite in Limestones using the Low-Temperature Transition. *Earth Planet. Sci. Lett.* **24**, 414–418, 1975
- Millot, G.: *Geology of Clays*, Berlin, Heidelberg, New York: Springer 1970
- Mojsisovics, E., Bittner, A.: Ischl und Hallstadt, 1:75.000. *Geol. Spezialkarte d. Österr. Ungar. Monarchie*, Bl. 4951, Geol. Reichsanst. Wien, 1905
- Molyneux, L.: A complete result magnetometer for measuring the remanent magnetization of rocks. *Geophys. J. Roy. Astron. Soc.* **24**, 429–433, 1971
- Opdyke, N.D. (1960) in Runcorn S.K.: *Continental Drift*. pp. 41–65, New York: Academic Press 1962
- Plöching, B.: Der Bau der südlichen Osterhorngruppe und die Tithon-Neokomtransgression. *Jb. Geol. Bundesanst. Wien* **96**, 357–372, 1953
- Plöching, B.: *Geologische Karte des Wolfgangseegebietes 1:25.000*. Geol. Bundesanst. Wien 1972
- Plöching, B.: Erläuterungen zur Geologischen Karte des Wolfgangseegebietes. *Geol. Bundesanst. Wien* 1973
- Plöching, B.: Das Juraprofil an der Zwölferhorn-Westflanke (Nördliche Osterhorngruppe, Salzburg). pp. 27–33, *Verh. Geol. Bundesanst. Wien* 1975
- Prey, S.: *Geologische Karte der Umgebung der Stadt Salzburg 1:50.000*. Geol. Bundesanst. Wien 1969
- Schlager, W., Schlager, M.: Clastic sediments associated with radiolarites (Tauglboden-Schichten, Upper Jurassic, Eastern Alps). *Sedimentology* **20**, 65–89, 1973
- Soffel, H.: Anticlockwise Rotation of Italy between the Eocene and Miocene: Palaeomagnetic Evidence from the Colli Euganei, Italy. *Earth Planet. Sci. Lett.* **17**, 207–210, 1972
- Tollmann, A.: *Der Bau der Nördlichen Kalkalpen*. Wien: Deuticke 1976
- Van den Berg, J., Wonders, A.A.H.: Palaeomagnetic Evidence of Large Fault Displacement around the Po-Basin. *Tectonophysics* **33**, 301–320, 1976
- Van der Voo, R., French, R.B.: Apparent Polar Wandering for the Atlantic-Bordering Continents: Late Carboniferous to Eocene. *Earth-Sci. Rev.* **10**, 99–119, 1974
- Van der Voo, R., Zijdeveld, J.D.A.: Palaeomagnetism in the Western Mediterranean Area. *Verh. Kon. Ned. Geol. Mijnbouwk. Gen. Volume XXVI*, 121–138, 1969
- Van Hilten, D.: Geology and Permian Palaeomagnetism of the Val-di-Non Area, *Geol. Ultraiectina* **5**, 95, 1960
- Vortisch, W.: Über schichtenparallele Bewegungen (Kammerker-Sonntagshorn-Gruppe und Osterhorngruppe). *Zentralblatt Mineral., B*, 263–286, 1937
- Wendt, J.: Stratigraphische Kondensation in triadischen und jurassischen Cephalopodenkalken der Tethys. *N. Jb. Geol. Paläont. Mh.*, 433–448, 1970
- Zijdeveld, J.D.A., Van der Voo, R.: Palaeomagnetism in the Mediterranean Area. In: *Implications of Continental Drift of Earth Sciences*, D.H. Tarling and S.K. Runcorn, eds.. New York: Academic Press 1973

Zur Korrelation zwischen der Vertikalintensität des erdmagnetischen Feldes und dem Schwerefeld im ostalpinen Raum

W. Seiberl, A. Franke, R. Gutdeutsch und P. Steinhauser

Institut für Meteorologie und Geophysik, Universität Wien,
Währingerstraße 17, A-1090 Wien, Österreich

Correlation Between Magnetic and Gravimetric Data in the East Alpine Area

Abstract. There is some evidence of a correlation between the Bouguer anomaly δg and the residuals δZ of the earth's magnetic field in the East Alpine area. If this correlation exists, it should be created by similar structures in the crust of the earth. To prove this, the gravimetric and magnetic data of parts of Central Europe were interpolated on a square grid with a grid spacing of $\Delta s = 10$ km. In a next stage the gradients

$$\frac{\partial \delta g}{\partial x}, \frac{\partial \delta g}{\partial y}, \frac{\partial \delta g}{\partial z}$$

were estimated with the aid of approximation formulas. A correlation of δZ with the gradients of δg exists only in the eastern parts of Austria.

Two-dimensional model calculations along a profile from St. Valentin (near Linz) toward Klagenfurt shows that the δZ anomaly is caused by the upper boundary of a weakly magnetized crystalline basement. The latter has also a positive density contrast as compared to the above-lying rock formations. In contrast to the magnetic anomaly the Bouguer anomaly is additionally caused by rocks the Curie point isothermal layer.

Key words: Correlation between magnetic and gravimetric data – East Alpine area.

Einleitung

Eine Korrelation zwischen der magnetischen Anomalie δZ und den Ableitungen der Schwereanomalie eines Störkörpers ist aufgrund potentialtheoretischer Zusammenhänge zu erwarten, wenn sich ein Störkörper sowohl in seiner homo-

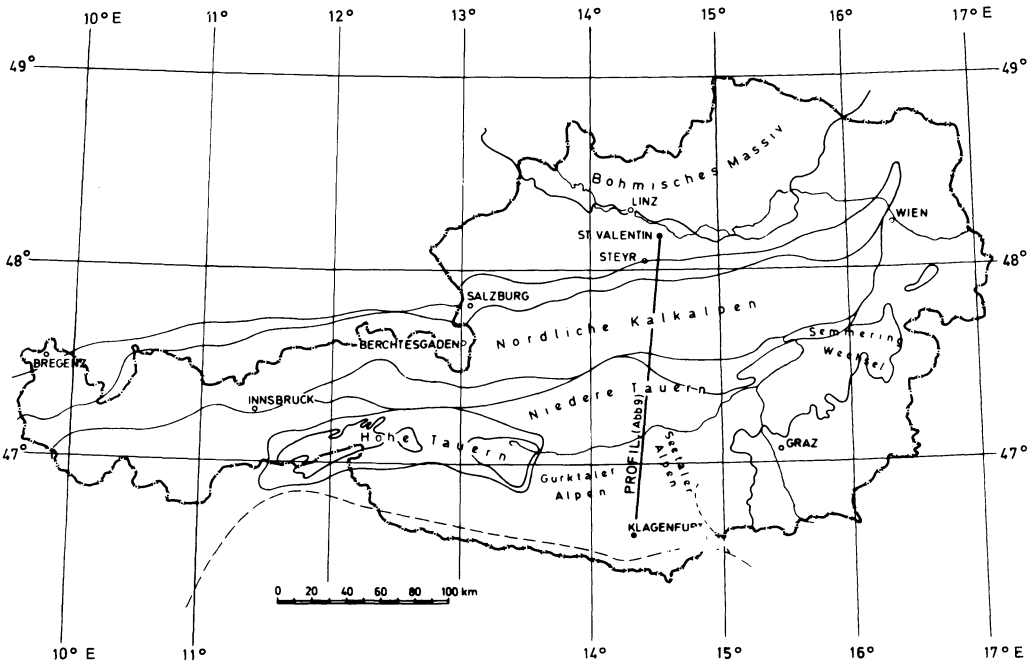


Abb. 1. Übersichtskarte des ostalpinen Raumes mit den wichtigsten geographischen Bezeichnungen

genen Magnetisierung als auch in seiner Dichte hinreichend von seiner Umgebung unterscheidet. Die simultane Untersuchung beider Meßgrößen und ihrer Korrelation kann daher insofern Zusatzinformationen über die stoffliche Zusammensetzung des Störkörpers liefern, als es auch nur wenige Gesteine gibt, bei denen Dichte und Magnetisierung gleichzeitig vom Durchschnitt abweichen. Hierzu gehören in erster Linie basische und ultrabasische Gesteine bei Temperaturen unterhalb des Curie-Punktes. Untersuchungen dieser Art wurden von Eötvös (1909) sowie später u.a. von Haalck (1929), Heiland (1946), Baranov (1957) und Linsser und Merritt (1970) durchgeführt und zeigten, daß die theoretisch gegebenen Beziehungen in der Praxis nicht immer klar erkennbar sein müssen, was zum Teil auf die oben erwähnten mineralogischen Voraussetzungen zurückzuführen ist. Überdies ist die Variationsbreite für Dichte und Magnetisierung von Gesteinen sehr unterschiedlich; die Dichteunterschiede erreichen im Extremfall nicht einmal den Betrag einer Größenordnung, während die Gesteinsmagnetisierung um etwa sieben Größenordnungen schwanken kann.

Die Vermutung, daß in Österreich eine Korrelation zwischen den gravimetrischen und geomagnetischen Feldgrößen besteht, legt ein Vergleich der Karten der geomagnetischen Landesaufnahme (Pühringer et al., 1975) und der Bouguer-Schwerekarte nahe. Von den bisher publizierten Bouguerkarten (u.a. Senftl, 1965; Makris, 1971) ist hier die Karte von Senftl (1965) verwendet worden. Die Bougueranomalie erreicht im Tauernfenster (Abb. 1) ihr Minimum von rund 160 mgal. Nördlich hiervon steigt δg langsam an, um bei Berchtesgaden (Abb. 1) ein schwaches Maximum zu durchlaufen. Das Bouguer-Minimum in den Hohen

Tauern (Abb. 1) korreliert recht gut mit einer kräftigen negativen Anomalie des Restfeldes δZ . Daher wurde als erster Test die Korrelation der δZ - und δg -Werte für ganz Österreich berechnet. Hierzu werden für die 227 Punkte der magnetischen Landesaufnahme, die praktisch gleichmäßig über das ganze Bundesgebiet verteilt sind, die Beträge der Bougueranomalie durch Interpolation aus der Schwerekarte bestimmt. Der so berechnete Korrelationskoeffizient beträgt $r = 0,34$ und ist nach dem t -Verteilungstest statistisch signifikant (Sachs, 1968). Regional gesehen ergeben sich systematische Unterschiede im Grad der Korrelation. Die beste Übereinstimmung ergibt sich in der Molasse des westlichen Donautales, den Niederen Tauern, Gurktaler- und Seetaler Alpen sowie Teilen der Hohen Tauern (Abb. 1), also auf einer Fläche, die etwa der Hälfte des gesamten Untersuchungsgebietes entspricht. Bei Beschränkung auf dieses Gebiet steigt der Korrelationskoeffizient auf $r = 0,66$ bei 138 Datenangaben und ist gemäß t -Test ebenfalls statistisch signifikant (Sachs, 1968). Eine wesentlich bessere Korrelation zwischen der Bougueranomalie und dem Vertikalintensitäts-Restfeld ist nicht zu erwarten, da ja die Korrelation nach der Theorie erst mit den Ableitungen der Schwerkraft gegeben sein soll, was daher näher untersucht werden soll.

Grundlagen der Bearbeitungsmethode

Die Anomalie des Magnet- und Schwerefeldes möge durch N Körper mit den Dichten ρ_i und den homogenen Volumenmagnetisierungen $\mathbf{m}_i = (m_{x_i}, m_{y_i}, m_{z_i})$ ($i = 1, 2, 3 \dots N$) hervorgerufen sein. Dann leitet man für die Vertikalintensität des erdmagnetischen Feldes ab:

$$\delta Z = \sum_{i=1}^N \delta Z_i = \frac{1}{f} \sum_{i=1}^N \left(\frac{m_{x_i}}{\rho_i} \frac{\partial \delta g_i}{\partial x} + \frac{m_{y_i}}{\rho_i} \frac{\partial \delta g_i}{\partial y} + \frac{m_{z_i}}{\rho_i} \frac{\partial \delta g_i}{\partial z} \right) + \delta Z_0(x, y, z), \quad (1)$$

($f = \text{Gravitationskonstante}$)

wobei δZ_i und δg_i die durch den i -ten Körper erzeugte Vertikalkomponente des magnetischen bzw. Schwerefeldes sind und δZ_0 einen Feldanteil bedeutet, der nicht von \mathbf{m}_i hervorgerufen wird. Da im allgemeinen nur $\delta g = \sum \delta g_i$ durch Messungen bestimmt wird, müssen die partiellen Ableitungen der Schwerebeschleunigung näherungsweise aus δg abgeleitet werden. Überwiegt unter N Körpern die Wirkung eines einzigen Körpers der Dichte ρ und der homogenen Magnetisierung (m_x, m_y, m_z) dann kann man Gl. (1) vereinfacht schreiben

$$\delta Z \approx \frac{1}{f\rho} \left(m_x \frac{\partial \delta g}{\partial x} + m_y \frac{\partial \delta g}{\partial y} + m_z \frac{\partial \delta g}{\partial z} \right) + \delta Z_0(x, y, z) \quad (2)$$

oder mit Abkürzungen

$$\delta Z = B \frac{\partial \delta g}{\partial x} + C \frac{\partial \delta g}{\partial y} + D \frac{\partial \delta g}{\partial z} + \delta Z_0(x, y, z). \quad (3)$$

Es ist möglich, den Ansatz (3) zu prüfen, wenn man $\delta Z_0(x, y, z)$ als Rest des Regionalfeldes interpretiert und mit $A = \text{const.}$ ansetzt. Unter diesen Voraussetzungen sind die Koeffizienten A , B , C und D durch Minimalisierung der Fehlerquadrate, integriert über die Fläche F ,

$$\sigma^2 = \iint_F \left(\delta Z(x, y) - A - B \frac{\partial g(x, y)}{\partial x} - C \frac{\partial g(x, y)}{\partial y} - D \frac{\partial g(x, y)}{\partial z} \right)^2 = \min \quad (4)$$

bestimmbar. Dieses Doppelintegral kann näherungsweise durch eine Doppelsumme ersetzt werden, weil δZ , sowie die Gradienten von g auf Gitterpunkten diskret vorgegeben sind. Im konkreten Fall wurde ein 5×5 -Raster mit einem Punktabstand von 10 km gewählt. σ_{\min}^2 kann dann als Maß für die Güte der Näherung und damit auch für die Wahrscheinlichkeit der Vermutung gelten, daß die magnetische und gravimetrische Anomalie auf den gleichen Störkörper zurückzuführen sind. Weiterhin wird eine über das gesamte Untersuchungsgebiet homogene Magnetisierung angenommen. Diese Annahme ist gerechtfertigt, wenn man nur induzierte Magnetisierung (derzeitige Feldrichtung) zuläßt. Die Richtung des geomagnetischen Feldes ändert sich im untersuchten Gebiet um kaum mehr als 2° bis 3° sowohl der geographischen Breite als auch der Länge nach. Diese Größen sind bei der Betrachtung des Restfeldes durchaus zu vernachlässigen.

Aufbereitung der Daten

Zunächst werden die Residuen δZ mit Hilfe der Ergebnisse der geomagnetischen Landesvermessungen von Bayern, Österreich und der südlichen Tschechoslowakei auf einem quadratischen Raster von 10 km Seitenlänge durch lineare Interpolation bestimmt (Pühringer et al., 1975; Wienert 1965; Burmeister, 1960; Bouska et al., 1959). Das Auflösungsvermögen des Verfahrens wird durch den mittleren Punktabstand von ca. 15 km bestimmt. Man muß daher Gebiete bzw. Anomalien ausschließen, die bei diesem Punktabstand nicht mehr aufgelöst werden (Nyquist-Wellenzahl $1/30$ km). Dieses ist in einigen interessanten Gebieten wie z.B. dem südlichen Burgenland (Szénás, 1967) und in den Hohen Tauern (Angenheister et al., 1972) der Fall. Diese Gebiete müssen deswegen gesondert untersucht werden.

In der gleichen Weise wurden die Bouguerkarten bearbeitet. Die so bestimmten, auf ein quadratisches Raster bezogenen δg -Werte wurden sodann überlappend in Flächenstücke zu je 7×7 Punkten bzw. $60 \times 60 \text{ km}^2$ aufgeteilt. Für jedes dieser Flächenstücke erfolgte eine Berechnung des Vertikalgradienten $\frac{\partial \delta g}{\partial z}$ nach dem von Jung (1961) beschriebenen Auszählendiagramm. Jung weist darauf hin, daß die Verwendung dieses Verfahrens nur zu Näherungen führt und für Punktmassen in der Tiefe s bzw. $2s$ ($s = \text{Rasterabstand}$, hier 10 km) 70% bzw. 90% des Extremwertes ergibt. Eine genaue Analyse zeigt weitere Fehler für große Tiefen des Störkörpers. Abbildung 2 stellt die exakten Ergebnisse für eine Punktmasse in der Tiefe z den Näherungen gegenüber. Für $z = 4s$ wird zwar die

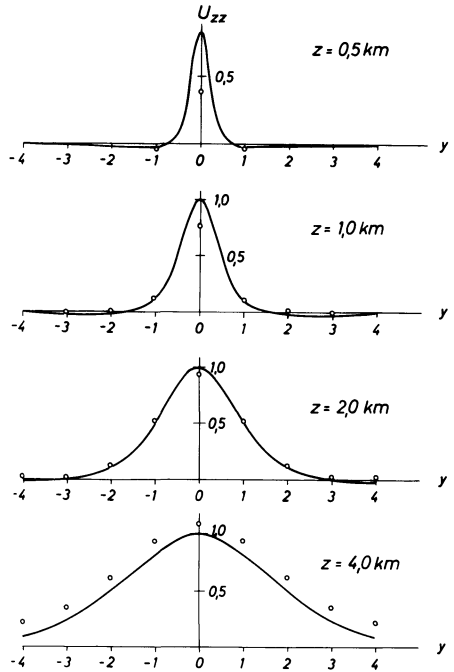


Abb. 2. Vergleich zwischen den theoretischen Werten von $\frac{\partial \delta g}{\partial z}$ über einem kugelförmigen Störkörper in verschiedenen Tiefen z (ausgezogene Linie) und den nach Jung (1961) bestimmten $\frac{\partial \delta g}{\partial z}$ -Werten (Punkte)

Form der Kurve recht genau wiedergegeben, doch erscheint sie parallel zu positiven Werten hin verschoben. Dieser Fehler muß als eine Folge der Vernachlässigung des außerhalb des Flächenstückes liegenden Integrationsgebietes angesehen werden. Die in Abbildung 3a wiedergegebenen $\frac{\partial \delta g}{\partial z}$ -Werte zeigen einen deutlichen Trend, der generell von NE nach SW abnimmt. Daraus wäre unter Umständen zu schließen, daß der Einfluß von Massen mit Tiefen über 40 km unter dem Alpenkörper stärker ist als außerhalb davon, was aus Überlegungen über den Aufbau der Erdkruste verständlich erscheint. In diesem Falle wäre der Trend als verfahrensbedingter Fehler anzusehen. Aus diesem Grund wurde der lineare Trend von den $\frac{\partial \delta g}{\partial z}$ -Werten subtrahiert. Das sich ergebende Feld $\frac{\partial \delta g}{\partial z}$ ist in Abbildung 3b wiedergegeben. $\frac{\partial \delta g}{\partial z}$ korreliert deutlich mit δZ (Abb. 6). Im Falle der Tauernanomalie erscheint jedoch das $\frac{\partial \delta g}{\partial z}$ -Minimum gegen das δZ -Minimum nach Norden verschoben, vermutlich als Folge einer gewissen Asymmetrie des δZ -Feldes.

Die Bestimmung von $\frac{\partial \delta g}{\partial x}$ und $\frac{\partial \delta g}{\partial y}$ an einem Punkt $x=i\Delta s, y=j\Delta s$ aus dem Schwerewert $\delta g_{i,j}$ erfolgte mit Hilfe folgender Näherungsformeln:

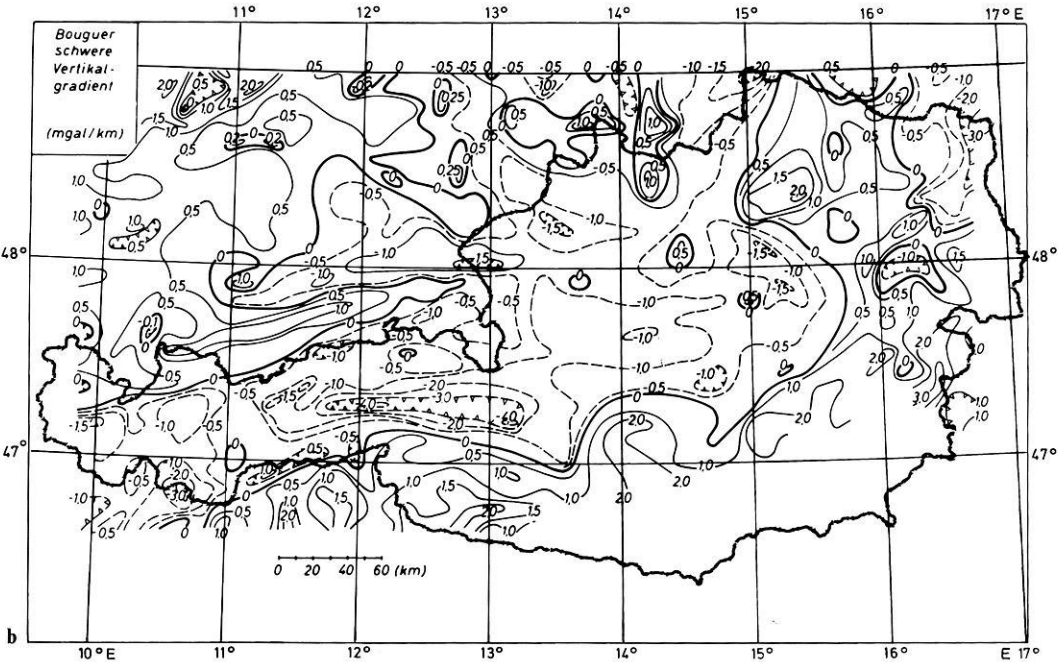
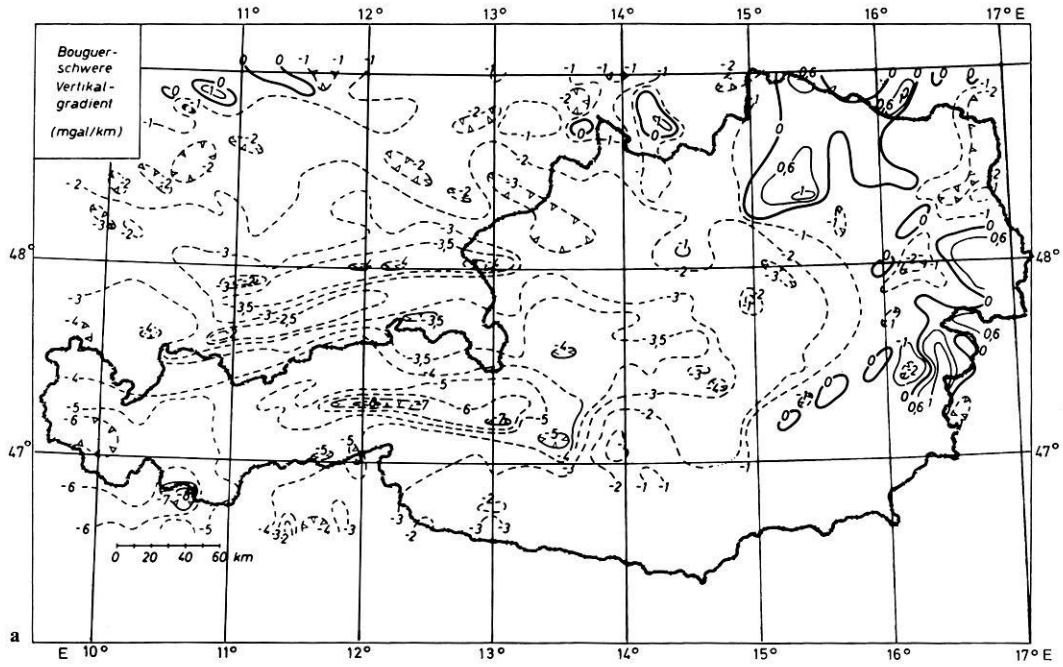


Abb. 3a und b. (a) Die regionale Verteilung des Vertikalgradienten $\left(\frac{\partial \delta g}{\partial z}\right)$ der Bouguerschwere im ostalpinen Raum; (b) Die regionale Verteilung des Vertikalgradienten $\left(\frac{\partial \delta g}{\partial z}\right)$ der Bouguerschwere nach Entfernung des linearen Trends

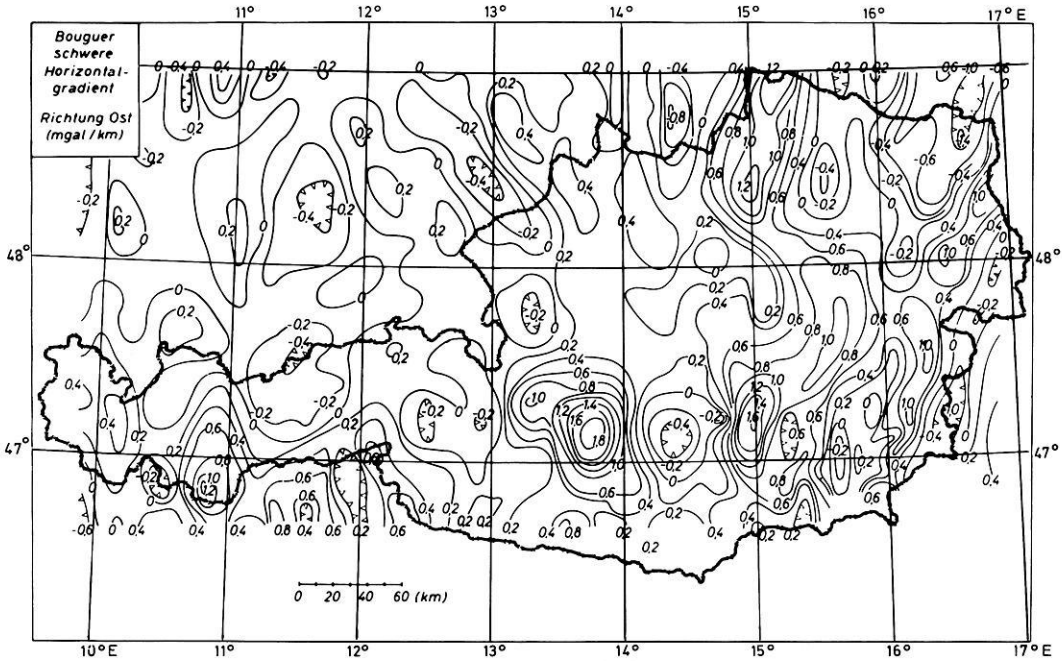


Abb. 4. Die regionale Verteilung des Horizontalgradienten $\left(\frac{\partial \delta g}{\partial y}\right)$, Richtung Ost, der Bouguerschwere im ostalpinen Raum

$$\frac{\partial \delta g}{\partial x}(x_i, y_i) \approx \sum_{v=1}^3 (\delta g(x_{i+1}, y_{j-2+v}) - \delta g(x_{i-1}, y_{j-2+v})) / 6s \quad (5)$$

$$\frac{\partial \delta g}{\partial y}(x_i, y_i) \approx \sum_{v=1}^3 (\delta g(x_{i-2+v}, y_{j+1}) - \delta g(x_{i-2+v}, y_{j-1})) / 6s \quad (6)$$

Die Ergebnisse sind in den Abbildungen 4 und 5 zu finden.

Stellt man die Abbildungen 3a, 4 und 5 der δZ_i -Karte (Abb. 6), die das Ergebnis einer Glättung der δZ_i -Werte auf einem 3×3 Gitterpunktnetz ist, gegenüber, so erkennt man, daß die Streichrichtung der Alpen in allen Karten

– bis auf die für $\frac{\partial \delta g}{\partial y}$ – dominant ist. Jedoch kann man schon visuell erkennen,

daß die Ableitungen der Schwere nur in wenigen engbegrenzten Gebieten mit δZ korrelieren. So ist z.B. die Korrelation im Bereich der Anomalie, die in den Nördlichen Kalkalpen im Raum von Berchtesgaden liegt („Berchtesgadner Anomalie“ (Gänger, 1954; Bleil und Pohl, 1976)), schlecht, hingegen weiter östlich im Raum um Steyr besser. Die Verteilung der Standardabweichung σ , angewendet auf kleinere Teilflächen mit einer Ausdehnung von $40 \text{ km} \times 40 \text{ km}$ gibt diesen Sachverhalt noch genauer wieder (Abb. 7). Diese Darstellung der „Fehlergebirge“ zeigt in den Zentralalpen große Werte, im Raum des Alpenvorlandes kleinere. Besonders sei auf die geringen Fehler im Gebiet des Semmerings und Wechsels, im östlichen Böhmischem Massiv und im Raum um Steyr (Abb. 1) hingewiesen.

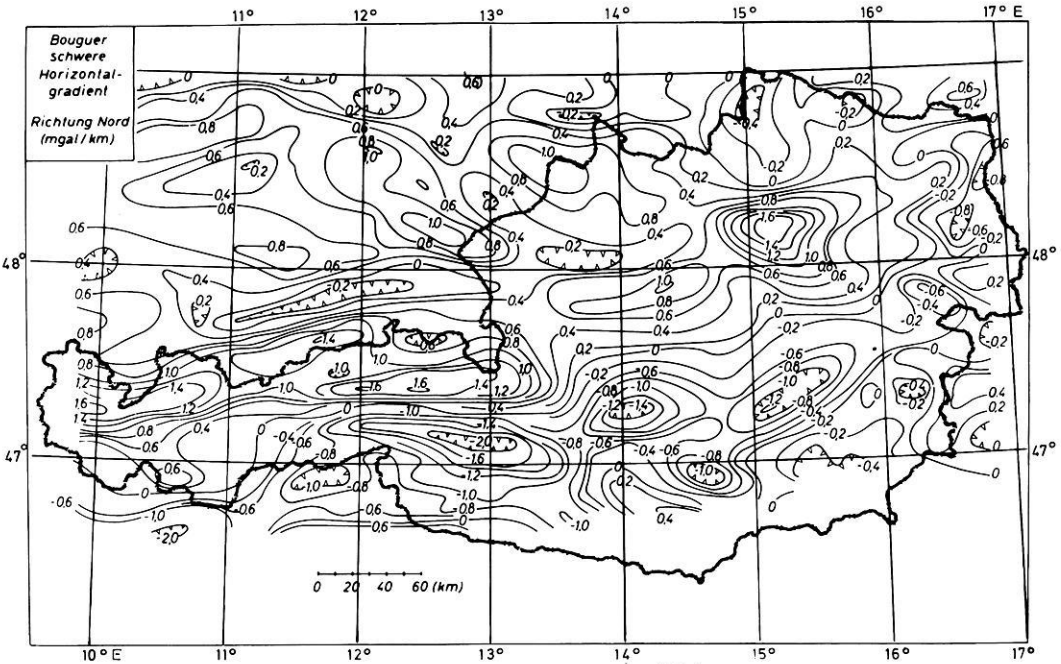


Abb. 5. Die regionale Verteilung des Horizontalgradienten $\left(\frac{\partial \delta g}{\partial x}\right)$, Richtung Nord, der Bouguer-schwere im ostalpinen Raum

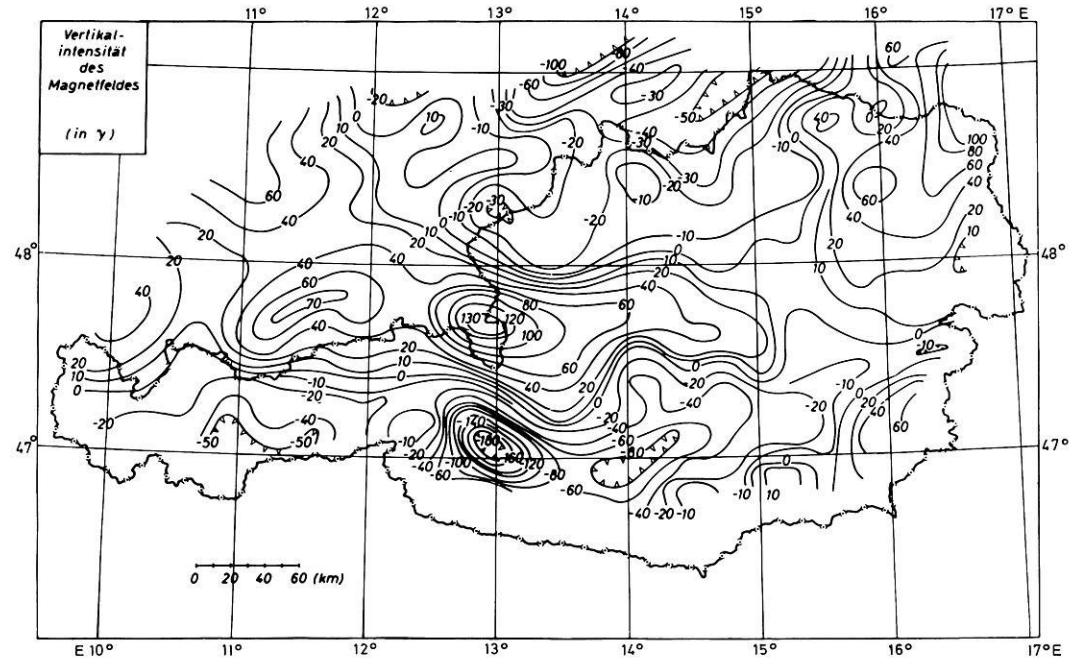


Abb. 6. Die Residuen (δZ) der Vertikalintensität des erdmagnetischen Feldes im ostalpinen Raum

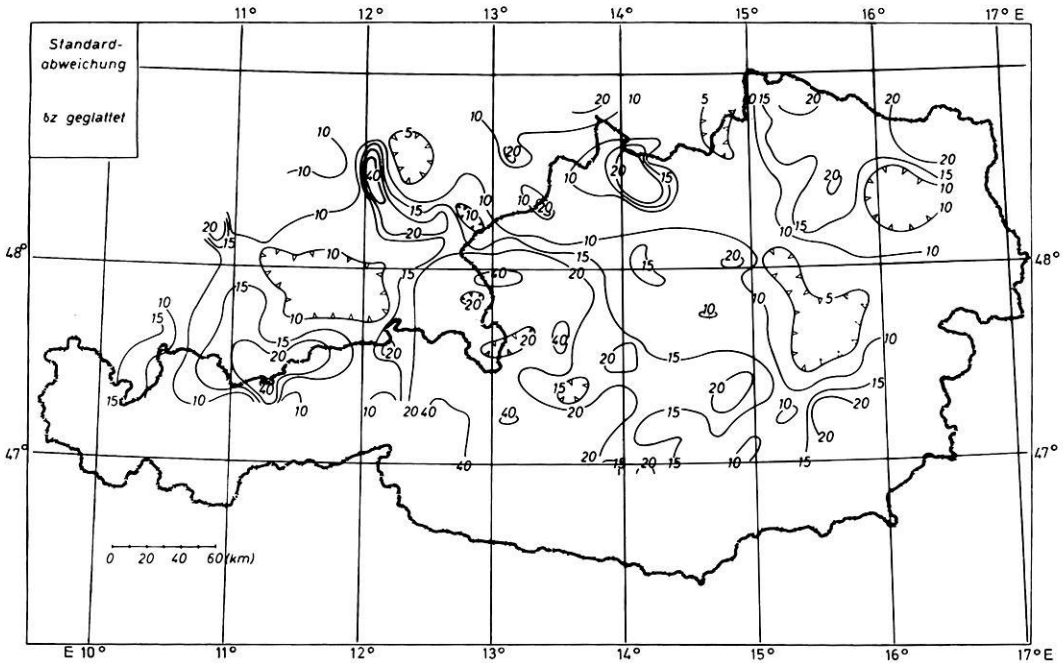


Abb. 7. Die regionale Verteilung der Isanomalien der Standardabweichung im ostalpinen Raum (δZ geglättet)

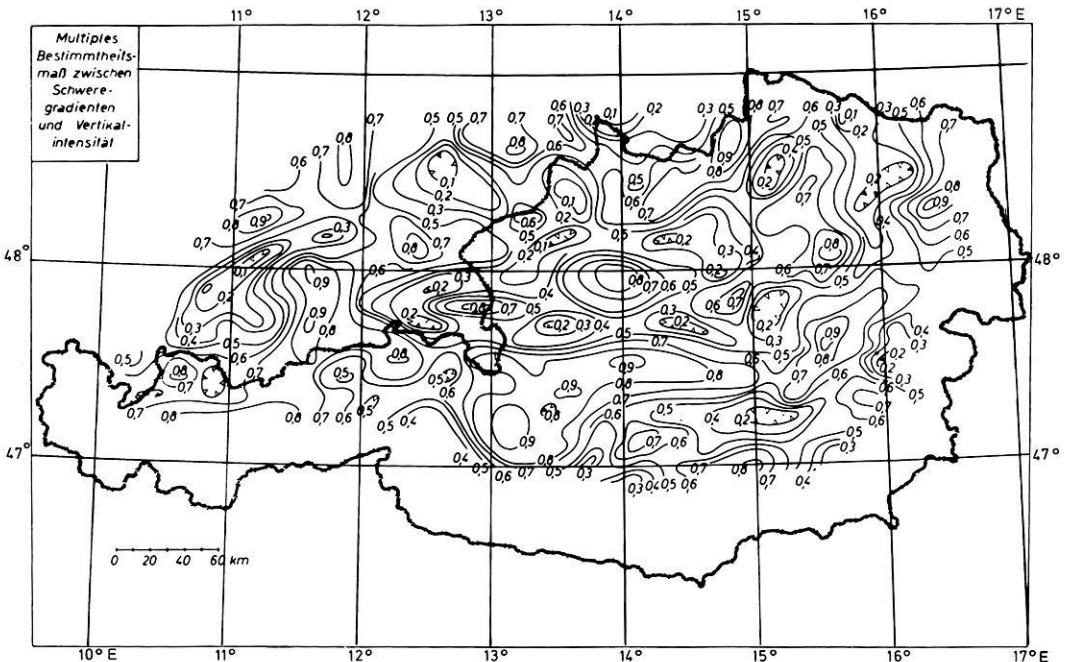


Abb. 8. Die regionale Verteilung des multiplen Bestimmtheitsmaßes (r^2) zwischen den Schweregradienten ($\frac{\partial \delta g}{\partial x}, \frac{\partial \delta g}{\partial y}, \frac{\partial \delta g}{\partial z}$) und der Vertikalintensität (δZ) im ostalpinen Raum

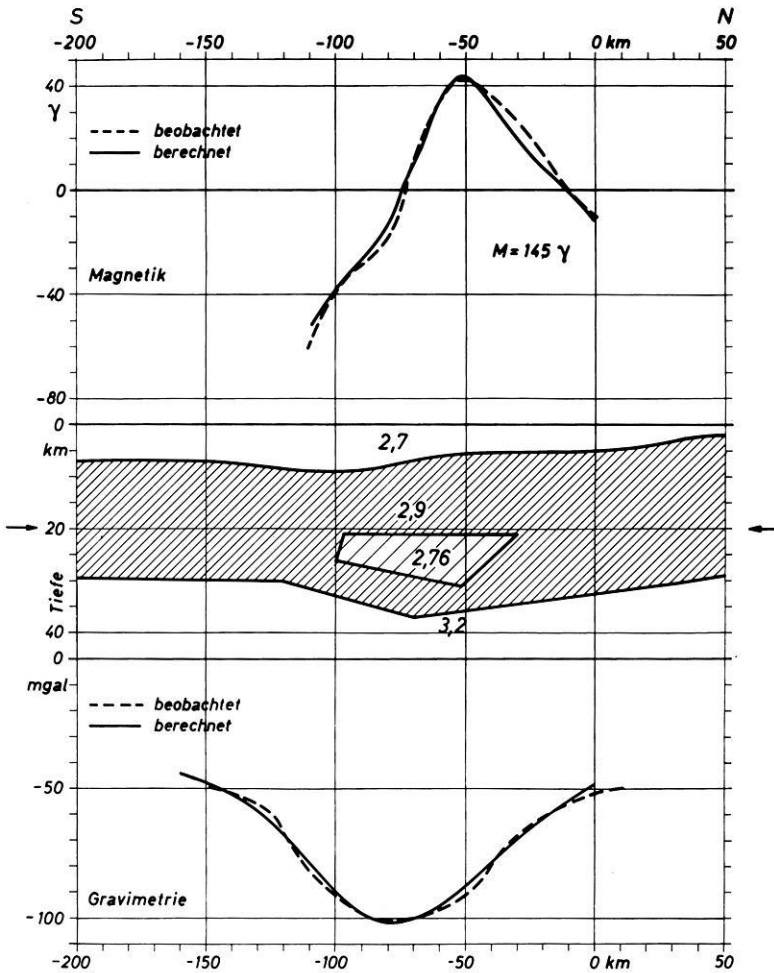


Abb. 9. Gravimetrische und magnetische zweidimensionale Modellrechnungsergebnisse entlang eines Profils von St. Valentin (bei Linz) in Richtung Klagenfurt (die Curiepunktisotherme liegt in 20 km Tiefe und ist mit einem Pfeil gekennzeichnet)

Da das multiple Bestimmtheitsmaß (r^2) (vgl. (Sachs, 1968)) ein noch allgemeineres Kriterium für die Korrelation zwischen δZ und den Ableitungen der Schwere bildet, wurde auch diese Größe bestimmt und wie die oben erwähnte Standardabweichung σ aufgetragen.

Das Ergebnis findet sich in Abbildung 8. Die vergleichsweise hohen Werte für r^2 dürfen nicht erstaunen, denn man muß ja in Betracht ziehen, daß $\frac{\partial \delta g}{\partial x}$, $\frac{\partial \delta g}{\partial y}$, $\frac{\partial \delta g}{\partial z}$ nicht unabhängig voneinander gemessen, sondern aus δg berechnet wurden. Das Resultat zeigt große Ähnlichkeit mit der σ -Verteilung in Abbildung 7.

Als einen ersten Versuch, einen gemeinsamen Störkörper für die beobachteten Schwere- und Magnetikwerte zu finden, wurde ein zweidimensionales Modell längs eines Profiles (Abb. 1), das von St. Valentin in Richtung Klagenfurt verläuft, gerechnet. Dabei wurde von einer möglichst einfachen Modellannahme ausgegangen. Die Tiefe zur Curiepunkt-Isotherme, unter der keine Magnetisierung mehr möglich ist, wurde mit einheitlich 20 km festgesetzt. Dieser Annahme liegt ein Temperaturgradient von $1^{\circ}\text{C}/33\text{ m}$ zugrunde. In Abbildung 9 sind sowohl die beobachteten als auch die berechneten Profilwerte, nebst dem zugehörigen Modell, zusammengefaßt. Die Magnetisierung des Störkörpers kann aus plausiblen Gründen nicht hoch sein; sie wurde mit $m = 145 \gamma$ angenommen. Die angenommenen Dichtewerte sind im Modell eingetragen und entsprechen den üblichen – etwas schematisierten Vorstellungen – über den Aufbau der Ostalpen. Demnach wird die magnetische Anomalie durch die obere Begrenzung eines schwach magnetischen Grundgebirges, das zusätzlich einen Dichtekontrast gegen die Überlagerung zeigt, verursacht. Die Tiefe bis zu dieser Grenzfläche beträgt im Norden des Profiles ca. 2 km. Sie erreicht unter den Alpen ihren größten Wert mit 9 km. Im Süden verläuft die Oberkante des Grundgebirges in einer Tiefe von etwa 7 km. Die Schwereanomalie wird zusätzlich noch durch Massen unterhalb der Curiepunkt-Isotherme verursacht, wobei die Moho-Diskontinuität eine Tiefenlage zwischen 29 km und 38 km aufweist.

Aus dieser Untersuchung ist zu folgern, daß entgegen dem visuellen Eindruck, den die gravimetrischen und magnetischen Anomalien in Österreich vermitteln, eine ursächliche Korrelation nur in Teilen besteht.

Danksagung. Diese Arbeit stellt einen Beitrag dar, der aus Mitteln des National Komitees „Geodynamisches Projekt“ der Österreichischen Akademie der Wissenschaften finanziert wurde. Hierfür sei der Österreichischen Akademie der Wissenschaften herzlich gedankt.

Literatur

- Angenheister, G., Bögel, H., Gebrande, H., Giese, P., Schmidt-Thomé, P., Zeil, W.: Recent investigations of surficial and deeper crustal structures of the Eastern and Southern Alps. *Geol. Rundschau* **61**, 349–395, 1972
- Baranov, V.: A new method for interpretation of aeromagnetic maps: Pseudo-gravimetric anomalies. *Geophysics* **22**, 359–383, 1957
- Bleil, U., Pohl, J.: The Berchtesgaden Magnetic Anomaly. *Geol. Rundschau* **65**, 756–767, 1976
- Bouska, J., Bucha, V., Koci, A.: Geomagnetische Karten der Tschechoslowakischen Republik für die Epoche 1958, 0. Travaux Inst. Géoph. Acad. Tchéc. Sci. Nr. 12, *Geophys. sborník*, Prague, 1959
- Burmeister, F.: Magnetische Vermessung II. Ordnung von Bayern 1955, 0. *Geoph. Observ. Fürstentfeldbruck d. Univ. München, Serie B, Nr. 1*, München, 1960
- Eötvös, R.: Bericht über geodätische Arbeiten in Ungarn, besonders über Beobachtungen mit der Drehwaage. *Verhand. 16. Konf. Int. Erdmessung*, 341 pp., London 1909
- Gänger, R.: Regionale magnetische Untersuchungen in den Berchtesgadner Kalkalpen und ihrem Vorland. *Diss. Naturwiss. Fak. Univ. München* 1954
- Haalck, H.: Zur Frage der Erklärung der Kursker magnetischen und gravimetrischen Anomalie. *Gerlands Beitr. Geophys.* **22**, 241–255 und 385–399, 1929
- Heiland, C.A.: *Geophysical Exploration*. New York: Prentice-Hall Inc. 1946
- Jung, K.: *Schwerkraftverfahren in der angewandten Geophysik*. Leipzig: Akademische Verlagsgesellschaft Geest & Portig K.G. 1961

- Linser, H., Merritt, R.K.: Comparison of gravimetric and magnetic data by the formation of pseudomagnetic fields. 32 nd EAEG-meeting. Edinburgh (Scotland) 1970
- Makris, J.: Aufbau der Erdkruste in den Ostalpen aus Schweremessungen und die Ergebnisse der Refraktionsseismik. Hamburger Geophys. Einzelschr., Heft 15, Hamburg 1971
- Pühringer, A., Seiberl, W., Trapp, E., Pausweg, F.: Die Verteilung der erdmagnetischen Elemente in Österreich zur Epoche 1970, 0. Arbeiten a.d. Zentralanstalt f. Meteor. u. Geod., Heft 14, Wien 1975
- Sachs, L.: Statistische Auswertemethoden. Berlin Heidelberg NewYork: Springer 1968
- Senftl, E.: Schwerekarte von Österreich, Bouguer-Isanomalien. Bundesamt f. Eich- und Vermessungswesen, Wien 1965
- Szénás, G.: Geofizikai Közlemények. Magyar Állami Eötvös Loránd Geofizikai intézet kiadványa, XVI. Kötet, 4. Szám Műszaki könyvkiadó, Budapest 1967
- Wienert, K.: Ergebnisse der erdmagnetischen Beobachtungen im Jahre 1964. Geoph. Observ. Fürstenfeldbruck d. Univ. München, Serie A, Nr. 7 (Einleitung), München 1965

Eingegangen am 23. Mai 1977/in revidierter Fassung am 16. Juni 1978

Some Aspects of Athabasca Oil Sand Behavior, Alberta, Canada

M.L. Jeremic

Associate Professor of Mining, Department of Mineral Engineering,
The University of Alberta, Edmonton, Canada T6G 2E1

Abstract. The basic behavior of Athabasca oil sand under uniaxial loading may be expressed as a property of both elastic and viscous bodies, where the predominance of each component depends on its composition.

Cyclic loading deformations showed that the shear strength of oil sand is almost half those of a static load, probably because of dissipation of energy and increase in temperature. However, a cyclic load with a previously applied static load, destroys the shear strength of oil sand, probably due to its structural viscosity.

Oil sand under hydrostatic pressure has a viscous deformation. The rate of deformation is a function of the bitumen viscosity. The bitumen viscosity greatly depends on the temperature, and so does the rate of deformation.

The represented investigations on disturbed (remoulded) samples without a gaseous phase, are intended to show the unique property of oil sand. However, a definite evaluation of the behavior of oil sand can be done only on intact of undisturbed deposits in the field.

Key words: Oil sand – Composition – Properties – Behavior – Structural deformation.

Introduction

The Lower Cretaceous sands, silts, and shales of the McMurray Formation lie unconformably on Devonian limestone and are overlain disconformably by marine shales of the Lower Cretaceous Clearwater Formation. Some time after the deposition of the McMurray Formation the bitumen probably migrated into waterwet sands (Hardy and Hemstock, 1963). The thickness of the oil sand formation varies between 6 and 60 m. It is covered by overlying strata up to 1300 m thick, some of which were later eroded. The present ground surface is the result of Pleistocene glaciation and recent erosion. The oil sand formation gently dips from its exposure at the Athabasca River to the east

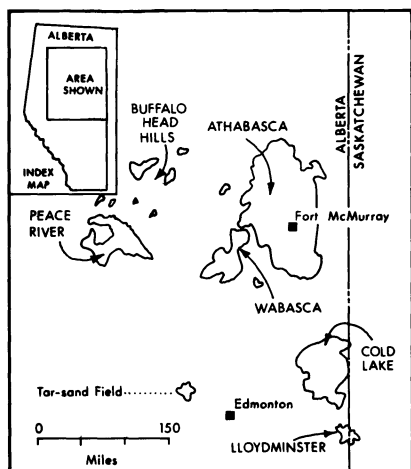


Fig. 1. Alberta's oil sand deposits

and west, where it is covered by up to 1300 m of overburden. The Athabasca oil sand deposit is the largest one (Fig. 1) in the province of Alberta.

Current estimates are that all oil sands deposits in Alberta contain about 700 billion bbl of crude oil (McConville, 1975). This is roughly equivalent to ten times that of the combined U.S.A. and Canadian total oil reserves. It is obvious that oil sand deposits are one of the more important sources of energy. At present the only developed method for oil sand exploitation is open-pit mining. By this method 10 percent of the total bitumen reserves can be obtained (pit limit 60 m of overburden). However, at present very intensive research work is in progress for "in situ" bitumen recovery. This method may perhaps be applied where the thickness of overlying strata exceeds 200–300 m. For this part of the oil sand deposits it is necessary to find some subsurface exploitation system or systems which might be applicable, for large scale production.

The oil sand has a unique composition as a four-phase system: solid-sand, viscous-bitumen, gaseous, liquid-water. This medium represents an enigma to develop some efficient mining system for subsurface production either of oil sand or just bitumen (Jeremic, 1975). It is obvious that the behavior of oil sand at depth is different from that at the surface or near the surface. The intention of this work is to point out those differences, and for this reason laboratory investigations of oil sand properties have been carried out. For uniaxial loading an Instron testing system (TT-D) has been used, and for triaxial loading, a triaxial cell (Soiltest) loaded by Instron an improvised apparatus for lateral pressure. All tests have been conducted in the laboratories of the Department of Mineral Engineering, the University of Alberta, Edmonton. The oil sand property delineated in this representation should be considered as preliminary because the testing has been done on disturbed (remoulded) samples without a gaseous phase. A definite evaluation of the behavior of an oil sand deposit can be done only by testing within an underground opening.

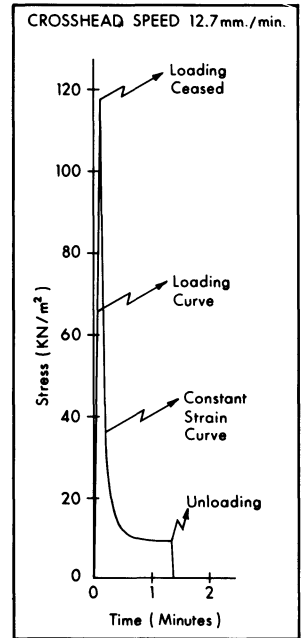


Fig. 2. Oil sand deformation at high speed of loading (high grade ore, room temperature)

Deformations as a Function of the Speed of Loading

Investigations of oil sand samples under unconfined pressure (Instron) at various constant crosshead speeds, and at various mixture composition showed their basic properties. Tests have been carried out on cylindrical samples (diameter — 43.7 mm) of remoulded oil sand. They have been compacted in layers to obtain densities in the range of 2 g/cm^3 .

The behavior of oil sand as a function of the high speed load mechanism is illustrated in Figure 2. The strain-rate sensitivity of the stress, at constant crosshead speed of 12.7 mm per minute shows the following deformation characteristics:

1. The loading deformation curve is instantaneous, and very steep.
2. when the cross head displacement was stopped, the sample relaxed and the relaxation was rapid.
3. After the load was removed, the curve dropped instantly to zero (like a spring release).

The behavior of oil sand as a function of the low speed load mechanism is illustrated in Figure 3. The strain-rate sensitivity of the stress, at constant crosshead speed of 0.127 mm per minute shows the following deformation characteristics:

1. The loading deformation curve is linear with a low slope.
2. When the crosshead displacement was stopped, the deformation continued and stress decreased.

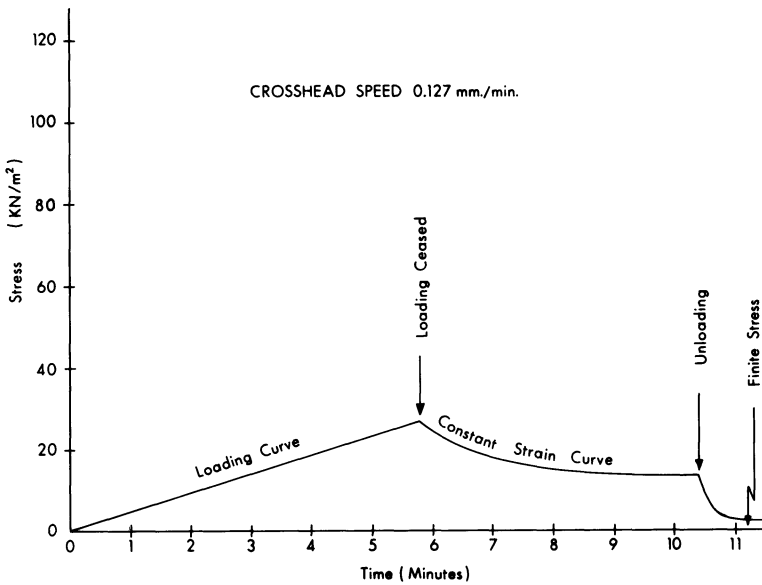


Fig. 3. Oil sand deformation at low speed of loading (high grade ore; room temperature)

3. After the load was removed the deformation curve declined to a certain point and became constant (similar to dashpot deformation).

Both tests show that oil sand may have the properties of two individual elements: elastic (spring) and viscous (dashpot). These two elements in its composition may control the basic deformation behavior of oil sand.

Deformations as a Function of Oil Sand Composition

Oil sand composition is one fundamental phenomenon which influences its behavior (Jeremic, 1975). For example, it has been established that oil sand increases strength and decreases the percent of strain to failure with increase in the content of the solid phase. The laboratory test (uniaxial load at room temperature) shows that the plotted curves of strain versus time are separate for two compositions of bitumen—solid phase mixtures (Fig. 4).

It could be assumed that external stress and sample contraction will be carried in different ways as a function of the magnitude of the elastic and of the viscous components of the system (Van Der Poel, 1960).

If it is assumed that with a stress increase the spring is fully contracted and takes the whole load, the shear strength of the system will depend on the magnitude of the elastic component. Thus the elastic component will break when the strength of the material is exceeded. From all the test data it is obvious that the magnitude of the elastic component (spring) is increased with decreasing bitumen content. The viscous deformation (dashpot) approached from the aspect of the bitumen content in the mixture suggests that shear

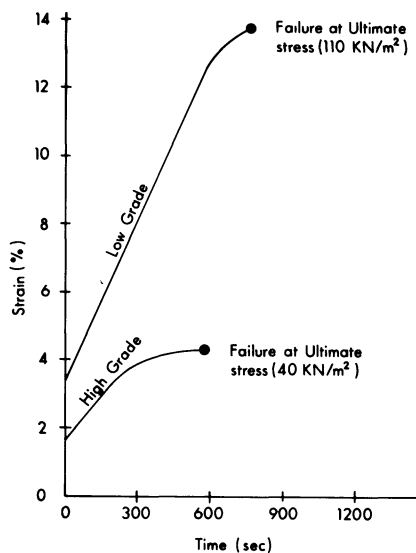


Fig. 4. Viscous flow of unconfined samples of various oil sand composition (at room temperature)

flow of the bitumen takes place some time before the sample failed, with mixtures of high bitumen content having a longer time of shearing motion than those of low bitumen content (Fig. 4). The viscous component will not show failure and so, an external stress can be carried to some extent by this component. Probably, the shearing displacement of the solid phase is governed by the flow of the dashpot, which separates sand grains along failure planes (Round, 1960).

However, the variation in flow for various compositions of oil sand is probably influenced not only by physical interaction between the solid and viscous phases, but also by some chemical interaction between the two of them (Carrigy, 1968). From visual observations of shear failures in the samples it could be concluded that interference of solid particles and their redistribution by bitumen during the loading process is a function of the percent of the solid phase (Jeremic, 1975).

Uniaxial Load-Time Deformations

Investigation of cylindrical remoulded oil sand samples has been conducted from two aspects: firstly, the deformation as a function of and instant constant load, and secondly, the deformation as a function of the removal of this constant load. The behavior of a bitumen-solid mixture for instant loading or unloading conditions with applied constant load as a function of time can be defined by rheological models (Van Der Poel, 1960; Ridgen, 1954). For example, the laboratory testing showed if the load was removed before failure set in, retarded elastic effects could occur and that part of the deformation becomes permanent: this suggests that a qualitative description of the bitumen-solid mixture might

be offered by a Kelvin element in series with a Maxwell element. Since the total strain is the sum of these two elements, subsequently

$$\varepsilon = \varepsilon_1 + \varepsilon_2$$

$$\varepsilon = \frac{\sigma_0}{E_1} + \frac{\sigma_0 t_1}{\eta_1} + \frac{\sigma_0}{E_2} \left(1 - e^{-\frac{E_2 t_2}{2}}\right)$$

where

$\frac{\sigma_0}{E_1}$ is instantaneous elastic strain (instantly recoverable)

$\frac{\sigma_0 t_1}{\eta_1}$ irrecoverable strain resulting from the steady strain rate (viscous flow)

$\frac{\sigma_0}{E_2} \left(1 - e^{-\frac{E_2 t_2}{2}}\right)$ exponential recoverable strain (retarded elasticity).

The time dependent phenomenon for volume deformation of oil sand can be assumed as follows:

- High grade oil sand shows an instant elastic effect at time zero, what is followed by retarded elasticity, and further deformation continues as a viscous effect.
- Simultaneous acting of all the elements of the model under loading and unloading conditions produces the volume-deformation effect of the oil sand.

The experiments on high grade oil sand samples showed that under repeated loading sometimes the retardation mechanism will have sufficient time to come into action and a failure stress below the original strength will be found. So actually at failure stress unloading and loading conditions, there is a clear tendency for the shear strength of the oil sand to deteriorate. This phenomenon has been noticed in the field during core sampling with increasing time from the recovery of the core (retardation mechanism), followed by volume of core deformation (Hardy and Hemstock, 1963), in agreement with our laboratory investigations (Jeremic, 1975).

Testing of the oil sand material in the field shows that its shear resistance decrease with depth (Hardy and Hemstock, 1963). This result suggests that retarded and viscous deformations have already developed in intact deposits due to geological cycles of loading and unloading during geological time, and that their values depend on the magnitude of the present load (i.e. weight of the overburden). From laboratory experiments it has been established that for a sample subjected to constant load, after unloading the shear strength of the sample deteriorated appreciably. In comparison, under very small load conditions (14 KN/m²) retarded and viscous deformations are almost negligible and for this condition described model is not applicable.

Cyclic Load Deformations

Oil sand behavior during unconfined cyclic loading as a function of time has been investigated from two different aspects.

Cyclic loading without previously applied static load shows that the stress changes sinusoidally with time, and from the analysis of viscous damping can be written as the equation (Van Der Poel, 1960)

$$\sigma = \hat{\sigma} \sin \omega t$$

so that the oil sand should display a sinusoidal deformation with the same angular frequency:

$$\varepsilon = \hat{\varepsilon} \sin (\omega t - \Theta)$$

which is delayed by the phase angle Θ . This is similar to the static loading ratio between σ and ε which depends on the temperature, composition of mixture etc., as well as, the dynamic ratio between $\hat{\sigma}$ and $\hat{\varepsilon}$ which depends on the magnitude of the dynamic load, the number of cycles, temperature, composition of the mixture, and also on the frequency.

Laboratory investigations showed that cyclic loading supplied information not only for conditions of shear flow, but also for the phase shift Θ . This phase angle is a measure of the amount of shear energy dissipated in the material during one cycle, given by the equation

$$W = \int_0^{2\pi} \sigma d\varepsilon$$

which represents the work done in that time per unit of volume, and which is directly proportional to $\sin \Theta$. The mechanical angle of loss is Θ and this phenomenon itself is denoted as damping. For the oil sand energy can only be dissipated in the dashpot (viscous phase).

The main parameter is the magnitude of the stress during one cycle of load. For example, with an increase of magnitude of the cyclic load, the shear resistance of oil sand shows a deterioration: a sample of high grade oil sand at room temperature failed at 22 KN/m² cyclic load (Fig. 5). This phenomenon suggests that sinusoidal deformations of oil sand decrease its shear strength with an increasing load amplitude.

Dynamic load can cause shear flow of the intact oil sand at the stress magnitude almost half that of a static load. If the oil sand is already loaded with overburden this phenomenon will be even grater, as shown in the next experiment.

Cyclic loading with previously applied static load simulated the oil sand deposit loaded by overburden under seismic effects. The test shows that for a small magnitude of cyclic loading, when the number of cycles is increased, the shear resistance of oil sand can be destroyed, probably due to structural viscosity. For example, a high grade sample was instantly loaded ($\sigma = 20$ KN/m²). The

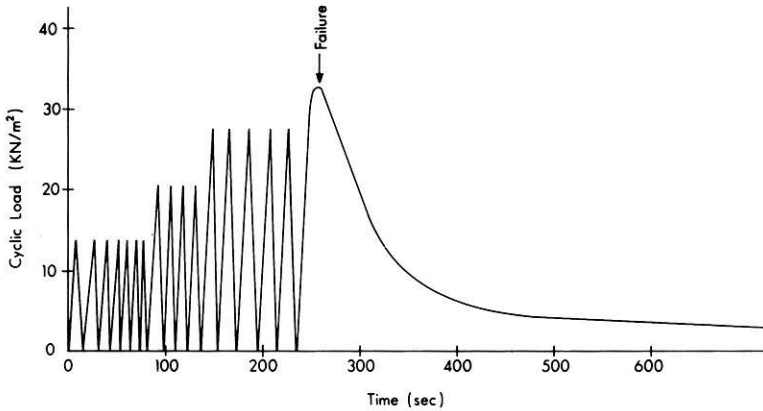


Fig. 5. Cyclic loading of high grade oil sand to failure at room temperature

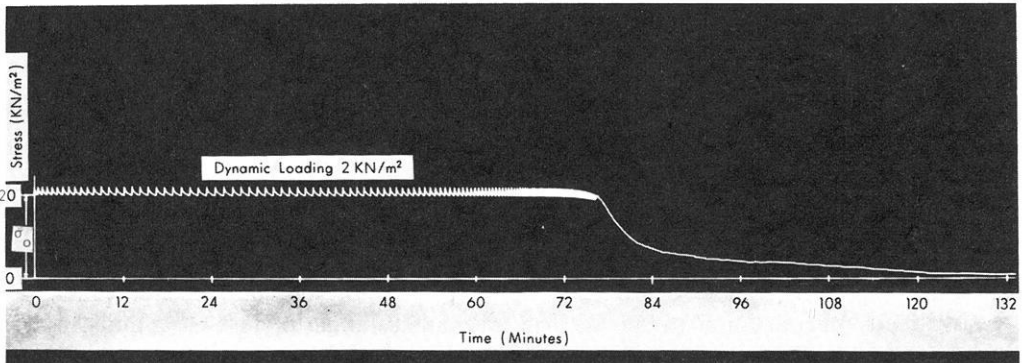


Fig. 6. High grade oil sand sample at instant stress cyclic loaded to failure at room temperature

experiment shows (Fig. 6) that with an increased number of cycles the retarded elastic recovery is also increased. The test carried on to failure shows a decrease of strain recovery before failure, probably due to shear flow already initiated. After failure occurs, the deformation curve as a function of time decreases almost parabolically and continues asymptotically to the times axis.

Hydrostatic Pressure Deformations

The laboratory investigations of oil sand under confined pressure in the triaxial cell showed that applied vertical pressure (higher magnitude) and lateral pressure (lower magnitude) tend to be redistributed. The redistribution of applied stress is toward their equalization, and they became equal at approximately 3.5 MN/m^2 . This phenomenon suggests that oil sand deposits exposed to overburden

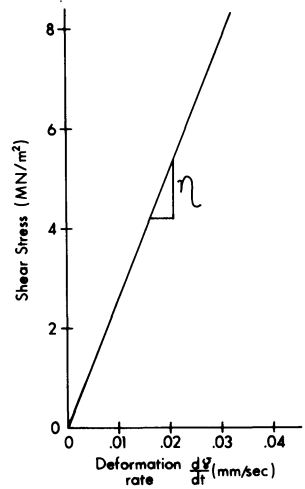


Fig. 7. Stress/deformation relations for hydrostatic pressure (high grade oil sand sample, at room temperature)

pressure at some depth might be in a state of hydrostatic pressure. Oil sand behavior under hydrostatic stress conditions has been investigated from two aspects.

Oil sand deformation under hydrostatic pressure (vertical and lateral pressures are equal) has been observed under laboratory conditions on cylindrical oil sand samples placed in a triaxial cell (Soiltest), loaded vertically by Instron frame and horizontally by improvised apparatus for lateral pressure. In figure 7 is illustrated a typical diagram of oil sand deformation under hydrostatic pressure. It is noticeable that for applied hydrostatic pressure, there are linear relations between stress and rate of deformation. This phenomenon suggests that at hydrostatic stress the shear strength of the oil sand is overcome and behaves like a Newtonian viscous substance (dashpot). This behavior can be represented by a rheological equation in which the shear stress is linearly related to the rate of shear strain, that is

$$\tau = \eta \frac{d\gamma}{dt}$$

where η represents the coefficient of proportionality and is determined by the viscosity of the pure bitumen. This equation clearly states that the intensity of deformation is a function of the magnitude of the coefficient of viscosity of the bitumen phase.

Accepting the possibility that the oil sand under hydrostatic pressure behaves like a Newtonian model, its deformation might be considered from the aspect of flow deformation. Oil sand properties as a four-phase system should be effected by behavior of each phase under hydrostatic pressure. It is obvious that solid phase (sand particles) and viscous phase (bitumen) will behave differently, under hydrostatic pressure due to their differing physical properties. These differences will effect the structural deformation of the system.

Structural deformation under confined pressure is mainly effected by the viscous flow of bitumen within the oil sand mixture. The flow of bitumen caused a noticeable change in the internal structure of the oil sand. For example a remoulded high grade oil sand sample with uniform bitumen distribution, after subjection to higher confinement has a bitumen content redistributed in a particular pattern. This pattern suggests that during loading pressure, the bitumen layers had been forced upwards and inwards by shearing stress. This is shown by the increase in bitumen concentration on the top of the sample and the sand concentration on the bottom and around the walls of the cylinder (Fig. 8). The sand particles were probably rearranged during bitumen flow, so as to make flow easier.

This phenomenon suggests that oil sand under higher confinement deforms by bitumen flow, which is mostly upward. Although structure deformation does not influence the mechanism of flow, it does follow the linear function of a Newtonian viscous body. It could be assumed that oil sand under sufficiently high pressure (zero shear strength) acts like an incompressible fluid without initial shear resistance. If this assumption is acceptable a hydrodynamic theory might be applied to analyse further the behavior of oil sand at higher confining pressures.

Conclusions

The behavior of oil sand is a very complex problem which should be investigated in the field in two ways: first, the behavior of oil sand in intact deposits as functions of the overburden pressure, composition of the mixture, and geothermal gradient; second, the behavior of oil sand within a mine structure as functions of the loading and unloading mechanism of deformation, increase of temperature, and also the size of the mine opening.

The laboratory investigations suggest that the main part of the intact oil sand deposits might behave like a Newtonian viscous body due to load (overburden pressure) and time (geological time). With the assumption of deformation sufficiently high that oil sand acts like a fluid without initial shear resistance, conventional subsurface mining systems cannot be applicable. For this possible behavior of oil sand, some unconventional exploitation method should be utilized to obtain a huge mass flow of caved oil sand.

Volume deformation, with a volume extension toward an opening, might be a phenomenon which will seal the opening and stop further caving and oil sand flow. Any shear strength in the material will deteriorate, but movement of the material will not be initiated.

At present many geophysical laboratories throughout the world conduct very sophisticated research involving explosion and their related seismic effects in thin layers, including hydraulic fracturing of rocks, temperature increases and heat flows in rock layers, and seismicity of rock layers under high pressure. Some of these research results might be applied to investigations of inducing flow of oil sand and accelerating its flow during mining. Thus geophysical applications may go beyond exploring for oil sand into methods of extracting oil sand.

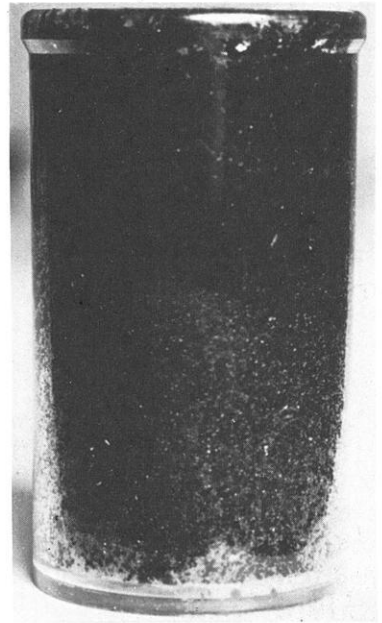


Fig. 8. Bitumen flow under higher confined pressure (7 MN/m^2) at room temperature

References

- Carrigy, M.A.: The Physical and Chemical Nature of Typical Tar Sand-Bulk Properties and Behaviour. Proceedings of the Seventh World Petroleum Congress, pp. 573-581, 1968
- Hardy, R.M., Hemstock, R.S.: Shearing Strength Characteristics of Athabasca Oil Sands. Clark Volume Research Council of Alberta, Edmonton, pp. 109-122, 1963
- Jeremic, M.L.: Tar sand influence of composition on its behaviour. *Western Miner* **48**, 25-31, 1975
- McConville, L.B.: The Athabasca Tar Sand. Mining Engineering Society of Mining Engineers. January, pp. 19-38, 1975
- Ridgen, P.J.: Road Research. Techn. Paper No. 38. London H.M.S.O., 1954
- Round, G.F.: The Shear Strength of McMurray Oil Sands. The Canadian Mining and Metallurgical Bulletin. Volume LXIII, pp. 145-150, 1960
- Van Der Poel, C.: Road Asphalt. Asphaltic Mixtures, CH. IX, pp. 360-413, 1960

Received November 18, 1976 / Revised version October 31, 1977

Shamil-Siahou Earthquake “North-East of Bandar-Abbas” of 21st March, 1977

M. Sobouti, I. Eshghi, and M.M. Mostaanpour

Institute of Geophysics, Tehran University, Tehran 14, Iran

Abstract. In this paper an attempt has been made to reveal the properties of forementioned earthquake from the field observations. The data has been obtained from the Iranian Seismological Stations, the International Seismological Center etc.

This report concerns different kind of data, preliminary studies on the regional seismicity, ground movements isoseismal maps, specifications of the major shocks, the subsequent aftershocks and some descriptions about the nature of the damaged buildings.

Key words: Iran – Earthquake – Regional seismicity – Destruction.

Introduction

In the recorded history of this region we repeatedly notice the occurrence of a series of destructive and devastating earthquakes in the various regions of the country. In the last few decades, some of the major shocks registered throughout the world have had their epicenters in the Plateau of Iran, approximately numbering 50.

Prior to the Shamil-Siahou earthquake, north-east of Bandar-Abbas, 4 earthquakes of $M > 6$ and 24 earthquakes of $6 > M > 5$ occurred around the epicentral zone of this earthquake and were registered in the seismological stations of the world.

Prior to the description of the Shamil-Siahou earthquake of the 21st March 1977, it seems necessary to discuss the geographical situation, the geological condition of the epicentral area and also the seismicity of the Bandar-Abbas region.

This discussion can help us the analysis of the results as obtained from the macro and micro-seismic studies. Consequently this report concerns:

1. A brief geological and geographical aspects connected to the region.
2. The seismicity of the Bandar-Abbas area.

3. Macro and micro-seismic data and their analysis.
4. Description and nature of the damaged buildings.

1. Geological and Geographical Aspects of the Earthquake Area

The region affected by the Shamil-Siahou earthquake of 21st March, 1977 accommodating 12,000 inhabitants, lies to the south of an elevation having a maximum height of 2,645 m (Pousht-Kuh). The western part (Khur-Kuh) has a maximum height of 1,471 m. This region is believed to have been on the extreme southern border of the Zagross mountains. This is the region where the general orientation of the mountain ridge is E-W (Fig. 3). This region is irrigated by the tributaries of three rivers, Shoor, Djalabi and Hassan-Langui. The springs feeding these rivers are mostly associated with some salt contents.

The area is part of the southeastern Zagross tectonic belt. The tectonic frame work consists of parallel east-west trending anticlines and synclines. Three salt plugs are shown in the map (Fig. 1). These salt plugs seem to have been active since the Jurassic and Cretaceous times. The major Zagross thrust fault zone lies to the north of the area. Apart from a major thrust fault on the southern flank of Pousht-Kuh few other minor faults are also present within the area. (Geological map of Bandar-Abbas area, N10 (1963.) The present structural setting of the area is the result of the Zagross orogeny which started in late Miocene time. Evidence of some tilting of sub-recent conglomerates indicates that this tectonic phase is still active to a certain degree. Apart from the Zagross movements, the area seems to be the site of a predominantly continuous deposition of limestone and shale, except for a few stratigraphic levels where minor disconformities are indicated.

The oldest exposures of the area consists of the Jurassic limestone outcropping at the eroded core of Pousht-Kuh. The Cretaceous and the lower Tertiary rocks are also exposed at the same places. The younger Tertiary rocks from the Asmarie and Fars group outcrop over the whole area. The Bakhtiary conglomerates from the youngest formation of the area overlies the older with an angular unconformity. The total known thickness of the sediment from Bakhtiary formation down to the lowest exposures of the Silurian rocks is approximately 8,300 m.

Silurian, Permo-Carboniferous and Triassic rocks are exposed at Kuh-e-Faragun about 20 km to the north of the area. Below Silurian the thickness of the remaining sediments is not known. But the salt rocks of the salt plug are thought to be of the Pre-Cambrian age.

The maximum intensity of the earthquake was found in the area between Sharu and Dimshahr villages. Field observations could not prove any relationships between the earthquake and the present structural features of the area.

2. Seismicity of the Bandar-Abbas Area

The region which lies between the latitudes 26° to 29° N and longitudes 54° to 58° E, having an area of 125,000 square km, has been known from immemorial

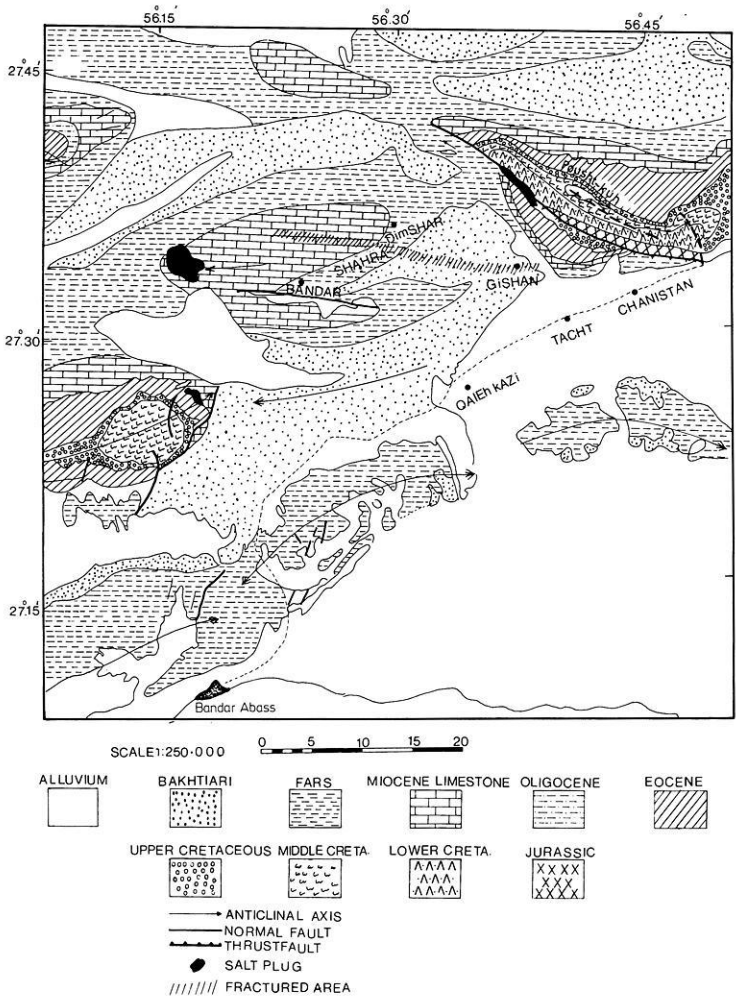


Fig. 1. Geological Map of the Region

times for its seismicity. Legends and history indicate severe and strong earthquakes causing heavy damages in this area.

Reference to the national and private libraries and the publications belonging to the various centers and various authors, has enabled us to discuss the seismic activities of the region. The region described above has had 263 destructive earthquakes that have taken place from 1900 up to the present time. In the case of early earthquakes before 1900, the vague accounts as given by ancient earthquakes for which a determination of epicentral coordinates is not easy to ascertain.

In order to give a picture of the seismic activities of the region, a map has been compiled (after Berberian, 1976). A large number of earthquakes prior to 1960 have remained unknown to us due to the lack of proper recording stations. The compilation of this map is based on the following sources:

1. Individual papers concerning the early earthquakes (see the list of references).
2. Seismicity of the Earth, by B. Gutenberg and C.F. Richter, 1954; and Rothé, 1969.
3. The Bulletins of the International Seismological Summary (ISS).
4. The Bulletins of the Bureau of the International Seismological Centers, Strasburg (BCIS).
5. Preliminary determination of epicenters by USCGS.
6. The Bulletins and Publications of The Seismological Service of the Institute of Geophysics, Tehran University.

Figure 2 represents the distribution of the epicenters and the magnitudes of 263 shocks. Sixty-five of these shocks have occurred prior to 1960 and are recorded by the neighbouring and the European seismological stations. The remaining shocks were recorded by the Iranian Seismological Stations which have been functioning since 1960.

3. Macro and Micro-Seismic Data and Their Analysis

3.1. Macro-Seismic Data

A. Epicentral Zone of the Earthquake. The region affected by the principal shock has an approximate surface area of 4,500 square km (Fig. 3). The damaged villages are grouped within the two districts, Shamil and Siahou and are situated in agricultural plains lying between rocky elevations and sometimes at the foot of the mountains of Pousht-Kuh and Khour-Huh. The villages lying in these districts and their agricultural plains are as mentioned, irrigated by the affluents of the three rivers. These tributaries, in different parts of the region, are known with varying names as, Khor-Joul, Viakan, Ab-Galamoun, Jamash etc. Numerous hot-water springs are located at the foot of the Pousht-Kuh and Khour-Kuh mountains. The water of some of these springs are sulphurous.

B. Visible Effects. The main shock has seriously destroyed the houses and the buildings of about 52 villages. The number of casualties, so far, out of a population of 12,000 people has reached to 168.

Minor cracks and undulations of the ground were seen in the area where the houses and buildings were seriously damaged (like Dimshahr, Jeghan, Guishan, Shahrou, etc. in Fig. 3).

The result of the observations reveal that the crust was fractured in a direction of $N 75 \pm 5 W$. This direction is detected by means of shattering and falling of rocks and overturning of the walls, etc. The water level and even the location of several hot-water springs located at the foot of the mountains has been considerably changed during the earthquake.

C. Intensity Distribution. An attempt was made to visit all the damaged region, but owing to the natural difficulties of the area such as the rocky elevations and lack of roads, only 70% of the villages in the damaged area were visited by the team. A great deal of information was obtained by local investigations from the

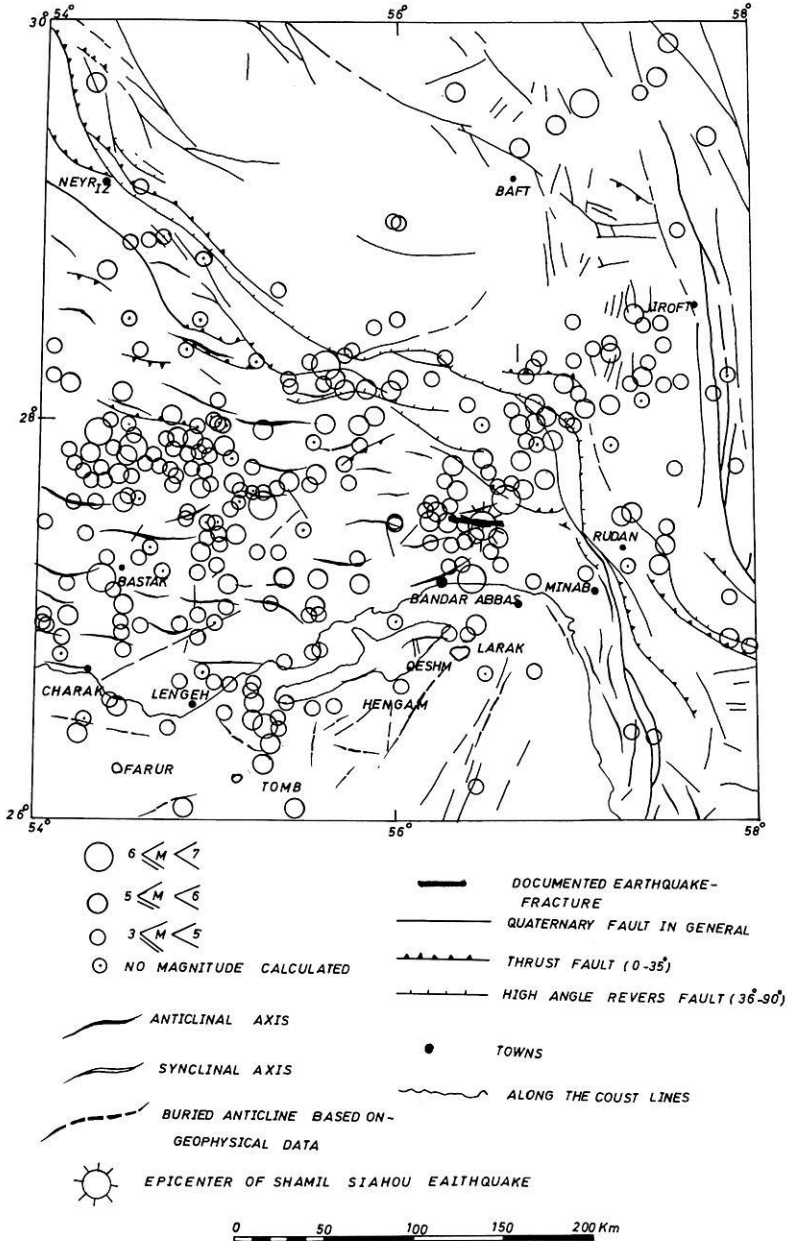


Fig. 2. Seismicity Map of Bandar Abbas. (After Berberian, 1976)

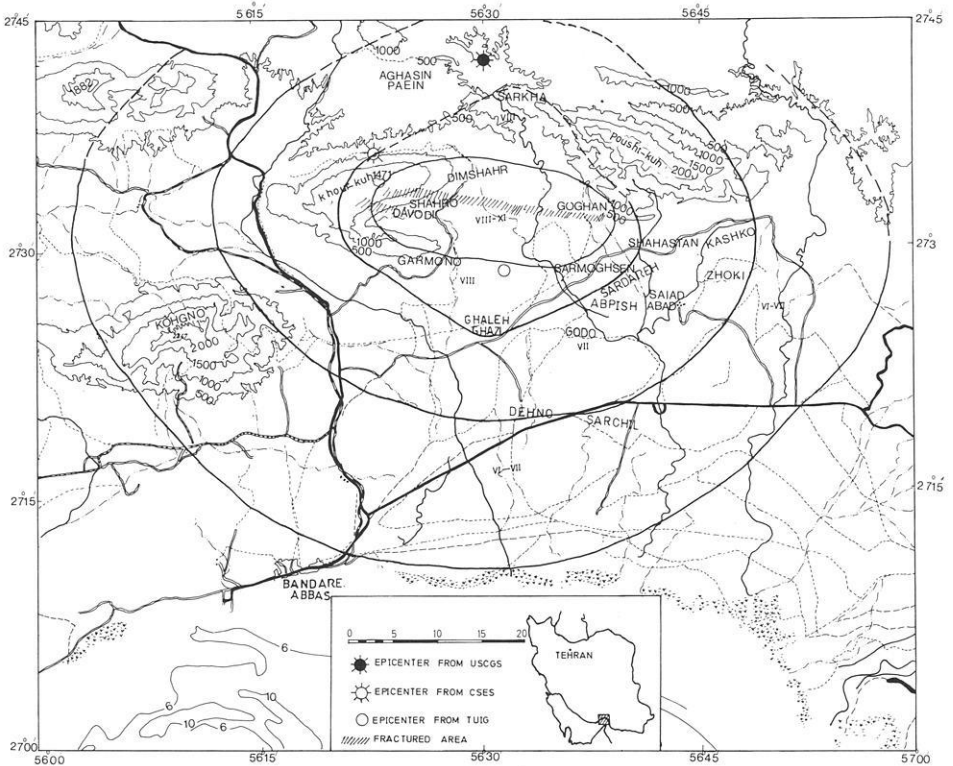


Fig. 3. ISO-Seismic Map of Earthquake

neighbouring villages and from the list of statistics as prepared by the governmental agencies of the Province of Hormozgan.

According to the results of these investigations, the maximum intensity of the earthquake in the damaged area is estimated VIII–IX on the Modified Mercalli scale. Lack of sufficient data and information has made the compilation of the isoseismal lines (Fig. 3) extremely difficult. Whenever the data was complete the isoseismal contour line is indicated by heavy lines and whenever the data has been insufficient or meager, the contour lines are represented by dotted lines.

D. Depth of Focus and Magnitude of the Earthquake as Computed From the Observation Data. In order to calculate the depth of focus, an empirical formula relating the depth of focus with r and I_m is used (Gutenberg's formula):

$$\frac{I_m - 6.5}{3} = \log \left[\left(\frac{r}{h} \right)^2 + 1 \right]$$

where

r = Radius of the isoseismal contour line having an intensity of VI–VII,

I_m = Maximum intensity on the ground surface.

h = Depth of focus.

In the case of the earthquake under discussion we have $I_m = \text{VIII-IX}$. For the radius of the isoseismal contour line, the mean of the minimum and the maximum radii are taken:

$$r = \frac{d1/2 + d2/2}{2}$$

consequently

$$r = 43.75 \text{ km}$$

and $h = 23 \text{ m}$.

As for the magnitude of the earthquake a formula is required relating the magnitude with the depth of focus and maximum intensity at the MM scale:

$$M = 0.7 I_m + 2.3 \log h - 2.0.$$

In the case of this earthquake we have:

$$I_m = 8.5 \text{ (the maximum intensity on the field),}$$

$$h = 23 \text{ (as determined in para. D).}$$

consequently $M = 7.0$.

3.2. Microseismic Data

A. Characteristics of the Main Shock. The geographical coordinates of the epicenter, origin time, depth of focus and magnitude as given by USCGS and CSES are the following:

Epic-coordinates			Origin time	Depth	Magnitude
(USCGS)	27.7°N,	56.5°E	21:18:54:6	33N	7.0
(CSES)	27.63°N,	56.36°E	21:18:54	—	6.75

The geographical coordinates of the epicenter and origin time of the main shock using the registered *P*-Travel times in Iranian seismological stations are given as follows:

Epicenter Coordinates			Origin Time
(UTIG)	27.5°N	56.5°E	21:18:55
(Tehran)			

The magnitude of this earthquake is calculated at the Tehran Seismological Station from the maximum amplitude (*A*) of *S* wave recorded by the short-period ($T = 0.8 \text{ s}$) Stuttgart-Hiller seismograph, using the formula:

$$M = \log \frac{A}{T} + 3.39 \log A - 4.49.$$

The result is:

$$M = 6.9.$$

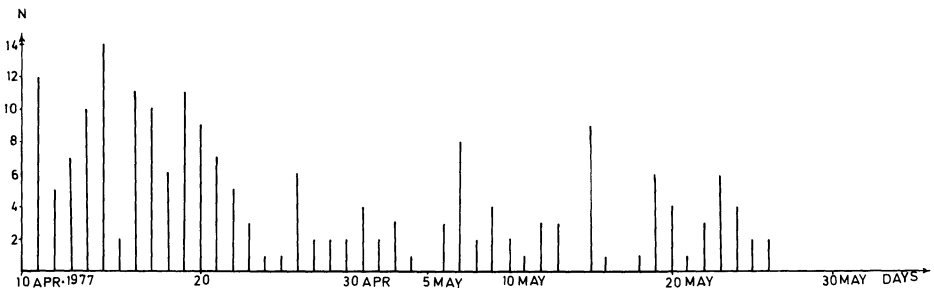
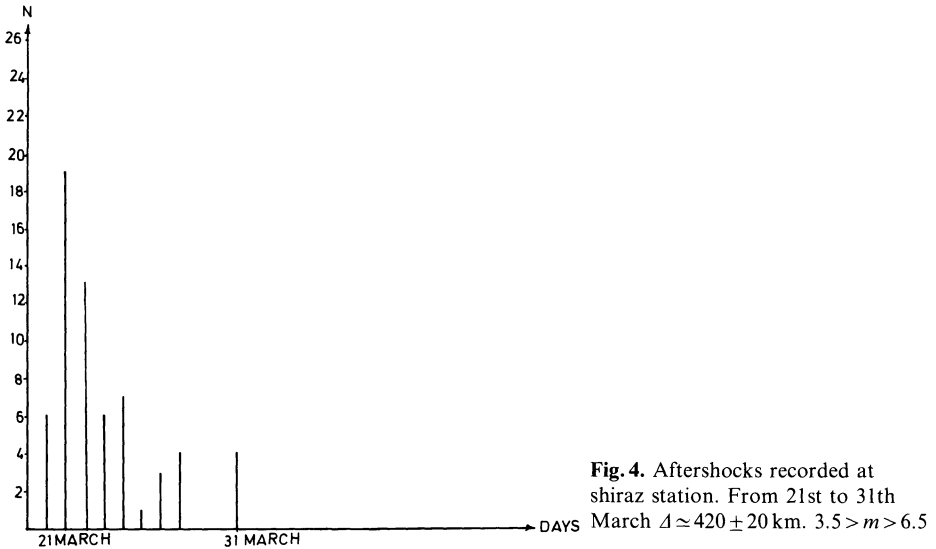
In order to evaluate the energy released in this earthquake, use is made of the Both's formula:

$$\log E = 12.24 + 1.44 M.$$

Using the value as calculated at the Tehran station we have:

$$E = 1.5 \times 10^{22} \text{ ergs.}$$

B. Aftershocks. As usual after the main shock a series of some hundreds of aftershocks took place in the epicentral area. The majority of these shocks were only felt, without causing material damage. Aftershocks with higher intensity are those that have been registered at the Shiraz station ($\Delta = 420 \pm 20$ km).



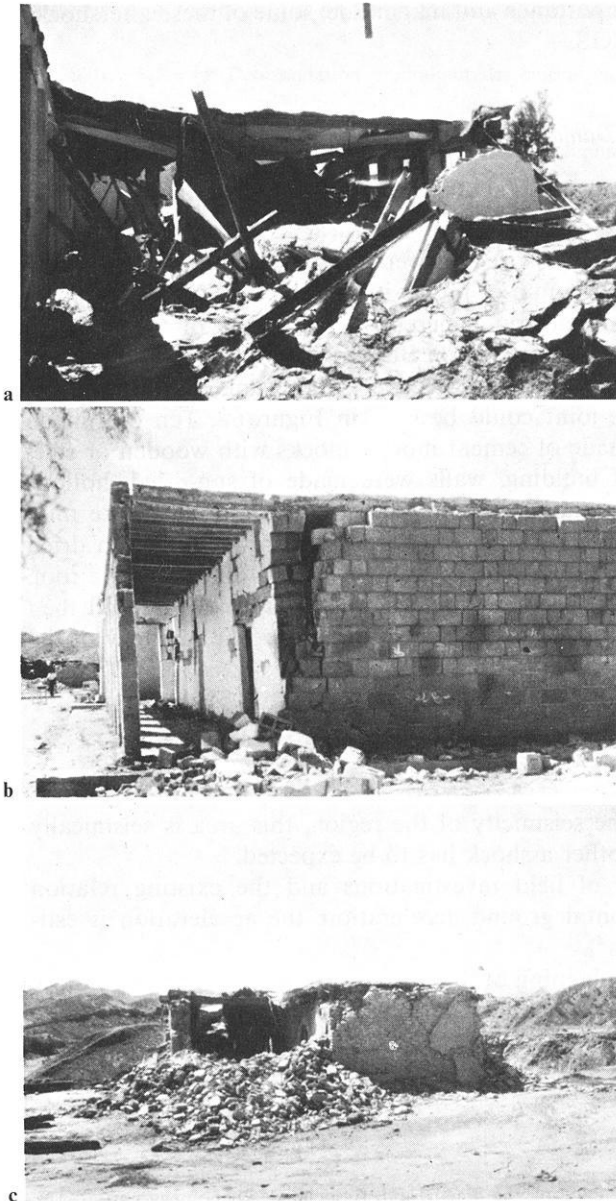


Fig. 6a-c. Damage to houses of different construction (see text)

These aftershocks caused the already damaged buildings and constructions to collapse further and thus causing more and more destructions.

Figure 4 describes graphically the aftershock actively from 21st March to 31st March 1977.

Figure 5 describes graphically the aftershocks recorded at Bandar-Abbas, by a portable Sprengnether seismograph during 48 days from 10th April to 27th

May, 1977. Owing to their importance and magnitude, some of these aftershocks had been delineated by USCGS.

4. Description and Nature of Damaged Buildings

The damage caused by the main shock was mainly due to the poor quality of the materials used and also to the construction of rural houses in this area.

About 10% of the houses in this region were made of bricks and the joint material was center mortar, pure mud or mud with lime. The roof is made up to steel beams resting on the reinforced concrete. An example of this kind of building was the newly built "Sharou School Building".

In this kind of building, the connection between the beams and the walls is unperfect. The details of the joint could be seen in Figure 6a. Ten or Fifteen percent of the houses were made of cement mortar blocks with wooden or steel roof beams. In this class of building, walls were made of sun-dried, hollow, cement mortar blocks. The material of joint was cement mortar or pure mud (Fig. 6b). Seventy-five or Eighty percent of the houses were made of sun dried bricks, with mud mortar, sometimes with a small amount of lime. For the roof, wooden beams are used which are then covered with a layer of mat and then with a 15 to 20 cm, layer of mud-straw (Kahguel) (Fig. 6c). The majority of the house in the epicentral region were of only one story.

Conclusion

From the point of view of the seismicity of the region, this area is seismically active and at one time or another a shock has to be expected.

According to the results of field investigations and the existing relation between intensity and horizontal ground acceleration, the acceleration is estimated to be ($\gamma = 150 \pm 50 \text{ cm/s}^2$).

In the reconstructing and planning of the urban or rural developement, those results must be taken into the design consideration.

References

- Gutenberg, B., Richter, C.F.: Seismicity of the Earth and Associated Phenomena, pp. 1-310. Princeton: Princeton University Press 1954
- Rothé, J.P.: La Séismicité du Globe, 1953, U.N.E.S.C.O. 1969
- Sobouti, M.: Report on the Seismological Activities in Iran, during the years 1969-1972, Publ. No. 63 of Geophysical Institute of Tehran University 1974
- Sobouti, M.: Le Séisme de Dacht-é-Baiyaz dans la province du Khorassan, Iran, 31 Aout, 1968. *Annali di Geofisica*, Roma **22**, No. 3, 229-266, 1968
- Sobouti, M., Eshghi, I., Hossein-Javaheri, J.: The Qir Earthquake of 10th April, 1972. *J. Earth Space Phys.* **1**, No. 2, 1972
- Taheri, J.Sh.: Magnitude Studies of Earthquakes of Iran. Publ. No. 49, 8-18. Geophysical Institute of Tehran University 1967

Bulletins and Publications of Some Seismological Centers

- B.C.I.S. (C.S.E.S.): (a) Determination preliminaires des epicentres, 1957–1977; (b) Bulletin mensuels, 1957–1973
- Geophysical Institute of Tehran University: (a) Reports on the Seismological Activities in Iran, Pubs. No. 3, 7, 14, 18, 26, 29, 41, 49, 60, Tehran; (b) Preliminary Readings of Earthquakes at the Seismological Stations of Iran, 1972–1977
- I.S.S.: (a) Bulletins, 1954–1973; (b) Regional Catalogue of Earthquakes 1954–1968
- U.S.C.G.S.: (a) Preliminary determination of epicenters, 1957–1977
- Geological and Exploration Division of NIOC: (a) Geological Map of Bandar-Abbas Area, 1:250,000, 1963, Tehran
- Geological Survey of Iran: (a) Tectonic and Seismotectonic Map of Iran, 1:2,500,000, 1976

Received October 3, 1977 / Revised version March 15, 1978

Short Communication

Anomalous *P*-Velocities in the Earth's Outer Core

J.A. Jacobs

Department of Geodesy and Geophysics, University of Cambridge, Madingley Rise,
Madingley Road, Cambridge CB3 0EZ, England

Key words: Earth's core – *P*-velocity.

Kind and Müller (1977) recently put forward a new model for the structure of the Earth's outer core based on SKS amplitudes and travel times. Specifically they used long period observations of SKS/SKKS amplitude ratios and travel time differences between SKS and SKKS from five deep-focus earthquakes in the Tonga-Fiji region, and obtained significant disagreements with conventional core models. They ruled out near source effects as the cause of these disagreements which they believe are caused by anomalous conditions around a depth of 3750 km. Their *P*-velocity structure around this depth is reproduced in Figure 1. It is the purpose of this short note to explore whether any physical-chemical model of the outer core could explain such a velocity structure, the validity of which demands further confirmation.

Since a light alloying element is required to account for the density of the core, it is probable that the core has a melting interval rather than a well-defined melting temperature. The solidus, or eutectic, temperature of the core could be quite a bit lower than the melting point of pure iron or the liquidus temperature of the alloy. Moreover since the liquidus is pressure dependent, the composition of the core would vary with depth. If core temperatures are below the liquidus solid iron would coexist with an ironrich melt solution. The solid iron could either be held in suspension by turbulent convection or settle out. An explanation for the behaviour of Figure 1 is put forward based on the supposition that between L_1 and L_2 the actual temperature in the outer core falls below the liquidus, crossing the solidus at L_2 . Between L_1 and L_2 there is then a slurry of solid iron particles. Between L_2 and L_3 the temperature falls below the solidus and the core is solid. At L_3 the temperature rises above the solidus again, crossing the liquidus at L_4 . Between L_3 and L_4 we again have a slurry of solid iron particles. It is further assumed that there is no abnormal behaviour in the incompressibility k which increases smoothly with depth (Bullen, 1949).

Consider first the region $L_1 L_2$ where the gradient of the velocity v_p of *P* waves is reduced. It is suggested that this reduction arises from the increased

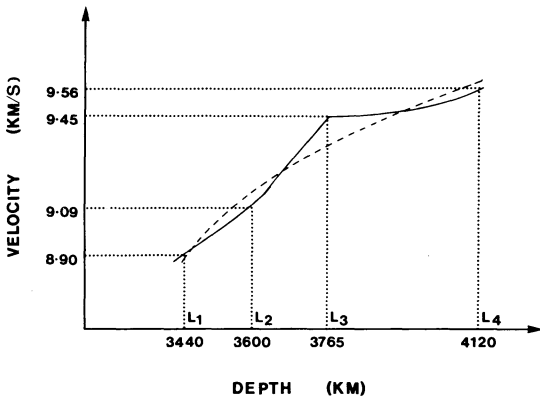


Fig. 1. Velocity of P waves versus depth in part of the outer core. Solid curve after Kind and Müller (1977), dashed curve, model 1066B (Gilbert and Dziewonski, 1975)

density in this region due to the solid iron particles in the slurry. Consider next the region $L_2 L_3$ where there is a rapid increase in v_p . This is accounted for by the elimination of a melt fraction in the core where the temperature has fallen below the solidus. If the material becomes sufficiently rigid, shear waves may be transmitted, and the abnormal increase in v_p given by $v_p^2 = k/\rho + \frac{4}{3}v_s^2$ where ρ is the density and v_s the velocity of shear waves. Taking the values of v_p from Kind and Müller (1977) and those of k and ρ from Model 1066B (Gilbert and Dziewonski, 1975) which Kind and Müller used for densities, values of v_s can be calculated throughout $L_2 L_3$. At L_3 , $v_s = 1.60$ km/s. Finally in region $L_3 L_4$ the temperature has risen above the solidus and we again have a slurry. v_s is now zero and the increase in v_p is reduced below that of 'normal models'. If the increase in ρ (due to the presence of the solid iron particles) is approx. equal to that in k , then v_p is approx. constant as indicated in Figure 1. As L_4 is approached, the temperature exceeds the liquidus again and the material would begin to melt. The latent heat absorbed on melting would probably keep the temperature near the liquidus. The density gradient would decrease and approach its more 'normal' value leading to more 'normal' values of the velocity gradient, as observed.

It should again be emphasized that it is not suggested that the above thermal structure actually occurs in the core—it is only put forward as a possible explanation of the behaviour of the v_p depth curve in the outer core (Fig. 1) should this be substantiated by further work. For this model the core would be stably stratified at least over part of its depth. It is interesting in this regard to note that in some of the models that have been proposed for the outer core, we have found some indication that there may be a central stable region, i.e., a region where the stability parameter $\beta = 1 + \frac{k}{g\rho^2} \frac{d\rho}{dr}$ introduced by Pekeris and Accad (1972) is negative. However the degree of stability in such a region and the composition gradient across the core appear slight and it seems doubtful whether such an abnormal velocity region as found by Kind and Müller does in fact exist.

References

- Bullen, K.E.: Compressibility-pressure hypothesis and the Earth's interior. *Monthly Notices Roy. Astron. Soc. Geophys. Suppl.* **5**, 355–368, 1949
- Gilbert, F., Dziewonski, A.M.: An application of normal mode theory to the retrieval of structural parameters and source mechanisms for seismic spectra. *Phil. Trans. Roy. Soc. London, Ser. A* **178**, 187–269, 1975
- Kind, R., Müller, G.: The structure of the outer core from SKS amplitudes and travel times. *Bull. Seism. Soc. Am.* **67**, 1541–1554, 1977
- Pekeris, C.L., Accad, Y.: Dynamics of the liquid core of the Earth. *Phil. Trans. Roy. Soc. London, Ser. A* **273**, 237–260, 1972

Received April 14, 1978 / Revised version May 31, 1978

In Memoriam

In Memoriam Alfred Schleusener



Am 13. April 1978 verstarb Professor Dr.-Ing. Alfred Schleusener, ein Pionier der Angewandten Geophysik, nach kurzer schwerer Krankheit in Hannover.

Alfred Schleusener wurde am 1. März 1898 in Staffelde, Kreis Soldin, geboren. Das Studium der Bergbauwissenschaften an der Technischen Hochschule Berlin-Charlottenburg vermittelte ihm u.a. eine gründliche Kenntnis in der Lagerstättenkunde sowie in Geologie und Mineralogie und führte ihn an die angewandte Geophysik heran. Diesem in den zwanziger Jahren sich stürmisch entwickelnden Bereich wandte er sich dann auch nach seinem Diplomexamen zu und trat 1925 in die Gesellschaft für Bodenforschung „Exploration“, Berlin, ein, welche 1928 mit der Seismos GmbH, Hannover, verschmolzen wurde.

Die ersten Jahre seiner beruflichen Tätigkeit führten den jungen Diplom-Bergingenieur sogleich in den Drehwaage-Boom der Erdöl-Exploration, in welchem deutsche Meßtrupps in Texas zahlreiche erdölführende Salzdomen entdeckten. Die in den dreißiger Jahren folgende Umwälzung in der gravimetrischen Methode, bei der in kurzer Zeit Drehwaage und Pendelapparat durch das Gravimeter verdrängt wurden, wurde wesentlich von A. Schleusener beeinflusst. Das

von ihm – nach einer Idee und Vorversuchen von Stephan von Thyssen-Bornemisza – im Jahre 1934 entwickelte astasierte Gravimeter erreichte als erster statischer Schweremesser eine serienmäßige Einsatzreife für die Geländearbeit. Rund 100 Geräte dieses Typs wurden von der Seismos hergestellt und in zahlreichen Ländern eingesetzt. Eine besondere Würdigung erfuhr diese Leistung durch die Auszeichnung des Thyssen-Schleusener-Gravimeters mit einer Goldmedaille anlässlich der Weltausstellung in Paris 1937.

Die hohe Genauigkeit dieses Gravimeters erlaubte auch die Durchführung regionaler Schweremessungen. So führten Meßtrupps der Seismos unter Leitung von A. Schleusener von 1935 bis 1945 eine detaillierte gravimetrische Vermessung Mitteleuropas im Rahmen der Geophysikalischen Reichsaufnahme durch, deren Resultate bis heute die Grundlage für großräumige gravimetrische Untersuchungen bilden. Nachdem hierauf aufbauend bereits 1949 in Zusammenarbeit mit H. Closs eine Freiluftschwerekarte Zentraleuropas entstanden war, konnten dann 1957 und 1959 die für geodätische Problemstellungen bedeutsamen Karten 1:1 Mill. der Bougueranomalien und der mittleren $6' \times 10'$ -Freiluftanomalien vom Institut für Angewandte Geodäsie, Frankfurt a.M., herausgegeben werden. Die von A. Schleusener hierfür abgeschätzten mittleren Höhen Zentraleuropas (1959) dienen auch heute noch als Geländemodell für Berechnungen der gravimetrischen Geodäsie.

Beim Wiederaufbau der Seismos nach 1945 wurde A. Schleusener die Leitung der Abteilung für Gravimetrie und andere nichtseismische Methoden übertragen, die er bis 1963 innehatte. Gravimetrische Meßtrupps – jetzt mit modernen amerikanischen Gravimetern ausgerüstet – führten in dieser Zeit groß- und kleinräumige Vermessungen in verschiedenen Gebieten Deutschlands (u.a. über zahlreichen Salzstöcken Norddeutschlands, im Saar-Nahe-Becken, am westlichen Rheintalgrabenrand und in der oberbayerischen Faltenmolasse), in Griechenland, in der Türkei, in Spanien und im Kongo aus. Dem Einsatz von A. Schleusener ist es entscheidend zu verdanken, daß die weltweite Aktivität der deutschen Angewandten Geophysik nach 1945 wiederum in starkem Maße auch die nichtseismischen Verfahren und besonders die Gravimetrie umfaßte.

Die wissenschaftliche Arbeit von A. Schleusener wird durch mehr als 30 Publikationen dokumentiert, welche seiner Doktorarbeit (1936) folgten. Diese von Professor Ludger Mintrop betreute Arbeit behandelt die gerade in der jüngsten Literatur wieder aufgegriffene Frage der Deformation von Niveauflächen durch Massenbewegungen, die Doktorwürde wurde ihm von der Technischen Hochschule Breslau verliehen. Schleuseners Veröffentlichungen befassen sich naturgemäß vor allem mit Fragen der angewandten Gravimetrie. So untersucht er die Genauigkeit und Einsatzmöglichkeit des Thyssen-Schleusener-Gravimeters, behandelt Eichprobleme und äußere Störeffekte, diskutiert die mit der Schwerereduktion und der Interpretation zusammenhängenden Fragen des Freiluftfaktors, der Dichtebestimmung sowie der Wirkung der Topographie und tiefer liegender Dichteanomalien. Bis heute benutzt werden seine Nomogramme zur Geländereduktion und die von ihm eingeführten unterschiedlichen Reduktionshorizonte.

Die Teilnahme an der von O. Niemczyk geleiteten deutschen Island-Expedition 1938 brachte ihn mit einer seit der Entwicklung der Plattentektonik beson-

ders aktuell gewordenen geowissenschaftlichen Problemstellung in Berührung, nämlich der Frage des Nachweises rezenter Krustenbewegungen im Bereich aktiver Plattengrenzen. Seine Idee, aus den 1938 durchgeführten Gravimetermessungen im Bereich der jungvulkanischen Zone Nordislands detaillierte Hinweise sowohl auf das regionale und lokale als auch – durch Wiederholungsmessungen – auf das langzeitige Verhalten des Schwerefeldes zu erhalten, konnte von ihm 1964/1965 in Verbindung mit den geodätischen Arbeiten von K. Gerke und H. Spickernagel wieder aufgegriffen werden. In diesen und in den 1967 und 1970 in Kooperation mit dem Institut für Theoretische Geodäsie der Technischen Universität Hannover durchgeführten Meßkampagnen wurde die Zahl der Gravimeterpunkte wesentlich erhöht und die Genauigkeit der jetzt dauerhaft vermarkten Punkte eines die Riftzone kreuzenden Profils auf $\pm 10^{-8}$ g gesteigert. 1971 konnte A. Schleusener dann zusammen mit dem Verfasser auf der XV. Generalversammlung der I.U.G.G. in Moskau die ersten Anzeichen für langfristige Schwereänderungen präsentieren.

A. Schleuseners wissenschaftliche Verdienste und seine reichen praktischen Erfahrungen veranlaßten die T.U. Hannover, ihm einen Lehrauftrag für Angewandte Geophysik, speziell Gravimetrie, zu erteilen und ihn zum Honorarprofessor zu ernennen. Von 1954 bis 1968 vermittelte er hier den Studenten der Geodäsie ein solides Grundwissen besonders in der Gravimetrie und konnte eine Anzahl von ihnen – den Autor eingeschlossen – so interessieren, daß sie sich später der Angewandten Geophysik oder der gravimetrischen Geodäsie zuwandten. Der Verfasser dieser Zeilen schätzt sich persönlich glücklich, daß er – bei seiner Diplomarbeit, in der Seismos und ab 1968 am Institut für Theoretische Geodäsie – die Gelegenheit zu einer engen und für ihn stets fruchtbaren Zusammenarbeit mit A. Schleusener hatte. Besonders gern erinnert er sich an die Meßkampagne in Island 1970, bei der A. Schleusener – im Alter von 72 Jahren – den anderen Expeditionsteilnehmern einschließlich der Studenten ein bewundernswertes Beispiel von Begeisterungsfähigkeit und persönlichem Einsatz gab.

Schleuseners Aktivität äußerte sich auch in einem starken Engagement in den Fachvereinigungen. So gehörte er 1951 zu den Gründern der European Association of Exploration Geophysicists. Er war Mitglied der Society of Exploration Geophysicists, der Internationalen Gravimetrischen Expedition und der Deutschen Geophysikalischen Gesellschaft, welche ihn für die Amtsperiode 1964–1966 zu ihrem Vorsitzenden wählte.

Alfred Schleusener, ein gründlicher Wissenschaftler und Praktiker und eine Persönlichkeit von ausgeprägtem Pflichtgefühl, dabei aber stets liebenswürdig und hilfsbereit, hat rund 50 Jahre besonders die Gravimetrie in Theorie und Anwendung gefördert und befruchtet und national wie international Anerkennung im Bereich von Geophysik und Geodäsie gefunden. Er hinterläßt einen Sohn, eine Schwiegertochter und zwei Enkelkinder; seine Ehefrau Lore, welche an seinen Arbeiten stets großen Anteil nahm, ist kurz nach ihm verstorben.

Die gravimetrische Gemeinschaft wird Alfred Schleusener nicht vergessen.